NIST Technical Note
NIST TN 2242

Tornado Wind Speed Maps for Building Design: Research and Development of Tornado Risk Assessment Methodology

Lawrence A. Twisdale, Jr.
Sudhan S. Banik
Lauren A. Mudd
Marshall B. Hardy
Shahriar Quayyum
Fangqian Liu
Melissa K. Faletra
Peter J. Vickery
Marc L. Levitan
Long Phan

This publication is available free of charge from:
https://doi.org/10.6028/NIST.TN.2242

NATIONAL INSTITUTE OF STANDARDS AND TECHNOLOGY
U.S. DEPARTMENT OF COMMERCE

NIST Technical Note
NIST TN 2242

Tornado Wind Speed Maps for Building Design: Research and Development of Tornado Risk Assessment Methodology

Marc L. Levitan
Long Phan
Materials and Structural Systems Division
Engineering Laboratory
National Institute of Standards and Technology

Lawrence A. Twisdale, Jr.
Sudhan S. Banik
Lauren Mudd
Marshall B. Hardy
Shahriar Quayyum
Fangqian Liu
Melissa K. Faletra
Peter J. Vickery
Applied Research Associates, Inc.
8537 Six Forks R., Suite 600
Raleigh, NC 27615

This publication is available free of charge from:
https://doi.org/10.6028/NIST.TN.2242

October 2023

U.S. Department of Commerce
Gina M. Raimondo, Secretary

National Institute of Standards and Technology
Laurie E. Locascio, NIST Director and Under Secretary of Commerce for Standards and Technology

NIST TN 2242
October 2023

Disclaimer No. 1

Certain commercial entities, equipment, or materials may be identified in this document in order to describe an experimental procedure or concept adequately. Such identification is not intended to imply recommendation or endorsement by the National Institute of Standards and Technology, nor is it intended to imply that the entities, materials, or equipment are necessarily the best available for the purpose.

Disclaimer No. 2

NIST takes no position as to whether the design or construction of any building discussed in this report was compliant with any code.

Disclaimer No. 3

The policy of NIST is to use the International System of Units in all publications. In this document, however, units are presented in the system prevalent in the relevant discipline, although in some cases more than one system of units may be presented.

Publication History
Approved by the NIST Editorial Review Board on 2022-11-14

How to Cite this NIST Technical Series Publication
Twisdale LA Jr., Banik SS, Mudd L, Hardy MB, Quayyum S, Liu F, Faletra MK, Vickery PJ, Levitan ML, Phan L (2023) Tornado Wind Speed Maps for Building Design: Research and Development of Tornado Risk Assessment Methodology. (National Institute of Standards and Technology, Gaithersburg, MD), NIST Technical Note (TN) NIST TN 2242. https://doi.org/10.6028/NIST.TN.2242

NIST Author ORCID iDs
Marc L. Levitan: 0000-0002-8053-2546
Long Phan: 0009-0009-4322-6193

Contact Information
marc.levitan@nist.gov
long.phan@nist.gov

Abstract

The first-ever engineering-derived tornado wind speed maps have been produced for the contiguous United States. Using multi-variate statistical analysis of 11 tornado and physiographic variables, we developed 9 broad tornado climatology regions. We analyzed regional and national data to produce probabilistic models that account for: population bias; EF-Scale distribution; tornado path length, width, direction, and translational speed; radius of maximum winds; tornado path length intensity variation; variable path widths within a tornado; mean to maximum path width ratios; and maximum damage widths relative to local path width. We used a probabilistic load and resistance modeling framework to develop engineering-derived wind speeds from the EF-Scale system by analyzing the most common Damage Indicator (FR12, one- and two-family residences) used to rate EF3-5 tornadoes. The developed wind speed distributions, based on 44 3-D models of FR12 structures, are broad and encompass the original judgment-based EF-Scale wind speeds. We used these data to support a probabilistic tornado wind field model, simulate tornado wind speed swaths, and develop regional tornado hazard curves. The tornado hazard curves depend on the building or "target" size. Fifty-one tornado wind speed maps were developed for target sizes ranging from geometric points to 4 million square foot (371612.2 square meter) targets and for 8 return periods that ranged from 300 to 10 million years. Numerous judgments and assumptions were required in the model development. Many of the probabilistic models consider both epistemic and aleatory uncertainties. The derived mean wind speeds are "best-estimates" and are intended for use in engineering design and safety analysis.

Keywords

Aleatory uncertainty; Enhanced Fujita (EF) Scale; epistemic uncertainty; population bias; radius of maximum winds (RMW); reference tornado wind speed (RWS); target size; tornado; tornado climatology; tornado damage; tornado hazard curve; tornado risk; tornado path length intensity variation (PLIV); tornado wind field model; tornado wind speed map; wind speed exceedance frequency (WEF).

Preface

On May 22, 2011, Joplin Missouri was struck by the deadliest and costliest single tornado since 1950, when the U.S. began keeping official records.[1] The mile-wide (1.6 kilometer-wide) tornado caused 161 fatalities, over a thousand injuries, and damaged or destroyed approximately 8,000 buildings at a cost of $2.8B (in 2011 dollars)[2]. Shortly following the tornado, the National Institute of Standards and Technology (NIST) launched a National Construction Safety Team (NCST) technical investigation, with a scope that included analyses of the wind environment and technical conditions that may have contributed to the fatalities and injuries, the performance of emergency communications systems, the public's response to emergency communications, and the performance of buildings and lifelines that affected buildings functionality. The findings and recommendations of this investigation provide a technical basis for improved codes, standards, and practices related to tornado hazard characterization, tornado–resilient design and construction, emergency communications systems, and emergency response.[3]

This report documents the development of a new generation of probabilistic tornado hazard maps for the contiguous US as a result of the implementation of Recommendation 3 from the NIST final report of Joplin tornado technical investigation, which states "*NIST recommends that tornado hazard maps for use in the engineering design of buildings and infrastructure be developed considering spatially based estimates of the tornado hazard instead of point–based estimates.*"[4] These maps represent a critical component needed for the implementation of Recommendations 5 and 6, development of performance-based standards and design methodologies, which together enable tornado-resistant design and construction of buildings and infrastructure in the US.

Following publication of the final Joplin report in March 2014, NIST stood up a new project focused on implementation of the 16 recommendations in the report. NIST contracted with Applied Research Associates, Inc (ARA) in September 2014 to lead development of the tornado hazard maps, with Dr. Lawrence Twisdale as the Principal Investigator. Dr. Twisdale and his team at ARA have a long history of engineering practice, research and development (R&D), and publications in areas of tornado and hurricane science, engineering, and probabilistic risk assessments. The project benefitted from this experience by scaffolding some of the needed tornado R&D onto existing ARA proprietary tools and software such as TORDAM (TORnado DAMage model), TORMIS (TORnado MISsile model) and TORRISK (tornado hazard curves). NIST staff worked closely with the ARA team over the next six years to formulate scope and develop the framework for probabilistic tornado hazard concept, contribute to the R&D effort, and continually provide technical guidance, review, and oversight for completion of the project.

NIST engaged the tornado hazard map stakeholder community early in the map development process. A NIST stakeholder workshop was held at the headquarters of the American Society of Civil Engineers (ASCE) in Reston Virginia on September 2, 2015, with close to 100 participants. The goals for that meeting were to: (1) inform key stakeholders about NIST

[1] "Final Report - National Institute of Standards and Technology (NIST) Technical Investigation of the May 22, 2011, Tornado in Joplin Missouri," NCSTAR 3, March 2014. Available at https://doi.org/10.6028/NIST.NCSTAR.3.
[2] "The 10 Costliest U.S. Tornadoes since 1950", National Oceanic and Atmospheric Administration/Storm Prediction Center. Available at https://www.spc.noaa.gov/faq/tornado/damage$.htm.
[3] Ibid., 1.
[4] Ibid.

plans and methodology for development of new tornado hazard maps; (2) review results from the first year of development work; and (3) obtain feedback on the proposed maps development methodology and prioritization of relevant R&D topics. A second workshop was conducted the next day on the NIST campus in Gaithersburg, Maryland, to brief federal agencies on this project and gather information about their needs in tornado mapping and tornado hazard reduction. Approximately 40 representatives from 14 federal agencies participated in this meeting. Feedback from both stakeholder groups was incorporated into the project plans.

In addition to the workshops, NIST used other venues to keep the broader stakeholder community and the public informed on the tornado map development progress. Briefings were provided at least annually to the NCST Advisory Committee (NCSTAC) in public meetings.[5] Within the Federal government, presentations were made to the National Windstorm Impact Reduction Program's Windstorm Working Group and the Office of Science and Technology Policy's Subcommittee for Disaster Reduction. The work in progress was also presented at a number of conferences and symposia, as well as seminars and webinars for universities, professional societies, and manufacturers associations.

NIST also engaged early and regularly with the United States Nuclear Regulatory Commission (NRC) as a key stakeholder, providing progress briefings and obtaining feedback. In 2017, the NRC provided funding to NIST (through an Interagency Agreement) to supplement the tornado map development. The primary scope of this additional work was to incorporate the effects of epistemic uncertainty (modeling) into the maps development process, in addition to consideration of the aleatory uncertainty (randomness). The final maps will therefore be applicable to the nuclear power industry in the US, where both aleatory and epistemic uncertainties are required in the risk analysis of nuclear power plants.

With the ultimate goal of having the tornado hazard maps incorporated into building standards and codes, NIST engaged with the ASCE Ad Hoc Committee on Performance-based Design for Wind Hazards from the beginning of the project. That committee initiated development of the overall framework for performance-based design for all windstorms, including tornadoes. The work of ASCE Ad Hoc Committee was transitioned to the ASCE 7-22 Wind Load Subcommittee (WLSC), which began meeting in January 2018. Several of the project team are members of the WLSC, including Dr. Levitan, who serves on the WLSC Steering Committee and chairs the Tornado Task Committee (TTC). The project team worked closely with the TTC and WLSC, drafting the standards provisions and commentary needed to bring the tornado hazard maps into a new chapter on tornado loads for the ASCE 7-22 Standard, *Minimum Design Loads and Associated Criteria for Buildings and Other Structures*. NIST and ARA also developed most of the other components of the tornado load methodology included in the new tornado loads chapter. The ARA component of the tornado load methodology R&D was led by Dr. Peter Vickery, under a separate contract with NIST.

A third workshop was held to inform stakeholders about draft project results and again obtain feedback. This workshop, jointly sponsored by NIST and the Structural Engineering Institute of ASCE, was conducted on May 14, 2019 at ASCE headquarters, with well over a hundred participants. Following detailed presentations on the tornado data, analysis, and map

[5] These presentations are available through the NIST Disaster and Failure Studies web site at https://www.nist.gov/topics/disaster-failure-studies/about-disaster-and-failure-studies-program, filed under the National Construction Safety Team menu, Advisory Committee Meetings submenu.

development methodology, the project team rolled out the draft tornado hazard maps and provided options for incorporation into the ASCE 7-22 standard. The project team similarly engaged the TTC and the WLSC during their meetings over the subsequent 3 days. Based on feedback obtained from the workshop and standards committee meetings, several technical updates were made to the map development methodology and the draft tornado hazard maps, which were provided back to the TTC and WLSC in October 2019.

NIST continued work on the near-final maps through December of 2020. This effort primarily consisted of several rounds of updates to the map cartography. These updates were in response to a series of ballot comments as the maps were incorporated into the draft of a new Tornado Loads chapter and then worked their way through the TTC, WLSC, and finally the ASCE 7-22 Main Committee. As of the completion of this report, the proposed new Chapter 32 on Tornado Loads of ASCE 7-22, including the set of tornado hazard maps provided in Appendix G of this report, was still working its way through the ASCE 7-22 committee approval process.

The tornado research and development documented in this report breaks new ground in a number of areas. For example, novel approaches to quantify the well-known problems of population bias (where more tornadoes are reported in areas having greater population) and to capture regional variation in tornado climate are presented in Sections 2 and 3. New tornado wind speeds associated with the Enhanced Fujita (EF) Scale intensity ratings have been derived through engineering analysis as described in Sections 5 and 6, instead of relying on the original EF Scale wind speeds based on expert elicitation. These wind speeds, denoted EF* herein, are defined as the maximum horizontal wind speed (assumed to be a nominal 3 second gust) at 33 ft (10 m) experienced over the plan area of the structure (target) as the tornado translates past the target. The tornado hazard maps take spatial effects of building size into account, where tornado wind speeds vary with the plan area (target) size of the building, as described in Section 7. The end result is production of state-of-the-art, probabilistic tornado hazard maps, prescribing tornado design wind speeds that cover a wide range of target sizes and return periods, that will enable tornado-resistant design of conventional buildings and infrastructure, essential facilities, and nuclear power plants.

The tornado map R&D also produced spin-off products and applications. The cleansed and augmented database of US tornadoes from 1950 through 2016, developed to support the tornado climatology analysis as described in Section 2 and Appendix A, is available for download at (DOI link pending). Several project team members are also active in the joint ASCE/American Meteorological Society (AMS) committee developing a new Standard on Wind Speed Estimation in Tornadoes and Other Windstorms. The engineering analysis of tornado wind speeds based on observed damage for the maps project is being adapted to propose a new, engineering-based wind speed estimation for inclusion of Wood Frame Residences (WFR) in an update to the Enhanced Fujita (EF) method. Additional components of the tornado map research also have broader applications to: improving tornado risk assessments of point and spatially-distributed targets; tornado damaging modeling of additional EF Scale Damage Indicators (DIs); and tornado loss estimation for catastrophic risk models; cost-benefit analysis for building code enhancements for wind/tornado design; and risk safety analysis applications to critical facilities, such as nuclear power plants, and ASCE Category IV facilities.

Acknowledgments

The authors gratefully acknowledge the support of the United States Nuclear Regulatory Commission (NRC) for the epistemic modeling task funding provided to NIST, as well as for the insightful technical comments of NRC's Dr. Elena Yegorova, Dr. Joseph Kanney, and others during this multi-year effort.

The authors appreciate the significant funding provided by ARA for multiple Internal Research and Development Projects in support of: field data planning and support; development and enhancement of multiple tornado and structural modeling computer codes; and building stock research. We acknowledge the tireless and professional effort of Ms. Lisa West of ARA in progress and final report document production.

The authors acknowledge the significant support and help from Mr. James LaDue of the NWS Warning Decision Training Division in Norman, OK. Jim answered numerous questions, provided contacts, and coordinated support for multiple damage surveys. The authors are also grateful to Ms. Pataya Scott, a guest researcher at NIST, for providing data and analysis from NIST's Residential Tornado Damage Database used to support the FR12 analysis in Sections 5 and 6.

The authors thank Ms. Cynthia Rivas of NIST for Geographic Information System (GIS) support and final cartography of the tornado wind speed maps, Mr. Nicholas de Toledo for assistance with editing, Ms Kathryn Miller for help with formatting the document, and Ms. Christina Kellerman for the cover design.

The American Society of Civil Engineers (ASCE) hosted two Tornado Map Stakeholder Workshops in support of the map development process and their contributions, along with those of Ms. Jennifer Goupil from ASCE, Mr. Donald Scott, chair of the ASCE 7 Wind Load Subcommittee, and the 100+ participants of these workshops, are gratefully acknowledged. The many members of the ASCE 7 Wind Load Subcommittee and Tornado Task Committee are gratefully acknowledged for their review and input on the draft tornado maps.

Table of Contents

List of Tables

List of Figures

List of Acronyms

ABL	Atmospheric Boundary Layer
AGL	Above Ground Level
AMS	American Meteorological Society
ANOVA	Analysis of Variance
ANS	American Nuclear Society
APA	American Plywood Association
APC	Atmospheric Pressure Change
AR	Aspect Ratio
ARA	Applied Research Associates
ASCE	American Society of Civil Engineers
ASME	American Society of Mechanical Engineers
B	Number of Building Damage Indicators
BBP	Bi-Linear Break Point
BD	Building Density
BLDG	Building
BSW	Building Stock Weighted
CAPE	Convective Available Potential Energy
CCW	Counterclockwise
CDF	Cumulative Distribution Function
CI	Confidence Interval
CMF	Cumulative Mass Function
COV	Coefficient of Variation
CRF	Cumulative Relative Frequency
CST	Central Standard Time
CT	Census Tract
C&C	Components and Cladding
DAT	Damage Assessment Toolkit
DI	Damage Indicator
DIR	Mean Tornado Path Direction
DPM	Damage Probability Matrix
DOD	Degree of Damage

DOE	Department of Energy
DOW	Doppler on Wheels
E	Uncertainty in Reporting Bias
EF	Enhanced Fujita
EF*	Refers to report development of engineering-based logic and wind speeds following NOAA's implementation (2007-2016) of the EF-Scale methodology
EML	Exponential Maximum Likelihood clustering procedure
EN	End-nail
EV1	Extreme Value Type I Distribution
EXP	Expected
F	Fujita
FE	Finite Element
FEA	Finite Element Analysis
FEM	Finite Element Model
FR12	One- or Two-Family Residence damage indicator for EF ScaleFSP Free Standing Pole Damage Indicator
GIS	Geographic Information System
GR	Geo-Referenced
H	Hit tornado counting method used in population bias analysis
HBD	High Building Density
HST	Hurricane Spawned Tornado
HRD	National Oceanic and Atmospheric Administration's Hurricane Research Division
HURDAM	ARA HURricane DAMage Model
HURDAT2	Hurricane Research Division Hurricane Database
HURMIS	ARA HURricane MISsile Model
HW	High-Wind
IBC	International Building Code
IP	In-Plane
IRC	International Residential Code
ITC	Inside the Tornado Core
KS	Kolmogorov-Smirnov test of equivalence of distributions
L	Length Fraction of Tornado

LB	Lower Bound
LBD	Low Building Density
LF	Length Fraction tornado counting method used in population bias analysis
LHS	Left Hand Side
LL	Latutude Longitude
LN	Lognormal Transformation of Metric
LPW	Local Path Width
LSD	Least Significant Difference
MDW	Maximum Damage Width
MMSA	United States Census Metro and Micro Statistical Area
MRI	Mean Recurrence Interval
MSB	Metal Building System Damage Indicator
MSE	Mean Square Error
MWFRS	Main Wind Force Resisting System
N	Normal Transformation of Metric
NAHB	National Association of Home Builders
NCDC	National Climatic Data Center
NCEI	National Centers for Environmental Information
NCMA	National Concrete Masonry Association
NCST	National Construction Safety Team
NCSTAC	National Construction Safety Team Advisory Committee
NCSTAR	National Construction Safety Team Act Report
NGR	Non-Geo-Referenced
NIST	National Institute of Standards and Technology
NLIN	procedure for Gauss Newton Method mentioned on page 101 of commentary
NOAA	National Oceanic and Atmospheric Administration
NRC	US Nuclear Regulatory Commission
NSSC	National Severe Storms Forecast Center
NUREG	U.S. Nuclear Regulatory Commission Technical Report Designation
NWS	National Weather Service
MHDW	Double Wide Manufactured Home Damage Indicator
MHSW	Single Wide Manufactured Home Damage Indicator
OP	Out-of-Plane

OR	Occurrence Rate
OR-All	Occurrence Rate – All Tornadoes
OR-M	Occurrence Rate – Moderate Intensity Tornadoes (F/EF2-F/EF3)
OR-S	Occurrence Rate – Strong Intensity Tornadoes (F/EF4-F/EF5)
OSB	Oriented Strand Board
OTC	Outside of the Tornado Core
PAEK	Polynomial Approximation with Exponential Kernel
PBD	Performance-Based Design
PD	Principal Diagonal
PDF	Probability Density Function
PL	Path Length
PLIV	Path Length Intensity Variation
PMF	Probability Mass Function
PP	Point Probability tornado counting method used in population bias analysis, or Point Strike Probability used in cluster analysis
PSW	Perforated Shear Wall
PW	Path Width
PWV	Path Width Variation
R	Region (in Section 3.3.3) or Reporting Accuracy (in Appendix C)
RHS	Right Hand Side
RMS	Root Mean Square
RMW	Radius to Maximum Winds
RP	Return Period
RWS	Reference Wind Speed
R&D	Research and Development
S	Statistical Accuracy (in Appendix C)
SDP	National Climatic Data Center Storm Data Publication
SF	Square Feet
SFR	Single-Family Residential Construction
SIC	Standard Industrial Codes
SLS	2016 American Meteorological Society Severe Local Storms Conference
SPC	Storm Prediction Center
SQFT	Square Feet (in Figures 8-5 and 8-7)

SR	Search Radius
SSW	Segmented Shear Wall
STD	Standard Deviation
TDPY	Number of Tornado Days per Year
TH	Hardwood Tree Damage Indicator
TN	Toe-Nail
TORDAM	ARA TORnado DAMage Model
TORMIS	ARA TORnado MISsile Model
TORRISK	ARA TORnado RISK Model
TORRISK2	Updated Version of TORRISK Model
TS	Softwood Tree Damage Indicator
TTC	Tornado Task Committee
TTU	Texas Tech University
U	Unadjusted Metric
UB	Upper Bound
UI-UO	Uniform In-Uniform Out test
W	Width Fraction of Tornado
WBD	Wind–Borne Debris
WEF	Wind Speed Exceedance Frequency
WFO	Weather Forecast Office
WINDMIS	ARA tornado generalized version of HURMIS
WLSC	Wind Load Subcommittee
WPM	Warning Preparedness Meteorologist
WSF	Wind Speed Frequency
WSR	Weather Surveillance Radar

1. Introduction

1.1. Objective

The objective of this report is to document the development of tornado risk maps for building design in the United States.

The work documented herein follows from the National Institute of Standards and Technology (NIST) National Construction Safety Team (NCST) Act Technical Investigation of the May 22, 2011 Joplin, MO, tornado. The final report[11] of that investigation was completed in March 2014, and detailed 16 recommendations in three broad areas; for improving tornado hazard characterization, for improving how buildings and shelters are designed; constructed, and maintained in tornado–prone regions; and for improving the emergency communications that warn of imminent threats from tornadoes. Key among the recommendations on building performance are those calling for the development and adoption of (1) nationally accepted Performance-Based Design (PBD) standards for the tornado-resistant design of buildings and infrastructure, including requirements for essential facilities such as hospitals and emergency operations centers to remain operational in the event of a tornado; and (2) design methods that will ensure all building components and systems meet the proposed performance objectives.[12]

To enable the development of PBD standards for tornado-resistant design, NIST initiated a multiyear project to develop a set of tornado hazard maps using up-to-date tornado databases and science-based tornado risk assessment methodology in order to accurately characterize tornado risk in the U.S. for building design purposes. This need is reflected in recommendation 3 of the NIST's Joplin tornado investigation final report, which states: "*NIST recommends that tornado hazard maps for use in the engineering design of buildings and infrastructure be developed considering spatially based estimates of the tornado hazard instead of point–based estimates.*"

1.2. Scope

The scope of this work has focused on the development of tornado wind speed risk maps for the contiguous US. The tornado risk map return periods follow ASCE 7 Risk Category return periods (300, 700, 1700, and 3,000 years) and then proceed to 10,000, 100,000, 1,000,000, and 10,000,000 years. These 8 return periods span the range needed for design of conventional facilities, essential facilities, and nuclear power plants.

Tornadoes often have modest path widths relative to the size of the structure. As a result, tornado wind speed risk depends on structure size. We evaluated 8 structure sizes from points to 4 million square feet (SF) (371612.2 m^2).

The maps are developed through probabilistic models that are "best estimates" rather than "conservatively based". This approach follows the intent of ASCE 7 wind speed maps for

---

[11] "Final Report - National Institute of Standards and Technology (NIST) Technical Investigation of the May 22, 2011, Tornado in Joplin Missouri," NCSTAR 3. Available at https://doi.org/10.6028/NIST.NCSTAR.3.

[12] The descriptions here are brief summaries of Recommendations 5 and 6. For the complete text of these and other recommendations, see the final report at the link provided in footnote 1.

other wind hazards, such as hurricanes (Vickery et al., 2009) and straight winds (Pintar et al., 2015).

Epistemic (modeling) uncertainties were also considered in the map development process. As a result, the maps are intended to provide results applicable to the nuclear power industry in the US, where both aleatory (randomness) and epistemic uncertainties are required in the risk analysis of nuclear power plants (ASME/ANS, 2009).

The development of probability distributions that relate tornado wind speed to observed damage was an important element of the work. Engineering models were developed to enable wind speed estimation for the Enhanced Fujita (EF) Scale Degrees of Damage (DOD) for one- and two-family residences (FR12) (TTU, 2006). This work used load path quality considerations that the National Oceanic and Atmospheric Administration (NOAA) (LaDue and Mahoney (2006), NOAA (2008), and NOAA (2016b)) employs in its damage assessment process to estimate wind speeds and assign EF ratings to tornadoes.

The work included field investigations of tornadoes for multiple purposes: gaining a better understanding of the field process used by the NOAA; investigating failure modes of Damage Indicators (DI): and, obtaining data for validation of the models used to estimate tornado wind speed from observed damage.

1.3. Methodology Overview

Figure 1-1 provides a schematic overview of the methodology components. The 6 main areas of analysis illustrated in Figure 1-1 are:

1. Tornado Data
2. Tornado Wind Field
3. Wind Speeds
4. Epistemic Uncertainties
5. Hazard/Risk Models
6. Tornado Wind Speed Maps

Sections 1.3.1 through 1.3.6 discuss these areas. Section 1.3.7 discusses the engineering load modeling process used to develop wind speeds applicable to engineering design and safety analysis.

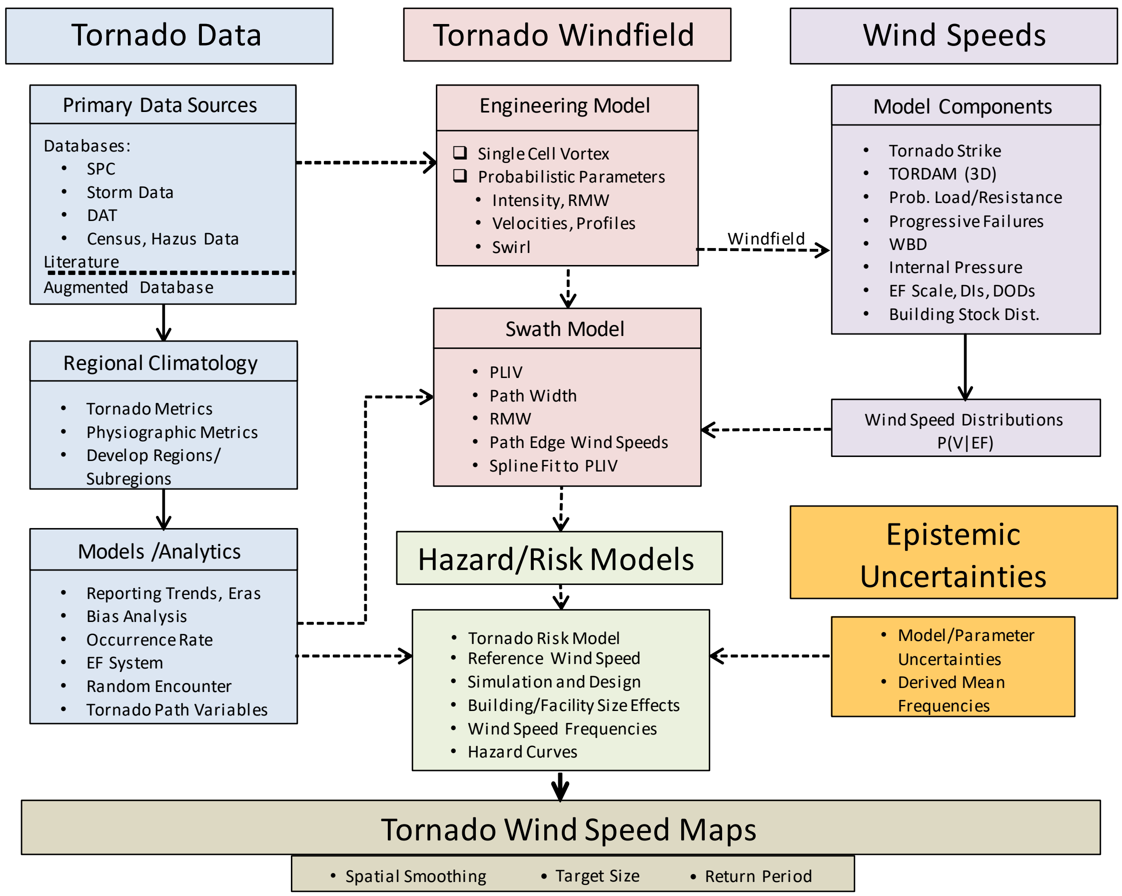

Figure 1-1. Tornado Risk Mapping Project Components

1.3.1. Tornado Data

The tornado data in Sections 2 and 3 includes analysis of the NOAA/National Weather Service (NWS) Storm Prediction Center (SPC) tornado database, to develop climatology metrics, analyze reporting trends, develop occurrence rates, and model EF-Scale distributions. As part of this process, we also investigated the Damage Assessment Toolkit (DAT) database (NOAA, 2016b), which was implemented in 2007. The DAT provides useful insights and data relationships on EF-Scale DIs and wind speed estimations for individual tornadoes. These analyses helped guide the development of the final methodology and data eras used in various components of research. For example, we used “modern era” data (1995 – 2016) for tornado occurrence rate analysis. However, we focused our analysis on tornado wind speed estimation from rated tornado intensities using data from the EF-Scale era, 2007-2016.

An augmented database was developed that includes some minor corrections to the SPC data and adds additional fields of data: (1) tornado path direction; (2) the National Centers for Environmental Information (NCEI) Weather Forecast Office (WFO) that produced the report; (3) the NCEI source of the tornado rating; and (4) the NCEI tornado ending date and time (NCEI, 2014). The agumentation included data cleansing and supplementation from the literature, merging of data from NCEI, and creating of additional fields with derived data, such as tornado path direction and average translation speed.

Regional climatology analysis is presented in Section 2. This work was performed using an empirical analysis of the augmented SPC database for the Years 1950-2016. We developed tornado metrics, such as tornado days per year, occurrence rates, point probability, and physiographic parameters. This analysis produced 6 broad tornado regions, considering a multivariate statistical analysis of the tornado risk metrics. We also performed within-region analysis to determine if tornado occurrence rates and intensities vary significantly over large sub-regions within the regions. Several sub-regions were identified resulting in the splitting of 3 of the 6 regions, producing a total of 9 final tornado regions. We did not attempt to produce maps that reflect smaller sub-region scales of tornado wind speed risk.

1.3.2. Tornado Wind Field

In this project, we started with a tornado wind field model developed for probabilistic tornado hazard analysis and wind-borne debris modeling (Twisdale et al., 1978, 1981; Dunn and Twisdale 1979). This model was augmented for use in wind field simulations for load modeling and hazard curve development. The main areas of augmentation included: models for path length intensity variation; radius to maximum winds; swirl model for radial inflow parameter; translational speed; path length and width statistics; path edge wind speeds; variable path width; and wind speed swath modeling. The model is based on a single cell vortex with probabilistic parameters that allow for simulations of different tornado sizes and parameters within each EF-Scale intensity. Different velocity profiles can be simulated based on the model inputs. Sections 3 and 4 describe this work.

1.3.3. Wind Speeds

Since tornado wind speeds are estimated based on observed damage in the field, a major component of the research focused on the development of engineering-based wind speed estimates from the EF-Scale rating data (EF0 through EF5). A method was developed to treat uncertainties in both the tornado wind field and the resulting damage to estimate the wind speeds probabilistically for each Degree of Damage (DOD). Then, by using conditional probability inference methods, a wind speed distribution is estimated from the observed DOD. This method is applied to a number of important DIs in order to develop probabilistic wind speed distributions for use in map development. An advantage of the probabilistic approach is that the wind speeds are based on engineering load/resistance and damage modeling. In this fashion, the resulting wind speeds in the maps can be interpreted and used for the engineering design of structures for tornado loads for specified return periods.

1.3.4. Epistemic Uncertainties

The treatment of epistemic uncertainties in the tornado wind speed map development follow from requirements in the US nuclear power industry. This work was added to the project in 2017.[13]

---

[13] Consideration of epistemic uncertainties in the map development process was funded by the Unitd States Nuclear Regulatory Commission through an Interagency Agreement with NIST.

Table 1-1 summarizes the areas that include epistemic modeling and references the section where they are discussed

The American Society of Mechanical Engineers (ASME)/American Nuclear Society (ANS) (ASME/ANS, 2009) Standard for Probabilistic Risk Assessment for Nuclear Power Plant Applications defines epistemic uncertainty as “the uncertainty attributable to incomplete knowledge about a phenomenon that affect our ability to model it. Epistemic uncertainty is reflected in ranges of values for parameters, a range of viable models, the level of model detail, multiple expert interpretations, and statistical confidence. In principle, epistemic uncertainty can be reduced with increased data and knowledge. (Epistemic uncertainty is often referred to as ‘modeling uncertainty’).”

The complement to epistemic uncertainty is aleatory uncertainty, which is defined in the ASME/ANS Standard as “the uncertainty inherent in a nondeterministic (stochastic, random) phenomenon. Aleatory uncertainty is reflected by modeling the phenomenon in terms of a probabilistic model. In principle, aleatory uncertainty cannot be reduced by the accumulation of more data or additional information. (Aleatory uncertainty is sometimes called ‘randomness.’)” A complete probabilistic model includes the major components of aleatory uncertainties through the use of random variables to describe inherently random processes. Such models often use simulation techniques to propagate randomness through various models and sub-models.

There are many epistemic uncertainties in the modeling and analysis of tornado risk. The modeling and analysis of epistemic uncertainties in this effort have focused on a practical set of uncertainties that are important drivers of tornado risk. The quantification of epistemic uncertainties is based on model sensitivity analysis, statistical and probabilistic model analysis, and engineering judgment.

We used a simulations process to propagate epistemic uncertainties. This process uses epistemic sampling for some variables and the use of derived mean” inputs for other variables.

Table 1-1 summarizes, by modeling component, what approach was used to propogate uncertainties.

Table 1-1. Epistemic Uncertainty Analysis Topics

Group	Epistemic Topic	Model/Parameter Uncertainty	Modeling Approach	Implementation	Epistemic Implementation Outside of TORRISK2	Epistemic Implementation in Hazard Curve Simulations	Report Section Location
1	**Tornado Regionalization**	**Region-Subregion Boundaries**	Uncertainties in location of regional boundaries modeled using Gaussian smoothing.	Implemented in the map production given the mean WEF's by region/subregion	Maps	NA	Section 2.1, Section 2.6, Section 8.3
2	**Tornado Occurrence Rates**	**Region/Subregion Occurrence Rates**	BD thresholds and uncertainty progagation to produce derived mean	Derived means are an input to TORRISK2.	Sampling	Derived Mean Occurrence Rates	Section 3.2.2.1, Section 3.2.4 (3.2.4.1, 3.2.4.2, 3.2.4.3, 3.2.4.4), Appendix C.5
3	**Tornado Intensity and Path Variables**	**a. EF-Scale**	BD thresholds and uncertainty progagation to produce derived mean		Sampling	Derived Mean EF Distribution	Section 3.3 (3.3.1, 3.3.2, 3.3.3), Appendix C.5
		b. Path Length	Uncertainties in distributions: use both Weibull and Lognormal models.	Sampling performed within TORRISK2.	NA	Sampling	Section 3.4 (3.4.1.3)
		c. Path Width	Max EF width to mean path width			Sampling	Section 3.5.3
		d. Rating Source for EF0 Tornadoes	Uncertainties in default tornado fractions for EF0's.			Sampling	Section 3.4.1.1
4	**Tornado Windfield and Swath Model**	**a. Windfield**	Uncertainties in swirl model.			Sampling	Section 4.3.3
		b. Swath	Uncertainties in mean PLIV fractions.			Sampling	Section 3.5.2
5	**Damage Modeling/EF Wind Speed Analysis**	**a. Engineering Interpretation in EF DODs Descriptions**	Uncertainties in EF Interpretation Parameters	Incoporated into TORDAM Sampling and Included in Resulting Derived Mean DOD Distribution	Sampling	6 Derived Mean EF Wind Speed Distributions	Section 6.2.1
		b. Structural Quality Factor	Judgment to reflect as-built structural resistances vs. lab-based resistances		Sampling	6 Derived Mean EF Wind Speed Distributions	Section 5.5.6
		c. DOD to EF Distribution	Uncertainties in EF DOD Mapping to EF Categories per Construction Quality Guidance		Sampling	6 Derived Mean EF Wind Speed Distributions	Section 6.6.2, 6.6.3
		d. House DOD 9-10 Model	Uncertainties in Wind Speeds Required to Blow Failed Components Off the "Slab"		Sampling	6 Derived Mean EF Wind Speed Distributions	Section 6.2.1.2
		e. Bayesian Prior Wind Speed Distribtuion	Estimated Bounds	Estimated Mean	Mean	6 Derived Mean EF Wind Speed Distributions	Section 6.4.4.2, 6.6.3

1.3.5. Hazard/Risk Models

We use Monte Carlo methods to simulate tornadoes, produce damage swaths, and score wind speed exceedances numerically over a wide range of wind speeds. This method follows from Twisdale and Dunn (1983a) with enhancements for: variable path width and radius of maximum winds (RMW); variable tornado path edge wind speeds; and importance sampling on target position. Hazard curves are developed for 8 return periods and 8 target sizes for each of 9 tornado regions. Section 7 documents the tornado hazard modeling methodology and presents the regional hazard curves.

1.3.6. Tornado Wind Speed Maps

The final component is the development of the tornado wind speed maps, which reflect the spatial variation in risk across the contiguous US and within the context of the broadly developed regions and sub-regions. We used a 1° grid to map the region and sub-region wind speeds for a given return period. We apply Gaussian smoothing to the grid to reflect epistemic uncertainties in the location of the region boundaries. An ArcGIS contouring algorithm is used to produce the wind speed contours from the smoothed grid. Example maps are provided in Section 8 and the full set of fifty-one maps (with non-zero tornado wind speeds) are provided in Appendix G.

1.3.7. Engineering Load Modeling Framework

Wind speed is a fundamental wind hazard parameter in wind engineering analysis and design. In conventional structural design in the US, the structure's Risk Category defined in the ASCE 7 standard (ASCE, 2016) determines the appropriate wind speed risk map. The wind speed risk map provides the spatially-dependent wind speed contours for a given mean recurrence interval (MRI) or return period (RP). Design loads typically vary with the square of wind speed. Therefore, errors in the wind speed associated with a return period can therefore have a significant impact on the reliability of designed structures. Consequently, the quantification of wind speeds for use with EF-Scale tornado frequencies is perhaps the most important step in the development of tornado wind speed risk maps for engineering applications.

Figure 1-2 illustrates our approach to developing EF-Scale wind speeds. A key element in this figure is that the methodology used to quantify wind speeds from damage (a reverse process) should be "consistent" with the methods used in structural analysis/design for a specified wind speed (a forward process). The left-to-right flow in the top portion of Figure 1-2 illustrates our modeling process from tornado occurrence with (unknown) wind speed (v) to loads to conditional damage probabilities $(d \mid v)$[14]. The process for estimating engineering-based wind speeds includes accounting for both the uncertainties in the estimated wind speeds and the sensitivities of the associated wind speeds with respect to uncertainties in structural resistances. In Box 4, we must reverse the process to produce the wind speed distribution given damage $(v \mid d)$[15]. The resulting wind speed probability mass functions

[14] The conditional event ($d|v$) denotes that d is conditional or dependent on v (e.g., Drake, 1967).
[15] The engineering analysis process for structural systems is a forward process that starts with loads, which are derived from wind speed, and determines the response of a structure. Hence, to ensure that we properly develop tornado wind speeds from tornado damage

(PMFs) provide the link between the Fujita/Enhanced Fujita (F/EF) intensity distributions and the development of a tornado wind speed climatology. This methodology is described in Section 6, using the damage modeling methodology developed in Section 5.

A key approach in our methodology is that by using the same probabilistic tornado wind field model in the hazard simulations (Boxes 1 and 5) and consistent load modeling effects (Box 2 vs. Box 8) for map development (Box 6), we have a reasonable framework for risk-based design standards (Boxes 7-9). In this manner, we are able to use a damage-based tornado intensity climatology, as embedded in the SPC database, to develop a tornado wind speed frequency climatology suitable for engineering applications.

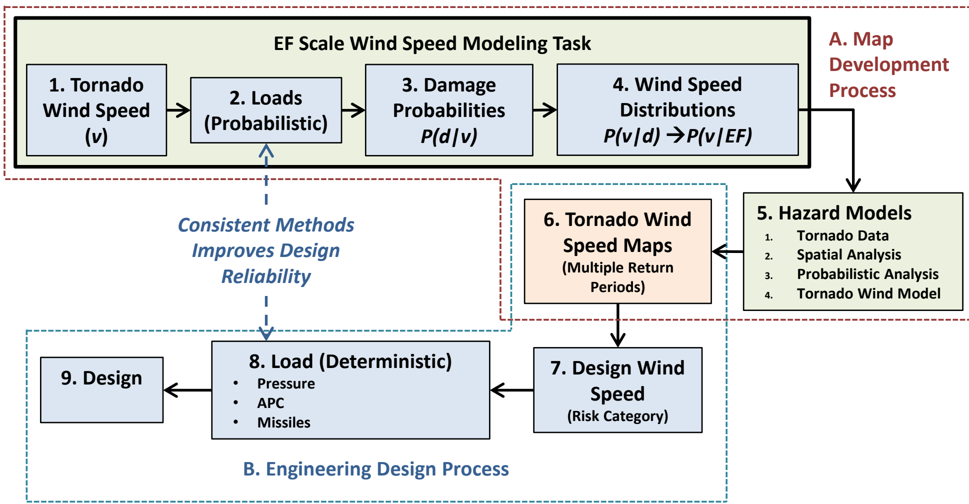

Figure 1-2. Framework for Estimating Tornado Wind Speeds for Engineering Design

observations, we must start with engineering-based damage given wind speed calculations ($d|v$) in order to obtain wind speed distributions given damage ($v|d$), which can be used in tornado wind speed quantification and risk map development.

2. Tornado Climatology Analysis

2.1. Overview

We analyze tornado databases and physiographic data to identify large-scale spatial patterns with similar tornado characteristics. From these patterns, we develop broad US regions with distinct tornado climatologies. Figure 2-1 illustrates the flow of the analysis process. The boxes colored green are described in this section. As noted, the blue-colored boxes are discussed in other sections.

We use the SPC tornado database and complement it with additional information from the National Center for Environmental Information (NCEI) Storm Events Database for the years 1950-2016. We found it useful to augment the SPC data fields with additional information from NCEI. The resulting "Augmented Database" is described in Appendix A.

With the Augmented Database, we perform trend analysis (Section 2.2) and analyze tornado climatology metrics and certain physiographic metrics (Section 2.3). This process is performed without attempting to correct for reporting biases based on population density or other factors (such biases are addressed in Section 3). We develop latitude-longitude grids to facilitate the spatial analysis of the data and to assess sensitivity of the results to a particular grid. A statistical multi-variate analysis method (cluster analysis) is used to determine how the grid cells group (Section 2.4). Eight models of climatology regions are developed to reflect differences in tornado region boundaries within the US. The epistemic uncertainties in the boundary locations are analyzed in Section 8 for smoothing the grid-cell wind speeds.

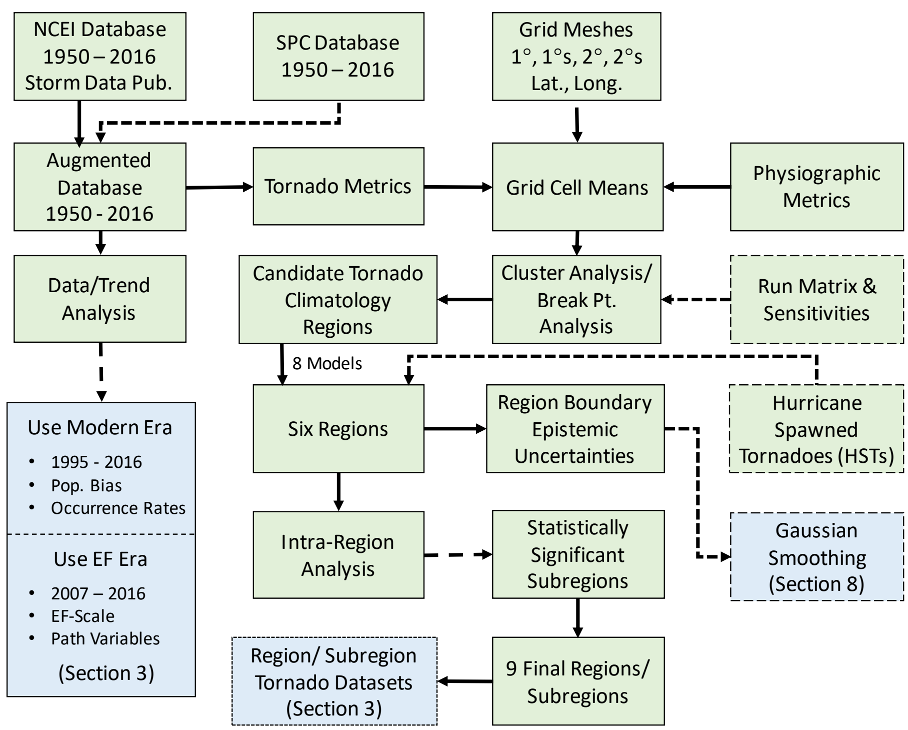

Figure 2-1. Overview of Development of Tornado Climatology Regions

In developing the broad tornado climatology regions (Section 2.5) we examine how the Gulf and Atlantic Coastal region is influenced by hurricane-spawned tornadoes (HSTs). This region is characterized by the highest frequency of EF0 tornadoes and reflects a large number of HSTs near the coast. This analysis provided supporting information in the development of the six tornado regions in Section 0.

In Section 2.7, we evaluate intra-regional variations in tornado occurrence for selected sub-regions. Based on this sub-region analysis, we divided 3 of the original 6 regions into 2 new sub-regions each, producing a total of 9 final regions/sub-regions that are used the tornado risk map development.

2.2. Use of Tornado Databases

There are two sources for tornado data: the National Climatic Data Center (NCDC) and the Storm Prediction Center (SPC). A good description of the data and how it is processed to produce the NCDC and SPC databases is summarized by McCarthy (2003). The SPC data are processed such that each record represents one tornado event, while the NCDC database includes a separate record for each tornado segment, defined according to county/state boundaries. In processing the data, the SPC has attempted to remove obvious errors in the database.

The NOAA SPC files for the years 1950 – 2016 were downloaded from the SPC website and are used as a basic source of data for this investigation.[16] These files are similar to the NSSC (National Severe Storms Forecast Center) database (Kelly et al., 1978). There remain many issues with the tornado database. The database includes tornadoes back to 1950, although Fujita's classification system did not emerge until 1971 (Fujita, 1971). Efforts were made to apply intensity classifications to pre 1970's events. Since the late 1970's, the data rely on local NWS meteorologists to collect the information. Spatial and temporal variability in these efforts and changes in NWS guidance over the years introduce further problems in the analysis of tornado risk; for examples see McCarthy (2003), Verbout et al., (2006), and Doswell and Burgess (1988). Edwards et al. (2013) also provides perspectives on tornado data.

2.2.1. Cleansing and Augmentation

During the course of the tornado risk mapping project, we discovered several errors and anomalies in the SPC database. To capture these discoveries, we developed "cleansed" data for several of the SPC fields. In addition, we found it useful to augment the SPC tornado data fields with additional data from the NCEI Storm Events Database and the Storm Data Publication (SDP). As part of this process, the tornado county segments in the Storm Events Database were linked together into full tornado tracks and matched, when possible, to their corresponding tornadoes in the SPC database. Our augmented data fields include: (1) tornado path direction; (2) the NCEI Weather Forecast Office (WFO) that produced the rating; (3) the NCEI source of the tornado report; and (4) the NCEI tornado start/end date and time.

[16] The SPC 2016 data became available in late Spring 2017. With the work on the Augmented Database and other simultaneous tasks, it was not practical to integrate additional years of SPC data after that time for this project.

The cleansed SPC database (1950 – 2016) with augmented data fields is described in Appendix A. “Augmented SPC Tornado Database (1950 – 2016)”, including a link to access the database. This augmented SPC data is used in this project to produce tornado wind speed risk maps for the US.

2.2.2. Views of the National Data

A national map view of SPC data for the period 1950-2016 is provided in Figure 2-2(a) with F/EF-Scale color-coded tornadoes. This map shows the reported variation in tornado occurrence and noticeable differences in reported tornado activity west of the Rocky Mountains and in portions of the Appalachians. In the Central and Southern US, one can see a broad area with a higher density of moderate and severe tornadoes. Figure 2-2(b) provides a tornado dot view with an elevation background. This figure shows the important effects of the Appalachian Mountain chain on tornadoes in the east and the dearth of reported tornadoes west of the Rockies.

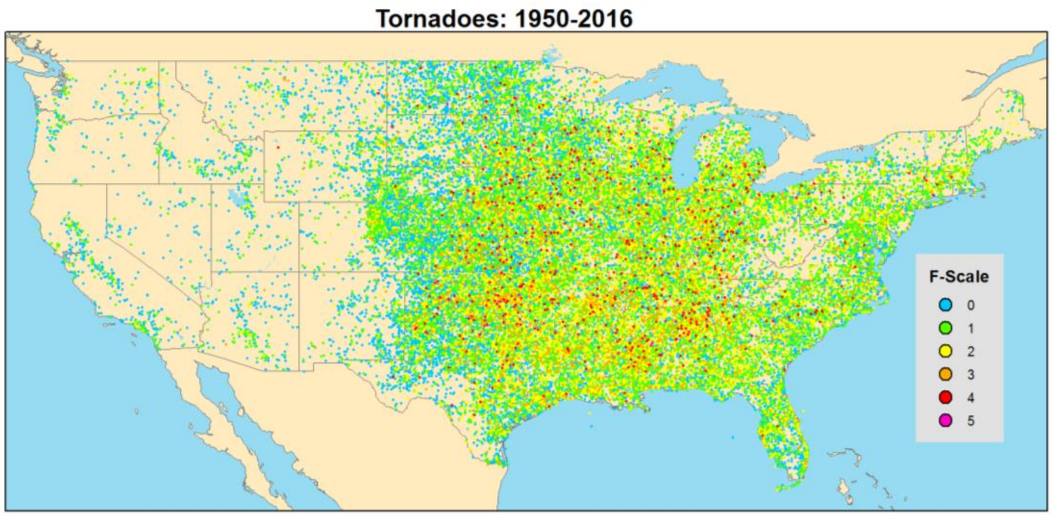

a) F/EF-Scale Color-Coded

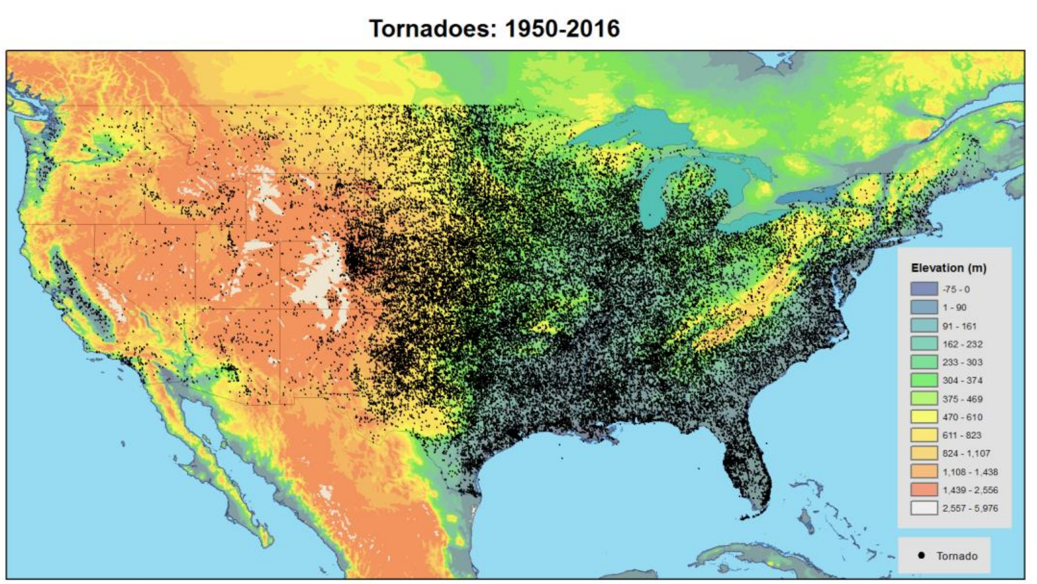

b) With Elevation-Colored Background (Note: 1 m = 0.32808 ft)

Figure 2-2. 1950-2016 SPC Tornadoes

Reported tornadoes have either a single latitude/longitude location, or a starting and ending latitude/longitude location. Figure 2-3 through Figure 2-5 plot tornadoes, colored by their F/EF-Scale, as either a point or a line, depending on if both starting and ending locations are given in the database. These figures readily show the predominant NE quadrant (storms travelling from SW quadrant toward NW quadrant) path direction of tornadoes and the correlation of path length with tornado intensity.

Figure 2-6 plots the F/EF-Scale distribution for tornadoes in the US from 1950-2016. The percentage of tornadoes of each F-Scale decreases with increasing F/EF-Scale. Forty seven percent of tornadoes are rated F/EF0, which decreases to 0.1 percent for F/EF5.

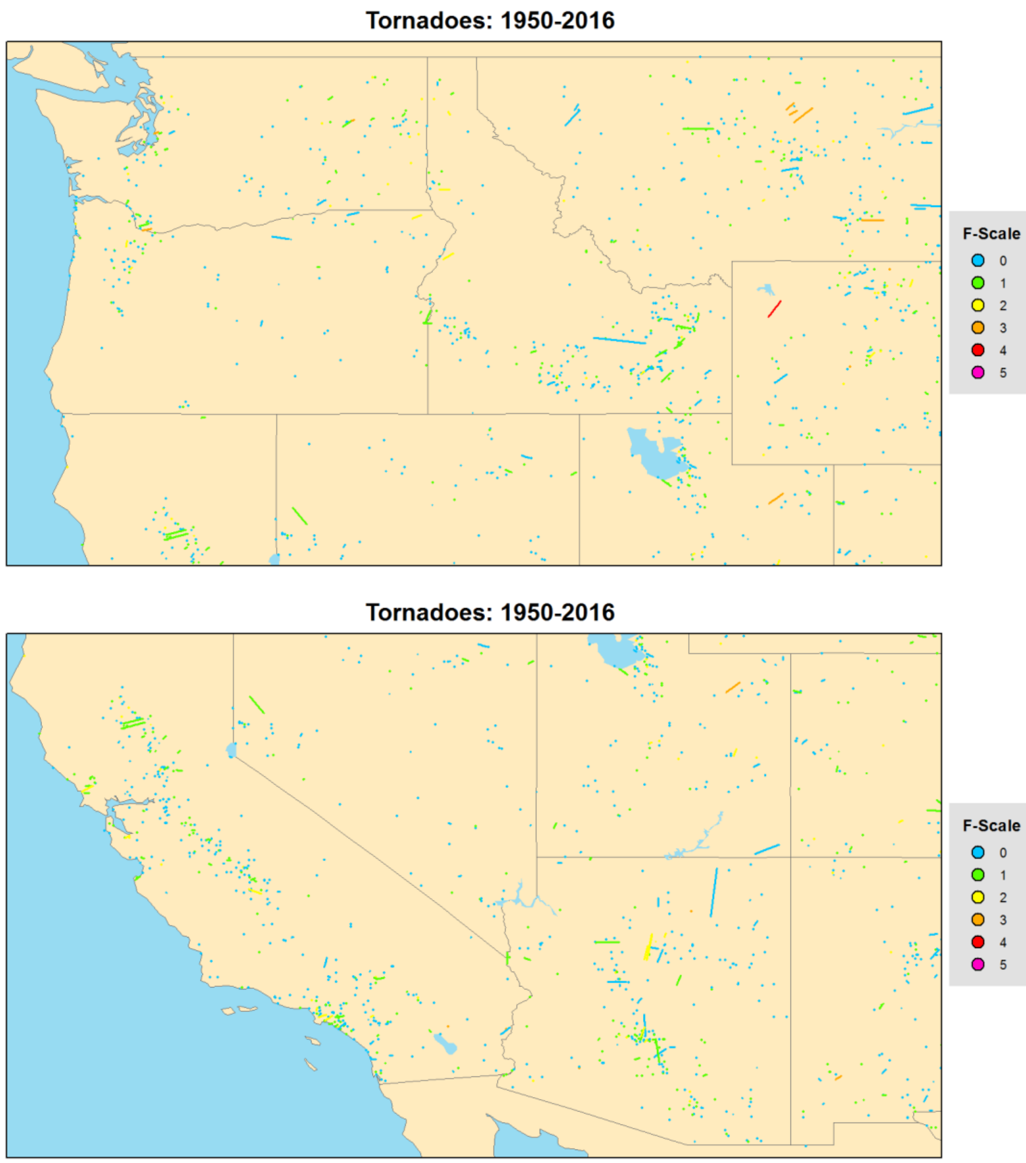

Figure 2-3. Western US Point and Line Tornadoes

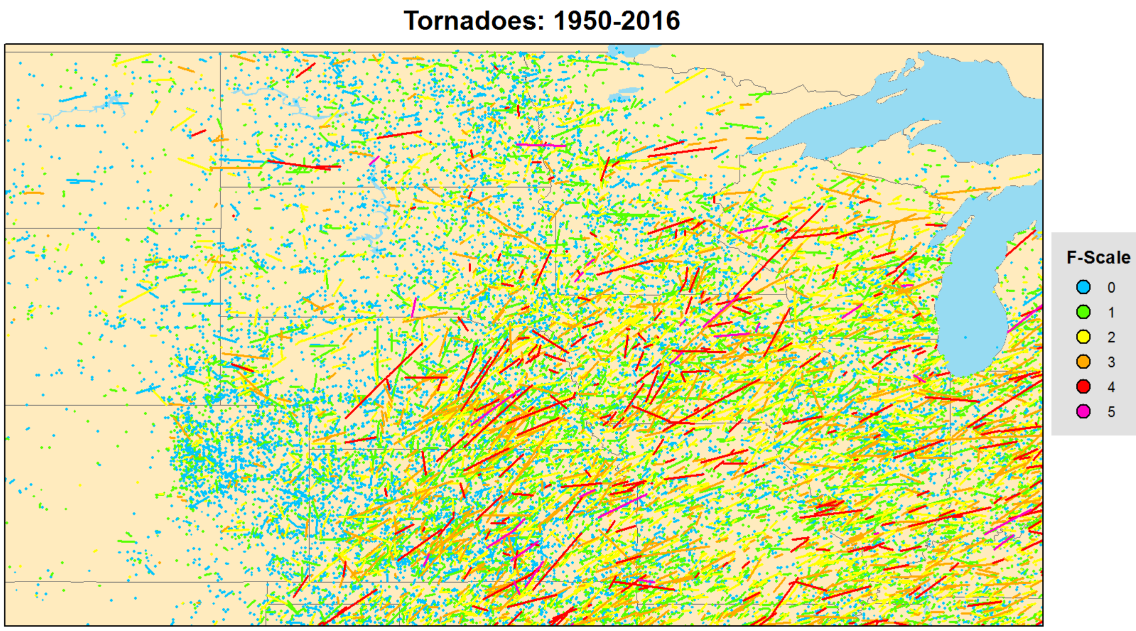

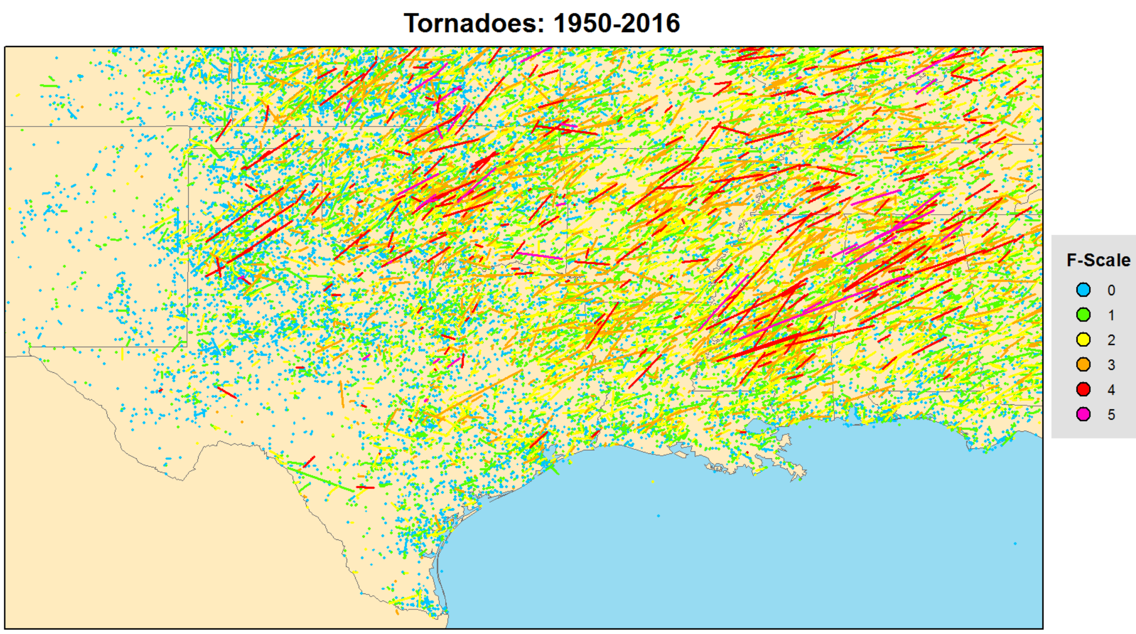

Figure 2-4. Central US Point and Line Tornadoes

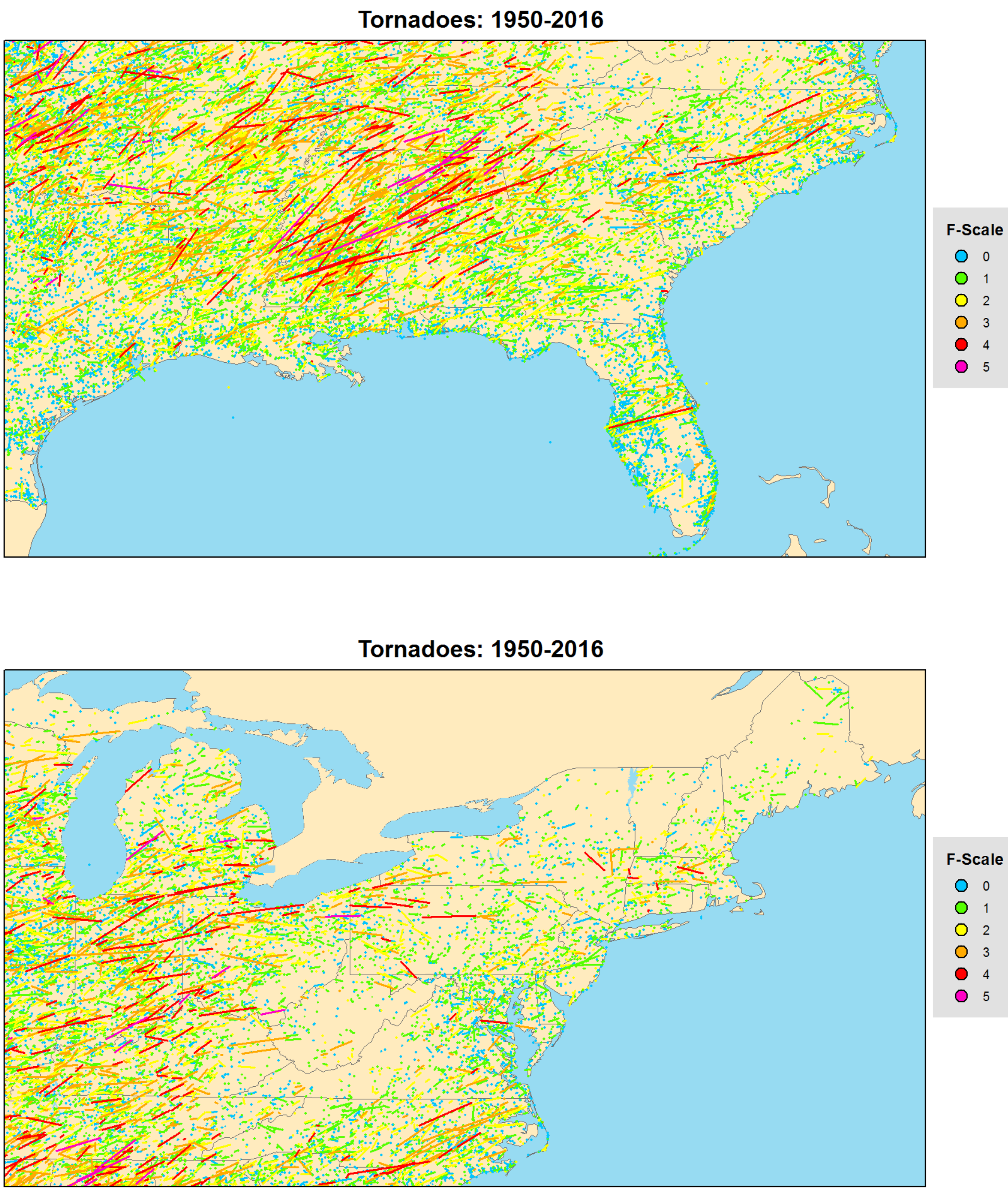

Figure 2-5. Eastern US Point and Line Tornadoes

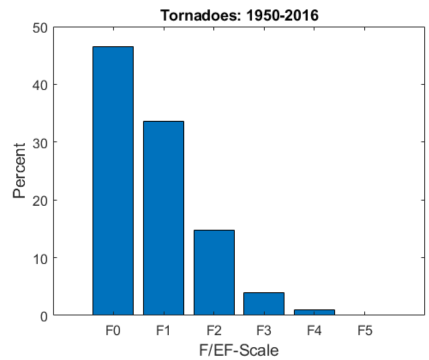

Figure 2-6. F-Scale Distribution (1950 to 2016)

Figure 2-7 shows the cumulative distribution function (CDF) of tornado path length for all tornadoes (left) and by F/EF-Scale (right). About 50% of all tornadoes are less than or equal to 1 mile (1.6 km) long, while 50% of F/EF5 tornadoes are less than or equal to 30 miles (48 km) long. The right side of Figure 2-7 shows the dramatic shifts with increasing path lengths by F/EF-Scale.

Figure 2-8 shows the CDF of tornado path widths for all tornadoes (left) and by F/EF-Scale (right). About 50% of all tornadoes are less than or equal to 50 yards (46 m) wide, while 50% of F/EF5 tornadoes are less than or equal to 600 yards (550 m) wide.

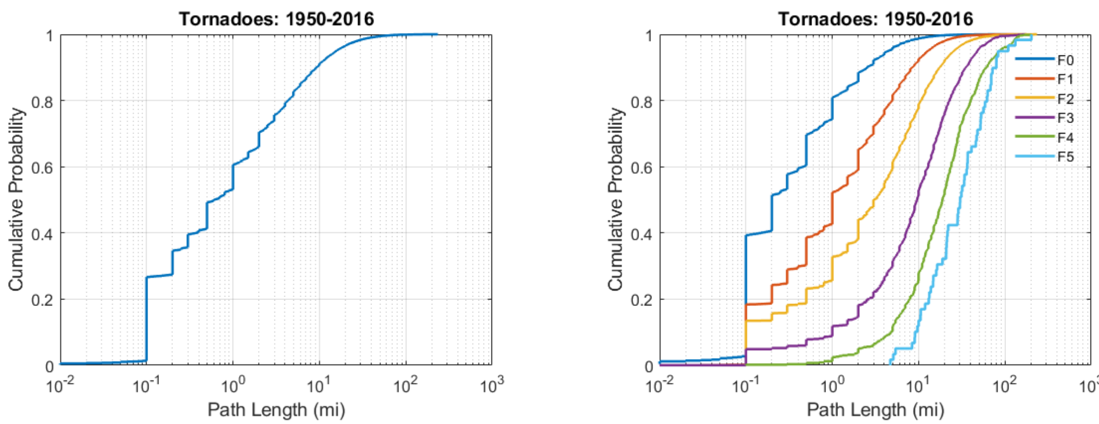

Note: 1 mi = 1.609344 km

Figure 2-7. Path Length CDFs (1950-2016)

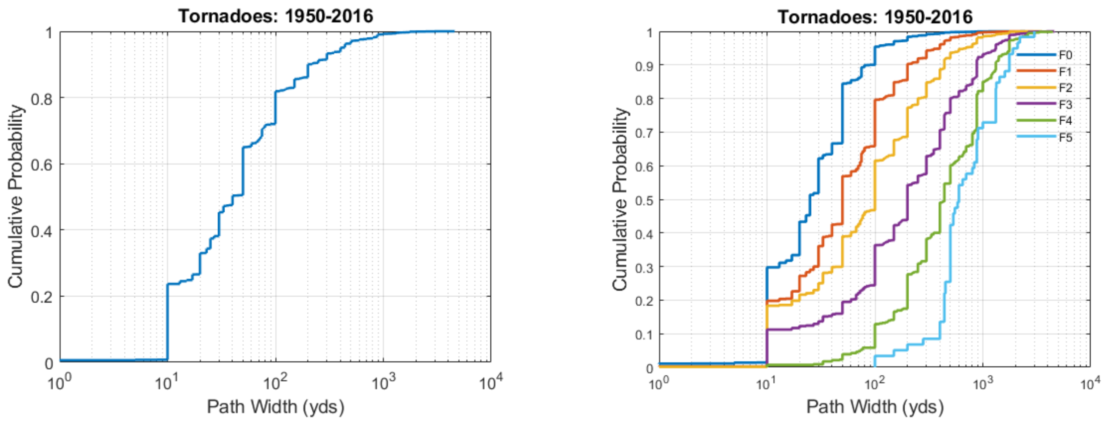

Note: 1 yd = 0.9144 m

Figure 2-8. CDF of Path Width and Path Width (1950-2016)

2.2.3. Tornado Reporting Eras and Trends

We separate tornado reporting into four eras:

1. Pre F-Scale Era: 1950 – 1976
2. F-Scale Era: 1977 –1994
3. Modern F-Scale Era: 1995 –2006
4. EF-Scale Era: 2007 – 2016

In the “Pre F-Scale Era” the majority of tornadoes were rated based on research on newspaper accounts of tornadoes, many years after the tornado had occurred. We expect this data to be the least accurate era. During the “F-Scale Era” the F-Scale was used to rate tornadoes through damage path surveys (Schaefer et al., 2002). In the early 1980’s the NWS warning program began, equipping each of the 52 weather forecast offices (WFO) with a Warning Preparedness Meteorologist (WPM). The responsibility the WPMs was to conduct damage surveys on significant tornadoes that occurred within their state. This program was further developed in the late 1980’s with the addition of 69 WFOs throughout the U.S. (McCarthy, 2003). The “Modern F-Scale Era” saw an increase in tornado reports (particularly for F0 and F1 events) due to the implementation of the WSR-88D Radar network, an increase in spotter networks, and the advent of cell phone usage, along with other societal factors (McCarthy & Schaefer, 2004). Additionally, during this era the NWS changed the survey protocol, requiring surveyors to report maximum path width, instead of the previously required mean path width (Schaefer et al., 2002). The introduction of the EF-Scale (TTU, 2006), its implementation in 2007 by NOAA (2008), associated training (Ladue and Mahoney, 2006), and damage assessment tools (NOAA, 2016b) was a significant milestone in estimating tornado wind speeds and assigning a damage-based intensity. Along with the EF-Scale came the NWS Damage Assessment Toolkit (NOAA, 2016b), an interface which allows surveyors to record geo-tagged details of their surveys, helping to increase both efficiency and accuracy.

Figure 2-9 illustrates our division of tornado reporting eras. With the exception of the EF-Scale Era, the exact year that divides these eras is debatable, but the improvement in the data collection guidelines and quality of data over time is irrefutable. Several analyses of tornado data trends are provid ed in the following sections and Appendix A. These analyses aid in the selection of data eras for tornado risk modeling components.

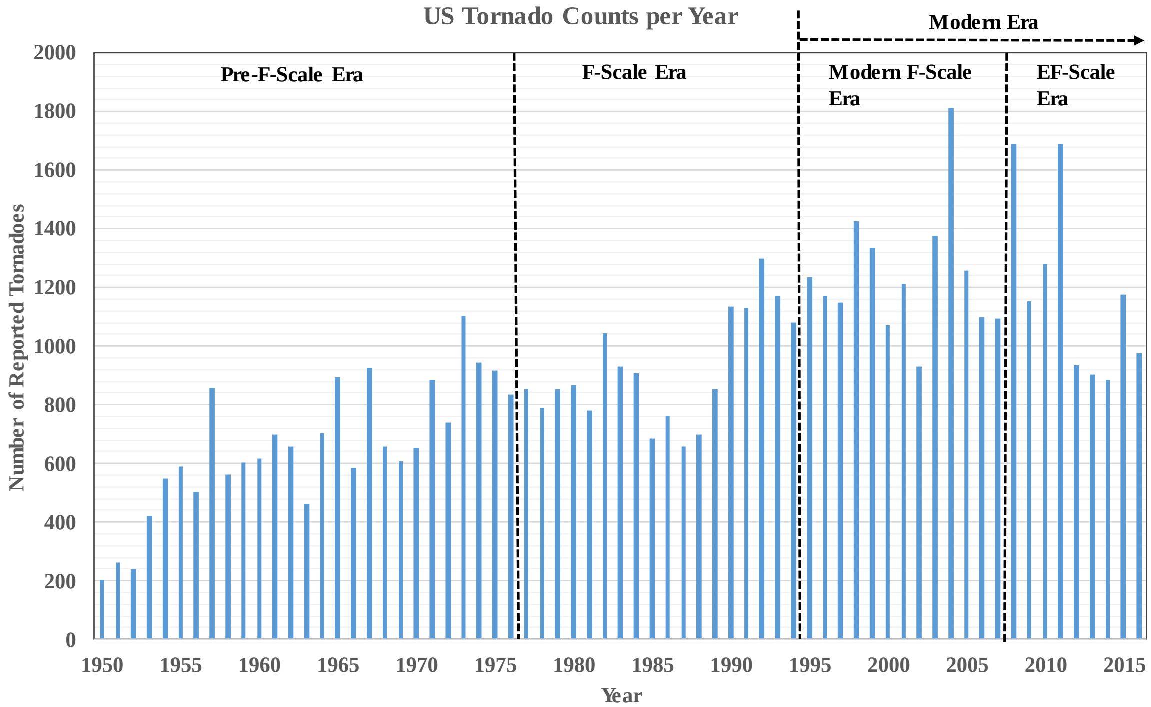

Figure 2-9. Reported Tornadoes (1950-2016) and Eras

2.2.3.1. Trend Analysis of Tornado Intensity and Path Variables

We examine reporting trends in F/EF-Scale, path length, width, area and path aspect ratio (length/width) using the Augmented Database. As described in Appendix A, the Augmented Database includes some corrections to path length and path width, including small values, and sets the default minimal values to 0.1 mile (0.16 km) for length and 10 yards (9.1 m) for width. The trend analysis in this section was performed in 2016 and includes data from 1950-2015.[17]

F/EF-Scale. Figure 2-10 shows the reported tornadoes by year by F/EF-Scale. This plot illustrates the significant increase in reported F/EF0 events in the modern era (beginning in the early 1990's in this plot), as noted by many others (Dean and Imy, 2006; McCarthy, 2003; Verbout et al., 2006). An interesting fact from Figure 2-10 is that F1 was the most frequently reported intensity until 1985. Over the full period of the plot, the trend of relative frequencies of F/EF0 and F/EF1 are increasing and the trends of the relative frequencies of F/EF1-5's are all decreasing. We do not believe these trends in Figure 2-10 reflect underlying tornado climatology trends, but rather the evolution of the tornado database with respect to reporting efficiency.

Figure 2-11 provides the F/EF-Scale relative frequency values, aggregated by era. The major differences in the Pre-F-Scale Era and all other eras is readily apparent and indicates that this early era should not be used in modeling the relative frequency of tornado intensity. Figure

[17] The tornado climatology analysis beginning in Section 2.3 is based on the data period 1950-2016.

2-11 also shows that there was not an abrupt change in the relative frequencies from the Modern F-Scale Era to the EF-Scale Era.

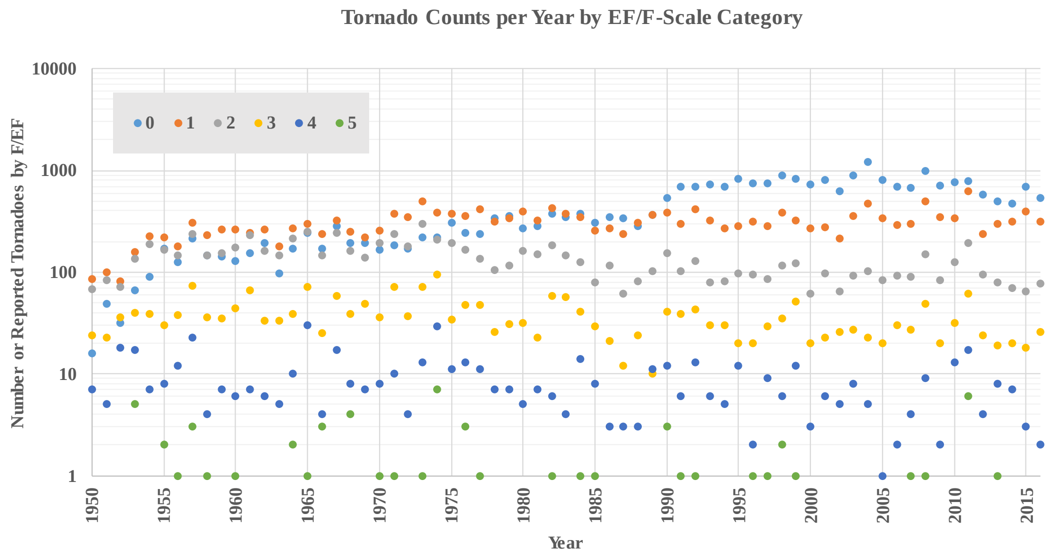

Figure 2-10. F/EF-Scale Trends Over Time

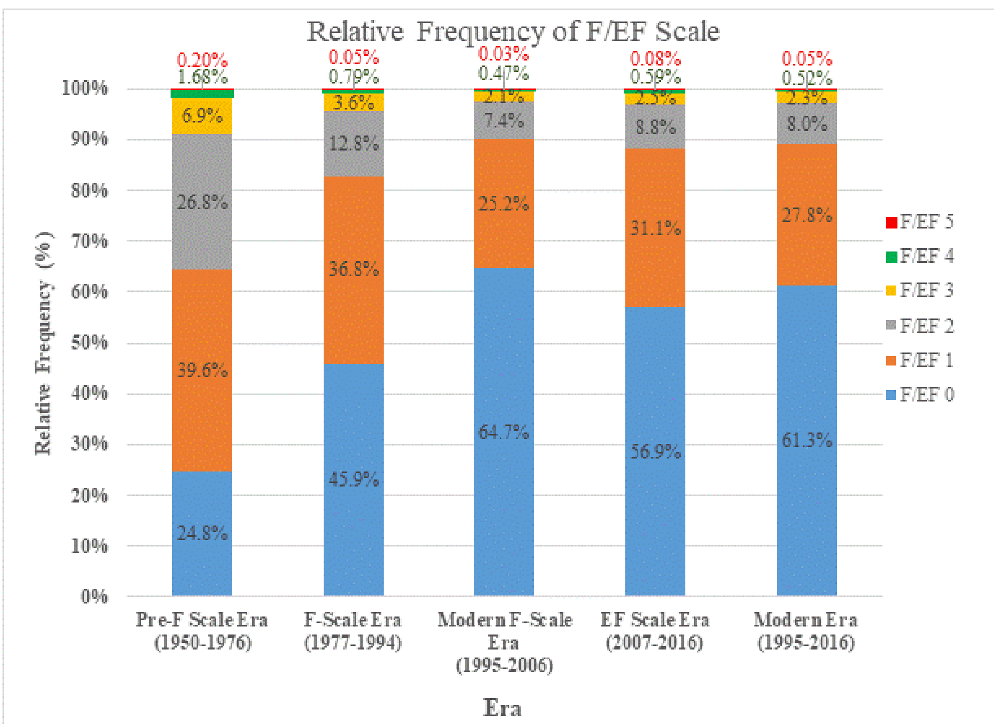

Figure 2-11. F/EF-Scale Relative Frequencies by Era

Path Length. Figure 2-12 shows the trend of mean, median, standard deviation and coefficient of variation (COV = σ/μ)[18] of path length (PL) and path width (PW), where σ is the standard deviation and μ is the mean. The trends in Figure 2-12 include significant year-to-year randomness but also show basic reporting trends.

The path length data inFigure 2-12 indicate a slight trend down with increasing year for the path length means, standard deviations, and COVs, while the medians have tended to increase. Within this overall trend, we see that the mean PLs for F/EF0 to F/EF2 trend down until about the 1990, where they begin gradual uptrends. With the medians remaining about even over time, these statistics suggest a trend of fewer reported PL extremes (particularly reductions in reported small PLs for F/EF0-F/EF1 beginning in the early 1990s).

With increased population/building density over time, one would expect a resulting increased ability to infer tornado starting and ending positions and a gradual increasing trend in reported PL. We see such a trend in the mean and median PLs for F/EF0-F/EF4 since the early 1990s (Figure 2-12). The banding of median PLs in the F/EF0-F/EF1 data begins to break up in the mid-1990s for F/EF1 and around 2005 for F/EF0. Reduced banding suggests more variation in low PW reporting and fewer default values, since the mean is also slightly increasing during this period.

Path Width. The PW trend statistics in Figure 2-12 are similar to PL but with some important differences. Maximum path width (vs mean path width) reporting began around 1994 (McCarthy, 2003). We see a more significant upward trend in all F/EF mean PWs beginning around 1985 and all F/EF median PWs beginning in the early to mid-1990s. The change from mean to maximum path width reporting appears to be more apparent in the median statistics since a noticeable jump can be seen at that time for most of the F-Scales. However, the conversion from mean path width reporting to maximum path width reporting in 1994 appears to be a non-event from the trend plots. Reported path widths continue their upward trend through today with noticeable jumps in the median and mean. The reported path widths in the EF era remain the largest ever, likely due to the improved training associated with the introduction of the EF-Scale in 2007.

There is significant banding of the median PWs up through F/EF2, which suggest use of rounded values and fairly crude estimates. The banded small median values of about 30, 50, and 100 yards (91 m) suggest narrow tornadoes in areas with sparse DIs, resulting in highly approximate width estimates. The COVs continue to trend slightly down for all F/EF-Scales. Reduction in the COV with time suggests more consistent reporting and fewer outliers/mistakes in entry. This data tends to agree with the points made earlier, that a large number of small width tornadoes continue to be reported with values modestly larger than 10 yards (9.1 m).

[18] The COV provides a dimensionless measure of dispersion and facilitates comparison of data sets with different means.

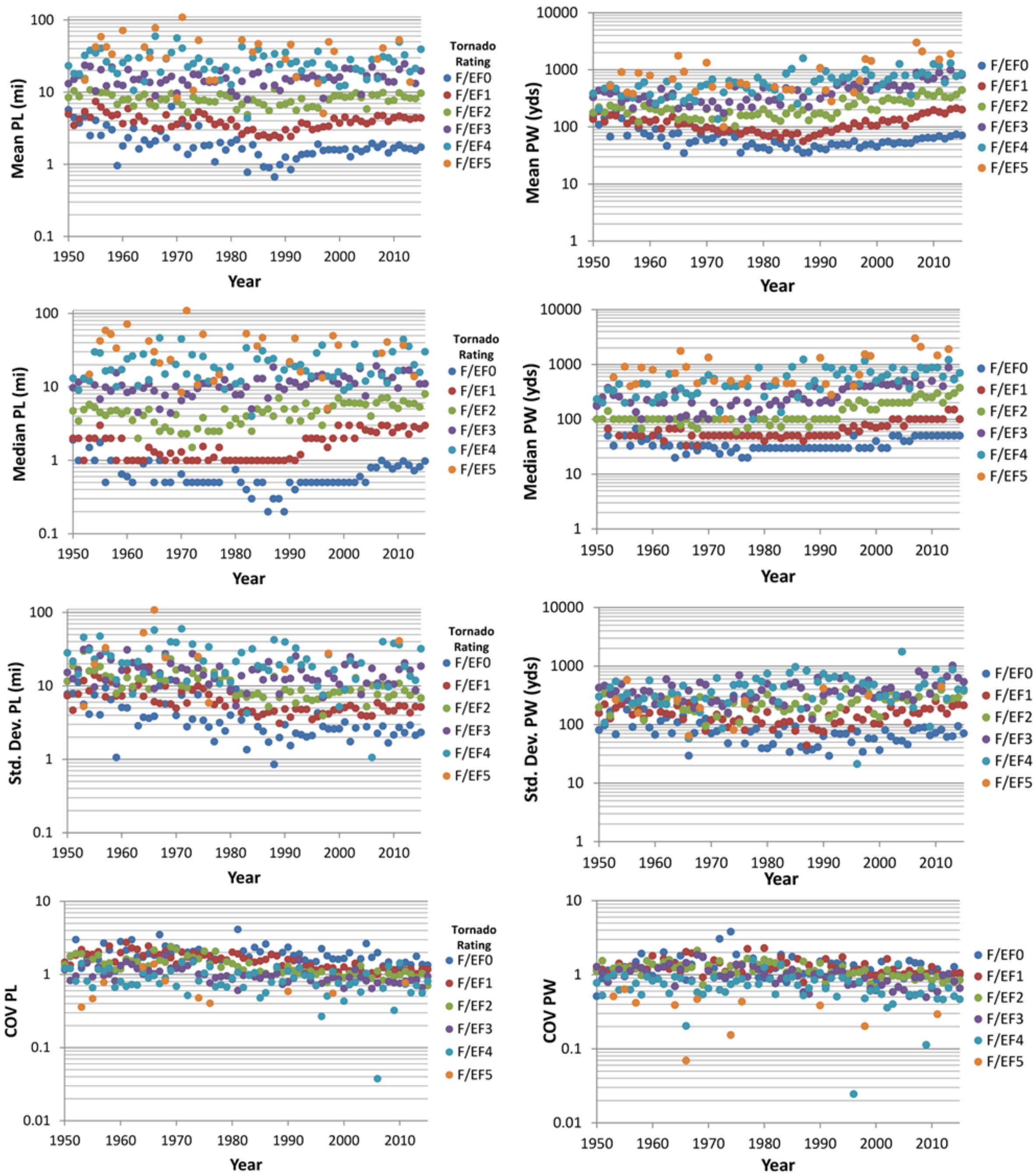

Note: 1 mi = 1.609344 km; 1 yd = 0.9144 m

Figure 2-12. PL and PW Statistics by F/EF-Scale and Year

Length vs. Width. The determination of a tornado's path length is generally viewed to be an easier task than the determination of path width. It therefore seems reasonable to assume that the path length reported values are more accurate. A comparison of the PL and PW COVs in Figure 2-12 indicates that both data sets have very large COVs with many > 1. We also see that the PL COV data has a slightly steeper down slope than the PW COV data. A possible explanation for this effect is that the methodology in reporting PL changed historically, moving from the idea of tornado skipping over the ground to the idea that a series of tornadoes touched down one after the other (McCarthy and Schaefer, 2004). As reviewed in a subsequent paragraph, the number of reported long track tornadoes has reduced over time, which would also tend to reduce the COV.

Inclusion of Default Minimum Data. We note that the above trend analysis was done with the default minimums (tornadoes with PL= 0.1 mile (0.16 km) or PW= 10 yards (9.1 m)) excluded. However, when the data are analyzed with the defaults included, many of the same observations are present, but are not as dominant, particularly for the low F/EF-Scales.

Reporting Era Trends. We investigated the statistical significance of differences in era, path length, and path width. A “separate slopes” model of path width versus path length was fit in log-log space with Era and F-Scale as categorical variables, using the SAS General Linear Models procedure (SAS, 1992) to test the null hypothesis, “H_o: Separate models, by the categorical variables, are not needed.” The resulting analysis of variance (ANOVA) rejected the null hypothesis. The resulting model explained 42% of the variation in $\ln(PW)$ with the main effects and interactions of all 3 input variables, $\ln(PL)$, Era, and F/EF-Scale, being highly significant.

An examination of the means of PL and PW by era is illustrated in Figure 2-13 and

Table 2-1. The eras correspond to those given in Figure 2-9 (Era 1= 1950-1976; Era 2 = 1977-1994; Era 3 = 1995-2006; Era 4 – 2007-2015). With the exception of F/EF0-F/EF2 between Era 1 and Era 2, the mean path width by F/EF has steadily increased over these eras. The percentage increases are significant and exceed 40% for several F/EF-Scales. The steady increase in PW suggests that path widths were not carefully estimated in the early years and that the more rigorous approach has produced more accurate path width estimates. The difficulties in determining path width are well known (McCarthy, 2003); Schaefer et al. 1986) due to asymmetries of tornado wind field structure and translation. The trends in Figure 2-12 show that the increase in path width means, medians and standard deviations appear likely to continue with improved training and attention. Increases in mean path length from Era 2 to Era 4 are also clear from Figure 2-13 and

Table 2-1. The fact that the mean path length increases within these eras similarly suggests improved reporting methods and increased population density (more DIs).

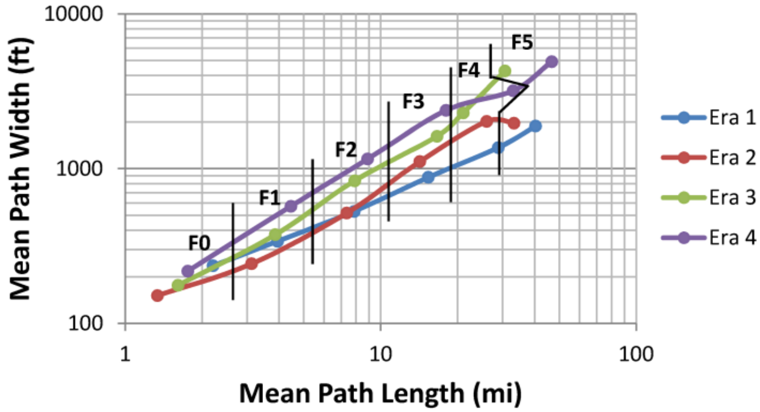

Note: 1 mi = 1.609344 km; 1 ft = 0.3048 m

Figure 2-13. Mean Path Width vs. Mean Path Length by Era and F/EF-Scale

Table 2-1. Mean Path Length and PW by Era and F/EF-Scale

Rating	Mean PL (mi)				Mean PW (ft)			
	Era 1	**Era 2**	**Era 3**	**Era 4**	**Era 1**	**Era 2**	**Era 3**	**Era 4**
F/EF0	2.2	1.3	1.6	1.8	236	152	177	218
F/EF1	3.9	3.1	3.9	4.5	340	243	375	573
F/EF2	7.9	7.4	7.9	8.9	531	518	836	1156
F/EF3	15.4	14.2	16.6	18.0	880	1114	1622	2381
F/EF4	28.8	26.0	21.0	33.0	1368	2023	2296	3191
F/EF5	40.4	33.2	30.7	46.7	1885	1970	4280	4913

Note: 1 mi = 1.609344 km; 1 ft = 0.3048 m

Path Aspect Ratio. Figure 2-14 plots the path width vs. path length by F/EF-Scale for the cleansed data. The mean trend line in log-log space indicates that longer tornadoes have wider path widths, on average, within each F/EF-Scale. The slopes of these fits are similar for F/EF0 through F/EF5. One can see the horizontal banding of rounded (and likely, roughly estimated) path widths up until about 1,000 yards (910 m). Banding of rounded path lengths is also apparent up to about 10 miles (16 kilometers).

There are still a large number of very narrow tornadoes that have path width values just above the default values in Figure 2-14. For example, there are many path widths in the 20 to 50 yard (18 to 46 m) range with lengths over 10 miles (16 kilometers).

Table 2-2 provides the 2 largest aspect ratios ($AR = PL/PW$) for each F/EF-Scale for all eras and for only Era 4. Many of these tornadoes are long but very narrow, for example, there are several ARs over 4,000.

Table 2-2 shows that the earlier eras contain many tornadoes with larger, less realistic aspect ratios, although this is less of an issue for the higher F/EF-Scale tornadoes. The maximum aspect ratios in Era 4 are much less extreme, showing that the corresponding PLs and PWs in this era are more reasonable.

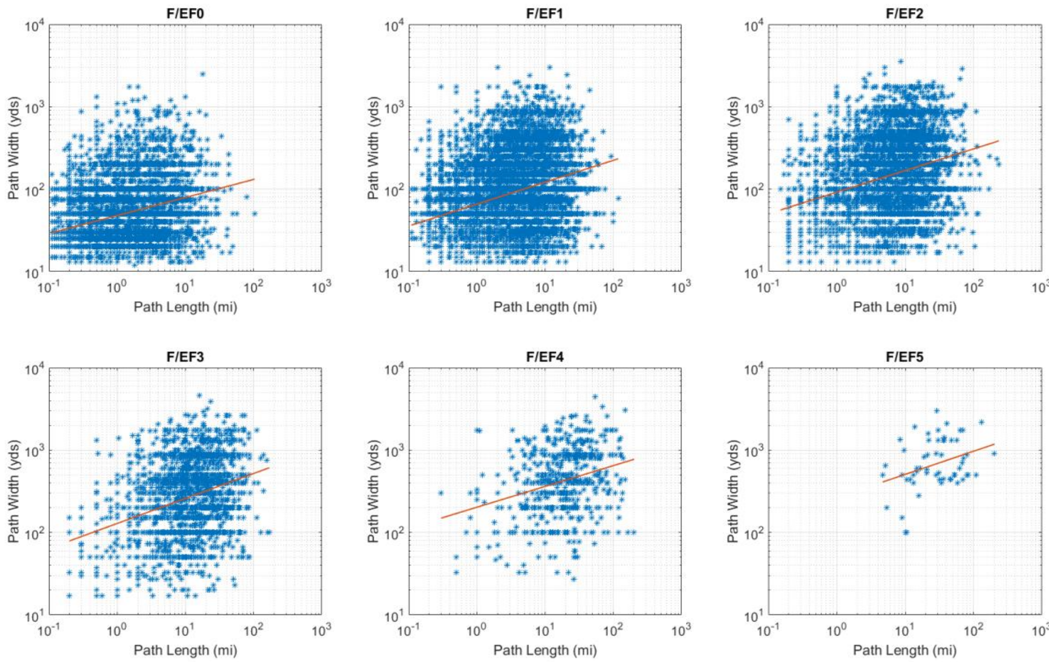

Note: 1 mi = 1.609344 km; 1 yd = 0.9144 m

Figure 2-14. Path Width vs. Path Length by F-Scale for SPC Tornadoes Including Corrections Described in Section 3 and Neglecting Tornadoes with Default Path Lengths and Widths

Table 2-2. Maximum ARs within Each F/EF-Scale for All Eras and for Only Era 4

All Eras					EF-Scale Era (Era 4)				
F/EF	Year	PL (mi)	PW (yds.)	AR	EF	Year	PL (mi)	PW (yds.)	AR
0	1958	45	17	4658	0	2012	15	20	1332
0	2004	50	20	4400	0	2013	14	25	1017
1	1975	68	20	5984	1	2014	18	20	1608
1	1980	99	40	4391	1	2011	28	50	975
2	1973	105	20	9275	2	2008	30	50	1050
2	1968	65	17	6771	2	2010	9	20	793
3	1978	53	23	4071	3	2013	38	100	667
3	1973	50	27	3266	3	2012	60	300	354
4	1971	202	100	3557	4	2012	50	400	221
4	1953	162	100	2851	4	2011	122	1050	205
5	1966	203	900	396	5	2011	132	2200	106
5	1971	109	500	384	5	2011	63	1760	63

Note: 1 mi = 1.609344 km; 1 yd = 0.9144 m

Figure 2-15 shows the time trend of the aspect ratio statistics. We see that the mean, standard deviation and COV of aspect ratio are still trending down, while the median AR has much less change over time. The downward trend in aspect ratio is significant, approaching a factor of about 5 over the 66 years of the data. Since the aspect ratio continues to trend down, the mean tornado path width is continuing to increase relative to path length. Thus, it is likely that tornado path widths are still underestimated based on these trends.

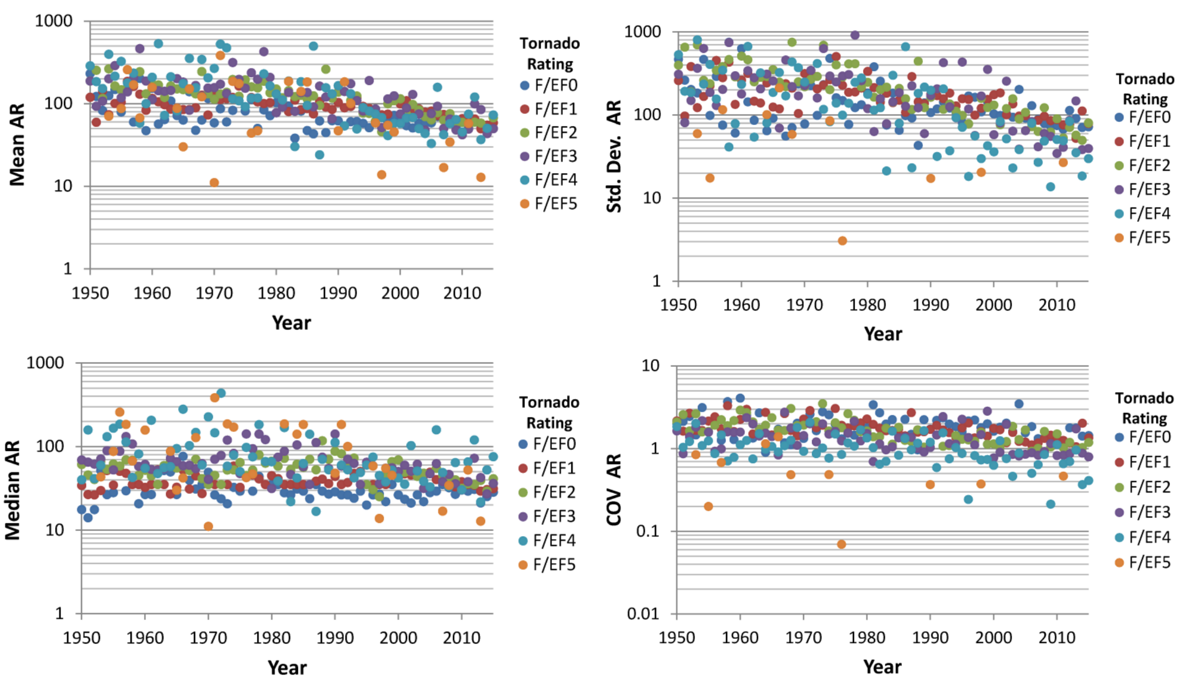

Figure 2-15. Mean, Median, Standard Deviation, and COV of AR by F/EF-Scale and Year

Long Track Tornado Trends. The reporting of long track tornadoes has decreased in time, as shown in Figure 2-16, which includes 3 PL thresholds of long tracks. The trends of long track and very long track tornadoes are captured in Figure 2-16, which shows slightly decreasing mean PL trends in the early years. Although, as discussed above, beginning in the early 1990s the mean PLs trend slightly upward (Figure 2-12), despite no increase in long track tornadoes (Figure 2-16). Hence, the increase in mean PL with time is not a result of more reporting of long track tornadoes. This result also suggests that PL accuracy may be increasing with time and the modern data is likely a better source for tornado path length statistics. This result also supports the logic provided in Doswell and Burgess (1988) regarding the reporting of long track tornadoes (where early era tornadoes were reported with a % ground factor, intended to reflect "skipping" of tornadoes. Modern observations with overhead imagery reflect that skipping tornadoes are generally separate tornadic events.)

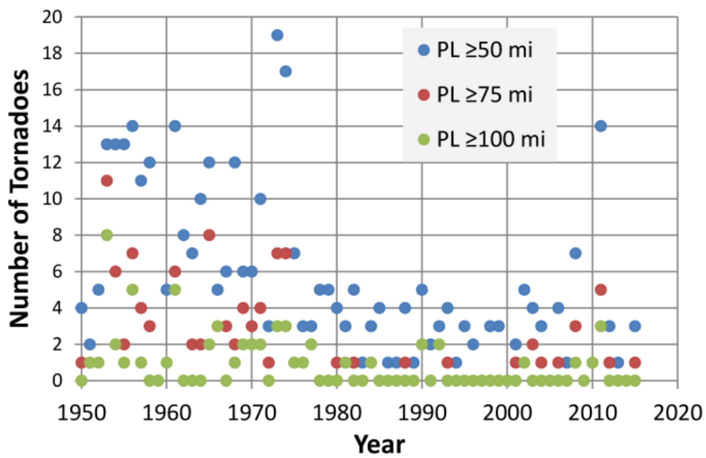

Note: 1 mi = 1.609344 km

Figure 2-16. Number of Long Track Tornadoes Reported by Year

Summary. These trend analyses illustrate the continued evolution of tornado reporting. The improvements in NOAA's damage survey methods, level of detail, as well as the trend statistics suggest that the most recent data are the best data to use for tornado risk modeling.

2.2.3.2. Unknown Tornadoes as EF0s

Since there is no F/EF unknown tornado category in the SPC database, tornadoes that are not surveyed or do not produce damage are generally given a default rating of F/EF0. This method officially began in 1982, when procedures were updated, instructing unknown ratings to be entered into the database as F0 (McCarthy, 2003).

The mining of early era data sets provide some clues regarding how many tornadoes that were unrated in early eras were rated F0. For example, data in Twisdale et al. (1981) show that 2,007 tornadoes out of 19,085 total were unrated in the years 1950-1978. Thus, about 10% of the reported tornadoes in that period were unrated due to lack of damage and/or other factors that prevented an F-Scale assignment.

In 2015, the SPC added a column that indicated whether or not a tornado's intensity rating had been estimated. The re-rating of originally un-rated events was based on an algorithm that used property loss and path length data. Figure 2-17 summarizes how the 1,843 originally unrated tornadoes from 1950 to1982 were fractionally rated by the SPC. Over 55% of these events were rated F0; 40% were rated F1; and less than 5% were rated F2 – F4. These results are very comparable to the tornadoes of the 1950-1978 Twisdale data set that were changed from missing F-Scales to assigned F-Scales. These data provide evidence that the early era tornadoes with no assigned F-Scale were from the population of all tornadoes rather than just F0 tornadoes.

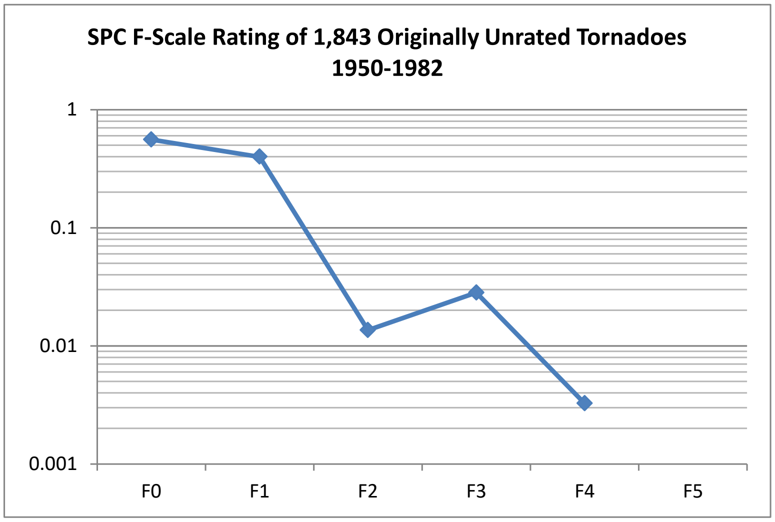

Figure 2-17. SPC F-Scale Fractional Rating of Unrated Tornadoes (1950-1982)

The practice since 1982 of rating unknowns as F/EF0 events has introduced a bias into the database. We do not know exactly which tornadoes were actually rated F/EF0 based on observed damaged and which tornadoes were rated F/EF0 based on lack of damage information. We seek to estimate the fraction of real F/EF0 events through population bias analysis in Section 3.

2.2.3.3. Damage-Based Intensity Ratings

Tornadoes are rated based on the damage that they produce. This fact makes ratings suspect in rural areas with wide spacing of structural (non-tree) damage indicators. Additionally, if a tornado's wind speed exceeds the maximum wind speed a DI can withstand, then the assigned F/EF-Scale may be biased low. Also, it is not always possible to ascertain if the structure experienced the tornado's maximum winds or if it was located in an area that experienced lower than maximum wind speeds. Finally, the level of damage is highly dependent on many structural variables, which have not been fully considered in F/EF ratings. These well known problems with damage-based intensity ratings complicate the modeling of the tornado F/EF distribution. We attempt to improve the modeling of the EF distribution by using building density data in Section 3.

2.3. Tornado Climatology Analysis

The important variables in modeling the frequency of a tornado strike on a target include the mean tornado occurrence rate, the F/EF-Scale distribution, and tornado path variables (path length and width).[19] The characteristics of these variables vary significantly over the contiguous US. For example, intense tornadoes occur much more frequently in the central and southern US than elsewhere. Weak tornadoes occur with high frequency along the

[19] Path direction is important in computing tornado strikes on long, linear targets such as electrical transmission systems.

hurricane prone coastline of the US, in part due to hurricane spawned tornadoes (HSTs). The path characteristics of tornadoes also vary regionally with the largest paths in the central and southern US.

Previous studies, including regional and site-specific analysis of tornado risk indicate that there is correlation among the important tornado variables of occurrence rate, intensity, and path length and width (e.g., Twisdale et al., 1978, 1981). For example, areas with higher tornado occurrence rates often have a more intense F/EF-Scale distribution than areas with lower tornado occurrence rates. Similarly, path lengths and widths depend on F/EF-Scale and these dependencies exhibit regional variations.

The correlation and spatial variability of important tornado variables suggests the use of multivariate analysis to identify regions with distinct tornado climatologies.[20] We develop empirical tornado metrics from the Augmented Database and include several physiographic variables to create a multivariate data set, as illustrated in Figure 2-1. We analyze these data using a multivariate statistical method to produce large-scale spatial patterns, or regions, with similar tornado characteristics. With the distinct regions developed in this section, the regional data are analyzed in Section 3.

2.3.1. Grids

We use four different grids covering the continental US in the analysis; a 1° grid (Figure 2-18), a 1° shifted grid (Figure 2-18), a 2° grid (Figure 2-18), and a 2° shifted grid (Figure 2-18). The 1° and 2° shifted grids are respectively shifted by 0.5° and 1° in both the latitudinal and longitudinal directions.[21] The shifted grids allow examination of any changes in the formed regions based on grid position. The smaller grids capture finer details in the tornado climatology, while the larger grids (with approximately four times the area) result in a larger sample size, and hencemore accuracy in the computation of the tornado cell means.

2.3.2. Metrics

We use the empirical, field-developed SPC tornado observational data to develop the tornado climatology metrics. In this research, we did not attempt to include climate data based on atmospheric variables such as convective available potential energy (CAPE), or wind shear, which have been shown to be relevant to tornado genesis (e.g., Brooks et al., 2003; Thompson et al., 2003; and Thompson et al., 2013).

In computing the tornado climatology metrics, each tornado is assigned to a cell or cells. For tornadoes with both a starting and ending point, the portion of the tornado's length that is located in a cell is allocated to that cell. If the entire tornado is located within a single cell, the entire tornado length is allocated to that cell. If the tornado's length spans more than one cell, the appropriate portion of tornado length is allocated to each intersected cell. If a tornado has no end point, then its entire length is assigned to a cell based on its starting latitude/longitude point. The allocation of tornado lengths to cells provides a way to properly

[20] An alternate approach is use a single variable, such as tornado occurrence rate as the sole spatially-dependent variable coupled with the use of singular (national) models of tornado intensity, path variables, and so forth for all locations or regions in the analysis (e.g., Ramsdell and Rishel, 2007). This approach generally underestimates the risk in the hottest tornado regions and overestimates the risk in the coolest tornado regions due to correlation of tornado frequency, intensity, and path area.

[21] The simultaneous latitude-longitude shifts produce the maximum shift for each size grid.

reflect long path tornadoes and tornadoes that cross cell boundaries. This allocation process allows tornado occurrences and path areas to be assigned to multiple cells in a manner that reflects the actual starting and ending points of the events. The role of tornado path length allocation is described for each metric. Basically, either the length value contained in each cell, or a count of one, is used, as appropriate, for each metric.

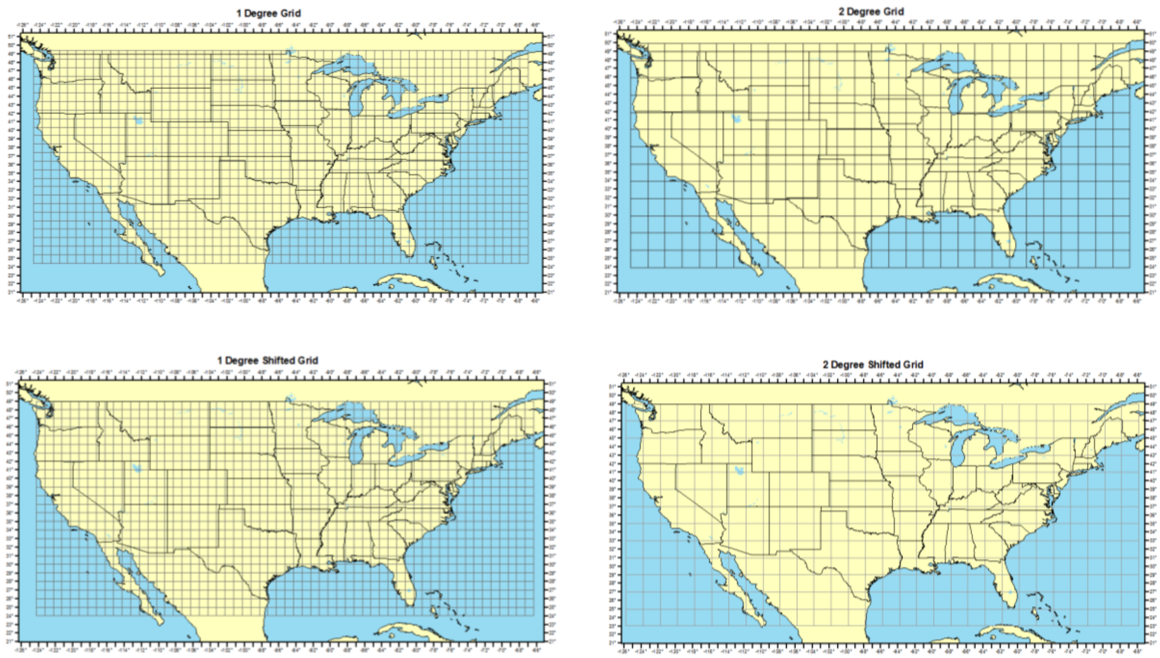

Figure 2-18. 1°, 1° Shifted, 2°, and 2° Shifted Grids

A total of eleven location, physiographic, and tornado climatology variables are considered in this study.[22] Location is described by latitude and longitude. Physiographic variables include mean elevation, standard deviation of elevation, and the cell fraction that is associated with a large body of water. Tornado climatology metrics include tornado days per year, occurrence rates, point strike probability, and path direction. These metrics are defined in the following paragraphs.

Latitude & Longitude Cell Mid-points. The mid-points of a cell's latitude and longitude boundaries are used as risk metrics to provide information on the cell's relative location to all other cells. To the extent that the tornado climatology differs latitude-wise and/or longitude-wise, this contributes to how regions are formed.

Mean and Standard Deviation of Elevation. These parameters provide physical measures of the topographic differences of the cells and likely influence the tornado climatology of the region. ArcGIS 10.2.2 (ESRI, 2014) was used to determine the mean and standard deviation elevations statistics for a cell. The "zonal statistics as a table" tool in ArcGIS is used to compute the mean and standard deviation for each cell. A raster file with a cell size of 1000 m by 1000 m (3281 ft by 3281 ft) is the source of the elevation data. These values provide a

[22] Appendix B.1 provides background on the names of US physiographic regions.

measure of the average elevation within a cell and the variation of elevation within a cell. Mountainous areas have high average elevations and high standard deviations of elevation.

Number of Tornado Days per Year. The number of tornado days per year is believed to be a basic indicator of tornado climatology. Brooks et al. (2003) show that the number of tornado days per year has less temporal variation than the number of tornadoes per year. A tornado day is a day in which at least one tornado is reported in the cell. Allocation of tornadoes is included in this metric. If any portion of a tornado's length is contained in a cell then the tornado contibutes towards that cell's integer number of tornado days. The number of tornado days per year (*tdpy*) for each cell "k," is normalized to a constant cell area A according to Eq. (2-1), where n_{td_k} is the number of tornado days in cell "k" during the number of years, $Y$and A is the nominal area of a square cell in the US. L_k is the US land fraction within cell k, and S_k is the total area of cell k. The value of A used in the calculations is 3,600 square miles (9300 km^2) for a 1° square cell in the US. For larger grid sizes the value of A is adjusted accordingly. Since the number or tornado days per year depends on the area over which a tornado may occur, the A term in Eq. 2-1 normalizes the results based on the actual cell size (S_k).

$$tdpy_k = \frac{n_{td_k} * A}{L_k S_k Y} \tag{2-1}$$

For cells larger than 1°, the normalizing land area in Eq. (2-1) is scaled accordingly.

Land Fraction. The ocean and large bodies of water may affect tornado risk (e.g. King et al., 2003). To assess the importance of large bodies of water, we defined a land fraction metric (the fraction of land vs. water) for each cell. This measure is 1 for cells that do not contain any portion of a large body of water. For cells that include a portion of a large lake (such as the Great Lakes), ocean, bay, or gulf, the fraction is less than one. Tornadoes are not reported for cells that are fully in the water.

Path Direction. The path direction (DIR) computation is discussed in Appendix A. This directional range (-150°, 210°) for tornado path is used for the Cluster Analysis since direction is a circular variable. Using this range of angles produces a bell-shaped direction distribution centered near the mean (tornadoes traveling Northeast), which is ideally suited for use in a clustering routine.

Occurrence Rate. The mean occurrence rate of tornadoes per year in cell k, ν_k is defined as:

$$\nu_k = \frac{n_k}{L_k\, S_k\, Y} \quad (tornadoes\ per\ sq\ mi\ per\ year) \tag{2-2}$$

where n_k is the number of tornadoes that occurred in cell k during the Y years. Tornado path length allocation is considered in determining the number of tornadoes that occurred in cell k. If all or a portion of a tornado path passed through cell k, then that tornado counts as one tornado towards n_k.

In addition to using the occurrence rate for all F/EF-Scale tornadoes (OR), moderate intensity (F/EF2-F/EF3) tornado occurrence rate (OR-M) and strong intensity (F/EF4-F/EF5) tornado occurrence rate (OR-S) metrics are also computed and used in the cluster analysis. Moderate occurrence rate and strong occurrence rate are calculated in the same way as occurrence rate, except n_k includes only tornadoes rated F/EF2-F/EF3 and F/EF4-F/EF5 for moderate and strong occurrence rates, respectively.

Point Strike Probability. The point strike probability (R_{k_i}) for cell *k* and tornado *i* is defined by:

$$R_{k_i} = \frac{A_i}{L_k\, S_k\, Y} \text{ (tornado 'i' point strike probability per year)} \qquad \textbf{(2-3)}$$

where A_i = path area (sq. miles) of tornado *i*. The cell total is:

$$R_k = \frac{\sum_{i=1}^{n_k} A_i}{L_k\, S_k\, \mathrm{Y}} \text{ (cell point strike probability per year)} \qquad \textbf{(2-4)}$$

where n_k is the number of tornadoes in cell *k*. Tornado path length allocation is used and R_k is therefore the probability of a tornado striking a point target in cell *k* per year, which corresponds to Thom's (1963) classical "point probability" definition.

2.3.2.1. Tornado Metric Data

Transformations of statistical data are often used to make a distribution more "normal," so that the data better conforms to the assumptions of the statistical procedure (e.g., Kennedy and Neville, 1974). The Exponential Maximum Likelihood (EML) clustering procedure and stepwise discriminant analysis procedures used in the clustering analysis assume the variables passed to them are normally distributed. Hence, we transform tornado metrics that have skewed distributions to achieve characteristics that are more like a normal distribution.

Normal distribution transformations are used for tornado days per year, path direction, and land fraction. Natural log transformations are used for occurrence rates and point probability. No transformations are used for latitude, longitude and the elevation metrics.

Normal Distribution Transformation. Transformations of non-nominal variates are often used in structural reliability and probability calculations (Ang and Tang, 1984; Rackwitz, 1976; Rosenblatt, 1952). A normal approximation can be computed by first calculating the Cumulative Relative Frequency (CRF) using Eq. (2-5a) (SAS, 1992), where I_k is the rank of the metric value of cell k, and N is the number of cells. After the CRF is computed, it is substituted for the CDF for the normal approximation, computed using Eq. (2-5b) and Eq. (2-5c) (Bell, 2015). We developed an improvement to the distribution's tails (Eq. (2-6)) to guarantee an absolute relative error < 1.42% in x, for CDF in [.00001, .99999].

The CRF is computed by:

$$CRF_k = \frac{I_k - 0.375}{N + 0.25} \qquad \textbf{(2-5a)}$$

And the transformed metric (*x*) is given by:

$$x = \sqrt{-\frac{\pi}{2}\ln\left(1-(2CDF-1)^2\right)} \qquad (CRF > 0.5) \qquad \textbf{(2-5b)}$$

$$x = -\sqrt{-\frac{\pi}{2}\ln\left(1-(1-2CDF)^2\right)} \qquad (CRF \le 0.5) \qquad \textbf{(2-5c)}$$

However, if $abs(0.5 - CDF) > 0.321$, the transformed x from Eq. (2-5) is further adjusted by:

$$x = 1.0032x^{1.0362} \qquad (CRF > 0.5) \qquad \textbf{(2-6a)}$$

$$x = -1.0032 * (-x)^{1.0362} \qquad (CRF \leq 0.5) \qquad \textbf{(2-6b)}$$

Natural Log Transformation. The natural log (ln) of each metric is computed according to the following protocol: If $\min(metric_{k=1:N}) > 0$, simply take the natural log of the value for each cell. If $\min(metric_{k=1:N}) = 0$, take ln $(metric_k + 0.5 * \min(metric_{k=1:N} \neq 0))$. For the path direction metric, we use: if $\min(metric_{k=1:N}) < 0$, then take the natural log of the metric plus 150° (direction is the only metric that can be negative).

2.3.2.2. Tornado Metric Maps

Plots of tornado risk metrics, are given in Figure 2-19 for the 1° grid shown in Section 2.3.1. The following paragraphs discuss the plots in Figure 2-19. Yellow cells in Figure 2-19 reflect no data.

Mean Elevation. The mean elevation for each 1° cell in the contiguous US is plotted in Figure 2-19 (a). You can see higher elevations shown in the Appalachian Mountains in the East, the Ozark Mountains in Arkansas, Missouri, and Oklahoma, and a transition to higher elevation starting in the high plains and moving West into the Rocky Mountains to the Pacific Mountain Systems.

Standard Deviation of Elevation. The standard deviation of elevation, which characterizes changes in elevation, is plotted in Figure 2-19 (b). High standard deviations can be associated with high as well as lower elevations and provides a measure of the “ruggedness” of the terrain. For example, the certain cells in the high plains of West Texas have elevations higher than the Appalachian System but much lower standard deviations.

Tornado Days per Year. The middle of the country, the Gulf of Mexico coastline, and the southeast coastline are characterized by highest numbers of tornado days per year. The tornado days per year metric is much lower west of the Rocky Mountains, in the Appalachian Mountains, and in the Northeast. Figure 2-19 (c), in comparison with Figures 2-19 (a) and (b), illustrates the importance of the major physiographic features in the US influence tornado climatology, as measured by tornado days per year (normalized to a 1° cell reference area).

Land Fraction. The inland cells in Figure 2-19 (d) have a land fraction of one, and cells along the coasts or along the great lakes have cell land fractions less than one. For cells in these locations, land fraction values are sensitive to the grid size and relative location.

Mean Tornado Path Direction. Mean tornado path direction (Figure 2-19 (e)) is toward the east or northeast for most of the country. The Rocky Mountains and areas west, Gulf and Atlantic coasts, and certain cells near the Great Lakes are the major exceptions. The orientation of the ridges and valleys in mountainous areas can produce a wide variation in mean tornado path direction for adjacent cells, as can be seen in the Rockies and areas west. Cells with no direction data are shown as yellow.

Occurrence Rate – All Tornadoes. Higher occurrences are visible in the mid-west, south, and southeast. Lower occurrences are seen in the cells west of the Rockies and in the Appalachian System. The tornado occurrence rates for all tornadoes in Figure 2-19 (f) is very similar to the tornado days per year plot. This result is expected since the plots would be identical if every tornado day in a cell produced a single tornado (compare Eq. (2-1) to (2-2)). The differences in these metrics occur when a tornado day produces multiple tornadoes within the cell.

Moderate Occurrence Rate. The moderate occurrence rate plot (Figure 2-19 (g)) plots (F/EF2-F/EF3) is very similar to the all-occurrence rate plot.

Strong Occurrence Rate. The strong occurrence rate plot (Figure 2-19 (h)) focuses the "hot" center even more. One can also see two apparent SW-NE axes in the central US in this plot. The Atlantic and Gulf coast cells and the northeast also have a significant drop off in the occurrence of strong tornadoes. Also, due to the rarity of these events, the hit and miss nature of these violent tornadoes is apparent from the dramatic color change from one cell to another, without any physiographic change in large-scale features.

Point Strike Probability. The difference in point strike probability (Figure 2-19 (i)) and the previous occurrence rate plots show the contrast in these two metrics. The former metric considers path areas and occurrences, while the latter metrics are a count of events, without consideration of path size. Since path area and intensity are highly correlated, we begin to see more similarity in the plots for the strong occurrence rate and the point probability plots. However, there are notable cell-to-cell differences in color scale throughout the US area east of the Rockies. The strong occurrence rate and the point probability metrics provide important inputs to the climatology analysis regarding the frequency of intense and large path area tornadoes.

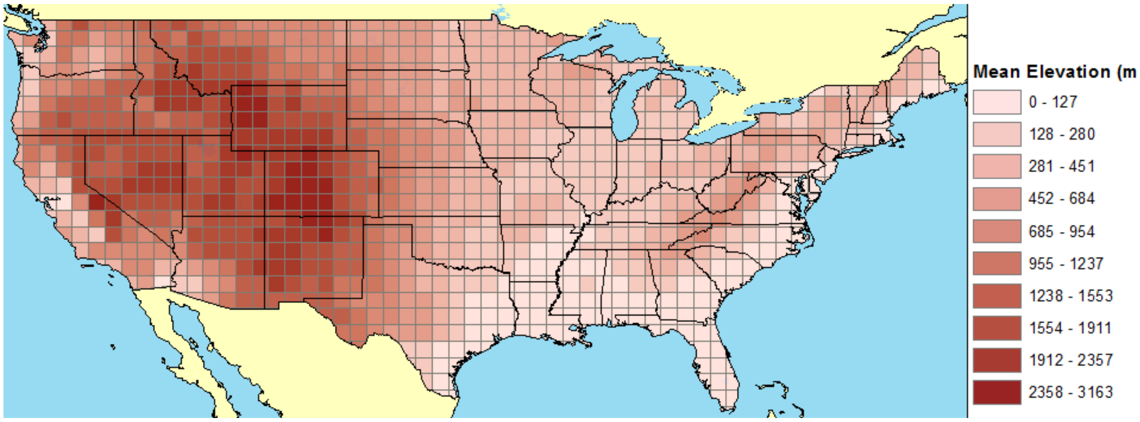

a. Mean Elevation

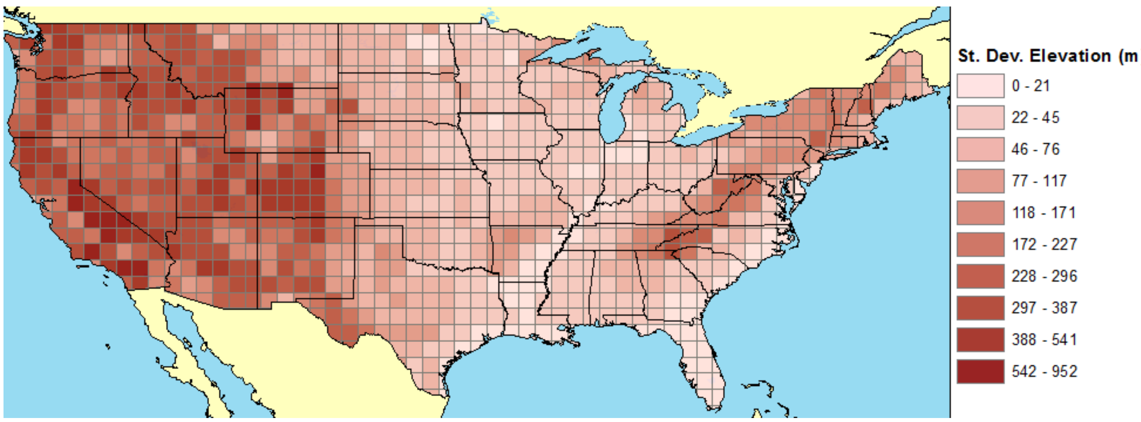

b. Standard Deviation of Elevation

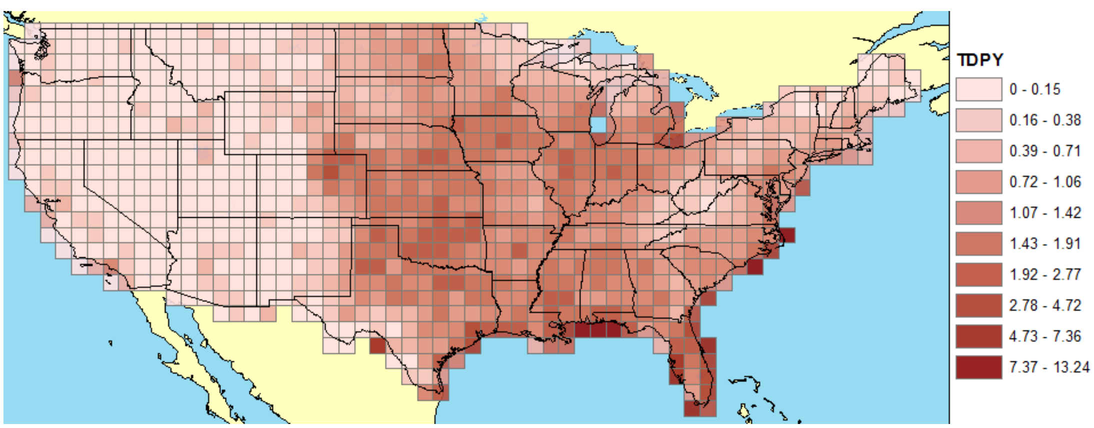

c. Tornado Days per Year

Note: 1 m = 3.28084 ft

Figure 2-19. 1° Cell Metrics for the Contiguous US

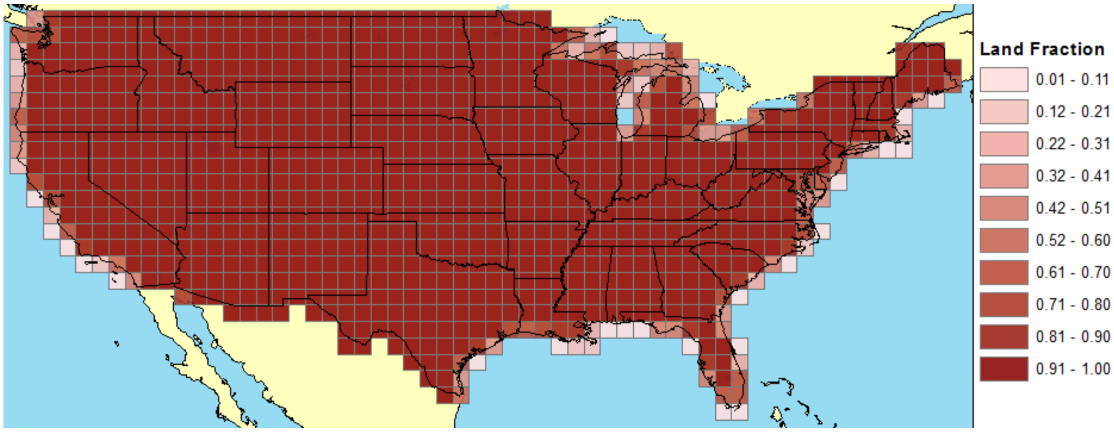

d. Land Fraction

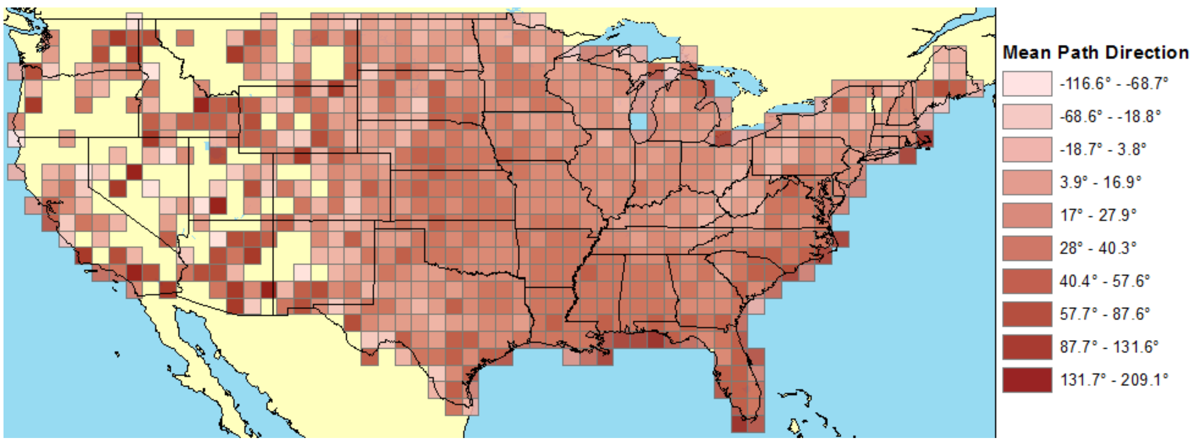

e. Mean Path Direction

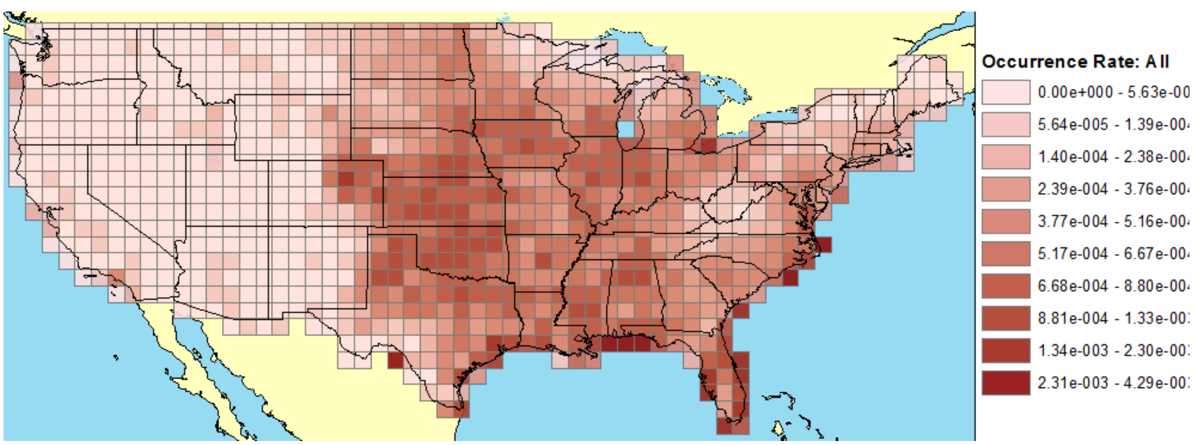

f. Occurrence Rate: All

Note: 1 m = 3.28084 ft

Figure 2-19. 1° Cell Metrics for the Contiguous US (continued)

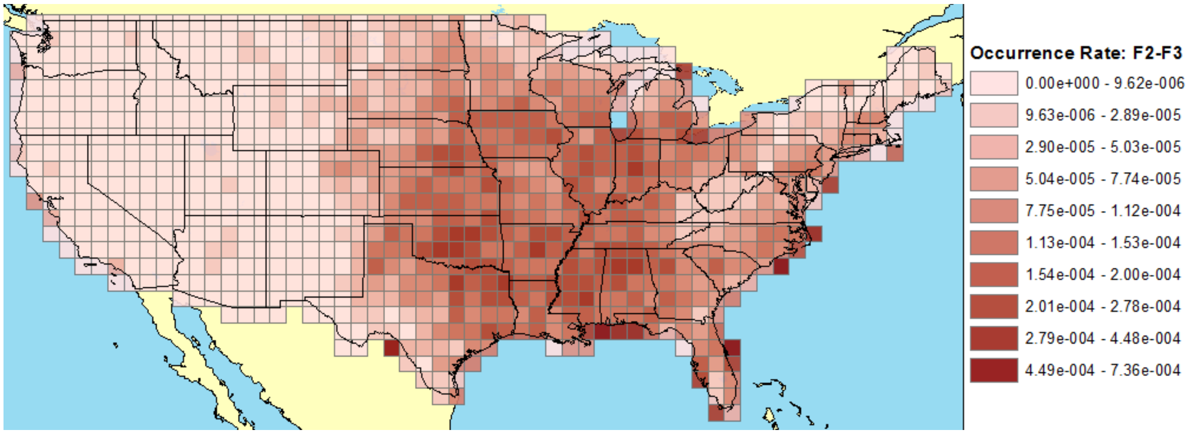

g. Occurrence Rate Moderate (F2-F3)

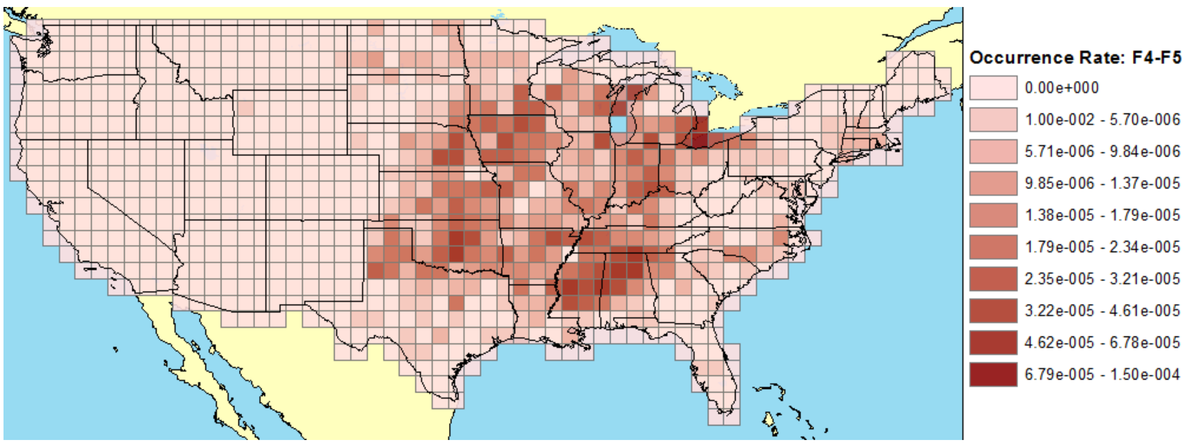

h. Occurrence Rate Strong (F4-F5)

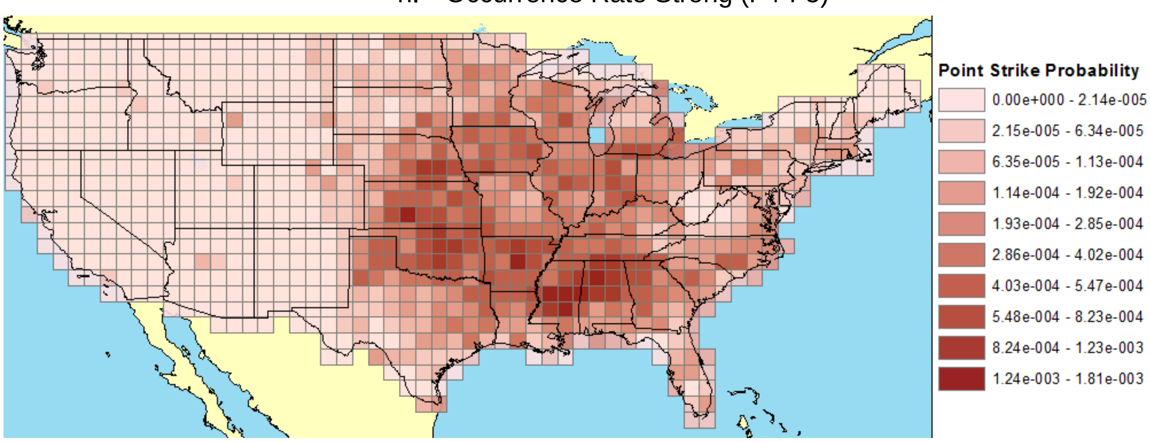

i. Point Strike Probability

Note: 1 m = 3.28084 ft

Figure 2-19. 1° Cell Metrics for the Contiguous US (continued)

2.4. Multivariate Statistical Analysis

We use the multivariate method broadly known as "cluster analysis," which is a method used to classify a set of objects into similar clusters of like characteristics. In this process, the method identifies objects that are more similar to each other than to those in other groups. Each resulting group is called a cluster. Therefore, cluster analysis is an explorative statistical method that tries to identify structures in the data. The method provides a way to identify how each object groups or "clusters" with other objects. In tornado risk analysis, it can be used to identify how the cells (objects) cluster due to similar tornado characteristics.

2.4.1. Background

Cluster analysis does not require prior knowledge or "training data," unlike discriminant analysis. Both cluster and discrimant analysis techniques have an advantage over "multiple comparison tests" and confidence interval techniques (Steel and Torrie, 1960; Walpole and Myers, 1978) in that they are not limited to using a single risk measure (like mean point strike probability) to similar groups or clusters. Instead, the procedures are free to find a combination of risk measures that best categorize the cells into distinct clusters or groups. There are many types of cluster models and algorithms.

The CLUSTER procedure of the SAS/STAT (SAS Institute, 1992) module was used for the cluster analysis. The cells are hierarchically clustered with the various risk metrics used as coordinates in an n-dimensional space. Hierarchical clusters are organized so that one cluster may be entirely contained within another, but no other kind of overlap between clusters is allowed. For any given number of clusters, the clusters are disjointed; hence, each cell may belong to only one cluster, for a given number of clusters.

The SAS CLUSTER methods used herein are based on the agglomerative hierarchical clustering procedure. Each cell begins in a cluster by itself. The two closest (distance-wise in n-dimensional risk metric space) clusters are merged to form a new cluster that replaces the two old clusters. Merging of the two closest clusters is repeated until only one cluster is left. The presentation of the clusters is in the reverse order of the SAS calculations.

The various clustering methods differ in how the distance between two clusters is computed. Many simulation studies have compared various methods of cluster analysis. In these studies, artificial data sets containing known clusters are produced using pseudo-random-number generators. The data sets are analyzed by a variety of clustering methods, and the degree to which each clustering method recovers the known cluster structure is evaluated (see Milligan, 1981 for a review of such studies). In most of these studies, a clustering method with best overall performance has been Ward's minimum variance method (Ward, 1963). In attempting to evaluate clustering methods, it is essential to realize that most methods are biased toward finding clusters possessing certain characteristics related to size (number of members), shape, or dispersion. Methods based on the least-squares criterion (see Sarle, 1982), such as Ward's, tend to find clusters with roughly the same number of cells in each cluster. Others are biased towards finding clusters of equal variance. Many clustering methods tend to produce compact, roughly hyper-spherical clusters and are incapable of detecting clusters with highly elongated or irregular shapes. The shape of a cluster refers to its shape relative to the distance function, which is computed from the multivariant tornado risk metrics.

2.4.2. Cluster Analysis Method

Based on ARA experience in tornado hazard modeling for over 30 nuclear plant sites in the US and Canada, we use the Maximum-Likelihood hierarchical clustering for mixtures of spherical multivariate normal distributions with equal variances but possibly unequal mixing proportions (EML). EML is similar to Ward's method (1963), but removes the bias toward equal-sized clusters. The EML method was derived by Sarle (1982) of SAS Institute from the maximum-likelihood formula obtained by Symons (1981) for disjoint clustering. EML joins clusters to maximize the likelihood at each level of the hierarchy under the following assumptions:

1. Multivariate normal mixture
2. Equal spherical covariance matrices
3. Unequal sampling probabilities

There is no generally satisfactory rule for determining the number of true population groups or clusters. At some point, the groupings become so fragmented that there is no practical need to continue to evaluate larger numbers of clusters. Appendix B.2 describes a method to assess the point of diminishing returns in cluster analysis, called the Bi-linear Break-Point (BBP). We use this information to identify a reasonable number of tornado regions.

As indicated in Table 2-3, cluster runs were performed for 76 different combinations of metrics and grids. The highlighted rows are the 8 model runs principally used to identify the tornado regions.

2.4.3. Cluster Analysis Results

The series designation in the table indicates what metric or group of metrics are used in that run. The W Series is the only one that includes all sets of metrics. The X Series includes all metrics except the elevation metrics and the Y Series includes no physiographic metrics. The Z Series includes only tornado metrics with no physiographic metrics or latitude longitude data.

The bi-linear break point (BBP) is shown in the last column in Table 2-3. For series with few metrics, the number of clusters indicated by the break point is generally less than when a large number of metrics are used. For example, for the single metric cases, the number of clusters at the break point are generally 3-5. When many metrics are used in the analysis, the BBP is generally in the 6-8 range.

Appendix B.3 presents the BBP clusters for the 1° and 2° runs for the individual tornado metrics, with and without the latitude-longitude metrics. Those plots show how clusters form when a single variable is used to assess spatial variation in tornado climatology. The basic regions formed in these single variable regions tend to be spatially similar to the multivariate analyses. As more metrics are added, we found that the general positions of the regions converged to the full multivariate case (W series).

W Series (All Metrics). The full variable W Series (Run 23) cluster sequence is given in Figure 2-20.[23] As indicated in Table 2-3, cluster runs were performed for 76 different combinations of metrics and grids.

[23] This figure shows Cluster 2 (CRc2) in the top left, Cluster 3 (CRc3) in the top right and so forth until Cluster 11 is in the bottom left. For brevity, we then jump to show the results for Cluster 22 (CRc22), the last cluster produced in all of our runs.

Table 2-3. Cluster Analysis Matrix

(U= Unadjusted Metric, N = Normal Transformation of Metric, LN = Natural Log Transformation of Metric, Blank = Not Used. Grids: 1 = 1° grid, 2 = 2° grid, 1S = 1° shifted grid, 2S = 2° shifted grid)

Years	Run ID	Case	Grid	Metric											
				Lat.	Long.	Mean Elev.	SD Elev.	TDPY	Land Frac.	Dir.	OR Moderate	OR Strong	PP	OR ALL	Bi-linear Break Point
	1	A	1					N							5.05
	2	B	1							N					4.14
	3	C	1								LN	LN			4.27
	4	D	1										LN		4.08
	5	E	1					N		N	LN	LN	LN		6.19
	6	F	1					N		N	LN	LN			6.17
	7	G	1					N			LN	LN	LN		6.14
	8	H	1	U	U			N							8.08
	9	I	1	U	U					N					7.23
	10	J	1	U	U						LN	LN			6.11
	11	K	1	U	U								LN		7.15
	12	L	1	U	U			N		N	LN	LN	LN		6.49
	13	M	1	U	U			N		N	LN	LN			6.48
	14	N	1	U	U			N			LN	LN	LN		7.01
	15	O	1											LN	3.23
	16	P	1	U	U									LN	8.09
	17	Q	1								LN				4.2
	18	R	1									LN			4.04
	19	S	1	U	U						LN				7.06
1950-2016	20	T	1	U	U							LN			5.44
	21	U	1	U	U										5.15
	22	V	1					N			LN	LN	LN	LN	7.35
	23	W	1	U	U	U	U	N	N	N	LN	LN	LN	LN	8.41
	24	X	1	U	U			N	N	N	LN	LN	LN	LN	7.43
	25	Y	1	U	U			N		N	LN	LN	LN	LN	7.09
	26	Z	1					N		N	LN	LN	LN	LN	6.27
	27	A	2					N							5.34
	28	B	2							N					4.21
	29	C	2								LN	LN			4.28
	30	D	2										LN		5.16
	31	E	2					N		N	LN	LN	LN		6.31
	32	F	2					N		N	LN	LN			6.14
	33	G	2					N			LN	LN	LN		7.27
	34	H	2	U	U			N							6.35
	35	I	2	U	U					N					6.23
	36	J	2	U	U						LN	LN			7.68
	37	K	2	U	U								LN		7.02
	38	L	2	U	U			N		N	LN	LN	LN		7.11
	39	M	2	U	U			N		N	LN	LN			6.47
	40	N	2	U	U			N			LN	LN	LN		8.18

Table 2-3. Cluster Analysis Matrix (continued)

(U= Unadjusted Metric, N = Normal Transformation of Metric, LN = Natural Log Transformation of Metric, Blank = Not Used. Grids: 1 = 1° grid, 2 = 2° grid, 1S = 1° shifted grid, 2S = 2° shifted grid)

Years	Run ID	Case	Grid	Metric											
				Lat.	Long.	Mean Elev.	SD Elev.	TDPY	Land Frac.	Dir.	OR Moderate	OR Strong	PP	OR ALL	Bi-linear Break Point
1950-2016	41	O	2											LN	4.12
	42	P	2	U	U									LN	6.07
	43	Q	2								LN				4.36
	44	R	2									LN			3.26
	45	S	2	U	U						LN				8.26
	46	T	2	U	U							LN			6.29
	47	U	2	U	U										5.03
	48	V	2					N			LN	LN	LN	LN	7.44
	49	W	2	U	U	U	U	N	N	N	LN	LN	LN	LN	7.44
	50	X	2	U	U			N	N	N	LN	LN	LN	LN	7.23
	51	Y	2	U	U			N		N	LN	LN	LN	LN	7.08
	52	Z	2					N		N	LN	LN	LN	LN	5.18
	53	A	2S					N							6.08
	54	B	2S							N					4.46
	55	D	2S										LN		4.01
	56	O	2S											LN	3.21
	57	Q	2S								LN				4.39
	58	R	2S									LN			3.21
	59	W	2S	U	U	U	U	N	N	N	LN	LN	LN	LN	8.1
	60	X	2S	U	U			N	N	N	LN	LN	LN	LN	8
	61	Y	2S	U	U			N		N	LN	LN	LN	LN	8.04
	62	Z	2S					N		N	LN	LN	LN	LN	6.32
	63	A	1S					N							5.08
	64	B	1S							N					5.06
	65	D	1S										LN		3.2
	66	O	1S											LN	3.23
	67	Q	1S								LN				4.2
	68	R	1S									LN			4.04
	69	W	1S	U	U	U	U	N	N	N	LN	LN	LN	LN	7.25
	70	X	1S	U	U			N	N	N	LN	LN	LN	LN	7.01
	71	Y	1S	U	U			N		N	LN	LN	LN	LN	7.11
	72	Z	1S					N		N	LN	LN	LN	LN	6.19
1995-2016	73	A	2					N							5
	74	B	2							N					4.21
	75	D	2										LN		4.05
	76	O	2											LN	5.21

The first grouping to form, and which is the most statistically significant, are cells west of the Rockies. This result can also be readily seen in the cell metric plots, which shows dramatic differences in reported tornado occurrence rates. For example, the three cluster results show a coastal and Great Lakes cluster forming around the edge of the broad central red cluster. Next, we see an Appalachian Mountain-New England break out along with the NW area of the central cluster. This appears to reflect the weakness of moderate and strong tornadoes in these areas, but there are also some similarities in mean elevation, and tornado path direction, for example (refer to the metric plots).

The breakpoint for Run 23 is 8.41. The 8 and 9 cluster groups show tornado climatology regions around the "hot center" that largely follow the main physiographic features of the US. The 9 cluster groups show that the Appalachian System breaking away from the Dakotas' region. Beyond that, we see small changes for smaller groups of cells regarding region membership. Complex areas like the Great Lakes, the mountainous western US, and areas around the center are mostly affected with relatively small changes. Three clusters out of the 9 cluster results are in the western US. In this region, the tornado occurrence rate is very low and many cells have no tornadoes.[24]

The continuity of the general shape of the large broad region beyond the breakpoint tends to demonstrate the validity of the BBP calculations (see $R^2_{partial\,(i)}$ in Appendix B.2). For example, we see that Cluster 22 shows the same general regionalization as Cluster 8 in Figure 2-20.

Figure 2-21 shows the W Series for the 1° shifted grid (Run 69). The results are similar with a few exceptions: the shifted grid results shows an extension of the center region into the Carolinas; the Appalachian System is distinct from the Dakotas by Cluster 8 in the shifted grid (Run 69) whereas it takes until Cluster 9 in Run 23 for this to occur; the latitude at which the boundary between the Dakotas region and the west Texas region varies from southern Nebraska to the Texas Panhandle. These variations in where the clusters form suggest uncertainties in the actual division of distinct tornado climatologies that depend on grid location.

The 8 cluster results (near BBPs) for the W Series 2° and 2° shifted grids are given in Figure 2-22. These plots show the central cluster extension into Georgia and the Carolinas. Due to the averaging of the tornado metrics over much larger areas that the 1° grids, the tradeoff in grid size can be seen in areas where there may be smaller scale differences in risk that are not apparent in the 2° results. Another difference is that the Appalachian System area does not form a separate cluster until the 12th Cluster for both the 2° and 2° shifted grids (see Appendix B.4). Cell memberships along the coast and at the periphery of the central region also vary with changes in grid size (averaging area).

A larger set of plots for the W (and other series) are provided in Appendix B.4.

[24] Previous work (e.g., Ramsdell and Rishel (2007), Twisdale et al. (1981)) shows that tornado risk in the western US is much less than the rest of the country. Due to the low level of risk and the complexity of potential sub-regions within the western US, our discussion of the cluster results focuses on the central and eastern US.

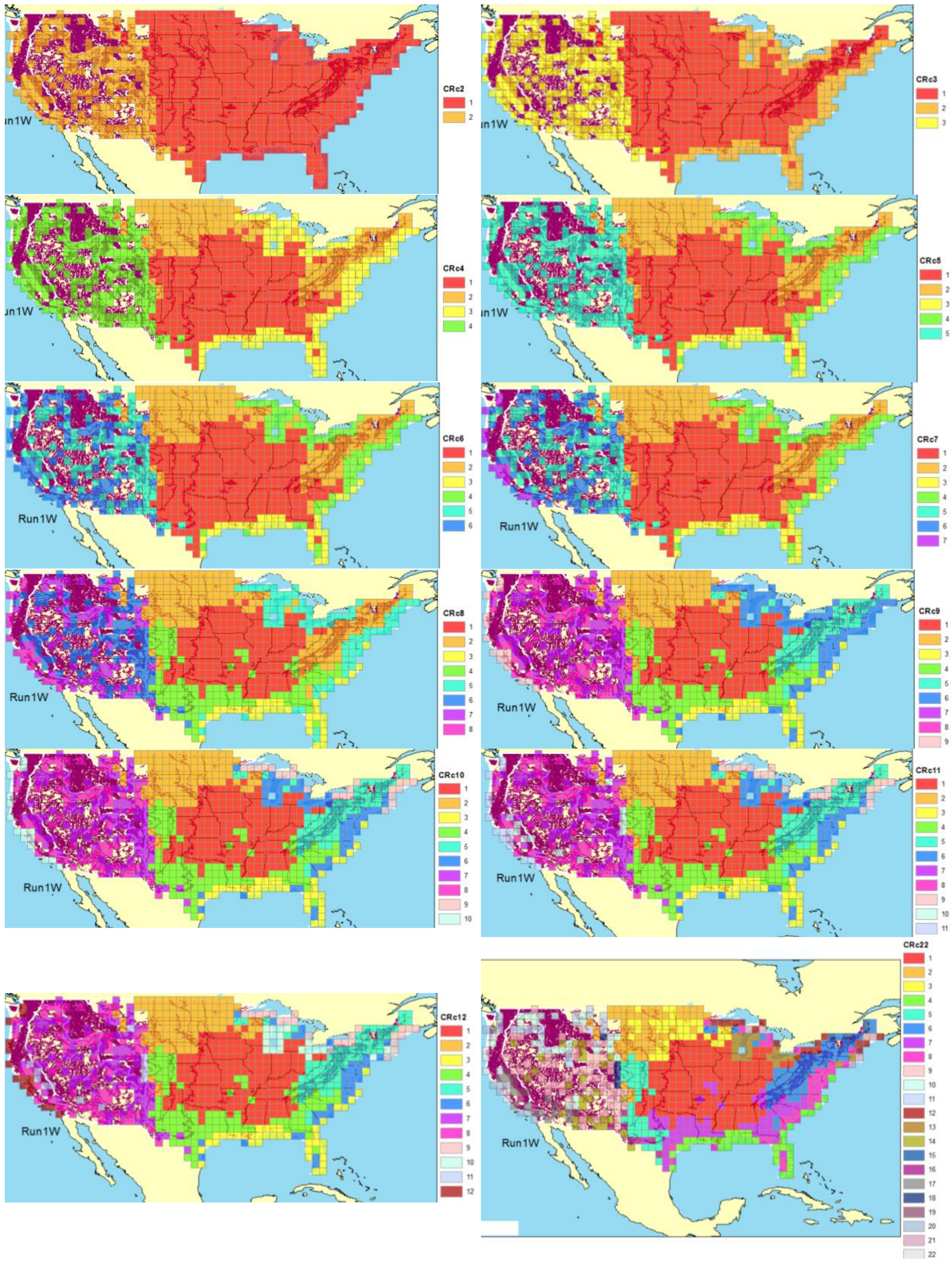

Figure 2-20. W Series 1°Grid Clusters (All Metrics, Run 23)

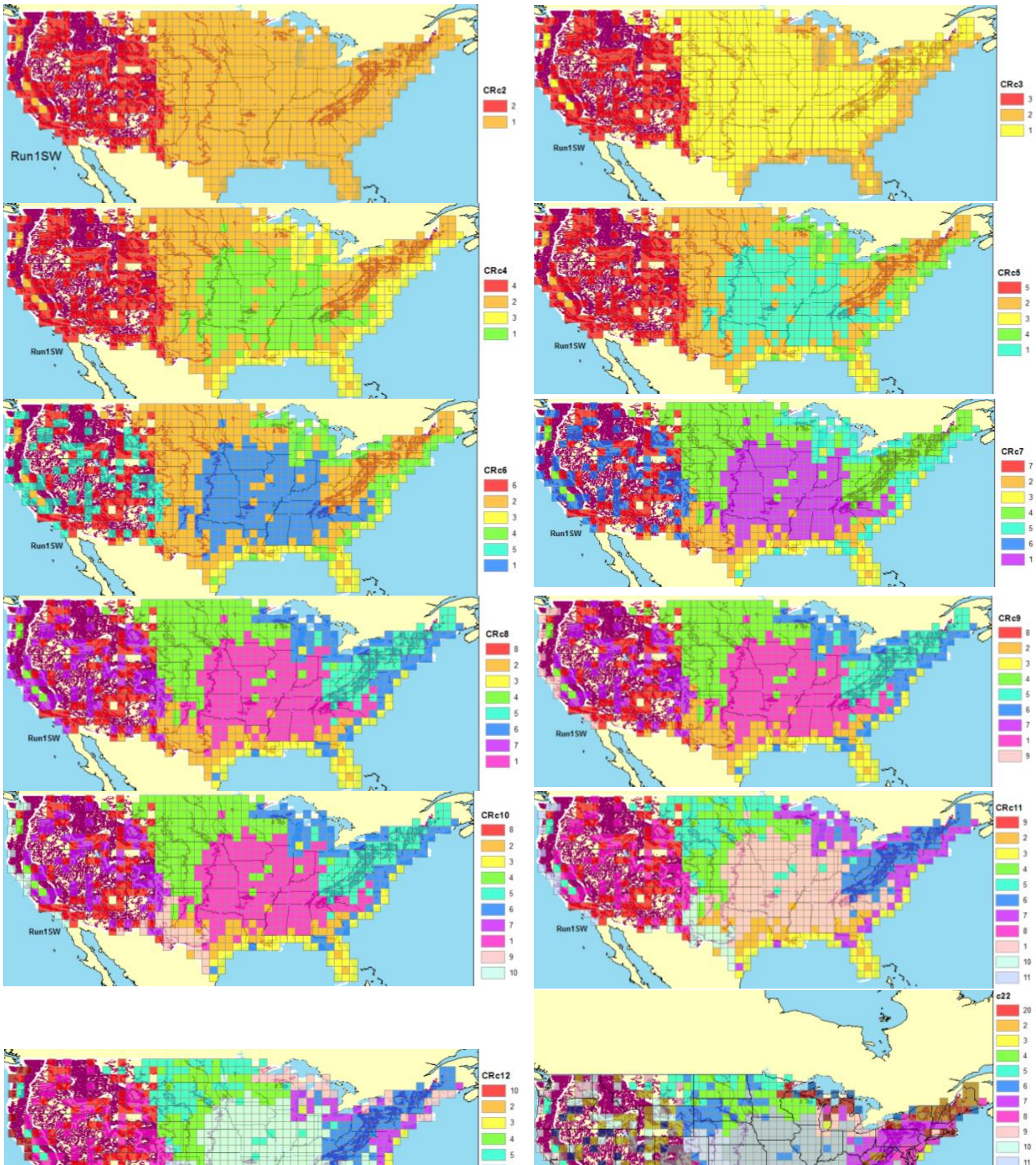

Figure 2-21. W Series 1° Shifted Grid Clusters (All Variables, Run 69)

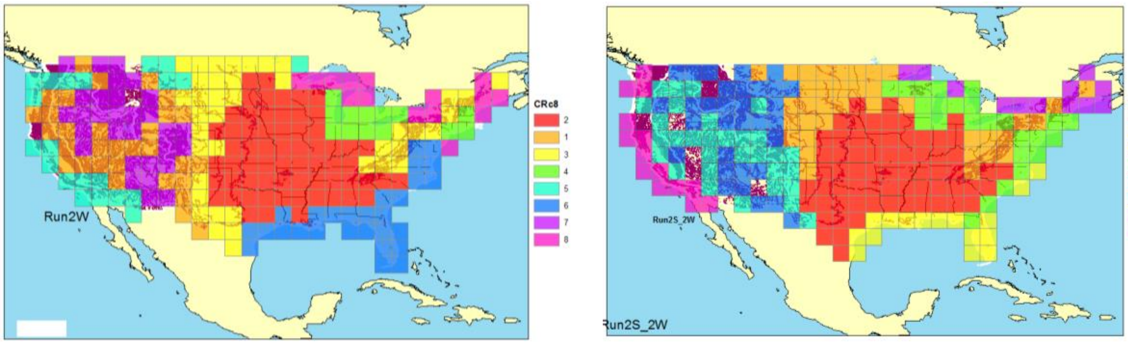

a. 8 Cluster for 2° Grid b. 8 Cluster for 2° Shifted Grid

Figure 2-22. W Series 2° and 2° Shifted Grid Clusters Near BBP (Runs 49 and 59)

Y Series (No Physiographic Metrics). The Y series includes all tornado metrics with latitude and longitude. No physiographic variables are included. This series provides a view of how the regions form without knowledge of mean elevation, standard deviation of elevation (ruggedness), or adjacent large bodies of water. Figure 2-23 shows the results for the 4 grids near BBPs. We see very similar formations with just tornado metrics and similar effects of grid size. There is more randomness within the formed regions when physiographic variables are not used and less connectivity in some areas near prominent physiographic features, such as mountains and water bodies. This effect is more apparent in the 1° grids. For example, for the 1° shifted grid at BBP we see more random cells within the central region, the Appalachians, along the coast, in the Dakotas, and Texas than the respective plots in Figure 2-20 and Figure 2-21. Hence, the additional physiographic information tends to provide some additional regional "glue," which eliminates some randomness for these 1° cells.

An important point is that the cluster analysis without the physiographic variables produce essentially the same regions as analyses with physiographics.

Z Series (All Metrics Except Latitude and Longitude). Figure 2-24 shows the results near the BBP for the 4 grids when all metrics are used except latitude and longitude (LL). In these figures, the clusters form without any cell location information. Without latitude and longitude data, there is much more randomness in the 1° results compared to the 2° results.

Use of Modern Era Data. We executed runs for the 2° grid with only the modern era data (1995-2016), which has about ½ of the number of tornadoes as the 1950-2016 dataset. Figure 2-25 shows these results near the BBP. We see similar regionalizations but with more randomness in the clusters due to the reduced amount of data.

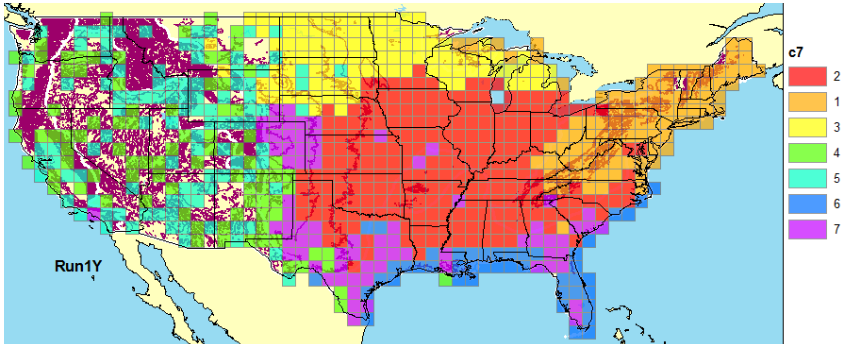

a. 1° Grid Results at 7 Clusters

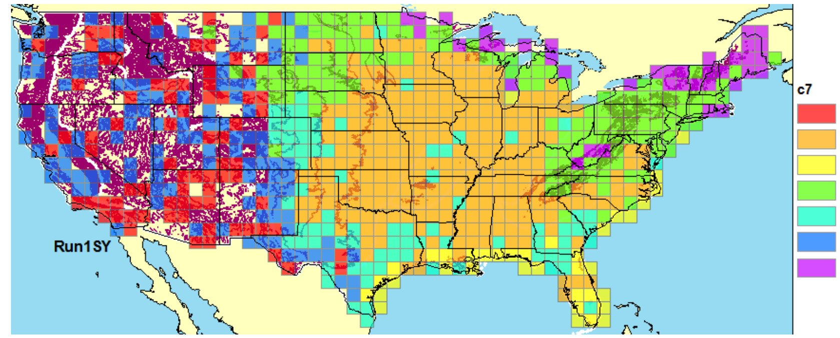

b. 1° Shifted Grid Results at 7 Clusters

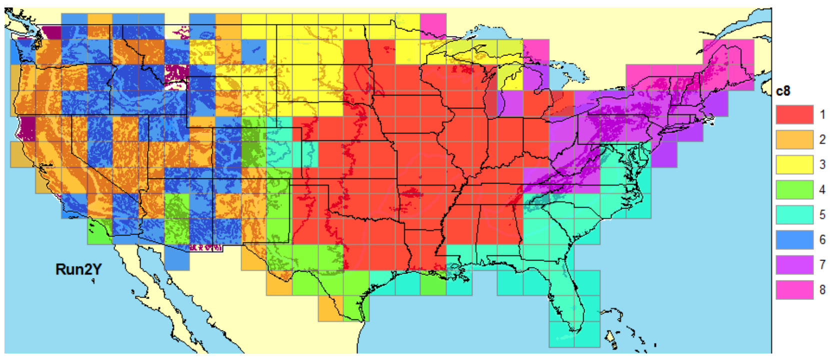

c. 2° Grid Results at 8 Clusters

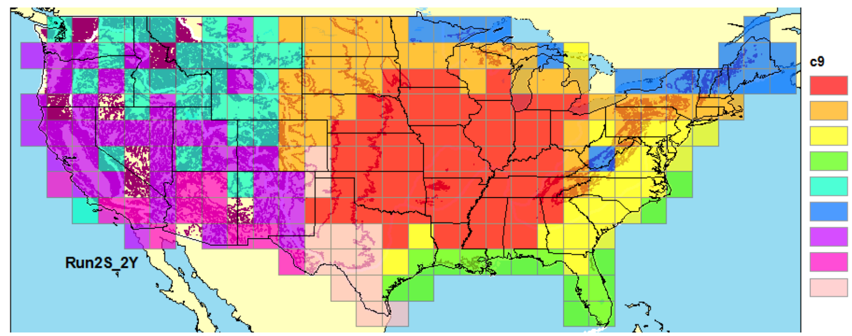

d. 2° Shifted Grid Results at 9 Clusters

Figure 2-23. Y Series Clusters Near BBP (No Physiographic Metrics)

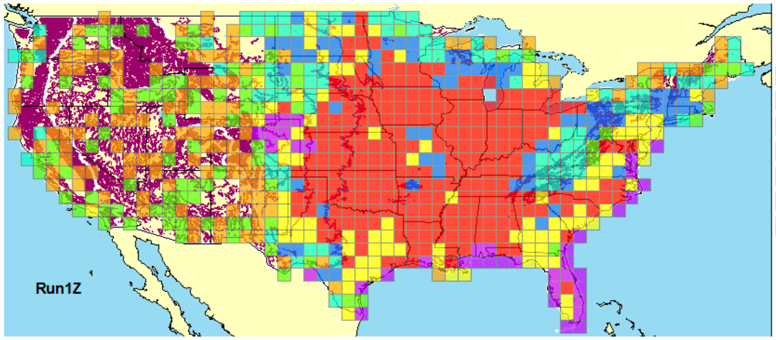

a. 1° Grid Results at 7 Clusters

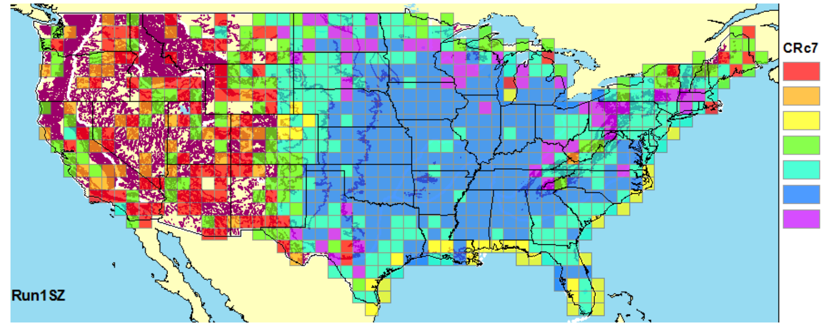

b. 1° Shifted Grid Results at 7 Clusters

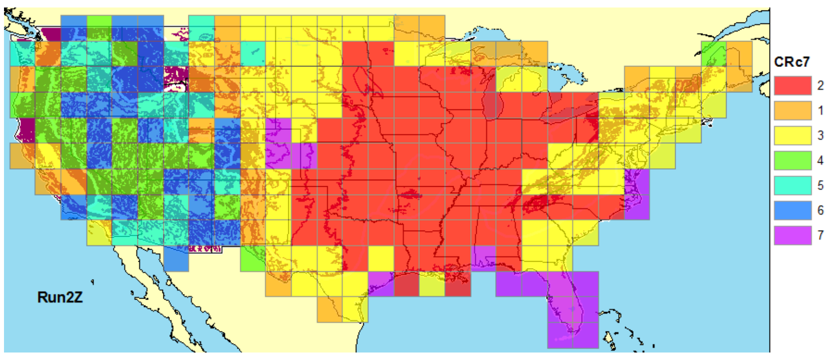

c. 2° Grid Results at 8 Clusters

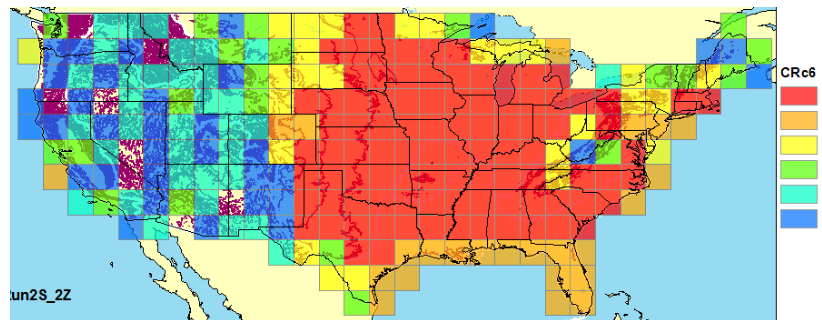

d. 2° Shifted Grid Results at 9 Clusters

Figure 2-24. Z Series Clusters Near BBP (All Metrics But LL)

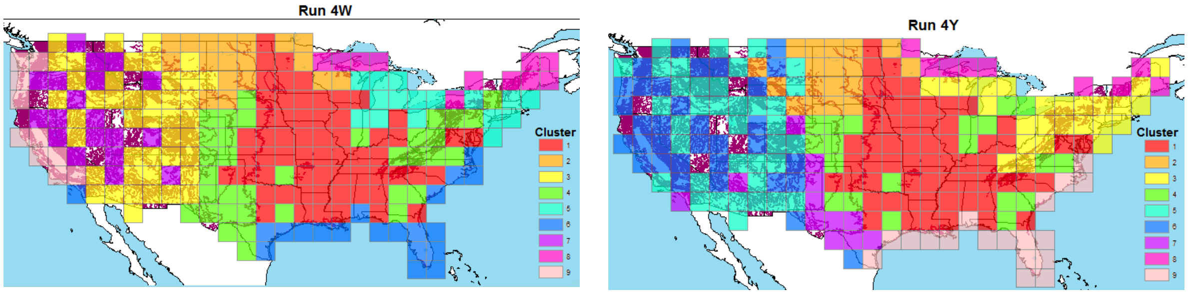

Figure 2-25. W and Y Series 2° Clusters Near BBP (1995-2016)

2.5. Hurricane Spawned Tornadoes (HST)

The formed tornado regions for various grids in both the W and Y series show a thin region forming along the Atlantic and Gulf coast. Further, in the Appendix B.3, we see similarities in the single tornado metric runs, like TDPY and moderate OR break point clusters (without latitude and longitude). The cell metric plots in Figure 2-19 show distinction in this area for TDPY and OR all. The fact that these metrics, independent of the land fraction metric, show climatology differences indicate that this region is characterized by higher occurrence rates, dominated by F/EF0 and F/EF1 events. For purposes of finalizing tornado regions, we examine the role of hurricane-spawned tornadoes and how far inland HSTs influence tornado climatology.

Past research has been performed on the likelihood of tornado genesis during a tropical cyclone event-making landfall in the United States. This past research has largely focused on tropical cyclone planning and preparedness. Similarly, tornadoes that could be attributed to a tropical cyclone event were identified herein, but with the aim of determining the significance of hurricane associated tornadoes relative to the non-hurricane historical tornado record.

Previous research has shown that most tropical cyclone generated tornadoes typically occur within 24 hours of landfall (Hill et al., 1966; Novlan and Gray, 1974; Gentry, 1983; McCaul, 1991) and in the outer rainbands of the hurricane structure (Hill et al., 1966; Novlan and Gray, 1974). It has also been found that approximately 85% of tropical cyclone induced tornadoes are attributed to hurricane strength storms (Weiss, 1985) and that the likelihood of tornado genesis increases with tropical cyclone intensity (Hill et al., 1966; Novlan and Gray, 1974; Gentry, 1983; Weiss, 1985; McCaul, 1991). Based on these findings, we focus on HSTs and investigate the inland extent that these events influence tornado climatology. The NOAA Hurricane Research Division’s (HRD) HURDAT2 hurricane database and the Storm Prediction Centers (SPC) tornado database were used in this assessment, including all events spanning the period 1950 to 2016.

2.5.1. HST Analysis

Our analysis uses only tropical cyclones of hurricane strength, and we use conservative limits to identify historical tornadoes that could be attributed to a hurricane. Any tornado that occurred within 1 day and approximately 300 miles (480 km) of any point along a hurricane track (not limited to landfall time/location) were retained. There are 1537 of these events, which are shown in Figure 2-26 and correspond to about 2.5 % of all reported U. S. tornadoes. Approximately 10

% of all tornadoes within 100 miles (160 km) of the coastline may be attributed to a hurricane event, as shown by the solid black line in Figure 2-27. Plotting the percentage of tornadoes attributed to a hurricane versus distance by EF-Scale magnitude ratings shows that EF-3 (dashed blue line) and EF-4 (dashed red line) hurricane induced tornadoes are more likely to occur very near the coast and more drastically decrease in likelihood as the distance is increased compared to weaker tornado events. No F/EF-5 (dashed green line) magnitude hurricane induced tornadoes were identified in the 66-year database; furthermore, no F/EF-5 tornadoes (hurricane induced or not) were found within approximately 125 miles (201 km) of the coast.

Figure 2-28 shows the percentage of tornadoes attributed to a hurricane on a 0.1° (6.9 miles) (11 km) grid basis within a radius of 50 miles (80 km) (0.72°), 100 miles (160 km) (1.45°), and 200 miles (320 km) (2.89°) of a grid point, respectively. Using a 50-mile (80 km) smoothing parameter, local hotspots of hurricane-associated tornadoes can be seen along the Texas and the Florida panhandle coastlines and inland in regions of North Carolina and Virginia. These local regions are highly dominated by a small number of hurricanes that have produced very large (100+) tornadoes upon transitioning from land to sea. As the smoothing parameter distance is increased, the percentage of hurricane-associated tornadoes becomes nearly constant along the coastline. For the 200-mile (320 km) smoothing distance, the percentage of HSTs resembles the mean percentage given in Figure 2-27.

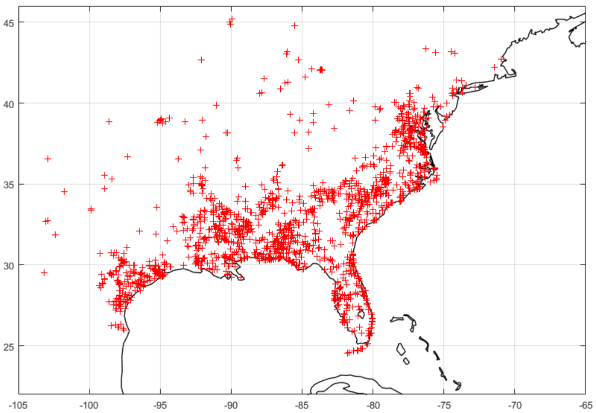

Figure 2-26. Tornadoes Occurring Within One Day and Approximately 300 Miles (480 km) of a Hurricane

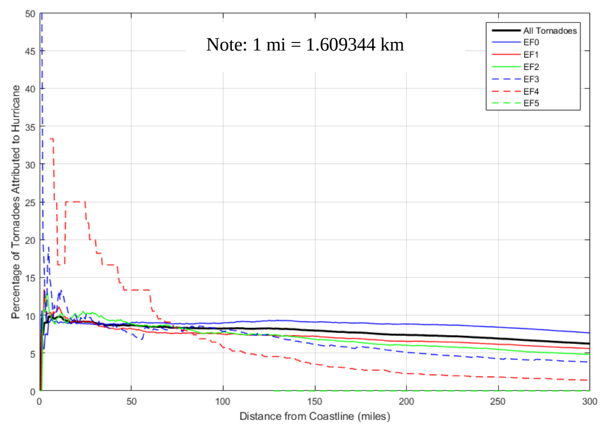

Figure 2-27. Percentage of Tornadoes Attributed To a Hurricane

Coastal segments, shown in Figure 2-29, were used to assess and display hurricane associated tornado characteristics against the non-hurricane tornado population. For example, Figure 2-30 shows the percentage of tornadoes attributed to a hurricane within approximately 25, 50 and 100 miles (40.2, 80 and 160 km) of the coast for each of these segments. The start latitude and longitude location of each tornado record was used to calculate the distance to the coastline. In each of the coastal distance ranges, all tornadoes that distance or less to the coastline were considered. The highest percentages of hurricane-associated tornadoes were observed near the coasts of Alabama and the Carolinas.

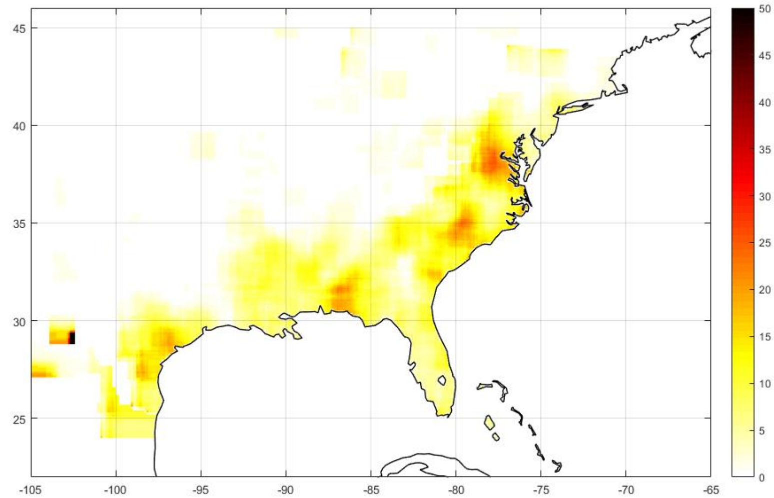

a. Radius of 50 miles (80 km) (0.72°)

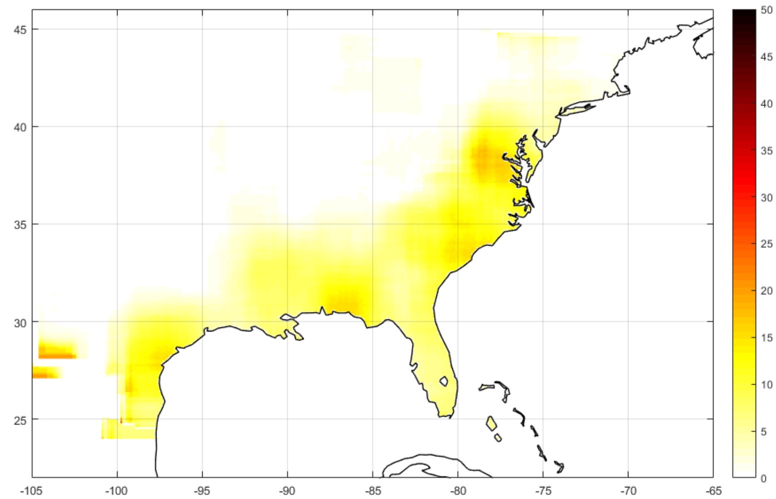

b. Radius of 100 miles (160 km) (1.45°)

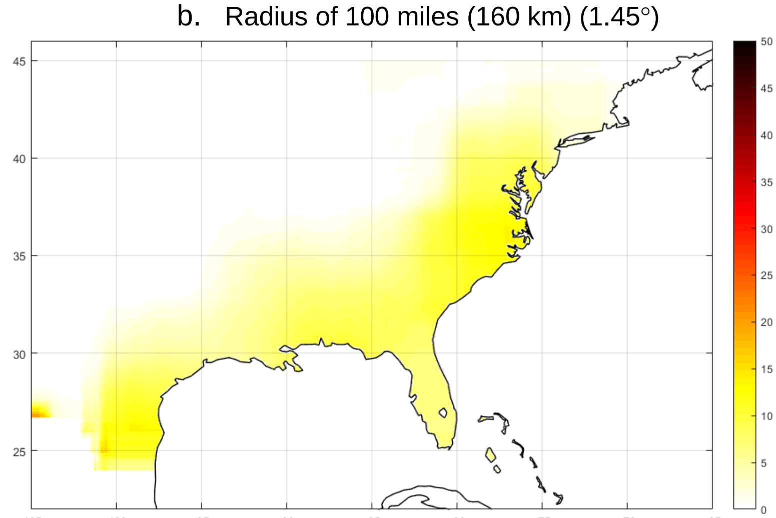

c. Radius of 200 miles (320 km) (2.89°)

Figure 2-28. Percentage of HSTs within a Radius of a Grid Location

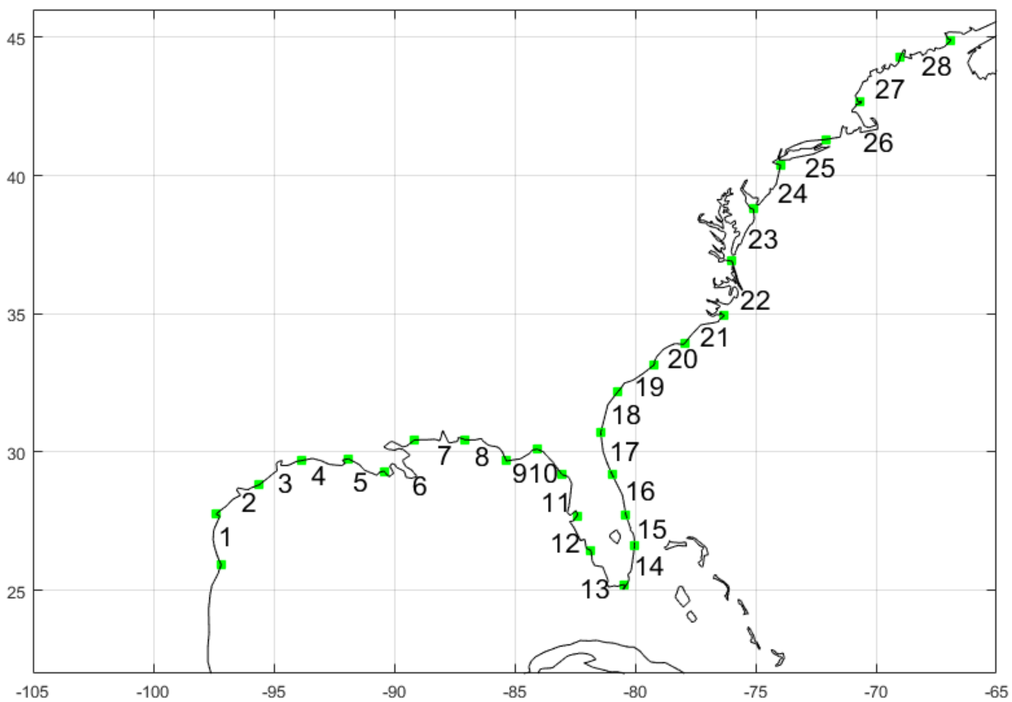

Figure 2-29. Coastal Segments Used To Compare Hurricane Associated Tornado Population to All Tornado Population

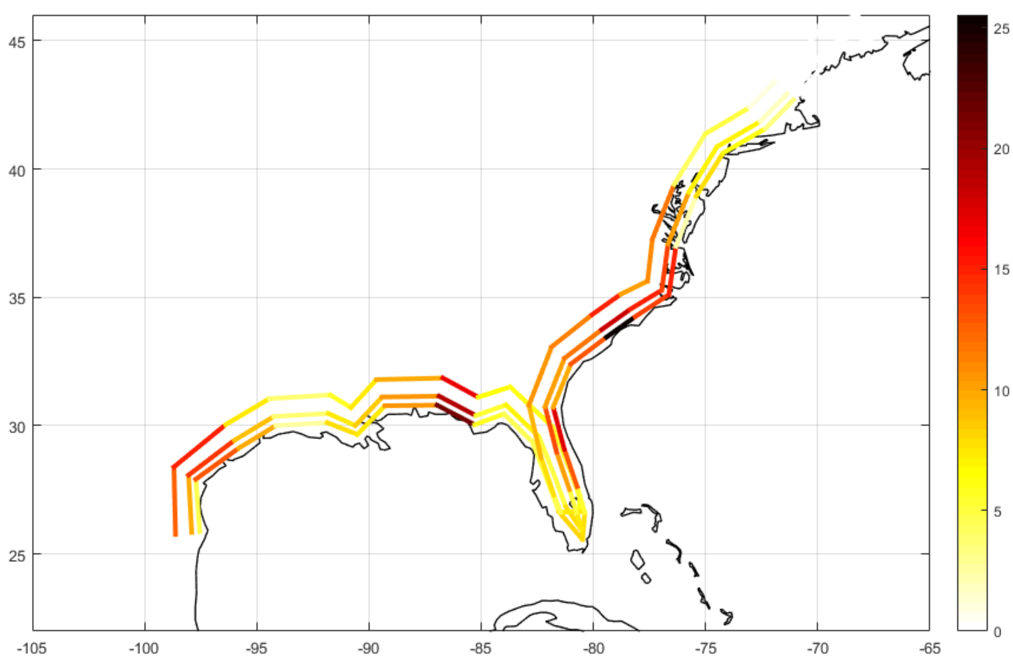

Figure 2-30. Percentage of Tornadoes Associated with a Hurricane Within Approximately 25, 50, and 100 Miles (40.2, 80, and 160 km) of the Coastal Segments Shown in Figure 2-29.

2.5.2. HST Intensity Distribution

Within each of the distance ranges, statistical tests were performed on the distribution of tornado intensity (F-/EF-Scale) between the hurricane and non-hurricane associated tornado populations. The statistical tests included the Kolmogorov-Smirnov (KS) test of equivalence of distributions, the t-test of the equivalence of means, and the F-test of the equivalence of variance. Counts of hurricane and non-hurricane associated tornadoes are provided in Table 2-4. The probability mass functions (PMFs) are presented in bar form in Figure 2-31 for both tornado populations in each of the distance to coastline ranges. Within 25 and 50 miles (40.2 and 80 km) of the coastline, the hurricane and non-hurricane associated tornado intensity distributions pass all three statistical tests at the 95% confidence level, indicating the magnitudes of the population of hurricane associated tornadoes are not statistically different than those of the non-hurricane associated tornado population. Within 100 miles (160 km) of the coastline, both the KS-test and t-test fail at the 95% confidence level, indicating the overall distributions and the mean of the distributions are statistically different. The PMFs within 100 miles (160 km) to the coastline indicate that EF0 tornadoes make up a larger portion of the hurricane associated tornado population than the non-hurricane associated tornado population.

Our HST modeling indicates that a separate tornado climatology is warranted for the Gulf and Atlantic coasts of the US. HSTs are an important contribution to the climatology of this area. The tornado occurrence rate (per square mile) is higher than the center of the country. Statistical tests indicate that F/EF0 HSTs occur at a more statistically significant rate than non-HSTs. The extent of this distance inland indicates that the width of this HST region between 100 and 200 miles (160 and 320 km) inland is reasonable and captures the HST impacts on the tornado climatology.

Table 2-4. Counts of Hurricane and Non-Hurricane Associated Tornadoes by Distance from the Coast and EF-Scale Magnitude (A Magnitude of -1 Indicates a Missing Record)

	Distance to Coast (miles)	EF-Scale Magnitude						
		-1	0	1	2	3	4	ALL
Hurricane	25	0	185	109	35	6	2	337
	50	0	310	168	55	10	2	545
	100	0	465	268	93	17	2	845
Non-Hurricane	25	1	1952	1017	332	53	3	3357
	50	1	2965	1756	581	114	7	5423
	100	1	4560	3224	1142	228	15	9141

Note: 1 mi = 1.609344 km

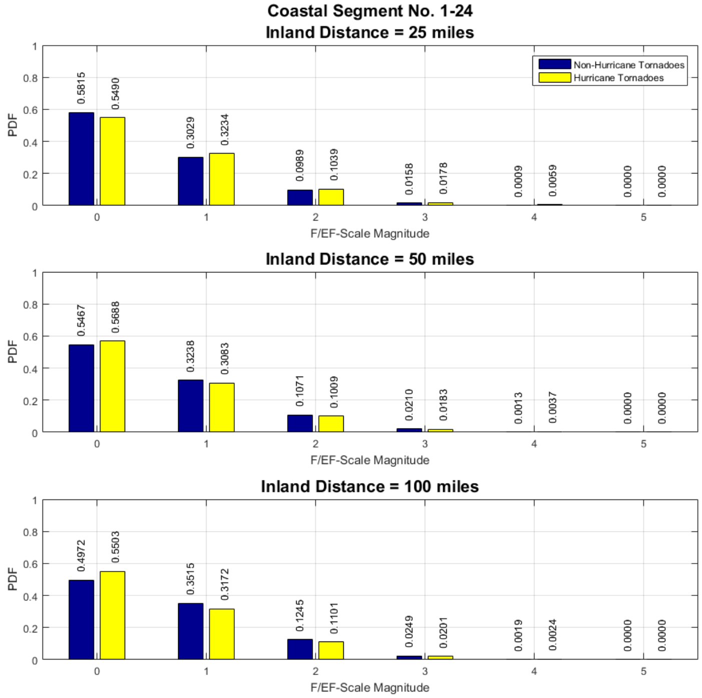

Note: 1 mi = 1.609344 km

Figure 2-31. Probability Mass Functions of the Magnitude of Non-HSTs (Yellow)

2.6. Regions with Boundary Uncertainties

We use the cluster analysis results and the analysis of HSTs (Section 2.5) to develop smoothed region contours that recognize the main regional climatologies as developed in Section 2.4. From the cluster series, we use the W (all metrics) and Y Series (tornado metrics). With 4 grids for each, we have 8 modeled sets of outputs from which to develop the regions and region-boundary uncertainties.

Epistemic Implementation. Each of these model outputs provides a viable spatial model of tornado climatology. Hence, by considering 8 such model outputs, we introduce modeling (epistemic) uncertainties into the spatial analysis. Our approach is to envelope the model-derived regional boundaries and to use these envelopes to characterize the transition areas (distances) from one region to another, all within our goal of developing broad tornado regions. In this section, we attempt to reasonably develop the regional envelopes from the 8 sets of model results and the associated "median" boundaries. In Section 8, we use these results to develop a boundary uncertainty distance and apply Gaussian smoothing to the grid-based wind speeds. The Gaussian smoothing serves to transition the wind speed climatology from one region to another across the median boundaries.

Western Region (Region 1). West of the Rockies, one broad region is used due to low tornado risk. This western region is significantly different than the rest of the country, as indicated by the first cluster to break away from the rest of the country.

The boundary of Region 1 was determined by examining the western boundary in a number of cluster runs. For each run, the western boundary was traced, as shown in Figure 2-32. All of the boundaries were overlaid on the same map (Figure 2-33), and a maximum and minimum boundary were determined (Figure 2-34). A boundary central to the maximum and minimum boundaries, and east of the highest elevation areas was determined to be the median boundary of Region 1 (see Figure 2-35).

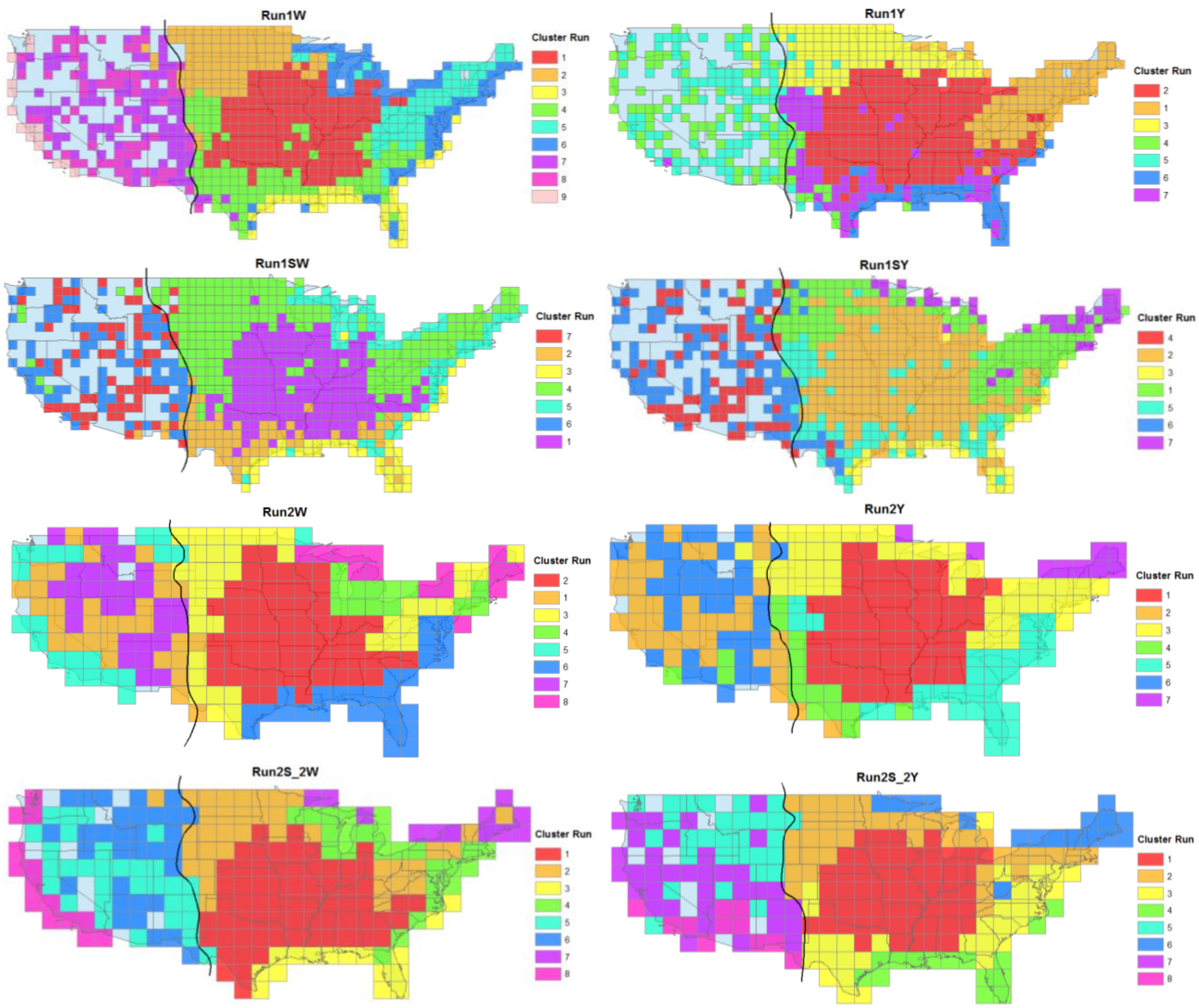

Figure 2-32. Outlines of Cluster Boundaries Separating Region 1

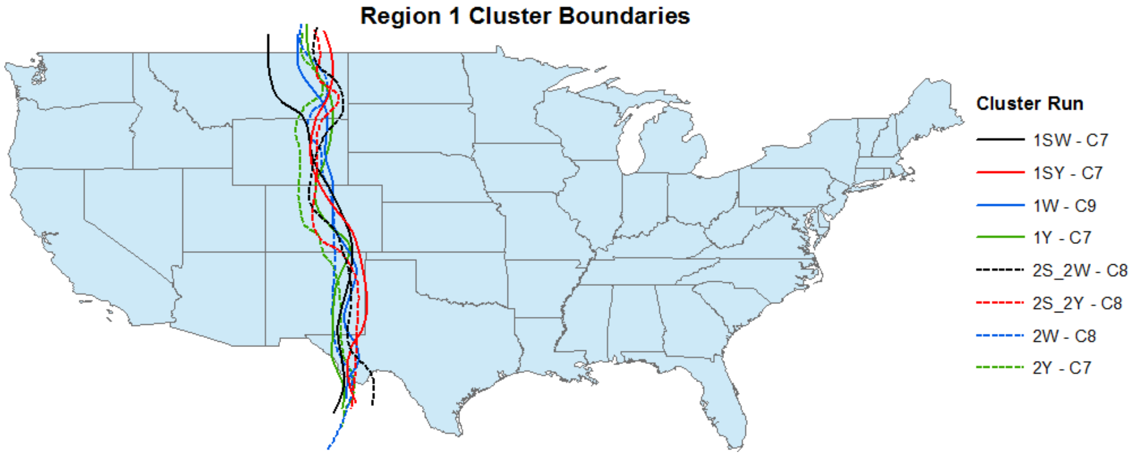

Figure 2-33. Region 1 Cluster Boundaries (Elevation (m))

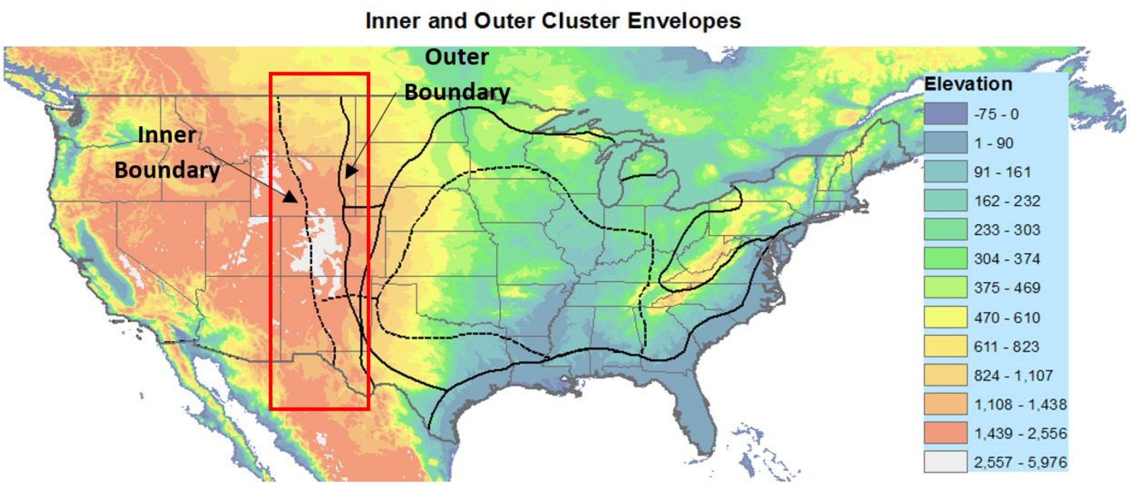

Note: 1 m = 3.28084 ft

Figure 2-34. Region 1 Inner and Outer Boundaries (Elevation (m))

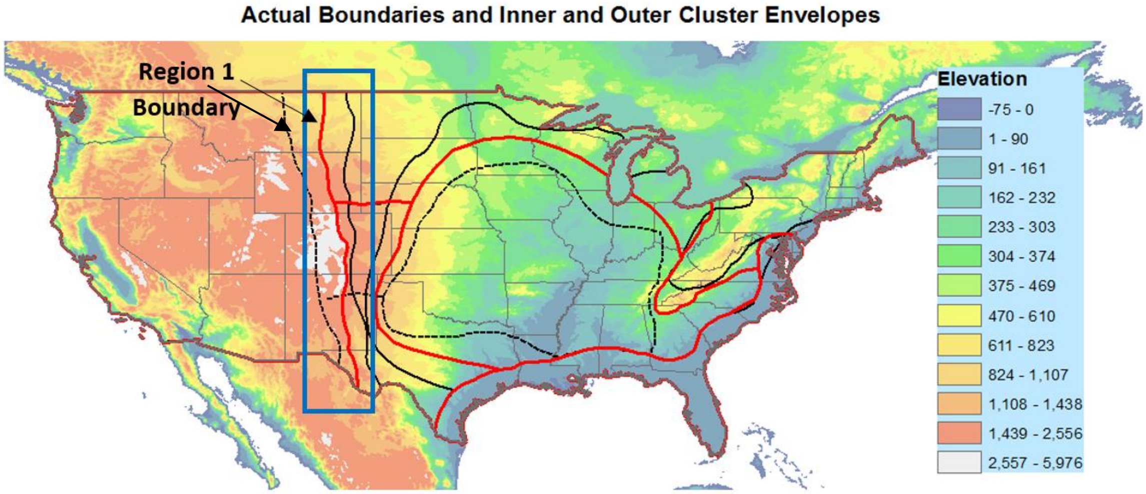

Note: 1 m = 3.28084 ft

Figure 2-35. Final Region 1 Boundary (Elevation (m)

Region 2 and Region 3. A North-South transition region is typically formed east of Region 1 and west of the central plains. This transition splits into a northern region (Region 2) from a southern region (Region 3). The boundary separating Region 2 and Region 3 is determined by tracing the boundary of the 8 model runs (Figure 2-36), and overlaying the boundaries on one map (Figure 2-37). The most northern and southern bounds based on these tracings are shown in Figure 2-38. The boundaries for half of the runs are almost overlapping, falling in the southern part of Wyoming and centrally in Nebraska. These northern boundaries were used to form the final Region 2-3 boundary, shown in Figure 2-39. This separation also tends to follow the TDPY and OR-all metric plots in Figure 2-19. The remaining boundaries for Region 2 and Region 3 were dictated based on analyses for Region 4.

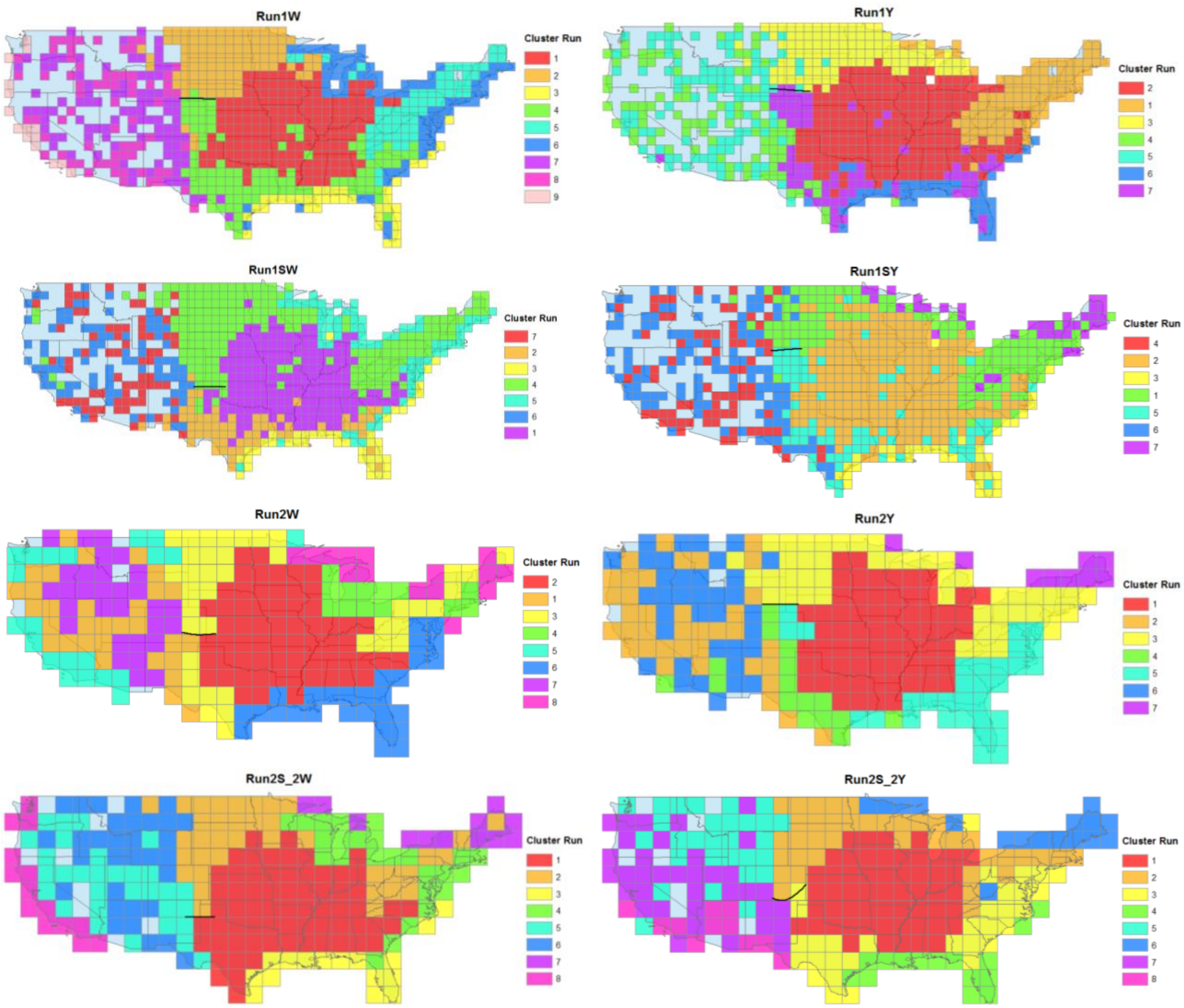

Figure 2-36. Outlines of Cluster Boundaries Separating Region 2 and Region 3

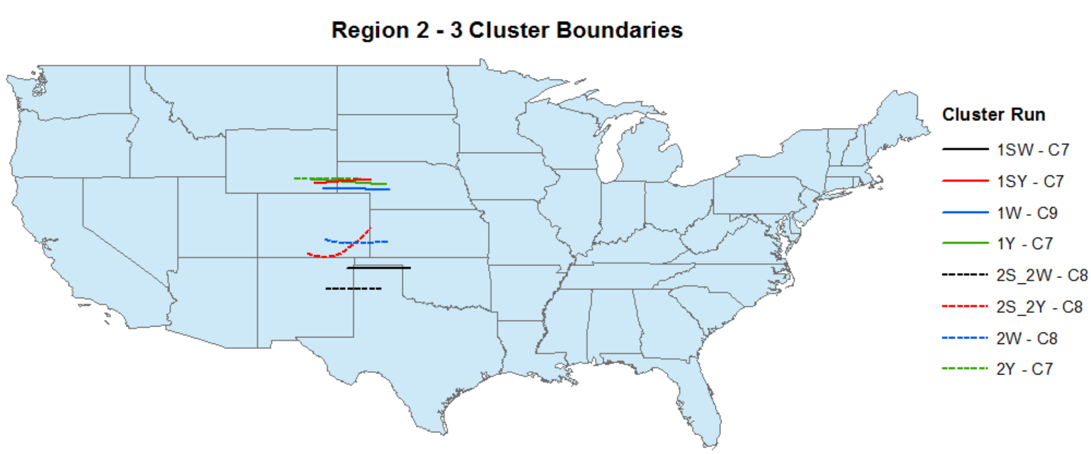

Figure 2-37. Region 2-3 Cluster Boundaries

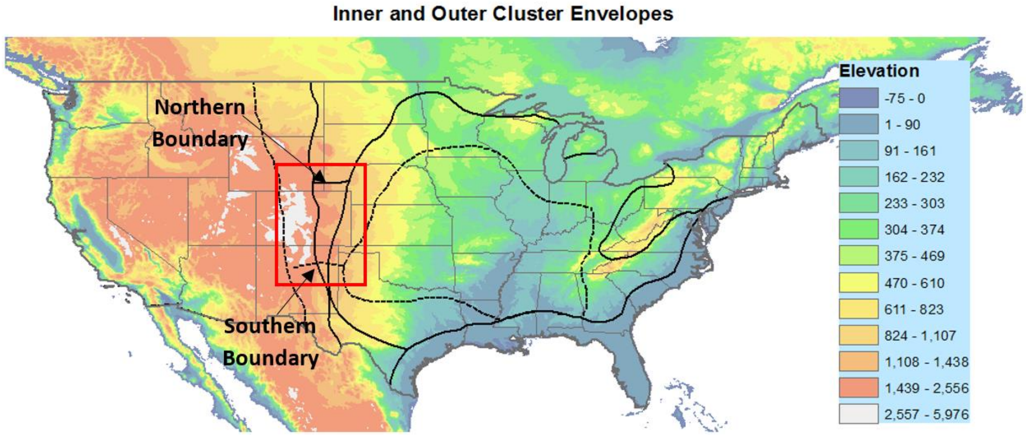

Note: 1 m = 3.28084 ft

Figure 2-38. Northern and Southern Extremes of the Region 2 to Region 3 Boundary (Elevation (m))

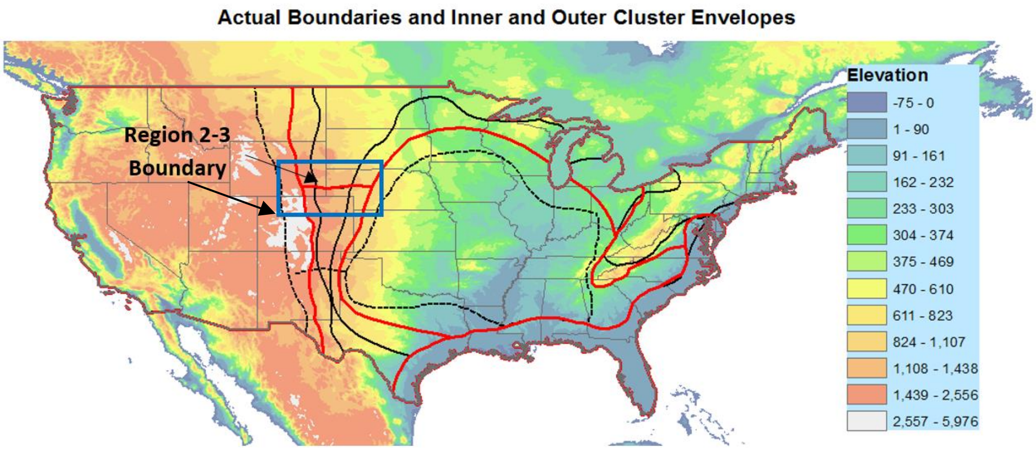

Note: 1 m = 3.28084 ft

Figure 2-39. Final Boundary Separating Region 2 and Region 3 (Elevation (m))

Central Regions (Region 4). The cluster results show that a broad, persistent central region exists, which is characterized by higher occurrence rates, higher occurrences of stronger tornadoes, and high point probabilities. Tracings of this central region from the 8 model runs are shown in Figure 2-40. Inner and outer cluster envelopes for Region 4 are given in Figure 2-41. The uncertainty distance in where the central region boundary falls is up to 300 miles (480 km). Additionally, many cluster results include an area protruding up into South Carolina and North Carolina in Region 4. The final Region 4 boundary (Figure 2-42) is determined to be approximately in the middle of the inner and outer boundaries, and it includes the Region 4 extension into the Carolinas. The extension into the Carolinas was included since it appears in 5 of the 8 plots in Figure 2-40.

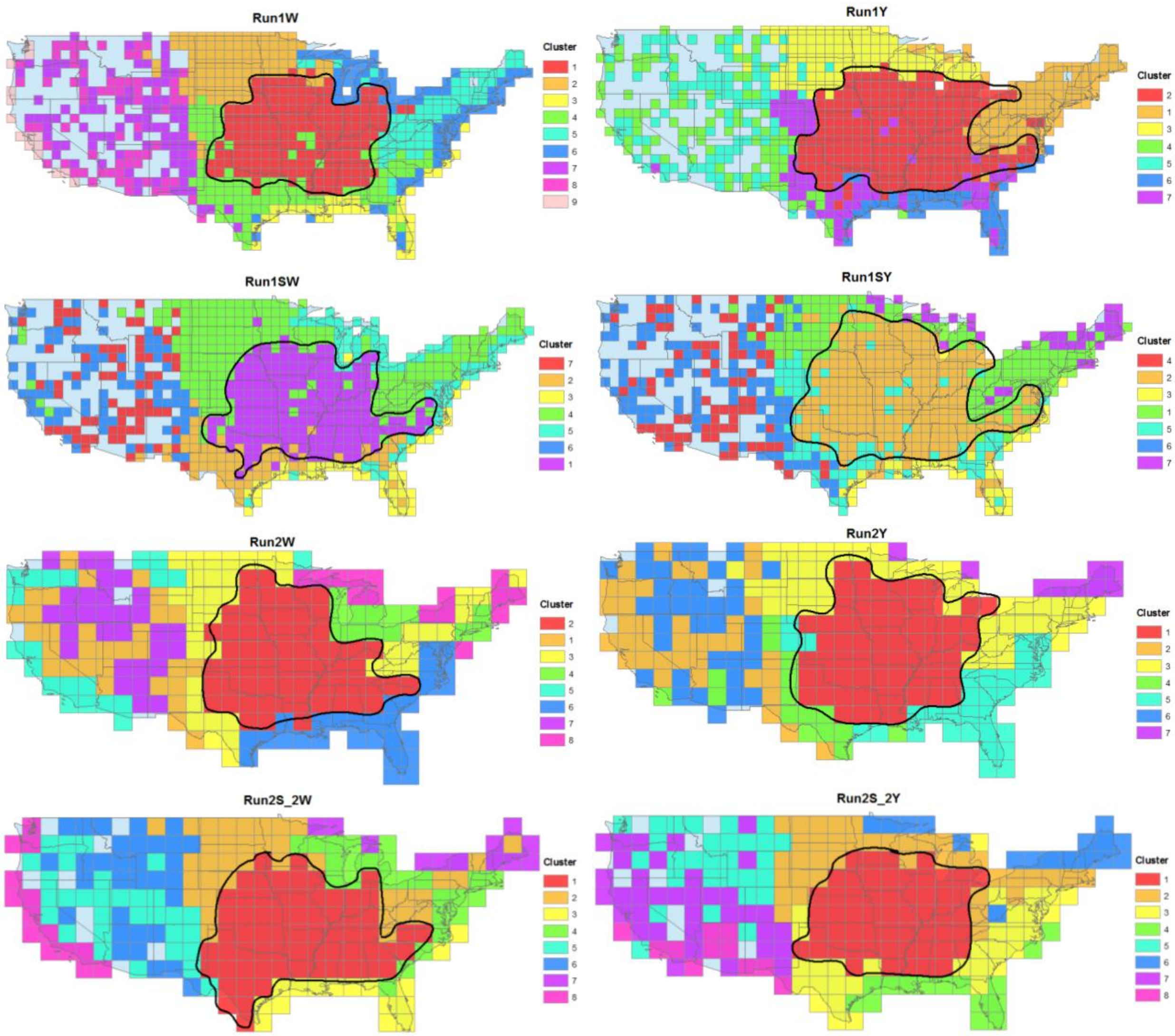

Figure 2-40. Region 4 Cluster Envelopes

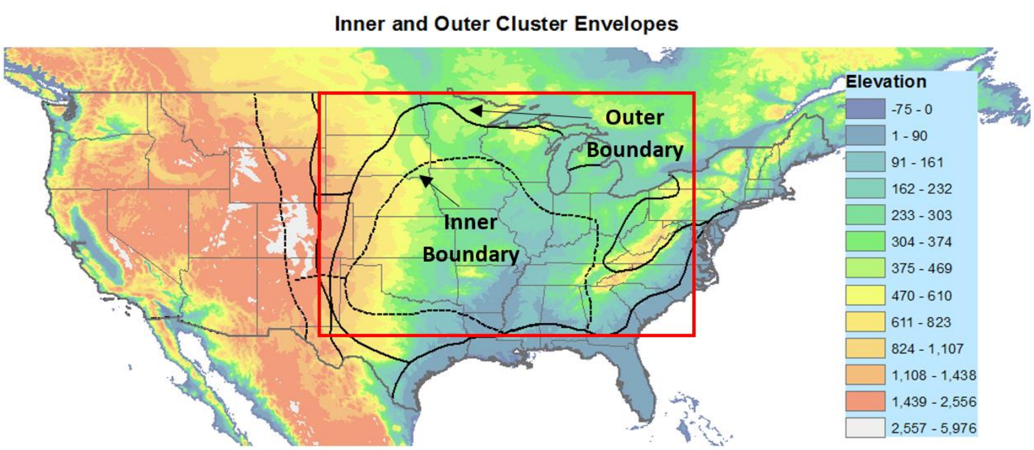

Note: 1 m = 3.28084 ft

Figure 2-41. Region 4 Inner and Outer Boundaries of Cluster Envelopes (Elevation (m))

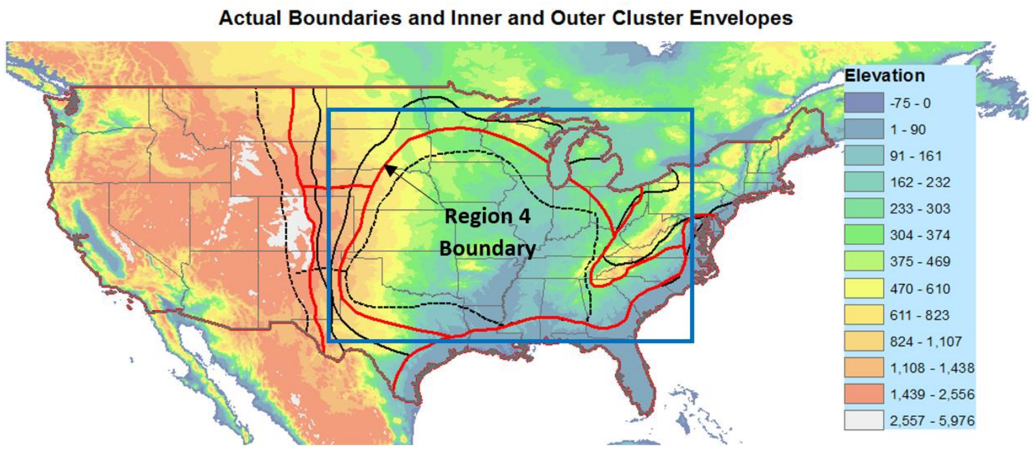

Note: 1 m = 3.28084 ft

Figure 2-42. Final Region 4 Boundary (Elevation (m))

Appalachian/Northeast Region (Region 5). The southern and southeastern boundaries of Region 5 were prescribed based on Region 4 and Region 6 boundaries. The boundary between Region 2 and Region 5, was set based on clustering the results and elevation trends, shown in Figure 2-43.

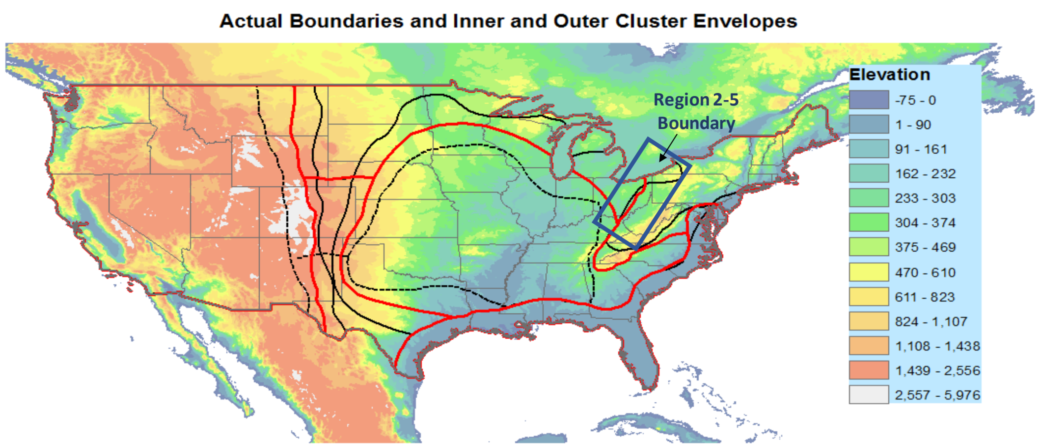

Note: 1 m = 3.28084 ft

Figure 2-43. Boundary between Region 2 and Region 5 (Elevation (m))

Coastal Region (Region 6). The Gulf and Atlantic coast region follows from the cluster maps and the HST analysis. We consolidate the coastal regions seen in Figure 2-40 in to a single region from Texas to the Chesapeake Bay. This region follows from the analysis of HSTs. Figure 2-44 shows the Region 6 boundary.

Final Regions. These 6 regions and their initial boundaries are given in Figure 2-45. This regionalization has some angular boundary intersections since it was developed generally as the mid-point of uncertainties in the 8 model run boundaries. We rely on the uncertainties and associated smoothing to average over the distinct climatology separations given in Figure 2-45.

As discussed in Section 8.2, we note that the boundary between Region 1 and Region 2 was subsequently adjusted westward to more closely follow the eastern edge of the Rocky Mountains, considering Canadian tornado data that became available later in the project. The

Region 2-5 boundary was also shifted slightly to the east, also to better follow elevation changes. These adjustments are described in Section 8.2. All of the region-level tornado statistics and hazard curves provided in this report are based on the region boundaries shown in Figure 2-45; only the final maps were drawn using the adjusted boundaries.

Table 2-5 gives the areas and tornado counts (1950-2016) for these regions. If a tornado crossed a region boundary, it was assigned to each of the crossed regions.

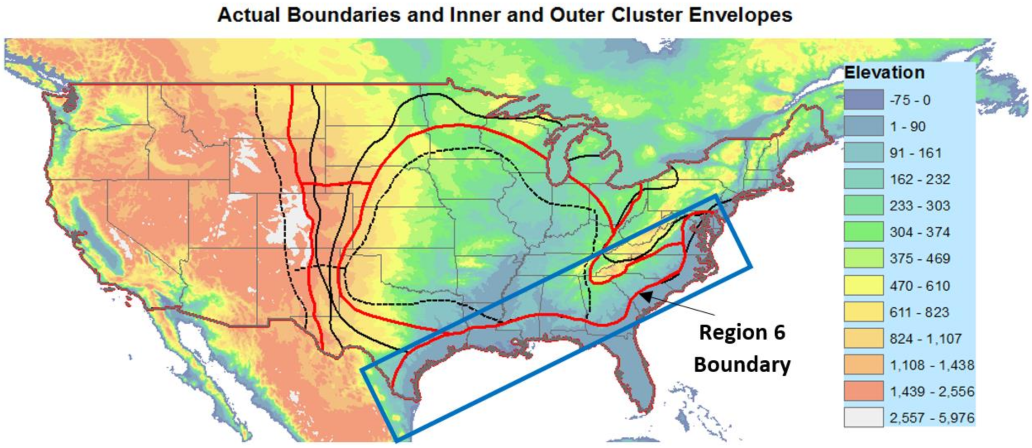

Note: 1 m = 3.28084 ft

Figure 2-44. Final Region 6 Boundary (Elevation (m))

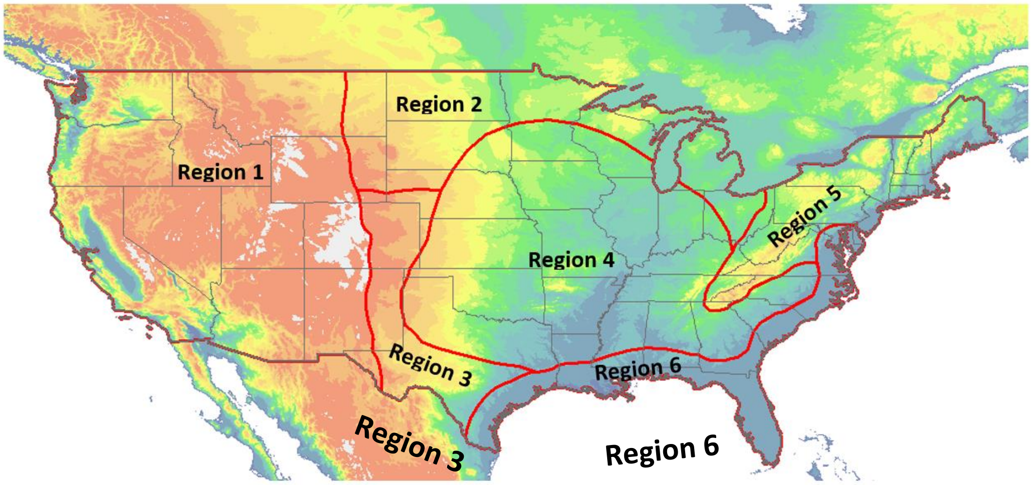

Note: 1 m = 3.28084 ft

Figure 2-45. Final Regions (Elevation (m))

Table 2-5. Area of Region and Number of Tornadoes within each Region (1950-2016)

Region	1	2	3	4	5	6
Region Area (sq mi)	1,043,932	359,330	204,664	913,341	250,134	232,116
No. Tors	2,015	6,013	4,751	35,900	2,689	9,938
Tors per sq mi per yr	2.9E-05	2.5E-04	3.5E-04	5.9E-04	1.6E-04	6.4E-04

Note: 1 mi^2 = 2.589988 km^2

2.7. Intra-Regional Analysis

The spatial patterns identified in the multi-variate analysis were selected near the BBP to develop broad regions with distinct tornado characteristics. The cluster-developed regions are intended to represent a reasonable high-level spatial pattern of tornado climatology.

Our focus on intra-regional analysis follows from: (1) the 8 model cluster results near the BBP; and (2), the HST analysis. The 8-model cluster results in Figure 2-40 shows several areas of interest. As previously discussed, Region 4 has a protrusion into Georgia and the Carolinas in about ½ of the cluster runs near the BBP. This result suggests that the protrusion may be a potential sub-region.

Another intra-regional area of interest regards Region 5. Region 5 has a south-west to north-east axis through mountainous terrain. We see from Figure 2-40 that the northern portion of Region 5 breaks away from the southern portion for Runs 1SY, 2W, 2S-2W, and 2S-2Y. Hence, we examine Region 5 to assess potential tornado occurrence rate weakening in the New England area.

A final area of interest is Region 6, which has multiple cluster variabilities in Figure 2-40. In addition, the HST analysis showed a declining tornado trend with distance from the coast; hence, we also examine potential sub-regions in Region 6.

Regions 1, 2, and 3 are generally more complicated regions for intra-region analysis. Regions 1 has very low tornado risk and is complicated by significant physiographic features within this region. One can see from Figure 2-40 that several clusters exist in Region 1 near the BBP. However, there is little connectivity with these clusters. Hence, we do not attempt to model tornado risk patterns within Region 1.[25] It remains a broad region and our analysis (in Section 3) will conservatively reflect the areas with high reported tornado densities.[26] Regions 2 and 3 border Region 4 and provide western transitions to Region 1. These regions have some intra-region variation as seen from the Cluster results in Figure 2-40. However, since our boundary uncertainty ranges in Figure 2-43 are very broad for Regions 2 and 3 (extending close to Canada and Mexico, respectively), intra-region variation is not analyzed for these two outward transition regions from Region 4.

In summary, our intra-region analysis is limited to specific cases of interest identified in the cluster analysis sequence and the variation of cell membership with series and grids. We do not consider small-scale variations in tornado risk.

---

[25] Most of the Region 1 population live in areas with low standard deviations of elevation and these areas have the highest tornado densities.
[26] The tornado risk for Region 1 is "best-estimate" for areas with low standard deviations of elevation, which is where the vast majority of people and structures are located. The Region 1 map wind speeds are believed to be conservative for other locations in the region.

2.7.1. Sub-region Analysis

We examine potential sub-regions using US Census Metro and Micro Statistical Areas (MMSAs) because we assume higher population and building density areas have higher tornado reporting efficiency. These MMSAs include counties associated with at least one urbanized area and at least a population of 50,000 (Metro) or between 10,000 and 40,000 (Micro) (US Census Bureau, 2017). Our approach consists of the following steps:

1. **Develop Initial Sub-regions**: Group together MMSAs by considering the natural connectivity/separation of their locations as well as similarities/differences in elevation metrics within the region.
2. **Perform Statistical Tests**: Determine if the sub-regions are statistically significant and how they group using multiple comparison means tests on mean tornado occurrence rates.
3. **Finalize Sub-regions**: Consolidate the initial sub-regions using the multiple comparison tests.

We used MMSAs to examine potential sub-regions. With this information, we examine tornado density conditional on population (US Census Bureau, 2017) and building density data developed in HAZUS (FEMA, 2006, 2007, 2011).[27] The developed MMSA groups are shown in Figure 2-46. From these MMSA groups, we developed tornado occurrence rates for multiple building density thresholds, as illustrated in Figure 2-47. The color code in Figure 2-47 shows how the mean allocated tornado occurrence rates (tornadoes per square mile per year) (tornadoes per square kilometer per year) vary by the specified building density (BD) threshold (buildings per square mile) (buildings per square kilometer). The numbers identify the MMSA groups. The black areas are the Micro Statistical Areas that meet the BD threshold shown for each figure. In examining the BD threshold data in Figure 2-47, we see greater variation and increases in tornado occurrence rates with increasing building densities. For example, for BD > 250, we can see a doubling or more of the tornado occurrence rates vs. the BD > 20 figure in some regions.[28]

[27] The use of building density thresholds is developed in Section 3 for occurrence rate modeling considering population bias.
[28] This characteristic is the theme developed in Section 3 for the analysis of tornado occurrence rates and population bias effects.

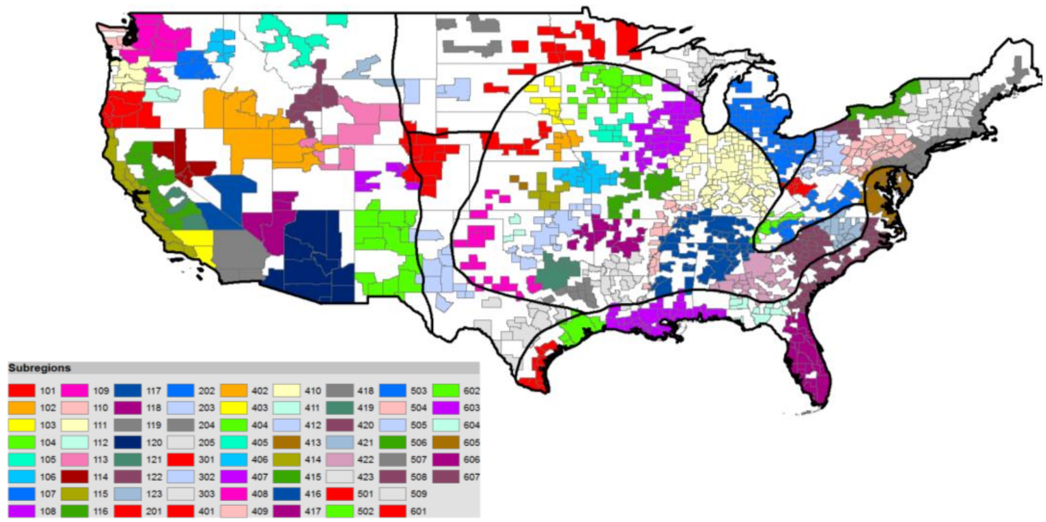

Figure 2-46. Metro and Micro Statistical Area Groupings to Form Initial Sub-regions

2.7.2. Mean Comparison Tests

We use SAS (SAS, 1992) procedures for analysis of variance and mean comparison tests (Waller-Duncan, Tukey's Studentized Range, and Least Significant Difference (LSD)) to analyze differences in mean tornado occurrence rates across potential sub-regions. We follow the convention of applying the mean comparison tests only if the null hypothesis that all the sub-region means are equal is rejected by an overall F test. If the overall F test is not significant, we do not perform the mean comparison tests. The Waller-Duncan test requires 3 means for comparison purposes so it was not used for comparisons of 2 means. These tests are applied separately for each BD threshold considered (BD0, BD20, BD50, BD100, and BD250).

2.7.2.1. Region 4

Region 4 sub-regions were consolidated by grouping sub-regions with similar occurrence rates from Figure 2-47. Figure 2-48 shows the sub-regions developed for Cases 1 and 2.

For Case 1, the F ratio is significant (all less than 0.0023) for each BD threshold for each of the 5 sub-regions. The mean occurrence rates are plotted in Figure 2-49. The mean comparison tests separated Sub-region 405 for BD0 and paired 403 with 405 for all other BDs. Hence, we then created Case 2 in which Sub-regions 403 and 405 were combined into a single sub-region (Sub-region 406, see right hand side of Figure 2-48) with Sub-regions 401, 402, and 404 as its complement (Sub-region 407). These final two sub-regions were significant with mean occurrence rate ratios (Sub-region 406/Sub-region 407) of about 1.8 for BD50 and above. They are therefore considered as separate regions in Section 3.

2.7.2.2. Region 5

We examined several Region 5 sub-regions and arrived at Case 4 as illustrated in Figure 2-50. Sub-region 511 is the northern portion of Region 5 and Sub-region 512 is the southern portion. The overall F test was significant for each BD threshold (all less than 0.0035) and the Tukey and

LSD test statistic also suggested separation. The mean occurrence rate ratios (Sub-region 512/Sub-region 511) are about 2 for BD20 and above. Sub-regions 511 and 512 are therefore considered as separate regions in Section 3.

2.7.2.3. Region 6

We examined several Region 6 sub-regions and arrived at Case 3 as illustrated in Figure 2-51. Sub-region 606 is the landward portion of Region 6 and Sub-region 609 is the coastal portion. The overall F test was significant for BD50, BD100, and BD250 thresholds (all less than 0.018). The Tukey and LSD tests maintained separation for these thresholds as well. The mean occurrence rate ratios (Sub-region 609/Sub-region 606) are 1.18, 1.25, 1.44, 1.60, and 2.02 for the BD0, BD20, BD50, BD100, and BD250 thresholds, respectively. Sub-regions 606 and 609 are, therefore, considered as separate regions in Section 3.

2.7.3. Final Sub-regions

The final regions and sub-regions are illustrated in Figure 2-52. The area of each sub-region and the number of tornadoes within each sub-region are given in Table 2-6. Subsequent minor adjustments to smooth sub-region boundaries were made to aid in contouring the final maps, as described in Section 8.2. The adjusted subregions have revised designations as follows (see also Figure 8-3):

406 → 4a
407 → 4b
511 → 5a
512 → 5b
606 → 6a
609 → 6b

All of the subregion-level tornado statistics and hazard curves provided in this report are based on the subregion boundaries shown in Figure 2-52; only the final maps were developed using the adjusted boundaries to determine cell regional membership.

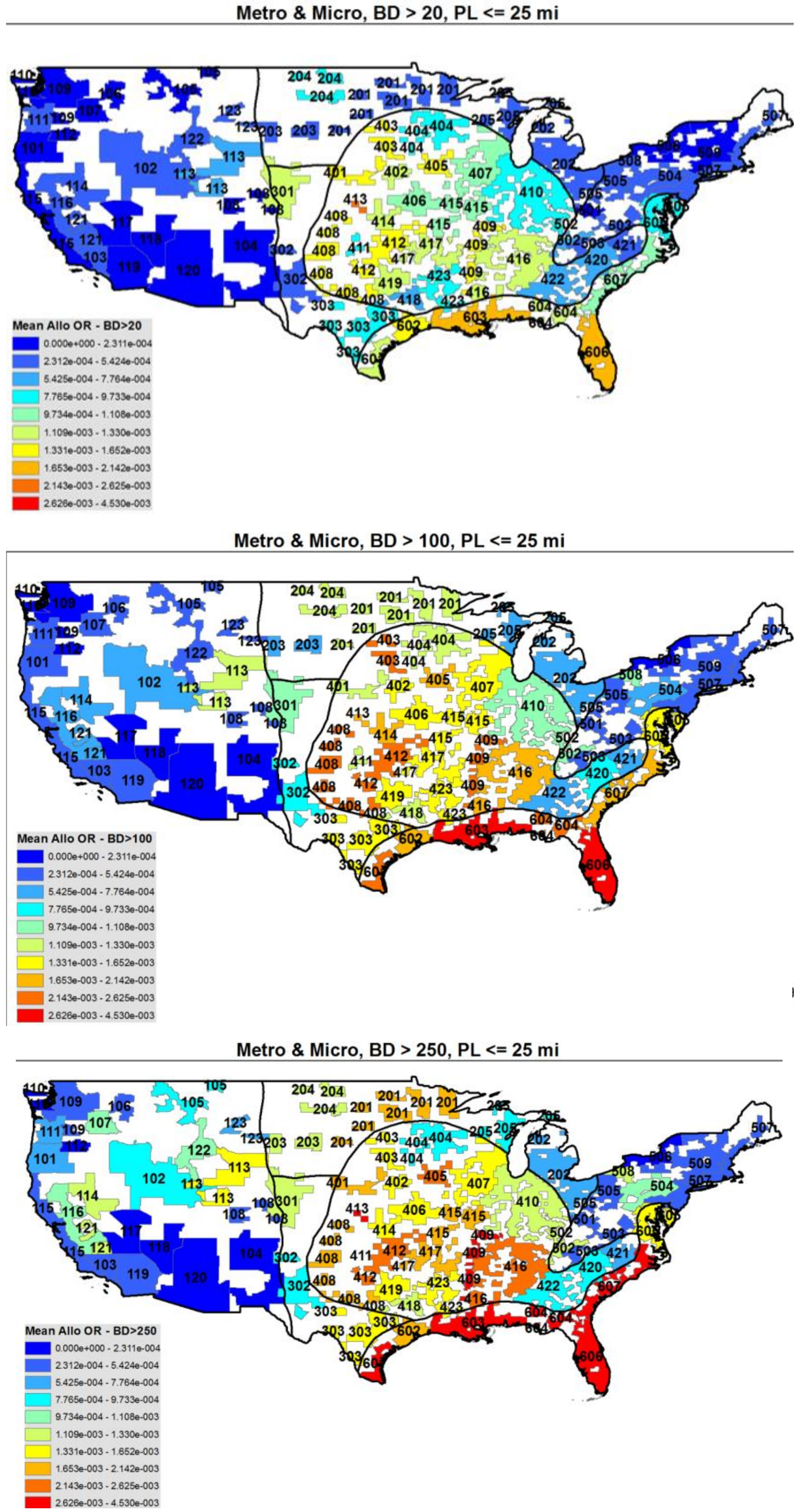

Note: 1 mi = 1.609344 km

Figure 2-47. MMSA Groups Colored by Mean Occurrence Rates

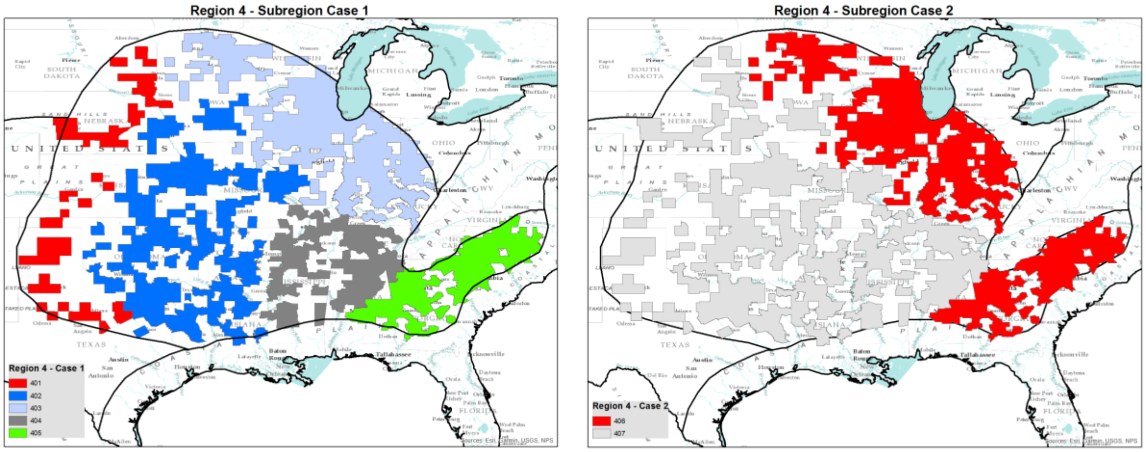

Figure 2-48. Region 4 Sub-region Cases 1 and 2

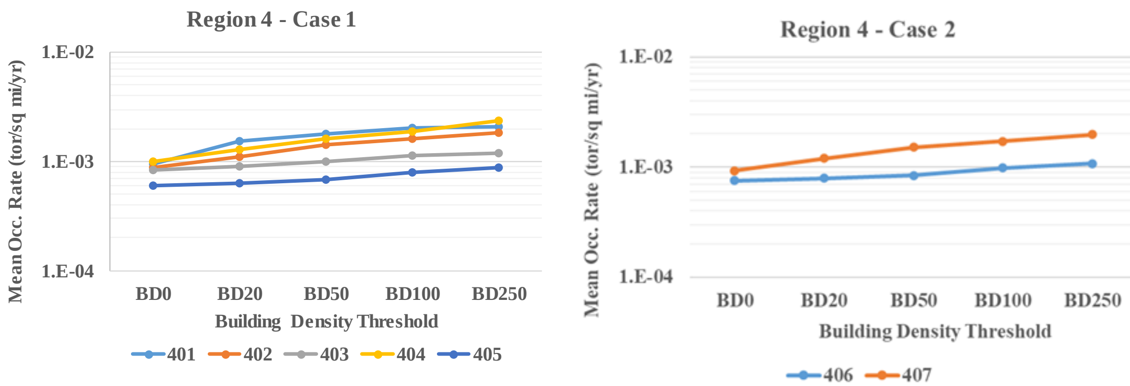

Note: 1 tornado per square mile per year = 0.386102 tornadoes per square kilometer per year

Figure 2-49. Region 4 Mean Occurrence Rates for Cases 1 and 2

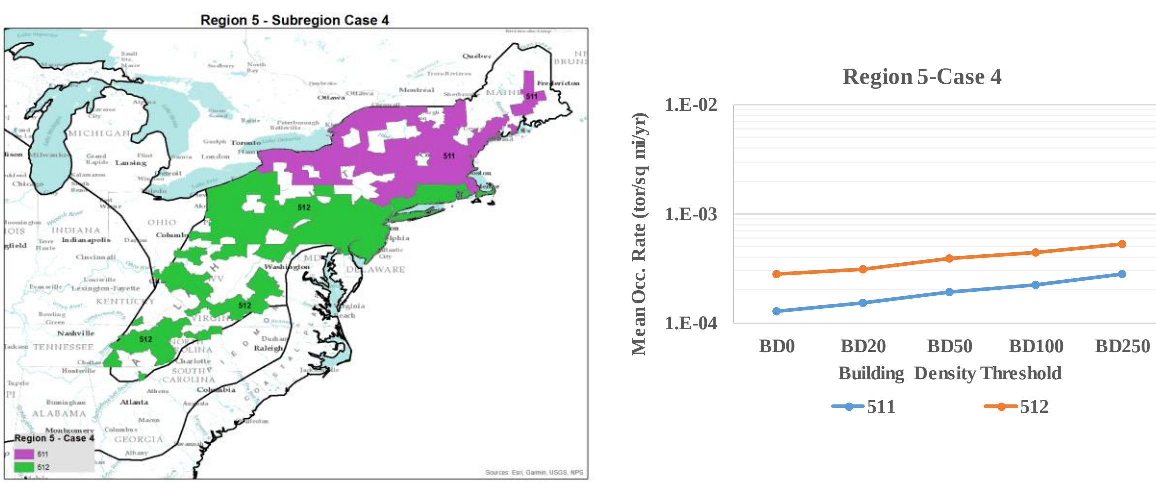

Note: 1 tornado per square mile per year = 0.386102 tornadoes per square kilometer per year

Figure 2-50. Region 5 Sub-region Case 4

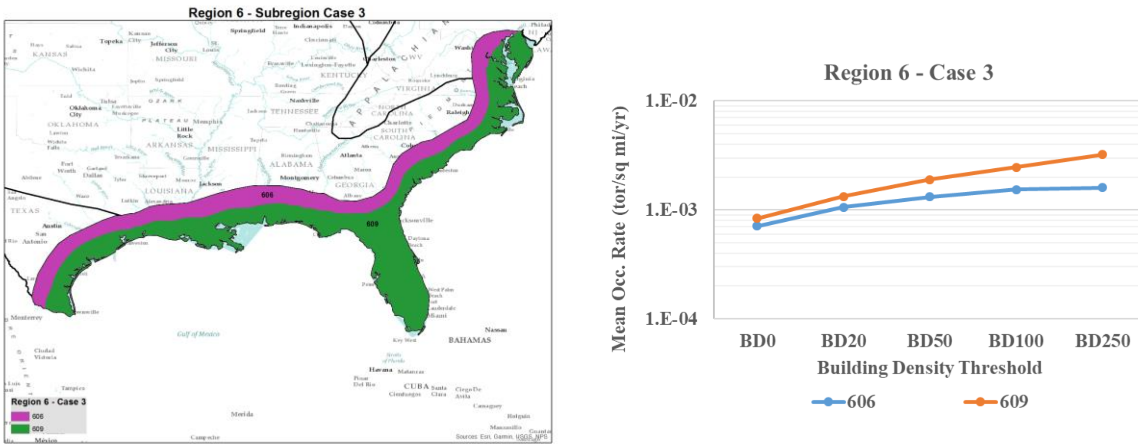

Note: 1 tornado per square mile per year = 0.386102 tornadoes per square kilometer per year

Figure 2-51. Region 6 Sub-region Case 3

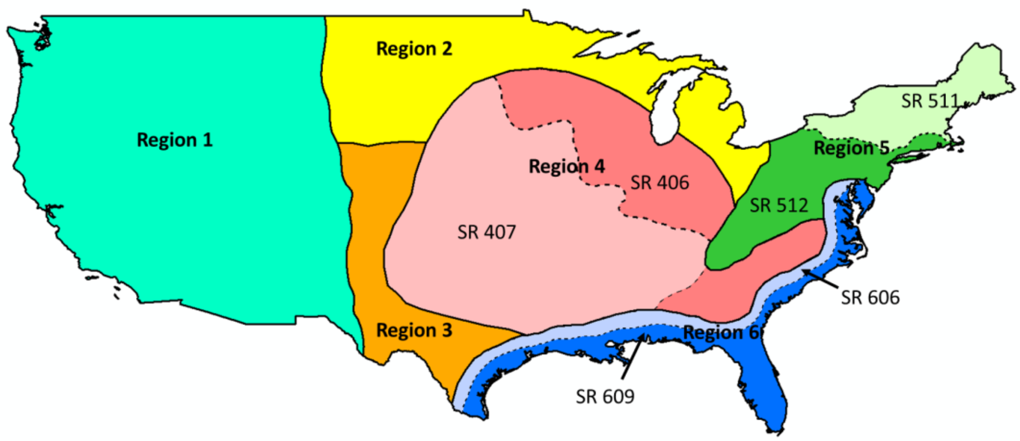

Figure 2-52. Map of Final Regions and Sub-regions

Table 2-6. Sub-region Area and Number of Tornadoes (1950-2016)

Sub-region	406	407	511	512	606	609
Area (sq mi)	303,007	610,330	101,751	148,379	87,355	144,760
No. Tors	10,066	25,834	731	1,958	2,819	7,119
Tors per sq mi per yr	5.0E-04	6.3E-04	1.1E-04	2.0E-04	4.8E-04	7.3E-04

Note: 1 square mile = 2.589988 km^2

3. Tornado Data Analysis

3.1. Data Elements

The broad tornado regions identified in Section 2 provide the starting point for the tornado data analysis. For this purpose, the regions are assumed to be homogeneous entities with uniform tornado risk. In this section, we analyze occurrence rate, EF-Scale intensity, and tornado path variables at a regional level. At a national level, we analyze within-path intensity variation data. The results of these analyses provide important inputs to tornado hazard modeling for the US.

A key element of the regional data analysis is the determination of "population bias" in the reporting of tornadoes. In order to assess population bias, we focus on the modern era and use census data for years 2000 and 2010 coupled with building density data. This analysis considers all tornadoes without the distinction of intensity rating. In Section 0, tornado intensity distributions (F-/EF-Scale rating) are developed from analysis of reported tornado intensities conditional on building density. Section 3.4 develops regional models of path length, width, and direction. Section 3.5 develops path length intensity variation (PLIV), path width variation (PWV), and maximum damage width (MDW) models for use in the tornado wind field and swath modeling in Section 4.

3.2. Tornado Occurrence Rate

Tornado occurrence rate is one of the fundamental inputs in the analysis of tornado wind speed risk. The units of tornado occurrence rate are tornadoes per unit area (square mile (square kilometers)) per year.

The reporting of the occurrence of a tornado requires confirmation (NOAA, 2016b). The overwhelming majority of tornadoes reported in the NCEI data and subsequently in the SPC database are based on observations of tornado damage and confirmation of rotational winds. Under-reporting of tornadoes in areas with few people and structures is a well-studied topic. The under-reporting of tornadoes has been generally referred to in the literature as "population bias". Numerous researchers have tackled the problem over the years. We summarize a few of these in the following paragraphs.

Population bias in tornado data in the US and Canada is well recognized in the literature. Snider (1977) studied Michigan tornado statistics from 1950 to 1973 and found tornado occurrences to be more accurate in urban areas than rural areas. Schaefer and Galway (1982) looked at tornadoes from 1950 – 1979 and their analysis showed that 1/3 of all tornadoes that occur are not reported. Twisdale et al. (1981) estimated tornado under-reporting of 20% to 35% for broad regions in the US. In Canada, Newark (1984) notes that population bias is an inherent source of error and concluded that in sparsely populated areas the probability of a tornado being observed is proportional to the population density in the area, until a threshold population density is reached where the probability is equal to one. Ray et al. (2003) studied a region within the Midwestern US and found that tornado density (years 1978 – 1992) decreases with increasing distance from NWS radar stations. Anderson et al. (2007) uses a Bayesian model to analyze population influences on tornado reporting for the years 1950 – 2001. By averaging Anderson's maximum and minimum probability of detection for several locations in the Midwest (Des

Moines, IA and Champaign, IL), an estimated bias factor for these areas was about 1.6 for all tornadoes and nil for F2 – F5 tornadoes.

Elsner et al. (2013) studied the effects of distance from a city on tornado reports during May and June from 1950 – 2011 in a region centered on Russell, Kansas. They found that on average, tornado reports in areas of higher population density exceeded those in lower population density areas by 70%. Their study also showed population bias to decrease with decade. Widen et al. (2013) perform similar statistical analysis for the years 1950 – 2011 and develop point probability risk estimates for selected states with bias correction for under-reporting of tornadoes. They compare to Simmons and Sutter (2011) and produce a bias correction factor on the order of two for several states in the Midwest. Cheng et al. (2013) use climatology data coupled with population bias analysis to produce updated maps of Canadian tornado occurrence rates. The study showed that tornado occurrence in sparsely populated areas is about a factor of two higher than is reported in the Canadian database. Cheng et al. (2015), subsequently, used a refined Bayesian analysis with monthly estimates to produce updated tornado occurrence rates on a 50 km grid.

The potential for both under-reporting of tornado frequency ("population bias") and under-estimation of tornado intensity (EF-Scale, as an intensity surrogate), is illustrated in Figure 3-1. In this figure, we have placed a scaled tornado in a rural area (top) and small city (bottom). Figure 3-1 suggests that tornadoes that occur in more densely settled areas have a higher probability of hitting a damage indicator and also of producing damage when the tornado is at its maximum intensity. If we assume the tornado strike location is independent of population/building density, using tornado data in areas where the reporting efficiency is expected to be greater provides us a method to quantify tornado occurrence rates and tornado intensity. Appendix C.1 provides tornado occurrence kernel density ArcGIS plots for various search radii and time periods. These plots indicate the inherent role of area-averaging in tornado risk assessment. Many of the high kernel density values in Appendix C.1 occur near cities and towns.

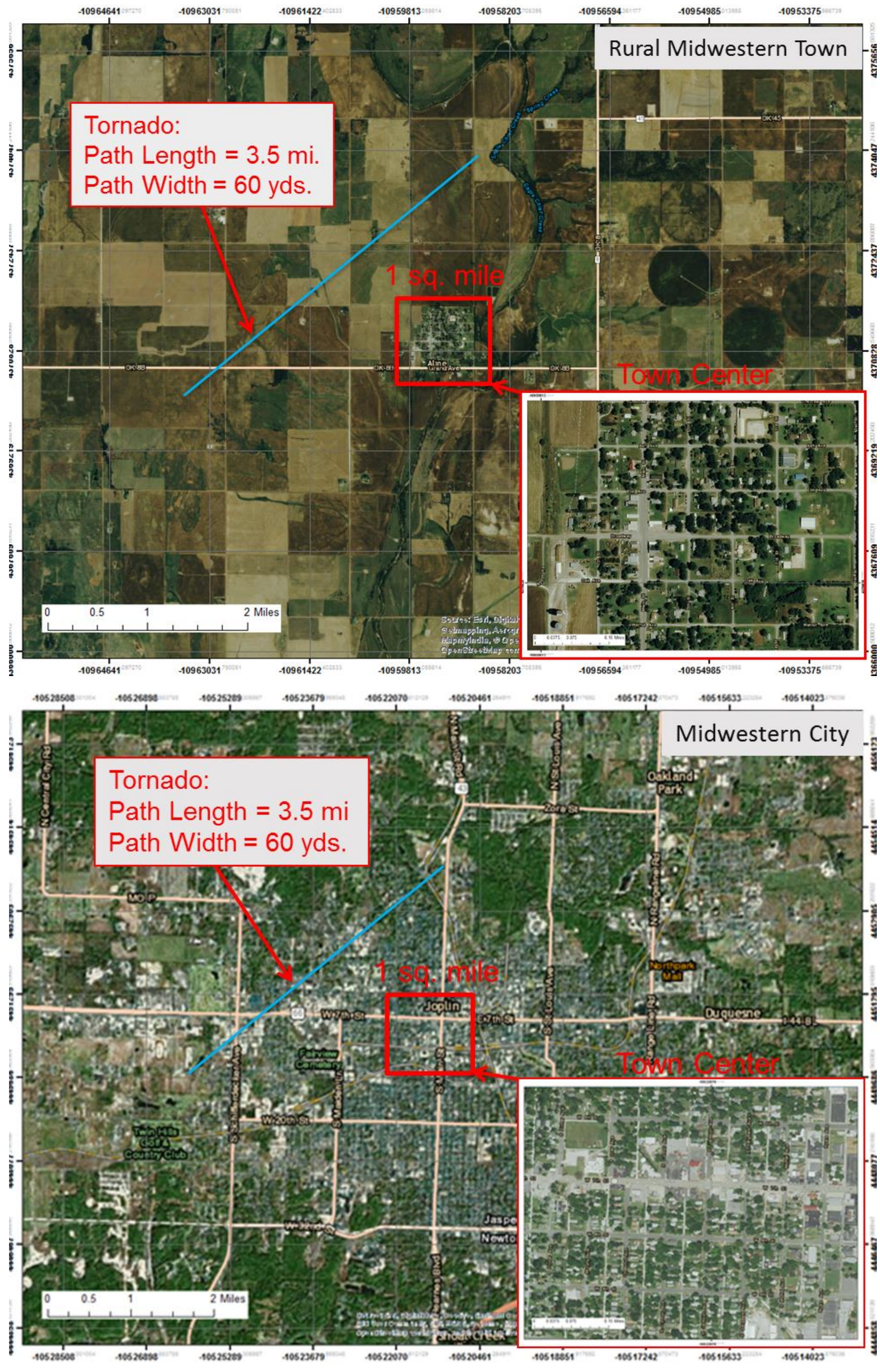

Note: 1 mi = 1.609344 km; 1 yd = 0.9144 m; 1 mi^2 = 2.589988 km^2

Figure 3-1. Tornado Scale Relative to Rural vs. Urban Population/Building Densities

3.2.1. Analysis Methodology

The basic hypothesis in population bias analysis is that tornadoes are reported with greater efficiency in locations with higher populations. Consequently, in areas with lower populations, not all tornadoes that occur are reported since they are not observed, they do not produce damage, or there is no confirmation of rotational winds. This hypothesis is generally tested by assuming uniform tornado occurrence rates over an area or region and comparing the densities of tornadoes with population densities. Since we have developed broad tornado regions based on multiple (empirical) tornado climatology metrics, the assumption of uniformity of risk over the region/sub-region is inherent in our mapping approach. Our population bias analysis follows the basic hypothesis that tornado reporting efficiency increases with increasing population density.

We use Census Bureau statistics for 2000 and 2010 coupled with FEMA's HAZUS BD data to analyze population bias. Building density and population bias are highly correlated. Calculation of Pearson correlation coefficients on the log of building density vs. log of population density on a census tract (CT) level was performed using SAS (1993) for the Regions 1, 2, 3, 4, 5, and 6. These correlation coefficients were 0.981, 0.986, 0.984, 0,983, 0.952, and 0.969, respectively. All tested significant for the null hypothesis with p values less than 0.0001.

We use building density since it has a practical density limit, whereas thousands of people can live in one high-rise building, which produces a long distribution tail for urban areas. The most common building type in the US is single-family residences (FEMA, 2007), which is also a dominant damage indicator (DI) in wind speed estimation in the EF-Scale.[29]

We use the HAZUS BD data, which was built-up from occupancy classes, as described in FEMA (2007, 2015). Our analysis method uses BD thresholds, which are BD exceedance values such as 20 buildings per square mile (7.7 buildings per square kilometer). We aggregate tornado metrics for all CTs that exceed a specified BD threshold. Our geospatial modeling is based on using census tracts. CTs appear to be the right level of granularity since they are contiguous, relatively homogeneous, and their spatial size depends on population density.[30] A basic model consisting of building density by CT data in conjunction with reported SPC tornado data is used to analyze tornado occurrence rate and regional reporting efficiency. The analysis is performed using the 2000 and 2010 US census tracts. Building density by census tract is computed from HAZUS data (described in Appendix C.2), which contains building counts by census tracts for the 2000 and 2010 US censuses. For example, Figure 3-2 illustrates an area in Alabama with reported tornadoes (2000-2016) overlaid on CTs, which are shaded according to building density (darker colors indicate towns/cities with higher BDs). Figure 3-3 illustrates how CTs vary by size for several states. Since each CT includes a similar range in total population, there are many small CTs in cities, whereas the CTs become much larger in rural areas where population and building density are much less.

[29] FR12 in the EF-Scale includes one- and two-family residences (TTU, 2006). FR12 is the most common EF-Scale DI used to rate tornadoes ≥ EF3 intensities.
[30] Census tracts average about 4,000 inhabitants, with a minimum of 1,200 and a maximim of 8,000 (US Census Bureau, 2020)

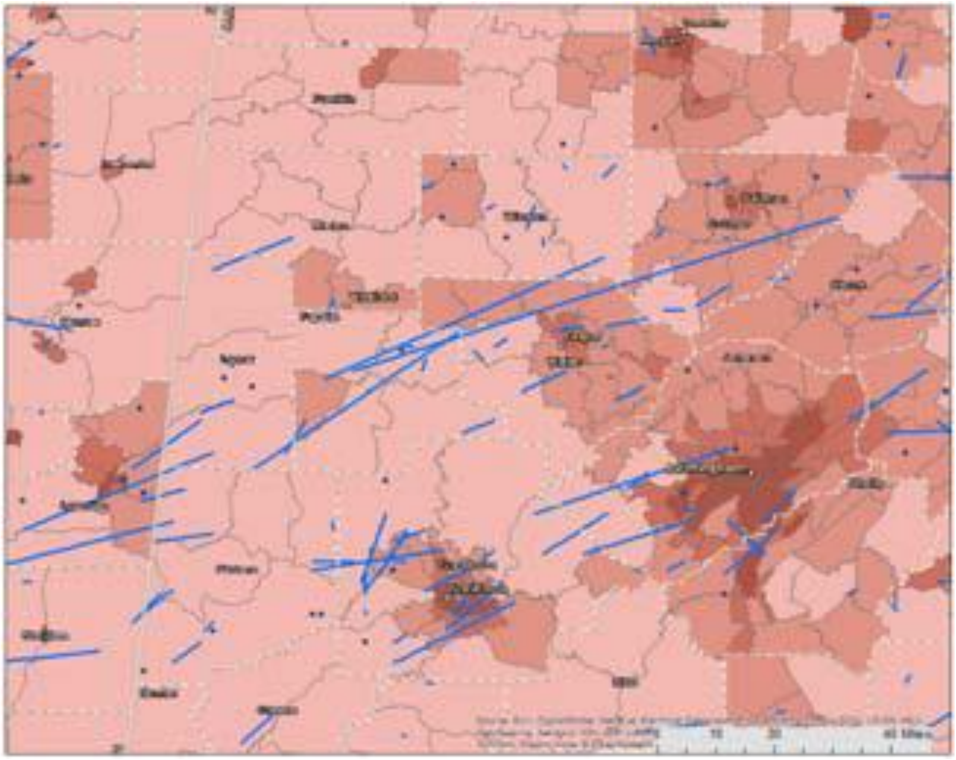

Figure 3-2. Reported Tornadoes (Blue, 2006-2016) Overlaid onto 2010 Census Tracts (BDs Shown by Shading)

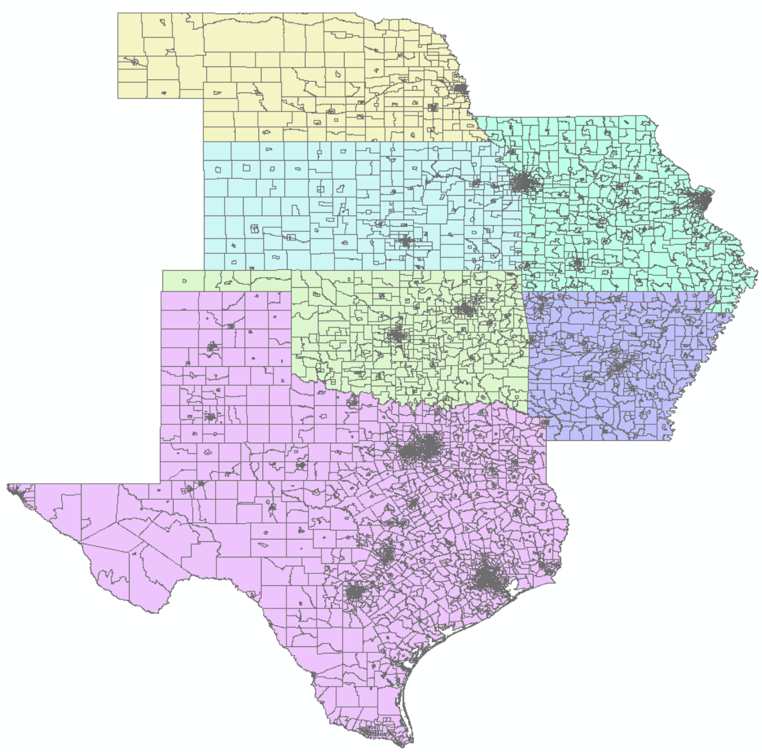

Figure 3-3. Example of Individual Census Tract Geometries and Areas

3.2.1.1. Tornado Reporting (Population) Bias

We use tornado density coupled with building density to quantify tornado population bias, *E, which* is a non-dimensional parameter that corresponds to the general definition of population bias parameters discussed in the literature, i.e., the "population bias factor". The inverse of *E*, 1/E, is reporting efficiency. We calculate *E* as a ratio of tornado densities

$$E_i = d_i/D \tag{3-1}$$

where d_i is a tornado density metric (such as tornadoes per square mile per year) for a building density threshold "i" and *D* is the nominal tornado density metric for the entire land area in the region. The threshold BD $\geq$ 0, herein denoted as BD_1, covers all the land in the region and Eq. 3-1 naturally reduces to E1 = D/D = 1. For BDs > 0, Eq. (3-1) provides a ratio of reported tornado densities in the associated BD areas to the nominal tornado densities in the entire region, thereby producing an estimate of population bias. For example, an E_i value of 1.5 means that the tornado metric for the BD_i threshold is 50 % greater than it is from the nominal value for the entire region. By evaluating different thresholds, we quantify the relationship of E_i vs. BD_i threshold. A mean value of *E* (reporting bias or population bias factor) is then estimated from E_i, considering epistemic uncertainties.

3.2.1.2. Tornado Density Metrics

We use three different metrics to quantify tornado density (d_i) within the context of our CT-based building density threshold analysis. Tornado density is defined as the tornado count metric divided by area. Three counting methods were considered in the population bias analysis. They include: (1) hit (H); (2) length fraction (LF); and (3) point probability (PP). A tornado hit is counted as one if any part of the tornado length intersects a CT within a CT threshold group. In LF counting, the fraction of the tornado length within a CT threshold group is recorded. Thus, if all of the length of a tornado is within a threshold group, it is counted as one, and a fraction otherwise.[31] For point probability method, the tornado's path area within a census tract is assigned to that census tract. The path areas of all the CTs in a CT threshold group are summed. The PP is the sum of the tornado path areas divided by the total CT threshold group area.

Each metric has its advantages and limitations. For example, hit counting produces a count of 1 in every CT threshold area that the tornado touches. Since a tornado may cross multiple CT thresholds (with each crossing produces a hit), hit counting does not conserve the total tornado count when the BD threshold counts are aggregated. Hit densities rise similarly for small BD threshold areas. Hit counting therefore has a potential for overestimating population bias. LF eliminates this potential for multiple counting of tornadoes in a threshold analysis since each tornado is counted fractionally. Hence, the sum of all counts is unity for each tornado, regardless of how many CTs it crosses. PP is based on tornado area density and provided a measure of tornado risk for a point within a CT threshold area. PP produces a true measure of risk (the probability of a point being within a tornado path over some period of time, typically a year). However, it is area-based and large (rare) tornadoes can produce high variance in the metric results.

[31] If tornadoes are assumed to be located at a single point in the calculation of population bias (such as Elsner et al. (2013) or Cheng et al. (2013, 2015)), H and LF produce the same tornado densities.

In the following section, we perform a statistical test to assess the efficacy of these tornado counting metrics to produce unbiased estimation of *E*.

3.2.2. Statistical Test of Tornado Counting Metrics

We develop a statistical test of the three counting metrics (H, LF, and PP) for the purposes of population bias analysis. We assesses the hypothesis: “an unbiased tornado density counting method is invariant with building density threshold for randomly positioned tornadoes.” We call this test “uniform in-uniform out?” (UI-UO) First, we simulate tornado positions uniformly over a region (“Uniform-In”). Second, we compute each tornado density metric for various BD thresholds (“Uniform-Out?”). Third, we determine if the metric output predicts the known input. From the test design, the metric density should not depend on BD threshold (since the simulated tornado density is statistically uniform over the region). If the metric is invariant with BD threshold (and hence, the output confirms the statistically valid input, “Uniform In”), we conclude that it is an “unbiased” metric for purposes of quantifying population bias. However, if the metric BD threshold counts suggest that the tornado density is not uniform, then we conclude that the metric is a biased estimator.

We begin by selecting ten rectangular polygons (see Figure 3-4) for the statistical test. These regions wer selected such that each region contained at least one polygon. We included several overalapping regions in “tornado alley”. These regions were positioned by hand to include major metropolitan areas in some cases and diverse topography in others. Regions 1, 2, 3, 5, and 6 each contain a single polygon, and Region 4 contains 5 polygons. These polygon sizes range from small to large, where the large polygons approach some regional sizes. The polygons, which are not numbered sequentially, include one polygon (Polygon 12) fully within another (Polygon10) and several partially enclosed polygons (Polygons 7 and 11). These overlapping polygons resulted as we continued to build-out the test to examine results across multiple polygon sizes and smaller areas within larger ones.

Area fraction CDFs of building density for the 2000 and 2010 census tracts within each polygon are given in Figure 3-5. These figures illustrate the differences in the polygon building density distributions. For example, half the land area in Polygon 1 has less than 1 building per square mile (less than 0.4 buildings per square kilometer), compared to only a few percent in Polygon 6.

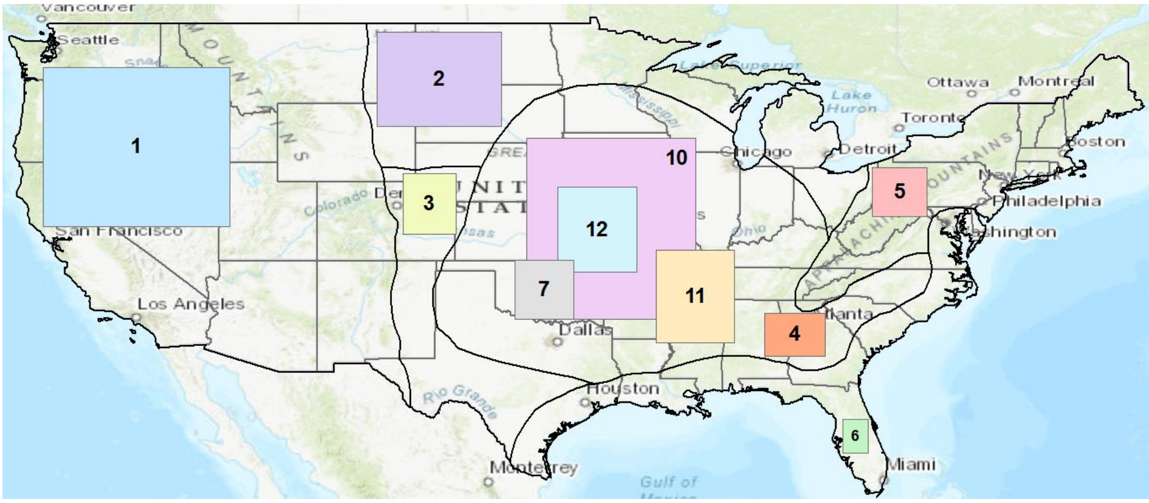

Figure 3-4. 10 Polygons Used for Uniform Statistical Tests

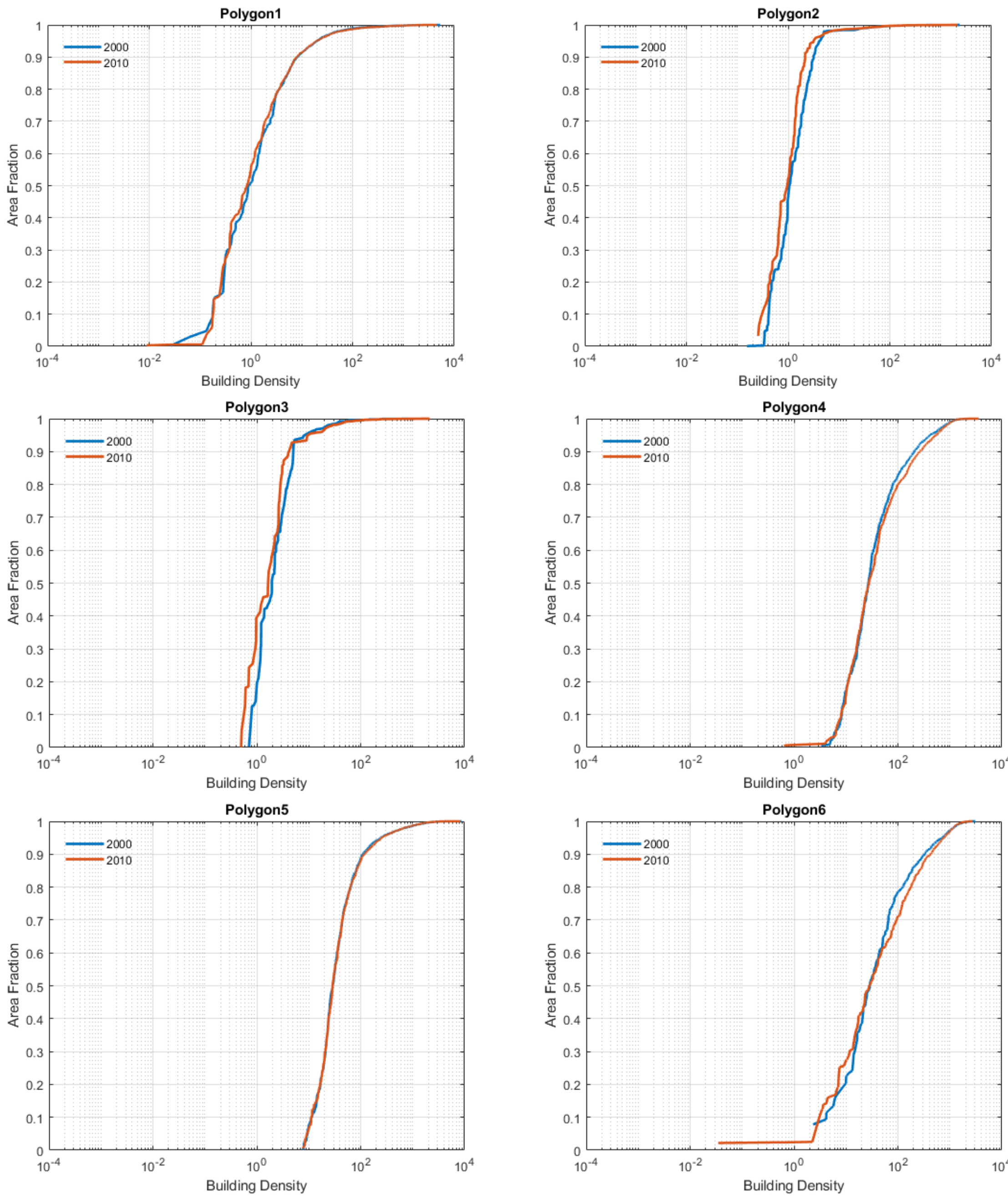

Figure 3-5. Polygon CDFs of Building Density by Area Fraction

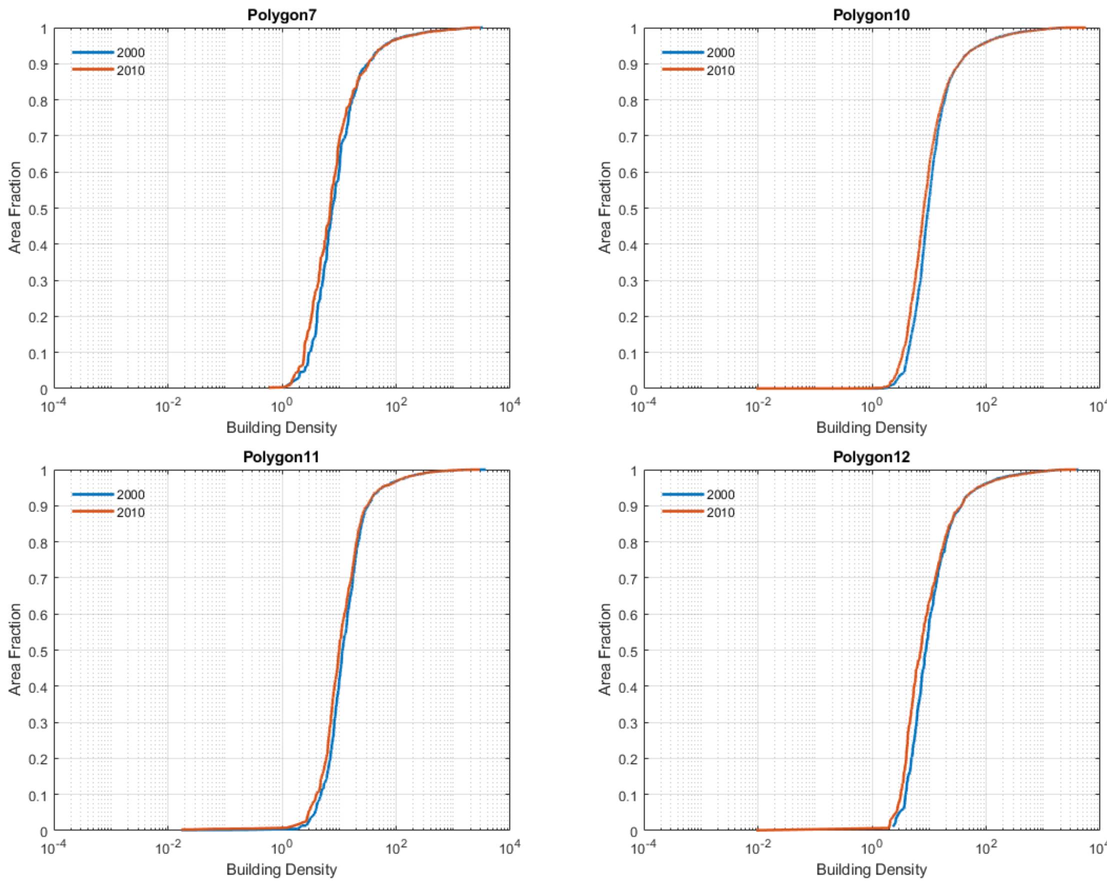

Figure 3-5. Polygon CDFs of Building Density by Area Fraction (continued)

The intersect tool in ESRI ArcMap is used to intersect SPC reported tornado data from 1995 to 2016 and CT shape files, separately for each of the two census periods. These results are then combined into one data set for analysis by BD density. The number of years of SPC tornado data in these calculations covers 1995-2005 (for the 2000 Census data) and 2006-2016 (2010 Census data). Hence we use 22 years of tornado data in the analysis and this period also corresponds to the so-called modern era, when Doppler Radars were available at the vast majority of NWS field offices.

We use the tornado data to generate 25 sets of uniformly-positioned tornadoes within the polygon, where each reported tornado in the 22-year period is included and the only change is that we simulate the tornadoes with random location. The numbers of tornadoes and polygon areas are given in Table 3-1.

Typically, the tornadoes within a polygon will consist of a mix of single-point and double point (line) tornadoes.[32] Because the point tornadoes actually have a reported path length in the database, we convert them to line tornadoes for use in the population bias analysis testing. A direction for each point tornado is sampled from the polygon path direction distribution of the line tornadoes. The reported path length and sampled direction are used to determine an ending point for the tornado, allowing for it to be treated as a line tornado. The tornado data within the

[32] Single-point means the tornado's position is given by a single latitude, longitude point in the SPC database.

polygon (now only consisting of line tornadoes) is the basis for the computation of the actual population bias factors and the bias factors of the uniformly-distributed tornadoes.

Table 3-1. Polygon Tornado Counts (1995-2016) and Land Areas

Polygon No.	Tornado Counts							Area (sq.mi.)
	EF0	EF1	EF2	EF3	EF4	EF5	All	
1	154	21	3	0	0	0	178	269,534
2	335	76	22	4	1	0	438	100,066
3	691	66	19	4	0	0	780	30,700
4	164	147	57	15	3	0	386	27,224
5	62	55	13	1	1	0	132	25,453
6	145	27	4	4	0	0	180	9,296
7	464	230	64	29	10	3	800	34,970
10	3152	1681	505	164	53	5	5560	294,682
11	528	488	173	82	20	4	1295	73,338
12	666	273	73	25	8	1	1046	64,228

Note: 1 mi^2 = 2.589988 km^2

3.2.2.1. Polygon Test Results

In the process of performing this UI-UO test, we develop statistics on the three tornado density metrics, conditioned on BD threshold, for two cases:

1. Case 1: Reported Tornadoes: Use SPC reported tornado locations (actual positions of reported tornadoes for the period 1995-2016).
2. Case 2: Uniformly Random Tornadoes “Uniform In-Uniform Out?” Test: Simulate uniform tornado locations with multiple replications (25 simulation replications of uniformly distributed tornadoes from the Case 1 data set).

Case 1 provides estimates of d_i (and E_i) for these polygons using actual tornado locations. We then perform the UI-UO Test Case 2 and assess the efficacy of the counting methods across the 10 polygons.

Reported Tornadoes. The computed tornado densities for the H, LF, and PP metrics are plotted in Figure 3-6. For the H (top figure) and LF (middle figure) the counting methods, we see strong and consistent trends of increasing tornado density with increasing BD. These trends indicates higher reported tornado densities in areas with higher BDs, and hence E values > 1.

The PP plots (bottom figure) show some mixed results with Polygons 4, 11, and 12 showing no increase in reported PP density with increasing BD. Seven of the 10 polygons suggest increasing PP risk with increasing BD threshold. PP quantifies the risk of being in a tornado path per year.

While the results in **Error! Reference source not found.** include some relatively small polygons and modest tornado counts, the results suggest that population bias is present in most, if not all of the polygons.

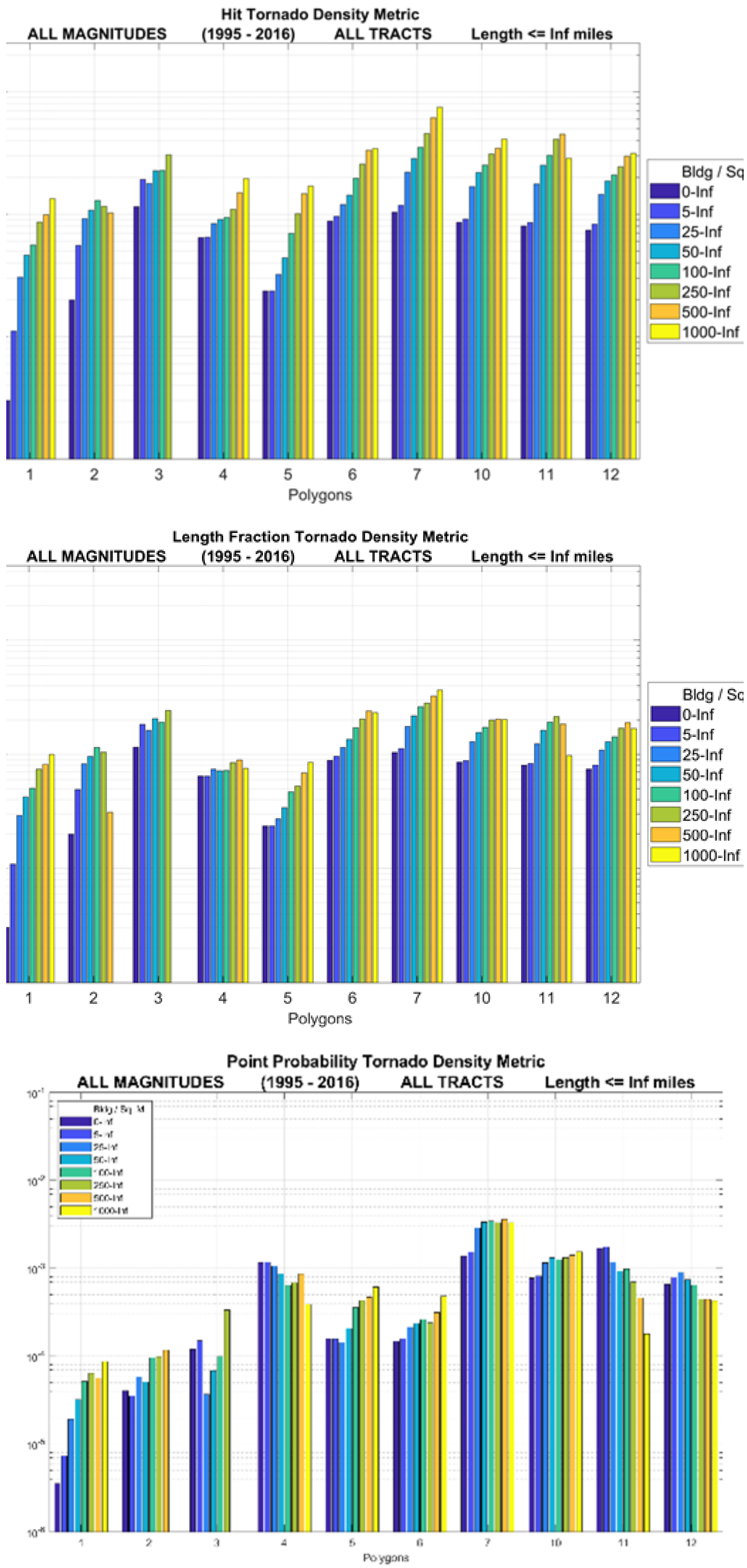

Note: 1 mi = 1.609344 km; 1 mi^2 = 2.589988 km^2

Figure 3-6. Case 1 Polygon Metrics: Reported Tornadoes

Statistically Generated Uniformly Distributed Tornadoes. We generated 25 sets of uniformly distributed tornadoes for each polygon. The tornado characteristics (length, width, and direction) were kept the same as the reported tornadoes in each replication. The tornado position changed from actual latitude and longitude to a uniformly random position in latitude-longitude space within the polygon. We created equal area sub-grids in each polygon to stratify the sampling of position (see Figure 3-7). Chi square tests were performed on each replication to ensure that the samples meet the 5% significance level for a uniform distribution. Rejection sampling was used to ensure that the tornado paths were fully within the polygon.

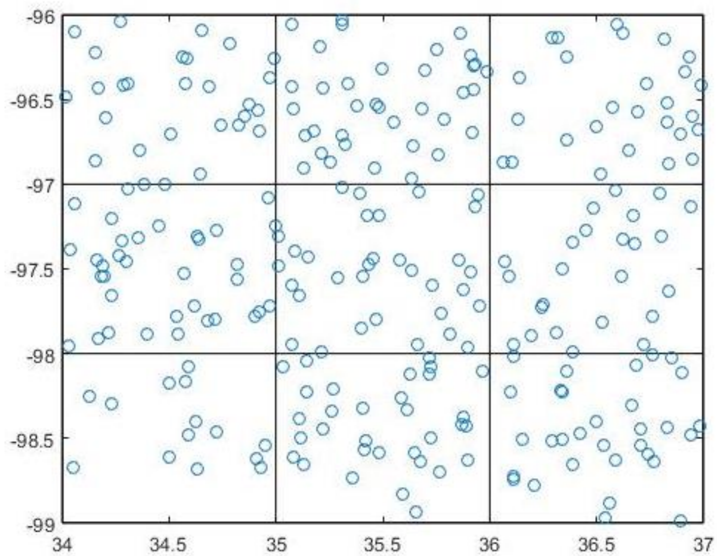

Figure 3-7. UI-UO Test Replication Example (9 sub-grids) of Uniformly-Distributed Tornadoes

The computed tornado densities for the H, LF, and PP metrics are plotted in Figure 3-8. For the *H* the counting methods, we see significant upward trend for all polygons. The hit counting suggest that most of the polygons are under reporting tornadoes by factors approaching two or more. For LF, we see mostly “flat” trends and modest estimates of under reporting. PP shows much more random variation by threshold, especially in the smaller regions with fewer tornadoes. PP produces essentially flat results (no bias) for 6 of 10 polygons. The high variance of PP shows that even with 25 replications of uniformly-distributed tornadoes, PP may not be reliable as a stand-alone metric.

Figure 3-9 shows the computed bias factors by polygon. Hit counting tends to produce biased estimations of *E* for all polygons. The H bias factors all have a positive slope with increasing BD threshold. The 10 polygon mean line (black dashed line) reaches 2 at BD250. The LF plots hug the E=1 line up until BD250 for all polygons except 1, 2, and 5. The mean LF bias factor line for all polygons does not deviate 5% from E =1 until BD500. The PP bias factors show significant variance around unity, but the mean PP across all polygons remains with 20% of unity for all BD thresholds.

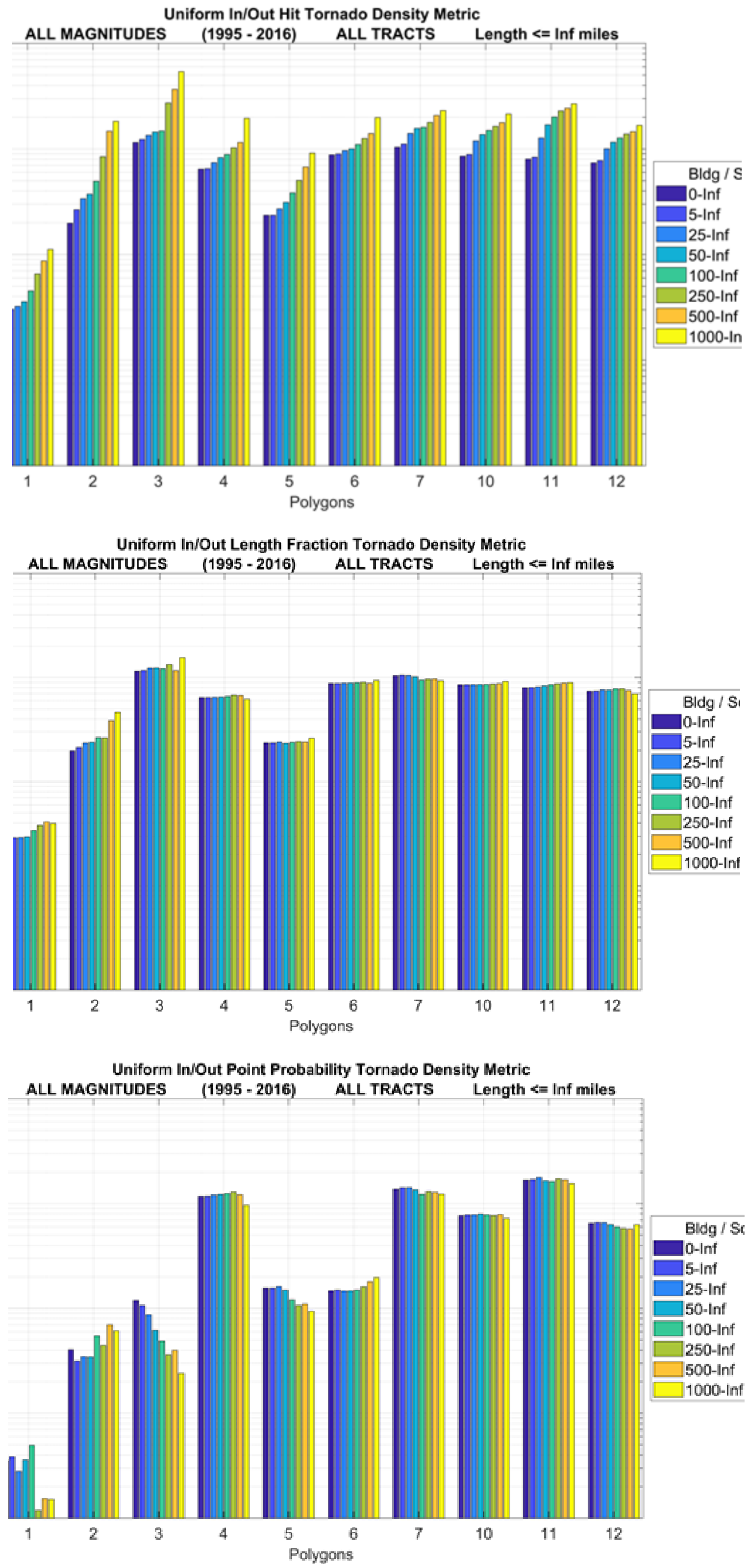

Note: 1 mi = 1.609344 km; 1 mi^2 = 2.589988 km^2

Figure 3-8. Case 2 Polygon Metrics: UI-UO Test

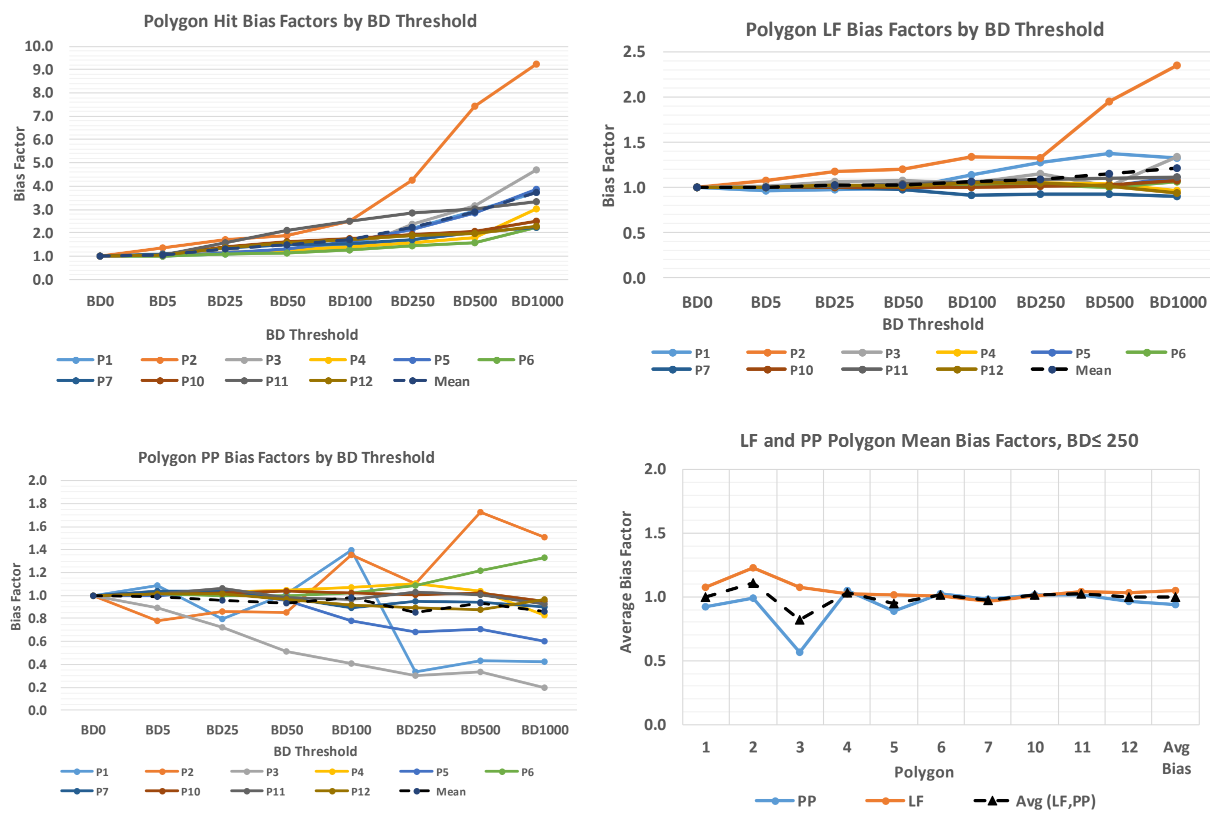

Figure 3-9. Computed UI-UO Bias Factors (E) by Metric and Polygon

The bottom right figure in Figure 3-9 shows the LF and PP polygon-by-polygon mean E's for BDs less than 250 buildings per square mile (less than 97 buildings per square kilometer). There is a negative correlation between LF and PP for this range of BD's. This negative correlation works in favor of correcting the potential bias in polygons with the largest deviations from unity (polygons 1, 2, and 3). LF does not consider tornado size or area (since all counts are a normalized fraction of length).

Epistemic Population Bias Model. With limited tornado counts in a polygon or a region and assumed randomness in tornado locations, any attempt to correct for population bias includes epistemic uncertainty in the estimation of the true number of tornado occurrences. Based on the UI-UO polygon test for BD threshold analysis: H produces positive bias in the estimation of E; LF seems to be the best overall single metric; and PP has high variance as a metric but tends to be generally unbiased when averaged over large areas, such as all the polygons. Due to its high bias, we eliminate hit counting as a viable approach for use with CT BD threshold analysis.[33]

Table 3-2 summarizes the polygon statistics for BD5 through BD250 for the three metrics. Across all polygons, we see that the mean E is 1.560, 1.047, and 0.994 for the H, PP, and LF, respectively. By averaging the PP and LF methods, the aggregate mean bias is near unity.

We believe that the average of the LF and PP bias factors for a region provides a reasonable method to estimate tornado-reporting bias E with BD threshold analysis. Across all polygons, the average of the LF and PP bias factors (for BD thresholds ≤ 250) is 0.994, its standard deviation is

[33] Analytic models for one dimension (line position with line segment tornadoes) also prove that H is a biased estimator.

0.073, and the standard error is 0.023 (see Table 3-2). In Section 3.2.4, we use these statistics to model the potential error in using LF and PP metrics for regional population bias analysis. Given the complexity of the CT threshold geometries intersected with tornado geometries (lines and areas, respectively for LF and PP metrics), this heuristic approach of averaging LF and PP provides a practical solution to estimating tornado under-reporting using two reasonable metrics, while eliminating a third.

Table 3-2. Polygon UI-UO Tornado Population Bias (E) Statistics

Polygon	Hit	Point Probability	Length Fraction Allocation	Mean: PP and LF
1	1.400	0.925	1.071	0.998
2	2.339	0.988	1.228	1.108
3	1.428	0.569	1.076	0.822
4	1.283	1.050	1.020	1.035
5	1.448	0.891	1.011	0.951
6	1.187	1.023	1.011	1.017
7	1.438	0.981	0.968	0.974
10	1.541	1.019	1.007	1.013
11	2.021	1.011	1.044	1.028
12	1.514	0.962	1.033	0.998
Aggregate Mean	1.560	0.942	1.047	0.994
Standard Deviation	0.351	0.139	0.071	0.073
Standard Error	0.111	0.044	0.023	0.023

3.2.3. Regional Tornado Densities

Based on the analysis in Section 3.2.2, we use LF and PP tornado density data (for BD ≤ 250) to quantify tornado reporting bias for the 9 regions developed in Section 2 and shown in Figure 2-52. We used 5 BD thresholds (BD1-BD5), where the first threshold (BD1) includes all the land area of the region. For BD1, H and LF counting reproduces the region's raw tornado counts. The remaining four thresholds for each polygon were produced using area decrements of about 0.5 such that BD2 had an area of about ½ of BD1 and so forth (BD5 has an area equal to about 1/16 of BD1). This process produces the BD thresholds in Table 3-3. For high-populated regions, the BD threshold for BD5 is much greater than for regions with less dense development (such as Regions 1 and 3). For example, BD5 for Region 512 has a threshold of 250, whereas BD5 for Region 1 has a threshold of 30 buildings per square mile. The use of the area decrement approach in determining the BD2-5 allows an even stratification by land area in the computations of *E*. It also reduces the potential bias of LF and PP for high BD thresholds (and the associated small land areas), as seen in Figure 3-9.[34]

The computed tornado densities for LF and PP are plotted in Figure 3-10. We see a notable increase in tornado densities for LF with increasing BD threshold for all of the regions.[35] As for the polygons, the increase in PP densities with BD is less than LF. The relative rankings of the regions by tornado density follows closely from the tornado metric plots in Section 2. We see the

[34] We initially used the same BD threshold values in all regions, but abandoned this approach to ensure a consistent area (percentage-wise) by region.

[35] Also plotted is a weighted BD tornado density for each region. This weighted BD is discussed in the following section.

highest occurrence rates by count (LF) in the central US and the Gulf/Atlantic coasts and the largest area tornadoes (as measured by PP) are in the central US (Regions 4, 406, and 407).

Table 3-3. Regional Building Thresholds Used for Reporting Bias Analysis

Region Label	BD Threshold Values (bldg/mi^2) for BD1-BD5				
	BD1	BD2	BD3	BD4	BD5
1	0	5	10	20	30
2	0	5	15	25	50
3	0	5	10	20	30
406	0	10	20	30	50
407	0	5	15	30	50
511	0	15	25	50	100
512	0	15	30	100	250
606	0	15	25	50	100
609	0	10	20	50	100

Note: 1 mi^2 = 2.589988 km^2

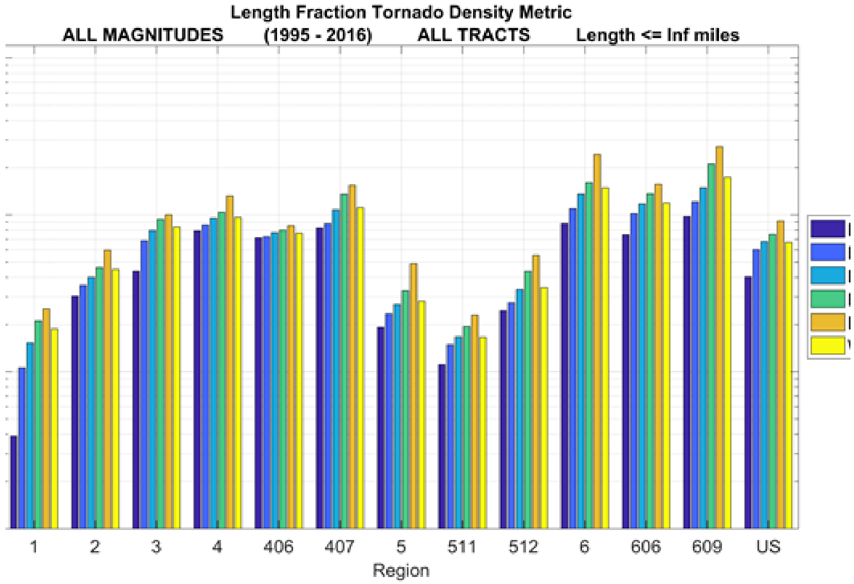

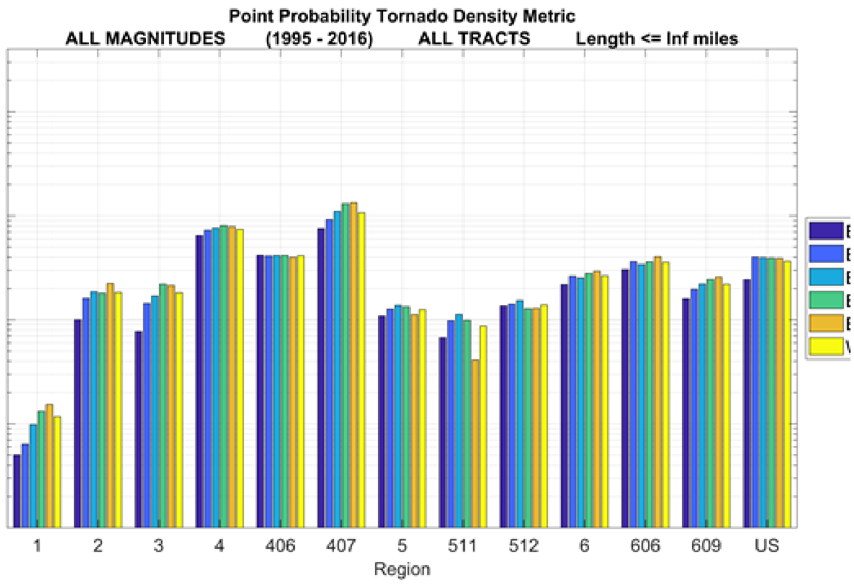

Note: 1 tornado per square mile per year = 0.386102 tornadoes per square kilometer per year; 1 mi = 1.609344 km

Figure 3-10. Regional LF and PP Tornado Densities by BD Threshold

Table 3-4 summarizes the LF and PP densities and regional population bias factors by BD threshold. Figure 3-11 plots the bias factors from Table 3-4. Region 1 (western US) has significantly higher bias factors, for reasons discussed in Section 2. Regions 406 and 407 have the lowest bias factors. All of the bias factors increase with BD except for the PP factors for Regions 406, 511, and 512 for BD4 and BD5. The following section discusses the use of these bias factors in the development of regional tornado occurrence rates.

Table 3-4. Regional LF and PP Densities and Bias Factors

Region	Length Fraction Densities (per sq. mi. per year)					Point Probability Densities (per year)				
	BD1	BD2	BD3	BD4	BD5	BD1	BD2	BD3	BD4	BD5
1	3.91E-05	1.07E-04	1.54E-04	2.12E-04	2.53E-04	4.71E-06	6.32E-06	9.72E-06	1.27E-05	1.50E-05
2	3.04E-04	3.57E-04	4.02E-04	4.62E-04	5.96E-04	1.00E-04	1.58E-04	1.84E-04	1.80E-04	2.21E-04
3	4.41E-04	6.86E-04	7.96E-04	9.40E-04	1.00E-03	7.72E-05	1.39E-04	1.59E-04	2.08E-04	1.99E-04
406	7.15E-04	7.27E-04	7.73E-04	8.00E-04	8.56E-04	4.16E-04	4.07E-04	4.11E-04	4.04E-04	3.91E-04
407	8.28E-04	8.82E-04	1.08E-03	1.35E-03	1.54E-03	7.32E-04	8.79E-04	1.05E-03	1.26E-03	1.30E-03
511	1.11E-04	1.49E-04	1.67E-04	1.95E-04	2.30E-04	6.72E-05	9.73E-05	1.11E-04	9.80E-05	4.12E-05
512	2.46E-04	2.77E-04	3.36E-04	4.39E-04	5.53E-04	1.26E-04	1.32E-04	1.42E-04	1.18E-04	1.16E-04
606	7.49E-04	1.02E-03	1.18E-03	1.36E-03	1.57E-03	3.10E-04	3.73E-04	3.41E-04	3.48E-04	4.00E-04
609	9.76E-04	1.21E-03	1.49E-03	2.11E-03	2.72E-03	1.62E-04	1.99E-04	2.23E-04	2.48E-04	2.62E-04
Region	**Length Fraction Bias Factors**					**Point Probability Bias Factors**				
	BD1	**BD2**	**BD3**	**BD4**	**BD5**	**BD1**	**BD2**	**BD3**	**BD4**	**BD5**
1	1.00	2.72	3.93	5.41	6.47	1.00	1.34	2.06	2.70	3.20
2	1.00	1.17	1.32	1.52	1.96	1.00	1.58	1.84	1.80	2.21
3	1.00	1.56	1.80	2.13	2.27	1.00	1.80	2.07	2.69	2.58
406	1.00	1.02	1.08	1.12	1.20	1.00	0.98	0.99	0.97	0.94
407	1.00	1.07	1.30	1.64	1.86	1.00	1.20	1.44	1.72	1.77
511	1.00	1.34	1.50	1.75	2.07	1.00	1.45	1.65	1.46	0.61
512	1.00	1.12	1.36	1.78	2.25	1.00	1.05	1.13	0.94	0.92
606	1.00	1.36	1.57	1.82	2.09	1.00	1.20	1.10	1.12	1.29
609	1.00	1.24	1.53	2.17	2.79	1.00	1.23	1.38	1.53	1.62

Note: 1 mi^2 = 2.589988 km^2

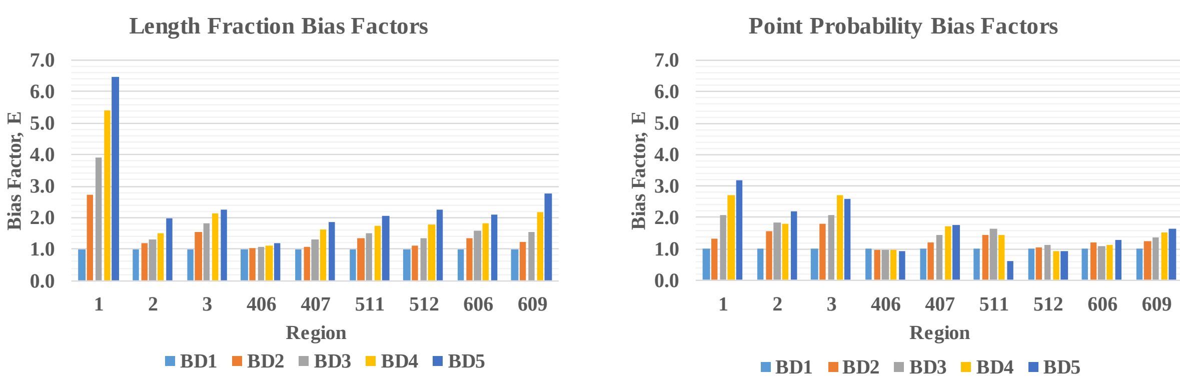

Figure 3-11. LF and PP Bias Factor Bar Plots

3.2.4. Regional Tornado Occurrence Rates

We develop regional tornado occurrence rates considering both aleatory and epistemic uncertainties. Using simulation, we compute a derived mean occurrence rate v from

$$v = v_n * E * \lambda \qquad \textbf{(3-2)}$$

where v_n = nominal occurrence rate (tor/sq mi/yr) with uncertainty based on tornado density metrics fitted with Type I distribution (e.g., Simiu and Scanlon, 1996); E = Reporting Efficiency, modeled with a log normal distribution; and λ is a judgment based epistemic uncertainty factor applied to the annual rate of tornado occurrences (modeled with a normal distribution).

The nominal (stationary) occurrence rates, v_n, are the tornado H (or LF since both are equal for BD1) count densities for the modern era (1995-2016), based on 22 years of data. Uncertainty in tornado reporting efficiency, *E*, is estimated from the UI-UO polygon test bias factor statistics. We introduce an epistemic uncertainty factor, λ, to reflect uncertain tornado climatology/trends. The details of the development of these variables are discussed in this section.

3.2.4.1. Uncertainty in Nominal Occurrence Rate

The hit tornado density per year (for BD>0) for each region was best fit with an Extreme Value, Type I (EV1) distribution. Figure 3-12 illustrates the 22 years of data and EV1 mean fits (solid lines) with 5^{th} and 95^{th} percentiles (dashed lines). The aleatory uncertainty (randomness) is measured by the slope of fit in Figure 3-12 to the 22 years of modern data. The epistemic uncertainty is measured by the uncertainty in the nominal mean, assuming a stationary process.

The uncertainties in the mean are illustrated in Figure 3-13. The 95% confidence interval (CI) is shown for two coefficients of variation (COV = σ/μ): 1.00 and 1.50, where the latter represents a 50% increase in the annual variability of tornado occurrences.

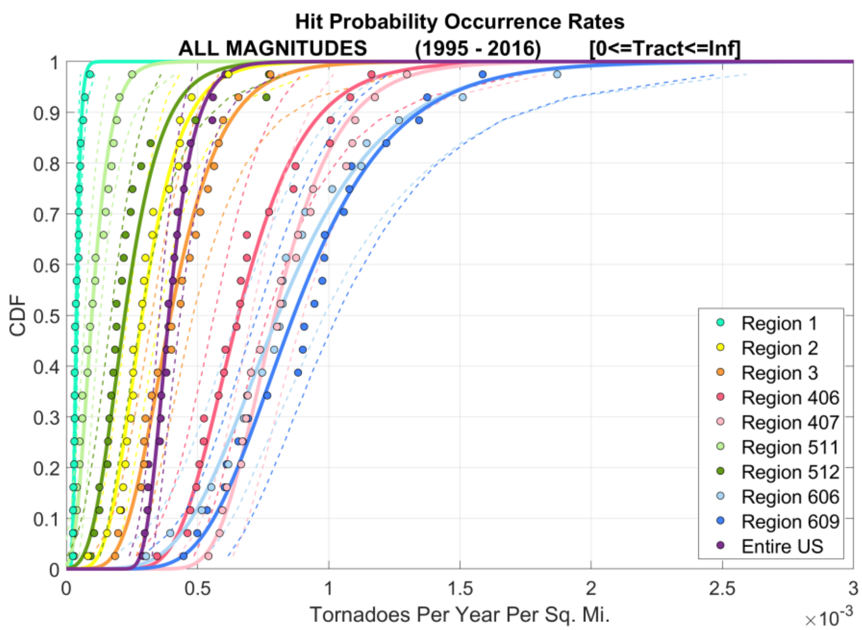

Note: 1 tornado per year per square mile = 0.386102 tornadoes per year per square kilometer

Figure 3-12. EV1 Fits to Nominal Tornado Densities with 5^{th} and 95^{th} Percentiles

To test whether a normal or lognormal model is the best fit for the epistemic uncertainty in v_n, we produced 1,000 percentile curves for each EV1 distribution fit to the 22-years of tornado occurrence metrics using the CDF (cumulative distribution function) in MATLAB. The percentile curves were then integrated to obtain a mean value of each percentile or confidence level. Figure 3-14 shows the PDF (probability density function) plots of the epistemic uncertainties in the nominal densities. The bottom chart in Figure 3-15 shows an example plot of the fit of the distribution of the resulting means, compared to lognormal and normal fits. We determined that the lognormal was the best fit, based on log-likelihood testing.

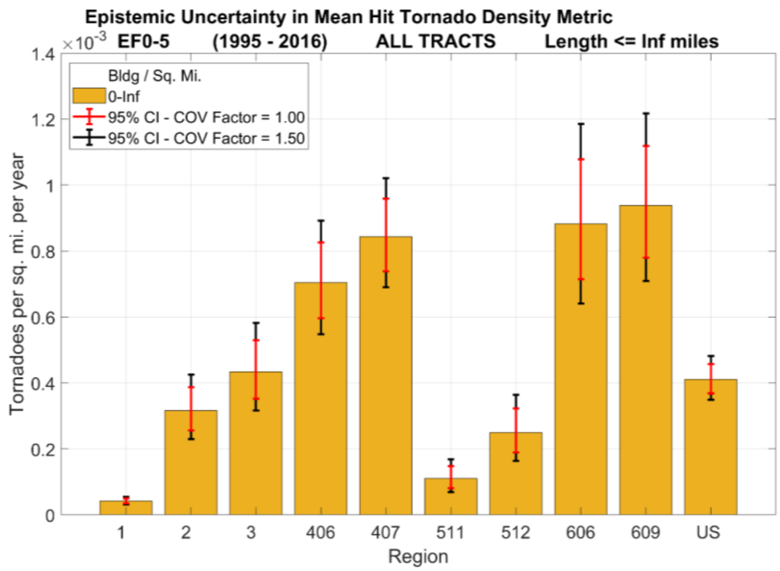

Note: 1 tornado per square mile per year = 0.386102 tornadoes per square kilometer per year; 1 mi^2 = 2.589988 km^2; 1 mi = 1.609344 km

Figure 3-13. Bar Chart of Nominal Means and Uncertainties

3.2.4.2. Uncertainty in Reporting Bias (E)

The regional tornado density plots in Figure 3-10 show how the density of reported tornadoes increases in areas with higher populations and numbers of building per square mile (per square kilometer). The modeling question is how to best use the trend data in these plots. There are two competing measures: (1) the relative accuracy in the mean estimate of tornado densities, which depends on the regional tornado sample size for each BD threshold; and (2), the relative accuracy of the tornado density mean as a measure of population bias for that BD threshold. The former reduces with increasing BD due to reduced land areas and associated tornado counts, while the latter is assumed to increase with increasing BD density since the expected number of building hits by the tornado increases with building density. Ignoring tornado occurrence rates based on roughness, we use a weighting approach with the BD Thresholds (BD1-BD5) to compute a mean bias factor E. This computation is performed by region from

$$E = \frac{1}{2} w_i \sum_{i=1}^{5} [E_i(LF) + E_i(PP)] \tag{3-3}$$

where w_i is the weight for BD_i and $E_i(LF)$ and $E_i(PP)$ are the LF and PP bias factors, respectively. The normalized weights reflect the relative statistical accuracy of the tornado densities (based on region sample sizes) times the relative accuracy of the population bias mean for that BD threshold.[36]

[36] The weights are developed in Appendix C.5.

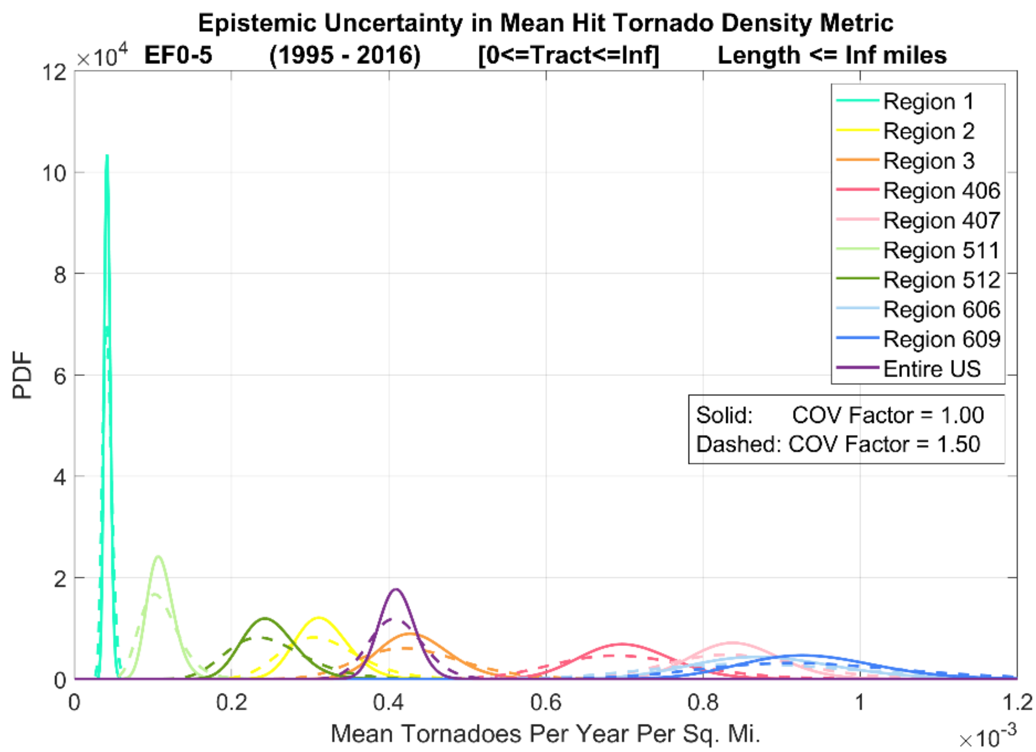

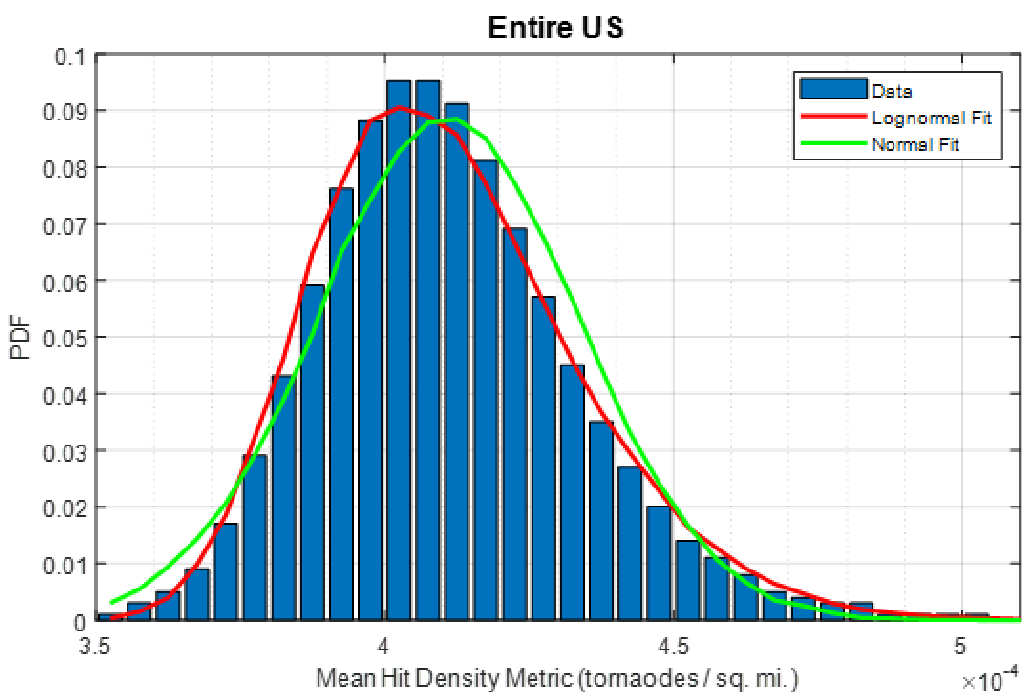

Note: 1 tornado per year per square mile = 0.386102 tornadoes per year per square kilometer; 1 mi^2 = 2.589988 km^2; 1 mi = 1.609344 km

Figure 3-14. Model of Epistemic Uncertainties in Tornado Nominal Occurrence Rate

The results of the calculation in Eq. (3-3) are the mean bias factors given in Table 3-5 and Figure 3-15. The bias factors range from 1.02 in Region 406 to 3.63 in Region 1. We see significant under reporting in Region 1 with a bias factor of 3.63. Recall that most of the reported tornadoes in Region 1 are in areas with higher populations and also lower standard deviations of elevation. Region 1 has vast mountainous areas with very low population densities. The high bias factor reflects this situation. The average bias factor, excluding Region 1 is 1.46, which means that about 46% of the tornadoes that occur east of the Rocky Mountain system are not reported. Excluding Region 3, which also has large areas with very low population, the average bias factor is 1.37. These values are generally comparable to previous studies typically using county level populations, instead of more homogenous CT data. For Region 406, this calculation produced 1.02, which was notably lower than the other regional factors. Based on other studies showing at least a 15% under-reporting of tornadoes, we increased this value to a minimal value of 1.15, based on judgment.

We estimate the uncertainty in the mean regional bias factors from the UI-UO test statistics. The mean and standard deviation of the UI-UO biases for the 10 polygons is 0.994 and 0.073. We use a lognormal distribution to model these potential errors as a product on the mean factors in Figure 3-15. The realized E's in the simulations or Eq. 3-2 were all constrained to be > 1.0, using rejection sampling.

Table 3-5. Mean Bias Factors

Region	Mean Bias Factor
1	3.63
2	1.65
3	2.07
406	1.15
407	1.31
511	1.39
512	1.21
606	1.37
609	1.58

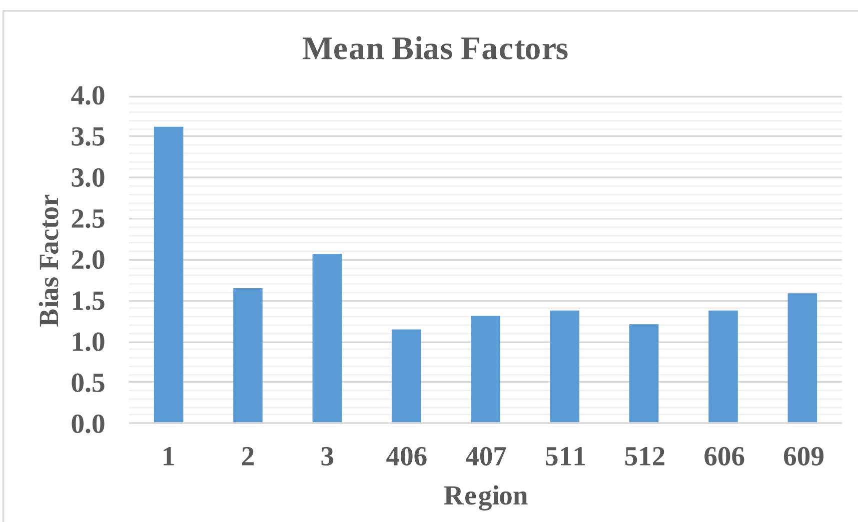

Figure 3-15. Plot of Mean Bias Factors

3.2.4.3. Occurrence Rate Uncertainty Factor (λ)

Previous work (e.g. Twisdale and Dunn, 1983a) has shown that Wind speed Exceedance Frequencies (WEF) are not sensitive to the stochastic model for WEF < 0.01 per year. Since tornado WEFs are < 0.01 in the US, we do not consider uncertainties in the stochastic model and use the simplifying computations outlined in Twisdale et al. (1978, 1981) and Twisdale and Dunn (1983a).

A major concern in the use of the modern era (1995 – 2016) data record for tornado occurrence rate modeling is the limited 22-year period of modern climatology data. As illustrated in Figure 3-16, very little is known regarding the impacts of global warming on Severe Convective Storms. Our approach is to examine simple trends in both the modern era and the entire data record period (1950-2016) to determine how the modern era compares to earlier periods.

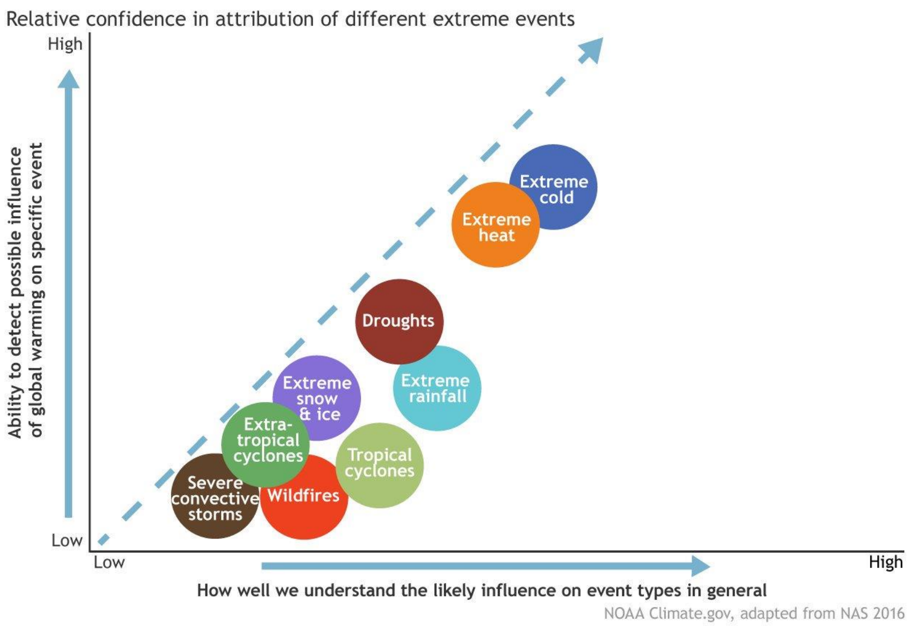

Figure 3-16. National Academy of Sciences Attribution Report Figure

Trends in the modern era data (1995 – 2016) are illustrated in Figure 3-18**Error! Reference source not found.**. The trend plots show H, PP, and LF for BD1 (top) and BD > 100 (bottom) for the entire US coupled with a 5-year running average trend with uncertainties. For the BD1 plots (nominal), the H and LF plots are identical, as discussed previously. These trend plots show a slight downward trend in H and LF, and a slight upward trend in PP (noting that part of this upward trend may well be due to the introduction of the EF system in 2007). The BD > 100 plot also illustrates the increase in tornado occurrence rates over the nominal values in the BD1 figure. This figure has differences in H and LF due to the different counting methods. Overall, we conclude that there is no dominant trend for the US in the modern era.

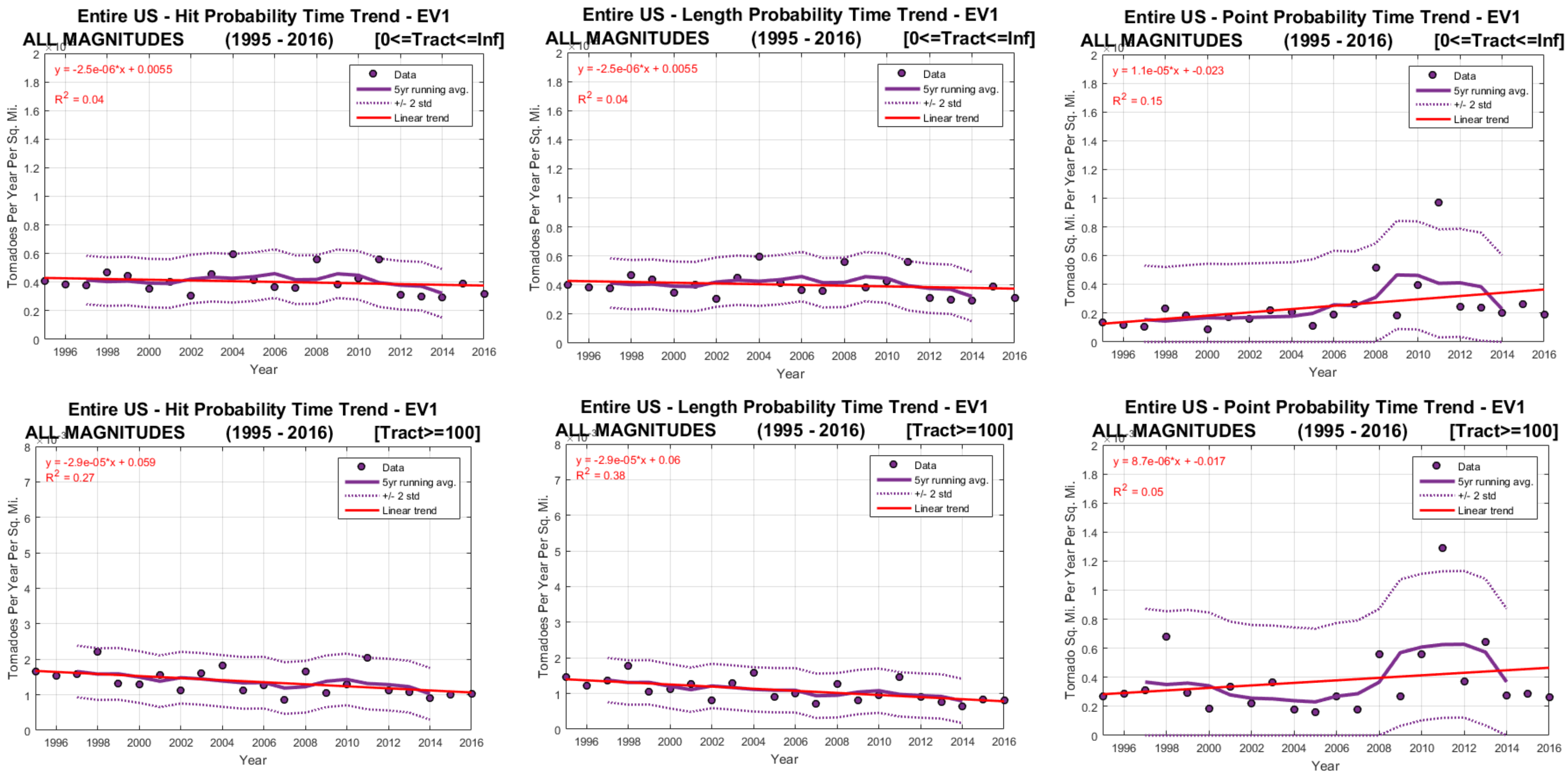

Note: 1 tornado per year per square mile = 0.386102 tornadoes per year per square kilometer

Figure 3-17. H, LF, and PP Modern Era Trend Plots for BD1 (top) and BD100 (bottom) for the Entire US

Next, we examine the 1950-2016 period for nominal occurrence rate trends using running averages. Appendix C.3 includes plots for mean and COV of occurrence rate for the US and the 6 main regions. We evaluated 5, 11, and 22-year periods. Our discussion focuses on the 22-year period plots, consistent with what our 22-year modern era occurrence rate analysis. Figure 3-18 shows the US plot from Appendix C.3. The top figure shows the mean annual occurrence rates (dots), the 22-year running average, and ± 2 standard deviation uncertainty intervals. The running average is plotted at the center of each 22-year period. Twenty-two years was used in these plots to reflect the modern era period of 22 years used to compute the nominal occurrence rate and population bias effects. We see that the 22-year mean is currently near its all-time high point. The coefficient of variation plot provides a view of the variability of the 22-year running mean over time. This plot shows a reduction in the COV in the Pre-F-scale era that continued until the mid-1970s, followed by an increasing trend in COV in the F scale era. The modern era has a COV of around 20%.

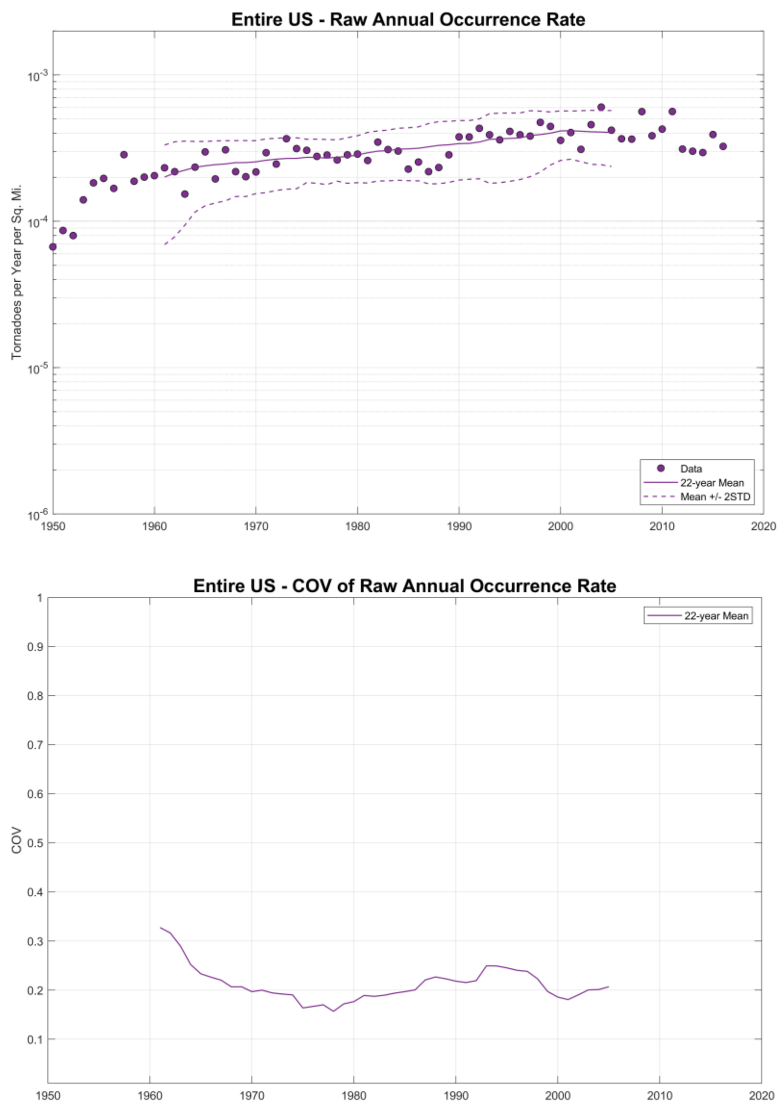

Note: 1 tornado per year per square mile = 0.386102 tornadoes per year per square kilometer

Figure 3-18. Historic US Trends (1950-2016) in Nominal Occurrence Rate

A brief summary of these data suggests:

1. The modern era (1995-2016) contains the highest number of reported tornadoes.
    a. For the 1995-2016 period, the 22-year mean is 97% of the maximum., Hence, our use of 1995-2016 does not represent the absolute maximum 22 year period of the raw recorded number of tornadoes.
2. The moving average (22 years) of the COV provides a measure of annual variability, averaged over 22 years.
    a. Ignoring the early prior F-Scale years, this metric peaked near the beginning of the modern era, after which there was a significant increase in tornado reporting efficiency.
    b. The modern era 22 year COV is currently a maximum.

To reflect: (1) the short 22-year modern-era period; (2) the 22-year analysis period corresponded to 0.97 of the maximum 22-year peak raw occurrence rate; (3) climatology modeling uncertainty; and (4), the increasing PP density trends in the modern era, we use a judgement–based value of 1.1 for λ in Eq. (3-2).

We model λ with a truncated normal distribution with a mean of 1.1, standard deviation = 0.05, minimum = 1.0, maximum = 1.25. This random variable λ is intended to capture unknowns beyond the occurrence rate model, reflect climatology uncertainties, and the shortness of the modern-era record.

3.2.4.4. Computation of Derived Mean Occurrence Rates

We performed 100,000 simulations of Eq. (3-2) assuming statistical independence among the variables. The resulting derived mean occurrence rates are given in Table 3-6 and the CDF plots are given in Figure 3-19. Recall that the Region 406 population bias factor was increased from 1.02 to 1.15 as a minimal bias factor. Hence, it shows more of a derived mean correction than the other regions.

The computed derived means average about 12% higher than the bias corrected mean. This minor increase is dominated by the judgement-based λ factor, which produces about 10% of the 12% increase. In summary, the propagation of uncertainties in the simulation produced a net average 2% increase in the derived mean over the nominal bias corrected mean. This modest increase is due to the general symmetry in the assumed occurrence rate uncertainties.

Overall, the development of v is dominated by the population bias modeling. The average 12% increase resulting from the propagation of uncertainties is not particularly significant in WEF space, which is illustrated in Section 7.

Table 3-6. Summary of Tornado Occurrence Rate Modeling Results

Region	Tornado Occurrence Rates (per sq mi per year)			Ratios	
	Nominal Mean	Bias Corrected Nominal Mean	Derived Mean	Der. Mean/ Nom. Mean	Der. Mean/Bias Corrected
1	3.94E-05	1.43E-04	1.58E-04	4.01	1.10
2	3.08E-04	5.08E-04	5.61E-04	1.82	1.10
3	4.44E-04	9.17E-04	1.01E-03	2.28	1.10
4	8.01E-04	9.43E-04	1.05E-03	1.31	1.11
406	7.06E-04	7.23E-04	9.01E-04	1.28	1.25
407	8.48E-04	1.17E-03	1.29E-03	1.52	1.11
5	1.97E-04	2.58E-04	2.85E-04	1.45	1.11
511	1.09E-04	1.51E-04	1.67E-04	1.53	1.11
512	2.56E-04	3.09E-04	3.43E-04	1.34	1.11
6	8.72E-04	1.26E-03	1.40E-03	1.60	1.11
606	7.77E-04	1.06E-03	1.17E-03	1.51	1.10
609	8.3461E-04	1.318E-03	1.45E-03	1.74	1.10

Note: 1 tornado per square mile per year = 0.386102 tornadoes per square kilometer per year

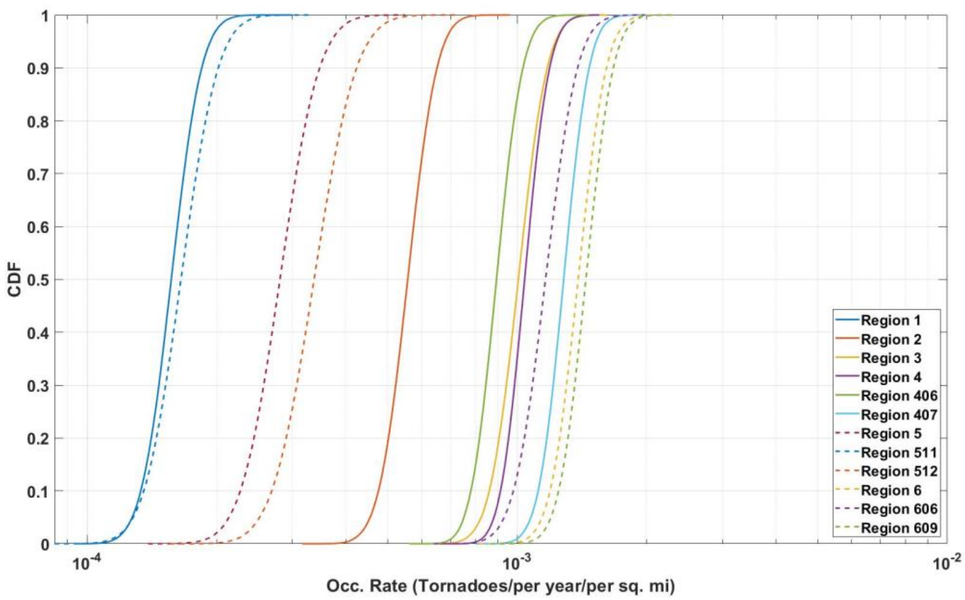

Note: 1 tornado per year per square mile = 0.386102 tornadoes per year per square kilometer

Figure 3-19. CDF Plots of Derived Means

3.3. EF-Scale Distribution

Tornado intensity modeling (F/EF-Scale probability distributions) is developed at a regional level using the EF era data (2007-2016). The methods used for estimating wind speeds and rating tornado intensity in this era are believed to be the best available data regarding the estimation of tornado wind speeds/intensity from observed damage. The NWS EF-Scale training (e.g., NOAA (2016b), Ladue and Mahoney (2006), Ladue and Ortega (2008)) includes a systematic basis for evaluating DIs and DODs that was not used in the F-Scale intensity ratings from earlier eras. In addition, important supporting information regarding numbers and types of DIs, estimated DI wind speeds, and associated EF ratings are documented in the DAT database (NOAA, 2016b). Hence, using the EF-Scale era data for modeling intensity distributions is consistent with the approach for the engineering modeling of EF-Scale wind speeds given an EF intensity rating.

Figure 3-20 provides a flow chart for the process used to develop the EF-Scale distribution. We use the LF metric, Weibull fits of the LF data in relative frequency space, and weighted simulations to produce a derived mean EF-Scale distribution. The following sub-sections present the key elements of this process.

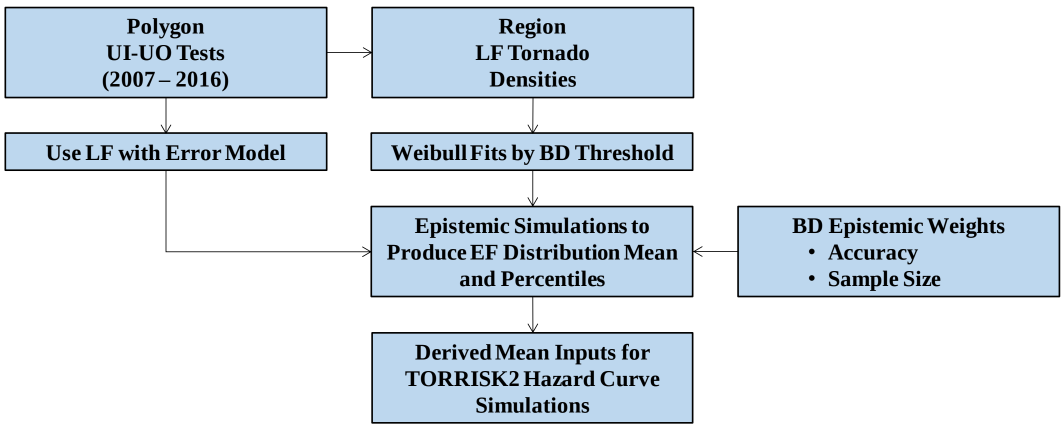

Figure 3-20. Tornado EF-Scale Distribution Intensity Modeling Steps

3.3.1. Building Density Analysis

Similar to the UI-UO tests reported in Section 3.2.2 for occurrence rate analysis, we subsequently expanded those tests to determine the best metric to estimate the EF-Scale intensity distribution, given a tornado occurrence. Appendix C.4 presents these results for the 10 polygon UI-UO tests. As was noted in Section 3.2.2 for occurrence rate analysis, H counting produces a high bias. PP has a somewhat higher variance than LF. Due to reduced variance in the bias factors, the LF metric is used to estimate the regional EF-Scale relative frequency.

We compute the LF metrics by CT BD threshold for the years 2007-2016 using the computational approach described in Section 3.2. The LF EF-Scale results for the 9 regions are given in Figure 3-21. The vast majority of regions have reductions in EF0 with increasing BDs. As noted previously, reduction in EF0 relative frequency means that the relative frequencies of the other EF's increase. For example, we see EF1 relative frequency increasing or flat with increasing BD for essentially all of the regions. EF2s and higher EFs show the same trend, but with more randomness across the BDs. Region 407 has the most tornadoes and one sees less randomness in this plot, which closely adheres to the "theoretically-expected" trends. Overall, these trends provide reasonable evidence for the use of BD threshold analysis to estimate EF intensity distributions. [37]

[37] Region 512 is the main outlier in these trends and this region also has the confounding standard deviation of elevation effects seen in Region 1. Nevertheless, the LF trends are strong considering all of the regions.

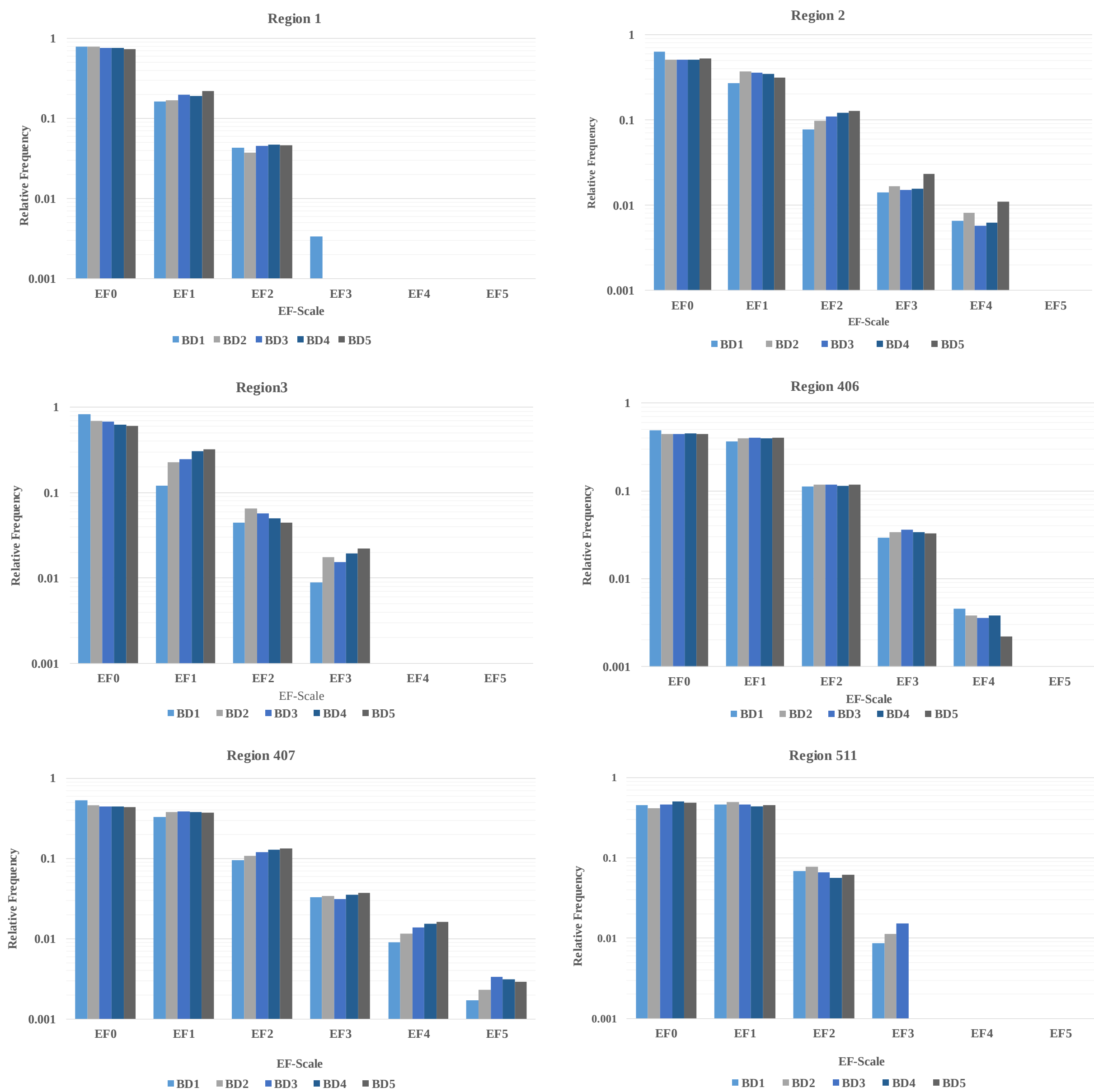

Figure 3-21. Regional EF-Scale Tornado Densities

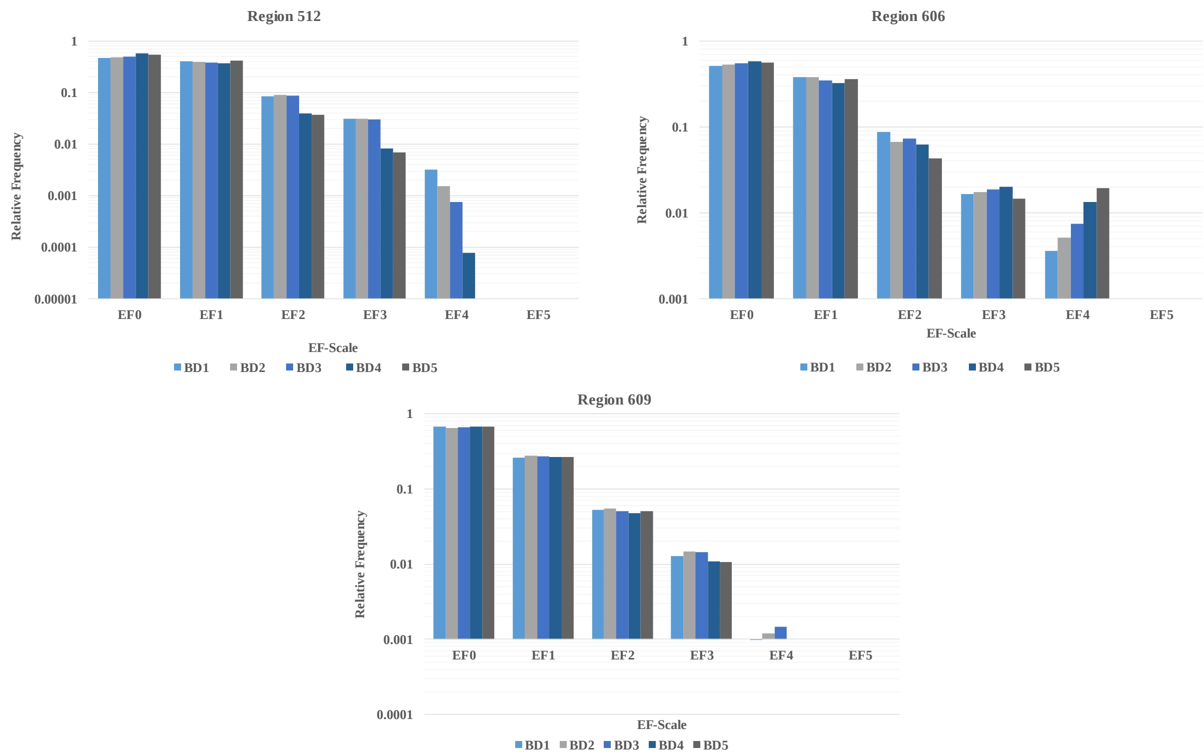

Figure 3-21. Regional EF-Scale Tornado Densities (continued)

These LF trends follow from the fact that there are more buildings within the tornado path in high building density (HBD) areas and a greater chance that one or more buildings are located within the high wind speed areas of the tornado path, thereby resulting in a greater chance of an EF rating associated with the maximum tornado intensity.

Discussion. The use of BD data to condition the EF-Scale distribution minimizes several problems:

1. ***EF0 Reporting Bias.*** Since 1982, the NWS has coded tornadoes with unknown intensity as EF0. With this practice continuing into the EF-Scale era, it is expected that a confirmed tornado that did not strike an EF-Scale DI, were generally rated EF0, regardless of its true maximum intensity. Hence, the EF0 counts include both tornadoes rated as EF0 based on observed EF0 damage, as well as tornadoes with unknown intensity. The fraction of EF0 tornadoes that were actually unknown intensity cannot be estimated accurately at this time on either a national or regional scale. Logically, some fraction of the EF0 tornadoes are not EF0 intensity. We term this potential over-reporting of EF0 intensity as "EF0 Reporting Bias". In HBD areas, tornadoes are more likely to strike DIs and produce damage, resulting in more accurate estimation of the true EF-Scale relative frequencies, given a tornado strike. In rural areas, with fewer DIs and large spacing of DIs, observed tornadoes are much less likely to strike one or more DIs with near-maximum winds and to be rated accordingly. These logical arguments are confirmed in most of the plots in Figure 3-21.

2. ***EF-Limited DIs.*** An EF-limited DI is one that has a maximum potential EF rating less than EF5. For example, a barn has a maximum rating of EF2; regardless of the tornado

wind speed the barn experiences. Our BD-conditioning approach also minimizes the bias from EF-limited DIs, such as barns, that have a max rating of EF2, regardless of the tornado's true intensity. Figure 3-23 shows the percentage of EF-Scale DIs that are EF-limited by quality condition (TTU, 2006). For example, for EF5 tornado ratings, a LB quality condition is not associated with EF5 tornadoes for any of the 28 DIs. About 82% of the DIs are not available at the EXP quality level for EF5s. Thus, intense storms that occur without several DIs (with UB conditions) are unlikely to be rated EF4 or EF5.[38]

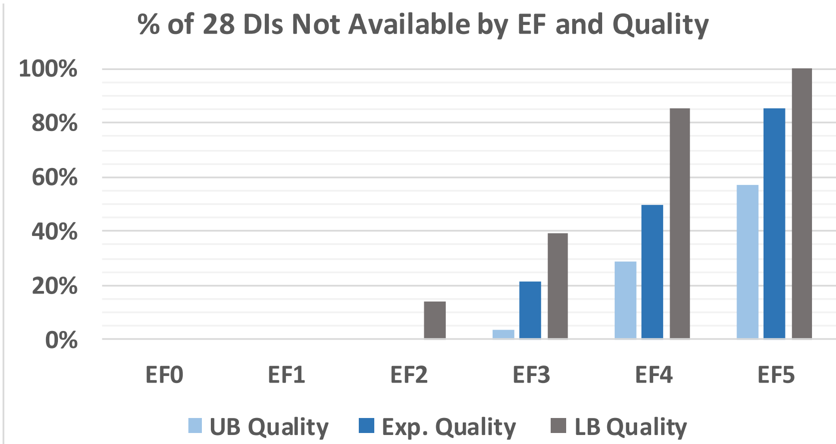

Figure 3-22. Percentage of EF-Scale DI's Not Available by EF and Quality Condition

As noted by Faletra and Twisdale (2016), houses are most often used to rate EF3, 4, and 5s and these DIs are very common in HBD areas. The inclusion of HBD areas, which are dominated by houses, in the development of the EF-Scale relative frequencies has the merits of minimizing effects of EF-limited DIs in the ratings.

3. ***Accuracy.*** The objective of both the F- and the EF-Scales are to quantify the maximum tornado wind speeds/intensity of the event, based on observed damage. It is reasonable to assume that increasing the number of DIs within the area of maximum winds produces more accurate tornado intensity ratings. The maximum wind speeds occur over a small area (a few percent to about 20 percent) of the total tornado path area. Tornadoes in low building density (LBD) areas have a much smaller chance of an accurate rating than those that strike HBD areas. For example, consider a region with 1 building per square mile and a tornado damage path of 1 square mile (2.6 km^2). If we assume that the building is a point and the maximum intensity damage swath area is 5% of the tornado path area, the probability of striking the building for each such tornado is 0.05 (from the binomial distribution). If there are 250 buildings per square mile, this probability is ≈ 1. Thus, in the case of 1 building per square mile and assuming the tornado was visually observed by a spotter or trained observer, it would most likely be rated an EF0 (unknown) since it will not typically strike a structure. However, if it strikes an area with 250 buildings per square mile, the tornado would be expected to damage to many Dis, with significantly improved chances of an accurate F/EF rating.

4. ***Confirmation.*** As noted the EF-Scale process, includes the desirable objective of confirmation of the tornado wind speeds. In higher BD area with multiple DIs in near

[38] See Section 6 for more detailed discussion on EF condition/quality attributes.

proximity, the opportunity for confirmation is clearly enhanced, improving the chances of an accurate final intensity. Typically, an EF-Scale rating is based on multiple DIs, particularly for more intense storms.[39] We believe that tornadoes that strike areas with reasonable BDs are more likely to have more confirmation that those in rural areas that may only strike several isolated structures, sometime many miles apart, all of which may not be evaluated due to awareness, time constraints, and logistics. Reasonable confirmation also requires the DIs to be in near proximity, which occurs more often in areas with higher BDs. For DIs widely separated, questions of inside/outside RMW, and well as PLIV, require more assumptions on the issue of confirmation and also inherently introduces larger uncertainties and potential errors in the EF-Scale rating.

These considerations reinforce the premise that areas with more structural DIs are expected to naturally produce the best chance for more accurate wind speed estimations and associated EF-Scale ratings.

This conclusion is also consistent with the realities of tornado damage surveys and EF-Scale ratings performed by the NWS and other professionals (engineers, architects, researchers, and building officials). Generally, due to time and resource constraints, the logistics of finding, accessing, and analyzing damage, the areas with more structural DIs are generally the ones that receive the most attention and would be expected to have more accurate ratings. Transportation systems are naturally more dense and this fact allows practical access to more accurately evaluate the damage. We therefore conclude that the EF-Scale condition on BD provides the most accurate data on which to probabilistically model tornado intensity.

Counter Arguments on the Use of BD Data. One counter argument follows from papers such as Cusack (2014), which suggests higher tornado frequency and severity in metro areas vs. non-metro areas based on heat island effects, roughness, and associated modifications of convective storms. Regarding this argument, consider the data in Figure 3-21, which shows the trend of increasing tornado severity with increasing BD even in areas where the BD threshold is less than 30 buildings per square mile such as BD2 and BD3 (see Table 3-1). These densities can hardly be condidered to be an urban heat island.[40]

In some parts of the country, tree DIs complicate the arguments for use of EF conditioning based on building density since trees or tree density are not directly considered when building density is the sole independent variable. Trees are often used for wind speed estimation and EF ratings for EF0-1 tornadoes. Table 5 in Faletra and Twisdale (2016) indicated that trees have the same rating as the tornado rating in 47% of EF0s and 42% of EF1s. However, for higher intensities, the fraction of time that trees have the same rating as the tornado drops to 6% and 4% for EF2s and EF3s. Both softwood and hardwood trees are EF-limited DIs, and max out at EF3 and EF4, respectively. In addition, the DAT data shows that trees have never been used to rate EF4s or EF5s. These facts regarding the important role of trees in estimating weak tornadoes (EF0-1) suggest that building density conditioning is suitable for modeling the EF-Scale distribution, particularly for ≥ EF2 tornadoes.

---

[39] See Faletra and Twisdale (2016).

[40] The question of tornado occurrence frequency in highly dense urban areas with high-rise buildings remains an open question and is not considered in this work. Further, while high-density urban areas and the associated ASCE 7 Exposure A (ASCE Commentary, 2016) could influence tornado occurrences, the amount of land area with these levels of roughness is small and would not have a significant impact on the region analysis, were they to be excluded. As previously noted, we limit all of the BD5 thresholds in the analysis to be no greater than 250 buildings per square mile.

3.3.2. Weibull Model of EF-Scale Distribution

Tornadoes generally strike multiple CTs and may interact with CTs that have notably different mean building densities. Our method of analysis follows from the background provided in Section 3.2 regarding the analysis of tornado occurrences. We use the "LF" counting method for the estimation of EF relative frequencies conditional on BD threshold. Using the data for multiple thresholds takes advantage of threshold data trends for Weibull fitting.

A consideration in this approach is that HBD census tracts have much smaller land exposure than LBD census tracts. Consequently, the tornado counts are smaller due to the significantly reduced land area exposure. With fewer tornado counts, the statistical uncertainties are larger as the BD threshold increases. Hence, we use a BD threshold "family-fitting" method that uses all 5 BD thresholds to capture the trends from the data with the most tornado counts (low BD thresholds) to the more accurate data (high BD thresholds).

The Weibull distribution provides a reasonable choice for fitting the EF-Scale distribution. We begin with the 3 parameter Weibull form presented by Dotzek et al. (2003), in which

$$p(x) = \frac{c}{b}\left(\frac{x-a}{b}\right)^{c-1} exp\left[-\left(\frac{x-a}{b}\right)^{c}\right], \qquad \forall x > a, \tag{3-4}$$

$$P(x) = 1 - exp\left[-\left(\frac{x-a}{b}\right)^{c}\right], \qquad \forall x > a, \tag{3-5}$$

In these equations, *p(x)* is the probability density function and *P(x)* is the probability distribution function. We use a location parameter $a = -1$ and define the scale parameter $b = b^*(1+\log(BD+1))^d$. The scale parameter model includes d as an additional fitting parameter and BD = building density threshold. Since the EF scale relative frequencies depend on BD, inclusion of BD into the fitting process is a key part of our modeling process. We constrain d to be ≥ 0. The shape parameter c is unconstrained in the fit. [41]

We fit the natural log of the EF-Scale relative frequency to the natural log of *p(x)* using nonlinear least squares regression using the Gauss Newton Method (NLIN Procedure in SAS/STAT Version 9.3, 2008).[42] The default procedure does not use explicit expressions for the partial derivatives of the model with respect to the parameters estimated, but rather estimates those derivatives at each step. After fitting, we normalize the p(x) to ensure an exact sum to unity over all EF-Scales by the simple logical adjustment *p(x)/P(x = EF5)*.

The LF Weibull input data is given in Table 3-7. Table 3-8 shows the three parameter Weibull fit for each BD threshold. The fitted parameter (*b*, *c*, and *d* in Eqs. (3-4) and (3-5)) values and the mean square error (MSE) of the least squares regression fits are summarized in Table 3-9. The fits in Table 3-9 with d=0 means that the BD family fitting approach did not improve the fit and that the fit reduced to a 2 parameter Weibull. The R-square values for these log-space fits are all greater than 95% for all regions and sub-regions.

---

[41] The Weibull allows us to use location (a), scale (b), and shape (c) parameters in the form described using BD as variable in the non-liner fitting process.
[42] Fitting in log relative frequency space produced the best fits, particularly for EF4/5.

Table 3-7. EF-Scale LF Input Data to Weibull Fits

Region	Building Density		EF0	EF1	EF2	EF3	EF4	EF5	Sum
	Label	Threshold (Bldg/ sq mi)							
Region 1	BD1	0	7.900E-01	1.633E-01	4.333E-02	3.333E-03	0.000E+00	0.000E+00	1.00
	BD2	5	7.925E-01	1.699E-01	3.763E-02	0.000E+00	0.000E+00	0.000E+00	1.00
	BD3	10	7.575E-01	1.969E-01	4.562E-02	0.000E+00	0.000E+00	0.000E+00	1.00
	BD4	20	7.623E-01	1.904E-01	4.738E-02	0.000E+00	0.000E+00	0.000E+00	1.00
	BD5	30	7.335E-01	2.201E-01	4.639E-02	0.000E+00	0.000E+00	0.000E+00	1.00
Region 2	BD1	0	6.302E-01	2.714E-01	7.767E-02	1.413E-02	6.593E-03	0.000E+00	1.00
	BD2	5	5.052E-01	3.720E-01	9.796E-02	1.667E-02	8.113E-03	0.000E+00	1.00
	BD3	15	5.112E-01	3.575E-01	1.103E-01	1.518E-02	5.775E-03	0.000E+00	1.00
	BD4	25	5.112E-01	3.466E-01	1.203E-01	1.567E-02	6.202E-03	0.000E+00	1.00
	BD5	50	5.235E-01	3.141E-01	1.281E-01	2.331E-02	1.096E-02	0.000E+00	1.00
Region 3	BD1	0	8.261E-01	1.207E-01	4.425E-02	8.878E-03	0.000E+00	0.000E+00	1.00
	BD2	5	6.895E-01	2.281E-01	6.483E-02	1.755E-02	0.000E+00	0.000E+00	1.00
	BD3	10	6.795E-01	2.480E-01	5.712E-02	1.533E-02	0.000E+00	0.000E+00	1.00
	BD4	20	6.262E-01	3.046E-01	4.969E-02	1.947E-02	0.000E+00	0.000E+00	1.00
	BD5	30	6.097E-01	3.237E-01	4.457E-02	2.203E-02	0.000E+00	0.000E+00	1.00
Region 4	BD1	0	5.200E-01	3.385E-01	1.008E-01	3.181E-02	7.718E-03	1.205E-03	1.00
	BD2	10	4.427E-01	3.981E-01	1.159E-01	3.279E-02	8.788E-03	1.639E-03	1.00
	BD3	20	4.427E-01	3.896E-01	1.202E-01	3.543E-02	1.018E-02	1.859E-03	1.00
	BD4	30	4.463E-01	3.848E-01	1.220E-01	3.468E-02	1.042E-02	1.790E-03	1.00
	BD5	100	4.408E-01	3.894E-01	1.262E-01	3.177E-02	1.034E-02	1.496E-03	1.00
Region 4 - Subregion 4a (406)	BD1	0	4.866E-01	3.668E-01	1.125E-01	2.949E-02	4.554E-03	0.000E+00	1.00
	BD2	10	4.440E-01	3.976E-01	1.183E-01	3.589E-02	4.159E-03	0.000E+00	1.00
	BD3	20	4.484E-01	3.980E-01	1.155E-01	3.466E-02	3.386E-03	0.000E+00	1.00
	BD4	30	4.426E-01	4.050E-01	1.176E-01	3.258E-02	2.183E-03	0.000E+00	1.00
	BD5	50	4.047E-01	4.623E-01	1.021E-01	2.961E-02	1.292E-03	0.000E+00	1.00
Region 4 - Subregion 4b (407)	BD1	0	5.335E-01	3.270E-01	9.605E-02	3.275E-02	9.000E-03	1.694E-03	1.00
	BD2	5	4.616E-01	3.816E-01	1.087E-01	3.430E-02	1.150E-02	2.297E-03	1.00
	BD3	15	4.482E-01	3.827E-01	1.205E-01	3.136E-02	1.381E-02	3.368E-03	1.00
	BD4	30	4.408E-01	3.773E-01	1.280E-01	3.527E-02	1.542E-02	3.138E-03	1.00
	BD5	50	4.340E-01	3.756E-01	1.342E-01	3.699E-02	1.630E-02	2.915E-03	1.00
Region 5	BD1	0	4.688E-01	4.217E-01	8.132E-02	2.572E-02	2.426E-03	0.000E+00	1.00
	BD2	15	4.673E-01	4.181E-01	8.675E-02	2.666E-02	1.195E-03	0.000E+00	1.00
	BD3	25	4.825E-01	4.076E-01	8.232E-02	2.707E-02	5.420E-04	0.000E+00	1.00
	BD4	50	5.149E-01	3.940E-01	7.715E-02	1.329E-02	6.907E-04	0.000E+00	1.00
	BD5	250	5.437E-01	4.013E-01	4.918E-02	5.849E-03	0.000E+00	0.000E+00	1.00
Region 5 - Subregion 5a (511)	BD1	0	4.569E-01	4.655E-01	6.897E-02	8.621E-03	0.000E+00	0.000E+00	1.00
	BD2	15	4.168E-01	4.950E-01	7.702E-02	1.125E-02	0.000E+00	0.000E+00	1.00
	BD3	25	4.594E-01	4.589E-01	6.649E-02	1.526E-02	0.000E+00	0.000E+00	1.00
	BD4	50	5.036E-01	4.397E-01	5.671E-02	0.000E+00	0.000E+00	0.000E+00	1.00
	BD5	100	4.883E-01	4.505E-01	6.121E-02	0.000E+00	0.000E+00	0.000E+00	1.00
Region 5 - Subregion 5b (512)	BD1	0	4.726E-01	4.079E-01	8.520E-02	3.109E-02	3.188E-03	0.000E+00	1.00
	BD2	15	4.810E-01	3.973E-01	8.938E-02	3.083E-02	1.518E-03	0.000E+00	1.00
	BD3	30	4.976E-01	3.840E-01	8.798E-02	2.969E-02	7.455E-04	0.000E+00	1.00
	BD4	100	5.816E-01	3.715E-01	3.863E-02	8.191E-03	7.718E-05	0.000E+00	1.00
	BD5	250	5.386E-01	4.181E-01	3.653E-02	6.778E-03	0.000E+00	0.000E+00	1.00
Region 6	BD1	0	6.147E-01	3.032E-01	6.603E-02	1.412E-02	1.960E-03	0.000E+00	1.00
	BD2	10	6.145E-01	3.094E-01	5.788E-02	1.565E-02	2.547E-03	0.000E+00	1.00
	BD3	20	6.283E-01	2.948E-01	5.795E-02	1.647E-02	2.460E-03	0.000E+00	1.00
	BD4	30	6.545E-01	2.789E-01	5.082E-02	1.289E-02	2.853E-03	0.000E+00	1.00
	BD5	100	6.904E-01	2.487E-01	4.826E-02	1.121E-02	1.416E-03	0.000E+00	1.00
Region 6 - Subregion 6a (606)	BD1	0	5.165E-01	3.760E-01	8.761E-02	1.636E-02	3.589E-03	0.000E+00	1.00
	BD2	15	5.328E-01	3.780E-01	6.676E-02	1.739E-02	5.094E-03	0.000E+00	1.00
	BD3	25	5.544E-01	3.469E-01	7.249E-02	1.875E-02	7.452E-03	0.000E+00	1.00
	BD4	50	5.818E-01	3.220E-01	6.273E-02	2.018E-02	1.325E-02	0.000E+00	1.00
	BD5	100	5.630E-01	3.605E-01	4.265E-02	1.462E-02	1.924E-02	0.000E+00	1.00
Region 6 - Subregion 6b (609)	BD1	0	6.735E-01	2.596E-01	5.310E-02	1.278E-02	9.833E-04	0.000E+00	1.00
	BD2	10	6.525E-01	2.761E-01	5.537E-02	1.479E-02	1.201E-03	0.000E+00	1.00
	BD3	20	6.605E-01	2.728E-01	5.089E-02	1.428E-02	1.473E-03	0.000E+00	1.00
	BD4	50	6.745E-01	2.671E-01	4.755E-02	1.089E-02	0.000E+00	0.000E+00	1.00
	BD5	100	6.731E-01	2.655E-01	5.088E-02	1.061E-02	0.000E+00	0.000E+00	1.00

Note: 1 mi^2 = 2.589988 km^2

Table 3-8. EF-Scale Weibull Family Fits

Region	Building Density		EF0	EF1	EF2	EF3	EF4	EF5	Sum
	Label	**Threshold (Bldg/sq mi)**							
Region 1	**BD1**	0	7.000E-01	2.520E-01	4.320E-02	4.250E-03	2.600E-04	1.050E-05	1.00
	BD2	5	6.840E-01	2.620E-01	4.870E-02	5.300E-03	3.660E-04	1.690E-05	1.00
	BD3	10	6.800E-01	2.640E-01	5.000E-02	5.580E-03	3.970E-04	1.880E-05	1.00
	BD4	20	6.770E-01	2.660E-01	5.130E-02	5.850E-03	4.270E-04	2.090E-05	1.00
	BD5	30	6.750E-01	2.670E-01	5.200E-02	6.000E-03	4.440E-04	2.210E-05	1.00
Region 2	**BD1**	0	5.660E-01	2.990E-01	1.030E-01	2.640E-02	5.380E-03	8.990E-04	1.00
	BD2	5	5.480E-01	3.030E-01	1.100E-01	3.040E-02	6.700E-03	1.220E-03	1.00
	BD3	15	5.420E-01	3.040E-01	1.130E-01	3.200E-02	7.250E-03	1.360E-03	1.00
	BD4	25	5.390E-01	3.050E-01	1.140E-01	3.270E-02	7.500E-03	1.430E-03	1.00
	BD5	50	5.360E-01	3.050E-01	1.160E-01	3.350E-02	7.810E-03	1.510E-03	1.00
Region 3	**BD1**	0	6.750E-01	2.520E-01	6.060E-02	1.080E-02	1.510E-03	1.730E-04	1.00
	BD2	5	6.260E-01	2.730E-01	7.960E-02	1.770E-02	3.180E-03	4.770E-04	1.00
	BD3	10	6.140E-01	2.770E-01	8.430E-02	1.970E-02	3.740E-03	5.960E-04	1.00
	BD4	20	6.030E-01	2.810E-01	8.880E-02	2.170E-02	4.330E-03	7.280E-04	1.00
	BD5	30	5.970E-01	2.830E-01	9.130E-02	2.280E-02	4.680E-03	8.100E-04	1.00
Region 4	**BD1**	0	4.920E-01	3.270E-01	1.320E-01	3.800E-02	8.210E-03	1.380E-03	1.00
	BD2	10	4.790E-01	3.290E-01	1.390E-01	4.210E-02	9.710E-03	1.760E-03	1.00
	BD3	20	4.760E-01	3.290E-01	1.400E-01	4.290E-02	1.000E-02	1.840E-03	1.00
	BD4	30	4.750E-01	3.290E-01	1.410E-01	4.330E-02	1.020E-02	1.880E-03	1.00
	BD5	100	4.710E-01	3.290E-01	1.430E-01	4.450E-02	1.060E-02	2.000E-03	1.00
Region 4 - Subregion 4a (406)	**BD1**	0	4.510E-01	3.710E-01	1.430E-01	3.050E-02	3.840E-03	2.940E-04	1.00
	BD2	10	4.510E-01	3.710E-01	1.430E-01	3.050E-02	3.840E-03	2.940E-04	1.00
	BD3	20	4.510E-01	3.710E-01	1.430E-01	3.050E-02	3.840E-03	2.940E-04	1.00
	BD4	30	4.510E-01	3.710E-01	1.430E-01	3.050E-02	3.840E-03	2.940E-04	1.00
	BD5	50	4.510E-01	3.710E-01	1.430E-01	3.050E-02	3.840E-03	2.940E-04	1.00
Region 4 - Subregion 4b (407)	**BD1**	0	5.080E-01	3.140E-01	1.280E-01	3.910E-02	9.540E-03	1.920E-03	1.00
	BD2	5	4.830E-01	3.170E-01	1.390E-01	4.640E-02	1.260E-02	2.830E-03	1.00
	BD3	15	4.740E-01	3.170E-01	1.430E-01	4.930E-02	1.380E-02	3.250E-03	1.00
	BD4	30	4.690E-01	3.170E-01	1.450E-01	5.100E-02	1.460E-02	3.510E-03	1.00
	BD5	50	4.660E-01	3.170E-01	1.460E-01	5.210E-02	1.510E-02	3.690E-03	1.00
Region 5	**BD1**	0	5.200E-01	3.600E-01	1.040E-01	1.510E-02	1.160E-03	4.930E-05	1.00
	BD2	15	5.200E-01	3.600E-01	1.040E-01	1.510E-02	1.160E-03	4.930E-05	1.00
	BD3	25	5.200E-01	3.600E-01	1.040E-01	1.510E-02	1.160E-03	4.930E-05	1.00
	BD4	50	5.200E-01	3.600E-01	1.040E-01	1.510E-02	1.160E-03	4.930E-05	1.00
	BD5	250	5.200E-01	3.600E-01	1.040E-01	1.510E-02	1.160E-03	4.930E-05	1.00
Region 5 - Subregion 5a (511)	**BD1**	0	5.110E-01	3.620E-01	1.090E-01	1.650E-02	1.340E-03	6.080E-05	1.00
	BD2	15	5.110E-01	3.620E-01	1.090E-01	1.650E-02	1.340E-03	6.080E-05	1.00
	BD3	25	5.110E-01	3.620E-01	1.090E-01	1.650E-02	1.340E-03	6.080E-05	1.00
	BD4	50	5.110E-01	3.620E-01	1.090E-01	1.650E-02	1.340E-03	6.080E-05	1.00
	BD5	100	5.110E-01	3.620E-01	1.090E-01	1.650E-02	1.340E-03	6.080E-05	1.00
Region 5 - Subregion 5b (512)	**BD1**	0	4.960E-01	3.360E-01	1.290E-01	3.290E-02	5.960E-03	7.980E-04	1.00
	BD2	15	4.960E-01	3.360E-01	1.290E-01	3.290E-02	5.960E-03	7.980E-04	1.00
	BD3	30	4.960E-01	3.360E-01	1.290E-01	3.290E-02	5.960E-03	7.980E-04	1.00
	BD4	100	4.960E-01	3.360E-01	1.290E-01	3.290E-02	5.960E-03	7.980E-04	1.00
	BD5	250	4.960E-01	3.360E-01	1.290E-01	3.290E-02	5.960E-03	7.980E-04	1.00
Region 6	**BD1**	0	6.120E-01	2.860E-01	8.190E-02	1.670E-02	2.580E-03	3.150E-04	1.00
	BD2	10	6.040E-01	2.890E-01	8.540E-02	1.810E-02	2.920E-03	3.740E-04	1.00
	BD3	20	6.030E-01	2.900E-01	8.600E-02	1.830E-02	2.980E-03	3.850E-04	1.00
	BD4	30	6.020E-01	2.900E-01	8.640E-02	1.850E-02	3.020E-03	3.910E-04	1.00
	BD5	100	6.000E-01	2.910E-01	8.730E-02	1.880E-02	3.110E-03	4.090E-04	1.00
Region 6 - Subregion 6a (606)	**BD1**	0	6.130E-01	2.720E-01	8.680E-02	2.230E-02	4.870E-03	9.250E-04	1.00
	BD2	15	5.710E-01	2.840E-01	1.040E-01	3.130E-02	8.090E-03	1.850E-03	1.00
	BD3	25	5.660E-01	2.850E-01	1.060E-01	3.240E-02	8.540E-03	1.990E-03	1.00
	BD4	50	5.600E-01	2.860E-01	1.080E-01	3.390E-02	9.130E-03	2.180E-03	1.00
	BD5	100	5.550E-01	2.870E-01	1.110E-01	3.520E-02	9.690E-03	2.370E-03	1.00
Region 6 - Subregion 6b (609)	**BD1**	0	6.260E-01	2.870E-01	7.280E-02	1.210E-02	1.410E-03	1.210E-04	1.00
	BD2	10	6.210E-01	2.900E-01	7.520E-02	1.290E-02	1.550E-03	1.380E-04	1.00
	BD3	20	6.200E-01	2.900E-01	7.570E-02	1.300E-02	1.580E-03	1.420E-04	1.00
	BD4	50	6.180E-01	2.910E-01	7.620E-02	1.320E-02	1.610E-03	1.460E-04	1.00
	BD5	100	6.170E-01	2.910E-01	7.660E-02	1.330E-02	1.640E-03	1.490E-04	1.00

Note: 1 mi^2 = 2.589988 km^2

Table 3-9. Model Results for Weibull Family Fit Results

Region	Sub-Region	Non-Linear Fit Status	Weibull Parameters			Fit MSE
			b	c	d	
1		Converged	1.2497	1.6320	0.0445	0.055
2		Converged	1.5102	1.4958	0.0548	0.104
3		Converged	1.2148	1.4289	0.1564	0.092
4		Converged	1.7487	1.6227	0.0340	0.022
4	406	Converged	1.8772	1.9171	0.0000	0.190
4	407	Converged	1.6876	1.5319	0.0790	0.033
5		Converged	1.6993	1.9202	0.0000	0.188
5	511	Converged	1.6736	1.9304	0.0000	0.190
5	512	Converged	1.6682	1.9057	0.0000	0.190
6		Converged	1.3985	1.5162	0.0202	0.047
6	606	Converged	1.3328	1.3679	0.1042	0.186
6	609	Converged	1.3912	1.5891	0.0134	0.044

3.3.3. Derived Mean EF Distribution

The BD fits in Table 3-8 provides the basis for modeling the EF-Scale distribution by region. Since there is no fundamental rule by which to select the best BD threshold fit, we develop a set of weights, by regions to compute a mean EF distribution for each region. Appendix C.5 develops these weights.

The statistical uncertainties in the Weibull model, developed in Section 3.2.2, are characterized by the MSE of the fit (see Table 3-9). This uncertainty in the fitting of the Weibull family of curves is a source of epistemic uncertainty. In addition, to reflect that other non-Weibull EF-Scale models are plausible, we apply a judgment factor (*J*) on the √MSE to reflect assumptions and uncertainties associated with the model development and form. A "*J*" value of 1.25 was selected by trial and error, based on plots of uncertainty bounds capturing the range of data, as described in the following implementation.

The epistemic uncertainties are propagated through these weighted family of curves and their statistical uncertainties using Monte Carlo simulation. A "realized" EF-Scale probability distribution function is created in an outer simulation loop to model epistemic uncertainties. That distribution is used in the inner loop simulations that produce the derived EF-Scale distribution. The following steps describe the implementation:

1. Sample from a uniform random number and select the associated BD threshold according to the weights in Table C-6 in Appendix C.5.
2. Sample a random number (ξ) from $N(0,1)$ and compute an EF distribution from the associated BD Weibull from Step 1 from the equation $p(EF_i) = \mu_i + \xi * J\sqrt{MSE}$, for i = 2, 3, 4, and 5. This form of modeling the statistical uncertainties follows from the fit of the Weibull family in ln space and assumes the Weibull statistical errors are lognormally distributed.
3. In developing the EF distribution, we use the reported relative frequencies for EF0 and EF1 for each associated BD threshold. This approach ensures reasonableness of the values for EF0 and EF1, which are based on large sample sizes (typically over 80% of the

tornadoes are ≤ EF1) and also include a large fraction of tornadoes based on non-structures, such as tree damage, which may not be directly related to BD threshold.[43]

4. Normalize the realized EF-Scale distribution to ensure that the CDF(EF5) ≡ 1.0.

The resulting derived mean and percentiles of the regional EF distribution are given in Table 3-10. Figure 3-23 plots the derived means and percentiles and also shows the LF BD data points.[44] We see that the derived mean values are generally in the range of the mid BD Threshold Curves. The 5th and 95th percentile curves around the derived mean provide the epistemic bounds on the EF-Scale distribution. The *J* value, described above, was selected such that the 1st and 99th percentile curves for the derived mean generally cover the full range of the raw data points for most regions. The derived mean distribution in Table 3-10 is an input to the TORRISK code used in the development of region and sub-region hazard curves.

***Region Comparison Discussion*. Error! Reference source not found.** compares the derived m ean EF relative frequencies for the 9 regions/sub-regions. This figure illustrates that the modeling approach produced significant differences in the EF-Scale distribution by region. Aside from the EF0-EF1 raw data (conditioned on BD) portion of these curves, the regional "curves" began to separate significantly for ≥ EF3 intensity. We see at least 3 groups. Region 407 is at the top with the highest relative frequencies for EF3-5. The second group of regions includes 606, 2, 3, 512, and 406. The regions with the lowest relative frequencies for EF3-5 includes 609, 511, and 1.

Table 3-10. EF-Scale Derived Mean Estimated Values

EF Scale	Region								
	Region 1	Region 2	Region 3	Region 406	Region 407	Region 511	Region 512	Region 606	Region 609
EF0	7.53E-01	5.16E-01	6.42E-01	4.70E-01	4.53E-01	4.37E-01	4.43E-01	5.26E-01	6.55E-01
EF1	1.95E-01	3.36E-01	2.60E-01	3.51E-01	3.58E-01	4.40E-01	3.83E-01	3.35E-01	2.64E-01
EF2	4.56E-02	1.08E-01	7.55E-02	1.40E-01	1.30E-01	1.09E-01	1.33E-01	9.85E-02	6.78E-02
EF3	5.19E-03	3.10E-02	1.81E-02	3.31E-02	4.43E-02	1.38E-02	3.39E-02	3.02E-02	1.17E-02
EF4	3.90E-04	7.34E-03	3.66E-03	5.19E-03	1.25E-02	9.00E-04	6.15E-03	8.28E-03	1.46E-03
EF5	1.97E-05	1.45E-03	6.26E-04	5.62E-04	2.98E-03	3.13E-05	8.23E-04	2.01E-03	1.35E-04
Sum	1.00E+00	1.00E+00	1.00E+00	1.00E+00	1.00E+00	1.00E+00	1.00E+00	1.00E+00	1.00E+00

[43] Trees, which are not necessarily correlated with building density, are often used to rate EF0 and EF1 tornadoes (see Section 3.3.1).
[44] These plots show continuous dashed lines for purposes of viewing the shape of the EF PMFs in log space.

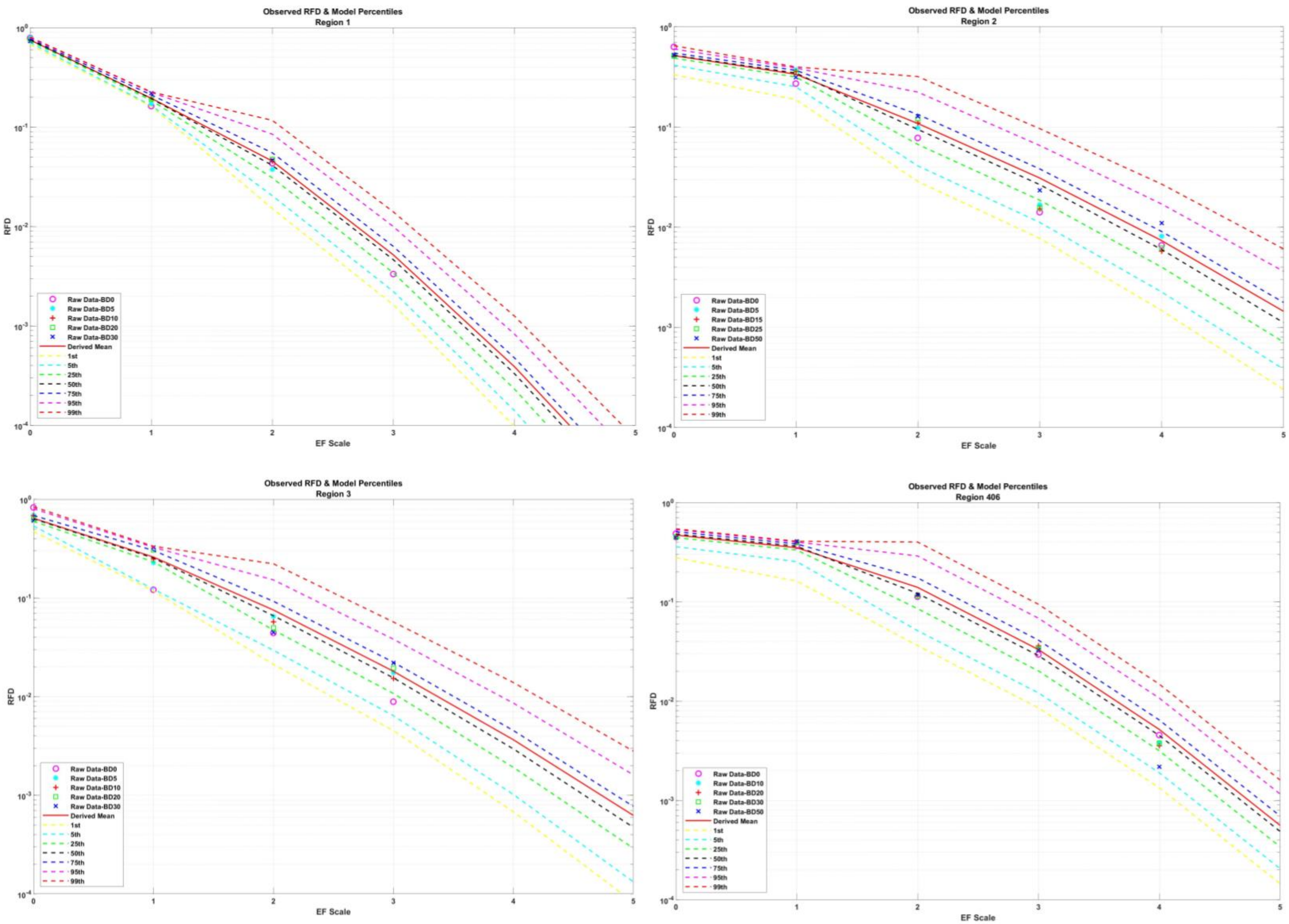

Figure 3-23. EF-Scale PMFs with Epistemic Uncertainties

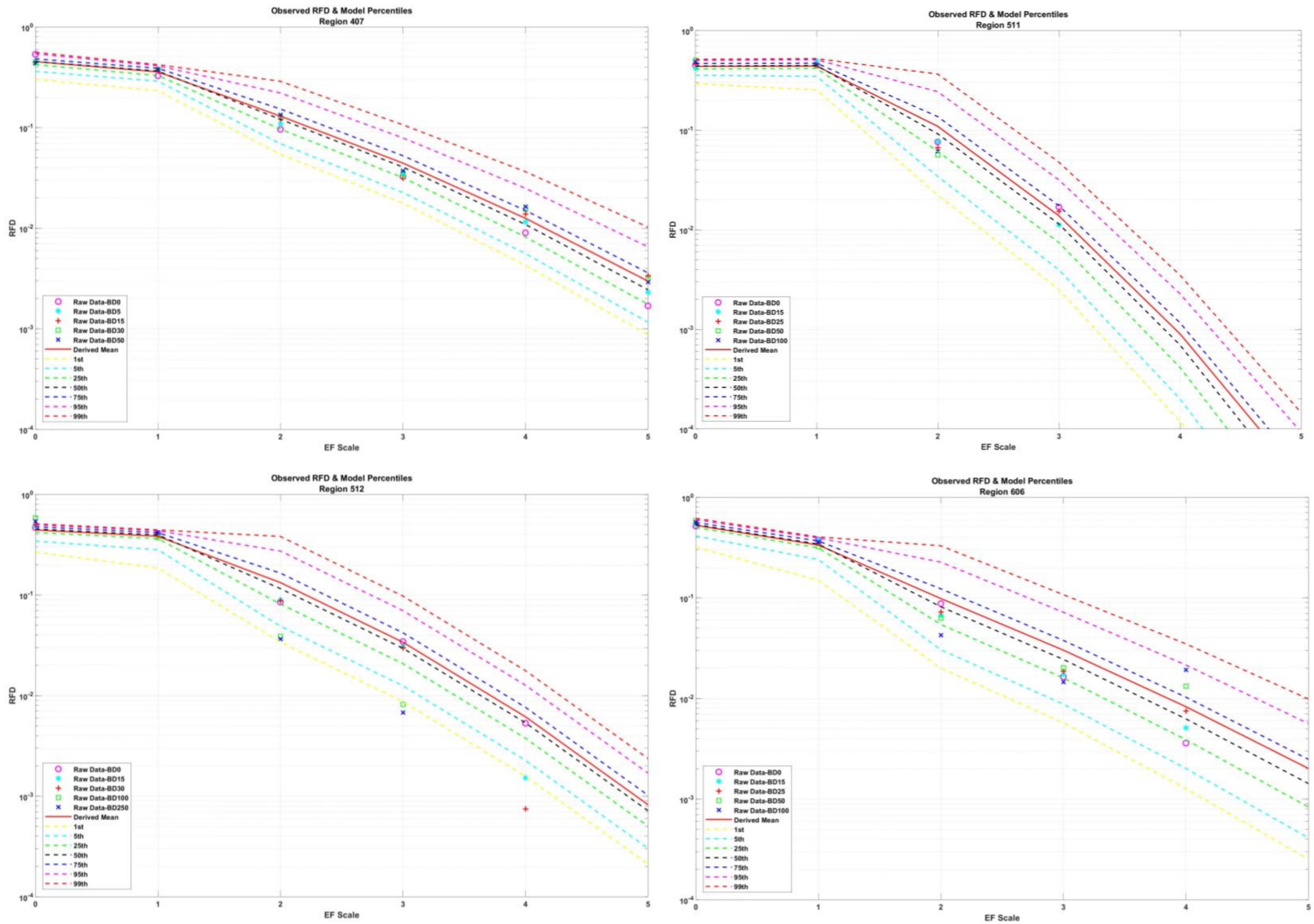

Figure 3-24. EF-Scale PMFs with Epistemic Uncertainties (continued)

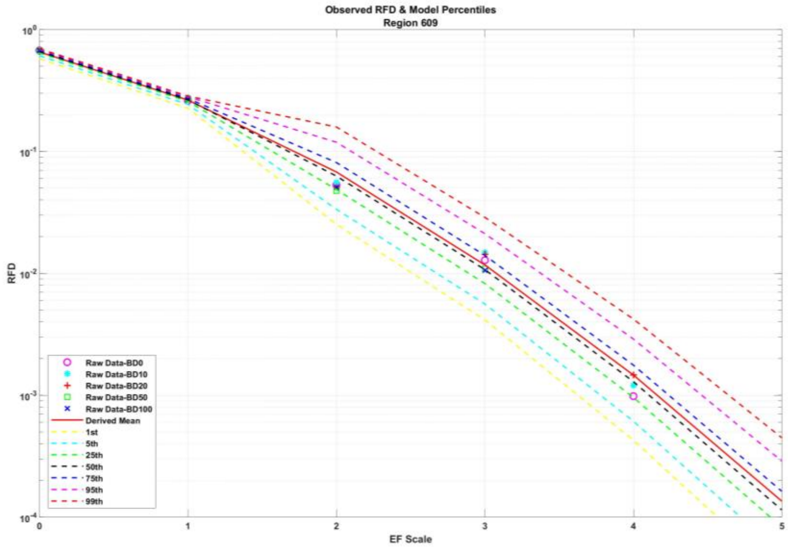

Figure 3-23. EF-Scale PMFs with Epistemic Uncertainties (continued)

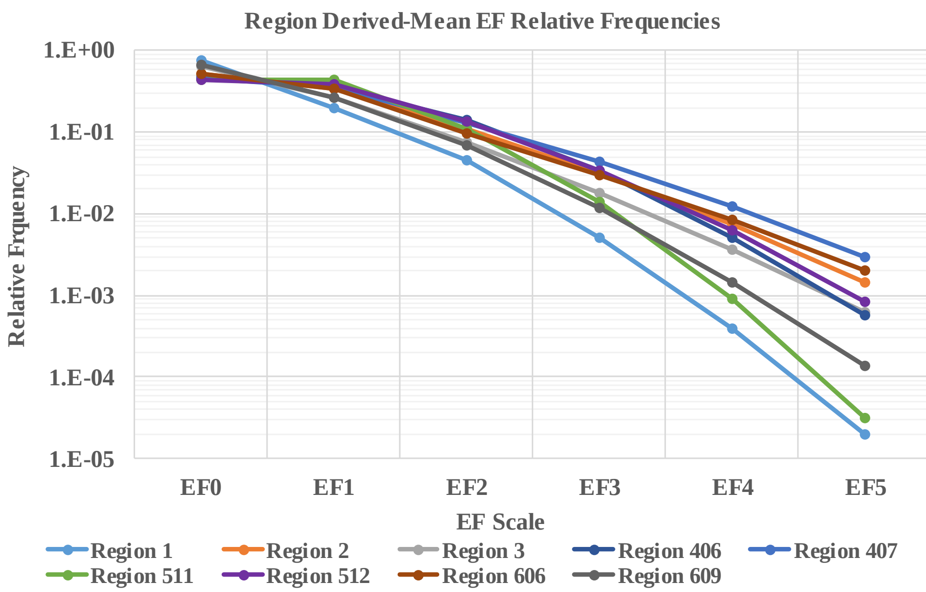

Figure 3-24. Derived Mean EF Relative Frequencies by Region

Another way to compare regional risk is the product of the derived mean tornado occurrence rates and the EF relative frequencies. This product gives the occurrence rate (tornadoes per square mile per year) by EF-Scale and is shown in Figure 3-25. The shapes of the individual curves remain unchanged from Figure 3-24**Error! Reference source not found.**, but their r elative positions shift with the regional occurrence rates. For example, we see that Regions 2, 3, and 406 are much closer together in Figure 3-25 once regional occurrence rates are factored in. This data product is an important element of the wind speed hazard curves in Section 7, although it does not include tornado path lengths, widths, and areas, which vary by region, and are further conditional on the EF-Scale.

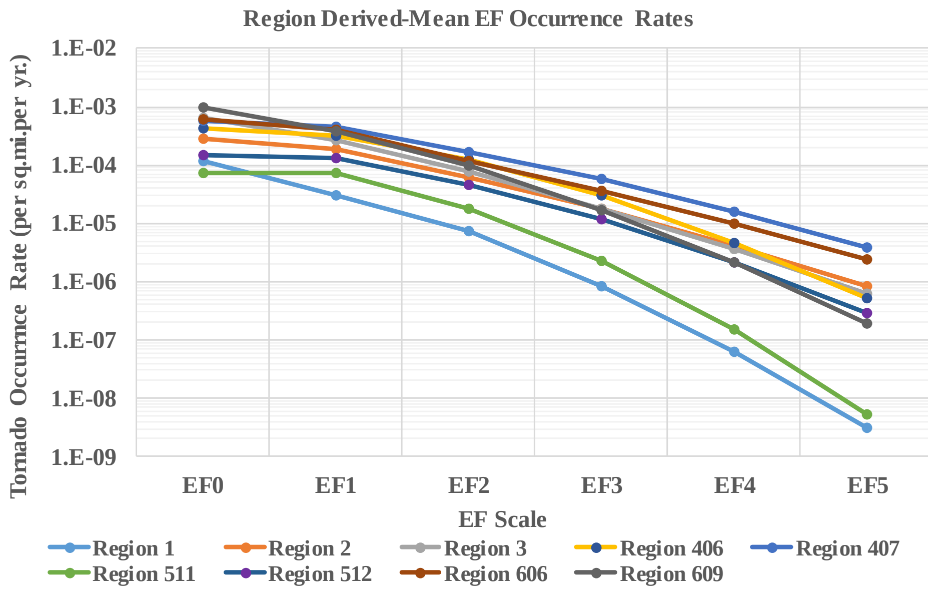

Note: 1 tornado per square mile per year = 0.386102 tornadoes per square kilometer per year

Figure 3-25. Derived Mean EF Relative Frequencies by Region

A simple ranking of the regions is illustrated in Figure 3-27**Error! Reference source not found.**, which plots mean tornado occurrence rates for ≥ EF3 intensity tornadoes. This ranking shows a two order of magnitude difference for ≥ EF3 risk from Region 407 to Region 1. The relative ranks place 407 at the top, followed by the regions adjacent to 407 (606, 406, 3, and 2), followed by 609, 512, 511, and 1. This pattern follows, reasonably well, the plots and climatology analysis developed in Section 2. As it turns out, including separate regions for Regions 2 and 3 served little purpose as seen from Figure 3-25 and 3-27**Error! Reference source not found.**. However, the creation of the sub-regions 406 and 407, 511 and 512, and 606 and 609, seems justified from the differences in the frequencies of the ≥ EF3 events in Figure 3-27**Error! Reference source not found.**.

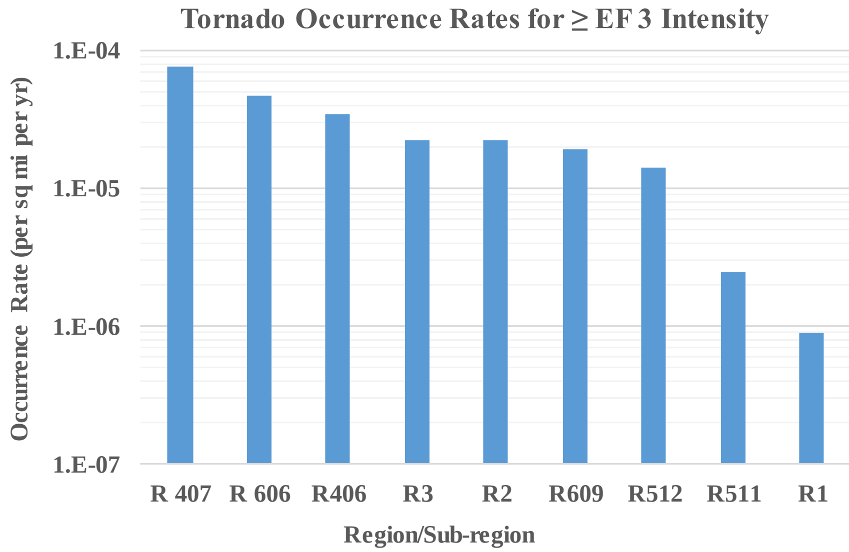

Note: 1 tornado per square mile per year = 0.386102 tornadoes per square kilometer per year

Figure 3-26. Region Ranking by Mean Occurrence Rate for ≥ EF3 Intensity

3.4. Tornado Path Variable Modeling

In tornado risk modeling, tornado wind field and path variables have been almost universally conditioned on the F/F-Scales (e.g., MacDonald et al. (1975), Twisdale et al. (1978), Reinhold and Ellingwood (1982), Brooks (2004), Ramsdell and Rishel (2007)). Intense tornadoes have much larger path areas, lengths, and widths than weak tornadoes. Further, since the EF scale is a discrete scale, this conditioning is easily handled from a modeling perspective. In addition, tornado occurrences, characteristics, and wind speed risk (which is derived from the F/EF scale distribution) have long been recognized as region-dependent (Wolford (1960), Court (1970), Abby (1975), MacDonald (1975), Fujita (1978), Twisdale (1978), NRC (2007) Banik and Kopp (2007), to name a few).

As previously discussed, we use region-dependent tornado modeling in which region (R) is the top variable (developed in Section 2), with EF dependent on region (Section 3.3)[45]. In this section, we continue the modeling sequence with PL dependent on EF and R (3.4.1); PW dependent on R, EF, and PL (3.4.1); and tornado path direction (ϕ) dependent on R (3.4.2). Within path models, which are not regional-dependent, include PLIV dependent on EF (3.5.2) and MDW dependent on EF and PLIV (3.5.4). Region dependence is not included for the within path variables since these data are derived from individual tornado studies and there is limited data.

Path length and path width data provide the basis for modeling tornado path geometries. Since tornadoes typically cross many CTs, there is no practical way to develop path variable distributions that reflect BD bin. We therefore use the regional path data for all ≥ EF1 tornadoes without considering BD data. For EF0 tornadoes, which have a large number of tornadoes with

[45] We note that EF is also conditioned to BD as part of the regional development of an EF scale distribution. The use CT modeling to extract EF counts based on BD is too fine a scale to extract tornado path variables, especially PL, which generally crosss many CTs. Hence CT conditioning is not used for any within path modeling.

SPC default minimal PL and/or PW entries (0.1 miles (0.16 km) for PL and 30 ft (9.1 m) for PW, respectively)[46], we consider BD and source rating data in the modeling of EF0 PL and PW.

Due to the limited amount of EF intensity data (2007 – 2016), we develop path models for Regions 1 – 6. We therefore use the Region 4 path models for 406 and 407, the Region 5 path models for Sub-regions 511 and 512, and the Region 6 path models for Sub-regions 606, and 609. The path variable models are conditioned on EF-Scale. MATLAB R2018a (MathWorks, 2018) and its statistical toolbox are used to analyze path length, path width, and path direction data. The statistical analyses are only carried out for the known values. Unknown or missing values are not considered.

Table 3-11 shows the counts of each EF-Scale tornadoes by region. Region 4 has the highest number of tornadoes and Region 1 has the least number of tornadoes in each EF-Scale among all the six regions. Regions 2, 5 and 6 do not have a recorded EF5 tornado. Regions 1 and 3 do not have recorded EF4 or EF5 tornadoes.

Table 3-11. EF-Scale Counts by Region (2007 – 2016)

F-scale	Region 1	Region 2	Region 3	Region 4	Region 5	Region 6
0	240	674	655	3889	229	1019
1	49	291	96	2537	207	496
2	13	83	37	759	40	111
3	1	15	7	242	14	25
4	0	7	0	58	2	4
5	0	0	0	9	0	0
Total	303	1070	795	7494	492	1655

3.4.1. Path Length and Width

A comparison of the mean values of the path length and width by EF-Scale are compared across regions in Figure 3-27 and Figure 3-28, respectively. Figure 3-27 shows that the mean lengths in Region 4 are higher than most of the remaining regions. Region 1 has the lowest mean lengths for EF0 through EF2. No significant difference is observed in mean path widths among all regions for EF1 and EF0 intensities. The mean lengths and widths show monotonic increase with EF-Scale except for a few cases where the sample size is very low, such as EF4 path length in Region 6. As discussed in Section 2, the EF era path length and width data has higher means than pre-EF eras.

[46] SPC default path widths were discussed in Section 2.2 and Appendix A.

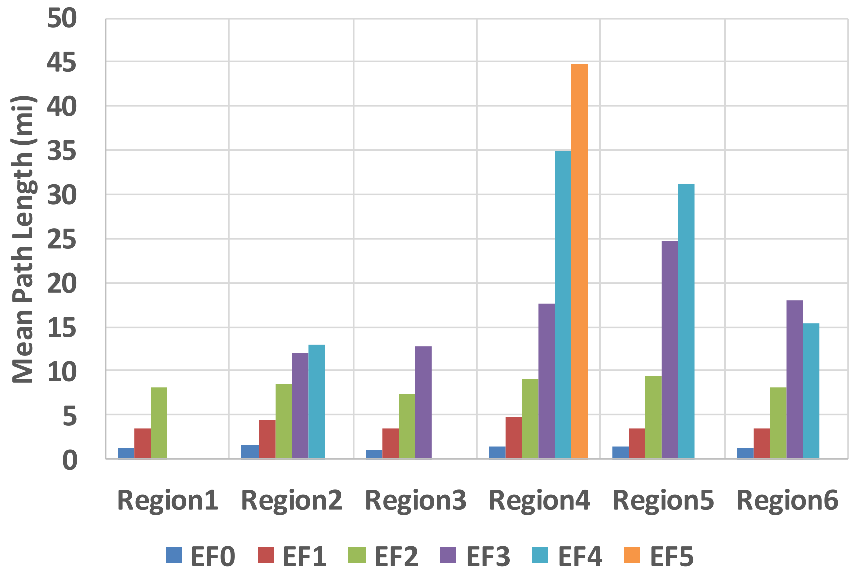

Note: 1 mi = 1.609344 km

Figure 3-27. Mean Path Lengths

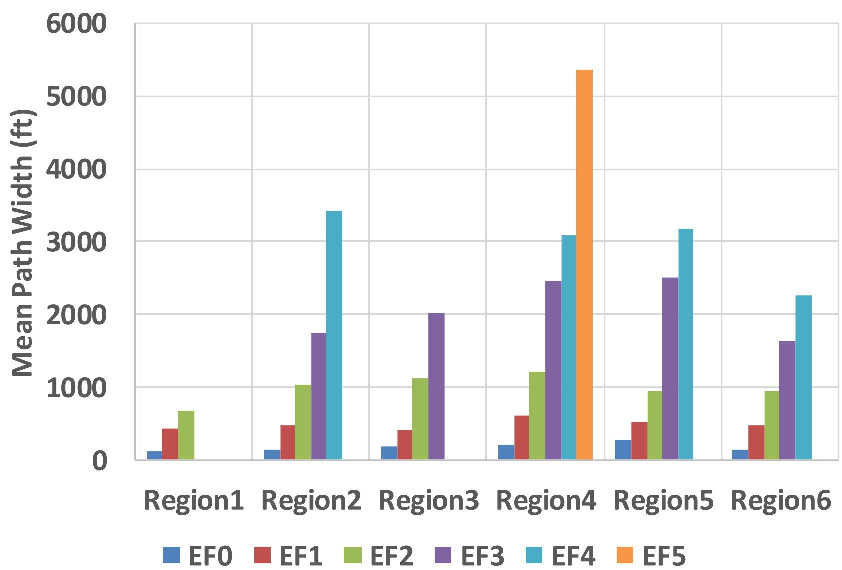

Note: 1 ft = 0.3048 m

Figure 3-28. Mean Path Widths

3.4.1.1. Default Minimal Values

As discussed in Section 2.2 and Appendix A, not all tornadoes are surveyed to determine a field-based estimate of PL or PW. Tornadoes that produce little or no damage may be given a default minimal PL or PW (0.1 miles (0.16 km) for PL and 30 ft (9.1 m) for PW). The frequency of these defaults depends on the EF-Scale and the rating source. In general, these default minimums are more frequently used by non-NWS rating sources. Default minimum tornadoes have path area that are notably less than the non-default tornadoes (Faletra et al. 2016a).

In modeling PL and PW, it is useful to consider separating tornadoes into a default group and a non-default group. In this context, a default tornado has either a default minimal PL, PW, or both. For non-default tornadoes, the majority are rated by the NWS and the differences in tornado path areas are not nearly as great as the difference among the areas of default and non-default tornadoes. Hence, for practical reasons, we do not distinguish rating source in modeling PL and PW for the non-default group. Figure 3-29 illustrates that EF0 tornadoes have relatively high number of tornadoes (2007 – 2016) that have default minimal PL/PW. About 40% of the EF0 tornadoes in R1 and R3 are defaults and over 25% of the EF0s in R2 and R6 are defaults. The other EF intensities have nil or very small percentage of defaults.

For default tornadoes, the impact of rating source is important only for EF0 tornadoes. Most of EF0 tornadoes are rated by non-NWS sources (see Faletra et al., 2016a). Our model of EF0 default tornadoes considers BD data in a similar fashion as was done for developing the EF-Scale distribution. We treat the fraction of EF0 tornadoes that are default minimal tornadoes with an epistemic uncertainty model that uses separate PL and PW models for default and non-default tornadoes.

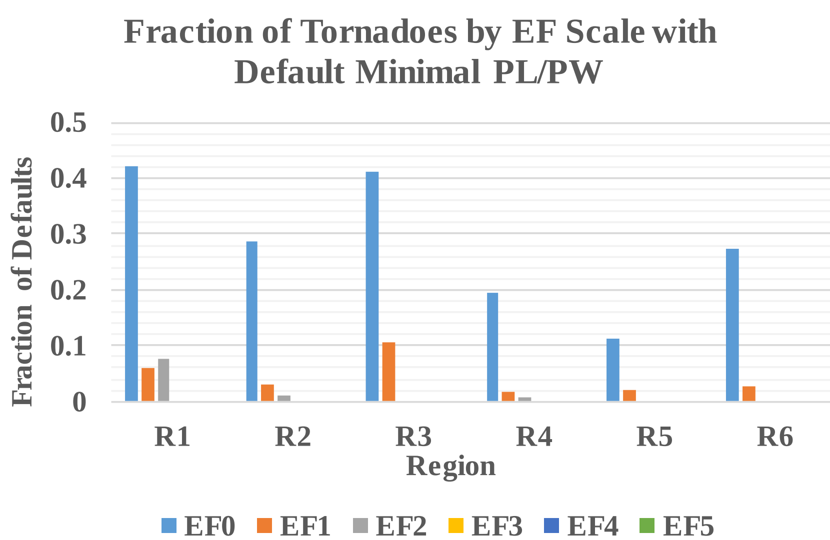

Figure 3-29. Fraction of Tornadoes by EF-Scale with Default Minimal PL/PW

Epistemic Model for Default EF0 Tornadoes. Table 3-12 shows the data used for the epistemic model. We use the reported data by rating source for the upper bound (UB) estimate of the percent of default EF0 tornadoes. For example, 46% of the tornadoes in Region 1 were rated by non-NWS sources and this is assumed to be an upper bound on the true percentage of very small (default minimum) tornadoes. The NWS default rating percentage is assumed to be a median estimate of the true percentage default.[47] A default percentage of zero is used for the epistemic

[47] This percentage is the percentage of NWS-rated EF0s that have a default PL or PW.

lower bound (LB). Accordingly, the lower bound in Table 3-12 does not include any default tornadoes in the modeling of EF0 path areas. [48]

Table 3-12. Epistemic EF0 Default Data and Results

Parameter	Epistemic Bounds	EF0 Percentages by Region						Comments
		1	2	3	4	5	6	
Default Fractions	UB	46%	18%	45%	15%	11%	26%	Raw Data EF0 Default Fraction
	Mid	13%	3%	25%	8%	6%	8%	NWS rated EF0 default fraction
	LB	0%	0%	0%	0%	0%	0%	Assumes no default tornadoes
Mean EF0 Default Area Increase		75%	76%	53%	27%	24%	65%	Increase in default path areas only

The regional epistemic model is implemented by sampling from a bi-linear probability distribution function that connects the percentages in Table 3-12. For example, for Region 4, the distribution is linear from 0% to 6% and then linear from 6% to 11%. Since the Mid case is assumed to be the median, one-half of the time the percentage will be less than the Mid percentage and ½ of the time it will be greater, with the limiting bounds shown in the table for each linear segment. Once the percentage is determined, a second uniform random number is sampled to determine if the EF0 tornado is a default or non-default tornado. Based on that outcome, the path length and width are sampled from the default or non-default distribution.

The impact of the default modeling approach for EF0 is given in the bottom row of Table 3-12. The percent increases in area range from about 24% to 76%. While these increases are notable, they have a much more modest impact on the overall EF0 path areas since the non-default EF0 path areas are significantly larger. Nevertheless, the EF0 default path variable model has been implemented with the epistemic sampling noted above. As pointed out in Faletra et al. (2016a), the percentage of default- rated tornadoes has declined in the modern era and this is reflected in the EF-Scale era data analyzed herein.

3.4.1.2. Path Length and Path Width Correlation

The analysis of correlation between path length and path width is carried out for the six regions. The analysis is only carried out for the EF-Scales where the path length and path width data are available. Table 3-13 shows the correlation coefficients and associated p-values in each F-Scale for the six regions. The p-value is associated with the null hypothesis that path length and width are not correlated. Any p-values less than 0.05 indicate the rejection of this hypothesis. As shown in Table 3-13 the null hypothesis is rejected for most cases where the correlation coefficient is low. The p-values for these cases are shaded in the table. The correlation of PL and PW by EF-Scale is therefore an important modeling consideration.

[48] There are many tornadoes in the database that have small values of PL or PW (some of which are only slightly greater than the default minimal values).

Table 3-13. Correlation Between Path Length and Path Width

EF-scale	Region 1		Region 2		Region 3		Region 4		Region 5		Region 6	
	Correlation Coeffcient	p-value	Correlation Coeffcient	p-value	Correlation Coeffcient	p-value	Correlation Coeffcient	p-value	Correlation Coeffcient	p-value	Correlation Coeffcient	p-value
0	0.2038	0.0015	0.1250	0.0011	0.2214	0.0000	0.3052	0.0000	0.2767	0.0000	0.2507	0.0000
1	0.1628	0.2637	0.1895	0.0012	0.1778	0.0831	0.3354	0.0000	0.2831	0.0000	0.3699	0.0000
2	0.8690	0.0001	0.3681	0.0006	0.3274	0.0479	0.4058	0.0000	0.3570	0.0237	0.3864	0.0000
3			0.6760	0.0057	0.9423	0.0015	0.3309	0.0000	0.5662	0.0348	0.0321	0.8789
4			0.4862	0.2686			0.5183	0.0000			0.6676	0.3324
5							0.2169	0.5751				
4 & 5			0.4862	0.2686			0.4793	0.0000			0.6676	0.3324

3.4.1.3. Path Length and Width Distributions

Path Length. Path length are conditioned to region (R) and EF. The path lengths of non-default tornadoes are fitted using a two-parameter shifted Weibull probability distribution and a shifted lognormal distribution. The shifted distributions are fitted using the reported path lengths minus the default value (i.e. 0.1 mile (0.16 km)) and fitting parameters of the distributions are based on maximum likelihood estimates (MLE). Banik et al. (2007) and Brooks (2004) also used Weibull distribution to model the path lengths conditional on F-Scale. The lognormal distribution was selected as a modeling alternative to capture the long tail of the distribution.

Figure 3-30 illustrates the path length data with the Weibull and lognormal model fits for Region 4. The data are plotted at 1 - CDF in log-log space to best illustrate the upper tail. We see that both models fit the data well until a CDF of about 0.9 or about 1 - CDF = 0.1. For lower values of 1 - CDF, the data deviate and tend to be bounded by the Weibull and lognormal models for most EFs. Appendix C.6 has similar plots for all the regions.

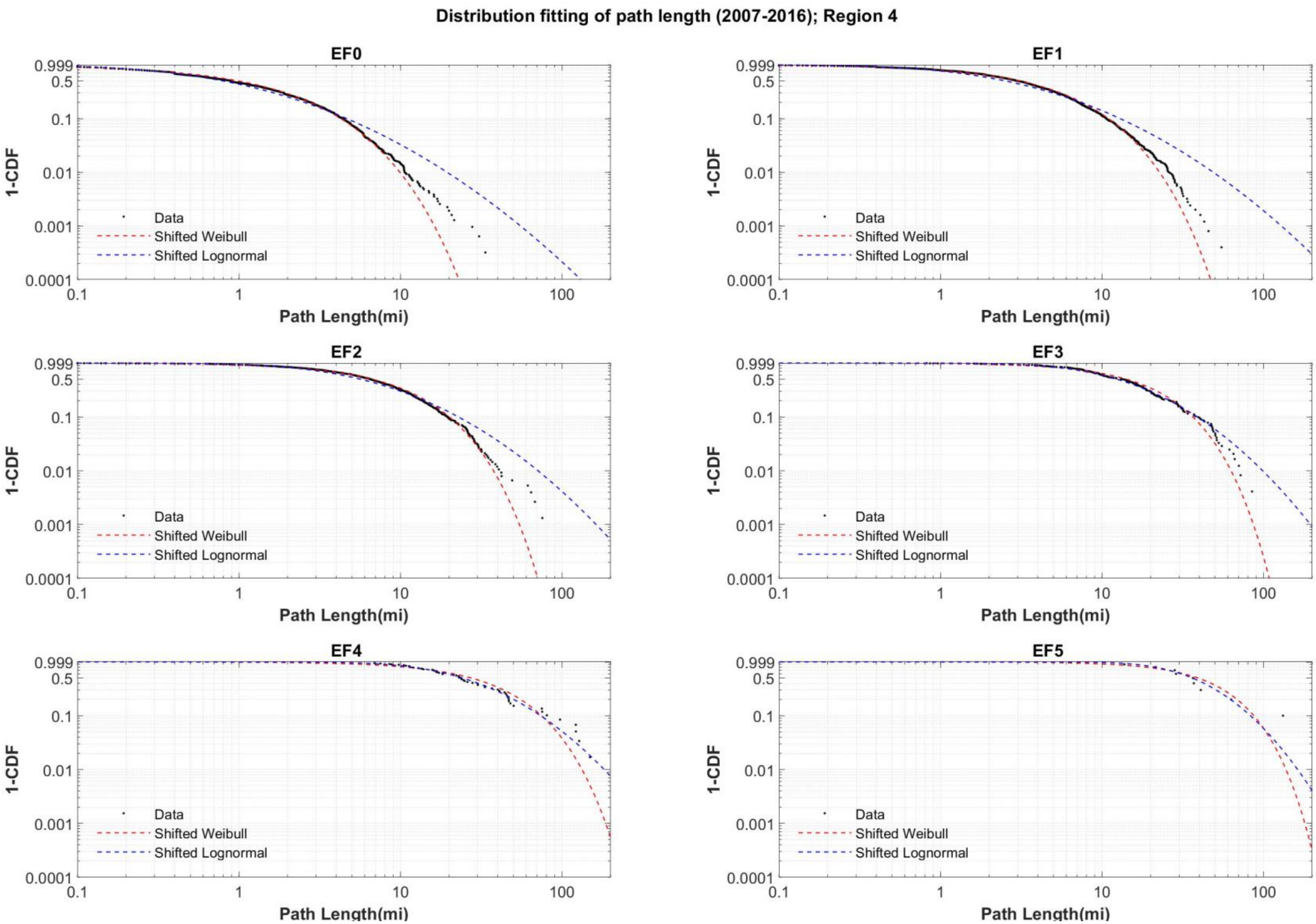

Note: 1 mi = 1.609344 km

Figure 3-30. Path Length Models for Region 4

Path Length Epistemic Implementation. We use both the Weibull and lognormal models in the path length sampling inside TORRISK2 with equal probabilities of 0.5. Hence, half the time, we sample from the Weibull and one-half the time we sample from the lognormal. The 0.5 estimate was based on judgment by reviewing the fits in Appendix C.6.

Path Width Given Length. Linear regression analysis is performed on the path length and path width data where path width (which is the assumed maximum width of the tornado) is a response variable and path length is the assumed independent given an EF-Scale within a region.[49]

The regression fits are done in (natural) logarithmic space. The residuals of these fits are modeled as normally distributed with a zero mean and a standard deviation equal to the standard deviation of the residuals in the fitting process. The path width is determined for a given length using the Eq. (3-6), which includes an error term

$$\ln(PW) = c + m * \ln(PL) + \varepsilon \qquad \textbf{(3-6)}$$

In Eq. (3-6), PW is the path width in feet, PL is the path length in miles, c is the constant of the linear fit, m is the slope of the linear fit, and ε is the random error obtained from a normal distribution with a zero mean.

Figure 3-31 illustrates the regression fits for Region 4. The horizontal data patterns result from the observed round offs of path width values. The regression fits (shown as red lines) and ±2 standard deviation lines (shown as blue lines) capture the data reasonably well. The (generally) positive correlation of PW to PL was computed in Table 3-13. Appendix C.6 includes all of the regional plots. EF-Scale data was grouped (for example, EF 4 and EF5 as EF4/5), as needed, for small sample sizes.

We did not include an epistemic model for PW. However, the epistemic implementation for PL carries over to the sampled values of PW due to the correlation of PW to PL.

3.4.1.4. Regional Path Area Scaling

As illustrated in Table 3-11, Region 4 is the only region with a rated EF5 tornado and Regions 1 and 3 do not have an EF4 rated tornado. The fact that intense tornadoes may not have been reported in these regions does not mean that they cannot happen. Our EF-Scale distribution frequencies in Figure 3-11 indicate that all regions have a possibility of intense tornadoes, regardless of how small the probability. Hence, path length and width modeling of tornadoes in all regions needs to reflect the possibilities of rare, intense tornadoes and their associated path sizes.

As discussed in the previous section, we grouped EF-Scales as appropriate to capture the PL and PW modeling in regions with limited data. The fact that we grouped the EFs does not mean that the positive correlation of increasing path sizes with EF-Scale should be neglected. For example, while no EF4s have been reported in Region 1, for example, it does not mean that we should model EF4 in Region 1 with EF2-3 path areas. Nor does it mean that we

[49] In the modern EF scale era, it is generally recognized that the relative uncertainties in the field in determining path length is much less than the uncertainty in determing the maximum path width due to: tornado aspect ratios (Section 2.2.3.1); tornado PLIV (3.5.2); tornado across width wind field asymmetry (Section 4); and issues with discerning damage from tornado rotation vs parent system translation speed along the path width edges (e.g.,NOAA, 2008).

should model EF5s in Region 406 with EF4 path areas simply because Region 406 has yet to experience a rated EF5 tornado in the relativity short EF-Scale period used in this project.

These observations lead us to a regional path-area scaling approach. Since the EF-Scale distribution model in Section 0 has frequencies, however small, for all EF-Scales in all regions, it is reasonable to extrapolate the data for the missing EFs in Table 3-11 for wind speed simulation purposes in Section 7. Extrapolation follows from the wind speed modeling scope of this effort, which includes very high return periods up to 10 million years.

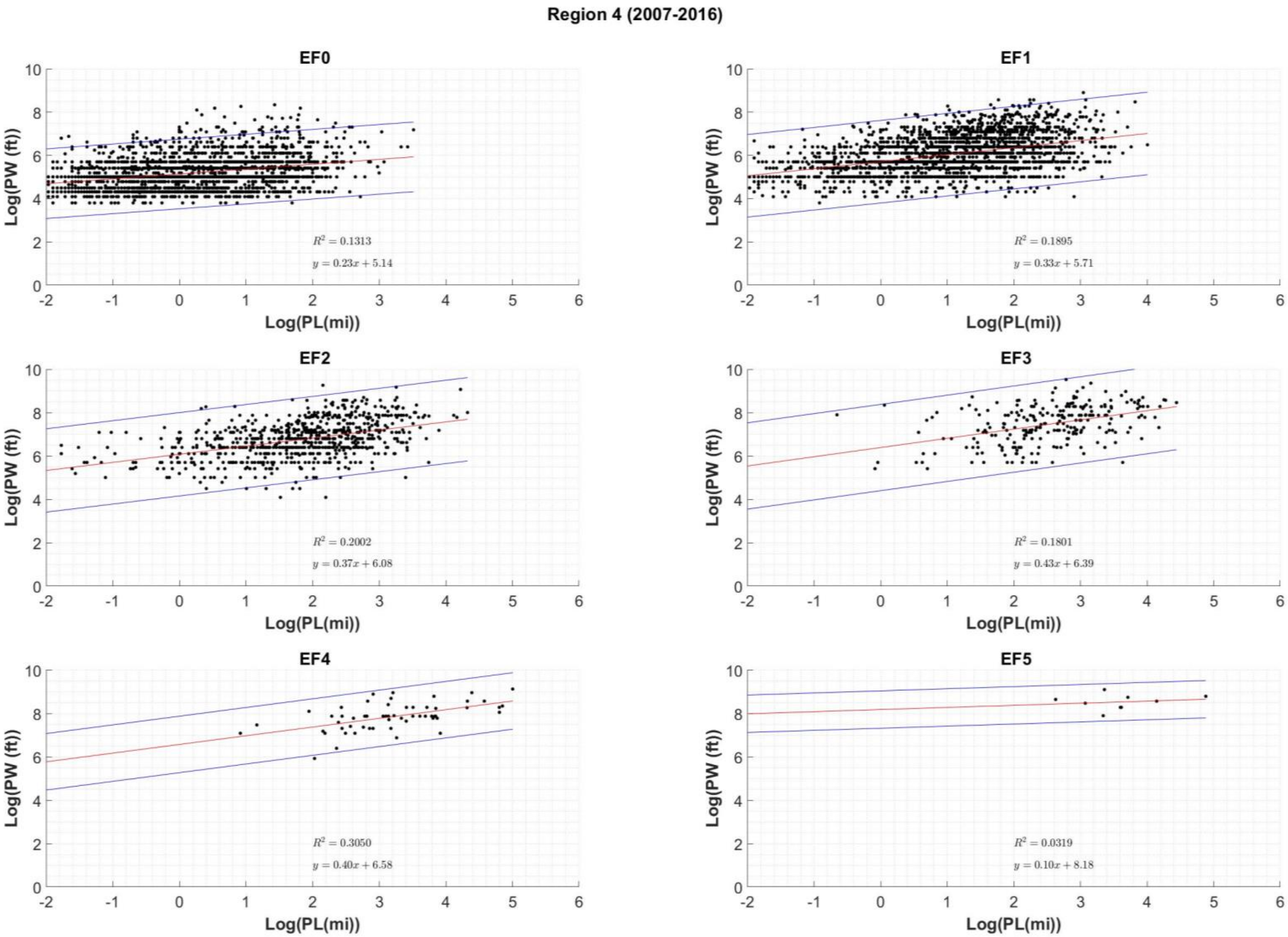

Note: 1 mi = 1.609344 km; 1 ft = 0.3048 m

Figure 3-31. Path Width Models for Region 4

Table 3-14 shows the mean path areas by region computed from the augmented database with the epistemic model for EF0 tornadoes. The grey areas were missing data where no EF events were reported. **Error! Reference source not found.** shows the data, power law fits, a nd final smoothed models. As seen from **Error! Reference source not found.**, the power law fit provided a reasonable approach to extrapolate data and to smooth variations from region-to-region.

Table 3-14. Mean Path Areas with Scaled Areas (Grey Cells)

Region	Mean Path Areas (sq. mi.) and Scaled Areas (grey cells)					
	EF0	EF1	EF2	EF3	EF4	EF5
1	0.05	0.45	1.98	4.00	7.00	12.00
2	0.06	0.52	2.05	5.30	10.78	16.00
3	0.05	0.45	2.09	5.80	12.00	20.00
4	0.09	0.77	2.90	10.06	26.45	45.64
5	0.10	0.61	2.28	9.24	16.33	26.00
6	0.05	0.48	1.99	5.64	8.11	16.00

Note: 1 mi^2 = 2.589988 km^2

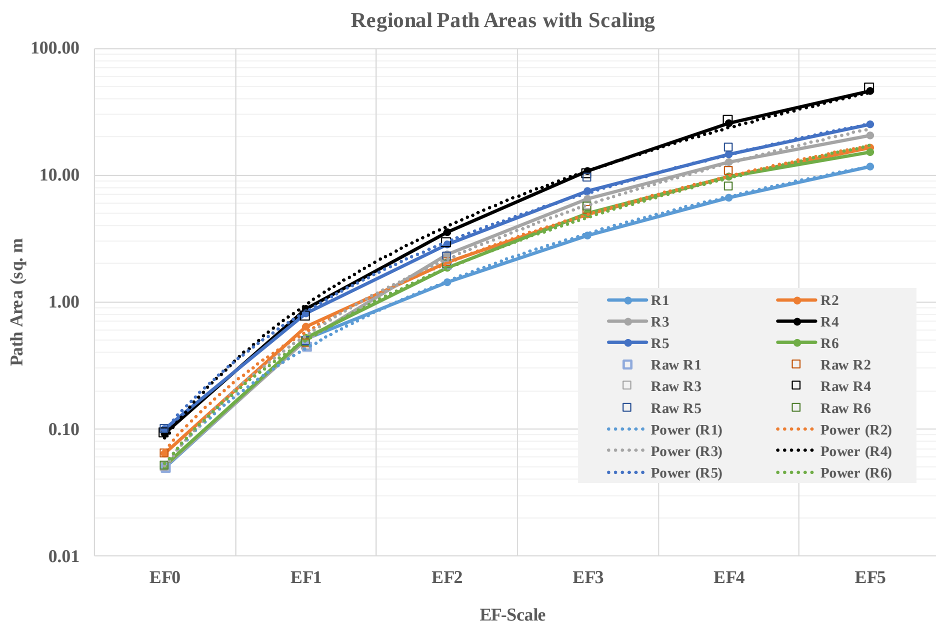

Note: 1 mi^2 = 2.589988 km^2

Figure 3-32. Region Path Areas with Smoothing and Scaling

We used the power law fit and judgement to develop the target path areas for the missing data in Table 3-14. The values in the grey cells in Table 3-14 represent these "target" path areas. Next, we performed simulations with the PL and PW models described in Section 3.4. For the target path areas in Table 3-14, we increased both the PL and PW by the square root of the area increase for the extrapolated area for each simulation. For example, in Region 1, for EF3 path simulations, we used the EF2 path data and sampled PL and PW. We increased both PL and PW by √ (4.00/1.98) = 1.42 to create a larger tornado per the extrapolated path area targets (grey cells) in Table 3-14. Table 3-15 shows the results of these simulations for all EF scales in all regions. The results of the simulations are plotted as the solid lines in Figure 3-33**Error! Reference source not found.**. We believe this approach overcomes many l imitations of regional data with limited sample sizes while reasonably preserving the raw path areas, smoothing the data, and providing scaling for missing data. The simulated results in Table 3-15 average about 5% higher than the data in Table 3-14.

Table 3-15. Simulated EF Scale Path Areas

Region	Simulated Path Areas with Scaling (sq. mi.)					
	EF0	EF1	EF2	EF3	EF4	EF5
1	0.05	0.51	1.77	3.98	6.69	11.61
2	0.06	0.64	2.06	4.87	9.79	16.40
3	0.05	0.50	2.38	6.48	12.53	20.54
4	0.09	0.88	3.55	10.83	25.51	45.64
5	0.10	0.82	2.86	8.71	14.58	25.19
6	0.05	0.52	1.88	5.02	9.74	15.24

Note: 1 mi^2 = 2.589988 km^2

3.4.2. Path Direction

Tornado path directions are calculated from the tornado starting coordinates and ending coordinates given in the Augmented Database (see Appendix A). MATLAB (MathWorks, 2018) mapping toolbox is used to compute the directions considering curved earth surface. The direction data is then analyzed to obtain distributions for 6 regions. The directions are not computed for tornadoes with missing end coordinates and for point tornadoes (i.e. same starting and ending coordinates). The right-handed Cartesian direction convention (where the positive x-axis is pointed to the East and direction angles are measured counter clockwise) are used to obtain the path directions. Since direction is a circular variable, the fitting is carried out in transformed directions (-150° to 210°) where 360° is deducted from the actual computed values if the computed value is greater than 210°.

Figure 3-33 shows the distribution of the path directions for six regions with both a Student's t fit (dashed red lines) and a normal fit (black lines). We see the Student's t fit in the path simulations The regional Student's t parameters μ, σ, and η are the location, scale, and shape parameters, respectively and are given in Table 3-16.

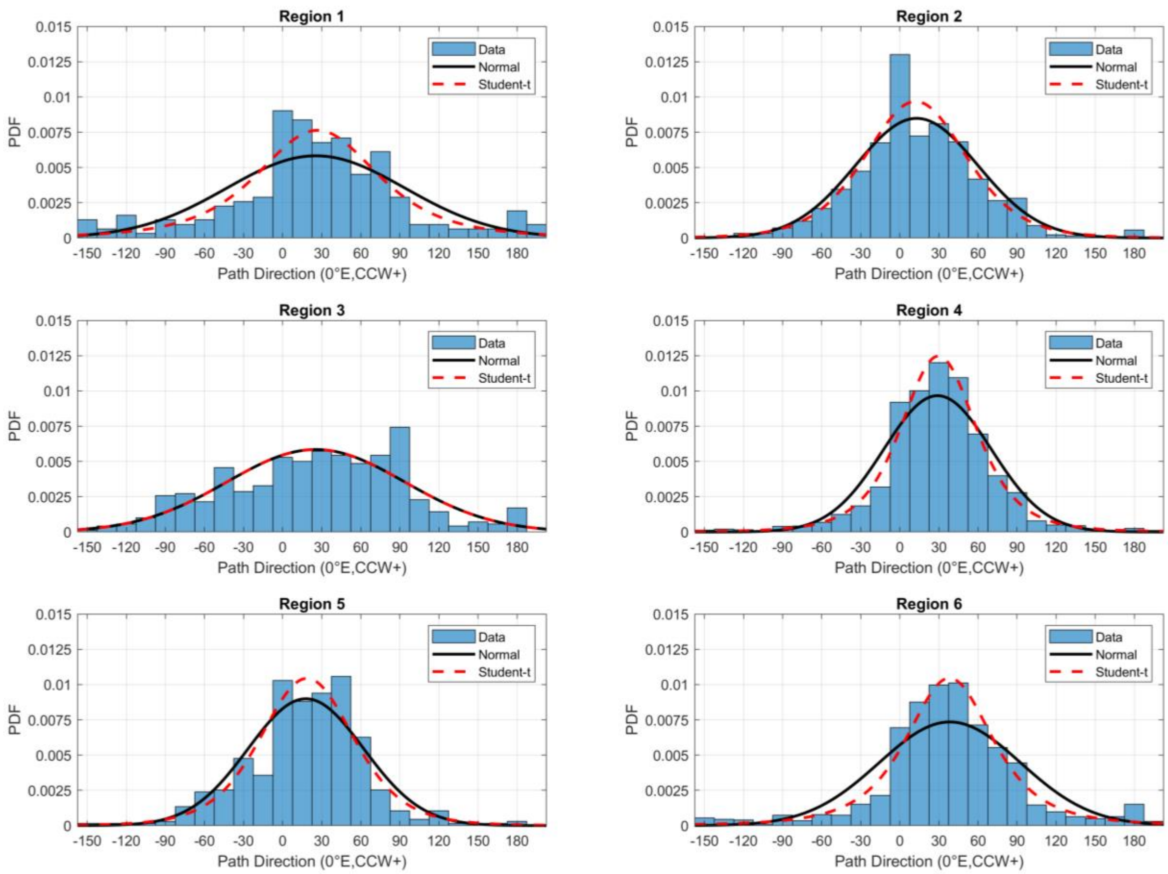

Figure 3-33. Distribution Plots of Path Directions by Region

Table 3-16. Distribution Parameters for Path Direction

Region	μ	σ	η
1	26.72	48.54	3.35
2	12.15	39.75	6.84
3	25.47	68.20	5.79
4	29.64	30.09	4.04
5	18.72	36.72	6.19
6	38.11	35.08	2.92

3.5. Within-Path Intensity Models

Tornado intensity variation within a tornado's path is an important element in tornado risk modeling for engineering analysis and design. As pointed out by Edwards et al. (2013), damage-based tornado intensity (F/EF) ratings are expected to have an important and continued role for the forseeable future regarding the modeling of tornado risk.

We examine tornado damage map data in order to extract important information on within-path variations of tornado intensity for the purposes of modeling tornado wind speed swaths in Section 4. We condition all data to F/EF damage-based intensities. Within-path means that we use estimates of F/EF intensity along (path length) and across (path width) within the overall path length (PL) and width (PW) of the tornado. These models are conditioned to the maximum tornado intensity (F/EF), L, and W of the event.

The across path data is used for two purposes: (1) to quantify the path width variation (PWV) of tornadoes, referenced to the mean path width of the event; and (2), to quantify the local maximum damage width (MDW) with respect to the local path width (LPW). Item 1 provides data needed in Section 4 to simulate tornado wind speed swaths with variable path widths, which are a characteristic of just about every tornado event. The second item provides a way to estimate the radius to maximum winds (RMW), which is a key variable in tornado wind field modeling. We develop the MDW data in this section and RMW is developed from the MDW data in Section 4.

Advantages of this modeling process are: it separates the analysis of damage intensity variation along a tornado path length from the estimation of wind speeds given a damage rating; and, similarly, the use of EF intensity models allow straightforward conditioning of the data and maintenance of important conditional PLIV, PWV, and MDW correlations in the data. In Section 6, we develop wind speed distributions that are conditioned on the same damage-based discrete intensities for the EF-Scale wind speeds.

The source of these data is based on tornado damage maps that show how the F/EF-Scale intensity changes within the tornado path. The data sources considered include both non-geo-referenced (NGR) and geo-referenced (GR) damage maps. The NGR maps are data sources that document historically-mapped tornadoes (e.g., see Figure 3-34). These publications provide the data needed to create catalogs of F/EF-Scale ratings regarding the path length intensity variation (PLIV) sequence. In addition, we develop PWV data from maps for each PLIV tornado segment. From a subset of these maps, we develop MDW data conditioned on segment local intensity and LPW.

The GR analysis was based on the NWS Damage Assessment Toolkit (DAT) data for the years 2008-2015. The DAT data contains a wealth of information, but due to practical time and resource constraints, does not necessarily include detailed and evenly spaced ground intensity ratings needed for systematic contours of damage for every tornado. Faletra et al. (2016b) present the details of DAT data analyses for purposes of estimating PLIV. The work herein follows from the conclusions in the Faletra analysis and focuses on the use of NGR damage map data, which we believe to be the best source of data at this time.[50]

[50] Portions of this section are taken from Faletra et al. (2016b). Details, analyses, and many plots of data views are provided in the paper and are not repeated herein. In this section, we update certain elements of this paper with additional data and extend the analysis to PWV and MDW.

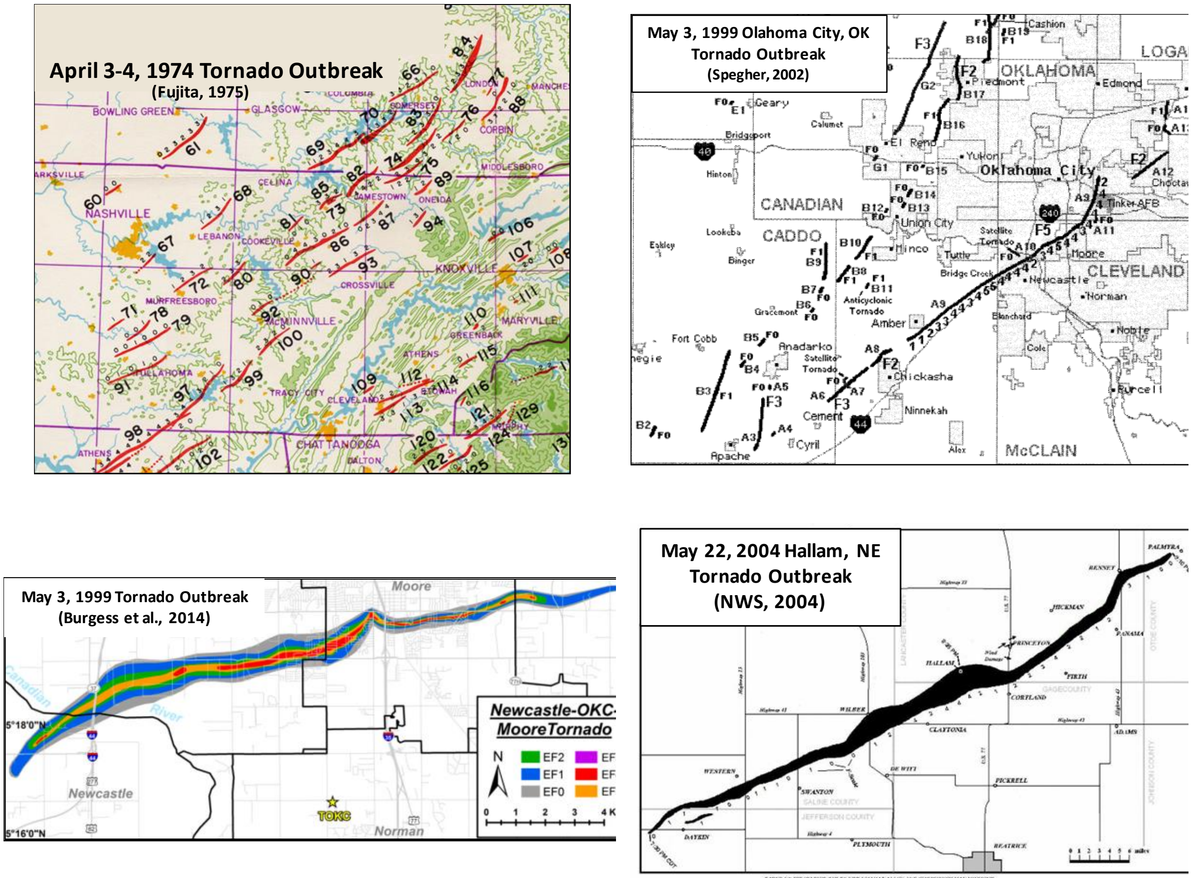

Figure 3-34. Examples of Non-geo-referenced Tornado Damage Maps (Fujita, 1975; Speheger, 2002; Burgess et al., 2014; NWS, 2004)

3.5.1. Data

The NGR map data use for the within-path analysis is given in Table 3-18. These data were re-developed from much of the original data in Twisdale et al. (1981) with new NGR PLIV data, as shown. A summary count of the events by F/EF-Scale is given at the bottom of the table. The data includes a total of 181 tornadoes of which 160 are ≥ EF1. The PWV column totals 171 events with acceptable data to develop PWV. A listing of the 181 tornadoes are given in Appendix C.7.

Table 3-17. Tornadoes Used for Within-Path Models

Event	Source	Date	No. Tors.						No. Tors with PWV	No. Tors. with PLIV
			F0	F1	F2	F3	F4	F5		
Pre-1981 NGR Data										
Red River Valley	Fujita & Wakimoto (1979)	Apr-79		1	5	2	2		10	10
April 3-4, 1974	Fujita (1975)	Apr-74	21	32	30	35	24	6	148	148
Union City Tornado	Golden & Purcell (1977)	May-73						1	1	1
Pre-1981 NGR Total No. Tors. = 159			21	33	35	37	26	7	159	159
Post-1981 NGR Data										
Chandler-Lake Wilson MN	NWS Sioux Falls (1992)	Jun-92						1	0	1
Kellerville & Alanreed	Wakimoto (2003)	Jun-95				1		1	2	2
Moore, OK	NWS Norman (1998)	Oct-98			1				1	1
24-Jun-03	NWS Sioux Falls (2003)	Jun-18			1	2	1		0	4
Coleridge	Smith (2003)	Jun-18					1		1	1
Walnut, IA	Smith (2004)	May-18		1					1	1
Hallam, NE	NWS Omaha/Valley (2004)	May-18					1		1	1
Clay Co., IA	NWS Sioux Falls (2004)	Jun-18			1	1			0	2
Beadle Co., SD	NWS Sioux Falls (2006)	Aug-18			1	1			0	2
Parkersburg, IA	Marshall (2008b)	May-18						1	0	1
Little Sioux Scout Camp	NWS Omaha/Valley (2008)	Jun-18				1			1	1
Hesston, KS	Davies et al. (1994)	Mar-90						1	1	1
Post-1981 NGR Total No. Tors. = 18			0	1	4	6	3	4	8	18
Detailed Contour Tornado Data										
Moore, OK	Burgess (2014)/DAT	13-May						1	1	1
Oklahoma City, OK	Speheger et al. (2002)	May-99						1	1	1
Joplin, MO	Marshall (2012)	11-May						1	1	1
El Reno, OK	Marshall (2014)	13-May				1			1	1
Detailed Contour Tornados = 4						1		3	4	4
Total No. Tors. = 181			21	34	39	44	29	14	171	181

This tornado data provides a means to construct “catalogs” of within-path tornado intensity variation conditioned on the maximum F/EF rating of the tornado. A “catalog” refers to a record of F/EF-Scale ratings and length for each segment in the PLIV sequence that they occur along the tornado path. Within each length segment, the catalog may also have suitable path width data. In this context, the catalog provides an image of the event with PLIV length segments, path width associated with each segment, and F/EF intensity for each segment. Some example catalogs are given in Table 3-18, which lists the first 8 tornado segments. The PLIV intensity is the local intensity shown on a damage map for that length segment. The W (Fraction) is the fraction of the width of the tornado, scaled to the maximum width shown on the damage map. The L (Fraction) is the length of that segment, scaled to the total length of the tornado. For example, for Segment 1 of the first tornado: its maximum local intensity is F/EF=1; the width is 0.375 times the maximum width of the tornado on the damage map; and the segment length is 0.125 of the length of the tornado. The analyses of these data are discussed in the following sections.

Table 3-18. Example Tornado Catalog Data

Tornado F/EF	Variable	No. Segments	Segment Number (first 8 shown)							
			1	2	3	4	5	6	7	8
5	PLIV (Local F/EF)	6	1	2	2	5	4	5		
	W (Fraction)		0.375	0.625	0.750	1.000	0.375	0.250		
	L (Fraction)		0.125	0.375	0.125	0.125	0.125	0.125		
2	PLIV (Local F/EF)	9	0	1	0	1	0	2	0	1
	W (Fraction)		0.667	0.667	0.667	0.667	0.667	1.000	1.000	0.667
	L (Fraction)		0.063	0.063	0.188	0.063	0.313	0.063	0.063	0.125
4	PLIV (Local F/EF)	17	0	1	2	2	2	3	4	3
	W (Fraction)		0.500	0.500	0.750	0.500	0.750	0.750	1.000	1.000
	L (Fraction)		0.038	0.038	0.115	0.038	0.077	0.038	0.038	0.038
2	PLIV (Local F/EF)	6	0	1	2	2	1	0		
	W (Fraction)		0.333	1.000	1.000	0.667	0.333	0.333		
	L (Fraction)		0.143	0.286	0.143	0.143	0.143	0.143		
1	PLIV (Local F/EF)	5	1	1	1	0	0			
	W (Fraction)		0.333	0.667	1.000	0.667	0.333			
	L (Fraction)		0.200	0.200	0.200	0.200	0.200			
3	PLIV (Local F/EF)	5	1	2	3	2	0			
	W (Fraction)		1.000	1.000	0.500	0.500	0.500			
	L (Fraction)		0.200	0.200	0.200	0.200	0.200			
2	PLIV (Local F/EF)	18	2	1	2	1	1	1	0	1
	W (Fraction)		0.800	0.800	0.600	0.600	0.800	1.000	1.000	0.800
	L (Fraction)		0.278	0.028	0.028	0.028	0.028	0.028	0.028	0.028
2	PLIV (Local F/EF)	1	2							
	W (Fraction)		1.000							
	L (Fraction)		1.000							
2	PLIV (Local F/EF)	8	0	1	1	0	0	1	2	1
	W (Fraction)		0.333	0.333	0.667	0.667	1.000	1.000	0.667	0.333
	L (Fraction)		0.111	0.222	0.111	0.111	0.111	0.111	0.111	0.111
4	PLIV (Local F/EF)	19	0	1	1	2	3	4	4	3
	W (Fraction)		0.400	0.400	0.600	0.600	0.800	1.000	0.800	1.000
	L (Fraction)		0.029	0.029	0.029	0.029	0.029	0.029	0.029	0.029
3	PLIV (Local F/EF)	13	1	2	2	3	3	2	1	1
	W (Fraction)		0.500	0.500	0.750	0.750	1.000	1.000	0.750	0.500
	L (Fraction)		0.286	0.048	0.048	0.048	0.048	0.048	0.048	0.048
0	PLIV (Local F/EF)	1	0							
	W (Fraction)		1.000							
	L (Fraction)		1.000							

3.5.2. Path Length Intensity Variation (PLIV)

Review. The intensity of a tornado varies over its life cycle and generally includes a formation stage, a mature stage and a dissipation stage (e.g., Golden and Purcell (1978), Grazulis (2001), Wakimoto et al. (2003), Atkins et al. (2014), etc.). As noted in Figure 3-34, tornadoes do not typically exhibit their maximum intensity over their entire recorded path length. Radar data demonstrates that tornado maximum wind speeds can both persist as well as change rapidly along the tornado path (e.g. Kosiba et al., 2013; and Burgess et al., 2002). While radar observations provide direct estimates of tornado wind speeds, sufficient radar data does not exist to probabilistically analyze intensity variation along complete tornado path lengths. Detailed damage maps in highly developed areas often demonstrate that tornadoes are capable of maintaining high intensity for relatively long distances. For examples see the 2013 Moore, OK tornado (Atkins et al., 2014), the Joplin, MO tornado of 2011 (Marshall et al., 2012), the Greensburg, KS tornado of 2007 (Marshall et al., 2008a), and the Parkersburg, IA tornado of May 25, 2008 (Marshall et al., 2008b) maps. While many tornadoes are capable of persistent intensity, non-supercell tornadoes are also likely to be brief and less intense (Wakimoto and Wilson, 1989).

Tornado wind speed risk is determined from the wind speed swaths (footprints) produced over the ground by a tornado.[51] Since damage observations are the basis for classifying tornado intensities, an approximate measure of a tornado's intensity variation during its life cycle can be obtained by analyzing F/EF-Scale rating variations along the length of the tornado's path. PLIV is determined from the maximum intensity observed along the path length at various stages in the tornado's life cycle. PLIV does not consider wind speed deviations from the maximum intensity across the path width. Variations in local wind speeds across the path width are best handled with a tornado wind field model. The use of a wind field model within a path length segment with a known local maximum intensity has the advantage of producing tornado wind speed time-histories (for modeling loads on buildings) and swaths (for wind speed frequency analysis) that also incorporate tornado life cycle intensity variation. The methods to model PLIV capture the macro-scale changes in tornado intensity, providing intensity estimates over intervals of tornado path length. Within this context, radar observations over a portion of a path length provide micro-scale level information on intensity variations.

The first attempt to model PLIV for tornado risk analysis was developed by Twisdale et al. (1978, 1981). This analysis used: Fujita's damage assessment and mapping of 148 tornadoes in the April 3-4, 1974 outbreak (Fujita, 1975); Red River Valley tornado outbreak of April 10, 1979 (Fujita and Wakimoto, 1979); the Bossier City, Louisiana tornadoes (Fujita, 1979); the Grand Gulf, Mississippi tornadoes (Fujita, 1978); and the Cabot, Arkansas tornado (Forbes, 1978). For these 150 ≥F1 tornadoes, the path lengths of each local F-Scale rating were summed and divided by the total length of all tornadoes in the tornado F-Scale rating, calculating the mean fraction of each local F-Scale intensity within each tornado F-Scale.

We note that this approach was adapted by others for simplified tornado risk assessment approaches, such as Reinhold and Ellingwood (1982), and Ramsdell and Rishel (2007).[52] The PLIV approach discussed herein is limited to macro-level intensity variation of the tornado along the path length, since a tornado wind field model is used for path width wind speed variation and to produce tornado wind speed swaths.

Analysis. We compute the F/EF-Scale fractional path lengths, conditional on the tornado maximum F/EF-Scale. We sum the lengths of each tornado's local intensity levels and then normalize each tornado by its path length (leaving us with fractions of each local intensity level, for each tornado). We then average the fractions for each local intensity level for tornadoes within each tornado rating. The result is conditional probabilities of the local path length intensity (I_i), given the maximum intensity rating of the tornado ($P(I_i|F/EF)$). From Faletra et al. (2016b), we know this will be somewhat conservative since the longer

[51] Each point in the swath grid calculations represents the maximum wind speed experienced at that point as the tornado vortex translates past the point.
[52] However, these papers used damage ratings to infer intensity across the path width in order to produce empirical estimates of damage areas by F/EF-Scale.

tornadoes have lower mean ratings over their path lengths.[53] Normalizing by length causes each tornado to have an equal input to the mean fraction summary, regardless of its length.

Table 3-19 summaries the PLIV catalog analysis into its simplest half-matrix form. This form has the mean fractions of length $P(I_i|F/EF_j)$, that an intensity segment (I_i) occurs for a tornado of intensity F/EF_j. The sum of each column is one, that is $\sum_{i=0}^{5} P(I_i|F/EF_j) = 1$. For example, the analysis indicates that the mean fractions of length that an F/EF3 tornado is F/EF0, F/EF1, F/EF2, and F/EF3 are 0.092, 0.260, 0.315, and 0.333, respectively. The principal diagonal (PD) values are the portions of the path that are rated the same as the tornado. These values represent the fraction of path length that the tornado sustains its maximum rating. From F/EF1 through F/EF5, the PD's are 62, 49, 33, 24, and 19%, respectively. These results indicate that the higher the intensity, the briefer the period of the tornado sustaining its maximum intensity. Figure 3-35 is a 3-D plot of the mean fraction half-matrix.

Table 3-19. PLIV Means, Standard Deviations, and Standard Errors

Local Intensity Rating	**Mean Fractions**					
	F/EF0	**F/EF1**	**F/EF2**	**F/EF3**	**F/EF4**	**F/EF5**
I0	1.000	0.380	0.199	0.092	0.134	0.056
I1		0.620	0.310	0.260	0.166	0.124
I2			0.491	0.315	0.252	0.248
I3				0.333	0.213	0.194
I4					0.235	0.188
I5						0.190
All	1.00	1.00	1.00	1.00	1.00	1.00

Local Intensity Rating	**Standard Deviations**					
	F/EF0	**F/EF1**	**F/EF2**	**F/EF3**	**F/EF4**	**F/EF5**
I0	0.000	0.327	0.215	0.135	0.137	0.080
I1		0.327	0.244	0.190	0.124	0.100
I2			0.307	0.180	0.144	0.170
I3				0.157	0.159	0.126
I4					0.117	0.145
I5						0.126

Local Intensity Rating	**Standard Errors (Increased by 50%)**					
	F/EF0	**F/EF1**	**F/EF2**	**F/EF3**	**F/EF4**	**F/EF5**
I0	0.000	0.084	0.052	0.031	0.038	0.032
I1		0.084	0.059	0.043	0.035	0.040
I2			0.074	0.041	0.040	0.068
I3				0.035	0.044	0.050
I4					0.033	0.058
I5						0.051

[53] This approach is slightly conservative relative to the method used by Twisdale (1978) and Twisdale et al. (1978, 1981), which added path length segments within each F-Scale.

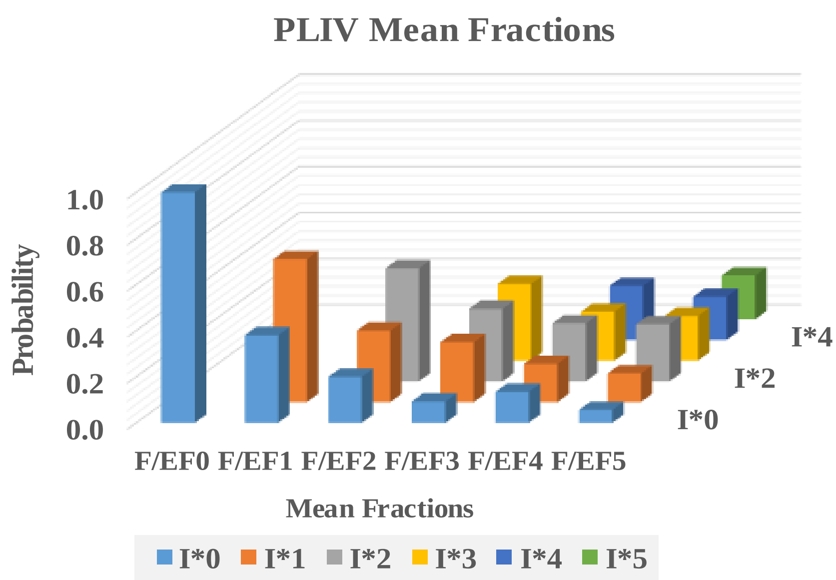

Figure 3-35. PLIV Mean Fraction Plot

Another insight from the PLIV catalog analysis is that the maximum intensity typically occurs near the center of the path. This observation is consistent with the generally recognized tornado life cycle characteristics of a formation stage, mature stage, and dissipation stage. Faletra et al. (2016b) found that the maximum intensity damage rating was observed 45 %, 90 %, and 52 % of the time within each sequential one third of the normalized path length, with similar trends observed when broken out by F/EF-Scale. Hence, these PLIV results agree with general meteorological tornado life-cycle observations. In addition, the percentage of the tornadoes that had a maximum rating unimodal life cycle was about 85%.

PLIV Epistemic Uncertainties. Damage-based PLIV analysis is limited because it is dependent on DI density and location along the tornado path. Damage maps in rural areas are more likely to have missed the maximum tornado intensity due to a lower likelihood of the tornado coming in contact with a DI. In addition, some DIs are wind speed-limited in the maximum intensity rating they can obtain (e.g. a barn can be rated a maximum of EF2), and this fact confounds the inference of PLIV from damage data. In addition, there are many uncertainties in F/EF-Scale assignments. PLIV analysis based on F/EF ratings is therefore subject to considerable uncertainties and potential biases. The results herein are subject to all of these limitations.

Comparisons of the NGR data and the DAT GR data are given in Faletra et al. (2016b). The GR data includes data from 550 ≥ F/EF1 tornadoes from the DAT database for the years 2010-2014. The GR PLIV analysis was based on DAT EF-Scale data. The analysis of the DAT data was complicated by many factors and required the use of statistical regression of the data coupled with a kernel length analysis to develop intensity variation data in a usable form. The results were highly dependent on the "kernel length" or the discretization length over which the maximum EF intensity rating was extracted. Figure 3-36 compares the DAT mean fraction data with the PLIV analysis in the paper. Short kernel lengths (*dx*) in Figure 3-36 produced smaller principal diagonal fractions than longer kernel lengths, as discussed in the paper. However, the 4-mile kernel length produced principal diagonal fractions similar to the NGR data, which had a mean rating spacing of 3.7 miles (6.0 km). The reasonably comparable results in Figure 3-36 for the 4-mile (6.4 km) kernel length provides some confirmation of the NGR data with a similar mean spacing of ratings.[54] This result is important since the NGR data is mostly composed of F-Scale era rating data.

In summary, as noted in Faletra et al. (2016b), the DAT analysis required many assumptions and was not viewed as reliable as the NGR damage maps. We believe the tornadoes in the NGR were more consistently mapped along the length and most, if not all of the surveys had aerial or satellite imagery available. The NGR results are also much more reasonable for the off-diagonal terms.

PLIV Epistemic Implementation. We model the uncertainties in the mean fractions as normally distributed with standard deviations equal to the standard errors given in Table 3-19. The standard errors are computed by $\sigma_e = 1.5 * (\sigma / \sqrt{n})$, where n are the total number of F/EF tornadoes in Table 3-17. We increased the standard errors by 50% to reflect data limitations and modeling issues previously described. The 50% increase in the standard error produces ranges of sampled fractions that cover most of the differences in the NGR and GR dx results illustrated in Figure 3-36, except for F/EF5.

The epistemic uncertainty model is implemented in TORRISK2 by a sampling approach. We sample the fractions independently (column wise for a given F/EF tornado simulation) such that they are within $2 * \sigma_e$ of the mean, constrain the sum to be unity, and use rejection sampling, as needed to meet the constraint. The dashed lines in Figure 3-37 illustrate the $\pm 2\sigma_e$ uncertainties in the principal diagonal (PD) mean fractions. The stacked bar chart provides a visual of the PLIV mean fractions and the modeled uncertainties in the principal diagonal. For example, an EF5 tornado may have EF5 intensity 9% to 30% of its length with an epistemic mean value of 19%.

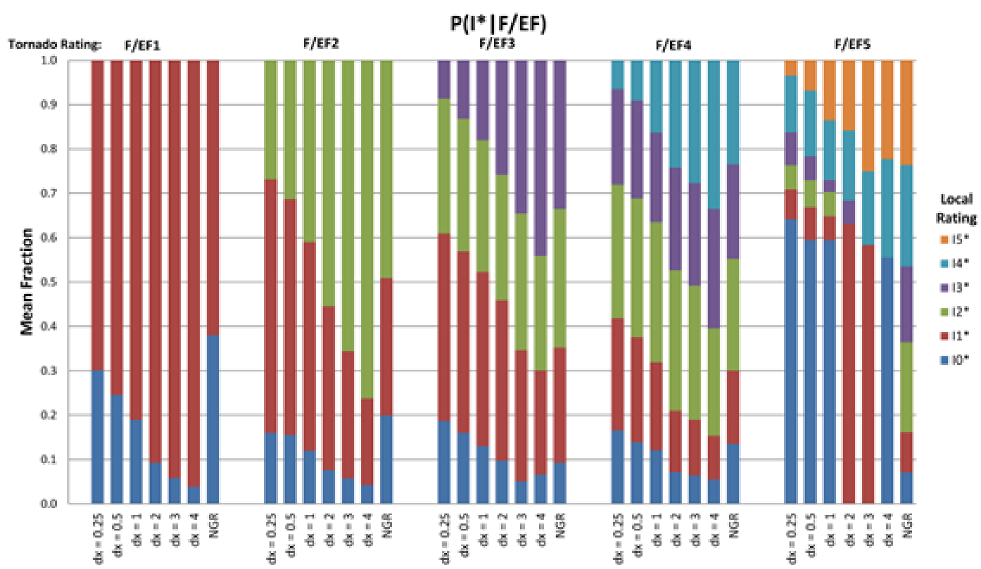

Figure 3-36. PLIV Cumulative Mean Fractions for NGR and GR Data (Faletra et al., 2016b)

[54] The DAT (GR) data included only 1 EF5 event. One can see the sensitivity of the results to dx in Figure 3-36.

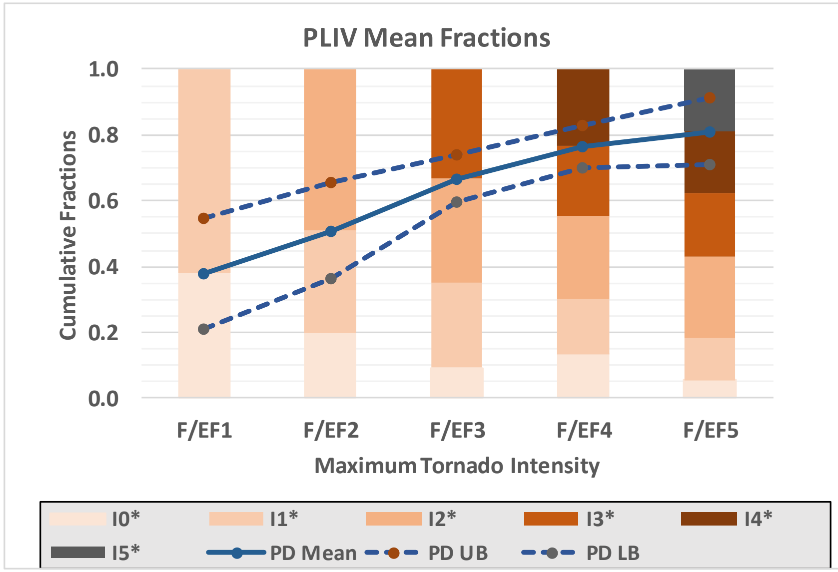

Figure 3-37. PLIV Mean Fractions and Principal Diagonal (PD) Uncertainties (± 2 σ_e)

3.5.3. Path Width Variation (PWV)

Tornado path widths often vary significantly over the life of the tornado as illustrated in Figure 3-28 . We used a subset of the damage maps to develop the PWV data in Table 3-17. The PWV data was developed by measuring width for every PLIV F/EF rating segment. The path widths were recorded and then converted to fractions ($\omega = W/W_{map}$, where W is the local path width and W_{map} is the maximum tornado width scaled from the map).

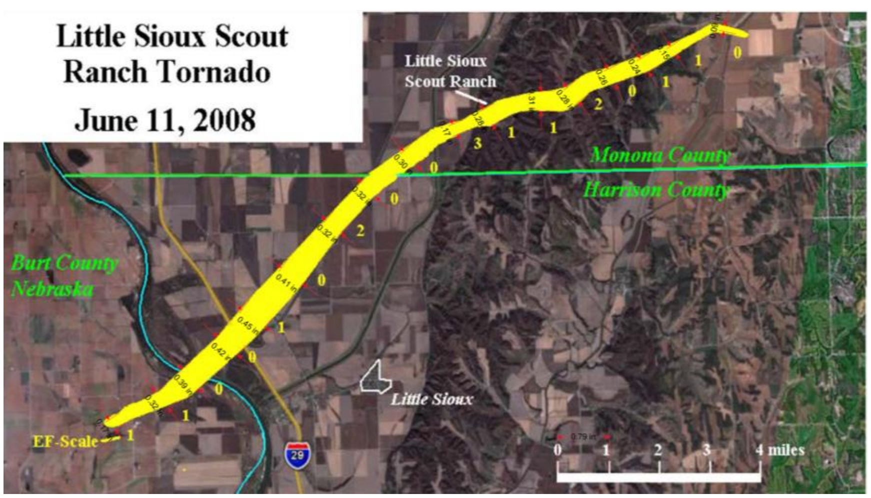

Note: 1 mi = 1.609344 km

Figure 3-38. Little Sioux Scout Ranch Tornado Damage Map Developed by NWS (2008)

As discussed in Section 2, our modeling of tornado paths uses EF-Scale data, which we concluded was the most accurate data for modeling tornado path lengths and widths. Prior to 1994, mean tornado path widths were reported in the database and since that time, maximum path widths were reported (McCarty, 2003). Mean tornado path widths must be used to simulate accurate tornado wind speed swaths. Simulating the maximum path widths over the full length of the tornado will overestimate the tornado wind speed risk due to significant path width variations observed in most tornadoes. For accurate tornado path simulations, we therefore need to replicate observed variations in tornado widths and, more importantly, ensure that our simulations match the best available data regarding mean-to-maximum path width ratios.

The process of developing map-derived path width variations is illustrated in Figure 3-38. We used a digital tool to record the segment widths and from that computed the mean scaled width for each segment. The segment widths were then scaled to dimensionless fractions by dividing all widths by the maximum path width. The map-derived scaled local path width mean-to-max ratios (ω) from the 181 tornadoes in Appendix C.7 are plotted in Figure 3-39. The map-derived mean ω ratios are 0.97, 0.91, 0.87, 0.78, 0.78, 0.66, respectively for F/EF0 to F/EF5 tornadoes. These results show a decreasing trend in the map-derived ω ratios. Since these ratios were developed from scaling of published maps in the "thin direction" of the tornado path, they are an approximate measure of the true ω. Tornadoes that are wider, on average, such as EF4-5's, are expected to produce a better estimate of ω since variations in path width are more accurately scaled for these events.

Due to the aforementioned limitations of map-derived PWV data, we made a data-based correction to the map data to facilitate a consistent application of PWV to EF-Scale maximum path width data. We computed the SPC mean to max data ratio (Ω) (from the Augmented Database) for the years 1982-1994 (mean path width data) and 2007-2016 (EF-Scale max path widths). Figure 3-39 shows these ratios by F/EF-Scale and they vary from 0.36 for EF1 to 0.73 for EF4. The weighted mean for all EFs is 0.498 ≈ 0.5. Due to the large (and inconsistent) variability of the SPC mean ratios in Figure 3-39, we use the all tornado mean of 0.5 for scaling purposes in the PWV modeling. This 0.5 mean is shown as the "Epistemic Mean" in Figure 3-39.

Implementation with Epistemic Uncertainties. With this approach, we correct the map-derived corrected ω_{ij} 's to agree with the SPC mean Ω ratio of 0.5 by the equations

$$(\omega_{mean})_i = \sum_{j=1}^{S_i} \omega_{ij} * \ell_{ij} \tag{3-7}$$

and

$$\Omega = \frac{1}{N}\sum_{i=1}^{N} (\omega_{mean})_i \tag{3-8}$$

Eq. (3-7) calculates the individual tornado mean-to-max ratio, $(\omega_{mean})_i$ from the sum-product of S_i length segments of local path width fraction (ω_{ij}) times the local PLIV length fraction (ℓ_{ij}). Eq. (3-8) simply computes the catalog average Ω across all tornadoes. For the mean catalog, we set Ω = 0.5. In these equations N = the number of tornadoes in the catalog (N= *181*).

This map-scaling correction was implemented to produce condensed PLIV-PWV catalogs, given in Appendix C.7 for a value of Ω = 0.5. The ω_{ij} and ℓ_{ij} fractions are provided for each tornado. At the bottom of Table C-5, the catalog corrected mean Ω is 0.5, which is the average of all 181 tornadoes as given by Eq. (3-8).

Epistemic Uncertainties. In recognition of the limitations of the SPC Ω ratios, which average 0.5 for all tornadoes, but have a range of 0.361 to 0.732 (or from 0.361 to 0.6 by combining F/EF4 and F/EF5), we model the uncertainty Ω from 0.4 to 0.6, uniformly distributed. Figure 3-39 shows the mean path width and the epistemic uncertainty range compared to the map-derived (ω_{mean}) prior to this correction.

In the epistemic implementation, an Ω value is sampled for each simulated tornado. The tornado condensed catalog is sampled by drawing a random number and associating that number with a catalog for the appropriate F/EF-Scale. For the sampled catalog (say the i^{th} catalog), its ω_{ij} values are adjusted by

$$(\omega_{ij})_{epistemic} = \omega_{ij}/0.5 \tag{3-9}$$

for each j or local EF-Scale intensity per the columns in Table C-5.

Figure 3-40 shows the possible range of simulated $(\omega_{mean})_i$ for Ω = 0.4, 0.5, and 0.6 (LB, mean, UB), respectively). We see that the range of catalog $(\omega_{mean})_i$ varies from 0.24 to 0.82 and the overall mean Ω of the tornadoes (3*181 = 543 tornadoes) in Figure 3-40 is 0.5. The sampled tornado mean width is determined from $W * (\omega_{mean})_i$ where W is the EF-Scale era sampled path width.

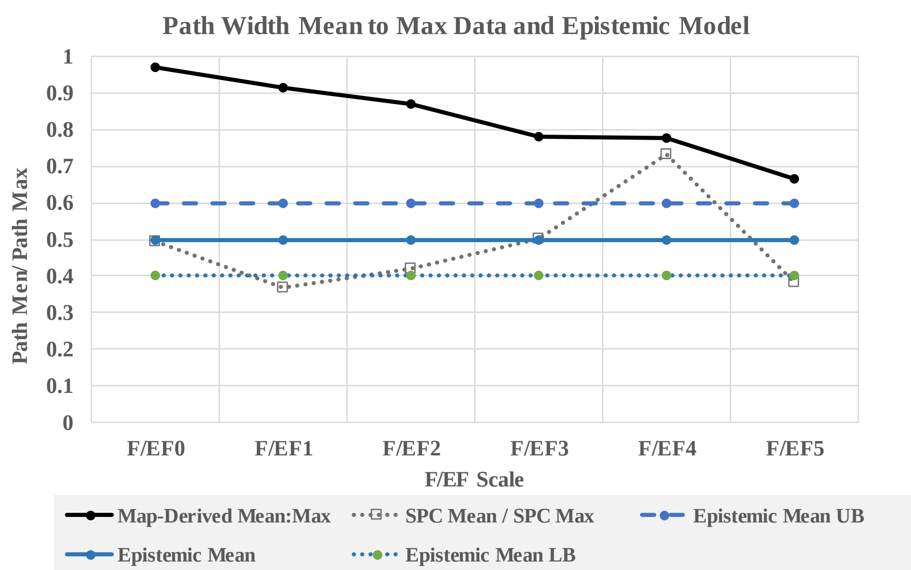

Figure 3-39. Path Width Mean-to-Max (**Ω**) Data and Epistemic Range

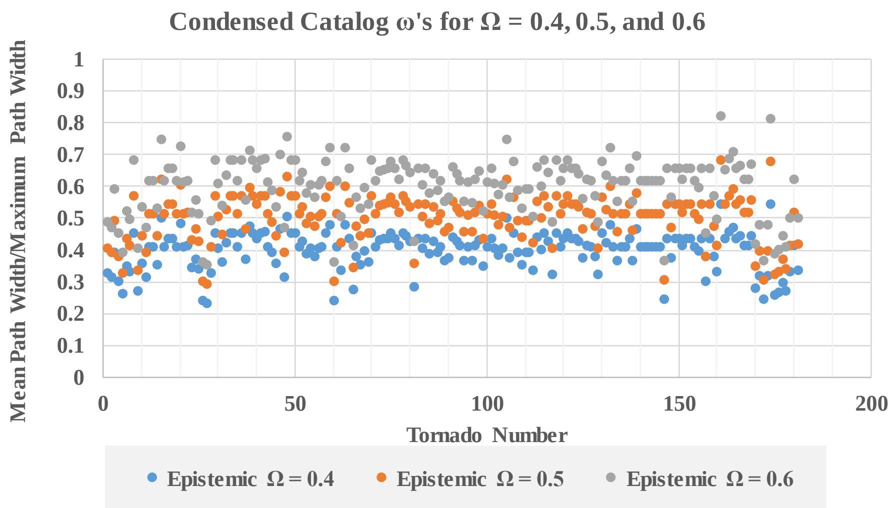

Figure 3-40. Condensed Catalog ω's for Ω = 0.4, 0.5, and 0.6

3.5.4. Maximum Damage Width

The purpose of maximum damage width (MDW) modeling is to obtain data to estimate RMW for the wind field modeling in Section 4. RMW is a key input to modeling tornado wind loads and estimating tornado wind speeds. MDW refers to the width of observed maximum damage for a PLIV segment. The MDW is the contour width within which the rated F/EF damage equals the maximum EF intensity for that segment.[55]

Figure 3-41 shows the transect analysis process used to obtain the MDW from the Moore, OK Tornado, May 20, 2013. The scaling approach was done similar to path width scaling from published maps. The measured MDW at each transect was converted to a fraction of the local path width. These fractions were analyzed by the tornado intensity and local path width intensity. Table 3-20 illustrates how the LPW and MDW are extracted to compute MDW/LPW fraction for each local intensity (I).

[55] As discussed in Section 4, prior to the idea of scaling local intensity MDW contour data, we attempted a literature review to obtain RMW data. Due to limitations of photogrammetric and radar data in terms of height above ground and knowledge of the local ground-level damage width associated with the RMW estimate, we concluded that damage-based observations were the most systematic data on which to develop statistical models of RMW conditioned on local path width (LPW), local intensity (I), and tornado maximum intensity (F/EF).

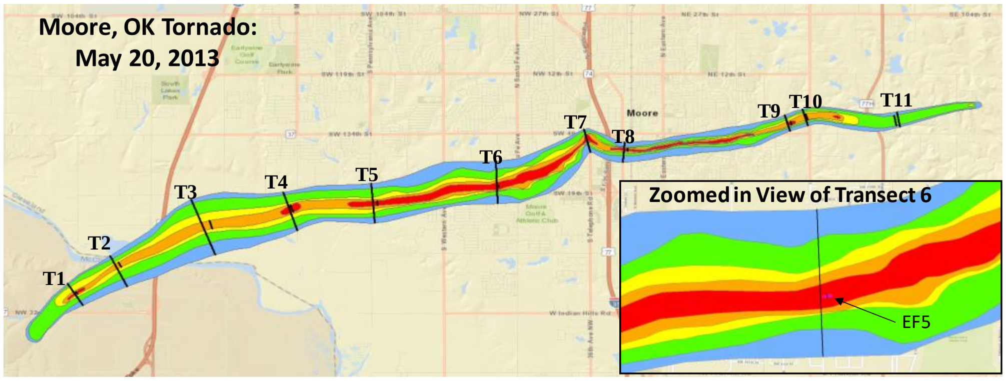

Figure 3-41. MDW Tornado Data Extraction Example

Table 3-20. MDW Data Developed from Figure 3-38 (widths in ft (1 ft = 0.3048 m)).

Transect No.	1	2	3	4	5	6	7	8	9	10	11
Max Damage Rating (F/EF)	4	3	3	4	4	5	5	4	4	3	1
Transect Width (LPW)	751	993	1744	1193	1177	1254	693	596	493	510	450
Max Damage Width (MDW)	76	154	249	202	137	32	29	74	99	177	310
MDW/LPW	0.10	0.16	0.14	0.17	0.12	0.03	0.04	0.12	0.20	0.35	0.69

A total of 243 tornadoes were evaluated with 671 transects. The MDW and LPW were measured and a statistical MDW/LPW dataset was produced, conditional on the segment intensity and tornado intensity. Table 3-21 summarizes the count by F/EF-Scale and local maximum intensity (I). Table 3-22 (top) summarizes the mean MDW/LPW fractions and the bottom provides the standard deviations. Figure 3-42 is a bar plot of the mean fractions in Table 3-21. We see that that the mean of the maximum damage width fractions for local maximum intensity *I* increases with F/EF-Scale, which is consistent with the increasing mean width of these events. There is also a decreasing principal diagonal value with increasing tornado F/EF-Scale. This data is used in Section 4 to develop RMW by EF-Scale and local intensity I.

Table 3-21. Summary of Tornado PLIV Segment Counts for MDW Intensity I

Tornado Rating	No. of Tornadoes	Number of Transects for each Local Maximum Intensity, I					
		I1	**I2**	**I3**	**I4**	**I5**	**Total**
F1	143	274	0	0	0	0	274
F2	62	101	84	0	0	0	185
F3	19	24	27	28	0	0	79
F4	11	17	28	23	14	0	82
F5	8	4	5	10	16	16	51
Total	243	420	144	61	30	16	671

Table 3-22. Mean and Standard Deviations of MDW/PW Fractions

Tornado Rating	Mean MDW/PW				
	I1	I2	I3	I4	I5
F1	0.513				
F2	0.571	0.322			
F3	0.551	0.382	0.282		
F4	0.611	0.451	0.386	0.231	
F5	0.686	0.490	0.322	0.197	0.128
Tornado Rating	**St. Dev. MDW/PW**				
	I1	**I2**	**I3**	**I4**	**I5**
F1	0.175				
F2	0.176	0.175			
F3	0.154	0.172	0.159		
F4	0.110	0.160	0.166	0.155	
F5	0.157	0.060	0.135	0.070	0.090

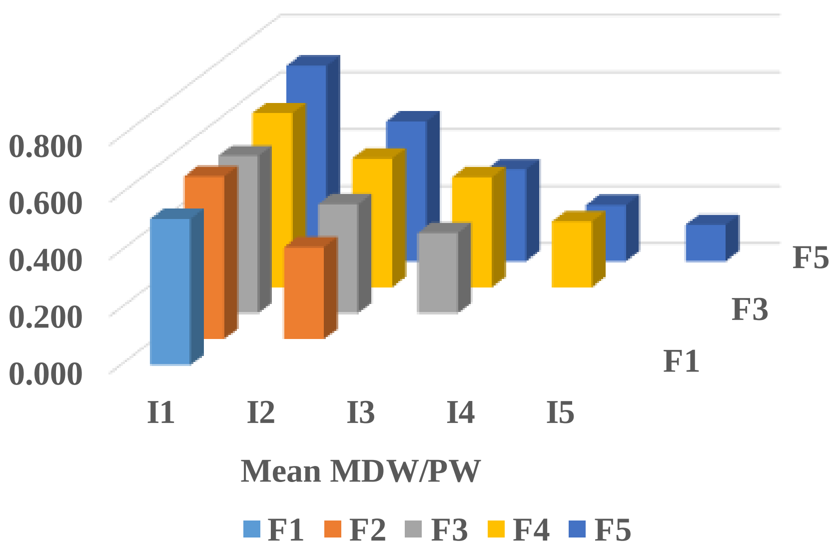

Figure 3-42. 3-D Plot of MDW/LPW Fractions

4. Tornado Wind Field and Tornado Swath Modeling

4.1. Objective and Scope

A tornado wind field model is required for developing tornado wind speed maps for engineering design and structure/system safety analysis. A wind field model provides a unifying link between engineering-based wind speed estimation and the development of wind speed exceedance frequencies (WEF). We therefore use a general tornado wind field model for each of the following applications:

1. Development of damage-to-wind-speed models for the engineering interpretation of EF-Scale wind speeds.
2. Validation of the damage-to-wind-speed models using observational data from specific tornadoes.
3. Production of tornado damage swaths for purposes of WEF tornado hazard calculations.

The implementation of a general wind field model in the above applications produces consistency in the interpretation of results and computation of the reference wind speed (RWS). The RWS is the wind speed magnitude that is used as an independent variable to facilitate discussion of results, produce tornado risk maps, and perform load calculations. Since RWSs are not directly measured in tornadoes, we must compute them as part of the tornado risk map development process so they can be applied consistently in engineering design (see Section 1.3.7). For non-tornadic winds, the term “Basic Wind Speed” (ASCE-7, 2016) is defined as a three-second gust at 33 ft (10.1 m) above the ground in Exposure C terrain. The Basic Wind Speed is determined from the appropriate wind hazard map in ASCE-7. Since tornado strikes on structures often produces different wind speed magnitudes at different locations on the structure, the definition of the RWS is critical to map development and design implementation.[56]

Tornadoes have a wide range of parameter characteristics, including path length, path width, radius of maximum winds (RMW), vortex structure, velocity components, maximum horizontal wind speed, translation speed, and life cycle intensity variation. In this regard, a fundamental objective of the wind field modeling is to capture the natural variability (randomness) and correlation of important parameters such that the tornado simulations are a reasonable representation of our knowledge of tornado characteristics. We also model epistemic uncertainties of several key parameters in the wind field modeling process.

An overarching objective in the wind field modeling is fast running simulations to support detailed, time-stepping load and resistance modeling calculations on 3-D modeled structures for all the degrees of damage (DOD) and associated failure modes (as developed in Section 5). In addition, in the production of WEFs, we must determine the RWS for a given structure at an arbitrary position within the tornado path. Determination of the RWS requires multiple calls to the wind field model as the tornado is advanced and each step evaluates a hundred or more loading points over the target’s plan area. For each simulated tornado, we create a

[56] We discuss RWS in Section 6, where it is defined as the maximum horizontal wind speed (assumed to be a nominal 3 second gust) at 33 ft (10.1 m) experienced over the plan area of the structure (target) as the tornado translates past the target.

physically realizable tornado by sampling from the probabilistic models (and associated correlations) that define the tornado's parameters. In summary, tornado wind field model validity, simplicity, scalability, and speed of calculations are important considerations in the wind field modeling approach described in the following sections.

4.2. Tornado Vortex Structure

Tornado vortex structure is very complex with three-dimensional flow structures and instabilities. In the past, many researchers attempted to characterize tornado vortex and provided conceptual models of typical tornado structures. Lewellen (1976) introduced a conceptual model of different regions that a typical tornado exhibits. Wurman et al. (1996) further refined this model with the help of Doppler radar derived data and identified five different flow regions as shown in Figure 4-1. Region I represents the outer flow region (above the boundary layer region) which is usually associated with the parent thunderstorm mesocyclone. Region II represents the core of a tornado which is usually axisymmetric and characterized by rotating flow of high winds that flows radially inward and then converted to upward flow near the center of a tornado. Region II extends up to RMW. This region is also associated with an atmospheric pressure drop. Region III is the corner flow region where tornado has intense radial flow that is affected by the surface friction and turns abruptly upward due to vertical pressure gradients. Region IV is the surface boundary layer region and Region V is the convective plume region.

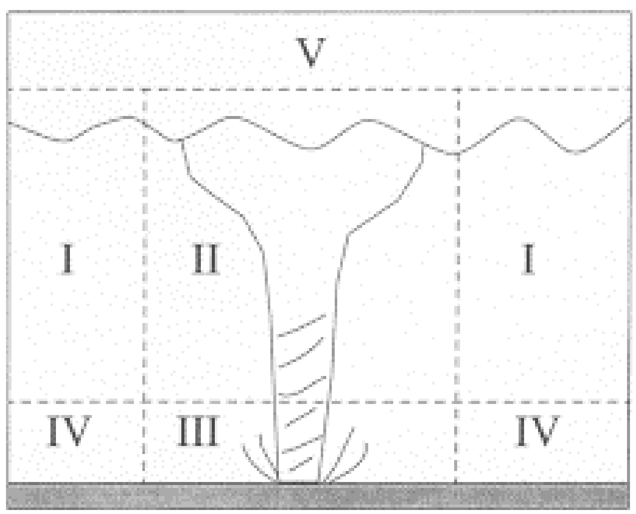

Figure 4-1. Elevation View of a Conceptual Model of Tornado Flow Regimes (Adapted from Wurman et al., 1996)

Tornado vortices are classified according to the vortex structure characteristics, which may vary during the lifetime of a tornado. Davies-Jones et al. (2001) provided schematic diagrams of tornadoes with different cell characteristics with increasing swirl ratio[57] as shown in Figure 4-2. For weak swirl, flow in the boundary layer separates and no tornado is formed. For low swirl, a smooth one-cell tornado is formed with only upward flow at the core of the tornado. With increasing swirl ratio, the one-cell vortex becomes unstable and breaks down

[57] Swirl ratio is discussed in section 4.3.3.

to a two-cell vortex with a downdraft at the center of the tornado. For large swirl, the tornado breaks down into multiple vortices.[58] Church et al. (1979) and Monji and Yasushi (1985) observed similar transitions in their experimental study. Matsui and Tamura (2009) observed transitions from laminar flow to turbulent flow with increasing swirl ratio. They also observed the expansion of core diameter with increased swirl ratio.

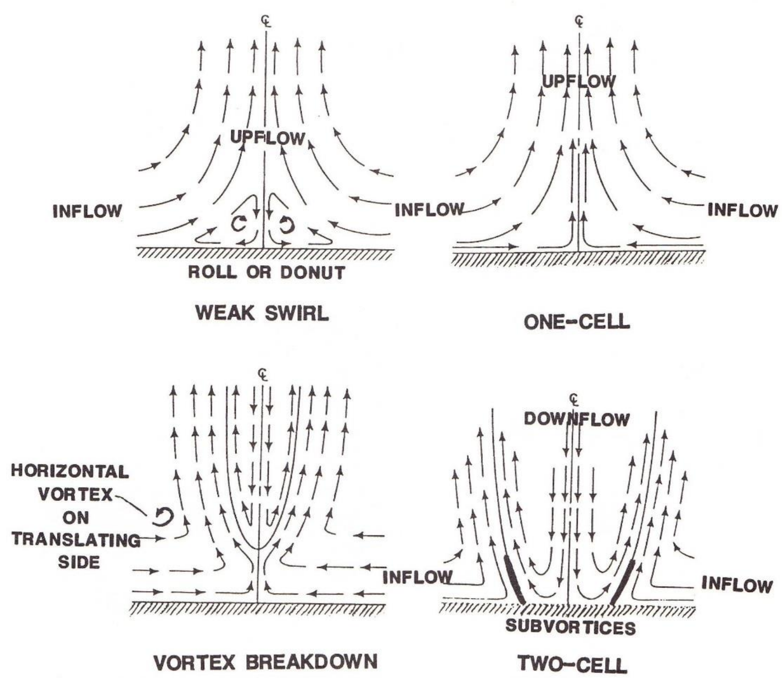

Figure 4-2. Schematic Diagrams of Tornado Vortices (Davies-Jones et al., 2001)

4.2.1. Simplified Vortex Models

There are several simplified vortex models that have been adopted by researchers to model tornado winds. These include the Rankine vortex model (Rankine, 1882), Burgers-Rott vortex model (Burgers, 1948), Sullivan vortex model (Sullivan, 1959), Wood and White (2011) model, Kuo's model (Kuo, 1971) and Baker's vortex model (Baker and Sterling, 2017). The following paragraphs provide a brief discussion of these models.

The Rankine vortex model is a one-dimensional model of the tangential component of the wind field. It assumes a rigid-body rotation within a core and decay of the velocity outside the core and hence it creates two separate flow regions: one is within the core and extends up to the RMW and the other one is outside the core. Inside the first region, wind speed increases linearly with distance from the vortex center and reaches to maximum at the RMW. Beyond RMW, it decays linearly. The Rankine vortex has been widely used to model tornadoes (Hoeker, 1960; Wurman and Gill, 2000; Lee et al., 2004; Peng et al., 2016; Refan and Hangan, 2016; etc.).

[58] The role of vortex breakdown and subvotices, as it applies to an engineering model, is discussed in Section 4.3.2.

The Burgers-Rott vortex model can simulate tangential, radial and vertical velocity components. The model is derived from an exact solution of the Navier-Stokes equations. It assumes the vortex is axisymmetric with steady state flow and has constant density and viscosity. The tangential and radial velocity components are only dependent on the radial distance and the vertical velocity component is linearly dependent on the height. This vortex model has also been used by researchers to model tornado flow field (Brown and Wood, 2004; Kosiba and Wurman, 2010; Wurman et al. 2013).

The Sullivan vortex model also simulates the three velocity components of a tornado wind field. Similar to Burgers-Rott model, the tangential and radial velocity components in the Sullivan model are only dependent on radial distance; and the vertical velocity component is dependent on radial and vertical distances. This model is capable of producing one-cell and two-cell vortices, while the Rankine model and Burgers-Rott model produce only one-cell vortices. The Sullivan model was used by Winn et al. (1999) and Wood and Brown (2011).

Wood and White (2011) developed a parametric tornado vortex model for tangential wind profiles. The model is able to produce sharply or broadly peaked tangential profiles that resemble realistic tornado vortices.

In Baker's vortex model, radial and vertical variations can be obtained for tangential, radial and vertical components. It can replicate flow characteristics of a single and two-celled vortex. Gillmeier et al. (2018) compared the results from physically simulated tornadoes with the results from the Baker's model. They found Baker's model could replicate the radial inflow only at heights near ground compared to experimentally simulated tornadoes. They concluded that Baker's model is not suitable to describe the overall three-dimensional flow structure in an experimentally simulated tornado.

None of these models described above treats radial and vertical variations of the three wind field components. In this context, Kuo (1971) solved nonlinear boundary layer equations to obtain radial and vertical distributions of the tangential, radial and vertical velocities. The vertical velocity function inside the core was developed from a continuity condition from the radial velocity mass flow rate. He solved the zeroth-order approximation of the axisymmetric boundary layer equation based on the assumption that the local boundary layer thickness is much smaller than the horizontal extent of the vortex. The upper boundary condition is imposed by a maintained Rankine vortex, and the ground boundary conditions are no slip for laminar flow and a geophysical boundary condition assumed at the sublayer surface for turbulent flow. He found that the flow inside the core behaves as a flow in an Ekman-layer with the velocity components showing oscillatory distribution. The flow outside the core is similar to a boundary layer flow. Kuo's model was adapted and generalized by Twisdale et al (1978,1981) for 3D simulations of wind-borne debris and fragility analysis of nuclear power plants.

4.2.2. Engineering Model Implementations

Many legacy-engineering models of tornado risk used empirical-based damage area modeling without the use of a wind field model. These include McDonald et al. (1975), DOE (1985), Abby and Fujita (1975). These models have many limitations and are not applicable to first-principal modeling of tornado damage.

Tornado wind field characteristics and models have also been used for engineering analysis. The engineering analysis includes analysis of inferring wind speeds from damage (Rouche et al. 2016; Kopp et al., 2016), assessing wind speed risk (McDonald et al., 1975; DOE, 1985; Abbey and Fujita 1975; Twisdale et al. 1978 and 1981; Banik et al., 2007) and engineering load analysis and design (NIST, 2014; Masoomi and van de Lindt, 2017; Roueche et al. 2017; Peng et al., 2016).

Fujita (1978) developed a tornado wind field model named DBT-77 that is similar to a Rankine vortex model. However, unlike Rankine vortex model, DBT-77 model can produce vertical and radial variation of wind speed components. Fujita (1978) also developed the DBT-78 model, which is a multi-vortex model capable of modeling suction vortices. There is a cyclostrophic balance of the flow near the vortex center when these suction vortices reach a steady state.

Twisdale et al. (1978, 1981) and Dunn and Twisdale (1979) developed a probabilistic "synthesized" wind field model to assess tornado missile risk for nuclear power plants. They adopted Kuo's (1970) representation of vertical and radial variations of tangential and radial components of the wind field. The tangential velocity follows the form of the Rankine vortex with probabilistic RMW. The model includes a variable vertical slope of the core, allowing for both cylindrical and conical wind fields (height-wise). Rate of decay parameters outside the core allow for probabilistic modeling and fitting a path width and RMW at a position along the tornado path. The relationship between the radial and tangential velocity components is modeled as a random variable, allowing the vortex wind fields to have a variable inflow relative to tangential velocity, similar to the classical laboratory models. The synthesized model assumes meridional flow continuity and the vertical component is computed from the continuity condition. The developed model included a probabilistic implementation with the following random variables: maximum horizontal wind speed; translational speed (dependent on intensity); boundary layer height; vertical slope of the tornado core; RMW (dependent on intensity); wind field inflow variable (γ ratio of radial to tangential flow at RMW); path width; decay parameters outside core; and reference boundary layer height. To our knowledge, this is the only wind field model that incorporates probabilistic modeling of important wind field parameters.

Banik et al. (2007) adopted Twisdale et al. (1978, 1981) probabilistic model to assess wind speed risk for southern Ontario. The NRC (2007) adopted tornado design parameters based on a Rankine vortex model was suitable for engineering design.

NIST (2014) used a tree-fall based tornado wind field model to compute structural loads. Their model is similar to a Rankine vortex model. The tree-fall data collected from Joplin tornado damage survey was used to provide basic inputs such as RMW, decay coefficient and radial inflow for this model.

Peng et al. (2016) adopted a Rankine type vortex model to predict tornado induced damage. Their wind field model simulates the radial variation of the tangential and radial components. The model does not include a height-wise variation of these components nor a vertical wind component.

Based on this review, the only tornado wind model developed with a key set of probabilistic parameters for engineering simulations of wind effects (pressure loads and wind-borne debris) is the Twisdale et al. (1978, 1981) model (also see Dunn and Twisdale (1979)). We apply this model, with enhancements, to this project. This synthesized model has desirable probabilistic features capable of capturing the range of tornadoes, RMWs, swirl ratios, path widths, path lengths, boundary layer profiles, and translational speeds for fast-running engineering simulations.

4.3. Wind Field Model

The Twisdale et al. (1978,1981) model is capable of producing spatial and radial variation of tangential, radial and vertical velocity components. It is scalable and maintains flow continuity between radial and vertical flow. Radial flow decreases with height and towards the center whereas vertical flow increases with height and towards the center. The tornado path edge wind speed was assumed to be a constant. Figure 4-3 shows an example of the radial and vertical variations of the wind speed components of an EF2 tornado with a maximum wind speed of 130 mph (58.1 m/s) and an RMW of 160 ft (48.8 m) at 33 ft (10.1 m) height above ground. The negative distances in the figure are distances from the center of the tornado towards negative x-axis. The complete set of model equations, solution algorithms, plots, and sensitivity analyses are provided in Twisdale et al. (1978, 1981) and Dunn and Twisdale (1979).

The wind field model is single-cell, so it does not produce two-cell flow structures or sub-vortices. For wind speed hazard swath simulations, the model is executed with time-stepping simulations that advance the wind field to produce digital calculations of reference wind speeds. The translation velocity of the tornado is vectorially added to the horizontal component, producing asymmetric flow. In building damage simulations, the wind field is simulated and time-stepped past the structure, producing the wind velocity vector components at each point needed for load calculations.

4.3.1. Wind Field Model Improvements and Implementation

The synthesized wind field model has been further enhanced for this project, including:

1. An updated RMW model
2. A swirl ratio model for estimation of radial inflow as a function of RMW
3. An updated translation speed model
4. An Atmospheric Pressure Change (APC) model
5. An improvement in the path width fitting routine

The updated RMW model is derived from the reported maximum damage width (MDW) data developed in Section 3. The model for the ratio of radial to tangential wind speeds (γ) are based on RMW and a swirl ratio relationship discussed in Section 4.3.3. The translation speed (assumed constant for a given tornado) is modeled as a regression on the tornado's path length in Section 4.3.4. APC is modeled using the cyclostrophic equation.[59] The wind speeds at the path edge boundaries are described in Section 4.3.5, using the distributions obtained from the EF-Scale wind speed analysis in 6. A new wind field fitting routine is implemented which fits probabilistic path edge wind speeds vs. a fixed path edge wind speed for all tornadoes is mentioned in Section 4.3.5 with details in Appendix D.2.

[59] The details of the APC model are given in Section 5.

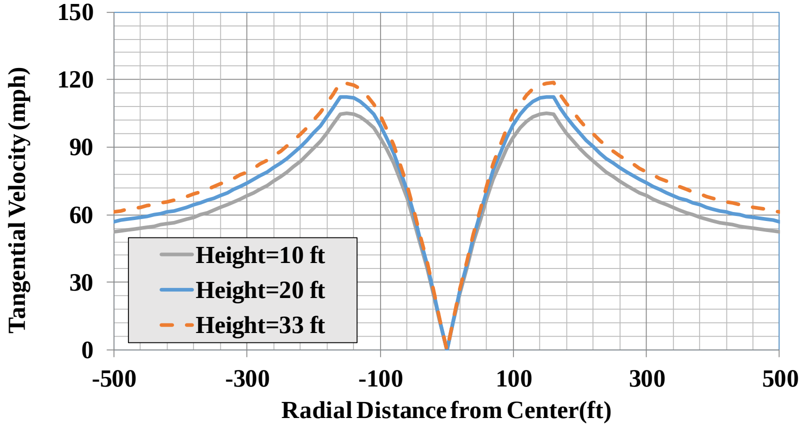

a. Tangential Velocity

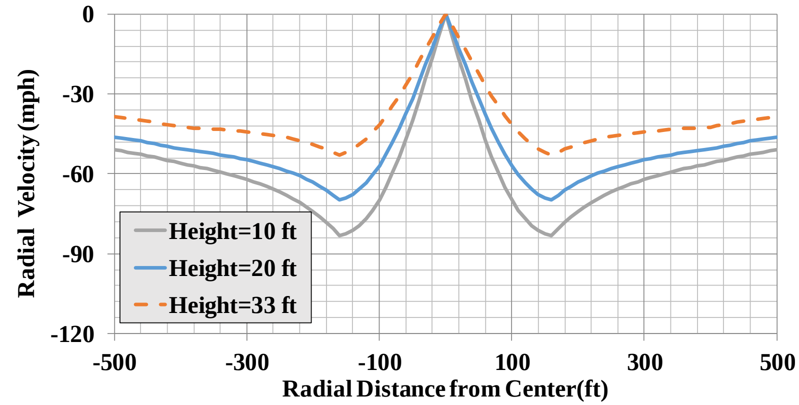

b. Radial Velocity

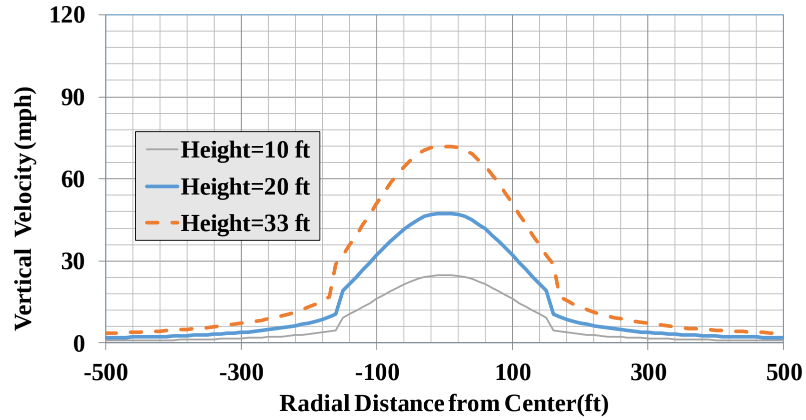

c. Vertical Velocity

Note: 1 mph = 0.44704 m/s; 1 ft = 0.3048 m

Figure 4-3. Spatial and Vertical Variation of Tornado Wind Field Components (EF2 tornado (130 mph (58.1 m/s)) with RMW = 160 ft (48.8 m)

4.3.2. RMW Model

RMW is an important parameter in tornado wind field modeling. It controls the variation of wind field components and pressure drop inside the core. Beginning in the late 1950's, film photogrammetry analysis was used to analyze tornado wind field flow patterns. From these analyses, RMW estimates could be inferred based on the location of the maximum horizontal or tangential velocities obtained from the analysis of the moving particles in a tornado (for example, Hoecker,1960; Fujita,1960; Agee et al, 1975; Fujita, 1975; Blechman, 1976; Golden,1976; Golden and Purcell, 1977; and Umenhofer and Fujita, 1977). Field damage surveys, still photography, and ground mark patterns have also been used to estimating tornado flows and radius of maximum observed damage (for example, Fujita, 1970a; Bleckman, 1975; Forbes, 1978; Marshall et al., 2008; Marshall et al., 2014). Radar observations of tornado wind fields includes those of Bluestein et al., 1993; Wurman, 2000; Bluestein, 2003; Wakimoto et al., 2003; Wurman and Alexander, 2005; and Wurman, 2014). Refan (2014) provided analyses of several radar observed tornadoes to estimate tornado wind field characteristics for laboratory experiments.

We examined a number of studies to assess the feasibility of developing conditional data on RMW from the literature. We found that RMW estimates in the literature were useful in development a relationship of RMW and tornado structure (observations of single vortex vs. multi-sub-vortex flows). The development of this relationship using the literature based RMW estimates is discussed in Section 4.3.3. However, the literature review was not suitable for developing a statistical distribution of RMW. The references did not generally have needed information on the tornado local path width (LPW) at the location of the estimated RMW. In addition, the height above ground of the estimated RMW was not necessarily included, particularly with radar observations. For these reasons, we used tornado ground level damage surveys that included F/EF contours of maximum damage width (MDW). As described in Section 3, for a PLIV F/EF segment, the MDW is the contour width within which the rated F/EF damage equals the maximum EF intensity for that segment. Using ground-level tornado damage survey data provides a systematic approach to conditioning MDW to the LPW at each PLIV segment along the tornado path. This method addresses many of the limitations of a literature-review approach to characterizing RMW.

The following paragraphs describe the development process for the RMW model as a path width dependent model from the MDW data.

MDW vs. LPW Regression Models. The first step to develop an RMW model was to develop the MDW and LPW data for a given EF intensity, using the detailed damage survey data described in Section 3. Using the data developed in Section 3, we performed linear regression analysis of MDW and LPW data for a given EF intensity in logarithmic space in which the natural logarithm of MDW is a function of the natural logarithm of local path width. LPW is the natural independent variable since it is developed empirically from tornado damage path data, as described in Section 3.5. The variation in LPW is captured from the catalogue of tornado eventThe regression plots are shown in Figure 4-4. The red line is the fitted regression line and the blue lines are the ±2 standard deviation lines from the regression lines. The standard deviation is computed from the residuals in the fitting process. Due to limited data, EF4 and EF5 data are combined into a single regression model EF0 tornadoes do not have a local MDW that differs from the local path width; hence, a regression fit is not shown in Figure 4-4.

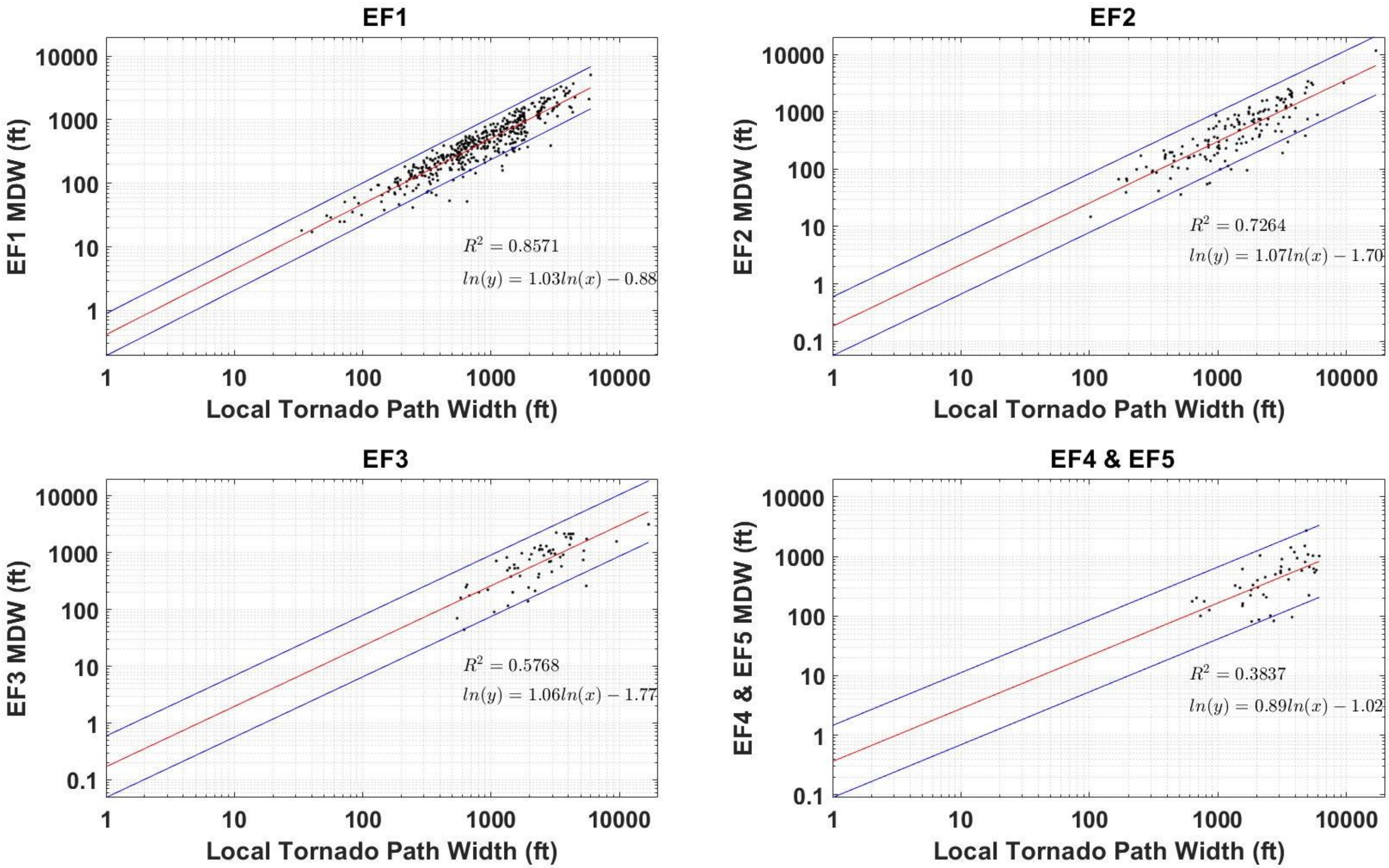

Note: 1 ft = 0.3048 m

Figure 4-4. Regression Plots for MDW vs. LPW Model

RMW vs. MDW. The second step was to develop RMW and MDW relationships for different EF intensities using simulations of tornado wind speed swaths. Figure 4-5 illustrates the steps to develop this model. This approach provides consistency in our spatial modeling of tornado windfields using empirically developed damage swaths and EF intensity contours.

Tornado simulations of intensities EF0-EF5 are performed using the Region 4 path model described in Section 0 and the wind field model with a range of RMW values. The radial inflow (γ) in the wind field model is computed using the swirl model discussed in Section 4.3.3. We used the Region 4 translation speed (U_T) model discussed in Section 0 for these simulations. The maximum wind speed (U_{max}) in each EF intensity is sampled from a uniform distribution using the wind speed ranges in the EF-Scale (TTU, 2004).[60] The wind field is fitted according to the path edge wind speed model as described in Section 0.

[60] This work was performed before the final EF* wind speeds were developed (Section 6).

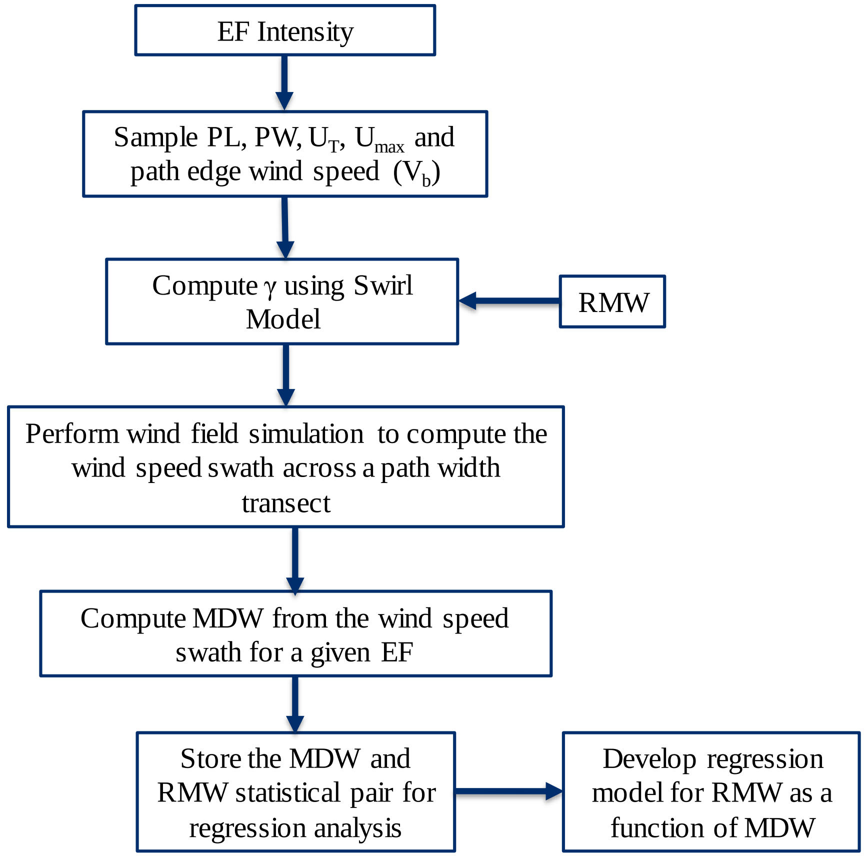

Figure 4-5. Steps to Develop RMW and MDW Relationship

For each simulated tornado, wind swaths are produced across the path width and MDW is calculated from the portion of the width where the swath wind speeds exceed the lower bound wind speed (TTU, 2006) for that intensity. For example, MDW in a simulated EF1 tornado is computed by evaluating the width where the swath wind speeds exceed 85 mph (38.0 m/s). MDW in a simulated tornado depends on RMW and the sampled values of maximum wind speed, translation speed, and path edge wind speed fitting.

The process of computing MDW from wind swath is performed for all of the simulated tornadoes. In this way, a range of RMW and corresponding MDW values are generated for each EF intensity. A linear regression analysis is then carried out to derive relationship between RMW and MDW, where MDW is the independent variable. The residuals of these fits are modeled as normally distributed variables with zero mean and a standard deviation, which is equal to the standard deviation of the residuals of each regression fit.

The regression plots are shown in Figure 4-6. The resulting mean RMW for each EF-Scale is about one-half of the MDW. In these plots, each black circle represents the RMW for the simulated MDW. The red line is the fitted regression line and the blue lines are the ± 2 standard deviation bounds from the fitted line. The standard deviation is computed from the residuals in the fitting process.

We illustrate examples of computed mean RMW values as a function of LPW for each EF scale in Table 4-1. The LPW values in Table 4-1 (Col. 1) for each EF-Scale are representative of Region 4 EF-Scale era data and are within about ± 1 Std from the mean PW of that region. The RMWs in Table 4-1 (Col. 3) are computed using two steps. In the first step, mean MDW (Col.2) is computed for a given LPW using the models shown in Figure 4-4.**Note**: 1 ft = 0.3048 m

Figure 4-4. Regression Plots for MDW vs. LPW Model

In the second step, mean RMW is computed from the models shown in Figure 4-6 for the mean MDW value computed in the first step. The ratio of mean RMW/ LPW (Col. 6) shows a decreasing tendency with increased tornado intensity. The ratio is greater than 0.5 for EF0 tornadoes whereas it is less than 0.15 for EF5 tornadoes. The decreasing tendency results from the fact that mean RMW is computed using the mean MDW and the ratio of mean MDW to LPW also decreases with increasing intensity. In an EF5 tornado, maximum wind speed is much higher than the path edge wind speed. Even with a rapid decay of wind speeds outside the core, MDW is much smaller than LPW due to the higher wind speed difference between the maximum wind speed and the path edge wind speed.

We also note that the MDW model is based on a limited set of data extracted from scaled damage maps. Due to this limitation, the MDW model may not capture the full range of variabilities in the MDW and LPW relationship. The ratio of mean RMW to mean MDW in Table 4-1 shows higher values for EF5 than for EF0. In an EF5 tornado, mean modeled translation speed is higher than that in an EF0 tornado and the path width fitting routine (discussed in Appendix D) may reduce the high translation speed to achieve the fitting in a simulation. The reduction of the translation speed results in a lower MDW than that without a reduction. Lower MDW also results when the sampled maximum wind speed is not significantly higher than the lower bound EF5 wind speed. As EF5 tornadoes generally have significantly higher RMWs than those in EF0 tornadoes, the ratio of RMW to MDW is higher when the computed MDW is low due to the aforementioned reasons.

Models for RMW and MDW are not regionally dependent but depend on regional tornado path width data. Hence, the RMW model implicitly incorporates regional variation and the epistemic uncertainties in path length and width.

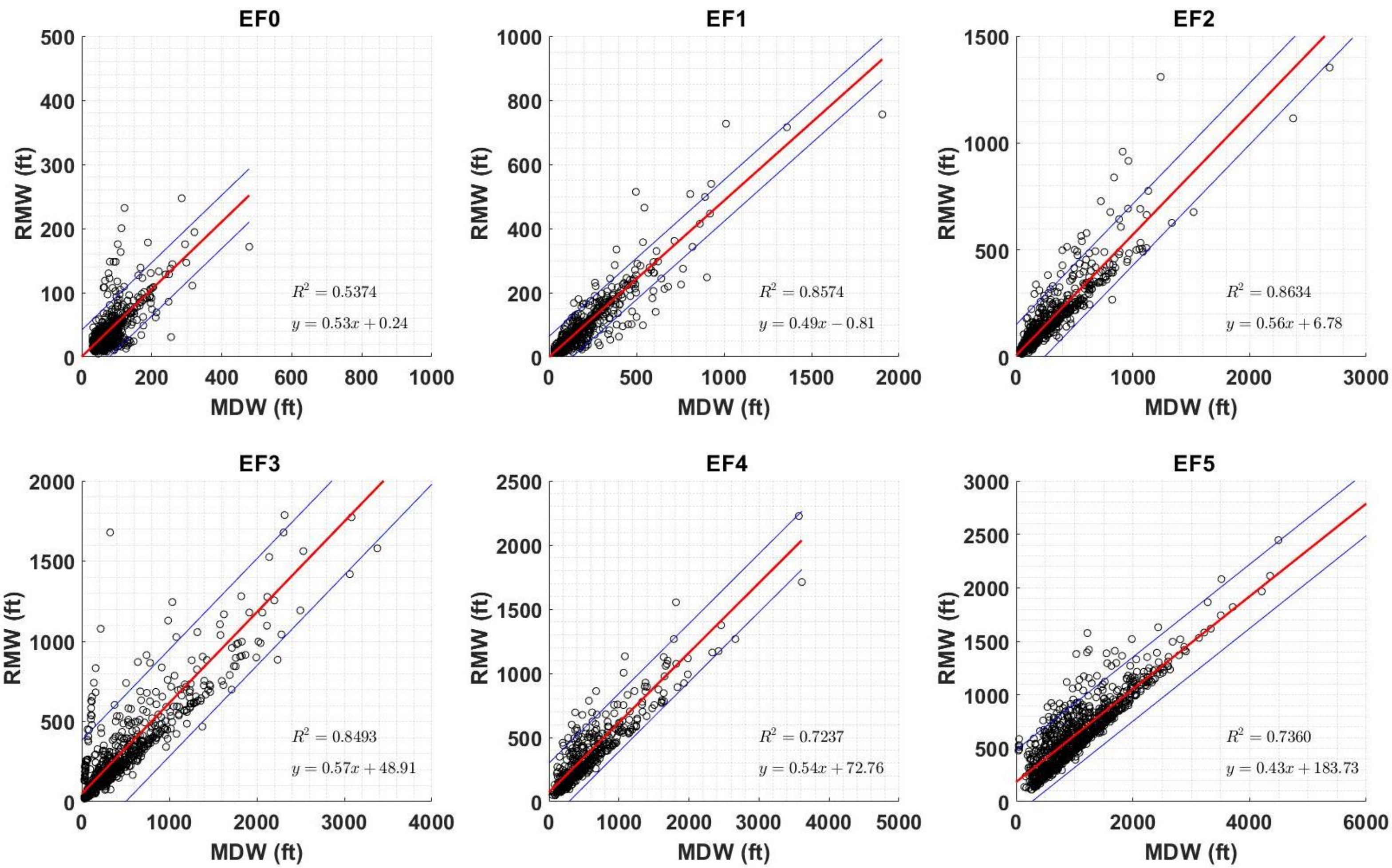

Note: 1 ft = 0.3048 m

Figure 4-6. Regression Plots for RMW Model

Table 4-1. Examples of Modeled MDW and RMW

Intensity	1. LPW (ft)	2. Mean MDW (ft)	3. Mean RMW (ft)	4. Mean MDW/LPW	5. Mean RMW/Mean MDW	6. Mean RMW/LPW
EF0	100	100	53	1.00	0.53	0.53
	200	200	106	1.00	0.53	0.53
	300	300	159	1.00	0.53	0.53
	400	400	212	1.00	0.53	0.53
	500	500	265	1.00	0.53	0.53
EF1	400	199	96	0.50	0.48	0.24
	500	250	122	0.50	0.49	0.24
	600	302	147	0.50	0.49	0.25
	700	353	172	0.50	0.49	0.25
	800	406	198	0.51	0.49	0.25
EF2	600	172	103	0.29	0.60	0.17
	700	202	120	0.29	0.59	0.17
	800	233	137	0.29	0.59	0.17
	900	265	155	0.29	0.58	0.17
	1000	296	173	0.30	0.58	0.17
EF3	1000	258	196	0.26	0.76	0.20
	1500	396	275	0.26	0.69	0.18
	2000	538	355	0.27	0.66	0.18
	2500	681	437	0.27	0.64	0.17
	3000	826	520	0.28	0.63	0.17
EF4	2000	313	242	0.16	0.77	0.12
	3000	448	315	0.15	0.70	0.11
	4000	579	386	0.14	0.67	0.10
	5000	706	454	0.14	0.64	0.09
	6000	831	521	0.14	0.63	0.09
EF5	3000	448	377	0.15	0.84	0.13
	4000	579	433	0.14	0.75	0.11
	5000	706	488	0.14	0.69	0.10
	6000	831	541	0.14	0.65	0.09
	7000	953	594	0.14	0.62	0.08

Note: 1 ft = 0.3048 m

4.3.3. Swirl Ratio Model

A swirl ratio model has been incorporated in the wind field model to facilitate physically-based modeling of the radial inflow parameter (γ), which is defined as the ratio of radial to tangential velocity at RMW (Twisdale et al. (1978,1981) and Dunn and Twisdale (1979)).

Swirl is a measure of the tornado-scale helicity. Swirl ratio can generally be defined as the ratio of the circulation of the tornado vortex to the inflow. Large swirl ratios imply increasing circulation mass. If the radial inflow is not sufficient to evacuate that mass, then the circulation "breaks down" into multiple circulation centers (i.e. sub-vortices). It has been widely reported in the literature (Church et al. 1979, Baker and Church 1979, Davies-Jones 1973, and Davies-Jones et al. 2001) that the swirl ratio is an important parameter to define the vortex structure within a tornado. Although, swirl ratio is widely used to explain the characteristic of a laboratory or numerically simulated tornadoes, no universal definition exists. It is particularly challenging to define swirl ratio at atmospheric level (Bluestein, 2017).

Swirl Definition. Several definitions of swirl ratio exist in the literature. The classical definition of swirl ratio referred by many researchers is given in Eq. (4-1), which represents the ratio of the angular momentum to the radial momentum in the vortex.

$$S = \frac{\Gamma r_o}{2Qh} \qquad \textbf{(4-1)}$$

where S is the swirl ratio; Γ is the circulation at the edge of the updraft; r_o is the updraft radius; Q is the volume flow rate through updraft hole per unit axial length of the updraft; and h is the height of the updraft.

Davies-Jones et al. (2001) defined swirl ratio as the ratio of the tangential velocity at the edge of the updraft to the mean vertical velocity through the updraft hole as given in Eq. (4-2).

$$S = \frac{v_0}{\overline{w}} \qquad \textbf{(4-2)}$$

where v_0 is the tangential velocity at the edge of the updraft and $\overline{w}$ is the average vertical velocity through the updraft. Eq. (4-2) can be obtained from Eq. (4-1) as the circulation at the edge of the updraft depends on tangential velocity and volume flow rate through updraft depends on mean vertical velocity through the updraft hole.

Swirl ratio can also be defined as the ratio of the tangent of the inflow angle to that of the aspect ratio, which is the ratio of the height of the inflow to the radius of the updraft.

$$S = \frac{\tan\theta}{a} \qquad \textbf{(4-3)}$$

This definition has been widely used in the laboratory experiments (Liu and Ishihara, 2012) since the values of inflow angle, height of the inflow and radius of the updraft are precisely known. In Eq. (4-3), θ is the inflow angle measured at the updraft radius and a is the aspect ratio which is the ratio of the height of the inflow/updraft (h) to the radius of the updraft (r_o). Liu and Ishihara (2012) shows that Eq. (4-1) can be converted to Eq. (4-3) for laboratory experiments that uses guide vanes to control the circulation.

Hann et al. (2008) modified the definition of swirl ratio given in Eq. (4-1) for their experiments in the following form

$$S = \frac{\pi V_{\theta\, max} r_c^2}{Q} \qquad \textbf{(4-4)}$$

where swirl ratio is measured at the radius of the maximum winds; $V_{\theta\, max}$ is the maximum tangential velocity at the radius of maximum wind speed; r_c is the radius of maximum wind speed; and Q is the volume flow rate.

These equations are different forms of tornado-scale helicity. For example, Eq. (4-4) can be reduced to Eq. (4-2) if the average volume flow rate (Q) is divided by the area of the core (i.e., πr_c^2). Thus, the definitions of swirl ratio given in Eq. (4-1), Eq. (4-3) and Eq. (4-4) are generally equivalent to that given in Eq. (4-2).

For establishing a general relationship between γ and swirl ratio, we adopt the equation form given in Eq. (4-2), use the tangential velocity at RMW, and compute the mean integrated vertical velocity inside the core ($\bar{w}$). Our computation of γ from swirl ratio is derived through a sensitivity analysis as discussed later in this section.

RMW, Swirl, and Vortex Breakdown. It is shown in the literature that the RMW is dependent on swirl ratio (Baker and Church, 1979, Davies-Jones, 1973). Vortex diameter tends to increase with increasing swirl ratio as reported in Davies-Jones (1973), Church et al. (1979), Baker and Church (1979), Hann et al. (2008) and Liu and Ishihara (2016). Baker and Church (1979) and Liu and Ishirara (2015) also shows swirl ratio increases more rapidly with respect to RMW after vortex breakdown. It is also reported in Rottuno (1977, 1979) and Baker and Church (1979) that the RMW is not dependent on radial Reynolds number and there is no well-defined relationship between swirl ratio and RMW for very small swirl ratio. Davies-Jones (1973) also found that the transition from single-cell vortex structure to two-cell vortex structure and multiple vortex is weakly dependent on radial Reynolds number.

Based on the above findings, we developed a simple RMW dependent model for swirl ratio. As breakdown from single vortex to multi-vortex structure depends on the swirl ratio, we also developed a logistic model based on vortex breakdown probabilities with respect to estimated RMW from literature review of 34 studies: 19 radar, 11 photogrammetric, and 4 damage survey given in Table 4-2. In some of the studies, the reported RMW values were measured at heights significantly higher than the typical height of observable damage. We generally used the reported value for these cases. For the studies reported in Table 4-2, we developed a table of 0's and 1's based on the researcher's conclusion of complete vortex breakdown (sub-vortices present) or not. To treat uncertainties in the data, and based on our interpretation of the researcher's presentation, we considered some of the data as not conclusive. We therefore developed lower bound and upper bound estimates of multi-vortex observations for each of the studies.

Epistemic Logistic Regression Models. Binomial logistic regression (using 0, 1 data, where 0 denotes no sub-vortices and 1 denotes observed sub-vortices) models were developed for an upper bound and a lower bound interpretation of the data using MATLAB (2018). The probabilities of vortex breakdown at a given RMW are then determined from the following logistic equation

$$P_{vb}(RMW) = \frac{1}{1 + e^{-(\beta_0 + \beta_1 * RMW)}} \quad \textbf{(4-5)}$$

where $P_{vb}(RMW)$ is the probability of vortex breakdown at a given RMW, β_0 and β_1 are the coefficients obtained from the regression.

As described previously, Table 4-2 has two columns regarding our interpretation of observed multi-vortices. Our interpretation places between 10 and 15 of the 38 cases as multi-vortices. Separate logistic fits are carried out using these two columns and the associated RMWs Figure 4-7 illustrates the fitted upper bound and lower bound logistic models. The large uncertainties in vortex breakdown probabilities for a given RMW is evident in the figure. At high RMW, vortex breakdown becomes highly probable, but not certain. The black circles and red ‘x’s (at 0 and 1 probabilities) in the figure represent the lower bound interpretation and the upper bound interpretation of the vortex breakdown data respectively for the estimated RMWs.[61] In a tornado wind field simulation, both the fitted models (shown in blue and orange curves in Figure 4-7) are used to determine the vortex breakdown. First, $P_{vb}(RMW)$ is computed from each of these models and then the mean of these computed $P_{vb}(RMW)$s is used to determine the vortex breakdown.

[61] There are 10 circles for $P_{vb} = 1$; 28 circles for $P_{vb} = 0$ for lower bound interpretation; 15 ‘x’s for $P_{vb} = 1$; and 23 ‘x’s for $P_{vb} = 0$ for UB interpretation.

Table 4-2. Tornado Vortex Breakdown Data obtained from Literature Review

Number	Location	Date	F/EF	Source Type	Est. RMW (ft)	RMW Source	Multi-Vortex Estimation	
							Lower Bound	Upper Bound
1	Greensburg, KS	5/4/2007	5	Damage	563	Marshall et al., 2008	0	1
2	Joplin, MO	5/22/2011	5	Damage	843	Lombardo et al., 2015	0	0
3	Dallas, TX	4/2/1957	3	Film Photogram.	79	Hoecker, 1960	0	0
4	Fargo, ND	6/20/1957	5	Film Photogram.	328	Fujita, 1960	0	0
5	Xenia, OH	4/3/1974	5	Film Photogram.	574	Fujita, 1975	1	1
6	Kankakee, IL	4/17/1963	4	Film Photogram.	252	Golden, 1976	0	0
7	Salina, KS	9/25/1973	3	Film Photogram.	66	Golden, 1976	0	0
8	Union City, OK	5/24/1973	4	Film Photogram.	273	Golden and Purcell, 1977	0	0
9	Great Bend, KS	8/30/1974	2	Film Photogram.	198	Umenhofer and Fujita, 1977	0	0
10	Great Bend, KS	8/31/1974	3	Film Photogram.	314	Umenhofer and Fujita, 1978	1	1
11	Parker, IN	4/3/1974	4	Film Photogram.	465	Agee, et. al., 1975	1	1
12	Oshkosh, WI	4/21/1974	4	Film Photogram.	380	Blechman, 1976	1	1
13	Oshkosh, WI	4/21/1974	4	Film Photogram.	479	Blechman, 1976	0	0
14	Attica, KS	5/12/2004	2	Radar	86	Bluestein, 2007	0	0
15	Bassett, NE	6/5/1999	0	Radar	75	Bluestein, 2003	0	0
16	Ceres, OK	4/26/1991	4	Radar	263	Bluestein et al., 1993	0	0
17	Clairemont, TX	6/12/2005	0	Radar	315	Refan, 2014	0	0
18	Clearwater, KS	5/16/1991	1	Radar	202	Bluestein et al., 1993	0	0
19	Dimmit, TX	6/2/1995	2	Radar	328	Wurman, 2000	0	1
20	Goshen, WY	6/5/2009	2	Radar	620	Refan, 2014	0	1
21	Happy, TX	4/21/2007	0	Radar	388	Refan, 2014	0	0
22	Kremlin,OK	4/12/1991	3	Radar	749	Bluestein et al., 1993	0	0
23	Mooreland, OK	5/26/1991	3	Radar	749	Bluestein et al., 1993	0	0
24	Mulhall, OK	5/3/1999	4	Radar	1550	Lee and Wurman, 2005	1	1
25	Orleans, NE	5/22/2004	0	Radar	150	Wurman, 2010	1	1
26	Prospect Valley,	5/26/2010	< 0	Radar	75	Tanamachi et al., 2013	0	0
27	Spearman,TX	5/31/1999	3	Radar	747	Bluestein et al., 1993	0	0
28	Spencer, SD	5/30/1998	4	Radar	199	Wurman and Alexander, 2005	0	0
29	Spencer, SD	5/31/1998	4	Radar	620	Refan, 2014	0	1
30	Stockton, KS	6/9/2005	1	Radar	682	Refan, 2014	0	0
31	Tribune, KS	5/25/2010	0	Radar	38	Tanamachi et al., 2013	0	0
32	Kellerville, TX	6/8/1995	5	Radar	142	Wakimoto et al. , 2003	0	0
33	Moore, OK	5/20/2013	5	Radar + Damage	300	Atkins, et al., 2014	0	0
34	Lubbock, TX	5/11/1970	5	Damage	744	Forbes, 1976; Fujita, 1970	1	1
35	Wisconsin	4/21/1974	3	Damage	211	Blechman, 1975	1	1
36	Cabot,Ark.	3/29/1976	3	Damage	101	Forbes and Bluestein, 2001; Forbes, 1978	1	1
37	Harper, KS	5/12/2004	0	Radar	75	Kosiba, Trapp, and Wurman, 2008	0	1
38	El Reno, OK	5/31/2013	3	Damage	1584	Marshall et al., 2014; Wurman et al., 2014	1	1
Estimated LB and UB Sums of Tornadoes with Multivortex Characteristics							10	15

Note: 1 ft = 0.3048 m

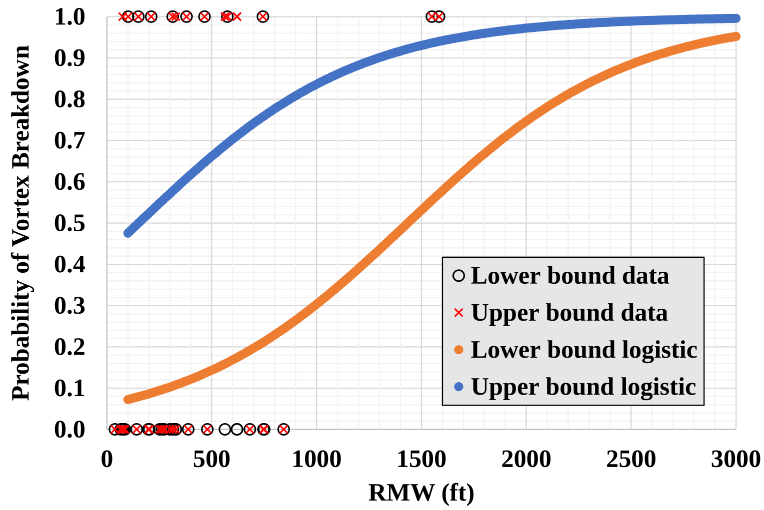

Note: 1 ft = 0.3048 m

Figure 4-7. Logistic Models for Vortex Breakdown

Epistemic Implementation. A laboratory-generated swirl ratio plot is given in Fig 8-4(a). This plot shows that swirl ratio increases linearly with RMW up to vortex breakdown and more rapidly thereafter, consistent with literature (e.g., Baker and Church, 1979; Liu and Isihara, 2016; Davies-Jones, 1973; Church et al., 1979 and Hann et al., 2008). The non-dimensional core radius in Figure 4-8(a) is the ratio of the RMW of the simulated vortex (in the experiment) to the updraft radius. As the updraft radius was kept constant in the experiment, the non-dimensional radius in the figure can be a substitute to represent RMW.

The mathematical formulation of the swirl ratio model is illustrated in Figure 4-8 (b). The black line illustrates the mean, which shows that Figure 4-8 (b) demonstrates the same form as classical laboratory plots as in Figure 4-8 (a).

Our mathematical formulation of a swirl ratio model is a bi-linear model as shown in Figure 4-8 (b). We discuss the bi-linear model in terms of the single-vortex region and the multi-vortex region (shaded area in Figure 4-8(b). The single-vortex region corresponds to the “linear” portion and the multi-vortex region corresponds to the “non-linear” portion of the curve in Figure 4-8(a). The linear segment employs lower and upper limits of swirl ratio and RMW to define this segment. In Figure 4-8 (b), S_s and R_s are the lower limits and S_{vb} and R_{vb} are the upper limits of swirl ratio and RMW respectively. The linear segment in the model shows the relationship between RMW and swirl ratio for a single vortex structure. The non-linear segment (shaded area) shows a multi-vortex region, which is defined in a simulation by the sampled values of S_{vb} and R_{vb}. The epistemic parameters include the logistic models and sampled values of (S_s, R_s) and (S_{vb}, R_{vb}). The sampling locates the positions of (S_s, R_s) and (S_{vb}, R_{vb}) in Figure 4-8 (b). The implementation of the swirl model follows.

Calculation Steps. The model calculation steps are given in Figure 4-9. The grey-shaded boxes indicate steps with sampling of epistemic uncertainties. These swirl calculations are performed for each PLIV intensity segment along the tornado path.

For a given EF intensity, the models of MDW and RMW given in Section 4.3.2 are used to compute RMW from a sampled PW (Steps 2 and 3). In Step 4, if the computed RMW is less than R_s, the swirl ratio is not computed since, at low RMW, swirl ratio and RMW relationship is not well-defined (e.g., Baker and Church, 1979) and we assume they are independent. We obtain γ from a uniform distribution between 1 and 3 and R_s is assumed to be 100 ft (30.5 m). If the computed RMW is greater than or equal to R_s, the values of S_s and S_{vb} are sampled from a uniform distribution between 0.1 and 0.4 and between 1 and 2, respectively (Step 5). The limits of S_s and S_{vb} distributions are inferred from literature as given in

Table 4-3.

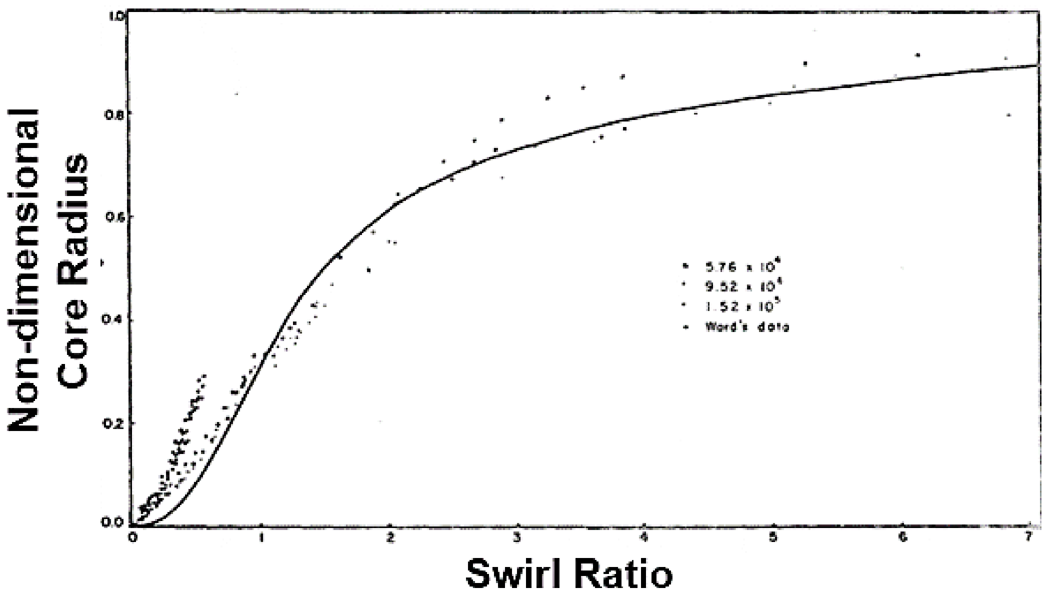

a. Variation of Non-Dimensional Core Radius with Swirl Ratio (Adapted from Baker and Church, 1979)

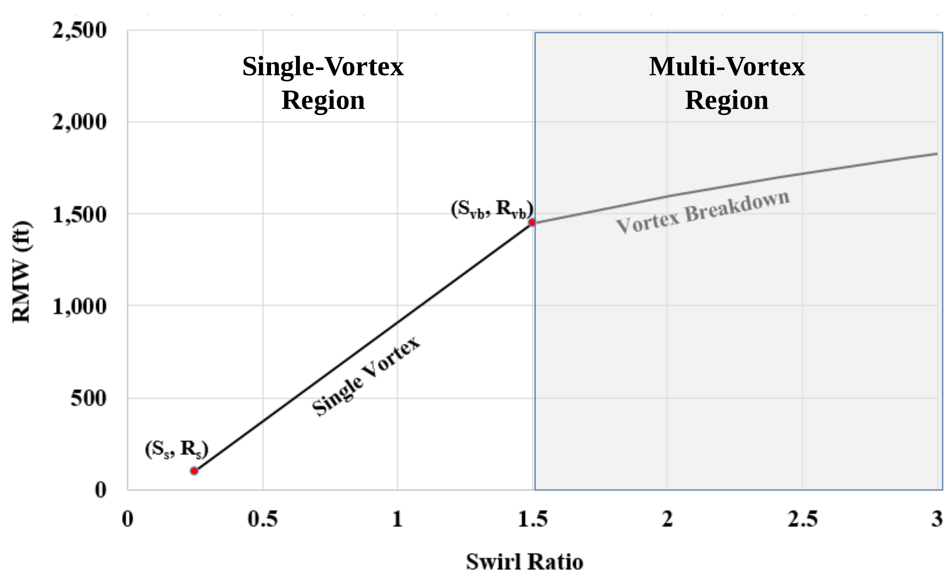

b. Mean Swirl Ratio Bi-Linear Model Illustrating Specific Sampled Values for S_S, S_{vb}, and R_{vb}

Note: 1 ft = 0.3048 m

Figure 4-8. Relationship between RMW and Swirl Ratio

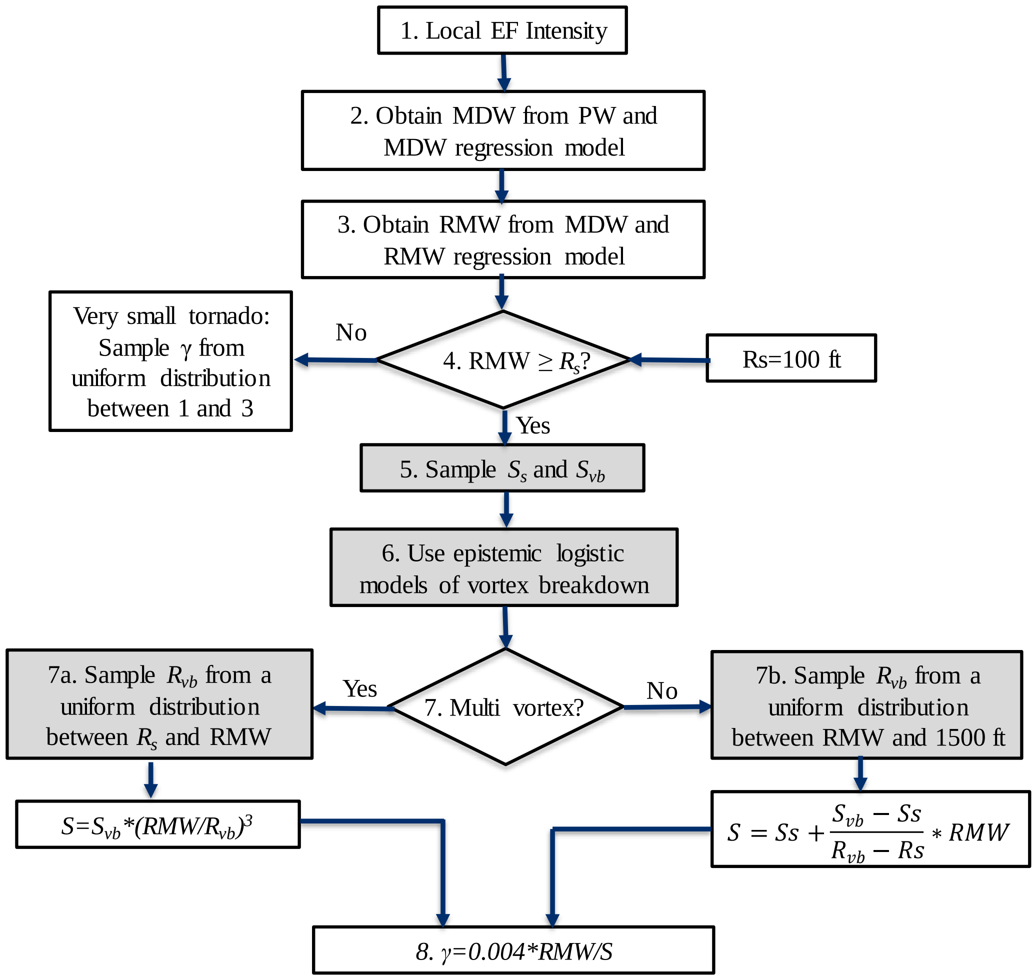

Note: 1 ft = 0.3048 m

Figure 4-9. Swirl Model Implementation

Table 4-3. Limits of S_s and S_{vb} Inferred from Literature

No.	**Reference**	S_s	S_{vb}
1	Baker and Church (1979)	0 to 0.4	1.5 to 2
2	Church et al. (1979)	≤0.1	>0.4
3	Davies-Jones et al. (2001)	<0.45	0.8 to 3
4	Lee and Wurman(2005)		>1
5	Monji (1985)	<0.2	0.5-1
6	Matsui and Tamura (2009)	<0.3	>1.1
7	Koshiba and Wurman (2013)		>1 to 7

In Step 6, we use the lower and upper bound logistic models for the vortex breakdown (shown in Figure 4-7) to determine vortex breakdown probabilities for the computed RMW. In Step 7, we sample from a normal distribution bounded between the lower bound and upper bound probabilities (computed in Step 6)to determine whether or not the vortex is single- or mulit-vortex for the computed RMW. If multi-vortex, then R_{vb} is obtained from a uniform distribution between R_s and the computed RMW; otherwise, R_{vb} is obtained from a uniform distribution between the computed RMW and 1,500 ft (457 m). The upper limit of 1,500 ft (457 m) is an estimate based on the information presented in Table 4-2, where no observations of a single vortex beyond RMW = 843 ft (256.9 m) exists in this data set. For the two cases in Table 4-2 with RMW > 1,500 ft (457 m), both resulted in multiple vortices. Hence, we chose 1,500 ft (457 m) as a modeled UB, which therefore cannot be exceeded in our simulations of RMW.

For a single vortex with RMW greater than or equal to R_s, swirl ratio linearly varies with RMW. In this case (Step 7a), the swirl ratio is computed from Eq. (4-6).

$$S = S_s + \frac{S_{vb} - S_s}{R_{vb} - R_s} * RMW \tag{4-6}$$

For the case of a vortex breakdown (Step 7b), swirl ratio is computed using a cubic equation to represent the rapid increase of swirl ratio with a modest increase of RMW. The following equation is employed for the model

$$S = S_{vb} * \left(\frac{RMW}{R_{vb}}\right)^3 \tag{4-7}$$

Once the swirl ratio is computed either by Eq. (4-6) or by Eq. (4-7), γ is obtained from Eq. (4-8) which was derived from a sensitivity analysis. The sensitivity analysis uses a set of RMW values (100 ft, 200 ft, 500 ft, 1,000 ft and 2,000 ft) (30.5 m, 61 m, 150 m, 305 m, 610 m) at which swirl ratio is computed using Eq. (4-2) for a given γ. For each of these RMW values the obtained swirl ratios are fitted with a power law as a function of γ as shown in Figure 4-10. The fitted equations show that swirl ratio is approximately an inverse function of γ which can be written as

$$\gamma = \frac{k * RMW}{S} \tag{4-8}$$

The coefficient (k) of this function is approximated as 0.004 by the power law fits. This relationship inherently reflects the mass flow continuity relationship between inflow and vertical flow in the synthesized wind field model.

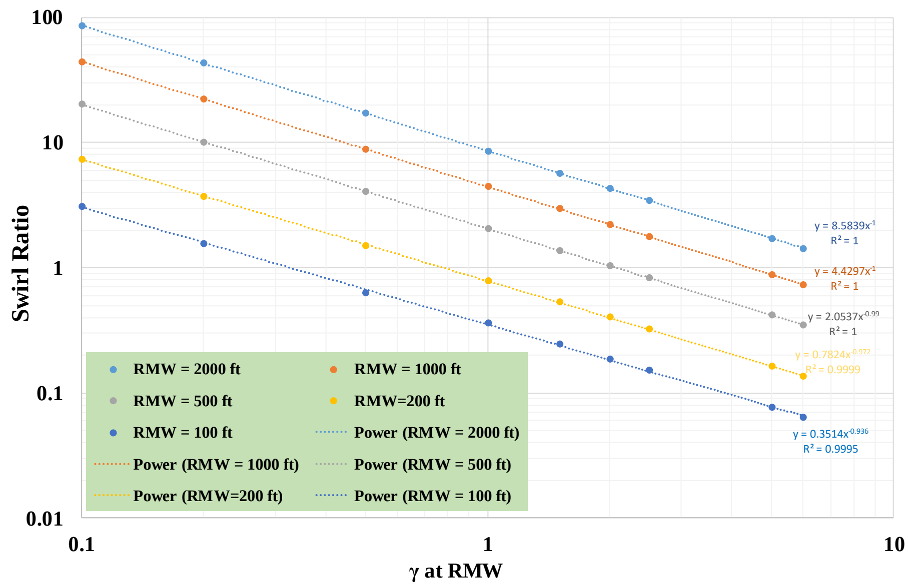

Note: 1 ft = 0.3048 m

Figure 4-10. Sensitivity of Swirl Ratio for Various γ and RMW Values

Swirl Model Results. We simulated 450 different EF intensity tornadoes with the Region 4 path models. Using the LPW to MDW and MDW to RMW models, we produced a realized RMW in each simulation.

Figure 4-11(a) shows the swirl ratios obtained from the simulated RMWs. Low RMW values produce low swirl ratios in most of the simulations and the value of modeled swirl ratio tends to increase with increasing RMW. High swirl ratios result when the vortex breaks down into multiple vortices.

Figure 4-11 (b) shows the computed γ values from the computed swirl ratios in Figure 4-11 (a). As expected, lower swirl ratio produces higher γ whereas higher swirl ratio produces lower γ.

In Figure 4-11 (c), γ is plotted vs. RMW. The model generates high γ when RMW is low. There is a decreasing trend of γ with increasing RMW. The trend is due to the fact that the model generates high swirl ratio when the RMW is high (when the vortex breaks into multiple sub-vortices). Figure 4-11 (c) also shows γ can be as high as 3 when RMW is less than 100 ft (30.5 m).

In these plots, the black dashed line is a power law fit to the simulated data. Overall, these plots show that the implemented swirl model produces values of swirl ratio and γ that have a consistent trend with the size of the vortex as generally captured in laboratory, numerical and radar studies. The fitted lines shown in Figure 4-11 (a), (b) and (c) produce R^2 values of about 0.8, 0.6 and 0.2, respectively.

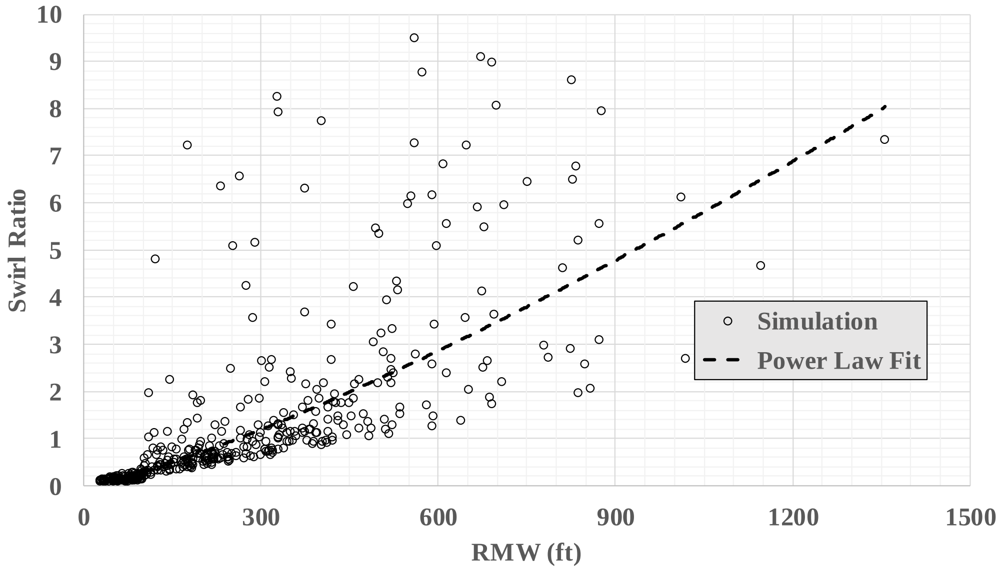

Note: 1 ft = 0.3048 m

a. Simulated RMW vs. Simulated Swirl Ratio

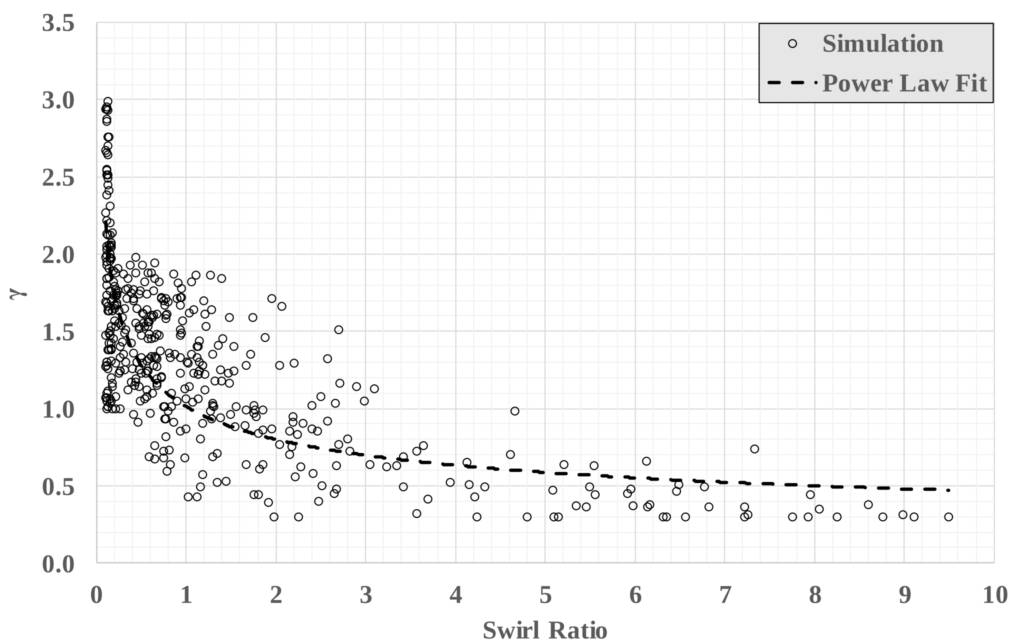

b. Swirl Ratio vs. γ

Figure 4-11. Swirl Model Plots

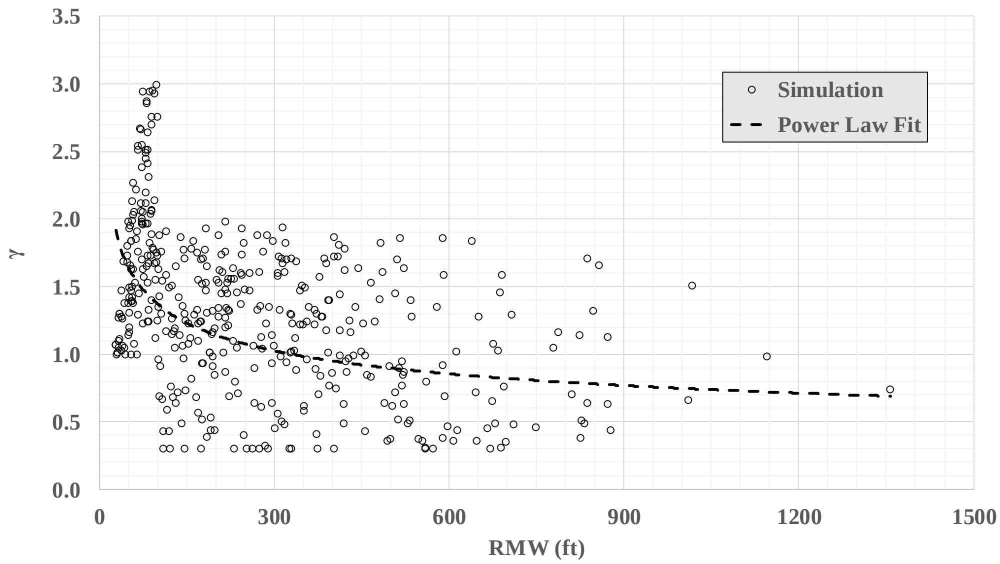

c. RMW vs. γ

Note: 1 ft = 0.3048 m

Note: 1 ft = 0.3048 m (continued)

4.3.4. Translation Speed Model

Translation speed is an important parameter of the wind field model as it vectorially increases the wind speed on the right-hand side of the track and decreases it on the left-hand side of the track.[62]

Translation speed is calculated for tornadoes in the EF-Scale era data (from 2007-2016) in the augmented database, which has information about the starting and ending locations as well as beginning and ending times of the tornado. It is assumed that the translation speed is constant during the life cycle of a tornado.

Translation speeds are analyzed for the six regions using the above-mentioned dataset. Analysis of correlation shows that the translation speed is generally well-correlated with the natural logarithm of the path length. Table 4-4 shows Pearson correlation coefficients for correlation of translation speed with natural logarithm of path length and natural logarithm of path width and their associated p-values for each EF-Scale for the six regions. A positive value of the correlation coefficient indicates a proportional relationship of the random variables whereas a negative value indicates the random variables are inversely correlated. The p-value is associated with the null hypothesis that translation speed is not correlated with either path length or path width. Any p-values less than 0.05 indicate the rejection of this hypothesis. The cells with p-value less than 0.05 are highlighted with light grey in the table. The blank cells in the table inidicate that no data is available in the augmented database for the region and the EF category. The 0 p-values shown in the table is a result of rounding of a

[62] Note that, nearly all tornadoes in the conterminous US rotate counterclockwise. Anti-cyclonic tornadoes are not modeled for this project.

slightly positive p-value to three significant digits after the decimal. As seen from the table, for a given EF, translation speed is well correlated with natural logarithm of tornado path length.

Table 4-4. Correlation Between Translation Speed and Path Length and Width

Length and Translation Speed Correlation												
EF	Region 1		Region 2		Region 3		Region 4		Region 5		Region 6	
	Corr. Coeff.	Pvalue	Corr. Coeff.	Pvalue	Corr. Coeff.	Pvalue	Corr. Coeff.	Pvalue	Corr. Coeff.	Pvalue	Corr. Coeff.	Pvalue
0	0.601	0.000	0.749	0.000	0.627	0.000	0.704	0.000	0.657	0.000	0.733	0.000
1	0.462	0.004	0.529	0.000	0.527	0.000	0.537	0.000	0.615	0.000	0.653	0.000
2	0.878	0.000	0.341	0.004	0.546	0.003	0.457	0.000	0.420	0.021	0.740	0.000
3			0.382	0.221	0.796	0.058	0.491	0.000	0.198	0.706	0.724	0.002
4			0.742	0.056			0.478	0.008				
5							0.430	0.570				
Width and Translation Speed Correlation												
0	0.142	0.063	0.435	0.000	0.125	0.011	0.309	0.000	0.329	0.000	0.293	0.000
1	0.098	0.563	0.303	0.000	-0.078	0.504	0.253	0.000	0.286	0.000	0.231	0.000
2	0.813	0.001	0.104	0.387	0.116	0.563	0.157	0.000	0.387	0.034	0.270	0.013
3			-0.274	0.388	0.482	0.333	-0.026	0.742	0.135	0.799	0.342	0.195
4			-0.046	0.923			-0.055	0.773				
5							-0.932	0.068				

Regression analyses have been carried out and intensity dependent regional models for translation speeds are developed as linear functions of the natural logarithm of path lengths.

$$U_T = c + m * \log(PL) + \varepsilon \quad \textbf{(4-9)}$$

where, U_T is the translation speed in mph, PL is the path length in miles, c is the constant of the linear fit, m is the slope of the linear fit and ε is the random error obtained from a normal distribution with a zero mean.

The regression plots for Region 4 are given in Figure 4-12. Regression plots for EF0, EF1 and EF2 tornadoes show a series of curved patterns. These patterns result from data round-off for short and modest path lengths and rounded time estimates in the database used to compute U_T. The red line shown in the plots are fitted lines and the blue lines are the ±2 standard deviation lines from the regression lines. The standard deviation is computed from the residuals in the fitting process. Regression plots for all other regions are given in Appendix D.1.

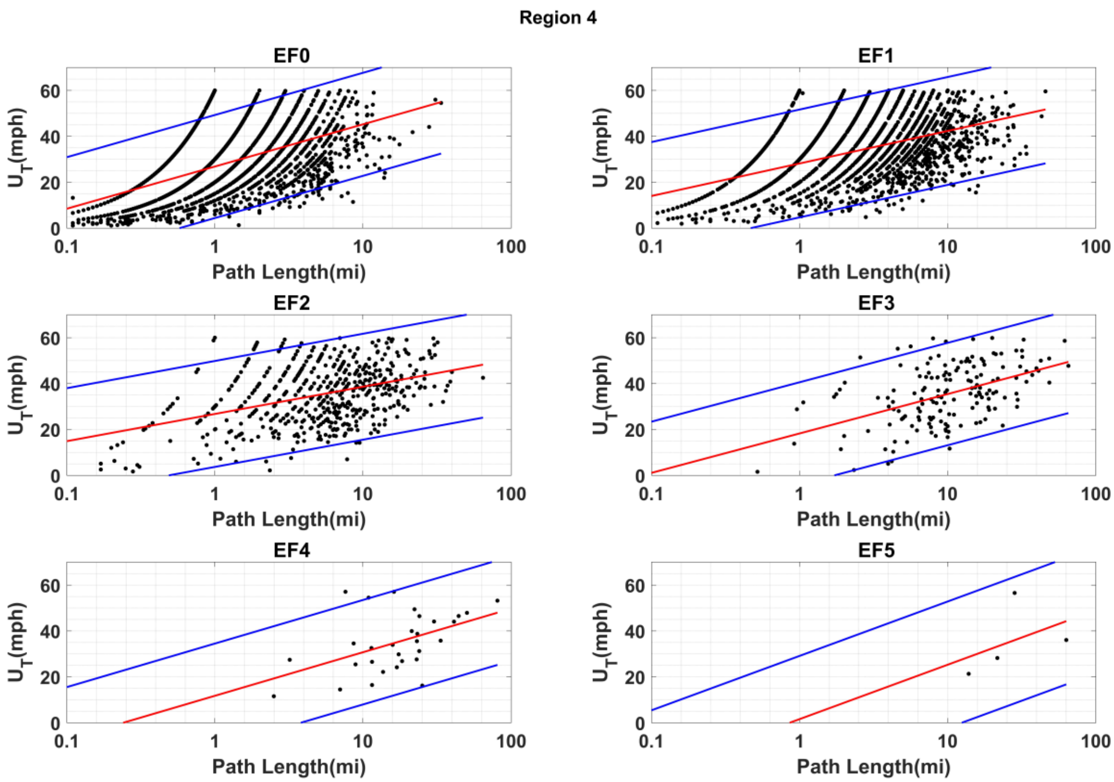

Note: 1 mph = 0.44704 m/s; 1 mi = 1.609344 km

Figure 4-12. Translation Speed Regression Models for Region 4

4.3.5. Path Edge Wind Speed Model

Path edge wind speed refers to the damaging wind speed at which the damage from rotational wind speed is evident. In the EF-Scale damage description (TTU, 2004, 2006), DOD 1 corresponds to the threshold of visible damage and this threshold maps to EF0 events. We use <EF0 wind speed distribution from our EF-Scale wind speed work described in Section 6 to define the boundaries between damaging wind inside the path and non-damaging wind outside of the path. This approach is a simplification (considering the field problems of distinguishing tornado rotational damage from the translation speed damage of the parent system), but provides a reasonable model for the distinction of observable threshold damage from no observable threshold damage.[63] The computed path edge wind speed probabilities (by 5 mph wind speed bin) that are used in the tornado map development are shown in Figure 4-13(a). These probabilities have a significant downward trend and are estimated to be less than 1/1000 at 100 mph (44.7 m/s). Figure 4-13(b) shows the cumulative distribution and

[63] The logic for ≤ EF0 (i.e., no observable damage) as the tornado path boundary threshold follows from the determination of the path boundaries as the edge of observable tornado damage is discussed in Section 6.2.1.1. It follows from simulations of tornadoes in which the RWS did not produce visible damage. For example, for a tornado with RWS = 50 mph (22 m/s), about 30% of the time the damage simulations do not produce observable threshold damage. See Section 6.2.1.1, 6.3, and Table 6-8 for discussion on DOD0 (no visible threshold damage).

indicated that the probability of no visible threshold damage is less than 50% for wind speeds greater than about 60 mph (26/8 m/s).

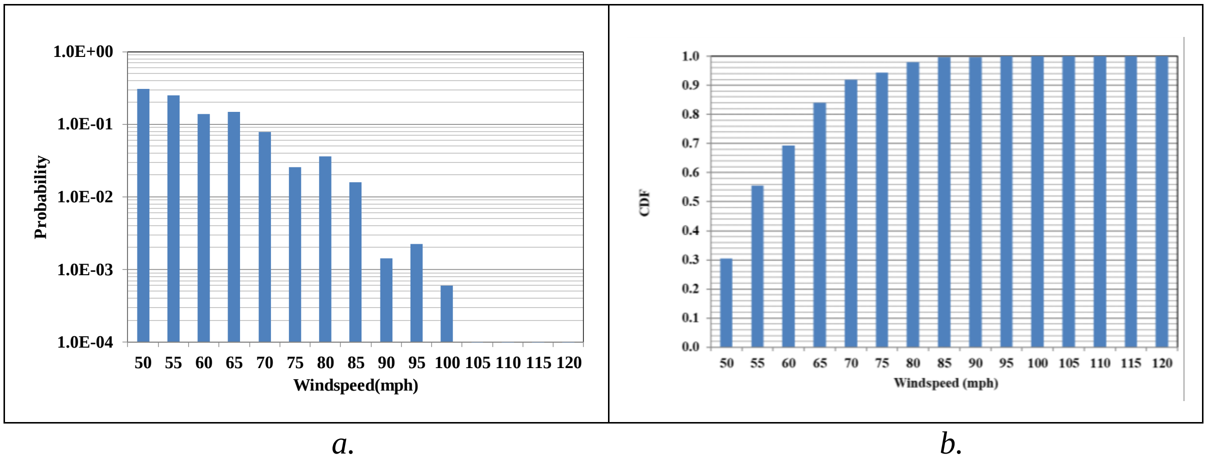

Note: 1 mph = 0.44704 m/s

Figure 4-13. Probability Distribution of Path Edge Wind Speed

Once the path edge wind speed is sampled from this distribution, the tornado wind field is "fitted" to the path width such that the produced swath from the wind field satisfies the damaging winds at the path boundaries. With a given maximum wind speed, translation speed, RMW and inflow, the model determines the appropriate decay parameters to ensure that the path edge wind speed is reached at the boundaries of the tornado path.

An iterative approach used to determine the appropriate decay parameters is given in Appendix D.2. This approach follows methods similar to Twisdale and Dunn (1981). An example of fitted wind field using this approach for a tornado with simulated maximum wind speed, path width, RMW, translation speed and path edge wind speed is shown in Figure 4-14. The sampled PW, RMW, maximum wind speed, and translation speed were 470 ft (143 m), 66 ft (21.1 m), 155 mph (69.29 m/s), and 19 mph (8.49 m/s) respectively. The sampled path edge wind speed was 70 mph (31 m/s) as shown by the dashed horizontal line in the figure. The dashed blue line is the maximum wind speed experiences (due to the passage of the sampled tornado) at each position relative to the tornado centerline across the path width. It is seen from the figure that with the appropriate decay parameters obtained from the iterative approach the simulated path edge wind speed is achieved at the edges of the path.

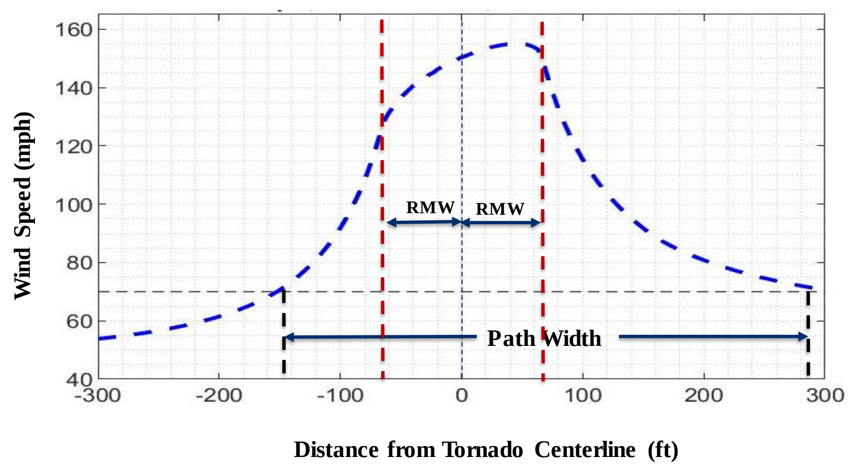

Note: 1 mph = 0.44704 m/s; 1 ft = 0.3048 m

Figure 4-14. An Example of Fitted Wind Field in a Tornado Path

4.4. Velocity Profile Modeling

The velocity profile is a specified input to the wind field model and important parameter to estimate wind loads at various heights. The velocity profile in the synthesized model depends on Kuo’s (1971) profile parameters, radial inflow, and position within the tornado path.

The profile parameters are α and ζ, where α adjusts the rate of increase of wind field components along height and ζ adjusts the magnitude of wind field components near ground. Figure 4-15 shows a set of velocity profiles of horizontal wind speeds as a function of γ and position with respect to the vortex center. Figure 4-15 (a) and Figure 4-15 (b) show velocity profiles at a distance from the center of the tornado, equal to RMW and 1.5 times RMW respectively. In both cases, similar shapes are observed for the velocity profiles for a given γ. However, it is evident from the figure that the height of the maximum wind speed is not the same for these cases. The velocity profiles shown in Figure 4-15 reflect $\alpha = 10$ and $\zeta = 25$.

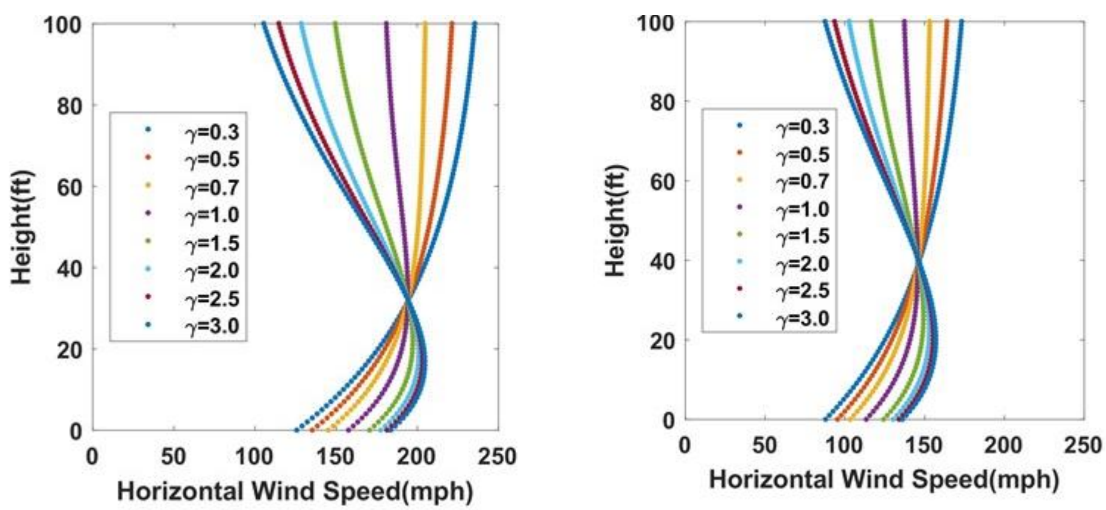

a. At RMW

b. At 1.5 RMW

Note: 1 mph = 0.44704 m/s; 1 ft = 0.3048 m

Figure 4-15. Probabilistic Profiles

Probabilistic Profiles. The profiles presented in Figure 4-15 are illustrative of many possible probabilistic profiles since the inflow parameter and RMW are random variables.

Field observations suggest significant variability in tornado velocity profiles. For example, Figure 4-16 shows some examples of velocity profiles obtained from radar observations, laboratory experiments, and numerical experiments. Figure 4-16 (a) shows radar-derived velocity profiles obtained from the 2012 Russel, Kansas tornado. Kosiba and Wurman (2013) obtained the data using Doppler radar at different times during the tornado. They were able to measure wind speeds as low as 5 m (16 ft) above ground. The velocity profiles are highly variable but show that maximum wind speeds may occur lower than 10 m (33 ft). Figure 4-16 (b) shows the variability in measured profile in a laboratory simulated stationary tornado by Refan (2017). The profiles vary with the swirl ratio and position within the simulated tornado. Figure 4-16 (c) shows velocity profiles obtained from a numerical study by Nolan et al. (2017) with different ground roughness values. They showed local maximum wind speed can occur at heights greater than 10 m (33 ft) and increases with roughness.

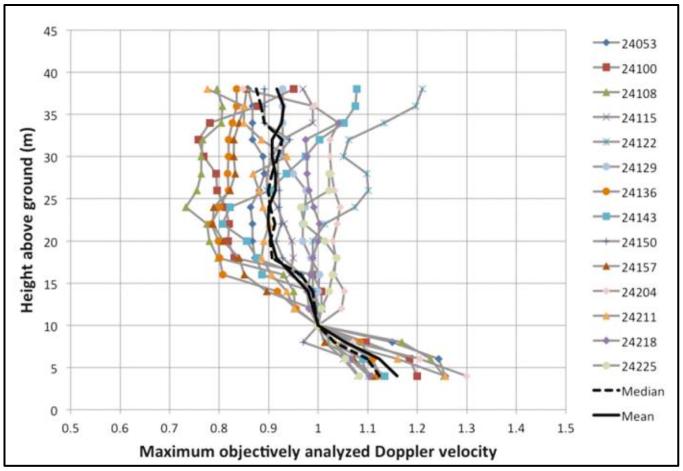

a. Adapted from Kosiba and Wurman (2013)

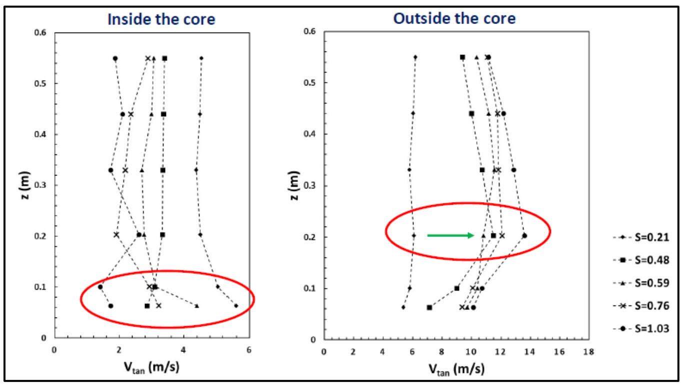

b. Adapted from Refan (2017); V_{tan} = tangential wind speed

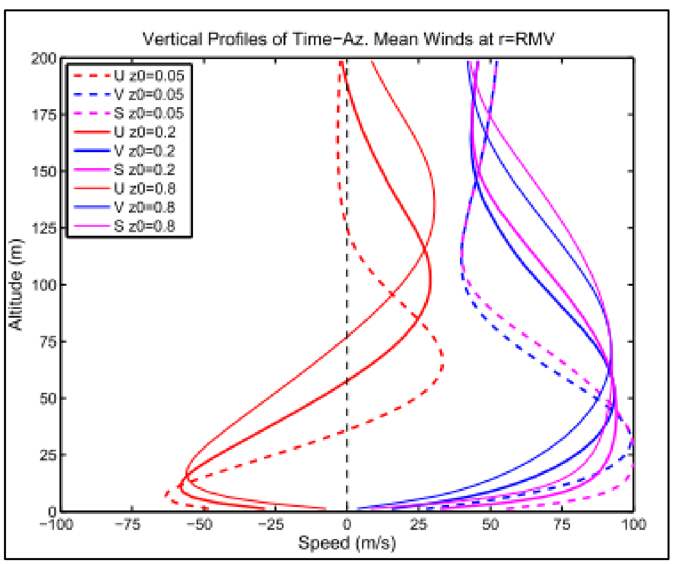

c. Adapted from Nolan et al. (2017); U=azimuthal mean of radial velocity; V= tangential velocity; S=azimuthal mean of surface wind speed

Note: 1 m = 3.28084 ft; 1 m/s = 2.2368 mph

Figure 4-16. Tornado Velocity Profiles Obtained from Radar Data, Laboratory and Numerical Simulations

As seen from Figure 4-16, tornado velocity profiles vary with swirl ratio, position within the core and surface roughness, among other possible variables. In light of these observations, the probabilistic profiles produced by the synthesized model seem to be reasonable.

Deterministic Profile. From a structural design standpoint, the velocity profile of horizontal winds is a critical structural design parameter. In consideration of simplified code-based tornado design approaches and the use of tornado wind speed risk maps, we use a deterministic vertical profile for horizontal winds. We compute the vector sum of radial, tangential, and translational speeds at 10 m (33 ft) and use that value (with its associated direction) for all load calculations. The tornado hazard simulations reflect these wind speeds for the standard 10 m (33 ft) height. Figure 4-17 illustrates a vertical profile for horizontal winds to a height of 200 ft (61 m).

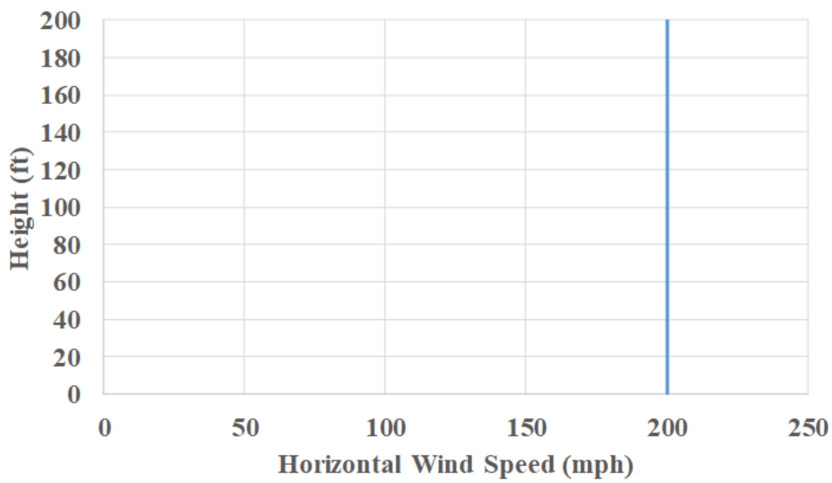

Note: 1 mph = 0.44704 m/s; 1 ft = 0.3048 m

Figure 4-17. Deterministic Profile

4.5. Tornado Wind Speed Swath Model

We have implemented a tornado swath wind speed model using the PLIV and PWV tornado catalogs (Section 3) with the wind field model discussed above. To achieve computational efficiency, we use a condensed version of these catalogs for hazard simulations, as given in Appendix C.

Given an EF intensity, we can compute a tornado wind speed swath by first sampling from the condensed catalog list for that EF intensity. The sampled catalog provides the length fractions for different intensity segments in that catalog and associated path width fractions. Using the sampled catalog, the tornado path is scaled using the simulated PL and PW of the tornado. The maximum wind speeds at the mid-point of EF intensity segments are sampled from EF-Scale wind speed distributions (discussed in Section 6). The sample maximum wind speeds are then fitted with a spline to ensure smooth transition of wind speeds from one intensity to another. The model then uses the scaled wind field model based on the sampled RMW and modeled γ for this RMW, sampled translation and path edge wind speeds to compute wind speed swath for the tornado.

For illustration of the swath model, we produced wind swath for an EF5 tornado using a condensed catalog. The simulated path boundary wind speed is 50 mph (22 m/s) and the translation speed is 10 mph (4.5 m/s). The wind speed swaths in Figure 4-18 are produced with and without spline-fitted wind speed to illustrate the effect of spline fitting on the produced swaths. The swaths include PLIV and PWV, as illustrated in Figure 4-18 (b) and (c), respectively. In Figure 4-18 (b), the sampled maximum wind speed in each segment is shown in red dots. The blue curve is a fitted curve using spline and is used to produce the wind speed swath in Figure 4-18 (a). The numbers shown in the x-axis of Figure 4-18 (a) are multiples of 10^4 ft.

Figure 4-18 (d) shows the wind speed swath produced without the spline (using only the sampled maximum wind speed in each segment). In this case, we assume that the sampled maximum wind speeds remain constant in each segment. The wind speed swath produced using spline fitted wind speeds shows a non-uniform path width for a given segment whereas the wind speed swath produced without spline fitted wind speeds shows uniform path width for a given segment and the path width variations matches with the PWV shown in Figure 4-18 (c).

We use the spline fitting swath model illustrated in Figure 4-18 (a) and (b) for the tornado hazard analysis and wind speed map development.

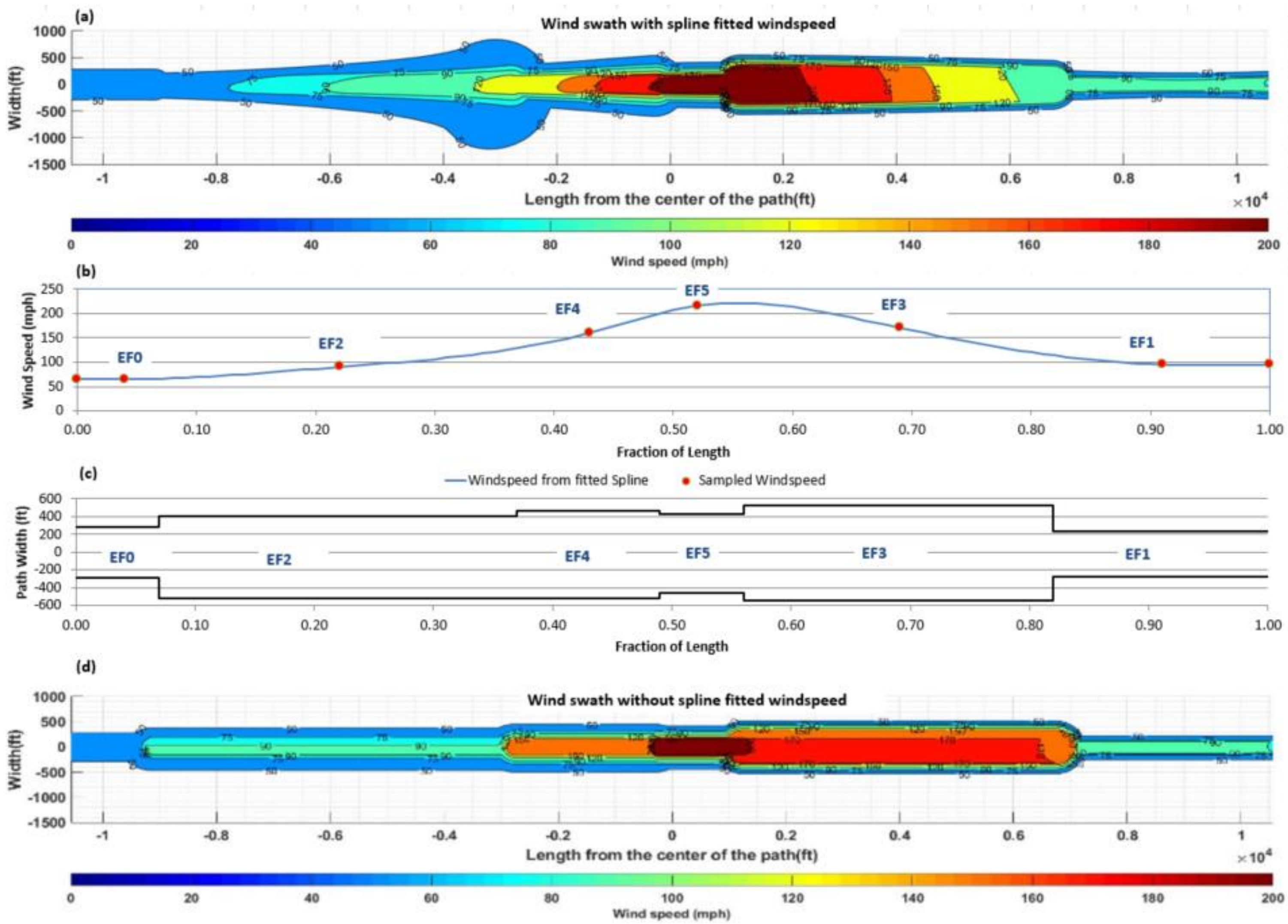

Note: 1 mph = 0.44704 m/s; 1 ft = 0.3048 m

Figure 4-18. Example Wind Swath Using a Condensed Catalog

5. Engineering-Based Tornado Damage Models

5.1. Overview

In this section we describe the development of the engineering-based tornado damage models for single-family residential structures. These models use 3-D physically-based, time-stepping, probabilistic load and resistance methods to treat the progressive failure of buildings in windstorms. The methodology has been adapted for tornado simulations by incorporating a tornado damage version (TORDAM), which includes a 3-D tornado wind field model and associated tornadic loads, including wind–borne debris (WBD), atmospheric pressure change (APC) and the effects of vertical winds. We apply the method for single-family residential (SFR) construction, which corresponds to the EF-Scale Damage Indicator (DI) denoted as "One- or Two-Family Residences (FR12)," (TTU, 2006).

The scope of this section is limited to SFR construction, which is a dominant subset of the EF-Scale FR12. The dominant role of FR12 in rating tornadoes is discussed in Faletra and Twisdale (2016). From the NWS's Damage Assessment Toolkit (DAT) database (NOAA, 2016b); over 75% of all tornadoes that are rated ≥ EF3 are based on FR12 damage.

5.2. Wind Damage Methodology Background

Explicit 3-D, time-stepping, probabilistic load and resistance modeling for progressive failure of buildings for windstorm damage and loss was pioneered by ARA in the mid-1990s by Twisdale et al. (1996). This approach analyzes individual buildings (or representative building classes) with known features using probabilistic engineering load and resistance models. This initial work continued to mature and evolve over two decades into a detailed and field-validated modeling system for hurricane wind effects for SFR and other buildings.

This modeling system has been used for a number of important applications: (1) the development of insurance mitigation credits for SFRs and other residential structures in the state of Florida (Twisdale et al., 2002, 2003, 2008); FEMA's HAZUS-US hurricane model for loss estimation (FEMA, 2006; Vickery et al., 2006a, b); insurance hurricane catastrophe loss modeling in the US (ARA, 2000-2019); assessment of state/region/city-level building code requirements, including cost-benefit metrics of loss avoidance in North Carolina (Twisdale and Young, 2002), Texas (ARA, 2003), New Orleans, Louisiana (ARA, 2010), and Mississippi (Lavelle and Vickery, 2012). Hundreds of thousands of SFRs have been inspected for important wind resistive features and other building characteristics in support of these studies. In addition, numerous field validation surveys were conducted to support model validation for hurricanes.

Pressure Loads. The tornado load model is coupled with ARA's time-stepping damage model and wind speed dependent WBD impact model. The wind loads include wind pressure (both external and internal) and APC. For external wind pressure loads, an empirical modeling approach is used to develop directionally dependent wind pressure coefficients acting on the building for each time step in the simulations as the storm passes the building. The pressure coefficient models are based on data from boundary layer wind tunnels for sloped and flat roofed buildings and are well validated. Figure 5-1 shows an example validation plot for one structure with complex geometry which is described in detail in FEMA (2006).

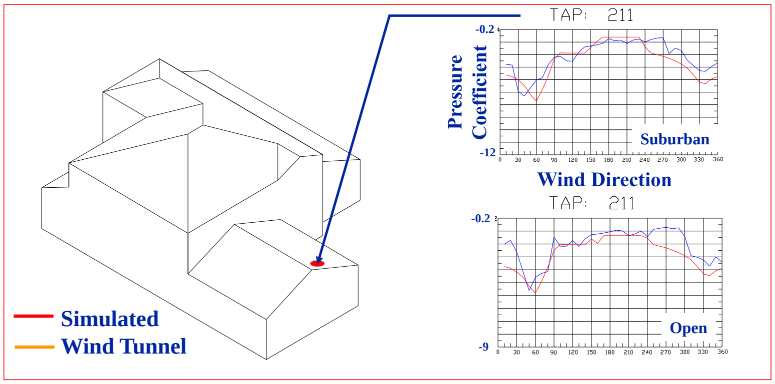

Figure 5-1. Aerodynamic Load Validation for Complex Geometry

Wind-Borne Debris. The wind generated-missile (debris) modeling for tornado damage model also follows from the previous referenced publications. The missile model is used to determine damage to glazed openings, which is critical to modeling the internal pressures in the building during the progression of the storm. The wind generated missile model is based on the parametric results of a 3-D physics based model, which was validated by performing simulations of entire subdivisions, flying individual debris missiles from failed upstream buildings, integrating the equations of motion for each, and scoring the impacts with respect to breaches in the envelope and glazed openings (see Figure 5-2(a)). The hurricane missile model was validated against field observations of numerous homes in multiple subdivisions in Hurricanes Andrew, Erin, and Opal (see Twisdale et al., 2002 and Vickery et al., 2006b). The 3-D trajectory model with drag, lift, and side force aerodynamics is described in Twisdale et al. (1979).

Figure 5-2 (b) illustrates one of the realizations for a subdivision and shows the missile impact points (blue) relative to the modeled SFRs (green), which are both missile sources and targets.

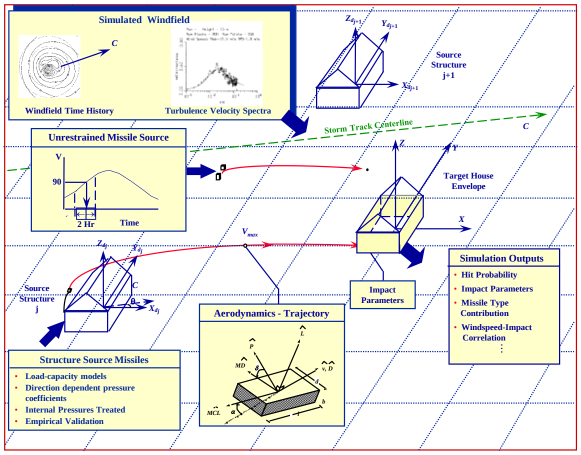

a) Wind generated missile source-target simulation modeling

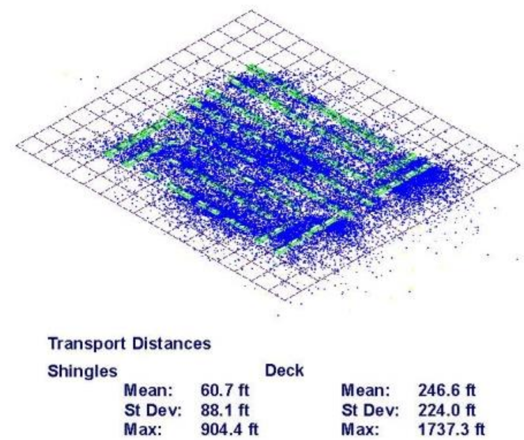

b) Realization of Missile Impact Points (blue) within a Subdivision

Note: 1 ft = 0.3048 m

Figure 5-2. Missile Model Simulation Approach

Resistance Models. The tornado damage model uses probabilistic resistance models for material strengths, connection strengths, wind-generated missile impact resistance, etc. These resistance models are based on laboratory and full-scale test data coupled with engineering analyses (including finite element analyses), and engineering judgment. For example, Figure 5-3 illustrates full-scale roof testing of roof-wall toenail connections (Judge and Reinhold, 2002). We note that these particular field tests indicated a notable increase over previously published test results (such as Canfield et al. (1991)). It is therefore important to model large variations in connection strength to cover strength and quality variations in “as-built” SFRs.

Figure 5-3. Full-Scale Testing of Roof-Wall Toenail Connection

5.3. The TORDAM Model

The TORnado DAMage model (TORDAM) builds on the hurricane damage model described above. This model has been extensively validated through comparisons of modeled and observed building damage states collected in post-storm damage investigations. The TORDAM model incorporates the direct action of wind using boundary layer wind tunnel derived pressure coefficients, coupled with a model for the change in pressure within the core of the tornado. A key to the success of the model is the inclusion of leakage, which enables some equalization of the external and internal pressures. The damage model is coupled with a probabilistic tornado wind field model in order to develop tornado fragility models.

Tornado Wind Field Model Integration. The tornado wind field model is based on previous work examining tornado wind speed and tornado generated missile risk (Twisdale et al., 1978, 1981; Dunn and Twisdale, 1979). The wind field model comprises a single cell vortex (see Figure 5-4(b)) with probabilistic parameters for path length, width, direction, RMW, translational speed, inflow, vertical profile for horizontal wind, and wind decay outside of RMW. Profile 5 in Figure 5-4(c) illustrates the steep (essentially vertical) profile of horizontal wind typically assumed in engineering models of tornado wind loads. As discussed in Section 4, we assume a vertical profile for horizontal winds over the building height. With the vertical profile assumption, the gust wind speed at the mean roof height of the building (upon which all the pressure coefficients are based) is the same as the gust wind speed at a height of 10 m (33 ft).

The tornado model incorporates the correlation of path width to path length and path length to intensity scale. Tornado path direction is modeled independent of intensity. The RMW is correlated to path width. The model simulates tight, rapidly translating vortices as well as large, slow moving tornadoes with large RMW. This modeling approach facilitates the simulation of tornado strikes on the structure that include the large variances in naturally occurring tornado wind field characteristics.

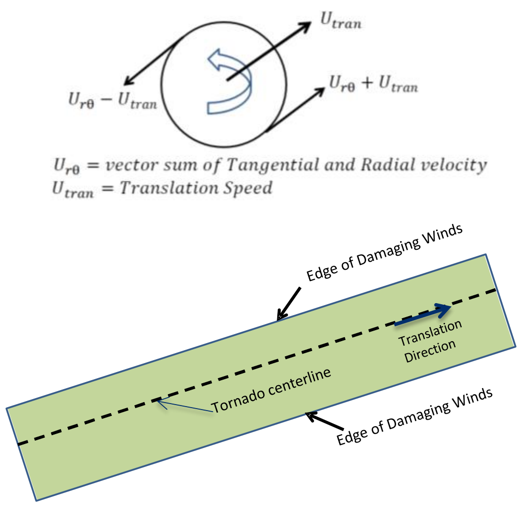

a. Vectorial Inclusion of Translation Speed Produces a Laterally Asymmetric Wind Field

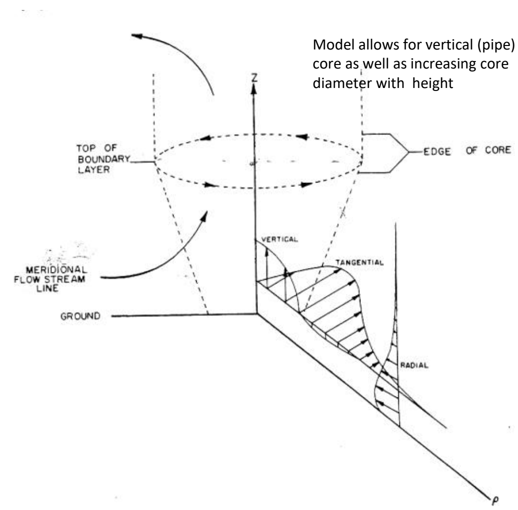

b. Probabilistic Wind Model Components Satisfy Flow Continuity

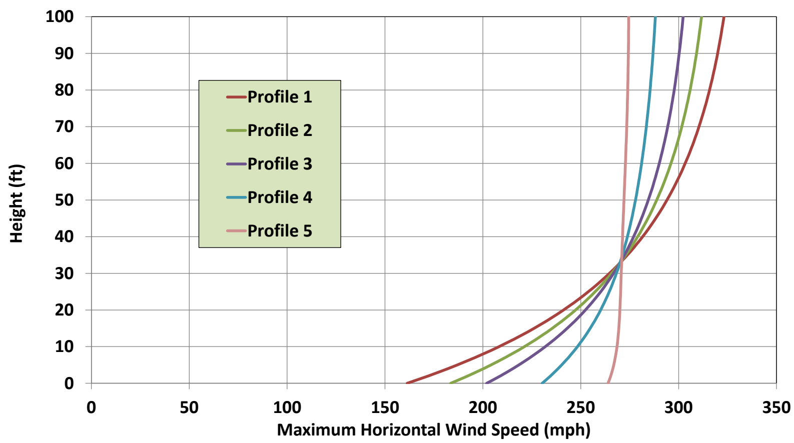

c. Parametric Profile Models of Horizontal Wind

Note: 1 mph = 0.44704 m/s; 1 ft = 0.3048 m

Figure 5-4. Probabilistic Tornado Wind Field Model

Simulation Sequence for TORRISK2 and TORDAM Models. The tornado strike parameters for a building simulation are created from a probabilistic tornado hazard model, which is incorporated into an updated version of the TORRISK model (Twisdale and Dunn, 1983a). The new model (TORRISK2) was developed under an ARA Internal Research and Development project (IR&D).[64] TORRISK2 is a simulation code that produces realizations of the tornado characteristics, track geometry, reference maximum wind speed, and structure position within the track. The reference maximum wind speed is the maximum peak gust wind speed at 10 m (33 ft) (above ground), over a specified horizontal reference area equal to the plan area of the modeled building.

[64] ARA developed and refined TORRISK2 to include many enhancements for tornado-target interaction modeling and scoring. With additional IR&D funding, TORRISK2 continued to evolve to support this project to include windfield enhancements; epistemic sampling; and other calculation improvements.

Figure 5-5 illustrates the process for simulating damage in TORDAM. The TORRISK2 produced tornado strike simulation files (i.e., the realized tornado strike and wind field parameters and reference maximum wind speeds) are an input to TORDAM.[65] Building orientation can be specified to be random (for unknown orientation or for a specified orientation distribution) or fixed (as in the forensic analysis of a particular building and tornado). TORRISK2 is executed separately by EF-Scale and produces realizations of the tornado wind field, strike parameters, and target position details in each simulation. These files are saved for later execution by TORDAM. TORDAM, which uses the same wind field module as TORRISK2, then executes the wind field deterministically (time-stepping the tornado past the target) for each simulated tornado and tornado- target interaction produced by TORRISK2. This process is repeated for all EF-Scales to produce a damage probability matrix (DPM) for a single structure type, DI, or DI class (e.g., a "sub-DI"). DPMs are discussed and illustrated in Section 6.3. TORDAM performs the load and resistance calculations to produce building damage states and/or fragilities.

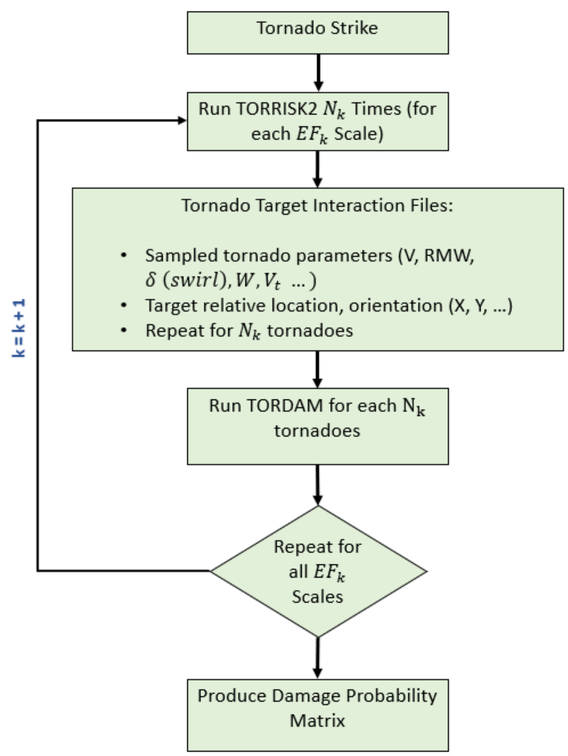

Figure 5-5. Simulation Sequence for Modeling of Tornado-Structure Interactions in TORDAM

Tornado Progressive Failure Model. TORDAM simulates the tornado strike on a specific building using the probabilistic wind field model and strike variables from the TORRISK2 code. In order to produce damage to a structure subjected to tornado wind loads, a progressive failure model is used where at each time step, loads produced by the tornado (including wind borne debris) are computed and compared to the resistances of the building components (e.g., windows, walls, roof cover, roof sheathing, etc.). Figure 5-6 presents a

[65] For purposes of damage modeling, we assume the target can be anywhere within the tornado core (See Section 7.4).

flow chart describing the time-stepping, progressive failure methodology. There are five major loops in the model:

1. Tornado Strike Simulation Loop (uses files from TORRISK2)
2. Building Replication Loop (samples component resistances and wind loading parameters)
3. Time Step Loop (moves the tornado along its path and computes new loads)
4. Internal Pressures Loop
5. Components/Systems Loop (fails components/systems)

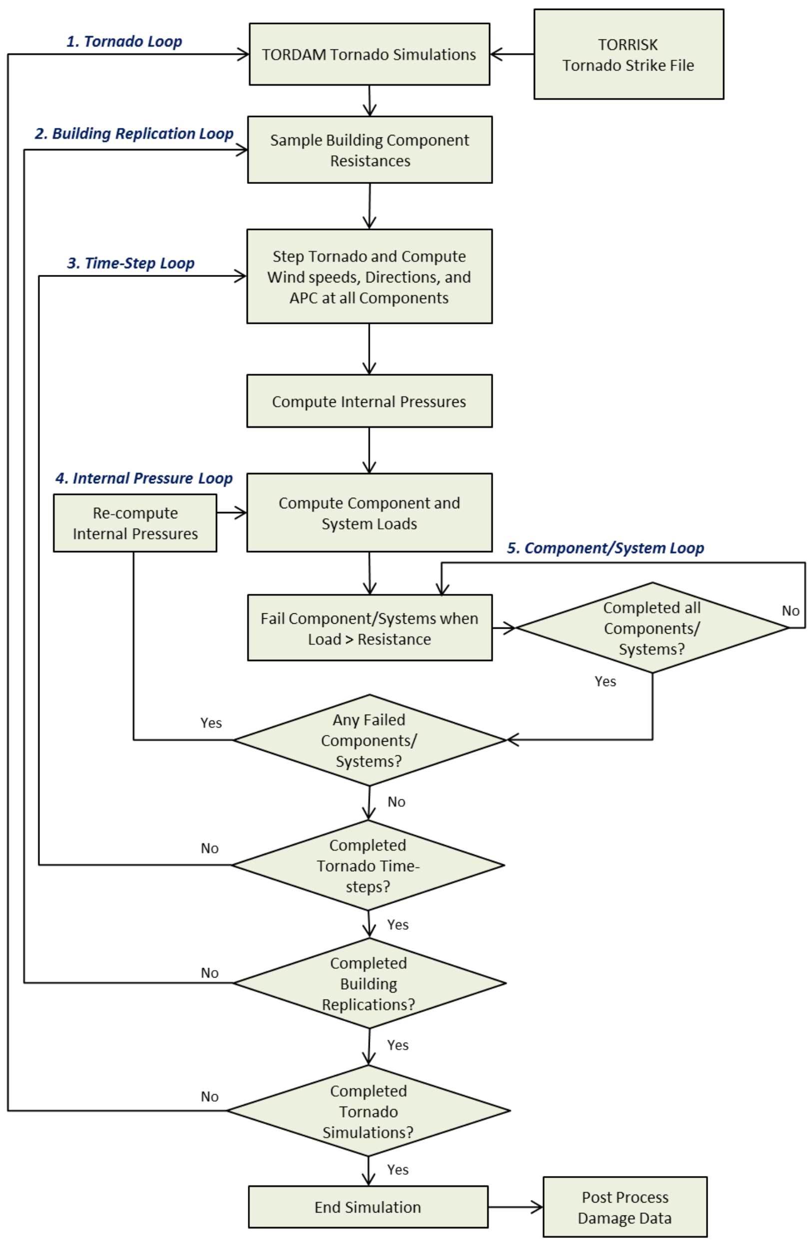

Figure 5-6. TORDAM Modeling System for Progressive Damage

For each simulated tornado (Loop 1), we replicate the building failure multiple times (Loop 2), in which we vary the resistances of the structure independently from the previous replication. This loop provides the natural structure-to-structure variability expected in full-scale structures, where construction quality, component resistances, and wind loads vary from structure-to-structure. The time-step loop (Loop 3) starts the tornado wind field simulations and steps the rotating vortex toward the building at the sampled translational speed. The load and damage calculations begin as soon as the maximum wind speed at mean roof height, somewhere within the footprint of the building exceeds 40 mph (18 m/s).

Within each time step, the internal pressures are computed, and the loads are calculated and compared to the sampled resistance for each component/system. For example, the system loads include all the integrated loads over the roof and wall systems. Internal pressures are computed at each time step, and include the contribution to the internal pressure due to the failure of windows and doors from pressure or wind generated missiles. All components and systems are evaluated in this manner in Loop 5. If any component or system fails in a time step in which a new breach in the structural envelope occurs, then the internal pressures are recomputed (Loop 4) with subsequent checks for any new failures (Loop 5 again). The internal pressure loop is repeated as many times as necessary until no more failures occur within the time step. The tornado is stepped forward and the analysis repeats itself with the new loads associated with the new position of the tornado. The time-step simulation for each tornado ends once the tornado has passed the structure and no more failures occur. The building damage statistics are stored for this tornado simulation and the whole process is repeated thousands of times.

Figure 5-7 illustrates a TORDAM-produced wind pressure time history for selected windows on an SFR. Also shown are the tornado wind vectors on the gable roof at two different times in the simulation of a rapidly translating vortex. The tornado translation path is parallel to the length of the SFR.When the tornado center is on the left-hand side of the house, Window 1 and Window 4 experience negative wind load whereas Window 2 and Window 3 experienced positive wind load. When the tornado center just passes the house, Window 1 and Window 4 experience positive wind load whereas Window 2 and Window 3 experienced negative wind load. In the latter position of the tornado center all windows experienced higher loads than that in the former position. This is due to the wind direction and larger wind vectors at this position.

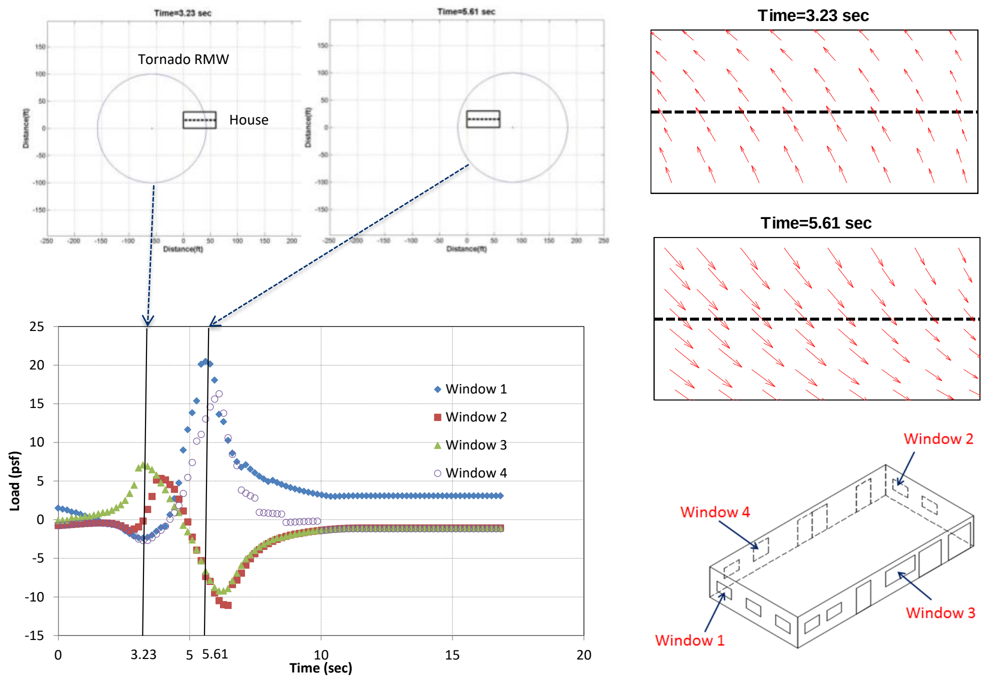

Note: 1 ft = 0.3048 m; 1 psf = 47.88026 Pa

Figure 5-7. Tornado Wind Pressure Time History for Example TORDAM Simulation

5.4. Tornado Load Model

5.4.1. Tornado Load Models Described in the Literature

Some previous studies have used modeling approaches similar to that used herein. The work of van de Lindt and coworkers (Amini and van de Lindt, 2014; Masoomi and van de Lindt, 2017), and Rouche and coworkers (Peng et al. 2016) are key examples. In tornado load modeling, a model is required to estimate the net pressures acting on the buildingand components thereof. The net pressure is the difference between the internal pressure, P_i and the external pressure, P_e. The external pressure is computed using

$$P_e = APC + \frac{1}{2}\rho G C_p V^2 \quad \textbf{(5-1)}$$

where V is the wind speed, and GC_p is product of gust effect factor and external pressure coefficients (e.g., ASCE, 2010, 2013, 2016).

The model developed by Amini and van de Lindt (2014), made use of the pressure coefficients described in Haan et al. (2010), which were obtained using a model of a house tested in a tornado simulator. The pressure coefficients measured by Haan et al. (2010) include the effects of the pressure due to the direct action of the wind (including the contribution due to vertical winds) as well as the contribution due to the APC. Haan et al. (2010) showed that the pressure coefficients measured in the tornado simulator (including the effects of APC) were much higher than those given is ASCE 7. Haan et al. (2010) found that the uplift loads acting on the entire roof of a single family home were increased by a factor of 1.8 to 3.2, and the product of gust effect factor and external pressure coeffcients (GC_p's) for components and cladding on the roof were increased by factors of 1.4 to 2.4. The Haan et al. (2010) data was implemented by Amini and van de Lindt (2014) in a load and resistance based model in order to develop fragility functions, by using the GC_p's given in ASCE 7, but increased by the factors presented in Hann et al. (2010). Amini and van de Lindt (2014) did not consider that the effect of the APC acting on the exterior of the building, which is ameliorated due to leakage of the external pressures into the interior of the building, (thereby reducing the net effect of the APC in increasing the negative roof and wall loads).[66] The effect of wind directionality was not taken into account, further increasing the apparent tornadic fragility of residential buildings.. In addition, their model does not consider damage to the building envelope due to windborne debris impacts.

Masoomi and van de Lindt (2017) expanded on the work of Amini and van de Lindt (2014), using a modified Rankine vortex (Refan, 2014) wind speed and APC model, coupled with the ASCE 7-10 (2010) pressure coefficients but allowed for load equalization through internal pressure using an empirical factor to vary the fraction of the APC which was allowed to propagate into the building.

Peng et al. (2016) developed a fragility model using taking into account the directionality of the wind through the use of directionally dependent GCp's developed using the results of wind tunnel tests performed at Tokyo Polytechnic University (Quan et al., 2007). The model takes into account leakage through the building envelope, but the effect of the vertical component of the wind is not modeled. The model does account for windborne debris.

Kopp et al. (2016) carried out a detailed fragility analysis of the roof structures of some of the damaged structures in the Angus, Ontario tornado of 17 June 2014. The paper discusses the role of roof shape, connection strength and quality on the observed damage. They used directionally dependent GCp's based on wind tunnel tests on different roof shapes and slopes for the fragility analysis. However, this work did not use a tornado wind field model in the analysis.

As described in previous sections, we use a 3-D time-stepping tornado wind field model with wind-borne debris, boundary layer wind tunnel measured pressure coefficients, and an internal pressure and APC model to compute tornado wind loads on a structure.

5.4.2. External Pressure Coefficients

5.4.2.1. Roof Pressure Coefficients

The pressures acting on the exterior of buildings in tornadoes are due to a combination of both the atmospheric pressure change within the tornado and the effect of the interaction of the wind with a bluff body. We have assumed that the wind induced pressures acting on the exterior of the building can be modeled using pressure coefficient information obtained from boundary layer wind tunnel experiments (such as those used to develop the GCps in ASCE 7). It is recognized that the turbulence characteristics in tornado winds are different than those associated with extratropical storm winds in the atmospheric boundary layer (ABL),

[66] The amount of reduction of the APC effect on the loads is a function of the building porosity (leakiness). The omission of leakiness in the development of the fragility models produces an overestimate of the expected damage to a building for a given wind speed.

which is well modeled in boundary layer wind tunnels. However, there is no evidence yet to indicate that the GCp's are notably different. When normalized by the peak gust wind speed at mean roof height, the GCp's are not sensitive to changes in the turbulence between open terrain and suburban terrain flow conditions. This observation lends some confidence to the assumption that the GCp's from ABL tests may be applicable to tornadoes. Any differences in GCp's for tornadoes associated with missing the low frequency components of atmospheric turbulence that exist the ABL are ignored, suggesting in some cases the assumption that the GCp's from tornadic and ABL winds are the same may be conservative.

The pressure coefficient models used in the tornado wind load model for the FR12 roof and wall loads were developed using data from tests performed at the boundary layer wind tunnel at the University of Western Ontario. The GCp's used for the gable roof buildings were developed using a combination of data given in Stathopoulus (1979), and described in Vickery, Kopp, and Twisdale (2011). The GCp's used for the hip roof buildings used a combination of the data given in Meecham (1988) and described in Vickery, Kopp, and Twisdale (2011).

The component and cladding wind loads on the gable roof building were modeled using a total of 8 different zones per quarter of the roof. The hip roof buildings were modeled using 14 different roof zones.

Roof zones are shown in Figure 5-8 and Figure 5-9 along with the wind direction used to define the coefficients. The pressure coefficients themselves are given in Figure 5-10 through Figure 5-13 for the gable and hip roof buildings with roof slopes of 4:14 and 7:12.

The component and cladding GCp's given in Figure 5-10 through Figure 5-13 are used directly with the wind speeds at mean roof height to compute loads on relatively small elements such as roof shingles and roof sheathing. Wind loads on larger elements (such as an entire roof) are computed by integrating the component and cladding loads coupled with a correlation function that ensures that the integration is not performed using the maximum value of each pressure at the same time. The correlation function methodology used herein is described in Vickery et al. (2006b)

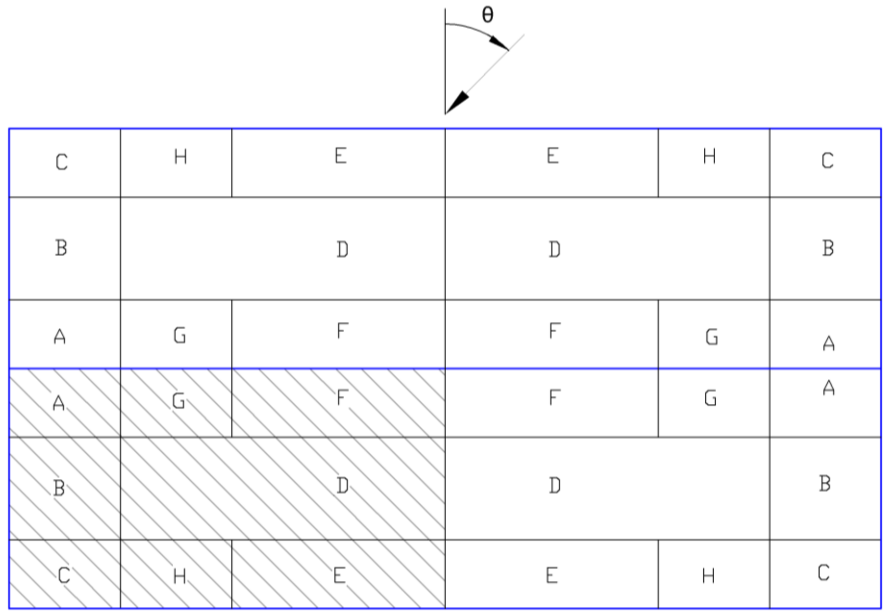

Figure 5-8. Roof Zones for Wind Loads for Gable Roof

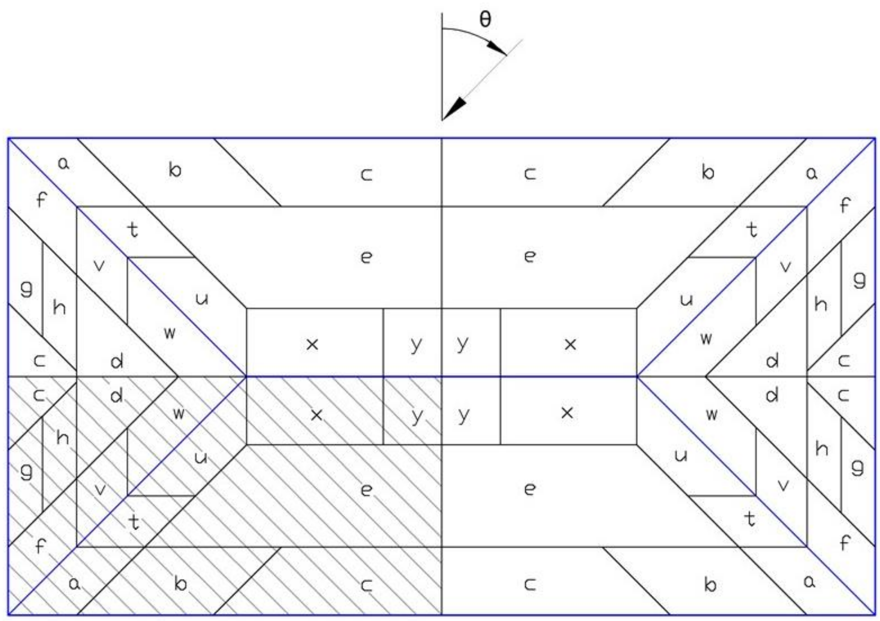

Figure 5-9. Roof Zones for Wind Loads for Hip Roof

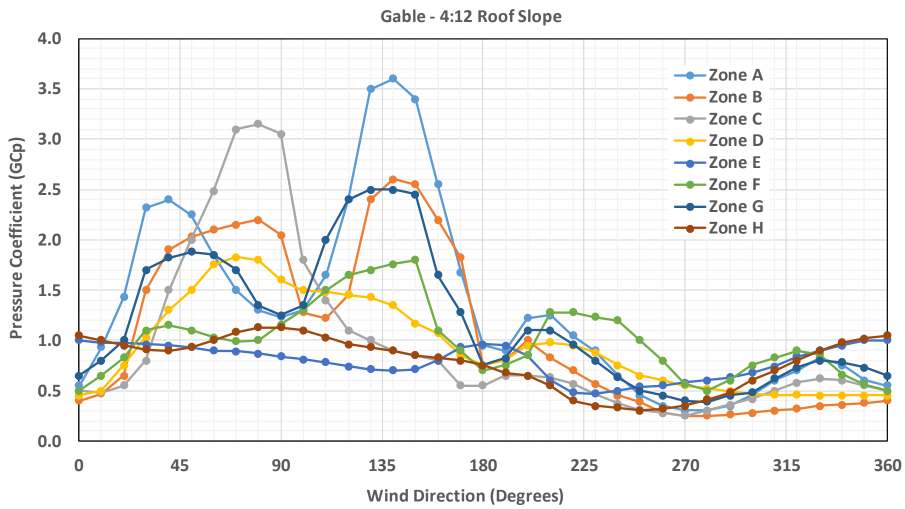

Figure 5-10. Roof GCp as a Function of Wind Direction and Roof Zone for Gable Roofed Buildings with a Slope of 4:12

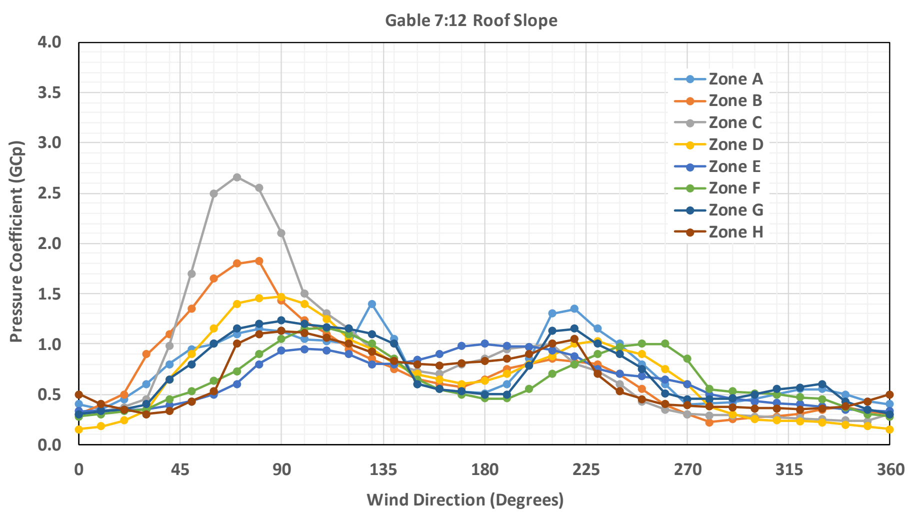

Figure 5-11. Roof GCp as a Function of Wind Direction and Roof Zone for Gable Roofed Buildings with a Slope of 7:12

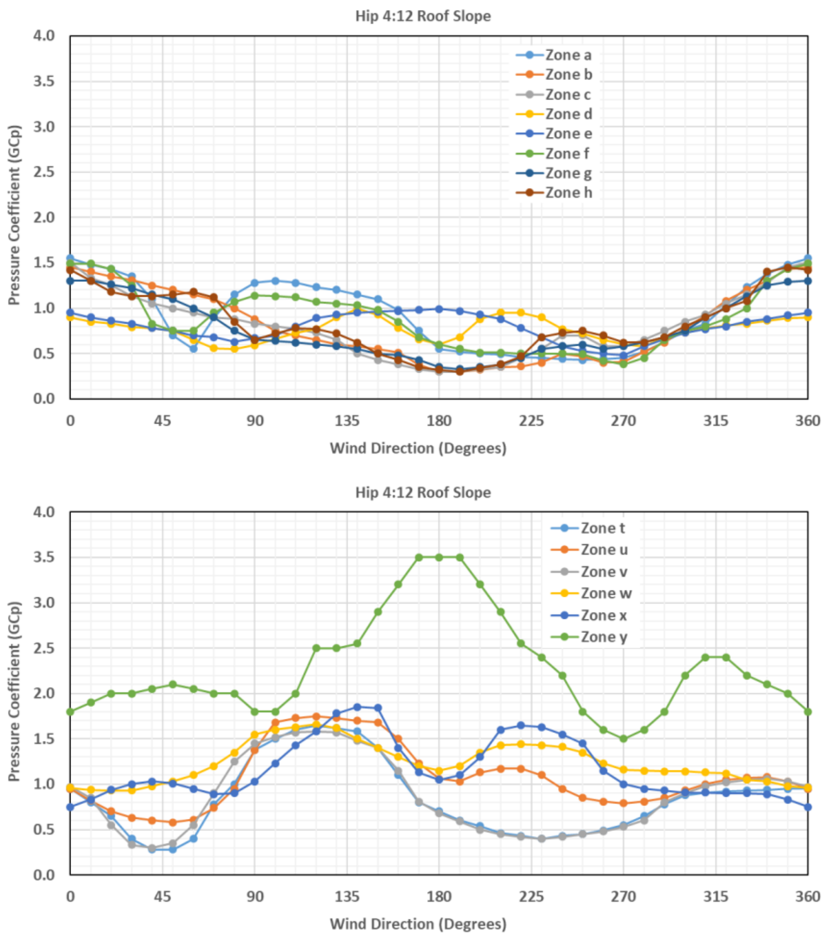

Figure 5-12. Roof GCp as a Function of Wind Direction and Roof Zone for Hip Roofed Buildings with a Slope of 4:12

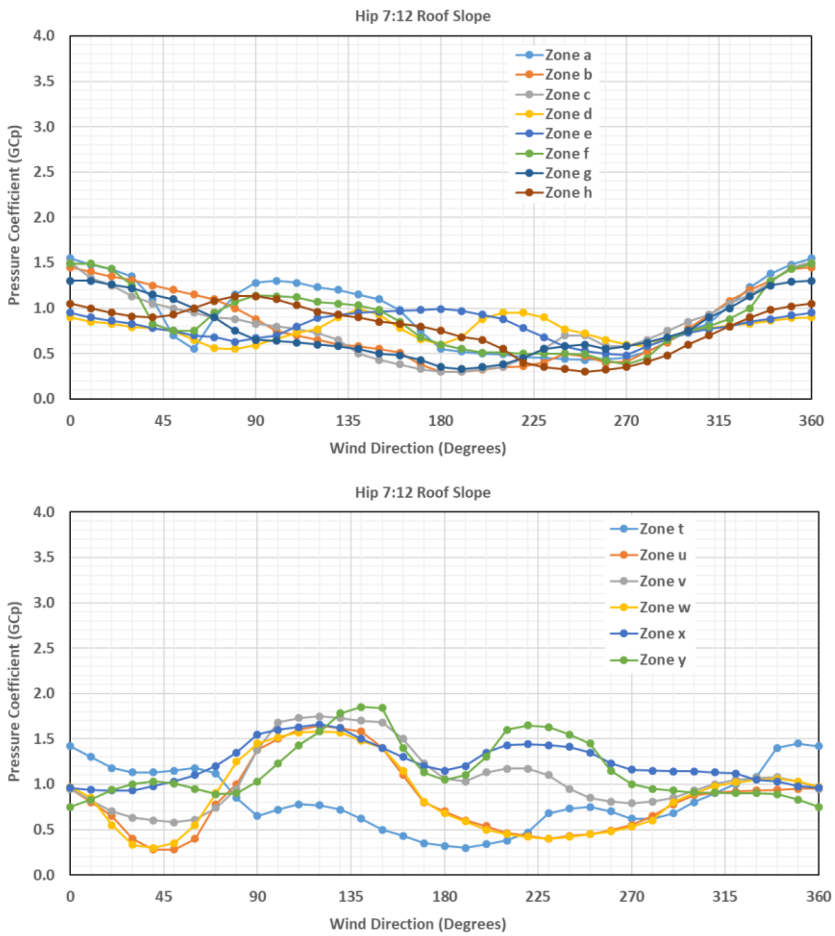

Figure 5-13. Roof GCp as a Function of Wind Direction and Roof Zone for Hip Roofed Buildings with a Slope of 7:12

5.4.2.2. Wall Pressure Coefficients

Pressures acting on wall surfaces (including windows and doors) are modeled using the methodology developed and described in FEMA (2006). The model for the GCp's for wall loads used in Hazus were developed using the wind tunnel data described in Ho et al. (2002). These data are available from NIST. The only difference between the methodology used in Hazus and that used herein is the minimum negative pressure coefficients were not forced to match the values given in ASCE 7 (as was the case in Hazus). In the case of wall Zone 4, forcing the coefficients to match those given in ASCE 7 would result in an overestimate of the magnitude of the negative pressures for a significant portion of the wall.

5.4.2.3. Effect of Vertical Winds on Roof Pressures

Tornadoes can have significant vertical winds inside the core. The magnitude and extent of vertical winds depends on the tornado maximum wind speed, cell structure, RMW, swirl ratio, radial inflow, and translational speed. From the perspective of the structure, its position within or very near the tornado core, its shape, orientation to tornado translation direction, roof slope and roof height play a significant role on the effect of vertical winds on the roof loads at each time step. All of these variables contribute to a complex range of possibilities that are explicitly produced in the simulations. For some tornadoes and structure positions, vertical wind effects will be nil; in others, they may be significant. In each TORDAM simulation, these factors are treated explicitly in the time-stepping 3D wind field model and in the structural model. Therefore, vertical wind effects are explicitly treated in our modeling and incorporated in the failure probability calculations on a component-by-component basis.[67]

As mentioned in Section 4, the tornado wind field model is a single cell model where the radial inflow converges to vertical outflow near the center of the tornado to maintain the flow continuity. In a single cell model, the maximum vertical wind speed occurs at the center of a tornado. In two-cell tornadoes, there is a central downdraft with an outer updraft annulus, as discussed in Section 4. We have not attempted to model two-cell tornadoes in this project, nor the resulting suction vortices when the tornado breaks down. Vortex breakdown is not a stable situation and it is unknown at this time how significant these wind field structures are from an engineering load modeling viewpoint.[68]

The effect of vertical winds on the roof deck fragility for a small gable SFR (4:12 roof slope) is illustrated in Figure 5-14. The fragilities are obtained using 6000 tornado strike simulations with tornado intensity ranging from EF0 to EF5 and 30 building simulations per tornado strike. The roof deck is attached to the roof frame using 6d nails at 6-12 spacing and has 3-8d toe nails for the roof-to-wall connection. Figure 5-14 shows increased vulnerability (up to 40% at about 95 mph (42.5 m/s)) due to vertical winds. The effect of vertical winds depends on many factors: roof shape, slope, structural resistance, and building size.

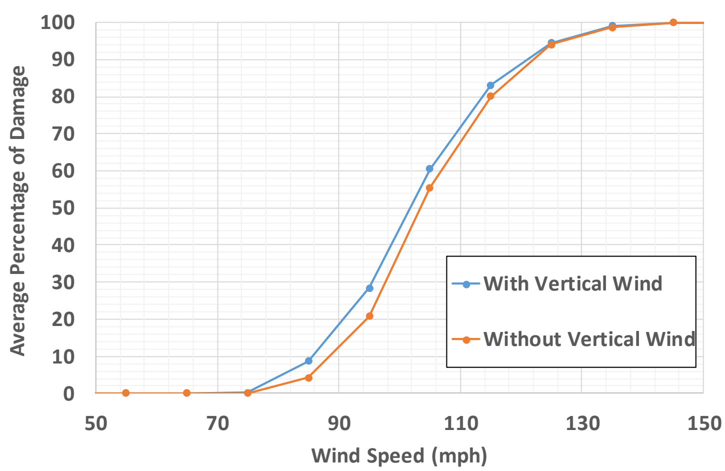

Note: 1 mph = 0.44704 m/s

Figure 5-14. Comparison of Roof Deck Fragilities with and Without Vertical Wind

---

[67] In a separate effort for NIST, ARA developed ASCE type *K* factors for tornado design, one of which is K_v for vertical wind effects. The developed *Kv* are based on the simulations, loads, and modeling parameters discussed in this report. Hence, our use of these models to estimated EF-Scale wind speeds for map development and the associated K factors suggested for ASCE 7 were consistently developed for the reference wind speeds shown on the tornado wind speed maps.

[68] For conventional design return periods, we do not believe that two-cell tornado wind field structures and sub-vortices are significant. It is possible, that sub-vortices are a potentially important loading condition (small vortices with very high translation speeds) for WEFs greater than about 1E-05 per year.

The pressure coefficients illustrated in Section 5.4.2.1 are based on horizontal winds; hence, we developed an adjustment to account for the angle of attack for the non-horizontal winds.[69] Wind tunnel studies (mentioned in Section 5.4.2.1) for different roof slopes and shapes are used for these adjustments. If the approaching wind is non-horizontal due to the presence of a vertical component, then based on the angle of attack, the effective roof slope is reduced, and the GCp's associated with a lower roof slope are used to compute the wind loads.

To estimate GCp's for an arbitrary roof slope an interpolation approach is employed using GCp's for roof slopes of 4:12 and 7:12. In the roof wind load model the single values of GCp are assigned to each of the 8 zones for a gable roof and 14 zones for a hip roof. The GCp data were created for ¼ of the roof resulting in an effective number of zones of 32 and 56 for the gable and hip roofs, respectively. The interpolation approach uses the angle of attack of the approaching wind on a roof element at a given time step of a tornado to compute the adjusted GCp's. The following equation is used for the interpolation approach

$$GC_{ap} = GC_p + c_{rt} * \tan^{-1}\frac{W_v}{W_h} \quad \textbf{(5-2)}$$

where GC_{ap} is the adjusted pressure coefficient, GC_p is the pressure coefficient based on horizontal wind, c_{rt} is the rate of change of pressure coefficient (derived from the GCp's of 4:12 and 7:12 roof slopes) with respect to the angle of attack, W_v is the vertical wind component and W_h is the horizontal wind component of the tornado wind. The inverse tangent of the ratio of W_v and W_h denotes the angle of attack. The approach used here is similar to that given in Letchford and Marwood (1997).

The adjustment of the pressure coefficients is performed for roof loads only. A comparison of the adjusted directional pressure coefficients for a 10° angle of attack is shown in **Error! Reference source not found.** along with the directional pressure coefficients for the two roof slopes that are used to determine the rate of change of pressure coefficients. The adjusted pressure coefficients increases significantly for winds from certain directions. Note that, the pressure coefficients shown in **Error! Reference source not found.** are for Roof Zone A (ASCE, 2016).

[69] The angle of attack from non-horizontal winds is the angle measured in vertical plane between the oncoming wind and the horizontal plane.

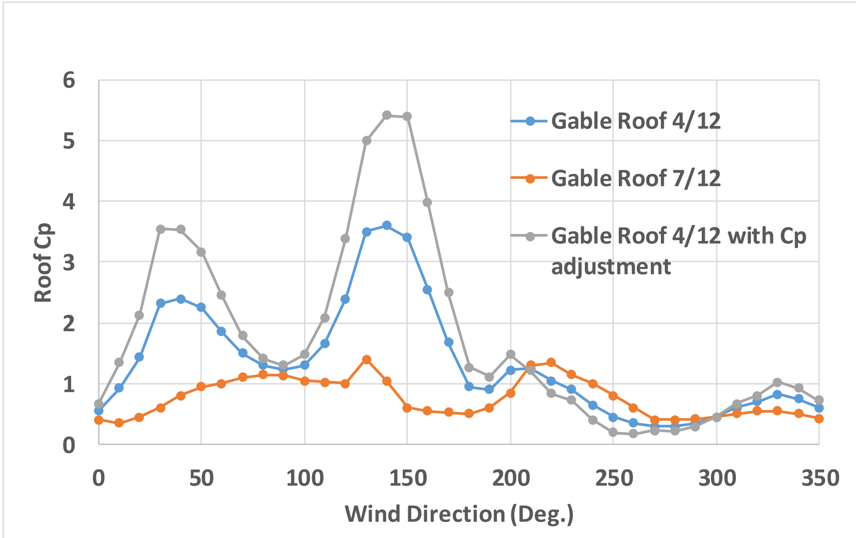

Figure 5-15. Comparison of Roof Pressure Coefficients for Gable Roof (Zone A) for a 10° Angle of Attack

5.4.3. Internal Pressure

The internal pressure experienced by the building components is estimated by solving the continuity equation using a quasi-static model (Cook, 1990). The following equations, derived from those given in Cook (1990), are used in the model to estimate the internal pressure

$$\sum_{j=1}^{N} Q_j + Q_B = 0 \tag{5-3}$$

where Q_j is the flow through j^{th} opening and Q_B is the total background flow through leakages assumed to be distributed uniformly over the building envelope. Equation (5-3) is the continuity equation. Q_B is modeled using Eq. (5-4)

$$Q_B = 3.4 * 10^{-4} * C_{D_B} \iint\limits_{A_s} \left[\frac{2 * (P_e(x,y,z) - P_{int})}{\rho}\right]^{0.6} dA \int_{A_s} \tag{5-4}$$

where A_s is the total exposed surface area of the building, C_{D_B} is the drag coefficient for the background flow, $P_e(x,y,z)$ is the external pressure at an arbitrary location on the exterior of the building, P_{int} is the internal pressure and ρ is the density of air, assumed to be invariant within the tornado (e.g., Simiu and Scanlan, 1996). The constant $3.4 * 10^{-4}$ is the assumed building porosity (e.g., Cook, 1990). Building porosity varies with building type, year of construction, and region of the country, being lower in both colder climates and recent constuction. These variations in building porosity are not considered herein. Q_j is modeled using

$$Q_j = C_{D_j} A_j \sqrt{\frac{2 * (P_{e_j} - P_{int})}{\rho}} \tag{5-5}$$

where $C_{D_j}$is the drag coefficient for flow through the jth opening, A_j is the area of the jth opening and $P_{e_j}$is the external pressure at the jth opening. Equation 5-4 is the the orifice-plate meter equation (Cook, 1990). Prior to failure of a building envelope component Q_j is zero and the internal pressure is controlled by the background leakage alone. Both $C_{D_j}$and $C_{D_B}$are taken as 0.61 (Cook, 1990).

Equations 5-3 through 5-5 are solved iteratively until the continuity equation is satisfied.

5.4.4. APC

APC is the reduction of atmospheric pressure within a tornado vortex. The gradient of the pressure change inside and outside the core of the tornado is modeled using the cyclostropic wind equation (e.g., Simiu and Scanlan, 1996)

$$\frac{dp_a}{dr} = \rho \frac{V_t^2}{r} \tag{5-6}$$

where $\frac{dp_a}{dr}$ is the change in the atmospheric pressure (p_a) at radius *r* from the center of the tornado vortex and V_t is the tangential velocity at a radius *r*. Eq. (5-7) and Eq. (5-8) are obtained by integrating equation Eq. (5-6) for inside and outside of the tornado vortex.

For *r* less than or equal to *RMW*,

$$p_a(r) = \rho \frac{V_{max}^2}{2}\left(2 - \frac{r^2}{RMW^2}\right) \tag{5-7}$$

For *r* greater than *RMW*

$$p_a(r) = \rho \frac{V_{max}^2}{2} \frac{RMW^2}{r^2} \tag{5-8}$$

where *RMW* is the radius of maximum wind and V_{max} is the maximum tangential velocity.

The methodology used to determine internal pressures due to the combined action of wind induced external pressures and APC described in Sections 5.4.2 and **Error! Reference source not found.** is reasonable until significant damage to the building envelope occurs. When the envelope of a building is sealed, leaky, or minimally breached, open to less than 10% or so, the methodology can be justified. However, as the building begins to “come apart” the structure will begin to behave as an open structure allowing flow through the building and changing the building aerodynamics. Since there have been no experimental studies performed that model internal and external wind pressures on severely damaged buildings, an internal pressure reduction factor was developed using engineering judgement. The function, given in Eq. (5-9), models the reduction in the effective internal pressure:

$$RF = \cos(B_0 * \pi/2)^{10} \tag{5-9}$$

where RF is the computed reduction factor and B_0 is the fraction of the area of the building envelope that is breached. As shown in Figure 5-16, the reduction factor approaches zero when the 60% of the building envelope is open, which is consistent with the definition of an open building in ASCE 7 (2010). -

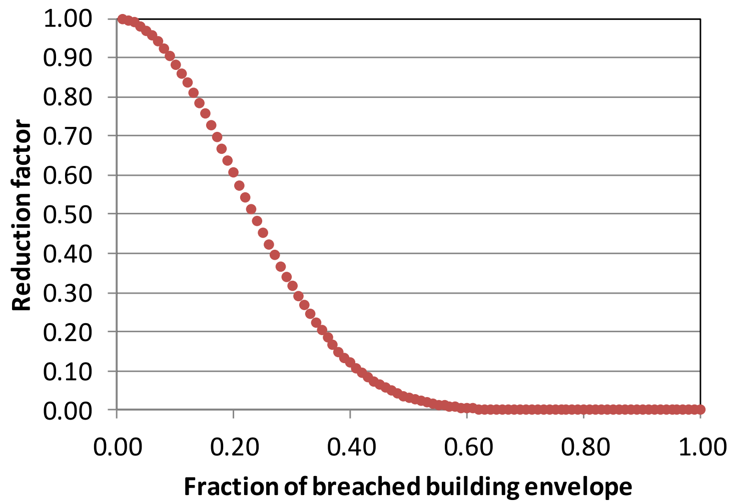

Figure 5-16. Model for Effective Internal Pressure Reduction Factor

5.4.5. Integrated Wind Loads

It is well known that the peak pressures acting on exterior elements of a building are not fully correlated (Davenport, 1961). As the area over which the pressures are averaged increases, the effective pressure coefficient decreases. The relationship of decreasing pressure coefficient with the increasing area of an element is provided in the wind loading codes such as ASCE-7.

The TORDAM wind load integration on roofs and walls is based on the methodology used in Hazus and described in FEMA (2011). The spatial extent of a tornado wind field is much smaller than that in hurricanes and the other straight-line winds, resulting in nominal (ignoring wind-structure interaction) mean wind speeds and directions that change over the exterior of the building. In the case of straight-line and hurricane winds, the nominal mean wind speed and direction is the same over the structure. In this case, the integration of the wind loads can be precomputed on a direction-by-direction basis, as the wind speed and wind direction are invariant over the structure. This procedure was used in Hazus, where integrated load effects such as truss loads, base shear, roof uplift, etc., were all precomputed and stored as directionally-dependent coefficients. For tornadic winds, which vary in both speed and direction over the exterior of the building, the use of the Hazus approach is not possible. Therefore, the integration is carried out at each time step during the tornado-damage simulation as opposed to using the integrated coefficients stored as a function of wind direction.

5.4.6. Effect of Nearby Buildings on Wind Loads

The wind loads derived from the pressure coefficients presented above are only applicable for isolated buildings in open or suburban terrain. However, in a real environment, the low-rise buildings (especially the one or two story houses) are surrounded by buildings of similar size. Due to the presence of surrounding structures, on average there is a reduction in wind loads experienced by these buildings. A wind tunnel study by Ho (1992) shows that the average reduction of wind loads on the roof is about 25% compared to the isolated building case. Ho (1992) found the coefficient of variation of the reduction of the roof loads is about 20%. The effect of nearby buildings on wall loads is somewhat less than on the roof loads. Ho (1992) did not separately study the effects of nearby buildings on the positive and negative pressures. Case (1996) attempted to fill that gap. Case (1996) found the negative roof and wall loads was similar to that reported in Ho (1992) and noticed on an average increase of positive wall pressures. Based on these studies, we have applied a factor with a mean value of 0.75 and a COV of 0.25 to the negative loads and a factor with a mean value of 1.0 and COV of 0.14 to the positive loads.

5.4.7. Wind Borne Debris

An explicit time-stepping model is used to predict the wind borne debris damage to structural components of the building and associated change in the internal pressure. ARA's prior work in this area for hurricanes was briefly reviewed in Section 5.2. This work is adopted herein for tornado WBD simulations as described in the following paragraphs.

5.4.7.1. Tornado Wind Field

The first step in implementing a tornado WBD model was the incorporation of the tornado wind field model (described in Section 4 and used in TORRISK2 and TORDAM) into ARA's HURMIS tool (see Figure 5-2). In HURMIS, missiles are flown, buildings impacted, and breaches are scored on a house-by-house and time-step basis. These data are then post-processed to produce impact flux parameters (impact probability per unit of wall area and impact energy CDF). This information becomes input to the individual building damage tool (HURDAM or TORDAM)

This initial tornado integration step produced WINDMIS (the tornado generalized version of HURMIS) and allowed us to test out the generation of tornado missiles in residential neighborhood on a house-by-house basis. This process was tested as illustrated in Figure 5-17 for a single tornado for roof cover debris. The blue squares in the plot represent the locations of the houses in a residential neighborhood. The orange line denotes the centerline of the tornado path. The effect of rotational wind on debris trajectory is evident from the figure. We performed a limited number of these simulations to determine how best to adapt the model.[70] The resulting adjustments are described in the next paragraphs.

[70] We did not have sufficient ARA resources or NIST funds to fully validate (with appropriatly developed field data) a tornado WBD model for this project.

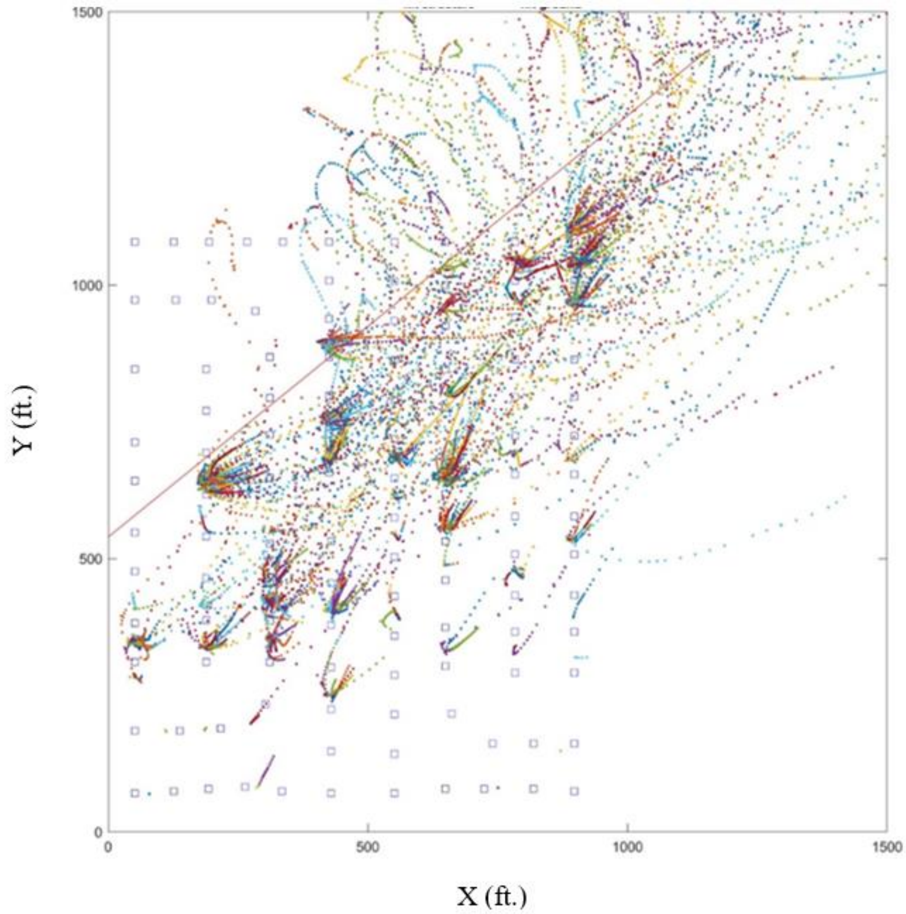

Note: 1 ft = 0.3048 m

Figure 5-17. Trajectories of Roof Cover Debris Generated in a Simulated Tornado

5.4.7.2. Step 1: Time Step Adjustment Factor

As part of the WBD tornado implementation, a time-step modification was necessary. The missile flux parameter (λ_h) used for hurricanes is conditioned on the number of missiles generated over a time step of 15 min. Since the TORDAM time steps are much less than 15 min, λ was adjusted in a two-step process.[71]

The first step was to produce a tornado flux (λ_t) that reproduces the hurricane WBD damage.[72] This step would then allow us to make tornado-specific adjustments to reflect the differences in the hazard wind fields in Step 2.

In Step 1, we simulated tornadoes (as illustrated in Figure 5-17) using the hurricane 15 min flux applied to each tornado time step. The simulation comparisons are shown in Figure 5-18. The wind speed in Figure 5-18 is the maximum reference (3-second gust) wind speed experienced over the plan area of each structures (per Section 7.3). The plotted values are by wind speed bin.

[71] The tornado time-steps are much smaller, fractions of a minute.
[72] The hurricane WBD model was validated with field data for multiple events.

The plotted values in Figure 5-18 show the increase in the mean percent of failed fenestrations from WBD. The tornado simulations produced more failures than hurricanes beginning at about 100 mph (45 m/s). From the data in Figure 5-18, we developed the missile flux parameter shown in Figure 5-19. This parameter is the ratio of the hurricane produced fenestration failures to the tornado-produced hurricane failures.

The computed ratios were fitted with a quadratic function of wind speed as shown in Figure 5-19. In TORDAM, the equation shown in Figure 5-19 is used to determine the reduction factor that is multiplied by the missile flux parameter. The modeled reduction factor becomes constant at wind speed greater than or equal to 200 mph (89 m/s).

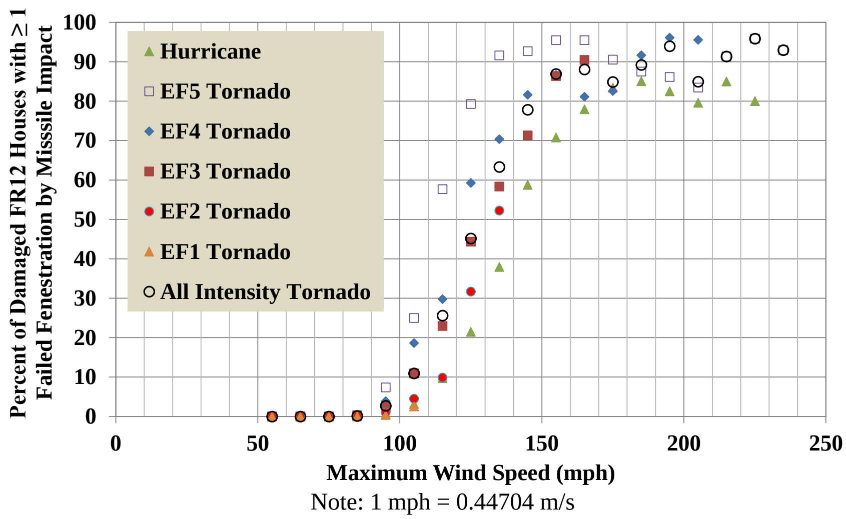

Figure 5-18. Missile Damage Fragilities (Hurricane vs. Tornado Winds)

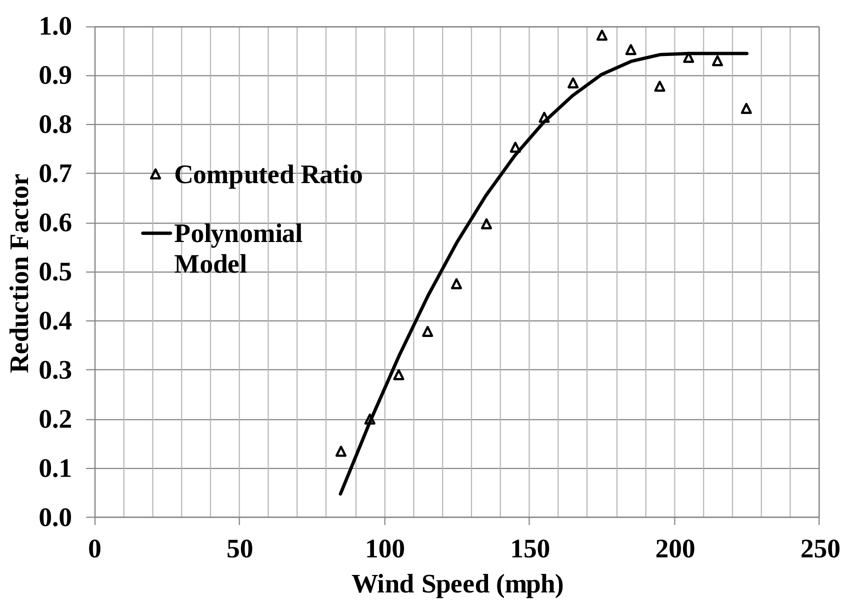

Note: 1 mph = 0.44704 m/s

Figure 5-19. Missile Flux Reduction Factor for Tornado Time-Step Simulations

5.4.7.3. Velocity Profile Adjustment Factor

The second step in the tornado WBD implementation considers tornado-specific factors that influence tornado missile flux relative to hurricane missile flux. Tornadoes are assumed to have a vertical profile, which increases damage for low-rise structures over hurricanes or straight winds. Tornado APC effects also produce higher-pressure loads. Vertical winds result in more missiles and lofted trajectories. However, the tornado RMW is much smaller than the RMW for hurricanes. RMW influences the number of missiles produced in the vicinity of the target and also affects missile duration before missiles enter wind field regions with lower wind speeds.

Nuclear power plant site-specific studies for both tornadoes and directional straight winds show similar contributions to WBD fragility risk, when averaged over all the component targets at the site.[73] However, nuclear plants have numerous missiles originating at heights over 33 ft (10.1 m). (due to the tall structures present), which tends to reduce the impact of strong low-level winds in tornadoes, which are important for low-rise residential buildings. As a result, we focus on using a horizontal wind profile adjustment approach to adjust the tornado time step adjusted flux obtained in Step 1.

The hurricane missile damage model is based on hurricane simulations in open country terrain. The reference wind speed at 33 ft (10.1 m) is used in the model to define wind-speed dependent missile hits. The hurricane boundary layer profile results in a lower wind speed at mean roof height for a one-story house than at 33 ft (10.1 m). Since the tornado damage model uses a constant vertical profile, the tornado wind speed at mean roof height equals the wind speeds at 33 ft (10.1 m). Therefore, the missile flux parameter is adjusted to reflect the enhanced missile environment due to the vertical profile used for tornadic winds. The adjustment multipliers are calculated using the following steps:

1. The equivalent hurricane wind speeds at 33 ft (10.1 m) for a constant vertical profile are calculated by comparing with an open country terrain profile (as used in ASCE 7 (2016)).
2. The resulting equivalent wind speeds are then used to derive the mean number of missile hits. These values are then normalized by the boundary layer wind speeds at 33 ft (10.1 m).

Figure 5-20 shows the profile adjustment multipliers vs. wind speed and the smoothed model implemented in TORDAM. The implemented model clearly enhances the missile environment in tornado winds compared to hurricane winds, particularly at low wind speeds. For example, at 100 mph (45 m/s), twice as many missiles are generated in tornadoes than in hurricanes.

[73] Twisdale (2016) compares straight wind vs. tornado WBD fragilities for one nuclear plant. The WBD straight wind fragilities were higher than their tornado counterparts for about 70% of the components. The wide breadth of straight winds (and hurricanes) produce missiles over the full width of the plant, whereas tornado WBD is often limited to a part of the plant and only affects a percentage of the targets in one event.

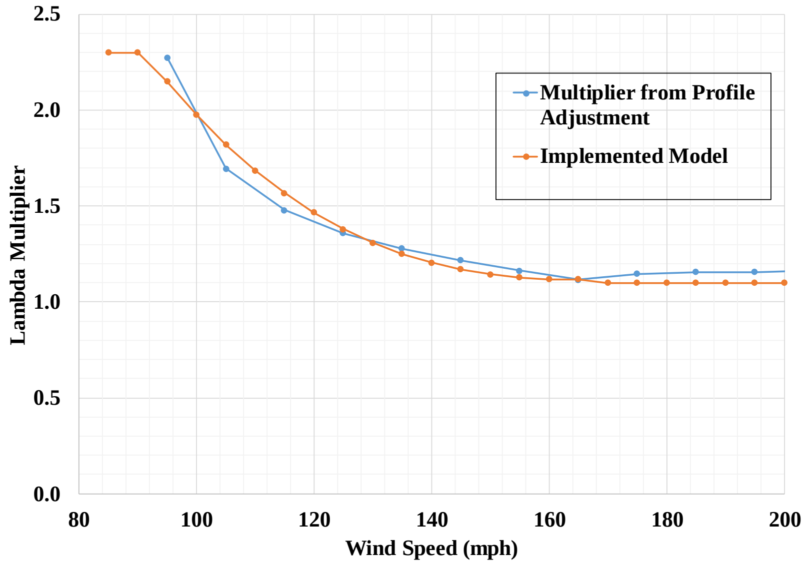

Note: 1 mph = 0.44704 m/s

Figure 5-20. Velocity Profile Adjustment Factor

5.5. FR12 Failure Modes and Resistance Models

The tornado damage model uses full load path to characterize the damage of FR12 due to tornado winds. For this reason, all the possible failure modes for an FR12 subjected to wind load are addressed in the model and the resistances for these failure modes are modeled. We modeled the component and system failure modes observed in the field damage surveys. These failure modes are shown in Figure 5-21. For component level, we modeled fenestration (such as windows and doors) failure, roof failure, wall failure and foundation failure. For system level such as whole building failure, we modeled sliding and overturning failures. The probabilistic resistance models for these failure modes (such as for material strengths, connection strengths, wind-generated missile impact resistance) are based on laboratory and full-scale test data coupled with engineering analyses (including finite element analyses), and engineering judgment.

Wall system failures have been studied extensively using finite element (FE) modeling and analysis. The FE model for wall and wall systems are validated against experimental studies and wall resistance models are developed for out-of-plane bending and in-plane shear. The house system effect on in-plane shear resistance is also investigated. The FE modeling overview and validation are given in Section 5.5.1. The detailed FE developed models are discussed in the respective component sections where they are used in the resistance models.

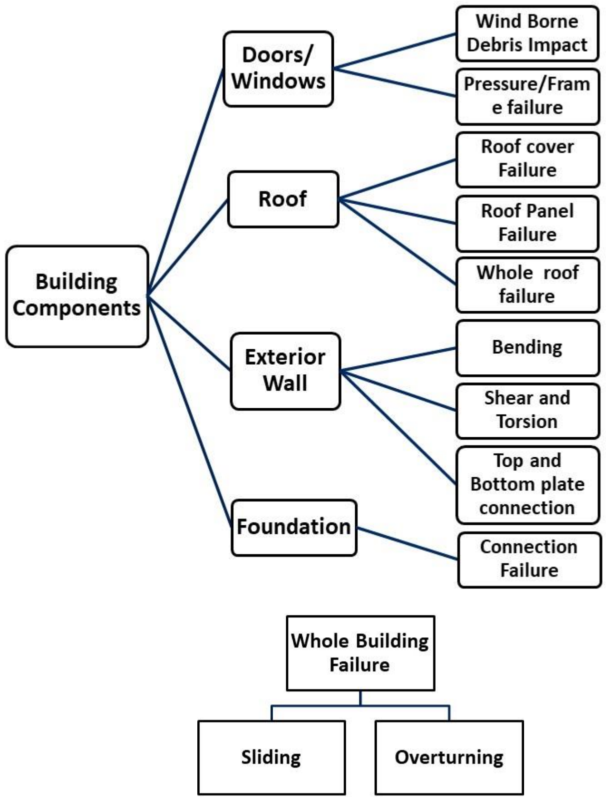

Figure 5-21. Modeled Building and Component Failure Modes

5.5.1. FE Resistance Modeling and Validation

To facilitate failure modeling of walls in the in-plane and out-of-plane directions, parametric models are developed to calculate the in-plane and out-of-plane load resistances of the walls and compare these resistances to applied wind loads. The parametric models for the walls are developed based on detailed finite element (FE) modeling and analysis of a standalone wood-frame wall and wall as a part of the house system. The finite element models (FEM) of the wood-frame houses are developed using the general-purpose finite element (FE) software ANSYS. The FE models consist of modeling wall and roof frames, concrete foundation and wood floor system, wall and roof sheathing, and connections between frame members, wall sheathing-to-wall frame, roof sheathing-to-roof frame, roof-to-wall, wall frame-to-concrete foundation, and wall frame-to-wood floor system.

Figure 5-22 shows a typical finite element mesh developed for a 15 m (50 ft) ×10 m (33.3 ft) wood-frame house used in the analysis. The connection between different components are considered to be as per the recommendations of IRC (2015) unless stated otherwise, e.g., the wall studs are connected to top and bottom plate by 2-16d end nails, sheathing is connected to wall and roof frame through 8d common nails spaced at 150 mm (6 in) on center along perimeter, roof-to-wall connection is established through 3-16d toe nails and wall bottom plate is connected to foundation through 12.7 mm (0.5 in) anchor bolts spaced at 1.8 m (6 ft) on center. Modeling of the connection between sheathing-to-frame, lumber-to-lumber and foundation-to-frame is of great importance in order to predict a realistic response of the walls under service loads. In this study, for the nonlinear springs representing connections between frame members, foundation-to-frame and sheathing-to-frame, force-displacement relationships are provided to define the stiffnesses in the axial and two lateral directions for different loading conditions. The force-displacement responses of the nails for different loading conditions are obtained from the test results reported by Mi (2004), Asiz et al. (2009) and Thampi (2010), whereas the force-displacement relationship of the anchor bolts connecting bottom plate-to-foundation is obtained from experimental responses reported by NAHB Research Center Inc. (2010).

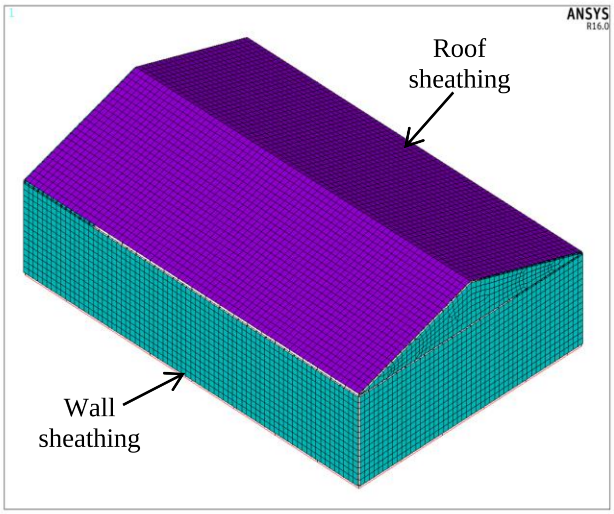

a. FE Mesh

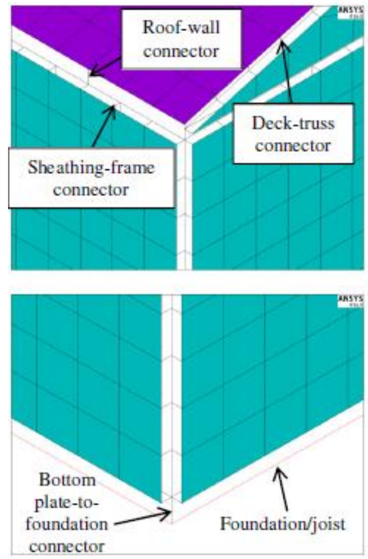

b. Connectors at Different Components

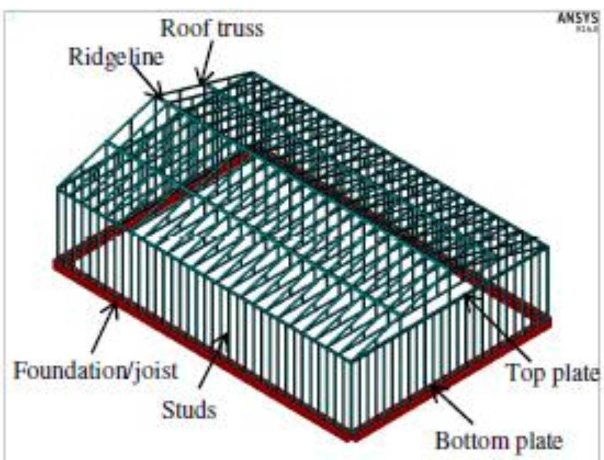

c. FE Mesh of Exterior Frame

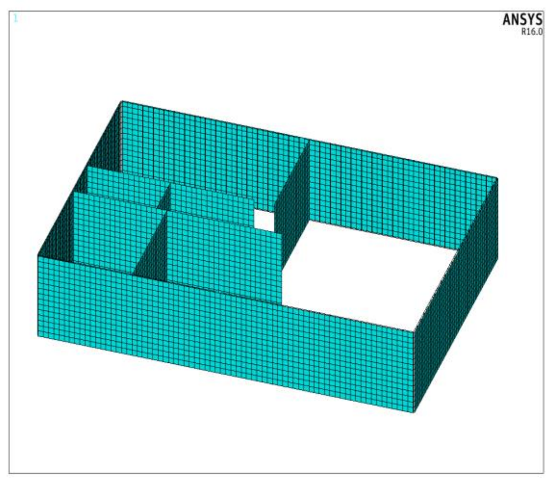

d. Interior Partition Walls

Figure 5-22. Finite Element Model of a Typical Wood-Frame House Used in the Analysis

The finite element models developed for the whole house are validated for three loading cases:

1. **In-Plane Wall Failures**: stand-alone wall of the house against experimental responses under in-plane lateral load response from Doudak et al. (2006) and Dolan and Heine (1997);

2. **Out-of-Plane Wall Failures**: stand-alone wall of the house against experimental responses under out-of-plane lateral load response from Gromala (1983); and
3. **Full House Wall System Effect**s: full house wind load damage against field observations from Thampi et al. (2011), and system level wall responses against experimental responses from Phillips et al. (1993) under in-plane lateral loads.

The finite element model validation cases and the simulation results are discussed briefly in the following section.

5.5.1.1. Validation of In-Plane Wall Model

The in-plane load-displacement responses of a stand-alone wall of the house model are validated against experimental responses from Doudak et al. (2006) and Dolan and Heine (1997). Doudak et al. (2006) tested seven 2.4 m (8 ft) × 2.4 m (8 ft) wood-frame wall under monotonic in-plane lateral loads where the connections between members were designed based on design code requirements. Two walls from these experiments are simulated by using the finite element models and the force-displacement responses are compared as shown in Figure 5-23e. The peak forces are accurately predicted, and the failure mode of the wall is captured well by the FE models which occurred by relative sliding and rotation of the OSB panels (Figure 5-23 (a-d)).

Dolan and Heine (1997) tested nine 12 m (40 ft) × 2.4 m (8 ft) walls under monotonic in-plane lateral loads with different anchorage conditions and partially sheathed cases. Two of the walls from this experimental study are simulated by using finite element models. Figure 5-23 (f) shows a comparison of the simulated force-displacement responses to experimental responses. It is seen that the simulated peak forces match well with the experimental results. The validation of the simulated results against experimental responses of Doudak et al. (2006) and Dolan and Heine (1997) indicates that the wall system of the house has been modeled accurately to realistically represent the in-plane load responses of a wood-frame wall.

a. Rotation of OSB Panel

b. Observed Wall Panel Relative Slip, Doudak et al. (2006)

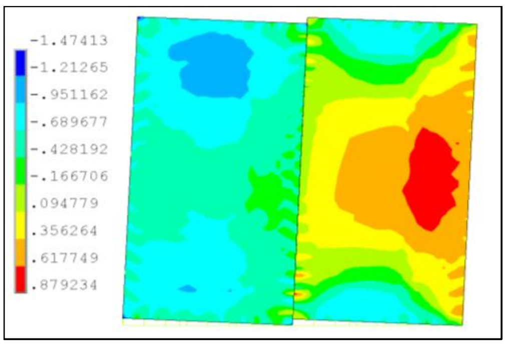

c. Simulated In-Plane Shear Stress (MPa) Response of Walls

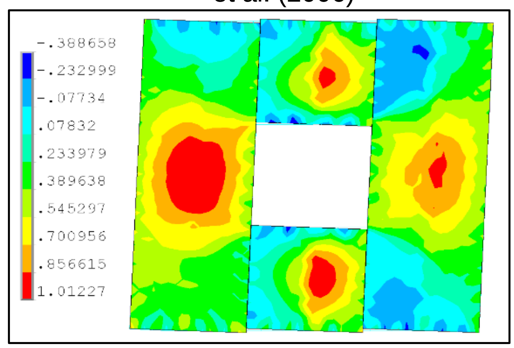

d. Simulated In-Plane Shear Stress (MPa) Response of Walls

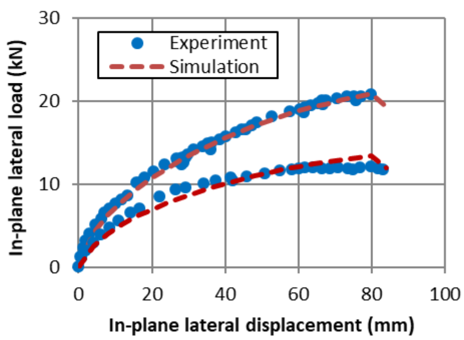

e. Comparison of Simulated Load-Displacement Responses to Experimental Responses from Doudak et al. (2006)

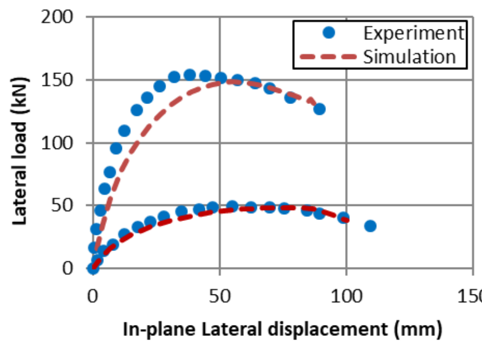

f. Comparison of Simulated Load-Displacement Responses to Experimental Responses from Dolan and Heine (1997)

Note: 1 MPa = 20885.43 psf; 1 mm = 0.03937 in; 1 kN = 224.8089 lbf

Figure 5-23. Experimental vs. Simulated Responses for In-Plane Shear Loads

5.5.1.2. Validation of Out-of-Plane Wall Model

The validation of the finite element models against out-of-plane loads is performed by comparing the responses from FEM simulation to those of the experiments performed by Gromala (1983), where 10 walls were tested under a positive out-of-plane uniform load provided by air bags. The tested walls had two different widths 3.6 m (12 ft) and 5.4 m (18 ft) with stud spacing of 400 mm (16 in) and 600 mm (24 in), respectively. The results of these tests revealed that under out-of-plane loads, failure occurred in the walls through stud splitting close to the bottom plate or bottom plate splitting. In both failure cases, the wall capacities were similar. These test walls are modeled following the experimental configurations. The FE models are able to predict the peak failure load and the failure mechanism of both walls. The simulated out-of-plane pressure-displacement response of one of the walls is shown in Figure 5-24a, which demonstrates that the FEM simulated response is in good agreement with that of the test results. The maximum principal stress contour of the studs shown in Figure 5-24b further demonstrates that the models can replicate the failure mechanism observed during the tests where maximum stresses occur in the studs close to the bottom plate or at the connection between the studs and the bottom plate. The ability of the FE models to predict the peak forces and the failure mechanism provides a good measure of validation of the developed finite element models in predicting the out-of-plane wall resistances.

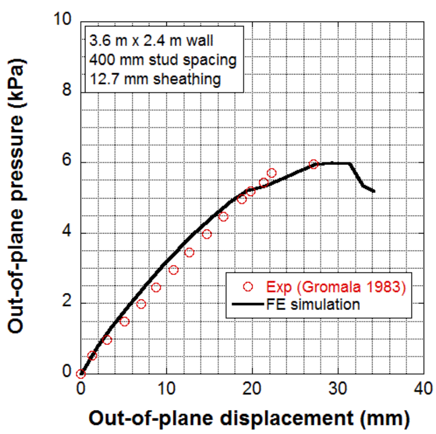

a. Measured (Gromala, 1983) and simulated force-displacement response of a wood-frame wall

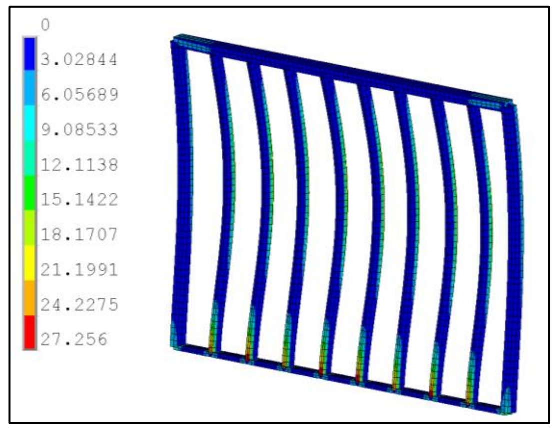

b. Simulated principal stress contour (MPa) of the studs, top and bottom plate showing maximum stresses at the bottom of the studs similar to the failure mechanism observed in Gromala (1983)

Note: 1 Pa = 0.02088543 psf; 1 mm = 0.03937 in

Figure 5-24. Experimental vs. Simulated Responses for Out-Of-Plane Loads

5.5.1.3. Validation of Full House Wall System Effects

To validate the house model as a system, a one story 15 m (50 ft) × 10 m (33.3 ft) gable-roofed house (Figure 5-22) is taken from the study of Thampi (2010) and Thampi et al. (2011) for analysis. This house was partially damaged (Figure 5-25(b)) during the EF5 Parkersburg Tornado in Iowa on May 25, 2008 (Sarkar and Kikitsu 2008). The house was located about 200 m (660 ft) away from the centerline of the tornado as shown in Figure 5-25(a). The house's major x-axis is in the direction of the translating tornado and all the distances measured are presented considering the origin is located at the center of the house.

In this study, the house components, members and connections are modeled based on the information provided in Thampi (2010). This house is analyzed under wind loads that are calculated from the net force coefficients and wind speeds on the building as reported in Thampi (2010). The reported maximum wind loads correspond to that of an EF5 tornado with wind speeds of 89.4 m/s (200 mph), 3-sec gust calculated with the pressure coefficients measured in the laboratory to preserve similarity to Parkersburg Tornado in Iowa on May 25, 2008 which was simulated in Iowa State University using their tornado/microburst simulator. The simulated tornado had a core radius of 40 m (130 ft) and a translation velocity of about 23 m/s (51 mph). Based on the measured wind pressure coefficients, Thampi (2010) reported net force coefficients (external minus internal) in the x, y and z directions for different ratio of $\frac{x}{r_c}$, where *x* is the distance between the tornado core and the center of the house as shown in Figure 5-25(a), r_c is the radius of the tornado core. These force coefficients are reported for a sealed building (closed doors and windows with porosity in the cladding) which takes into account both external and internal pressures. In order to calculate the net force coefficients Thampi (2010) integrated the x, y, z components of the net pressure coefficients (i.e., the difference between the external and internal pressure coefficients) over the entire surface of the building and normalized the integrated results by the projected area of the building corresponding to each building axis. These force coefficients along with the wind speeds on the house have been employed in this study to generate the relevant wind forces on the walls and roof of the house for various locations of the tornado.

The load is calculated for x, y and z directions and applied in a quasi-static manner by applying loads in time steps and updating the response in each time step. Due to unavailability of the detailed time histories of the pressure coefficients on different parts of the walls and roof of the house, the wind pressure is applied uniformly on the walls and roof of the house. In the analysis, several locations of tornado are considered starting from $x = -4r_c$ to $x = -r_c$ and wind speed on the building is taken for each location along with the force coefficients and the projected area of the wall and roof to calculate the wind loads on each component of the building. For tornado location of $x = -4r_c$, wind speed on the building is taken as ~25 m/s (55 mph) and as the tornado approaches the house, the wind speed on the building is increased with a maximum wind speed of ~56 m/s (125 mph) for tornado location of $x = -1.65r_c$. In other words, the wind pressures on the wall and roof of the house is ramped up as the tornado approaches the building based on the measured wind speed on the building and the force coefficients for the corresponding tornado location. The analysis presented in this study is an approximate approach to simulate the house damage that was observed by Sarkar and Kikitsu (2008).[74]

In this analysis, flexural failure of the frame members are defined by the modulus of rupture values as obtained from Ross (2010). For sheathing, failure is defined by axial, shear and bending failure stress criteria as given by APA (1997) and excessive displacement failure criteria as reported by 2012 IBC (2011). Whenever any fastener has a displacement of 20 mm (0.8 in.) or more along the axial direction the connection is assumed failed based on the guidelines of ASTM-D1761-12 (2012) "Standard test methods for mechanical fasteners in wood". Whenever any connection fails, the members or sheathing elements associated to that connection is also assumed failed. In addition to the displacement failure criteria for the connection, reaction force based failure criteria is also used using both transverse and axial reactions as reported in Thampi (2010). During analysis, the failed components are deactivated i.e. their stiffness is set to zero in the next analysis step. By incorporating the aforementioned failure criteria for different components of the wall and roof system, the house is analyzed under the wind loads for different locations of the tornado and the damage

[74] The analysis could have been improved with actual time-history data from the measured pressure coefficients at each location of the wall and roof.

to the building is compared to that of field observation from Sarkar and Kikitsu (2008). The simulated maximum principal stress distribution contour of the house is presented in Figure 5-25(c-d) for two locations of the tornado by physically removing the failed components from the model.

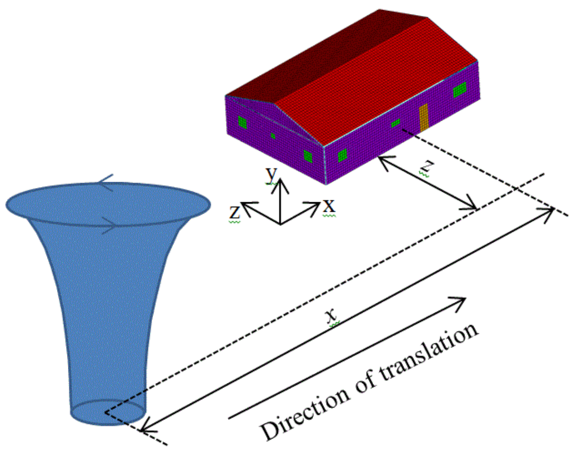

a. Location of the Example House

b. Damage Observed During Field Survey

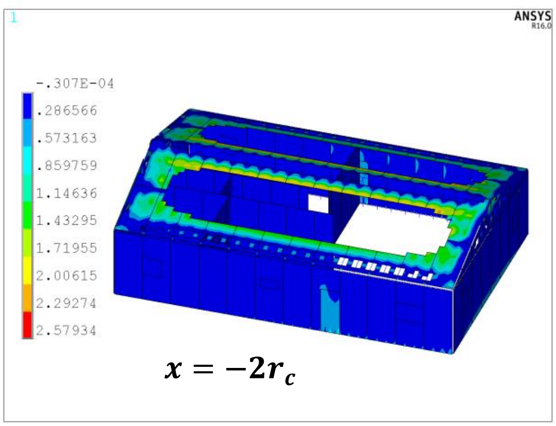

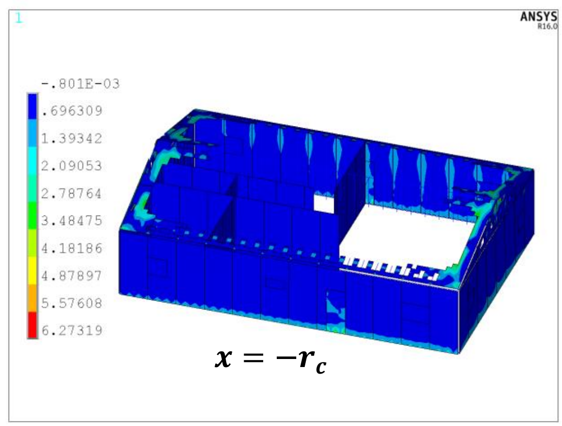

c.- d. Simulated Damage of the Example House

Figure 5-25.Validation of the Full House Model

As the tornado approaches the house, the extent of damage increases with the maximum damage occurring for tornado location between $x = -2r_c$ to $x = -r_c$, which correspond to a wind speed of 56 m/s (125 mph) on the building. It is consistent with the observation from the numerical analysis of Thampi et al. (2011). The extent of damage obtained from the simulated results is comparable to the field observation (compare Figure 5-25(d) to Figure 5-25(b)) where it is seen that most of the failure occurred in the roof of the house. The validation of the house model against the study by Thampi et al. (2011) and field observation from Sarkar and Kikitsu (2008) shows that the interaction between various components of the house are modeled accurately and the failure and damage mechanisms of the house components are predicted accurately by the finite element model. However, the full house model is developed to address the system effects on the load resistances of the walls, and the FE model validation case presented in this analysis has failure mostly in the roof panels of the house. Hence, another validation of the full house model is conducted on the individual wall responses of the house system against the experimental responses from Phillips et al. (1993) which is more relevant to the intent of full house model developed.

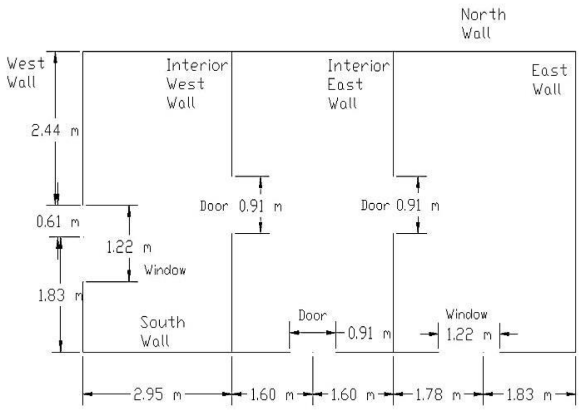

a. Plan Dimensions

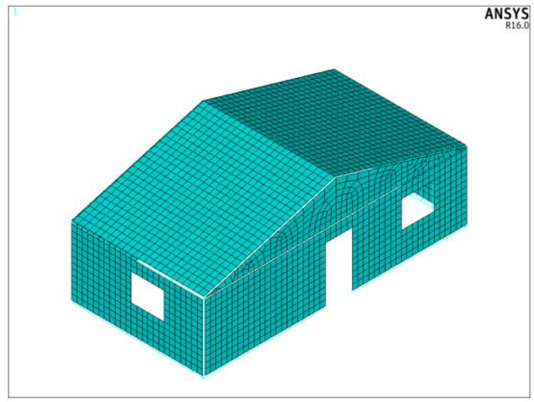

b. Finite Element Model of the Building Tested by Phillips et al. (1993)

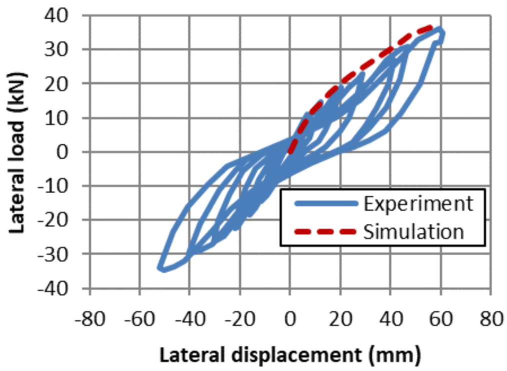

c. Simulated and Measured (Phillips et al. 1993) Load-Displacement Response of West Wall

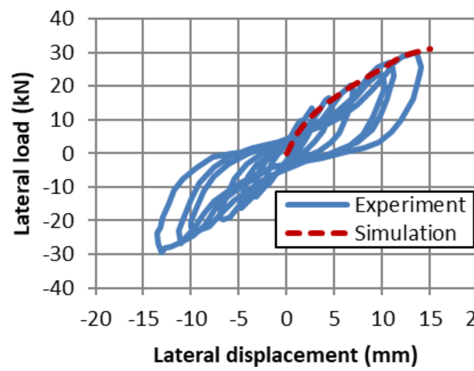

d. Simulated and Measured (Phillips et al. 1993) Load-Displacement Response of East Wall

Note: 1 m = 3.28084 ft; 1 mm = 0.03937 in; 1 kN = 224.8089 lbf

Figure 5-26. Validation of the Full House Model for In-Plane Shear Loads

To further validate that the wall resistances of the house at the system level are predicted well by the finite element models, the house model developed is validated against the study by Phillips et al. (1993) where they experimentally investigated a gable-roofed house under lateral force to quantify the load sharing characteristics among the wall and roof diaphragms. The plan dimensions and the finite element model of the house are shown in Figure 5-26(a) and Figure 5-26(b), respectively. The finite element model for this house is developed precisely so that it resembles the experimental setup as closely as possible (Figure 5-26(b)). The properties of the nails are obtained from the experimental results reported in Phillips (1990). The lateral loads are applied to the south side of the house as point loads on each of the shear walls where the load was increased monotonically instead of cyclic loads applied in the experiments. The simulated lateral force-displacement responses of west and east walls are compared to the cyclic load-displacement responses from the experimental results in Figure 5-26(c) and Figure 5-26(d), respectively. It is observed that the simulated load-displacement responses resemble closely the monotonic envelope of the cyclic load-displacement responses from the experiments. This indicates that the developed house model can predict the lateral load resistances of wood-frame wall as a part of the house system.

Overall, the simulated responses demonstrate that the developed full house model is able to predict the peak load resistances of the walls and the observed damage of the house reasonably well. Moreover, the stand-alone wall from the house model is able to predict the experimental peak load resistances and failure mechanism with good accuracy. The experimentally validated FE models are utilized to investigate the influence of different design variables on the in-plane and the out-of-plane load resistances of wood-frame walls. Details of the finite element models and analysis results are presented in Quayyum (2019a, 2019b, 2020). The specific models developed for the 3 loading cases described above are discussed in the respective section on wall and house system response.

5.5.2. Fenestration Failure Model

Two failure modes are considered in the fenestration failure model. These are failure due to wind borne missile impact and failure from wind pressure load.

5.5.2.1. Missile Damage Failure

Missile impact is checked at each time step for the undamaged fenestrations considering wind speed and direction at the centroid of the fenestration. If a fenestration is damaged by a missile, the internal pressure is recomputed. Missile impact resistances are obtained from HAZUS (FEMA, 2011). We have used an enhanced missile model compared to that used in HAZUS. The enhanced missile model was discussed in Section 5.4.7.

5.5.2.2. Wind Pressure Failures

The wind pressure failure of the fenestration results from either a pressure failure of the glass or a failure in the connection between the frame and the house. The wind pressure resistances vary widely between manufacturers and the required design pressure. For this study, we used a mean failure resistance of 40 psf (1.92 kPa) with a COV of 0.2. These values are the same as those used in the HAZUS (FEMA, 2011) damage model.

When the computed wind load (i.e. algebraic summation of external pressure, internal pressure and APC) is greater than the fenestration resistance, the fenestration is considered to have failed. The internal pressure is recomputed when a fenestration is failed. A flow chart is given in Figure 5-27 showing the steps to determine fenestration failure. The flowchart also shows how the internal pressure is computed before and after a fenestration failure. Fenestrations failures due to wind borne debris impact are checked first. If one or more fenestrations are failed by debris impact, then the internal pressure is recomputed using the steps shown in the internal pressure routine flowchart illustrated in the left side of Figure 5-27. The internal pressure is computed using the external wind induced pressures and APC at the locations of failed components in conjunction with the computation of the internal pressures due to uniformly distributed background leakage. Details of the internal pressure model and APC are discussed in Sections **Error! Reference source not found.** and 5.4.4. N ext, wind pressure failure is checked against the combined load from external pressure, internal pressure and APC. If one or more fenestrations are failed by wind pressure then internal pressure is recomputed.

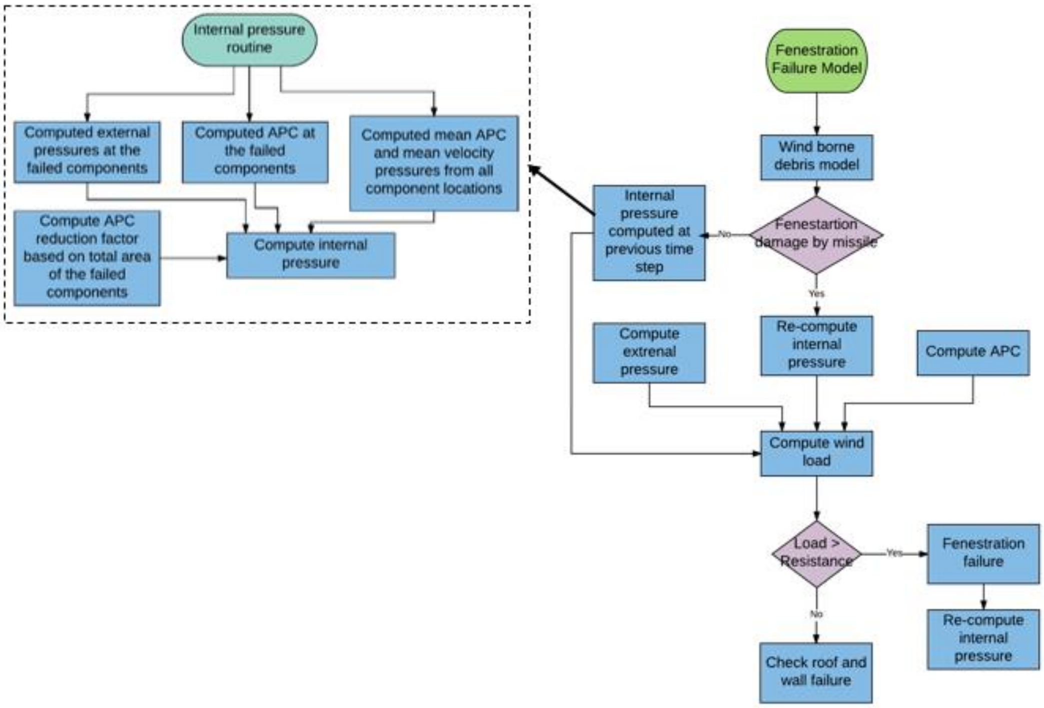

Figure 5-27. Flowchart for Fenestration Failure Steps

5.5.3. Roof Component Failure Model

Three failure modes are considered for the roof. These are failure of roof cover, failure of roof panels and failure of roof-to-wall connections (whole roof failure). Partial failure of the roof frame due to splitting of rafters or truss top chord members are not considered in the roof deck failure.

5.5.3.1. Roof Cover

The failure model for shingle and tile roof cover is the same as that used in Hazus (FEMA, 2011). The failure model is based on the methodology described in Cherry (1991). Using this model, overturning moments on individual tile elements are computed and compared to the tile moment resistances, which are provided for a range of tiles with different shapes and attachment techniques. The failure of a roof cover element is determined by comparing the tile moment resistance with the moment from the wind uplift calculation. The shingle failure model is the same as the tile model except the uplift capacity has been reduced by 10%. The approach has been validated through comparisons with field observations as discussed in FEMA (2011). APC and internal pressure are not required in the roof cover failure model, since the shingles and tiles are modeled as air permeable and the internal pressure is assumed to be contained by the roof sheathing

5.5.3.2. Roof Deck

The roof deck failure model is based on the experimental uplift failure tests performed on 8 ft (2.4 m) by 4 ft (1.2 m) panels of plywood and Oriented Strand Board reported in Cunningham (1993), Mizzel (1994), Shane (1996), Rosowsky and Schiff (1996). The uplift capacities vary with nail size and spacing.

Failure of the roof deck is determined by comparing the withdrawal resistance of the nails connecting deck elements to the roof frame (obtained from experimental results) with the uplift pressure, which is an algebraic summation of external pressure, internal pressure and APC. The material failure of the deck elements such as splitting of plywood or OSB is not modeled. The resistances that are used in the model are summarized in Table 5-1.

5.5.3.3. Whole Roof

The whole roof failure model depends on the strength of the roof to wall connection. The resistances of different roof-to-wall connections developed using experimental data provided by Canfield et al. (1991), Judge and Reinhold (2002) and FEMA (2011) are used herein. The capacity statistics of roof-to-wall connections that are used for this study are summarized in Table 5-1.

Failure of whole roof is determined by comparing the resistance of the roof to wall connections to the integrated net uplift roof pressure on the entire roof at a given time step. The net uplift load is obtained by deducting the gravity load from the gross uplift load due to wind. The whole roof failure model takes into account the load reduction in the wind uplift due to failed roof panels by setting the loads on failed panels to zero. The dead load due to the weight of the failed shingles and failed sheathing is also taken into account in the computation of net uplift load.

Figure 5-28 illustrates the steps in roof failure model. Failure of roof cover is evaluated in the beginning of the roof failure model. Only the external pressure is used in the load computation for roof cover elements since these elements will not experience any internal pressure or APC effect. The failure of roof deck panels is evaluated next. Load on the roof deck panels is based on the algebraic sum of external pressure, internal pressure, APC and weight of the panels. In case of any roof cover failure, the weight of the corresponding roof deck panel is reduced. Finally, the failure of the whole roof is evaluated using the integrated load on the entire roof.

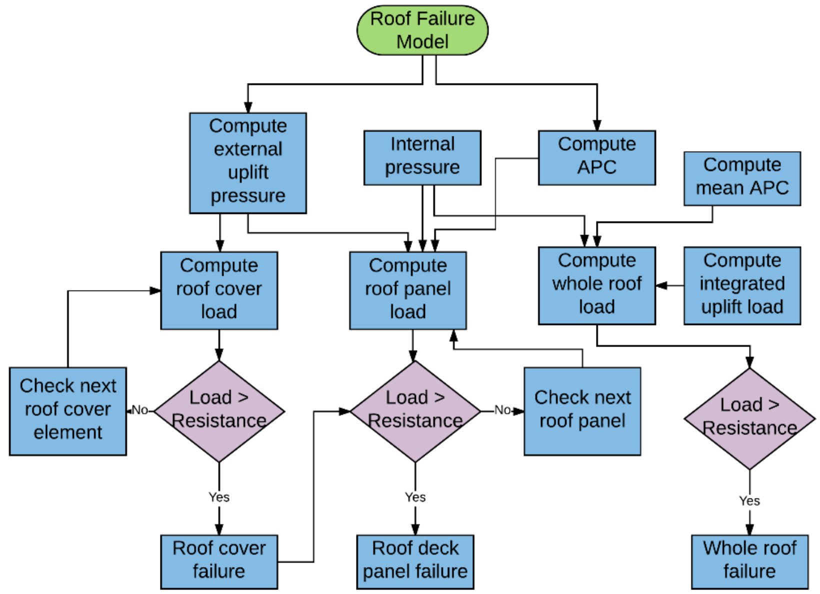

Figure 5-28. Flowchart for Roof Failure

5.5.4. Wall Failure Model

The walls of each side of the building are divided into multiple sections to compute loads and determine failure of these sections. The wall section failure modes include in plane shear failures, out-of-plane bending failures, failure of top plate to stud connections, bottom plate to stud connections, and failure of bottom plate to foundation connections. The entire wall on each side of the building is used to determine the in-plane-shear failure. The out-of-plane bending and in-plane shear failure models includes partially and fully sheathed walls, with or without drywall. A flow-chart describing the wall failure model is given in Figure 5-29. Computation of wall loads begins with the computation of out-of-plane loads comprising the algebraic sum of the external wind induced pressure, internal pressure and the APC. The out-of-plane resistance depends on the presence of top-support, which is determined by whether or not the roof remains attached to the wall. As indicated in Figure 5-29 the failure of the roof is computed using a load and resistance-based model.

When the roof-to-wall connection fails, the walls will lose top-support and the out-of-plane bending resistances are re-sampled. In this case, the house system effect on in-plane resistance is also affected and results in lower in-plane resistance than that if the roof is intact. The in-plane loads are computed using the out-of-plane wall loads and horizontal component of the roof load. The vertical load on a wall that resulted from the vertical component of the roof load is used in the wall failure model. This vertical load affects the resistance for in-plane shear and the loads on stud to top plate and bottom plate connections and bottom plate to foundation connection.

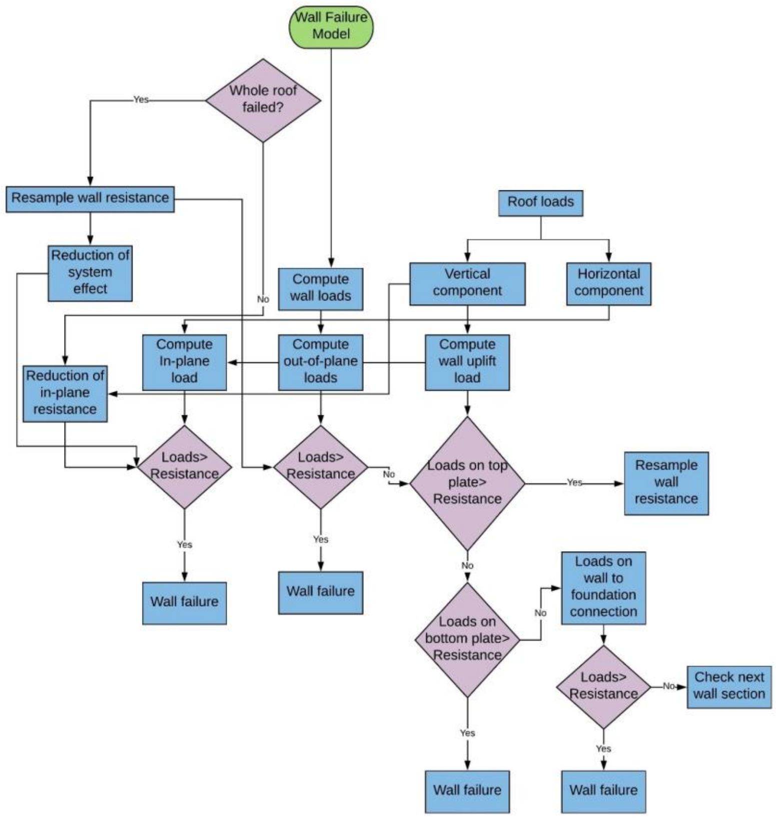

Figure 5-29. Flowchart for Wall Failure

The wall failure modes that are considered in the house damage model are described in the following sections. The description includes modeling of the resistance and its implementation in the model.

5.5.4.1. Out-of-Plane Bending Failure

The out-of-plane (OP) load resistance of the walls is investigated considering both positive and negative out-of-plane loads for different wall length, height, stud and sheathing nail spacing, sheathing thickness, presence of drywall and opening, and different boundary conditions. Figure 5-30 shows one set of FE simulated out-of-plane load responses of the wood-frame wall. It is evident that with increase in wall height, stud spacing and sheathing nail spacing, the out-of-plane load resistance of the wall decreases, whereas it increases with increases in sheathing thickness. On the other hand, the presence of openings in the wall in the form of windows, doors or even partially sheathed panels decreases the out-of-plane load capacity of the wall. Moreover, it is observed that wall support conditions significantly influence the out-of-plane load resistances of the wall, where the wall resistances can decrease by 50% or even more with the loss of top and/or side supports. Similar analyses are performed on wood-frame walls by varying the design variables and a broad set of data is generated for the out-of-plane load resistance of the wall.

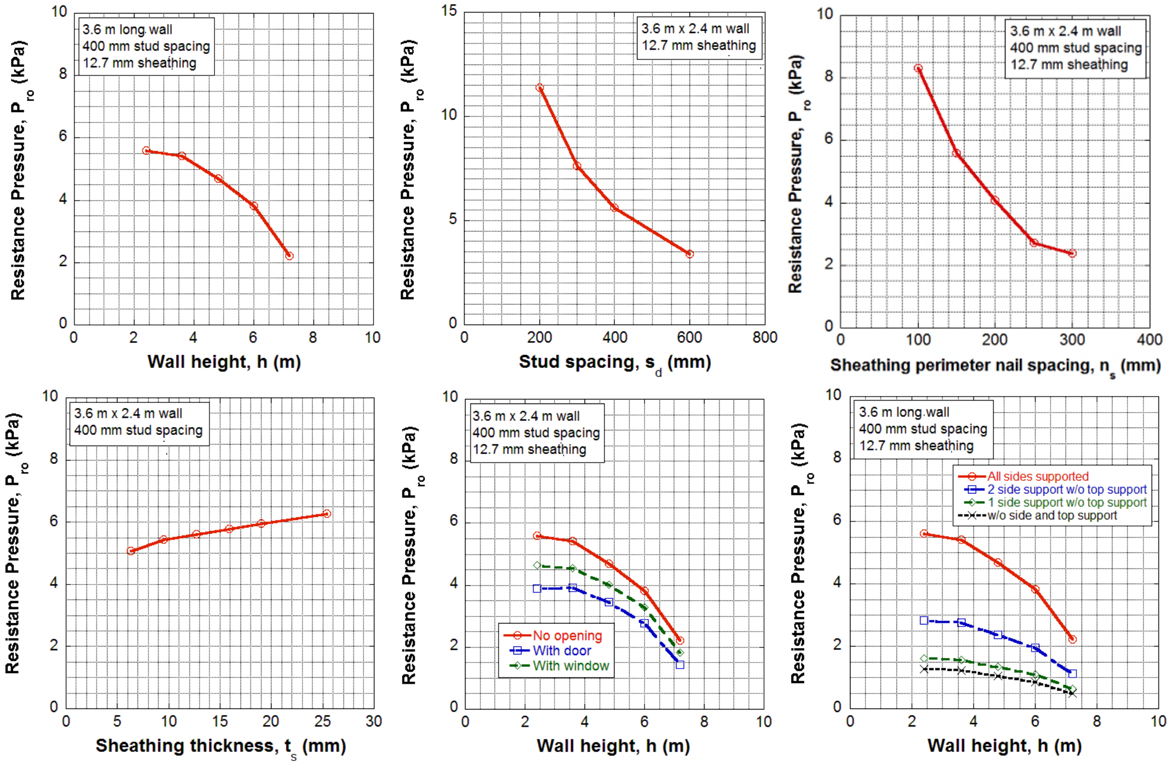

Note: 1 kPa = 20.88543 psf; 1 m = 3.28084 ft; 1 mm = 0.03937 in

Figure 5-30. Sensitivity Analysis of Wall Load Resistance Out-Of-Plane

Parametric Resistance Model. Based on the responses obtained from the FEM sensitivity analyses, a parametric model is developed that provides the out-of-plane wind load resistances of wood-frame walls for different heights, stud spacing, sheathing nail spacing, sheathing thickness, opening area, and support conditions. Details of the sensitivity analyses and the development of the parametric models and modification factors for evaluating the out-of-plane load resistances of the walls are presented in Quayyum (2019a, 2020). The parametric model to calculate the OP load resistance of the wood-frame walls is expressed as:

$$P_{ro} = k_{ns} k_{ts} k_o k_s k_p a(s_d)^b \qquad \textbf{(5-10)}$$

where P_{ro} is the OP load resistance (in kPa) of walls; a and b are constants expressed by Eqs. (5-11) and (5-12), respectively; h and s_d are height and stud spacing of walls in meters; $k_{ns}, k_o, \; k_{ts}, k_s$ and k_p are modification factors for sheathing-to-frame nail spacing, wall opening, sheathing thickness, support condition, and loading direction, respectively. The modification factors for sheathing-to-frame nail spacing (k_{ns}), sheathing thickness (k_{ts}) and wall opening (k_o) are calculated by using Eqs. (5-13), (5-14), and (5-15), respectively, where n_s and t_s are perimeter sheathing-to-frame nail spacing and sheathing thickness in millimeters; and ρ_o is the percentage of opening in the total wall area (Quayyum, 2020).

$$a = 2.434 - 450.98e^{-14.37h^{-0.413}} \qquad \textbf{(5-11)}$$

$$b = -1.069 + 674.83e^{-31.37h^{-0.751}} \quad \textbf{(5-12)}$$

$$k_{ns} = 107.7(n_s)^{-0.934} \quad \textbf{(5-13)}$$

$$k_{ts} = 0.0113t_s + 0.8609 \quad \textbf{(5-14)}$$

$$k_o = 1 - 0.01\rho_o \quad \textbf{(5-15)}$$

The modification factors for support condition ($\boldsymbol{k_s}$) vary with the base, top and side support conditions and the values of these factors are reported in Quayyum (2019a, 2020). In addition, a reduction factor of $\boldsymbol{k_p = 0.8}$ is proposed when the wall is subjected to negative pressure in the out-of-plane direction (Quayyum, 2019a). The prediction of the out-of-plane load resistances of the parametric models are verified against experimental and simulated results from literature as shown in Figure 5-31 through equity line plots. Equity line refers to a line through a scatter plot of data points that gives a quantitative measure of the relationship between one or more independent variables and a resulting dependent variable (i.e. how well the model predictions compare to the measured data points). It is demonstrated from the equity line plots in Figure 5-31 that the models can reliably predict the out-of-plane load resistances of the wood-frame walls of single-family houses.

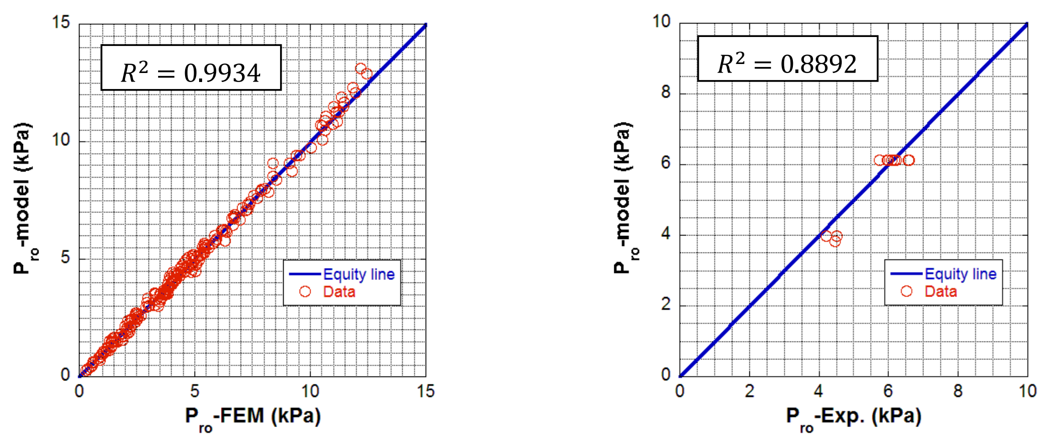

Note: 1 kPa = 20.88543 psf

Figure 5-31. Equity Line Plots Showing OP Load Resistance Comparison

TORDAM Implementation. The out-of-plane bending failure of an undamaged wall section is determined by comparing the wind pressure acting perpendicular to the wall section with the resistance computed from the parametric equations developed from Finite Element Analysis (FEA) described above. The parametric equations yield wall resistances for with or without top support and is a function of wall height, wall thickness, stud spacing, percent of opening, spacing of sheathing to stud nails and wall to foundation connection. All of the parameters needed to compute the OP resistances are obtained from model inputs except the percent opening. For the partially sheathed wall, the percent opening value is set to 80%, which reflects the case where the wall is only sheathed at the corner. For a fully sheathed wall, the percent opening is computed using the area of the doors and windows present at the wall. The computed resistance obtained from Eq. (5-10) is used as a resistance for positive wind loads. To compute the resistance for negative wind loads, a reduction factor of 0.8 (as given in Quayyum, 2019a) is used with the positive load resistance. The computed values of resistances are used as a mean resistance in the damage simulation. Using the mean and a coefficient of variation of 15% (modeled as normally distributed) sampled values of the wall resistance are obtained at the beginning of each simulation. The wind pressures acting on the wall sections are computed using the load integration discussed in Section 5.4.5. The wind pressure is compared with the appropriate resistance to determine if the wall has failed.

5.5.4.2. In-Plane-Shear Failure

To study the in-plane (IP) load resistances of the wood-frame walls, nonlinear pushover analyses are performed. The top of the wall is subjected to a gradually increasing displacement in the lateral direction until the maximum lateral strength reduces by more than 40%. The sensitivity of in-plane load resistance of wood-frame walls is investigated for wall length, height, stud and sheathing nail spacing, presence of opening and drywall, sheathing thickness, foundation connection, and combined in-plane and uplift loads. Figure 5-32 presents one set of simulated in-plane load responses of the wood-frame wall. It is noted that with increase in wall height, stud and sheathing nail spacing, and with presence of opening in the forms of windows, doors and/or partially sheathed panels, the in-plane load resistance of wall decreases. On the other hand, with increase in wall length and presence of drywall, the in-plane load capacity of wall increases. Similar analyses are performed by changing all the design variables studied and a broad set of in-plane load resistance data is generated based on finite element simulation results.

Parametric Resistance Model. Based on the responses obtained from the FEM sensitivity analyses, a parametric model is developed that provides the in-plane load resistances of wood-frame walls for different lengths, heights, stud spacings, sheathing nail spacings, opening area, drywall, combined loads, and foundation connections. Details on the sensitivity analyses responses and the development of the parametric models and modification factors for evaluating in-plane load resistances of the walls are presented in Quayyum (2019a, 2019b, 2020).The parametric model to calculate IP load resistance of the wood-frame walls is expressed as:

$$P_{ri} = 9.174 k_{ns} k_o k_{dw} k_c k_b \left(\frac{l^2}{h s_d}\right)^{0.4405} \quad \textbf{(5-16)}$$

where $P_{ri}$is the IP load resistance (in kN) of walls, l, h and s_d are length, height and stud spacing of walls in meters, and $k_{ns}, k_o, k_{dw}, k_c, k_b$ are modification factors for sheathing-to-frame nail spacing, wall opening, drywall, combined lateral and uplift loads, connection between foundation and bottom plate, respectively. The modification factors for sheathing-frame nail spacing (k_{ns}), wall opening (k_o) and combined lateral and uplift loads (k_c) are calculated by using Eqs. (5-17), (5-18), and (5-19), respectively, where n_s is the perimeter sheathing-to-frame nail spacing in mm, ρ_o is the percentage of opening in the total wall area and R_L is the ratio of uplift load to lateral load. The modification factor for drywall (k_{dw}) is taken as 1.12 when drywall is present; otherwise it is taken as 1. Similarly, the modification factor for the connection between bottom plate and lower structure (k_b) is calculated using Eq. (5-20) when the connection is established through nails to wood joist system (where n_{bs} = nail spacing between bottom plate to wood joist); otherwise, it is taken as 1 for anchor bolted connection to concrete foundation. Details of wall-foundation connection analysis are presented in Quayyum (2019b).

$$k_{ns} = 119.2(n_s)^{-0.954} \tag{5-17}$$

$$k_o = 0.000053\,\rho_o^2 - 0.0153\,\rho_o + 1 \tag{5-18}$$

$$k_c = 0.0187\,R_L^{\ 2} - 0.1375\,R_L + 1 \tag{5-19}$$

$$k_b = \frac{0.24}{1 - 0.763e^{-0.0015\left[\frac{n_{bs}}{\left(\frac{l}{h}\right)}\right]}} \tag{5-20}$$

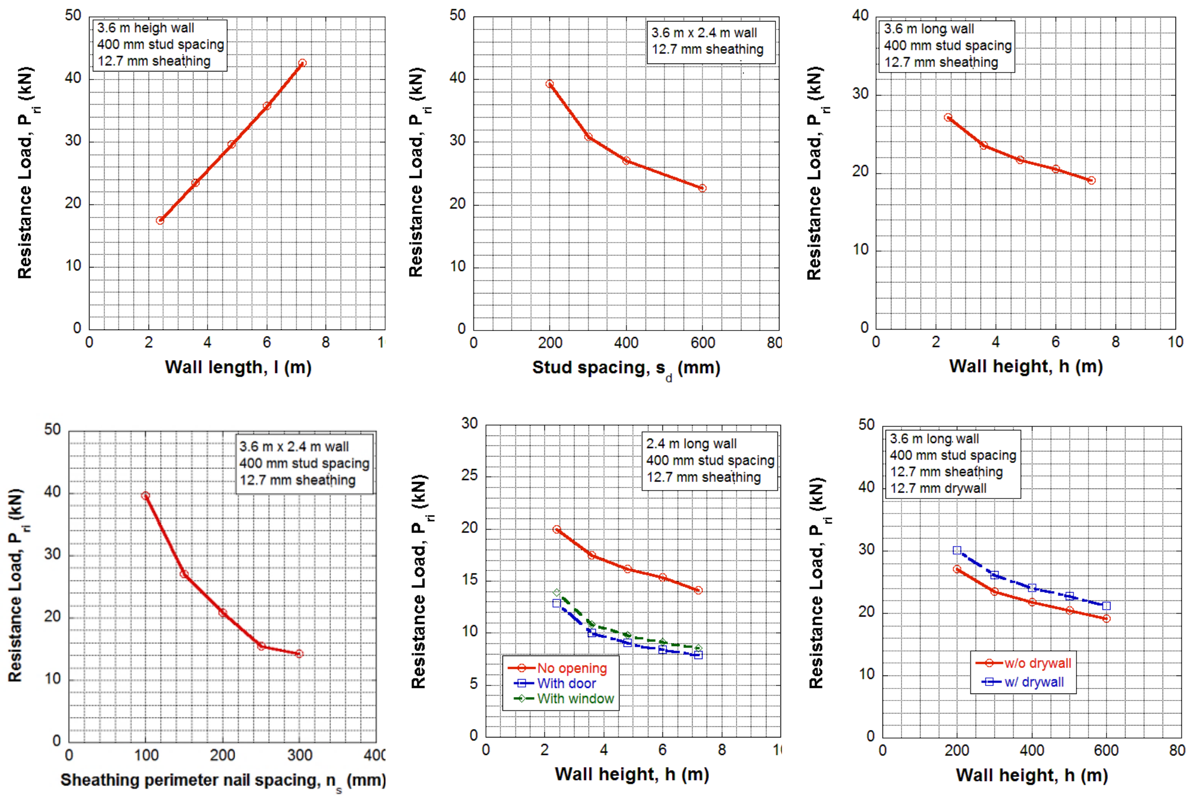

Note: 1 kN = 224.8089 lbf; 1 mm = 0.03937 in; 1 m = 3.28084 ft

Figure 5-32. Sensitivity Analysis of Wall In-Plane Load Resistance

Predictions of the in-plane load resistances derived from the parametric models are verified against experimental and simulated results from the literature as shown in the equity line plots in **Figure 5-33** where it is seen that the models reliably predict the in-plane load resistances of the wood-frame walls of single-family houses.

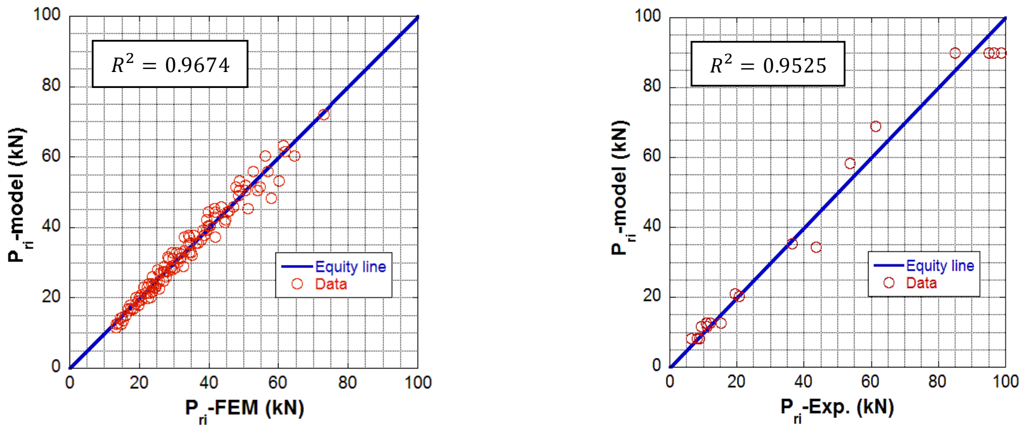

Note: 1 kN = 224.8089 lbf

Figure 5-33. Equity Line Plots Showing IP Load Resistance Comparison

TORDAM Implementation. In-plane-shear failure or racking failure is determined by comparing the in-plane resistance of each wall obtained from the FEA to the computed in-plane load for the wall. In-plane shear loads are determined by the vector sum of the shear and torsional loads. Shear loads computed for each wall from the integrated wall load and the integration of the horizontal components of the roof panel loads.

In-plane resistance of a wall depends on the wall to foundation connection, percent of openings in the wall, presence of drywall, spacing of the studs, spacing of the stud nails and whether the wall has a top support or not. All of the parameters needed to compute the IP resistances are obtained from model inputs except the percent opening and presence of top support. The determination of the percent opening is discussed in the out-of-plane bending failure section. The factor for top support is governed by the whole roof failure and the top plate to stud failure. In the model, a reduction factor of 0.7 is used when the roof to wall connection has failed but the top plate is intact. This factor becomes 0.3 when the top plate to stud connection has failed. The reduction factors are discussed in Quayyum (2019a). In the presence of any uplift load the in-plane shear resistance is reduced by a factor obtained from parametric equation developed from FEM (Quayyum, 2020). The reduction factor is a function of the ratio of the uplift load and in-plane shear load and is capped at 0.5 since no experimental results available for values below 0.5.

5.5.4.3. House System Effects on Wall Failures

As discussed in (Thurston 2003, 2006), the load resistance of a wall increases when it works as a part of the house system instead of a stand-alone wall due to contributions from the roof, side and interior partition walls. To incorporate this increase in the load resistance due to system effects in the parametric models for calculating in-plane and out-of-plane load resistances, further analyses are performed. For evaluating the out-of-plane load resistances of the walls, the displacements in the out-of-plane direction are constrained for the side and top of the wall, and out-of-plane load resistances are calculated based on different support conditions on the sides and top. Hence, there is no need to further analyze the system effect for out-of-plane load resistance of the walls (Quayyum, 2019a).

In order to investigate the system effect (i.e. contribution of roof, side and partition walls on the in-plane load resistance of wood-frame wall) the load resistance is evaluated for a wall as a component of the house system and as a stand-alone wall. The ratio of the load resistance of the wall in a house to that of a stand-alone wall gives the system effect factor to be considered in the calculation of in-plane load resistance of wall in a wood-frame house. In the simulation, the length and height of the wall are varied to study the influence of wall aspect ratio on the system effect. Moreover, while evaluating the in-plane load resistance of a wall as a part of the house system, two cases are considered: 1) the roof is intact indicating system effects from roof, side and partition walls, and 2) the roof is missing indicating system effect from side and partition walls only. In all the analysis cases, it is assumed that each component and the connection between various components of the house are designed based on the recommendations from IRC (2015). Hence, the walls are anticipated to develop ultimate capacity under in-plane lateral loads failing by relative sliding and rotation of the OSB panel.

Based on the finite element analysis results it is observed that failure of the walls occur through relative sliding and rotation of the OSB panels as shown in Figure 5-34(a) – (d) for both a stand-alone wall and a wall as a part of the house system. However, the load resistance increases significantly when the wall acts as a part of the house system either with or without the roof as shown in Figure 5-34 (e) and Figure 5-34 (f) for a house having either a 7.2 m (24 ft) of 14.4 m (48 ft) long wall with a height of 3 m (10 ft). It is found that for a 14.4 m (48 ft) a long wall, the in-plane load resistance increases by 72% compared to a stand-alone wall in presence of roof, side and partition walls (Figure 5-34 (f)). On the other hand, this increase is only 15% when the roof is missing and system effect is provided by side and partition walls only (Figure 5-34 (f)). Likewise, for a 7.2 m (24 ft) long wall, the in-plane load resistance increases by 56% when roof, side and partition walls are present, whereas the increase is only 28% in presence of side and partition walls only (Figure 5-34 (e)).

The system effect increases the in-plane load resistance of wood-frame wall significantly, especially when the roof is in place. The influence of the system effect also varies with wall aspect ratio and top support (roof) condition. Therefore, several analyses have been performed on the house and stand-alone walls by varying the length and height of the wall and changing the top support condition with and without the roof. The system effect factor is evaluated for these walls by taking a ratio of the load resistance of the walls as part of house system to that of stand-alone walls. Figure 5-35 shows the system effect factor plotted against wall aspect ratio $\left(\frac{l}{h}\right)$ for two top support conditions. When the roof is intact, the system effect factor increases linearly with wall aspect ratio (blue dots in Figure 5-35). This is anticipated, since with increasing wall length, the lateral load capacity of walls increases linearly. Moreover, with an increase in the wall length, the number of roof trusses between side walls increases providing more stiffness to the wall system. Hence, based on the FEA data, a linear expression is proposed in Eq. (5-21) for the system effect factor as a function of wall aspect ratio when the roof is undamaged. When roof is damaged, the system effect factor decreases with an increase in the wall aspect ratio as shown in Figure 5-35 (red squares). This is due the fact that when the roof is damaged, side and partition walls are the only component providing the system effect and as the unsupported length of the wall increases, the stiffness of the wall system decreases. Hence, based on the FEA data, the nonlinear expression given in Eq. (5-22) is used for the system effect factor as a function of wall aspect ratio when roof is damaged. Details of the development of these factors are given in Quayyum (2019b).

$$k_{sys} = 0.0398\frac{l}{h} + 1.4477 \quad \textbf{(5-21)}$$

$$k_{sys} = \frac{1}{1-0.35e^{-0.16\left(\frac{l}{h}\right)}} \quad \textbf{(5-22)}$$

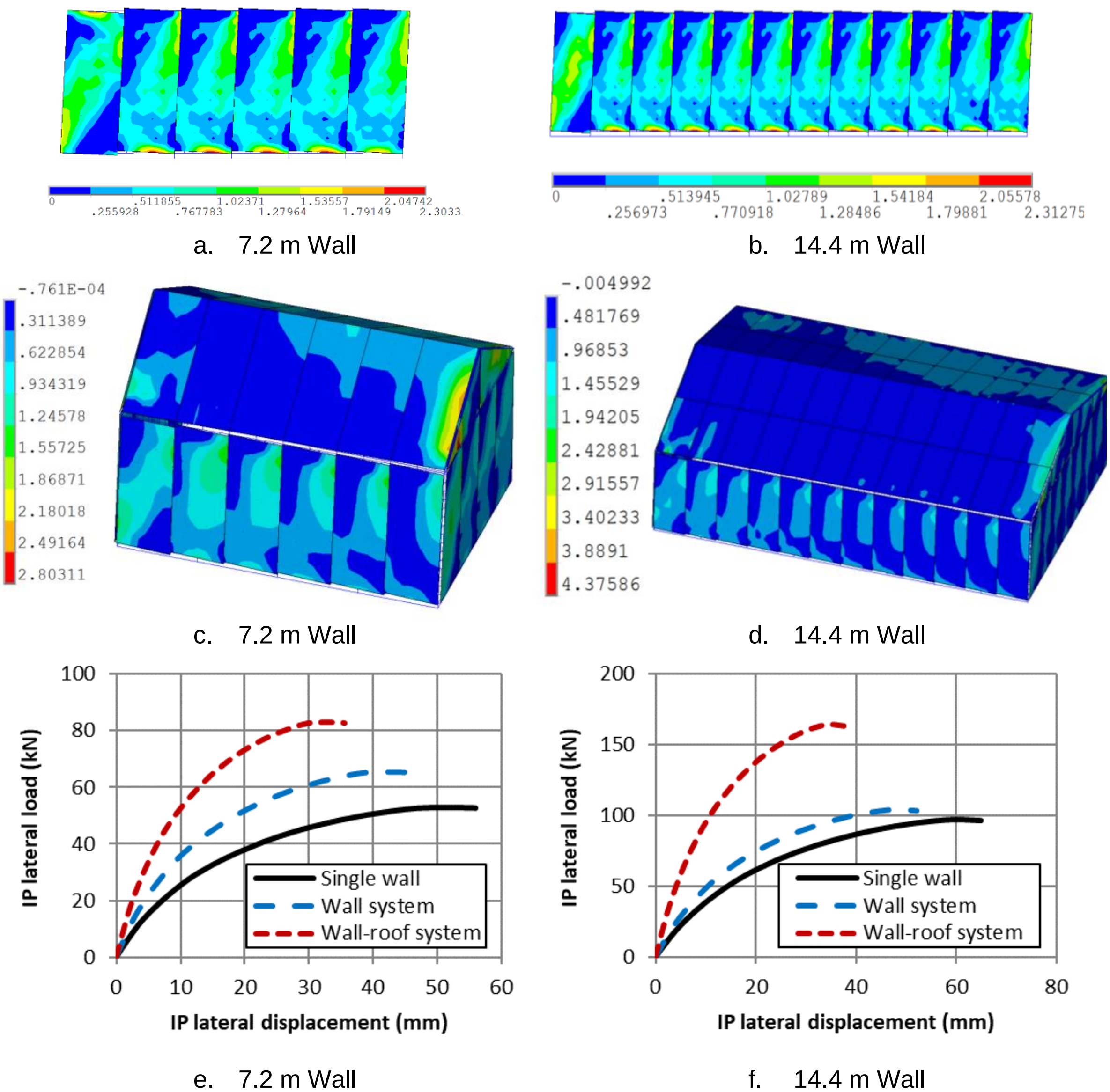

Note: 1 kN = 224.8089 lbf; 1 mm = 0.03937 in; 1 m = 3.28084 ft

Figure 5-34. IP Load Response of Wall from Stand-Alone and Full House Models

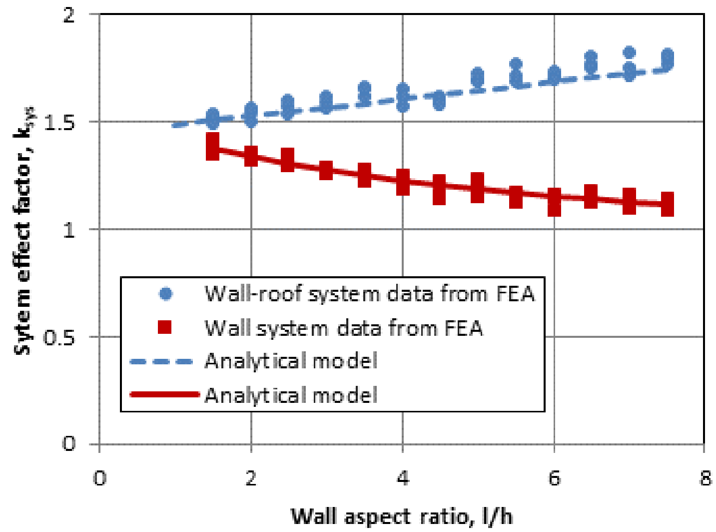

Figure 5-35. Factor to Account for System Effect on IP Load Resistance of Walls

The system effect factor calculated using Eq. (5-21) yields factors varying between 1.48-1.73 for wall lengths ranging between 2.4 m (8 ft) – 15 m (50 ft). This is consistent with the findings of the NAHB Research Center Inc. (2009), where they reported system effect factors based on a review of 42 experimental studies on full-scale house tests. The tested ultimate strengths of the walls are compared to the predicted strengths of the walls by using the Perforated Shear Wall (PSW) Method (Sugiyama 1981) and Segmented Shear Wall (SSW) Method (ANSI/AWC-SDPWS 2015). It is reported that by using the PSW Method (Sugiyama 1981), the system effect factor for 4.8 m (16 ft)-11.3 m (37.7 ft) long walls varies between 1.54 - 1.7. On the other hand, it is found that the system effect factor calculated based on the SSW Method (ANSI/AWC-SDPWS 2015) varies between 1.72 - 1.8 for wall lengths ranging between 1 m (3.3 ft) and 8 m (26.7 ft). These system effect factors are even higher when the same calculations are done using design code and seismic code limitations. Therefore, the system effect factor calculated by the proposed equations (Eq. (5-21) and Eq. (5-22) provide a conservative and reasonable estimate of the increase in the in-plane load resistances of wood-frame walls because of the stiffness contribution from the roof, side and partition walls. In this study, no attempt has been made to separate out the contributions of the roof, side, and partition walls on the system effect factor which will be considered in a future study.

TORDAM Implementation. The in-plane load resistances of walls increase when the roof and the walls are intact. Therefore, a system effect factor based on Eq. (5-21) is applied to the in-plane-shear resistance of a wall. When the entire roof is failed, the system effect factor is determined using Eq. (5-22).

5.5.4.4. Wall Uplift Failure

The wall uplift resistances and failure are modeled for the following two scenarios:

Failure of Top Plate to Stud Connection. The failure of the connection is determined by comparing the failure load with the sampled resistance of the connection. The uplift load acting at the top of each wall section is computed from the share of the vertical component of the pressure load acting on each roof deck element. The net uplift load in the wall section is computed by deducting the share of the roof weight assigned to the section. Four connection options are available. These are 2-16d straight nail, 3-8d toenail, single clip, and double wrap. The resistance of these connections are given Table 5-1.

Failure of Bottom Plate to Stud Connection. The failure of the connection is determined by comparing the failure load with the sampled resistance of the connection. The net uplift load acting in the bottom of a wall section is computed by deducting the wall dead load from the net uplift computed at the top of each wall section. The bottom plate-to-stud connections are modeled using the same four connections used to model the top plate-to-stud connections.

The failure of the top plate to stud connection is evaluated first. If there is no failure, then the bottom plate to stud connection is assessed. A wall is considered to have failed when the bottom plate to stud connection fails. The failure of the top plate to stud connection yields a decrease in the bending resistances of a wall.

5.5.4.5. Wall-Foundation Failure

Failure of foundations, especially failure at the bottom plate to foundation connections, was the main failure mode observed in the damage surveys performed during this project. The failure can be due to splitting of the bottom plate as shown in Figure 5-36 or due to the uplift of the foundation connection as shown in Figure 5-37 and Figure 5-38.

Figure 5-36. Splitting of Bottom Plate at Foundation Connection

Figure 5-37. Uplift Failure of Bolted Connection

Figure 5-38. Uplift Failure of End-Nailed Connection

Three types of foundation connections are considered in the model: cut-nails, shot-pins, and anchor bolts. The net uplift load computed at the bottom of each wall section is used to determine the failure of the connection by comparing it with the resistance of the connection. The statistics of the uplift resistances for the cut-nail and shot-pin are given in Mahaney et al. (2002), Filiatrault, A. (Ed.). (2001), and Hairstans (2007). The statistics of the resistances for the (1/2 inch (1.3 cm)) anchor bolt are given in NAHB (2010). The failure of the bolted connection includes splitting of the bottom plate, concrete spall, and tension failure of the bolt. The failure model currently uses failure of bolted connection with nuts and cut washers. The model does not consider anchor bolts without nuts and washers, or anchor bolts with square washers.

Table 5-1. Values of the Test-Based Resistances Used in Damage Model

Resistance type	Connection type	Mean	COV	Source
Roof deck	6d common nail @ 6/12 spacing	65 psf	0.12	Cunningham (1993), Mizzel (1994), Shane (1996), Rosowsky and Schiff (1996)
	8d common nail @ 6/12 spacing	122 psf	0.12	
	8d common nail@ 6/6 spacing	215 psf	0.12	
	8d ring shank nail@ 6/6 spacing	469 psf	0.12	
Roof to wall connection	8d common toenail	208 lb	0.16	Canfield et al. (1991)
	16d box toenail	550 lb	0.26	Judge and Reinhold (2002)
	Single clip	866 lb	0.15	FEMA(2011)
	One-sided wrap	1200 lb	0.30	
	Two-sided wrap	2400 lb	0.30	
Strength of stud connection with top and bottom plate	Straight nail	218 lb	0.26	Marshall (1983), Rammer et al. (2001)
	Toe-nail	288 lb	0.30	Marshall (1983)
Uplift strength of foundation connections	Anchor Bolt	5000 lb	0.05	NAHB (2010)
	Shotpin	650 lb	0.38	Mahaney et al. (2002)
	Cut nails	325 lb	0.15	Hairstains R. (2007)
Shear strength of foundation connections	Anchor Bolt	4700 lb	0.10	NCMA(2013)
	Shotpin	180 lb	0.10	Mahaney et al. (2002)
	Cut nails	180 lb	0.10	Hairstans R. (2007)

Note: 1 psf = 47.88026 Pa; 1 lb = 0.4535924 kg

In addition to the failure of the foundation connection by uplift, sliding and overturning of the whole building are also checked. The sliding loads are calculated from shear and torsional loads on the building. The resistance for sliding failure is calculated from the shear resistances of the foundation connections (given in Table 5-1) and the static frictional resistance. We used a value of 0.62 for the coefficient of friction between concrete and wood (https://www.engineersedge.com/coefficients_of_friction.htm) in conjunction with the net gravity load of the building (i.e. gravity load of the building minus the uplift load on the building) to determine the dry static frictional resistance to sliding. Sliding failure is checked for both principal directions.

Overturning resistances are modeled and failure due to overturning is checked. We modeled a rigid body rotation for overturning failure with the assumption that the house remains intact during overturning. Overturning resistance is computed using the uplift resistance of the foundation connections and the restoring moment due to gravity. Overturning failure is checked for both principal directions. Rigid body overturning failure is rare during windstorms. Quantifying the frequency of failures due to overturning is challenging since no damage states for FR12 in the EF-Scale include this failure mode. As such, the overturning failure is checked but not used in the damage scoring for the purpose of estimating wind speeds.

5.5.5. Small Interior Room

In the progressive failure modeling, we included a small interior room since this is a potentially important feature of the EF damage scale DODs for FR12. In the DOD progression, the transition from DOD 8 to DOD 9 requires failure of all walls, including those of small interior rooms. In the progressive failure model, we begin to apply loads to a small interior room once the exterior walls have failed. This section summarizes how we model the loads and resistance on small interior rooms. We use the Joplin tornado data to develop information regarding the size, top support, and debris pile-up adjacent to FR12's with DOD 8 classifications (which includes standing small interior rooms).

Joplin Tornado Data Analysis. A total of 143 houses from the NIST Joplin Tornado Damage Database (ref.) were extracted for photograph review for the conditions: (1) greater than 80% exterior wall damage and (2) small interior rooms still standing. Of these 143 houses, 86 were found to meet these criteria and have photographs with enough clarity to complete the review.

A subset of the interior picture review data was used to develop information to inform the modeling of interior rooms in TORDAM. This population was limited to homes that had (1) an estimated wind speed greater than 160 mph (71.5 m/s), and (2) were found to be truly interior rooms (i.e. the room had no exterior walls). This reduced the data population to 28 houses. Figure 5-39 and Figure 5-40 show example photos from four of the 28 houses in the reduced dataset. The house numbers in the photos refer to the house numbers as reported in the NIST Joplin Tornado Damage Database.

Figure 5-39. Example Aerial and Elevation Photos of House 2818 (top) and 803 (bottom) with Interior Room Standing after Joplin Tornado (Scott, 2021)

Figure 5-40. Example Aerial and Elevation Photos of House 1661 (top) and 2819 (bottom) with Interior Room Standing after Joplin Tornado (Scott, 2021)

Aerial and elevation photos of these 28 houses were evaluated to determine the overall footprint area of the interior rooms left standing as a percentage of the total building footprint area and the average depth of debris adjacent to the room as a percentage of the wall height. Average debris depth around the interior room is used in the interior room wall load calculations.

The key points developed from the photo review of the final set of 28 houses include:

1. Average area of an interior room was 9.7% of the plan area of the building. The CDF of the standing interior room area, as a percentage of home area, is shown in Figure 5-41.

2. Average depth of debris over all walls was is just over 15% of the wall height, or about 1.65 ft (0.5029). The CDF of debris depth, as a percentage of wall height, is shown in Figure 5-42.

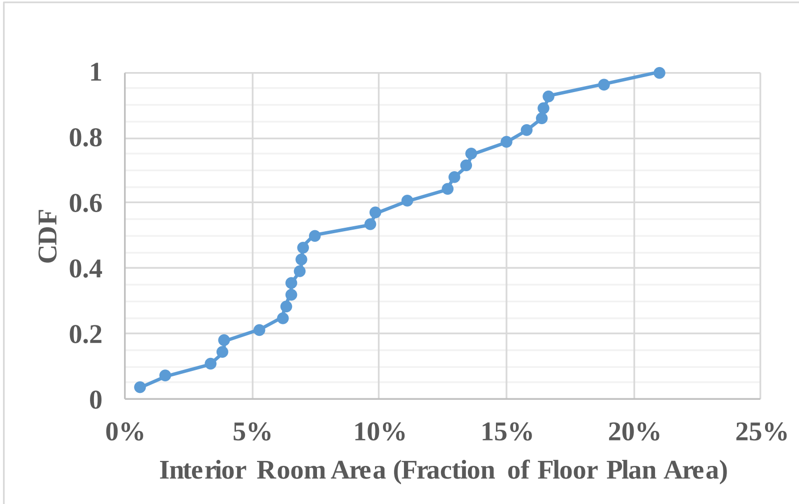

Figure 5-41. CDF of Interior Room Area as a Fraction of Floor Plan Area

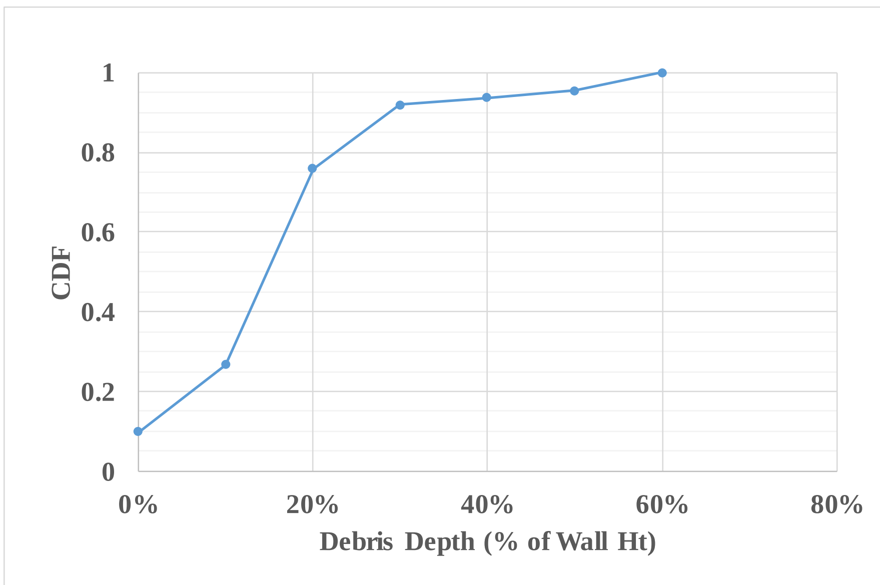

Figure 5-42. CDF of Debris Depth as a Percentage of Wall Height

Small Interior Room Model. Based on the Joplin data, summarized above, we implemented a small interior room model into TORDAM. The interior room is modeled as a square room in the center of the house plan. The plan area of the interior room is sampled from the distribution shown in Figure 5-41. The height of the room is modeled as 8 ft (2.4 m). The walls are considered fully sheathed with drywall and have an opening of 30% of the wall area to account for the presence of doors.

The height of the debris pile up is computed from the cumulative distribution plot in Figure 5-42. The maximum height is set to 4.8 ft (1.46 m), which is the largest height of the debris pile up found in the Joplin data. The debris pile-up height is used to compute the effective wall load which is the wind load on exposed wall area and determine the center of pressure of the horizontal wind loads. Possible bracing effects from the debris ramp (as seen for some of the rooms in Figure 5-39 and Figure 5-40) are ignored in the resistance calculations.

We consider in-plane-shear and overturning failure modes to determine the failure of the small room. The out-of-plane bending failure of the walls is not considered due to their small size. The in-plane resistances are based on the FEM resistance model discussed in Section 5.5.4.2. The overturning resistance is based on nail pullout resistance of the bottom plate. The bottom plate is connected to the wall studs with 2-16 straight nails. The nail pull out resistance is obtained from Marshall (1983).

The computation of wind loads and failures of internal rooms initiates when the vast majority of exterior walls (about 75% to 95%) have failed.[75] The in-plane wind loads that are acting on the walls are computed using the wind speed and direction at the center of the house and drag coefficients for a box (Blevins, 2003). Computation of in-plane wind loads considers the debris pile up on the walls, which is discussed above. Computation of overturning load also considers debris pile up.[76] In this case, the center of the load shifts upward from the center of the wall. The in-plane and overturning loads are computed for each of the two principal directions. A load interaction formula is used to combine the loads and assign them to the appropriate load resisting elements.

5.5.6. Epistemic Structural Quality Factor

We introduced an epistemic structural quality factor for all metal connection resistances in the house model to reflect uncertainty in "as-built" construction quality. That is, since the resistance statistics are based on laboratory tests, we introduced an epistemic resistance factor that reflects field installations such as: missing or insufficient number of nails in a strap, or clip connection; improperly driven toe-nail connections; fasteners that split the wood material: insufficient spacing of connections; use of wrong nail sizes, etc.

Based on our experience in FR12 inspections (e.g., Twisdale et al., 2002), we used judgment in modeling this structural resistance "quality" factor to reflect as-built vs. laboratory resistances. We modeled the structural quality factor as $Y = 1.1-X$ shown in Figure 5-43, where is X is a lognormally distributed variable with a mean of 0.21 and a COV of 0.31. The median value of this model is 0.9, which means than ½ of the sampled values will be less than 0.9 and ½ greater. We truncate the sampled resistance factor to the range (0.7, 1.05). The model allows the sampled resistance factor to exceed 1 about 1% of the time. This epistemic factor is sampled once for each house damage simulation, which means that the factor is applied in a correlated fashion across all metal connectors. The sampling of randomness proceeds independently for each connection (see Table 5-1) to produce a realized strength, which is then multiplied by the sampled epistemic quality factor for that house simulation.

[75] See Table 6-4.
[76] We performed a sensitivity analysis (with and without debris pile-up around the small interior room). We found only modest differences in the results due to the higher center of pressure but lower net drag force for the debris pile-up simulations.

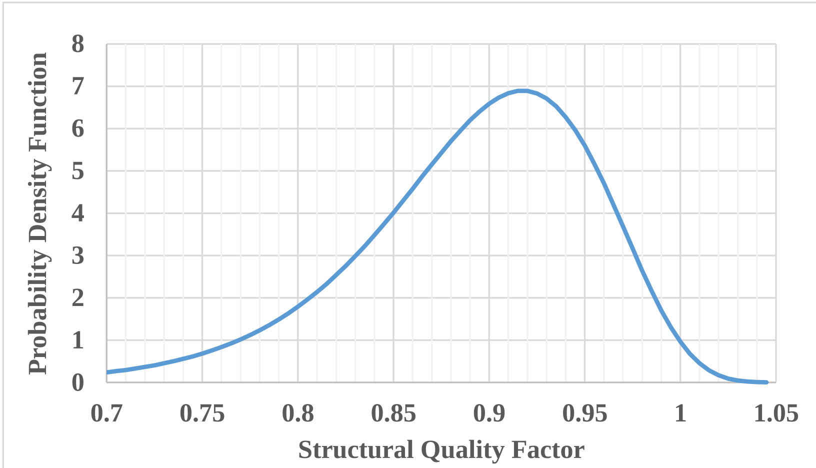

Figure 5-43. Probabilistic Model for Structural Quality Factor (Y)

5.6. Tornado Fragility Examples

In this section, we illustrate several component fragilities developed with the TORDAM implemented FR12 progressive failure model. We also illustrate specific fragilities developed from the TORDAM methodology for a commercial building that was damaged in the Joplin Tornado.

5.6.1. FR12 Examples

Using the TORDAM FR12 model described herein, we have developed fragility plots for roof cover, roof deck, wall and fenestration for several example houses. The house cases include both simple (Class 1, 13, and 21) and complex (Class 23, 35, and 43) gable shape houses and three strength categories (weak, mid and strong).[77] Descriptions of these house cases are given in Table 5-2. In these simulations we use a fixed orientation of the building (i.e. building is oriented such that its length is parallel to the East). Fragility plots are shown in Figure 5-44 and Figure 5-45. Fragilties are expressed as average percentage of damage of the respective components. The number of samples used for averaging varies with wind speed bins and house cases. We used 6000 simulated tornadoes and 30 replications of each house cases per tornado. For simple gable house cases, the total number of roof cover elements, roof deck panels, wall sections and fenestrations are 1464, 64, 8 and 15 respectively. For complex gable house cases, the total number of roof cover elements, roof deck panels, wall sections and fenestrations are 1947, 128, 15 and 15 respectively.

[77] These houses correspond to Houses 1, 13, and 21 for simple plan and 23, 35 and 43 for complex plan in Table 6-7.

Table 5-2. House Cases used for Fragility Comparisons

FR12 Class	Description	Roof Cover	Roof Deck to Roof Truss Connection	Roof to Wall Connection	Wall Sheathing	Stud to Bottom Plate Connection	Foundation Anchor	Opening Protection	Garage Door Strength
1, 23	Weak Gable	Asphalt Shingle 110	6d Common Nail, 6/12 spacing	3-8d Toenail	Minimal	2-16d Straight Nail	Nail	None	Standard
13, 35	Mid Gable	Asphalt Shingle 110	6d Common Nail, 6/12 spacing	3-16d Toenail	Sheathed	2-16d Toe Nail	Bolt	None	Standard
21, 43	Strong Gable	Asphalt Shingle 130	8d Ring Shank Nail, 6/6 spacing	Double Wrap	Sheathed	Double Wrap	Bolt	Yes	High Wind Design

Small Gable. For the simple house plans, the roof deck fragilities in Figure 5-44 move to the right with the increasing house strength. The weak house has 6d nails for roof deck attachment and 8d toe nails for the roof-to-wall connection. Due to the weak roof-to-wall connection, the roof deck failure is dominated by the whole roof uplift failure, rather than the failure of individual pieces of roof sheathing.

The mid-strength house also has 6d roof deck nails, but the roof deck fragility curve is shifted slightly to the right. This shift results from less frequent whole roof failures due to 16d toe nails used to connect the roof to the wall.

For the strong house, the roof fragility curve shifts to the right. This shift is due to the stronger roof deck attachment with tighter nail spacing and stronger roof-to-wall connections. The wall fragilities also show a rightward shift with the increased house strength. The weak house has partially sheathed walls whereas mid and strong cases have fully sheathed walls. The wall fragility curves shift to the right when the walls are fully sheathed. The wall fragilities are also influenced by the strength of the roof-to-wall connection.[78]

The fragilities for the fenestration damage in Figure 5-44 include pressure damage and WBD damage. In the strong house case, the fenestrations are protected by shutters, and the garage doors are strong. The strong house fenestration fragility curve reflects these conditions. The mid strength case has slightly higher fragilities than the weak case. This difference is due to the wall strength and the method for computing fenestration failure. Since the fenestration fragilities reflect only the failure of fenestration, either by debris impact or wind pressure, early failure of walls reduces the count of fenestration failures. Hence, the fenestration fragility curve appears slightly stronger for the weak house.

Complex Gable. Similar observations are noticed for the complex house cases shown in Figure 5-45. The fragilities of the complex houses show that these houses are somewhat stronger than the simple houses in their respective strength categories. This is due to the complex geometry and presence of multiple roofs. The complex geometry and the complex roof structure requires strong winds from more directions and over a larger area to produce equivalent levels of damage vs. the simple plan house cases.

[78] Wall resistances reduce with whole roof failure (loss of top support).

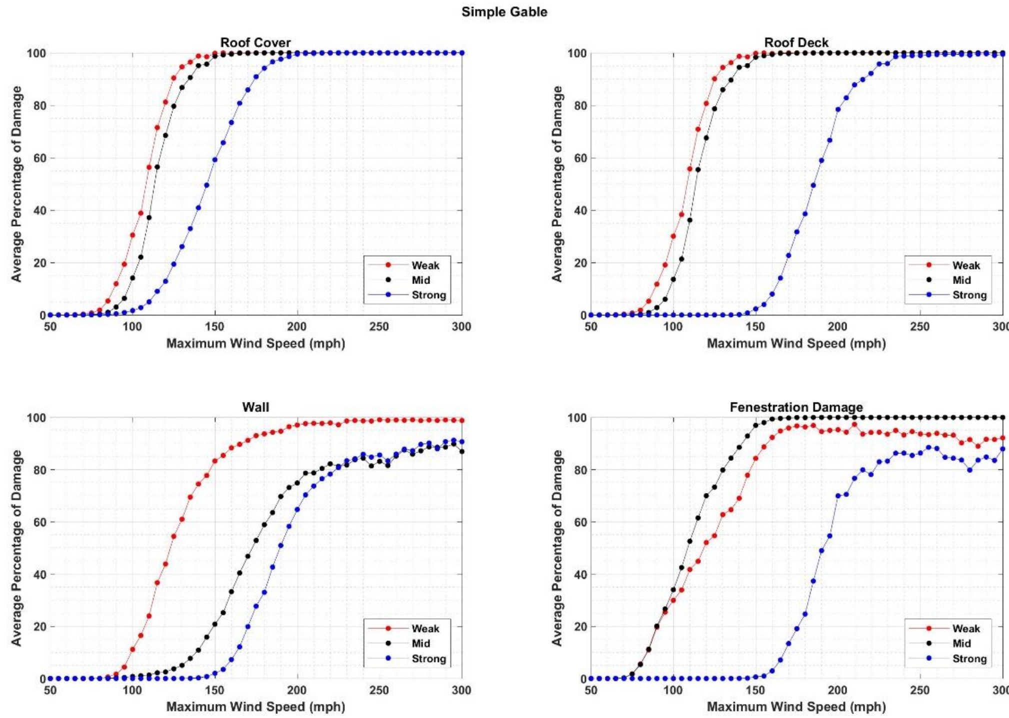

Note: 1 mph = 0.44704 m/s

Figure 5-44. Small Rectangular Gable House Fragilities

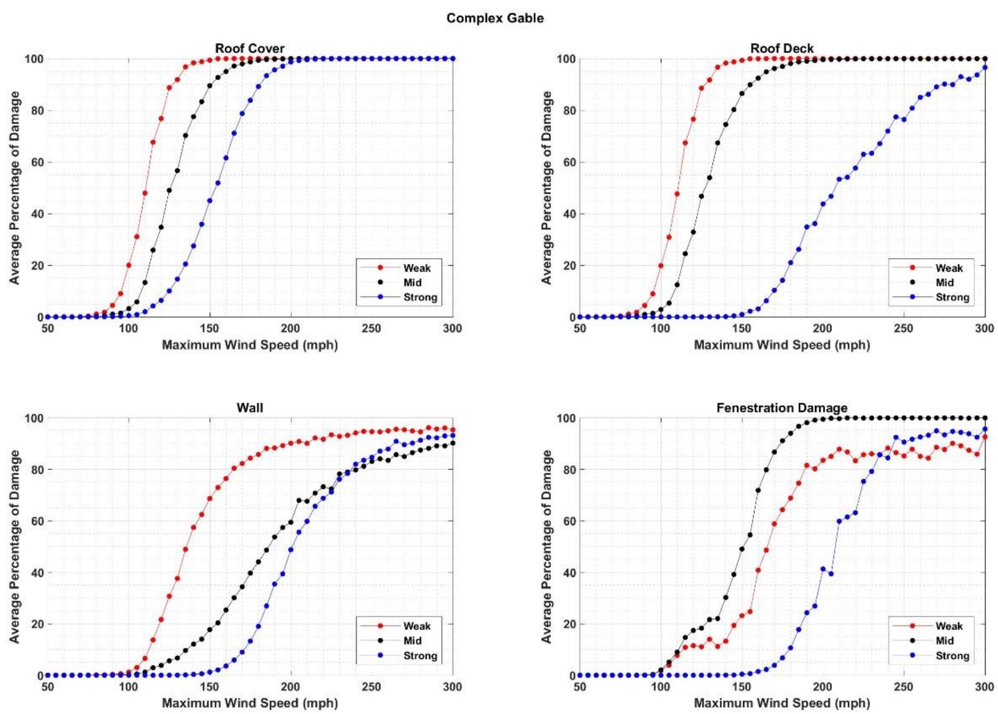

Note: 1 mph = 0.44704 m/s

Figure 5-45. Complex House Fragilities

Tornado, Hurricane, and Straight-Wind Fragilities. Tornado fragilities are compared with those obtained from hurricane and straight wind damage simulations in Figure 5-46 through Figure 5-48.[79] The hurricane and straight-wind simulations are carried out in open terrain which produces wind speeds at the roof height that are (about 15%) less than the reference wind speed at 33 ft (10.1 m).

Figure 5-46 shows the comparison of the roof deck fragilities for the weak simple gable house and the weak complex gable house cases given in Table 5-2. We see that the tornado fragility curve for the simple plan house is about 20 to 25 mph (8.9 to 11 m/s) shifted to the left of the other storms. This shift is due to the fact that tornadoes have vertical winds that enhances the roof deck wind load. The tornado wind loads are also enhanced by a vertical velocity profile and the effects of APC. Thus, for the same reference wind speed, building components experience higher wind loads in tornadoes than in hurricanes or straight winds. The tornado simulations also use an enhanced missile model compared to hurricanes and straight winds. In Figure 5-46, fragilities for hurricanes are slightly weaker than straight winds due to wind directionality effects.

For the complex plan house in Figure 5-46, the tornado fragility curve has a much steeper slope than the non-tornadic storms. This result is due to the fact that the complex plan house has multiple roofs and wind directionality effects are different for each roof. Therefore, strong winds from multiple directions are needed to fail a large number of roof deck elements for this house. In the simulated tornadoes, strong winds can come from multiple directions in the same storm since the structure is located within the tornado core in the simulations.

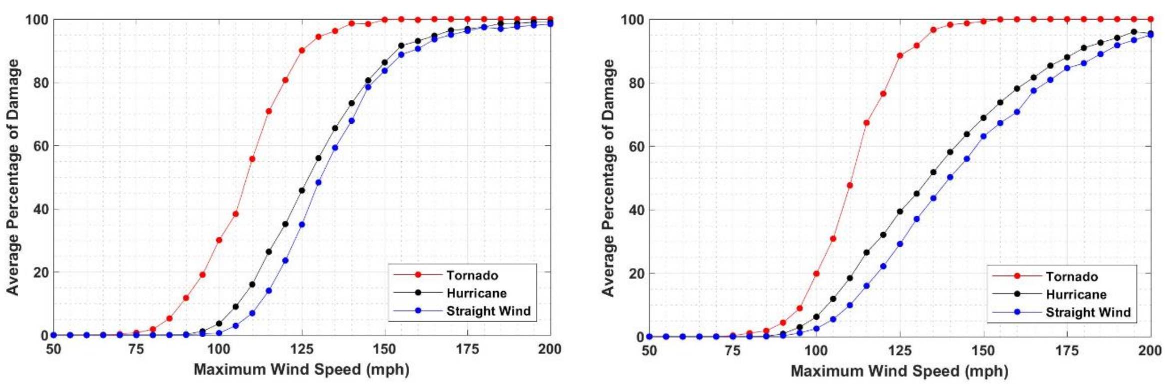

a. Simple House b. Complex House

Note: 1 mph = 0.44704 m/s

Figure 5-46. Comparison of Roof Deck Fragilities for Different Storm Types

Vertical Profile Sensitivity. We performed a sensitivity analysis for the simple and complex weak gable cases in which the hurricane and straight wind simulations used a vertical profile of horizontal winds, similar to tornadoes. Figure 5-47 shows that both the hurricane and straight wind fragility curves are shifted to the left compare to those shown in Figure 5-46. This shift is about 15% of the wind speed. Tornado fragilities for the simple case remain weaker than the other fragilities. For the complex case, tornado fragilities are stronger than the hurricane and straight wind when the wind speeds are lower than 90 mph (40.2 m/s). This

[79] These simulations use generic locations; the straight-wind simulations also use a generic wind-direction distribution.

reduction reflects the contributions of small tornadoes with a small RMW at these wind speeds.[80]

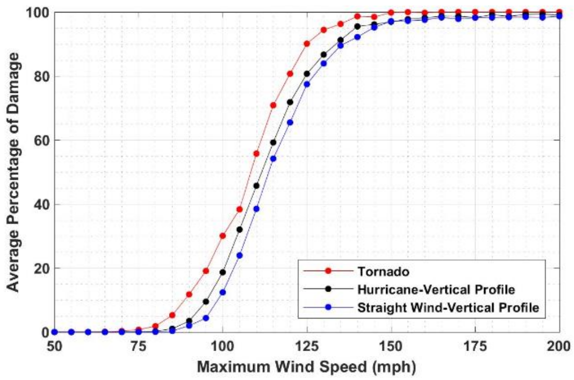

a. Simple House

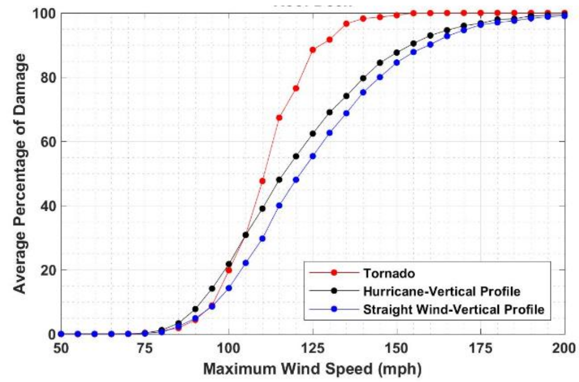

b. Complex House

Note: 1 mph = 0.44704 m/s

Figure 5-47. Comparison of Roof Deck Fragilities for Sensitivity Case 1

Tornadoes Without Vertical Winds or APC Sensitivity. This sensitivity removed the vertical winds and APC effects from the tornado simulations and used the same vertical profile for all hazards. Hence, we have only the wind field, RMW, and storm directionality distribution differences. Figure 5-48 shows these comparisons. The results show that the order of weak-to-strong fragilities is: hurricane, straight wind, tornado. Hence, the tornado fragilities appear stronger (lower damage for a given wind speed). This order reflects differences in directionality and RMW. Hurricanes have more wind directionality in an event than straight winds whereas tornadoes have about the same directionality as a hurricane, but a much smaller RMW.[81]

The comparisons in Figure 5-47 and Figure 5-48 are for only for weak roof decks and reflect a single generic case of typical hurricane, straight wind, and tornado path directionality distributions. Hence, these plots should be viewed as one example only, which is not a site-specific analysis.

[80] As a result, the whole structure may not experience the same maximum wind speed as for that in hurricanes or straight winds. The complex house has larger building footprint than the simple house.
[81] Hence, the RWS definition impacts the fragility plot comparisons in these figures.

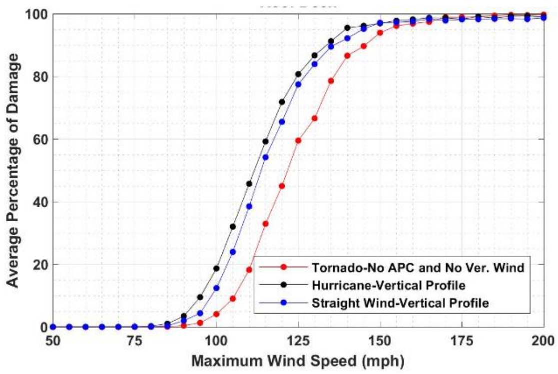

a. Simple House

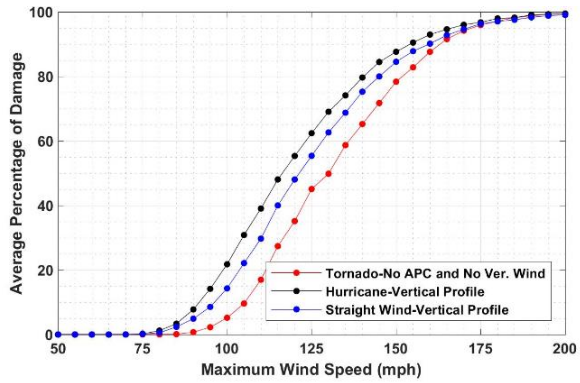

b. Complex House

Note: 1 mph = 0.44704 m/s

Figure 5-48. Comparison of Roof Deck Fragilities for Sensitivity Case 2

5.6.2. Commercial Building Example

The tornado damage model described herein was previously applied to a commercial building as an example validation for a FEMA best available refuge area project (ARA, 2016). The validation was carried out for two large commercial structures (Walmart Supercenter and Home Depot) that collapsed during the 2011 Joplin tornado. The Walmart store was partially collapsed with the failure of a significant portion of the roof and walls. The structure was located on the left (weak) side of the tornado centerline.

The construction characteristics of the buildings were obtained using the engineering drawings and damage assessment reports. These characteristics, including the roof-to-wall connection, type of roof and wall systems, were used to create the TORDAM model. Reasonable values of the tornado characteristics including RMW, maximum wind speeds and location of the structure relative to the tornado centerline were obtained from the NIST NCSTAR3, Joplin Tornado Investigation and other Joplin studies were used in the damage model.

The damage model reasonably predicted the observed damage as seen in Figure 5-49. The comparison of the damage picture on the left with those in the middle and the right shows the model reasonably predicts wall and roof failures compared to the observed damage. The picture on the left includes the model-predicted probability of failure of different walls (shown in red inside yellow highlighted text boxes). The plan view of the damaged area shows that the walls on the south side of the building collapsed, along with a significant portion of the east side walls, and a small portion of the west side walls. The results from our probabilistic analysis also show higher probability of wall damage (i.e. greater than 0.5) on these sides.

The middle picture in Figure 5-49 shows the probability of failure of the roof (shown in black inside yellow highlighted text boxes). The portion of the roof on the south and the southeast side of the building shows higher probability of failure (i.e., greater than 0.5) which resembles the observed damage.

The picture on the right side of Figure 5-49 shows section of the roof with higher probability of failure. In the probabilistic analysis, we positioned the south wall of the building on the left side of the tornado centerline. We used variable positions of the tornado centerline with respect to the south wall of the building, variable RMW and inflow (based on tree-fall studies by NIST, 2014 and Karstens et al., 2013) and variable maximum wind speeds.

A similar analysis was carried out for the Joplin Home Depot. We obtained reasonably good comparisons for observed vs. predicted damage.

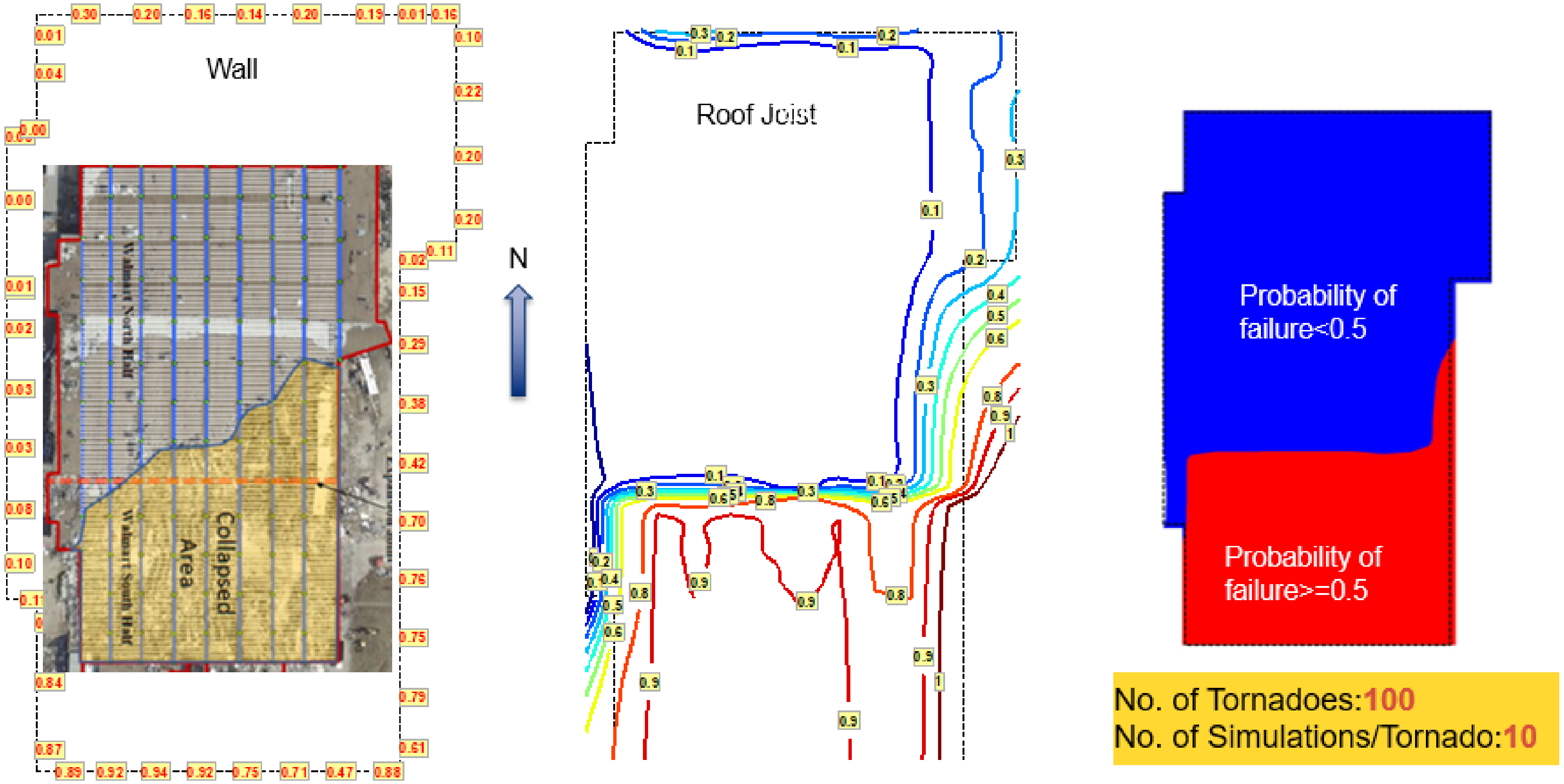

Figure 5-49. Comparison of Model Predicted Damage with the Observed Damage of Walmart Supercenter in Joplin Tornado

6. Engineering-Derived EF-Scale Wind Speeds

6.1. Overview

This section develops engineering-derived tornado wind speeds for single-family residential structures. The methodology in this section tackles a main technical challenge in the quantification of wind speeds from observed damage: how to model and analyze the separate contributions of the variability in tornado wind characteristics, the variability in structure position within the tornado path, and the variability in loads and structural resistances. The analysis framework uses conditional probability concepts to decipher these variability contributions and produce consistent estimates of wind speeds given an observed damage state. Through application of this method to the training, protocols, and context of the Enhanced Fujita (EF) Scale system, the goal is to develop wind speed distributions for the EF-Scale's Damage Indicators/Degrees of Damage (DIs/DODs) commonly used to rate tornadoes.

The wind speeds developed in this section are based on ARA's engineering modeling system, as adapted to tornadoes in Section 5. We apply the method for single-family residential (SFR) construction, which corresponds to the EF-Scale Damage Indicator (DI) denoted as One- or Two-Family Residence (FR12). FR12 are one of the most common DIs used in wind speed estimation in the EF-Scale and essentially all severe tornadoes rated EF4 or EF5 are based on observations of damage to FR12.

6.1.1. Background

Fujita introduced the concept of rating tornadoes based on observed damage in 1971 (Fujita, 1971). Fujita's method of damage-derived intensity classification used photos and brief word descriptions to describe typical damage for each Fujita-, or F-Scale, intensity level. The Enhanced Fujita (EF) Scale rating system was developed through an expert elicitation process in 2004 (TTU, 2004, 2006). The EF-Scale includes 28 damage indicators (DIs), each with various degrees of damage (DOD), and subjectively estimated wind speed ranges for each DOD. The EF-Scale was officially adopted by the National Weather Service (NWS) in 2007 and implemented into the NWS's EF-Scale Toolkit (Ladue and Mahoney, 2006). These tornado damage intensity scales and their associated deterministic and non-overlapping wind speed intervals are shown in Table 6-1. For reference, we also show a simplified engineering-derived Bayesian update of the F-Scale wind speeds (termed F′), which was suggested by Twisdale in 1978 (Twisdale, 1978 and Twisdale et al., 1978). The 1978 F′ wind speeds are remarkably similar to the EF2, EF3, EF4, and lower bound EF5 wind speeds developed in 2004. Note that the wind speeds in the F-Scale were said to be fastest ¼-mile wind speeds, and those in the EF-Scale were based on 3-second gust speed. The important and continuing role of damage-based tornado intensity ratings in providing data for risk assessment of tornadoes is discussed by Edwards et al. (2013).

Table 6-1. Tornado Damage Intensity Wind Speed Scales (mph)

Damage Intensity Scale	F (Fujita, 1971)		F ' (Twisdale, 1978)		EF (TTU, 2004)	
	Lower	Upper	Lower	Upper	Lower	Upper
0	40	73	40	73	65	85
1	73	112	73	103	86	110
2	112	157	103	135	111	135
3	157	206	135	168	136	165
4	206	260	168	209	166	200
5	260	318	209	277	≥ 200	
All	40 - 318		40 - 277		65 - 200+	

Note: 1 mph = 0.44704 m/s

The significance of tornado damage ratings and the use of National Oceanic and Atmospheric Administration's Storm Prediction Center (NOAA's SPC) tornado database (NOAA, 2016a) to develop tornado hazard wind speeds for engineering design and risk assessment were highlighted by Twisdale (2010a, b) at the first EF-Scale Stakeholders Meeting. Tornadoes are generally considered to be the ultimate wind hazard for most regions in the United States. New efforts are underway to develop standards for tornado wind speed estimation (LaDue, 2016), tornado hazard maps for the U.S. (Phan et al., 2016), and tornado-resistant design of buildings and other structures (Kuligowski et al., 2014). In the nuclear power industry, tornado design requirements (e.g., US Nuclear Regulatory Commission (NRC) Reg. Guide 1.76 (USNRC, 2007) and ongoing safety risk assessments (ASME/ANS, 2013) demand consideration of extremely rare tornado frequency levels (1E-07 per year).

There are many issues with damage observations that can make them highly uncertain and unreliable in terms of a field-based intensity rating system. These challenges have been documented in numerous papers (e.g., Phan and Simiu, 1998a, b). A well-recognized and long-term challenge in estimating wind speeds from damage has been how to decipher the contributions of the variability in tornado wind characteristics from the variability in structural loads and response (NOAA, 2003). That is, was the observed damage caused by low winds-low resistance, medium winds-medium resistance, or high winds-high resistance, and so forth? Until we can answer such questions, tornado intensity ratings make tornado wind speed climatology development more of a subjective exercise than a scientific one. This issue permeates the practical application and interpretation of any damage-based intensity scale and one can see its nuances throughout EF-Scale training materials (NOAA, 2008).

Another challenge in estimating tornado wind speeds from damage regards the spatial scale of damage over which the tornado wind speeds are estimated. For cases where the DI characteristic horizontal dimension is about the same or greater than a tornado's radius of maximum winds (RMW), looking for DI confirmation outside of RMW will lead to an underestimate of the peak wind speeds. Another issue is how to best deal with multiple nearby DIs and the potential for confirmation or conflict that results from similar or different levels of damage. The NWS training considers several of these challenges through examples of "confirmation" and "exposure" (e.g., see Ladue and Ortega, 2008). A major bias regarding the underestimation of intensity is also introduced when "wind speed-limited" DIs are used to rate a tornado's intensity.[82] Without more guidance, standards, and comprehensive reporting of intensity rating data, consistent intensity rating for climatological modeling is impossible.

A unique aspect of the approach is the simulation of variabilities (randomness and modeling uncertainties) in each of three critical areas that affect the DOD: (1) tornado strike[83], (2) tornado wind characteristics, and (3) structural characteristics and strength. The analysis framework uses conditional probabilities to decipher variability contributions and to process the data in two distinct steps. In this manner, we correctly model both: (1) the forward process of calculating damage from simulated tornadoes, and (2) the reverse process of determining wind speeds from a field-observed damage state. By applying this method to the training, protocols, and context of the EF-Scale system, we are able to develop wind speed probabilities for discrete wind speed bins (probability mass functions (PMFs) and cumulative mass functions (CMFs), e.g., see Drake, 1967)) for FR12s. The developed wind speed PMFs provide the probabilistic quantification of wind speed given the modeled variabilities in tornado strike, wind characteristics, and structural resistances/failure modes.

6.1.2. EF-Scale Wind Speed Estimation Process

As discussed in Section 1.3.7, a fundamental goal of this project was to develop engineering-derived tornado wind speeds for use in engineering design and safety analysis. Section 5 describes the basic engineering models used in this project to estimate damage from tornado strikes on houses. This section describes how we used the DPMs to estimate wind speeds corresponding to the EF-Scale FR12 DODs. The estimation of wind speeds from observed damage is not the same problem as developing fragilities. Wind speed is the independent variable for fragility computations and damage is the independent variable for wind speed estimation. The conditional probability formulation requires reversal for the latter.

Figure 6-11 summarizes the process used to estimate EF-Scale wind speeds. We term these updated wind speeds EF* to distinguish them from the EF-Scale wind speeds in Table 6-1. The main data sources for this work includes the EF-Scale documentation (TTU, 2006), NOAA's training and documentation regarding implementation of the EF-Scale, and NOAA's Damage Assessment Toolkit (DAT). From those main data sources: we analyzed the DAT data to quantify both damage indicator (DI) frequency and load path quality; developed an engineering interpretation of the FR12 degrees of damage (DOD); and applied the damage methodology in Section 5 to multiple FR12 engineering models.

The use of Bayes Theorem to reverse the conditioning from forward fragility simulations to estimation of wind speeds requires the use of a "prior" estimate of tornado wind speed frequencies. Considering radar estimates of extreme tornadic wind speeds, we develop a range of possible priors and use an epistemic weighted prior for the final EF* wind speed calculations. Due to the complexities of tornado interactions with DIs, lack of detailed structural information on damaged DIs, and few direct measurements of wind speeds at locations of surveyed damage, the estimation of wind exceedance frequencies (WEFs) for extreme tornado wind speeds requires numerous judgments in the modeling process. Our

[82] Many of the DIs in the EF-Scale are wind speed-limited in that the maximum possible EF rating is less than EF5, for example a destroyed barn maxes out at EF2.
[83] By tornado strike, we include random variables such as tornado path direction, building azimuthal orientation, position of tornado centerline relative to the DI, radius of maximum winds (RMW), translational speed, inflow, etc.

goal was to use a rational framework on which to integrate available data, detailed engineering models, and judgments.

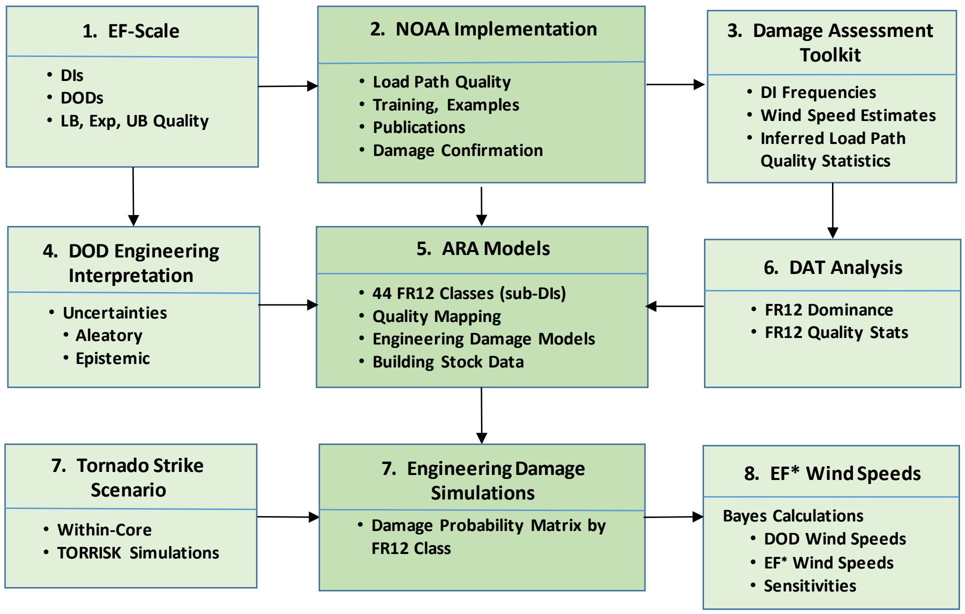

Figure 6-1. EF-Scale Wind Speed Estimation Process

6.1.3. EF-Scale DIs Commonly Used in Wind Speed Estimation

The EF-Scale (TTU, 2006) consists of 28 different damage indicators (DIs) with different degrees of damage (DOD) that are used to estimate wind speeds and rate tornado intensity. The NWS developed the Damage Assessment Toolkit (DAT) (NOAA, 2016) as a GIS based framework that is used to collect and store geo-referenced tornado data. Tornado data is entered into the DAT during NWS damage surveys. The DAT interfaces with hand-held devices that allow surveyors to enter geo-tagged details for each DI, including, its location, DOD, EF rating, and damage photos. Contours of the damage intensity levels for the tornado path can also be drawn. The DAT is a significant resource that has increased the efficiency and accuracy of tornado damage surveys, as well as providing a central database for detailed tornado damage survey data. Data exists in the publicly available DAT database from 2008 to present. The amount of data has increased in recent years as more Weather Forecast Offices (WFOs) use the DAT.

To focus our resources in the estimation of EF-Scale wind speeds, we analyze the frequencies that individual DIs are used to estimate wind speeds. Our initial analysis of DI frequencies was presented at the 2016 AMS Severe Local Storms Conference (Faletra and Twisdale, 2016). Following that work, we updated our analysis to include DAT tornadoes through November 2017. Our DAT processing resulted in 2,639 tornadoes, which are plotted in Figure 6-2. Table 6-1 shows the percentage of tornadoes with at least one DI with an EF-Scale damage-rating equal to the tornado rating. Table 6-2 provides a summary ranking of the top DIs used in tornado EF-Scale ratings.

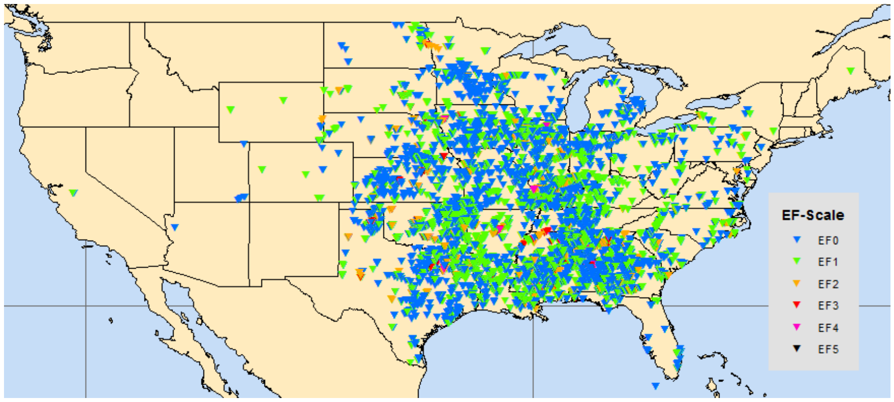

Figure 6-2. DAT Tornadoes (2008-November 2, 2017)

Table 6-2 and Table 6-3 suggest that FR12 and trees (TH and TS) are dominant DIs when it comes to having ratings equal to the max EF rating assigned to the tornado. For example Table 6-2 shows that FR12 has the top frequency for EF2-EF5 events for this time period. The FR12 frequencies dominate EF3-EF5 in that from 75 to 100% of the time their rating equals the tornado ratio. Table 6-2 provides a ranking of the top 10 DIs by EF-Scale. We see that FR12 are the fourth top ranked DI for EF0 and EF1 and, as mentioned, the top ranked DI for EF2 through EF5. We also note that there was no difference in the ranking position of FR12 in our initial analysis (through 2016) and the expanded analysis, summarized in Table 6-2.

We used this information to develop a priority list of structures, excluding trees, that we could effectively apply modern engineering load and resistance damage modeling. We initially investigated, FR12, MHSW (manufactured home-single wide), MHDW (manufactured homes-double wide), FSP (free-standing poles), and MBS (metal building system). As the work evolved, we focused on wood-frame houses for EF-Scale wind speed estimation. To distinguish our engineering-derived wind speeds from the 2006 estimated wind speeds, we use the notation EF* in figures and tables to avoid confusion. The wind speed distributions, $P(v \mid EF^*)$, denote our model estimated wind speeds of the historical (2007-2016) EF-Scale wind speeds. This approach ensures consistency with our use of the SPC EF era data for 2007-2016 in the development of the probability distributions of EF-Scale intensity (see Section 3).

Table 6-2. Percentage of DAT Tornadoes with at Least One DI (TTU, 2006) Equal to the Tornado EF Rating (2008 – 2017) (See TTU (2006) for full names of the DIs)

DI NO	DI Description	EF0	EF1	EF2	EF3	EF4	EF5
1	SBO	30.7	39.1	24.7	0.0	0.0	0.0
2	FR12	28.2	30.1	55.1	75.2	96.7	100.0
3	MHSW	6.4	11.6	15.6	8.8	0.0	0.0
4	MHDW	1.3	3.2	6.5	9.7	0.0	0.0
5	ACT	0.5	1.3	3.4	0.9	10.0	0.0
6	M	0.3	0.4	0.5	0.0	0.0	0.0
7	MAM	0.4	0.3	1.6	0.9	3.3	0.0
8	SRB	1.1	2.0	2.1	2.7	3.3	0.0
9	SPB	2.0	1.6	1.6	5.3	0.0	0.0
10	SM	0.9	1.0	0.5	0.0	3.3	0.0
11	LSM	0.1	0.1	0.0	0.0	0.0	0.0
12	LIRB	0.3	0.6	0.3	1.8	0.0	0.0
13	ASR	0.1	0.1	0.5	0.0	0.0	0.0
14	ASB	0.7	1.0	0.5	1.8	0.0	0.0
15	ES	0.8	0.5	1.3	0.0	0.0	0.0
16	JHSH	0.3	0.3	1.3	0.9	0.0	0.0
17	LRB	0.8	0.6	1.8	3.5	3.3	0.0
18	MRB	0.1	0.1	0.3	0.0	0.0	0.0
19	HRB	0.0	0.0	0.0	0.0	0.0	0.0
20	IB	0.8	0.6	1.0	1.8	0.0	0.0
21	MBS	4.0	6.6	11.7	20.4	13.3	0.0
22	SSC	0.8	0.8	0.5	0.0	0.0	0.0
23	WHB	1.3	2.0	2.9	5.3	3.3	0.0
24	ETL	2.4	9.8	18.2	16.8	0.0	0.0
25	FST	0.7	0.3	1.3	1.8	0.0	0.0
26	FSP	2.1	3.6	3.6	0.9	0.0	0.0
27	TH	58.3	62.3	19.5	15.0	13.3	0.0
28	TS	50.1	45.8	9.4	4.4	0.0	0.0

Note: see TTU (2006) for an explanation of each DI acronym.

Table 6-3. Top DIs Used in Tornado EF-Scale Determination

DI Rank	Top DIs Used to Rate Damage					
	EF0	EF1	EF2	EF3	EF4	EF5
1	TH	TH	FR12	FR12	FR12	FR12
2	TS	TS	SBO	MBS	MBS, TH	
3	SBO	SBO	TH	ETL	ACT	
4	FR12	FR12	ETL	TH	WHB, LRB, SRB, MAM, SM	
5	MHSW	MHSW	MHSW	MHDW		
6	MBS	ETL	MBS	MHSW		
7	ETL	MBS	TS	WHB		
8	FSP	FSP	MHDW	SPB		
9	SPB	MHDW, WHB	FSP	TS		
10	MHDW, WHB	SRB	ACT	LRB		

Note: see TTU (2006) for an explanation of each DI acronym.

6.2. FR12 EF-Scale Models

6.2.1. DOD Probabilistic Quantification

The descriptions in the EF-Scale guidance document and the National Weather Service (NWS) EF training documents provide the basis for probabilistic modeling of the FR12 DOD transitions. The TTU (2006) document provides the DOD damage descriptions and the definitions of construction conditions associated with the judgment-based EXP (expected), LB (lower bound), and UB (upper bound) wind speeds given in Table 6-4. One- and two-family residences (FR12) have 10 DODs, ranging from the threshold of visible damage to a “clean slab.”

***Epistemic Uncertainties*.** We developed judgment-based engineering descriptions and epistemic distributions for our implementation of the EF Scale damage descriptions in Table 6-4. The epistemic distributions given in Table 6-4 are used in the DOD modeling to capture a range of reasonable interpretations of the EF DOD descriptions. For example, the EF description for DOD 8 includes “most walls collapsed.” This statement is interpreted as being a majority of collapsed walls. We use a uniform epistemic distribution range [75-95%] of wall failures (see far right column in Table 6-4). In our damage simulations, we sample from this uniform distribution to obtain a realized value and compare that value to the simulated % wall failures. If the modeled wall failures are ≥ the sampled value and the small interor room survives, the realized damage for this simulation would be DOD 8.

Section 6.2.1.1 provides discussion on the EF* damage descriptions for DOD 1-9. The DOD 10 epistemic model is discussed in Section 6.2.1.2.

Table 6-4. EF and EF* Damage Descriptions

DOD	EF Damage Description	EF Wind Speed (mph)			EF* Probabilistic Damage Interpretations	Distribution of EF* Epistemic Means
		EXP	LB	UB		
1	Threshold of visible damage	65	53	80	Roof cover damage between 0.25% and 1-5%; OR threshold visible damage to exterior attachments	Roof Cover Uniform: 1 to 5%
2	Loss of roof covering material (<20%), gutters and/or awning, loss of vinyl or metal siding	79	63	97	Roof cover damage greater than DOD 1 but less than or equal to approximately 20%; OR failures (> threshold level damage) of exterior attachments	Roof Cover Uniform: 15 to 25%
3	Broken glass in doors and windows	96	79	114	Failure of one or more glazed openings	None
4	Uplift of roof deck and loss of significant roof covering material (>20%); collapse of chimney; garage doors collapse inward; failure of porch or carport	97	81	116	Roof deck damage exceeds approximately 10%; roof cover damage greater than approximately 20%; garage door damage	Rook Deck Uniform: 5 to 15%
5	Entire house shifts on foundation	121	103	141	House rigid body sliding failure	None
6	Large sections of roof structure removed; most walls remain standing	122	104	142	Roof deck damage greater than approximately 80%; OR one or more major roof structure sections fall (which includes whole roof failure)	Roof Deck Uniform: 70 to 90%
7	Exterior walls collapsed	132	113	153	Exterior wall collapse exceeds about 25%	Wall Uniform" 15 to 35%
8	Most walls collapsed, except small interior rooms	152	127	178	Exterior wall failures exceed approximately 85%; AND small interior room survives	Wall Uniform: 75 to 95%
9	All walls	170	142	198	Exterior wall failure ≥ DOD8 AND failure of small interior room	No additional epistemic uncertainty. See Section 5.5.5.
10	Destruction of engineering and/or well constructed residence; slab swept clean	200	165	220	DOD 9 is attained AND additional wind speeds to produce a "clean" slab/foundation. Floor plate may or may not remain bolted to foundation	See Section 6.2.1.2 for epistemic models.

Note: 1 mph = 0.44704 m/s

6.2.1.1. DODs 1 - 9

For DOD 1, based on numerous wind damage surveys (Twisdale et al., 1996; Vickery et al., 2006a, b; Twisdale et al., 2009), we modeled the threshold of visible damage or damage to exterior wall accessories and other non-engineering features. Visible wind damage can occur at wind speeds as low as 40-50 mph (Twisdale, et al., 2009).[84] In addition, as part of the threshold damage model from Twisdale et al. (2009), which included detailed reviews of over a thousand insurance claims, we used an ARA-developed insurance claim-based damage function for residential “exterior accessories”, such as exterior trim, lights, soffits, decorative shutters, etc. Hence, we modeled the DOD 1 threshold as either visible threshold roof cover damage or visible damage to exterior accessories.[85]

DOD 2 occurs when roof cover damage exceeds DOD 1 roof cover loses (but is less than about 20%), or loss of vinyl/metal siding, gutter, or awning damage. We include an epistemic uncertainty range of 15% to 25% for the roof cover threshold damage for DOD 2, which allows a reasonable variance in the observer’s estimation process. In addition, exterior accessory damage that results in failure/detachment of trim, gutters, lights, etc. is considered greater than visual threshold damage and falls into DOD 2.

DOD 3 corresponds to “broken glass in doors and windows.” For the engineering model, we interpret this simply as “at least one glazing failure”. We include fenestration glazing failure from any failure mode (i.e., glazing failures from either wind-generated missiles, wind pressure loads, or window/glass door frame failures) as meeting the DOD 3 threshold.

DOD 4 has a total of 6 features listed (roof deck, roof cover, chimney, garage door, porch, and carport). The use of 6 features, each with potential independent strengths, confounds the efficacy of DOD 4 regarding the ability to infer reasonably accurate wind speeds. From an engineering perspective, we focus on the roof deck, roof cover, and garage door features for DOD 4.[86] We note that the garage door failures are heavily dependent on wind direction and often fail at lower wind speeds than a well-attached roof deck.

DOD 5 is interpreted as a rigid body sliding failure of the house. This DOD is dependent on the type of foundation and the attachment of the wood frame sill plates. Sliding failures are relatively rate and most often occur for small houses with simple floor plans and weak foundation anchorages (including no anchorage attachment or cut nail attachments). Sliding is often accompanied by torsion and twisting of the house due to the variations in the shear resistance along the footprint, and the fact that the shear center is not co-located with the instantaneous center of pressure of the building. In our modeling of sliding failures, the house can still be damaged to higher DODs, which is consistent with the EF-Scale documentation (TTU, 2006).

We interpret DOD 6 as sheathing damage greater than approximately 80% roof deck damage or whole roof failure of one or more major roof sections at the roof-wall connections. We use

---

[84] From multiple surveys, we found that roof cover damage greater than 0.25% was generally captured by ARA damage surveyors with a 360° walk-around of a house. With a less detailed approach, such a more distant (street level) view, roof cover loss less than about 5% was readily detected by surveyors. Hence, we used these values in an epistemic model of threshold roof cover damage for DOD 1.

[85] For hurricane wind speeds less than about 80 mph, roof cover damage dominates threshold losses, based on 1,109 claim reviews in 4 events (Twisdale et al., 2009).

[86] The performance of -roof covers and roof decks has been reasonably well validated with hurricane field data (Vickery et al. 2006a, b), Our building models considered herein do not include porches or carports. Porches, carports, attached screen enclosures, and attached sheds are termed “exterior” structures, since they are exterior to the main dwelling structure. See Twisdale, et al. (2007) for damage survey data on exterior structures and their associated vulnerabilities.

an “OR” logic since loss of most of the roof deck leads to instability of the trusses or rafters and results in an appearance of roof structure failure with leaning or collapsed trusses or rafters. Whole roof failure of a small house or roof failure of a major roof section (over a wing of a complex house) are considered as DOD 6 damage. Whole roof failures typically occur from failed roof-to-wall connections. Occasionally, the wood roof trusses or rafters may fail (split) due to excessive stresses within the members without failure of the roof-to-wall connection.

DODs 7-9 involve wall failures. The EF descriptions are minimal and require significant observer judgements. We interpret DOD 7 as less than or about 25% failure of the exterior wall perimeter. We interpret DOD 8 as more than about 85% perimeter wall failure with interior room walls standing. We model a small interior room for each house. If the small interior room walls fail at the same wind speeds that fail the exterior walls, then the damage state is DOD 9. The epistemic ranges for wall failures for these DODs in Table 6-4 allow for a 20% range of uncertainty for both the DOD 7 and 8 thresholds. This range corresponds to about 1/5 of the exterior wall perimeter.

DOD 10 has an important implication regarding construction quality in that it says “destruction of an engineered or well- constructed residence; slab swept clean.” This terminology implies that a house that is not interpreted as well constructed would be a LB condition. As described by McDonald, et al., (2009), the EF-Scale expected wind speeds (Table 6-1) are associated with a set of “normal” conditions. For buildings, normal implies no glaring weak links in the load path, and conditions worse/better than normal should be associated with the lower/upper bound wind speeds, respectively.

6.2.1.2. DOD 10 Wind Speeds

The EF-Scale descriptions for DOD’s 9 and 10 describe a transition from failure of “all walls” to “slab swept clean”. This transition implies that essentially all walls (including interior room walls) have failed by DOD 9 and that the vast majority of the house walls and components have been displaced from the slab/foundation area. This transition presents a challenging structural and wind-borne debris-modeling problem. Modeling this transition requires detailed data on debris fields, structural details, as well as tornado information for EF5 tornadoes. Considering analysis complexities and the lack of detailed data, we did not implement an engineering model for the DOD 9-10 transition. In the following paragraphs, we use judgement to develop epistemic wind speed factors that are applied to the engineering-derived DOD 9 wind speed to quantify the DOD 10 wind speeds.

Background. We examined a number of FR12 photographs for all DODs. The DOD 9 photographs illustrate cases with several standing walls (or wall remnants) to cases of no standing walls or remnants. Photos of DOD 10 also show a range of cases, some with very few remaining wall components, while others show some standing exterior and/or interior walls (e.g. see Figure 6-3). The amount of debris within the foundation footprint also ranges from none to notable amounts. In some cases, the debris on the slab/foundation may have originated from another building. This confounding effect may not be easily determined in the field for closely spaced houses.

Many parameters influence the final resting position of walls and other components regarding the appearance of the slab as “clean”. They include:

1. Tornado characteristics such as RMW, translational speed, vertical winds, and presence of sub-vortices
2. Position of the building with respect to the translating tornado
3. Building characteristics, including strength, orientation, size, plan, and roof complexity
4. Wall failure dynamics, including inward collapse with no significant translation.

Numerous tornado photos and videos show dramatic images of building failures with components lifting and rotating about the vortex. For these cases, the incremental wind speeds to achieve DOD 10 are likely nil with respect to the failure wind speed. The other extreme includes cases where wall sections and other component collapse without translation. The wind forces required to lift or push these horizontal elements off the slab or away from the foundation may be a significant increment over the collapse wind speed. In some cases, pile-ups may form against anchored or braced vertical wall remnants (such as small interior rooms, plumbing or other slab penetrations, bolted bottom plates, and braced corners). Such configurations likely require additional wind forces to clear the slab. These forces may well exceed the wind force required to fail vertical walls, especially those with weak connections.

In summary, the DOD 9-10 transition for FR12 is complex and uncertain. It may require very little additional wind force to produce a “clean” slab. It may also require large wind forces (from multiple directions) to push or lift debris elements individually and/or as groups of tangled pile-ups.

Figure 6-3. DOD10 Photos from NIST Joplin Database (Scott, 2021)

Epistemic DOD 9-10 Wind Speed Factors. Transition Model. An examination of the assumptions made in the EF-Scale provide a starting point for developing judgment-based DOD 9 to 10 wind speed ratios. The EF-Scale committee estimated that 16, 18, and 11% higher wind speeds (based on the lower bound (LB), expected (EXP), and upper bound (UB) construction conditions, respectively) are required to transition from DOD 9 to DOD 10 (TTU, 2006). The EF rows in Table 6-5 provides the EF wind speeds and the resulting wind speed ratios from DOD 9 to DOD 10. We use these data in a judgment-based approach to develop the EF* DOD 10/DOD 9 wind ratios for implementation in a probabilistic wind speed transition model in the following paragraphs.

Table 6-5. EF and EF* DOD 9-10 Transition Wind Speed Parameters (Wind Speeds in mph)

EF or EF*	Parameter	LB	EXP	UB
EF	DOD 9	142	170	198
	DOD10	165	200	220
	DOD 10/DOD 9	1.16	1.18	1.11
EF*	Mean DOD 10/DOD 9	1.16	1.125	1.09
	COV DOD 10/DOD 9	0.4	0.35	0.3
	10% DOD 10/DOD 9	1.09	1.08	1.04
	90% DOD 10/DOD 9	1.25	1.18	1.12

Note: 1 mph = 0.44704 m/s

First, we plot these EF-Scale DOD 10/ DOD 9 parameters in Figure 6-4. A linear fit of the EF LB (142 mph (63.48 m/s)), EXP (170 mph (76.00 m/s)), and UB (198 mph (88.51 m/s)) ratios smooths the kink in the EF ratios. This fit takes out the anomaly that the ratio is highest for EXP vs UB conditions (strengths). The EF linear fit in Figure 6-4 shows a downward trend, which suggests that the incremental wind speed to produce DOD 10 is less for well-built houses than for houses with below normal conditions.

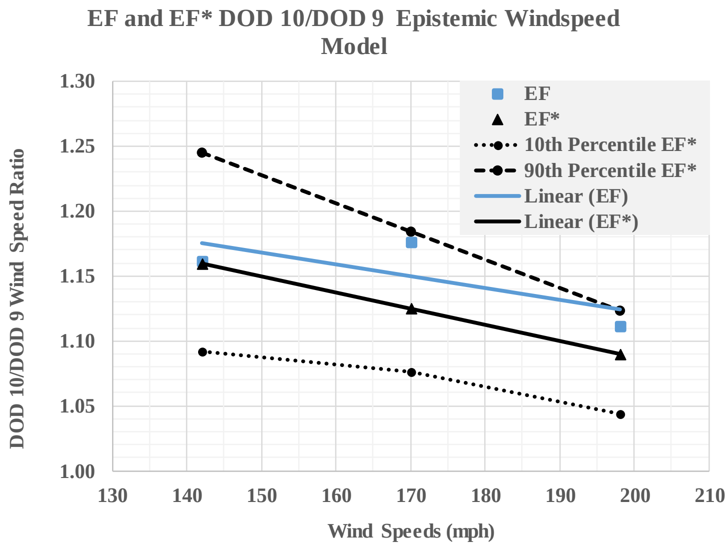

Note: 1 mph = 0.44704 m/s

Figure 6-4. DOD 10/DOD 9 Wind Speed Ratios

For the engineering-derived EF* model, we use the LB EF ratio of 1.16 (at 142 mph (63.48 m/s)). This LB condition ratio is judged to be reasonable, based on the significant amount of field experience and surveys in regions where LB construction quality conditions are prevalent (e.g., Marshall, 2002). The EF-Scale committee, which included engineers and meteorologists, used this knowledge in their estimation of DOD 9 and DOD 10 wind speeds for LB construction/conditions.

We also use a linear model for EF* and therefore the next step is to estimate the ratio for UB conditions. The EF Scale UB DOD 10/DOD 9 ratio is 1.11. In consideration of the increased aerodynamic pressures that exist at high wind speeds (198 mph (88.51 m/s) in Table 6-5 for EF-Scale DOD 9 failures, we use some simple calcluations to infer a reasonable EF* DOD 10/DOD 9 ratio. From the EF-Scale wind speeds, the EF LB ratio produces an excess force that is proportional to $(1.16*142)^2 - 142^2 \sim 7{,}000$. We found that a UB ratio of 1.09 produces a similar magnitude of excess force (i.e., $1.09*198)^2 - 198^2 \sim 7400$. Hence, using 1.09 for the UB ratio provides approximately the same net excess aerodynamic force to displace a component from the slab, once it has failed.[87]

With these ratios and a linear model, the EXP ratio is computed as 1.125, as shown in Table 6-5. In consideration of the potentially large epistemic and aleatory uncertainties in the transition from DOD 9-10 (see background discussion), we use a lognormal distribution to model the incremental fractions.[88] The judgmentally developed lognormal COVs are given in Table 6-5.

Figure 6-4 shows the resulting 10^{th} to 90^{th} ratio range, computed with the lognormal parameters. The distribution range seems reasonable and well captures the EF scale deterministic ratios. The COVs used in the model allow for much greater variation about the mean at low wind speeds than at high wind speeds.

Figure 6-5 shows the CDFs of these LB, EXP, and UB lognormals. In the damage simulations, we sample from the appropriate lognormal, based on the load path quality of the FR12 to obtain a realized EF* DOD 10/DOD 9 ratio and that ratio times the DOD 9 computed windspeed (in that simulation) becomes the DOD 10 wind speed used to build the DPMs.

We believe this model supports the concept of large epistemic modeling uncertainties in the estimation of DOD 10 wind speeds. We also tested the model to confirm that the uncertainties in the DOD wind speeds were similar to those for DODs 8 and 9. The standard deviations of DOD 10 wind speeds were similar in magnitude to those of DODs 8 and 9.

[87] That is, since DOD 9 failure wind speeds depend largely on connection strength rather than weight of the component (for wood frame structures), we assume a component that fails at low wind speeds is less likely to clear the slab than the same component (with stronger connections) that fails at high wind speeds.

[88] The incremental fraction is the DOD 9-10 wind speed ratio -1.

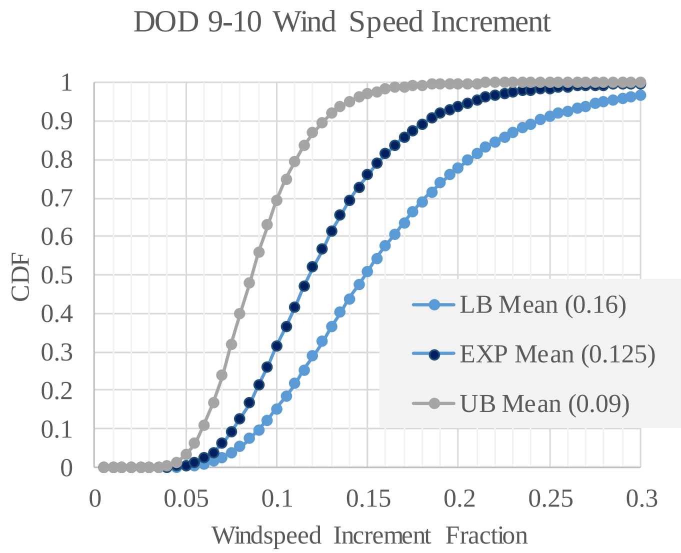

Figure 6-5. DOD 10 Wind Speed Increment Fraction Model

6.2.2. Load Path Quality

Table 6-4 shows the EF-Scale DOD wind speeds for LB, EXP, and UB conditions. Per TTU (2006), "The expected value of wind speed to cause a given DOD is based on a set of "normal conditions: No glaring weak links, traditional construction quality, appropriate building materials, compliance with local building code, and continuous maintenance." Figure 6-6 plots these FR12 DOD wind speeds. The important role of deviations from normal conditions increases in significance for higher DODS: for example, we see 51, 56, and 55 mph (22.8, 25.0, and 24.6 m/s) ranges from LB to UB conditions for DODs 8, 9, and 10, respectively.

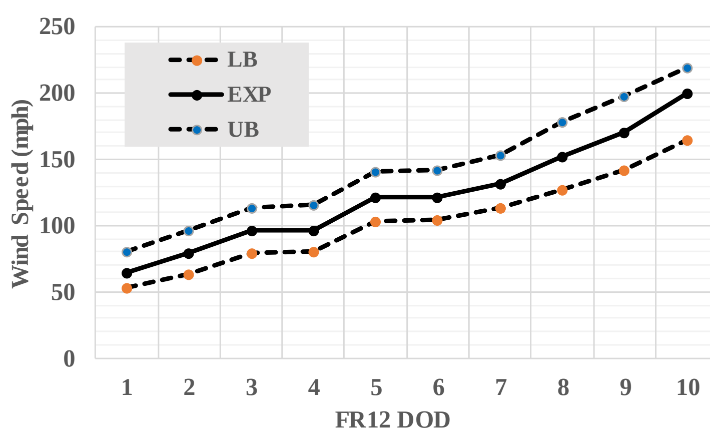

Note: 1 mph = 0.44704 m/s

Figure 6-6. FR12 DOD Lower, Expected, and Upper Bound Wind Speeds (TTU, 2006)

NOAA's EF Toolkit incorporates LB, EXP and UB conditions considering the structure's load path from the foundation to the roof (Ladue and Mahoney, 2006). The NOAA/NWS Warning Decision Training Division (https://training.weather.gov/wdtd/courses/EF-Scale/) EF training portal provides lessons, cases, and quizzes regarding NOAA's implementation of the EF-Scale. For example, Lesson 2, Slides 15, 17, 19, and 20, illustrated in Figure 6-7, provide a glimpse of the training for "load path quality, surveying damage, and rating a tornado event". The information in this figure is explained in detailed text notes in the Lessons and Cases. From these materials, we conclude: roof-to-wall clips exceed EXP quality; straight-nailed studs to sill plates are weaker than EXP (Marshall, 2002); sliding failures typically suggest a LB quality; toe-nailed bottom plate and wall sheathing are examples of EXP quality; and wall sheathing, anchor bolts, and toe nails up the load path meet EXP quality. For DOD 4, load path connections are not evaluated when assessing wind speeds.

The NOAA process involves a determination of the DOD and the construction quality to produce a wind speed estimate. Lesson 2 Guidance, and the Case 2 study indicate that the tornado's EF rating is based on the highest estimated wind speeds, provided: there is a confirming DI of similar rating; or, the highest-rated DI makes sense given surrounding damage. Collateral damage and confirmation of wind speed is an important theme in both the EF-Scale documentation and NOAA's implementation. Ladue and Ortega (2008) provide discussion on these issues, advantages of the EF-Scale system and challenges in field implementation.

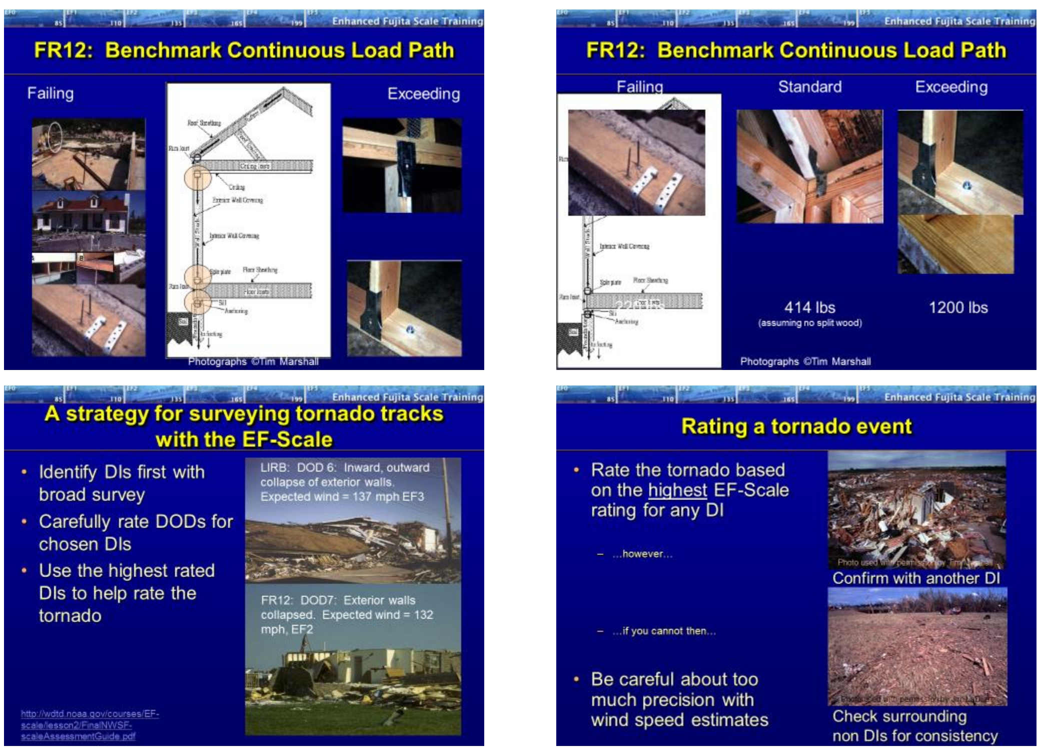

Note: 1 lb = 0.4535924 kg

Figure 6-7. Load Path Quality and Tornado Event Rating Slides from EF Training Toolkit (Source NWS, https://training.weather.gov/wdtd/courses/EF-Scale/)

Table 6-6, developed from a review of the EF training materials and associated publications, provides a summary of the FR12 load path construction quality conditions. We use the 4 main quality attributes discussed in the training materials and training examples: roof-to-wall connection, wall sheathing, stud-to-bottom plate, and foundation anchorage.

As indicated in the training materials and examples, load path quality does not materially affect the levels of damage for DODs 1-4. We note that DOD 4 involves uplift of roof deck, but there is no roof deck quality level (such as fastener size and spacing) in the NOAA materials. The foundation connection is the main quality condition for sliding failures (DOD 5), bolted connections are required for EXP, and UB wind speeds. DOD 6 includes roof structure failures. Hence, roof-wall connection quality is an important attribute in assessing DOD 6 wind speeds. Similarly, DODs 7-9 involve wall failures. For these DODs, one or more low quality wall connections place the FR12 into the LB condition. Houses with all four expected quality connections, per Table 6-6), would correspond to the EXP wind speeds. One or more weaker connection in the load path, if observed, would result in a downward adjustment from EXP. UB quality consists of clips or better for the roof-to wall connection, sheathed walls, clips or better for the wall to sill plate connection, and a properly-bolted foundation.

Table 6-6. EF-Scale Condition (Construction Quality) Mapping to DOD

DOD Groups	Associated Damage	EF Scale Quality Protocol	Roof-Wall	Wall Sheathing	Stud-to-Bottom Plate	Foundation Anchor
DOD 1-4	Threshold: roof cover; uplift of roof deck; garage door, etc.	LB	These connections are not generally applicable or observable for DODs 1-4 damage.			
		Exp				
		UB				
DOD 5	Sliding Failure	LB	These connections are not generally observable for DOD 5 damage.			Nails
		Exp				Bolts
		UB				Bolts
DOD 6	Large sections of roof failed; Most walls standing	LB	TN	Minimal	EN	Nails
		Exp	TN	Sheathed	TN	Bolts
		UB	≥ Clip	Sheathed	≥ Clip	Bolts
DOD 7-10	Wall failuires, internal room failures, to "clean slab"	LB	TN	Minimal	EN	Nails
		Exp	TN	Sheathed	TN	Bolts
		UB	≥ Clip	Sheathed	≥ Clip	Bolts

In summary, the EF documentation and training materials provide the critical information on how to develop engineering-derived wind speeds from the EF-Scale for FR12. They provide a basic protocol from which to infer the connections used in the ratings of tornado intensities. While one would not expect the field implementation of this guidance to be perfect, the protocols well support a probabilistic engineering-derived evaluation of EF wind speeds for historically rated (2007 – 2016) FR12s.

6.2.3. FR12 House Models

Progressive failure models require 3-D structural models. We use 44 house models with different sets of structural strengths. These strengths include the EF-Scale quality levels and several additional important FR12 features.

6.2.3.1. 3-D Models

We use "simple" and "complex" plan models of one-story wood frame houses for the EF-Scale wind speed analysis. The simple plan houses have a rectangular shape with an 1800 square foot (167 m^2) plan area, built-in garage, 4/12 roof slope and 14% wall area glazing (ARA Model No. 1304, Twisdale et al., 2008). The complex shape has a 2,400 square foot (223 m^2) plan area, built-in garage, 4/12 roof slope, and multiple roof sections, of which two are "large" roof sections (ARA Model No. 0014, Twisdale et al., 2008). The one-story house models are shown in Figure 6-8.[89]

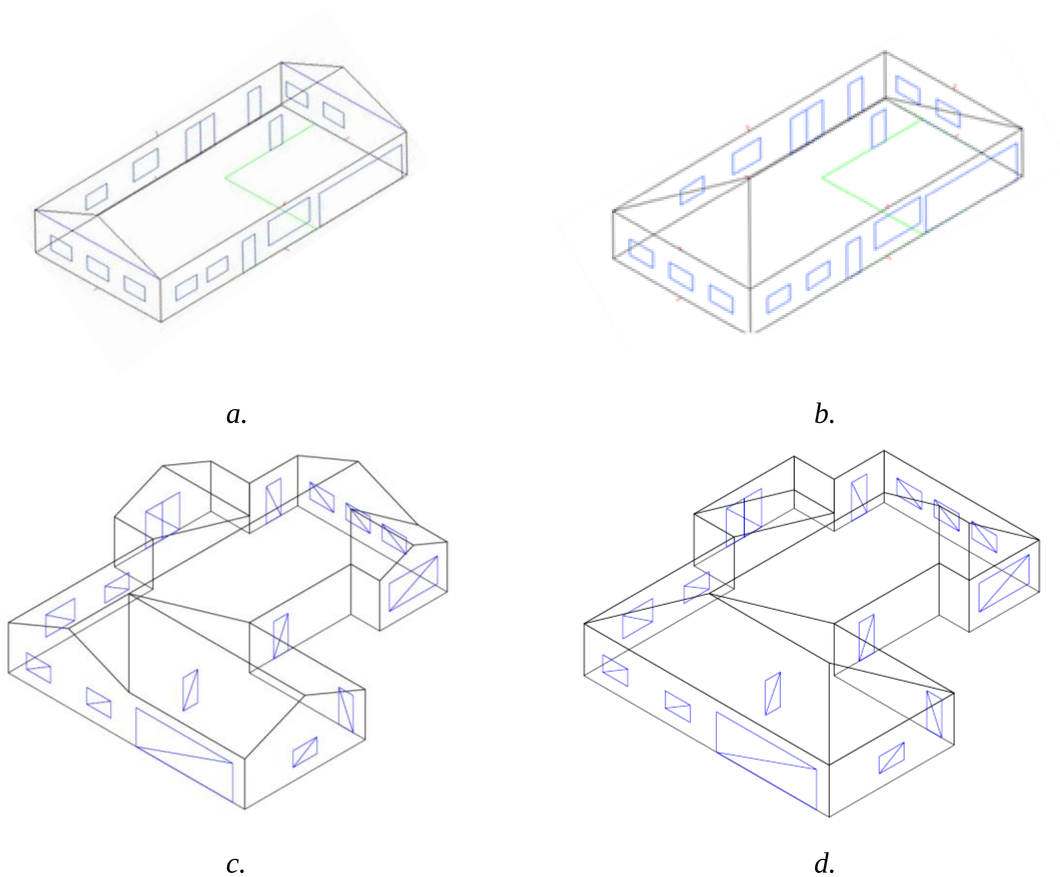

Figure 6-8. 3D View of House Models: (a) Simple Gable (b) Simple Hip (c) Complex Gable and (d) Complex Hip

[89] We also investigated some two-story FR12 models, but focused on one-story models due to a large amount of guidance material for one-story houses and the fact that DODs 8 – 10 require wall failures at the foundation or first story levels. See Twisdale et al., (2008) for information on CAD model data.

6.2.3.2. FR12 Classes (sub-DIs)

Table 6-7 lists 44 FR12 house models or classes, with variations on 10 features[90]:

1. Plan complexity
2. Roof shape
3. Roof cover
4. Roof-to-wall connection
5. Roof deck-to-roof truss connection
6. Wall sheathing
7. Stud-to-bottom plate connection
8. Bottom plate-to-foundation anchorage
9. Glazed opening protection
10. Garage Door Strength

Plan complexity and roof shape are systematically varied in these 44 classes. The remaining features are grouped into strength levels: weak (W), mid (M), strong (S), and super strong (SS). Grouping was used since a full combinatorial combination of features would require more than 1,000 classes. Classes 1-8 and 23-30 have weak TN roof-to-wall connections, minimal wall sheathing, straight-nailed stud to bottom plate, and nailed foundation. Classes 9-16 and 31-38 have EXP level strengths (stronger TN roof-to-wall connections, sheathed walls, TN stud-to-bottom plate, and pinned or bolted foundation connections).[91] Classes 17-20 and 39-42 are examples of UB construction with stronger than expected connections.

The final two classes in these groups (21-22 and 43-44) are examples of SS houses that exist in high hurricane risk areas near the Gulf and Atlantic Coasts. These houses have strong connections, glazed opening protection, and high-wind (HW) garage door strengths. The SS houses are very rare in other parts of the country and do not materially affect the quantification of EF*-Scale wind speeds. They provide an engineering estimate of how strong houses perform in tornadoes.

[90] The notation/abbreviations in the table include: 6d and 8d are common labels for nail size; fdn= foundation; aspht= asphalt; com= common; TN = toe-nail; 6/12 and 6/6 refer to fastener spacing (inches) on edge/field of structural wood panels; str= straight; and HW= high wind.

[91] Pinned foundations were included in this group as a sub-group.

Table 6-7. FR12 House Class Descriptions

House Plan Shape	Class No.	Label	Case	Roof Shape	Roof cover	Roof-to-wall connection	Roof deck to roof truss connection	Wall Shear Strength	Stud to Bottom Plate	Fdn. Anchor	Opening Protection	Garage Door Strength
Simple	1	W6dG	Weak: 6d deck, gable, corner bracing, nailed fdn	Gable	Aspht. Shing.	8d Com. 3TN	6d, 6/12 spacing	Minimal (Corners)	Str. Nail	Nailed	None	Standard
	2	W6dH	Weak: 6d deck, hip	Hip								
	3	W8dG	Weak: 8d deck, gable	Gable			8d, 6/12 spacing					
	4	W8dH	Weak: 8d deck, hip	Hip								
	5	W8dPDGN	Weak: Plank Deck (<1966), gable,	Gable	Aspht. Shing.	8d Com. 3TN	8d, 6/6 spacing	Minimal (Corners)	Str. Nail	Nailed	None	Standard
	6	W8dPDHN	Weak: Plank deck, hip	Hip								
	7	W8dPDGB	Weak: Plank Deck (<1966), gable,	Gable			8d, 6/6 spacing			Bolts		
	8	W8dPDHB	Weak: Plank deck, hip	Hip								
	9	M6dG	Mid: 6d deck, sheathing, gable, pinned	Gable	Aspht. Shing.	16d Com. 3TN	6d, 6/12 spacing	Sheathed	TN	Pinned	None	Standard
	10	M6dH	Mid: 6d deck, sheathing, hip	Hip								
	11	M8dG	Mid: 8d deck, sheathing, gable	Gable			8d, 6/12 spacing					
	12	M8dH	Mid: 8d deck, sheathing, hip	Hip								
	13	M6dBG	Mid: 6d deck, sheathing, bolts gable	Gable		16d Com. 3TN	6d, 6/12 spacing	Sheathed	TN	Bolts	None	Standard
	14	M6dBH	Mid: 6d deck, sheathing, bolts, hip	Hip								
	15	M8dBG	Mid: 8d deck, sheathing, bolts gable	Gable			8d, 6/12 spacing					
	16	M8dBH	Mid: 8d deck, sheathing, bolts, hip	Hip								
	17	SG6D	Strong: 6d deck, sheathing, bolts gable	Gable	Aspht. Shing.	Clip	6d, 6/12 spacing	Sheathed	Clip	Bolts	None	Standard
	18	SH6D	Strong: 6d deck, sheathing, bolts, hip	Hip								
	19	SG	Strong: 8d deck, sheathing, bolts gable	Gable		Clip	8d, 6/12 spacing	Sheathed	Clip	Bolts	None	Standard
	20	SH	Strong: 8d deck, sheathing, bolts, hip	Hip								
	21	SSG	Stronger: 8d deck, sheathing, bolts gable, shut.	Gable	Aspht. Shing. 130	Double Wrap	8d-ring shanked, 6/6 spacing	Sheathed-Nailed to bottom & top plates	Double Strap	Bolts	Impact Resistance Glazing	HW Design
	22	SSH	Stronger: 8d deck, sheathing, bolts, hip, shut.	Hip								
Complex	23	W6dG	Weak: 6d deck, gable, corner bracing, nailed fdn	Gable	Aspht. Shing.	8d Com. 3TN	6d, 6/12 spacing	Minimal (Corners)	Str. Nail	Nailed	None	Standard
	24	W6dH	Weak: 6d deck, hip	Hip								
	25	W8dG	Weak: 8d deck, gable	Gable			8d, 6/12 spacing					
	26	W8dH	Weak: 8d deck, hip	Hip								
	27	W8dPDGN	Weak: Plank Deck (<1966), gable,	Gable	Aspht. Shing.	8d Com. 3TN	8d, 6/6 spacing	Minimal (Corners)	Str. Nail	Nailed	None	Standard
	28	W8dPDHN	Weak: Plank deck, hip	Hip								
	29	W8dPDGB	Weak: Plank Deck (<1966), gable,	Gable			8d, 6/6 spacing			Bolts		
	30	W8dPDHB	Weak: Plank deck, hip	Hip								
	31	M6dG	Mid: 6d deck, sheathing, gable, pinned	Gable	Aspht. Shing.	16d Com. 3TN	6d, 6/12 spacing	Sheathed	TN	Pinned	None	Standard
	32	M6dH	Mid: 6d deck, sheathing, hip	Hip								
	33	M8dG	Mid: 8d deck, sheathing, gable	Gable			8d, 6/12 spacing					
	34	M8dH	Mid: 8d deck, sheathing, hip	Hip								
	35	M6dBG	Mid: 6d deck, sheathing, bolts gable	Gable		16d Com. 3TN	6d, 6/12 spacing	Sheathed	TN	Bolts	None	Standard
	36	M6dBH	Mid: 6d deck, sheathing, bolts, hip	Hip								
	37	M8dBG	Mid: 8d deck, sheathing, bolts gable	Gable			8d, 6/12 spacing					
	38	M8dBH	Mid: 8d deck, sheathing, bolts, hip	Hip								
	39	SG6D	Strong: 6d deck, sheathing, bolts gable	Gable	Aspht. Shing.	Clip	6d, 6/12 spacing	Sheathed	Clip	Bolts	None	Standard
	40	SH6D	Strong: 6d deck, sheathing, bolts, hip	Hip								
	41	SG	Strong: 8d deck, sheathing, bolts gable	Gable		Clip	8d, 6/12 spacing	Sheathed	Clip	Bolts	None	Standard
	42	SH	Strong: 8d deck, sheathing, bolts, hip	Hip								
	43	SSG	Stronger: 8d deck, sheathing, bolts gable, shut.	Gable	Aspht. Shing. 130	Double Wrap	8d-ring shanked, 6/6 spacing	Sheathed-Nailed to bottom & top plates	Double Strap	Bolts	Impact Resistance Glazing	HW Design
	44	SSH	Stronger: 8d deck, sheathing, bolts, hip, shut.	Hip								

6.3. FR12 Damage Simulations

With our probabilistic interpretation of the EF DODs and FR12 models, we use the methodology described in Section 5 to simulate structural response and damage to the FR12 class models. The process follows the TORRISK-TORDAM coupled simulation modeling approach where we used the strike set-up for randomly positioned buildings inside the tornado core. Figure 6-9 shows 3 hypothetical positions in which at least one point of the structure is inside the core.[92] This strike definition is chosen for EF*-Scale wind speed analysis since the EF-Scale tornado rating is based on the maximum observed damage in the tornado, which almost always occurs within the tornado core.[93]

We use 53 wind speed bins that covered the range 50 to 310 mph (22 to 139 m/s) in 5 mph (2.2 m/s) increments for the damage simulations. A total of 6,000 tornado strikes are

[92] Additional discussion of tornado strike set-up alternatives is given in Section 7.
[93] See Section 7.6.2.

simulated for each FR12 class with sampled tornado and building parameters for each strike. For each of the 6,000 tornado strikes, 30 building simulations are performed (each with new sampled strength values) in a sub-loop, producing 180,000 results. The tornado, house position, and load/strength values were sampled from the appropriate probability distributions in the Monte Carlo simulations (see Section 5). These data are processed to create a DOD damage probability matrix (DPM) for each FR12 class. The DPMs include all the modeled aleatory and epistemic uncertainties regarding tornado characteristics, building position and orientation, load/resistance parameters, and DOD probabilistic interpretations.

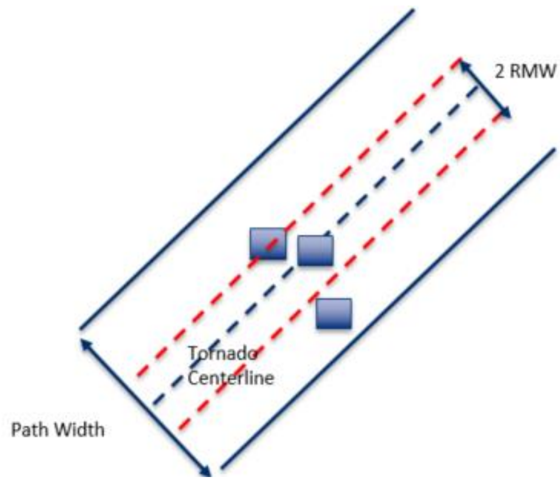

Figure 6-9. Tornado Strike Set-Ups

A condensed (25 mph (11.2 m/s) wind speed increments) DPM for Class 13 in Table 6-7 is illustrated in Table 6-8. Each column in the table provides the DOD damage probabilities conditional on the wind speed bin.[94] For each simulation, the house damage is classified into the highest observed DOD. Hence, the vertical statistics in Table 6-8 are the fractions of time the house is damaged to each DOD level for a given wind speed bin.

Table 6-8 includes a no damage level, herein termed DOD 0. This null damage state ensures that each simulation results in the house being classified into a mutually exclusive and collectively exhaustive damage state. If the house is not damaged to the DOD 1 threshold, then it is counted as DOD 0. The introduction of DOD 0 is analogous to not observing damage. With the inclusion of DOD 0, the columns in Table 6-8 all sum to one, producing discrete probability mass functions (PMFs).

The PMFs in Table 6-8 are broad in terms of the number of impacted DODs for a given wind speed bin. The range of non-zero DODs depends on the FR12 class and the wind speed bin. The broad vertical range reflect randomness and epistemic uncertainties, such as:

- Variations in tornado characteristics (such as RMW, translation speed, swirl ratio, and path width).
- Variation of house position within the tornado core.
- Variation of house strength characteristics for a given class. For example, for Class 13, the 16d roof-wall toe-nailed connection has a mean strength of about 550 lbs (249

[94] The wind speeds in Table 6-8 correspond to the reference wind speed (RWS), defined in Section 7. The RWS is the maximum wind speed at 10 m (33 ft) height experienced within the plan area of the structure as the tornado passes through.

kg) and a standard deviation of 143 lbs (64.86 kg). Hence, in 95% of the simulations, a 2σ simulated connection strength would cover a wide range of 264 (119.7 kg) to 836 lbs 379.2 (kg). Similarly, roof deck strength, roof-to-wall strength, wall-to-foundation resistances also vary significantly.

Table 6-8. DOD Damage Probability Matrix for FR12 Class 13

DOD	Wind speed (mph)														
	50	75	100	125	150	175	200	225	250	255	260	265	270	275	300
DOD 0	8.79E-01	3.46E-01	5.28E-02	1.63E-04											
DOD 1	1.25E-02	3.33E-01	1.55E-01	4.88E-04											
DOD 2	1.08E-01	2.69E-01	1.90E-01	1.55E-02											
DOD 3		2.68E-02	1.50E-01	3.95E-02											
DOD 4		2.52E-02	3.42E-01	1.85E-01	1.70E-02										
DOD 5															
DOD 6		2.74E-04	1.03E-01	7.20E-01	6.35E-01	1.75E-01	1.08E-02	9.01E-04							
DOD 7			6.44E-03	3.66E-02	2.37E-01	2.89E-01	1.32E-01	1.05E-01	1.16E-01	1.38E-01	9.71E-02	6.23E-02	9.74E-02	6.26E-02	9.55E-02
DOD 8				2.44E-03	1.08E-01	4.45E-01	5.34E-01	4.12E-01	2.99E-01	3.13E-01	2.57E-01	2.62E-01	2.46E-01	2.67E-01	2.02E-01
DOD 9					3.91E-03	7.24E-02	1.83E-01	1.60E-01	1.73E-01	1.51E-01	1.10E-01	1.18E-01	1.43E-01	1.13E-01	2.53E-01
DOD 10					2.30E-04	1.85E-02	1.40E-01	3.23E-01	4.11E-01	3.98E-01	5.36E-01	5.57E-01	5.14E-01	5.58E-01	4.50E-01
Sum	1.00E+00	1.00E+00	1.00E+00	1.00E+00	1.00E+00	1.00E+00	1.00E+00	1.00E+00	1.00E+00	1.00E+00	1.00E+00	1.00E+00	1.00E+00	1.00E+00	1.00E+00

Note: 1 mph = 0.44704 m/s

Figure 6-10 shows plotted DPM results for selected wind speed bins (75 to 275 mph (33.5 to 122.9 m/s) in 25 mph (11.2 m/s) increments) for four simple plan, gable house classes (1, 13, 17, and 21).[95] With increasing wind speeds, we see the bar plots shift to the right for a given house class. We see significant shifts in the modes of these DOD distributions for the different classes, reflecting the significant differences in the quality levels and associated strengths. For example, at 125 mph (55.9 m/s), we see that House 1 is most likely to be in DOD 8, followed by DOD 7 and DOD 6, whereas: House 13 is most likely to be in DOD 6, followed by DOD 4 and DOD 3; House 17 is most likely to be in DOD 4, followed by DOD 6 and DOD 3; and House 21 is most likely to be in DOD 4, followed by DOD 2 and DOD 3. Hence, for a given wind speed, the most likely observed DOD depends on the house class. The above example illustrates that Class 21 does not reach a DOD 8 mode until 200 mph (89 m/s), while Class 1 reaches it at 125 mph (55.9 m/s).

The effect of foundation strength in Figure 6-10 can be readily seen for DOD 5, which corresponds to sliding failures (see Table 6-4). House 13, which has a bolted foundation, does not experience sliding failures as an end-state DOD.[96] Figure 6-10 shows that House 1 has non-zero DOD 5's at 100 and 125 mph (45 and 55.9 m/s).

[95] Note that the probability axis has a log scale, which allows visualization of the tails of the DOD PMFs.
[96] A house that slides may still be damaged to higher DODs and would be classified at a higher DOD.

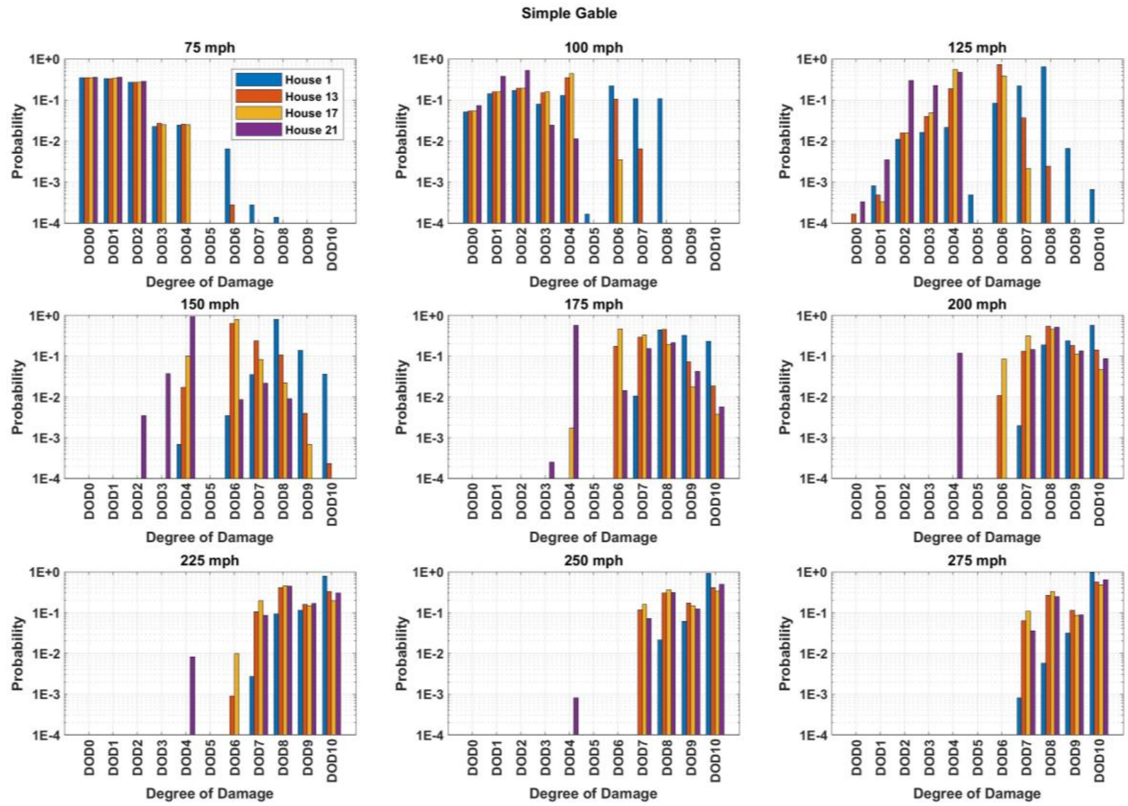

Note: 1 mph = 0.44704 m/s

Figure 6-10. DPM DOD Probability Plots for House 1

Appendix F.1 shows DPM bar plots for additional classes, including simple hip, complex gable, and complex hip houses. The bar plots show how a change in one or two strength features can significantly change the DOD progression and frequencies reflecting the system of connections and any "weak-links".

6.4. Methodology for EF-Scale Wind Speed Estimation

The DPMs contain the engineering information required to estimate wind speeds from damage states. However, since the data in the DPMs are conditioned on wind speed, we must reverse the conditioning to infer wind speeds given an observed DOD. In the following sections, we develop the probabilistic models that enable us to infer tornado wind speeds from observed damage using NOAA's EF-Scale process.

6.4.1. Bayesian Model for DOD Wind Speeds

We develop the distribution of wind speed given an observed damage state using conditional probabilities. The basic expression is

$$P(v_i|d_j)P(d_j) = P(d_j|v_i)P(v_i) \quad \textbf{(6-1)}$$

where v_i denotes wind speed bin *i* (*i* = 1, 53); d_j is the observed damage state (such as a DOD in the EF-Scale); $P(v_i|d_j)$ is the probability of v_i given d_j; and $P(d_j|v_i)$ is the probability of d_j given v_i. The $P(d_j|v_i)$ follow from the DPM columns (e.g., see Table 6-8). There are 11 possible mutually exclusive and collectively exhaustive damage states for FR12 (including the no damage state, DOD 0).

Using Bayes Rule (e.g., Ang and Tang, 1975), we write Eq. (6-1) as

$$P(v_i'|d_j) = \frac{P(d_j|v_i)P(v_i)}{P(d_j)} \quad \textbf{(6-2)}$$

where we denote the Bayesian updated (posterior) wind speed as $P(v_i'|d_j)$. From the Total Probability Theorem (Ang and Tang, 1975), Eq. (6-2) becomes

$$P(v_i'|d_j) = \frac{P(d_j|v_i)P(v_i)}{\sum_{i=1}^{b} P(d_j|v_i)P(v_i)} \quad \textbf{(6-3)}$$

where the summation is over all velocity bins (*b*). For an observed DOD damage level, the wind speed distribution is given by the right hand side of Eq. (6-4) where *i* is sequentially varied from 1 to *b* to produce the distribution of v_i' over all *i*. Performing these calculations for all DOD levels; one obtains the wind speed distribution for each possible observed damage state.

These expressions are the well-developed equations for Bayesian inference, which has been applied to a number of applications (e.g. Benjamin and Cornell (1970); Ang and Tang (1975); Kapur and Lamberson (1977); Twisdale et al. (1995); (Berliner et al. (1998); Jiang and Mahadevan (2008); and An et al. (2012), to name a few) including tornado risk assessments (e.g. Twisdale et al. (1978); Twisdale (1978); Cheng et al. (2015)).

The basic interpretation of Eq. (6-3) is:

$$\begin{pmatrix} Posterior\ Windspeed\ "v_i" \\ Given\ Obs.Damage\ "d_j" \end{pmatrix} = \frac{\begin{pmatrix} Damage\ "d_j" \\ Given\ "v_i" \end{pmatrix}\begin{pmatrix} Prior \\ Prob\ of\ "v_i" \end{pmatrix}}{Normalizing\ Constant} \quad \textbf{(6-4)}$$

where the normalizing constant is the sum product of $P(d_j|v_i)$ and $P(v_i)$.

The $P(v_i)$ is the prior probability of wind speed v_i. The $P(v_i)$ in these equations form the prior PMF of wind speed. The prior reflects the knowledge of the tornado wind speed distribution before new data is available to update the distribution. This new information is represented by the engineering-derived DPM data, $P(d_j|v_i)$. The development of the prior distribution is discussed in Section 6.4.4.

6.4.2. Bayesian Model for EF-Scale Wind Speeds

EF-Scale wind speeds are related to the DOD wind speeds by the FR12 quality level. We express the relationship between DOD (d_j in Eq. (6-1)) and EF using conditional probabilities as

$$P_m(EF_k|v_i, h_m) = \sum_{j=1}^{D} P_m(EF_k|\, d_j, h_m)\ P_m\left(d_j\middle|v_i, h_m\right) \quad \textbf{(6-5)}$$

where D = number of DOD damage states (including DOD 0), and $P_m(EF_k|\, d_j, h_m)$ conditionally relates the EF-Scale assignment to the observed DOD for FR12 house (h) class subscript m (h_m). From Table 6-6 and Table 6-7, the house classes can be directly associated with the EF LB, EXP, and UB conditions (qualities). We can now use Bayes Theorem to reverse the conditioning in $P_m(EF_k|v_i, h_m)$ to obtain

$$P_m\left(v_i'\middle|EF_k^*, h_m\right) = \frac{P_m(EF_k|v_i, h_m)\, P(v_i)}{\sum_{i=1}^{b} P_m(EF_k|v_i, h_m)\ P(v_i)} \quad \textbf{(6-6)}$$

Eq. (6-6) is similar to Eq. (6-3), where $P(v_i)$ is the wind speed prior and $P\left(v_i'\middle|EF_k^*, h_m\right)$ is the posterior wind speed. Next, we compute the mean posterior FR12 wind speed distribution, $P\left(v_i'\middle|EF_k^*\right)$ from the total probability theorem for the FR12 classes

$$P\left(v_i'\middle|EF_k^*\right) = \sum_{m=1}^{H} P\left(v_i'\middle|EF_k^*, h_m\right) P(h_m) \quad \textbf{(6-7)}$$

where h = the number of house classes for FR12 and $P(h_m)$ = the building stock-based relative frequency of house class m. In this work, we use H = 44 house classes per Table 6-7. Eq. (6-7) is executed over all (i, m) to produce the expected value distribution of EF_k^* wind speeds based on one damage observation. As indicated in Eq. (6-7), we denote these updated EF-Scale wind speeds as $P\left(v_i'\middle|EF_k^*\right)$.

6.4.3. Recursive Calculations

An advantage of the Bayesian approach is the ability to update the wind speed distribution based on additional observations of damage. As previously discussed, NOAA's EF protocols (LaDue and Ortega, 2008; NOAA, 2016b) require confirmation in the wind speed estimation process.

The process of updating the posterior with additional information (such as damage to additional DIs or DI classes) is a recursive process in which the posterior becomes the prior in each succeeding update. The recursive process is invariant to the sequence, i.e., the order of the new damage observations.

For wind speed estimation, the form of the recursive equations depends on the application. For field applications, in which multiple DIs, or DI classes, are evaluated, the process is applied using equations that follow from Eq. (6-3). For the estimation of EF* wind speeds, we do not have all the data needed for using individual FR12 classes in the updating process. Hence, we apply the recursive equation to the FR12 mean wind speed distribution as given in Eq. (6-7). With this simplification, the recursive equation for EF confirmation is

$$P(v''_i|EF_k^*) = \frac{P(EF_k^*|v'_i)\ P(v'_i|EF_k^*)}{\sum_{i=1}^{b}\ P(EF_k^*|v'_i)\ P(v'_i|EF_k^*)} \qquad \textbf{(6-8)}$$

The previously computed $P(v'_i|EF_k^*)$ in Eq. (6-7) becomes the prior wind speed distribution in the recursive calculation. The resulting $P(v''_i|EF_k^*)$ is the updated wind speed PMF based on confirmation. Eq. (6-8) is used to produce the EF* wind speeds developed herein.

6.4.4. Prior Wind Speed Distributions

As described, the estimation of wind speeds from observed damage using Bayes Theorem requires a prior distribution, $P(v_i)$, of tornado wind speed frequencies. The $P(v_i)$ prior reflects the knowledge of the tornado wind speed distribution before new information is available. Bayes Theorem provides the logic to update prior knowledge with new information to produce a posterior distribution of EF-Scale wind speeds. The new information consists of the FR12 damage modeling methodology and outputs, as captured in the DPMs.

The prior appears in both the numerator and denominator in Bayes' equations. Hence, it can be multiplied or divided by a constant with no effect on the updated wind speed frequencies (WSF). The impact of the prior is therefore effectively captured by the rate of change (i.e., the slope) of WSF vs. wind speed.[97] A vertical or horizontal shift in the position of the prior hazard curve does not influence the updated WEF. We consider several sources of data to estimate plausible priors for the EF-Scale wind speed calculations.

6.4.4.1. Plausible Tornado Wind Speed Hazard Priors

The prior distribution is generally formulated from sources of relevant prior knowledge, including relevant data, models, and expert judgments. An obvious choice for the prior tornado wind speed distribution consists of previously developed tornado hazard curves.[98] One publically available methodology with wide-spread use is the work of (Ramsdell and Rishel, 2005, 2007). These NUREG publications represent the Nuclear Regulatory Commission approved tornado wind speeds for nuclear plant design. The 2005 publication uses the F-Scale wind speeds in the analysis and the 2007 publication updated the results to the EF-Scale wind speeds. Both studies use the SPC database for the years 1950-2003. The resulting hazard curves from these publications provide a useful indication of how the WEF hazard slope changes from a narrow-banded scale (EF wind speeds) to the broader F-Scale wind speeds.

Figure 6-11 shows the Ramsdell and Rishel (2007) WEFs, (1E-05, 1E-06, and 1E-07) for the central US (NRC Region 1). These WEFs are for a 200 ft x 200 ft (61 m x 61 m) building. As

---

[97] The WSF are directly derived from the WEF tornado hazard curve by $WSF_i = WEF_i - WEF_{i+1}$. For convenience, our discussion uses WEFs, recognizing that WSF are a a straight forward derivation for uniformly-spaced wind speed intervals.
[98] In the intial phases of this work, we used a prior based on an earlier project version of the $P(V_i|EF_r)$. However, we abandoned this approach in favor of independently developed tornado hazard curve WEFs.

expected, the slope of the F-Scale curve is flatter than the EF-Scale slope.[99] The differences in these two slopes provides a view of plausible slopes of the prior wind speed distribution. A tornado hazard curve from Twisdale et al. (2015a) is also shown for a plant location in the southeast US for a point target.[100] The Twisdale hazard curve (follows the method and computer model described in Twisdale and Dunn (1983), with enhancements for propagating uncertainties. The Twisdale hazard curve is a more recent effort than the Ramsdell and Rishel (2005, 2007) data and includes EF-Scale data through 2014. The hazard curve is a derived mean and includes several epistemic uncertainties: occurrence rate, F/EF damage scale distribution, wind speed distribution, and overall modeling uncertainties.

Since the Twisdale et al. (2015a) tornado hazard curve considered uncertainties in the tornado wind speeds; it is not surprising that the Twisdale data lies between the NUREG F and EF data. It is important to note that Ramsdell and Rishel (2007) and the Twisdale et al. (2105) use different datasets, assumptions, and approaches for modeling wind speed swath areas. Hence, the data in Figure 6-11 provides reasonably independent data for estimating tornado wind speed priors.

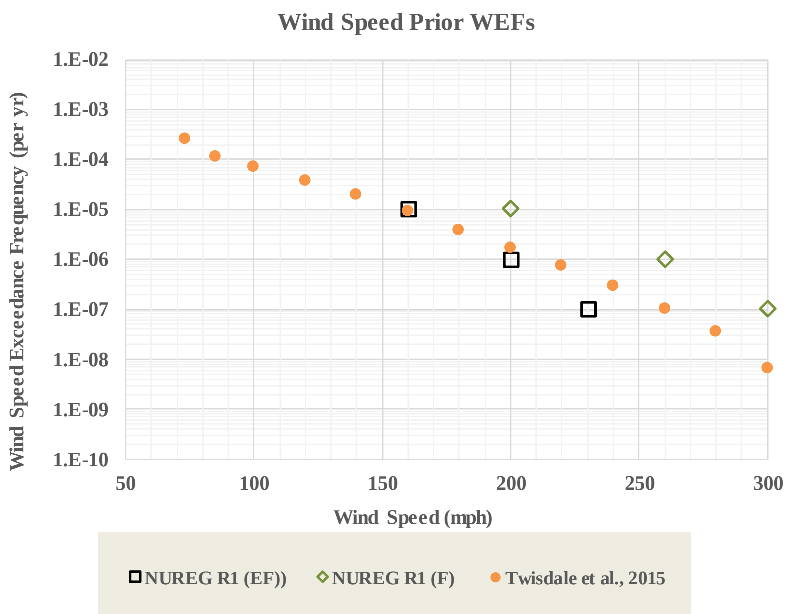

Note: 1 mph = 0.44704 m/s

Figure 6-11. Prior Tornado Wind Speed Tornado Hazard Curves

6.4.4.2. Epistemic Uncertainties in the Wind Speed Prior

A plausible wind speed prior should reflect the potential for extreme and uncertain tornado wind speeds. To supplement the tornado hazard priors illustrated in Figure 6-11, we review data from radar-derived tornado wind speeds.The radar data is evaluated in a simple "ball-park" model to estimate plausible frequencies of observing 300 mph (134 m/s) tornadic wind

[99] The flatter F-Scale slope provides a more "diffuse prior" than the EF-Scale slope.
[100] The Twisdale et al. (2015) hazard example used a simpler methodology than the modeling approach developed herein.

speeds. This analysis is then compared to Figure 6-11 to aid the quantification of epistemic uncertainties.

Doppler Radar Derived Wind Speeds. A large number of mobile Doppler radar tornado observations have occurred over the past two decades. Alexander and Wurman (2005) indicate that radar observations have been acquired for over 150 supercell tornadoes. These high-resolution radars have measured some extreme tornado wind speeds, which are fundamental to estimating uncertainties in tornado priors. The highest radar-derived wind speed measured in a tornado is the EF5 Bridge Creek-Moore, OK tornado of May 3, 1999 (Wurman et al., 2007). In this observation, wind speeds of approximately 300 mph (134 m/s) were measured at 105 ft (32.00 m) above ground level (AGL). This wind speed magnitude far exceeds the EF5 threshold wind speed of 200 mph (89 m/s) and indicates that extremely high tornado speeds are attainable near ground level. Although Wurman's ~ 300 mph (134 m/s) wind speed was derived well above 33 ft (10.1 m), multiple radar datasets indicate that wind speeds in the first 33 ft (10.1 m) AGL could equal or possibly exceed the wind speeds at 100 ft (30.5 m) (e.g., see Wurman and Kosiba, 2014).[101]

There have been other high tornadic wind speeds derived from radar measurements, mostly in rural areas. For example, Snyder and Bluestein (2014) discuss several high wind speed radar measurements: (1) 263 mph (117.6 m/s) (2 second average, with a maximum "objectively- analyzed" 289 mph (129.2 m/s) peak) in the May 24, 2011 tornado near the West and North sides of El Reno, Oklahoma and (2) ≥ 130 m/s (290 mph) in a sub-vortex (translating at 175 mph (78.23 m/s)) in the 31 May 2013 tornado across rural areas in southwestern El Reno. Other radar-derived high wind speeds include: Wurman et al.'s estimated speeds of 234 mph (104.6 m/s) in the Mulhall, OK tornado of May 4, 1999, and Wurman and Alexander's (2005) estimated wind speeds of 250 mph (112 m/s) in the Spencer, SD F4 tornado of May 30, 1998.

There are many factors that affect the chance of measuring wind speeds in the proximity of significant EF-Scale ground level damage (e.g., see Snyder and Bluestein, 2014). Often, the maximum radar derived wind speed occurs where there are no DIs or the tornado's EF-Scale rating was based on DIs at other locations along the tornado path. [102]

Priors Based on Radar Analyzed Wind Speeds.For purposes of quantifying a prior wind speed distribution, we consider the observed 300 mph (134 m/s) tornadic wind speed in an area close to EF5-rated tornado damage as a "threshold" event. Wurman's (2007) ~300 mph (134 m/s) observation meets this threshold. A number of additional high wind speed measurements have been made in tornadoes in proximity to moderate and intense damage, but Bridge Creek stands out as an event with both EF5 rated damage and proximity radar-derived wind speeds that exceeded 300 mph (134 m/s). This single event is assumed to be our threshold wind speed exceedance event ≥ 300 mph (134 m/s) in a simple "ball park" analysis[103].

---

[101] In addition, a review of available data has been produced by the ASCE Tornado Wind Speed Estimation Committee, which is proposing a vertical profile for horizontal wind speeds to an elevation of 200 ft (61 m) AGL (see Section 4.4).

[102] Marshall et al. (2014) also discuss the lack of DIs in the areas of maximum measured wind speeds in the El Reno tornado of 2013. It was rated EF3 based on multiple damage observations.

[103] "Ball-park" is a colloquial term often used to identify an approximation of an outcome that is based on information that is readily available. In this case, since we assume that ≈ 300 mph (134 m/s) tornadoes exist from Wurman's Bridge Creek-Moore, OK analysis, the ball-park approximation is to estimate the frequency of being in the right place for an EF5 tornado (event) to quantify a 300 mph (134 m/s) wind speed threshold measurement.

A "ball-park" threshold exceedance calculation for observing an exceedance frequency of 300 mph (134 m/s) wind speeds given EF5-rated damage is developed from

$$P_{ci}(V > 300) \approx P_{ci}(V > 300|\, EF\,5)\, P\,(EF5) \tag{6-9}$$

where the left hand side is the threshold wind speed exceedance frequency for a given confidence interval (P_{ci}). The right-hand side of Eq. (6-9) includes the conditional probability of observing > 300 mph (134 m/s) wind speeds from a radar position in "close proximity to EF5 tornado damage," which is defined as the conditioning event (*EF5*) in the above equation. We use simple two-sided binomial confidence intervals subsequently in order to reasonably bound the event in our analysis of plausible wind speed priors. We approximate the event (*EF5*) "close proximity to an EF5 tornado damage" as the probability of EF5 damage within the path of an EF5-rated tornado. We estimate $P(EF5)$ from

$$P(EF5) = v\, P(EF5|v)\mu_{\mathrm{A}}(EF5) \tag{6-10}$$

where v is the tornado occurrence rate (per square mile per year), $P(EF5|v)$ is the frequency of EF5s given the occurrence of a tornado, and $\mu_{\mathrm{A}}(EF5)$ is the mean EF5 wind speed swath area within an EF5 tornado.

1. This simple model is used to "ball park" the chances of Wurman "being in the right place at the right time" regarding measuring wind speeds in near proximity to EF5 rated damage. We use the data for Region 407 (Sections 3 and 4) for this analysis. The steps are: The mean occurrence rate (v) for tornadoes is 1.17 E-03 tornadoes per square mile per year.
2. The mean EF5 tornado relative frequency given a tornado occurrence, $P(EF5|v)$, in Region 407 is 2.98E-03 per tornado.
3. The path model estimated EF5 wind speed swath area, $\mu_{\mathrm{A}}(EF5)$ is 0.77 mi^2 (2.0 km^2).
4. The product of these 3 terms in Eq. (6-10) is *P (EF5)* = 2.68E-06 per year. In this analysis, we use the area of the EF5 swath as a surrogate to close proximity for radar measurements. The units are per year for the event of close proximity to EF5 rated damage area. This value is used in Eq. (6-9).
5. The next step is to evaluate $P_{ci}(V > 300|\, EF\,5)$ in Eq. (6-9). Using the binomial distribution, we compute the 95$^{\text{th}}$ two-sided confidence intervals, P_{ci}, in a sensitivity analysis. For example, the two-sided 95% P_{ci} for one successful observation out of 1 try is (0.025, 1), whereas for 1 success in 200 super cell radar observations is (0.00013, 0.02754). We did not consider sample size in the computation of the binomial confidence intervals.
6. The product of these quantities provides for a "ball-park" sensitivity analysis of the epistemic ranges of plausible WEFs for observing a single event with 300 mph (134 m/s) threshold tornado wind speeds near ground level.

Statistical uncertainties from binomial observations are illustrated in Figure 6-12, which shows the means and ranges of two-sided 95% confidence intervals for a single success out on *N* trials. The range of uncertainty (UB/LB) begins at 40 for 1 out of 1, increases to 175 at 1 out of 10, and then grows gradually to less than 1 in 200 as the number of assumed trials reaches 100. Assuming an unknown number of EF5 observations, these statistics suggest a potentially broad binomial uncertainty range in the prior WEF for a 300 mph (134 m/s) measurement wind speed threshold.

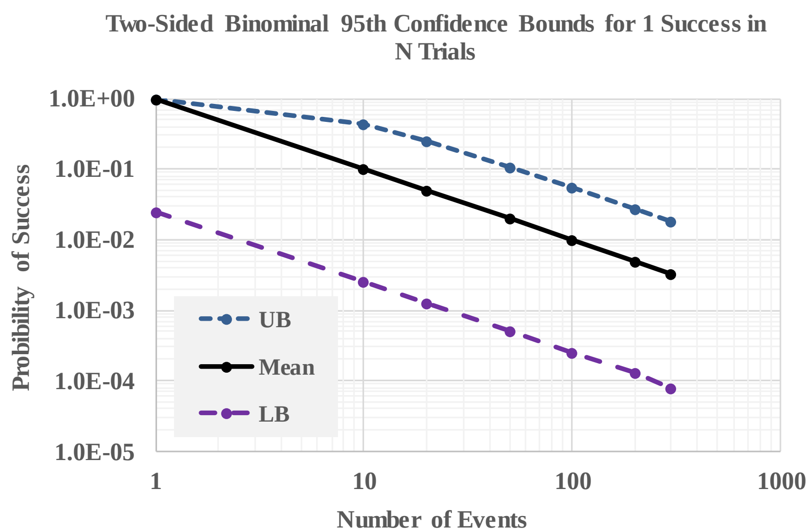

Figure 6-12. Two-Sided Binomial Confidence Bounds: 1 Success in N Trials

Figure 6-13 shows the results of P_{ci} computations (using Eq. (6-9)), plotted as symbols at 300 mph (134 m/s). For example, we see that 1 out of 1 (Bridge Creek) plots a P_{ci} range of 6.69E-08 to 2.68E-06, where 1 out of 200 shows a range of 3.48E-10 to 7.37E-08. This range of possibilities includes: (1) an upper-bound "lucky" 1 for 1 Bridge Creek observation (being in the right place at the right time)[104]; and (2) a lower-bound, frequency-based 1 success in 200 radar observations of supercell tornadoes. The LB estimate effectively assumes that all supercells produce EF5 wind speeds and the confidence interval, $P_{ci}(V > 300|\ EF\ 5)$, is based on 1 success in some 200-supercell radar observations. Since all supercell tornadoes do not produce EF5 wind speeds, we use these data to postulate the lower bound. The true, but unknown frequency of 300 mph (134 m/s) EF5s is assumed to be between these limits. The 1 in 200 frequency is based on Alexander and Wurman (2005) estimate of 150 radar observations of supercell tornadoes with an extra 50 added as a guess on the total current number.

The resulting range from the radar sensitivity analysis in Figure 6-13 is about 1E-09 to about 1E-06 for 300 mph (134 m/s) WEFs.

Comparing the Ball-Park Analysis to Hazard Model Wind Speeds. Figure 6-13 also shows the Ramsdell and Rishel (2007) WEFs. The F-Scale WEF results cross 300 mph (134 m/s) at about 1E-07 whereas the EF-Scale WEF results (extrapolated) cross at about 1E-09. From Figure 6-13, the 1 in 1 binomial 95% confidence bounds from the ballpark model place the 300 mph (134 m/s) threshold between 7E-08 and 3E-06 WEF, whereas the 1 in 200 binomial place it between 3E-10 and 7E-08. These ball-park analyses tend to bound the WEFs at 300 mph (134 m/s).

[104] The term "lucky" means radar measurements of ~ 300 mph (134 m/s) wind speeds "close" to EF5 rated damage. While other radar measurements in the same 300 mph (134 m/s) ballpark wind speed have been recorded, they were not as lucky, being within a lesser-rated tornado.

With these results, our approach is to use the data in Figure 6-13 to develop three plausible priors (simply denoted as LB, EXP, and UB). The LB curve (1E-09 WEF at 300 mph (134 m/s)) in Figure 6-13 corresponds to the NUREG EF slope and is within the 95% confidence bounds for the 1 in 200 case. The UB (1E-06 WEF at 300 mph (134 m/s)) curve is above the F slope, but below the upper bound confidence interval of the 95% interval for the 1 in 1 case. The base prior WEF for 300 mph (134 m/s) is the log median (3.16E-08) between the UB and LB WEFs at 300 mph (134 m/s). These values are connected to a common WEF of 5E-04 (a rounded value for Region 407) at 100 mph (45 m/s) and 1E-03 (a rounded value occurrence rate for Region 407) at 50 mph (22 m/s), producing bilinear exponential priors.

Since the slope of the prior influences the resulting Bayesian wind speeds, the computed WEFs are invariant with rigid body vertical shifts in the priors. The slope of the prior from 100 to 300 mph (45 to 134 m/s) is the area of interest for engineering design purposes. We assess the sensitivity of EF* wind speeds to those slopes and develop an epistemic prior in Section 6.6.3.

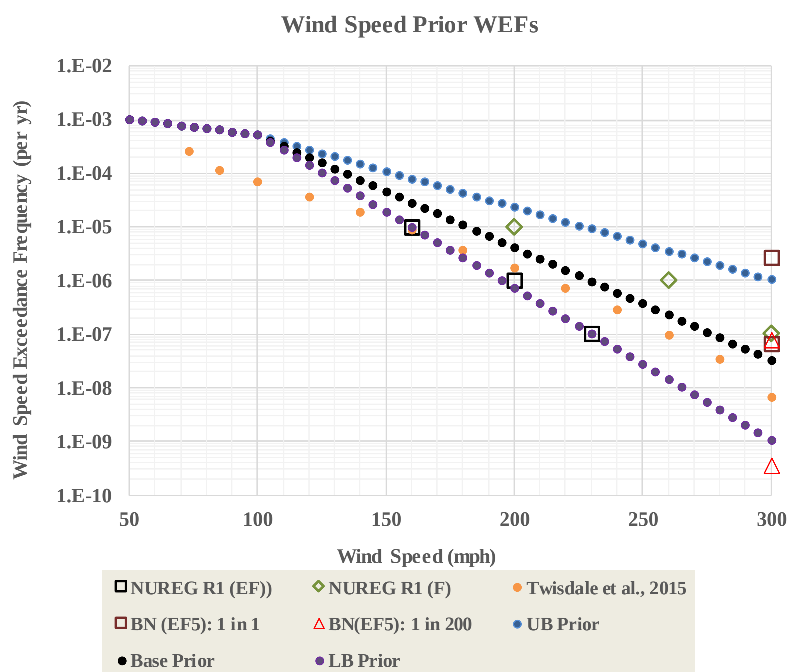

Note: 1 mph = 0.44704 m/s

Figure 6-13. Assumed Lower, Base, and Upper Range of Plausible WEF Priors

6.5. FR12 Derived DOD Wind Speed Distributions

The derived epistemic mean FR12 DOD wind speeds are presented in this section using the calculations developed in Section 6.4.1.

The resulting Bayesian processed $P\left(v'_i \middle| d_j\right)$ PMFs for House 1, 14, and 41 are shown in Figure 6-14 through Figure 6-16. These PMFs capture the full set of 53*11 = 583 data points that reflect the 180,000 damage simulations for each house class. The red vertical dashed lines in these figures correspond to the EF-Scale range (TTU, 2006) for that DOD and the black vertical dashed lines correspond to the model computed wind speed ranges. While the log plots readily show the tails of the PMFs, there is less than about a 5% chance that the wind speeds are outside of the ($\mu \pm 2\sigma$) black vertical lines.

House 1: Weak Gable. This small gable house has weak connections through out (see Table 6-7). The engineering-derived DOD wind speeds in Figure 6-14 are captured reasonably well by the EF-Scale wind speeds. The means and standard deviations of the DOD wind speeds are shown on each plot. The broad uncertainties in the DOD wind speeds reflect the aforementioned randomness in tornado characteristics, position and orientation of the house inside the tornado core, and uncertainties in DOD interpretations, structural loads, and structural strengths. The EF-Scale wind speeds do very well in capturing the center of these PMFs, but the EF range of wind speeds is too narrow for high DODs.

House 14: Mid Hip. This small plan, hip house has some improved connections over House 1: larger roof to wall toe nails, sheathed walls, TN stud-to-bottom plate, and bolted sill plates. In Figure 6-15, we see the role of roof shape in the DOD 4 wind speeds with a mean wind speed of 122 vs. 96 mph (54.54 vs. 42.9 m/s) for House 1. The effect of sheathed walls and bolted foundation result in 30 to 40 mph (13 to 18 m/s) increases in DOD 7-10 over House 1. We also see larger standard deviations in stronger houses and houses with hip vs. gable roofs. The EF-Scale wind speeds do reasonably well up to DOD 3, but significantly underestimate the wind speeds for higher DODs for this hip-roof structure with EXP quality.

House 41: Strong Gable. This complex shape gable has strong connections with clip roof-to-wall connections, 8d nails at 6/12 spacing, clip stud-to-bottom plate, and bolted foundation. The EF-Scale wind speeds in Figure 6-16 do not capture the wind speed PMFs of this strong, complex house very well for ≥ DOD 4.

Appendix F.2 includes the DOD PMF plots for all 44 FR12 Classes.

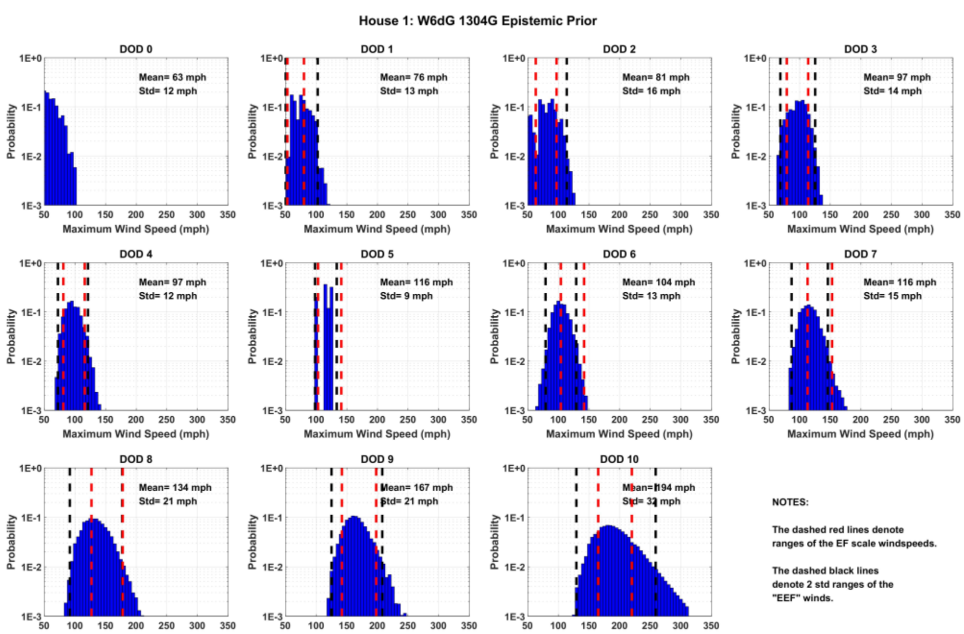

Note: 1 mph = 0.44704 m/s

Figure 6-14. Engineering-Derived DOD Wind Speed PMF Plots for House 1

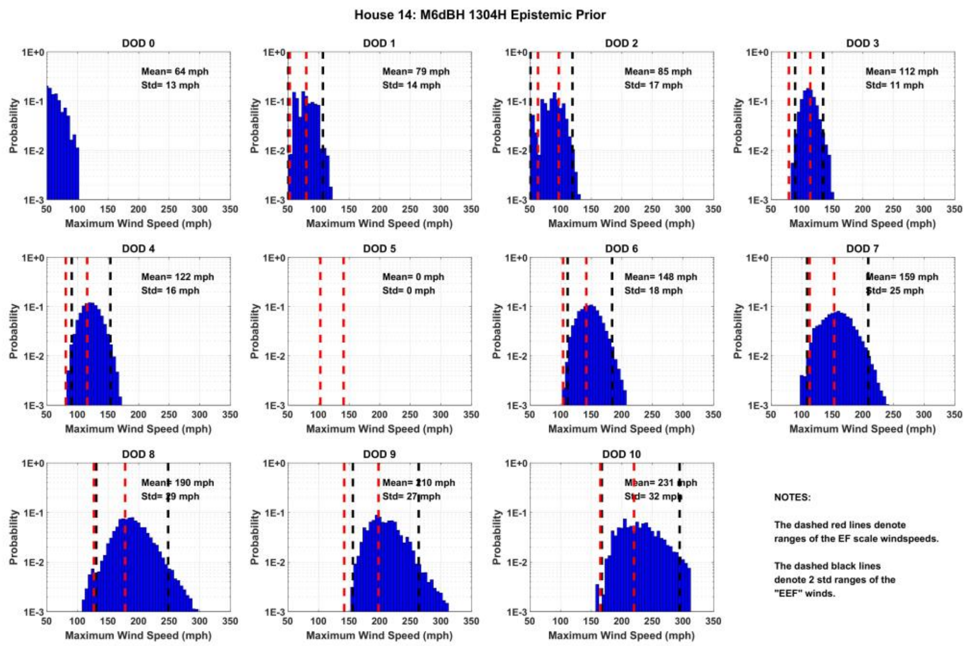

Note: 1 mph = 0.44704 m/s

Figure 6-15. Engineering-Derived DOD Wind Speed PMF Plots for House 14

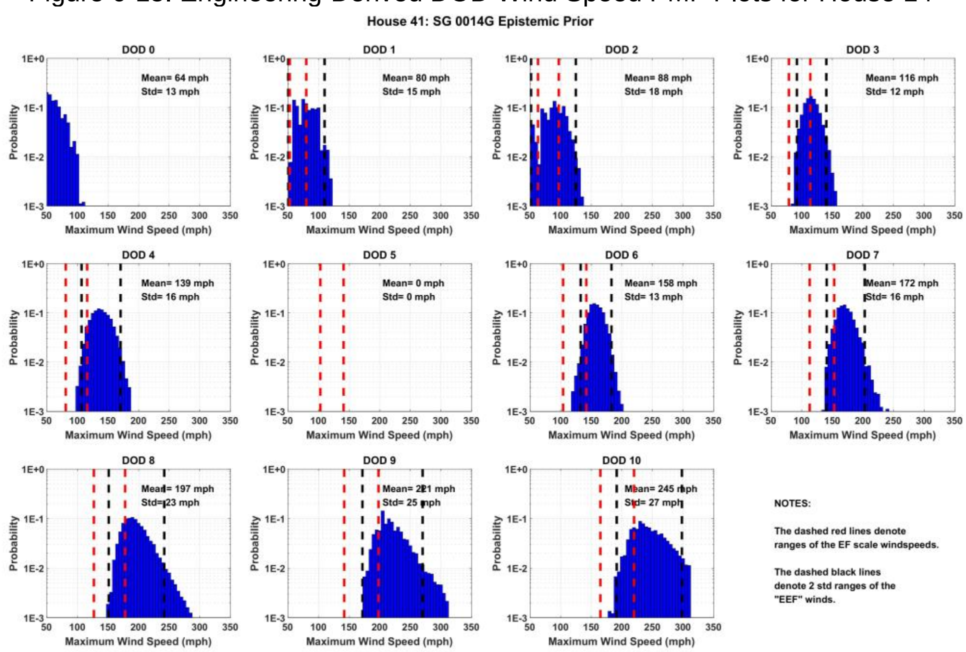

Note: 1 mph = 0.44704 m/s

Figure 6-16. Engineering-Derived DOD Wind Speed PMF Plots for House 41

DOD Wind Speed Summary. Figure 6-17 plots the EF-Scale DOD LB, EXP, and UB wind speeds, illustrating the tight ranges and progressive steps of these wind speeds. Figure 6-18 through Figure 6-20 plot the EF* DOD Mean, Mean – 2σ, and Mean + 2σ wind speeds, respectively, for the selected house classes (which include weak, mid, strong, and super-strong classes, gable vs. hip, and simple vs complex plans). These 16 house classes are the same houses shown in the DOD PMF plots in Appendix F.2.

Figure 6-18 shows that the DOD EXP wind speeds plot reasonably well against the mean DOD wind speeds for the weak house classes (1, 2, 23, and 24) and the simple shape gable mid house class (13). The other house classes begin to deviate toward higher wind speeds beginning with DOD 4 and show significant separations from the EF wind speeds beginning with DOD 6. We see that most of the house classes plotted here do not have DOD 5 (sliding) as an end state. Houses 1 and 2 are the only classes plotted with nailed foundations and hence are the only ones that experience sliding as an end state with a non-zero wind speed.[105] A second point regarding sliding failures is that the house may still be damaged to a higher DOD, which determines its final state in the EF-Scale protocol. We see, for example for House 1 that the mean wind speed for DOD 6 is less than the mean wind speed for DOD 5.[106] These types of reversals can occur due to the EF-Scale pre-determined failure progression order, which works well but is not perfect for all house classes.

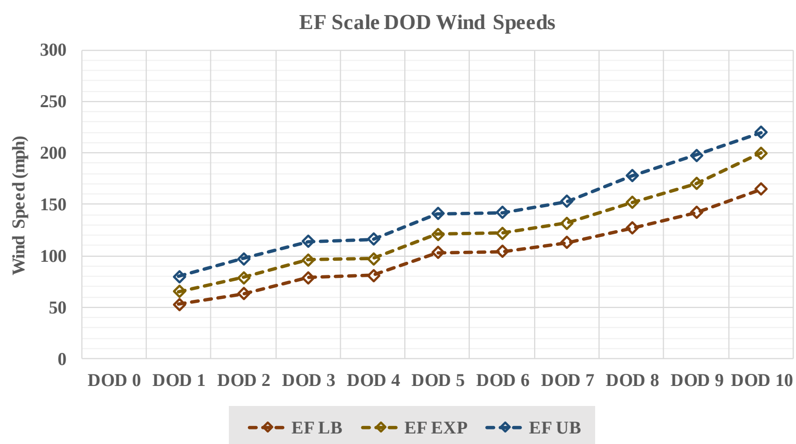

Note: 1 mph = 0.44704 m/s

Figure 6-17. EF-Scale FR12 DOD (LB, EXP, and UB) Wind Speeds

[105] There are a total of 6 classes with nailed foundation and 4 classes with pinned foundations in Table 6-7. Recall from Eq. 6-5 through 6-7 that the house classes are building stock weighted in the computation of EF* wind speeds. Weak houses are common in many parts of the country and have much higher weights than strong houses.

[106] However, House 2, which is the hip shaped version of the same house does not have this reversal in the mean wind speed. The hip roof house requires higher wind speeds to achieve DOD 6 than does its gable counterpart, whereas both houses have the same mean DOD 5 wind speed for sliding failures.

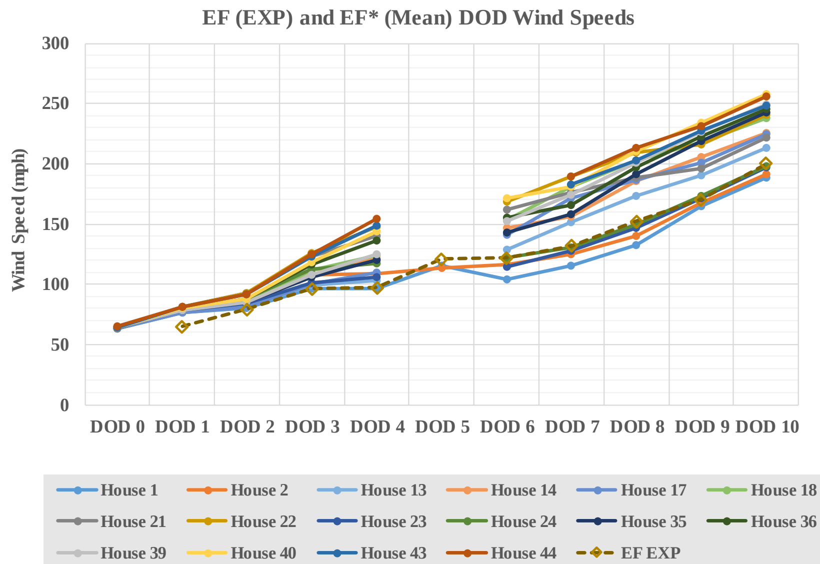

Note: 1 mph = 0.44704 m/s

Figure 6-18. EF-Scale EXP vs. EF* Mean DOD Wind Speeds

Figure 6-19 shows that the EF DOD LB wind speeds are higher than the wind speeds for the weakest houses (1, 2, 23, and 24), reasonable for simple shape mid houses (13, 14, 17, and 18), with wind speed underestimation of 20-40 mph (8.9-18 m/s) for the remaining classes. The DOD wind speeds would be expected to occur less than about 2.5% of the time, and hence represent rare observations. Nevertheless, Figure 6-19 points out that the engineering-derived wind speeds well capture the potential for failures at all DODs at very modest wind speeds. For example, we see "clean slabs" for small simple houses occurring at wind speeds of about 130 mph (58.1 m/s), which corresponds to the upper tail of loads and lower tails of resistances for poorly-built structures. We also see that even for super strong structures that clean slabs can occur at 200 mph (89 m/s). These cases also reflect a "weakness" alignment in the simulations where several parameters such as house position, orientation, tornado RMW, APC, vertical winds, and excessive wind borne debris coincide to produce failures.

Figure 6-20 shows the other end of the DOD spectrum that is observed rarely (about 2.5% of the time for DOD wind speeds). These cases represent alignments of "strength". We see that the EF DOD UB wind speeds do not compare well with the EF* DOD ($\mu + 2\sigma$) wind speeds except for the weakest house classes (1, 2, 23, and 24). For the other house classes plotted, the wind speed differences in Figure 6-20 are from 30 to 80 mph (13 to 36 m/s) for high DODs.

In summary, the engineering-derived DOD wind speeds produce a range of wind speeds that reflect the 10's of variables that influence structure response in tornadoes. We see that when plotted with for the RWS, that these variables produce much broader range of possible wind speeds than is captured in the EF-Scale DOD wind speeds. These broad ranges show the difficulties of quantifying wind speeds and rating tornado intensities for FR12s without knowledge of additional wind-resistive construction features. As demonstrated herein, with additional observables (principally, plan complexity, roof shape, and roof-deck connection), wind speeds can be quantified much more accurately than using a single generic FR12 class. The current EF-Scale protocol requires examination of several important observables, so modest enhancement to the protocol could have big payoffs in terms of estimating wind speeds and accurately rating tornado damage intensity.

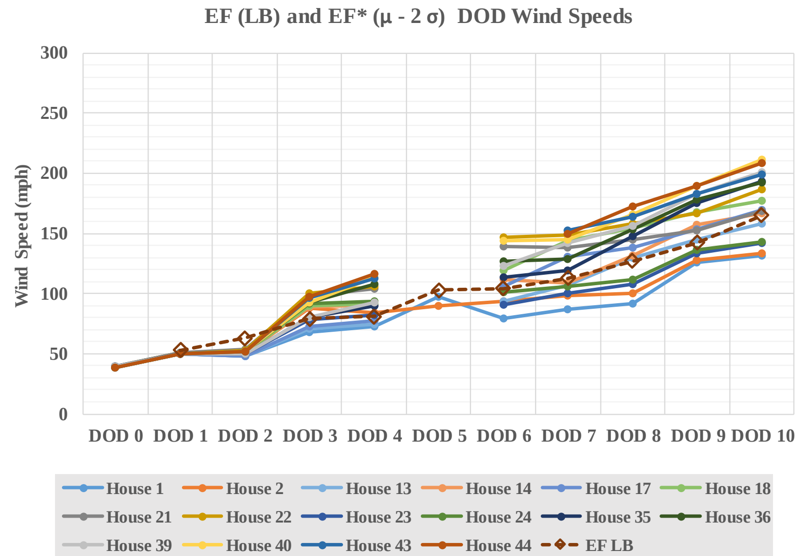

Note: 1 mph = 0.44704 m/s

Figure 6-19. EF-Scale LB vs. EF* (*μ – 2σ)* DOD Wind Speeds

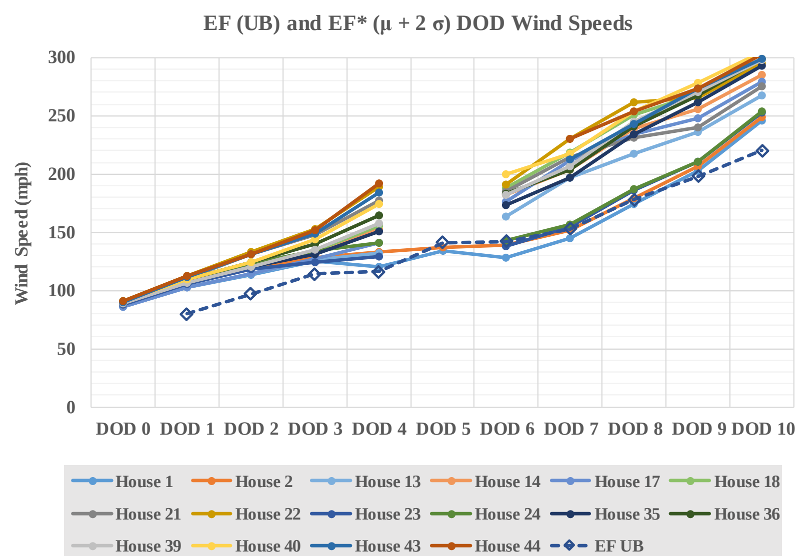

Note: 1 mph = 0.44704 m/s

Figure 6-20. EF-Scale UB vs. EF* (μ + 2σ) DOD Wind Speeds

6.6. EF* Wind Speeds

The above modeling of the $P(v_i|d_j)$ wind speeds (i.e., DOD wind speeds) provides a way to use engineering-derived wind speeds in the field to estimate tornado wind speeds and classify tornado intensity ratings. In this section we use these wind speeds in the development of the EF* wind speeds from the equations in Section 6.4.2.

6.6.1. Building Stock Weights

The work on general building data development for this project was based on previous ARA detailed wind mitigation inspections, field damage surveys, and literature (e.g., Twisdale et al. (2002), ARA (2000 – 2019), and FEMA (2007)). For this project, ARA also integrated data from the American Housing Survey (US Census Bureau , 2017) and selected county tax records to develop the FR12 building stock weights. [107]

Several example plots for the building data from the American Housing Survey and tax data are shown in Figure 6-21(a). The top left chart shows relative frequency of year built eras by region. Many houses built before 1965, when plywood became the dominant roof decking material, were built with dimensional lumber decks with 2 nails per board connections.[108] The top right chart shows that most house roof shapes are non-hips (most of these non-hips are gables), which are not as aerodynamically efficient as hips. Roof shape is an important variable in wind speed estimation and influence roof cover, deck, and structure failures. Square footage is useful in identifying size of building and associated complexity of the footprint and number of roof sections. Roof-deck nail size and spacing are a primary strength factor in deck failures (DOD 4), where 8d nails have about twice the pullout resistance of 6d nails.

Building stock weights were developed using multiple public data sources and ARA proprietary data. These weights for the 44 classes were initially developed by region for use with the epistemic DOD to EF model (described in the following section). However, the wind speed results did not vary significantly by region. We therefore used Region 407 data for the epistemic model in the calculations of EF* wind speeds. The FR12 class weights for Region 407 are illustrated in Figure 6-21(b). The percentages of classes by weak (LB), mid (EXP), and strong (UB) qualities are 38%, 54%, and 12%. About 78% are gables with 22 % hips; 58% are simple with 42% complex plans. The probabilities for Classes 21, 22, 43, and 44 (super strong class) are assumed to be zero for Region 407, as seen in Figure 6-21.

---

[107] All of the work on building data for purposes of this project were funded by an ARA Internal Research and Development (IRD) effort. The building stock work was not originally anticipated for this project scope and since ARA has developed building stock data since 1998 for use in loss mitigation and insurance catastrophe models, it was efficient for ARA to apply this data without requiring NIST resources. As we later discovered, the EF* wind speeds were not particularly sensitive to the use of building stock data vs. the DAT frequency data, which is described in Sections 6.6.2 and 6.6.3.

[108] Conditioning the building data by year-built era is useful for modeling building characteristics (Twisdale et al., 2002).

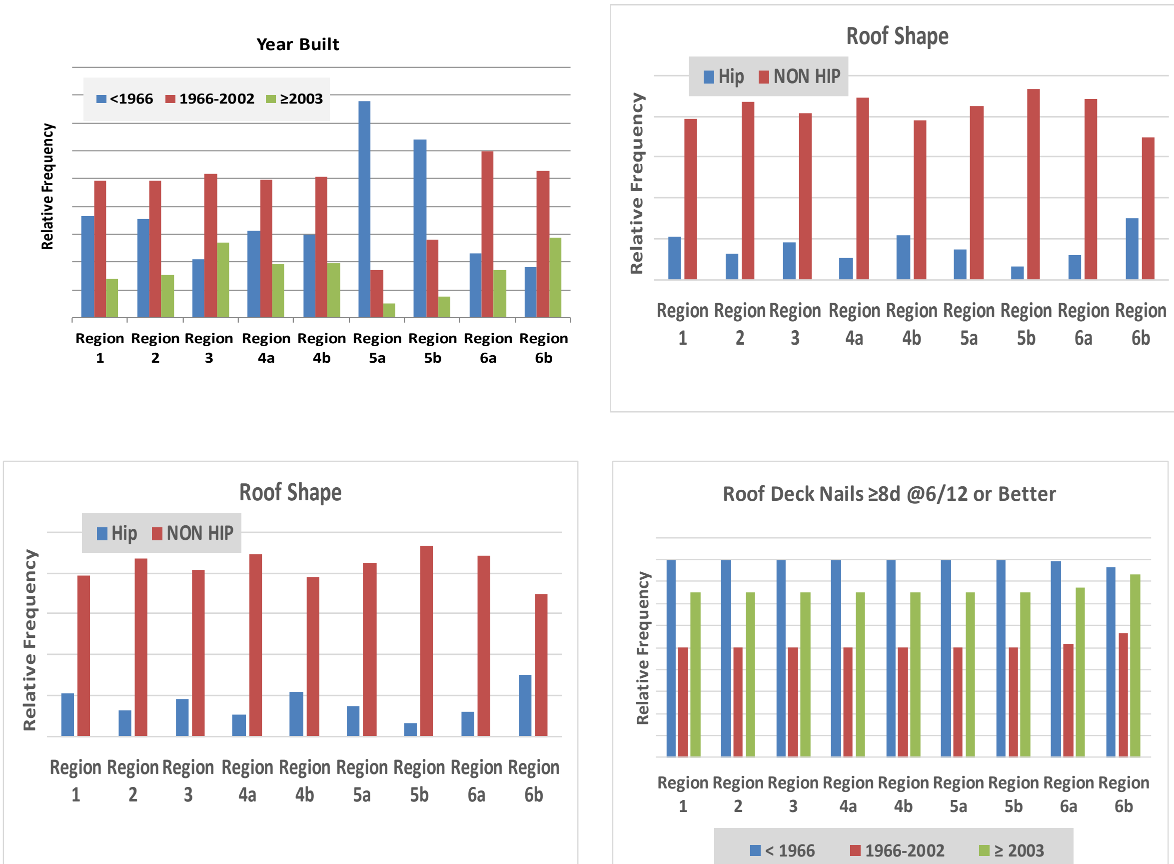

a. Examples of Regional Data

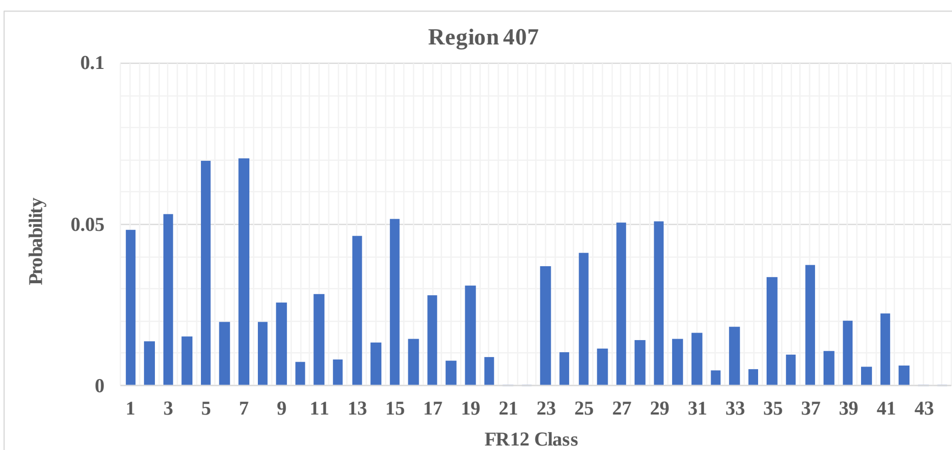

b. Region 407 Probabilities for 44 FR12 Classes

Figure 6-21. Example FR12 Building Data

6.6.2. DOD to EF* Model with Epistemic Uncertainties

The product $P_m\left(EF_k \middle| d_j, h_m\right) P_m(d_j | v_i, h_m)$ in Eq. (6-5) determines how the DODs are related to the EF-Scale wind speeds based on quality levels. The first term $P_m\left(EF_k \middle| d_j, h_m\right)$ relates how the load path features of various house classes are mapped to NOAA quality levels. We obtained data to support this mapping from our analysis of the DAT. As described in the Augmented Database, we linked DAT and SPC data to capture the tornado EF rating as part of this analysis. We performed this analysis two ways: (1) using FR12 as the sample space, and (2) using the tornado event as the sample space. The tornado event basis statistics are conditioned on a constraint that the FR12 EF rating equals the tornado EF rating. The two analyses produced similar results. We use the second approach herein since it limits the analysis to house EF ratings that match the tornado EF rating. The second approach ensures consistency with our use of the SPC EF-Scale frequencies to model the distribution of tornado intensities in the hazard curve simulations.

The event-based counts are provided in Table 6-9(a). This table show the EF frequencies for each DOD. For example, we find that for DOD 6, 305 out of 423 DOD 6 assignments resulted in an EF2 wind speed. The grey shaded areas in Table 6-9 correspond to the range of EFs corresponding to the LB, EXP, and UB wind speeds. Assigned EFs outside of the grey cells were exceptional cases.[109] Table 6-9(b) shows the relative frequencies by DOD without outliers. This table provides the basis for our conditional probability model ($P_m\left(EF_k \middle| d_j, h_m\right)$) needed to develop EF* wind speeds. It ensures that our use the EF-Scale frequency data from the SPC (used to develop the EF-Scale distribution model in Section 3) is consistent with the engineering derived EF* wind speeds.

Table 6-9(b) is next used to map the FR12 individual classes to the EF-Scale according the NOAA training and implementation of load path quality evaluation (NOAA, 2016b; LaDue and Ortega (2008); Ladue and Mahoney (2006)). Using the load path quality mapping (Table 6-6) to the EF-Scale Conditions (LB, EXP, and UB), Table 6-10 shows the resulting house class frequencies based on Table 6-9(b). Table 6-10 presents the first 22 classes, recognizing that the second 22 are identically mapped. The mixed quality houses (Classes 7-12) are not shown as mapped in this table in order to have a “frequency” mapping with no other interpretations; that is, Table 6-10 is a mapping which exactly follows the DAT data and the NOAA EF load path quality training (without any considerations of errors, observer interpretation variations, and unknowns with respect to the FR12 load path observations, mixed quality FR12 classes, or building stock data). Table 6-10 is termed a “frequency” implementation of the data.

[109] These rare outliers may also include data entry errors.

Table 6-9. FR12 DAT Database DOD and EF Data Conditioned on Tornado Event EF Rating

DOD	EF0	EF1	EF2	EF3	EF4	EF5	Total
DOD 1	91	0	2	0	0	1	94
DOD 2	340	121	0	0	0	0	461
DOD 3	13	93	0	0	0	0	106
DOD 4	43	481	27	1	0	0	552
DOD 5	1	33	48	4	0	0	86
DOD 6	0	89	305	29	0	0	423
DOD 7	0	5	110	42	3	0	160
DOD 8	0	0	24	114	9	0	147
DOD 9	0	1	4	96	77	6	184
DOD 10	0	0	0	17	77	31	125
Total	488	823	520	303	166	38	2338

a. Raw Counts

DOD	EF0	EF1	EF2	EF3	EF4	EF5	Total
DOD 1	1.00						1.00
DOD 2	0.74	0.26					1.00
DOD 3	0.12	0.88					1.00
DOD 4	0.08	0.87	0.05				1.00
DOD 5		0.39	0.56	0.05			1.00
DOD 6		0.21	0.72	0.07			1.00
DOD 7			0.72	0.28			1.00
DOD 8			0.16	0.78	0.06		1.00
DOD 9				0.55	0.45		1.00
DOD 10				0.14	0.61	0.25	1.00

b. EF Relative Frequency Given DOD (without outliers)

Table 6-10. DOD to EF Relative Frequencies According to DAT Quality Inference (“ Frequency Implementation”)

FR12 Class and Load Path Quality Attribute						DOD1	DOD2		DOD3		DOD4			DOD5			DOD6			DOD7		DOD8			DOD9		DOD10		
						EF0	EF0	EF1	EF0	EF1	EF0	EF1	EF2	EF1	EF2	EF3	EF1	EF2	EF3	EF2	EF3	EF2	EF3	EF4	EF3	EF4	EF3	EF4	EF5
Class	RW	Wall Sh.	Stud-BP	Fdn	Quality	All	L, E	U	L	E, U	L	E	U	L	E	U	L	E	U	L, E	U	L	E	U	L	E, U	L	E	U
1	8TN	M	SN	N	LB	1.00	0.74		0.12		0.08			0.39			0.21			0.72		0.16			0.55		0.14		
2	8TN	M	SN	N	LB	1.00	0.74		0.12		0.08			0.39			0.21			0.72		0.16			0.55		0.14		
3	8TN	M	SN	N	LB	1.00	0.74		0.12		0.08			0.39			0.21			0.72		0.16			0.55		0.14		
4	8TN	M	SN	N	LB	1.00	0.74		0.12		0.08			0.39			0.21			0.72		0.16			0.55		0.14		
5	8TN	M	SN	N	LB	1.00	0.74		0.12		0.08			0.39			0.21			0.72		0.16			0.55		0.14		
6	8TN	M	SN	N	LB	1.00	0.74		0.12		0.08			0.39			0.21			0.72		0.16			0.55		0.14		
7	16TN	M	SN	B	LB-EXP																								
8	16TN	M	SN	B	LB-EXP																								
9	16TN	F	TN	P	LB-EXP																								
10	16TN	F	TN	P	LB-EXP																								
11	16TN	F	TN	P	LB-EXP																								
12	16TN	F	TN	P	LB-EXP																								
13	16TN	F	TN	B	EXP	1.00	0.74			0.88		0.87			0.56			0.72		0.72			0.78			0.45		0.61	
14	16TN	F	TN	B	EXP	1.00	0.74			0.88		0.87			0.56			0.72		0.72			0.78			0.45		0.61	
15	16TN	F	TN	B	EXP	1.00	0.74			0.88		0.87			0.56			0.72		0.72			0.78			0.45		0.61	
16	16TN	F	TN	B	EXP	1.00	0.74			0.88		0.87			0.56			0.72		0.72			0.78			0.45		0.61	
17	C	F	C	B	UB	1.00		0.26		0.88			0.05			0.05			0.07		0.28			0.06		0.45			0.25
18	C	F	C	B	UB	1.00		0.26		0.88			0.05			0.05			0.07		0.28			0.06		0.45			0.25
19	C	F	C	B	UB	1.00		0.26		0.88			0.05			0.05			0.07		0.28			0.06		0.45			0.25
20	C	F	C	B	UB	1.00		0.26		0.88			0.05			0.05			0.07		0.28			0.06		0.45			0.25
21	DW	F	DS	B	UB	1.00		0.26		0.88			0.05			0.05			0.07		0.28			0.06		0.45			0.25
22	DW	F	DS	B	UB	1.00		0.26		0.88			0.05			0.05			0.07		0.28			0.06		0.45			0.25

In the “frequency” implementation (Table 6-10), consider FR12 Class 1 and DOD 5 as an example. We see that class always produces an EF1 wind speed as a LB quality house and that this occurs 39% of the time. Alternately, for House 13, which has EXP quality connections, the DAT data indicates that 56% of the time DOD 5 damage is associated with

EF 2 wind speeds. Thus, the data in Table 6-10 corresponds to an EF-Scale "historical" interpretation of NOAA developed tornado wind speeds and EF ratings associated with each DOD. We use these results without building stock weights on the house classes since we are using the NOAA data to indicate the frequency of LB, EXP, and UB conditions, as indicated in the DAT database wind speeds. In reading Table 6-10, note that the grouped entries for the columns under a DOD sum to unity (i.e., 0.39 + 0.56 +0.05 = 1.00), which reflect the DAT data.

Epistemic Uncertainties. Any system that attempts to estimate tornado wind speeds from observed damage is fraught with uncertainties.[110] For example, the user may have to infer certain features since time may not be available to do a thorough assessment or to gain entry into a partially-damaged structure. In the DAT toolkit, the user can adjust his/her wind speed estimation to reflect professional judgments regarding damage observables.

To reflect the realities of tornado wind speed estimation and the associated tornado EF damage rating, we developed several epistemic versions of Table 6-10. The epistemic version with very broad uncertainties is shown in Table 6-11. This table is used with building stock data, which provides the weighting for each row.[111] For a given DOD relative frequency (Eq. (6-5)) from the DPM table for that house class, the entries in Table 6-11 provide the relative frequency of the EF-Scale classification, reflecting the aforementioned uncertainties. For example, for Class 1 and DOD 5, we see that that this does not always produce EF1 tornado wind speeds. Considering uncertainties, we assigned a 60% weight to EF1, a 25% weight to EF2, and a 15% weight to EF3.[112] Hence, Table 6-11 allows for large uncertainties in the evaluation of load path quality and the associated LB, EXP, and UB wind speed estimations.

Table 6-11. DOD to EF Relative Frequencies According to DAT Quality Inference ("Epistemic with Building Stock Implementation")

FR12 Class and Load Path Quality Attribute						DOD1	DOD2		DOD3		DOD4			DOD5			DOD6			DOD7		DOD8			DOD9		DOD10		
						EF0	EF0	EF1	EF0	EF1	EF0	EF1	EF2	EF1	EF2	EF3	EF1	EF2	EF3	EF2	EF3	EF2	EF3	EF4	EF3	EF4	EF3	EF4	EF5
Class	RW	Wall Sh.	Stud-BP	Fdn	Quality	All	L, E	U	L	E, U	L	E	U	L	E	U	L	E	U	L, E	U	L	E	U	L	E, U	L	E	U
1	8TN	M	SN	N	LB	1.00	0.60	0.40	0.60	0.40	0.60	0.25	0.15	0.60	0.25	0.15	0.60	0.25	0.15	0.60	0.40	0.60	0.25	0.15	0.60	0.40	0.60	0.25	0.15
2	8TN	M	SN	N	LB	1.00	0.60	0.40	0.60	0.40	0.60	0.25	0.15	0.60	0.25	0.15	0.60	0.25	0.15	0.60	0.40	0.60	0.25	0.15	0.60	0.40	0.60	0.25	0.15
3	8TN	M	SN	N	LB	1.00	0.60	0.40	0.60	0.40	0.60	0.25	0.15	0.60	0.25	0.15	0.60	0.25	0.15	0.60	0.40	0.60	0.25	0.15	0.60	0.40	0.60	0.25	0.15
4	8TN	M	SN	N	LB	1.00	0.60	0.40	0.60	0.40	0.60	0.25	0.15	0.60	0.25	0.15	0.60	0.25	0.15	0.60	0.40	0.60	0.25	0.15	0.60	0.40	0.60	0.25	0.15
5	8TN	M	SN	N	LB	1.00	0.60	0.40	0.60	0.40	0.60	0.25	0.15	0.60	0.25	0.15	0.60	0.25	0.15	0.60	0.40	0.60	0.25	0.15	0.60	0.40	0.60	0.25	0.15
6	8TN	M	SN	N	LB	1.00	0.60	0.40	0.60	0.40	0.60	0.25	0.15	0.60	0.25	0.15	0.60	0.25	0.15	0.60	0.40	0.60	0.25	0.15	0.60	0.40	0.60	0.25	0.15
7	16TN	M	SN	B	LB-EXP	1.00	0.50	0.50	0.50	0.50	0.40	0.42	0.18	0.40	0.42	0.18	0.40	0.42	0.18	0.60	0.40	0.40	0.42	0.18	0.50	0.50	0.40	0.42	0.18
8	16TN	M	SN	B	LB-EXP	1.00	0.50	0.50	0.50	0.50	0.40	0.42	0.18	0.40	0.42	0.18	0.40	0.42	0.18	0.60	0.40	0.40	0.42	0.18	0.50	0.50	0.40	0.42	0.18
9	16TN	F	TN	P	LB-EXP	1.00	0.50	0.50	0.50	0.50	0.40	0.42	0.18	0.40	0.42	0.18	0.40	0.42	0.18	0.60	0.40	0.40	0.42	0.18	0.50	0.50	0.40	0.42	0.18
10	16TN	F	TN	P	LB-EXP	1.00	0.50	0.50	0.50	0.50	0.40	0.42	0.18	0.40	0.42	0.18	0.40	0.42	0.18	0.60	0.40	0.40	0.42	0.18	0.50	0.50	0.40	0.42	0.18
11	16TN	F	TN	P	LB-EXP	1.00	0.50	0.50	0.50	0.50	0.40	0.42	0.18	0.40	0.42	0.18	0.40	0.42	0.18	0.60	0.40	0.40	0.42	0.18	0.50	0.50	0.40	0.42	0.18
12	16TN	F	TN	P	LB-EXP	1.00	0.50	0.50	0.50	0.50	0.40	0.42	0.18	0.40	0.42	0.18	0.40	0.42	0.18	0.60	0.40	0.40	0.42	0.18	0.50	0.50	0.40	0.42	0.18
13	16TN	F	TN	B	EXP	1.00	0.50	0.50	0.40	0.60	0.20	0.60	0.20	0.20	0.60	0.20	0.20	0.60	0.20	0.60	0.40	0.20	0.60	0.20	0.40	0.60	0.20	0.60	0.20
14	16TN	F	TN	B	EXP	1.00	0.50	0.50	0.40	0.60	0.20	0.60	0.20	0.20	0.60	0.20	0.20	0.60	0.20	0.60	0.40	0.20	0.60	0.20	0.40	0.60	0.20	0.60	0.20
15	16TN	F	TN	B	EXP	1.00	0.50	0.50	0.40	0.60	0.20	0.60	0.20	0.20	0.60	0.20	0.20	0.60	0.20	0.60	0.40	0.20	0.60	0.20	0.40	0.60	0.20	0.60	0.20
16	16TN	F	TN	B	EXP	1.00	0.50	0.50	0.40	0.60	0.20	0.60	0.20	0.20	0.60	0.20	0.20	0.60	0.20	0.60	0.40	0.20	0.60	0.20	0.40	0.60	0.20	0.60	0.20
17	C	F	C	B	UB	1.00	0.40	0.60	0.40	0.60	0.15	0.25	0.60	0.15	0.25	0.60	0.15	0.25	0.60	0.40	0.60	0.15	0.25	0.60	0.40	0.60	0.15	0.25	0.60
18	C	F	C	B	UB	1.00	0.40	0.60	0.40	0.60	0.15	0.25	0.60	0.15	0.25	0.60	0.15	0.25	0.60	0.40	0.60	0.15	0.25	0.60	0.40	0.60	0.15	0.25	0.60
19	C	F	C	B	UB	1.00	0.40	0.60	0.40	0.60	0.15	0.25	0.60	0.15	0.25	0.60	0.15	0.25	0.60	0.40	0.60	0.15	0.25	0.60	0.40	0.60	0.15	0.25	0.60
20	C	F	C	B	UB	1.00	0.40	0.60	0.40	0.60	0.15	0.25	0.60	0.15	0.25	0.60	0.15	0.25	0.60	0.40	0.60	0.15	0.25	0.60	0.40	0.60	0.15	0.25	0.60
21	DW	F	DS	B	UB	1.00	0.40	0.60	0.40	0.60	0.15	0.25	0.60	0.15	0.25	0.60	0.15	0.25	0.60	0.40	0.60	0.15	0.25	0.60	0.40	0.60	0.15	0.25	0.60
22	DW	F	DS	B	UB	1.00	0.40	0.60	0.40	0.60	0.15	0.25	0.60	0.15	0.25	0.60	0.15	0.25	0.60	0.40	0.60	0.15	0.25	0.60	0.40	0.60	0.15	0.25	0.60

[110] One can either attempt to model them or not. As a major theme of this work, modeling these inherent uncertainties allows us to propagate them through the process to order to develop probabilistic wind speed distributions.

[111] The row-wise sum under each DOD group is unity to reflect the use of row-wise building stock weights.

[112] These broad uncertainties reflect up to two EF-Scale variation in wind speeds for a given class with the majority of the weight going to the DAT frequencies. They reflect user interpretations, variance, inability to ascertain load path quality conditions, mistakes, etc.

6.6.3. Sensitivity Analyses and Epistemic Distributions

We performed several sensitivity analyses on key judgments used in the development of the EF* wind speeds.

Prior Distribution. The effect of the prior wind speed distribution is illustrated in Figure 6-22. The mean and mean ± 2 standard deviation (SD) wind speeds are given for the UB, Base, and LB Priors. We also show a weighted Epistemic Prior, which was produced by weighting the EF* wind speeds for LB, Base, and UB and combined the results to produce a weighted mean EF* wind speed distribution. We used weights of 0.1, 0.5, and 0.4 for the LB, Base, and UB, respectively. This judgment-based weighting places the half the weight on the Base case, a very modest weight (0.1) on the LB case, and the remaining (0.4) weight on the UB case. The modest LB weight reflects the fact that the engineering-derived wind speeds show that the EF-Scale wind speeds are reasonable for LB FR12 conditions, but do not adequately reflect EXP or stronger conditions.

We see that the epistemic EF* mean wind speeds are slightly above the Base. For example, the mean weighted Epistemic EF* 3, 4, and 5 wind speeds are about 3, 5 and 6 mph (1.3, 2.2, and 2.7 m/s) larger, respectively, than the Base. The differences for lower EF* mean wind speeds are less than 1 mph (0.45 m/s).

The range of wind speeds within from LB to UB priors (V_{UB} - V_{LB}) provide a measure of the range of uncertainty in wind speed estimation given the probabilistic engineering derived wind speed distributions and available data regarding the frequency of extreme tornado wind speeds. This range is very modest for LB wind speeds, as seen by the tight grouping and minor impact of the prior assumption. This LB range approaches 20 mph (8.9 m/s) for EF*5 wind speeds. For mean EF* wind speeds, the range is about 20 mph (8.9 m/s) at EF*3 and increases to about 30 mph (13 m/s) for EF*5 wind speeds. The range is greatest for UB wind speed and reaches about 50 mph (22 m/s) at EF*5 wind speeds. If we divide the range by 2, a rough estimate of the residual uncertainty in extreme EF*5 wind speeds is about ± 25 mph (11.2 m/s).

The Epistemic Prior is used for the final EF* wind speed distributions for the tornado wind speed maps. Additional sensitivities are illustrated regarding the prior assumption are provided in Section 7 in terms of its impact on hazard curves.

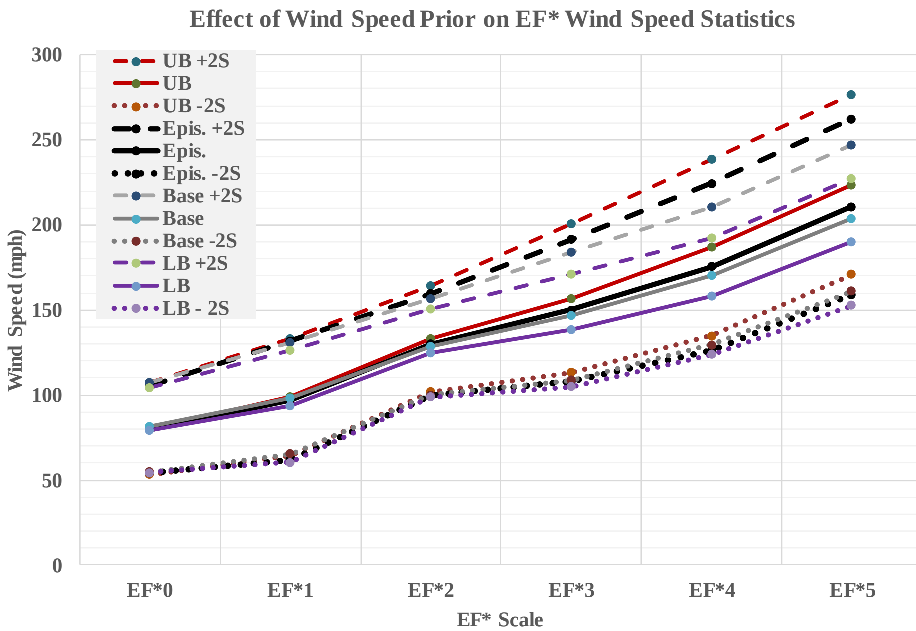

Note: 1 mph = 0.44704 m/s

Figure 6-22. EF* Wind Speed Sensitivity to Prior Wind Speed Distribution

DOD to EF Frequency Distribution. We computed EF* wind speeds from the equations in Section 6.4 for both the " frequency implementation" and the "epistemic" DOD to EF models in Table 6-10 and Table 6-11, respectively. Figure 6-23 shows the EF* wind speed means and means plus 2 standard deviations wind speeds obtained from these DOD to EF implementations.

We see that the epistemic implementation provides slightly higher results for EF3-5. These results reflect the fact that: (1) there are broad and overlapping wind speed distributions for the EF* DODs; (2) there are very minor differences in the DOD wind speeds for different house qualities for the lower DODs; and (3) there is an invariance regarding EF5 wind speeds since only UB conditions warrant these wind speeds (TTU, 2006: NOAA, 2016). As a result of these facts, there is little sensitivity to the EF* wind speeds with the notable differences from Table 6-9 to Table 6-10. The frequency results have EF*5 wind speeds based only on UB conditions and this fact ameliorates the large differences in the conditional probabilities between Table 6-9 and Table 6-10.

Based on this analysis, we use the epistemic implementation in Table 6-10 for the development of EF* wind speeds to reflect uncertainties in the DOD to EF wind speed estimation process.

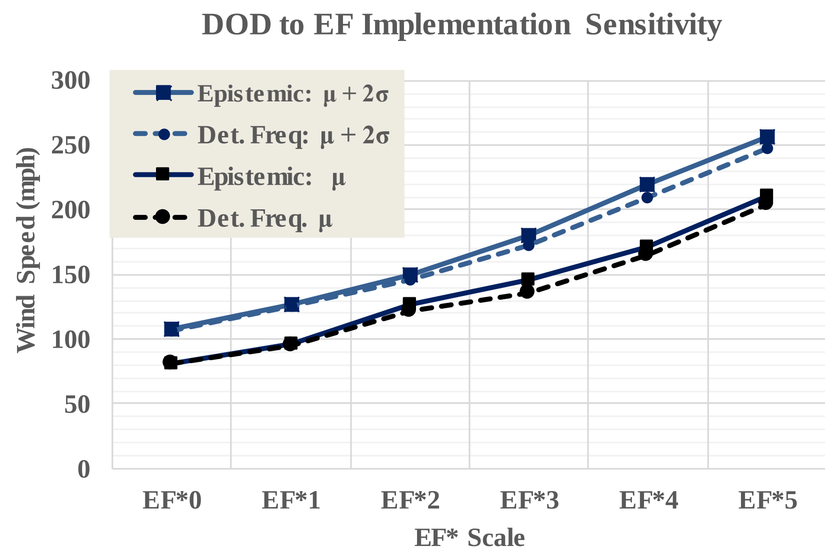

Note: 1 mph = 0.44704 m/s

Figure 6-23. EF* Wind Speed Statistics for Different DOD to EF Implementations

Bayesian Recursive Updating (Damage Confirmation). With each succeeding damage observation, the Bayesian model updates the wind speed distribution (per Eqs. (6-6) and (6-8)). We illustrate this process for Eq. (6-8) in which we assume that each new observation is confirming damage on the weighted mean FR12 class (per Eq. (6-7)). Figure 6-24 illustrates the results for up to 10 (repetitive) confirming observations. Under these assumptions, the mean EF* wind speeds change very little as a result of the additional observations. We see that the mean of the 1st observation and the 10th observation show little variation. The mean generally reduces slightly with each succeeding observation due to the long right-hand tails of the EF* wind speeds and the elimination of very high wind speeds due to confirmation.

The tightening of the *2σ* wind speed ranges illustrate how the process works with this ideal case of confirming damage observations. This tightening occurs with several observations and then shows a gradual reduction. It is seen most readily in the higher EF* wind speeds. For example, the EF5* standard deviations for 1 to 10 observations are 32, 22, 17, 14, 13, 11, 10, 10, 9, and 8 mph (14.3, 9.83, 7.60, 6.26, 5.81, 4.92, 4.47, 4.47, 4.0, and 3.6 m/s) (as rounded integer values).

We use the EF* wind speeds based on two observations, which are assumed to be statistically independent. This approach agrees with the general NOAA concept of at least a second "independent" confirmation of the wind speeds in the field as part of the rating of the tornado. Figure 6-24 shows that this approach produces mean wind speeds that are not sensitive to the number of observations and that the distribution variance is reduced by about 30% with the second observation. [113]

[113] It is important to note that our use of identical confirmations is a simplification over a field implemented recursive updating of wind speeds. In field implementation, each succeeding DI may be a different DI or a different class of the same DI. In addition, field observations have variation in observed DOD frequencies. Such results may increase the mean, reduce the mean, expand or reduce the uncertainties, as noted by Twisdale et al. (2016). However, the use of identical confirmations serves the purpose of tightening uncertainties in a reasonable fashion as shown in Figure 6-24.

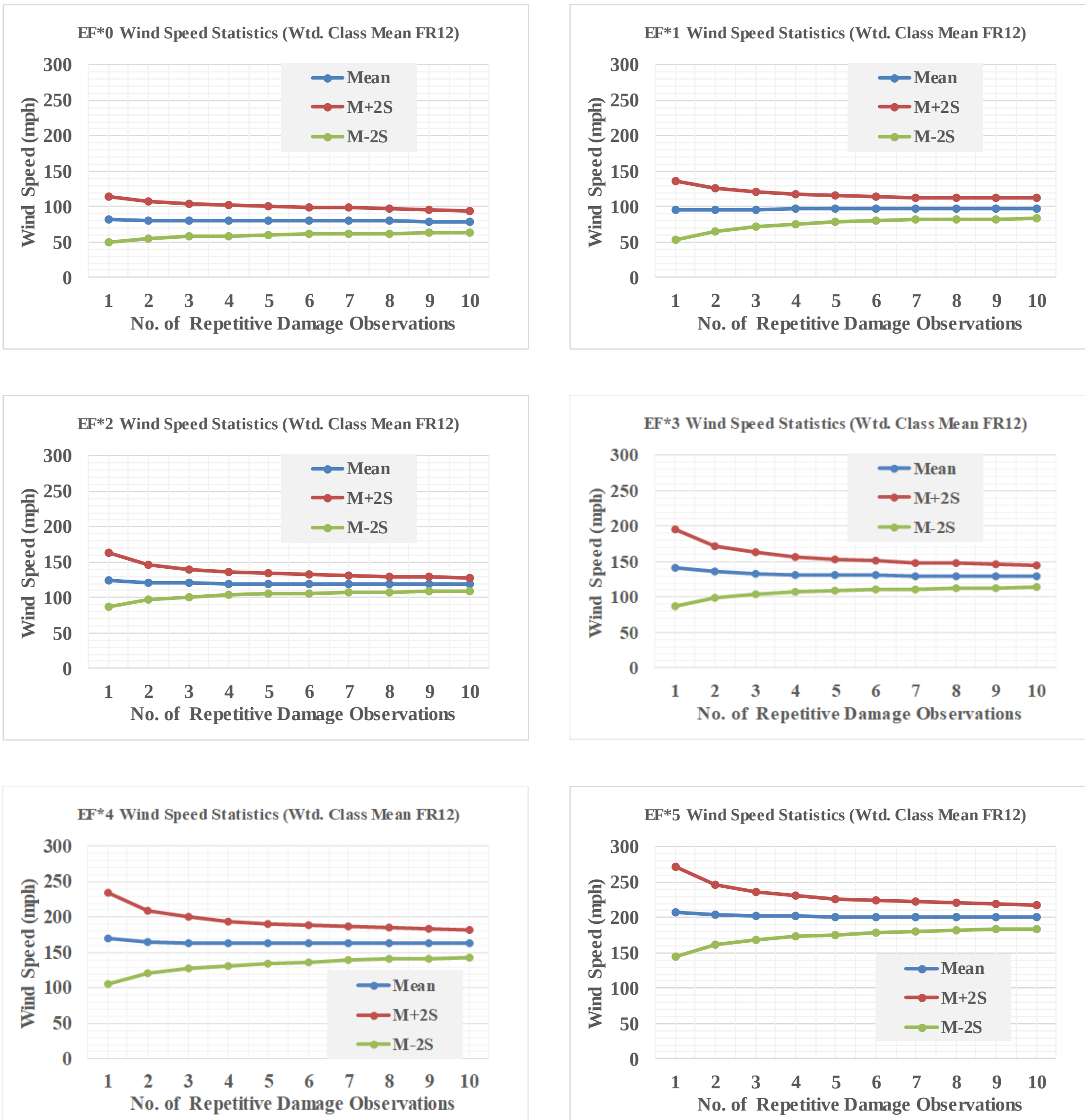

Note: 1 mph = 0.44704 m/s

Figure 6-24. Illustration of Repetitive Confirming Damage Observations on EF* Wind Speed Statistics

6.6.4. EF* Wind Speed Distributions

The engineering-derived EF* wind speed PMFs used in the map development are given in Figure 6-25 through Figure 6-27. The PMFs naturally sum to one for each EF*-Scale. The wind speeds represent the distribution of wind speeds associated with the SPC tornado EF-Scale intensity ratings, which are dominated by the FR12 DI. The wind speeds are RWS,

.

which are defined as the maximum tornado wind speed (nominal peak gust) experienced within the FR12 plan area at 33 ft (10.1 m).

The black dashed vertical lines on the figures are the EF-Scale wind speed ranges (TTU, 2006). The EF-Scale wind speed ranges are well captured in the EF* wind speeds. The EF* 2-5 wind speeds have long upper tails compared to the EF wind speed upper ranges.

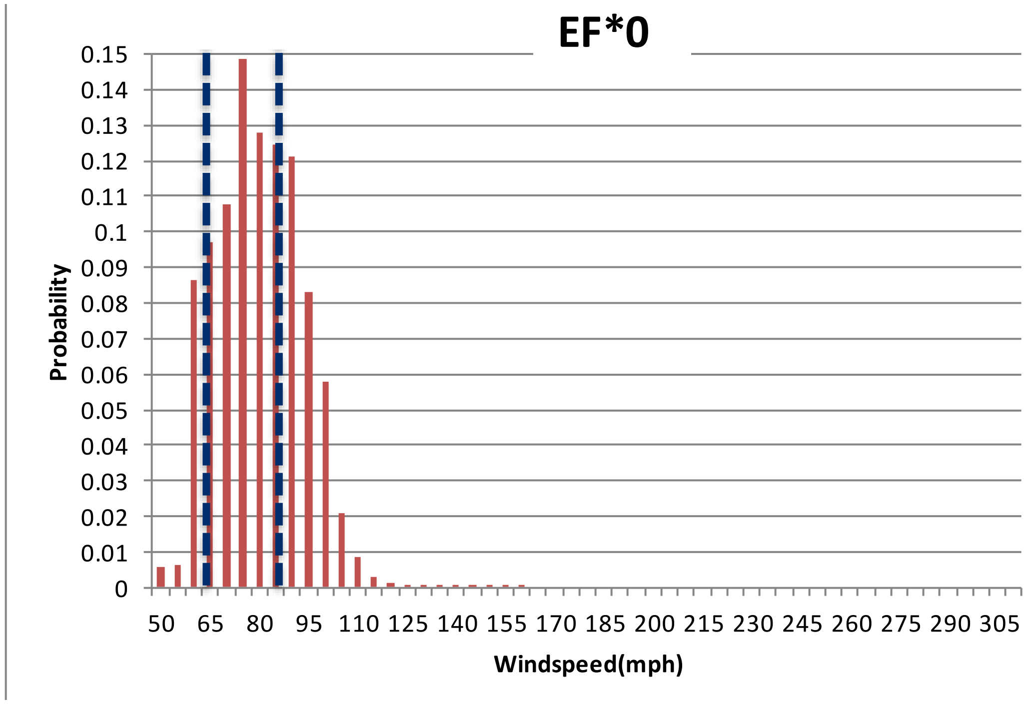

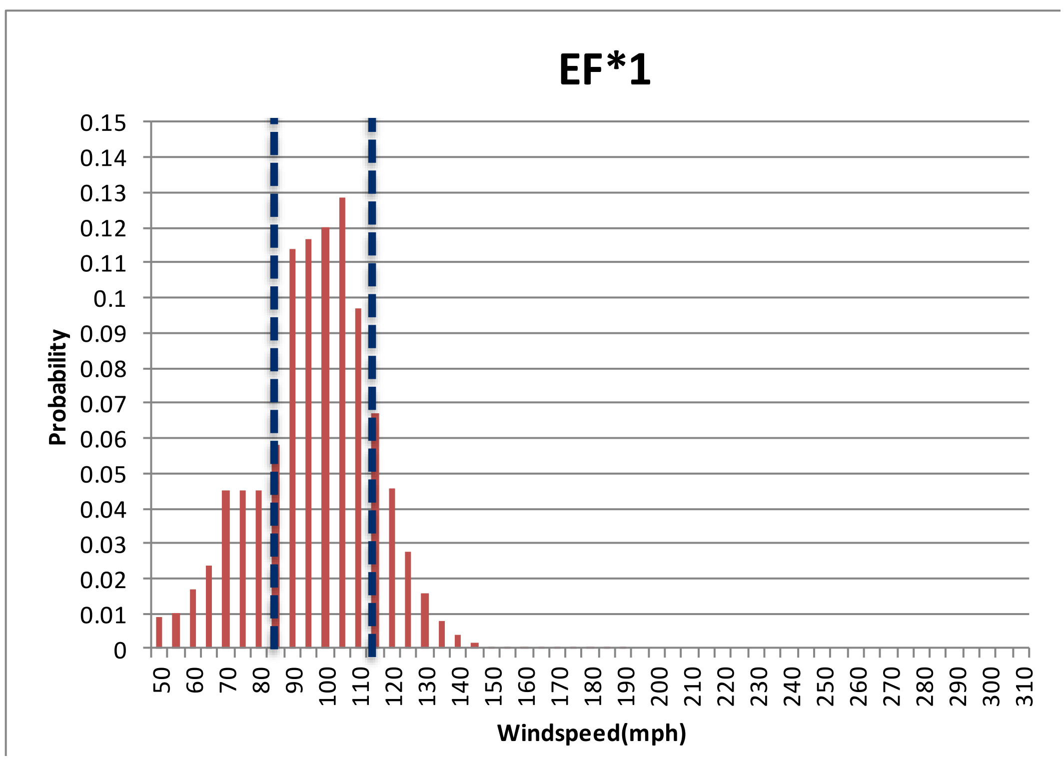

Note: 1 mph = 0.44704 m/s

Figure 6-25. EF*0 and EF*1 Wind Speed PMFs

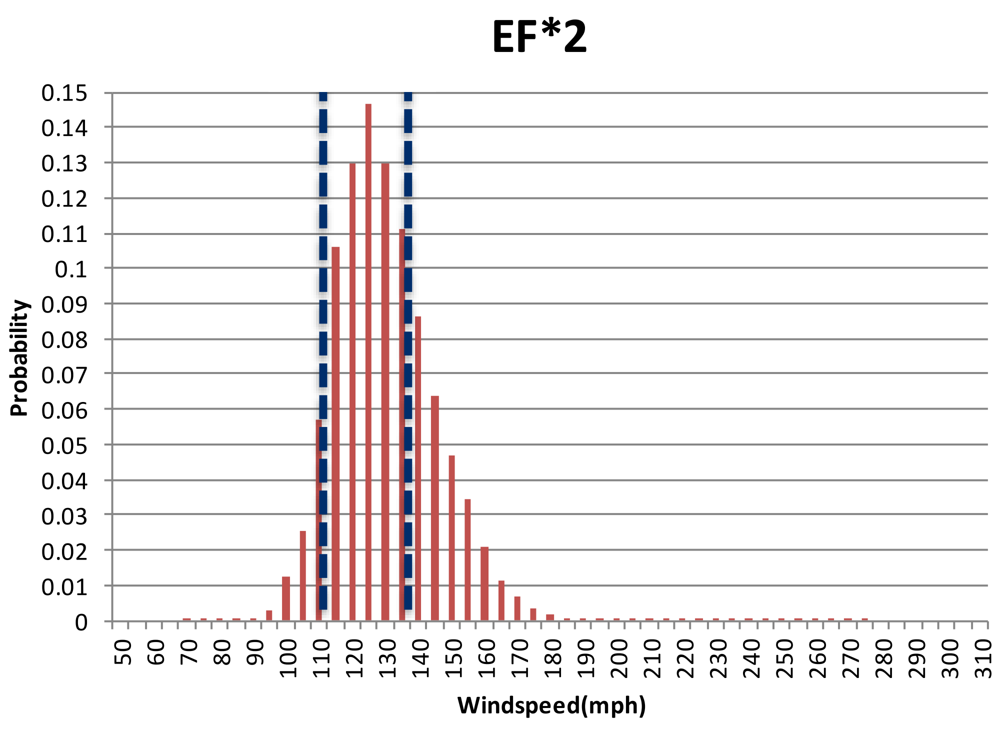

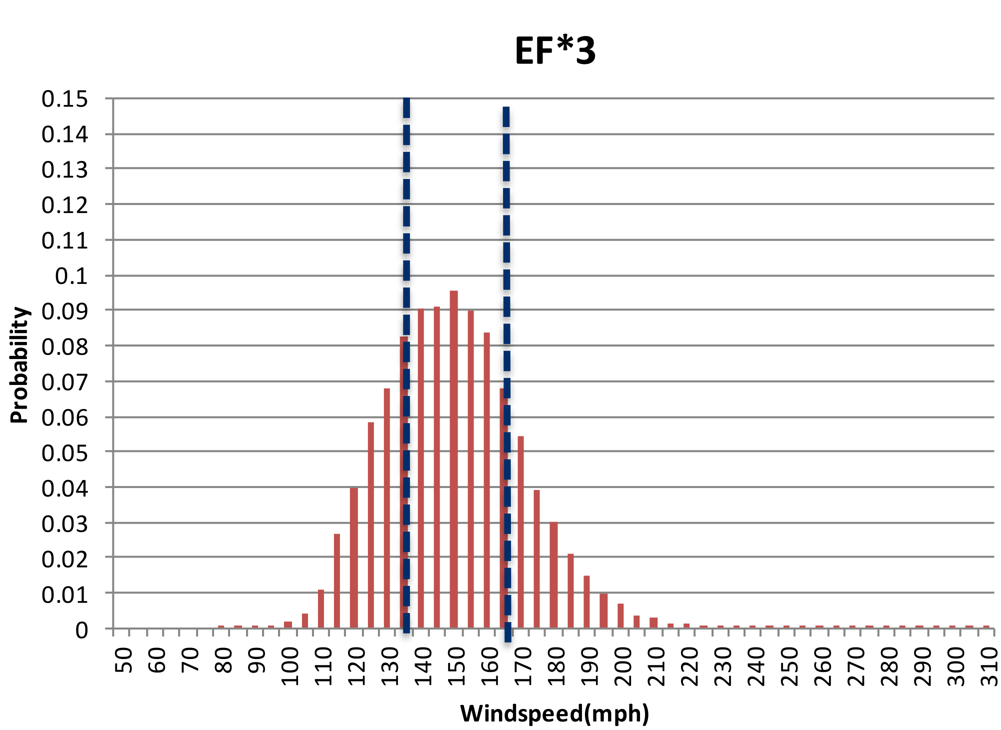

Note: 1 mph = 0.44704 m/s

Figure 6-26. EF*2 and EF*3 Wind Speed PMFs

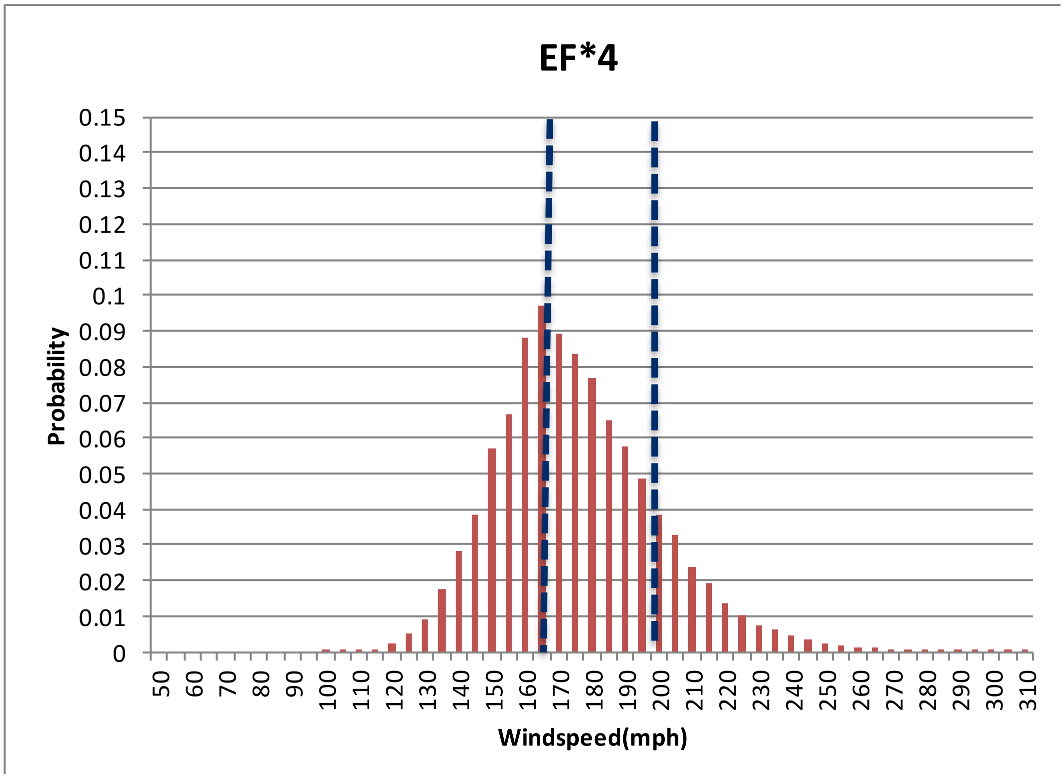

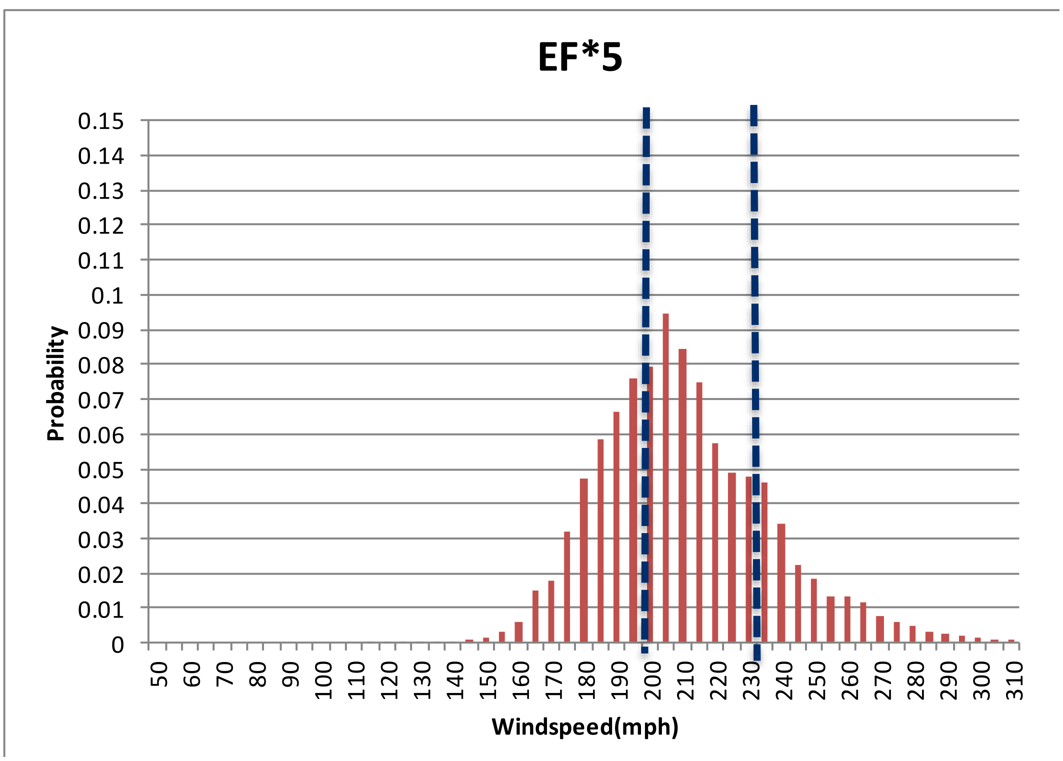

Note: 1 mph = 0.44704 m/s

Figure 6-27. EF*4 and EF*5 Wind Speed PMFs

Similar to the DOD wind speeds, the EF* wind speeds are much broader than the EF-Scale ranges, due to the aforementioned variations in: tornado characteristics; building position and orientation; randomness in pressure coefficients; tornado wind directionality; and structural loads/resistances. Epistemic uncertainties are included in two ways: (1) explicitly by sampling within the simulations; and (2) through inputs of derived means to the simulations (e.g., the prior wind speed distribution).

Figure 6-28 provides log scale probability plots of the EF* wind speeds and includes the ≤ EF*0 category. As mentioned in Sections 3 and 6.4, the ≤ EF*0 distribution is developed naturally from the DPM calculations by scoring when the FR12 does not experience D0D 1 threshold damage. As seen from Figure 6-28, these ≤ EF*0 wind speeds are less than 85 mph (38.0 m/s) about 99% of the time. The log scale plots for all the EF* wind speeds show the long right-hand tail of the engineering-derived wind speeds.

Figure 6-29 provides cumulative distribution function (CDF) plots of the EF* wind speeds. The cumulative functions show reasonable separation and smoothness. The slope of the functions generally increase with EF*-Scale, reflecting increasing uncertainties with increasing EF*.

Table 6-12 provides the PMF values over the range of 50 to 310 mph (22 to 139 m/s) in 5 mph (2.2 m/s) increments. Zero PMFs mean that none of the simulations produced a result in that wind speed bin for that EF*-Scale. From Table 6-11, we see, for example, that 1 in 10, 1 in 100, and 1 in 1,000 (2007-2016, historically rated) EF5 tornadoes are expected to have a maximum peak gust wind speed of about 240 mph (107 m/s), 280 mph (125 m/s), and about 300 mph (134 m/s), respectively, using the epistemic prior. These wind speeds are associated with an area of 2,050 square feet (190.5 m^2), which is the area weighted of the simple and complex plans. These results also indicate that the slope of the prior distribution governs its impact on the engineering-derived wind speeds and not the actual WEF values used to estimate plausible priors in Section 6.4.4. We will see in Section 7 that as the building size increases, the chances of experiencing 300 mph (134 m/s) wind speeds, increases notably. [114]

Since our upper wind speed bin for the DPM calculations was 310 mph (139 m/s) (range of 307.499 mph to 312.5 mph (137.4644 m/s to 139.70 m/s)), we do not have information for wind speeds greater than 312.5 mph (139.70 m/s). From the EF*5 PMF plots in Appendix F.2, one can see that small probabilities would be expected at somewhat higher wind speeds.

Table 6-13provides the mean, standard deviation, and selected CDF percentiles for the EF* wind speed distributions.

[114] Similarly, a mobile radar with an accurate viewable window over, say, fractions of a square mile plan area has a much greater chance of observing 300 mph (134 m/s) wind speeds than observing these wind speeds over a much smaller area, such as a 2000 SF (7E-05 mi^2) (190 m^2) house.

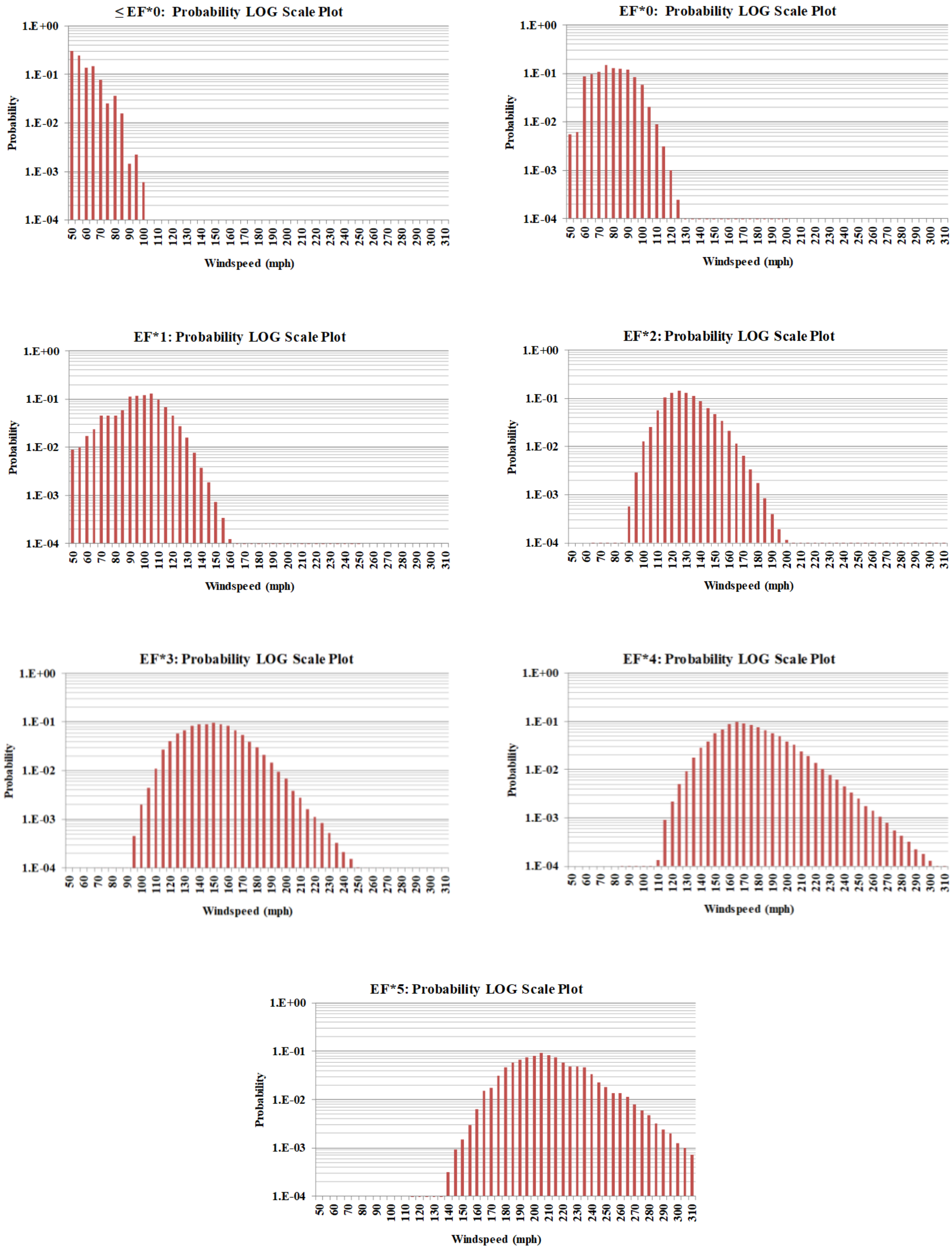

Note: 1 mph = 0.44704 m/s

Figure 6-28. Log Scale Probability Plots of the EF* Wind Speeds

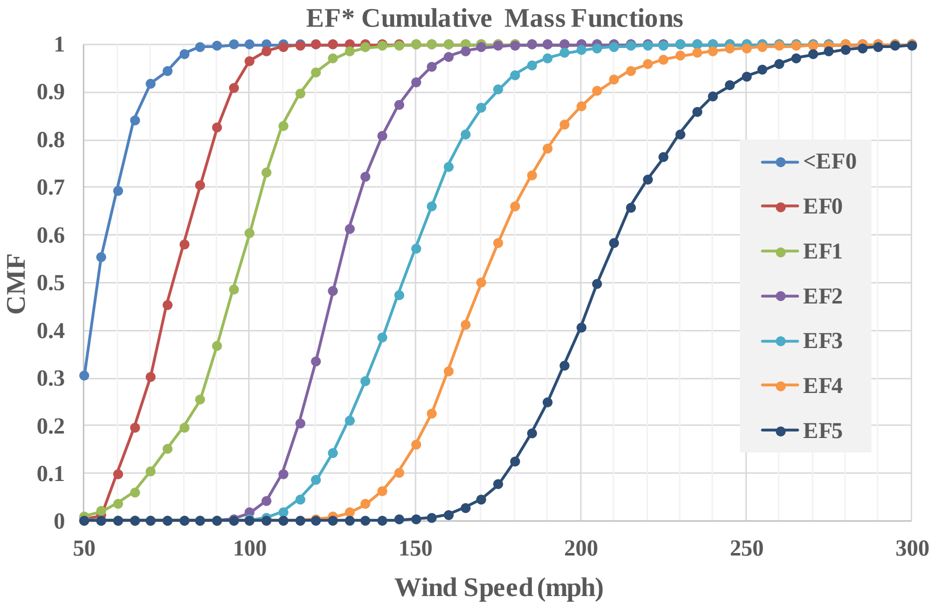

Note: 1 mph = 0.44704 m/s

Figure 6-29. EF* Cumulative Distribution Function Plots

Table 6-12. EF* Probabilities by Wind Speed Bin

Wind Speed (mph)	EF* Scale						
	<EF*0	EF*0	EF*1	EF*2	EF*3	EF*4	EF*5
50	3.04E-01	5.47E-03	8.97E-03	0.00E+00	0.00E+00	0.00E+00	0.00E+00
55	2.51E-01	6.08E-03	1.01E-02	0.00E+00	0.00E+00	0.00E+00	0.00E+00
60	1.39E-01	8.64E-02	1.68E-02	0.00E+00	0.00E+00	0.00E+00	0.00E+00
65	1.47E-01	9.71E-02	2.36E-02	8.02E-10	0.00E+00	0.00E+00	0.00E+00
70	7.78E-02	1.08E-01	4.52E-02	4.91E-08	8.80E-10	0.00E+00	0.00E+00
75	2.54E-02	1.49E-01	4.52E-02	3.84E-07	9.09E-09	0.00E+00	0.00E+00
80	3.59E-02	1.28E-01	4.53E-02	4.06E-06	2.71E-07	0.00E+00	0.00E+00
85	1.58E-02	1.25E-01	5.81E-02	5.47E-05	6.89E-06	2.44E-09	0.00E+00
90	1.44E-03	1.21E-01	1.14E-01	5.68E-04	7.53E-05	9.74E-09	0.00E+00
95	2.22E-03	8.28E-02	1.17E-01	2.90E-03	4.46E-04	1.70E-08	0.00E+00
100	5.95E-04	5.78E-02	1.20E-01	1.26E-02	2.02E-03	4.47E-07	0.00E+00
105	5.26E-06	2.06E-02	1.29E-01	2.55E-02	4.44E-03	2.21E-05	0.00E+00
110	5.28E-06	8.76E-03	9.70E-02	5.73E-02	1.08E-02	1.36E-04	0.00E+00
115	2.80E-07	3.08E-03	6.71E-02	1.06E-01	2.68E-02	9.05E-04	4.25E-08
120	9.03E-09	1.01E-03	4.56E-02	1.30E-01	4.00E-02	2.16E-03	1.92E-07
125	1.08E-09	2.46E-04	2.75E-02	1.47E-01	5.83E-02	4.92E-03	3.41E-07
130	3.10E-11	9.70E-05	1.58E-02	1.30E-01	6.77E-02	9.30E-03	1.15E-05
135	0.00E+00	3.06E-05	7.63E-03	1.11E-01	8.28E-02	1.75E-02	6.21E-05
140	0.00E+00	1.00E-05	3.70E-03	8.64E-02	9.04E-02	2.81E-02	3.17E-04
145	0.00E+00	6.19E-06	1.86E-03	6.37E-02	9.10E-02	3.86E-02	9.34E-04
150	0.00E+00	1.26E-06	7.24E-04	4.69E-02	9.56E-02	5.69E-02	1.49E-03
155	0.00E+00	4.21E-07	3.41E-04	3.42E-02	9.01E-02	6.67E-02	2.95E-03
160	0.00E+00	1.52E-07	1.25E-04	2.11E-02	8.39E-02	8.83E-02	6.30E-03
165	0.00E+00	2.17E-08	3.34E-05	1.15E-02	6.77E-02	9.69E-02	1.51E-02
170	0.00E+00	4.37E-09	1.03E-05	6.57E-03	5.42E-02	8.93E-02	1.77E-02
175	0.00E+00	9.02E-10	3.19E-06	3.34E-03	3.94E-02	8.34E-02	3.18E-02
180	0.00E+00	1.02E-10	7.45E-07	1.73E-03	3.04E-02	7.66E-02	4.72E-02
185	0.00E+00	1.09E-11	1.91E-07	8.52E-04	2.11E-02	6.50E-02	5.87E-02
190	0.00E+00	1.48E-12	3.28E-08	3.97E-04	1.49E-02	5.75E-02	6.61E-02
195	0.00E+00	1.71E-13	8.81E-09	1.94E-04	9.56E-03	4.84E-02	7.58E-02
200	0.00E+00	7.58E-16	1.87E-09	1.14E-04	6.72E-03	3.84E-02	7.95E-02
205	0.00E+00	0.00E+00	4.34E-10	4.37E-05	3.80E-03	3.30E-02	9.43E-02
210	0.00E+00	0.00E+00	1.04E-10	3.35E-05	2.80E-03	2.36E-02	8.46E-02
215	0.00E+00	0.00E+00	3.34E-11	1.49E-05	1.62E-03	1.90E-02	7.48E-02
220	0.00E+00	0.00E+00	1.85E-11	8.97E-06	1.13E-03	1.38E-02	5.71E-02
225	0.00E+00	0.00E+00	3.57E-12	6.13E-06	8.37E-04	1.02E-02	4.88E-02
230	0.00E+00	0.00E+00	4.85E-13	3.11E-06	5.16E-04	7.62E-03	4.76E-02
235	0.00E+00	0.00E+00	6.31E-14	1.72E-06	3.27E-04	6.16E-03	4.63E-02
240	0.00E+00	0.00E+00	4.23E-14	1.32E-06	2.13E-04	4.50E-03	3.42E-02
245	0.00E+00	0.00E+00	1.17E-15	7.08E-07	1.50E-04	3.37E-03	2.27E-02
250	0.00E+00	0.00E+00	3.18E-16	4.35E-07	1.04E-04	2.55E-03	1.82E-02
255	0.00E+00	0.00E+00	0.00E+00	3.83E-07	7.39E-05	1.77E-03	1.36E-02
260	0.00E+00	0.00E+00	0.00E+00	1.73E-07	4.59E-05	1.39E-03	1.34E-02
265	0.00E+00	0.00E+00	0.00E+00	1.26E-07	3.13E-05	1.06E-03	1.14E-02
270	0.00E+00	0.00E+00	0.00E+00	8.00E-08	2.25E-05	7.81E-04	7.82E-03
275	0.00E+00	0.00E+00	0.00E+00	3.77E-08	1.58E-05	5.42E-04	5.85E-03
280	0.00E+00	0.00E+00	0.00E+00	2.55E-08	1.11E-05	4.20E-04	4.84E-03
285	0.00E+00	0.00E+00	0.00E+00	1.57E-08	7.36E-06	3.25E-04	3.21E-03
290	0.00E+00	0.00E+00	0.00E+00	1.20E-08	4.72E-06	2.22E-04	2.39E-03
295	0.00E+00	0.00E+00	0.00E+00	9.22E-09	3.80E-06	1.80E-04	2.01E-03
300	0.00E+00	0.00E+00	0.00E+00	6.48E-09	2.68E-06	1.29E-04	1.23E-03
305	0.00E+00	0.00E+00	0.00E+00	3.36E-09	2.00E-06	9.25E-05	9.97E-04
310	0.00E+00	0.00E+00	0.00E+00	3.33E-09	1.44E-06	6.69E-05	7.16E-04
Sum	1.00E+00	1.00E+00	1.00E+00	1.00E+00	1.00E+00	1.00E+00	1.00E+00

Note: 1 mph = 0.44704 m/s

Table 6-13. EF* Wind Speed Statistics

Statistic		EF*-Scale Wind Speeds (mph)						
		<EF*0	EF*0	EF*1	EF*2	EF*3	EF*4	EF*5
Mean		58.86	79.86	96.87	129.89	149.84	175.5	210.55
Std. Dev.		9.04	12.79	17.42	14.9	20.78	24.42	25.82
Percentile (%)	0.1%	50	50	50	91	97	115	144
	0.5%	50	50	50	96	103	122	154
	1.0%	50	54	51	98	107	126	159
	2.5%	50	57	57	102	112	133	164
	5.0%	50	58	63	106	116	138	171
	10.0%	50	60	70	110	122	145	178
	25.0%	50	68	85	117	133	157	190
	50.0%	54	77	96	126	146	170	205
	75.0%	62	87	106	137	160	187	224
	90.0%	69	95	115	148	174	205	242
	95.0%	76	99	121	154	183	217	256
	97.5%	79	102	127	160	192	229	268
	99.0%	83	107	133	168	202	244	281
	99.5%	85	110	137	173	210	256	290
	99.9%	94	117	147	184	230	280	304

Note: 1 mph = 0.44704 m/s

6.7. Validation Testing of the Damage Model

Tornado damage model was tested against some of the damaged structures in three different tornadoes to assess the damage prediction of the model for these structures. The first two validation examples are based on the ARA surveyed tornadoes and the third one is based on the NIST Joplin Tornado database (Scott, 2021).

6.7.1. Galatia Tornado

The data collected from the Galatia tornado damage survey was used to validate the tornado damage model. Details of this damage survey are given in Appendix E. We used one of the houses that was damaged in the tornado for the validation. The house is a one story wood frame house with gable roof. The shingles were observed as poor quality. The roof deck was attached to the roof frame by 8d nails spaced at 9 inches (23 cm) at the edge and 17 inches (43 cm) at the field. 3-16d toe nails were used to attach to the roof frame to the wall. Walls were not sheathed and the top plate was connected to wall studs using 16-d straight nails. The foundation connection of this house is unknown. The house had a significant roof damage and a few windows were failed. A small portion of the south wall failed due to wind borne debris impact. We did not observe any failure of the foundation. We performed probabilistic analysis to test model performance for this Galatia house. Tornado strikes were simulated based on the best estimates of tornado path from NWS survey data. In the probabilistic analysis, we considered location of the structure with respect to the tornado track, translation speed of the storm, estimates of RMW, and a range of maximum wind speeds for the tornado. For the analysis, we varied the maximum wind speed, RMW and path width to simulate tornado strikes on the structure. For each tornado strike, we used 30 realizations of the building. Comparison of the fragilities shown in Figure 6-30 implies the failure of roof dominates over other failure modes for wind speed greater than 110 mph (49.2 m/s). Failure probability of foundation connection is very low even with the minimal connection assumption. The comparison indicates that the wind speeds were likely greater than about 115 mph (51.41 m/s) and less than 150 mph (67.1 m/s), based on the whole roof failure and modest wall failures.

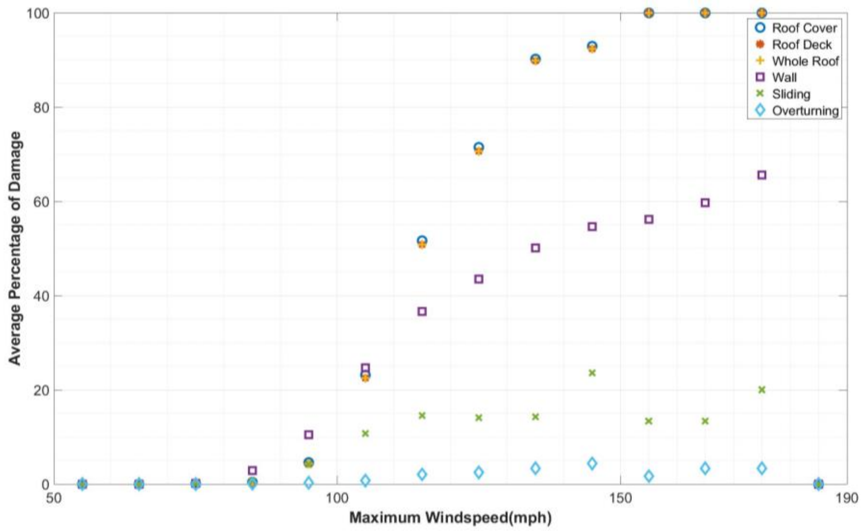

Note: 1 mph = 0.44704 m/s

Figure 6-30. Comparison of Fragilities for a Damaged House in Galatia Tornado

6.7.2. Greensboro, NC Tornado

One of the (surveyed) damaged houses in Greensboro, NC tornado was used for the validation. This house had a strong roof-to-wall connection (i.e. a single clip) and weak stud-to-top plate and bottom plate-to-stud connection (i.e. straight nails), as shown in Figure 6-31. In the figure, we illustrate the model predicted roof deck failure for the 8d/6-12 observed roof deck. The house was located on the LHS (left hand side) of the tornado according to the NWS tornado path. We ran two cases for the tornado-damaged house in Greensboro, NC to illustrate model performance.

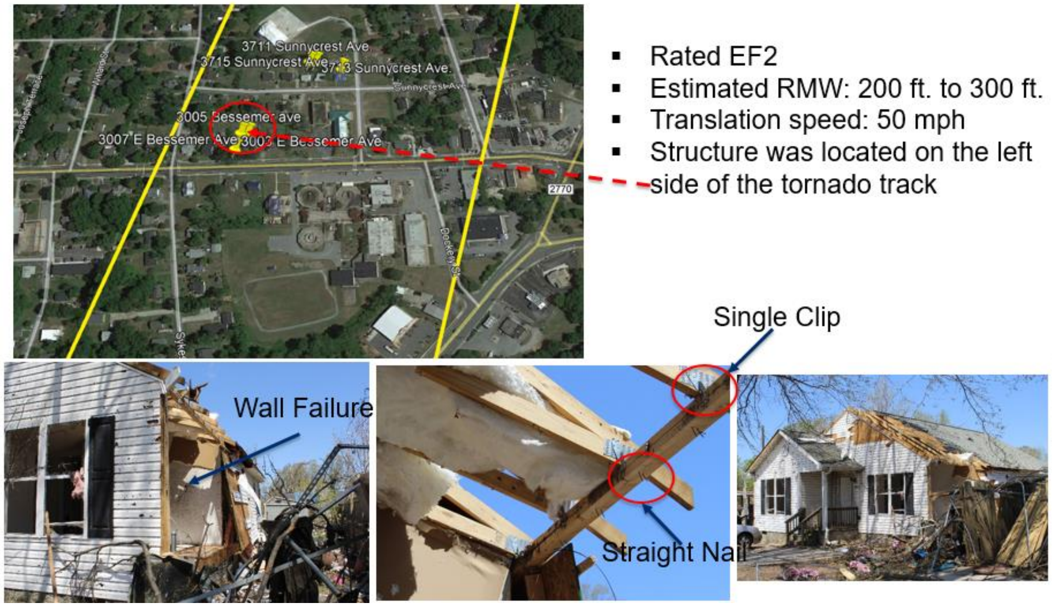

Note: 1 mph = 0.44704 m/s; 1 ft = 0.3048 m

Figure 6-31. Damaged House in Greensboro, NC Tornado

The first case is our best estimate of the location of the house with respect to tornado centerline. The first case illustrates the performance of the model compared to the observed damage (failure of the portion of the east wall and damaged sheathing on the southeast corner of the roof). As seen on the plots on the left side of Figure 6-32, there is a higher probability of wall failure on the east wall and failure probability of the sheathing is high on the southeast side of the roof.

The second case is a sensitivity case (shown in the right-hand side of Figure 6-32), where we place the house on the right-hand side of the track within the core. The sensitivity case (right hand side (RHS) of tornado) shows a much higher probability of failure for the roof and walls. In both cases, we used 1000 probabilistic tornadoes that best represent the Greensboro tornado in terms of wind speeds, RMW and the location of the structure. These illustrations show how building position influences damage and that the use of a time-stepping tornado wind field model with directional wind pressure coefficients, etc. can reasonably estimate location of damage on a building.

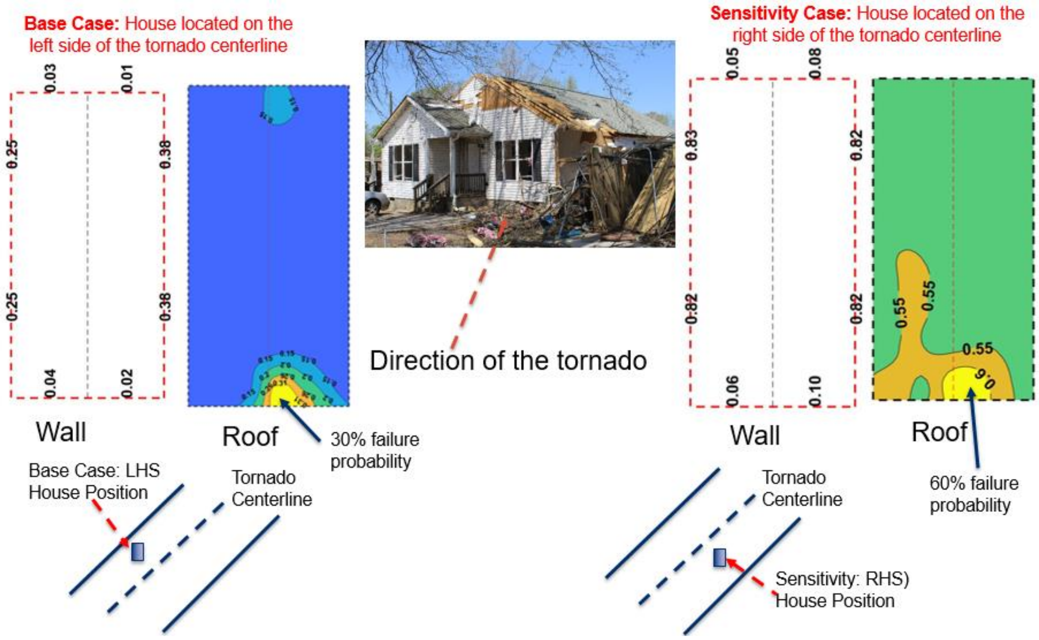

Figure 6-32. Failure Probabilities of the House Components

6.7.3. Joplin Tornado

We used NIST's preliminary Joplin database to compare our wind speeds from damage simulations based on known house characteristics. House case shown on Figure 6-33 had major roof damage and was assigned DOD 6. Since we do not know the connection type of the roof structure, we compared the estimated wind speed of this house with our generic wind speed distributions for DOD 6 from two similar houses. These houses are simple gable but the size of the deck nails and roof to wall connection are different. We show our DOD 6 wind speed ranges for these houses with:

- Simple rectangular plan
- Roof deck nails from 6d to 8d
- Gable roof shape
- Two toe nail Roof-wall connection types

The dashed red lines in the bottom left plots denote ranges of EF-Scale wind speeds and black dashed lines denote the ±2 std. deviations of the modeled wind speeds.

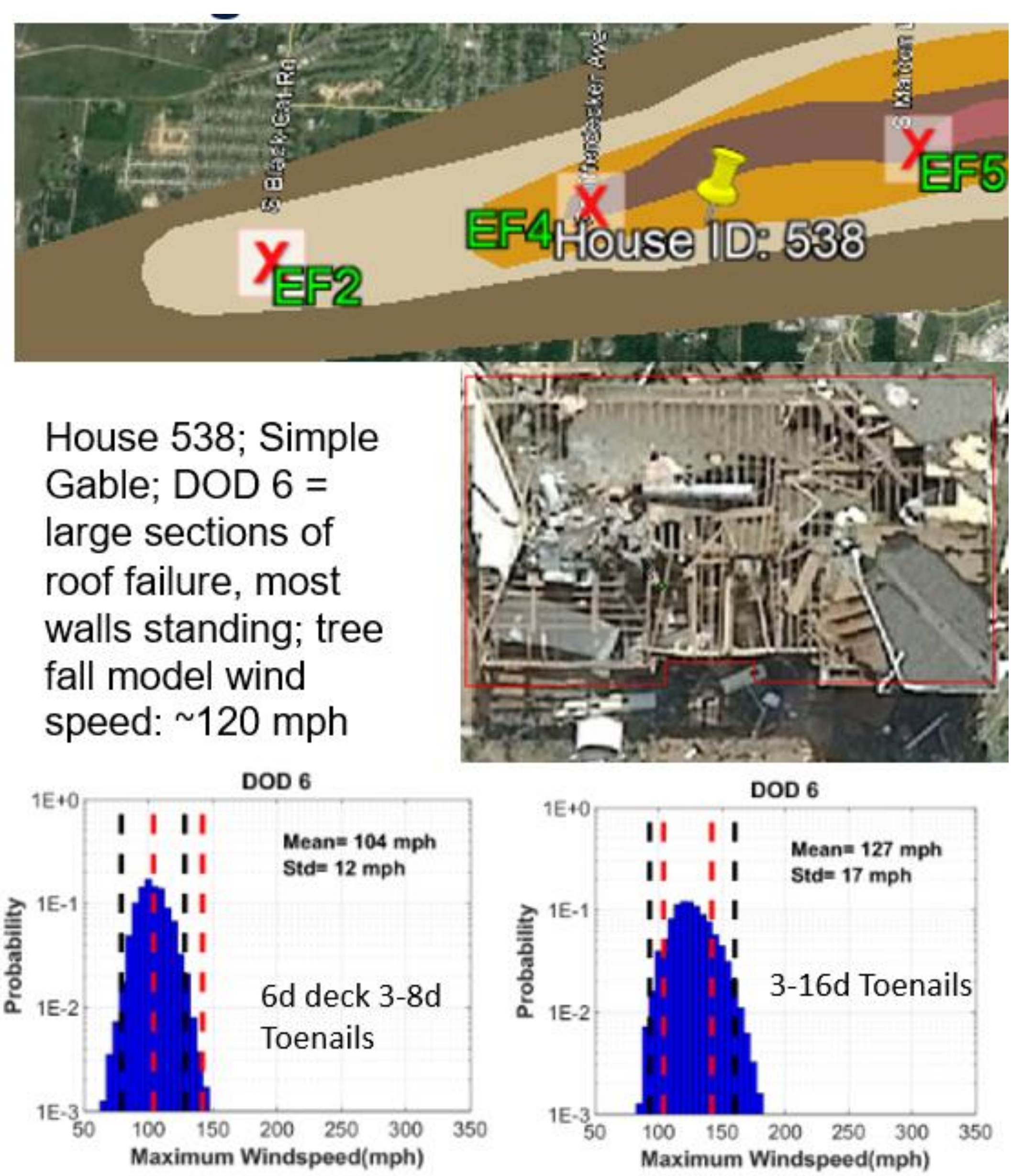

Note: 1 mph = 0.44704 m/s

Figure 6-33. Comparison of the Estimated Wind Speeds for a House Damaged in Joplin Tornado

Without more structural specifics, there is a wide range of possible wind speeds for DOD 6. The NIST tree fall model wind speeds for this house location are within the mean values of the distributions of the modeled houses. The tree fall wind speeds are based on NIST NCSTAR3, Joplin Tornado Investigation.

Comparison of DOD wind speeds are shown here for two additional houses. The house shown in Figure 6-34 on the left-hand side is similar to our complex hip house and had major wall damage and was assigned DOD 8. Without the connection details, we compared the estimated wind speed for this house with DOD 8 distributions from two of our previously modeled complex hip houses. For the partially sheathed and nailed foundation case, the wind speed range is 149±38 mph (66.6±17.0 m/s), whereas for the fully sheathed and bolted foundation case, the range is 197±44 mph (88.1±19.7 m/s). The tree fall wind speed for this house was 172 mph (76.89 m/s), which is within the range of wind speeds for these two houses. With more information on structural details, our model-based wind speed range could be refined.

A similar comparison is shown for the simple gable house shown on the right. The house was assigned DOD 10 since its slab was “swept clean”. Our estimation for the partially sheathed and nailed foundation case is 189±58 mph (84.5±25.9 m/s), whereas for the fully sheathed and bolted foundation case, the estimation is 213±54 mph (95.2±24.1 m/s).

Since we did not specifically model the Joplin houses, (in terms of strength, position, and house orientation) the wind speed ranges are very broad, and obviously bound the NIST tree-fall model based estimated wind speeds at these locations.

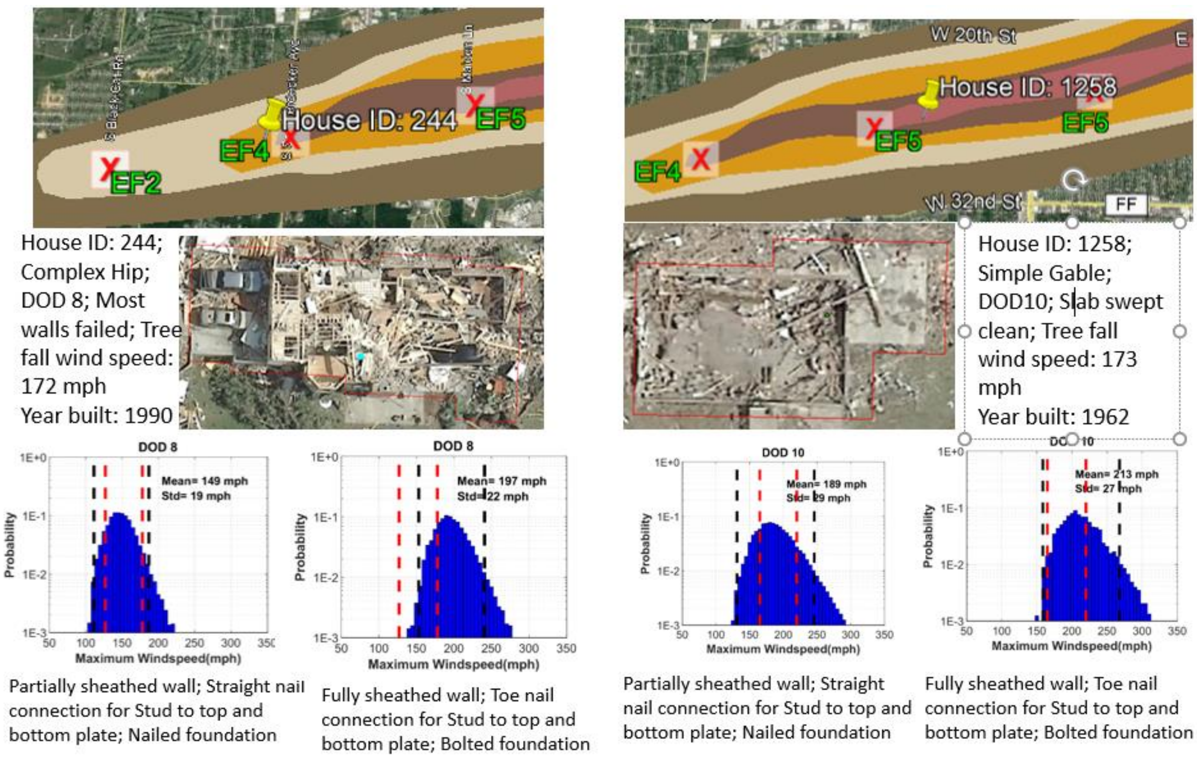

Note: 1 mph = 0.44704 m/s

Figure 6-34. Comparison of the Estimated Wind Speeds for Two Houses Damaged in Joplin Tornado

7. Tornado Wind Speed Hazard Analysis

7.1. Overview

The tornado hazard modeling inputs and analysis process are illustrated in Figure 7-1. The tornado inputs include both regional level data and national level data. We use national level data for modeling the within-path tornado models, where regional data is sparse or does not readily exist. The epistemic uncertainty models have been incorporated into the analyses described in previous sections. In this section, we compute tornado wind speed exceedance frequencies (hazard curves). The tornado hazard curves depend on the size of the component, equipment, building, structure, or facility (all referred to generically as a "target").[115]

The hazard analysis process involves: tornado target interaction modeling for a defined Reference Wind Speed (RWS), tornado risk model, simulation design, and the WEF computations. We develop hazard curves for each region and 8 target sizes. Sensitivity analyses illustrate how important variables propagate through the models to influence the computed WEFs.

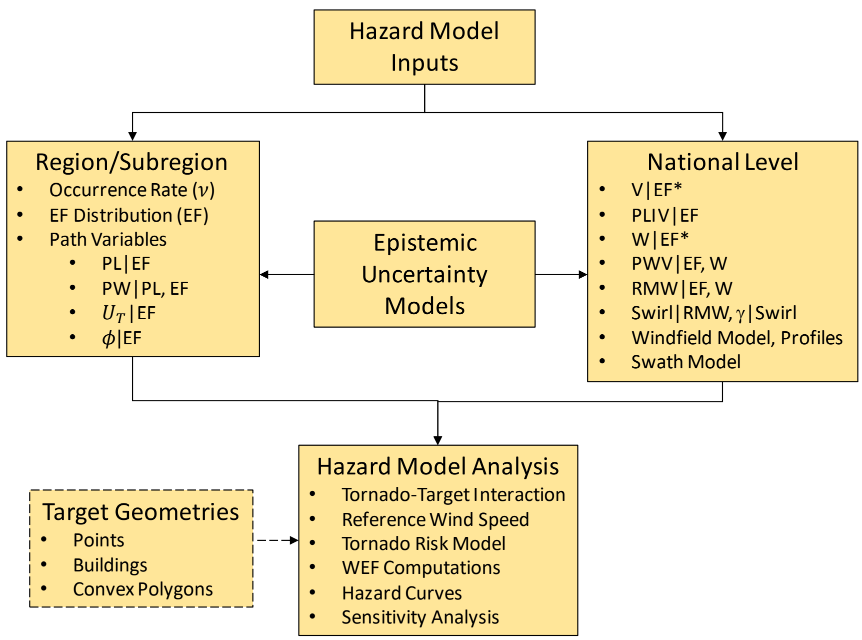

Figure 7-1. Overview of Tornado Hazard Model

7.2. Tornado-Target Interaction Background

Tornadoes are small and potentially powerful storms with much smaller path areas than other extreme winds. Mean tornado path area ranges from about 0.0006 to about 50 square miles (0.0016 to 130 km^2), producing a range ratio of about 1E05. In this regard, the modeling of tornado strikes on individual structures and large facilities is unique among extreme wind

---

[115] A target may be anything from a single geometrical point (such as a pole or tower, with minimal plan area), to a single building, to a system of spatially-distributed points, components, structures, etc. Boolean logic can be used to specify the performance function of the system, as is done in nuclear power plant risk and safety analysis for tornadoes and high winds (Twisdale, 1988; Twisdale, et al., 2015a, b). The hazard curves developed herein focus on buildings.

hazards. For hurricanes, extratropical cyclones, and thunderstorm winds the size of the target is almost always negligible compared to the extent of the storm.[116] For tornadoes, target size is a critical input in quantifying tornado WEF.

Another important consideration for tornadoes is that they have large aspect ratios (*L/W*) and highly asymmetric path directions. These attributes are important for modeling risk to structures/systems that also have high aspect ratios, such as lifeline systems (for example, see Twisdale and Dunn (1983a). The combination of tornado attributes and target size, shape, and orientation produce non-linear effects in the WEF computations. Hence, multiple hazard curves are required to capture these complexities.

7.2.1. Tornado-Target Interaction Geometry

Models for tornado target interaction assume that tornadoes occur in equally likely positions near the target and the same assumptions are made herein for hazard curve development. Figure 7-2 illustrates several tornado-target interaction scenarios. For example, small shifts in the tornado path can miss a small point target (red dashed path in left figure), but hit an area target (middle figure). As the tornado position is shifted laterally, the larger target will be hit more often than a smaller target.

Thom (1963) developed the basic geometrical equations for point targets (tornado point strike probability). Area target tornado interaction equations were developed by Garson et al. (1975), Wen and Ang (1975) and further generalized by Twisdale et al. (1978, 1981). Life-line targets analysis was included in Twisdale and Dunn (1983a). Large spatially diverse systems, such as multiple separated critical structures (or, for example, the targets illustrated in the right side of Figure 7-2) often require consideration of how the facilities and systems interact to produce functional failures (Twisdale, 1988).

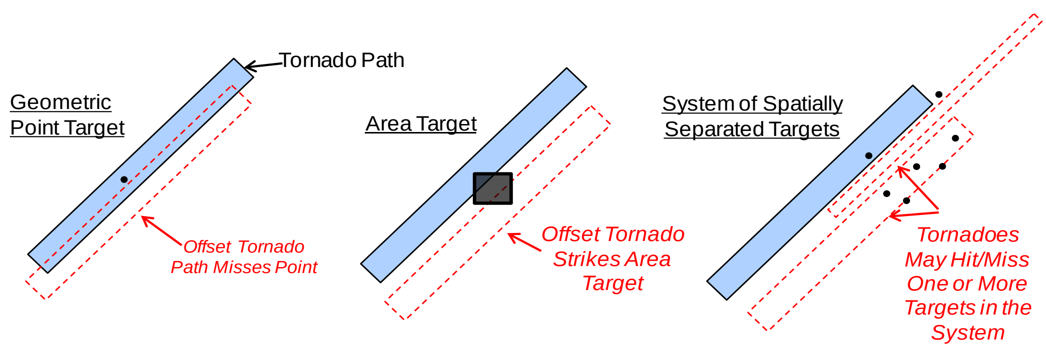

Figure 7-2. Target Size and Tornado Target Interactions

The computation of tornado strike probabilities involves the geometric union or intersection of a typically rectangular tornado path model with the target plan area geometry. The target plan area may be small, such as towers and poles, medium in size, such as a typical commercial building, or large, such as a manufacturing facility, school campus, or a nuclear power plant. Since tornado paths have variable azimuthal directions and targets may be of many sizes, shapes, and orientations, the possibilities are endless for computing tornado-target interactions. In addition, we know that there is significant variation of tornado wind

[116]Exceptions include insurance portfolios, widely-distributed facilities, and transmission line systems.

speed across the path width. These facts suggest that simulation methods are best suited for tornado hazard curve development.

7.2.2. WBD Considerations

The scope of this project did not include a separate analysis of tornado wind-borne debris analysis for purposes of developing engineering design standards, which typically requires specification of the types, masses and impact speeds of individual missiles. Thus, although wind borne debris was explicitly considered in the damage modeling work in Section 5, the determination of design basis missiles for tornadoes is a separate problem from the inclusion of WBD in damage calculations and wind speed estimation.

A significant amount of work has taken place in the nuclear power industry regarding tornado missiles. The Nuclear Regulatory Commission has published regulatory guides and standards (USNRC, 2007a, 2007b). Important considerations for tornado WBD include vertical winds, vertical profile of horizontal winds, tornado strike definition, and extent of missile transport distances. Failed structural cladding, roof components, and temporary structures are a major contributor to tornado WBD risk for nuclear facilities (Twisdale, 2016).

7.3. Reference Wind Speed

For the tornado hazard, we define the reference wind speed (RWS) as the maximum 10 m (33 ft) (above ground) horizontal wind speed produced within the target plan area by the translating tornado. Due to the limited state of knowledge with respect to terrain effects on tornado structure and wind speeds near the ground, RWS is defined independently of terrain. Similarly, due to the limited state of knowledge regarding tornado gust characteristics, we assume that the wind speeds are associated with the nominal 3 second gusts used in wind load computations (ASCE, 2016). As with non-tornadic winds, the RWS is the free-field wind speed ignoring presence of the target.

For the RWS computation in each target simulation, we develop a uniform (11x11) 121 point grid over the plan area of the target and compute the maximum wind speed experienced at each point in the grid as the tornado translates past the target. Once the target is positioned (randomly in both path length and width directions) within the tornado path, the RWS is computed at each grid point for each tornado time step. This calculation considers the target position in the path width direction and the target position in the path length direction. In the path length direction, we sample from the appropriate EF-Scale PLIV intensity distribution. The RWS calculation is performed by translating the tornado center 3*RMW in front of the target to 3*RMW beyond the target. The RWS is the maximum wind speed over all 121 points and all time steps. Figure 7-3 illustrates that the RWS depends on the target position within the tornado path and that the RWS can occur anywhere in the plan area of the structure.

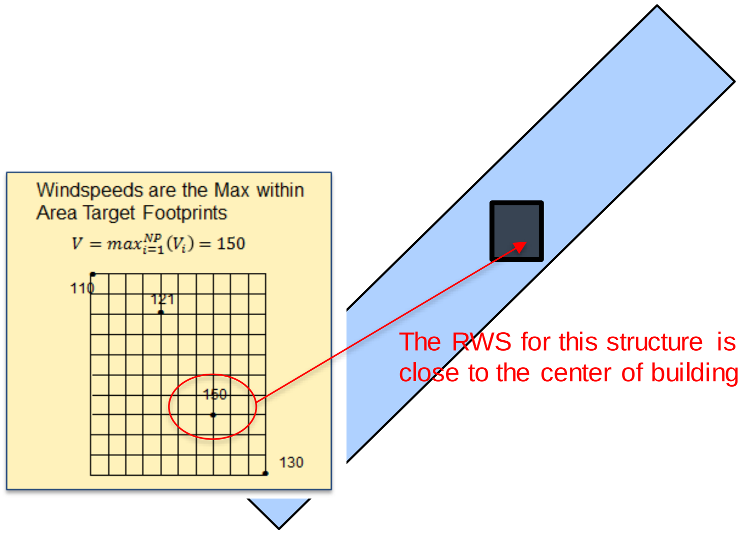

Figure 7-3. Schematic Illustration of RWS Computation for Tornado Hazard Simulations

We develop tornado hazard curves conditional on the tornado EF intensity and simulate EF0 to EF5 tornado strikes. From Section 3, we know that a tornado has maximum intensity over a generally small fraction of the total path length. And, from Section 4, we know that there is generally a modest width across the tornado associated with the maximum tornado winds. Hence, with random target positioning within an EF-Scale tornado, the RWS produced by the tornado will contain values from EF0 tornadoes up to the tornado intensity being analyzed. For example, for an EF4 simulation, the range of RWS from all the EF4 simulations will vary from EF0 to EF4 wind speeds, because the target can experience this full range of wind speeds based on its position within the simulated EF4 wind swath.

For area targets, the RWS in any simulation may occur over a small or large part of the target. For large target areas, a small part of the target may actually experience the maximum RWS. For example, Figure 5-49 illustrates the Joplin Wal-Mart, which was damaged in the May, 2011 Joplin Tornado. From the NIST Joplin report (Kuligowski et al., 2014), tree fall analysis positioned the tornado centerline approximately 800 ft (240 m) to the south of the building. Hence, the building did not experience the maximum wind speed of the tornado and only the southern portion of the building experienced the RWS. Nevertheless, the Joplin Walmart suffered collapse failures over a significant part of the building. While the damage did not propagate to collapse level in the northern part of the structure, the building was not functional, nor repairable and was demolished. The Joplin Walmart example illustrates how high tornadic winds over a part of the building can produce catastrophic damage over part of the structure that renders the entire structure functionally destroyed. Loading considerations, such as APC and propagation of internal pressures, uncertainties in progressive collapse, and vulnerability to wind borne debris entering the non-collapse portions of the building also suggest the use of a RWS based on the entire plan area.

In summary, we believe that our RWS definition is the most appropriate definition for structural design and safety analysis.[117] Use of the maximum horizontal wind speed as the RWS require appropriately developed parameters for Main Wind Force Resisting System

[117] For very large structures/facilities where loss of function is acceptable, use of a RWS for a smaller area may be possible. However, this requires careful considerations of independent structural systems, safety distance from failed elements, and wind borne debris trajectories into adjacent non-failed independent structures.

(MWFRS) and Components and Cladding (C&C) loads, wind directionality effects, influence of vertical winds, APC/internal pressures, and wind borne-debris.

7.4. Target Strike Simulation Design

Figure 7-4 illustrates several possible tornado strike scenarios for tornado-target interaction. Three target strike designs are illustrated:

1. Target Strike Design 1: Target randomly positioned within tornado path
2. Target Strike Design 2: Target randomly positioned within the core of the tornado
3. Target Strike Design 3: Target deterministically positioned

Design 1 allows the target to be uniformly randomly positioned anywhere within the tornado path. This design is appropriate for hazard curve development since high wind speeds can be experienced outside the core for moderate and intense tornadoes. In this case, target position is assumed to be uniformly likely from the left hand side of the tornado to the right hand side and along the entire path length of the tornado. Obviously, the vast majority of positions do not experience the maximum wind speeds within the simulated tornado. We note that for point targets, about ½ the target will be inside the core and about ½ the time it will be outside the core in Design 1. The hazard curve simulations reported in Section 7.4 are based on Design 1, which is used for map development.

In Design 2, the target is positioned uniformly random within the core of the tornado, defined as within ± RMW of the tornado centerline. Since the target is within the core, about ½ the time a point target will be on the RHS of the centerline and have a good chance to experience the highest local wind speeds for that PLIV position. EF-Scale tornado wind speed estimation and damage-based ratings are intended to reflect the highest observed damage in the tornado. In the F- and EF-Scale rating processes, the observer finds the most significant damage for purposes of estimating maximum wind speeds and the tornado's EF rating. In locations with moderate and high DI densities, the most significant observable damage will be for those DIs within the tornado core. Since our EF-Scale distribution is based on damage ratings in moderate and high building densities, Design 2 was used in Section 6 to produce the EF* wind speeds.[118]

[118] The relationship of Design 1 and Design 2, in terms of the fraction of time the RWS is governed by target position inside the core, is estimated in Section 7.6.2 as a function of target size and wind speed.

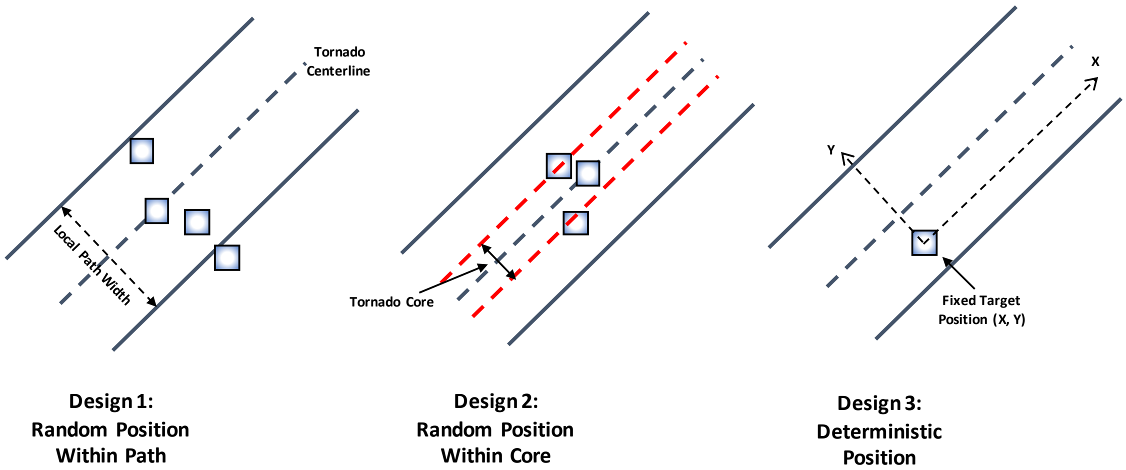

Figure 7-4. Tornado Strike Simulation Scenarios

Design 3 is typically used for damage model validation based on field-collected data for specific tornado events. This set up takes advantage of observables about the tornado and the target. Important tornado information includes position of tornado relative to target (tornado centerline relative to target, approximate RMW, translational speed, vortex structure, estimated maximum wind speed range, and so forth). Important target information includes DI structural details such as plan shape, roof shape, orientation, connection strength, presence of nearby structures, and so forth). Information on a few key variables can significantly improve the wind speed estimation and reduce the uncertainties in estimated wind speeds. This set up is used for several of the damage model validation studies.

An important point is that the hazard curve development is not based on a conservative simulation design, in which the target is constrained to be near the tornado centerline or near the RMW on the right-hand side. In addition, from the PLIV work in Section 3, the hazard curves reflect the fact that the target is unlikely to experience a RWS when the tornado is not at its maximum intensity. Requiring the target to be positioned at/near the maximum wind speed in each tornado path is not realistic, nor would it produce hazard data suitable for risk-informed or reliability-based design (e.g., McAllister et al., 2018).

An alternative to the RWS definition used herein would be to develop analysis/design scenarios for tornado strikes for use in a scenario-based analysis/design. A scenario approach for tornado strike was rejected in this project due to the complexities of identifying bounding scenarios for design for a wide range of structure types, sizes, tornado interaction geometries, and variable tornado characteristics.

Target Strike Designs 1 and 2 follow from a "union" definition of tornado strike (Twisdale and Dunn, 1983a).[119] The use of a union definition for the RWS results in considerable variance in the resulting design parameters, which requires explicit consideration in structural reliability calculations and computation of failure frequencies.

[119] The term union refers to at least one point of the target defines a tornado strike, whereas the term intersection refers to the requirement that the entire target experiences the defined event, such as $P(v>V)$.

7.5. WEF Computational Methodology

Monte Carlo simulation is a useful method to quantify tornado risk. The efficiency of the simulation approach for tornadoes is improved by using variance reduction methods, such as importance sampling, stratified sampling, and analytical equivalence (Twisdale et al., 1978, 1981). An efficient simulation method for producing tornado hazard curves was similarly developed by Twisdale and Dunn (1983a). We use a similar approach in this work with generalizations to the scoring methods, including treatment of epistemic uncertainties within the simulations, incorporation of variable path width modeling, and PLIV importance sampling. For convenience, we present the basic equations herein (following the notation in Twisdale and Dunn, 1983a).

7.5.1. Tornado Risk Model

A total probability formulation of risk probabilities for hazards that occur randomly over time is given by

$$P_T(\xi) = \sum_{N=0} P(\xi\,|N)\,P_T(N) \tag{7-1}$$

in which $P_T(N)$ = probability of N tornadoes during time T; $P(\xi|N)$ = probability of event (i.e.., wind velocity exceedance, $v > V$) given the occurrence of the N storms; and $P_T(\xi)$ = stochastic model of event ξ during time period T. The most commonly applied stochastic models of tornado occurrence assume that tornado events constitute a Poisson process in which the probability of N tornadoes during the time period T is given by

$$P_T(N) = \frac{(\lambda T)^N}{N!}exp(-\lambda T) \tag{7-2}$$

in which λ = mean rate of occurrence. By substituting this relation into Eq. (7-1) and evaluating $P(\xi|N)$ from a union combination of independent events, we obtain

$$P(\xi|N) = 1 - [1 - P(\xi)]^N \tag{7-3}$$

Eq. 7-3 provides the probability of at least one event ξ, which means at least one wind exceedance for $P(\xi) = P(v > V)$. Combining Eq. (7-1), (7-2), and (7-3), Wen and Chu (1973) presented the above equations and also developed the analytic solution

$$P_T(\xi) = 1 - exp[-\lambda P(\xi)\,T] \tag{7-4}$$

For $\lambda P(\xi)\,T \leq 0.01$, Eq. (7-4) can be approximated by

$$P_T(\xi) \cong \lambda P(\xi)\,T \tag{7-5}$$

with an accuracy of 0.5%. The simplified risk model represented by Eq. (7-5) has been used, in a number of studies that have attempted to characterize tornado related risk (e.g., Abby and Fujita, 1975; Garson et al., 1975; McDonald et al., 1975; Ramsdell and Rishel, 2007; Thom, 1963; Wen and Ang, 1975).

In addition to the Poisson process, other stochastic models that have been suggested for tornado occurrence include the Polya, Weibull, Bayesian Poisson, and Bayesian Weibull processes, which are given in Twisdale and Dunn (1983a). The Polya model generally provides the best fit for tornado occurrences and is needed for modeling short-term risk, such as inter-annual tornado risk (seasonality). As noted, Eqs. (7-4) and (7-5) are adequate for tornado risk assessment for $\lambda P(\xi)\, T \leq 0.01$, assuming reporting time trends and population bias corrections have been applied to the mean occurrence rate.

As described in Section 3, we consider epistemic uncertainties in v that include population bias corrections for the modern era, model uncertainties in tornado density analysis and annual variability, and a judgment-based uncertainty factor.

7.5.2. EF-Scale Total Probability Formulation

A convenient formulation of total tornado risk uses the mean occurrence rate, v, for all intensities and the calculation of $P(\xi)$ in Eq. (7-4) using the discrete EF-Scale intensities in a total probability equation

$$P(\xi) = P(v > V) = \sum_{k=0}^{5} P(v > V|EF_k)\, P(EF_k) \qquad \textbf{(7-6)}$$

where EF_k = tornado EF-Scale category. In this work, we use the EF-Scale as a mutually exclusive and collectively exhaustive event set for the total probability formulation.[120] See Twisdale and Dunn (1983a) and Twisdale (1986) for discussion of alternate formulations and bounds on total risk.

7.5.3. Tornado Target Geometry

In this section, we summarize the well-known expressions for tornado target interactions of a convex polygon target, typical of a single building or the enveloping polygon drawn around a series of functionally related structures or components at a site. A fundamental expression in tornado-target probability calculations is

$$P(\xi) = \frac{A_0}{S}, \qquad if\ A_0 \leq S\ = 1, otherwise \qquad \textbf{(7-7)}$$

in which P(ξ) = the tornado strike probability from (Thom's (1963) point probability); A_0 = tornado origin area; and S = tornado reference area used in the calculation of v. Eq. (7-7) assumes that tornado occurrence is uniformly random over S. A_0 is the locus of all points, with respect to the center of the tornado, that result in a tornado strike on the target, as illustrated in Figure 7-5. Figure 7-5 illustrates the A_0 for a "union" tornado strike, which means that at least one target point is within the tornado path (Twisdale and Dunn, 1983a). We use the union strike concept in hazard simulation calculations with the RWS defined in Section 7.3.

[120] This approach does not logically inhibit the use of overlapping wind speed distributions (non mutually exclusive) $P(v_i|EF_k)$ in Section 6.

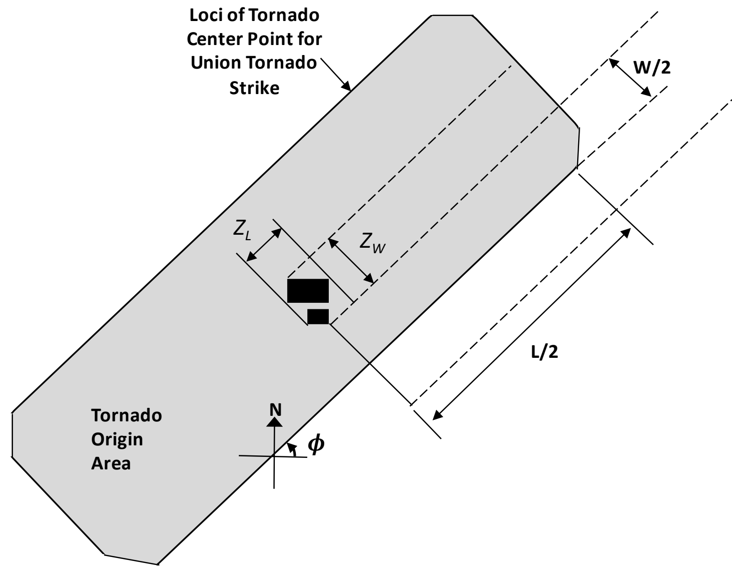

Figure 7-5. Tornado Origin Area for Tornado Strike (Twisdale and Dunn, 1983a)

The tornado origin area depends on the tornado path geometry and the target geometry. Tornado paths have many shapes and include rectangular, dogleg, and loop shapes. We use a rectangular tornado path geometry for purposes of the tornado strike simulations with the path defined by *W* (*W* = EF-Scale maximum path width) and the tornado length, *L*. The use of *W* ensures that we do not miss any hits using the variable path wind swath model, as developed in Section 4.

Twisdale et al. (1978) performed a sensitivity study that showed that the rectangular path model yields tornado origin areas only several percent smaller than equal area curved-track tornadoes represented by a 30° arc. Hence, we use rectangular path models in this study for tornado-target interaction modeling.

As described in Section 4, we use a single-cell vortex wind field model to develop wind speed swaths. This approach is reasonable up to vortex breakdown, at which multiple sub-vortices (Fujita's "suction vortices") may form. Regarding sub-vortices, we note that a simple analysis of the area swept out by sub-vortices was performed in Twisdale and Dunn (1983b). This analysis suggested that the cycloidal paths of sub-vortices would likely sweep out high wind speed swaths within the tornado core that are similar to that of the single cell parent vortex. For example, Twisdale and Dunn (1983b) showed that a continuous single sub vortex would hit a point target (randomly positioned inside the tornado core) about 40% of the time. With multiple sub-vortices forming around the core, one would expect this value to approach 100%. Hence, we conclude that using a single cell-vortex wind model for purposes of modeling tornado wind swaths is reasonable for wind speed swath simulations and it considerably simplifies the computations.

A simple expression for A_0 can be used if the target geometry can be described as a convex polygon.[121] In this case,

$$A_0 = WL + WZ_L + LZ_W + A_S \tag{7-8}$$

where WL = tornado area based on maximum path width; W = tornado path width; Z_L = maximum projection of target polygon in the tornado length direction; L= tornado path length; Z_W = maximum projection of target convex polygon in the tornado width direction; and A_S = area of the target. This expression is valid for a single line segment or a circular target and agree with expressions in Garson et al. (1975) and Wen and Ang (1975) for rectangular targets. We use Eq. (7-8) for the WEF computations herein.

7.5.4. Tornado Path Data Probabilistic Model Summary

The tornado path data models, developed in Section 4, are inputs to the TORRISK2 simulation code, used to generate the regional hazard curves. The path geometry is defined by L, W, and ϕ (path direction). These variables are region (R) dependent and generally conditional on EF-Scale intensity. The conditioning and joint probability (f) sampling approach is illustrated by

$$f(EF_k, L, W, |R) = P(EF_k|R) \cdot f(L|EF_k, R) \cdot f(W|EF_k, L, R) \cdot f(\phi|R) \tag{7-9}$$

The models for these variables were developed in Section 3. They uniquely define a realized tornado path. The tornado maximum wind speed is sampled from $P(v''_i|EF_k^*)$and the translation speed (v_T) is sampled from $f(v_T|EF_k, L, R)$. Once these variables are sampled, the simulation proceeds with the target position sampling, PLIV sampling, and tornado wind field sampling.

7.5.5. Simulation Methodology

Monte Carlo techniques are used with variance reduction (e.g. Law and Kelton, 1982; Bratley et al., 1983) to quantify tornado WEFs using the TORRISK2 code. The developed Monte Carlo technique uses an analytical equivalence technique similar to Twisdale et al. (1981), which is implied in the computation of A_0, and stratified sampling of EF-Scale tornado intensity to quantify $P(v > V)$. Splitting and importance sampling are used for target positioning within the tornado path.

The calculational procedure proceeds as follows for a given EF-Scale simulation: (1) the tornado maximum wind speed, path length, width, direction, and translational speed are sampled per Section 7.5.4; (2) the target orientation is determined (sampled if random) and A_0 is computed; (3) the tornado PLIV fractions are sampled; (4) the maximum wind speed along the path length is created from the spline fit discussed in Section 4; (5) the target is positioned within a PLIV segment, using importance sampling; (6) the target lateral position (local path width position) is then sampled within the maximum path width; (7) if the target position is outside of the local path width (Design 1), or the core (Design 2), then there is no successful tornado hit for the simulation design and a new target simulation begins (Step 5); (8) the tornado wind field parameters are sampled and the wind field is locally fit to the local

[121] A convex polygon is one where all the interior angles are less than 180°.

intensity segment in the variable path width model; (9) the RWS is computed by advancing the tornado past the target; and (10) the appropriate wind speed exceedance threshold is scored.

The simulation scoring equation for *P(v>V)* uses the wind speed thresholds v, and is given by

$$P_{T=1}(v > V) = \lambda \sum_{k=0}^{5} P(EF_k) \left[\frac{1}{N_k} \sum_{r=1}^{N_k} (A_0)_{kr} \frac{1}{N_S} \sum_{q=1}^{N_S} \left(\delta_{krq} | v > V \right) \right] \quad \textbf{(7-10)}$$

where the outputs are per year (T=1); N_k is the number of simulations for EF_k intensity; N_S = number of sub-loop simulations for target position; the term $(\delta_{krq}|v > V)$ represents the target position importance sampling weight, aggregated in the appropriate wind speed exceedance threshold, $(v > V)$. The target positioning sub-process defined by steps 5-8 is repeated in the "N_S" sub-loop to improve computational efficiency. For the WEF computations, we use wind speed bins from 50 to 300 mph (22 to 134 m/s) in 10 mph (4.5 m/s) increments. Once all of the N_k simulations are complete for an EF-Scale, the next EF-Scale is processed and so on.

Table 7-1 summarizes the simulation design. It includes information on tornado sample sizes; number of target positions sampled per tornado; local EF-Scale importance sampling weights for the PLIV positioning; and estimates of the number of wind speeds and associated WEFs by individual EF-Scale simulations. Column 1 shows an increase in the number of tornado simulations (N_i) by EF-Scale in order to produce a reasonable number of outcomes for the tails of the wind speed distributions. We sample 10 target positions per realized tornado (Column 2). Column 3 shows the PLIV importance sampling position frequency times a factor of 1/3 to estimate the number of times the target will be in the "sweet spot" on the right hand side of the core and capable of producing near maximum EF-Scale simulated wind speeds. Column 4 is the product of Columns 1-3, producing the effective number of calculations producing local EF wind speeds. Column 5 is the Region 4 point probability by EF-Scale. Column 6a shows the number of wind speed exceedances for the 0.99 position on the wind speed cumulative distribution function (CDF) and the associated WEF. Similarly, Column 6b shows these results for the 0.999 CDF position.

The calculation illustrate that the simulation design has a reasonable chance of producing a reasonable number of wind speed exceedances (around 30) for the 99% CDF for each simulated EF-Scale. The associated WEF for EF5 simulations is crudely estimated to be about 1E-07 per year. Column 6b, which only shows a few exceedances, indicated that we expect to see noticeably jagged results by 1E-08 WEF per year.

Table 7-1. Simulation Design to Produce Low WEFs

EF-Scale	1. Number of Tornadoes (N_k)	2. Target Positions per Tornado (N_S)	3. PLIV Sampling Position Wts. *1/3	4. No. of WEF Calcs Producing EF Wind Speeds	5. Region 4: Point Probability (Yrs)	6a. Est. No. of 0.99 EF CDF Wind Speeds & Associated WEF		6b. Est. No. of 0.999 EF CDF Wind Speeds & Associated WEF	
						No. of Wind Speeds	WEF (Yr-1)	No. of Wind Speeds	WEF (Yr-1)
EF0	1,000	10	0.333	3,333	4.8E-05	33	4.8E-07	3	4.8E-08
EF1	1,000	10	0.167	1,667	3.2E-04	17	3.2E-06	2	3.2E-07
EF2	2,000	10	0.143	2,857	4.6E-04	29	4.6E-06	3	4.6E-07
EF3	2,000	10	0.121	2,424	5.2E-04	24	5.2E-06	2	5.2E-07
EF4	4,000	10	0.104	4,166	3.8E-04	42	3.8E-06	4	3.8E-07
EF5	4,000	10	0.091	3,636	1.6E-04	36	1.6E-06	4	1.6E-07

7.5.6. WEF Return Periods and Target Sizes

The WEF computations are performed for the matrix of return periods and target sizes given in Table 7-2. Target sizes range from geometric points to 4 million square feet (371612.2 m^2). The targets are modeled as squares. Sensitivities on non-square target shapes are discussed in Section 0.

The return periods cover ASCE 7 Risk Categories II, III, and IV. Return periods from 10,000 years to 10 million years are included for performance-based design (PBD), critical facilities, and nuclear power plants. A total of 56 WEF wind speeds are derived from the 8 target sizes and 8 return periods for each region. With 9 regions, we have a total of 504 derived mean wind speeds.

Table 7-2. WEF Calculation Matrix

Target		WEF (per yr) and Return Period (yrs)								Target Count
Area (sf)	Plan Dimensions (sf)	3.33E-03	1.43E-03	5.88E-04	3.33E-04	1.00E-04	1.00E-05	1.00E-06	1.00E-07	
		300	700	1,700	3,000	10,000	100,000	1,000,000	10,000,000	
Point	NA	ASCE Cat I	ASCE Cat II	ASCE Cat III	ASCE Cat IV	Performance Based Design, Critical Facilities, and Nuclear Power Plants				1
2,000	45 x 45									2
10,000	100 x 100									3
40,000	200 x 200									4
100,000	316 x 616									5
250,000	500 x 500									6
1,000,000	1,000 x 1,000									7
4,000,000	2,000 x 2,000									8
WEF Count		1	2	3	4	5	6	7	8	Product = 56
Number of Tornado Regions		9								Product = 504

Note: 1 SF = 0.09290304 m^2; 1 ft = 0.3048 m

7.6. Regional Tornado Hazard Curves and Sensitivities

The tornado hazard curves, analysis of tornado inside core vs outside core target hits, and a sensitivity analysis are presented in this section. The hazard curves in Section 7.6.1 provide the basis for the maps provided in Section 8.

7.6.1. Hazard Curves

Figure 7-6 through Figure 7-13 provide the 8 target size hazard curves for each of the nine regions. The regional order (highest wind speed for a given return period) of the hazard curves is:

1. Region 407
2. Region 406, 606
3. Regions 2 and 3
4. Regions 512 and 609
5. Region 511
6. Region 1

Regions 406 and 606, 2 and 3, as well as 512 and 609, are grouped together in the above list since the hazard curves are very close and cross each other. The regional order is driven largely by the occurrence rate, EF-Scale distribution, and path areas. For example, Region 407 has the second highest occurrence rate, but the most intense EF-Scale distribution, and the largest path areas. At the other end of the spectrum, Region 1 has the lowest occurrence rates, weakest EF-Scale distribution, and smallest path areas.

Crossing hazard curves are a result of the EF-Scale distribution and path area dependence on EF-Scale. For example, we see that the coastal Region 609 has the highest occurrence rate (dominated by weak EF0/EF1 events and hurricane spawned tornadoes), which places it above Regions 2, 3, and 512 for lower wind speeds but it drops to the bottom of this group for higher wind speeds, reflecting the lower frequencies for EFs 3, 4, and 5 as well as smaller modeled path areas for these events. Similarly, we see that Regions 406 and 606 are in a tight race and cross for similar reasons.

The overall shape of the curves start out flat (parallel to the wind speed axis) and then curve downward with a very slight convex downward shape. The initial flat range reflects the variable DOD 0 wind speeds (including the epistemic uncertainties in Table 6-4), which define the tornado path edges for all EF-Scales. From Section 5, the wind speed distribution for DOD 0 defines the range of potential tornado boundary wind speeds. DOD 0 reaches its 75 percentile by about 75 mph (33.5 m/s). The initial low wind speed flatness of the hazard curves seems reasonable regarding observer interpretations of visible damage, which also varies with structure class.

The effect of target sizes can be seen by reviewing the hazard curves for the same region in the different figures. There are notable increase in the wind speeds for the very large targets compared to the small targets at the same return period. This effect is greater at low return periods. Direct comparison plots illustrating target size sensitivity are given in Section 7.6.3.

The hazard curves in Figures 7-6 through 7-13 are not smoothed. One can see some local randomness with increasing *V*. More simulations would reduce these local variations, but overall, the curves are accurate to about 5 mph (2.2 m/s) over most of the hazard curve. For WEF less than about 1E-06, the local variations become much more apparent.

Table 7-3 provides the hazard curve interpolated return period wind speeds for the return periods and target sizes. The blank spaces, shaded light green, mean that there is nil tornado risk for that target size, return period, and region.

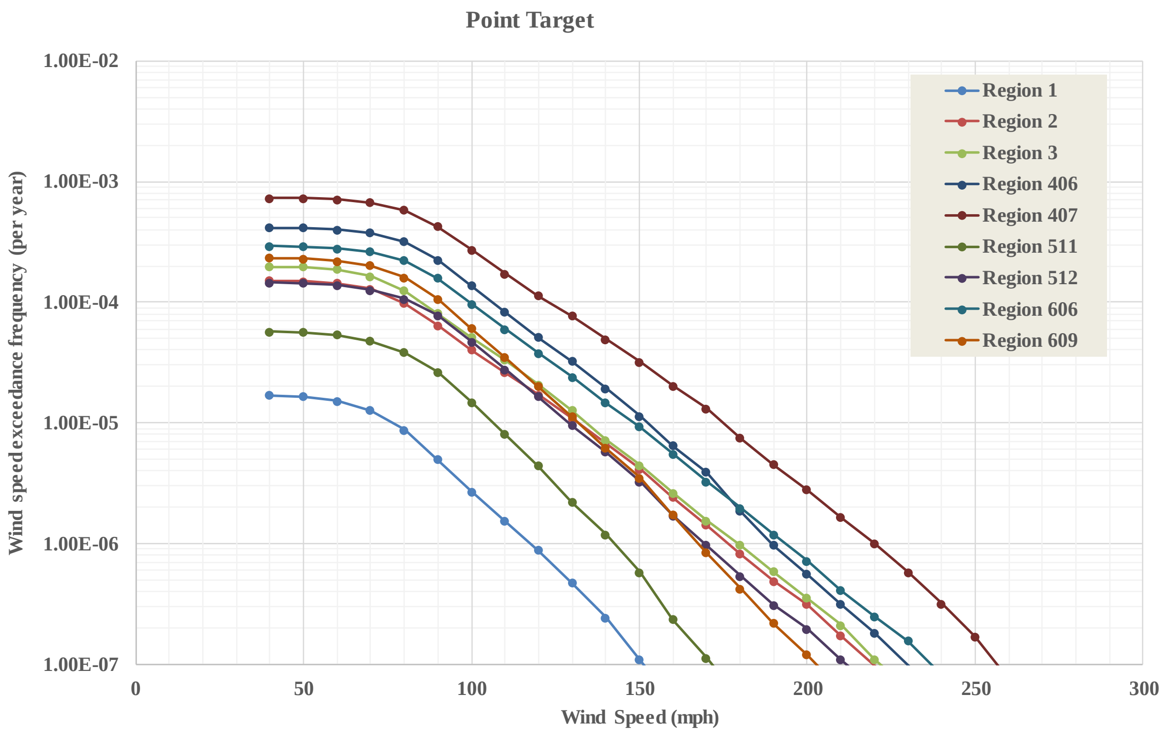

Note: 1 mph = 0.44704 m/s

Figure 7-6. Point Target WEFs

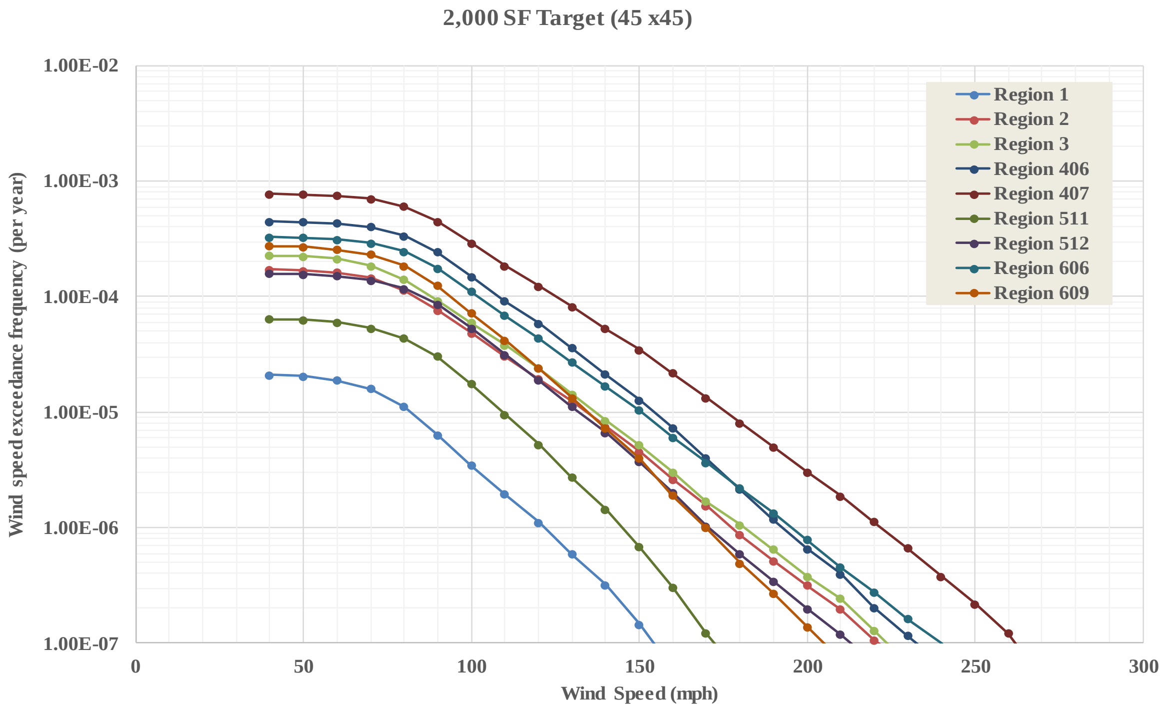

Note: 1 mph = 0.44704 m/s

Figure 7-7. 2,000 SF (185.8 m^2) Target WEFs

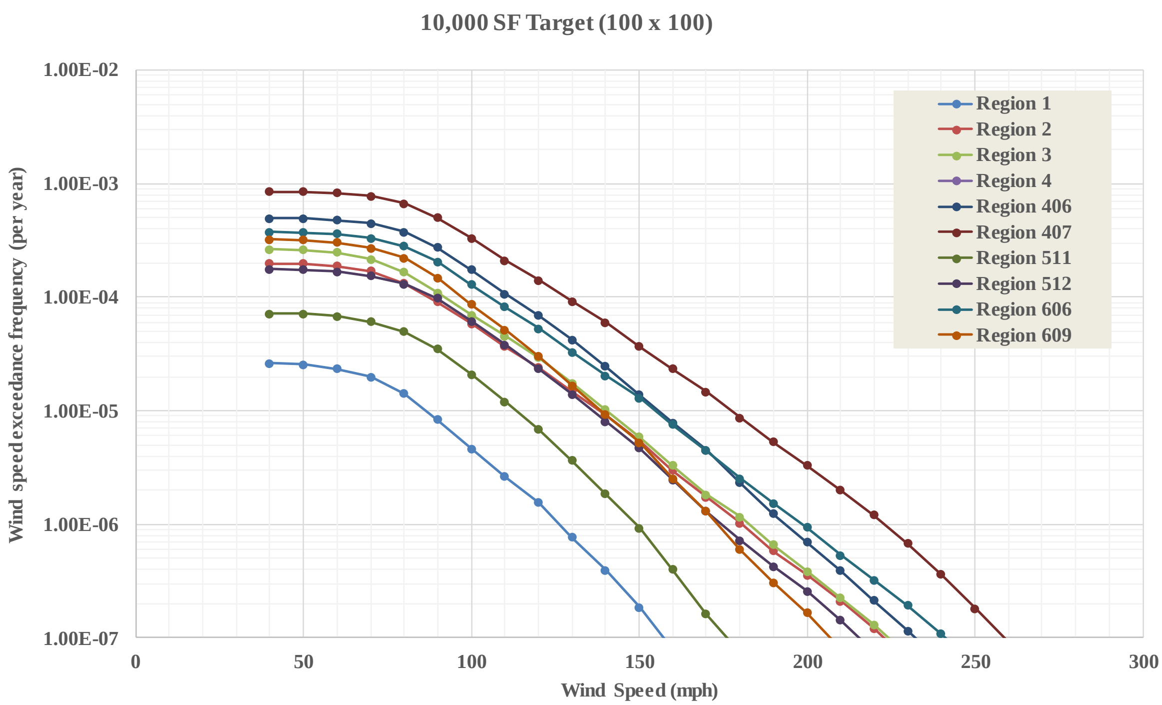

Note: 1 mph = 0.44704 m/s

Figure 7-8. 10,000 SF (929.0 m^2) Target WEFs

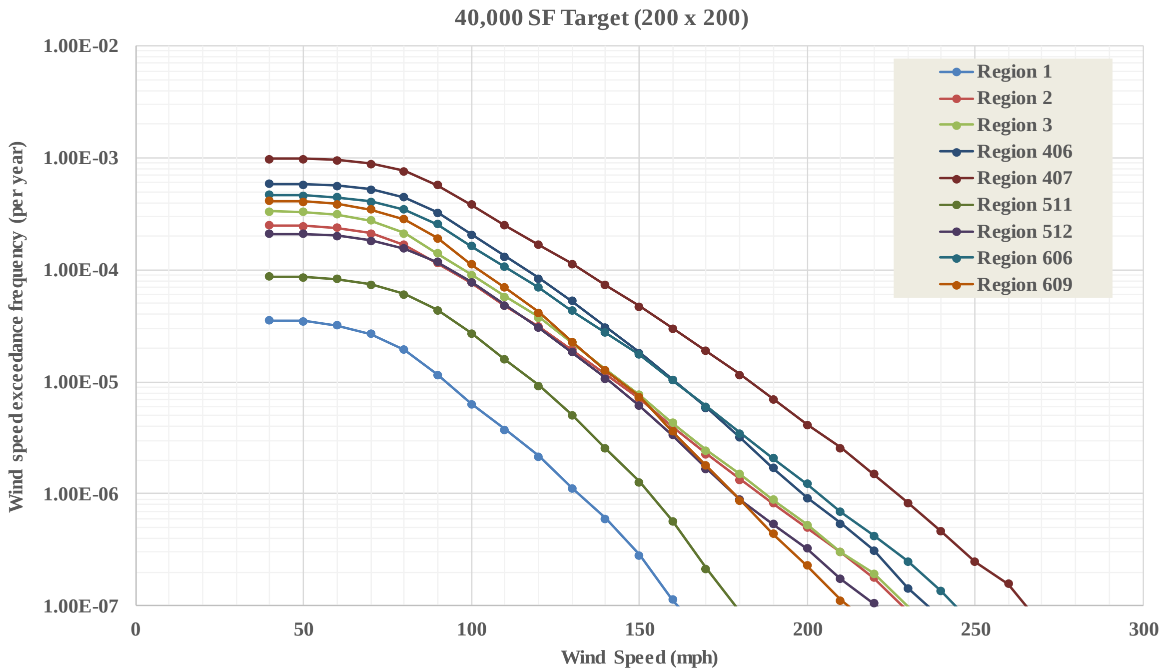

Note: 1 mph = 0.44704 m/s

Figure 7-9. 40,000 SF (3716.1 m^2) Target WEFs

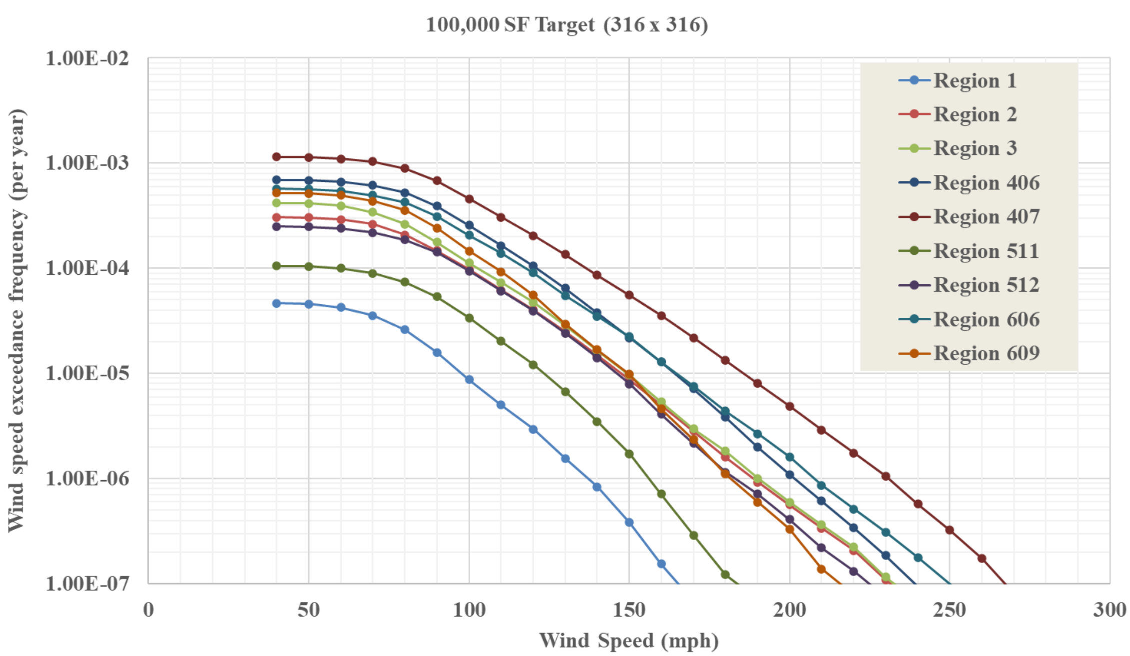

Figure 7-10. 100,000 SF (9290.3 m^2) Target WEFs

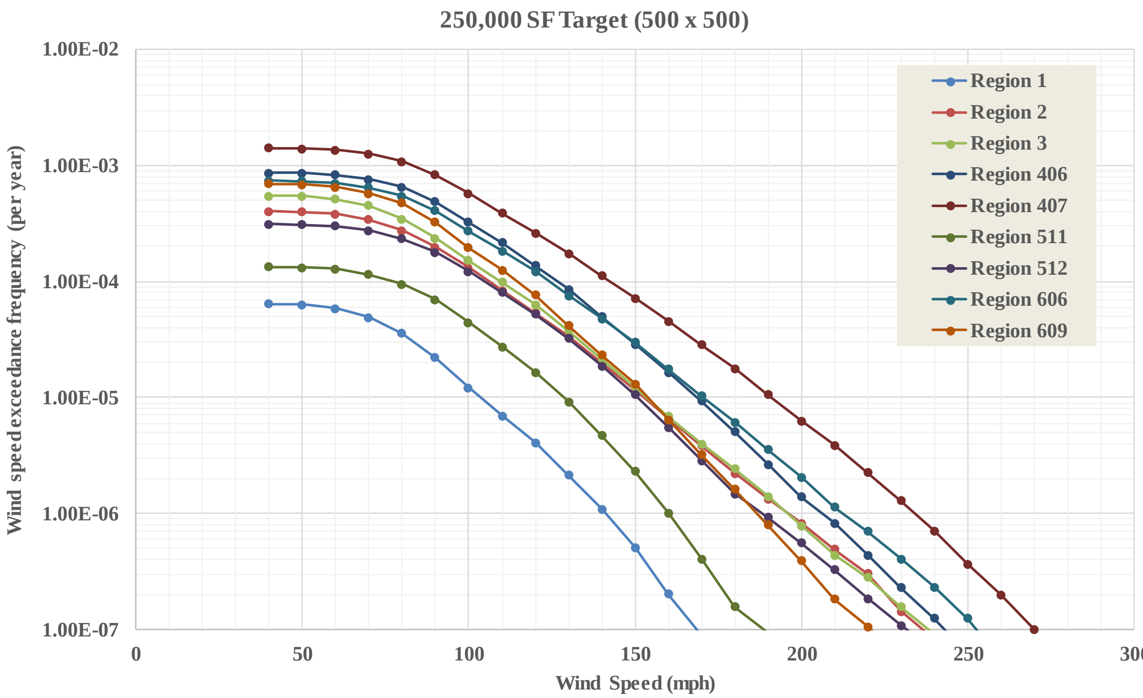

Note: 1 mph = 0.44704 m/s

Figure 7-11. 250,000 SF (23225.8 m^2) Target WEFs

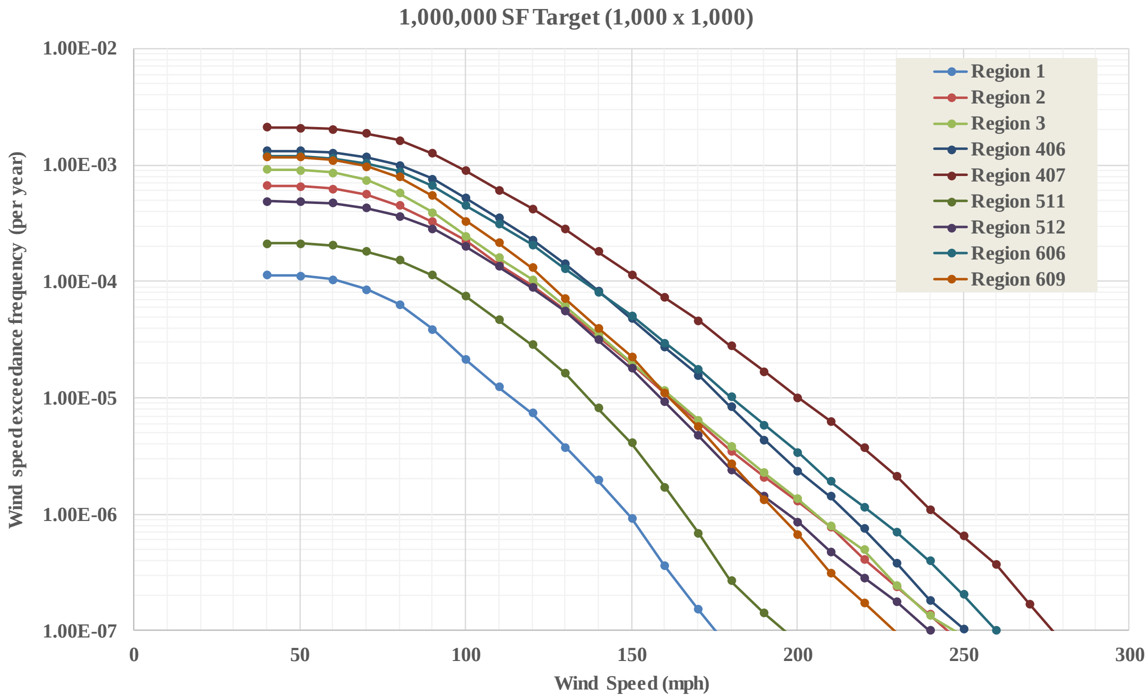

Note: 1 mph = 0.44704 m/s

Figure 7-12. 1,000,000 SF (92903.0 m^2) Target WEFs

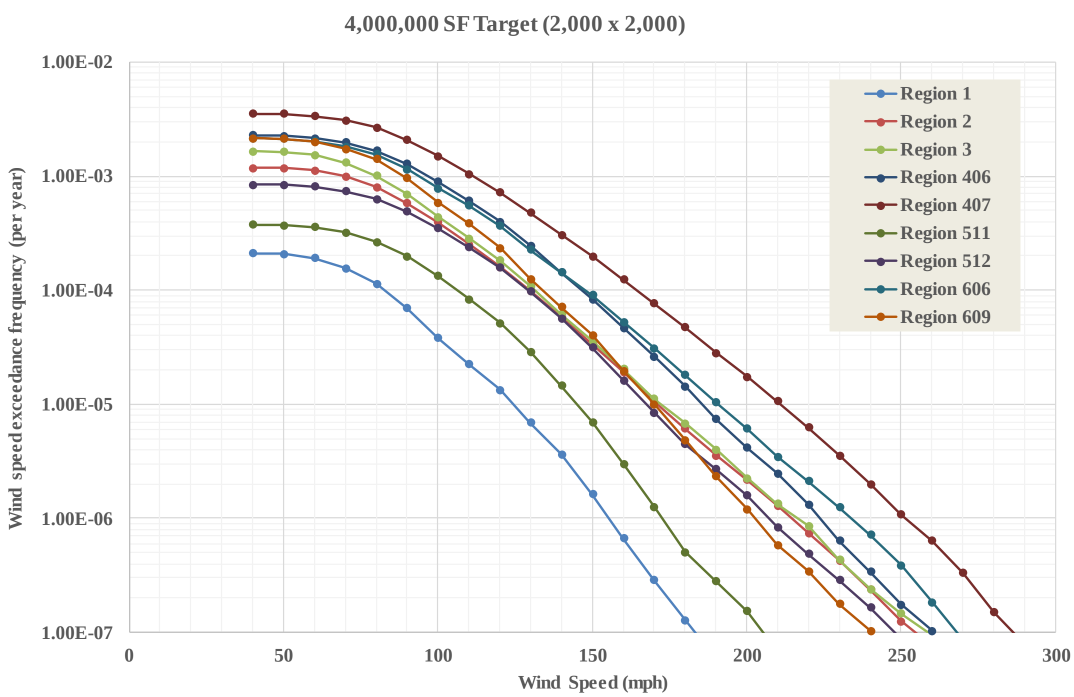

Note: 1 mph = 0.44704 m/s

Figure 7-13. 4,000,000 SF (371612.2 m^2) Target WEFs

Table 7-3. Region Wind Speeds by Target Size and Return Period

Region	Target Area (sf)	Tornado Windspeed (mph)								
		RP300	RP700	RP1000	RP1700	RP3000	RP10,000	RP100,000	RP1,000,000	RP10,000,000
Region 1	Point							76	118	151
	2,000							82	122	154
	10,000							87	126	157
	40,000							93	132	162
	100,000							98	137	165
	250,000							103	141	169
	1,000,000						62	114	149	175
	4,000,000						83	124	155	183
Region 2	Point						79	132	176	220
	2,000						83	134	178	221
	10,000						87	138	180	223
	40,000						94	143	186	228
	100,000						99	147	189	232
	250,000					71	106	153	196	237
	1,000,000				66	89	118	162	205	245
	4,000,000			70	90	104	130	171	215	254
Region 3	Point						85	134	179	222
	2,000						88	137	181	224
	10,000						92	140	183	224
	40,000					42	98	145	188	230
	100,000					71	103	149	190	233
	250,000					81	110	154	196	238
	1,000,000				79	94	121	162	206	247
	4,000,000		65	80	94	106	131	172	217	258
Region 406	Point					77	106	152	190	230
	2,000					80	108	154	193	232
	10,000					84	112	156	194	234
	40,000					89	116	161	199	236
	100,000				73	94	121	164	202	239
	250,000				84	99	127	169	206	243
	1,000,000			80	97	111	137	177	216	251
	4,000,000		86	97	111	124	147	185	224	260
Region 407	Point				79	95	123	175	220	257
	2,000				81	97	125	176	222	260
	10,000				84	100	128	177	223	261
	40,000				89	103	133	183	227	265
	100,000			72	94	108	137	186	231	267
	250,000			83	99	114	142	191	234	270
	1,000,000		85	97	111	126	153	200	242	277
	4,000,000	62	101	111	125	138	165	211	251	286
Region 511	Point							106	142	171
	2,000							109	145	172
	10,000							113	149	176
	40,000							119	153	179
	100,000						60	123	156	184
	250,000						77	128	160	189
	1,000,000						93	137	166	196
	4,000,000					66	106	145	173	205
Region 512	Point						82	129	169	212
	2,000						85	132	171	213
	10,000						89	136	175	216
	40,000						94	141	178	221
	100,000						99	146	183	225
	250,000						105	151	188	232
	1,000,000					84	117	159	197	240
	4,000,000				83	101	130	167	207	248
Region 606	Point						99	148	193	237
	2,000						102	151	195	240
	10,000					70	106	155	199	241
	40,000					81	112	161	204	244
	100,000					88	118	165	208	250
	250,000				76	95	124	171	213	253
	1,000,000			72	93	108	135	180	223	260
	4,000,000		83	94	108	122	148	191	234	268
Region 607	Point						91	132	168	203
	2,000						94	135	170	205
	10,000						97	139	173	207
	40,000					72	102	144	178	212
	100,000					82	108	150	182	216
	250,000				69	89	114	154	187	221
	1,000,000			68	88	100	124	161	194	229
	4,000,000		80	89	100	113	134	170	203	240

Note: 1 SF = 0.09290304 m^2; 1 mph = 0.44704 m/s

7.6.2. Inside Tornado Core vs Within Tornado Path Analysis

The hazard curves in this section are based on at least one point of the target plan area being within the tornado path, as described in Section 7-4 (also see left hand figure, Design 1 in Figure 7-4). To ascertain the contribution of wind speed risk to a structure outside of the tornado core (OTC), we recomputed the WEFs for Design 2 in Figure 7-4 in which any point of the target inside the tornado path is simulated.[122] The fraction (D2-D1)/D2 in $P(v > V)$ is the fractional contribution of the outside the core *P(OTC)* strikes to the total WEF for a given wind speed.

Figure 7-14 shows *P(OTC)*, which is the relative contribution of OTC hits to the total WEF for point, 40,000 SF (3716.1 m^2) target and the 4 million SF (371612.2 m^2) target. We see that OTC hits are more important for small targets (such as points) than for larger targets. For point targets, we see that OTC hits contribute about 50% to the WEF in the range of 40 to about 90 mph (18 to about 40.2 m/s). This percentage decreases to less than 10% by about 150 mph (67.1 m/s). The OTC contribution is greatest for Region 407, which has the largest tornadoes and path widths, and less for regions with smaller tornadoes areas (such as Region 1).

For the 40,000 SF (3716.1 m^2) target, OTC fractions range from about 0.4 at low wind speeds to less than 0.1 by about 130 mph (58.1 m/s). For the 4 million SF (371612.2 m^2) target, OTCs contribute about 10% of the WEF at low wind speeds and drops to less than 5% by about 120 mph (53.6 m/s).

These results follow from physical arguments that the target must be inside the core in order to experience the highest wind speeds in a tornado. At high wind speeds, contributors from low EF-Scale intensities becomes nil. Hence, all the curves approach nil OTC risk fractions with increasing *V*. The complement event is that for low wind speeds, and point targets, the target has about equal contributions from inside the tornado core (ITC) and OTC, particularly for regions with large tornado areas.

An important conclusion of this analysis is that for engineering design wind speeds greater than about 100 mph (45 m/s), ITC hits dominate the risk and design loads can reasonably be determined assuming that the target is inside the core.

[122] In discussions with the ASCE Tornado Load Subcommittee, a question was raised regarding when to consider APC loads, which occurs for buildings inside the tornado core (Design 2 in Figure 7-4). Buildings OTC do not experience APC loads. We performed the simulations described in this section to quantify the fraction of tornado WEF for building strikes OTC. The results in this section show that one should design for APC once wind speeds are greater than about 100 mph (45 m/s) with the hazard curves herein, since OTC risk is a small fraction of the total WEF. Further, since tornado wind speeds do not dominate designs until the wind speeds are greater than 100 mph (45 m/s), these results can be used without reference to a wind speed threshold.

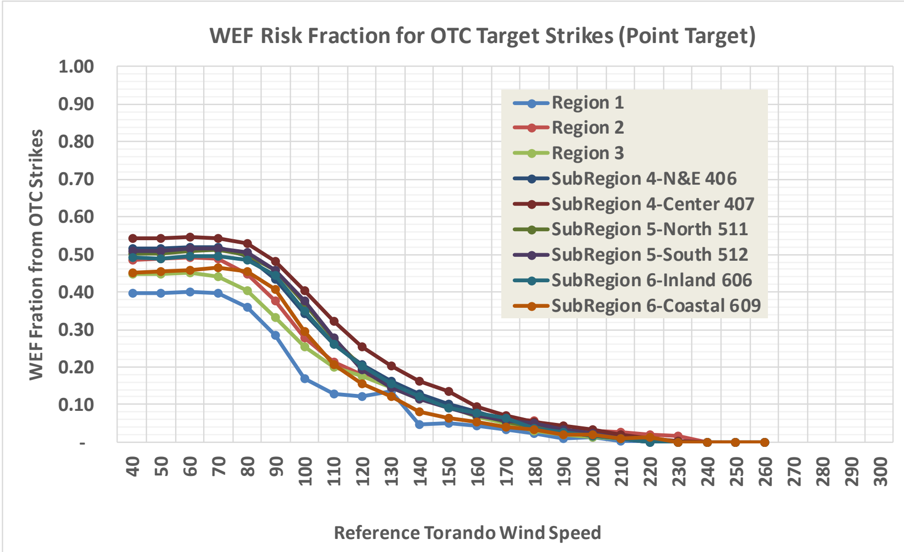

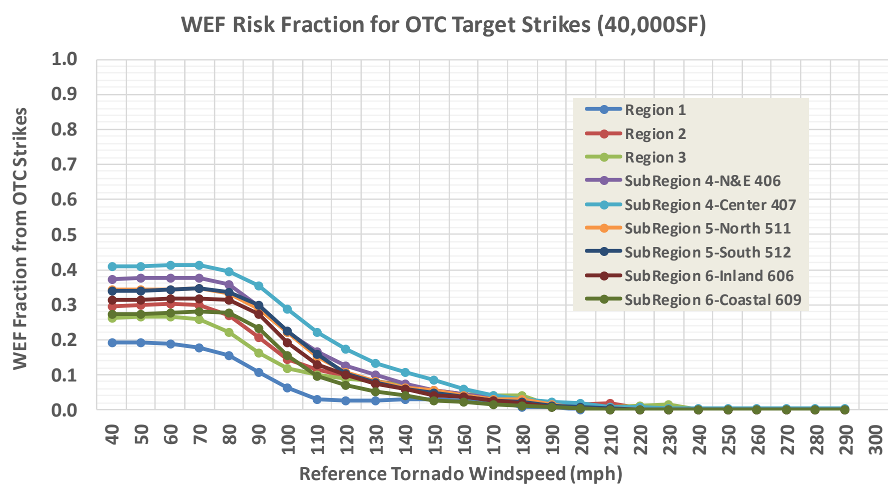

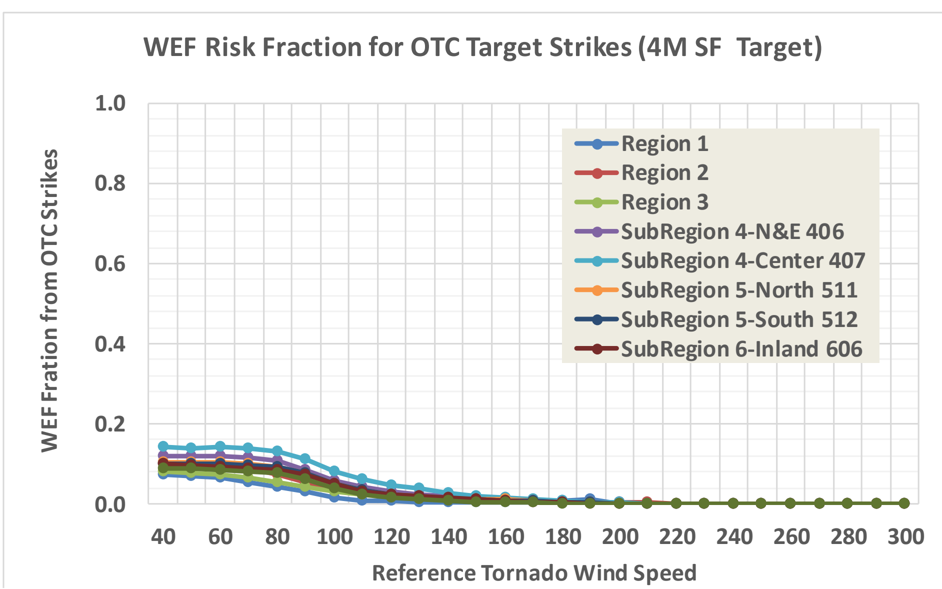

Note: 1 SF = 0.09290304 m^2; 1 mph = 0.44704 m/s

Figure 7-14. WEF Risk Fraction for OTC Target Strikes

7.6.3. Sensitivity Analysis

The following paragraphs present sensitivity analyses for:

1. Target Size
2. Target Aspect Ratio
3. Approximate Nominal Hazard
4. Region 407: Miscellaneous Sensitivities
5. Region 407: EF* Wind Speeds
6. Region 407: Prior Wind Speed Distribution

The last three sensitivities are limited to Region 407 due to simulation run times and post-processor steps.

7.6.3.1. Target Size

Target size effects are significant for our RWS definition. The effect of target size depends on the region and the return period. Target size effect is illustrated in Figure 7-15 for point, 40,000 SF (3716.1 m^2) and 4M SF (371612.2 m^2) targets in Regions 1 (lowest tornado hazard) and 407 (highest tornado hazard).

The effect of target size generally diminishes within a region with increasing return periods (lower WEFs). For example, in Region 1, the increases in wind speed from point to 40,000 SF to 4 M SF (3716.1 to 371612.2 m^2) at 1E-05 WEF are 16 and 48 mph (7.15 and 21.5 m/s), whereas; at 1E-07 WEF, they are 11 and 32 mph (4.92 and 14.3 m/s). This trend follows from Eq. (7-8), where the A_0's increase with tornado intensity, producing less sensitivity to target size at high wind speeds

The effect of target size varies across regions. Generally, regions with larger size tornadoes have less sensitivity to target size effects, but the differences also depend on intra-region EF-Scale distribution and tornado path areas.

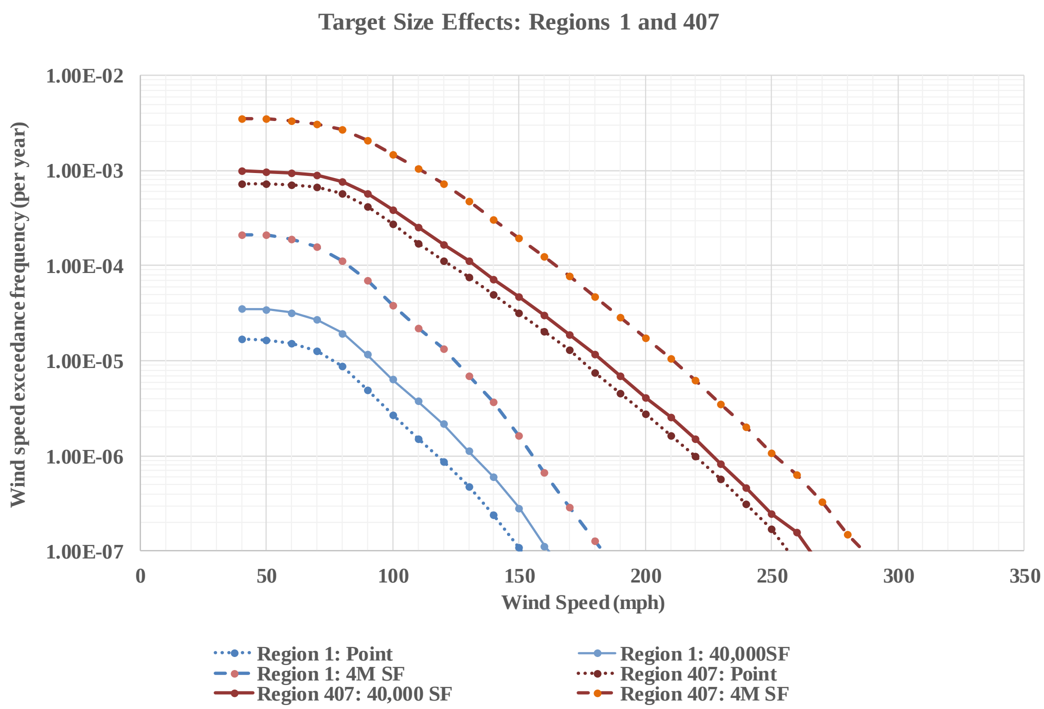

Note: 1 SF = 0.09290304 m^2; 1 mph = 0.44704 m/s

Figure 7-15. Within Region Target Size Effects Comparisons

For a given wind speed, the effect of increasing target size, produces an upward shift in the hazard curve. This upward shift means that the larger target size is more likely to experience the same RWS as a smaller target. This shift also means that a larger target may experience a return period wind speed whereas a smaller target is not hit by a tornado at that return period. For example, the point target in Region 407 is not hit by tornadoes at the 1E-03 per year WEF in Figure 7-15, whereas the 4 Million SF (371612.2 m^2) Target has a 1E-03 wind speed of 111 mph (49.62 m/s). Similarly, for Region 1, the point and the 40,000 SF (3716.1 m^2) Targets do not have wind speeds for 1E-04 per year WEF, whereas the 4M SF (371612.2 m^2) Target wind speed is 83 mph (37.1 m/s).

7.6.3.2. Target Orientation and Aspect Ratio Sensitivity

We evaluated several cases to assess sensitivity of target orientation and aspect ratio for Regions 1 and 407. These runs were all made with the targets positioned parallel and perpendicular to the mean tornado path direction. The runs were made with the Base Prior for three target sizes:

1. 4:1 Aspect Ratio: 800 ft x 200 ft (160,000 SF) (243.84 m x 60.96 m (14864.5 m^2))
2. 10:1 Aspect Ratio: 800 ft x 80 ft (64,000 SF) (243.84 m 24.384 m (5945.8 m^2))
3. 40:1 Aspect Ratio: 800 ft x 20 ft (16,000 SF) (243.84 m 6.096 m (1486.4 m^2))

Figure 7-16 shows these results for Regions 1 and 4. Both regions show minor sensitivities that reduce modestly with increasing aspect ratio. As can be seen from the directional distribution plots in Section 3.4.2, Region 1 has a broader distribution of tornado path direction. This effect reduces the influence of target orientation. For example, for Region 407 the 4:1 aspect ratio target, the wind speed differences (perpendicular-parallel) for a 3,000 yr. RP wind speed are 116.4 - 112.6 = 3.8 mph, 114.8 - 109.6 = 5.2 mph, and 114.6 - 107.7 = 6.9 mph (52.035 – 50.337 = 1.698 m/s, 51.320 – 48.996 = 2.324 m/s, and 51.231 – 48.146 = 3.085 m/s) for the 4:1, 10:1, and 20:1 aspect ratios, respectively. These differences tend to reduce for higher RPs. For example, at a 1 million yr. RP, the aspect ratio differences are all in the 1 to 2 mph (0.45 to 0.89 m/s) range for these cases.

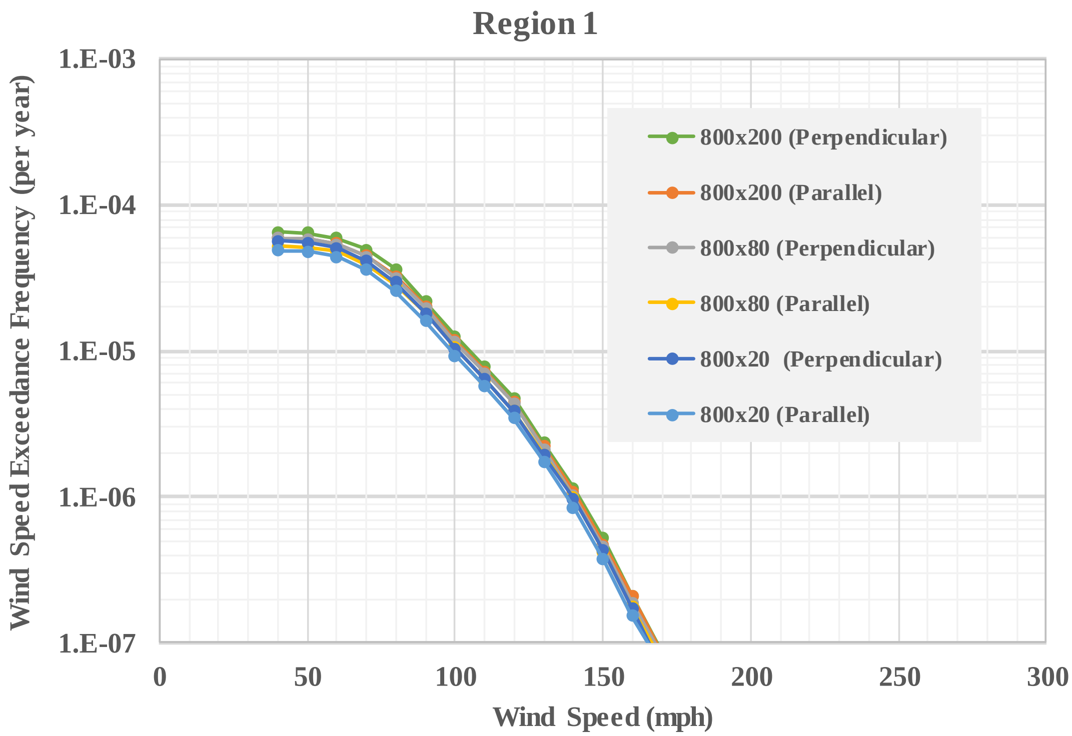

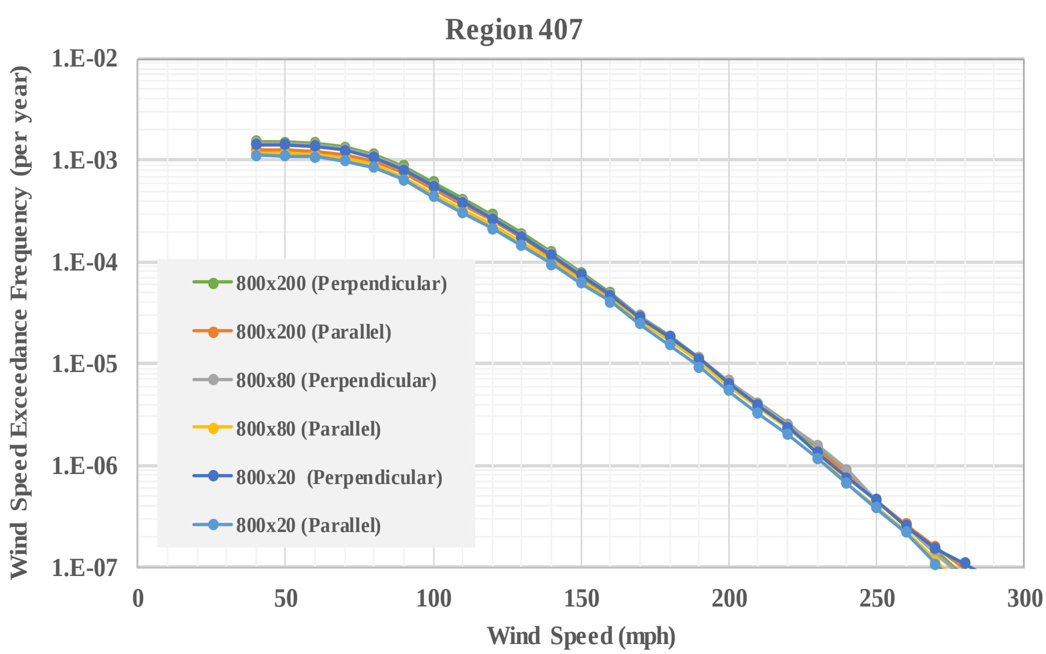

Note: Target dimensions in feet. 1 ft = 0.3048 m; 1 mph = 0.44704 m/s

Figure 7-16. Target Orientation and Aspect Ratio Sensitivity

Table 7-4 summarized the mean ratios of the increase in the WEF when the target is oriented perpendicular to the mean tornado path direction vs. parallel to it. Target orientation sensitivity is governed by Eq. (7-8) (and the cosine and sin functions that influence the computation of the *ZL* and *ZW* projections), the directional distribution for ϕ, and the tornado path length and width distributions.

These results do not apply to lifeline targets with long length and extremely high aspect ratios; for examples see Twisdale and Dunn (1983a). The effects of orientation can be much more significant for these long, linear targets.

Table 7-4. Mean WEF Ratios (Perpendicular/Parallel) for Targets in Figure 7-16 and 40 < V ≤ 260 mph (18< V ≤ 116 m/s)

Aspect Ratio	Region 1	Region 407
4:1	1.05	1.11
10:1	1.06	1.18
40:1	1.08	1.22

7.6.3.3. Approximate Nominal Hazard

Nominal hazard curves are based on the nominal or raw data without considering possible biases, errors, or uncertainties.

The subjective EF wind speed ranges (TTU, 2006) are used in these nominal simulations with nominal occurrence rates (no population bias correction) and the nominal EF distribution. However, for the tornado path model data and wind field simulations, we used the epistemic models developed herein. Hence, this is an “approximate” nominal analysis in that regard. This approximate nominal case was executed in TORRISK2.

The approximate nominal curves given in Figure 7-17 are for the 40,000 SF (3716.1 m^2)Target. For comparison, we include the hazard curves from Section 7.6.1 for Regions 1 and 4. For a given RP, the nominal hazard wind speeds are notably smaller. For example, at a 1E-06 WEF, the Regions 1 and 407 epistemic mean wind speeds are about 20 mph (8.9 m/s) greater than their respective nominal means. Beginning at about 1E-06 WEF, the increasing downward curvature in the nominal curves result from use of the EF-Scale deterministic wind speed ranges with a 234 mph (104.6 m/s) upper bound for EF5. The differences in epistemic and approximate nominal means therefore increase for these WEFs.

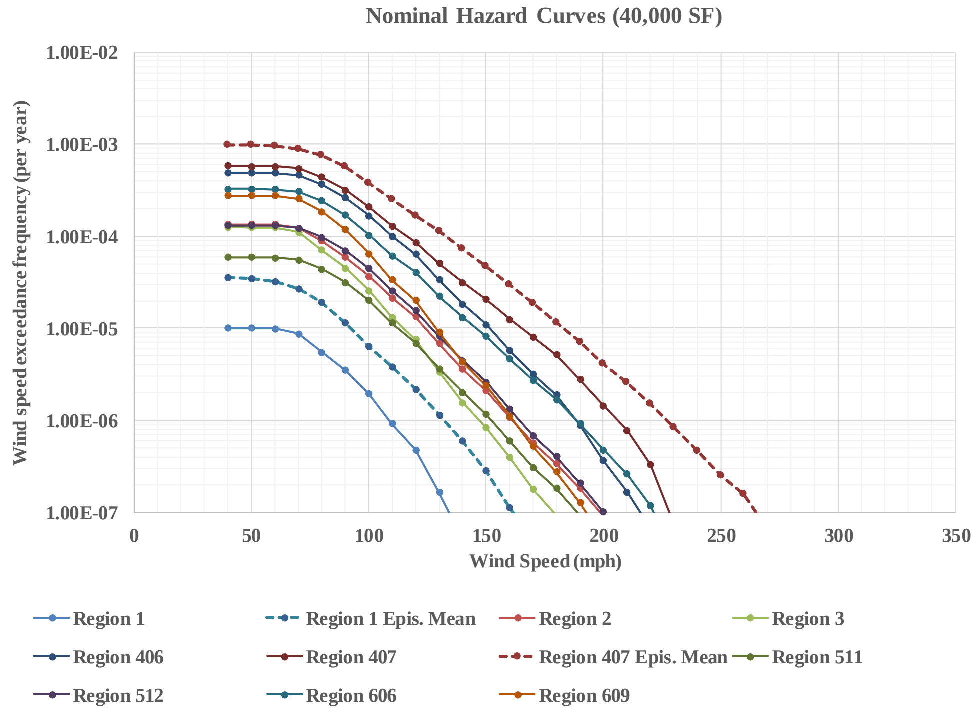

Note: 1 SF = 0.09290304 m^2; 1 mph = 0.44704 m/s

Figure 7-17. Approximate Nominal Hazard Curves

7.6.3.4. Region 407: Miscellaneous

Figure 7-18 shows multiple sensitivities for Region 407 for the 40,000 SF (3716.1 m^2) Target. The mean hazard curve (Base Prior) is shown with a black dashed line and hollow square symbols.

These one-at-a-time sensitivities show how changes to one variable or input file affect the results:

1. **Reduced Occurrence Rate:** Use of the Region 1 occurrence rate produces a rigid body shift in the Region 4 hazard curve as shown. The WEFs are reduced by the ratio of the derived mean input occurrence rates, which corresponds to a WEF reduction factor of 81.6 for this case. With the Region 1 occurrence rate, the wind speed reductions are about 57 mph (25.5 m/s) at 1E-04 WEF and about 45 mph (20.1 m/s) at 1E-06 WEF.

2. **Reduced Path Areas:** Use of the Region 1 path models produces a modest downward WEF shift of about 1.5 from the base curve. In terms of wind speeds, the reduction ranges from about 10 mph (4.5 m/s) at WEF = 1E-04 to about 4 mph (1.8 m/s) at WEF = 1E-06.

3. **Low Gamma:** For this case, gamma (wind field radial velocity/tangential velocity ratio) was set to 0.3.[123] We see that this sensitivity produces a slight downward shift in the hazard curve of about 1.2 for wind speeds greater than about 100 mph (45 m/s).

[123] This case was created without using the swirl model and RMW was set to ½ the maximum damage width.

Low gamma results in higher tangential velocity components in the total horizontal wind speeds and slightly reduces the swath area of high wind speeds.

4. **Reduced RMW:** We reduced the mean simulated RMWs to 0.5 of those in the base case. From the swirl model, reduced RMW results in low swirl (higher inflows relative to tangential wind speed). We see modest reductions in the hazard curve of a few percent due to the offsetting effect of high gamma at low swirl ratios and the resulting wider swaths for the same maximum wind speeds.
5. **EF Era *W*:** The use of the EF era maximum path width (*W*), without the epistemic mean width reduction factor of about 0.5, produces a factor of about 1.8 increase in WEF in the horizontal portion of the hazard curve. As expected, increasing the widths of all the EF intensities results in a similar (1/0.5 = 2) increase in WEF at low wind speeds. This effect reduces with wind speed to a factor of about 1.35 at 160 mph (71.5 m/s) and 1.2 at 220 mph (98.3 m/s). The lessened effect at higher wind speeds is due to larger tornadoes and the associated tradeoffs of larger RMW and higher swirls, with associated lower inflows.

These results show that changes in occurrence rate produce a rigid body shift in the WEFs. In terms of wind speeds, we note, for example, that a factor of 2 increase/reduction in occurrence rate results in about a 10-15 mph (4.5-6.71 m/s) change in the wind speed in the main part of the hazard curve.

Tornado path area (length and width models) have a modest effect. For example, the use of the Region 1 path areas for Region 4 produces a 10-15 mph (4.5-6.71 m/s) shift in the central part of the hazard curve.

For the remaining cases in Figure 7-18, the sensitivities show generally modest impacts. Of these, the largest sensitivity is the doubling of the path width, which effectively assumes that the EF-Scale maximum-recorded path width is constant over the full length of the tornado. For the 40,000 SF (3716.1 m^2) Target, doubling the path width produces increases of about a 10 mph (4.5 m/s) for RP= 3,000 years and 5 mph (2.2 m/s) for RP = 100,000 years.

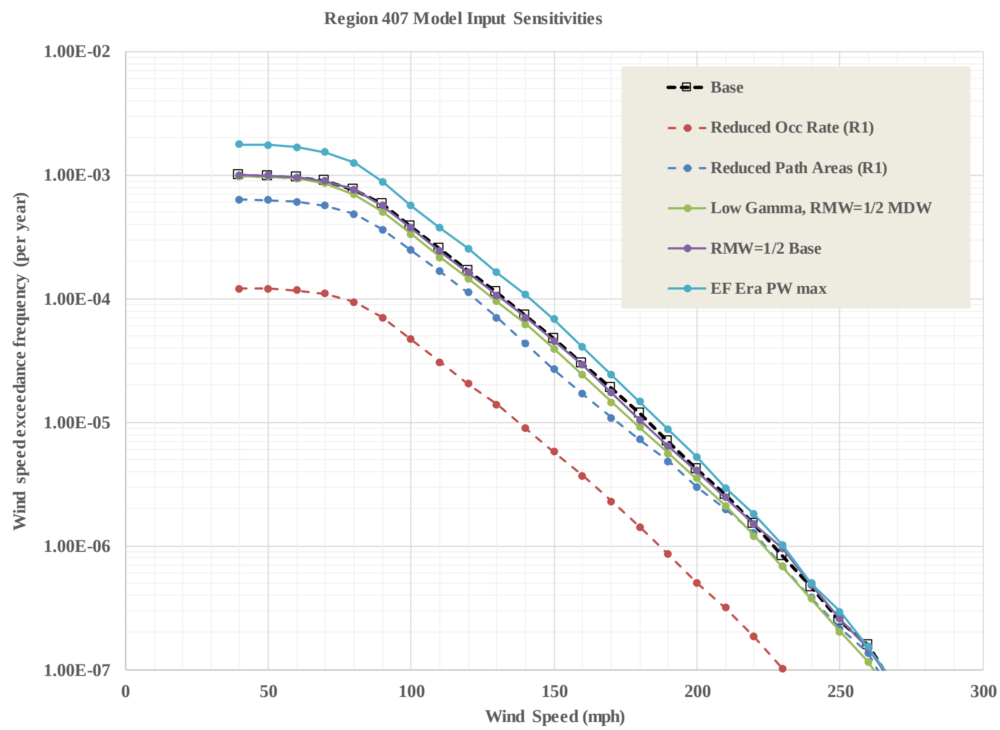

Note: 1 mph = 0.44704 m/s

Figure 7-18. Region 407 Model Input Sensitivities

7.6.3.5. Region 407: EF* Wind Speed Sensitivity

As described in Section 6, we use a building stock weighted (BSW) mean FR12 wind speed distribution for each EF-Scale in the hazard curve development. The BSW mean is a weighted mean of the EF* wind speed distributions over the 44 house types. In this section, we illustrate hazard curves based on several individual FR12 classes compared to the BSW mean house.

Individual House EF* Wind Speeds. Figure 7-18 shows the results for 6 FR12 classes (Nos. 1, 13, 21, 26, 42, and 44) for Region 407.[124] We see that the weakest house (Class No. 1) produces the lowest hazard curve (lowest wind speed for a given return period). The strongest house (Class No. 44) produces a hazard curve well shifted to the right (higher wind speeds for the same WEF), beginning at about 120 mph (53.6 m/s). In between, we see a range of curves that reflect how that the FR12 class characteristics are reflected in the wind speed hazard curves.

The BSW weighted mean curve is closer to the weaker houses since they are the most frequent construction classes. The BSW hazard curve is slightly below No. 13, which falls into the EF load-path condition protocol as EXP.

The range in wind speeds in Figure 7-18 for a given WEF depends on a complicated convolution of many probabilistic parameters. These include: tornado wind field parameters; tornado path variables; loads; and structure size, geometry, and resistances. Tornado size,

[124] Table 6-7 provides the characteristics of these classes.

vertical winds, APC effects, WBD, and directional winds vary significantly with RWS. House complexity, orientation, component resistances also vary significantly with FR12 class, producing the significant across-class differences in the hazard curves.

The range of resulting wind speeds for a WEF in Figure 7-18 broadens significantly once the building begins to experience notable structural damage ≥ DOD 4. We see a range of about 40 mph (18 m/s) beginning at about 1E-04 WEF for Region 407. This range increases for lower WEFs as a result of the more complex structural damage DODs that involve a system of components. At a WEF of 1E-05, we see a range of 170 to 225 mph (76.0 to 100.6 m/s) from the weakest to the strongest modeled FR12 class. This wind speed range produces a ratio of 1.5. The ratio of the resistance of the various components for the two respective house classes exceeds a factor of 4 for all of the connections, which would produce at least a wind speed factor range of 2 or more. However, with increasing wind speeds, we also have more energetic WBD, higher vertical wind speeds and larger RMWs. In addition, wood frame walls can fail when the material reaches its stress limits, becoming the weak link in the load path. Another potential weak link in strong house occurs when individual wood roof structural elements (chords, webs, tie beams, or rafters) reach their stress limits and fail prior to roof-to-wall connection failures. With these effects, one should not expect wind speed capacities to continue to increase for wood frame construction in proportion to the square root of the ratio of metal-connection resistances.[125]

[125] Classes for masonry wall FR12 (reinforced and unreinforced) should be included in the new EF-Scale wind speed standard. Properly reinforced masonry walls will result in a significant increase in DOD 7-10 wind speeds.

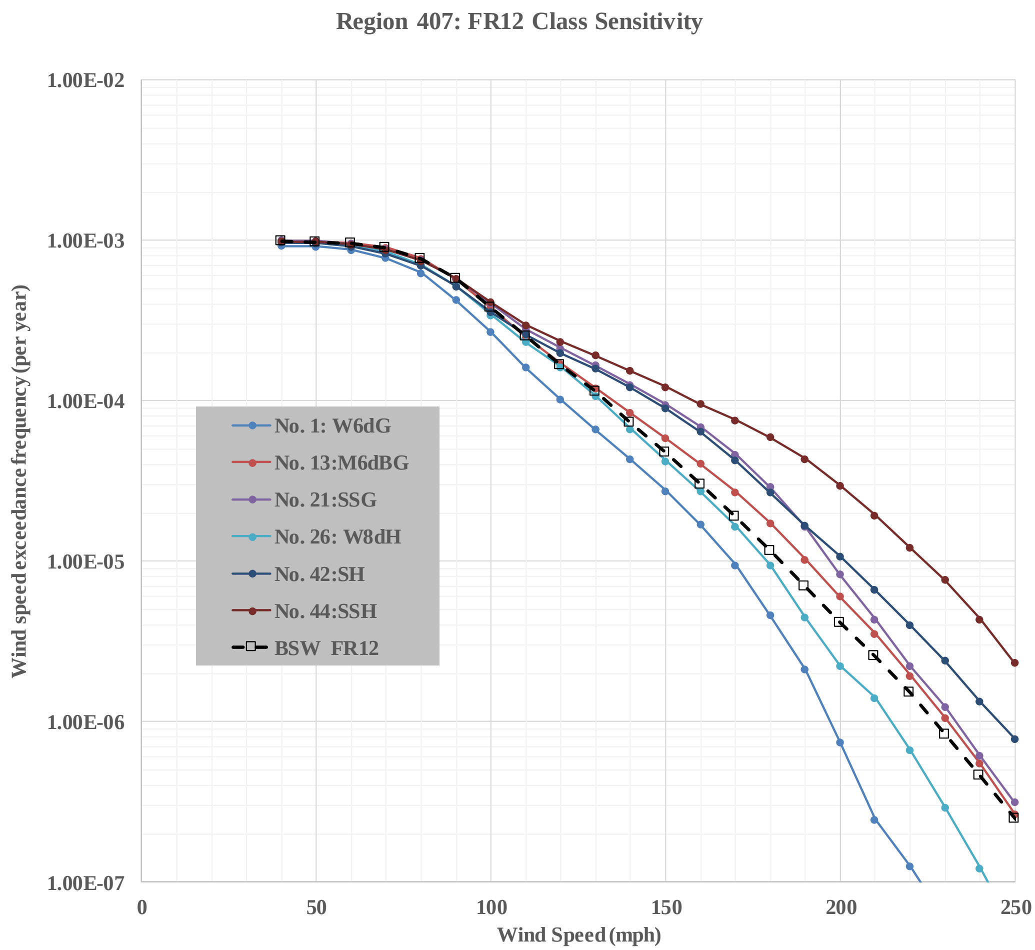

Note: 1 mph = 0.44704 m/s

Figure 7-19. Region 407: Sensitivity to FR12 Class

7.6.3.6. Region 407: Prior Wind Speed DistributionNote: 1 SF = 0.09290304 m2; 1 mph = 0.44704 m/s

Figure 7-20 illustrates the sensitivity of the hazard curves to the prior wind speed distribution for the 40,000 SF (3716.1 m^2) target for Regions 1, 3, and 407. These 3 regions represent a very weak tornado climatology, a mid-range tornado climatology, and a strong U.S. tornado climatology, respectively. The results are shown for the LB, Epistemic, and UB Priors, as developed in Section 6.4.3. Recall that the mean epistemic prior was based on judgmental weights of UB = 0.4, Base = 0.5, and LB = 0.1; hence, its hazard curve lies closer to the UB curve than the LB. The Base prior results are not shown as they are essentially mid-way between the UB and LB.

The effect of the prior assumption has virtually no effect on wind speeds corresponding to a 3,000 year RP wind speeds for this target size. For a 100,000 year RP, there is no appreciable effect for Region 1, minor effect for Region 2 (<10 mph (4.5 m/s)), and modest effect for Region 407 (< 20 mph (8.9 m/s)). These effects become larger at higher RPs as the LB prior hazard curve wind speeds begin to turn concave down in shape.

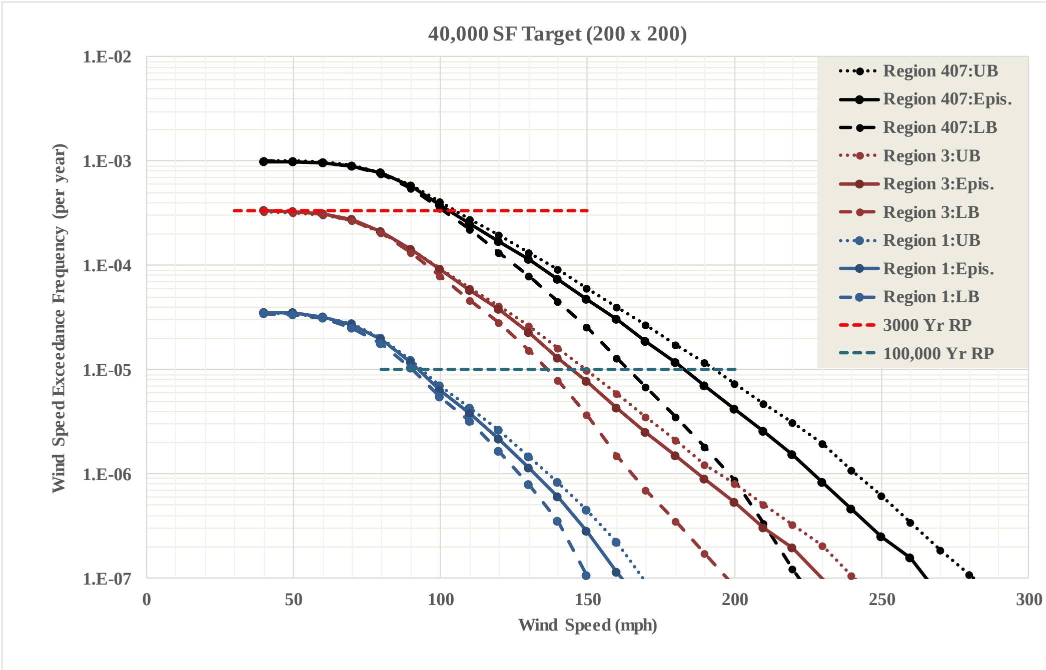

Note: 1 SF = 0.09290304 m^2; 1 mph = 0.44704 m/s

Figure 7-20. Wind Speed Prior Distribution Sensitivities

7.6.3.7. Sensitivity Discussion

The one-at-a-time hazard curve sensitivity analyses show how changes in inputs to one or more of the embedded models impacts the resulting wind speeds for a given WEF (or, alternately, the WEFs for a given wind speed). We offer a few remarks on these analyses:

1. Target size sensitivity is non-linear and generally decreases with lower WEFs. Also, regions with larger tornadoes generally have lower sensitivity to target size. The target size sensitivity analysis presented herein does not address lifelines or systems of spatially-separated targets.
2. The hazard curve is not particularly sensitive to the azimuthal orientation of typical individual buildings and structures with aspect ratios less than about 10:1.
3. WEFs are linear in tornado occurrence rate in all hazard curves, regardless of target size.
4. Tornado wind field parameters gamma and RMW are related through the swirl model. We found minor sensitivity in terms of the computed hazard curve with an RMW-dependent swirl model.
5. Uncertainties in path width data and the relationship of maximum tornado path width to mean path width have a greater impact at low wind speeds than high wind speeds.
6. There is wide variation in EF* wind speeds for weak to strong FR12 classes for WEFs less than about 2E-04 in Region 407.
7. The prior wind speed distribution assumption has virtually no impact on RP ≤ 3,000 years and very modest impacts for RP = 100,000 years. At 10 million years, the

sensitivity depends on the region. For example, the wind speed sensitivity, expressed as the range divided by 2 is about 10, 20, and 30 mph (4.5, 8.9, 13 and m/s) for regions with weak (Region 1), moderate (Region 3), and severe (Region 407) tornado risk.

8. Tornado Wind Speed Maps

8.1. Overview

Figure 8-1 summarizes the map development process. The first step involved the application of minor judgment-based adjustments to the mapped tornado climatology regional boundaries developed in Section 2. These adjustments were made late in the project without re-analysis of data. The second step involved interpolation of the regional tornado hazard curves. We used log interpolation on WEFs and linear interpolation on wind speed. In Step 3, the interpolated wind speeds were mapped to each 1° grid cell in the 1° shifted grid. Gaussian smoothing was applied in Step 4 to the grid wind speeds to reflect uncertainties in the region boundaries. In Step 5, the wind speed grids corresponding to each return period and target area combination were converted to shapefiles of grid points. Next, the wind speed grid points were interpolated using ordinary kriging in ArcMap 10.8 (ESRI, 2019a) to produce wind speed rasters. Finally, wind speed contours were derived from these rasters, smoothed, and manually adjusted to create the final wind speed maps.

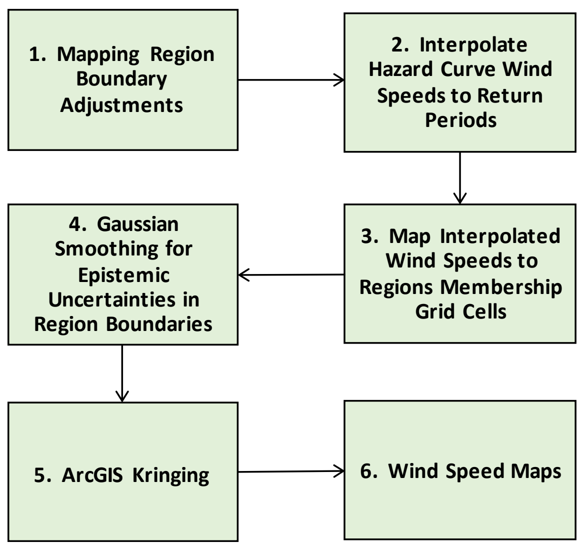

Figure 8-1. Map Development Process

8.2. Region Boundary Adjustments

In Sections 2.6 and 2.7 we developed tornado climatology region boundaries from the cluster analysis boundaries, resulting in the region map shown in Figure 2-52. Several region boundary adjustments were made during the tornado hazard map development process, which included:

Adjusting Region 1-2 boundary in Montana-Wyoming to follow Rocky Mountain elevations and tornado trends. We evaluated combined US-Canadian tornado map data (see Figure 8-2) and Canadian map regions being developed in a separate project. The red line R1-R2, in Figure 8-2, shows the position of the Region 1–Region 2 boundary after the manual adjustment. This boundary was shifted west to follow the elevation changes of the Rockies and reflected the tornado densities that extend approximately to the eastern edge of the Canadian Rockies. This adjustment, while somewhat outside of the Region 1-2 boundary uncertainties as shown in Figure 2-40, ensures that the Region 2 wind speeds do not weaken prematurely in central Montana-Wyoming.

Adjusting the Region 2-5 boundary by shifting 1 cell east in northeastern Ohio. This adjustment was made to more closely follow elevation differences and ensure that the tornado risk in this part of Ohio is not overly affected by the Gaussian smoothing from cells further east. This shift is illustrated by red line R2-R5 in Figure 8-2. This shift is within the epistemic uncertainty boundary shown in Figure 2-40.

1. Smoothing certain boundaries to improve map contouring in vicinity of Regions 4a-4b, 4b-6a, 6a-6b, and 5a-5b. This smoothing improves the boundaries developed in the original sub-region analysis and eliminates excessive curvatures in these areas.

The original region boundaries given in Figure 2-422 are reproduced in Figure 8-3 (top), along with the final adjusted boundaries (bottom). These adjustments were well within the cluster group formation trends. In these adjustments, we updated grid-cell region membership before the final grid smoothing and Kriging.

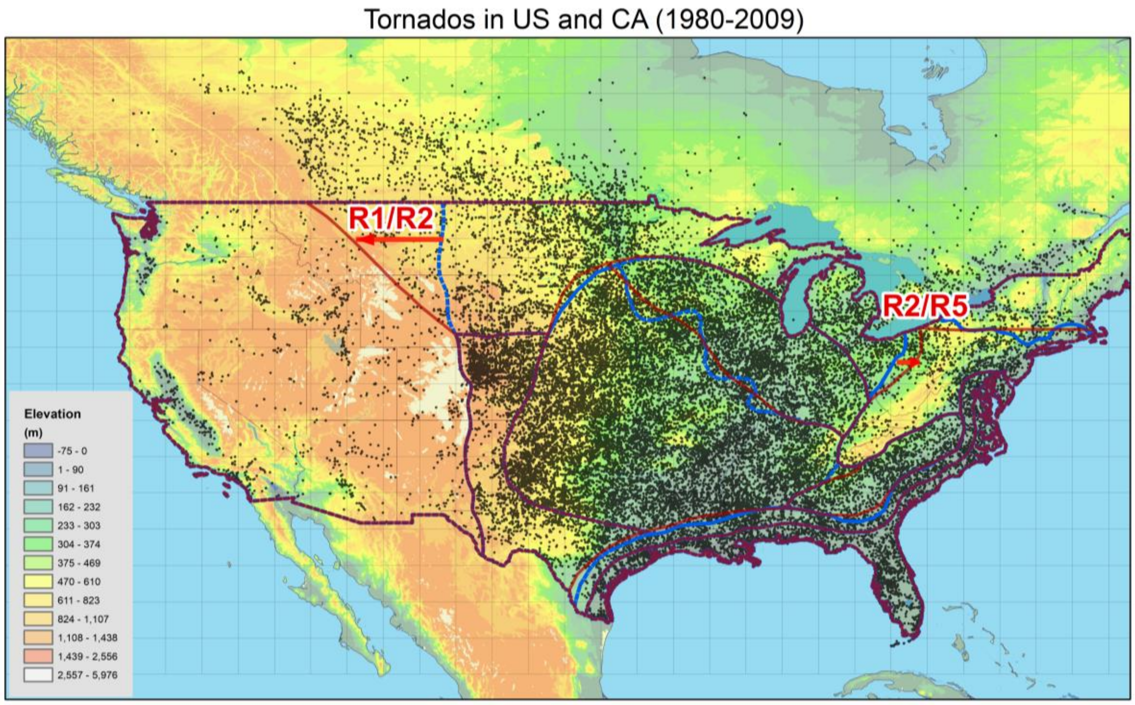

Note: 1 m = 3.28084 ft

Figure 8-2. Regional Boundary Adjustments for Regions 1-2 and 2-5

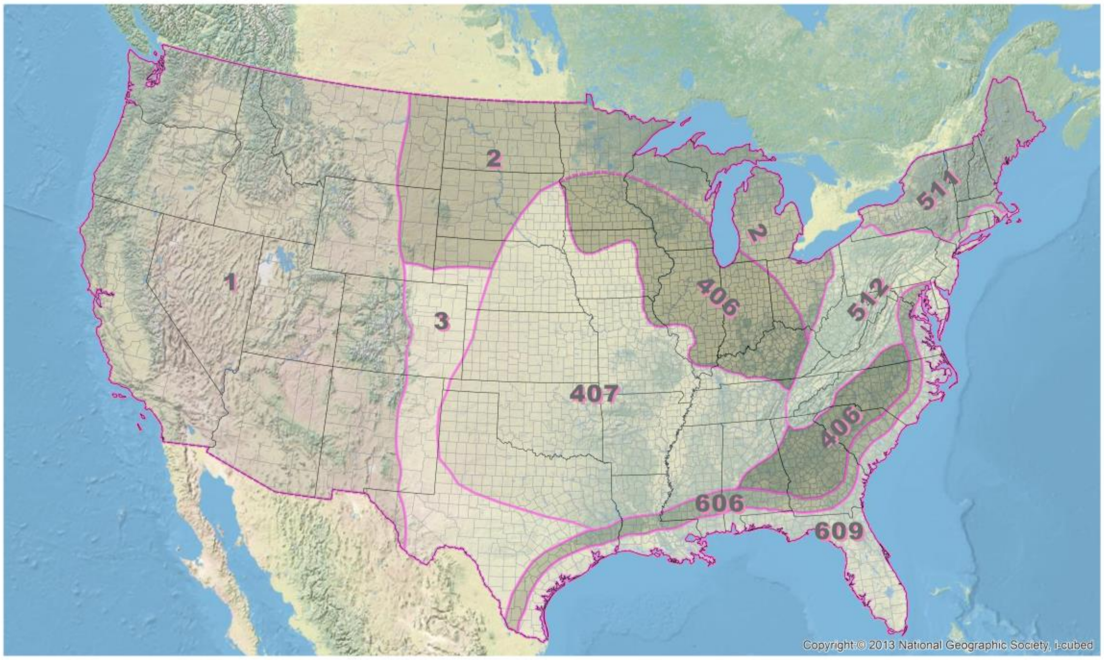

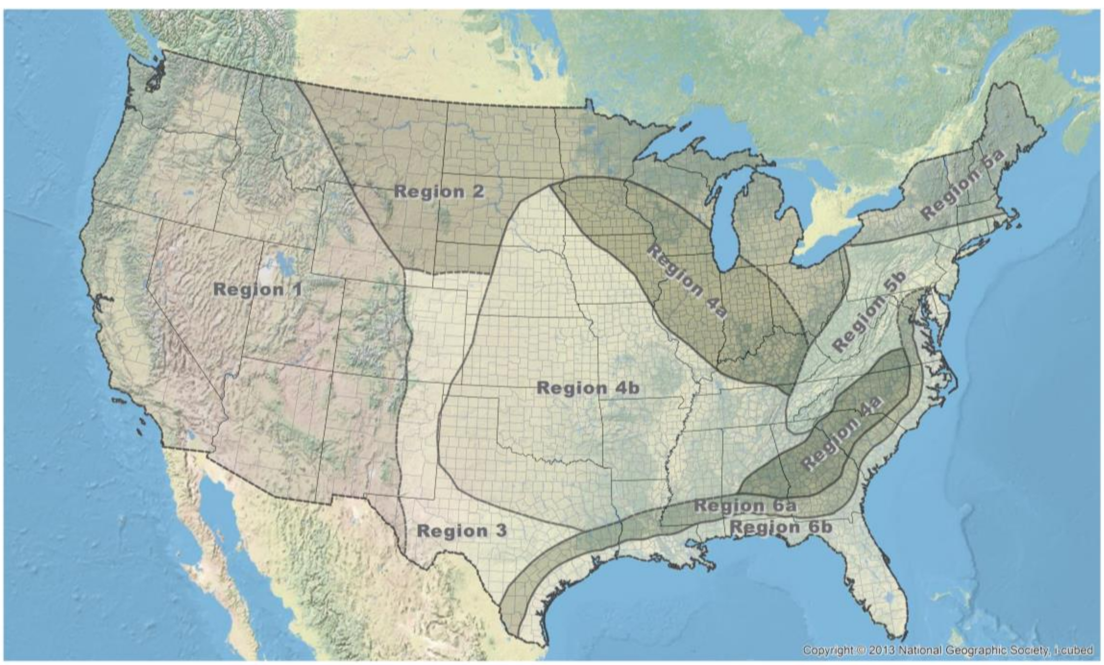

Figure 8-3. Regional Boundary Maps Before (top) and After Adjustments (bottom)

8.3. Wind Speed Grids and Spatial Smoothing

The 1° shifted grid in Figure 8-4 was used for map development. This grid was evaluated as one of the four grids considered in Section 2 (see Figure 2-9) and used in the epistemic analysis of region boundary uncertainties developed in Section 2.4.

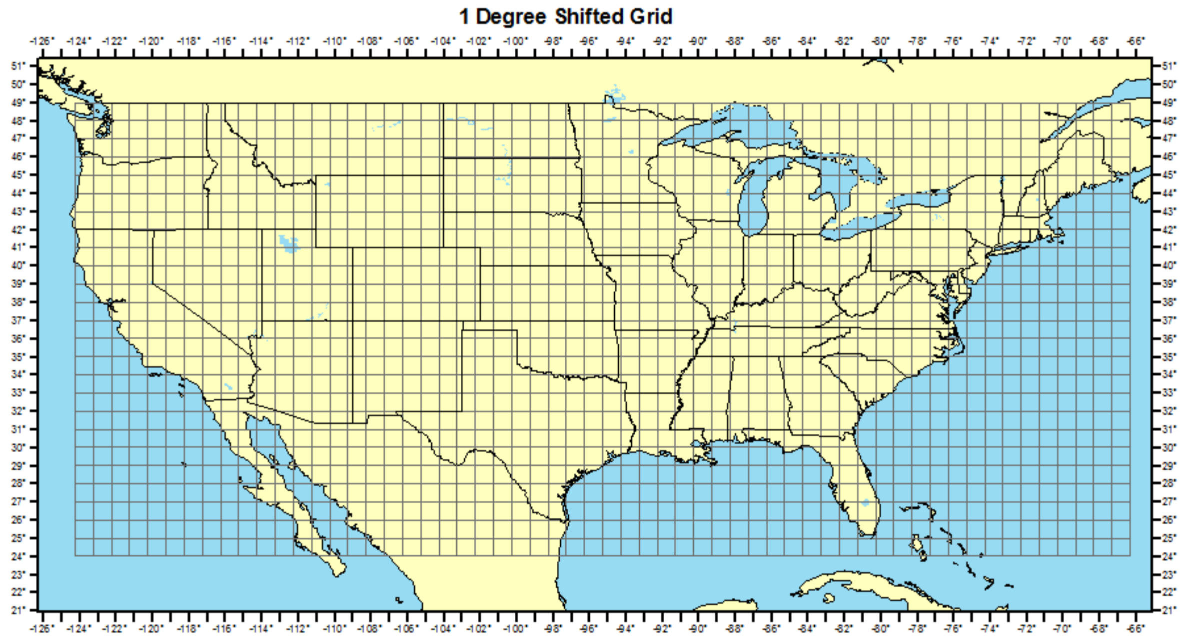

Figure 8-4. 1° Shifted Grid Used for Map Development

The return-period-interpolated wind speeds are mapped to each grid cell according to region membership. Figure 8-5 shows example wind speed grids for the 40,000 SF (3716.1 m^2) target and return periods of 3,000, 10,000, 100,000 and 10,000,000 years.

The next step involved spatial smoothing of the grid wind speeds to reflect the epistemic uncertainties in the region boundary locations. We used a 5x5 cell grid smoothing approach. This smoothing range includes a one-cell uncertainty range due to a possible ½° shift in cell center from a shifted 1° grid. In addition, we computed the regional mean epistemic boundary uncertainty range of 3 cells (about 180 miles (290 km)) from Section 2.4. We included an additional 1 cell smoothing width uncertainty to reflect non-modeled uncertainties as an epistemic adjustment. Combining 1 + 3 + 1 produces a 5-cell width range for spatial smoothing. The two-way 5 x 5 Gaussian-smoothing grid is shown in Figure 8-6. The two-way smoothing weights range for 0.0099 in the outer corner cells to 0.1031 in the center cell and sum to one over all 25 cells.

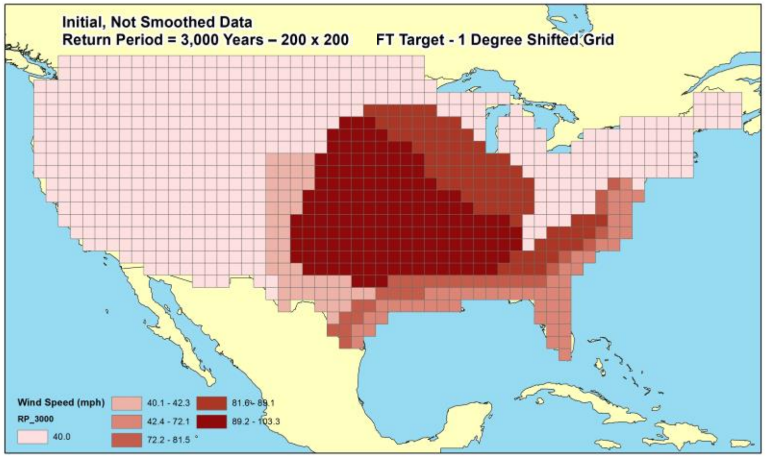

a. 3,000 Year Return Period

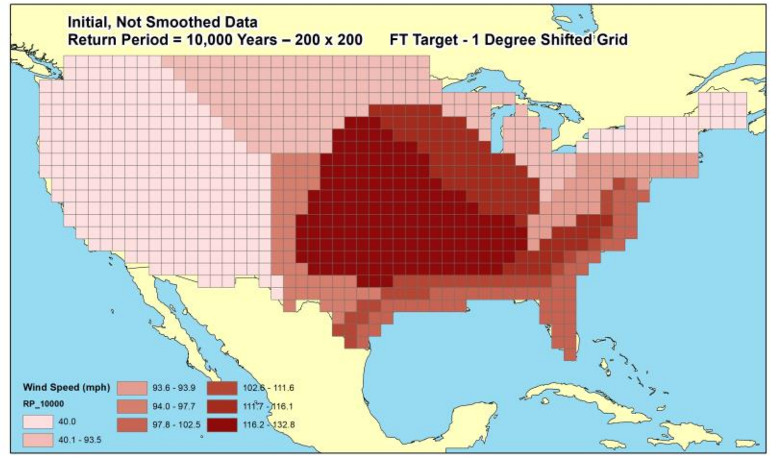

b. 10,000 Year Return Period

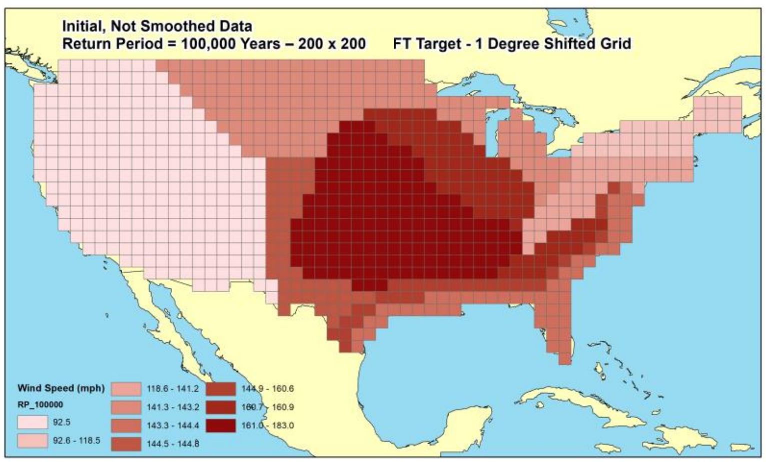

c. 100,000 Year Return Period

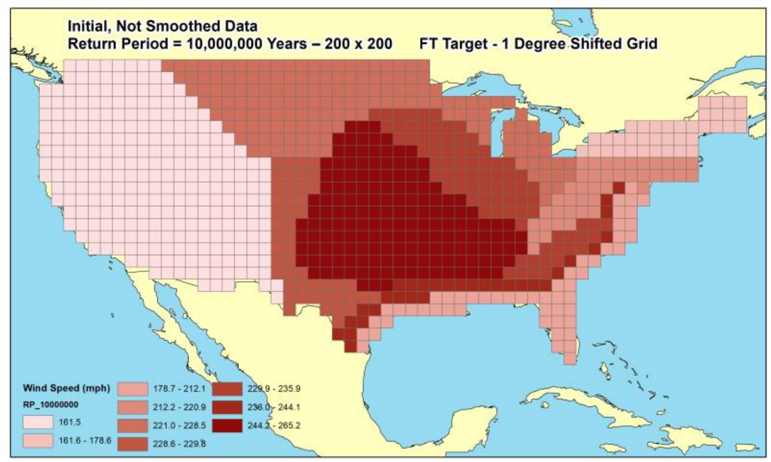

d. 10,000,000 Year Return Period

Note: 1 ft = 0.3048 m; 1 mph = 0.44704 m/s

Figure 8-5. Non-Smoothed Wind Grids for 4 Return Periods

0.0099	0.0239	0.0320	0.0239	0.0099
0.0239	0.0575	0.0770	0.0575	0.0239
0.0320	0.0770	0.1031	0.0770	0.0320
0.0239	0.0575	0.0770	0.0575	0.0239
0.0099	0.0239	0.0320	0.0239	0.0099

Figure 8-6. Regional Boundary Uncertainty Gaussian 5 x 5 Cell Smoothing Weights

In the application of the Gaussian smoothing to the wind speed grids illustrated in Figure 8-5, we used the following process to reduce the amount of smoothing toward high wind speed cells from low wind speed cells:

1. The original hazard curve grid wind speeds is denoted as Set A.
2. We smooth Set A with Gaussian weights to produce Set B.
3. On a cell-by-cell basis:
    a. Set C is determined by:
        i. Set C = Set B if the cell wind speeds are less than Set A.
        ii. Otherwise, Set C = Set A.
    b. Average Set B and Set C to create the cell wind speeds for Kriging.

These steps produce ½ of the smoothing for cells whose values are reduced by Gaussian smoothing. For example, this approach reduces the spatial extent of the weakening within Region 407.

The results of the wind speed grid smoothing process are illustrated in Figure 8-7. This figure illustrates that the smoothing steps were an important part of the spatial modeling of broad tornado regions. The Gaussian smoothing aided in the production of maps that could handle “sharp” convergences of multiple regions and important physiographic features.

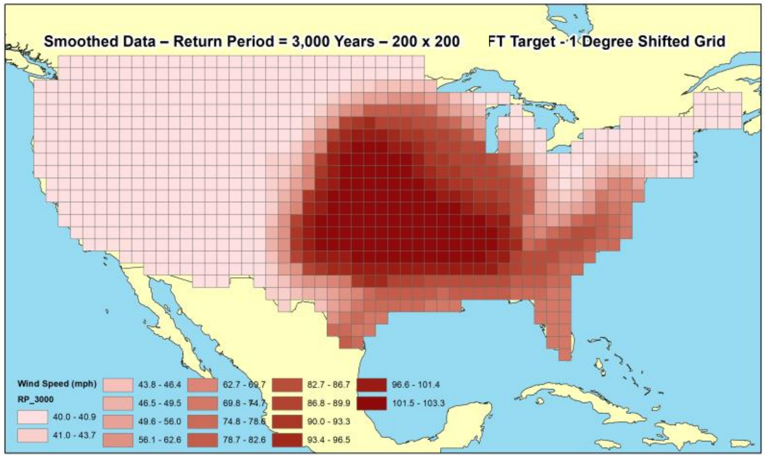

a. 3,000 Year Return Period

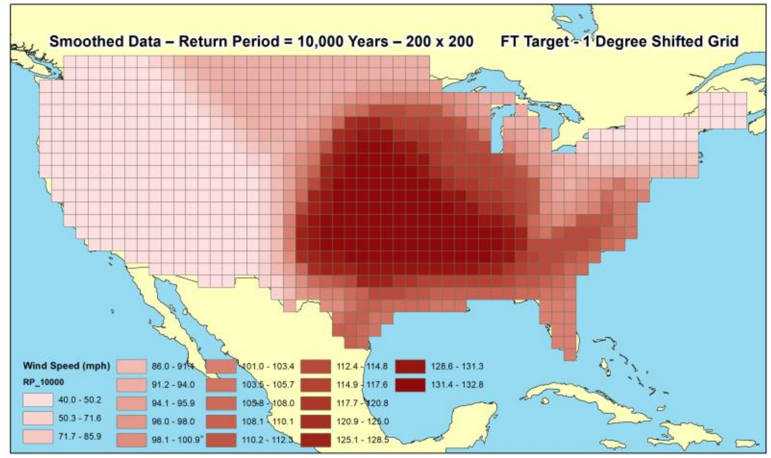

b. 10,000 Year Return Period

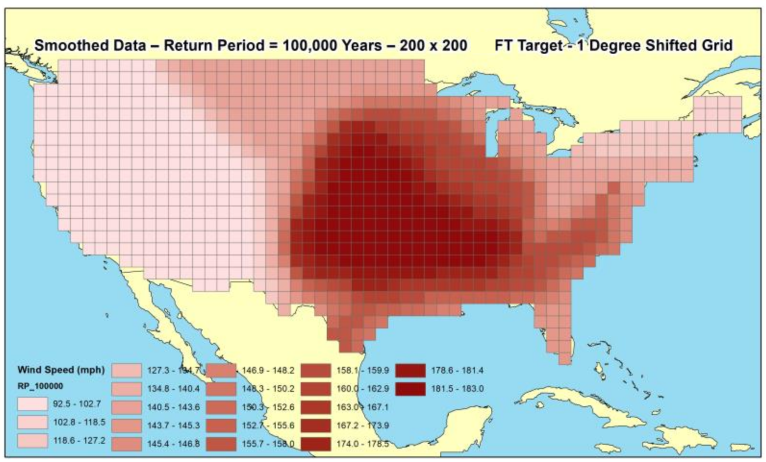

c. 100,000 Year Return Period

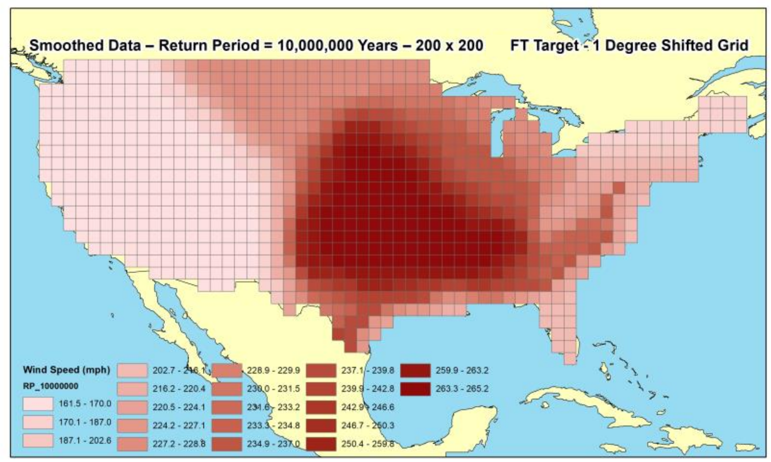

d. 10,000,000 Year Return Period

Note: 1 ft = 0.3048 m; 1 mph = 0.44704 m/s

Figure 8-7. Smoothed Wind Maps for 4 Return Periods

8.4. Tornado Wind Speed Maps

Using the wind speed grids previously described, the wind speed maps were produced in ArcMap 10.8 (ESRI 2019a) by creating wind speed rasters and then deriving wind speed contours from those rasters. The Kriging tool in the ArcGIS Spatial Analyst Toolbox (ESRI 2019a) was used to create wind speed raster surfaces from the grid points, for each combination of effective area and return period. The default method of ordinary kriging with a spherical semivariogram model was employed. The kriging configurations, namely cell size and search radius, were set as the default values in the tool (as a default, the output "cell size is calculated from the shorter of the width or height of the extent divided by 250" (ESRI 2019b)). The search radius was set as "variable," with a search range of the nearest 12 points from the sample location.

Contours were created at 10 mph (4.5 m/s) intervals using the Contour tool in the ArcGIS Spatial Analyst Toolbox. Inner and outer contours were also added for the nearest single mph value, to capture the maximum and minimum values and aid in interpolation for geographic location and target size. Contours with a value of 40 mph (the lower bound of the wind speed manually assigned to invalid grids in the modeling phase) were all deleted, along with irregularities like extremely small contour rings or pieces. The contours were then smoothed to remove minor 'wiggles' related to the selected grid size. This was accomplished using the ESRI Smooth Line tool and Polynomial Approximation with Exponential Kernel (PAEK) method in the ArcGIS Cartography Toolbox (ESRI 2019a). The Smoothing Tolerance parameter was set to 600 km. This value was selected to best smooth out the minor 'wiggles' without significantly impacting the overall shape and location of the contour lines. Lastly, many of the contours were selectively hand smoothed to further remove superfluous and uncertain detail introduced through the GIS process.

The final cartography of the maps is consistent with that used in the ASCE 7 Standard, and was informed by feedback from the ASCE 7-22 Wind Load Subcommittee. In South Texas where the wind speeds in the narrow strip of Region 6a are greater than those in surrounding regions (3 and 6b, see Figure 8-3), this sometimes resulted in a small plateau of greater speeds, and sometimes in a local maximum value. In the latter case, this was represented as a point value instead of a contour, consistent with the treatment of local maxima and minima in ASCE 7-16 and later editions for maps of nontornadic wind speeds.

Table 8-1 summarizes the tornado wind speed maps by return period and target size that have non-zero tornado wind speeds. The complete set of the 51 non-zero maps ordered by target size, is given in Appendix G. The targets are modeled as square targets oriented with global NS-EW orientations. Orientation is not important for square targets in terms of the RWS calculations.

Table 8-1. Count of Return Periods and Target Sizes with Non-Zero Tornado Wind Speeds

Target Area (SF)	Tornado Return Period (RP) (years)							
	RP300	RP700	RP1700	RP3000	RP10,000	RP100,000	RP1,000,000	RP10,000,000
Point			1	2	3	4	5	6
2,000			7	8	9	10	11	12
10,000			13	14	15	16	17	18
40,000			19	20	21	22	23	24
100,000			25	26	27	28	29	30
250,000			31	32	33	34	35	36
1,000,000		37	38	39	40	41	42	43
4,000,000	44	45	46	47	48	49	50	51

Note: 1 SF = 0.09290304 m^2

Figure 8-8 through Figure 8-16 present 6 of the 51 maps in Appendix G. These include point, 40,000 SF (3716.1 m^2) and 4,000,000 SF (371612.2 m^2) targets for 3,000, 100,000, and 10,000,000 year return periods. The point and 4,000,000 SF (371612.2 m^2) targets bound the sizes analyzed. The 40,000 SF (3716.1 m^2) target is representative of a medium size (200 ft x 200 ft) (61 m x 61 m) commercial building. All the maps begin at 50 mph (22 m/s).

Figure 8-8 through Figure 8-16 show significant wind speed sensitivity to target size. For the same return period, the wind speed differences exceed 40 mph (18 m/s) for a point vs. a 4,000,000 SF (371612.2 m^2) target. These wind speed differences reduce with increasing return period and are typically about 30 mph (13 m/s) for a 10,000,000 year RP.

Discussion Regarding Map Contour Locations. There is considerable spatial uncertainty in the process of mapping tornado wind speeds for broad tornado regions of similar climatology. One issue regards contouring in the vicinity of significant physiographic structures such as the western and eastern US mountain systems. In these regions, there may be sharp transitions in tornado risk, as indicated by the densities of the reported tornadoes (for example see Figure 8-2). Our approach was to apply regional boundary uncertainty smoothing, reflective of broad regional mapping with no attempt at micro-level mapping of tornado sub-regions over much smaller areas. Thus, the contours in these transition regions provide the mechanism to average the tornado wind speed transition over hundreds of miles. The exact location of a contour, in terms of the presence of (possible) dramatic physiographic features in rugged terrain, is meaningful only in the context of a transitioning tornado risk from one broad region to another.

In the same fashion, the map contours near large bodies of water have a similar limitation. Since the smoothing approach was not dynamically adapted to the presence of these physiographic features, the contours should be viewed as a spatially reasonable wind speed transition between regions. For example, the smoothing did not produce contours parallel to the Atlantic or Gulf coast for many of the return periods or target sizes. Another illustration is that the results for higher return period maps may show a contour across central Florida (see the 170 mph (76.0 m/s) contour in Figure 8-13, for example). This contour is the result of the transition to the grid wind speed of 170 mph (76.0 m/s) for Region 609. Its exact contour location is a Kriging result of the smoothing process.

The smoothing approach, described in Section 8.3, attempts to limit the smoothing towards regions with higher tornado risk by averaging Gaussian smoothing and no smoothing results.

For example, in Region 407 there is an inner contour with a wind speed that reflects the region's hazard curve wind speed (95 mph (42.5 m/s) in Figure 8-8). This value matches the 95 mph (42.5 m/s) (±1 mph (0.45 m/s) due to round off) value in

Table 7-3 for this region, target size, and return period. We debated several ways to show this wind speed and decided to be consistent with the Kriging process by developing a new contour and locating it according to its ArcGIS Kriging-produced location.[126]

Target Size vs. Tornado Path Width Graphic. Figure 8-17 graphically shows the scale differences area for the range of target sizes. Reasonably-sized large, moderate, and small tornado core widths are also shown. One can visualize how target and tornado core sizes significantly impact the frequency of tornado hits on a target. The illustrated tornado widths cover a reasonable range of tornado sizes, but do not include the largest or smallest possible core widths.

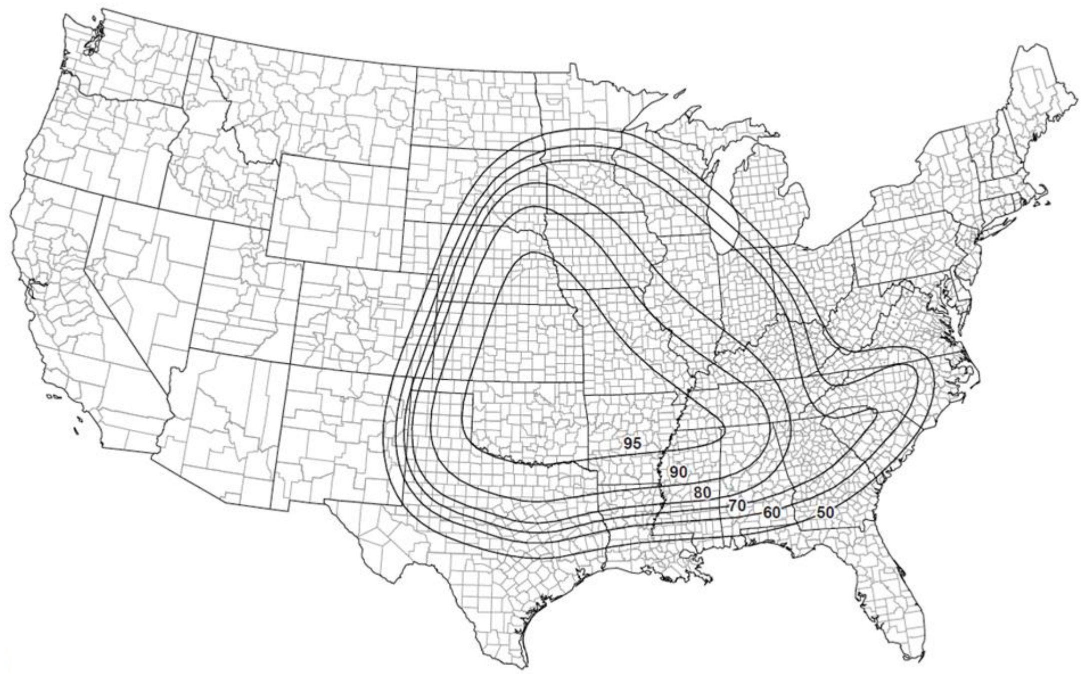

Note: 1 mph = 0.44704 m/s

Figure 8-8. 3,000 Year RP Map Design Tornado Wind Speeds (mph) for Point Targets

[126] For example, we also considered an approach that avoids the interior weakening from the Gaussian smoothing by showing the Table 7-3 value of 95 mph (42.5 m/s) on the 90 mph (40.2 m/s) contour. This approach, however, would have broken the 10mph (4.5 m/s) wind speed mapping interval and would have required an inserted contour between the new 95 mph (42.5 m/s) contour and the 80 mph (36 m/s) contour. Another idea was to create the 95 mph (42.5 m/s) very close to the 90 mph (40.2 m/s) contour, but again, a modification that is not true to the contour creation process involving rasters made by Kriging. In summary, the inner-most contour location in Region 407 is a result of the decision to locate it in its exact Kriged position. This inner contour is therefore the result of this decision and it cannot be argued that this smaller area has different tornado risk that areas just to the outside of the inner-most contour.

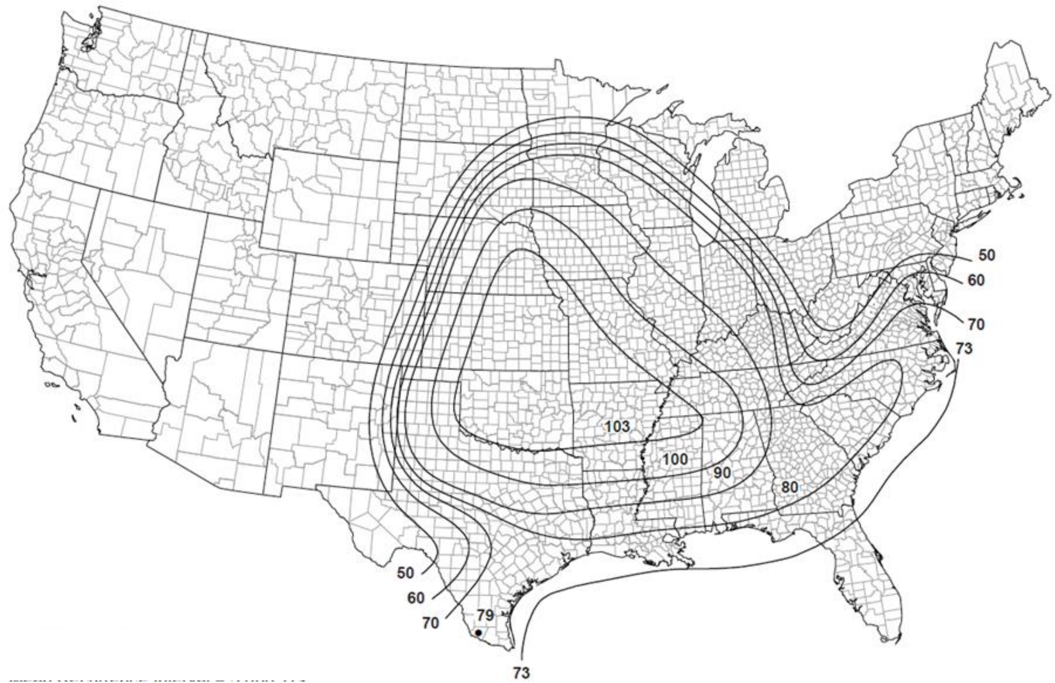

Note: 1 mph = 0.44704 m/s

Figure 8-9. 3,000 Year RP Map Design Tornado Wind Speeds (mph) for 40,000 SF (3716.1 m^2) Targets

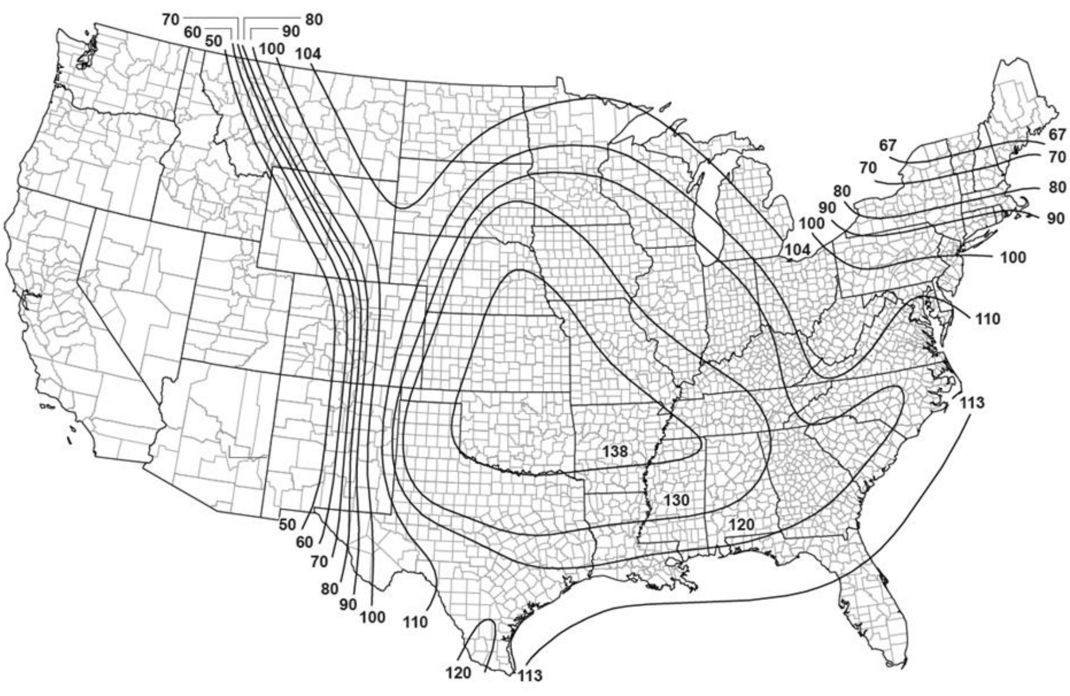

Note: 1 mph = 0.44704 m/s

Figure 8-10. 3,000 Year RP Map Design Tornado Wind Speeds (mph) for 4,000,000 SF (371612.2 m^2) Targets

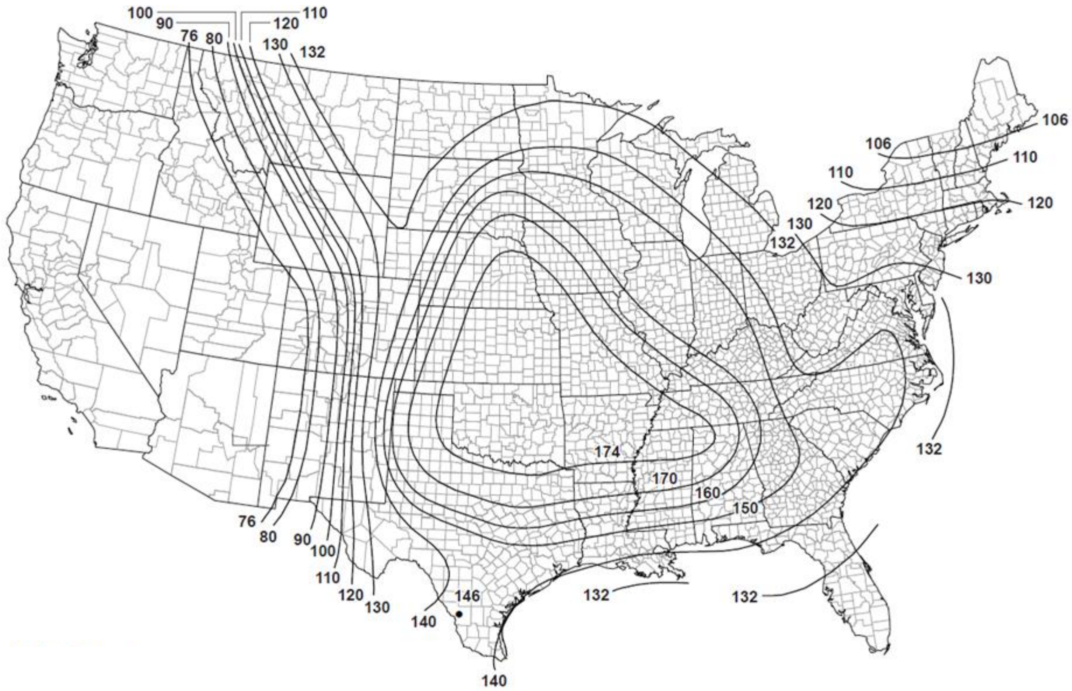

Note: 1 mph = 0.44704 m/s

Figure 8-11. 100,000 Year RP Map Design Tornado Wind Speeds (mph) for Point Targets

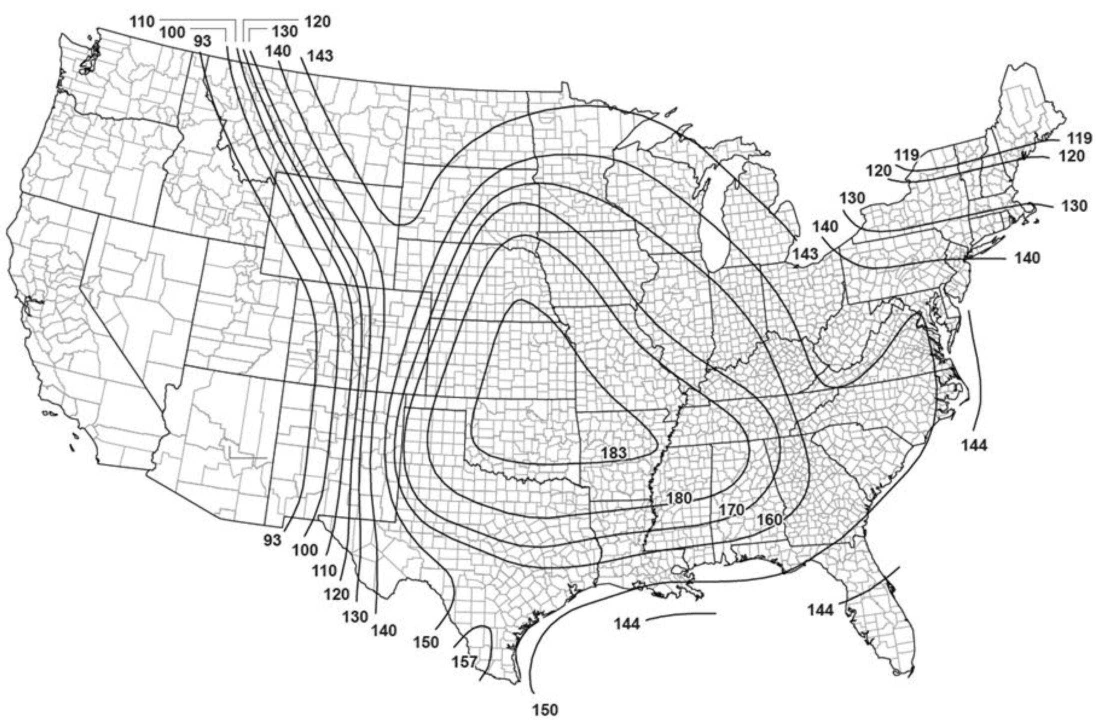

Note: 1 mph = 0.44704 m/s

Figure 8-12. 100,000 Year RP Map Design Tornado Wind Speeds (mph) for 40,000 SF (3716.1 m^2) Targets

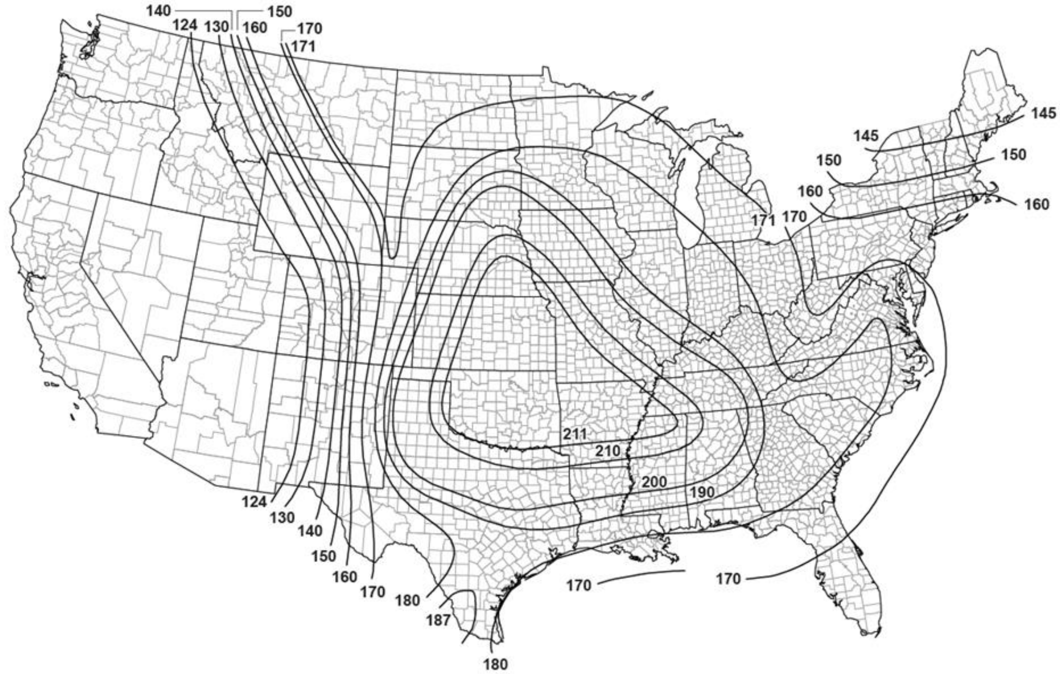

Note: 1 mph = 0.44704 m/s

Figure 8-13. 100,000 Year RP Map Design Tornado Wind Speeds (mph) for 4,000,000 SF (371612.2 m^2) Targets

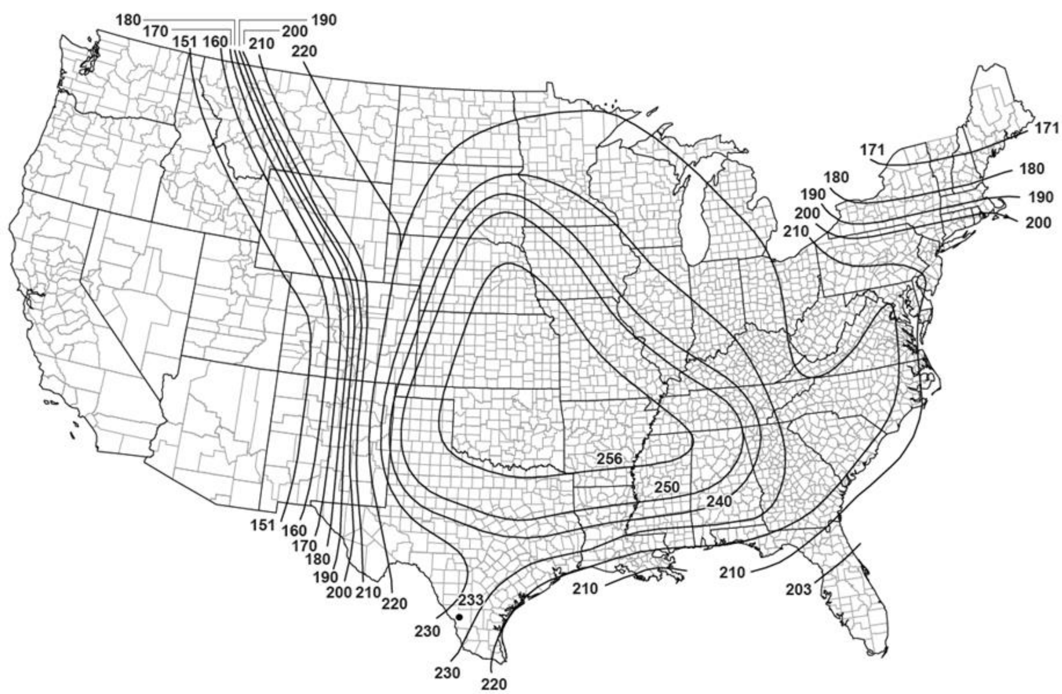

Note: 1 mph = 0.44704 m/s

Figure 8-14. 10,000,000 Year RP Map Design Tornado Wind Speeds (mph) for Point Targets

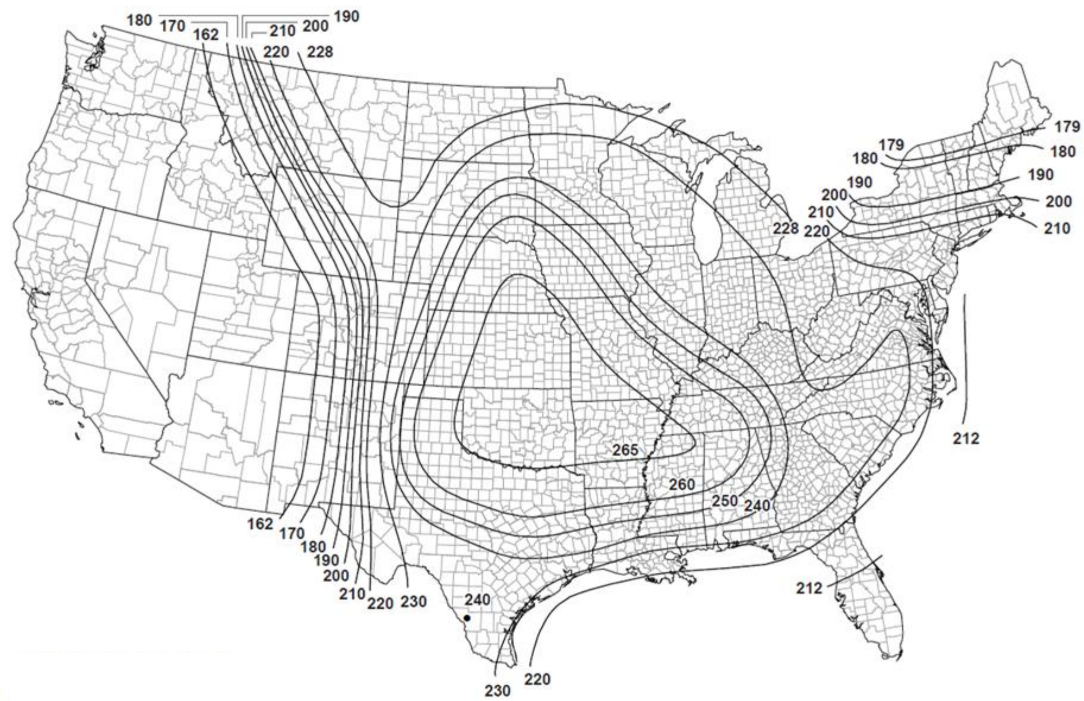

Note: 1 mph = 0.44704 m/s

Figure 8-15. 10,000,000 Year RP Map Design Tornado Wind Speeds (mph) for 40,000 SF (3716.1 m²) Targets

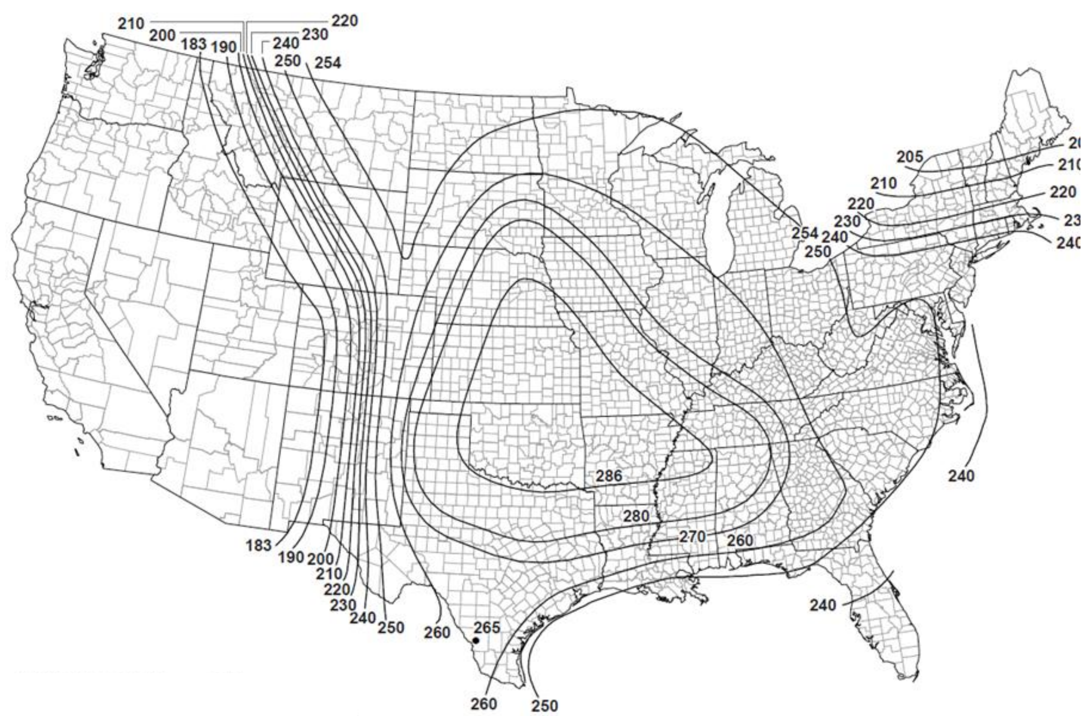

Note: 1 mph = 0.44704 m/s

Figure 8-16. 10,000,000 Year RP Map Design Tornado Wind Speeds (mph) for 4,000,000 SF (371612.2 m²) Targets

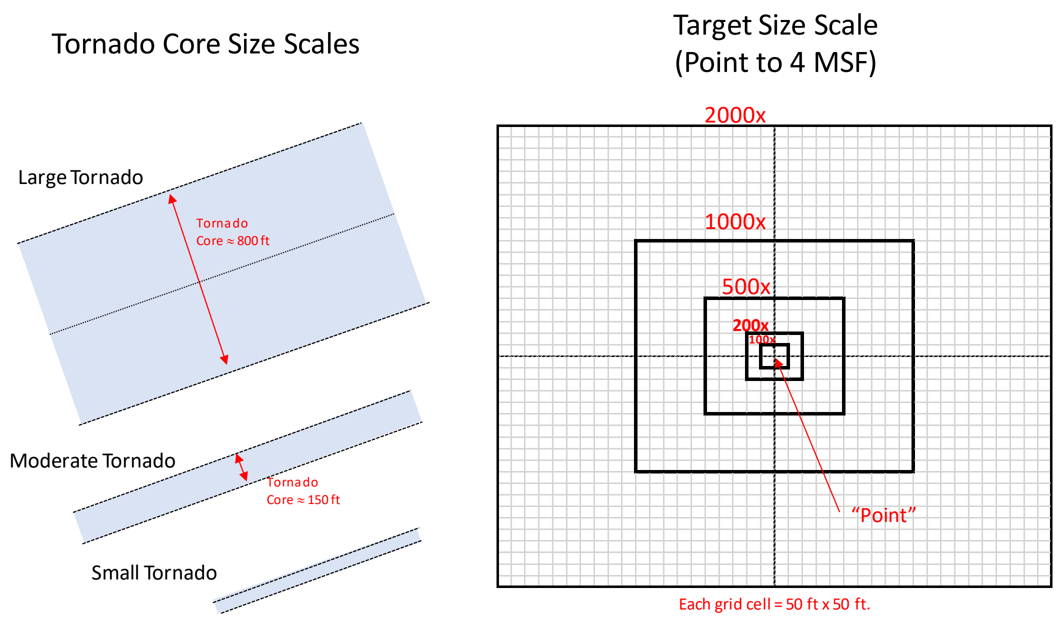

Note: 1 ft = 0.3048 m; 1 SF = 0.09290304 m^2

Figure 8-17. Illustration of Scales Involved in Tornado-Target Interactions

9. Summary

The first-ever engineering-derived tornado wind speed maps have been produced for the contiguous United States. This work follows from recommendations in the NIST technical investigation of the May 22, 2011 Joplin, MO, tornado (Kuligowski et al., 2014). The probabilistic methodology considered both epistemic and aleatory uncertainties. The following paragraphs summarize the analysis methods and some of the high-level results.

Tornado Data. We used the NOAA/NWS Storm Prediction Center (SPC) database to develop climatology metrics, analyze reporting trends, develop occurrence rates, and model EF-Scale distributions. As part of this process, we also investigated the Damage Assessment Tool (DAT) database (NOAA, 2016b), which was implemented in 2007. These analyses helped guide the development of the final methodology and data eras used in various components of research, including: the "modern era" (1995 – 2016) for tornado occurrence rate analysis and the EF-Scale era (2007-2016) for tornado wind speed estimation.

Augmented Database. An augmented database was developed that includes some minor corrections to the SPC data and adds additional fields of data, (1) tornado path direction; (2) the NCEI Weather Forecast Office (WFO) that produced the rating; (3) the NCEI source of the tornado rating; and (4) the NCEI tornado ending date and time (NCEI, 2014). The tornado data analyses were made with the augmented database.

Broad Climatology Regions. The goal of the climatology analysis was to develop broad tornado regions under the assumption of uniform tornado climatology within each region. This work was performed using an empirical analysis of the augmented SPC database for the Years 1950-2016. We developed tornado metrics, such as tornado days per year, occurrence rates, point probability, and several physiographic metrics. This analysis produced 6 broad tornado regions, considering a multivariate statistical analysis of the tornado risk metrics. Several sub-regions were also identified resulting in a total of 9 final tornado regions. We did not attempt to produce maps that reflect smaller sub-region scales of tornado wind speed risk. Epistemic uncertainties in region boundary locations, considering spatial variations from multiple analyses, were processed using a Gaussian smoothing approach at the map grid level.

Population Bias Analysis of Reported Tornado Occurrences. We used US 2010 and 2010 census data at the census tract level to estimate population bias in tornado reporting. We coupled the census with data with Hazus data on building inventory to produce building density data. These data were combined with the US tornado database for the years 1995-2016. We found that fractional counting of tornado lengths and tornado point probability metrics, conditioned on building density at the census tract level, were suitable for estimating population bias. There are considerable uncertainties in population bias estimates due to the numerous assumptions required. We propagated epistemic uncertainties with simulations that considered the annual variability in occurrences, the population bias analysis method, and trend analysis of the modern era data. The resulting population bias estimates of tornado under-reporting varied from a few percent to several hundred percent on a regional basis.

EF Scale Distribution. We also conditioned EF-Scale intensity data on a census-tract-based building density analysis. This approach overcomes several limitations of using raw tornado counts, including: EF0 reporting bias, which includes unknown intensities rated as EF0 tornadoes; EF-limited DIs, like barns and trees; and more accurate EF ratings due to improved chances of the maximum wind speeds in the tornado hitting multiple buildings. With this method, we found in most regions that the nominal frequencies of moderate and severe tornadoes are underestimated and EF0s are overestimated. We produced derived mean EF distributions from simulations that reflected Weibull fitting errors, tornado sample size, and estimates of tornado rating accuracy based on building density threshold.

Tornado Wind Field Model. A tornado wind field model was used to simulate loads on structures for wind speed estimation and to produce wind speed swaths for wind speed frequency analysis. The 3-D probabilistic wind field model is a single cell model that includes models for: path length intensity variation; radius to maximum winds; radial inflow parameter dependent on swirl ratio; translational speed; path length and width statistics; path edge wind speeds; variable path width; and damage swath modeling. The model is based on a single-cell vortex with probabilistic parameters that allow for simulations of different tornado sizes and parameters within each EF-Scale intensity. A uniform vertical profile of horizontal winds was used for the final load modeling and wind speed hazard curve development.

Engineering-Derived EF*Tornado Wind Speeds. We used a framework to develop engineering-derived wind speeds that is consistent to the load and resistance modeling process for engineering design. The wind speed estimation approach tackled a main technical challenge in the quantification of wind speeds from observed damage, including: how to model and analyze the separate contributions of the variability in tornado wind characteristics, the variability in structure position within the tornado path, and the variability in loads and structural resistances? The analysis framework uses Bayesian conditional probability concepts to decipher these variability contributions and produce consistent estimates of wind speeds given observed damage. Through application of this method to the training, protocols, and context of the Enhanced Fujita (EF) Scale system, we developed wind speed distributions for the EF-Scale Damage Indicator (DI) denoted as One- or Two-Family Residence (FR12). FR12 are one of the most common DIs used in wind speed estimation in the EF-Scale and essentially all severe tornadoes (EF4-5) have been rated based on observations of damage to this DI. The derived wind speed distributions are based on 3D progressive failure probabilistic simulations of 44 house models. The developed EF* wind speed probability distributions are much broader that the tight, deterministic EF-Scale wind speeds and the EF3-5 distributions have long right-hand tails. We found that the judgment-based EF-Scale wind speeds (TTU, 2006) were good estimates for houses with weak connections, but significantly under-estimates the wind speeds for houses with modest and strong construction characteristics, which exist in some counties, states and regions.

Reference Wind Speed. For the tornado hazard, we defined the reference wind speed (RWS) as the maximum 10 m (33 ft) above ground horizontal wind speed produced within the target plan area by the translating tornado. The RWS was computed in each simulation by analyzing the wind speeds over a grid within the target plan area, stepping the tornado along its path, and saving the maximum wind speed produced as the RWS. Due to the limited state of knowledge with respect to terrain effects on tornado structure and wind speeds near the ground, RWS is defined independently of terrain. Similarly, due to the limited state of knowledge regarding tornado gust characteristics, we assume that the wind speeds are associated with the nominal 3 second gusts used in wind load computations (ASCE, 2016).

As with non-tornadic winds, the RWS is the free-field wind speed ignoring presence of the target.

Target Size-Dependent Tornado Wind Speed Hazard Curves. Tornado wind speed hazard curves provide the basis for interpolating the wind speed associated with a return period for a given target size. Tornado wind speed hazard curves were developed for each of the 9 region-sub-regions for 8 target sizes. Since tornadoes often have narrow widths and even smaller areas with the maximum wind speeds, tornado wind speed risk depends on the target size. We considered target sizes ranging from a geometrical point to 4 million square feet (371612.2 m^2). The effect of target size on the hazard curve depends on the region and the return period. For a given return period, wind speed differences from a point to a very large target size range from about 10 mph (4.5 m/s) to about 50 mph (22 m/s). The hazard curves were developed for square-shaped targets. Minor sensitivities were noted for oblong targets with aspect ratios less than about 10. These results were not sensitive to target azimuthal orientation. The hazard curve results do not apply to line targets with long lengths, such as transmission line systems. Spatially-distributed targets also require separate computations and are not addressed in this report.

Wind Speed Maps. The maps were developed on a broad scale using the 9 tornado climatology regions. The following table (similar to

Table 8-1) summarizes the 51 maps developed by return period and target size. The maps have broad similarity to previous tornado maps and closely reflect the empirical database with regard to the spatial variabilities in occurrence rates and tornado intensity distributions. Appendix G provides a complete set of maps.

Target Area (SF)	Non-Zero Tornado Wind Speed Maps by Target Area and Return Period (RP) (years)							
	RP300	RP700	RP1700	RP3000	RP10,000	RP100,000	RP1,000,000	RP10,000,000
Point								
2,000								
10,000								
40,000								
100,000								
250,000								
1,000,000								
4,000,000								

Note: 1 SF = 0.09290304 m^2

Epistemic Uncertainties. Numerous judgments and assumptions were made to produce these maps. We modeled epistemic uncertainties in 9 areas of the work. The results do not reflect a two-loop simulation with epistemic uncertainties in the outer loop, but rather a combination of simulation sampling from epistemic and aleatory distributions coupled with derived mean inputs for select variables.

The engineering-derived wind speeds have considerable uncertainties. These uncertainties are judged to be modest (say ± 10 mph (4.5 m/s) for 3,000 year RPs), but are likely on the order of ± 30 mph (13 m/s) for 10 million year return periods.

There is also considerable spatial uncertainty in the process of mapping tornado wind speeds for broad tornado regions. Our approach was to apply regional boundary uncertainty smoothing, reflective of broad regional mapping with no attempt at micro-level mapping of tornado sub-regions over much smaller areas. Thus, the contours in these transition regions provide the mechanism to average the tornado wind speed transition over hundreds of miles. The exact location of a contour, in terms of the presence of significant physiographic features, such as mountain systems, very large lakes, and/or oceans, is meaningful only in the context of a transitioning tornado risk from one broad region to another.

The modeling approach used throughout was “best-estimate” rather than “conservative-based.” This approach follows the intent of ASCE 7 wind speed maps for other wind hazards. The use of best estimate modeling allows for use of load and resistance factors in design in a logical way to meet appropriate structural reliability goals.

10. References

Abbey, R. F. (1975). “Establishment of Maximum Regional Tornado Criteria for Nuclear Power Plant,” presented at the October 21-23, 1975, American Meteorological Society Ninth Conference on Severe Local Storms, held at Norman, OK.

Abbey, R. F., and Fujita, T. T. (1975). “Use of Tornado Path Lengths and Gradations of Damage to Assess Tornado Intensity Probabilities. Proc., 9th Conference on Severe Local Storms, Norman, OK, American Meteorological Society, 286-293.

Agee, E. M., Church, C. R., Morris, C., and Snow, J. T., (1975). “Some Synoptic Aspects and Dynamic Features of Vortices Associated with the Tornado Outbreak of 3 April 1974,” *Monthly Weather Review*, 103, 318-333.

Alexander, C. R. and Wurman, J. (2008). “Updated Mobile Radar Climatology of Supercell Tornado Structures and Dynamics,” 24th Conference on Severe Local Storms, Savannah, GA, Oct. 27-31.

An, D., Choi, J-H. and Kim, N. H. (2012). “Identification of Correlated Damage Parameters under Noise and Bias Using Bayesian Inference,” Structural Health Monitoring, Vol. 11, No. 3, p. 293-303.

Anderson-Spreher, R., (1994). “Model Comparison and R2,” American Statistics, 48, 113-117.

Anderson, Christopher J., Wikle, Christopher K., Zhou, Qin, and Royle, J. Andrew (2007). “Population Influences on Tornado Reports in the United States,” *Weather and Forecasting*, Vol. 22, pp. 571-579, June.

Ang, A.H-S. and Tang, W.H. (1984). *Probability Concepts in Engineering Planning and Design, Volume II: Decision, Risk, and Reliability*, John Wiley & Sons, New York, NY.

ANSI/AWC-SDPWS (2015). *Special Design Provisions For Wind and Seismic*. American Wood Council, Leesburg, VA.

APA (1997). *Plywood design specification*, The Engineered Wood Association, Tacoma, WA.

Applied Research Associates (2000-2019), *HurLoss*, Florida Commission on Hurricane Loss Projection Methodology, 1999-2014 Standard Submissions (Annual and/or Bi-annual), Tallahassee, FL.

Applied Research Associates (2003). “Analysis of Loss Reduction Benefits of Improvements to International Residential Code for Texas Tier I Locations,” Prepared for Institute for Business and Home Safety, Tampa, FL, (February).

Applied Research Associates (2010). “Insurance and Rehab Mitigation Study for New Orleans,” Prepared for New Orleans Redevelopment Authority, New Orleans, LA, (July).

Applied Research Associates, (2015). “FCALC Computer Code, Volume 1 – User Manual, Ver. 2.0” Applied Research Associates, Inc., Raleigh, NC, January.

ASCE, (2000). *Minimum Design Loads for Buildings and Other Structures, ANSI/ASCE 7-98,* American Society of Civil Engineers, Reston, VA, January.

ASCE, (2010). *Minimum Design Loads for Buildings and Other Structures*. Second Edition, American Society of Civil Engineers, Reston, VA.

ASCE (2013). “Minimum Design Loads for Buildings and Other Structures,” American Society of Civil Engineers, ASCE/SEI 7-2010, American Society of Civil Engineers, Reston, VA (March).

ASCE (2016). “ASCE 7-16, Minimal Design Loads for Buildings and Other Structures,” American Society of Civil Engineers, ASCE/SEI 7-2016, American Society of Civil Engineers, Reston, VA.

Asiz, A., Chui, Y. H., Smith, I., and Zhou, L. (2009). Development of Advanced System Design Procedures for the Canadian Wood Design Standard. Final Report. Ottawa: Natural Resources Canada, 107.

ASME/ANS (2009). “Standard for Level 1/Large Early Release Frequency Probabilistic Risk Assessment for Nuclear Power Plant Applications,” Addenda to ASME/ANS RA-Sa-2009, American Society of Mechanical Engineers, New York, New York, February.

ASME/ANS (2013). “Standard for Level 1/Large Early Release Frequency Probabilistic Risk Assessment for Nuclear Power Plant Applications,” Addenda to ASME/ANS RA-S-2008, American Society of Mechanical Engineers, New York, New York, September.

ASTM-D1761-12 (2012). *Standard Test Methods for Mechanical Fasteners in wood*, ASTM International, West Conshohocken, PA.

Atkins, N.T., Butler, K.M., Flynn, K.R., and Wakimoto, R.M. (2014). “An Integrated Damage, Visual, and Radar Analysis of the 2013 Moore, Oklahoma, EF5 Tornado,” *Bulletin of the American Meteorological Society*, Vol. 95/10, pp. 1549–1561.

Baker, G. L. and Church, C. R. (1979). “Measurements of Core Radii and Peak Velocities in Modeled Atmospheric Vortices.” *Journal of Atmospheric Sciences*. Vol 36, pp 2413-2424.

Baker, C. J. and Sterling, M. (2017). “Modeling Wind Field and Debris Flight in Tornadoes,” *Journal of Wind Engineering and Industrial Aerodynamics*, Vol. 168, pp. 312-321.

Banik, S.S., Hong, H.P., and Kopp, G.A. (2007). “Tornado Hazard Assessment for Southern Ontario.” *Canadian Journal of Civil Engineering*, Vol. 34. No. 7. pp. 830-842.

Beebe, R.C., et al. (1978), “Some Synoptic Aspects and Dynamic Features of Vortices Associated with the Tornado Outbreak of April 3, 1974,” *Monthly Weather Review,* Vol. 103, pp. 318-333, April.

Bech, J., Gaya, M., Aran, M., Figuerola, F., Amaro, J., and Arus, J. (2009). “Tornado Damage Analysis of a Forest Area using Site Survey Observations, Radar Data and a Simple Analytical Vortex Model,” *Atmospheric Researc*h, Vol. 93, pp. 118-130.

Beck, J.L. and Au, S.K. (2002). “Bayesian Updating of Structural Models and Reliability using Markov Chain Monte Carlo Simulation,” ASCE, *Journal of Engineering Mechanics,* Vol. 10.

Beck, V. and Dotzek, N. (2010). “Reconstruction of Near-Surface Tornado Wind Fields from Forest Damage,” *Journal of Applied Meteorology and Climatology*, Volume 49, pp. 1517–1537.

Bell, Jeff. (2015). “A Simple and Pragmatic Approximation to the Normal Cumulative Probability Distribution,” available at SSRN: http://ssrn.com/abstract=2579686 or http://dx.doi.org/10.2139/ssrn.2579686.

Benjamin, J.R., and Cornell, C. A. (1970). *Probability, Statistics, and Decision for Civil Engineers*, McGraw-Hill, New York, NY.

Berliner, L. M., Royle, J. A., Wilke, C. K., and Milliff, R. F., (1998). “Bayesian Methods in the Atmospheric Sciences,” *Bayesian Statistics,* 6.

Blechman, J. B. (1975) “The Wisconsin Tornado Event of April 21, 1974: Observations and Theory of Secondary Vortices,” Preprints, *9th Conf. on Severe Local Storms*, Norman, OK, American Meteorologica Society, 344–349.

Bluestein, H., Ladue, J.G., Stein, H., Douglas, S. (1993). “Doppler Radar Wind Spectra of Supercell Tornadoes,” *Monthly Weather Review*, Vol. 121, pp. 2200-2221.

Bluestein, H. B., Lee, W., Bell, M., Weiss, C. C., & Pazmany, A. L. (2003). “Mobile Doppler Radar Observations of a Tornado in a Supercell near Bassett, Nebraska, on 5 June 1999. Part II: Tornado-Vortex Structure,” *Monthly Weather Review*, 131(12), 2968-2984.

Bluestein, H.B., French, M. M., Tanamachi, R. L., Frasier, S., Hardwaick, K., Junyent, F. and Pazmay, A. L. (2007). “Close-Range Observations of Tornadoes in Supercells Made with a Dual-Polarization, X-Band, Mobile Doppler Radar”, *Monthly Weather Review*, Vol. 135, pp. 1522-1543.

Bluestein, H. B. (2017). *Tornadoes and Their Parent Convective Storm*, Oxford Handbooks Online, Oxford University Press.

Bock, H.H. (1985). “On Some Significance Tests in Cluster Analysis,” *Journal of Classification*, Volume 2, pp. 77-108.

Bratley, P., Fox, B. L. and Schrage, L. E. (1983). *A Guide to Simulation*, Springer-Verlag New York, Inc. New York, NY.

Brooks, Harold E., Doswell III, Charles A., and Kay, Michael P., (2003). “Climatological Estimates of Local Daily Tornado Probability for the United States.” *Weather and Forecasting*, Vol. 18, pp. 626-640, August.

Brooks, H. E. (2004). “On the Relationship of Tornado Path Length and Width to Intensity,” *Weather and Forecasting*, Vol. 19, pp. 310-319.

Brown, R. A. and Wood, V. T. (2004). “Comparisons of Doppler Velocity Tornadic Vortex Signatures from Model Vortices,” 22nd Conference on Severe Local Storms, *American Meterological Society*, MA.

Burgess, D. W., Magsug, M. A., Wurman, J., Dowell, D. C., and Richardson, Y., (2002). “Radar Observations of the 3 May 1999 Oklahoma City Tornado,” *Weather and Forecasting*, Vol. 7.

Burgers, J. M. (1948). “A Mathematical Model Illustrating the Theory of Turbulence.” *Advances in Applied Mechanics*, 1, 171–199.

Canfield, L.R., Niu, S., and Liu, H., (1991). “Uplift Resistance of Various Rafter-Wall Connections,” *Forest Products Journal*, 41.

Caprolu, G., Girhammar, U.A., Kallsner, B. and Johnsson, H. (2012). "Tests on the Splitting Capacity of the Bottom Rail Due to Uplift in Partially Anchored Shear Wall," WCTE, Auckland, New Zealand, July.

Case, P.C. (1996). "Wind Loads on Low Buildings with 4:12 Gable Roofs," M.S. Thesis, University of Western Ontario, London, Ontario, Canada, May.

Cheng, V. Y. S. Arhonditsis, G. B., Sills, D. M. L., Auld, H., Shephard, M. W., Gough, W. A., and Klaassen, J. (2013). "Probability of Tornado Occurrence across Canada," *Journal of Climatology*, 26, 9415–9428.

Cheng., V. Y. S., Arhonditsis, G. B., Sills, D. M. L., Gough, W. A., Auld, H. (2015). "A Bayesian Modelling Framework for Tornado Occurrences in North America," *Nature Communications*, doi: 10.1038/ncomms7599, March.

Cherry, N.J. (1991). "Fixing Studies for MRTI Normal Weight Tiles" SBCCI Submission, Redland Technology Limited, New Technology & Product Development Centre, Horsham, West Sussex, England, December.

Church, C. R., Snow, J.T., Baker, G. L, and Agee, E.M. (1979). "Characteristics of Tornado-Like Vortices as a Function of Swirl Ratio: A Laboratory Investigation." *Journal of Atmospheric Sciences*, Vol. 36, pp 1755 – 1776.

Cook, N.J. (1990). *The Designer's Guide to Wind Loading of Building Structures: Part 2 Static Structures*, London, UK.

Coleman, T. A. and Dixon, P. G. (2014). "An Objective Analysis of Tornado Risk in the United States," *Weather and Forecasting*, Vol. 29, 366-376.

Court, A. (1970). "Tornado Incidence Maps," *ESS Technical Memorandum ERTLM-NSSL 49*, National Severe Storms Laboratory, Norman, OK.

Crawford, K. (2012). "Experimental and Analytical Trajectories of Simplified Debris Models in Tornado Winds." Master of Science Thesis. Iowa State University.

Cunningham, T. P. (1992). "Evaluation of Roof Sheathing Fastening Schedules for High Wind Uplift Pressures," ASCE Symposium on Hurricanes of 1992, Miami, FL, December.

Cunningham, T.P. (1993). "Roof Sheathing Fastening Schedules for Wind Uplift," APA Report T92-28, American Plywood Association, Tacoma, WA, March.

Davies-Jones, R. P. (1973). "The Dependence of Core Radius on Swirl Ratio in a Tornado Simulator." *Journal of the Atmospheric Sciences*, Vol. 30.

Davies-Jones, R. P., Trapp, R. J. and Bluestein, H. B. (2001). "Tornadoes and Tornadic Storms." *Meteorological Monographs*, Vol. 28, Chap. 5, pp. 167-221.

Davenport, A.G. (1961). "The Application of Statistical Concepts to the Wind Loading of Structures," *Proceedings Institute of Civil Engineers,* Volume 19, pp. 449-472.

Dean, A.R., and Imy, D.A., (2006). "A Look at the Tornado Report and Watch Climatology for the Continental United States from 1986-2005." *Preprints*, 23rd Conference on Severe Local Storms, St., Louis, MO.

Dessens, J. (1972). "Influence of Ground Roughness on Tornadoes: A Laboratory Simulation," *Journal of Applied Meteorolog*y. Vol. 11, pp. 72-75.

Ditlevsen, O. (1979). "Generalized Second Moment Reliability Index," *Journal of Structural Mechanics*, 7, 4, 435-451.

DOE (1985). "Natural Phenomena Hazards Modeling Project: Extreme Wind/Tornado Hazard Models for Department of Energy sites," Report prepared by Lawrence Livermore National Laboratory, Livermore, California.

Dolan, J.D., and Johnson, A.C. (1996). "Monotonic Tests of Long Shear Walls with Openings," *Report No. TE-1996-001*, Virginia Polytechnic Institute and State University, Blacksburg, Virginia.

Dolan, J.D., and Heine, C.P. (1997). "Monotonic Tests of Wood-frame Shear Walls with Various Openings and Base Restraint Configurations. *Report No. TE-1997-001,* Virginia Polytechnic Institute and State University, Blacksburg, Virginia.

Doswell, III, C.A and Burgess, D.W., (1988). "On Some Issues of United States Tornado Climatology" *Monthly Weather Review*, 116, pp. 495-501, February.

Dotzek, N., Grieser, J., and Brooks, H. E. (2003). "Statistical Modeling of Tornado Intensity Distributions," *Atmospheric Research*, 67-68, pp. 163-187.

Doudak, G., Smith, I., McClure, G., Mohammad, M., and Lepper, P. (2006). "Tests and Finite Element Models of Wood Light-frame Shear Walls with Openings," *Progress in Structural Engineering and Materials*, 8(4), 165-174.

Dun and Bradstreet (2006). *Business Population Report* Aggregated by Standard Industrial Classification (SIC) and Census Block.

Dunn W.L. and L.A. Twisdale, (1979). "A Synthesized Windfield Model for Tornado Missile Transport," *Journal of Nuclear Engineering and Design,* Vol. 52.

Drake, A.W. (1967). *Fundamentals of Applied Probability Theory*, McGraw Hill, New York.

Edwards, Roger (2003). "Rating Tornado Damage: An Exercise in Subjectivity," First Symposium on the F-Scale and Severe-Weather Damage Assessment, Long Beach, CA, February.

Edwards, R., and Brooks, J.R., (2010): "Possible Impacts of the Enhanced Fujita Scale on United States Tornado Data." *Preprints*, 25th Conf. Severe Local Storms, Denver, CO.

Edwards, R., LaDue, J. G., Ferree, J. T., Scharfenberg, K, Maier, C. and Coulbourne, W. L. (2013) "Tornado Intensity Estimation: Past, Present, and Future." *Bulletin of the American Meteorological Society*, 94, 641-653.

Ellingwood, B, Galambos, T.V., MacGregor, J.G. and Cornell, C.A. (1980). "Development of a Probability Based Load Criterion for American National Standard A58, Building Code Requirements for Minimum Design Loads in Buildings and Other Structures," National Bureau of Standards, Washington, D.C., June.

Elsner, James B., Michaels, Laura E., Scheitlin, Kelsey N., and Elsner, Ian J. (2013). "The Decreasing Population Bias in Tornado Reports across the Central Plains," *Weather, Climate, and Society*, Vol. 5, pp. 221-232, July.

ESRI (2014). ArcGIS Desktop Release 10.2.2, Environmental Systems Research Institute, Redlands, CA.

ESRI (2001). ArcGIS Desktop: Release 10, Environmental Systems Research Institute, Redlands, CA.

ESRI (2019a). ArcGIS Release 10.8, Environmental Systems Research Institute, Redlands, CA.

ESRI (2019b). "Kriging (3D Analyst)," ArcGIS 10.8 Help, ArcGIS Release 10.8, Environmental Systems Research Institute, Redlands, CA.

Everitt, B.S. (1979). "Unresolved Problems in Cluster Analysis," Biometrics, Volume 35, pp. 169-18.

Everitt, B.S. (1980). *Cluster Analysis*, 2nd Edition, Heineman Educational Books Ltd., London.

Faletra, M. K., and Twisdale, L. A., (2016). "Frequency Analysis of EF-Scale Tornado Damage Indicators," 28th Conference on Severe Local Storms, American Meteorology Society, Portland, OR, November.

Faletra, M.K., Twisdale, L. A., Hardy, M. (2016a). "Tornado Database Cleansing and Augmentation for Use in Tornado Risk Modeling", Poster Paper, 28th Conference on Severe Local Storms, Portland, OR, Nov 7-11.

Faletra, M.K., Twisdale, L.A., and Banik S.S. (2016b). "Probabilistic Modeling of Tornado Path Length Intensity Variation Using F/EF-Scale Damage Data" American Meteorological Society Severe Local Storms Conference, Portland, Oregon, November.

FEMA (2006). *Multi-hazard Loss Estimation Methodology- Hurricane Model- Hazus-MH2.1, User Manual*, Washington, D.C.

FEMA (2007). "MultiHazard Loss Estimation – Hurricane Model, HAZUS MH MR3 Technical Manual," Federal Emergency Management Agency, Mitigation Division, Washington, D.C.

FEMA (2011). *HAZUS-MH 2.1 Technical Manual*, Federal Emergency Management Agency, Department of Homeland Security, Washington, DC.

FEMA (2015). HAZUS Release 2.2 User Release Notes. Version 1.

Fenneman, Nevin M. (1917). "Physiographic Subdivision of the United States," Proceedings of the National Academy of Sciences of the United States of America. 3 (1): 17–22, January. doi:10.1073/pnas.3.1.17. OCLC 43473694. PMC 1091163. PMID 16586678.

Fenneman, N. M. 1928. Physiographic divisions of the United States. Annals of the Association of American Geography, 3rd Ed. 1 18:4:261-353, December.

Fenneman, Nevin Melancthon (1931). *Physiography of western United States*, McGraw-Hill, 534 pp, OCLC 487636.

Fenneman, Nevin Melancthon (1938). *Physiography of eastern United States*, McGraw-Hill. OCLC 487628.

Filiatrault, A. (Ed.). (2001). "Woodframe Project: Testing and Analysis Literature Reviews," Consortium of Universities for Research in Earthquake Engineering, Richmond, CA.

Fisher, R.A. (1936): "The Use of Multiple Measurements in Taxonomic Problems." *Annals of Eugenics* 7: 179–188.

Forbes, G. S. (1978). The Cabot, Arkansas Tornado of March 29, 1978, *Satellite & Mesometeorology Research Project*, 167, Department of the Geophysical Sciences, the University of Chicago.

Forbes, G. S., and Bluestein, H. B. (2001) “Tornadoes, Ttornadic Thunderstorms, and Photogrammetry: A Review of the Contributions by T. T. Fujita,” *Bulletin of the American Meteorological Society*, 82, 73–96.

Fujita, T. T. (1960). “A Detailed Analysis of the Fargo Tornadoes of June 20, 1957,” US Weather Bureau Tech. Report 5.

Fujita, T. T. (1970). “Lubbock Tornadoes of 11 May, 1970,” SMRP Res. Paper No. 88, Univ. of Chicago, 23 pages. (see also *Weatherwise*, 23, 1970, 160-173).

Fujita, T. T. (1971). “Proposed Characterization of Tornadoes and Hurricanes by Area and Intensity,” SMRP Research Paper No. 105, University of Chicago, Chicago, Ill., February.

Fujita, T. T. and Pearson, A. D., (1973). “Results of FPP Classification of 1971 and 1972 Tornadoes,” Eighth Conference on Severe Local Storms, American Meteorological Society, Boston, MA, October.

Fujita, T. T. (1975). “New Evidence from April 3-4, 1974 Tornadoes,” Preprints, *Ninth Conf. on Severen and Local Storms*, Norman, OK, American Meteorological Society, 248-255.

Fujita, T. T. (1975). “Super Outbreak of Tornadoes of April 3–4, 1974, Map printed by University of Chicago Press.

Fujita, T. T. (1978). “Aerial Survey of Grand Gulf Plant and Vicinity after the April 17, 1978 Tornado, *Satellite & Mesometeorology Research Project*, 162, Department of the Geophysical Sciences, the University of Chicago.

Fujita, T. T. (1978). “Workbook of Tornadoes and High Winds for Engineering Applications,” University of Chicago, SMRP Research Paper 165, September.

Fujita, T. T., and Wakimoto, Roger M. (1979). “Red River Valley Tornado Outbreak of April 10, 1979,” Map printed by the University of Chicago.

Gardner, A., Mehta, K. C., Tanner, L. J., Zhou, Z., Conder, M., Howard, R., Martinez, M. S., and Weinbeck, S., (2000). “The Tornadoes of Oklahoma City of May 3, 1999,” Report, Wind Science and Engineering Research Center, Texas Tech University.

Garson, R. C., Catalan, J. M., and Cornell, C. A. (1975). “Tornado Design Winds Based on Risk,” *Journal of Structural Division*, ASCE, Vol. 101, No ST9, September.

Gentry, R.C. (1983). “Genesis of tornadoes associated with hurricanes.” *Monthly Weather Review*, 111: 1793–1805.

Gillmeier, S., Sterling, M., Hemida, H. and Baker, C.J. (2018). “A reflection on analytical tornado-like vortex flow field models.” *Journal of Wind Engineering and Industrial Aerodynamics*, Vol. 174, pp. 10-27.

Golden, J.H., (1976). “An Assessment of Wind Speeds in Tornadoes,” *Proceedings of the Symposium on Tornadoes: Assessment of Knowledge and Implications for Man*, Texas Tech University, June 22-24.

Golden, J. H., and D. Purcell, (1978). “Airflow Characteristics Around the Union City Tornado,” *Monthly Weather Review*, 106, 22–28.

Grazulis, T.P., (1993), *Significant Tornadoes (1680-1991)*, Environmental Films, St. Johnsbury, Vermont.

Grazulis, T. P., (2001). *The Tornado: Nature's Ultimate Windstorm*, University of Oklahoma Press.

Gromala, D.S. (1983). *Light-frame Wall Systems: Performance and Predictability, (No. FSRP-FPL-442)*. Forest Products Lab, Madison, WI.

Guyer, Jared L. and Shea, Todd J. (2003). “An Assessment of the Variability in Operational Assignment of F-Scale Damage,” First Symposium on the F-Scale and Severe-Weather Damage Assessment, Long Beach, CA, February.

Haan, F.L., Sarkar, P.P., and Gallus, W.A. (2008). “Design, Construction and Performance of a Large Tornado Simulator for Wind Engineering Applications.” *Engineering Structures*, Vol. 30, pp. 1146-1159.

Hairstans, R. (2007). “Optimization of Timber Platform Frame Construction,” Doctoral dissertation, Edinburgh, Napier University.

Hardy, M. and Faletra, M. K. (2016). “TorDat Computer Code Suite, Ver. 1.0,” Applied Research Associates, Inc., October.

Hartigan, J.A. (1985). “Statistical Theory in Clustering,” *Journal of Classification*, Volume 2, pp. 63-76.

Hill, E.L., Malkin, W., Schulz, W.A. Jr. (1966). “Tornadoes Associated with Cyclones of Tropical Origin-Practical Features.” *Journal of Applied Meteorology*, 5: 745–763.

Hill, R. R. and Goldstein, K. L. (1981). “A Non-Fibonacci Search Plan With Fibinacci-Like Result.” Published in www.semanticsscholar.org.

Ho, T. C. E., (1992). “Variability of Low Building Wind Loads,” Thesis, Department of Civil Engineering, University of Western Ontario, London, Ontario, July.

Ho, T. C. E., Surry, D., and Morrish, D. P. (2003). “NIST/TTU Cooperative Agreement — Windstorm Mitigation Initiative: Wind Tunnel Experiments on Generic Low Buildings,” BLWT-SS20-2003,” http://fris2.nist.gov/winddata/uwo-data/blwt-ss20-2003.pdf.

Hoecker, W. H., Jr., (1960). “Wind Speed and Air Flow Pattern in the Dallas Tornado of April 2, 1957,” *Monthly Weather Review*, Vol. 88, pp. 167-180.

IBC (2011). *2012 International Building Code*, International Code Council, Country Club Hills, IL.

IRC (2015). *International Residential Code for One- and Two-Family Dwellings*, International Code Council, Illinois.

Jiang, X. and Mahadevan, S. (2008). “Bayesian Probabilistic Inference for Nonparametric Damage Detection of Structures,” *Journal of Engineering Mechanics,* Vol. 134, No, 10, p. 820-831.

Judge, E. K., and Reinhold, T.A., (2002). “Practicality and Effectiveness of Wind Resistant Retrofit Measures,” Proceedings of Solutions to Coastal Disasters, ASCE, San Diego, CA.

Kapur, K. C., and Lamberson, L. R., (1977). *Reliability in Engineering Design*, John Wiley and Sons, Inc., New York, NY.

Karstens, C. D., Gallus, W. A., Lee, B. D., and Finley, C. A. (2013). “Analysis of Tornado-Induced Tree Fall Using Aerial Photography from Joplin, Missouri, and Tuscaloosa-Birmingham, Alabama, Tornadoes of 2011,” *Journal of Applied Meteorology and Climatology,* Vol. 52.

Kelly, D.L., J.T. Schaefer, R.P. McNulty, C.A. Doswell, III, and R.F. Abbey, Jr. (1978). “An Augmented Tornado Climatology, *Monthly Weather Review*, Volume 106, pp. 1172-1183, August.

Kennedy, J. B, and Neville, A. M. (1974). *Basic Statistical Methods for Engineers and Scientists,* Thomas Cromwell Company, INC, New York, International Textbook.

Ketchen, D.J. and C.L. Shook (1996). “The Application of Cluster Analysis in Strategic Management Research: An Analysis and Critique,” *Strategic Management Journal*, Vol. 17, Issue 6, 441-458, June.

King, P. W. S., Leduc, D.M., Sills, M.L., Donaldson, N.R., Hudak, D.R., Joe, P., and Murphy, B.P. (2003), “Lake Breezes in Southern Ontario and Their Relation to Tornado Climatology,” *Weather and Forecasting*, Vol. 18, pp. 795-807.

Kopp, G.A., Hong, E., Gavanski, E., Stedman, D., and Sills, D.M.L. (2014). “Assessment of Winbd Speeds Based on Damage Observations from the Angus (Ontario) Tornado of 17 June 2014,” *Canada Journal of Civil Engineering*, 44, 37-47.

Kosiba, K., Trapp, R. J., and Wurman, J. (2008) “An Analysis of the Axisymmetric Three-Dimensional Low Level Wind Field in a Tornado Using Mobile Radar Observations,” *Geophysical Research Letters*, Vol. 35, L05805.

Kosiba, K. and Wurman, J. (2010). “The Three-Dimensional Axisymmetric Wind Field Structure of the Spencer, South Dakota, 1998 Tornado,” *Journal of Atmospheric Science,* Vol. 67, pp. 3074-3083.

Kosiba, K. and Wurman, J. (2013). “The Three-Dimensional Structure and Evolution of a Tornado Boundary Layer,” *Weather and Forecasting,* Vol. 28, pp. 1552-1561.

Kosiba, K., Wurman, J., Richardson, Y., Markowski, P., Robinson, P., and Marquis, J., (2013). “Genesis of the Goshen County, Wyoming, Tornado on 5 June 2009 during VORTEX2,” *Monthly Weather Review,* Vol. 141.

Kuo, H. L. (1971). “Axisymmetric flows in the boundary layer of a maintained vortex,” *Journal of Atmospheric Sciences*. Vol. 28, pp. 20 – 41.

Kuligowski, E., Lombardo, F., Phan, L., Levitan, M. and Jorgensen, D. (2014). “Final Report - National Institute of Standards and Technology (NIST) Technical Investigation of the May

22, 2011, Tornado in Joplin Missouri," NCSTAR 3, (March). https://doi.org/10.6028/NIST.NCSTAR.3.

LaDue, J., and Mahoney, E., (2006). "Implementing the New Enhanced Fujita Scale with the NWS", 23rd Conference on Severe Local Storms, St. Louis, AMS.

LaDue, J., and Ortega, K. (2008). "Experience in Using the EF-Scale Since its Inception," 24th Conference on Severe Local Storms, Savannah, GA, AMS.

Ladue, J.G. (2016). "About the ASCE Tornado Wind Speed Estimation Committee," 28th Conference on Severe Local Storms, American Meteorological Society, Portland, OR.

Lavelle, F.M. and P.J. Vickery, (2012) "Interactions among Wind Mitigation Features in Benefit/Cost Analysis," Advances in Hurricane Engineering: Learning from our Past, 2012 ATC & SEI Conference, Miami, FL.

Law, A. M. and Kelton, D. K. (1982). *Simulation Modeling and Analysis*, McGraw-Hill, New York, NY.

Lee, J. J., T. M. Samaras, and C. R. Young (2004). "Pressure measurements at the ground in an F-4 tornado," Preprints, 22nd Conf. on Severe Local Storms, Hyannis, MA, American Meteorological Society.

Lee, W and Wurman, J. (2005). "Diagnosed Three-Dimensional Axisymmetric Structure of the Mulhall Tornado on 3 May 1999," *Journal of the Atmospheric Sciences*, Vol. 62, pp. 2373-2393.

Lewellen, W. S. (1976). "Theoretical Models of the Tornado Vortex," Symposium on Tornadoes: Assessment of Knowledge and Implications for Man (Texas Technological University, Lubbock, Texas, June 1976), 105–150.

Letchford, C.W., and Marwood, R. (1997). "On the influence of *v* and *w* component turbulence on roof pressures beneath conical vortices," *Journal of Wind Engineering and Industrial Aerodynamics*, 69-71.

Liu, Z. and Ishihara, T. (2016). Study of the effects of translation and roughness on tornado-like vortices by large-eddy simulation. *Journal of Wind Engineering and Industrial Aerodynamics*. Vol. 151, pp. 1-24

Lombardo, F.T., Roueche, D.B., and Prevatt, D.O., (2015). "Comparison of two methods of near-surface wind speed estimation in the 22 May, 2011 Joplin, Missouri Tornado," *Journal of Wind Engineering and Industrial Aerodynamics*, 138, pp. 87-97.

Mahaney, James A., and Kehoe, Brian E. (2002). "Anchorage of Wood-frame Buildings: Laboratory Testing Report (CUREE Publication No. W-14)," CUREE, Richmond, CA.

Main, J. A., and Fritz, W. P. (2006). *Database-assisted design for wind: Concepts, software, and examples for rigid and flexible buildings*, National Institute of Standards and Technology, Technology Administration, U.S. Dept. of Commerce, Gaithersburg, MD, http://www.itl.nist.gov/div898/winds/wind_pressure/wind_pressure.htm.

Marshall, T. P. (1993). Lessons Learned from Analyzing Tornado Damage. The Tornado: Its Structure, Dynamics, Prediction, and Hazards. *Geophysical Monograph*, 79. American Geophysical Union.

Marshall, T. P., (2002). “Tornado Damage Survey at Moore, Oklahoma,” *Weather and Forecasting*, Vol. 17.

Marshall, T. P., McCarthy, D., and LaDue, J. (2008). “Damage Survey of the Greensburg, KS Tornado,” 24th Conference on Severe Local Storms, Savannah, GA.

Marshall, T. P., McCarthy, D., LaDue, J. G., Wurman, J., Alexander, C. R., Robinson, P., and Kosiba, K. A. (2008a). Damage Survey of the Greensburg, KS Tornado,” *24th Conference on Severe Local Storms,* Savanah, GA.

Marshall, T. P., Jungbluth, K., and Baca, A. (2008b). “The Parkersburg, IA Tornado: 25 May 2008,” *24th Conference on Severe Local Storms,* Savanah, GA.

Marshall, T. P., Davies, W., and Runnels, S. (2012). “Damage Survey of the Joplin Tornado: 22 May 2011,” *26th Conference on Severe Local Storms,* Nashville, TN.

Marshall, T. P., Burgess, D., Garfield, G., Smith, R., Speheger, D., Snyder, J., and Bluestein, H. (2014). “Ground-based Damage Survey and Radar Analysis of the El Reno, Oklahoma Tornado,” *Proc. 27th Conf. on Severe Local Storms*, Madison, WI, Amer. Meteor. Soc., Paper 13.1.

Masoomi, H. and Van de Lindt, J.W. (2017). “Tornado community-level spatial damage prediction including pressure deficit modeling.” *Sustainable and Resilient Infrastructure*.

MATLAB (2018), MATLAB Mapping Toolbox Release 2018a, Mathworks, Inc.

Matsui, M and Tamura, Y (2009). “Influence of incident flow conditions on generation of tornado-like flow”, 11th American Conference on Wind Engineering, Sun Juan, Puerto Rico, June 22-26.

McAllister, T. P., Wang, N., and Ellingwood, B. R. (2018). “Risk-Informed Recurrence Intervals for Updated Wind Maps in ASCE 7-16,” *Journal of Structural Engineering*, 144(5): 06018001.

McCarthy, D.W. (2003). “NWS Tornado Surveys and the Impact on the National Tornado Data Base.” Preprints, *Amer. Met. Society,* 1st Symposium on F-Scale and Severe Weather Damage Assessment, Long Beach, CA.

McCarthy, D., & Schaefer, J. (2004). Tornado trends over the past thirty years. In Preprints, 14th Conf. Applied Climatology, Seattle, WA, *Amer. Meteor. Soc* (Vol. 3).

McCaul, E.W. Jr. (1991). “Buoyancy and Shear Characteristics of Hurricane-Tornado Environments.” *Monthly Weather Review*, 119: 1954–1978.

McDonald, J. R., Mehta, K. C., Minor, J. E., and Benson, L. (1975). “Development of a wind speed risk model for the Argonne National Laboratory site,” Institute for Disaster Research and Department of Civil Engineering, Texas Tech. University. Lubbock, Texas.

McDonald, J. R. and Mehta, K. C. (2004). “A recommendation for an Enhanced Fujita Scale,” Submitted to the National Weather Service, Texas Tech University, Lubbock, Texas.

McDonald, J.R., Mehta, K.C., Smith, D.A., and Womble, J.A. (2009). “The Enhance Fujita Scale: Development and Implementation,” Proceedings, 5th Congress on Forensic Engineering, Washington, DC, November 10-15, 2009, pp. 719-728 (publication and presentation).

Meecham, D. (1988). “Wind Action on Low-Rise Buildings,” M.E.Sc. Thesis, The University of Western Ontario, London, ON, Canada.

Mehta, K.C., et al. (1976). “Windspeed Estimates: Engineering Analysis,” presented at Symposium on Tornadoes, held at Lubbock, Texas, June.

Mi, H. (2004). “Behavior of Unblocked Wood Shearwalls,” *MS Thesis*, University of New Brunswick, Canada.

Milligan, G. W. (1981). “A Review of Monte Carlo Tests of Cluster Analysis,” *Multivariate Behavioral Research*, Volume 16, pp. 379-407.

Mizzell, D. P., and Schiff, S. D. (1994). “Wind Resistance of Sheathing for Residential Roofs.” Wind Load Test Facility Rep., Department of Civil Engineering, Clemson University, Clemson, S.C.

Mizzell, D. P., 1994. Wind Resistance of Sheathing for Residential Roofs. Master Thesis, Clemson University, Clemson, USA.

Monji, N. (1985). “A Laboratory Investigation of the Structure of Multiple Vortices.” *Journal of Meteorological. Society Japan, Vol.* 63, pp. 703–712.

Monji, N. and Yasushi M (1985). “A Laboratory Experiment on the Multiple Structure in Tornado-like Vortices”, *Disaster Prevention Research Institute Annals*, No.26, B-1, 427-436

NAHB Research Center, Inc. (2009). *Evaluation of Full-Scale House Testing Under Lateral Loading*. Upper Marlboro, MD: NAHB Research Center, Inc.

NAHB (2010). “Evaluation of Wood Sole Plate Anchorage to Concrete Under Monotonic and Cyclic Loading,” Report prepared by National Association of Home Builders Research Center, MD.

National Centers for Environmental Information (NCEI), (2014). “Storm Data Export Format, Field names,” https://www.ncdc.noaa.gov/stormevents/ftp.jsp.

Newark, M.J. (1984), “Canadian Tornadoes, 1950-1979,” *Atmosphere-Ocean*, Vol. 22, pp. 343-353.

NIST (2014). “Technical Investigation of the May 22, 2011, Tornado in Joplin, Missouri,” Report prepared by National Institute of Standards and Technology, Gaithersburg, Maryland.

NOAA (2003). *A Guide to F-Scale Damage Assessment*, National Weather Service, April.

NOAA (2008). “EF-Scale Training,” http://www.wdtb.noaa.gov/courses/EF-scale/index.html, Warning Decision Training Division, National Weather Service.

NOAA SPC (2012). “Severe Weather Database Files.” www.spc.noaa.gov/wcm/#data.

NOAA (2016a). SPC Actual Tornadoes Database 1950-2015, Storm Prediction Center, http://www.spc.noaa.gov/wcm/#data

NOAA (2016b). NWS Damage Assessment Toolkit (DAT), https://apps.dat.noaa.gov/StormDamage/DamageViewer/

Nolan, D. S., Dahl, N. A., Bryan, G. S. and Rotunno, R. (2017). “Tornado Vortex Structure, Intensity, and Surface Wind Gusts in Large-eddy Simulations with Fully Developed Turbulence,” *Journal of the Atmospheric Sciences*, Vol. 74, pp. 1573-1596.

Novlan, D.J., Gray, W.M. (1974). "Hurricane-Spawned Tornadoes." *Monthly Weather Review*, 102: 476–488.

NRC (2007). "Design Basis Tornado and Tornado Missiles for Nuclear Power Plants. Regulatory Guide 1.76," *Office of Nuclear Regulatory Research*, U.S. Nuclear Regulatory Commission.

NWS Sioux Falls, (1992). Chandler-Lake Wilson Minnesota F5 Tornado of June 16, 1992. Map. NWS NOAA. 7 Dec. 2016 http://www.weather.gov/fsd/19920616-tornado-chandlerlakewilson

NWS (1998). "The Moore, Oklahoma Tornado of 4 October 1998," Map. NWS NOAA. 7 Dec. 2016. https://www.weather.gov/oun/events-19981004-mooretornado, Norman, OK.

NWS Sioux Falls, (2003). 24 June 2003 Tornado Tracks. Map. NWS NOAA. 7 Dec. 2016. http://www.weather.gov/fsd/20030624-tornadotracks

NWS Omaha/Valley & Emergency Management, (2004). Hallam, NE Tornado May 22, 2004. Map. NWS NOAA. http://w2.weather.gov/images/oax/Archives/hallam/hallammap.jpg

NWS Sioux Falls, (2004). Tornado Tracks over Clay County Iowa on June 11, 2004. Map. NWS NOAA. http://www.weather.gov/fsd/20040611-tornado-claycounty

NWS Sioux Falls, (2006). Maps of the Beadle County Tornado Paths – August 24, 2006. Map. NWS NOAA. http://www.weather.gov/fsd/tor2006aug24_path

NWS Omaha/Valley, (2008). Little Sioux Scout Ranch Tornado, June 11, 2008. Map. NWS NOAA. http://w2.weather.gov/oax/LittleSioux

OSHA (2019). "Standard Industrial Classification (SIC) System Search," Occupational Safety and Health Administration, https://www.osha. gov/pls/imis/sicsearch.html, Washington, DC.

Peng, X., Rouche, D., Prevatt, D. O. and Gurley, K. R. (2016). "An Engineering-based Approach to Predict Tornado-Induced Damage," Wall of Wind Research and Testing to Enhance Civil Infrastructure to Hurricane Multi-Hazards. Chapter 15, pp. 311-335.

Phan, L. and Simiu, E., (1998a). "Fujita Tornado Intensity Scale: A Critique Based on Observations of the Jarrell Tornado of May 27, 1997", NIST TN 1426, July 1998.

Phan, L. and Simiu, E., (1998b). "Tornado Aftermath: Questioning the Tools", ASCE Civil Engineering Magazine, December 1998.

Phan, L., Levitan, M., Twisdale, L. A., (2016). "Tornado Hazard Mapping for Tornado-Resistant Design of Buildings and Infrastructure," 28th Conference on Severe Local Storms, *American Meteorology Society*, Portland, OR, November.

Phillips, T.L. (1990). "Load Sharing Characteristics of Three-Dimensional Wood Diaphragms," MS Thesis, Washington State University, Pullman, WA.

Phillips, T. L., Itani, R. Y., and McLean, D. I. (1993). "Lateral Load Sharing by Diaphragms in Wood-Framed Buildings," *Journal of Structural Engineering*, 119(5), 1556-1571.

Pintar, A. L., Simiu, E., Lonbardo, F. T., Levitan, M. (2015). "Maps of Non-hurricane Nontornadic Wind Speeds With Specified Mean Recurrence Intervals for the Contiguous United States Using a Two-dimentional Poisson Process Extreme Value Model and Local

Regression," NIST Special Publication 500-301, National Institute of Science and Technology, Washington, (Available through NIST website: via link https://nvlpubs.nist.gov/nistpubs/SpecialPublications/NIST.SP.500-301.pdf)

Potter, S. (2007). "Fine Tuning Fujita," *Weatherwise*, 60 (2), 64-71.

Quayyum, S. (2020). "Parametric Models for Wind Load Resistances of Wood-Frame Walls," *Journal of Structural Engineering*, Vol. 146, 2, November.

Quayyum, S. (2019a). "Finite Element Analysis of Wood-Frame Houses Under Lateral Loads," *Journal of Structural Engineering*, Vol. 145, 12, December.

Quayyum, S. (2019b). "Refined Parametric Models for Wind Load Resistances of Wood-Frame Walls," *Engineering Structures*," *183*, 841-859, January.

Rackwitz, R. (1976). "Practical Probabilistic Approaches to Design," Bulletin 112, Comite European du Breton, Paris France.

Rammer, R. D., Winistorfer, S. G. and Bender, D. A. (2001). "Withdrawal Strength of Threaded Nails," *Journal of Structural Engineering*, Vol. 127, No. 4, pp. 442-449.

Ramsdell, J.V., Jr., and Rishel, J.P. (2007). "Tornado Climatology of the Contiguous United States," U.S. Nuclear Regulatory Commission Report NUREG/CR-4461, Revision 2, PNNL-15112, Revision 1, February.

Rankine, W. J. M. (1882). *A Manual of Applied Physics*. 10th Ed., Charles Griff and Co., pp. 663.

Ray, P. S., Bieringer, P., Niu, X., and Whissel, B. (2003). "An Improved Estimate of Tornado Occurrence in the Central Plains of the United States," *Monthly Weather Review*, Vol. 131, pp. 1026-1031, May.

Refan, Maryam, (2014). "Physical Simulation of Tornado-Like Vortices" Electronic Thesis and Dissertation Repository. 1923.

Refan, M. and Hangan, H. (2016). "Characterization of Tornado-like Flow Fields in a New Model Scale Wind Testing Chamber," *Journal of Wind Engineering and Industrial Aerodynamics*, Vol. 151, pp. 107-121.

Refan, M. (2017). "Near surface wind field characteristics of tornadoes," Presentation to ASCE wind speed committee webinar, November.

Reinhold, T. A. and Ellingwood, B., (1982). *Tornado Damage Risk Assessment*, NUREG/CR-2944; BNL-NUREG-51586. National Bureau of Standards, Washington, DC. Center for Building Technology.

Roueche, D. B. and Prevatt, D.O. (2013). "Residential Damage Patterns Following the 2011 Tuscaloosa, AL and Joplin, MO Tornadoes," *Journal of Disaster Research*, Vol. 8, No. 6.

Roueche, D.B., Lombardo, F.T. and Prevatt, D.O. (2015). "Development of Empirically-Based Fragilities of Residential Damage in the 2011 Joplin, Missouri Tornado," *Geotechnical and Structural Engineering Congress 2016*, Phoenix, AZ.

Roueche, D. B., Lombardo, F. T. and Prevatt, D. O. (2017). “Empirical Approach to Evaluating the Tornado Fragility of Residential Structures,” *Journal of Structural Engineering.* Vol. 143, issue 9, pp. 04017123-1 - 04017123-10.

Rosenblatt, M. (1952). “Remarks on Multivariate Transformations,” *Annals of Math. Stat.*, No. 3, September.

Rosowsky, D.V. and Schiff S.D. (1996). “Probabilistic Modeling of Roof Sheathing Uplift Capacity,” Specialty Conference on Probabilistic Mechanics and Structural and Geotechnical Reliability. Reston, VA.

Ross, R. J. (2010). *Wood handbook: Wood as an engineering material*, USDA Forest Service, Washington, DC.

Rotunno, R. (1977). “Numerical Simulation of a Laboratory Vortex.” *Journal of Atmospheric Science*, Vol. 30, pp. 1599-1619.

Rotunno, R. (1979). “A Study in Tornado-Like Vortex Dynamics.” *Journal of Atmospheric Sciences*, Vol. 36, pp. 140-155.

Sarkar, P. P., and H. Kikitsu (2008). “Damage Survey Report on Parkersburg and New Hartford,” Iowa City, IA: Iowa State University.

Sarle, W.S. (1982). “Cluster Analysis by Least Squares,” Proceedings Seventh Annual SAS Users Group International Conference, SAS Institute Inc., Cary, North Carolina, pp. 651-653.

SAS Institute Inc. (1992). SAS/STAT User’s Guide, Version 6, 4th Edition, Volume 1, SAS Institute Inc., Cary, North Carolina.

Sassa, K., Takemura, S. and Yamashtha, K. (2009). “The Behavior of Windborne Debris Accompanied by a Traveling Tornado,” The Seventh Asia-Pacific Conference on Wind Engineering, Taiwan, November.

Schaefer, J. T. and Galway, J. G. (1982). “Population Biases in Tornado Climatology,” Preprints, 12th Conference on Severe Local Storms, San Antonio, TX, *American Meteorological Society*, 51-54.

Schaefer, J. T., Kelly, D., and Abbey, R. F. (1986). “A Minimum Assumption Tornado-Hazard Probability Model,” *Journal of Climate and Applied Meterology*, Vol. 25, 1934-1945.

Schaefer, J. T., R. S. Schneider, and M. P. Kay (2002). “The Robustness of Tornado Hazard Estimates,” Preprints, Third Symp. on Environmental Applications, Orlando, FL, *Amer. Meteor. Soc.*, 35–41, January.

Scott, P. (2021) “Analysis of Residential Building Performance in Tornadoes as a Function of Building and Hazard Characteristics. Dissertation. Texas Tech University. https://ttu-primo.hosted.exlibrisgroup.com/primo-explore/fulldisplay?docid=01TTU_DSPACE_ML2346%2F87580&context=L&vid=01TTU&lang=en_US&search_scope=01TTU_ALL&adaptor=Local%20Search%20Engine&tab=default_tab&query=any,contains,pataya%20scott&mode=Basic

Simiu, E. and Scanlan, R.H. (1996). *Wind Effects on Structures, An Introduction to Wind Engineering*, 3rd Edition, Wiley-Interscience, New York, NY.

Simmons, K.M. and Sutter, D. (2011). *Economic and Societal Impacts of Tornadoes*, American Meterological Society, Massachusetts.

Smith, B. and Zapotocny, C. (2003). Coleridge, NE Tornado, June 23, 2003. Map, NWS, NOAA, 7 Dec. 2016. http://w2.weather.gov/oax/coleridge

Smith, B. and Adams, B., (2004). Walnut, IA Tornado May 8, 2004. Map. NWS NOAA. 7 Dec. 2016. http://w2.weather.gov/images/oax/Archives/walnut_tor/scanmap.jpg

Snider, C. R., (1977). “A Look at Michigan Tornado Statistics,” *Monthly Weather Review*, 105, 1341-1342.

Snyder, J. C., & Bluestein, H. B. (2014). “Some Considerations for the Use of High-Resolution Mobile Radar Data in Tornado Intensity Determination,” *Weather and Forecasting*, 29, 799–827.

Speheger, D. H., C. Doswell, G. Stumpf (2002), “The Tornadoes of 3 May 1999: Event Verification in Central Oklahoma and Related Issues,” *Weather and Forecasting*, Vol. 17, June, 2002.

Steel, R.G.D. and J.H. Torrie (1960). *Principles and Procedures of Statistic*s, McGraw-Hill, New York, New York.

Straub, D. and Papaioannou, I., (2105), “Bayesian Updating with Structural Reliability Methods,” *Journal of Engineering Mechanics*, Vol. 141, No. 3, March.

Storm Prediction Center, (2010). “SPC Tornado, Hail, and Wind Database Format Specification,” https://www.spc.noaa.gov/wcm/data/SPC_severe_database_description.pdf.

Sugiyama, H. (1981). “Evaluation of Wood-based Shear Walls with Opening,” *Wood Industry*, 36(7): 3-8.

Sullivan, R. D., (1959). “A Two-cell Vortex Solution of the Navier-Stokes Equations,” *Journal of Aerospace Science*, Vol. 26, pp. 767–768.

Symons, M.J. (1981). “Clustering Criteria and Multivariate Normal Mixtures,” *Biometrics*, Volume 37, pp. 35-43.

Tanamachi, R. L., Bluestein, H. B., Xue, M., Lee, W., Orzel, K. A., Frasier, S. J., & Wakimoto, R. M. (2013). “Near-Surface Vortex Structure in a Tornado and in a Sub-Tornado-Strength Convective-Storm Vortex Observed by a Mobile, W-Band Radar during VORTEX2,” *Monthly Weather Review*, 141(11), 3661-3690.

Texas Tech University (TTU) (2004), “A Recommendation for an Enhanced Fujita Scale,” Wind Science and Engineering Center, Lubbock, TX, June.

TTU (2006), “A Recommendation for an Enhanced Fujita Scale,” Wind Science and Engineering Center, Lubbock, TX, Revision 2, October.

Thampi, H. (2010). “Interaction of a Translating Tornado with Low-Rise Building,” *MS Thesis*, Iowa State University, Ames, Iowa.

Thampi, H., Dayal, V., and Sarkar, P. P. (2011). “Finite Element Analysis of Interaction of Tornados With a Low-Rise Timber Building,” *Journal of Wind Engineering and Industrial Aerodynamics*, *99*(4), 369-377.

Thom, H. C. S. (1963). “Tornado Probability,” *Monthly Weather Review*, Vol. 91, October-December.

Thompson, R. L., Edwards, R., Hart, J.A., Elmore, K. L. and Markowski, P. (2003). “Close Proximity Soundings within Supercell Environments Obtained From the Rapid Update Cycle,” *Weather and Forecasting*, 18, 1243-1261.

Thompson, R. L., Smith, B. T., Dean, A. R., and Marsh, P. T. (2013). “Spatial Distributions of Tornadic Near-Storm Environments by Convective Mode,” Electronic *Journal of Severe Storms Meteorology*, 8, 1-22.

Thorndike, Robert L. (1953). “Who Belongs in the Family?” *Psychometrika* 18 (4): 267–276, December.

Thurston, S.J. (2003). “Full-sized House Cyclic Racking Test,” *BRANZ study report No. 119*, Building Research Association of New Zealand, Judgeford, New Zealand.

Thurston, S.J. (2006). “Racking Tests on Rooms and Isolated Walls to Investigate Uplift Restraint and Systems Effects,” *BRANZ study report No. 154*, Building Research Association of New Zealand, Judgeford, New Zealand.

Toro, W. M., Salenikovich, A., Mohammad, M., and Beauregard, R. (2007). “Racking and Bending Tests for Prefabricated Wall Panels,” *Maderas. Ciencia y Tecnología*, *9*(1), 3-14.

Twisdale, L. A., Dunn, W. L., Lew, S. T., David, T. L., Hsu, J. C., and Lee, S. T. (1978), *Tornado Missile Risk Analysis*, Electric Power Research Institute, EPRI NP-768 and NP-769 (Appendixes), Palo, Alto, CA, May.

Twisdale, L. A., (1978), “Tornado Data Characterization and Wind Speed Risk,” *Journal of the Structural Division*, ASCE, Vol. 104, No. ST10, October.

Twisdale, L. A., Dunn, W. L., and Davis, T.L. (1979), “Tornado Missile Transport Analysis,” *Nuclear Engineering and Design*, Vol. 51, 1979.

Twisdale, L.A. Dunn, W. L., Lew, S. T., David, T. L., Hsu, J. C., and Lee, S. T. (1981). *Tornado Missile Simulation and Design Methodology*, EPRI NP-2005, Volumes 1 and 2, Electric Power Research Institute, Palo Alto, CA, August.

Twisdale, L.A. and Dunn, W. L. (1983a). “Probabilistic Analysis of Tornado Wind Risks.” *Journal of Structural Engineering*, Vol. 109, No. 2, 468-488.

Twisdale, L.A. and Dunn, W. L. (1983b). “Wind Loading Risks from Multivortex Tornadoes,” *Journal of Structural Engineering*, Vol. 109, No. 8, 2016-2022.

Twisdale L. A. (1983). Wind Loading Risks from Multivortex Tornadoes. *Journal of Structural Engineering*, Vol. 109.

Twisdale, L.A., (1986). “Reliability and Risk Models Based on Independent Trials,” *Probabilistic Engineering Mechanics*, Vol. 1, No. 4, 202 – 207, September.

Twisdale, L.A. (1988). “Probability of Facility Damage From Extreme Wind Effects,” *Journal of Structural Engineering*, Volume 114, Number 10, October.

Twisdale, L.A., Vickery, P.J. and Steckley, A.C. (1996). “Analysis of Hurricane Windborne Debris Risk for Residential Structures,” Technical Report. Applied Research Associates, Inc. Raleigh, NC.

Twisdale, L.A. et al., (2002). “Development of Loss Relativities for Wind Resistive Features of Residential Structures,” prepared for Florida Department of Community Affairs, Tallahassee, FL, March.

Twisdale, L.A., and Young, M., (2002). “Analysis of Costs and Loss Reduction Benefits of Windborne Debris Protection- North Carolina Coast Exposure C Locations,” prepared for Institute for Business and Home Safety, Tampa, FL, (May).

Twisdale, L.A., (2003). “Loss Relativities for FBC Wood Panel Shutters,” prepared for Florida Department of Community Affairs, Tallahassee, FL, June.

Twisdale, L.A., (2007). “Evaluation and Report on the Insurability of Attached and Free Standing Structures,” prepared for Florida Office of Insurance Regulation, Tallahassee, FL, May).

Twisdale, L.A. et al., (2008). “2008 Florida Residential Wind Loss Mitigation Study,” prepared for Florida Office of Insurance Regulation, Tallahassee, FL, ARA Report 18401, October.

Twisdale, L. A. (2010a). “Tornado Data and EF Winds: Impact on Engineering Analysis,” Presentation at EF-Scale Stakeholders Meeting, Norman, OK, March.

Twisdale, L. A. (2010b), “Determining Wind speeds from Damage,” Presentation at EF-Scale Stakeholders Meeting, Norman, OK, March.

Twisdale, L. A., Vickery, P.J., Sciaudone, J.C., Banik, S.S., Mizzen, D. R., (2015a). “Advances in Wind Hazard and Fragility Methodologies for HW PRAs”, ANS International Topical Meeting ON Probabilistic Safety Assessment, Sun Valley, Idaho, April.

Twisdale, L.A., Lovelace, N. and Slep, C. (2015b). “High Wind PRA Failure Calculations, Error Estimations, and Use of CAFTA,” ANS International Topical Meeting on Probabilistic Safety Assessment, Sun Valley, Idaho, April 26-30.

Twisdale, L.A., Banik, S.S., Vickery, P. J., Levitan, M. and Phan, L. (2016). “A Methodology for Improving Tornado Damage-Based Intensity Ratings.” 28th Severe Local Storm Conference, *American Meteological Society*, Portland, November.

Twisdale, L. A. (2016). “Risk Assessment for High Winds:State of the Art,” 10th Nuclear Plant Current Issues Symposium, North Carolina State University, Charlotte, NC, December.

Twisdale, L. A. (2017). “Non-Parametric Method for Wind Pressure Fragility Analysis.” ANS 2017 International Topical Meeting on Probabilistic Safety Assessment and Analysis, Pittsburg, PA, September 24-28

Umenhofer, T. A., Fujita, T. T., and Dundas, R. (1977). “Great Bend Tornadoes of August 30, 1977,” Preprints, 10th Conf. on Severe Local Storms, Omaha, NE, *American Meteorological Society*, 457-462.

US Census Bureau (2000). Census of Population and Housing, 2000: Summary Tape File 1B Extract on CD-ROM, US Census Bureau, Washington, DC.

US Census Bureau (2000). Census of Population and Housing, 2000: Summary Tape File 3 on CD-ROM, US Census Bureau, Washington, DC.

US Census Bureau (2010). Census of Population and Housing, 2010: Summary File.

US Census Bureau (2017). 2017 Census Tracts and Blocks REST File, https://catalog.data.gov/ dataset/2017-census-tracts-and-blocks-rest-file1f2c7, US Census Bureau, Washington, DC, May

US Census Bureau (2017). American Housing Survey: AHS 2017 Summary Tables, , https://www.census.gov/programs-surveys/ahs/data.html.

US Census Bureau (2020). Glossary. https://www.census.gov/programs-surveys/geography/about/glossary.html#par_textimage_13

US Nuclear Regulatory Commission (2007a), "Design-Basis Tornado and Tornado Missiles for Nuclear Power Plants," Regulatory Guide 1.76, Revision 1, United States Nuclear Regulatory Commission, Washington, DC, March.

US Nuclear Regulatory Commission (2007), "Standard Review Plan, NUREG 0800, Section 3.3.2 Tornado Loads," Revision 3, United States Nuclear Regulatory Commission, Washington, DC, March.

Verbout, S. M., Brooks, H. E., Leslie, L. M., and Schultz, D. M. (2006). "Evolution of the U.S. Tornado Database: 1954-2003." Weather and Forecasting, Vol. 21, February.

Vickery, P.J., Chen, J., and Sciaudone, J. (2006), "Mitigation of Two Story Single Family Residences," prepared for Florida Department of Community Affairs, Tallahassee, FL, July.

Vickery, P.J., J. X. Lin, P. F. Skerlj, and L. A. Twisdale, Jr., (2006a). "The HAZUS-MH Hurricane Model Methodology Part I: Hurricane Hazard, Terrain and Wind Load Modeling," *Natural Hazards Review*, 7, 82-93.

Vickery, P.J., P F. Skerlj, J. X. Lin, L. A. Twisdale Jr., M.A. Young and F.M. Lavelle, (2006b) "The HAZUS-MH Hurricane Model Methodology Part II: Damage and Loss Estimation", *Natural Hazards Review*, 7, 94-103.

Vickery, P. J., Wadhera, D., Twisdale, L.A., Lavelle, F. M. (2009). "United States Hurricane Wind Speed Risk and Uncertainty," *Journal of Structural Engineering*, 135, 301-320.

Vickery, P. J., G. A. Kopp and L. A. Twisdale, Jr. (2011). "Component and Cladding Wind Pressures on Hip and Gable Roofs: Comparisons to the US Wind Loading Provisions," *13th International Conference on Wind Engineering*, Amsterdam, The Netherlands.

Vickery, P. J., Banik, S. S. and Twisdale, L. A. (2019). Development of Tornado Design Criteria for Buildings and Shelters Subject to Tornado Induced Loads," 2019 Disaster Resilience Symposium, National Institute of Standards and Technology, DC, August.

Wakimoto, R. M. and Wilson, J. W. (1989). "Non-supercell Tornadoes," *Monthly Weather Review*, 117, 1113-1140.

Wakimoto, R. M., Murphey, H. V., Dowell, D. C., and Bluestein, H. B. (2003). "The Kellerville Tornado During VORTEX: Damage Survey and Doppler Radar Analyses," *Monthly Weather Review*, 131, 2197–2221.

Wakimoto, R. M., Atkins, N. T., and Wurman, J. (2011). "The LaGrange Tornado During VORTEX. Part 1: Photogrammetric Analysis of the Tornado Combined with Single-Doppler Radar," *Monthly Weather Review*, 139, 2233-2258.

Walpole, R.E. and Myers, R.H. (1978). Probability and Statistics for Engineers and Scientists, 2nd Ed., Macmillan, New York, New York.

Wang, J., Cao, S. and Pang, W. (2017). “Experimental Study on Effects of Ground Roughness on Flow Characteristics of Tornado-like Vortices,” *Boundary Layer Meteorology*. Vol. 162, pp. 319-339.

Ward, J.H. (1963). “Hierarchical Grouping to Optimize an Objective Function,” *Journal of the American Statistical Association,* Volume 58, pp. 236-244.

Weiss, S.J. (1985). “On the Operational Forecasting of Tornadoes Associated with Tropical Cyclones.” Preprints 14th Conf. on Severe Local Storms, Indianapolis, IN, *American Meteorological Society*, pp 293–296.

Wen, Y. K. and Ang A. H. S. (1975). “Tornado Risk and Wind Loading Effect on Structures,” Proceedings, Fourth International Conference on Wind Effects on Buildings and Structures, London, England, September.

Wen, Y.K., and Chu, S.L. (1973). “Tornado Missile Simulation and Design Wind Speed,” *Journal of the Structural Division,* ASCE, Vol. 99, No ST12, December.

Widen, Holly M., Elsner, James B., Amrine, Cameron, Cruz, Rizalino B., Fraza, Erik, Michaels, Laura, Migliorelli, Loury, Mulholland, Brendan, Patterson, Michael, Strazzo, Sarah, and Xing, Guang (2013). “Adjusted Tornado Probabilities,” *Electronic Journal of Severe Storms Meterology,* Vol. 8, pp. 1-12, December.

Winn, W. P. Hunyardy, S. J. and Aulich, G. D. (1999). “Pressure At the Ground in a Large Tornado,” *Journal of Geophysical Research Atmosphere*, Vol. 104, pp. 22067-22082.

Wolford, L. V. (1960). “Tornado Occurrences in the United States,” *U.S. Weather Bureau Technical Paper No 20,* Washington, D.C.

Wood, V. T. and Brown, R.A. (2011). “Simulated Tornado Vortex Signatures of Tornado-like Vortices Having One and Two-Celled Structures,” *Journal of Applied Meteorology Climatology,* Vol. 50, pp. 2338-2342.

Wood, V.T. and White, L.W. (2011). “A New Parametric Model of Vortex Tangential Wind Profile: Testing and Verification,” *Journal of Atmospheric Science*, Vol. 68, pp. 990-1006.

Wurman, J., Straka, J. M. and Rasmussen, E. N. (1996). “Fine-Scale Doppler Radar Observation of Tornadoes,” *Science,* Vol. 272, pp. 1774-1777.

Wurman, J. and Gill, S. (2000). “Finescale Radar Observations of the Dimmit, Texas (2 June 1995), Tornado,” *Monthly Weather Review,* Vol. 128, pp. 2135-2164.

Wurman, J. and Alexander, C. R. (2005). “The 30 May 1998 Spencer, South Dakota, Storm. Part II: Comparison of Observed Damage and Radar-Derived Winds in the Tornadoes.” *Monthly Weather Review*, Vol. 133, pp. 97-119.

Wurman, J., Robinson, P., Alexander, C., & Richardson, Y. (2007). “Low-Level Winds in Tornadoes and Potential Catastrophic Tornado Impacts in Urban Areas. *Bulletin of the American Meteorological Society*, 88(1), 31-46.

Wurman, J. and Kosiba, K., and Robinson, P. (2013). "In Situ Doppler Radar Interior Structure of a Tornado and Wind-Damage Relationship," *Bulletin of the American Meteorological Society*, 134, 835-846.

Wurman, J. and Kosiba, K. (2014). "Radar and In Situ Wind Measurements vs. Damage Measurements," Presentation from Enhanced Fujita (EF) Scale Open Feedback Forum, Atlanta, GA, February.

Wurman, J., Kosiba, K., Robinson, P., and Marshall, T. (2014) "The Role of Multiple Vortex Tornado Structure in Causing Storm Researcher Fatalities," *Bulletin of the American Meteorological Society*, 95, 31–45, doi:https://doi.org/10.1175/BAMS-D-13-00221.1.

Zhang, W. and Sarkar, P. P. (2008). "Effects of Ground Roughness on Tornado-like Vortex Using PIV," AAWE workshop, Vail, Colorado, August.

Appendix A. Augmented SPC Tornado Database (1950-2016)

A.1. Introduction

The Storm Prediction Center (SPC) tornado database provides the data that is typically used in tornado climatology and risk modeling. SPC links together the tornado county segment data obtained from the National Center for Environmental Information (NCEI) Storm Events Database in order to produce full tornado track data. SPC has made edits and corrections to the data over the years. Similarly, the NCEI Storm Events Database and its sources have evolved over time. As a result of the evolution, maintenance, and updating activities of the various databases since 1950, along with transitions from printed to digital records, one would expect some errors and anomalies in the current tornado data.

During the course of the tornado risk mapping project, we discovered possible errors and anomalies in the SPC database. To capture these discoveries, we developed “cleansed” data for several of the SPC fields. In addition, we found it useful to augment the SPC tornado data fields with additional data from the NCEI Storm Events Database. As part of this process, the tornado county segments in the Storm Events Database were linked together into full tornado tracks and matched, when possible, to their corresponding tornadoes in the SPC database. Our augmented data fields include: (1) tornado path direction; (2) the NCEI Weather Forecast Office (WFO) that produced the rating; (3) the NCEI source of the tornado report; and (4) the NCEI tornado start/end date and time.

The cleansed SPC database with augmented data fields created and described in this Appendix documents the augmented SPC data used in this project to produce tornado wind speed risk maps for the U.S. This augmented database for the years 1950-2016 can be obtained from NIST (DOI: x). This database does not contain probabilistic modeling results, nor bias corrections of the type discussed in the body of this report. It includes some cleaning of errors we were able to discover and several augmented fields. The augmented fields are separated from the SPC data. This separation allows the user to see each element of cleansing/augmentation on a tornado-by-tornado basis. The data cleansing performed herein does not include the tornado intensity field (F or EF rating). Finally, the SPC data corrections/cleansing should not be considered to consist of a systematic review of the entire database, but rather specific issues we discovered incidental to our work.

The work described herein was originally performed on data through 2015 and reported in a Poster Session at the 2016 American Meteorological Society (AMS) Severe Local Storms Conference (SLS) in Portland Oregon. Information presented in this appendix has been updated to reflect that the augmented database covers the years 1950-2016, instead of 1950-2015, as originally reported in the 2016 SLS.

A.2. Background and Data Format

Two of the main digital databases that contain temporal tornado records are the NCEI Storm Events Database (NCEI, 1950-2016), herein referred to as the NCEI database, and the SPC tornado database (NOAA, 2016a). The SPC and the NCEI databases contain key inputs in the development of tornado wind speed risk maps for engineering design (Phan et al., 2016). Other tornado databases that are referenced in this work are Grazulis' Significant Tornadoes (Grazulis, 1993) and the NCDC Storm Data publication (NCEI, 1959-2015), which we will refer to as "SDP".

The NCEI Database contains records entered by the National Weather Service (NWS) from 1950 to present. This database consists of records for all types of significant weather phenomena, including tornadoes. Tornado records in this database are segmented, i.e. entered as separate lines of data, by the county in which the tornado occurred. If a tornado only took place in one county, then the data entry includes the information for the entire tornado track, although if it crossed through more than one county, then the overall tornado track information is gained by linking the individual county segments.

The SPC database is created by extracting the tornado data from the NCEI database and linking together the county segments into full track tornado data. We note that if at any point in time the SPC finds conflicting information on a tornado in the SPC database, including missing tornadoes, they will correct the data as seen fit. NCEI on the contrary does not correct data after it is submitted to them by the local NWS Weather Forecast Offices (WFOs). Hence, the NCEI and SPC tornado databases do not necessarily contain the exact same tornado data (Speheger, 2002).

Table A-1 provides a summary of the fields in the augmented database. Each row in the database represents a tornado. Column 1 contains a unique ID number for each tornado.

A.3. SPC Data

Columns 2 through 22 are fields from the SPC database, which are described in the SPC Tornado, Hail, and Wind Database Format Specification document (SPC, 2010), which is shown as a table at the end of this appendix.

The user should interpret the zero entries in the SPC ending latitude and longitude columns (Columns 18 and 19) as missing data.

The 1950-2016 SPC tornado database was downloaded from the SPC website in June of 2017.

A.4. Augmented Fields

Columns 23 to 27 contain augmented fields. Columns 23 and 24 contain corrected path lengths and widths. The corrections include an F/EF4 and F/EF5 path length and width correction, a year 1999 path width correction, path length and width minimal values, and unrealistically small path aspect ratio. These three corrections are described in Section B.4.1. Column 25 gives whether the tornado has both starting end location information. Columns 26 and 27 contain computed path direction and translation speed, respectively. The entry -9 in the augmented fields denotes that the augmented field could not be computed from the available data

A.4.1. Path Length and Width Augmentation (Cols. 23 and 24)

Path length and width augmentation has included the following elements: review of small values; F/EF4-5 tornado length and width review; year 1999 path width corrections; setting consistent default minimums; and aspect ratio corrections for tornadoes with width greater than length. The following paragraphs describe these updates.

Table Error! No text of specified style in document.**-1. Summary of Fields in the Cleansed and Augmented Database**

	Column	Field Name	Number of Known Values
	1	Unique_ID	61,020
SPC Database	2	Year_SPC	61,020
	3	Month_SPC	61,020
	4	Day_SPC	61,020
	5	Hour_SPC	61,020
	6	Minute_SPC	61,020
	7	Time_Zone_SPC	61,020
	8	State_SPC	61,020
	9	stf_SPC	61,020
	10	stn_SPC	61,020
	11	Fscale_SPC	60,990
	12	Injuries_SPC	61,020
	13	Fatalities_SPC	61,020
	14	Property_Loss_SPC	37,721
	15	Crop_Loss_SPC	631
	16	Start_Lat_SPC	61,020
	17	Start_Lon_SPC	61,020
	18	End_Lat_SPC	35,881 (different than start lat.)
	19	End_Lon_SPC	35,881 (different than start longitude.)
	20	FC_SPC	1,843 (FC=1)
	21	PL_SPC (mi)	61,020
	22	PW_SPC (yds)	61,020
Augmented Fields	23	PL_Corrected (mi)	61,020
	24	PW_Corrected (yds)	61,020
	25	PT1_LN0	61,020
	26	Direction (deg)	35,881
	27	Trans_spd_mph (mph)	18,338
NECI Database	28	NCEI_Match	56,342
	29	NCEI_Year_s	56,342
	30	NCEI_Mo_s	56,342
	31	NCEI_Day_s	56,342
	32	NCEI_Hr_s	56,342
	33	NCEI_Min_s	56,342
	34	NCEI_Year_e	56,342
	35	NCEI_Mo_e	56,342
	36	NCEI_Day_e	56,342
	37	NCEI_Hr_e	56,342
	38	NCEI_Min_e	56,342
	39	NCEI_Fscale	54,454
	40	NCEI_PL (mi)	49,442 (PL≠0)
	41	NCEI_PW (yds)	56,283 (PW≠0)
	42	NCEI_Source	20,254
	43	NCEI_WFO	24,873

Note: 1 mi = 1.609344 km; 1 yd = 0.9144 m; ; 1 mph = 0.44704 m/s

Review of Small Path Lengths and Widths. One problem that arises in the tornado database is the existence of unrealistically small path length (PL) and path width (PW) values that appear to be default values. A comparison of the Storm Data publication, the NCEI database, and the SPC tornado database gives insight on these default values. In many cases from 1950 to the mid-1980s, a tornado path length shows as zero if it was missing from Storm Data tables or reported as “short”. Similarly, if a tornado’s path width was missing from Storm Data tables or reported as “narrow,” it was often in the Storm Events database as 33 yards (30.2 m). Comparing the small path widths and lengths in the Storm Events database, it was found that from 1950 to 1998, all zero length tornadoes in Storm Events are equal to 0.1 miles (0.16 km) in the SPC tornado database, and most cases of path widths equal to 33 yards (30.2 m) in Storm Events are equal to 10 yards (9.1 m) in SPC database. While in some cases these default values were used when tornadoes were in fact small, research using Storm Data narratives and entries in Grazulis’ (1993) database showed that in some cases tornadoes that were notable events in actuality have small (or default) path length and width values in the SPC database.

Figure A-1 and Figure A-2 support these observations, showing the fraction of tornadoes by year with path lengths and path widths equal to small values. The figures reveal disproportionately high fractions of tornadoes with path lengths equal to 0.1 miles (0.16 km), and tornadoes with path widths equal to 10 yards (9.1 m). We suspect that these minimal values, which are used disproportionately compared to other small values, are default values that were likely unknown or not measured.

Figure A-1 shows a disproportionately large fraction of path lengths equal to 0.1 miles (0.16 km) from 1950 to 1985 and from 1992 to approximately 2006, suggesting that 0.1 miles (0.16 km) was used as a default path length in those years. A spike in 0.2 miles (0.32 km) from 1986 to 1991 suggests that 0.2 miles (0.32 km) was probably used as a default path length. In 2007, the fraction of path lengths equal to 0.1 miles (0.16 km) decreased significantly. The amount of path lengths less than or equal to 0.1 miles (0.16 km) also decreased, but less so. These decreases may correspond with an increase in precision in the path length values from one decimal place to two in 2007. We suspect that many of these small values from 2007 to 2015 are default path lengths that have increased precision.

Figure A-2 shows that from 1950 to the mid-1990s there are a large amount of path widths equal to 10 yards (9.1 m), compared to other similar small values, such as 20 yards (18.3 m). In the mid-1990s the fraction of tornadoes with path widths equal to 10 yards (9.1 m) decreased significantly, and the proportion of tornadoes with path widths equal to 50 yards (45.7 m) increased to a significantly higher amount than other similar small path width values. While this increase could have been caused by the NWS policy change to record maximum tornado path width instead of mean path width, which occurred around the same time, more investigation is needed on this increase in path widths equal to 50 yards (45.7 m).

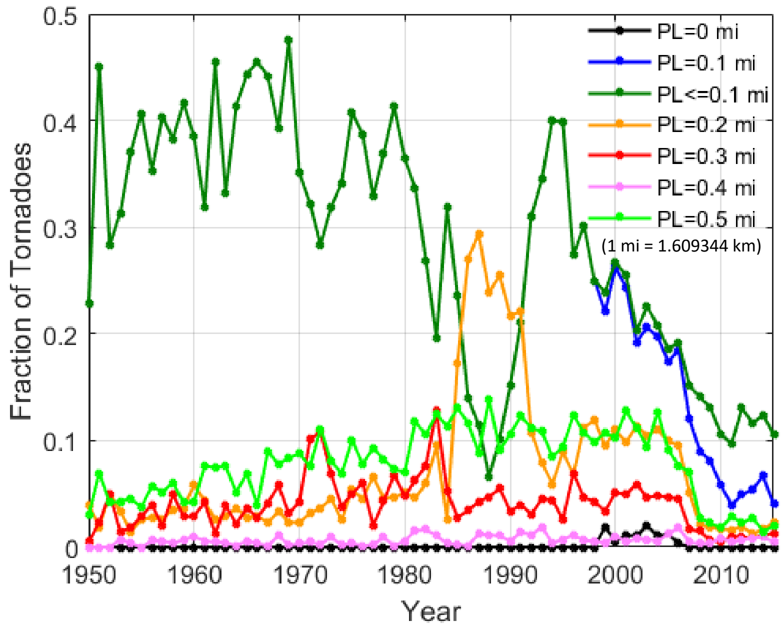

Figure Error! No text of specified style in document.**-1. Fraction of Tornadoes by Year with Small Path Lengths**

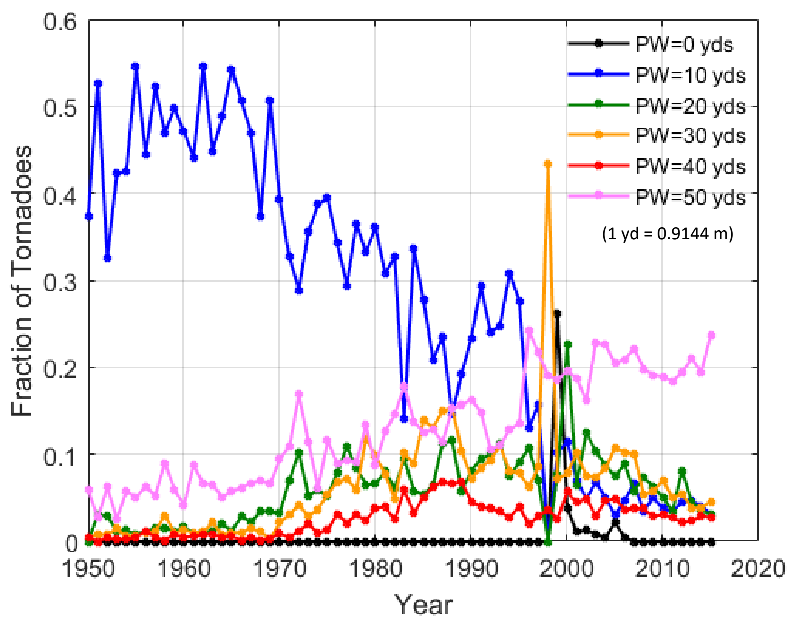

Figure Error! No text of specified style in document.**-2. Fraction of Tornadoes by Year with Small Path Widths**

PL and PW Review for F/EF4 and F/EF5 Tornadoes. We reviewed all F/EF4 and F/EF5 tornadoes in the SPC with default minimal path lengths (≤ 0.1 mi) (≤ 0.16 km) or default minimal path widths (≤ 10 yd) (≤ 9.1 m). The 6 F/EF4-F/EF5 events with path lengths ≤ 0.1 mi (≤ 0.16 km) and the 33 F/EF4-F/EF5 events with path widths ≤ 10 yd (≤ 9.1 m) were individually researched to determine the most accurate path length and width values for these events.

The SDP, the NCEI Storm Events Database, and Grazulis' Significant Tornadoes Database were used to research individual tornadoes and compare the records with those in the SPC database. Table Error**! No text of specified style in document.**-3 summarizes the information found for each event and provides the augmented PL and PW values for these tornadoes resulting from the research. This effort resulted in information allowing us to change 5 of the 6 F/EF4-F/EF5 tornadoes with path lengths ≤ 0.1 mi (≤ 0.16 km) and 29 of the 33 F/EF4-F/EF5 tornadoes with path widths ≤ 10 yd (≤ 9.1 m).

In order to keep the SPC data as consistent as possible when making corrections, information from the NCEI Storm Events database and the Storm Data publication superseded data from the Grazulis database because the NCEI Storm Events database and the Storm Data publication have the same source as the SPC database. In Table Error**! No text of specified style in document.**-3, the source of each corrected value in the "Updated" column is highlighted in yellow. Path width and length changes to these 33 tornadoes resulted in a 5,804% increase in area of these 33 tornadoes. However, when considered with the total population of F/EF 4's and 5's, the area increases are 5.4% and 2.3% for F/EF4 and F/EF5 tornadoes, respectively. The mean areas of F/EF4 and F/EF5 tornadoes for the entire database before and after the corrections are shown in Table Error**! No text of specified style in document.**-2. These corrections suggest that additional work to research individual events would be beneficial.

Table Error! No text of specified style in document.**-2. Mean Area of F/EF4 and F/EF5 Tornadoes in the Entire Database Before and After F/EF4-5 Corrections**

Rating	Mean Area (mi^2) Before	Mean Area (mi^2) After
F/EF4	10.63	11.20
F/EF5	20.40	20.87

Note: 1 mi^2 = 2.589988 km^2

Year 1999 Path Width Corrections. In our review of the SPC database, we noted a peak in 1999 of tornadoes with path widths equal to zero, where 26.2% of tornadoes have path widths equal to zero. A review of other years indicated that number of zero path width tornadoes was an anomaly (See Figure A-2). This percentage is zero or close to zero for all other years. A comparison of individual events in the SPC tornado database with individual events in the NCEI Storm Events database revealed that in 1999 any tornado in the NCEI Storm Events Database with a path width equal to a number ending in "5" in the NCEI Storm Events database is equal to "0" in the SPC database. This difference affects the path widths of F0 through F3 tornadoes, with 32%, 20%, 12% and 14% of F0-F3 tornadoes, respectively, having path widths equal to 0 yards (0 m). We concluded this was likely some type of inadvertent administrative error and corrected these path width anomalies in the augmented database.

The path width error for tornadoes in 1999 with original widths ending in a "5" was therefore corrected by replacing the zero path widths with the path widths from the matched NCEI Storm Events database tornadoes. This effort resulted in 246 of the original 350 tornadoes with zero path lengths being corrected to non-zero values. Table A-4 shows the effects of these corrections on the 1999 mean path widths and on the mean path widths of all the data.

These corrections caused a modest increase in mean path widths for 1999 and a minor change to the mean path widths for 1950-2016. Obviously, for certain applications, these effects may be greater if the cleansed data is averaged over fewer years and/or more heavily impacted areas.

Table Error! No text of specified style in document.**-3. Summary of Individual Corrections to Default F/EF4-5 Path Lengths and Widths. PW (yd), PL (mi), PA (mi^2). Source of Each Correction is Highlighted in Yellow.**

Date	Location	Rating	SPC			NCEI		Storm Data Pub.		Grazulis		Updated		
			PW	PL	Area	PW	PL	PW	PL	PW	PL	PW	PL	Area
3/21/1952	Cross, Co., AR	4	880	0.1	0.05	880	0					880		
3/21/1952	Lonoke, AR	4	10	7.6	0.04	417				800	70	417	7.6	1.8
5/1/1953	Choctaw Co., AL	4	100	0.1	0.01	100	0			200	10	100	10	0.57
6/27/1953	Adair Co., IA	5	100	0.1	0.01	100	0			200	10	100	10	0.57
5/10/1953	Wayne, IA	4	10	6.4	0.04	33	6.4			200	8	200	6.4	0.73
5/10/1953	Hancock, … IA	4	10	26.6	0.15					800	28	800	26.6	12.09
5/1/1954	Pottawatomie, …OK	4	10	59.2	0.34	33	59.2			800	30	800	59.2	26.91
6/27/1955	Scottsbluff, Morrill, NE	4	10	26	0.15	33	26			400	11	400	26	5.91
7/7/1955	Lincoln/Lyon, MN	4	10	30	0.17	33	30			200	20	200	30	3.41
1/22/1957	Sequoyah, OK	4	880	0.1	0.05	880	0			50	5	880	5	2.5
12/19/1957	Columbia, Ouachita, AR	4	10	17.7	0.1	33	17.7			300	15	300	17.7	3.02
4/15/1958	Polk, Co., FL	4	300	0.1	0.02	300	0			300	5	300	5	0.85
5/4/1960	Pottawatomie, OK	4	10	8	0.05	33	8			400	6	400	8	1.82
5/5/1960	Sequoyah, OK	4	10	5.4	0.03	33	5.4			200	5	200	5.4	0.61
5/19/1960	KS	4	10	20.6	0	33	20.6	.5-3 mi					20.6	
5/30/1961	NE	4	10	48.1	0.27	33	48.1	narrow	40	400	45	400	48.1	10.93
6/29/1961	MT	4	10	15.9	0.09	33	15.9		15				15.9	
5/5/1964	Greeley, Boone, NE	4	10	51.2	0.29	33	51.2	narrow	60				51.2	
4/11/1965	St. Joseph, Elkhart, IN	4	10	21.2	0.12	33	21.2			400	22	400	21.2	4.82
4/11/1965	Branch, … MI	4	10	80.5	0.46	1760	80.5	.5-1mi	70			1760	80.5	80.5
4/11/1965	Blackford, …IN; …OH	4	10	52.5	0.3	33	52.5			600	55	600	52.5	17.9
5/8/1965	Howard, NE	4	10	78.9	0.45	33	78.9	narrow	80	400	90	400	78.9	17.93
5/8/1965	Hall, … NE	4	10	125.7	0.71	33	125.7	narrow	120	400	85	400	125.7	28.57
6/10/1967	Blaine Co., OK	4	10	0.1	0	33	0			100	5	100	5	0.28
2/21/1971	Warren, … MS	4	10	65.2	0.37	33	65.2		69	800	70	800	65.2	29.64
4/19/1972	Carter, … OK	4	10	28.2	0.16	33	28.2	50	20-25	50	27	50	28.2	0.8
4/3/1974	Anderson, … KY	4	10	79.4	0.45	33	80			800	36	800	36	16.36
4/3/1974	Perry, … IN	5	10	68	0.39	33	68	700	67	1000	62	700	68	27.05
4/3/1974	Hancock, … IN	4	10	18.9	0.11	33	18.9	1000	21	800	20	1000	18.9	10.74
4/3/1974	Jefferson, … KY	4	10	18.5	0.11	33	18.5			200	21	200	18.5	2.1
4/3/1974	Hardin, … KY	4	10	37.9	0.22	33	37.9			400	42	400	37.9	8.61
4/3/1974	Green, … KY	4	10	20.2	0.11	33	20.2			800	29	800	20.2	9.18
4/3/1974	Cumberland, … KY	4	10	38.4	0.22	33	38.4	440-1760	35	800	30	800	38.4	17.45
4/3/1974	Garrard, … KY	4	10	31.9	0.18	33	31.9	133-400	22	300	35	300	31.9	5.44
4/3/1974	Wayne, McCreary, KY	4	10	16.1	0.09	33	16.1			500	26	500	16.1	4.57
6/18/1975	Custer, NE	4	10	15.2	0.09	33	15.2	100-500			15	300	15.2	2.59
6/3/1980	Allegheny, … PA	4	10	11.8	0.07	33	11.8		14		14		11.8	
4/27/1984	Waukesha, WI	4	10	6.5	0.04	10	6.5	100	6.5	100	6.5	100	6.5	0.37
Total Area					6.04	Total Area								356.62
Mean Area					0.18	Mean Area								10.81

Note: 1 yd = 0.9144 m; 1 mi = 1.609344 km; 1 mi^2 = 2.589988 km^2

Table Error! No text of specified style in document.**-4. Mean Path Widths for Year 1999 and All Years Before and After 1999 Path Width Corrections**

Rating	Mean PW (yds.): Year 1999		Mean PW (yds.): All Years	
	Before	After	Before	After
F0	31.64	39.05	42.12	42.33
F1	89.46	96.78	97.58	97.69
F2	176.09	185.72	175.79	177.91
F3	386.35	388.8	365.68	365.73

Note: 1 yd = 0.9144 m

Minimal Path Width and Length. After the corrections described above were made, any path lengths less than 0.1 miles (0.16 km) were set equal to 0.1 miles (0.16 km) and any path widths less than 10 yards (9.1 m) were set equal to 10 yards (9.1 m). 336 path widths and 825 path lengths were affected by these minimal requirements.

Aspect Ratio < 1. Tornado path aspect ratio (dimensionless metric) is defined as path length divided by path width. Aspect ratios of tornadoes in the SPC average from 55 for F/EF0 to over 100 for F/EF 3-5 tornadoes. The mean, median, and standard deviation of aspect ratios have been trending down since the early 1980s. Aspect ratios in the EF era are somewhat less than those in earlier eras.

Aspect ratios less than one are assumed to be outliers in the data, since the tornado is wider than it is long. This result is not physically realistic for either a stationary or translating vortex. The augmented path length and width data therefore includes corrections for 175 tornadoes with reported path widths greater than the path length. In these cases, we set the path width equal to the path length based on the assumption that the path length is the more likely correct value.

A.4.2. Point or Line Tornado Information (Col. 25)

The SPC database includes latitude and longitude fields for the tornado starting and ending positions (Columns 16-19). We added a field that indicates whether or not both starting and ending positions are known for each tornado. The “PT1_LN0” field in Column 25 contains a “1” if the tornado data only consists of one latitude/longitude point (point tornado) or if the starting and ending points are identical. A “1” therefore identified a “point” tornado. The field contains a “0” otherwise, which can be inferred to be “line” tornado, for which a direction can be computed. Within this context, there are 25,139 line tornadoes in the SPC latitude longitude data. This can be computed by counting the zeros in Column 25.

The distinction of point or line tornado is applicable to the computation of tornado direction. We note that the SPC Path Length data (Column 21) includes only 119 zero length tornadoes. Hence, the vast majority of point tornadoes, as denoted in Column 25, actually have a length denoted in Column 21. Many (34,569) of the early chronological entries in the SPC database have zeros entered for latitude and longitude ending points, implying missing ending point data for these tornadoes.

A.4.3. Computed Path Direction (Col. 26)

Path direction, shown in Column 26, is calculated for line tornadoes. For point tornadoes, we show a "-9" in Column 26, signifying that the direction is unknown.

Path directions are calculated using MATLAB (2018) mapping toolbox with the "great circle approach" for curved earth surface. We compared these great circle path directions with the MATLAB "rhumb line approach" and found no material differences. These calculations produced 25,139 tornado directions.

A right-hand Cartesian system is used to report the direction angle (degrees) of the tornado path where the x-axis is pointed East with positive direction angles measured counterclockwise (see Figure A-3). Figure A-4 shows the histogram of path direction data in Column 26 in 15° bins. For this figure, we plotted angles greater than those in the 210° bin as negative angles from the X-axis. With this type of transformation, one can readily fit a normal or Student's T distribution to tornado path data. Path directional data may have some EF-Scale and PL dependencies

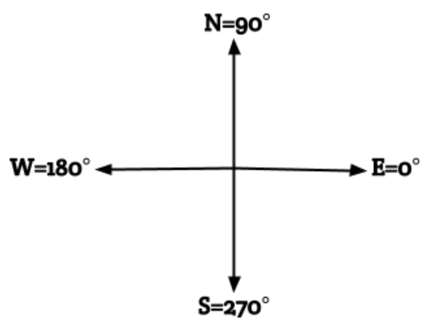

Figure Error! No text of specified style in document.**-3. Angle Convention for Path Direction**

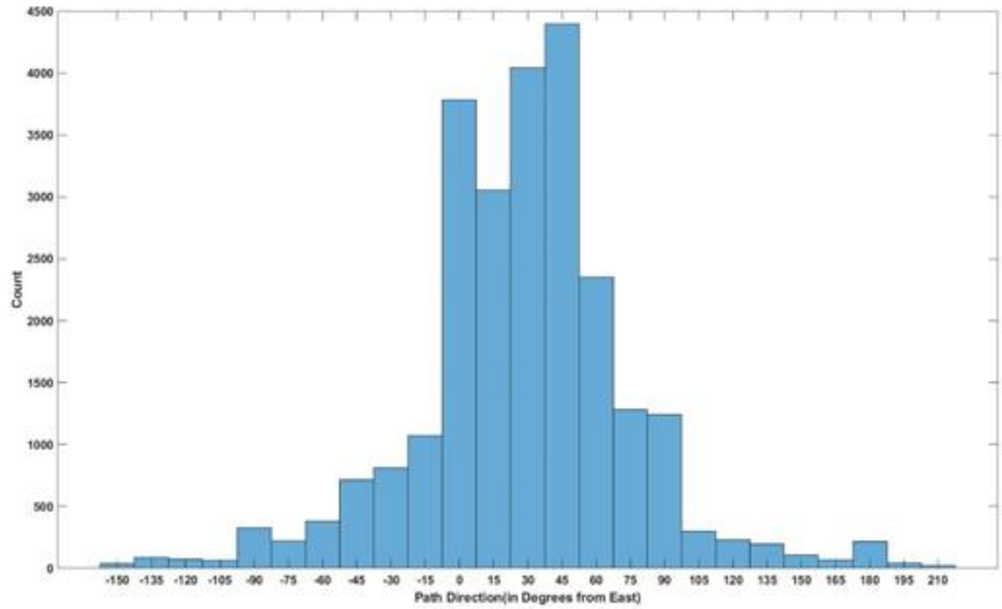

Figure Error! No text of specified style in document.**-4. Tornado Path Direction Histogram**

As discussed in Section 3.4.2, the tornado path direction data includes rounding errors from the number of significant latitude/longitude digits in the historical SPC records. In addition, anomalous spikes exist at 0, 90, 180, and 270°. These spikes are likely from observers or database administrators reusing starting and ending latitude/longitude values. Fitting a probability distribution to the data is one convenient way to minimize the impact of these limitations.

A.4.4. Translational Speed (Col. 27)

NCEI Tornado data, which was augmented to the SPC data (described in the following section), contains both a tornado start and end time. We use these times and the corrected SPC path length (Column 23) to compute an estimated average translational speed:

$$Translational\ Speed = \frac{PL(mi)}{End\ Time_{NCEI} - Start\ Time_{NCEI}(hours)} \quad \textbf{(A-1)}$$

The NCEI time data in the above equation was extracted from Columns 37-38 and 32-33, respectively. The path length data in the above equation comes from Column 23. The computed translational speed values are limited to a range of 1 mph to 60 mph (0.4 m/s to 27 m/s) in order to remove likely erroneous data. This range is generally consistent with the literature. For example, Alexander and Wurman (2008) analysis of Doppler on Wheels (DOW) mobile radar observations from 69 different tornadoes from 1995 to 2003 give translational speeds ranging from near stationary to 56 mph (25.0 m/s), with a median value of 29 mph (13.0 m/s). Translational speed values falling outside of 1 mph to 60 mph (0.4 m/s to 27 m/s) are set to “-9” signifying that they are unknown.

Figure **Error! No text of specified style in document.**-5 plots the mean translational speed by tornado rating and month. Figure **Error! No text of specified style in document.**-5(a) shows the mean translational speed increasing with F/EF scale. Figure Error**! No text of specified style in document.**-5(b) shows the mean translational speed reaches a minimum in the summer months.

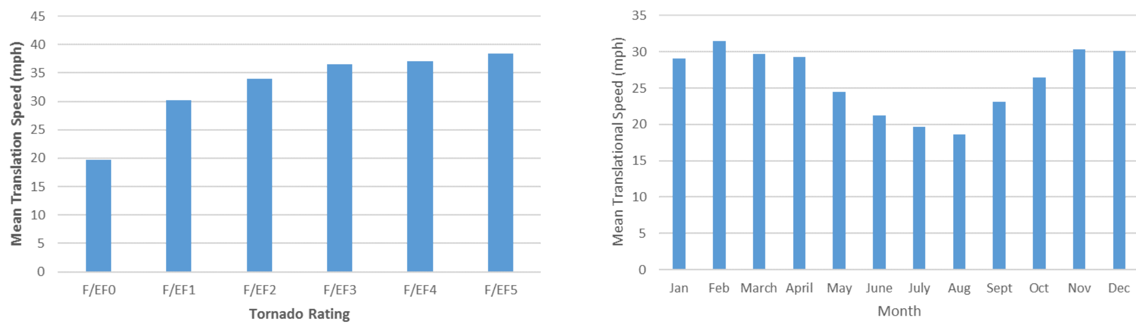

a. Tornado Path *b. Month*

Figure Error! No text of specified style in document.**-5. Mean Tornado Translational Speed in mph (1 mph = 0.44704 m/s)**

A.5. Augmentation of Data Fields from NCEI (Storm Data)

The NCEI Storm Events Database contains additional beneficial information that is not included in the SPC Tornado Database. For example, the NCEI database includes the WFO that produced the rating, the source of the rating, and the tornado ending date and time. To facilitate the use of this information, we “matched” the NCEI database tornadoes to the SPC database tornadoes.

The first step in the process required that the tornado county segments in the NCEI Storm Events database be linked together to form full track data. Tornado segments from October 2006 to 2016 were matched using the methodology described in the NCEI Storm Data Export Format document (NCEI, 2014). The tornado county segments from 1950 to September 2006 were matched based on their starting and ending date and time as well as their starting and ending latitude and longitude. If not already in Central Standard Time (CST), NCEI tornado starting and ending times were converted to CST to match the SPC database.

Once the county segments in the NCEI Storm Events database were linked together, the full track tornado data were matched to the SPC tornadoes based on their starting and ending location and their date and time. 56,342 of the 61,020 total tornadoes in the SPC tornado database were matched to NCEI tornadoes. We were unable to match all of the SPC tornadoes to tornadoes in NCEI for several reasons. One reason is that the two databases do not contain all of the same tornadoes, as described above. NCEI is missing some tornadoes from 1993, and SPC corrects their data, including the addition or deletion of tornadoes. Secondly, there are likely some errors in the linking of the NCEI tornado county segments, which would produce differences between the NCEI and the SPC tornadoes. Finally, the use of an automated approach to match tornadoes has limitations. For example, slight differences or errors in the location or time data of a tornado in either database might not result in a match.

Since our tornado matching approach was limited to comparisons of position, date, and time and we did not use any other criteria (such as F/EF scale, PL, PW, etc.), our matching approach was not unique. However, for the EF era (2007-2016), we note that the approach produced exact EF, PL, and PW matches on about 96%, 92%, and 92% of the tornadoes. Hence, for our principal use of the EF era data for tornado risk modeling, the matching criteria seems sufficient for producing data such as translational speed and rating source. We did not use the NCEI data for any other purpose in this study.

NCEI_Match:

NCEI_Match = 1 if a NCEI Storm Events tornado was matched to the SPC tornado

NCEI_Match = 0 if a NCEI Storm Events tornado was NOT matched to the SPC tornado

NCEI_Year_s*:* NCEI Tornado Start Year

NCEI_Mo_s*:* NCEI Tornado Start Month

NCEI_Day_s*:* NCEI Tornado Start Day

NCEI_Hr_s*:* NCEI Tornado Start Hour (CST)

NCEI_Min_s*:* NCEI Tornado Start Minute (CST)

NCEI_Year_e*:* NCEI Tornado End Year

NCEI_Mo_e*:* NCEI Tornado End Month

NCEI_Day_e*:* NCEI Tornado End Day

NCEI_Hr_e*:* NCEI Tornado End Hour (CST)

NCEI_Min_e*:* NCEI Tornado End Minute (CST)

NCEI_Fscale*:* NCEI Tornado F/EF-Scale Rating

NCEI_PL*:* NCEI Tornado Path Length in miles

NCEI_PW*:* NCEI Tornado Path Width in yards

NCEI_Source*:* The “Source” field states the source of the tornado record in the database. The field began being used in 1998 in the NCEI database, although it wasn’t until 1999 that all NCEI tornado records included source information. The field is a free-fill entry, and from 1998 through 2016, 38 different source descriptions were entered into this field; one of which is “NWS Storm Survey.” Examples of other sources used include: emergency manager, law enforcement, newspaper, social media, etc. We reduced this field down to the following 3 sources:

NCEI_Source = 0, unknown source

NCEI_Source = 1, source is a NWS Damage Survey

NCEI_Source = 2, source is not a NWS Damage Survey

NCEI_WFO*:* The NWS weather forecast office that the report came from. This field began being used in 1996.

A.6. SPC Database Format Specification

The SPC tornado database format is available from (https://www.spc.noaa.gov/wcm/data/SPC_severe_database_description.pdf).

Appendix B. Tornado Climatology

B.1. Physiographic Regions

The Association of American Geographers appointed a committee in 1915 to create a map of physiographic divisions, described in Fenneman (1917). This work was then further extended and explained more fully in Fenneman (1928, 1931, and 1938). The physiographic regions were created based on the features that were believed to be the most outstanding characteristics of an area. The main principles considered are the geologic structure, process (erosive agency by which the original structure is being destroyed), and stage of the process in a location (Fenneman, 1928). In other words, these regions typically have similar topographic features, often being described by mountains, plateaus, and plains. The physiographic regions, consist of 8 major divisions, 25 provinces, and 85 sections, shown in Figure B-1.

Figure Error! No text of specified style in document.**-6. US Physiographic Regions**

B.2. Bi-linear Break Point (BBP)

Appendix B.2 describes a method developed by ARA (Hardy and Faletra, 2016) to assess the point of diminishing returns in cluster analysis. A goodness-of-fit criterion (R^2) is used to determine clusters of diminishing return for increasing numbers of clusters by measuring the proportion of response variation attributable to the independent variable(s) added to the model (Steel & Torrie, 1960). The R^2 for each variable is pooled over all variables and compared for each number of clusters. Plots of R^2 vs. the number of clusters is used to identify a "bi-linear breakpoint" (BBP) or "elbow", which is interpolated as a reasonable point of diminishing returns. We use this information to identify a reasonable number of tornado regions.

Since cluster identity is a categorical variable having no inherent ordering among the clusters, a categorical response modeling method must be used to calculate an R^2. Accordingly, the SAS STEPDISC procedure (SAS, 1992, pp. 1493-1509) was chosen for its ability to choose variables automatically, in a stepwise manner, and build an explanatory model for a fixed number of clusters. A partial R^2 is produced for each new variable added to the model, at each step. This coefficient is used to provide insight into whether or not one or more additional predictors may be useful in a more fully specified regression model. Calculating these for each number of clusters produces a record of which risk variables are driving the clustering procedure at each step over its entire run.

In Eq. (B-1) and Eq. (B-2), R^2 refers to the coefficient of determination and $R^2_{partial(i)}$ refers to the coefficient of partial determination (Anderson-Spreher, 1994). R^2 is given by

$$R^2 = (SST - SSE) / SST \qquad \textbf{(B-1)}$$

where SST is total sum of squared deviations about the mean and SSE is sum of squared residuals from a model. Eq. (B-1) is analogous to $R^2_{partial(i)}$ for simple regression. The coefficient of partial determination is given by

$$R^2_{partial(i)} = (SSE_{i-1} - SSE_i) / SSE_{i-1} \qquad \textbf{(B-2)}$$

where i is the step number in which variable x_i is added to the model. The partial R^2 can be seen as the proportion of unexplained variation reduced by adding x_i to the model. These are pooled, by averaging over all candidate variables for a model, at each clustering, and plotted against the number of clusters. Variables rejected have $R^2_{partial(i)} = 0$.

We evaluate the number of clusters by plotting the average added proportion of variance explained by the variables for each clustering against the number of clusters. The first clusters' variables will add much information (i.e. explain a lot of variance), but at some point the marginal gain of additional clusters begins to drop at the bi-linear break point, or, the "elbow". This "elbow" cannot always be unambiguously identified (Ketchen & Shook 1996). This method can also be traced to speculation by Robert L. Thorndike (1953).

Figure B-2 shows an application of the elbow method to Fisher's Iris Data (Fisher 1936). In effect, one looks for a cluster number representing a local maximally negative second derivative, imagining a minimally deviating, smooth curve connected the plotted points. In this example, the correct number of species is 3, identified by the "sharpest elbow." The 3 clusters in the data do, in fact, correspond mainly to the 3 species. Figure B-2 also identifies a "Bi-Linear" Elbow, or BBP, at Cluster 9. Since all of Fisher's measurements were lengths and widths of different features, the 9 clusters identified by bi-linear breakpoint in the plot, fit by least squares, represent different size characteristics within the species. In the development of tornado climatology regions, sharp elbows are not always apparent due to the fact there is no distinct true number of unique clusters (as in Fisher's data).

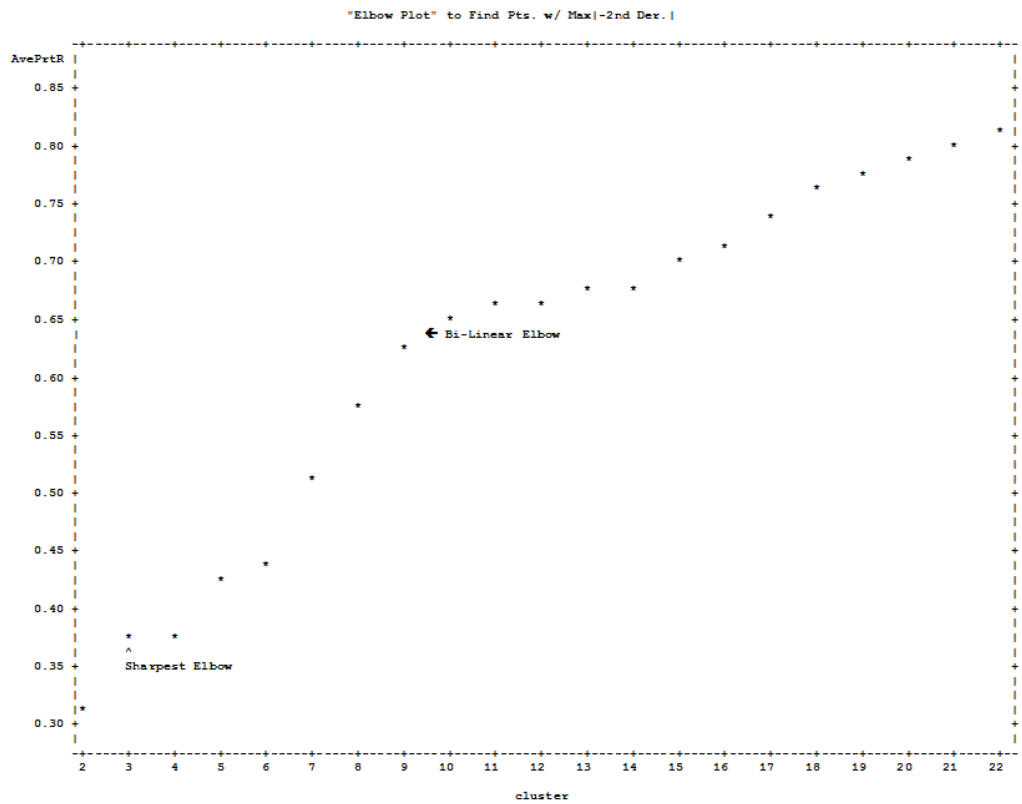

Figure Error! No text of specified style in document.**-7. Implemented Elbow Plot Example of Fisher's Irises (SAS, 1992)**

B.3. Cluster Analysis

In this appendix, we present cluster results for individual tornado metrics. This data shows how regions form based on a single variable. For most cases, we also include results with latitude and longitude to illustrate how position controls the clustering.[1] Latitude and longitude position has a notable impact on these one-variable results. These cases were run with the 1° and 2° grids. The Run ID corresponds to Column 1 in Table 2-3.

Table B-1 presents the matrix of runs illustrated in the appendix. All plots are shown at the break point. Each figure is labeled with the variables included and the run number. The 8 major physiographic division outlines are included as a white background line on these sets of plots. The run number is also given in Table B-1.

[1] For convenience, the plots with latitude-longitude have an LL in the lower right label.

Table Error! No text of specified style in document.**-5. Tornado Metric Cluster Analysis**

Run ID		Metric							Break Pt.		Page
1°	2°	TDPY	DIR	PP	OR-All	OR-M	OR-S	Lat-Long	1°	2°	
1	27	N							5	5	B-5
8	34	N						U	8	6	B-6
2	28		N						4	4	B-7
9	35		N					U	7	6	B-8
4	30			LN					4	5	B-9
11	37			LN				U	7	7	B-10
15	41				LN				3	4	B-11
16	42				LN			U	8	6	B-12
17	43					LN			4	4	B-13
18	44						LN		4	3	B-14

Notes: TDPY=Number of Tornado Days per Year; DIR=Computed Path Direction; PP=Point Strike Probability; OR= Occurrence Rate – All Tornadoes; OR-M= Occurrence Rate – Moderate Intensity Tornadoes (F/EF2-F/EF3); OR-S= Occurrence Rate – Strong Intensity Tornadoes (F/EF4-F/EF5); Lat-Long= Latitude Longitude; N=Normal Transformation of Metric; LN=Lognormal Transformation of Metric; U=Unadjusted Metric.

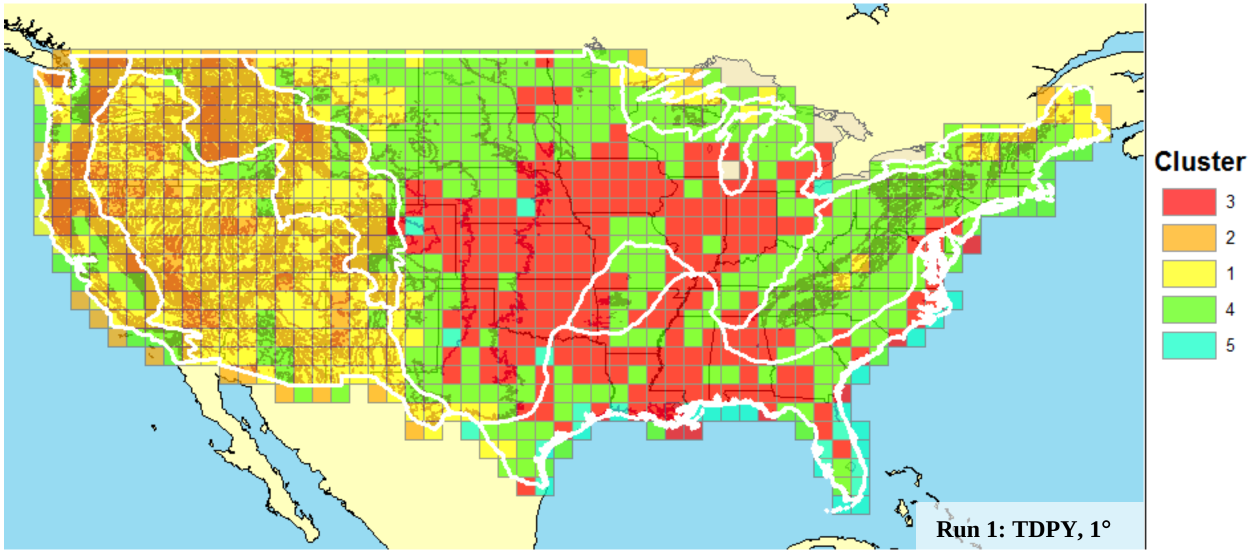
Cluster
3
2
1
4
5
Run 1: TDPY, 1°

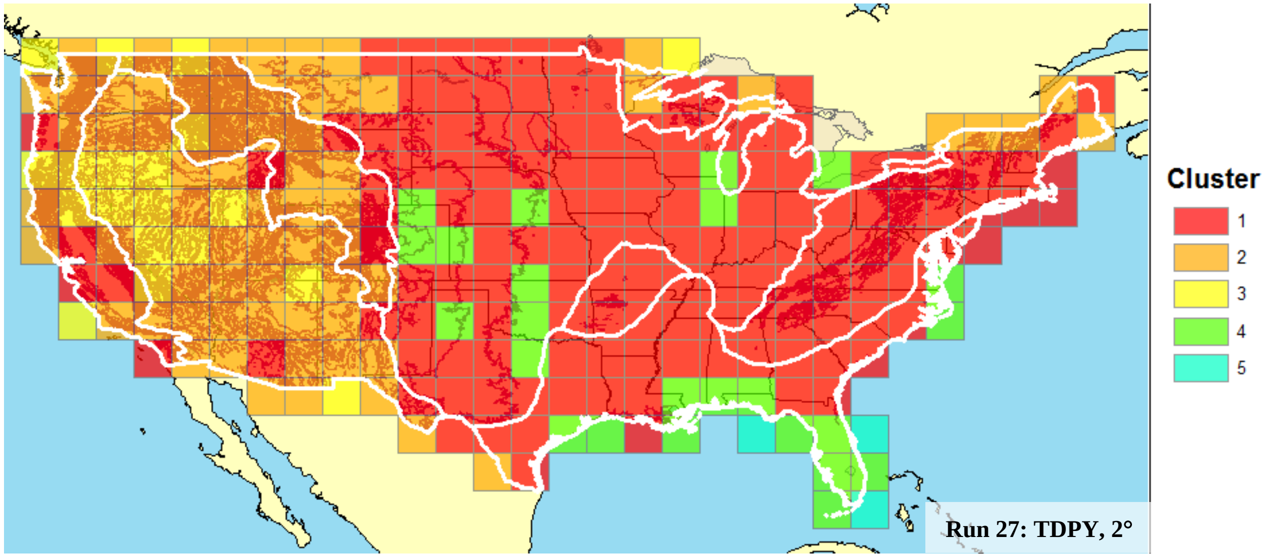
Cluster
1
2
3
4
5
Run 27: TDPY, 2°

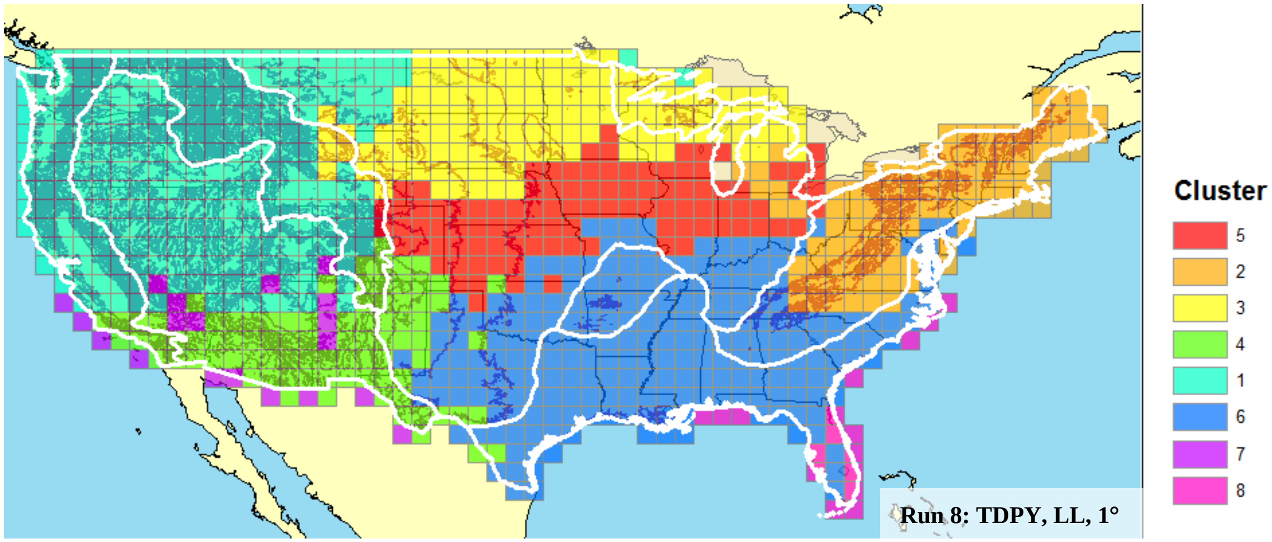
Cluster
5
2
3
4
1
6
7
8
Run 8: TDPY, LL, 1°

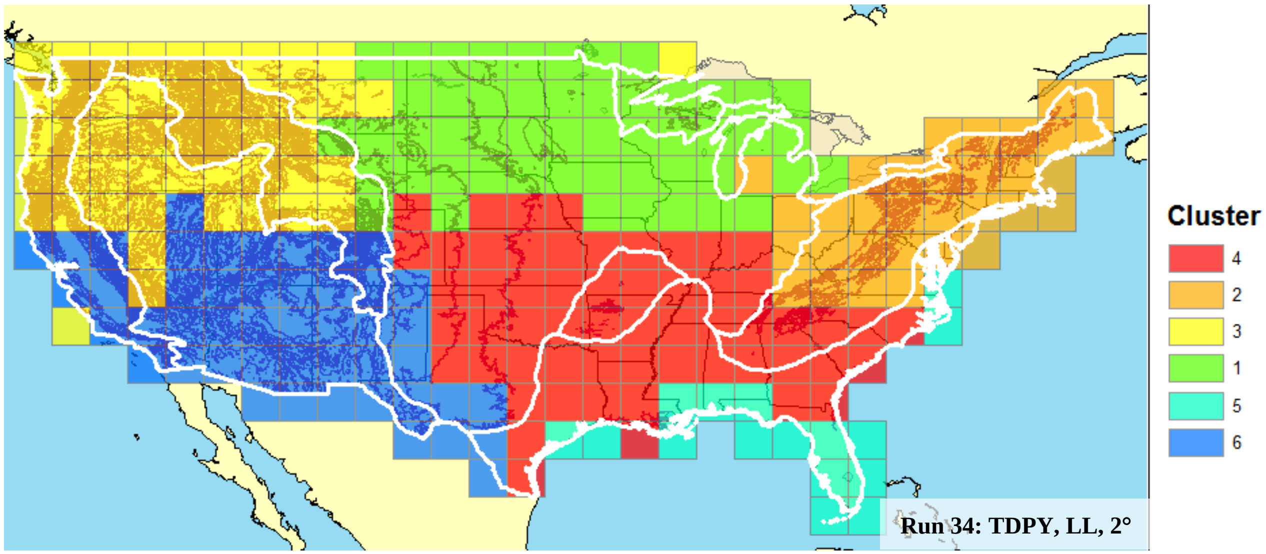
Cluster
4
2
3
1
5
6
Run 34: TDPY, LL, 2°

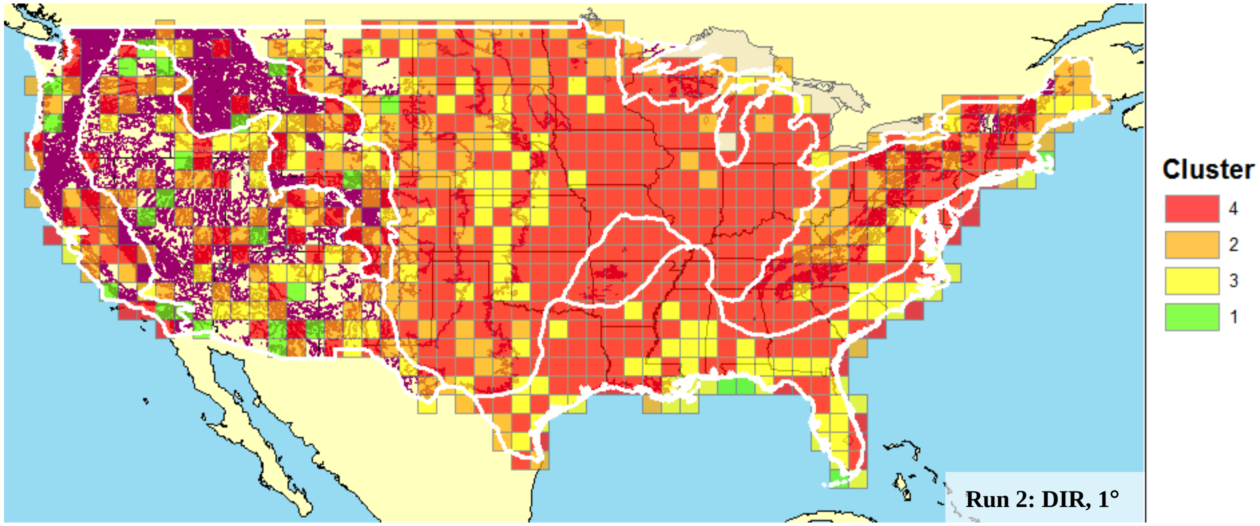
Cluster
4
2
3
1
Run 2: DIR, 1°

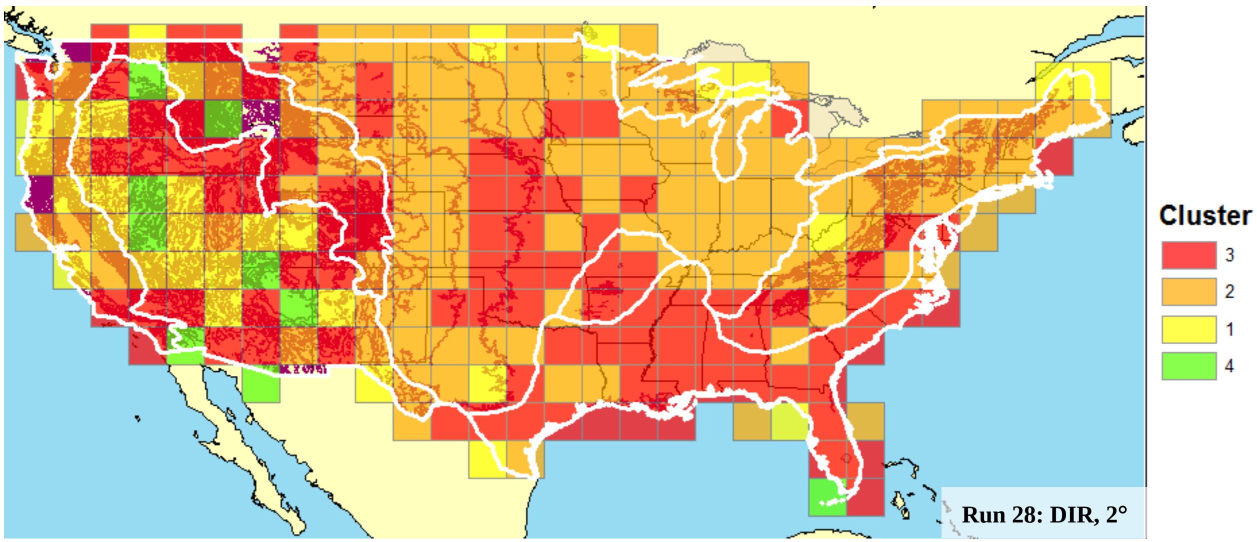
Cluster
3
2
1
4
Run 28: DIR, 2°

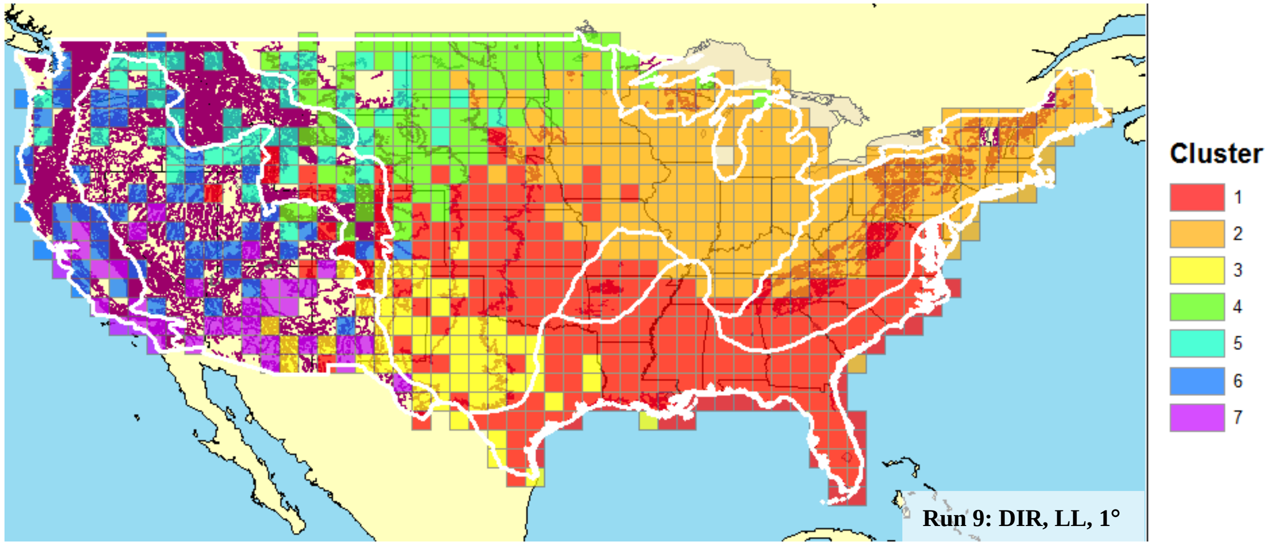
Cluster
1
2
3
4
5
6
7
Run 9: DIR, LL, 1°

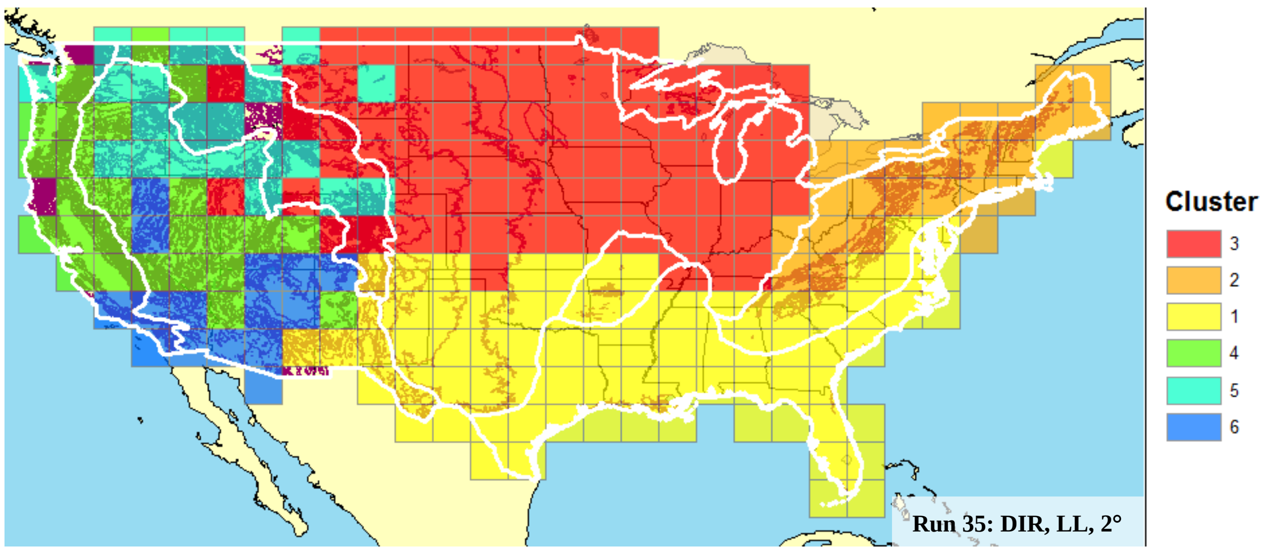
Cluster
3
2
1
4
5
6
Run 35: DIR, LL, 2°

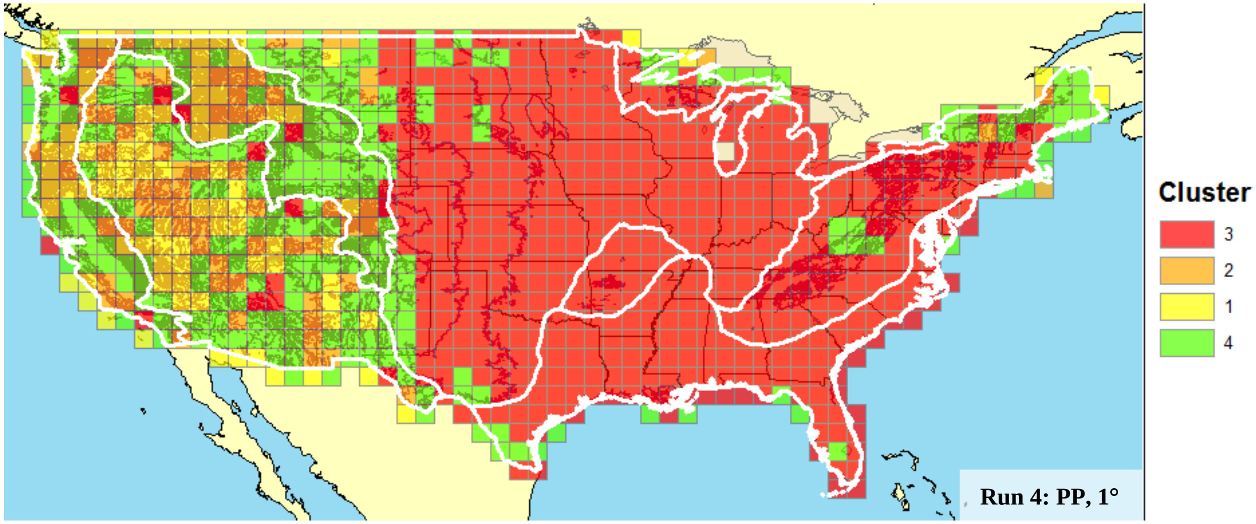
Cluster
3
2
1
4
Run 4: PP, 1°

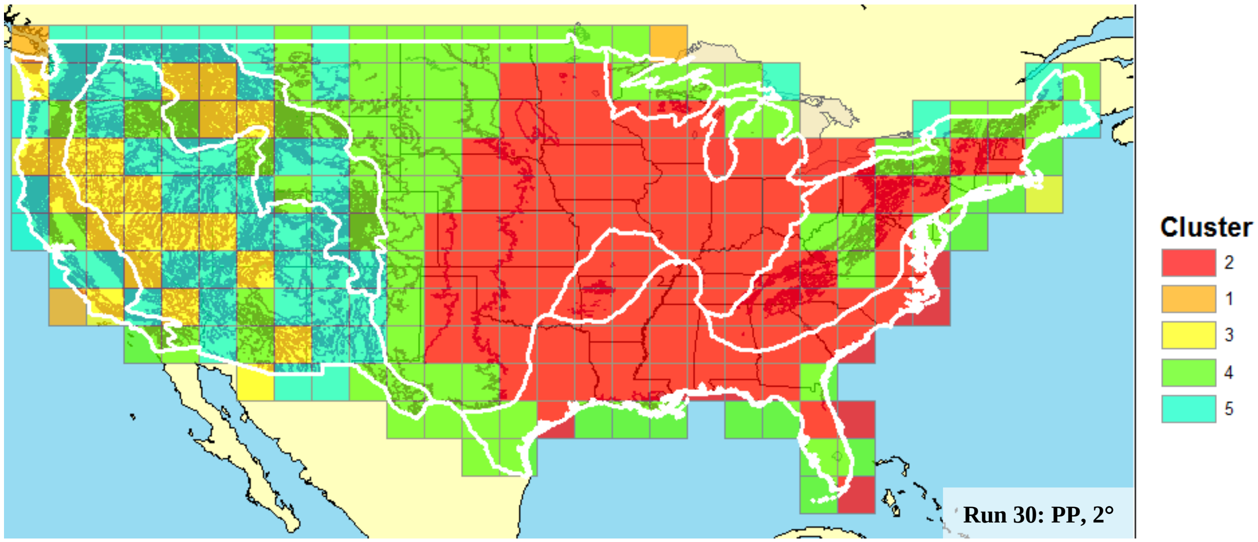
Cluster
2
1
3
4
5
Run 30: PP, 2°

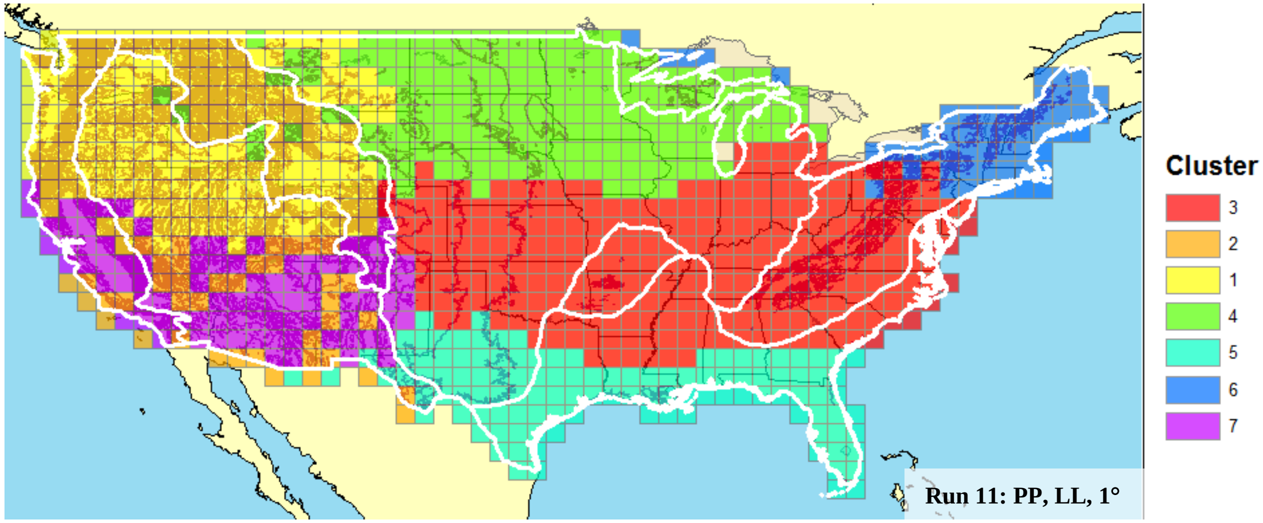
Cluster
3
2
1
4
5
6
7
Run 11: PP, LL, 1°

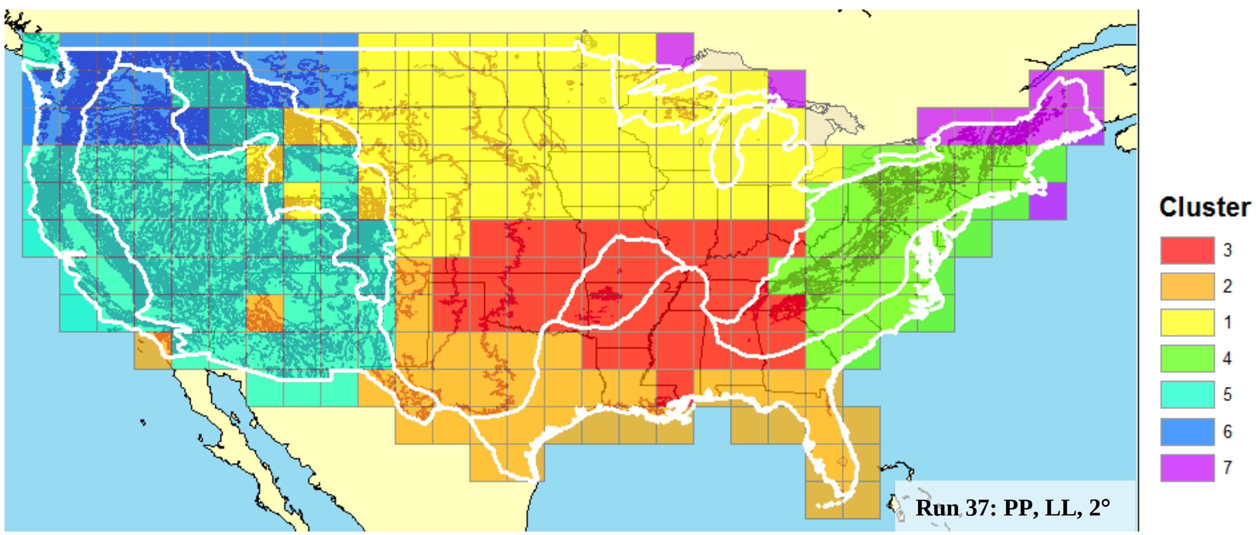
Cluster
3
2
1
4
5
6
7
Run 37: PP, LL, 2°

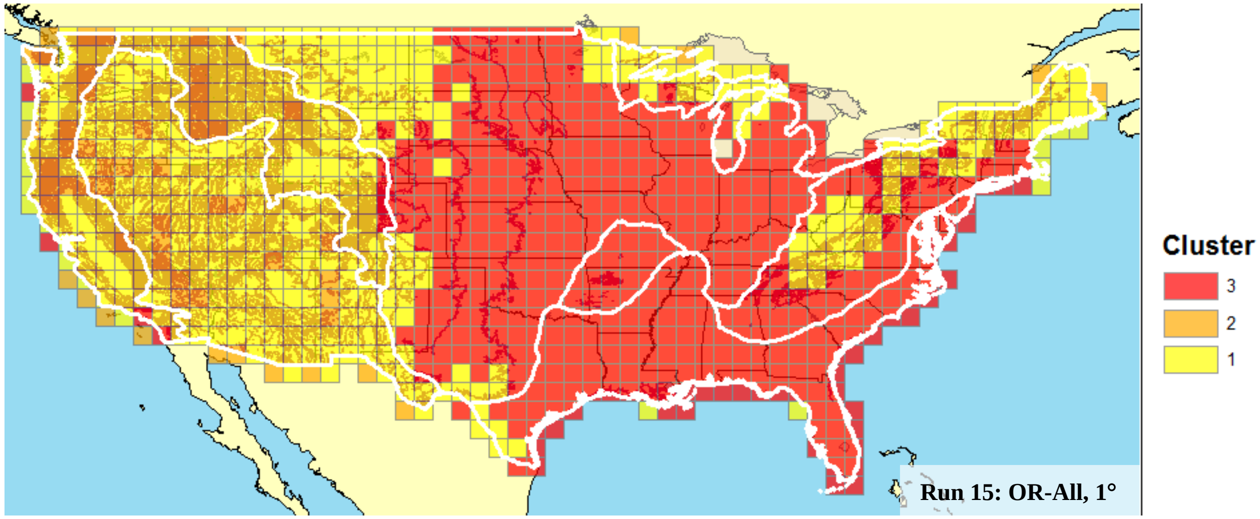
Cluster
3
2
1
Run 15: OR-All, 1°

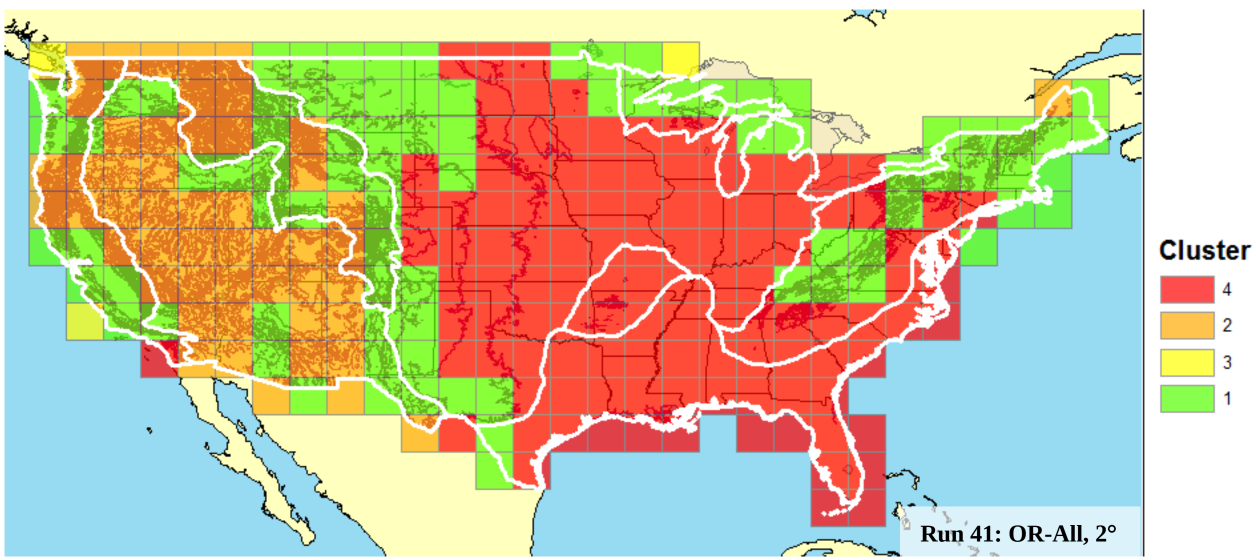
Cluster
4
2
3
1
Run 41: OR-All, 2°

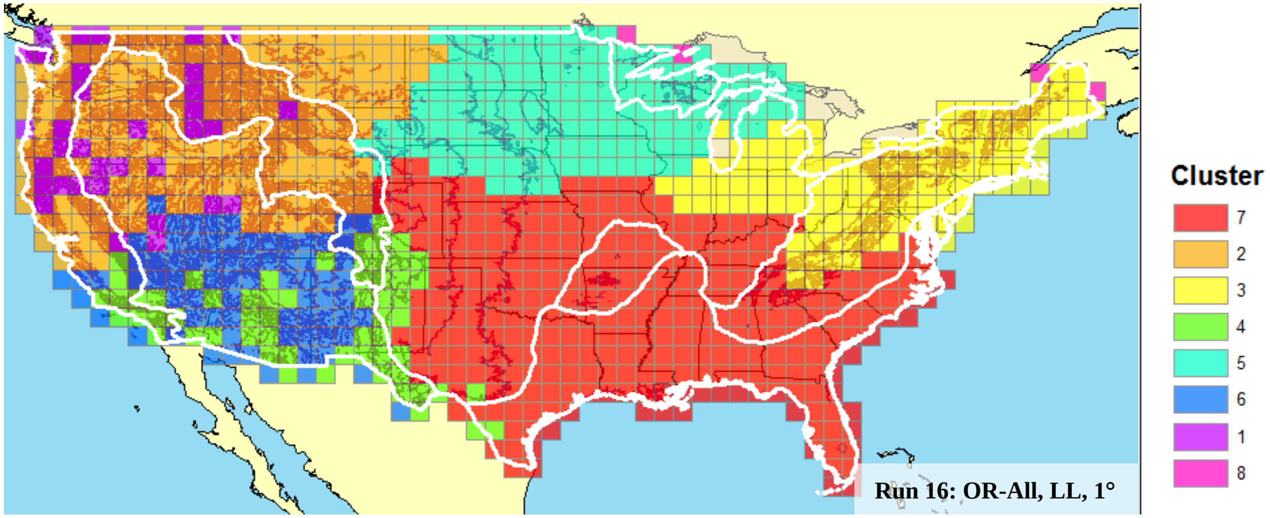
Cluster
7
2
3
4
5
6
1
8
Run 16: OR-All, LL, 1°

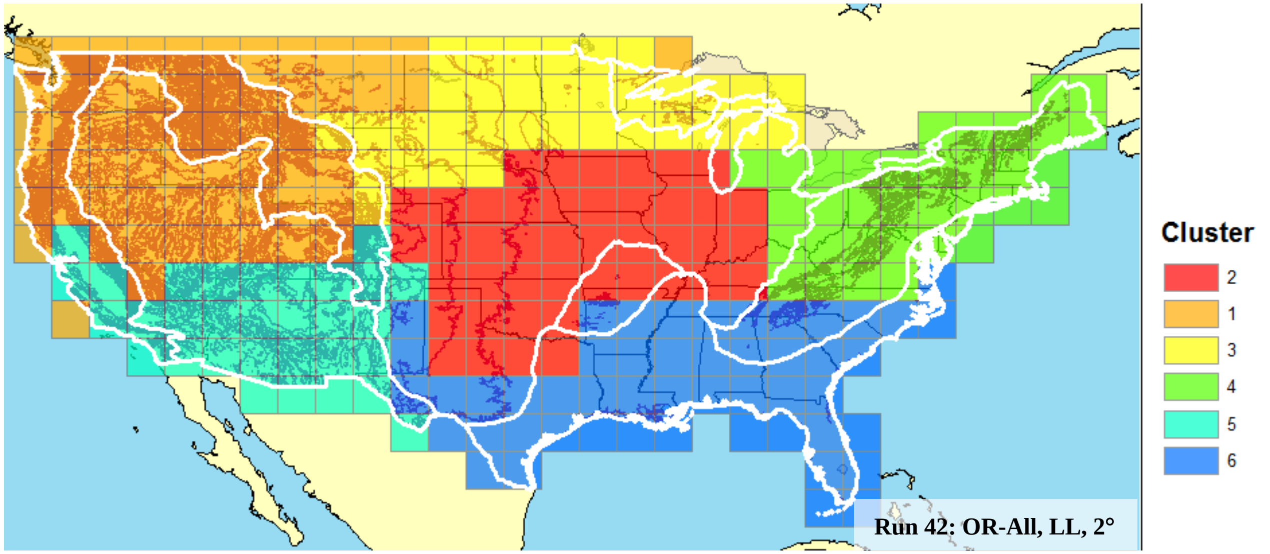
Cluster
2
1
3
4
5
6
Run 42: OR-All, LL, 2°

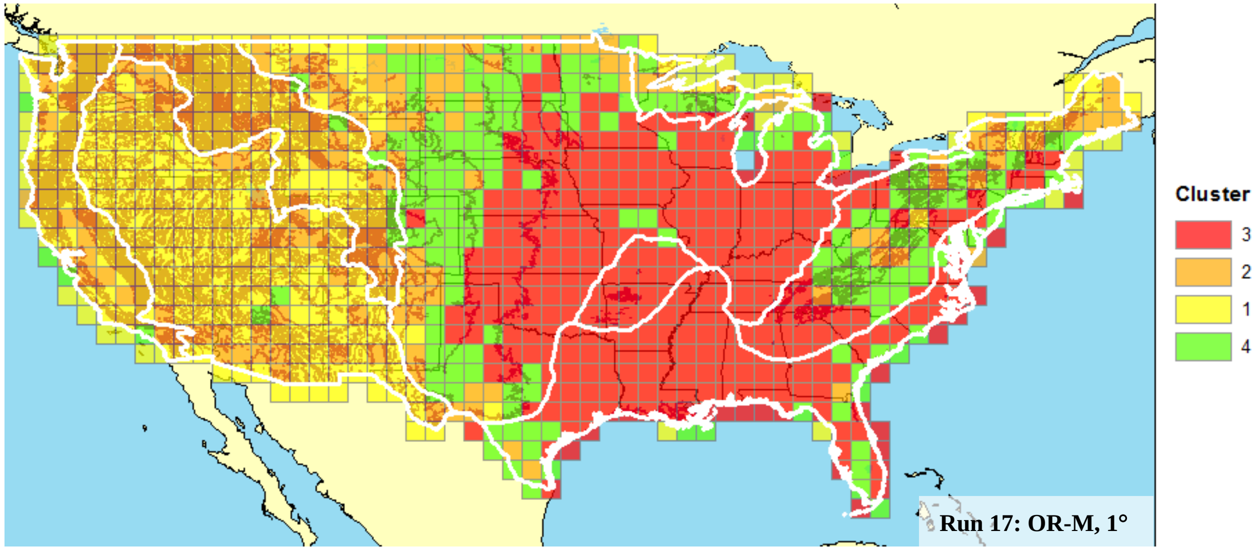
Cluster
3
2
1
4
Run 17: OR-M, 1°

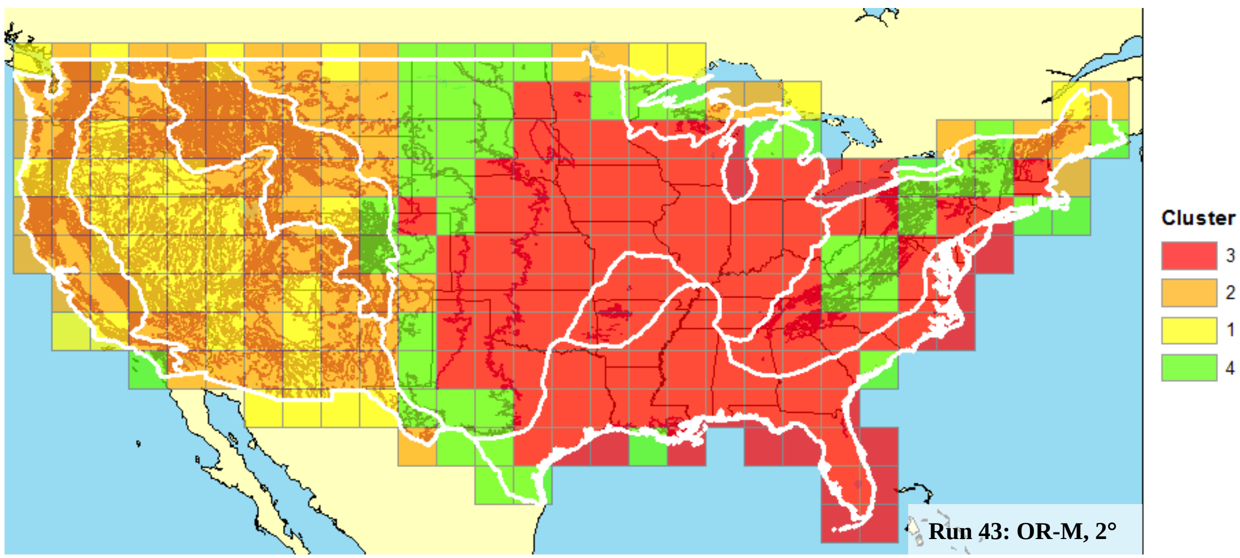
Cluster
3
2
1
4
Run 43: OR-M, 2°

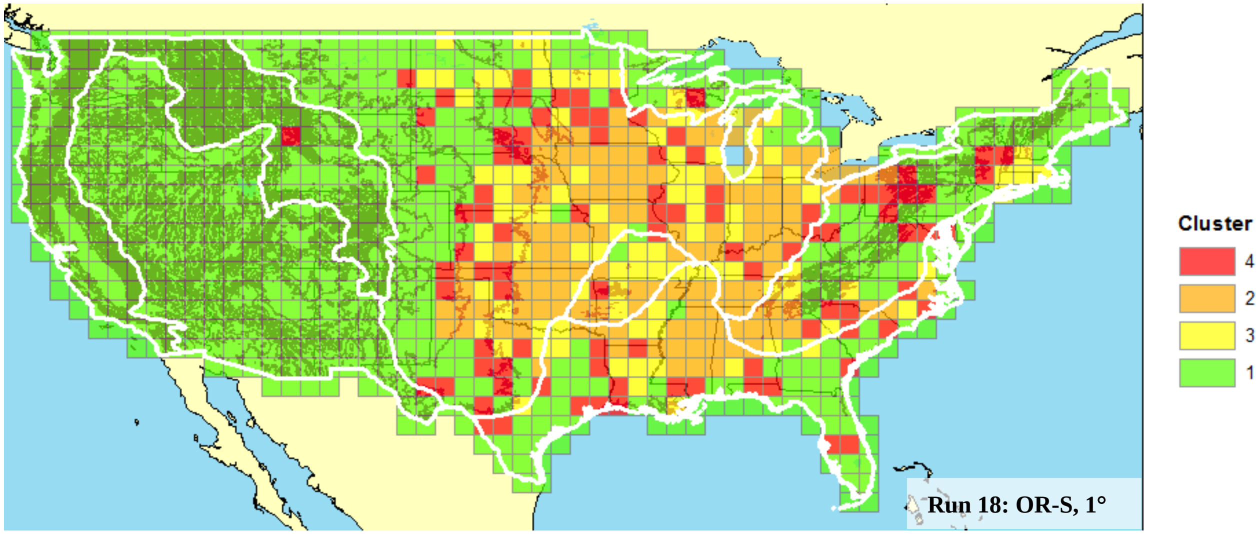
Run 18: OR-S, 1°
Cluster
4
2
3
1

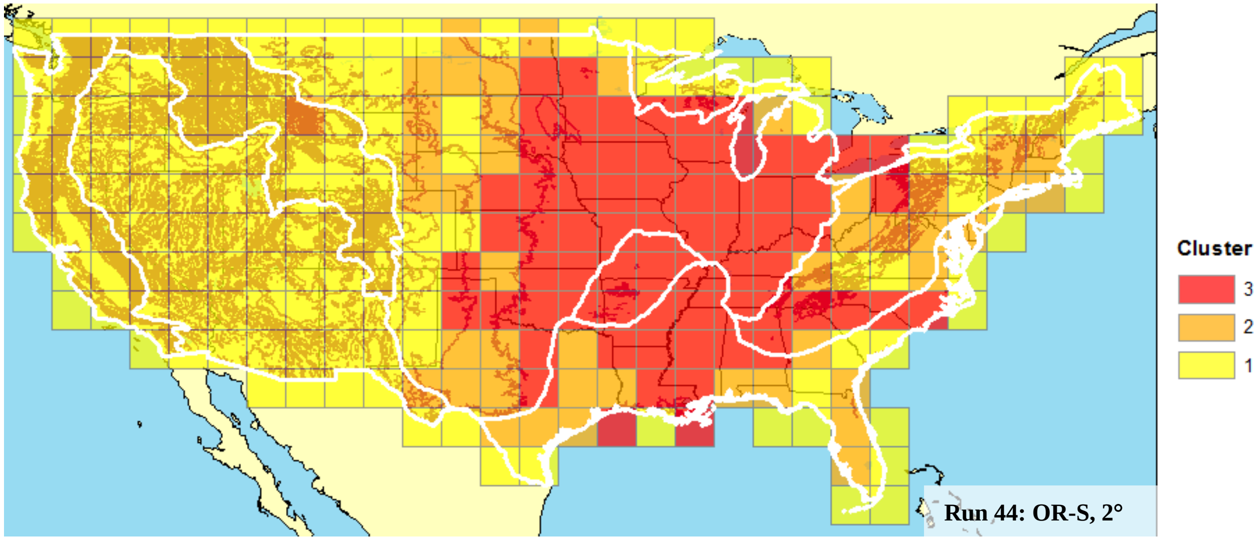
Run 44: OR-S, 2°
Cluster
3
2
1

B.4. Region Cluster Maps

As discussed in Section 2.4, a hierarchical cluster method was used to identify regions using 6 tornado variables that contribute to tornado climatology, 3 physiographic variables, and 2 location variables (latitude-longitude). Table 2-3 describes the many runs that were made. The final regions were selected based on W and Y series for 1°, 1° shifted, 2° and 2° shifted. The following plots provide pictures of the cluster groupings for 2 through 12 clusters and the 22nd cluster, which was the highest grouping we evaluated. The order of the figures are given in Table B-2. A description of legend format for the figures in Appendix B.4 is provided in Section 2.4.3.

Table Error! No text of specified style in document.**-6. Tornado Region Cluster Maps**

Series	Run No.	Grid				Pages
		1°	1°s	2°	2°s	
W	23	•				B-16 - B-18
	69		•			B-19 - B-21
	49			•		B-22 - B-24
	59				•	B-25 - B-27
Y	25	•				B-28 - B-30
	71		•			B-31 - B-33
	51			•		B-34 - B-36
	61				•	B-37 - B-39

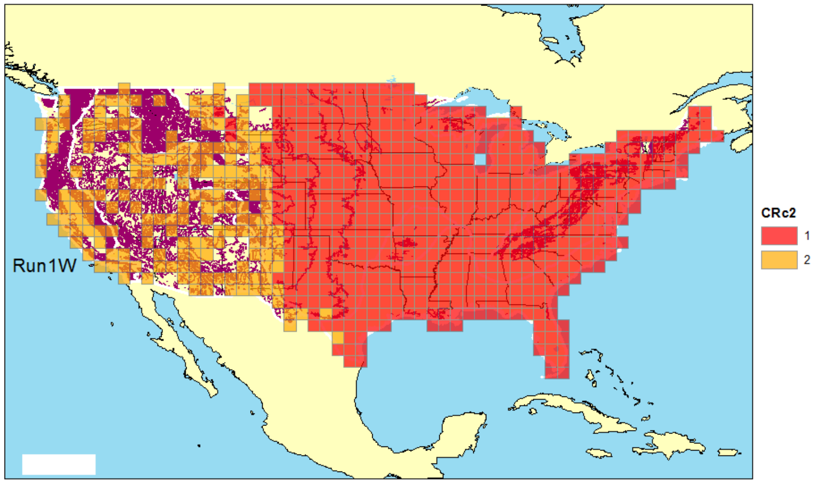
Run1W
CRc2
1
2

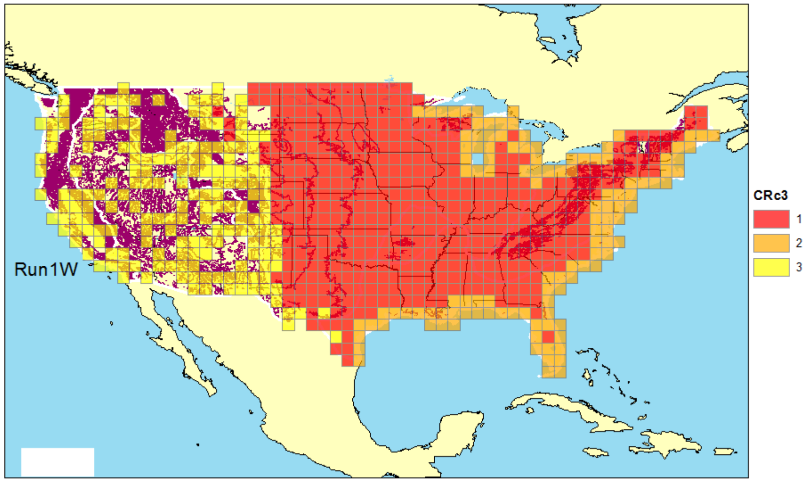
Run1W
CRc3
1
2
3

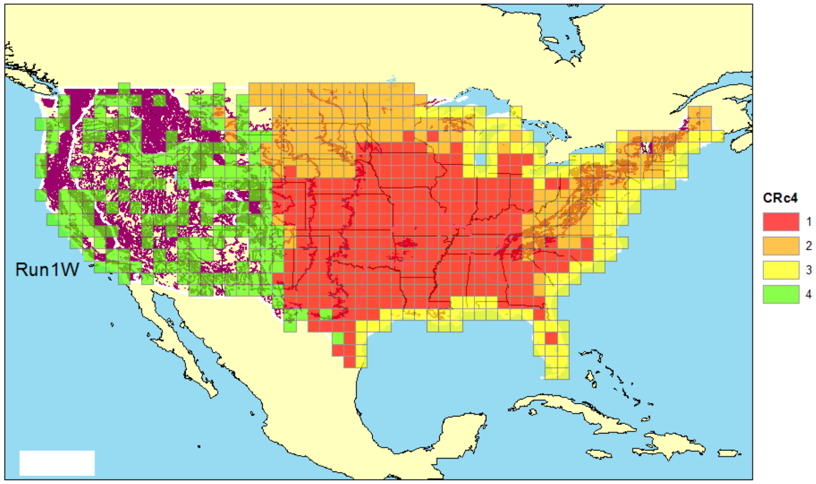
Run1W
CRc4
1
2
3
4

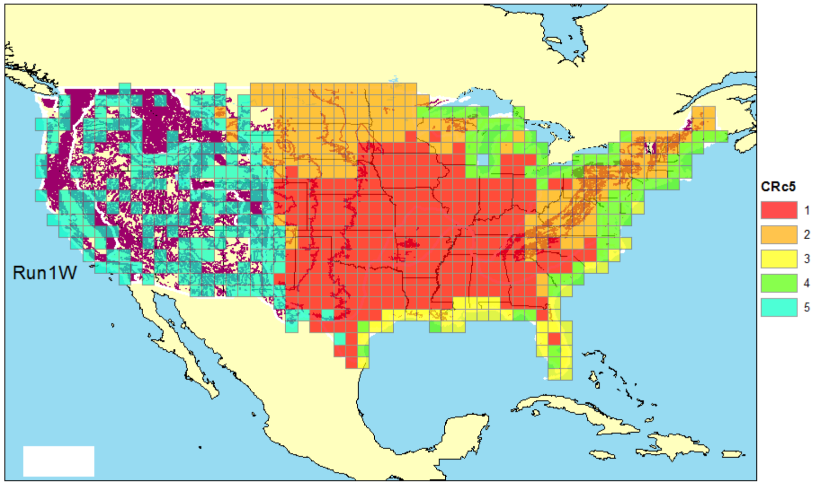
Run1W
CRc5
1
2
3
4
5

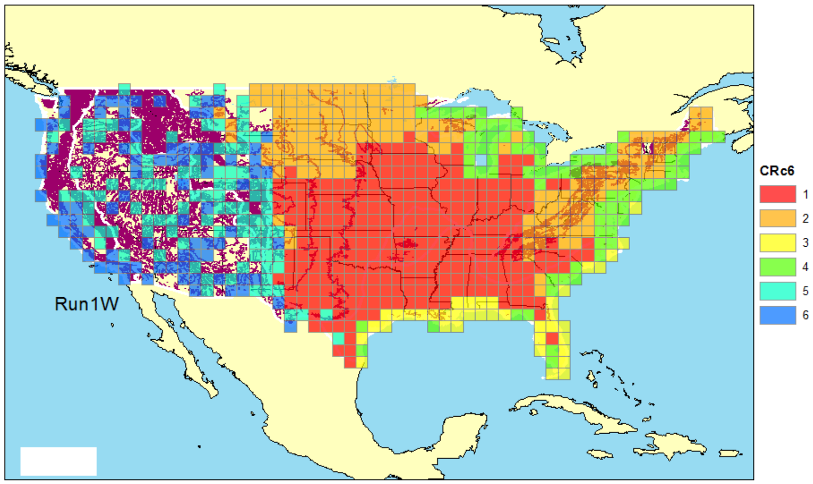
Run1W
CRc6
1
2
3
4
5
6

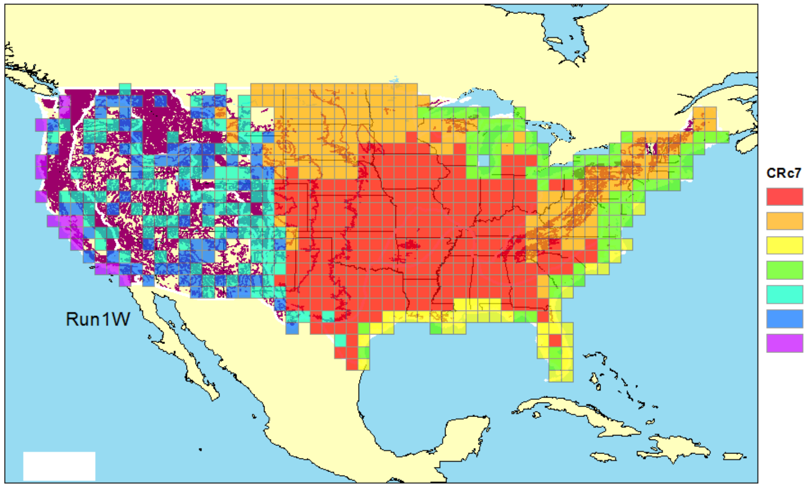
Run1W
CRc7
1
2
3
4
5
6
7

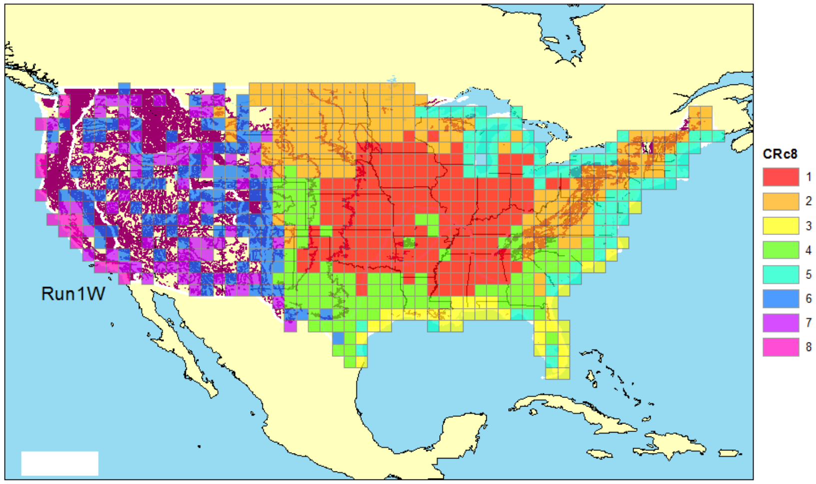
Run1W
CRc8
1
2
3
4
5
6
7
8

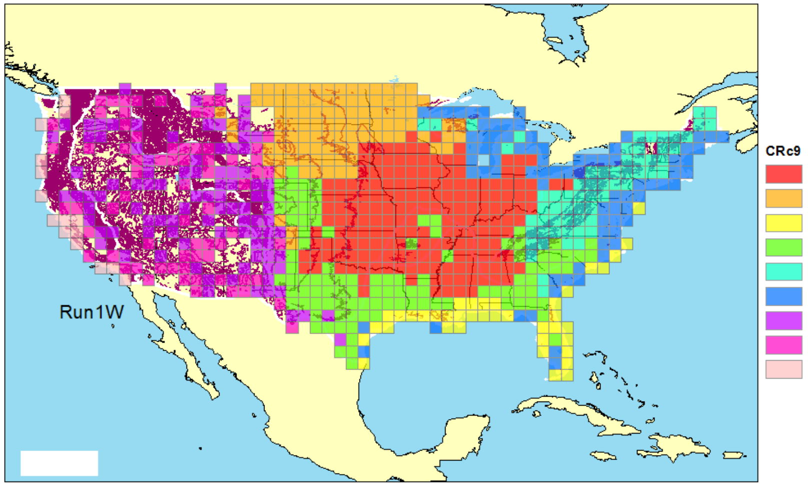
Run1W
CRc9
1
2
3
4
5
6
7
8
9

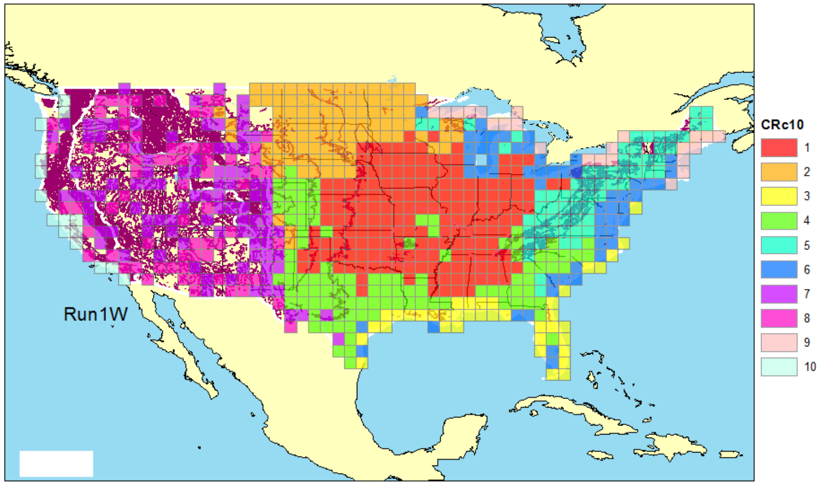

Run1W
CRc10
1
2
3
4
5
6
7
8
9
10

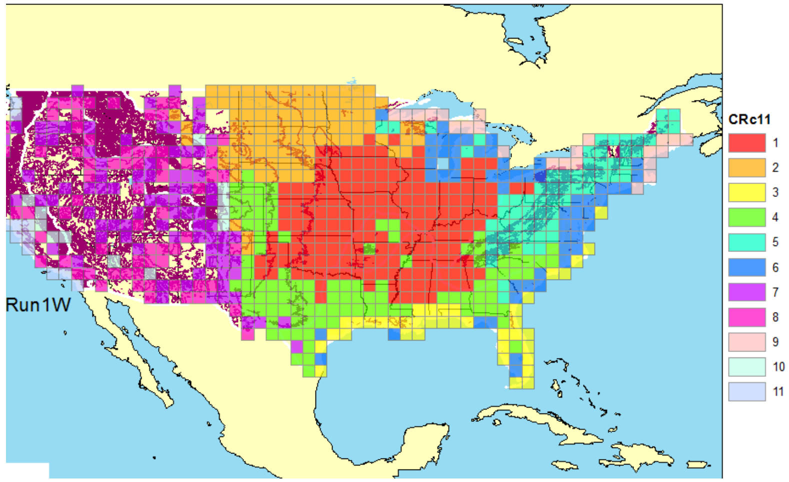

Run1W
CRc11
1
2
3
4
5
6
7
8
9
10
11

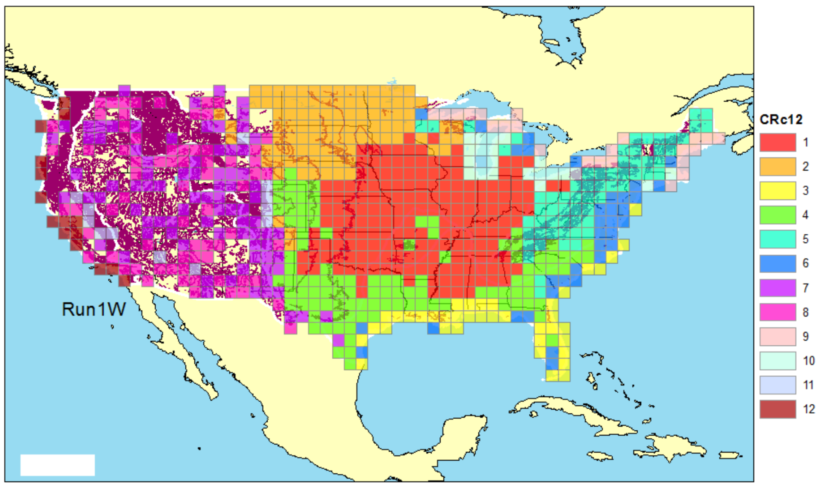

Run1W
CRc12
1
2
3
4
5
6
7
8
9
10
11
12

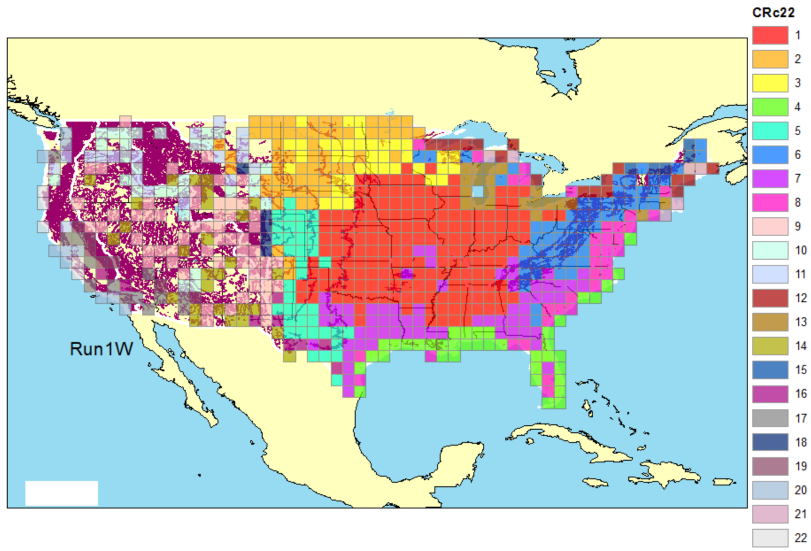

Run1W
CRc22
1
2
3
4
5
6
7
8
9
10
11
12
13
14
15
16
17
18
19
20
21
22

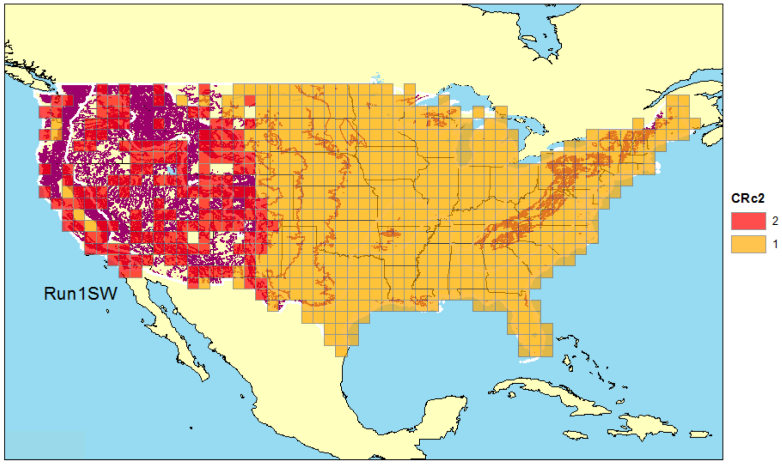
Run1SW
CRc2
2
1

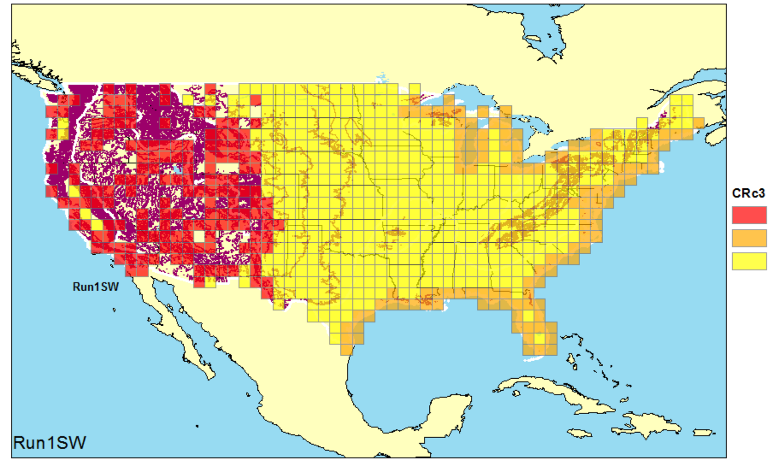
Run1SW
Run1SW
CRc3
3
2
1

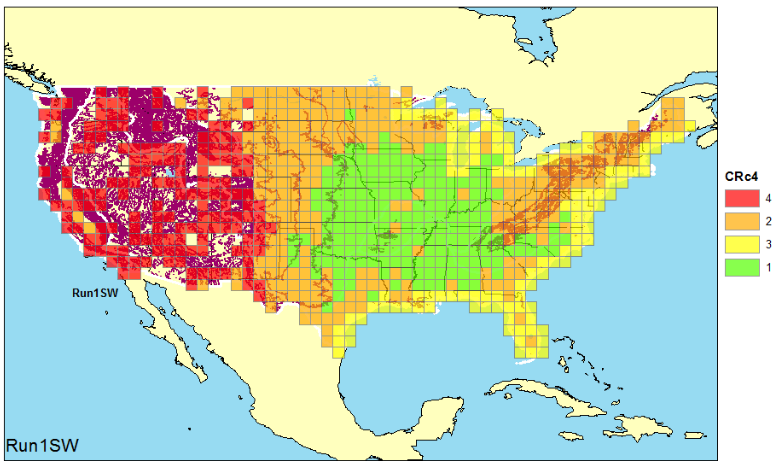
Run1SW
Run1SW
CRc4
4
2
3
1

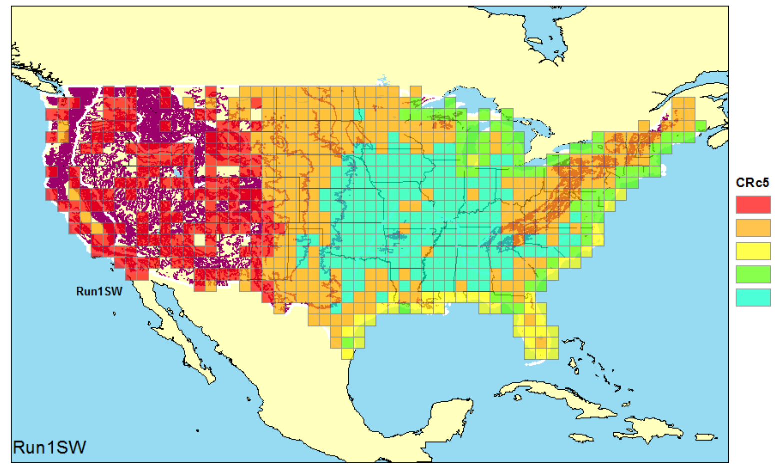
Run1SW
Run1SW
CRc5
5
2
3
4
1

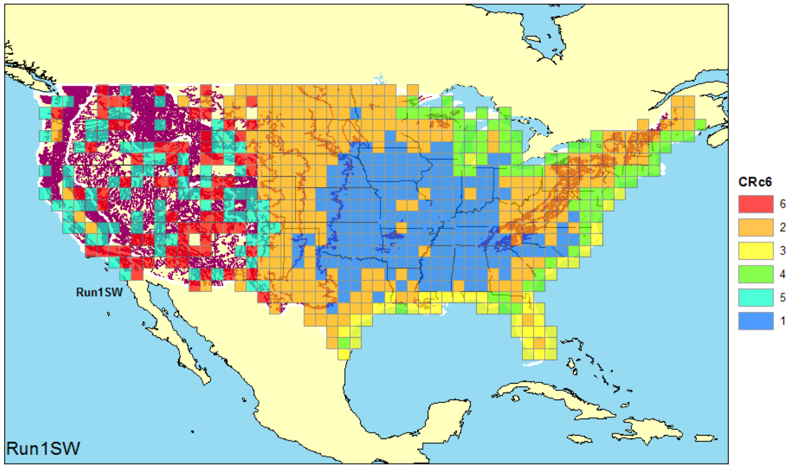
Run1SW
CRc6
6
2
3
4
5
1
Run1SW

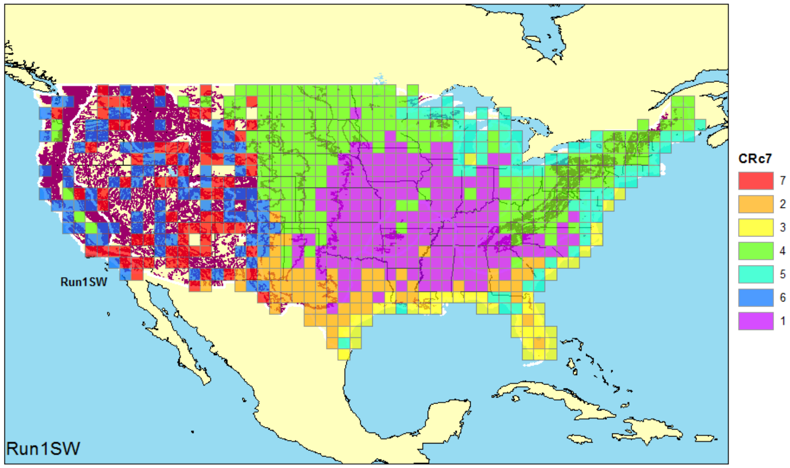
Run1SW
CRc7
7
2
3
4
5
6
1
Run1SW

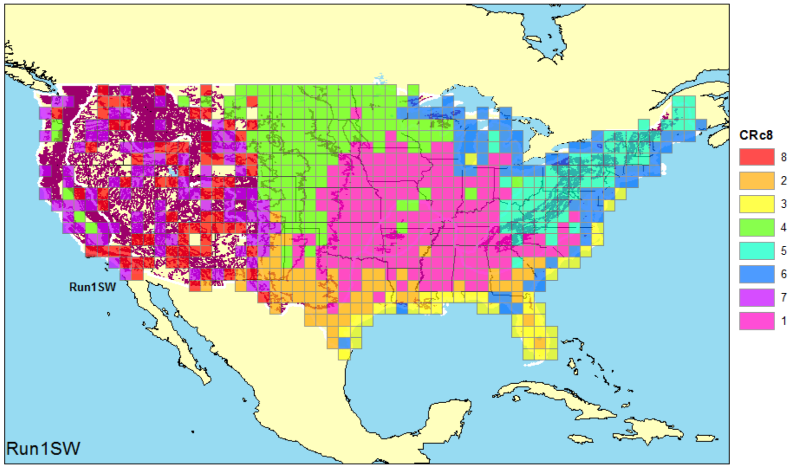
Run1SW
CRc8
8
2
3
4
5
6
7
1
Run1SW

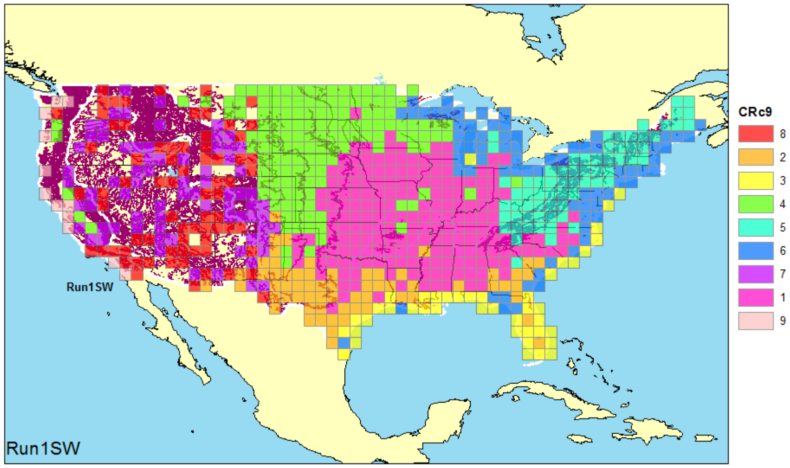
Run1SW
CRc9
8
2
3
4
5
6
7
1
9
Run1SW

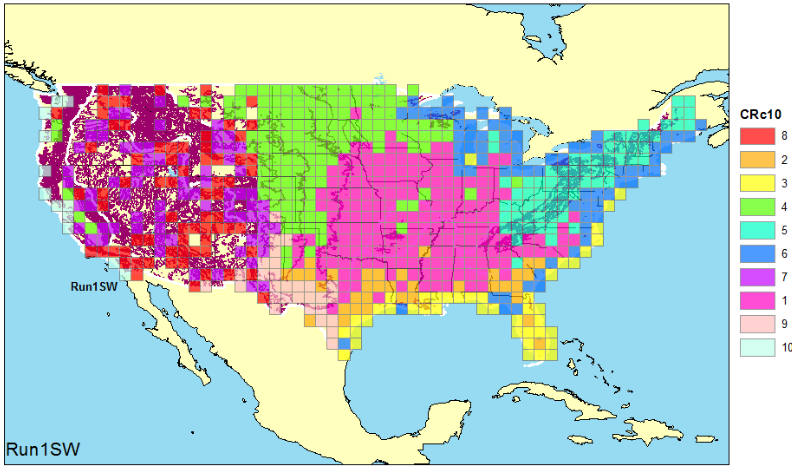
Run1SW
CRc10
8
2
3
4
5
6
7
1
9
10
Run1SW

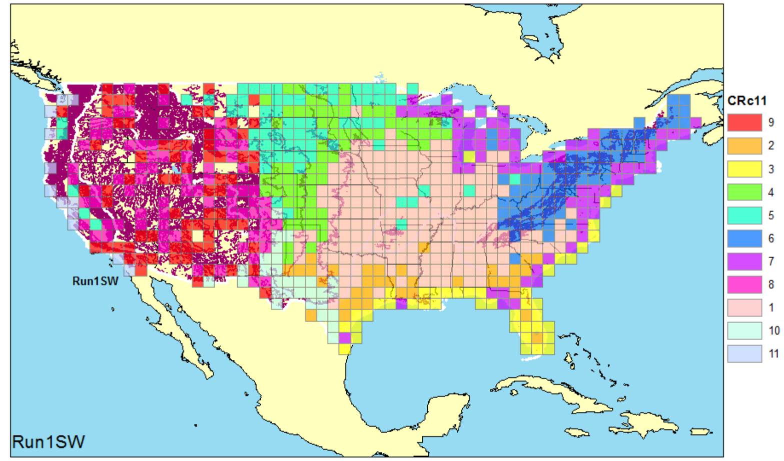
Run1SW
CRc11
9
2
3
4
5
6
7
8
1
10
11
Run1SW

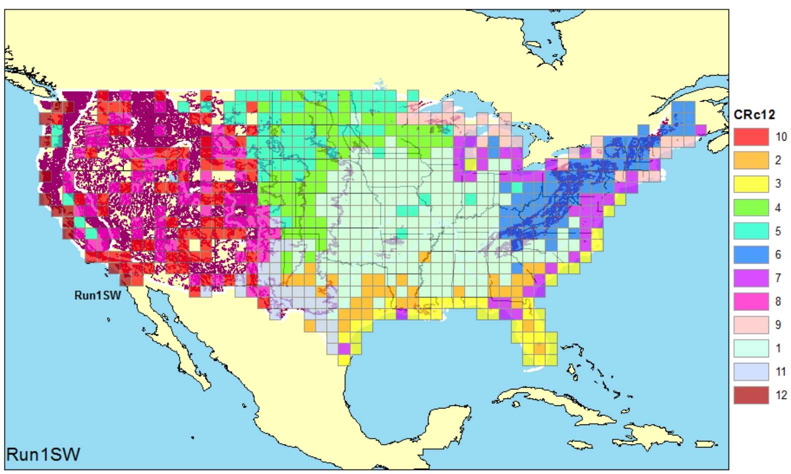
Run1SW
CRc12
10
2
3
4
5
6
7
8
9
1
11
12
Run1SW

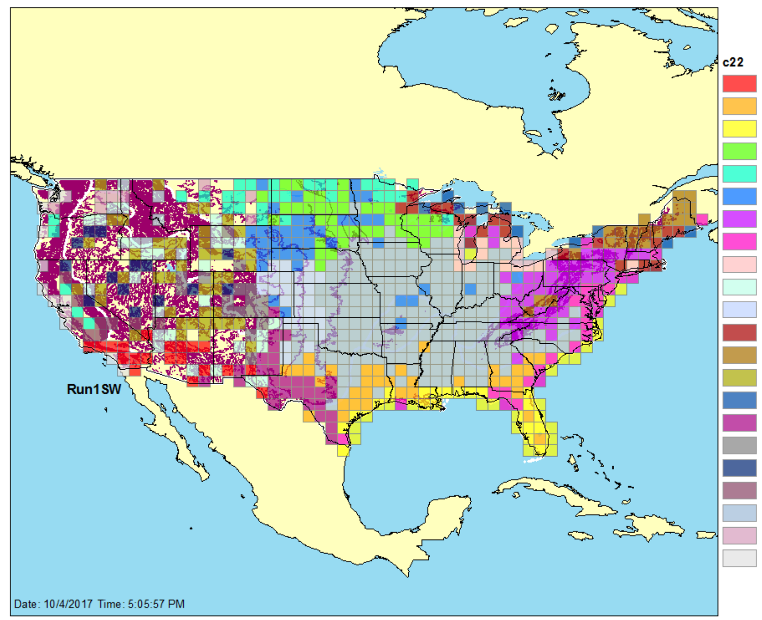
Run1SW
c22
20
2
3
4
5
6
7
8
9
10
11
12
13
14
15
16
17
18
19
1
21
22
Date: 10/4/2017 Time: 5:05:57 PM

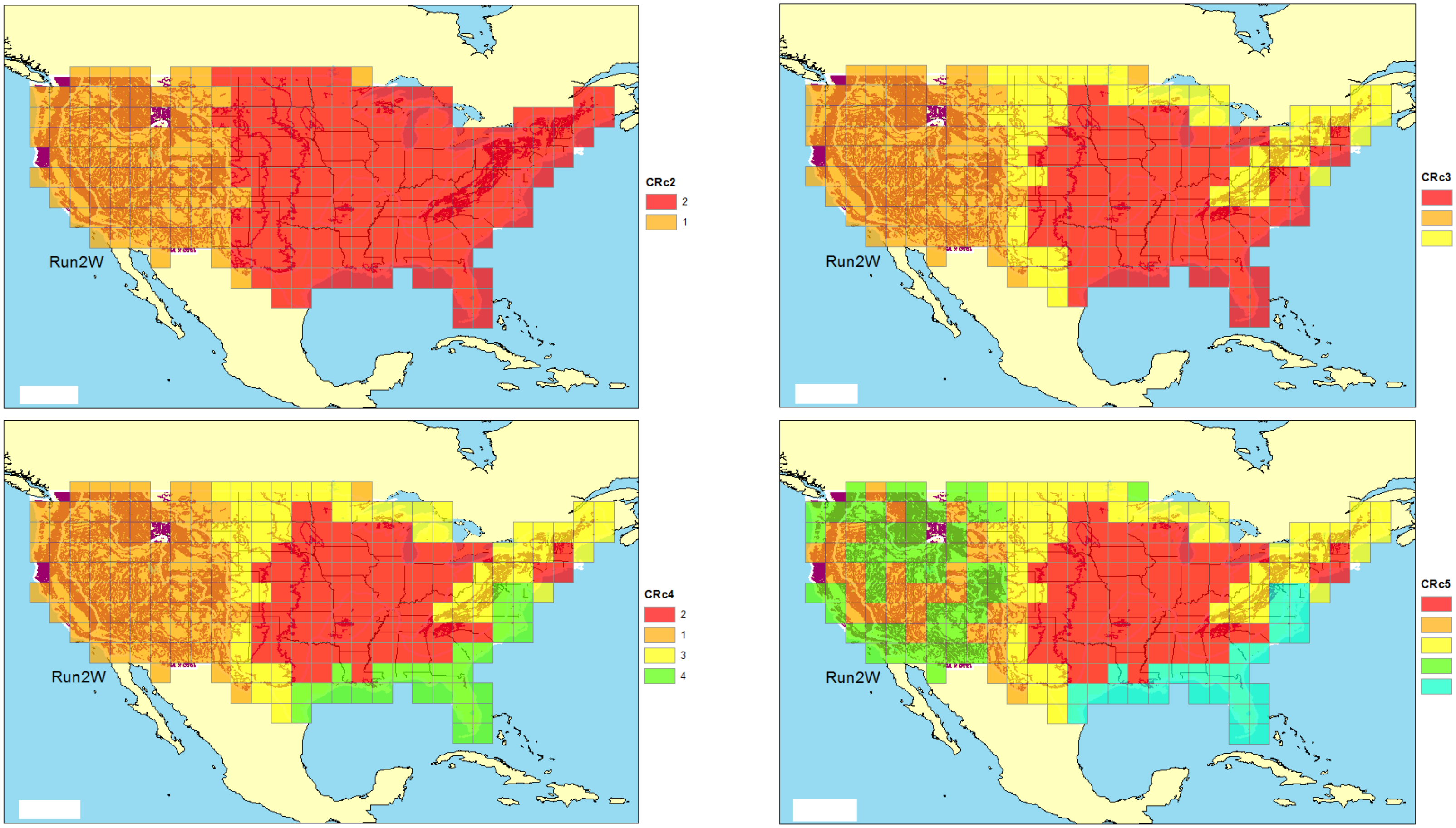
CRc2
2
1
Run2W
CRc3
2
1
3
Run2W
CRc4
2
1
3
4
Run2W
CRc5
2
1
3
4
5
Run2W

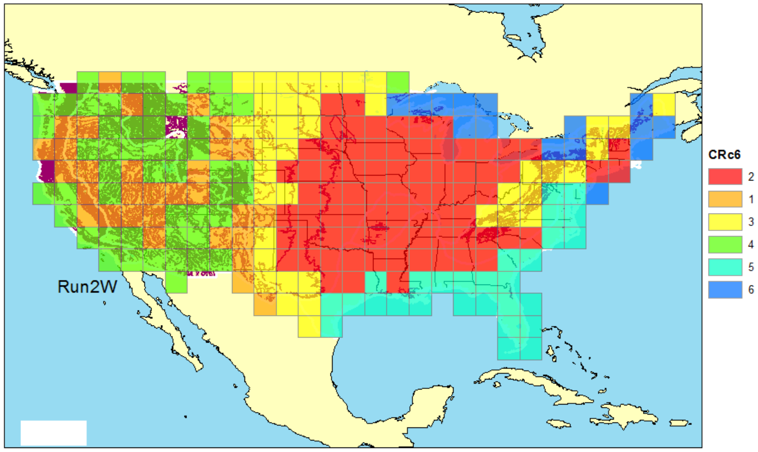
Run2W
CRc6
2
1
3
4
5
6

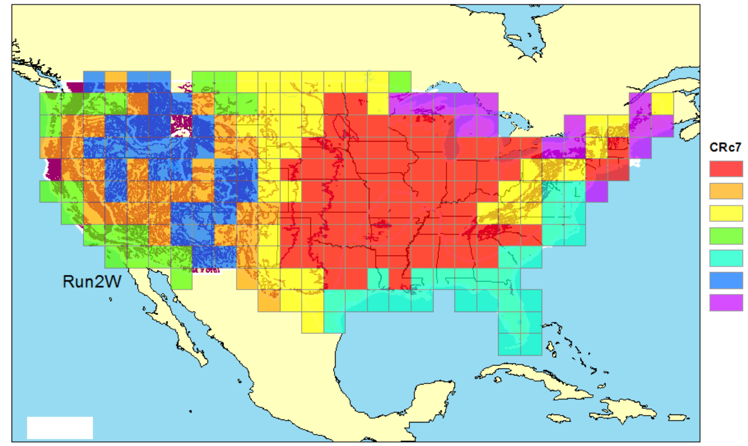
Run2W
CRc7
2
1
3
4
5
6
7

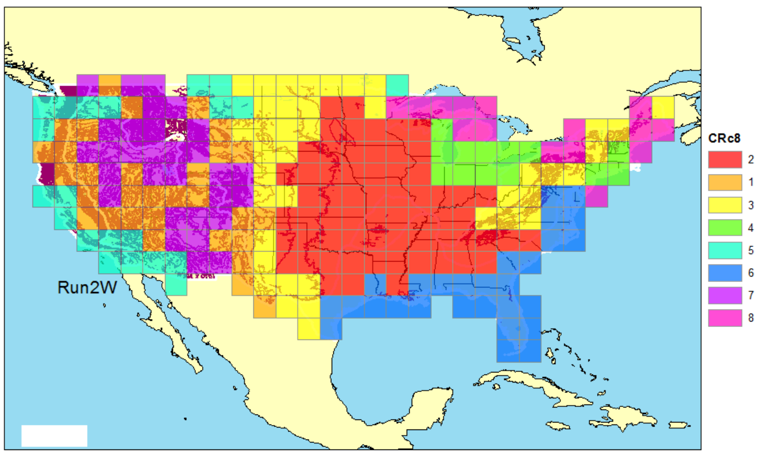
Run2W
CRc8
2
1
3
4
5
6
7
8

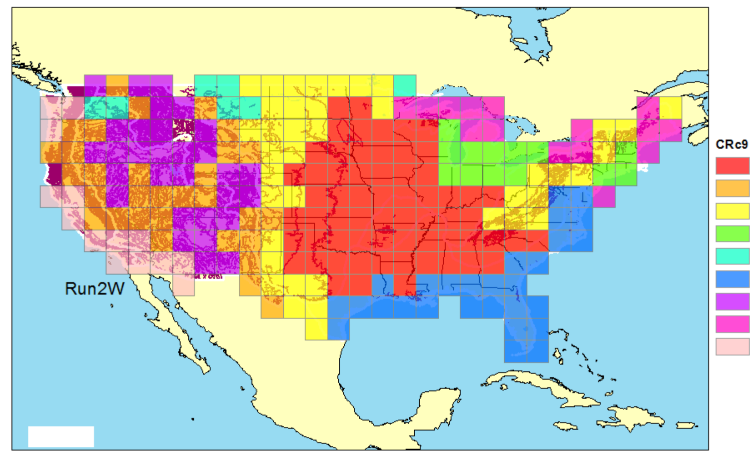
Run2W
CRc9
2
1
3
4
5
6
7
8
9

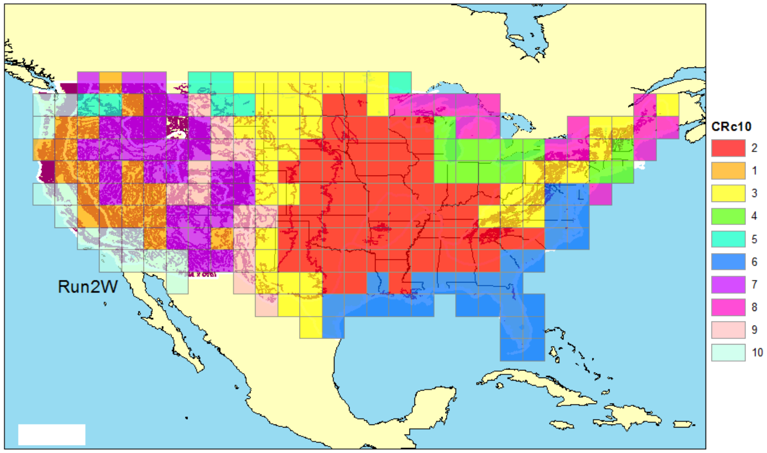
Run2W
CRc10
2
1
3
4
5
6
7
8
9
10

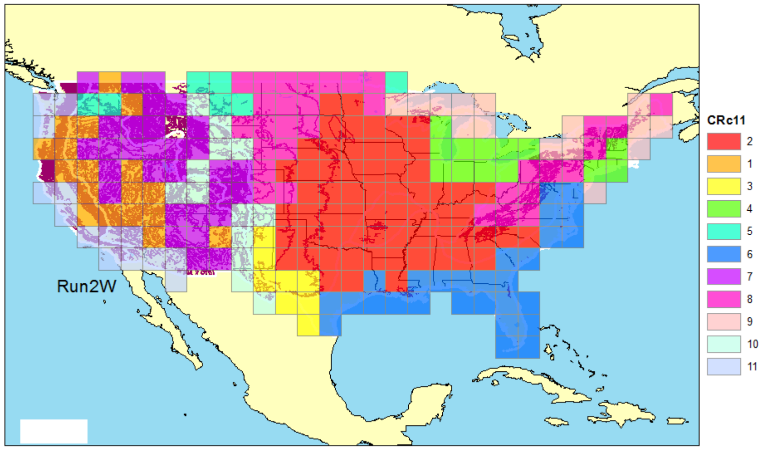
Run2W
CRc11
2
1
3
4
5
6
7
8
9
10
11

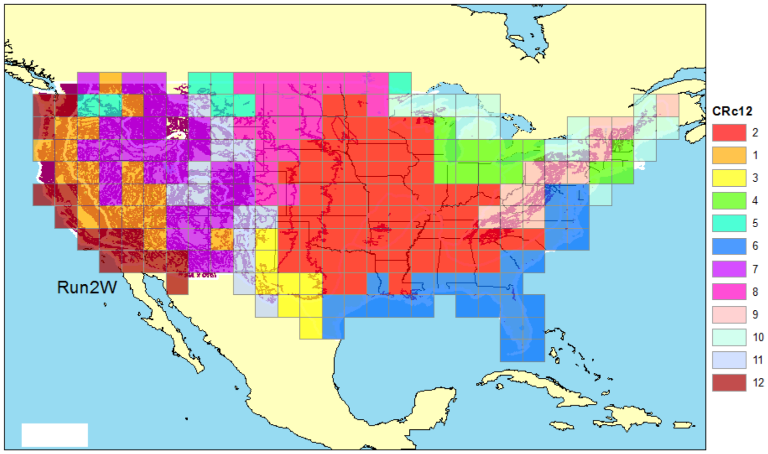
Run2W
CRc12
2
1
3
4
5
6
7
8
9
10
11
12

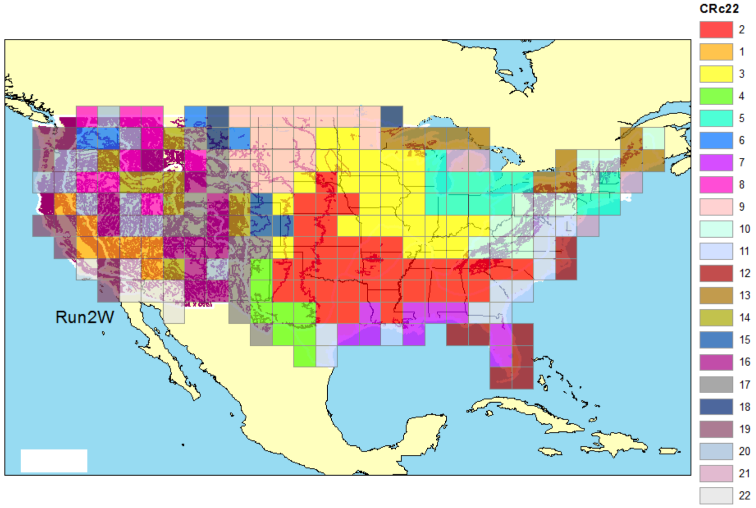
Run2W
CRc22
2
1
3
4
5
6
7
8
9
10
11
12
13
14
15
16
17
18
19
20
21
22

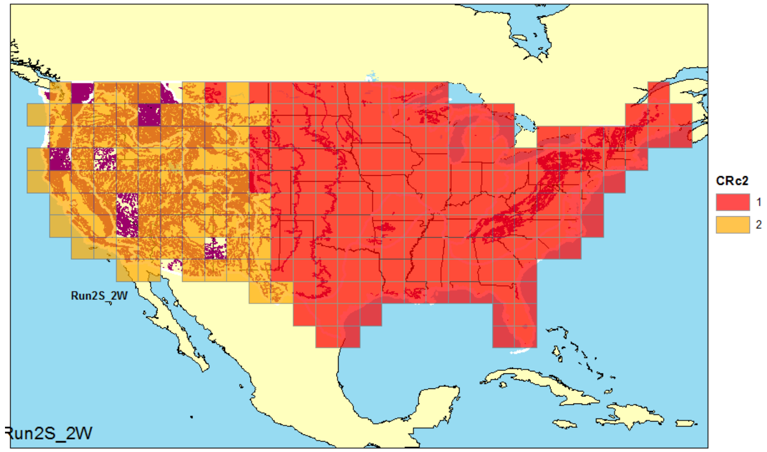
Run2S_2W
CRc2
1
2

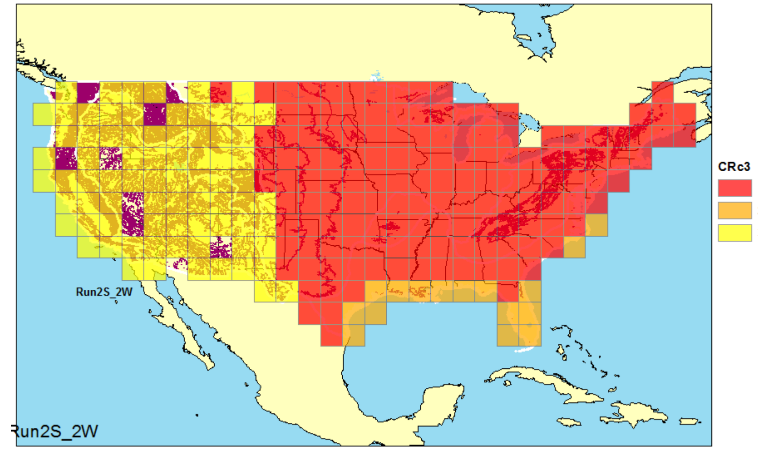
Run2S_2W
CRc3
1
2
3

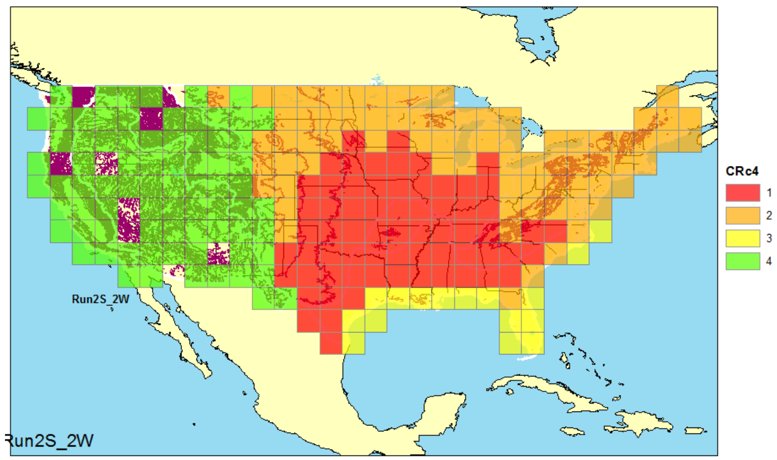
Run2S_2W
CRc4
1
2
3
4

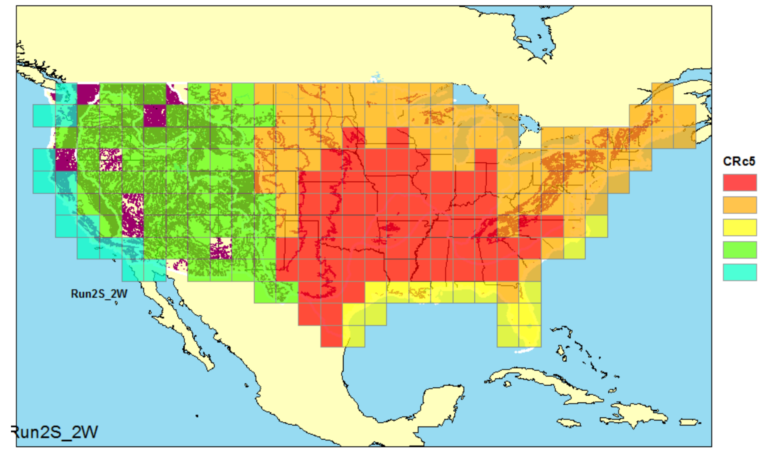
Run2S_2W
CRc5
1
2
3
4
5

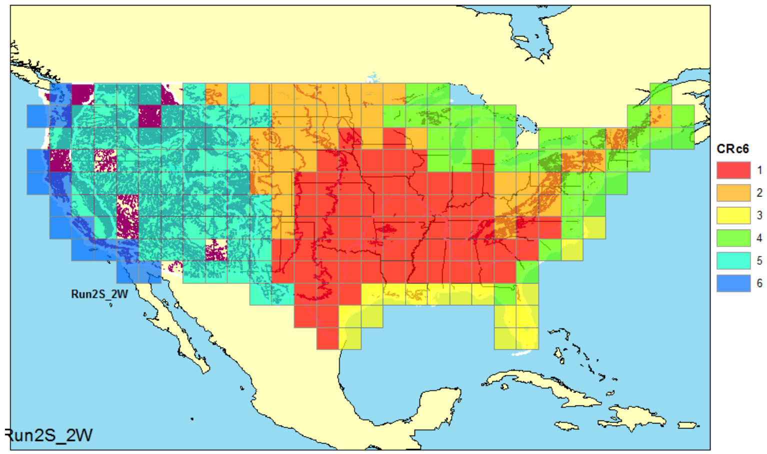
CRc6
1
2
3
4
5
6
Run2S_2W
Run2S_2W

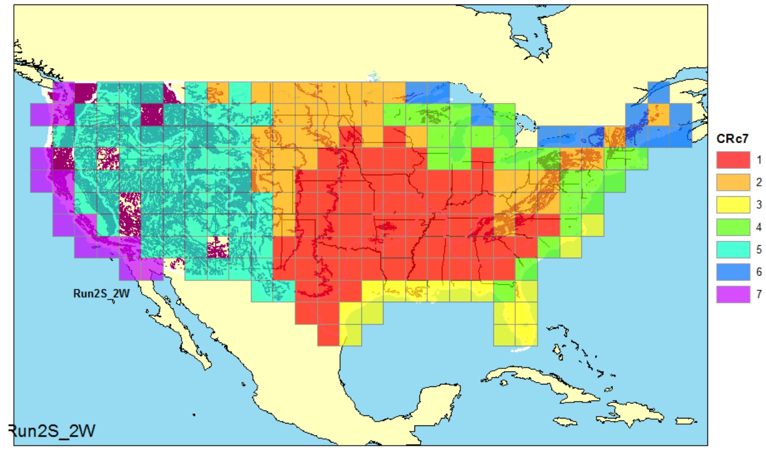
CRc7
1
2
3
4
5
6
7
Run2S_2W
Run2S_2W

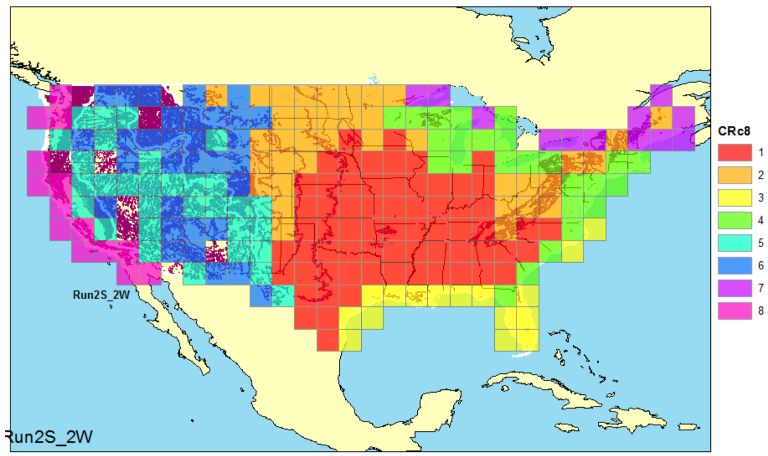
CRc8
1
2
3
4
5
6
7
8
Run2S_2W
Run2S_2W

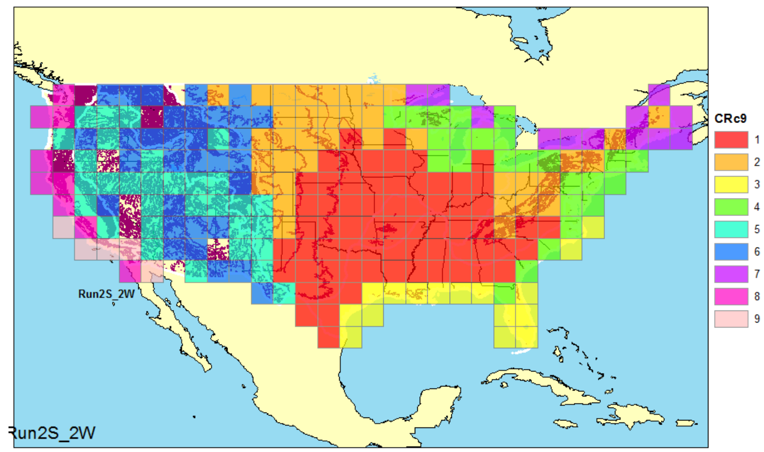
CRc9
1
2
3
4
5
6
7
8
9
Run2S_2W
Run2S_2W

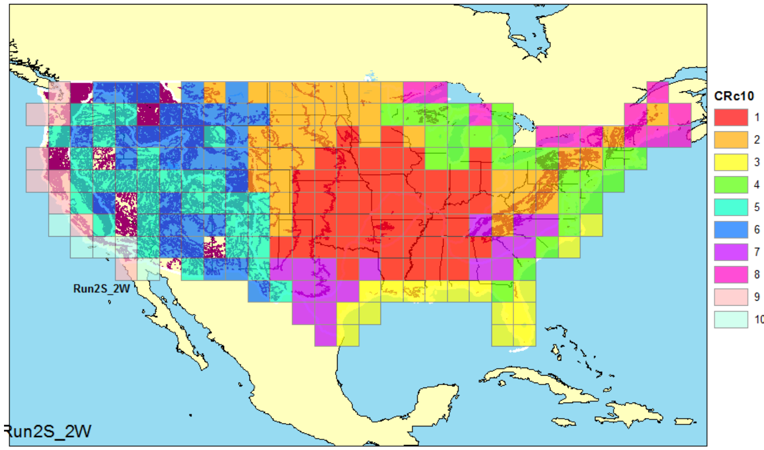
CRc10
1
2
3
4
5
6
7
8
9
10
Run2S_2W
Run2S_2W

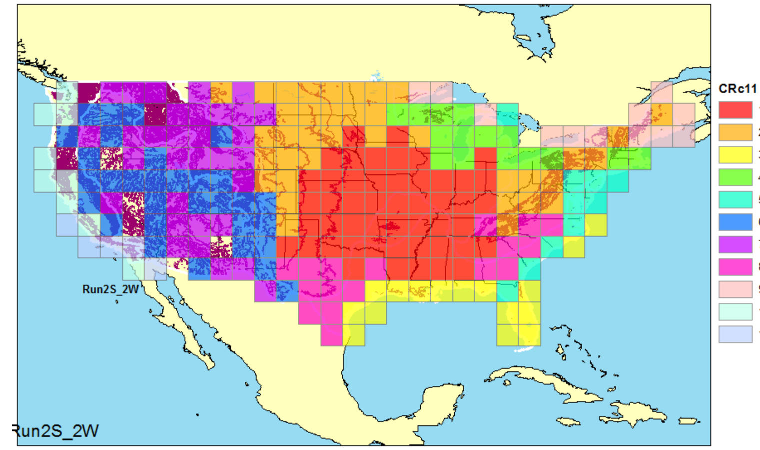
CRc11
1
2
3
4
5
6
7
8
9
10
11
Run2S_2W
Run2S_2W

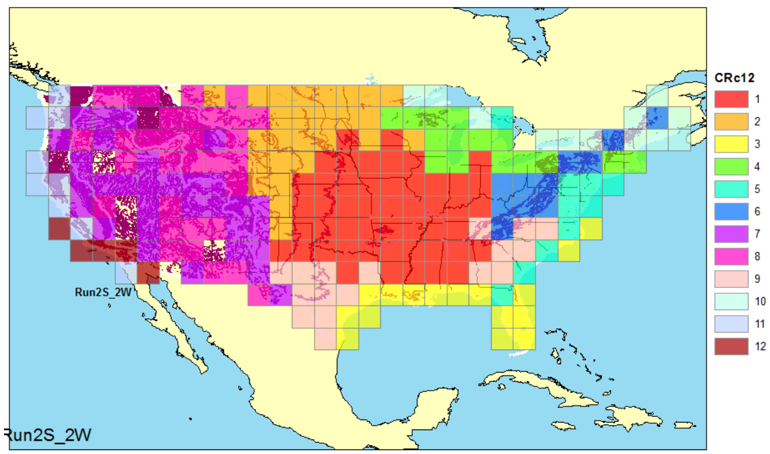
CRc12
1
2
3
4
5
6
7
8
9
10
11
12
Run2S_2W
Run2S_2W

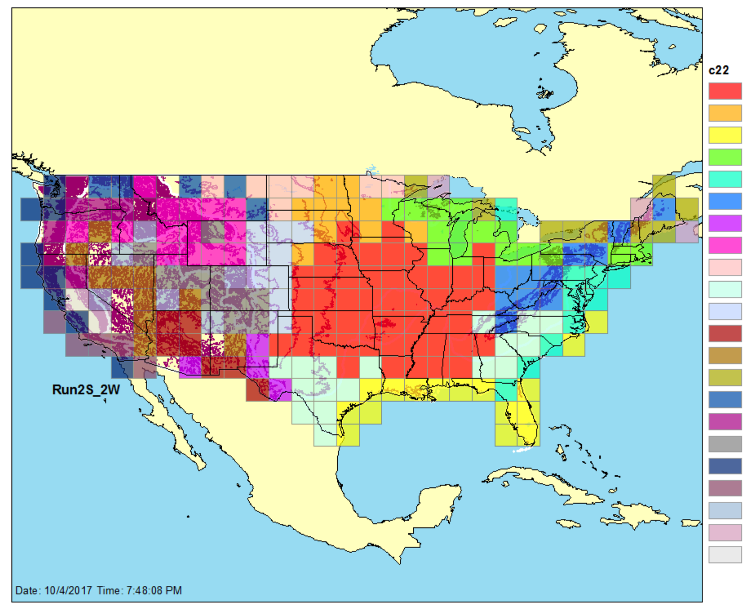
c22
1
2
3
4
5
6
7
8
9
10
11
12
13
14
15
16
17
18
19
20
21
22
Run2S_2W
Date: 10/4/2017 Time: 7:48:08 PM

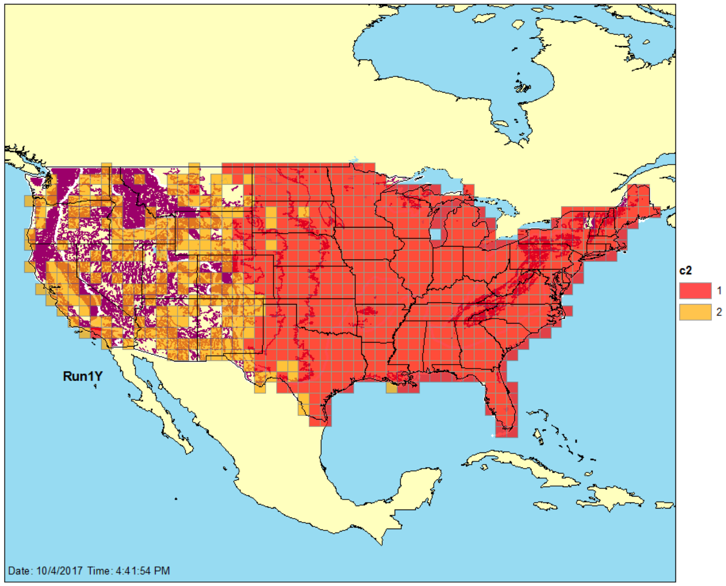
Run1Y
c2
1
2
Date: 10/4/2017 Time: 4:41:54 PM

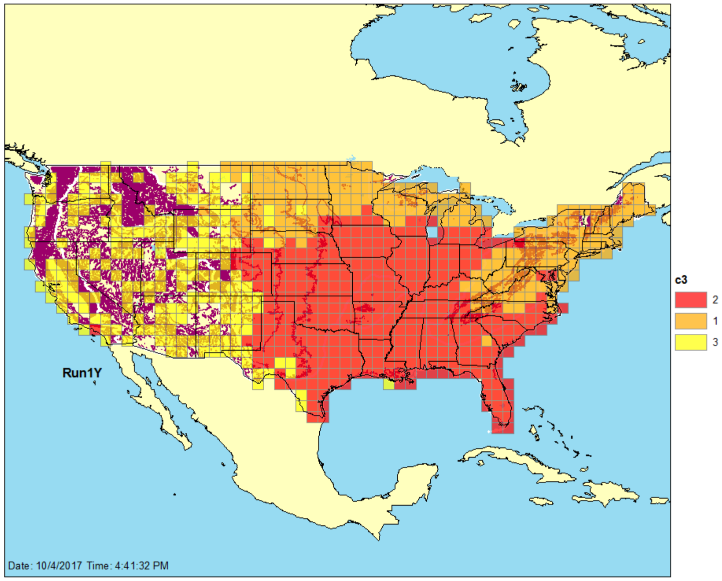
Run1Y
c3
2
1
3
Date: 10/4/2017 Time: 4:41:32 PM

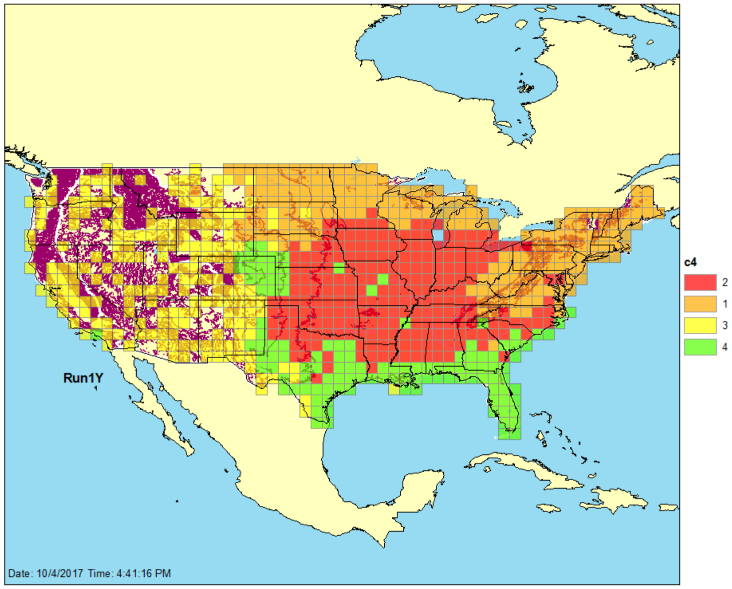
Run1Y
c4
2
1
3
4
Date: 10/4/2017 Time: 4:41:16 PM

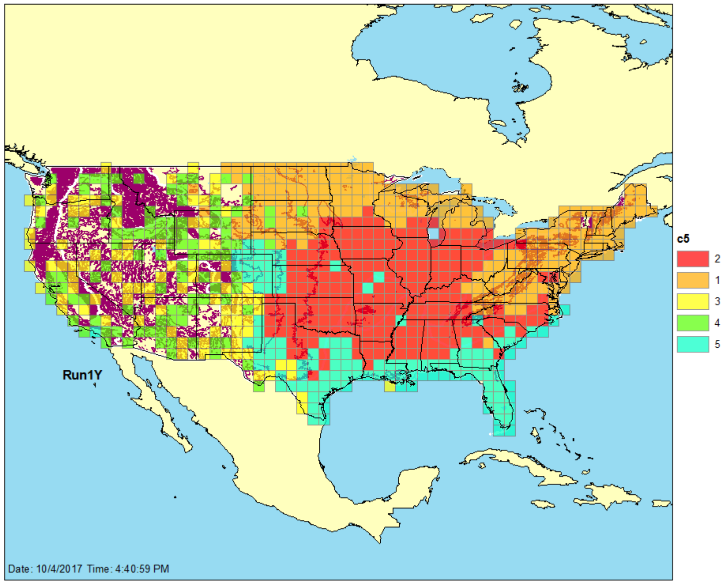
Run1Y
c5
2
1
3
4
5
Date: 10/4/2017 Time: 4:40:59 PM

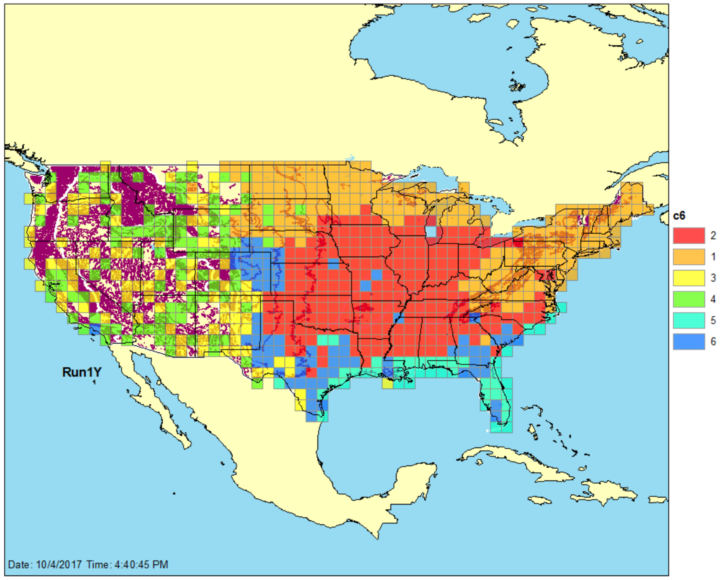

c6
2
1
3
4
5
6
Run1Y
Date: 10/4/2017 Time: 4:40:45 PM

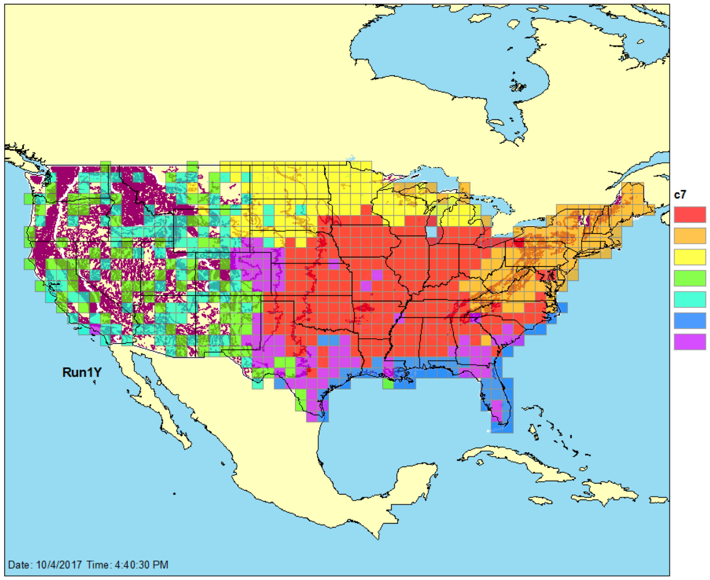

c7
2
1
3
4
5
6
7
Run1Y
Date: 10/4/2017 Time: 4:40:30 PM

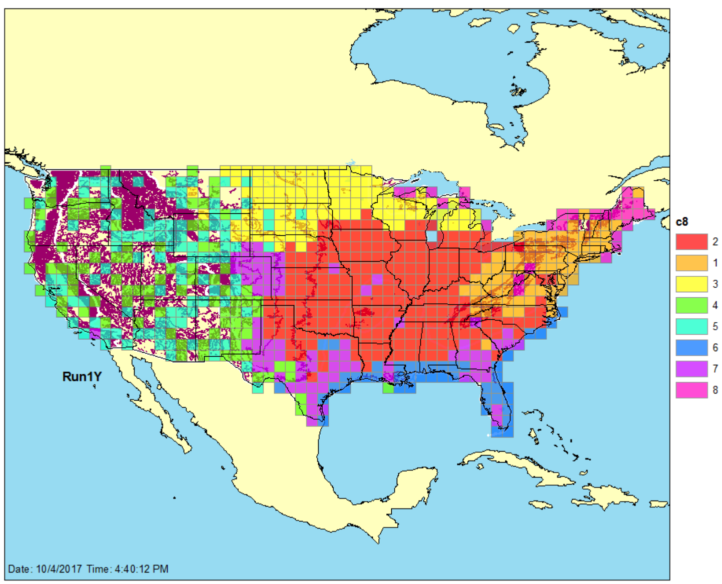

c8
2
1
3
4
5
6
7
8
Run1Y
Date: 10/4/2017 Time: 4:40:12 PM

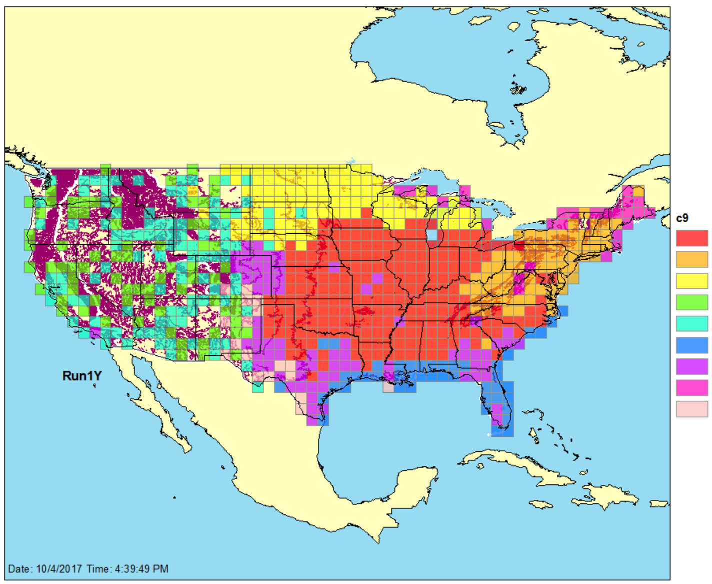

c9
2
1
3
4
5
6
7
8
9
Run1Y
Date: 10/4/2017 Time: 4:39:49 PM

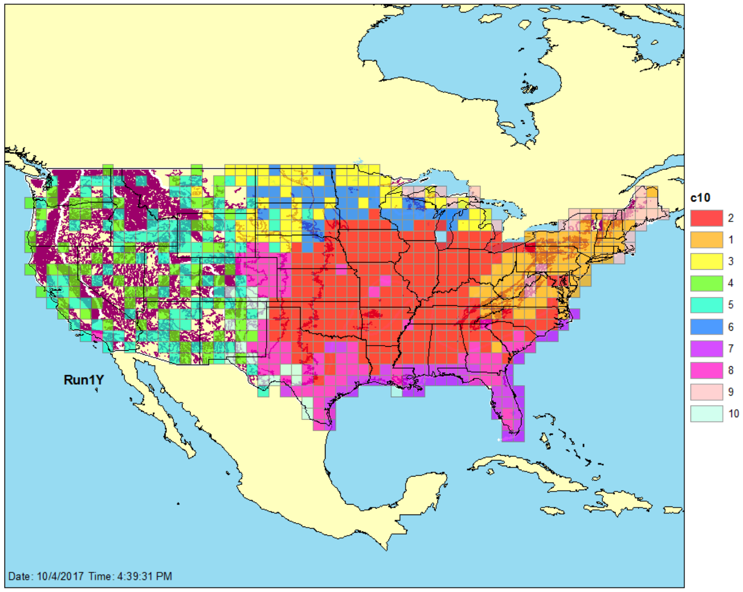
c10
2
1
3
4
5
6
7
8
9
10
Run1Y
Date: 10/4/2017 Time: 4:39:31 PM

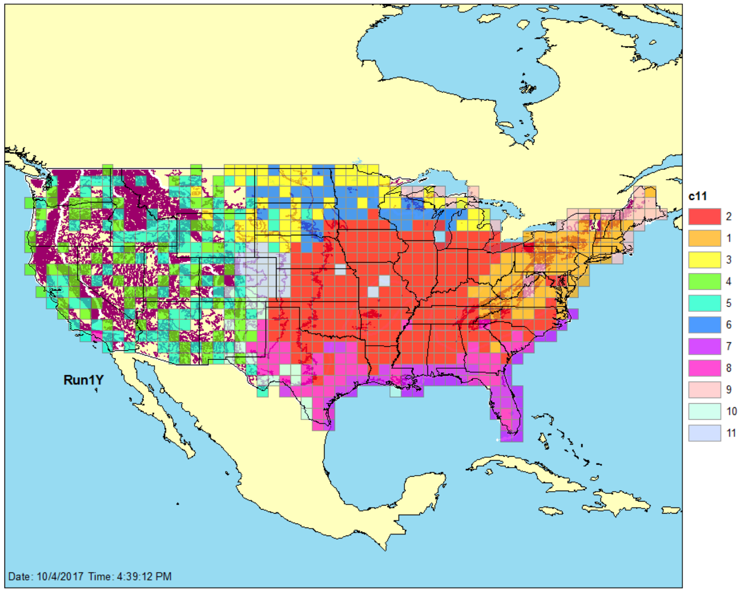
c11
2
1
3
4
5
6
7
8
9
10
11
Run1Y
Date: 10/4/2017 Time: 4:39:12 PM

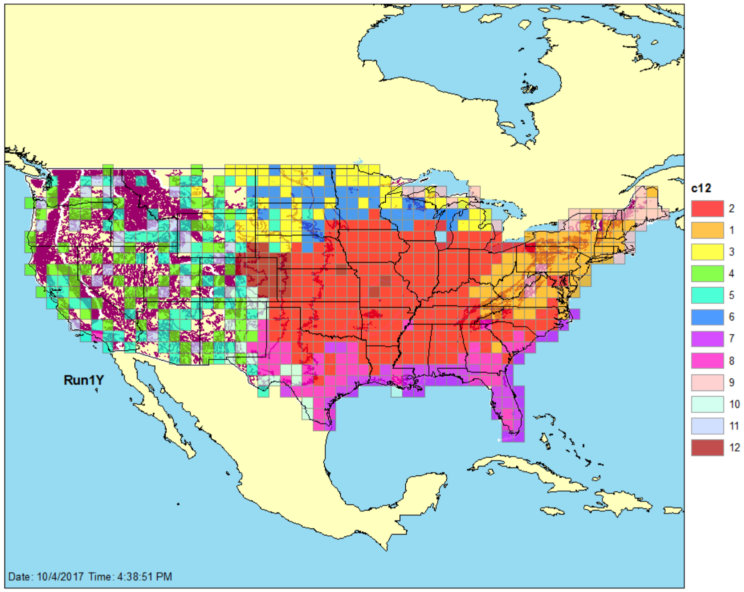
c12
2
1
3
4
5
6
7
8
9
10
11
12
Run1Y
Date: 10/4/2017 Time: 4:38:51 PM

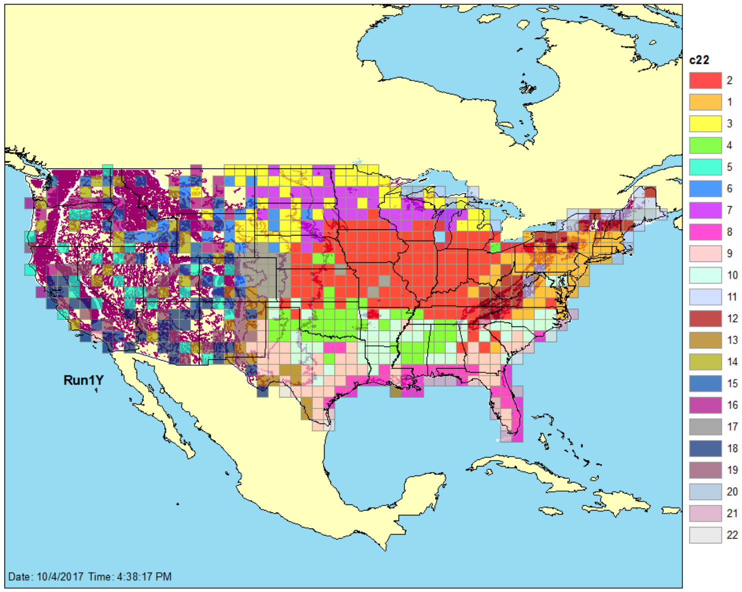
c22
2
1
3
4
5
6
7
8
9
10
11
12
13
14
15
16
17
18
19
20
21
22
Run1Y
Date: 10/4/2017 Time: 4:38:17 PM

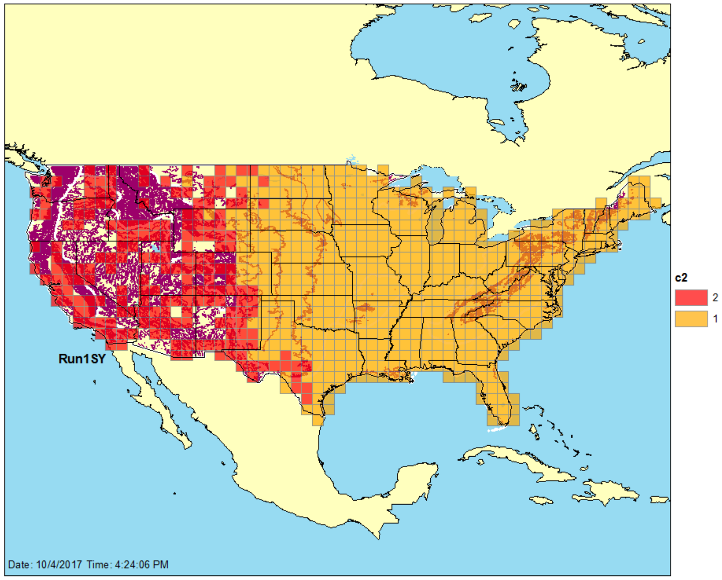
Run1SY
c2
2
1
Date: 10/4/2017 Time: 4:24:06 PM

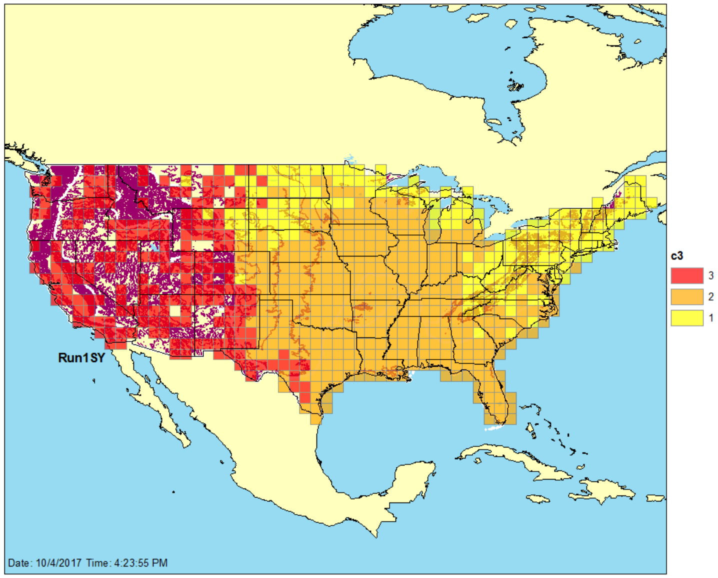
Run1SY
c3
3
2
1
Date: 10/4/2017 Time: 4:23:55 PM

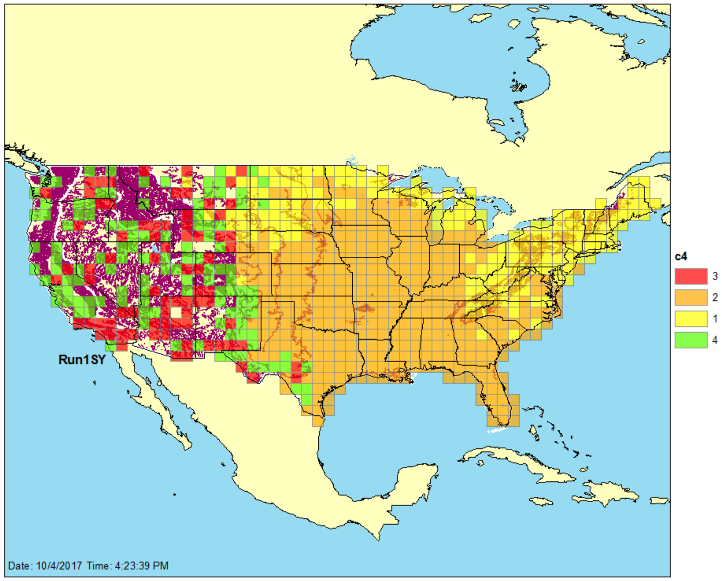
Run1SY
c4
3
2
1
4
Date: 10/4/2017 Time: 4:23:39 PM

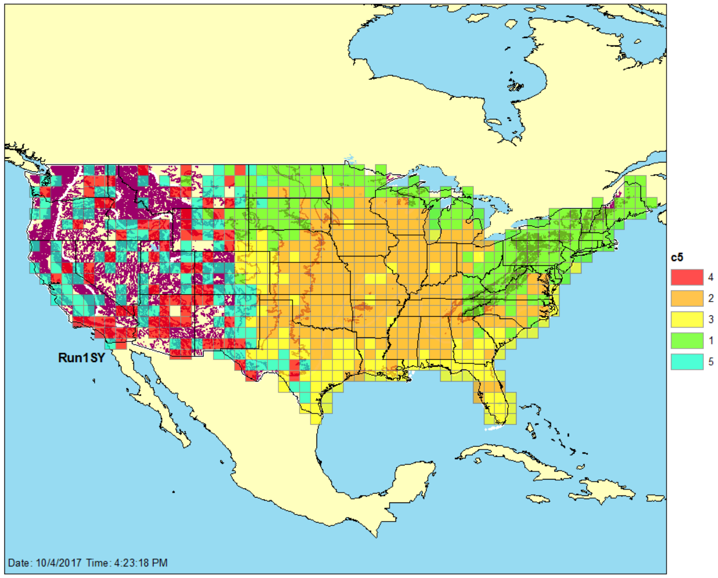
Run1SY
c5
4
2
3
1
5
Date: 10/4/2017 Time: 4:23:18 PM

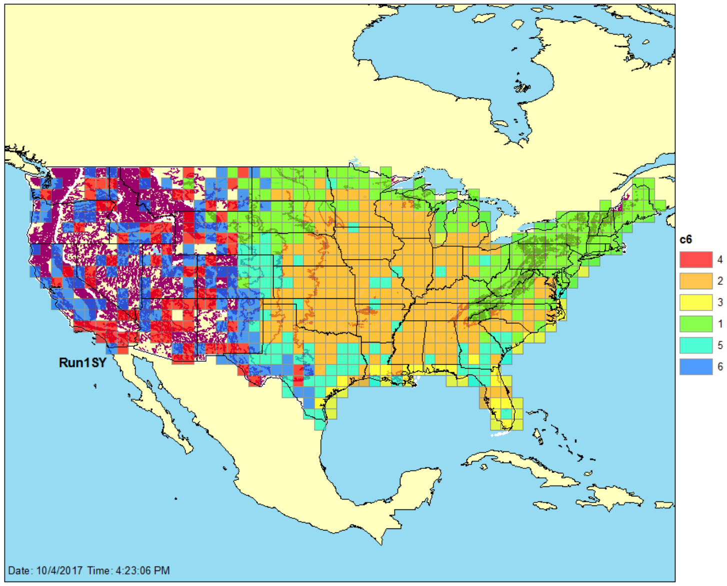
Run1SY
c6
4
2
3
1
5
6
Date: 10/4/2017 Time: 4:23:06 PM

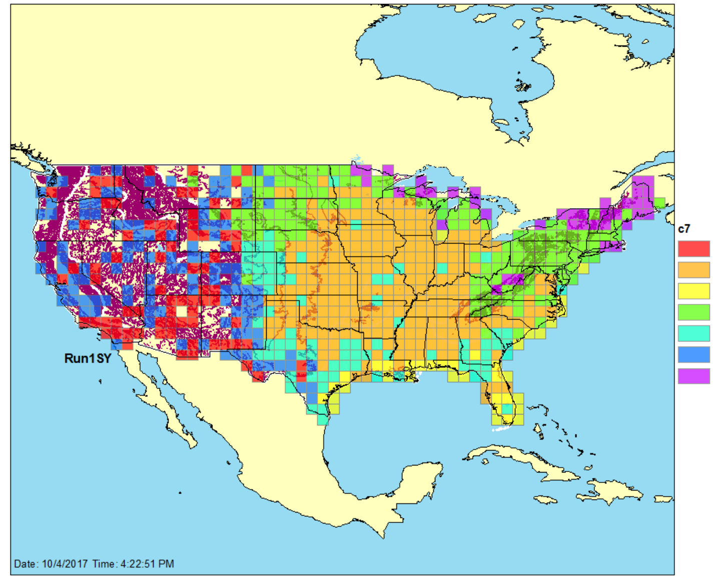
Run1SY
c7
4
2
3
1
5
6
7
Date: 10/4/2017 Time: 4:22:51 PM

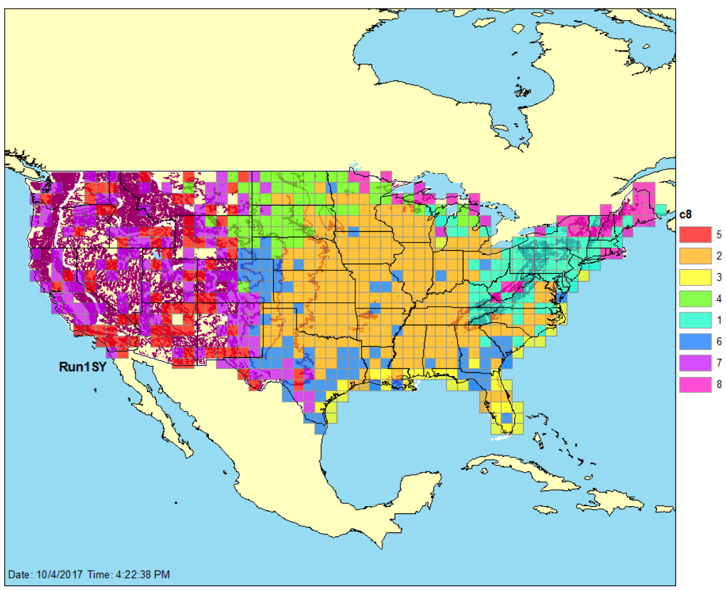
Run1SY
c8
5
2
3
4
1
6
7
8
Date: 10/4/2017 Time: 4:22:38 PM

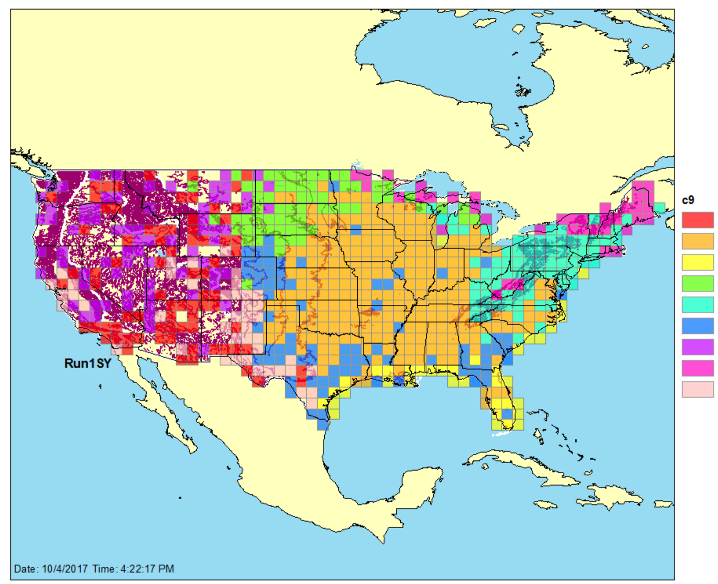
Run1SY
c9
5
2
3
4
1
6
7
8
9
Date: 10/4/2017 Time: 4:22:17 PM

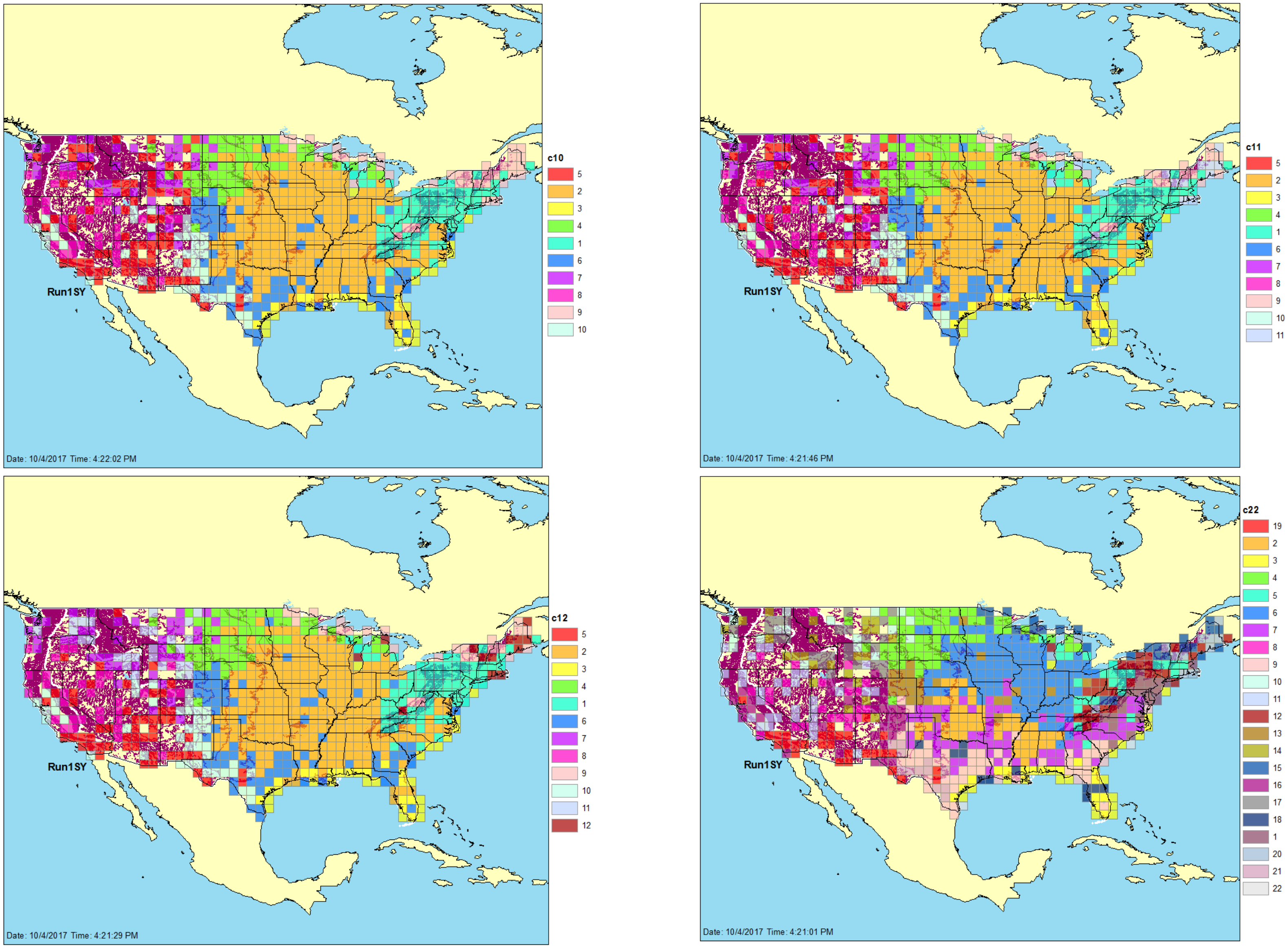

Run1SY
c10
5
2
3
4
1
6
7
8
9
10
Date: 10/4/2017 Time: 4:22:02 PM
Run1SY
c11
5
2
3
4
1
6
7
8
9
10
11
Date: 10/4/2017 Time: 4:21:46 PM
Run1SY
c12
5
2
3
4
1
6
7
8
9
10
11
12
Date: 10/4/2017 Time: 4:21:29 PM
Run1SY
c22
19
2
3
4
5
6
7
8
9
10
11
12
13
14
15
16
17
18
1
20
21
22
Date: 10/4/2017 Time: 4:21:01 PM

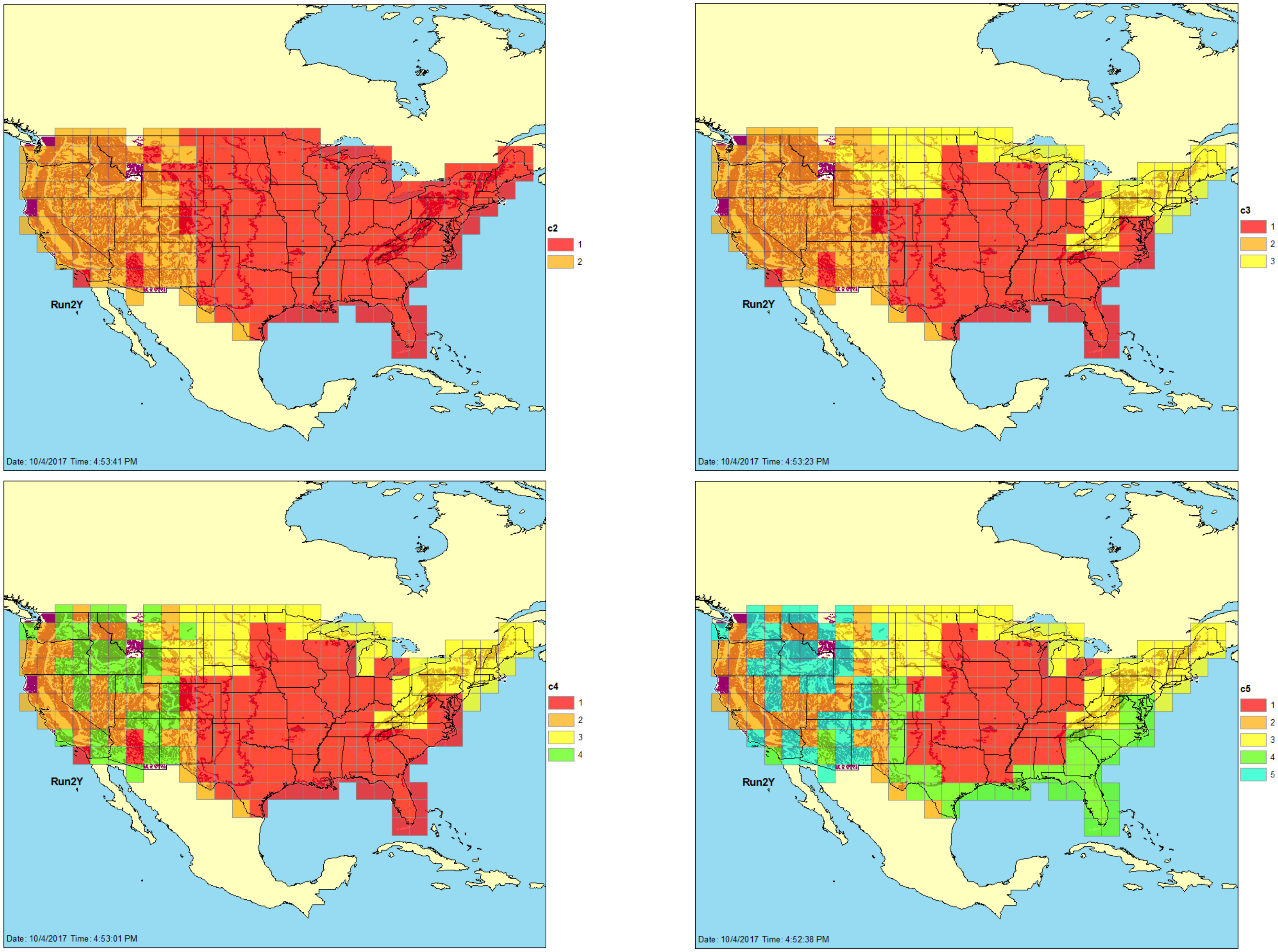
c2
1
2
Run2Y
Date: 10/4/2017 Time: 4:53:41 PM
c3
1
2
3
Run2Y
Date: 10/4/2017 Time: 4:53:23 PM
c4
1
2
3
4
Run2Y
Date: 10/4/2017 Time: 4:53:01 PM
c5
1
2
3
4
5
Run2Y
Date: 10/4/2017 Time: 4:52:38 PM

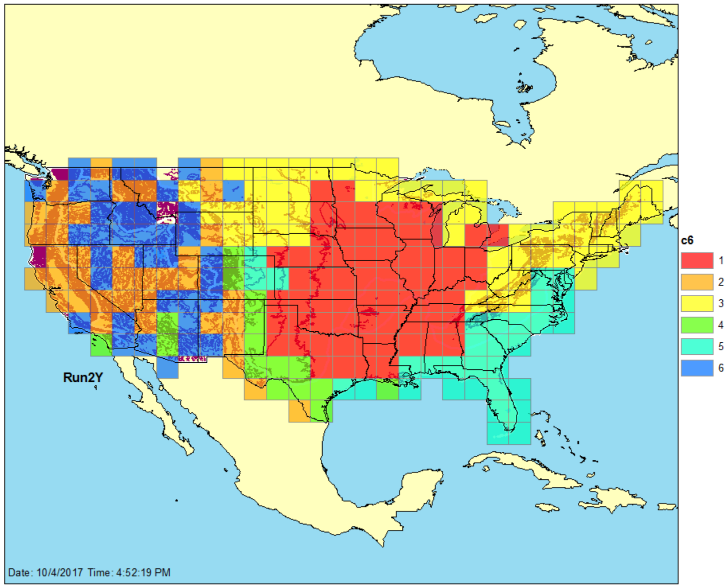
c6
1
2
3
4
5
6
Run2Y
Date: 10/4/2017 Time: 4:52:19 PM

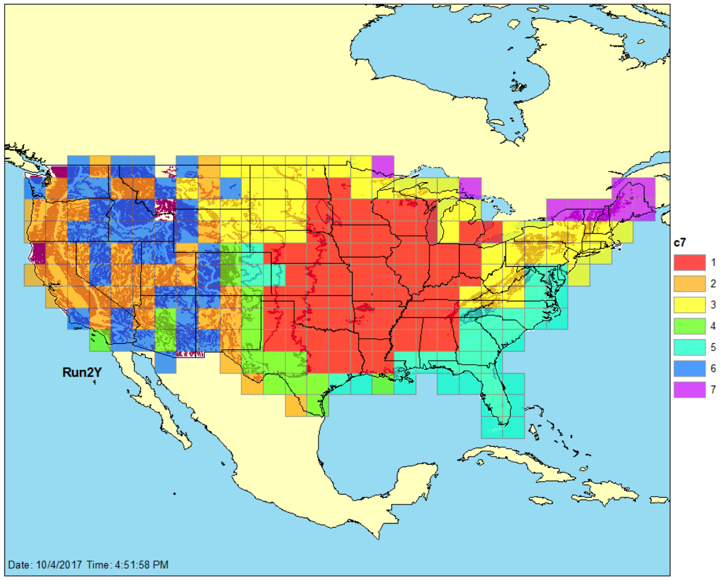
c7
1
2
3
4
5
6
7
Run2Y
Date: 10/4/2017 Time: 4:51:58 PM

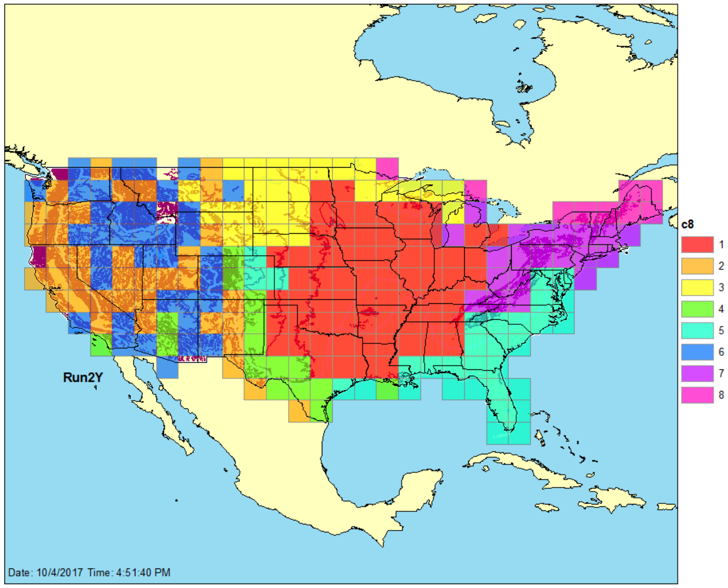
c8
1
2
3
4
5
6
7
8
Run2Y
Date: 10/4/2017 Time: 4:51:40 PM

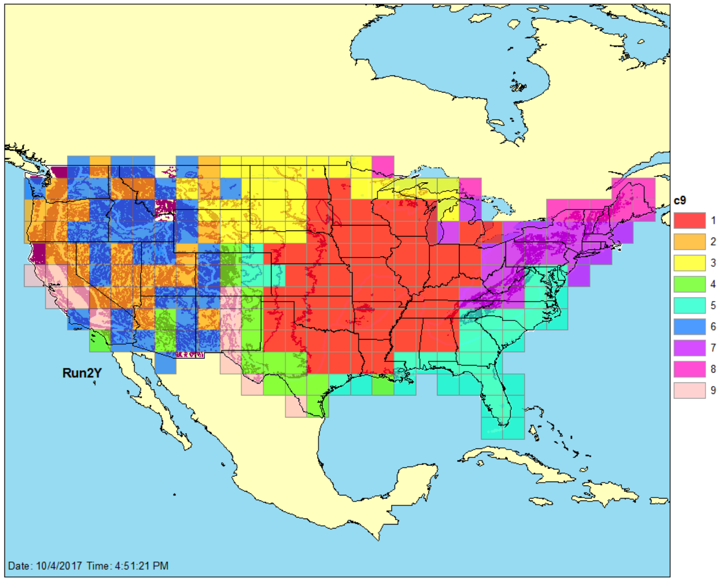
c9
1
2
3
4
5
6
7
8
9
Run2Y
Date: 10/4/2017 Time: 4:51:21 PM

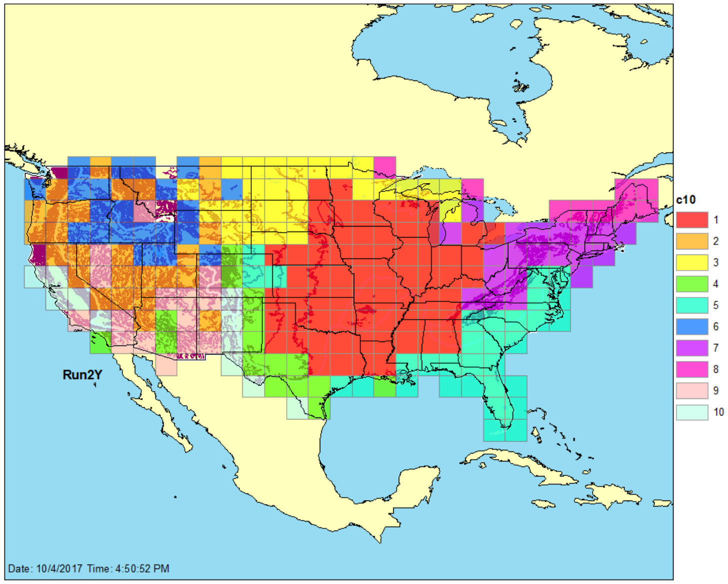
c10
1
2
3
4
5
6
7
8
9
10
Run2Y
Date: 10/4/2017 Time: 4:50:52 PM

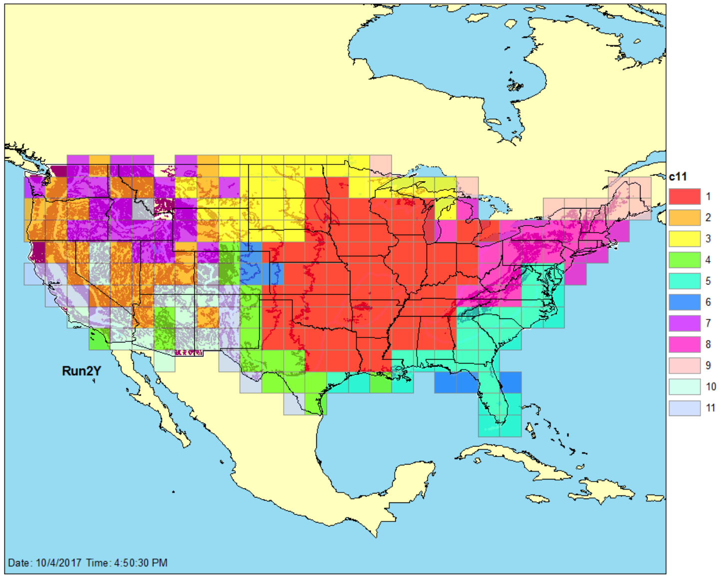
c11
1
2
3
4
5
6
7
8
9
10
11
Run2Y
Date: 10/4/2017 Time: 4:50:30 PM

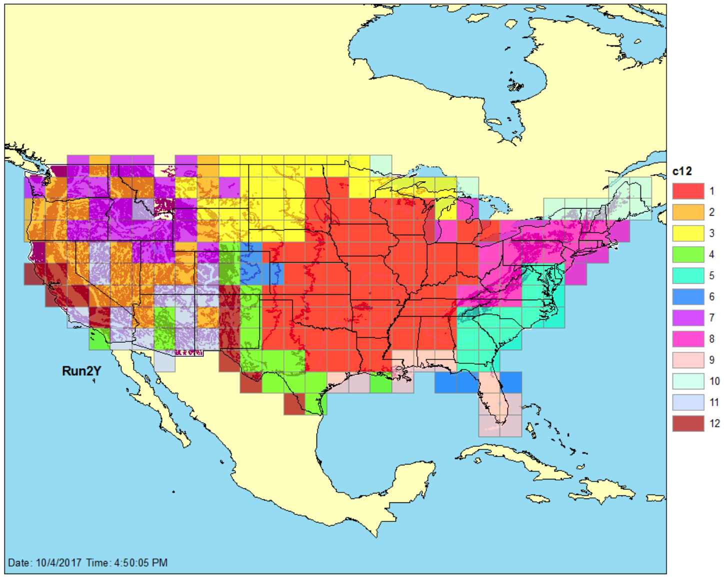
c12
1
2
3
4
5
6
7
8
9
10
11
12
Run2Y
Date: 10/4/2017 Time: 4:50:05 PM

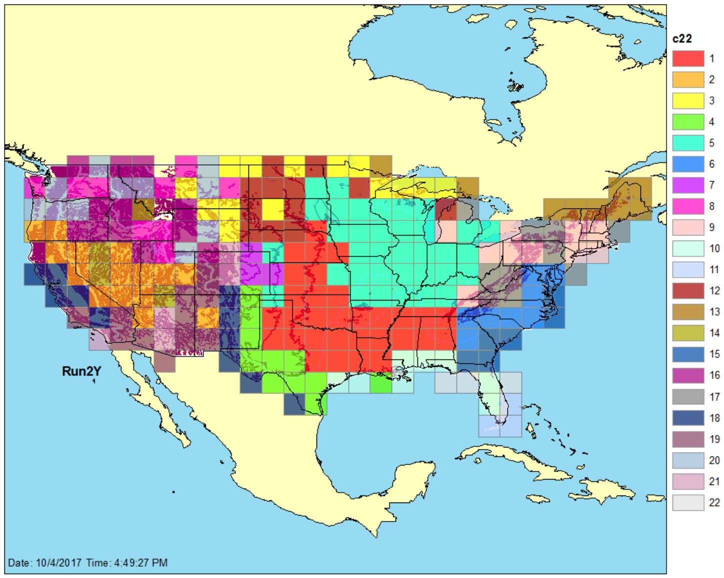
c22
1
2
3
4
5
6
7
8
9
10
11
12
13
14
15
16
17
18
19
20
21
22
Run2Y
Date: 10/4/2017 Time: 4:49:27 PM

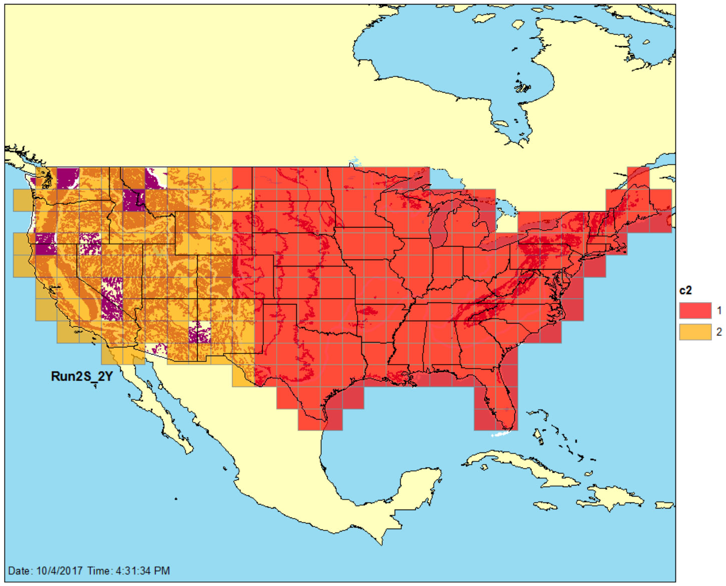
c2
1
2
Run2S_2Y
Date: 10/4/2017 Time: 4:31:34 PM

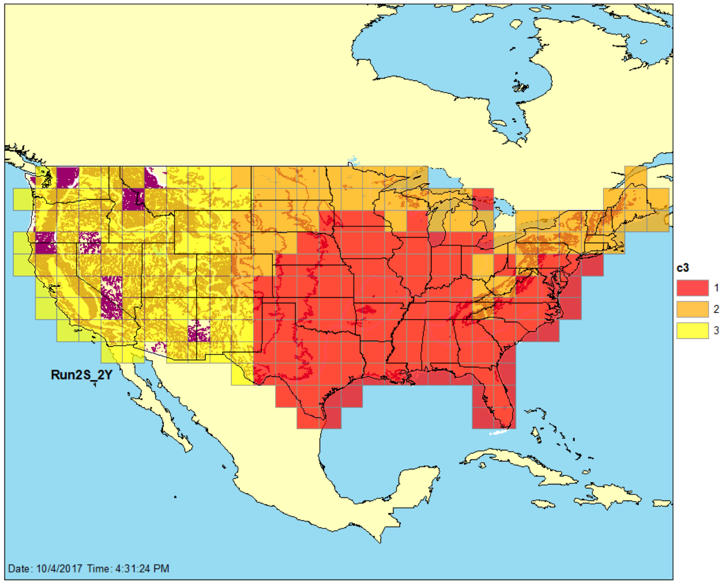
c3
1
2
3
Run2S_2Y
Date: 10/4/2017 Time: 4:31:24 PM

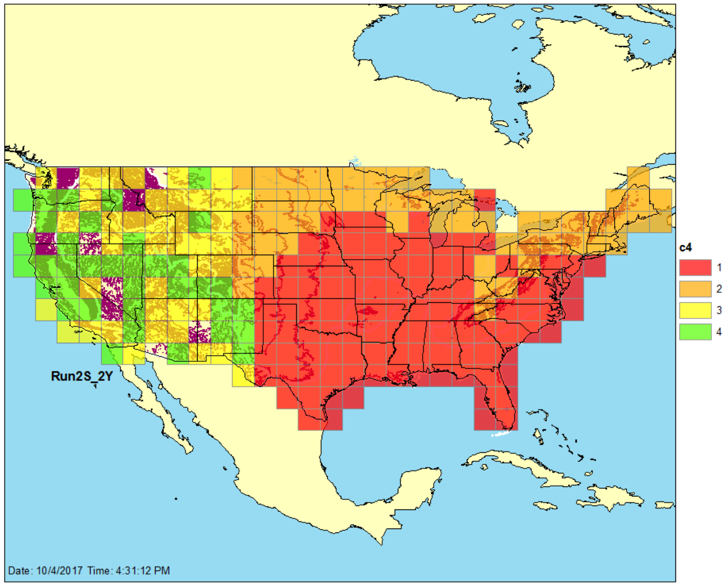
c4
1
2
3
4
Run2S_2Y
Date: 10/4/2017 Time: 4:31:12 PM

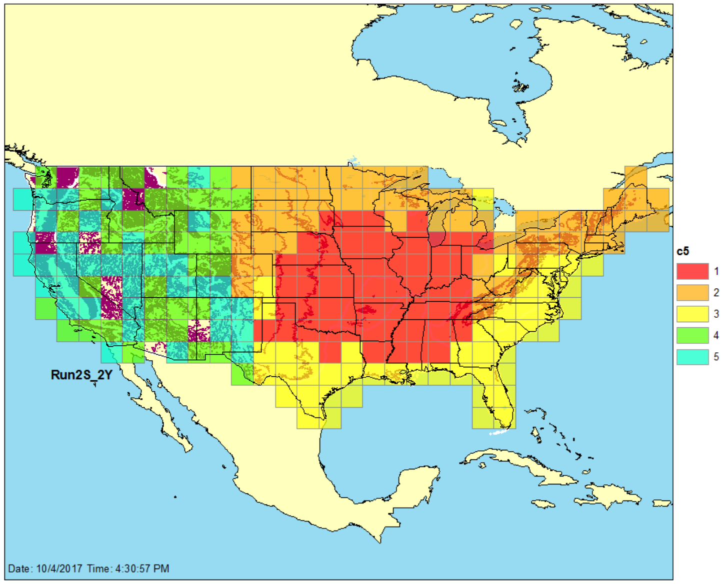
c5
1
2
3
4
5
Run2S_2Y
Date: 10/4/2017 Time: 4:30:57 PM

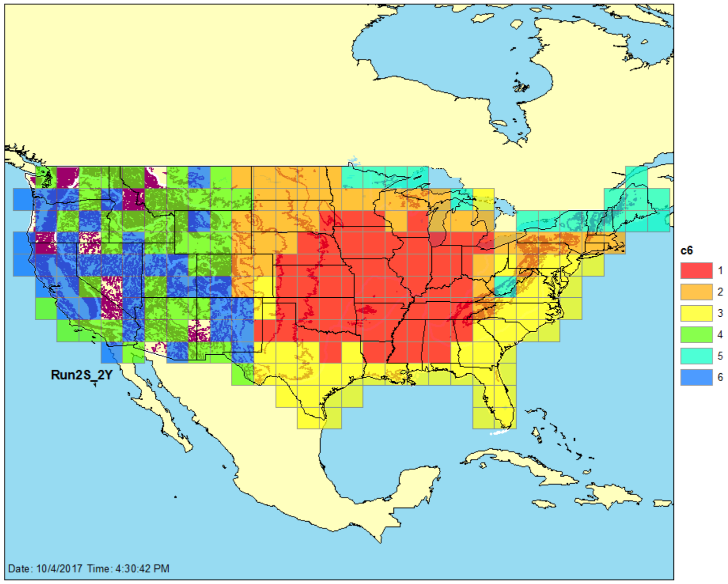
Run2S_2Y
c6
1
2
3
4
5
6
Date: 10/4/2017 Time: 4:30:42 PM

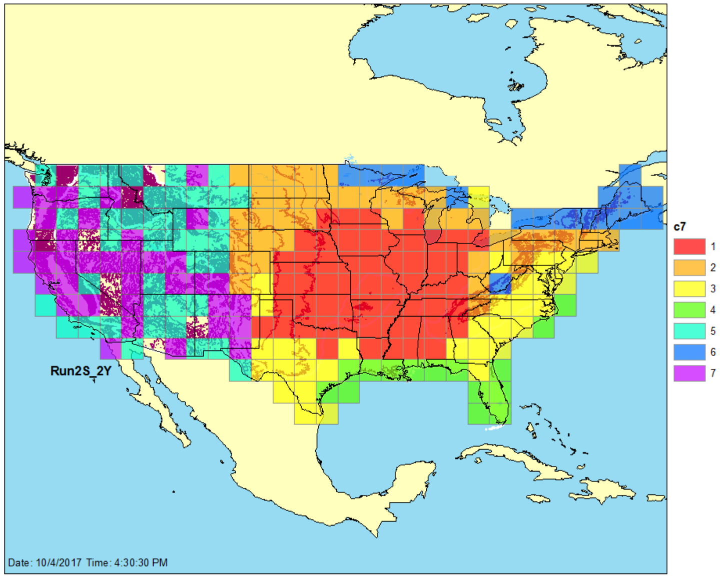
Run2S_2Y
c7
1
2
3
4
5
6
7
Date: 10/4/2017 Time: 4:30:30 PM

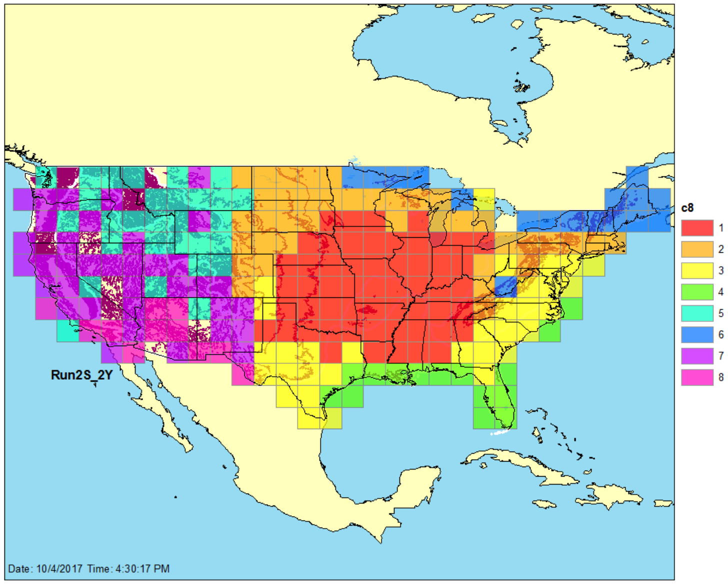
Run2S_2Y
c8
1
2
3
4
5
6
7
8
Date: 10/4/2017 Time: 4:30:17 PM

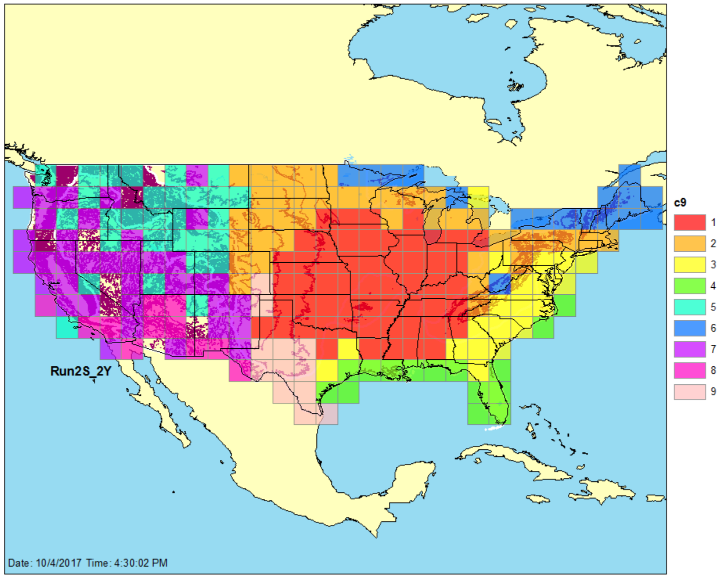
Run2S_2Y
c9
1
2
3
4
5
6
7
8
9
Date: 10/4/2017 Time: 4:30:02 PM

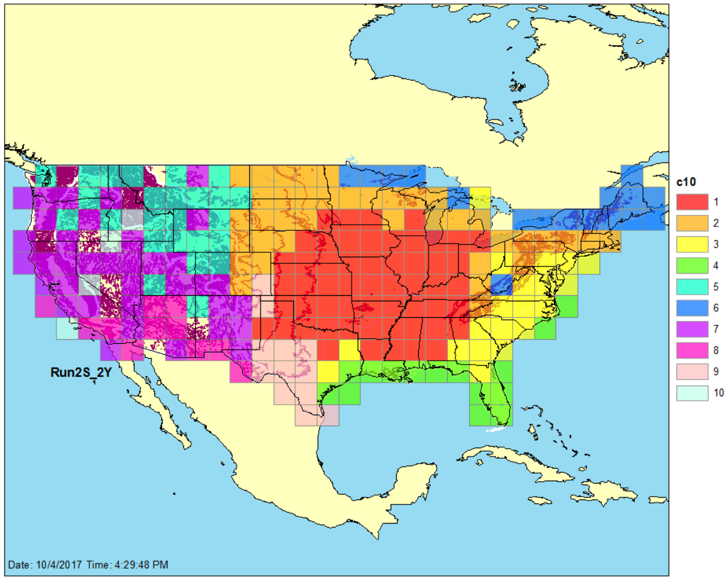
c10
1
2
3
4
5
6
7
8
9
10
Run2S_2Y
Date: 10/4/2017 Time: 4:29:48 PM

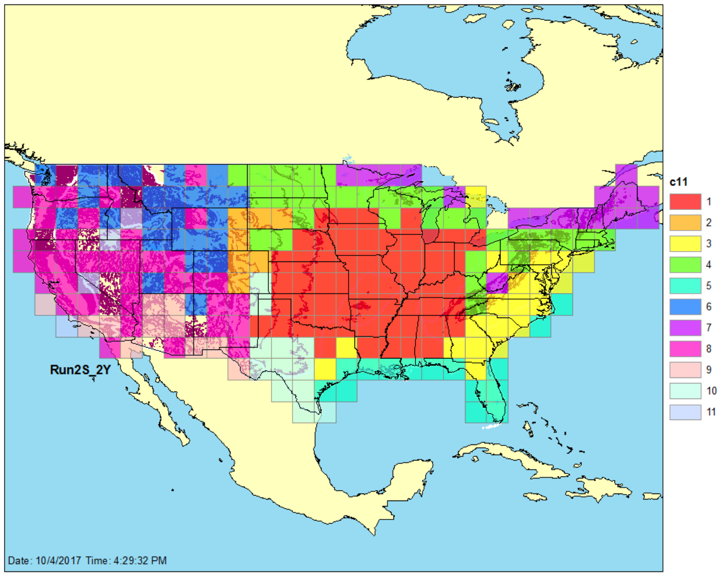
c11
1
2
3
4
5
6
7
8
9
10
11
Run2S_2Y
Date: 10/4/2017 Time: 4:29:32 PM

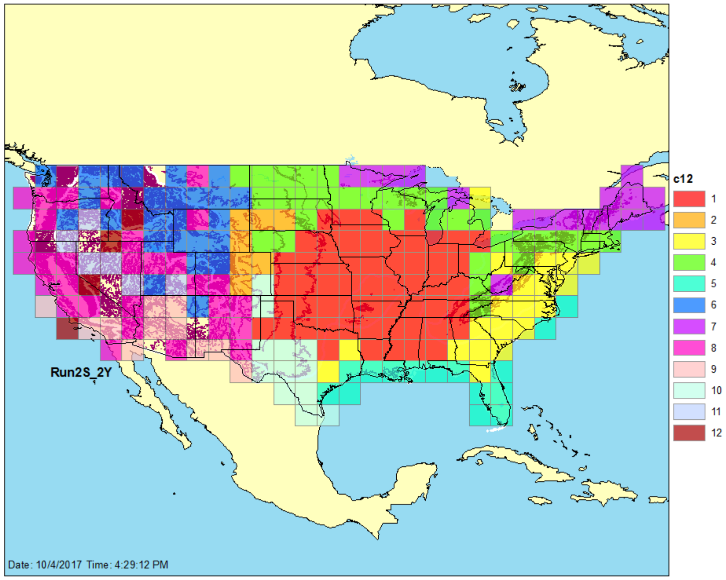
c12
1
2
3
4
5
6
7
8
9
10
11
12
Run2S_2Y
Date: 10/4/2017 Time: 4:29:12 PM

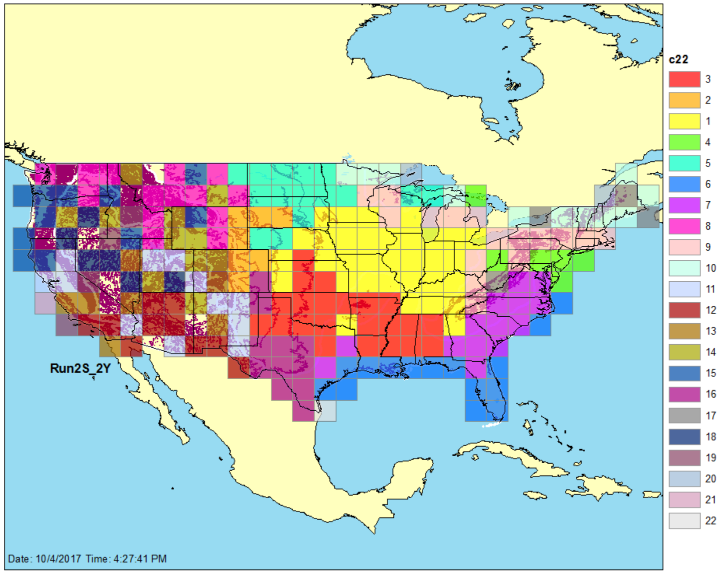
c22
3
2
1
4
5
6
7
8
9
10
11
12
13
14
15
16
17
18
19
20
21
22
Run2S_2Y
Date: 10/4/2017 Time: 4:27:41 PM

Appendix C. Region/Sub-region Models

C.1. Kernel Density Plots

Tornado kernel density plots provide a visualization of the SPC tornadoes computed as tornado densities for a specified search radius (SR). The plots in this appendix include search radius (SR) results for 0.5 to 3°. They are not normalized by the time period, so the main visual effect is location of the color shading. The smaller the SR, the smaller the averaging area used to produce the kernel density plot. SR is varied to illustrate how averaging area affects the kernel density plots. Many of the plots with small SRs show high kernel densities near towns and cities (such as Denver, Oklahoma City, Little Rock, Houston, Jackson, Huntsville Atlanta, and Tampa). The kernel densities vary with averaging area (as determined by the search radius).[2] The plots are not normalized by the time period, so the value of the densities shown depends on the years used in the time period considered. Hence the main visual effect is how the degree of shading changes spatially, near urban areas and broadly over regions.

Table C-1 summarizes key information about the 22 kernel density plots in this appendix. Plots 1-14 are for the period 1950 – 2016, excluding hurricane-spawned tornadoes. Plots 15-22 include hurricane-spawned tornadoes for 4 periods: 1950 – 2016, 1950 – 1977, 1997-1994, and 1995 – 2016. Plots 17 and 18 show how the high spots of kernel densities vary over different time periods, reflecting spatial variability of reported tornado occurrences. Tornado outbreaks, which may include large numbers of events in a region, are expected to influence how these densities change over time.

A main characteristic of these plots is how the density increases around many urban area. The significant improvement in reporting efficiency in the modern era can be seen by comparing Plots 17 to 18 and 21 to 22.

[2] The conversion between kernel density map degrees and miles is approximately 1 degree ≈ 69 miles (1 degree ≈ 111 km). The kernel density units are the number of tornadoes per the period considered per square degree.

Table Error! No text of specified style in document.**-7. Order of Kernel Density Plots**

Plot	Data	Hurricane-Spawned Tornadoes	SR	Page
1	All tornadoes - 1950-2016	No	0.5	C-2
2	All tornadoes - 1950-2016	No	1	C-2
3	All tornadoes - 1950-2016	No	1.5	C-2
4	All tornadoes - 1950-2016	No	2	C-2
5	All tornadoes - 1950-2016	No	3	C-3
6	All tornadoes - 1950-2016	No	4	C-3
7	Tors>=2 - 1950-2016	No	2	C-3
8	Tors>=4 - 1950-2016	No	2	C-3
9	Tors>=4 - 1950-2016	No	3	C-4
10	Tors>=4 - 1950-2016	No	4	C-4
11	Tors>=4 - 1950-2016	No	1.5	C-4
12	Tors>=2 - 1950-2016	No	1	C-4
13	Tors>=2 - 1950-2016	No	1.5	C-5
14	Tors>=2 - 1950-2016	No	3	C-5
15	All tornadoes - 1950-2016	Yes	1	C-5
16	All tornadoes - 1950-1977	Yes	1	C-5
17	All tornadoes - 1977-1978	Yes	1	C-6
18	All tornadoes - 1995-2016	Yes	1	C-6
19	All tornadoes - 1950-2016	Yes	0.5	C-6
20	All tornadoes - 1950-1977	Yes	0.5	C-6
21	All tornadoes - 1977-1978	Yes	0.5	C-7
22	All tornadoes - 1995-2016	Yes	0.5	C-7

Note: Tors = tornadoes

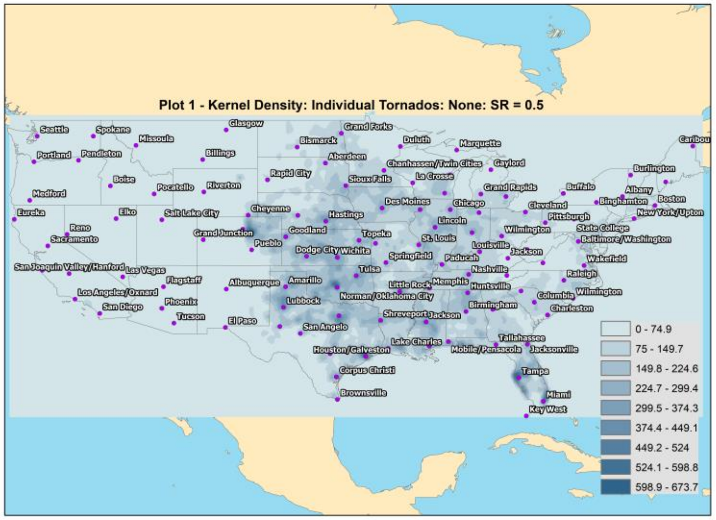
Plot 1 - Kernel Density: Individual Tornados: None: SR = 0.5
0 - 74.9
75 - 149.7
149.8 - 224.6
224.7 - 299.4
299.5 - 374.3
374.4 - 449.1
449.2 - 524
524.1 - 598.8
598.9 - 673.7

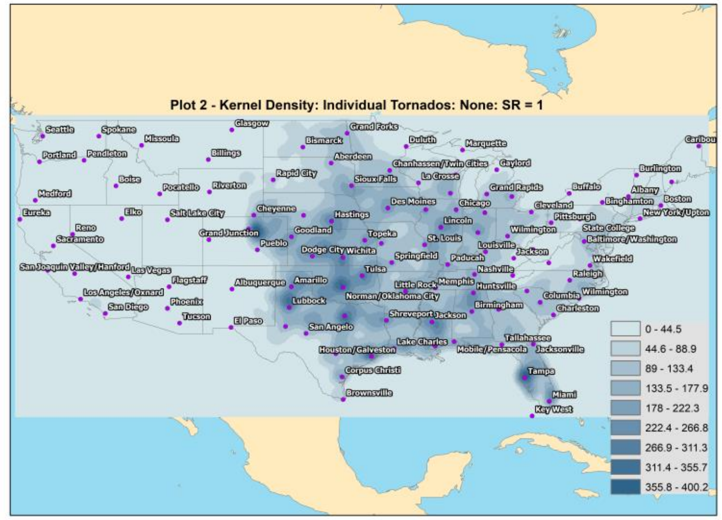
Plot 2 - Kernel Density: Individual Tornados: None: SR = 1
0 - 44.5
44.6 - 88.9
89 - 133.4
133.5 - 177.9
178 - 222.3
222.4 - 266.8
266.9 - 311.3
311.4 - 355.7
355.8 - 400.2

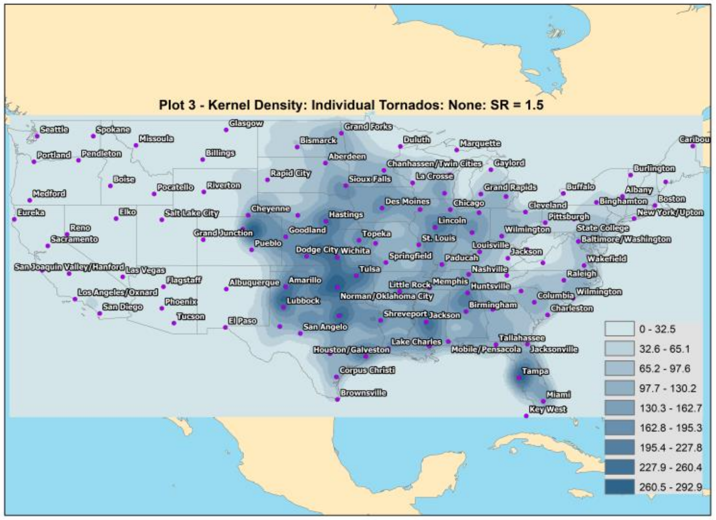
Plot 3 - Kernel Density: Individual Tornados: None: SR = 1.5
0 - 32.5
32.6 - 65.1
65.2 - 97.6
97.7 - 130.2
130.3 - 162.7
162.8 - 195.3
195.4 - 227.8
227.9 - 260.4
260.5 - 292.9

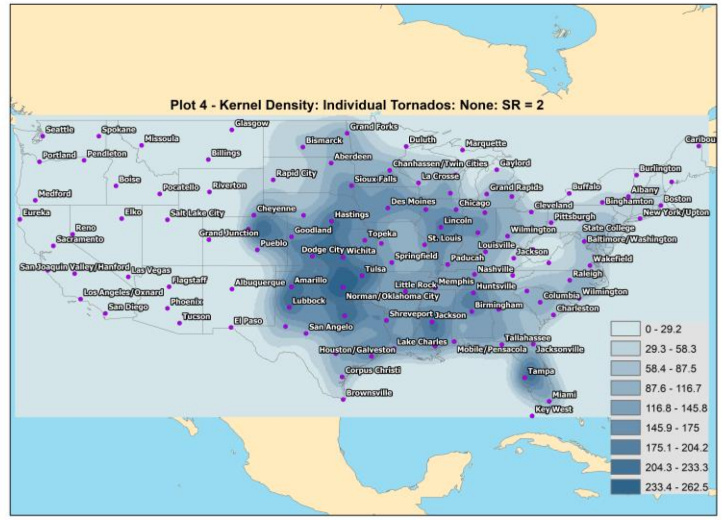
Plot 4 - Kernel Density: Individual Tornados: None: SR = 2
0 - 29.2
29.3 - 58.3
58.4 - 87.5
87.6 - 116.7
116.8 - 145.8
145.9 - 175
175.1 - 204.2
204.3 - 233.3
233.4 - 262.5

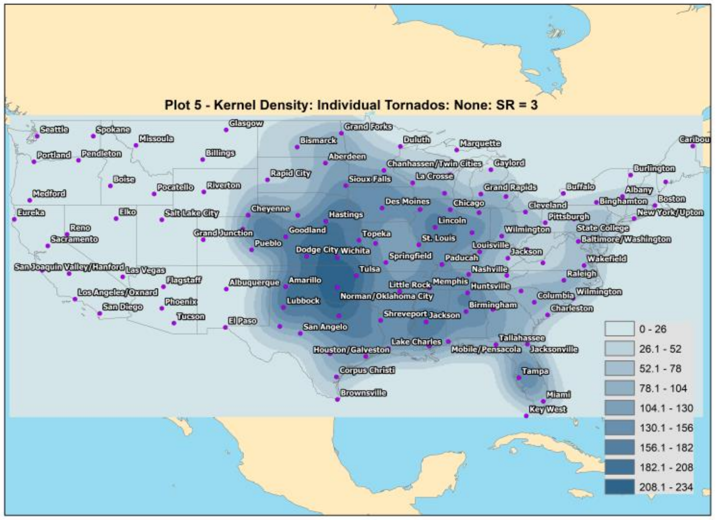
Plot 5 - Kernel Density: Individual Tornados: None: SR = 3
0 - 26
26.1 - 52
52.1 - 78
78.1 - 104
104.1 - 130
130.1 - 156
156.1 - 182
182.1 - 208
208.1 - 234

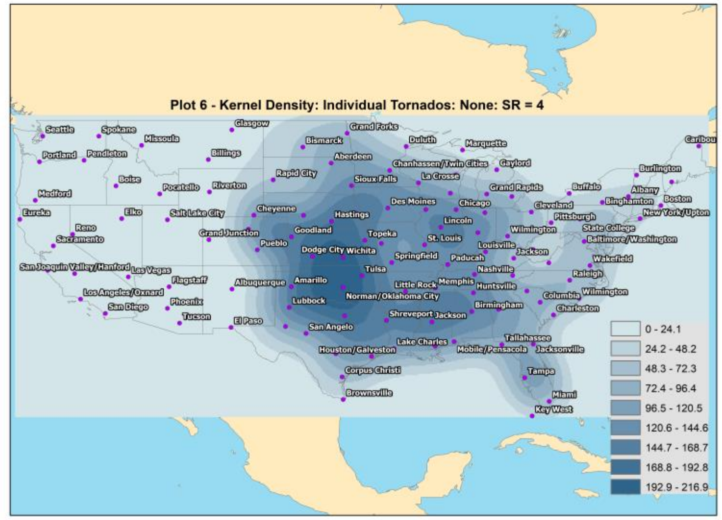
Plot 6 - Kernel Density: Individual Tornados: None: SR = 4
0 - 24.1
24.2 - 48.2
48.3 - 72.3
72.4 - 96.4
96.5 - 120.5
120.6 - 144.6
144.7 - 168.7
168.8 - 192.8
192.9 - 216.9

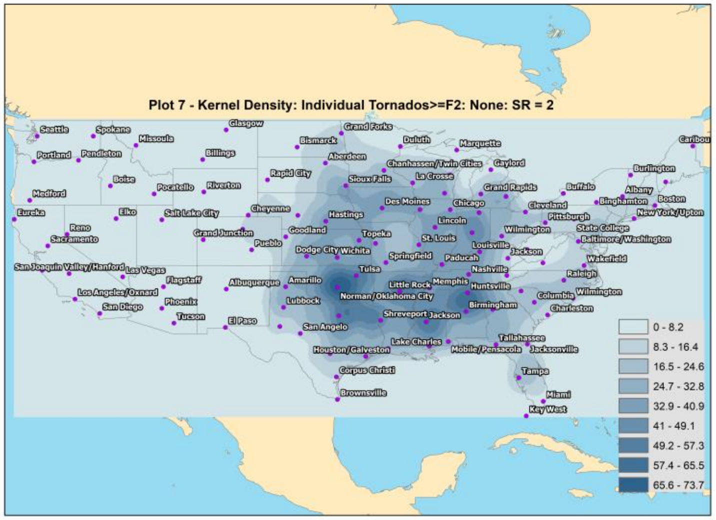
Plot 7 - Kernel Density: Individual Tornados>=F2: None: SR = 2
0 - 8.2
8.3 - 16.4
16.5 - 24.6
24.7 - 32.8
32.9 - 40.9
41 - 49.1
49.2 - 57.3
57.4 - 65.5
65.6 - 73.7

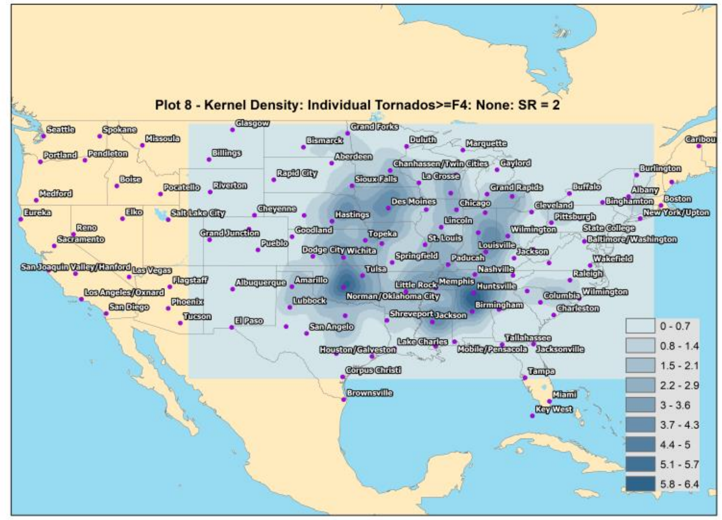
Plot 8 - Kernel Density: Individual Tornados>=F4: None: SR = 2
0 - 0.7
0.8 - 1.4
1.5 - 2.1
2.2 - 2.9
3 - 3.6
3.7 - 4.3
4.4 - 5
5.1 - 5.7
5.8 - 6.4

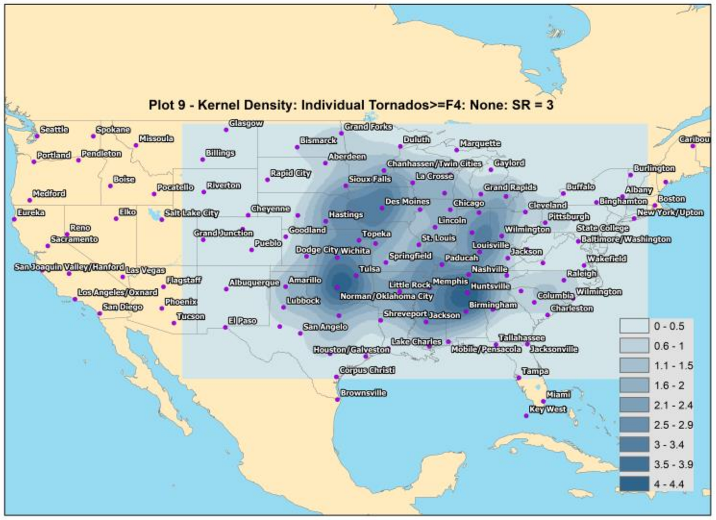
Plot 9 - Kernel Density: Individual Tornados>=F4: None: SR = 3
0 - 0.5
0.6 - 1
1.1 - 1.5
1.6 - 2
2.1 - 2.4
2.5 - 2.9
3 - 3.4
3.5 - 3.9
4 - 4.4

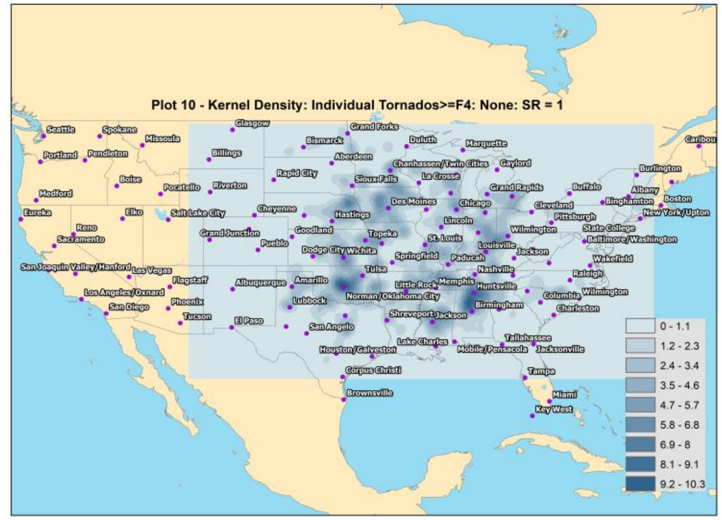
Plot 10 - Kernel Density: Individual Tornados>=F4: None: SR = 1
0 - 1.1
1.2 - 2.3
2.4 - 3.4
3.5 - 4.6
4.7 - 5.7
5.8 - 6.8
6.9 - 8
8.1 - 9.1
9.2 - 10.3

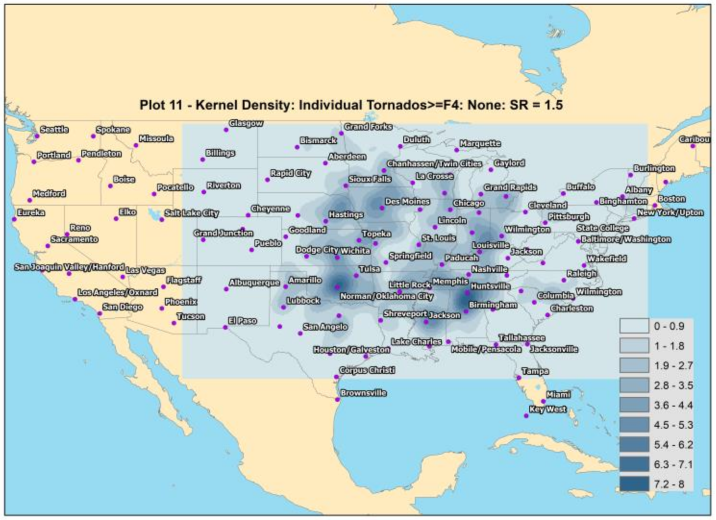
Plot 11 - Kernel Density: Individual Tornados>=F4: None: SR = 1.5
0 - 0.9
1 - 1.8
1.9 - 2.7
2.8 - 3.5
3.6 - 4.4
4.5 - 5.3
5.4 - 6.2
6.3 - 7.1
7.2 - 8

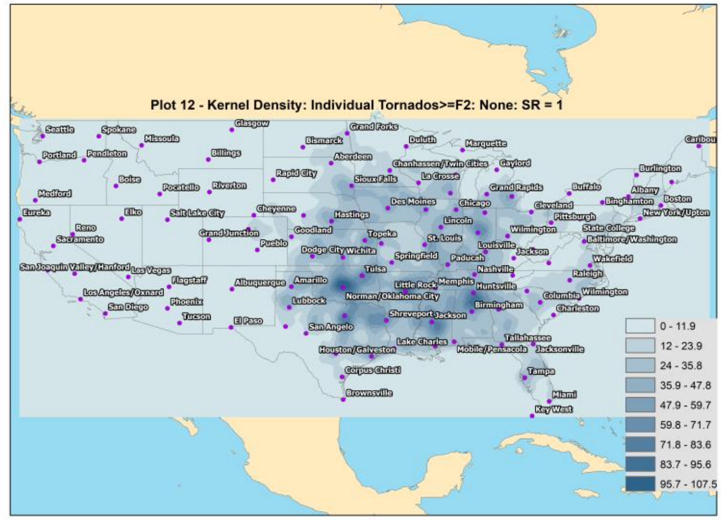
Plot 12 - Kernel Density: Individual Tornados>=F2: None: SR = 1
0 - 11.9
12 - 23.9
24 - 35.8
35.9 - 47.8
47.9 - 59.7
59.8 - 71.7
71.8 - 83.6
83.7 - 95.6
95.7 - 107.5

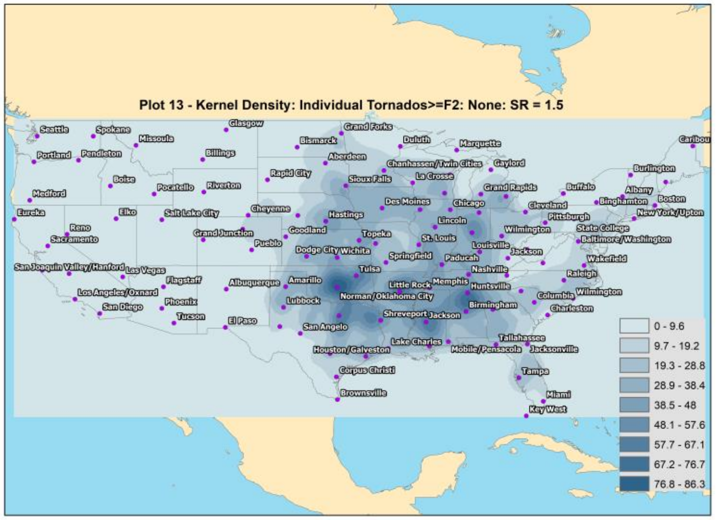
Plot 13 - Kernel Density: Individual Tornados>=F2: None: SR = 1.5
0 - 9.6
9.7 - 19.2
19.3 - 28.8
28.9 - 38.4
38.5 - 48
48.1 - 57.6
57.7 - 67.1
67.2 - 76.7
76.8 - 86.3

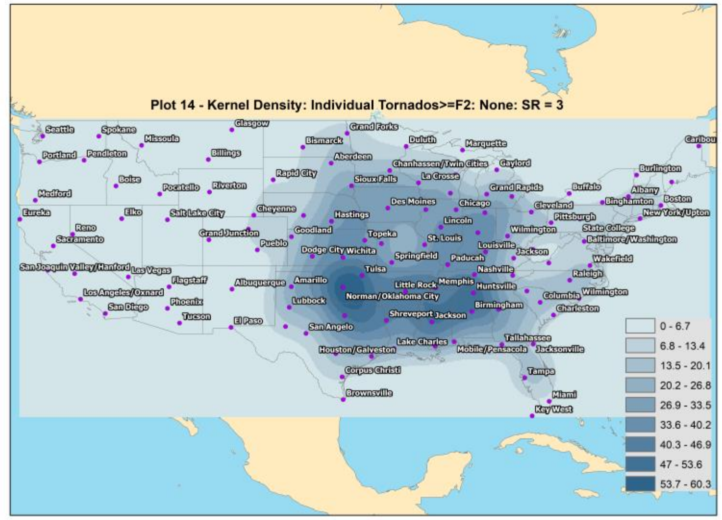
Plot 14 - Kernel Density: Individual Tornados>=F2: None: SR = 3
0 - 6.7
6.8 - 13.4
13.5 - 20.1
20.2 - 26.8
26.9 - 33.5
33.6 - 40.2
40.3 - 46.9
47 - 53.6
53.7 - 60.3

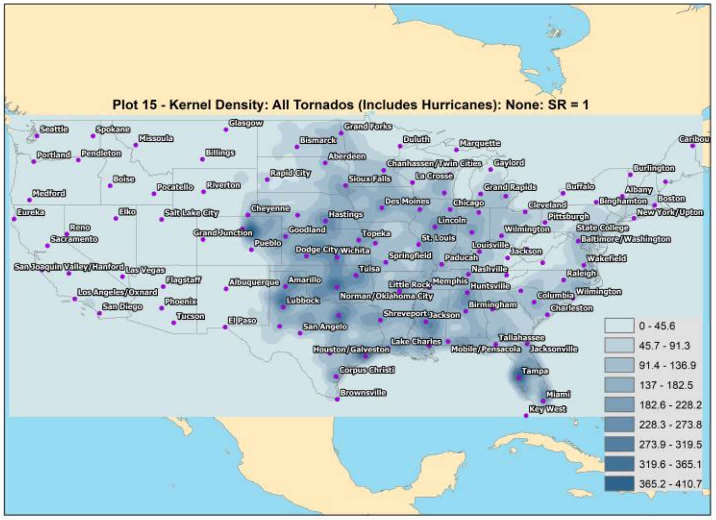
Plot 15 - Kernel Density: All Tornados (Includes Hurricanes): None: SR = 1
0 - 45.6
45.7 - 91.3
91.4 - 136.9
137 - 182.5
182.6 - 228.2
228.3 - 273.8
273.9 - 319.5
319.6 - 365.1
365.2 - 410.7

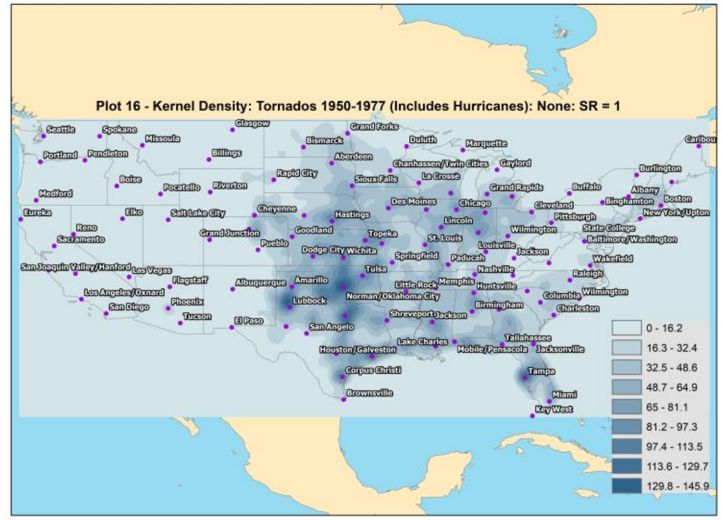
Plot 16 - Kernel Density: Tornados 1950-1977 (Includes Hurricanes): None: SR = 1
0 - 16.2
16.3 - 32.4
32.5 - 48.6
48.7 - 64.9
65 - 81.1
81.2 - 97.3
97.4 - 113.5
113.6 - 129.7
129.8 - 145.9

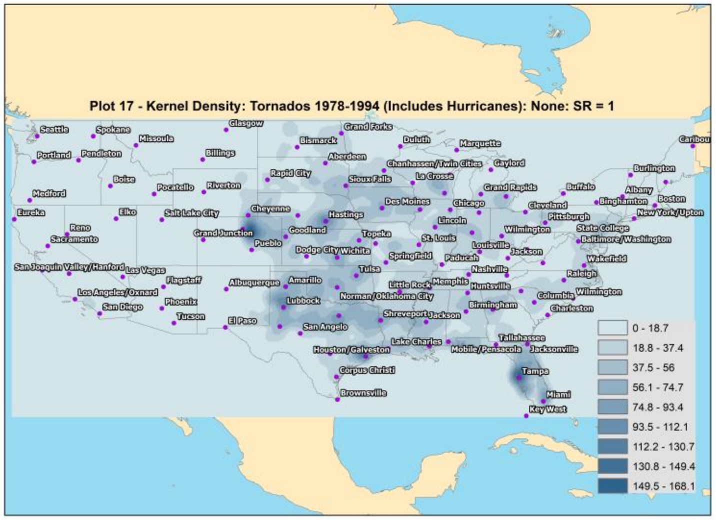
Plot 17 - Kernel Density: Tornados 1978-1994 (Includes Hurricanes): None: SR = 1
0 - 18.7
18.8 - 37.4
37.5 - 56
56.1 - 74.7
74.8 - 93.4
93.5 - 112.1
112.2 - 130.7
130.8 - 149.4
149.5 - 168.1

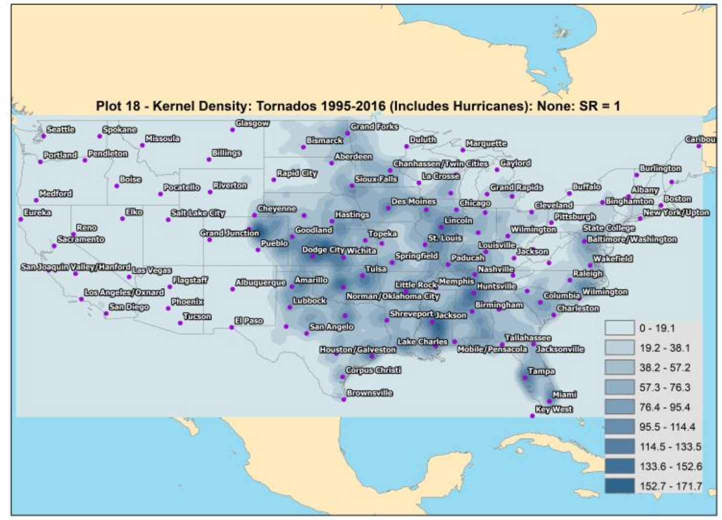
Plot 18 - Kernel Density: Tornados 1995-2016 (Includes Hurricanes): None: SR = 1
0 - 19.1
19.2 - 38.1
38.2 - 57.2
57.3 - 76.3
76.4 - 95.4
95.5 - 114.4
114.5 - 133.5
133.6 - 152.6
152.7 - 171.7

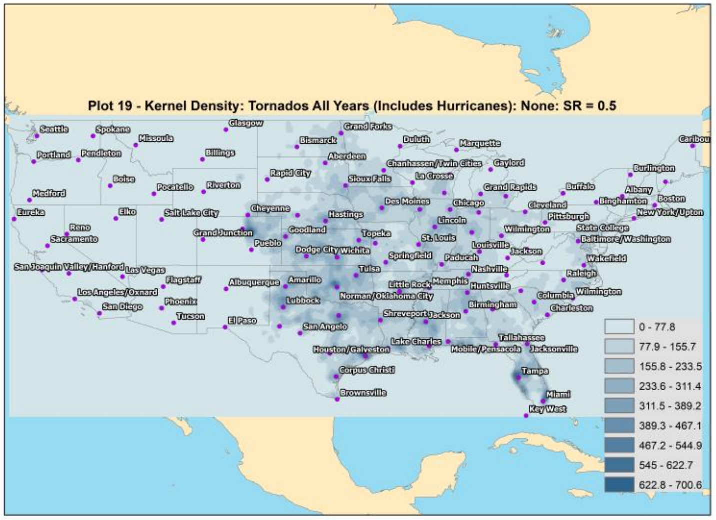
Plot 19 - Kernel Density: Tornados All Years (Includes Hurricanes): None: SR = 0.5
0 - 77.8
77.9 - 155.7
155.8 - 233.5
233.6 - 311.4
311.5 - 389.2
389.3 - 467.1
467.2 - 544.9
545 - 622.7
622.8 - 700.6

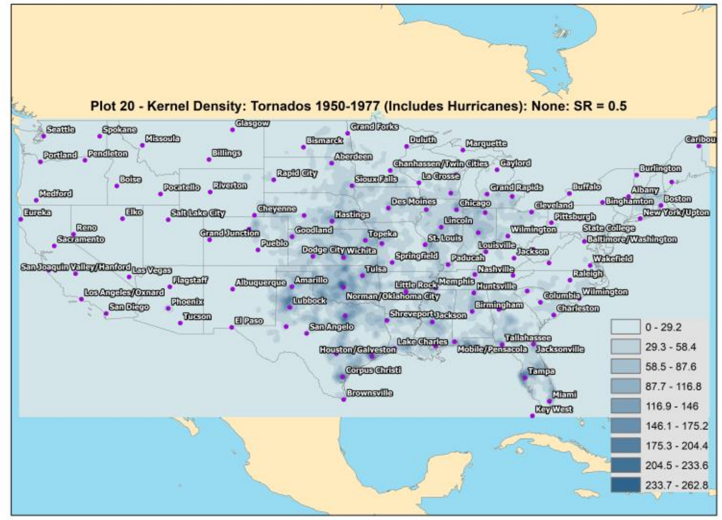
Plot 20 - Kernel Density: Tornados 1950-1977 (Includes Hurricanes): None: SR = 0.5
0 - 29.2
29.3 - 58.4
58.5 - 87.6
87.7 - 116.8
116.9 - 146
146.1 - 175.2
175.3 - 204.4
204.5 - 233.6
233.7 - 262.8

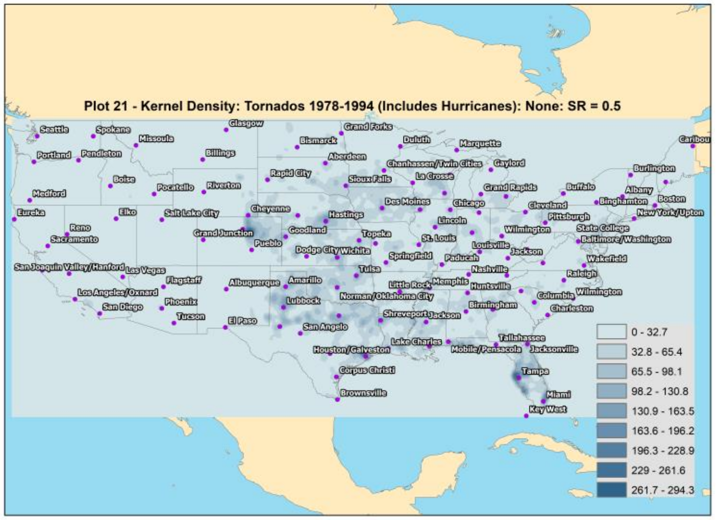
Plot 21 - Kernel Density: Tornados 1978-1994 (Includes Hurricanes): None: SR = 0.5
0 - 32.7
32.8 - 65.4
65.5 - 98.1
98.2 - 130.8
130.9 - 163.5
163.6 - 196.2
196.3 - 228.9
229 - 261.6
261.7 - 294.3

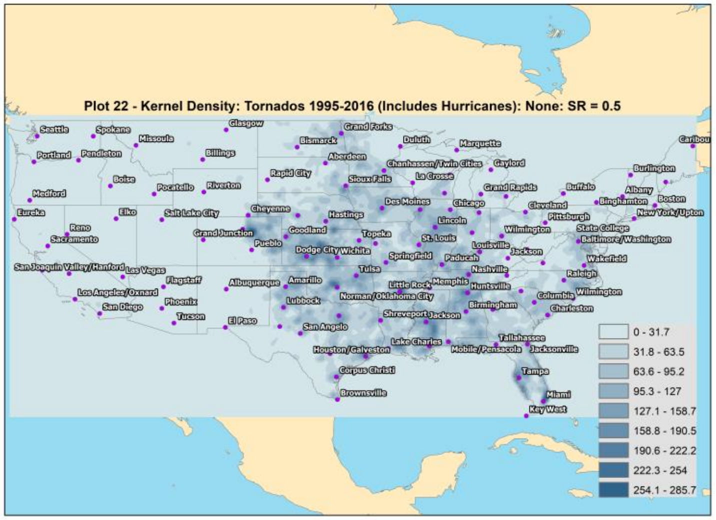
Plot 22 - Kernel Density: Tornados 1995-2016 (Includes Hurricanes): None: SR = 0.5
0 - 31.7
31.8 - 63.5
63.6 - 95.2
95.3 - 127
127.1 - 158.7
158.8 - 190.5
190.6 - 222.2
222.3 - 254
254.1 - 285.7

C.2. Population and Building Data

C.2.1. Background

In our analysis of tornado reporting efficiency, we use data associated with the US Census Bureau statistical divisions, including census tracts, census block groups, and census blocks. The population bias analysis uses building density data for the 2000 and 2010 census tracts.

A *Census tract* is the largest division of tracts, group, and blocks. Census tracts generally have a population size of 1,200 to 8,000 people, with an optimal size of 4,000 people. Census tracts are contiguous, and their spatial size varies based on the population density in the area (larger/smaller for lower/higher populated areas). Census tracts do not cross state or county boundaries (state and county boundaries are also census tract boundaries) (US Census Bureau, 2017).

Census Block Groups are statistical divisions of census tracts that typically contain between 600 and 3,000 people. Block groups consist of clusters of blocks and help to control block numbering (US Census Bureau, 2017).

A *Census Block* is the smallest census statistical division. Blocks are bounded by visible features such as roads and streams, or non-visible boundaries such as city or county limits. Block are typically spatially smaller in densely populated areas and spatially larger and more irregularly shaped in rural areas. Blocks are fully contained within both block groups and tracts. Census tracts, block groups, and blocks cover the entire United States, Puerto Rico, and the Island areas (US Census Bureau, 2017).

Population Density. The population density of a tract (ρ_{pT}) is computed as the number of people living in a tract (N_p), divided by the area of the tract (A_T).

$$\rho_{p_T} = \frac{N_p}{A_T}\left(\frac{people}{mi^2}\right). \qquad \textbf{(C-3)}$$

Building Density. The building density of a tract (ρ_{bT}) is computed as the number of buildings in a tract (N_b), divided by the area of the tract (A_T).

$$\rho_{b_T} = \frac{N_b}{A_T}\left(\frac{bldg.}{mi^2}\right). \qquad \textbf{(C-4)}$$

C.2.2. Hazus Methodology for Year 2000 and 2010 Number of Buildings Estimates

Hazus-MH MR3 (FEMA, 2007) and Hazus 2.2 (FEMA, 2015) data is used to compute tract building density. The 2000 data is from Hazus-MH MR3 and the 2010 data is from Hazus 2.2. The methods used in Hazus to develop building counts are described below.

The Hazus data contains building counts per tract by building occupancy class. Thirty-three specific occupancy classifications are used, which fall into 7 general occupancies. The occupancy classes and their general classifications are given in Table C-2. Standard Industrial Codes (SIC) refer to the 1987 SIC manual.

The number of buildings in each occupancy class within a tract are summed to get the total number of buildings in a tract (N_b), used in Eq. (C-4).

Table Error! No text of specified style in document.**-8. Hazus Building Occupancy Classes (reproduced from Hazus-MH MR3 (FEMA, 2007))**

HAZUS Label	Occupancy Class	Standard Industrial Codes (SIC)
Residential		
RES1	Single Family Dwelling	
RES2	Mobile Home	
RES3A	Multi Family Dwelling - Duplex	
RES3B	Multi Family Dwelling – 3-4 Units	
RES3C	Multi Family Dwelling – 5-9 Units	
RES3D	Multi Family Dwelling – 10-19 Units	
RES3E	Multi Family Dwelling – 20-49 Units	
RES3F	Multi Family Dwelling – 50+ Units	
RES4	Temporary Lodging	70
RES5	Institutional Dormitory	
RES6	Nursing Home	8051, 8052, 8059
Commercial		
COM1	Retail Trade	52, 53, 54, 55, 56, 57, 59
COM2	Wholesale Trade	42, 50, 51
COM3	Personal and Repair Services	72, 75, 76, 83, 88
COM4	Business/Professional/Technical Services	40, 41, 44, 45, 46, 47, 49, 61, 62, 63, 64, 65, 67, 73,78 (except 7832), 81, 87, 89
COM5	Depository Institutions	60
COM6	Hospital	8062, 8063, 8069
COM7	Medical Office/Clinic	80 (except 8051, 8052, 8059, 8062, 8063, 8069)
COM8	Entertainment & Recreation	48, 58, 79 (except 7911), 84
COM9	Theaters	7832, 7911
COM10	Parking	
Industrial		
IND1	Heavy	22, 24, 26, 32, 34, 35 (except 3571, 3572), 37
IND2	Light	23, 25, 27, 30, 31, 36 (except 3671, 3672, 3674), 38,39
IND3	Food/Drugs/Chemicals	20, 21, 28, 29
IND4	Metals/Minerals Processing	10, 12, 13, 14, 33
IND5	High Technology	3571, 3572, 3671, 3672, 3674
IND6	Construction	15, 16, 17
Agriculture		
AGR1	Agriculture	01, 02, 07, 08, 09
Religion/Non-Profit		
REL1	Church/Membership Organizations	86
Government		
GOV1	General Services	43, 91, 92 (except 9221, 9224), 93, 94, 95, 96, 97
GOV2	Emergency Response	9221, 9224

Education		
EDU1	Schools/Libraries	82 (except 8221, 8222)
EDU2	Colleges/Universities	8221, 8222

The HAZUS building count data is given by both census tract and census block.

C.2.2.1. Year 2000 Building Count

The year 2000 building count data was calculated through Year 2000 Census of Population and Housing (US Census Bureau, 2000) and Dun and Bradstreet (2006) data. The census data was used to determine the inventory of residential buildings (RES1-RES3) and the Dun and Bradstreet (2006) data was used to determine the inventory of non-residential/commercial structures (FEMA, 2007). The Dun and Bradstreet (2006) data was also used for facilities that are commercial in nature, but provide housing for people (RES4, RES5, and RES6). The Dun and Bradstreet (2006) data represents approximately 76% of the total businesses in the United States, and approximately 98% of the gross national product. This means that the businesses not in the Dun and Bradstreet (2006) database are smaller and mostly home based, in which case they are accounted for in the Census of Population and Housing data (FEMA, 2007).

The Census of Population and Housing (2000) data gave the total count of all housing units in each housing category (1 unit detached, 1 unit attached, 2 units, 3 or 4 units, 5-9 units, 10-19 units, 20-49 units, 50+ units, and mobile homes) down to the block group level. At the block level, only the total number of housing units was given (i.e. the count was not broken out by housing category). The single family, RES1, occupancy was estimated as the sum of "1 unit detached" and "1 unit attached." The RES2 occupancy was set equal to the mobile home count. The building count data by tract for RES1 and RES2 occupancies was taken directly from the block group counts. The building count data by block for RES1 occupancies was computed as the ratio of the number of RES1 occupancies within a block group to the total number of occupancies in a block group, multiplied by the total number of occupancies in the block. The same method was used to compute the number of RES2 occupancies by block (FEMA, 2007).

The building counts for all of the other occupancy classifications were derived using total square footage by occupancy and census block/tract. The building count for each occupancy type was calculated by dividing the total unit square footage of each occupancy type within a tract by the typical building size for each occupancy. The assumed typical building square footage by specific occupancy are given in Table C-3 (FEMA, 2007).

Table Error! No text of specified style in document.**-9. Assumed Typical Building Square Footage by Specific Occupancy (reproduced from Hazus -MH MR3 (FEMA, 2007))**

Occupancy	Square Footage	Occupancy	Square Footage	Occupancy	Square Footage
RES3A	3,000	COM2	30,000	IND2	30,000
RES3B	3,000	COM3	10,000	IND3	45,000
RES3C	8,000	COM4	80,000	IND4	45,000
RES3D	12,000	COM5	4,100	IND5	45,000
RES3E	40,000	COM6	55,000	IND6	30,000
RES3F	60,000	COM7	7,000	AGR1	30,000
RES4	135,000	COM8	5,000	REL1	17,000
RES5	25,000	COM9	12,000	GOV1	11,000
RES6	25,000	COM10	145,000	GOV2	11,000
COM1	110,000	IND1	30,000	EDU1	130,000
				EDU2	50,000

Note: 1 square foot = 0.09290304 m^2

C.2.2.2. Year 2010 Building Count Data

Hazus 2.2 (FEMA, 2015) data was used for the year 2010 building count data. The Hazus 2.2 data was produced using the year 2010 Census of Population and Housing (US Census Bureau, 2010) and Dun and Bradstreet (2006) data. Aside from using 2010 Census of Population and Housing data (new tract and block boundaries and data), the only change in the methods used by Hazus to produce the building counts, described in the previous sections, were in computing the RES3 building counts (FEMA, 2015).

Two changes were made in the way the RES3 building counts were produced. The first change was an update of FEMA (2007), which contains the typical floor areas for multi-family buildings. Newly available Environmental Impact Assessment data was used to develop estimated housing unit floor areas that varied by census region. The second change was that RES3 building counts were no longer estimated based on total unit square footages (making the first change have no effect on our use of the data). In the Hazus 2.2 data the building counts were estimated directly from the housing unit data by assuming a typical unit count per building (FEMA, 2015).

C.3. Time Trends of Tornado Occurrences

Moving average trend plots for 5, 11, and 22-year periods of mean tornado occurrence rates (1950 – 2016) by region are provided in the first group of plots in Table C-4. The second group of plots provide the COVs of the mean occurrence rates for the same periods.

Table Error! No text of specified style in document.**-10. Tornado Occurrence Rate Time Trends**

Metric	Region	Average (yrs)	Page
Nominal Occurrence Rate	1	5, 11, 22	C-12
Nominal Occurrence Rate	2	5, 11, 22	C-13
Nominal Occurrence Rate	3	5, 11, 22	C-14
Nominal Occurrence Rate	4	5, 11, 22	C-15
Nominal Occurrence Rate	5	5, 11, 22	C-16
Nominal Occurrence Rate	6	5, 11, 22	C-17
Nominal Occurrence Rate	US	5, 11, 22	C-18
COV	1	5, 11, 22	C-19
COV	2	5, 11, 22	C-20
COV	3	5, 11, 22	C-21
COV	4	5, 11, 22	C-22
COV	5	5, 11, 22	C-23
COV	6	5, 11, 22	C-24
COV	US	5, 11, 22	C-25

Notes: Occurrence rates are shown in the plots as tornadoes per year per square mile (1 tornado per year per square mile = 0.386102 tornadoes per year per square kilometer). 2STD = two standard deviations.

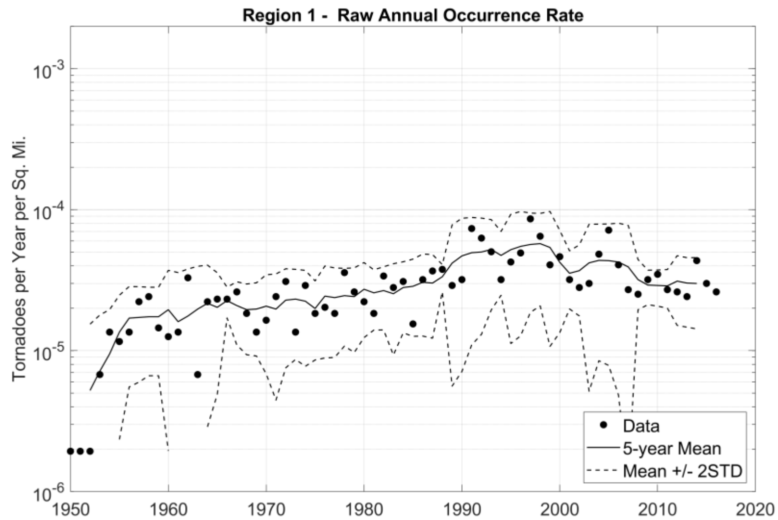
Region 1 - Raw Annual Occurrence Rate
Tornadoes per Year per Sq. Mi.
Data
5-year Mean
Mean +/- 2STD

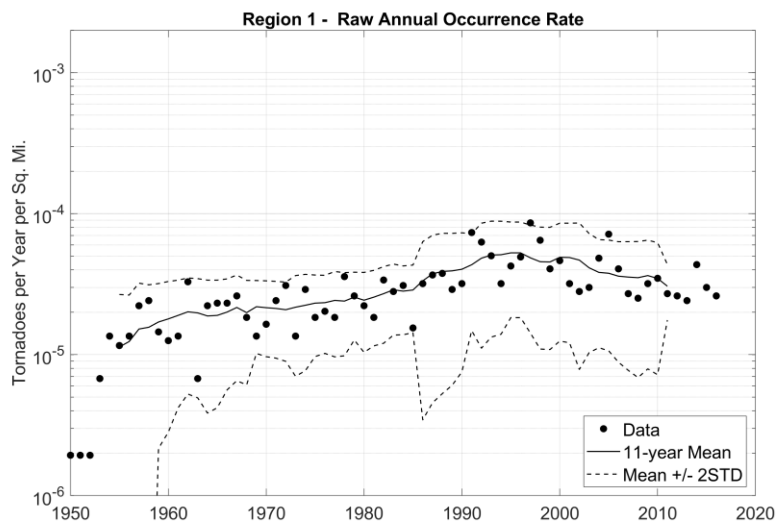
Region 1 - Raw Annual Occurrence Rate
Tornadoes per Year per Sq. Mi.
Data
11-year Mean
Mean +/- 2STD

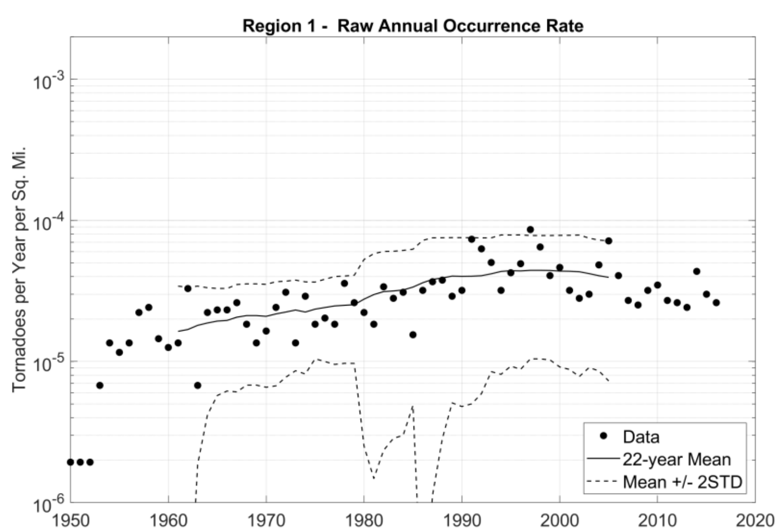
Region 1 - Raw Annual Occurrence Rate
Tornadoes per Year per Sq. Mi.
Data
22-year Mean
Mean +/- 2STD

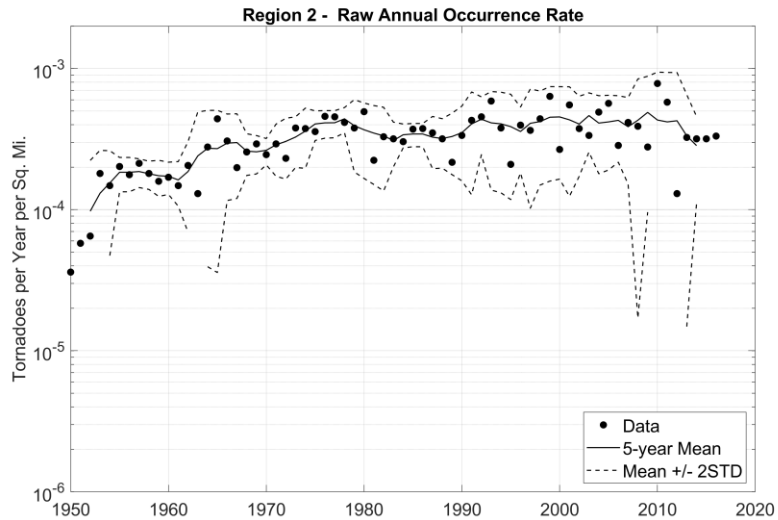
Region 2 - Raw Annual Occurrence Rate
Tornadoes per Year per Sq. Mi.
Data
5-year Mean
Mean +/- 2STD

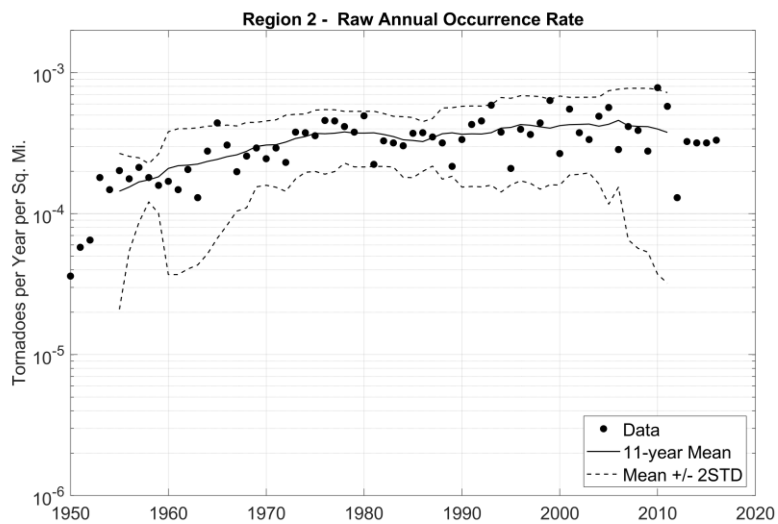
Region 2 - Raw Annual Occurrence Rate
Tornadoes per Year per Sq. Mi.
Data
11-year Mean
Mean +/- 2STD

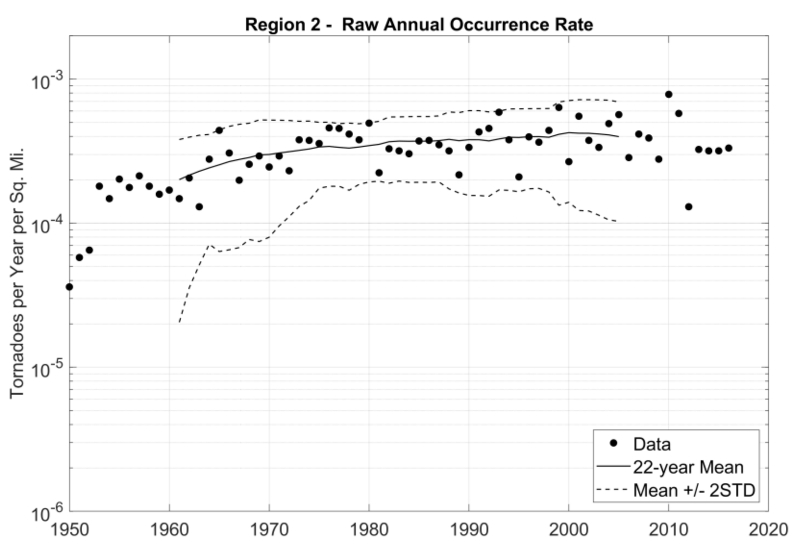
Region 2 - Raw Annual Occurrence Rate
Tornadoes per Year per Sq. Mi.
Data
22-year Mean
Mean +/- 2STD

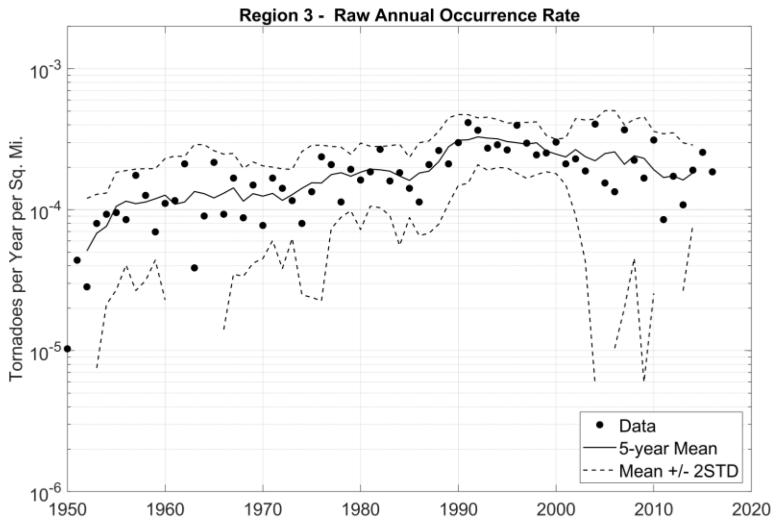
Region 3 - Raw Annual Occurrence Rate
Tornadoes per Year per Sq. Mi.
10^-3
10^-4
10^-5
10^-6
1950
1960
1970
1980
1990
2000
2010
2020
Data
5-year Mean
Mean +/- 2STD

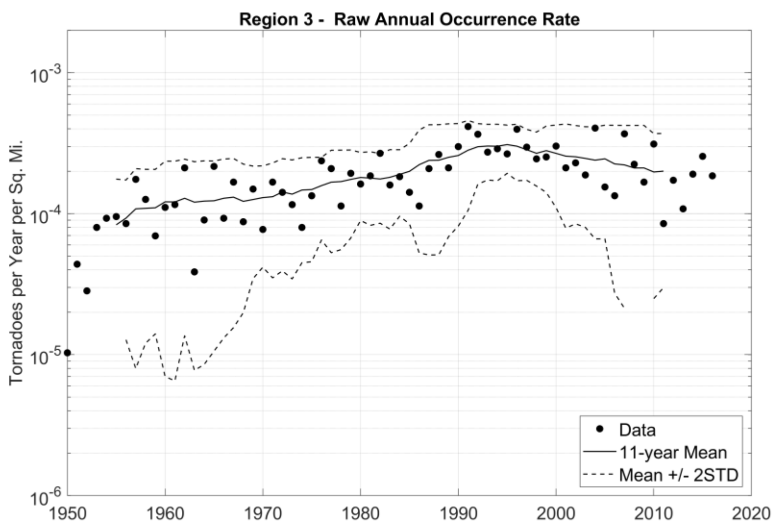
Region 3 - Raw Annual Occurrence Rate
Tornadoes per Year per Sq. Mi.
10^-3
10^-4
10^-5
10^-6
1950
1960
1970
1980
1990
2000
2010
2020
Data
11-year Mean
Mean +/- 2STD

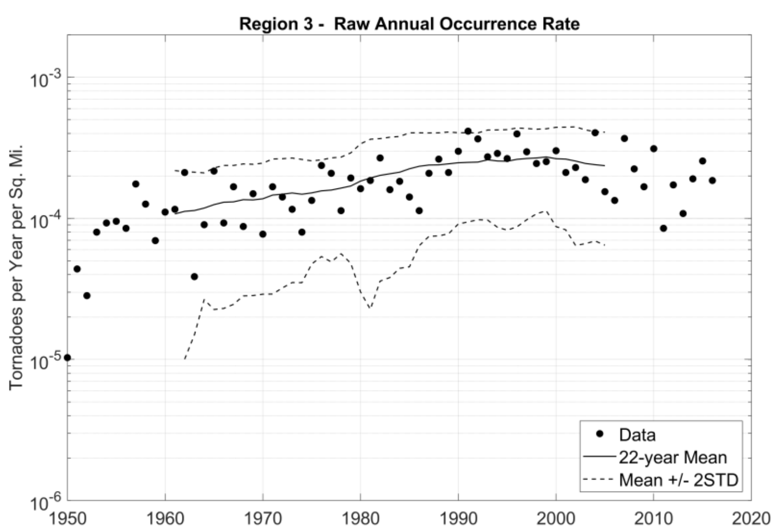
Region 3 - Raw Annual Occurrence Rate
Tornadoes per Year per Sq. Mi.
10^-3
10^-4
10^-5
10^-6
1950
1960
1970
1980
1990
2000
2010
2020
Data
22-year Mean
Mean +/- 2STD

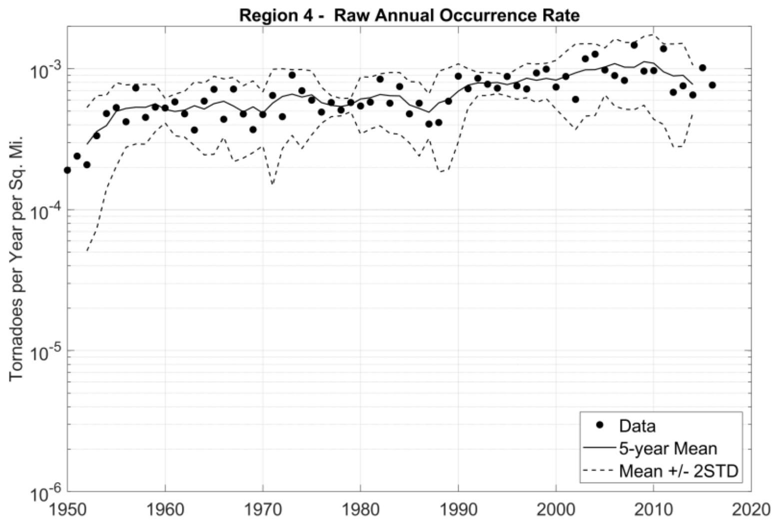
Region 4 - Raw Annual Occurrence Rate
Tornadoes per Year per Sq. Mi.
Data
5-year Mean
Mean +/- 2STD

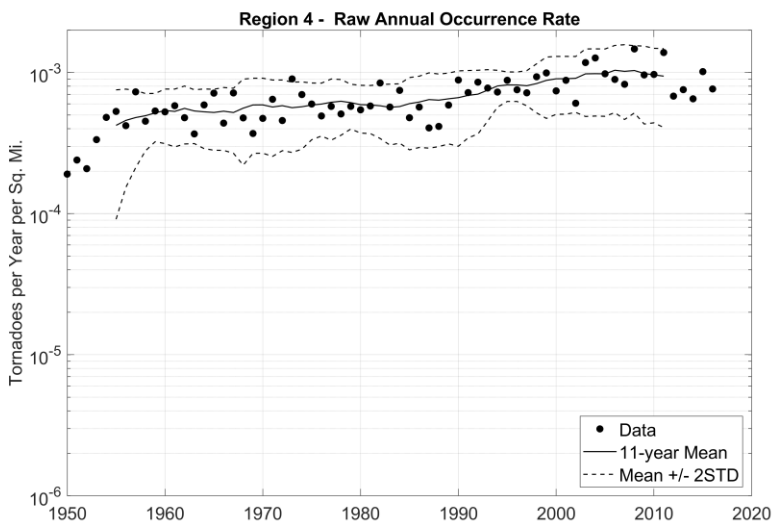
Region 4 - Raw Annual Occurrence Rate
Tornadoes per Year per Sq. Mi.
Data
11-year Mean
Mean +/- 2STD

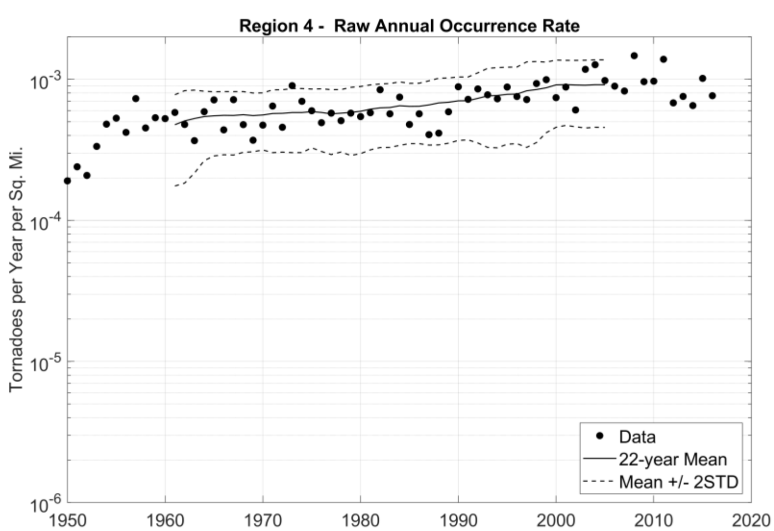
Region 4 - Raw Annual Occurrence Rate
Tornadoes per Year per Sq. Mi.
Data
22-year Mean
Mean +/- 2STD

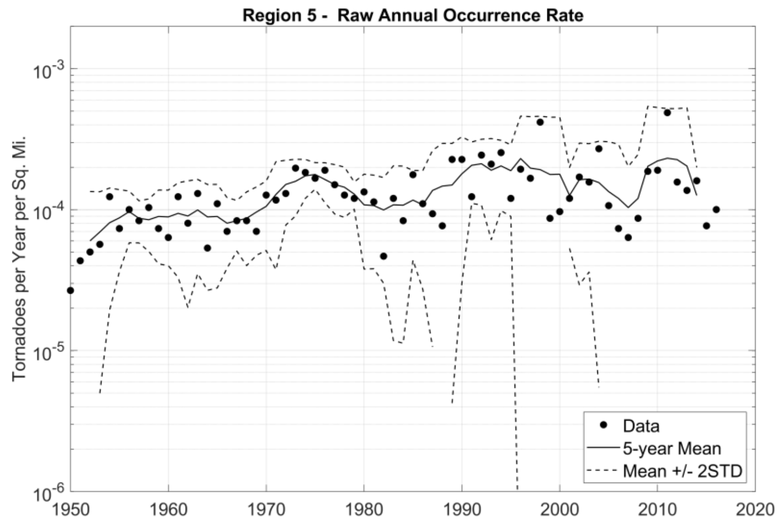
Region 5 - Raw Annual Occurrence Rate
Tornadoes per Year per Sq. Mi.
Data
5-year Mean
Mean +/- 2STD

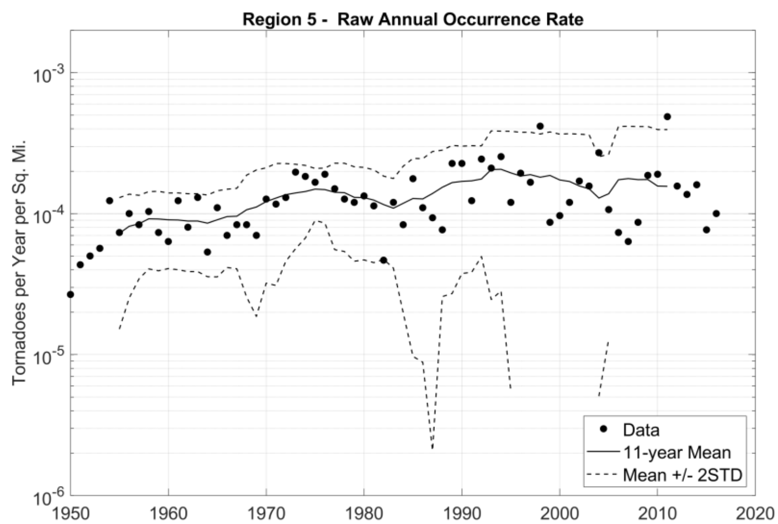
Region 5 - Raw Annual Occurrence Rate
Tornadoes per Year per Sq. Mi.
Data
11-year Mean
Mean +/- 2STD

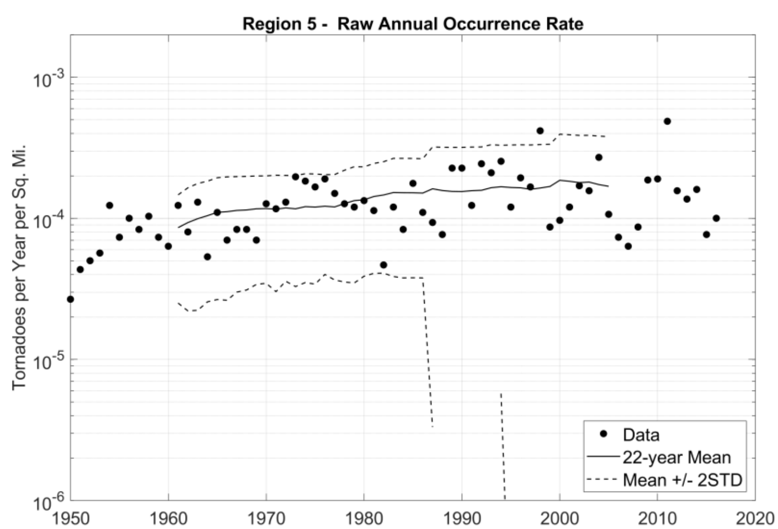
Region 5 - Raw Annual Occurrence Rate
Tornadoes per Year per Sq. Mi.
Data
22-year Mean
Mean +/- 2STD

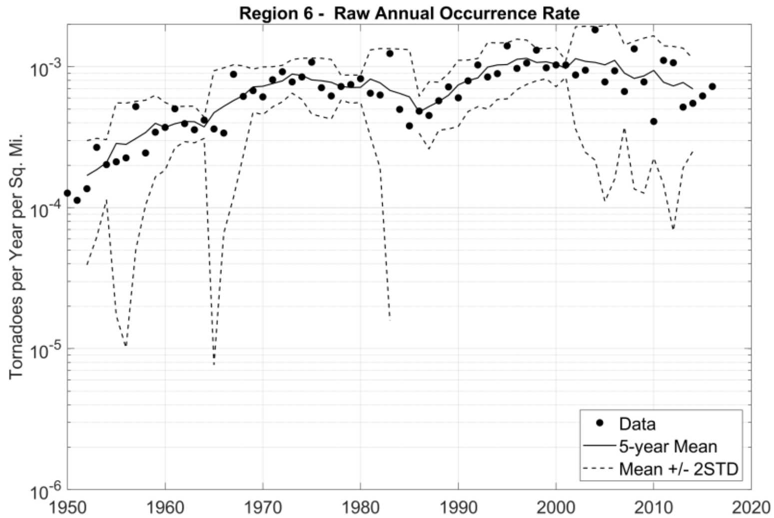
Region 6 - Raw Annual Occurrence Rate
Tornadoes per Year per Sq. Mi.
Data
5-year Mean
Mean +/- 2STD

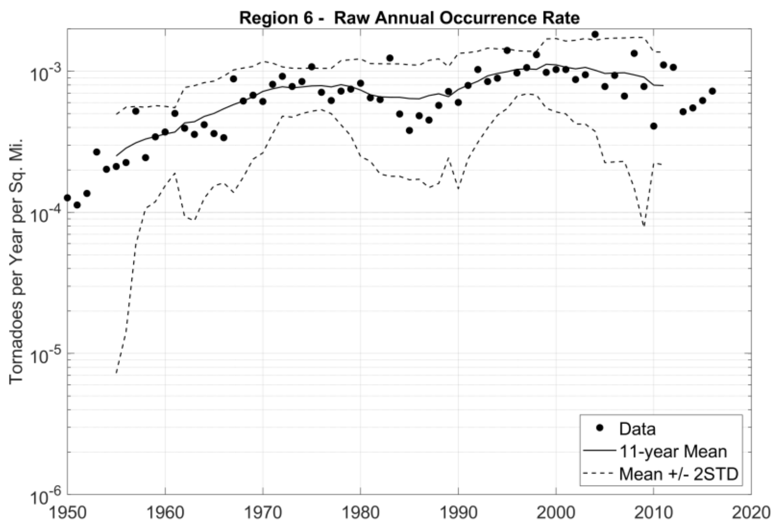
Region 6 - Raw Annual Occurrence Rate
Tornadoes per Year per Sq. Mi.
Data
11-year Mean
Mean +/- 2STD

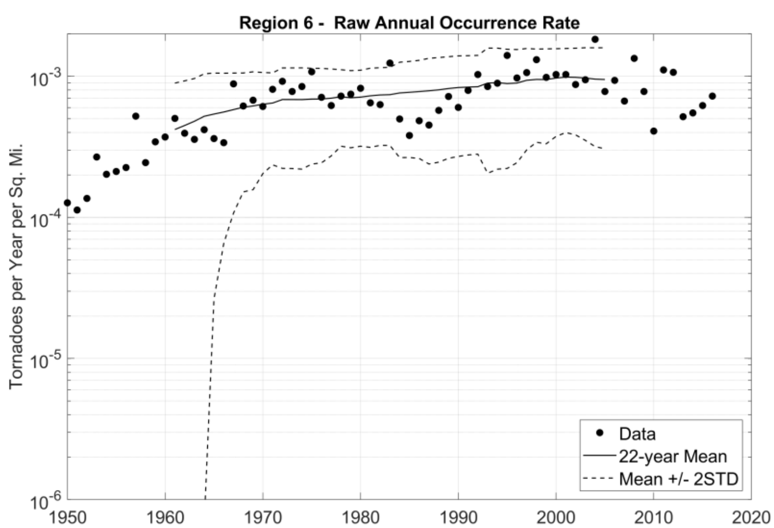
Region 6 - Raw Annual Occurrence Rate
Tornadoes per Year per Sq. Mi.
Data
22-year Mean
Mean +/- 2STD

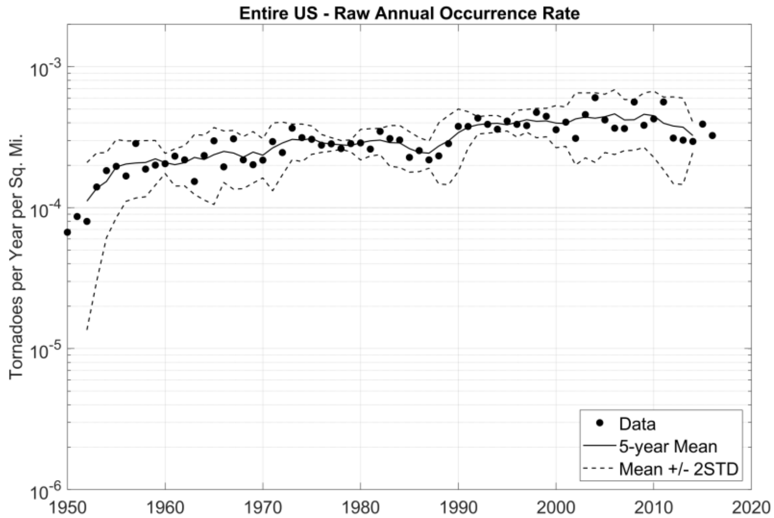
Entire US - Raw Annual Occurrence Rate
Tornadoes per Year per Sq. Mi.
10^{-3}
10^{-4}
10^{-5}
10^{-6}
1950
1960
1970
1980
1990
2000
2010
2020
Data
5-year Mean
Mean +/- 2STD

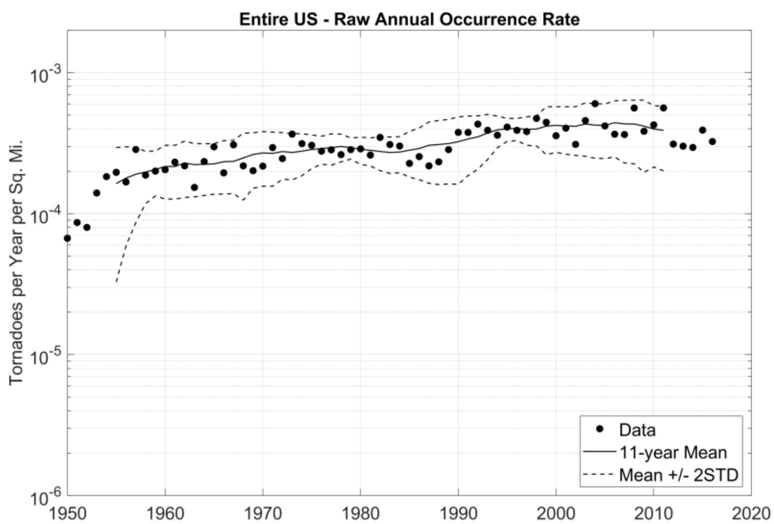
Entire US - Raw Annual Occurrence Rate
Tornadoes per Year per Sq. Mi.
10^{-3}
10^{-4}
10^{-5}
10^{-6}
1950
1960
1970
1980
1990
2000
2010
2020
Data
11-year Mean
Mean +/- 2STD

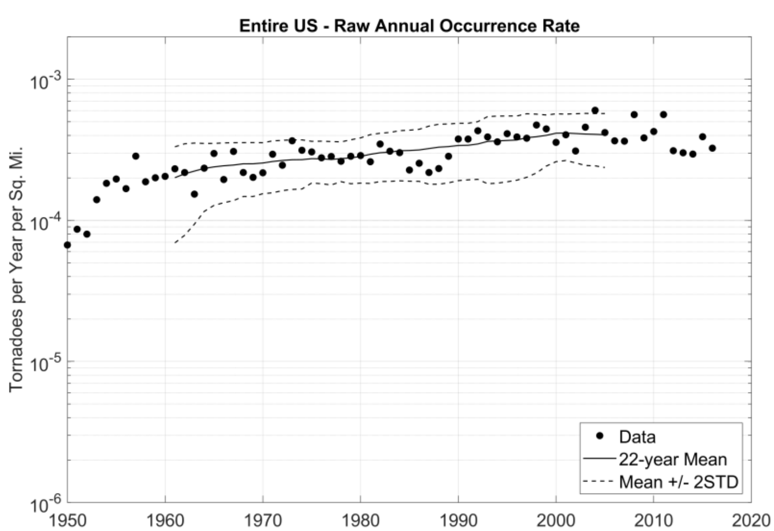
Entire US - Raw Annual Occurrence Rate
Tornadoes per Year per Sq. Mi.
10^{-3}
10^{-4}
10^{-5}
10^{-6}
1950
1960
1970
1980
1990
2000
2010
2020
Data
22-year Mean
Mean +/- 2STD

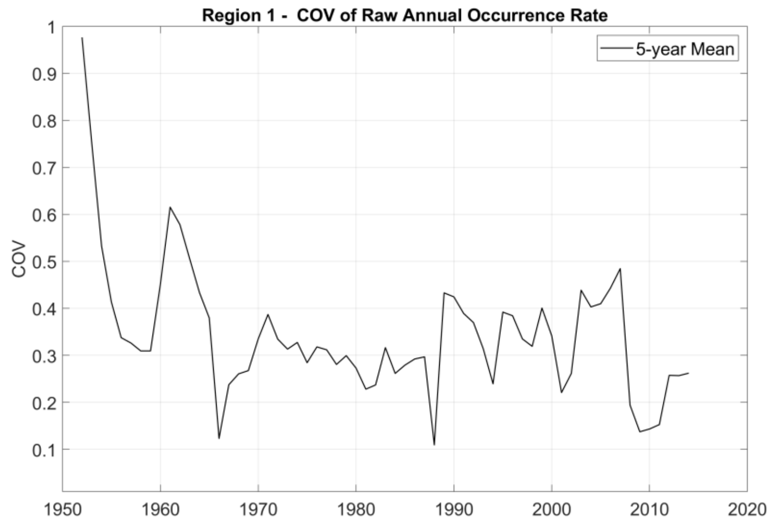
Region 1 - COV of Raw Annual Occurrence Rate
5-year Mean
COV
1
0.9
0.8
0.7
0.6
0.5
0.4
0.3
0.2
0.1
1950
1960
1970
1980
1990
2000
2010
2020

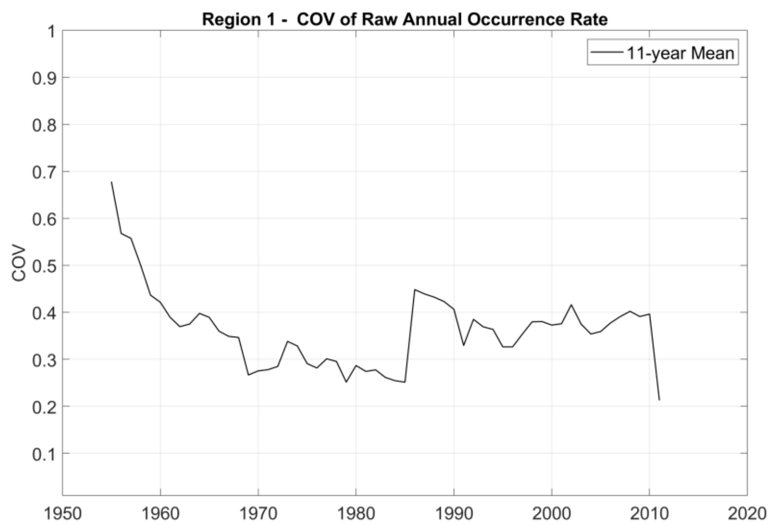
Region 1 - COV of Raw Annual Occurrence Rate
11-year Mean
COV
1
0.9
0.8
0.7
0.6
0.5
0.4
0.3
0.2
0.1
1950
1960
1970
1980
1990
2000
2010
2020

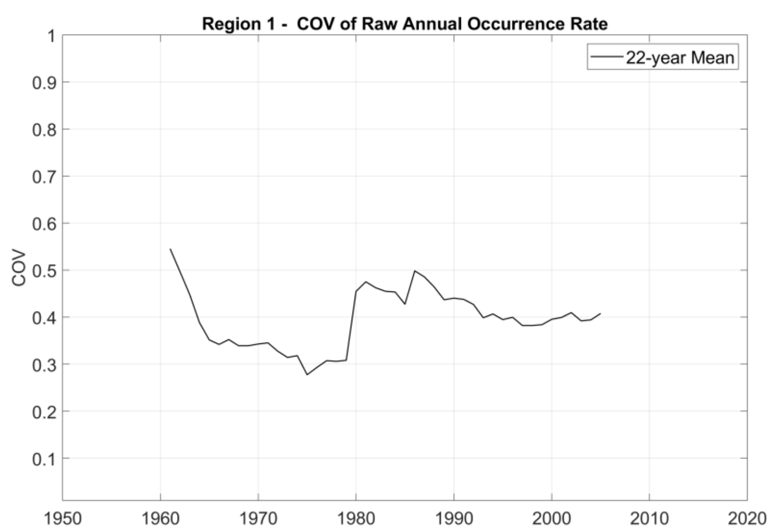
Region 1 - COV of Raw Annual Occurrence Rate
22-year Mean
COV
1
0.9
0.8
0.7
0.6
0.5
0.4
0.3
0.2
0.1
1950
1960
1970
1980
1990
2000
2010
2020

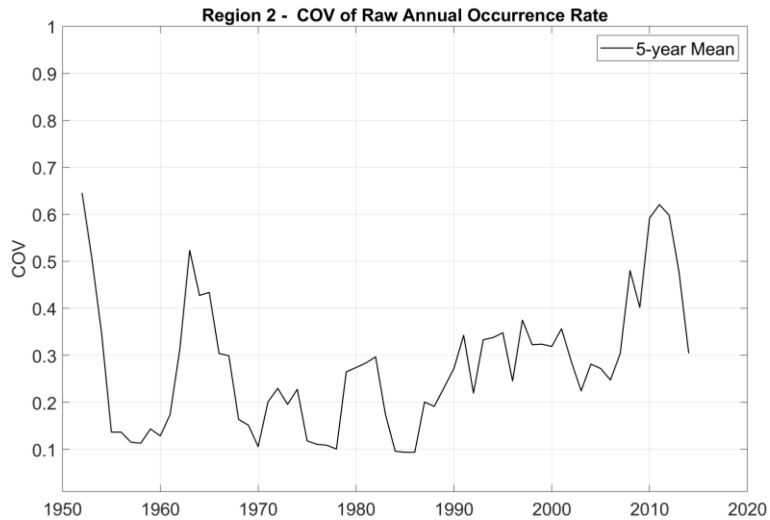
Region 2 - COV of Raw Annual Occurrence Rate
5-year Mean
COV
1
0.9
0.8
0.7
0.6
0.5
0.4
0.3
0.2
0.1
1950
1960
1970
1980
1990
2000
2010
2020

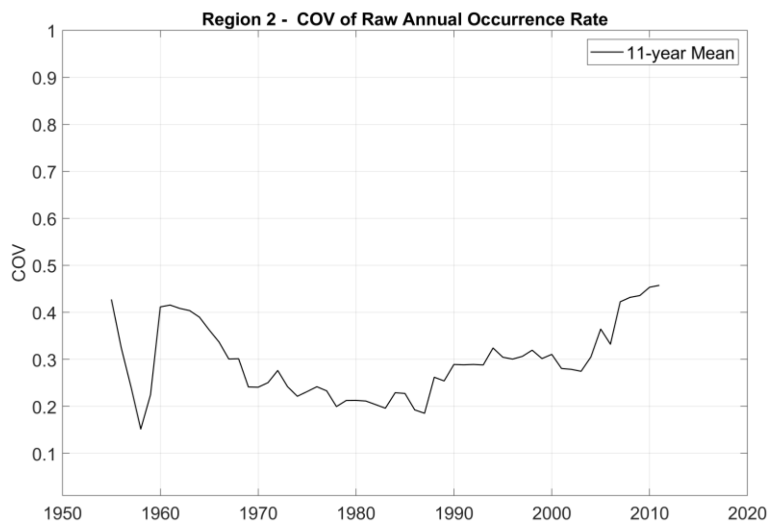
Region 2 - COV of Raw Annual Occurrence Rate
11-year Mean
COV
1
0.9
0.8
0.7
0.6
0.5
0.4
0.3
0.2
0.1
1950
1960
1970
1980
1990
2000
2010
2020

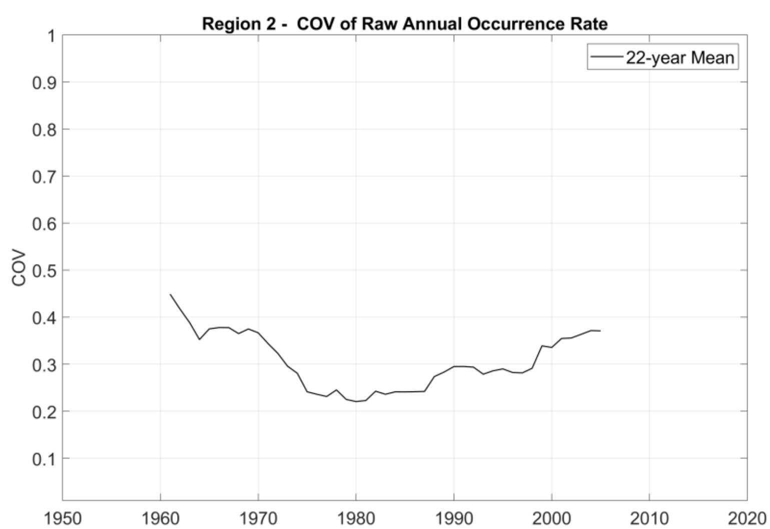
Region 2 - COV of Raw Annual Occurrence Rate
22-year Mean
COV
1
0.9
0.8
0.7
0.6
0.5
0.4
0.3
0.2
0.1
1950
1960
1970
1980
1990
2000
2010
2020

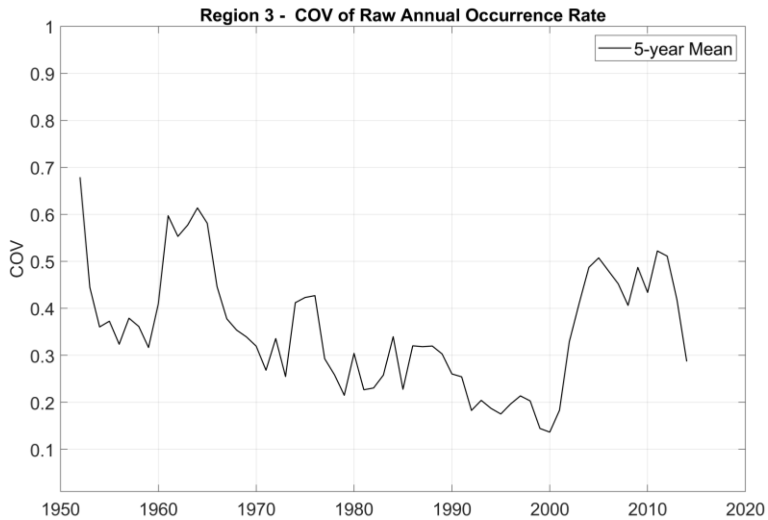
Region 3 - COV of Raw Annual Occurrence Rate
5-year Mean
COV
1
0.9
0.8
0.7
0.6
0.5
0.4
0.3
0.2
0.1
1950
1960
1970
1980
1990
2000
2010
2020

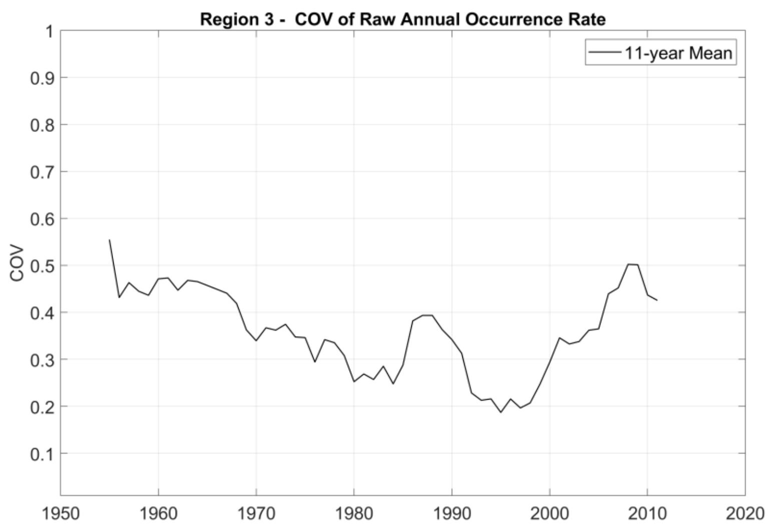
Region 3 - COV of Raw Annual Occurrence Rate
11-year Mean
COV
1
0.9
0.8
0.7
0.6
0.5
0.4
0.3
0.2
0.1
1950
1960
1970
1980
1990
2000
2010
2020

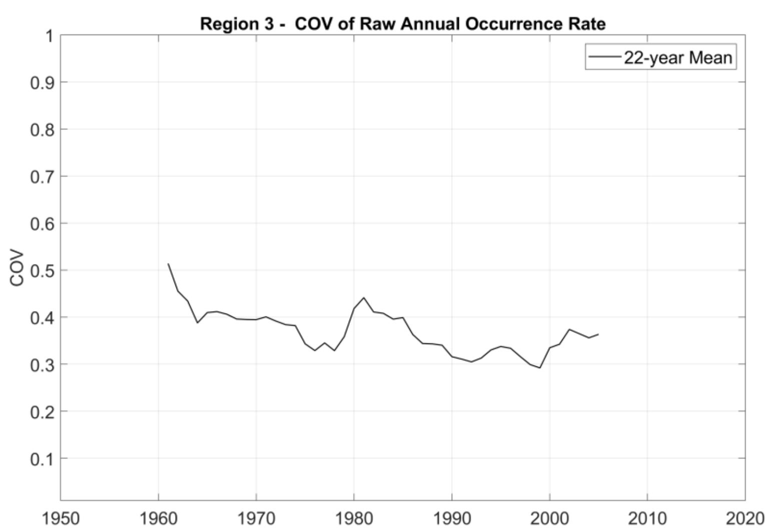
Region 3 - COV of Raw Annual Occurrence Rate
22-year Mean
COV
1
0.9
0.8
0.7
0.6
0.5
0.4
0.3
0.2
0.1
1950
1960
1970
1980
1990
2000
2010
2020

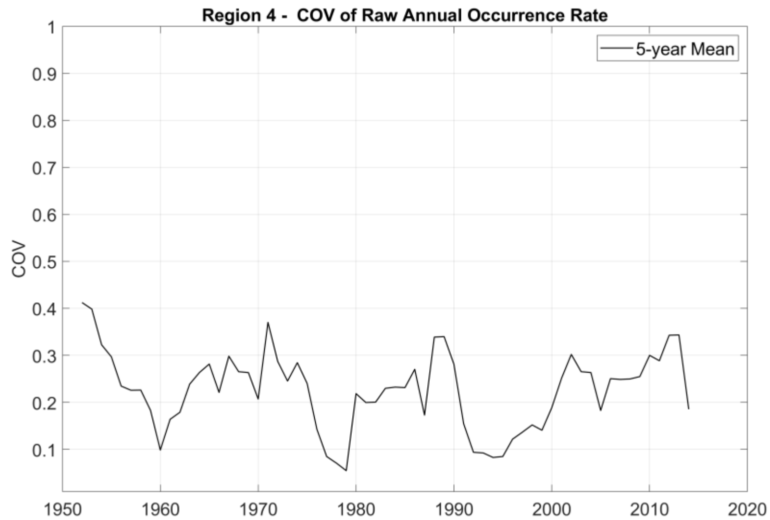
Region 4 - COV of Raw Annual Occurrence Rate
5-year Mean
COV
1
0.9
0.8
0.7
0.6
0.5
0.4
0.3
0.2
0.1
1950
1960
1970
1980
1990
2000
2010
2020

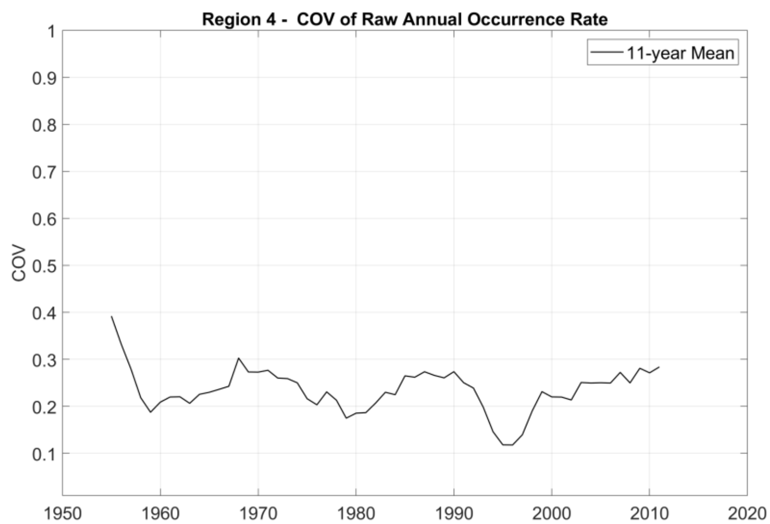
Region 4 - COV of Raw Annual Occurrence Rate
11-year Mean
COV
1
0.9
0.8
0.7
0.6
0.5
0.4
0.3
0.2
0.1
1950
1960
1970
1980
1990
2000
2010
2020

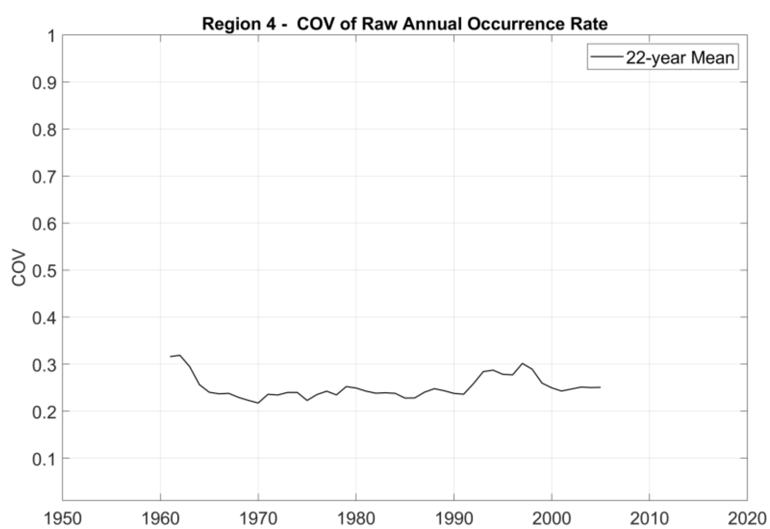
Region 4 - COV of Raw Annual Occurrence Rate
22-year Mean
COV
1
0.9
0.8
0.7
0.6
0.5
0.4
0.3
0.2
0.1
1950
1960
1970
1980
1990
2000
2010
2020

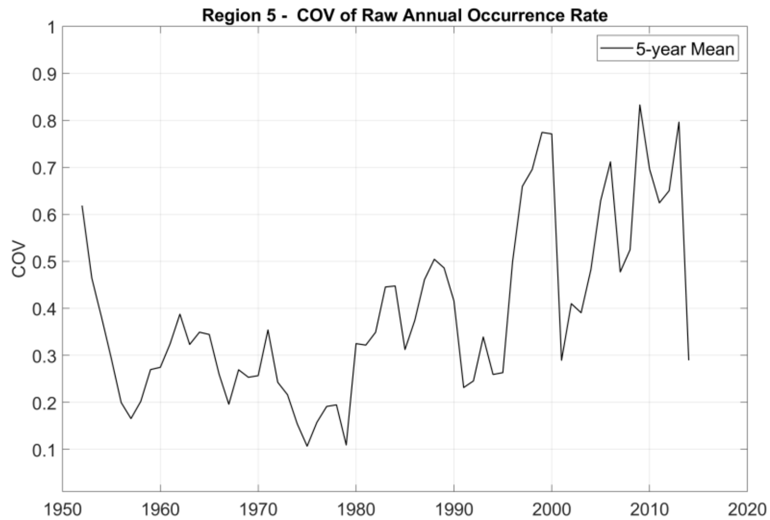
Region 5 - COV of Raw Annual Occurrence Rate
5-year Mean
COV
1
0.9
0.8
0.7
0.6
0.5
0.4
0.3
0.2
0.1
1950
1960
1970
1980
1990
2000
2010
2020

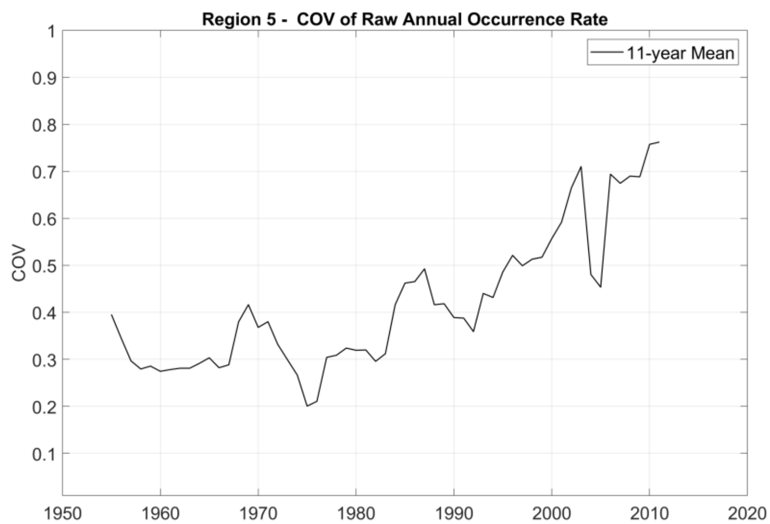
Region 5 - COV of Raw Annual Occurrence Rate
11-year Mean
COV
1
0.9
0.8
0.7
0.6
0.5
0.4
0.3
0.2
0.1
1950
1960
1970
1980
1990
2000
2010
2020

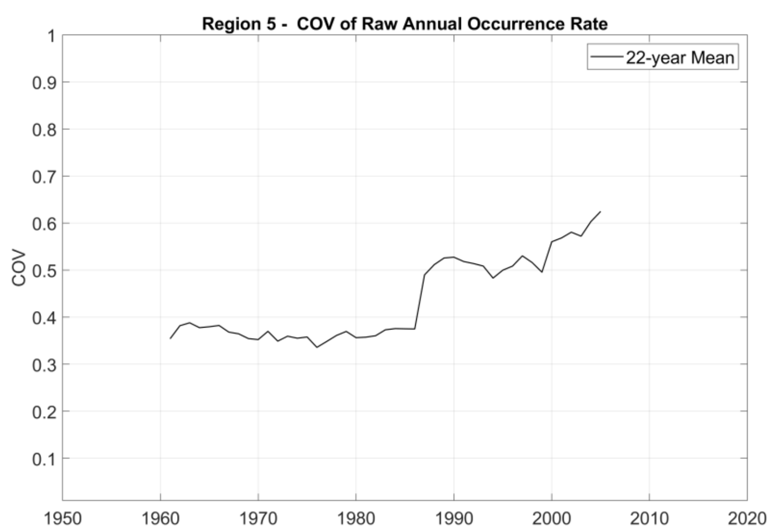
Region 5 - COV of Raw Annual Occurrence Rate
22-year Mean
COV
1
0.9
0.8
0.7
0.6
0.5
0.4
0.3
0.2
0.1
1950
1960
1970
1980
1990
2000
2010
2020

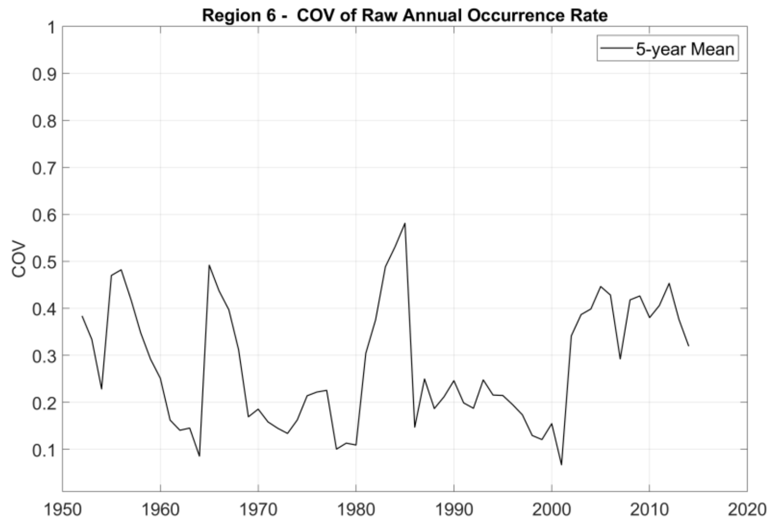
Region 6 - COV of Raw Annual Occurrence Rate
5-year Mean
COV

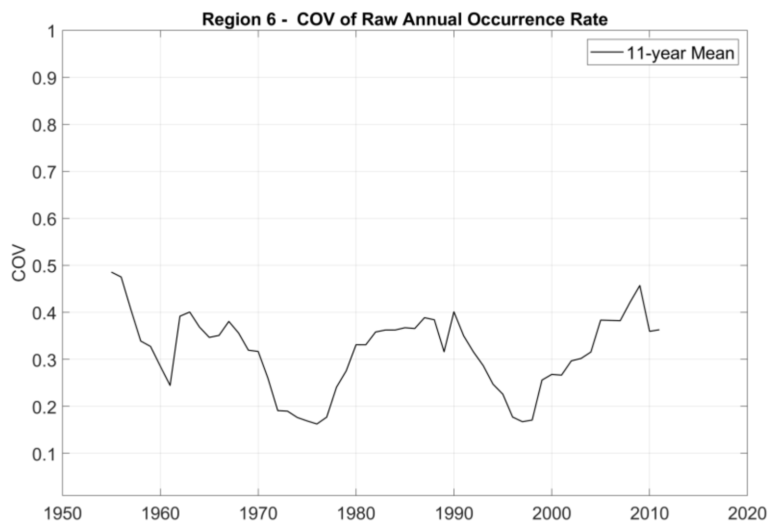
Region 6 - COV of Raw Annual Occurrence Rate
11-year Mean
COV

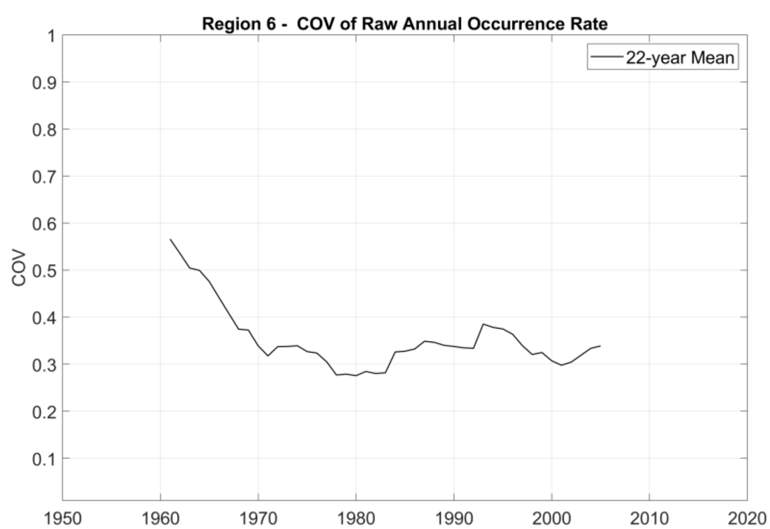
Region 6 - COV of Raw Annual Occurrence Rate
22-year Mean
COV

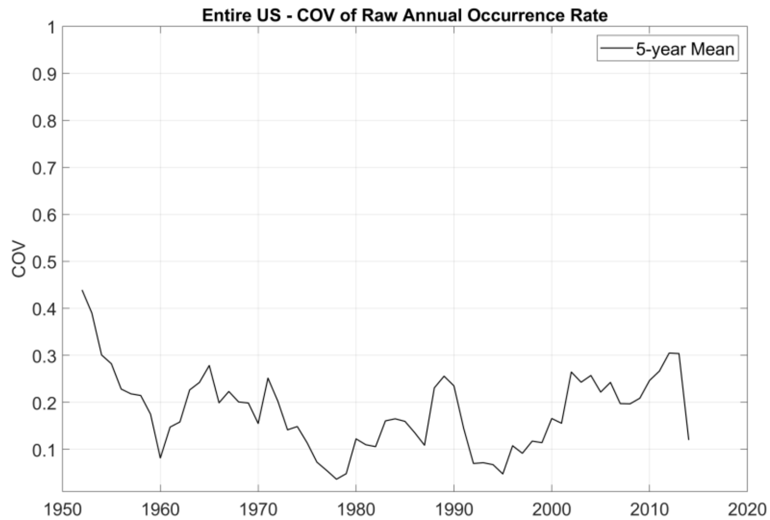
Entire US - COV of Raw Annual Occurrence Rate
5-year Mean
COV
1
0.9
0.8
0.7
0.6
0.5
0.4
0.3
0.2
0.1
1950
1960
1970
1980
1990
2000
2010
2020

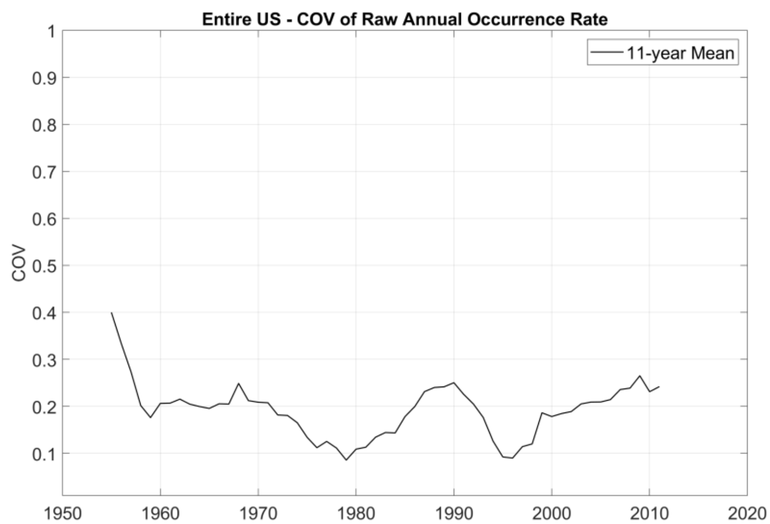
Entire US - COV of Raw Annual Occurrence Rate
11-year Mean
COV
1
0.9
0.8
0.7
0.6
0.5
0.4
0.3
0.2
0.1
1950
1960
1970
1980
1990
2000
2010
2020

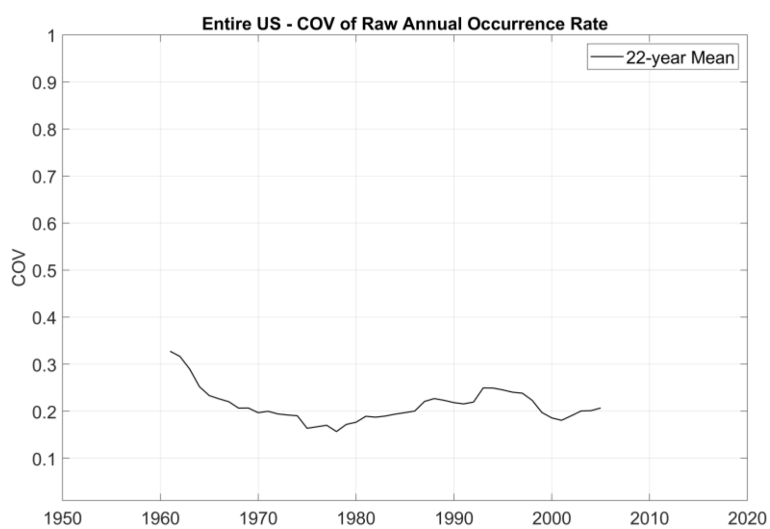
Entire US - COV of Raw Annual Occurrence Rate
22-year Mean
COV
1
0.9
0.8
0.7
0.6
0.5
0.4
0.3
0.2
0.1
1950
1960
1970
1980
1990
2000
2010
2020

C.4. UI-UO Polygon Test Results for EF-Scale Distribution Modeling

Similar to the UI-UO tests reported in Section 3.2.2 for occurrence rate analysis, we subsequently reproduced the results to determine the best metric to estimate the EF-Scale intensity distribution, given a tornado. The results for H, LF, and PP are given in Figure C-1 through Figure C-3. Occurrence rates are shown as tornadoes per square mile per year (1 tornado per square mile per year = 0.386102 tornadoes per square kilometer per year). [Tract??] length is <u>less than or equal to infinity miles (infinity km).</u> The LF results have slightly better statistics than PP and we chose to use LF for EF-Scale distribution modeling due to the larger variance in PP results.

We analyzed the bias for the polygons in Region 4, which have the largest number of tornadoes, particularly EF4-5's. Figure C-4 shows the resulting bias factors for these polygons. From Figure C-1, we developed bias uncertainty terms of 0.1, 0.15 and 0.2 for EF01, EF1-2, and EF4-5, respectively. These terms increase with EF-Scale groups, reflecting the bias ratios illustrated in the figue. These terms are applied as additional uncertainty terms in the Weibull fit RMS error term in the epistemic simulations to produce the Weibull derived mean EF relative frequencies. This approach is expected to reasonably estimate the uncertainties resulting from using the LF modeling approach for the regional EF distributions.

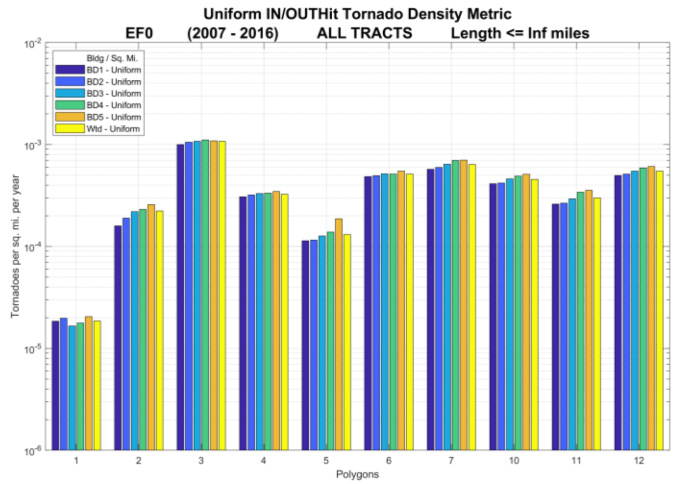

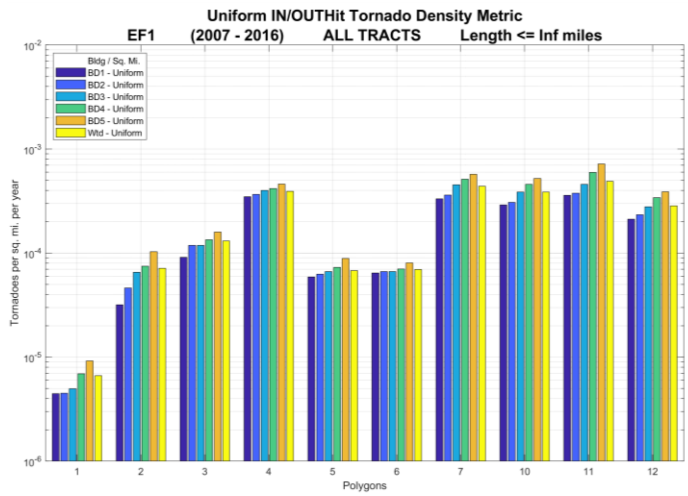

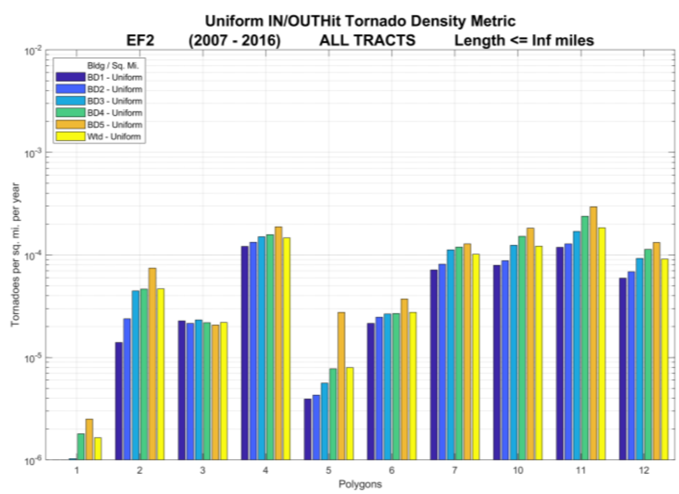

Figure C-1. UI-UO EF-Scale Hit Results by Polygon for EF0 through EF5

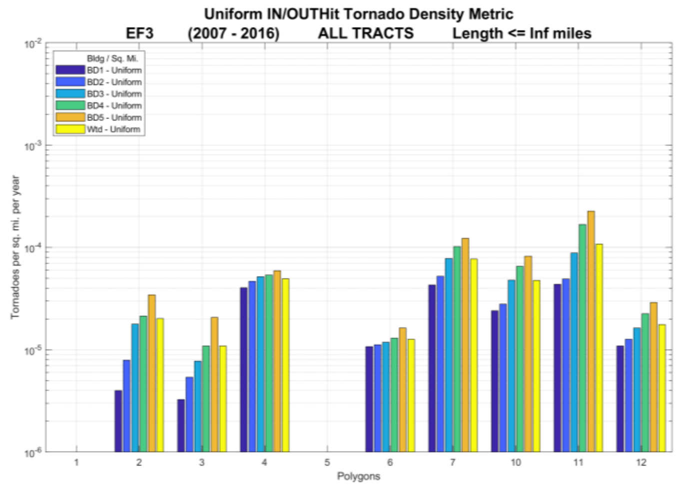

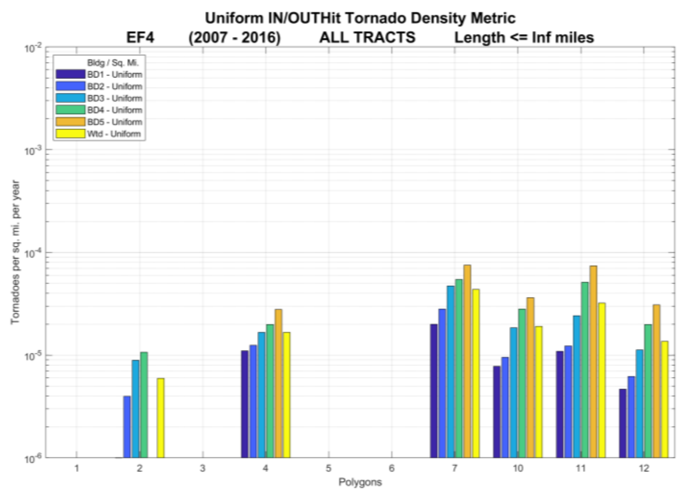

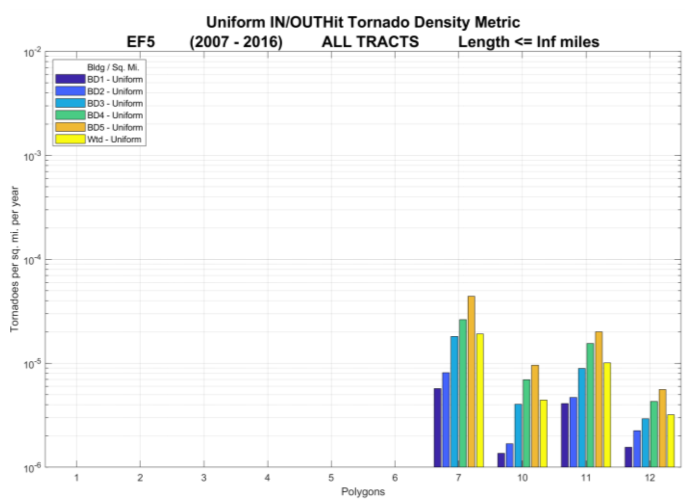

Figure C-1. UI-UO EF-Scale Hit Results by Polygon for EF0 through EF5

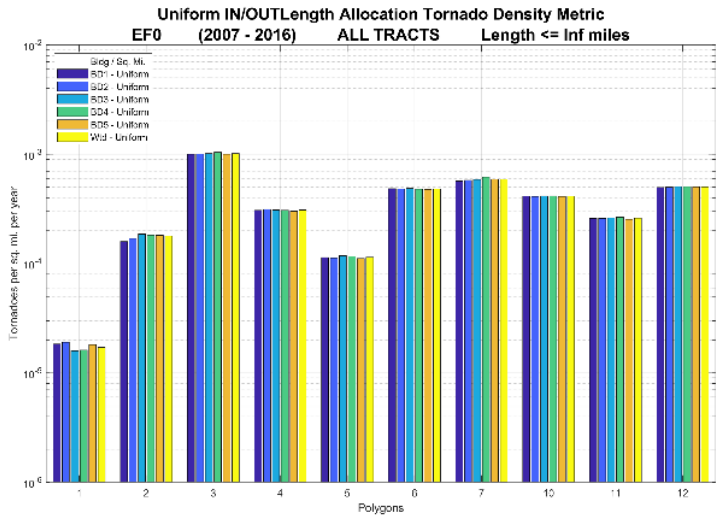

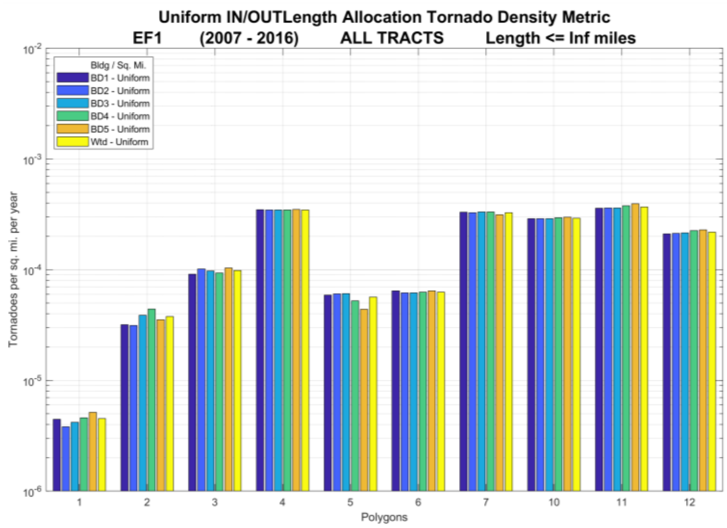

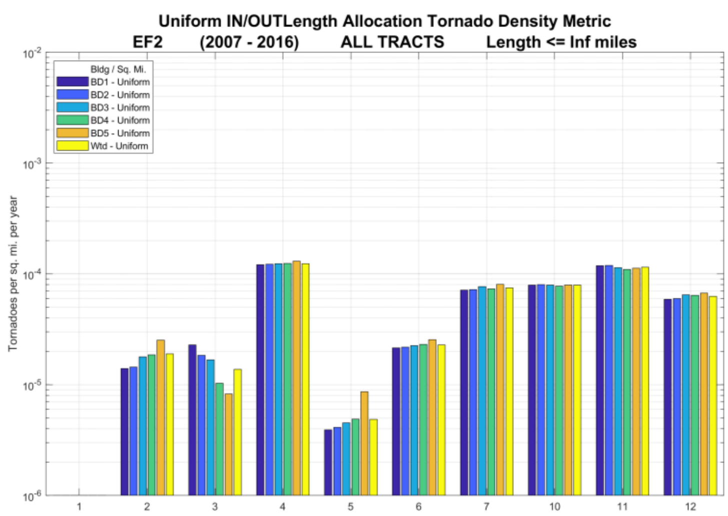

Figure C-2. UI-UO EF-Scale LF Results by Polygon for EF0 through EF5

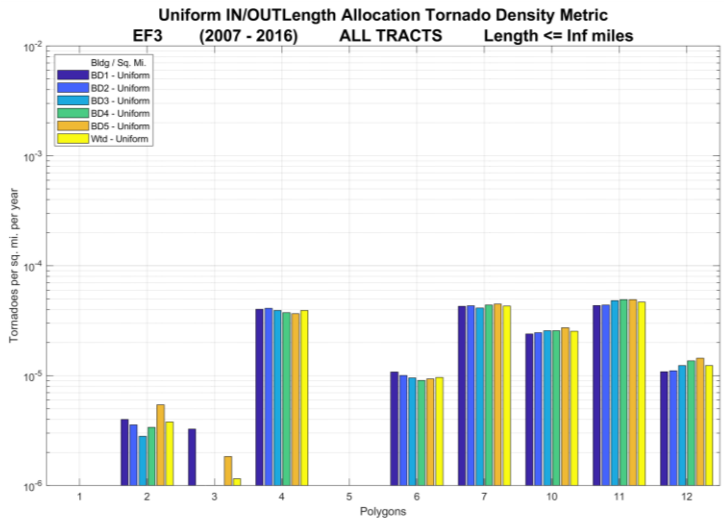

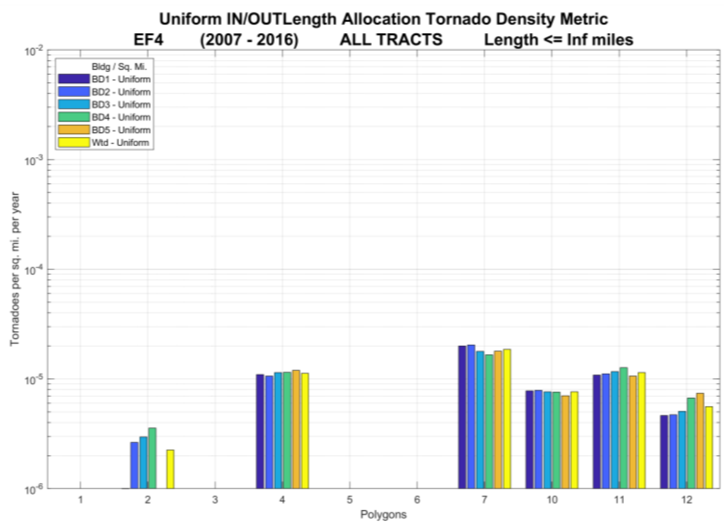

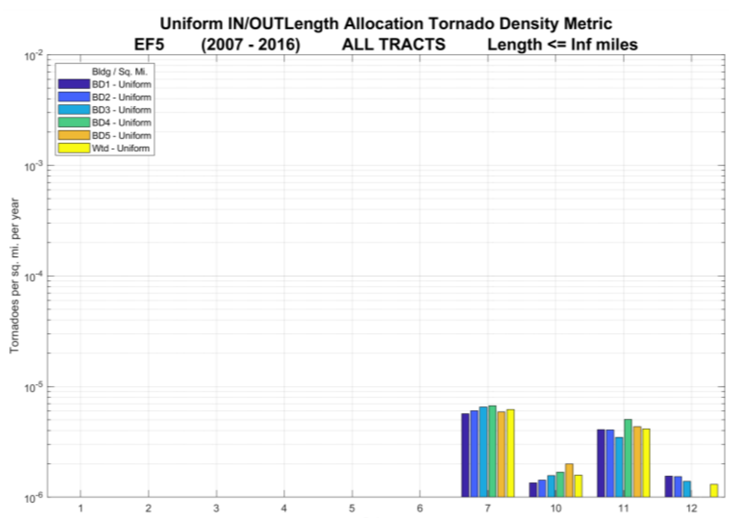

Figure C-2. UI-UO EF-Scale LF Results by Polygon for EF0 through EF5

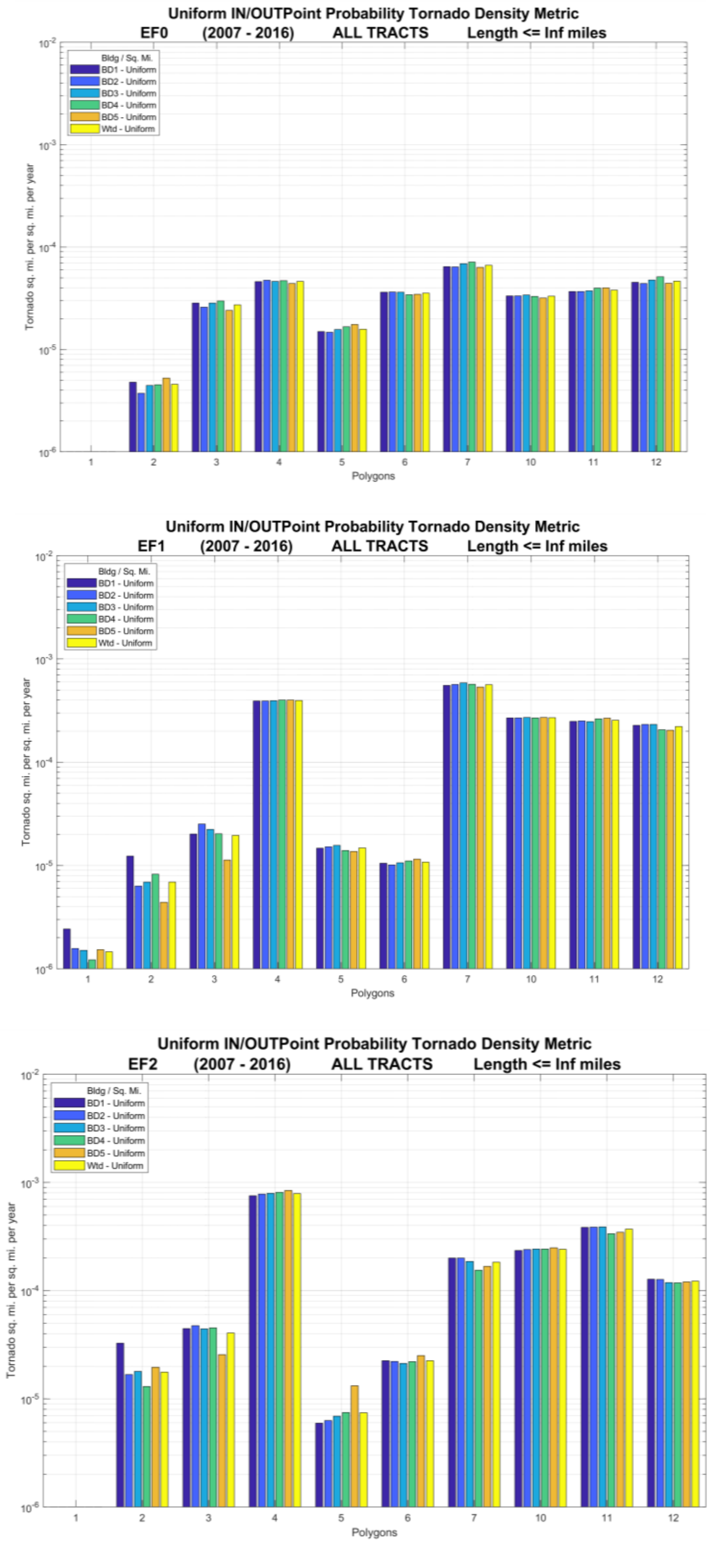

Figure C-3. UI-UO EF-Scale Point Probability by Polygon for EF0 through EF5

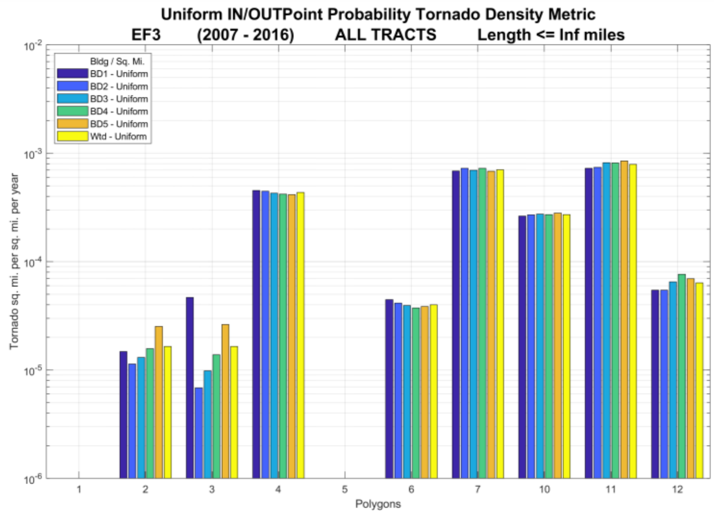

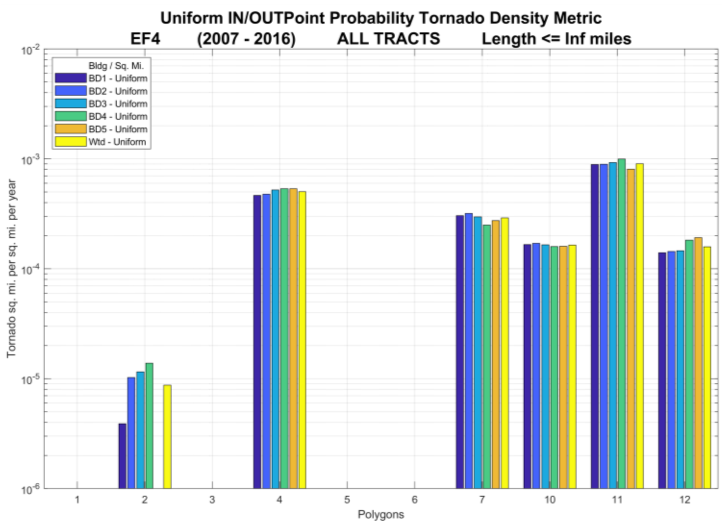

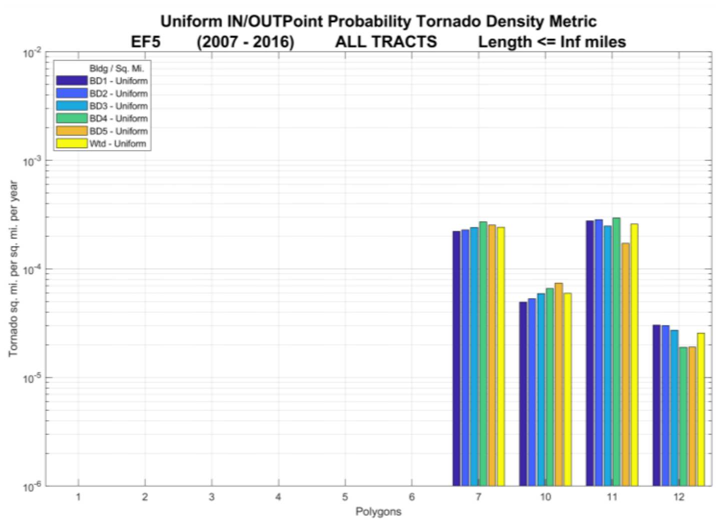

Figure C-3. UI-UO EF-Scale Point Probability by Polygon for EF0 through EF5

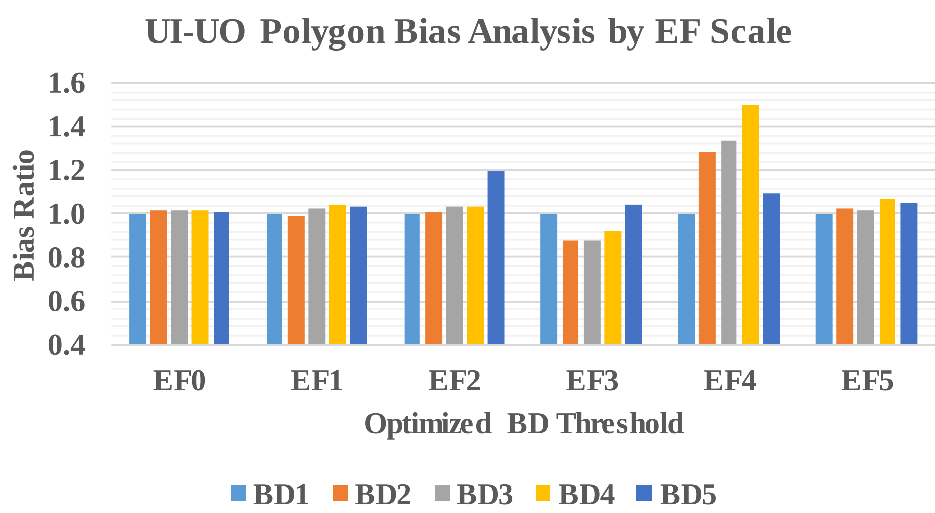

Figure C-4. UI-UO Polygon Bias Analysis Ratios for EF-Scale Distribution Modeling

C.5. Epistemic Weights for BD Threshold Analysis

BD threshold analysis is a key element of the tornado occurrence rate and EF-Scale intensity distribution analysis. Data is developed and modeled for 5 BD thresholds (BD1- BD5).[3] Table 3-3 provided the BD thresholds for BD1-BD5 by region. In this appendix, we address the question of how to probabilistically weight these threshold results in order to develop derived means. We develop the weights considering the EF-Scale, since that is a subset of the occurrence rate modeling. For consistency, we use the same probabilistic weights for both occurrence rate and EF-Scale distribution modeling. Hence, the discussion that follows is aimed at the EF-Scale intensities, all of which contribute to the occurrence of a tornado.

The basic question is how to model uncertainties for families of BD data (BD1 – BD5) for each region. Each data set in the family represents an estimation of plausible relative frequencies (or occurrence rates) for that region. The BD1 frequencies include all land area, but are expected to be the least accurate data. On the other hand, the BD5 frequencies may be the most accurate data, but that data is based on the fewest number of tornadoes.

Our initial approach regarding how to weight the BD data was a very simple judgment approach based on using the square root of building density (normalized). However, we abandoned that approach in favor of the following method, which is considerably more complicated, but nevertheless conceptually simple. We consider that each BD data set has two important statistical attributes: reporting accuracy (R) and statistical accuracy (S). The product of these individually-estimated measures produces as an epistemic probability weight for each BD. With weighted BD data, we use simulation to produce final derived mean distributions. This approach applied the computation of both the derived means for tornado occurrence rates and EF-Scale distributions.

[3] For tornado occurrence rate modeling, Table 3-4 has the LF and PP tornado densities and for the EF-Scale distribution modeling and Table 3-8 has the Weibull fits (based on LF analysis by EF-Scale) for the BD1-BD5 thresholds.

C.5.1. BD Threshold Accuracy

Accuracy is estimated by the building density threshold associated with a particular curve. We compute the expected number of DIs within the maximum EF-Scale wind swath for each BD threshold from simulation. The mean of the maximum EF_i wind swath area, $A_{EF(max)}$, is computed from simulations of the wind swath model described in Section 4, and summarized in Table C-5.

The expected number of building (B) DIs within this area is estimated by $B = BD^* A_{EF(max)}$, where BD is the building DI density. To convert the number of DIs hit by the tornado to a measure of accuracy, we evaluated the DAT data to determine the mean number of DIs with the EF_{max} rating. This analysis produces averages of 5, 6.7, 3.7, 4.5, 6.6, and 19 for EF0 through EF5, respectively. This value includes all 28 DI's. Thus, with the exception of EF5, which is based only on 2 events, the mean number is approximately 5 DI's. From this analysis, we concluded that a reasonable accuracy scoring equation is $R = max(0, min(B\text{-}5, 20)$. This expression scores a zero if $B \leq 5$ and scores a maximum of 20. Twenty is chosen as the practical upper limit of an accuracy score since assessing more than 20 DIs with the maximum rating is very unusual and limited to a few detailed studies of EF5's.

The computed accuracy weights (R) are based on summing across each *EF* within a BD threshold and normalizing the results. The "Reporting Accuracy" rows in Table C-6 provide these results. This approach produces a reasonable accuracy weighting that increases with BD threshold. For example, the values produce the smallest weights for BD1 and max largest weights for BD5. The top plot in Figure C-5 shows how the accuracy weights vary by region and BD.

Table Error! No text of specified style in document.**-11. Simulated Mean Areas, $EF_{i(Amax)}$**

EF Scale	Mean EFi(max) Damage Area (sq mi)					
	R1	R2	R3	R4	R5	R6
EF0	0.03	0.04	0.03	0.04	0.05	0.03
EF1	0.06	0.09	0.05	0.12	0.07	0.07
EF2	0.17	0.17	0.18	0.22	0.16	0.16
EF3	0.25	0.27	0.41	0.56	0.83	0.29
EF4	0.24	0.24	0.32	0.53	0.34	0.13
EF5	0.32	0.29	0.43	0.77	0.64	0.26

Note: 1 square mile = 2.589988 km^2

Table Error! No text of specified style in document.**-12. Epistemic BD Threshold Weights**

Epistemic Uncertainty	BD	Region/Subregion											
		R1	**R2**	**R3**	**R4**	**R406**	**R407**	**R5**	**R511**	**R512**	**R6**	**R606**	**R609**
Accuracy (R)	BD1	0.013	0.030	0.023	0.127	0.164	0.106	0.159	0.131	0.169	0.097	0.080	0.114
	BD2	0.130	0.128	0.157	0.185	0.184	0.159	0.183	0.187	0.176	0.181	0.161	0.174
	BD3	0.230	0.231	0.248	0.215	0.205	0.236	0.197	0.199	0.198	0.224	0.218	0.216
	BD4	0.307	0.284	0.276	0.230	0.223	0.243	0.222	0.229	0.229	0.248	0.264	0.248
	BD5	0.320	0.326	0.296	0.243	0.223	0.256	0.240	0.254	0.229	0.250	0.277	0.248
Sample Size (S)	BD1	0.303	0.337	0.399	0.319	0.272	0.314	0.266	0.281	0.274	0.256	0.307	0.248
	BD2	0.202	0.213	0.182	0.237	0.240	0.254	0.247	0.246	0.258	0.230	0.240	0.224
	BD3	0.184	0.178	0.158	0.186	0.196	0.182	0.219	0.211	0.220	0.198	0.195	0.202
	BD4	0.161	0.155	0.138	0.157	0.164	0.138	0.173	0.151	0.144	0.180	0.146	0.174
	BD5	0.150	0.117	0.122	0.101	0.128	0.111	0.095	0.110	0.104	0.137	0.112	0.151
Total (Normalized Product of R and S)	BD1	0.023	0.063	0.061	0.219	0.230	0.186	0.221	0.197	0.241	0.131	0.141	0.147
	BD2	0.155	0.170	0.189	0.237	0.227	0.225	0.236	0.245	0.237	0.220	0.220	0.204
	BD3	0.249	0.256	0.259	0.216	0.207	0.241	0.224	0.224	0.226	0.234	0.242	0.228
	BD4	0.291	0.274	0.252	0.195	0.189	0.188	0.200	0.185	0.172	0.235	0.220	0.225
	BD5	0.282	0.237	0.239	0.133	0.147	0.160	0.118	0.149	0.124	0.181	0.177	0.196

We believe this approach has its advantages over a simple judgment-based estimate of BD accuracy and weighting of BD curves in the development of a derived mean EF-Scale distribution. It is based on mean areas of the maximum EF_i intensity with EF_i tornado swaths, BD as a measure of DI's within that area, and the mean number of DI's associated with the maximum rating of a tornado. All these variables have been quantified from empirical data within the above databases and swath modeling discussed in Section 4.

C.5.2. BD Statistical Accuracy

The second part of the BD data weighting is statistical uncertainty of the BD threshold data. We use the tornado counts (sample size) by BD threshold within each region to estimate the accuracy of the BD data for that region. The statistical accuracy is assumed to be proportional to the square root of sample size (tornado counts); i.e., $S = \sqrt{n}$, where n is the tornado count for a BD threshold within a region or sub-region. The normalized weights for each BD threshold are given in Table C-6. The middle plot in Figure C-5 illustrates how these weights reduce with increasing BD.

C.5.3. Combined Epistemic Weights

The combined weights are used in the EF-Scale distribution epistemic modeling are proportional to the product of the weights (R and S) in Table C-6. The normalized products are given in Table C-6. Regions with large open space areas (such as R1, R2, and R3) have small weights for BD1, whereas, other more populated regions have higher weights for BD1. The mode of the BDs generally lies between BD2 – BD4. In summary, the combined epistemic weights are associated with a middle threshold density and are not dominated by the very high BDs that have relatively high statistical uncertainties.

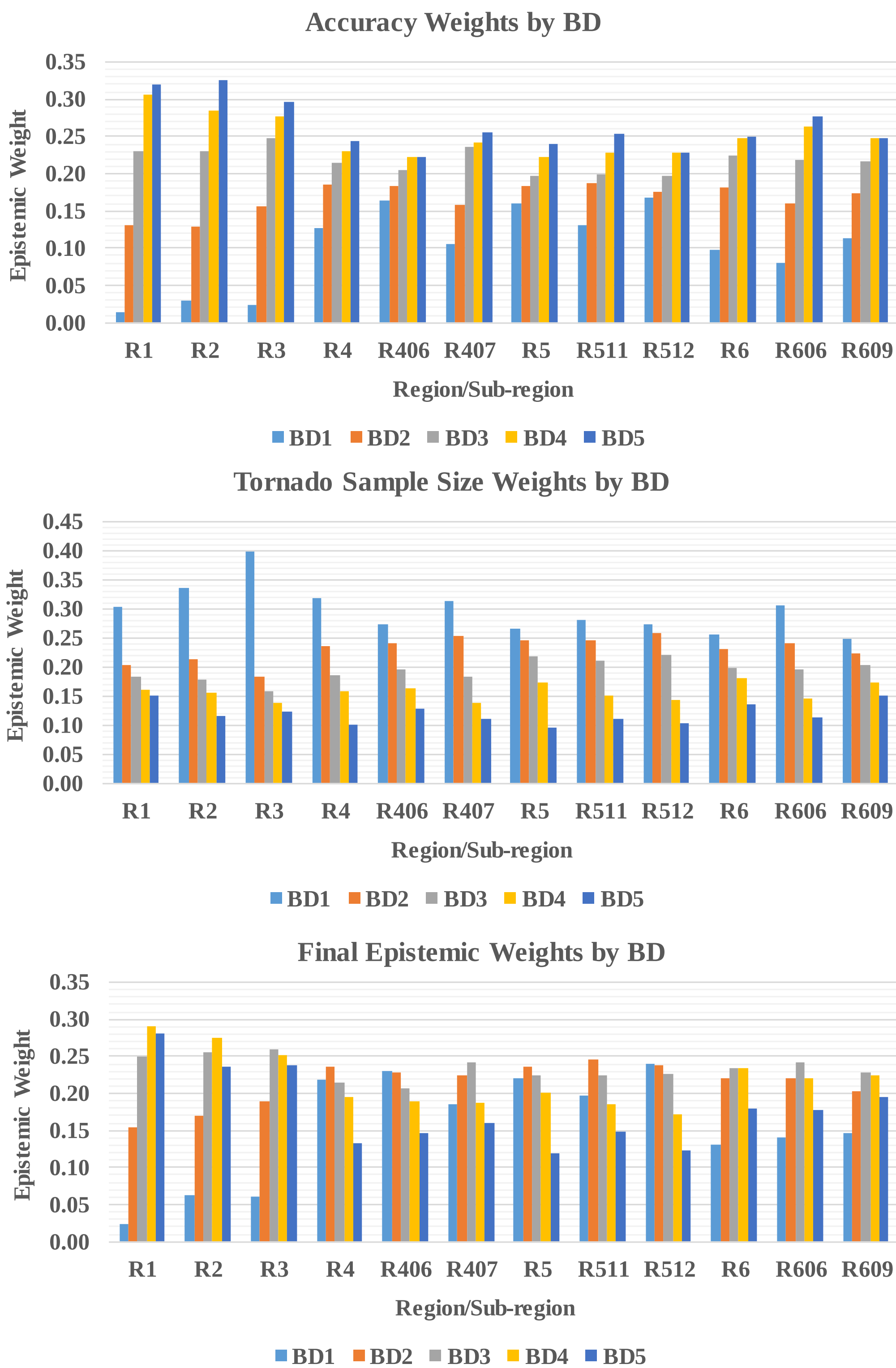

Figure C-5. Plots of Epistemic BD Threshold Weights

C.6. Tornado Path Length and Width Disribution Plots

Table C-7 provides the figure index for the regional models for path length and path width. The following plots use path length in miles (1 mile = 1.609344 km) and/or path width in feet (1 ft = 0.3048 m).

Table Error! No text of specified style in document.**-13. Regional Tornado Path Variables**

Variable	Region	Page
Path Length	1	C-38
Path Length	2	C-39
Path Length	3	C-40
Path Length	4	C-41
Path Length	5	C-42
Path Length	6	C-43
Path Width	1	C-44
Path Width	2	C-45
Path Width	3	C-46
Path Width	4	C-47
Path Width	5	C-48
Path Width	6	C-49

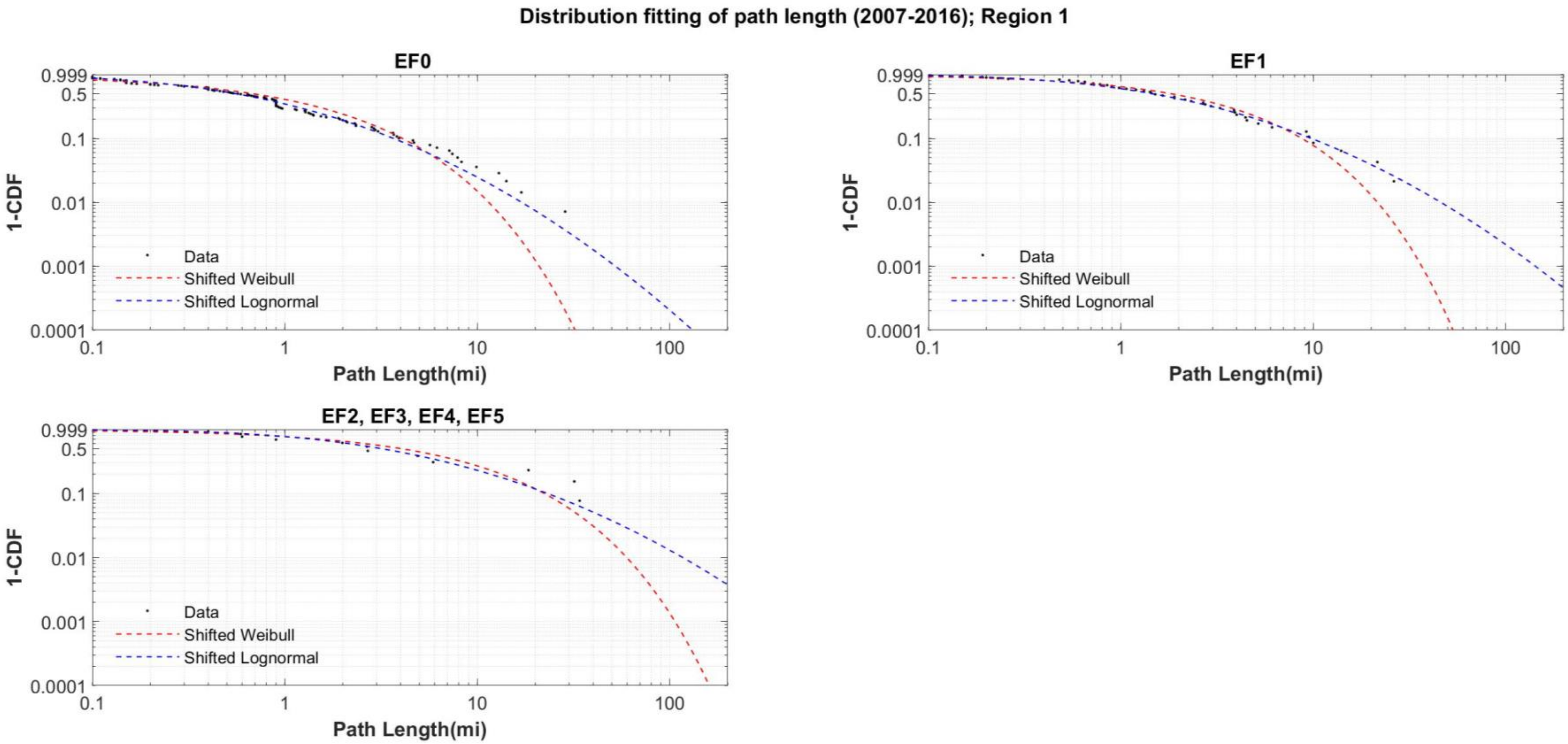
Distribution fitting of path length (2007-2016); Region 1
EF0
EF1
EF2, EF3, EF4, EF5
1-CDF
Path Length(mi)
0.999
0.5
0.1
0.01
0.001
0.0001
0.1
1
10
100
Data
Shifted Weibull
Shifted Lognormal

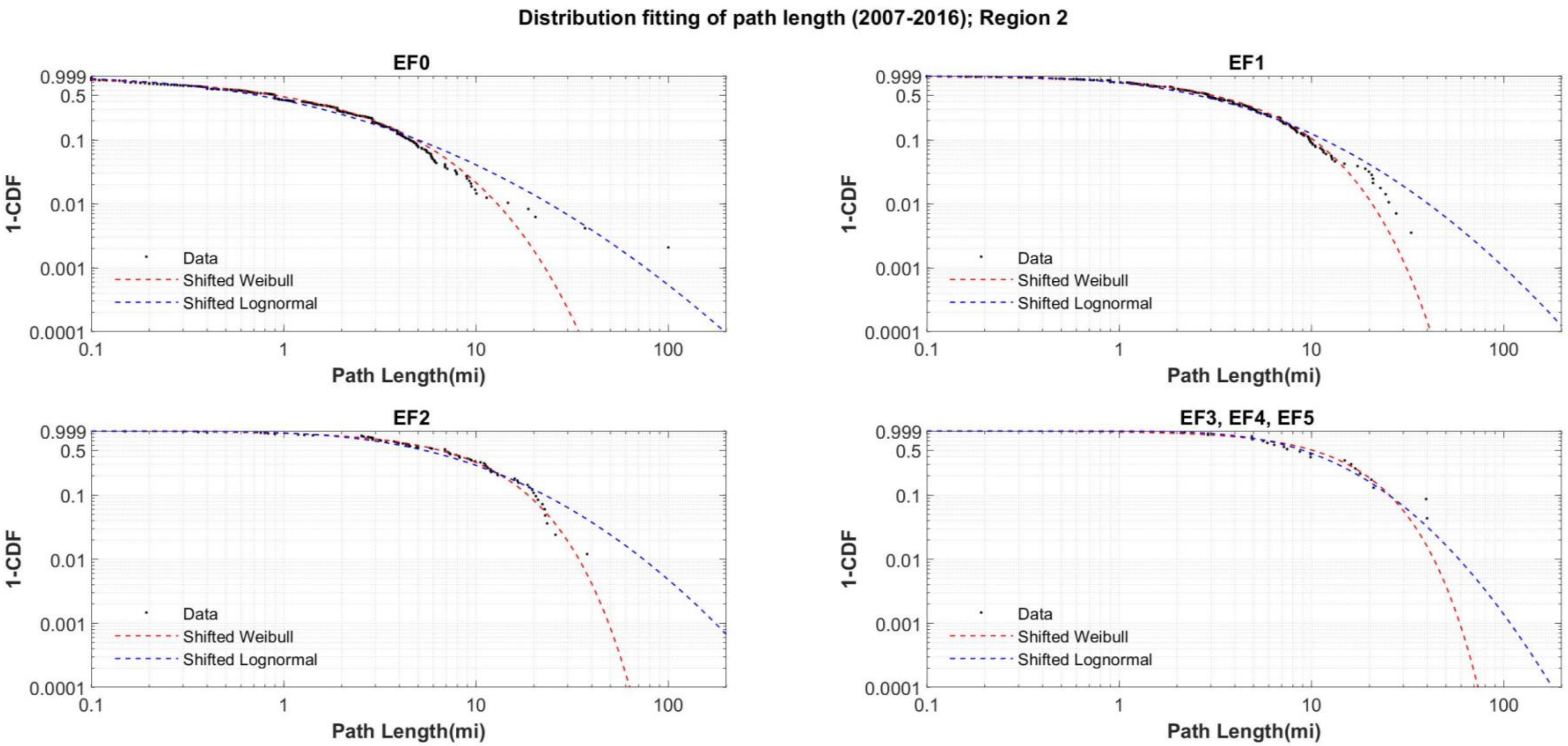

Distribution fitting of path length (2007-2016); Region 2
EF0
EF1
EF2
EF3, EF4, EF5
1-CDF
Path Length(mi)
Data
Shifted Weibull
Shifted Lognormal
0.999
0.5
0.1
0.01
0.001
0.0001
0.1
1
10
100

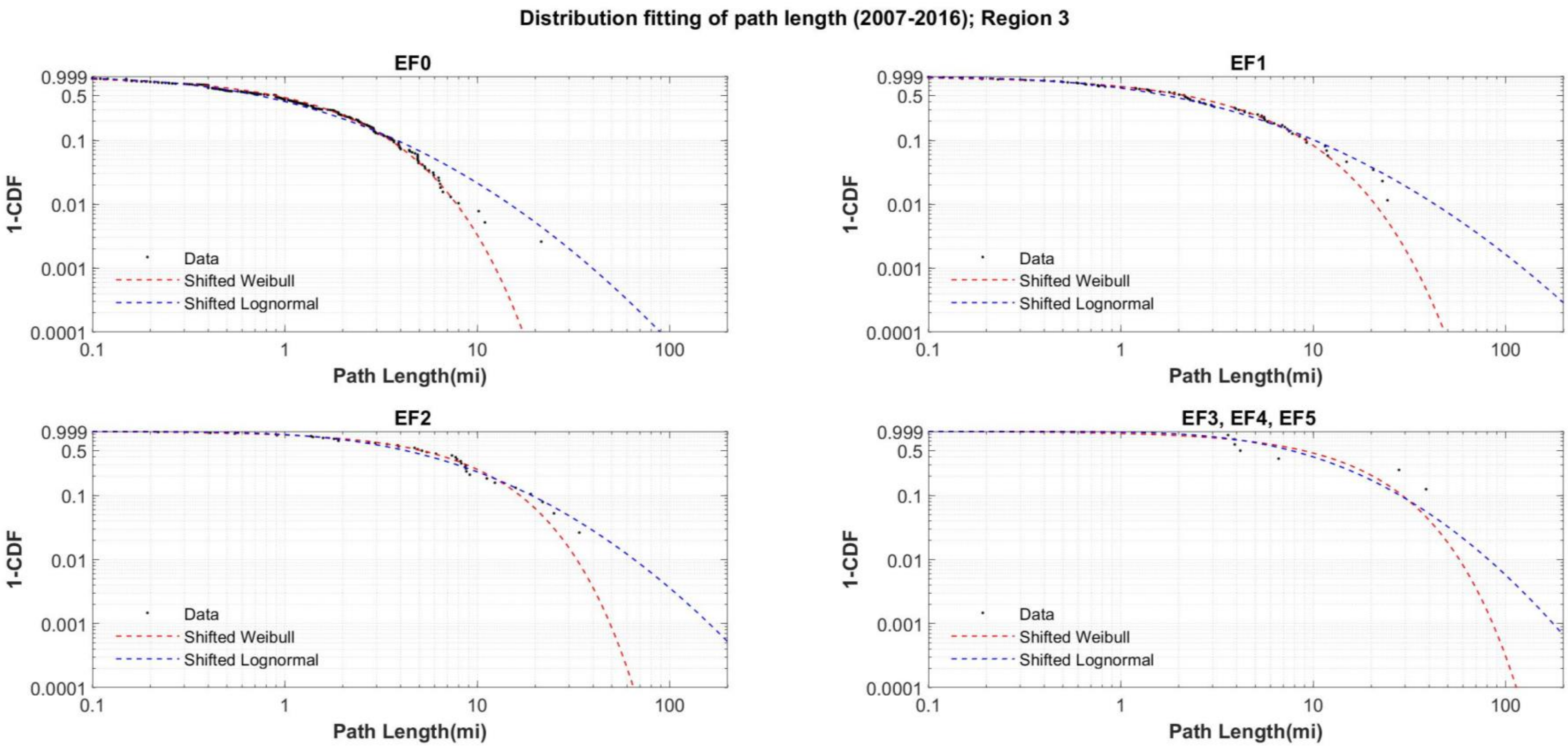

Distribution fitting of path length (2007-2016); Region 3
EF0
EF1
EF2
EF3, EF4, EF5
1-CDF
Path Length(mi)
Data
Shifted Weibull
Shifted Lognormal
0.999
0.5
0.1
0.01
0.001
0.0001
0.1
1
10
100

Distribution fitting of path length (2007-2016); Region 4

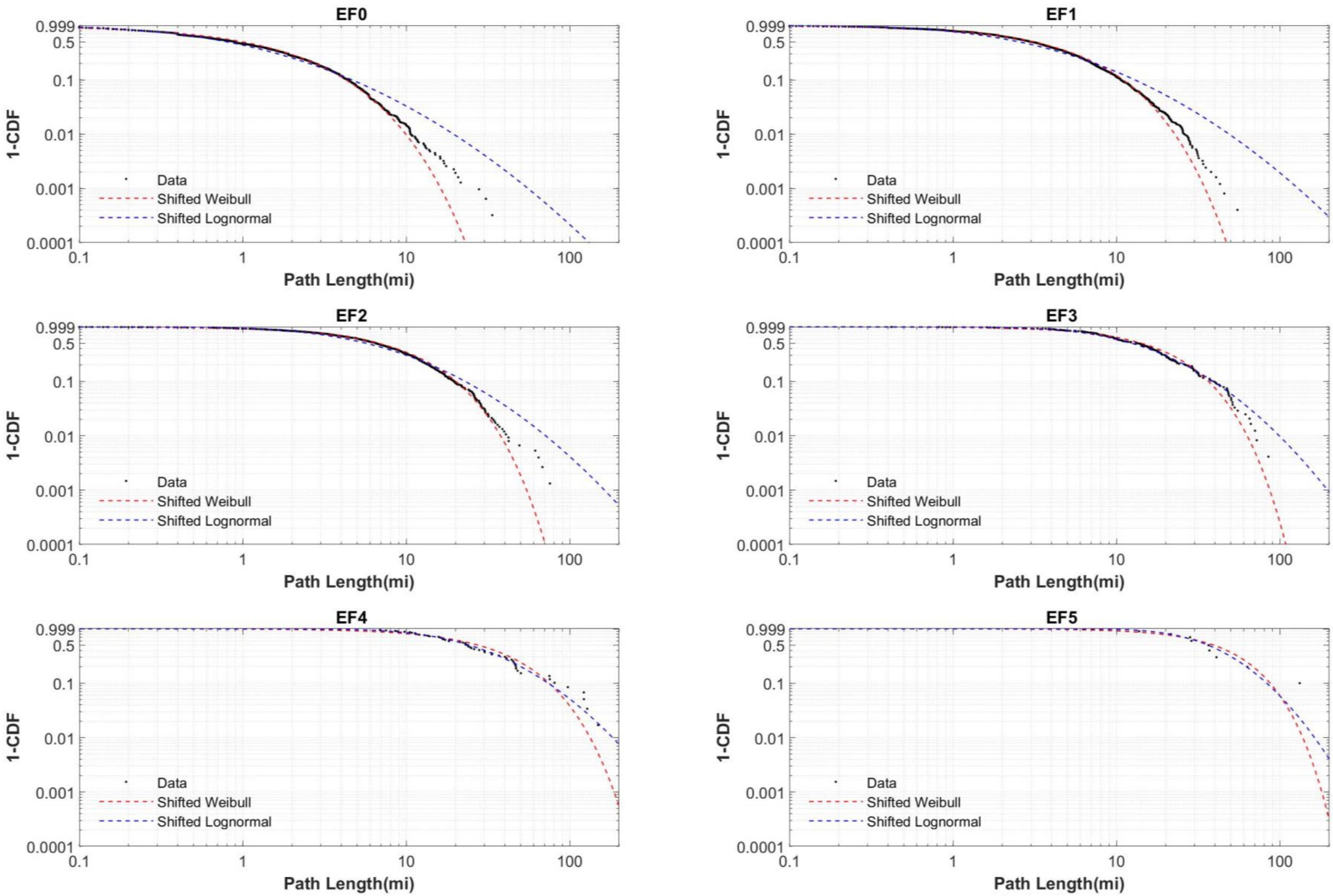

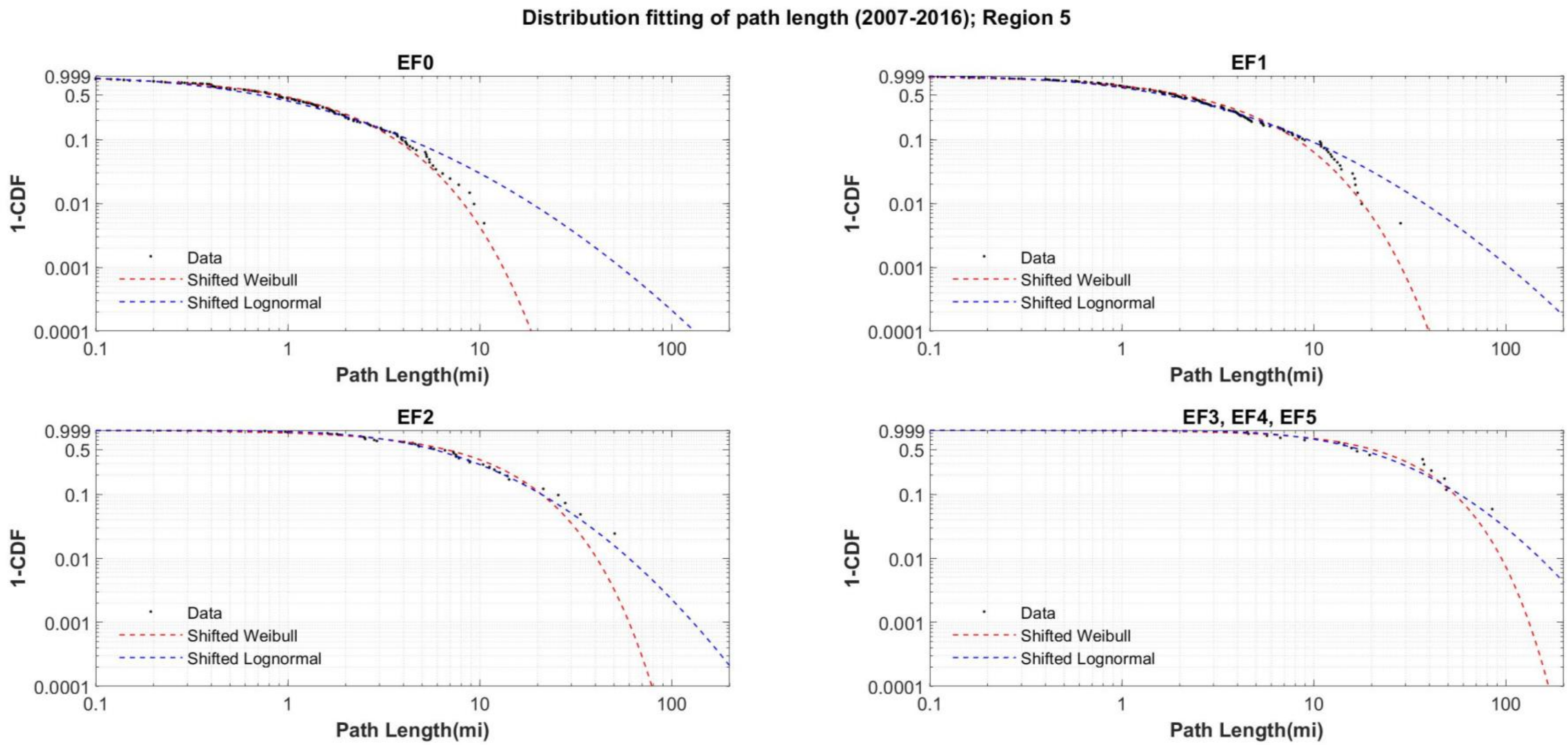
Distribution fitting of path length (2007-2016); Region 5
EF0
EF1
EF2
EF3, EF4, EF5
1-CDF
Path Length(mi)
0.999
0.5
0.1
0.01
0.001
0.0001
0.1
1
10
100
Data
Shifted Weibull
Shifted Lognormal

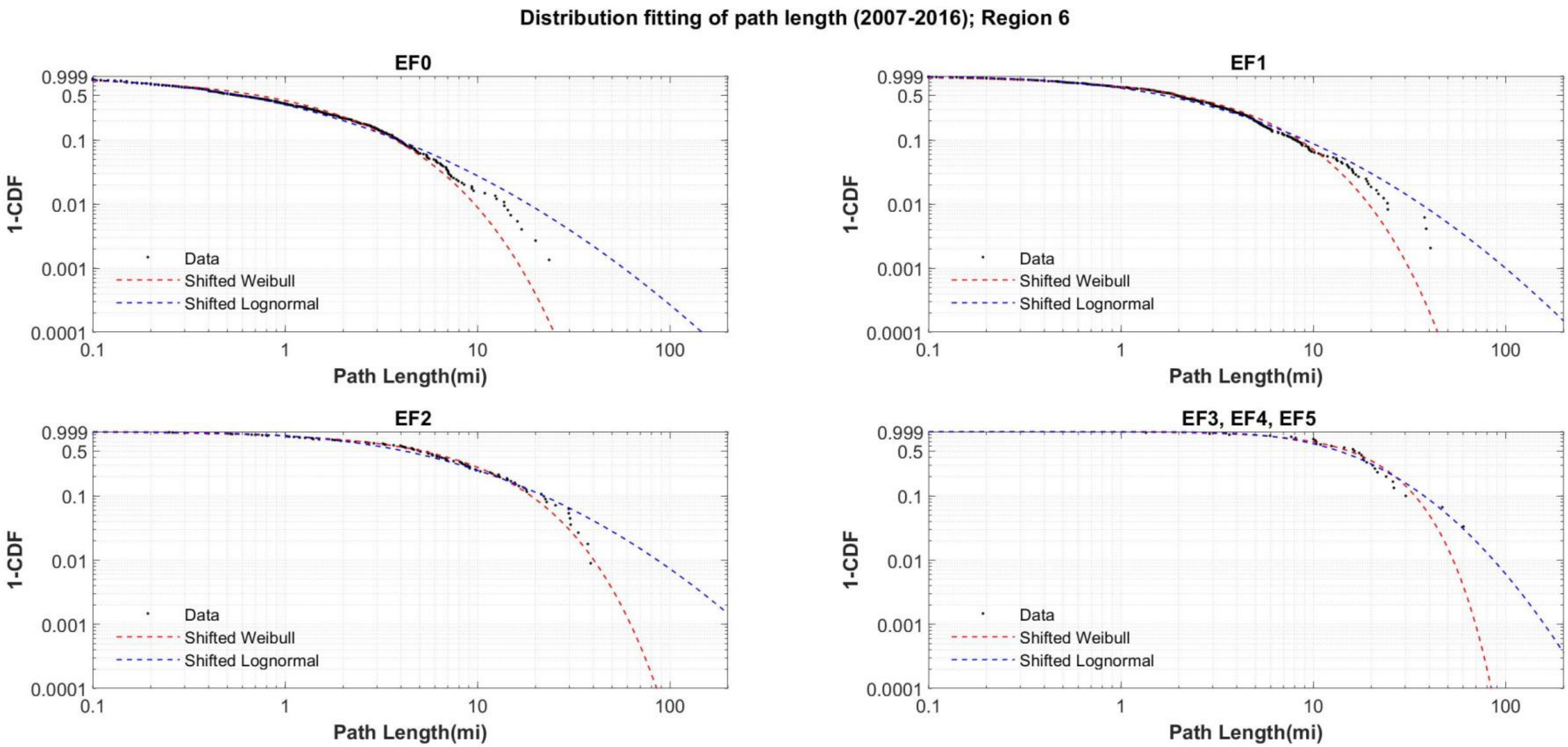
Distribution fitting of path length (2007-2016); Region 6
EF0
EF1
EF2
EF3, EF4, EF5
1-CDF
Path Length(mi)
0.999
0.5
0.1
0.01
0.001
0.0001
0.1
1
10
100
Data
Shifted Weibull
Shifted Lognormal

Region 1 (2007-2016)

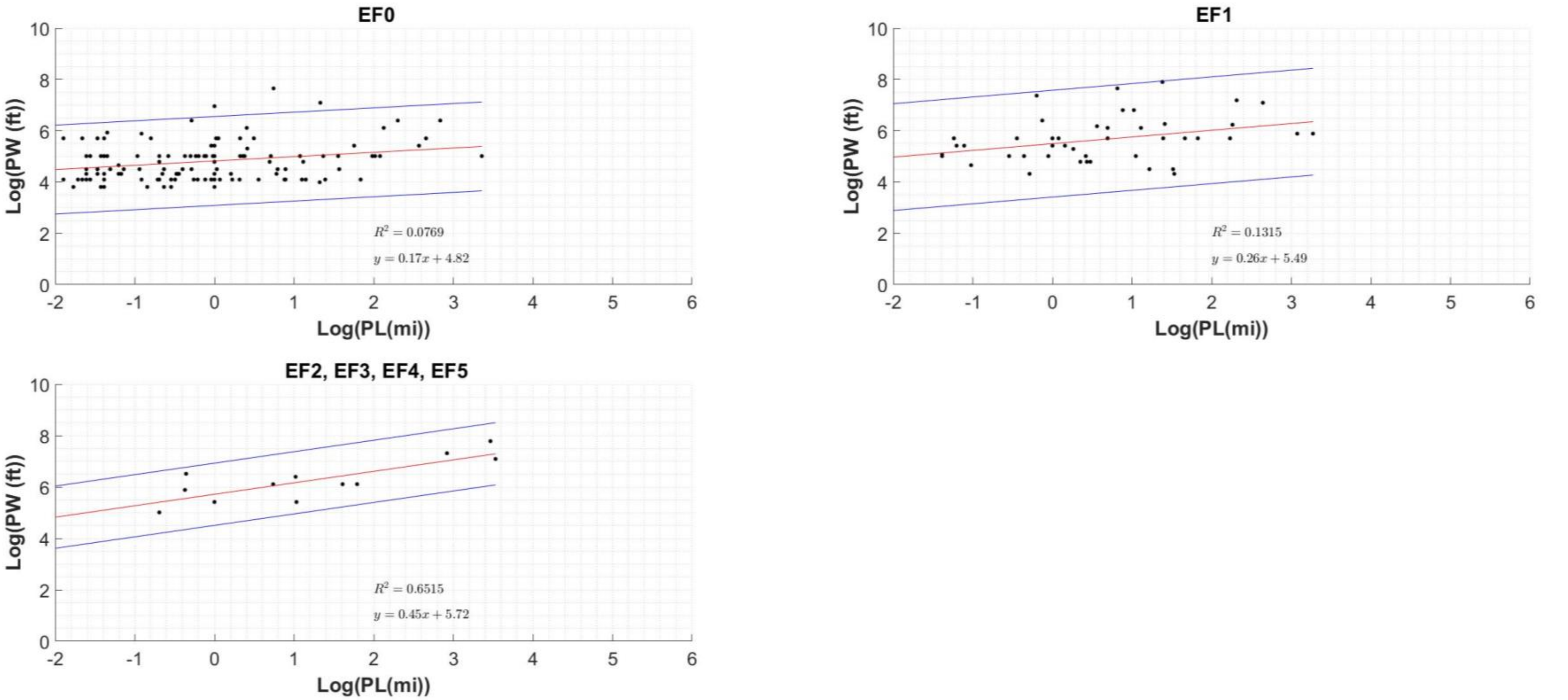

Region 2 (2007-2016)

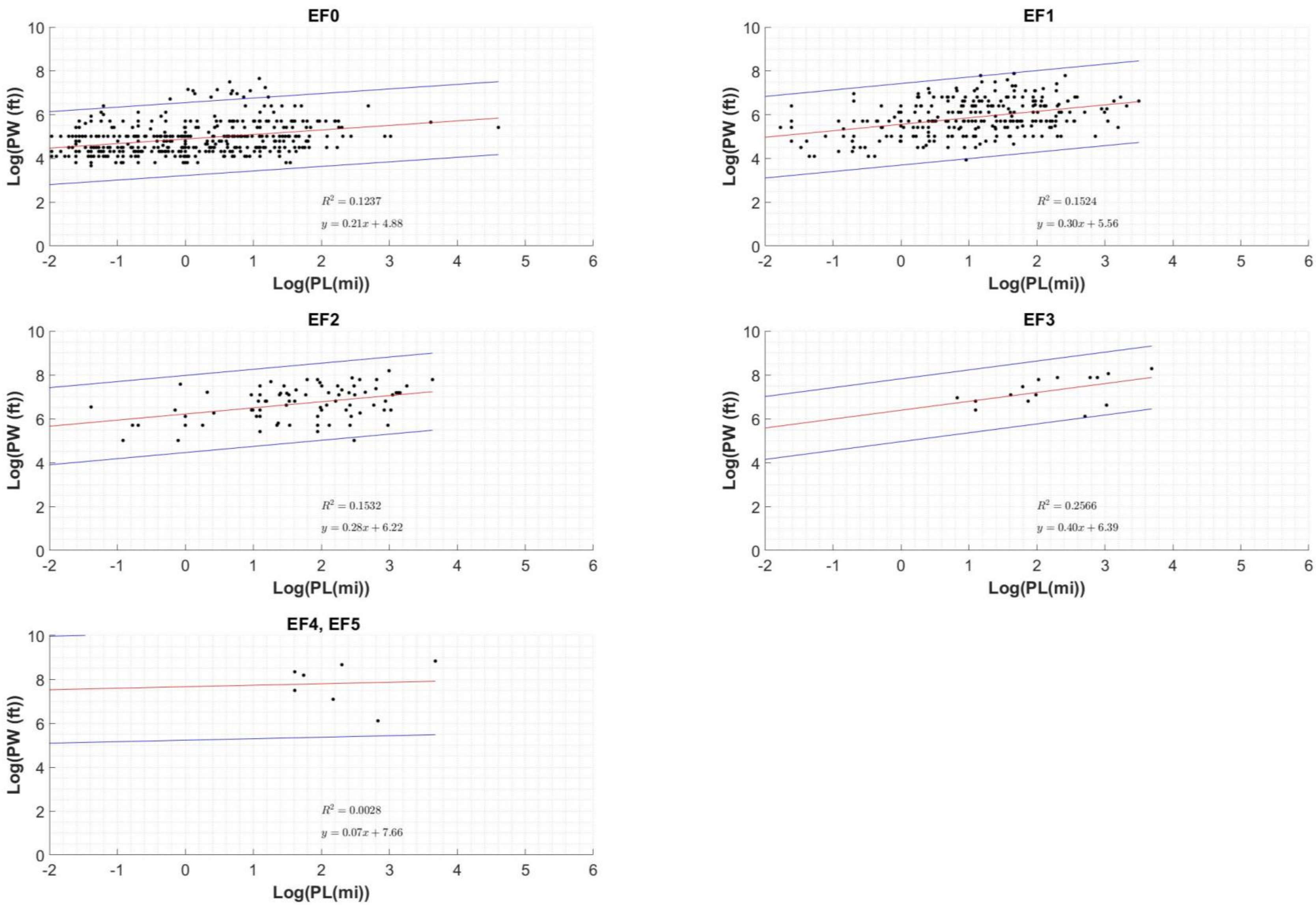

Region 3 (2007-2016)

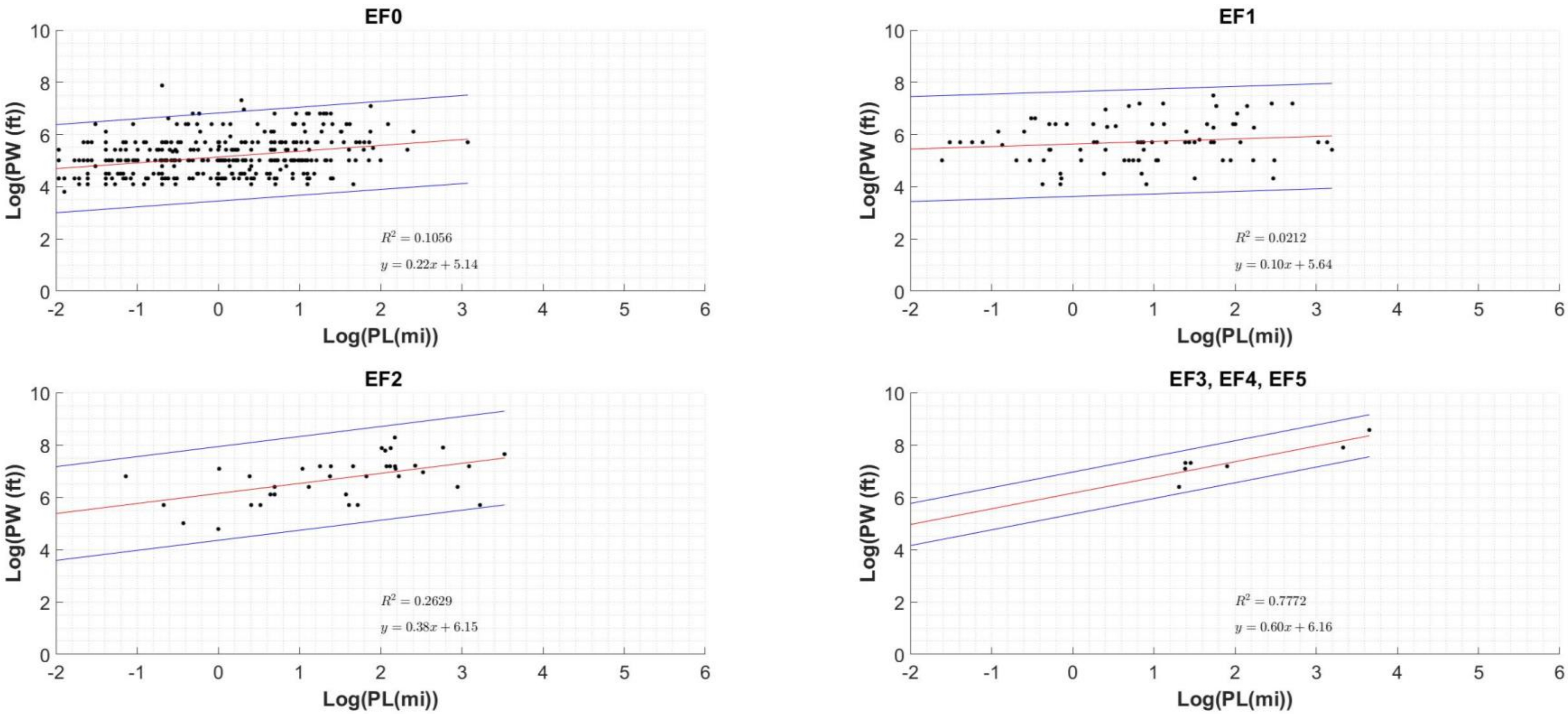

Region 4 (2007-2016)

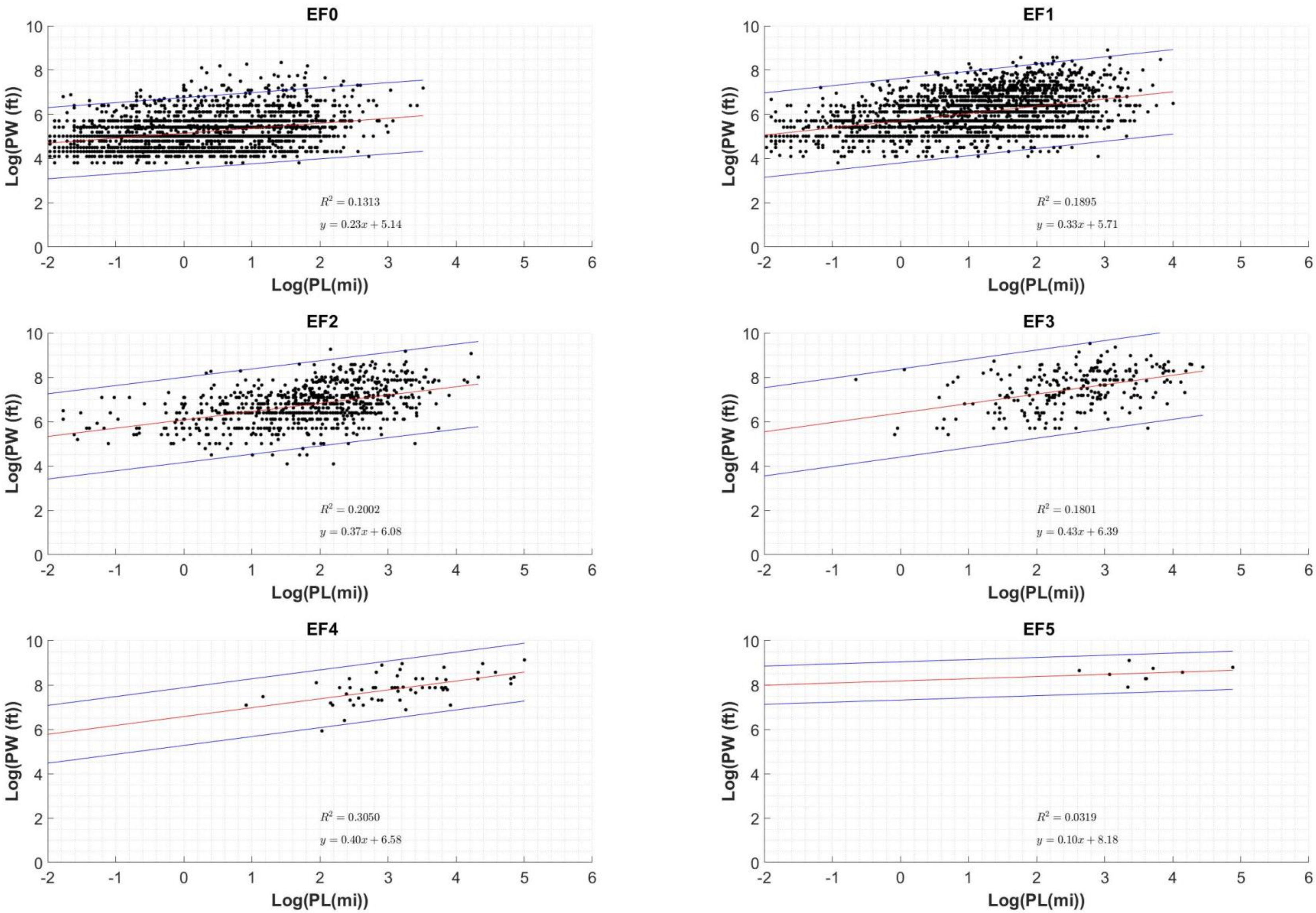

Region 5 (2007-2016)

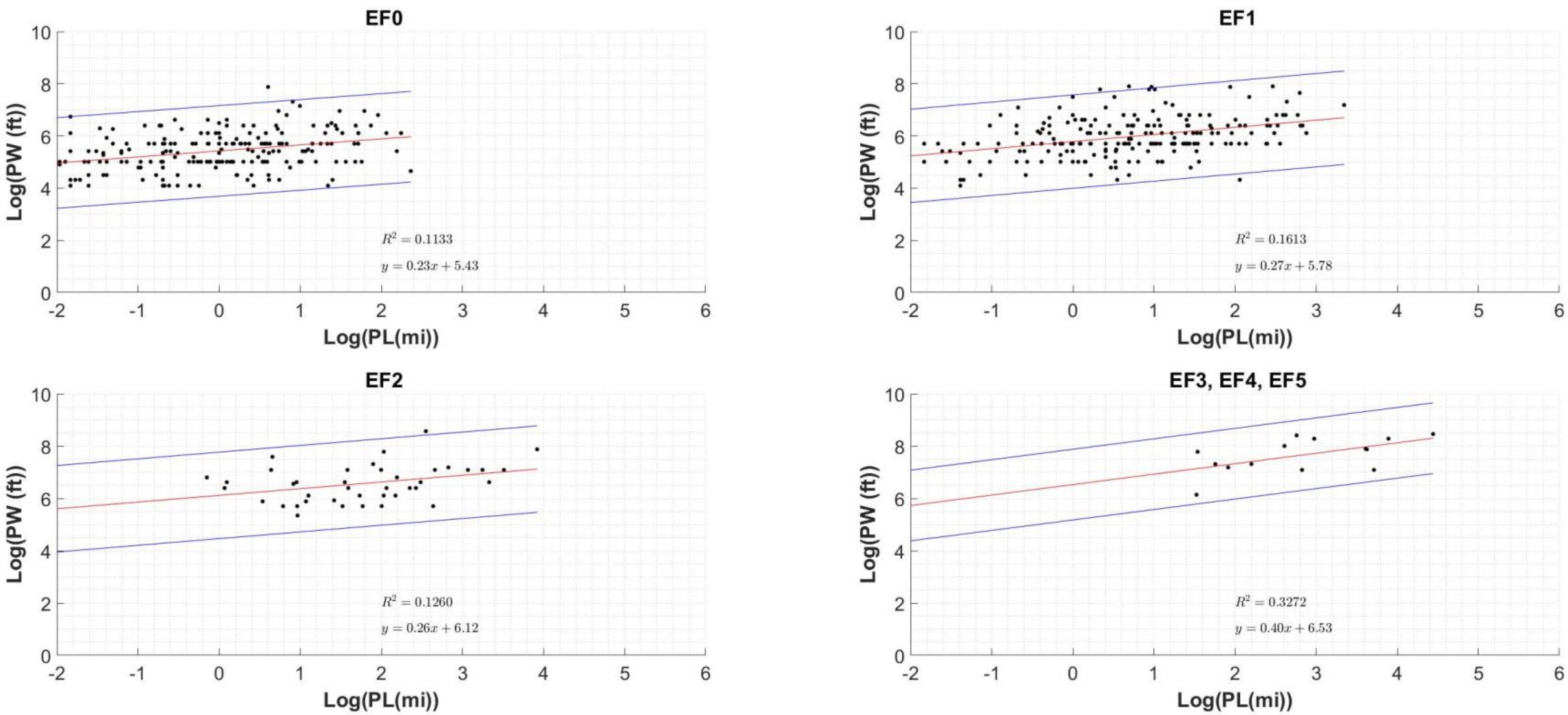

Region 6 (2007-2016)

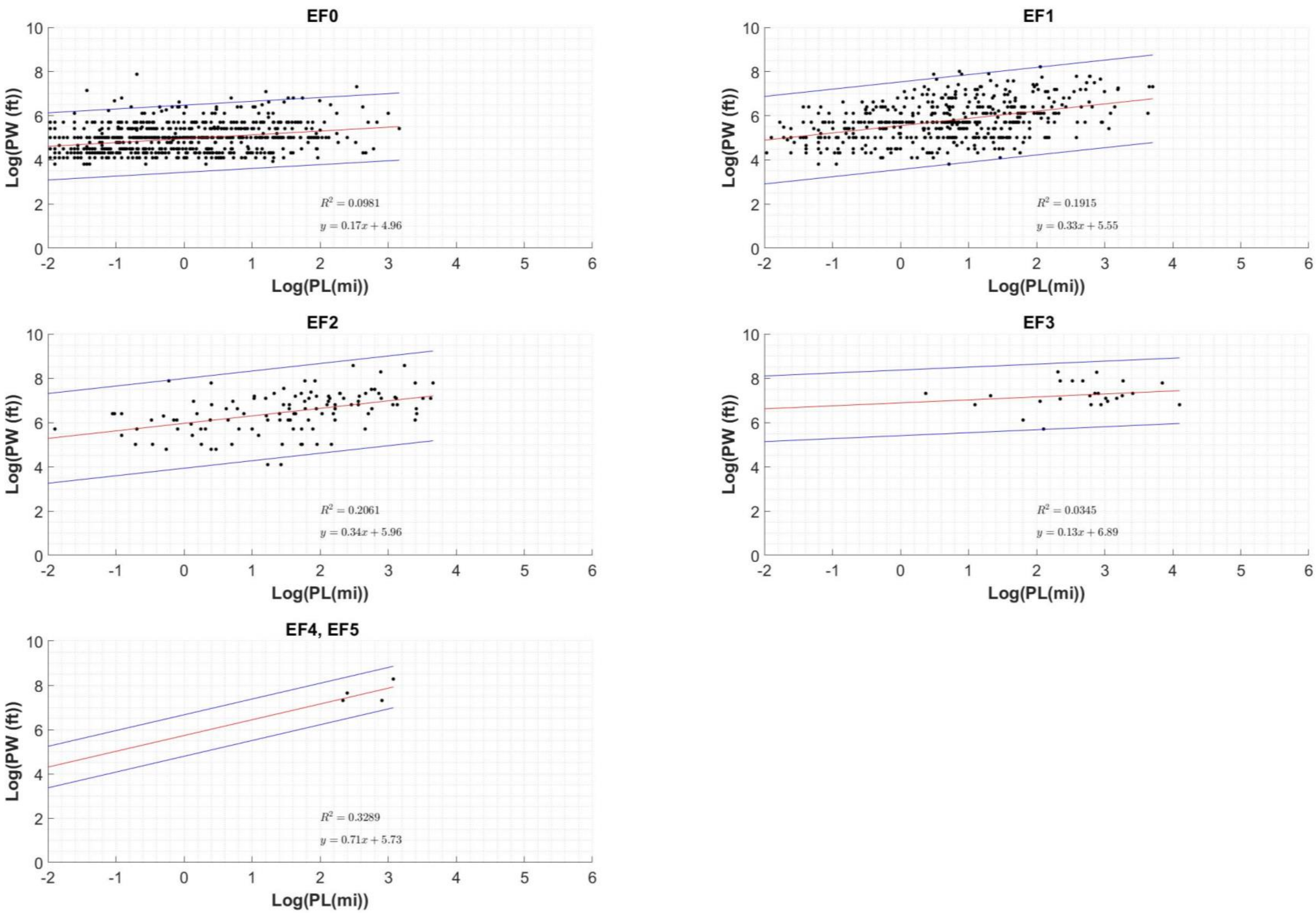

C.7. Within-Path Intensity Variation Data

Within-path intensity models are developed from tornado intensity contour damage maps. This appendix lists sources and the condensed PLIV-PWV catalog. Table C-8 provides a listing of the 181 tornadoes used for PLIV-PWV analysis. Reported path length and average PLIV spacing are given in miles (1 mile = 1.609344 km). Table C-9 lists the condensed catalogs for the 181 tornadoes in Table C-8. The condensed catalog is used for hazard curve development in the simulations in Section 7.

Table Error! No text of specified style in document.**-14. Tornado Listing for PLIV Analysis**

Tornado No.	Name (if applicable)	Outbreak/Group Name	Date	Reported Path Length (mi)	Avg. PLIV Spacing (mi)	No. of PLIV F/EF Ratings	Tornado F/EF Rating
1	Union City Tornado		24-May-73	10.56	1.32	8	5
2	Crowell	Red River Valley	10-Apr-79	23	1.44	16	2
3	Vernon	Red River Valley	10-Apr-79	39	1.50	26	4
4	Hollister	Red River Valley	10-Apr-79	8	1.14	7	2
5	Faxon	Red River Valley	10-Apr-79	7	1.40	5	1
6	Lawton	Red River Valley	10-Apr-79	4	0.80	5	3
7	Grandfield	Red River Valley	10-Apr-79	64	1.78	36	2
8	Noble	Red River Valley	10-Apr-79	2	2.00	1	2
9	Seymour	Red River Valley	10-Apr-79	11	1.22	9	2
10	Wichita Falls	Red River Valley	10-Apr-79	47	1.34	35	4
11	Pruitt	Red River Valley	10-Apr-79	27	1.29	21	3
12		Fujita Mapped-74	3,4-Apr-74	0.5		1	0
13		Fujita Mapped-74	3,4-Apr-74	0.5		1	0
14		Fujita Mapped-74	3,4-Apr-74	15	3.75	4	1
15		Fujita Mapped-74	3,4-Apr-74	8	2.00	4	3
16		Fujita Mapped-74	3,4-Apr-74	19	3.80	5	3
17		Fujita Mapped-74	3,4-Apr-74	13	4.33	3	1
18		Fujita Mapped-74	3,4-Apr-74	8	2.67	3	1
19		Fujita Mapped-74	3,4-Apr-74	4		1	0
20		Fujita Mapped-74	3,4-Apr-74	8	2.67	3	3
21		Fujita Mapped-74	3,4-Apr-74	17	4.25	4	3
22		Fujita Mapped-74	3,4-Apr-74	7	2.33	3	2
23		Fujita Mapped-74	3,4-Apr-74	26	4.33	6	3
24		Fujita Mapped-74	3,4-Apr-74	121	4.17	29	4
25		Fujita Mapped-74	3,4-Apr-74	8	2.67	3	1
26		Fujita Mapped-74	3,4-Apr-74	36	5.14	7	3
27		Fujita Mapped-74	3,4-Apr-74	21	5.25	4	2
28		Fujita Mapped-74	3,4-Apr-74	16	5.33	3	1
29		Fujita Mapped-74	3,4-Apr-74	2	2.00	1	2
30		Fujita Mapped-74	3,4-Apr-74	7	3.50	2	1
31		Fujita Mapped-74	3,4-Apr-74	10	2.50	4	2
32		Fujita Mapped-74	3,4-Apr-74	19	4.75	4	2
33		Fujita Mapped-74	3,4-Apr-74	11	3.67	3	2
34		Fujita Mapped-74	3,4-Apr-74	7	7.00	1	2
35		Fujita Mapped-74	3,4-Apr-74	12	4.00	3	2
36		Fujita Mapped-74	3,4-Apr-74	8	8.00	1	2
37		Fujita Mapped-74	3,4-Apr-74	13	4.33	3	1
38		Fujita Mapped-74	3,4-Apr-74	10	3.33	3	3
39		Fujita Mapped-74	3,4-Apr-74	0.5	0.50	1	2
40		Fujita Mapped-74	3,4-Apr-74	0.5	0.50	1	1

Table C-8. Tornado Listing for PLIV Analysis (continued)

Tornado No.	Name (if applicable)	Outbreak/Group Name	Date	Reported Path Length (mi)	Avg. PLIV Spacing (mi)	No. of PLIV F/EF Ratings	Tornado F/EF Rating
41		Fujita Mapped-74	3,4-Apr-74	6	2.00	3	2
42		Fujita Mapped-74	3,4-Apr-74	17	4.25	4	3
43		Fujita Mapped-74	3,4-Apr-74	20	5.00	4	4
44		Fujita Mapped-74	3,4-Apr-74	22	3.14	7	4
45		Fujita Mapped-74	3,4-Apr-74	13	3.25	4	1
46		Fujita Mapped-74	3,4-Apr-74	38	4.75	8	3
47		Fujita Mapped-74	3,4-Apr-74	37	5.29	7	4
48		Fujita Mapped-74	3,4-Apr-74	32	5.33	6	5
49		Fujita Mapped-74	3,4-Apr-74	15	3.75	4	2
50		Fujita Mapped-74	3,4-Apr-74	5	1.67	3	2
51		Fujita Mapped-74	3,4-Apr-74	62	4.77	13	5
52		Fujita Mapped-74	3,4-Apr-74	38	4.75	8	4
53		Fujita Mapped-74	3,4-Apr-74	28	4.00	7	4
54		Fujita Mapped-74	3,4-Apr-74	21	4.20	5	5
55		Fujita Mapped-74	3,4-Apr-74	20	4.00	5	4
56		Fujita Mapped-74	3,4-Apr-74	10	5.00	2	2
57		Fujita Mapped-74	3,4-Apr-74	0.5		1	0
58		Fujita Mapped-74	3,4-Apr-74	34	4.25	8	5
59		Fujita Mapped-74	3,4-Apr-74	21	4.20	5	4
60		Fujita Mapped-74	3,4-Apr-74	21	2.33	9	1
61		Fujita Mapped-74	3,4-Apr-74	1		1	0
62		Fujita Mapped-74	3,4-Apr-74	16	3.20	5	3
63		Fujita Mapped-74	3,4-Apr-74	28	5.60	5	4
64		Fujita Mapped-74	3,4-Apr-74	42	4.67	9	4
65		Fujita Mapped-74	3,4-Apr-74	36	4.50	8	4
66		Fujita Mapped-74	3,4-Apr-74	25	4.17	6	3
67		Fujita Mapped-74	3,4-Apr-74	9	3.00	3	1
68		Fujita Mapped-74	3,4-Apr-74	14	4.67	3	2
69		Fujita Mapped-74	3,4-Apr-74	18	3.60	5	2
70		Fujita Mapped-74	3,4-Apr-74	9	4.50	2	2
71		Fujita Mapped-74	3,4-Apr-74	6		2	0
72		Fujita Mapped-74	3,4-Apr-74	25	3.57	7	3
73		Fujita Mapped-74	3,4-Apr-74	29	4.14	7	4
74		Fujita Mapped-74	3,4-Apr-74	18	3.60	5	3
75		Fujita Mapped-74	3,4-Apr-74	35	5.00	7	4
76		Fujita Mapped-74	3,4-Apr-74	7	7.00	1	1
77		Fujita Mapped-74	3,4-Apr-74	24	4.00	6	3
78		Fujita Mapped-74	3,4-Apr-74	12	6.00	2	2
79		Fujita Mapped-74	3,4-Apr-74	21	5.25	4	3
80		Fujita Mapped-74	3,4-Apr-74	30	4.29	7	4
81		Fujita Mapped-74	3,4-Apr-74	24	6.00	4	3
82		Fujita Mapped-74	3,4-Apr-74	10	10.00	1	1
83		Fujita Mapped-74	3,4-Apr-74	19	4.75	4	3
84		Fujita Mapped-74	3,4-Apr-74	4	4.00	1	1
85		Fujita Mapped-74	3,4-Apr-74	26	4.33	6	4
86		Fujita Mapped-74	3,4-Apr-74	20	5.00	4	2
87		Fujita Mapped-74	3,4-Apr-74	13	4.33	3	2
88		Fujita Mapped-74	3,4-Apr-74	3		1	0
89		Fujita Mapped-74	3,4-Apr-74	15	5.00	3	1
90		Fujita Mapped-74	3,4-Apr-74	26	4.33	6	1

Table C-8. Tornado Listing for PLIV Analysis (continued)

Tornado No.	Name (if applicable)	Outbreak/Group Name	Date	Reported Path Length (mi)	Avg. PLIV Spacing (mi)	No. of PLIV F/EF Ratings	Tornado F/EF Rating
91		Fujita Mapped-74	3,4-Apr-74	15	5.00	3	3
92		Fujita Mapped-74	3,4-Apr-74	10	3.33	3	1
93		Fujita Mapped-74	3,4-Apr-74	19	3.80	5	4
94		Fujita Mapped-74	3,4-Apr-74	29	4.83	6	3
95		Fujita Mapped-74	3,4-Apr-74	30	5.00	6	3
96		Fujita Mapped-74	3,4-Apr-74	13	4.33	3	3
97		Fujita Mapped-74	3,4-Apr-74	32	4.00	8	4
98		Fujita Mapped-74	3,4-Apr-74	13	2.60	5	4
99		Fujita Mapped-74	3,4-Apr-74	21	3.50	6	3
100		Fujita Mapped-74	3,4-Apr-74	12	6.00	2	2
101		Fujita Mapped-74	3,4-Apr-74	4	4.00	1	1
102		Fujita Mapped-74	3,4-Apr-74	28	5.60	5	1
103		Fujita Mapped-74	3,4-Apr-74	11	3.67	3	1
104		Fujita Mapped-74	3,4-Apr-74	26	5.20	5	3
105		Fujita Mapped-74	3,4-Apr-74	12	4.00	3	3
106		Fujita Mapped-74	3,4-Apr-74	12	4.00	3	2
107		Fujita Mapped-74	3,4-Apr-74	51	5.67	9	5
108		Fujita Mapped-74	3,4-Apr-74	36	5.14	7	4
109		Fujita Mapped-74	3,4-Apr-74	50	4.55	11	4
110		Fujita Mapped-74	3,4-Apr-74	20	5.00	4	3
111		Fujita Mapped-74	3,4-Apr-74	16	4.00	4	3
112		Fujita Mapped-74	3,4-Apr-74	102	4.86	21	5
113		Fujita Mapped-74	3,4-Apr-74	41	3.42	12	3
114		Fujita Mapped-74	3,4-Apr-74	103	5.42	19	4
115		Fujita Mapped-74	3,4-Apr-74	1	1.00	1	2
116		Fujita Mapped-74	3,4-Apr-74	12	2.40	5	3
117		Fujita Mapped-74	3,4-Apr-74	9		2	0
118		Fujita Mapped-74	3,4-Apr-74	4	2.00	2	2
119		Fujita Mapped-74	3,4-Apr-74	5		2	0
120		Fujita Mapped-74	3,4-Apr-74	6	6.00	1	1
121		Fujita Mapped-74	3,4-Apr-74	2	2.00	1	2
122		Fujita Mapped-74	3,4-Apr-74	1	1.00	1	1
123		Fujita Mapped-74	3,4-Apr-74	4	4.00	1	1
124		Fujita Mapped-74	3,4-Apr-74	13	4.33	3	3
125		Fujita Mapped-74	3,4-Apr-74	24	4.80	5	3
126		Fujita Mapped-74	3,4-Apr-74	9	4.50	2	1
127		Fujita Mapped-74	3,4-Apr-74	3		1	0
128		Fujita Mapped-74	3,4-Apr-74	12	4.00	3	2
129		Fujita Mapped-74	3,4-Apr-74	14	2.80	5	3
130		Fujita Mapped-74	3,4-Apr-74	26	4.33	6	4
131		Fujita Mapped-74	3,4-Apr-74	17	4.25	4	3
132		Fujita Mapped-74	3,4-Apr-74	22	4.40	5	4
133		Fujita Mapped-74	3,4-Apr-74	1		1	0
134		Fujita Mapped-74	3,4-Apr-74	19	4.75	4	2
135		Fujita Mapped-74	3,4-Apr-74	0.5		1	0
136		Fujita Mapped-74	3,4-Apr-74	0.5		1	0
137		Fujita Mapped-74	3,4-Apr-74	1	1.00	1	1
138		Fujita Mapped-74	3,4-Apr-74	65	5.42	12	2
139		Fujita Mapped-74	3,4-Apr-74	24	6.00	4	4
140		Fujita Mapped-74	3,4-Apr-74	0.5		1	0

Table C-8. Tornado Listing for PLIV Analysis (continued)

Tornado No.	Name (if applicable)	Outbreak/Group Name	Date	Reported Path Length (mi)	Avg. PLIV Spacing (mi)	No. of PLIV F/EF Ratings	Tornado F/EF Rating
141		Fujita Mapped-74	3,4-Apr-74	0.5		1	0
142		Fujita Mapped-74	3,4-Apr-74	0.5		1	0
143		Fujita Mapped-74	3,4-Apr-74	1		1	0
144		Fujita Mapped-74	3,4-Apr-74	0.5		1	0
145		Fujita Mapped-74	3,4-Apr-74	0.5		1	0
146		Fujita Mapped-74	3,4-Apr-74	26		4	0
147		Fujita Mapped-74	3,4-Apr-74	2	2.00	1	1
148		Fujita Mapped-74	3,4-Apr-74	35	4.38	8	3
149		Fujita Mapped-74	3,4-Apr-74	5	2.50	2	1
150		Fujita Mapped-74	3,4-Apr-74	9	9.00	1	1
151		Fujita Mapped-74	3,4-Apr-74	12	6.00	2	3
152		Fujita Mapped-74	3,4-Apr-74	0.5	0.50	1	1
153		Fujita Mapped-74	3,4-Apr-74	0.5	0.50	1	1
154		Fujita Mapped-74	3,4-Apr-74	8		2	0
155		Fujita Mapped-74	3,4-Apr-74	9	3.00	3	3
156		Fujita Mapped-74	3,4-Apr-74	18	4.50	4	1
157		Fujita Mapped-74	3,4-Apr-74	9	3.00	3	2
158		Fujita Mapped-74	3,4-Apr-74	1	1.00	1	1
159		Fujita Mapped-74	3,4-Apr-74	5	2.50	2	2
160	Hesston		13-Mar-90	48	1.78	27	5
161	Chandler-Lk.Wilson		16-Jun-92	35	8.75	4	5
162	Manchester		24-Jun-03	10	1.67	6	4
163	Woonsocket		24-Jun-03	5	1.67	3	3
164	Cavour		24-Jun-03	3.5	1.75	2	3
165	Mount Vernon		24-Jun-03	6	2.00	3	2
166	Beadle County		24-Aug-06	24.5	1.75	14	3
167	Beadle County		24-Aug-06	7	1.40	5	2
168	West of Everly		11-Jun-04	5.5	1.38	4	2
169	West of Webb		11-Jun-04	5.8	1.16	5	3
170	Coleridge		24-Jun-03	13	1.08	12	4
171	Walnut		8-May-04	6	1.00	6	1
172	Hallam		22-May-04	52	1.53	34	4
173	Little Sioux		11-Jun-08	14	0.82	17	3
174	Parkersburg		25-May-08	43.5	8.70	5	5
175	Kellerville		8-Jun-95	31	1.15	27	5
176	Alanreed		8-Jun-95	10	1.11	9	3
177	Moore		4-Oct-98	3	0.43	7	2
178	Moore		20-May-13	14.3	0.60	24	5
179	OKC (A9)		3-May-99	37	1.03	36	5
180	Joplin		22-May-11	22.1	0.92	24	5
181	El Reno		31-May-13	16.3	1.16	14	3
Sum				**3253.06**	**574.05**	**1078.00**	**430.00**
Mean				**17.97**	**3.59**	**5.96**	**2.38**

Table Error! No text of specified style in document.**-15. PLIV-PWV Condensed Catalogs for Ω = 0.5**

No.	Tornado F/EF	L or W	EF0	EF1	EF2	EF3	EF4	EF5	Mean F/EF and Mean ω for Epistemic Ω = 0.5 (F/EF in L row and ω in W row)
1	5	L	0.000	0.125	0.500	0.000	0.125	0.250	2.875
		W		0.265	0.464		0.265	0.442	0.409
2	2	L	0.688	0.250	0.063	0.000	0.000	0.000	0.375
		W	0.380	0.380	0.570				0.392
3	4	L	0.077	0.192	0.538	0.115	0.077	0.000	1.923
		W	0.321	0.449	0.504	0.534	0.641		0.493
4	2	L	0.286	0.429	0.286	0.000	0.000	0.000	1.000
		W	0.190	0.444	0.475				0.380
5	1	L	0.400	0.600	0.000	0.000	0.000	0.000	0.600
		W	0.274	0.365					0.328
6	3	L	0.200	0.200	0.400	0.200	0.000	0.000	1.600
		W	0.313	0.626	0.469	0.313			0.438
7	2	L	0.222	0.556	0.222	0.000	0.000	0.000	1.000
		W	0.399	0.416	0.428				0.415
8	2	L	0.000	0.000	1.000	0.000	0.000	0.000	2.000
		W			0.570				0.570
9	2	L	0.333	0.556	0.111	0.000	0.000	0.000	0.778
		W	0.380	0.304	0.380				0.338
10	4	L	0.143	0.229	0.286	0.229	0.114	0.000	1.943
		W	0.333	0.417	0.410	0.545	0.545		0.447
11	3	L	0.429	0.286	0.190	0.095	0.000	0.000	0.952
		W	0.348	0.365	0.469	0.547			0.395
12	0	L	1.000	0.000	0.000	0.000	0.000	0.000	0.000
		W	0.515						0.515
13	0	L	1.000	0.000	0.000	0.000	0.000	0.000	0.000
		W	0.515						0.515
14	1	L	0.750	0.250	0.000	0.000	0.000	0.000	0.250
		W	0.462	0.391					0.444
15	3	L	0.000	0.250	0.500	0.250	0.000	0.000	2.000
		W		0.626	0.626	0.626			0.626
16	3	L	0.200	0.000	0.400	0.400	0.000	0.000	2.000
		W	0.400		0.488	0.601			0.516
17	1	L	0.667	0.333	0.000	0.000	0.000	0.000	0.333
		W	0.547	0.547					0.547
18	1	L	0.667	0.333	0.000	0.000	0.000	0.000	0.333
		W	0.547	0.547					0.547
19	0	L	1.000	0.000	0.000	0.000	0.000	0.000	0.000
		W	0.515						0.515
20	3	L	0.000	0.667	0.000	0.333	0.000	0.000	1.667
		W		0.597		0.626			0.607
21	3	L	0.000	0.250	0.500	0.250	0.000	0.000	2.000
		W		0.450	0.488	0.626			0.513
22	2	L	0.000	0.667	0.333	0.000	0.000	0.000	1.333
		W		0.491	0.570				0.518
23	3	L	0.000	0.333	0.333	0.333	0.000	0.000	2.000
		W		0.356	0.485	0.453			0.431
24	4	L	0.138	0.138	0.414	0.138	0.172	0.000	2.069
		W	0.343	0.426	0.472	0.503	0.553		0.466
25	1	L	0.667	0.333	0.000	0.000	0.000	0.000	0.333
		W	0.443	0.396					0.428

Table C-9. PLIV-PWV Condensed Catalogs for Ω = 0.5 (continued)

No.	Tornado F/EF	L or W	EF0	EF1	EF2	EF3	EF4	EF5	Mean F/EF and Mean ω for Epistemic Ω = 0.5 (F/EF in L row and ω in W row)
26	3	L	0.143	0.143	0.429	0.286	0.000	0.000	1.857
		W	0.626	0.179	0.298	0.207			0.302
27	2	L	0.250	0.250	0.500	0.000	0.000	0.000	1.250
		W	0.570	0.183	0.211				0.294
28	1	L	0.667	0.333	0.000	0.000	0.000	0.000	0.333
		W	0.342	0.547					0.410
29	2	L	0.000	0.000	1.000	0.000	0.000	0.000	2.000
		W			0.570				0.570
30	1	L	0.500	0.500	0.000	0.000	0.000	0.000	0.500
		W	0.547	0.469					0.508
31	2	L	0.250	0.500	0.250	0.000	0.000	0.000	1.000
		W	0.570	0.428	0.380				0.452
32	2	L	0.250	0.500	0.250	0.000	0.000	0.000	1.000
		W	0.570	0.489	0.570				0.530
33	2	L	0.333	0.333	0.333	0.000	0.000	0.000	1.000
		W	0.570	0.570	0.570				0.570
34	2	L	0.000	0.000	1.000	0.000	0.000	0.000	2.000
		W			0.570				0.570
35	2	L	0.667	0.000	0.333	0.000	0.000	0.000	0.667
		W	0.489		0.570				0.516
36	2	L	0.000	0.000	1.000	0.000	0.000	0.000	2.000
		W			0.570				0.570
37	1	L	0.667	0.333	0.000	0.000	0.000	0.000	0.333
		W	0.456	0.486					0.466
38	3	L	0.000	0.667	0.000	0.333	0.000	0.000	1.667
		W		0.626		0.536			0.596
39	2	L	0.000	0.000	1.000	0.000	0.000	0.000	2.000
		W			0.570				0.570
40	1	L	0.000	1.000	0.000	0.000	0.000	0.000	1.000
		W		0.547					0.547
41	2	L	0.333	0.333	0.333	0.000	0.000	0.000	1.000
		W	0.570	0.570	0.570				0.570
42	3	L	0.000	0.250	0.250	0.500	0.000	0.000	2.250
		W		0.556	0.626	0.556			0.574
43	4	L	0.000	0.250	0.250	0.250	0.250	0.000	2.500
		W		0.385	0.577	0.449	0.641		0.513
44	4	L	0.286	0.143	0.286	0.143	0.143	0.000	1.714
		W	0.630	0.310	0.453	0.442	0.509		0.490
45	1	L	0.750	0.250	0.000	0.000	0.000	0.000	0.250
		W	0.452	0.428					0.446
46	3	L	0.250	0.125	0.250	0.375	0.000	0.000	1.750
		W	0.585	0.517	0.598	0.598			0.585
47	4	L	0.143	0.143	0.286	0.286	0.143	0.000	2.143
		W	0.249	0.303	0.490	0.392	0.445		0.394
48	5	L	0.167	0.000	0.333	0.167	0.167	0.167	2.667
		W	0.582		0.665	0.624	0.624	0.624	0.631
49	2	L	0.500	0.250	0.250	0.000	0.000	0.000	0.750
		W	0.570	0.570	0.570				0.570
50	2	L	0.000	0.667	0.333	0.000	0.000	0.000	1.333
		W		0.570	0.570				0.570

Table C-9. PLIV-PWV Condensed Catalogs for Ω = 0.5 (continued)

No.	Tornado F/EF	L or W	EF0	EF1	EF2	EF3	EF4	EF5	Mean F/EF and Mean ω for Epistemic Ω = 0.5 (F/EF in L row and ω in W row)
51	5	L	0.154	0.077	0.154	0.154	0.385	0.077	2.769
		W	0.390	0.439	0.524	0.573	0.575	0.414	0.516
52	4	L	0.000	0.000	0.250	0.500	0.250	0.000	3.000
		W			0.431	0.542	0.630		0.536
53	4	L	0.286	0.286	0.143	0.000	0.286	0.000	1.714
		W	0.380	0.416	0.546		0.629		0.485
54	5	L	0.200	0.200	0.200	0.200	0.000	0.200	2.200
		W	0.412	0.471	0.707	0.412		0.530	0.506
55	4	L	0.200	0.200	0.200	0.200	0.200	0.000	2.000
		W	0.289	0.321	0.481	0.641	0.641		0.474
56	2	L	0.000	0.000	1.000	0.000	0.000	0.000	2.000
		W			0.507				0.507
57	0	L	1.000	0.000	0.000	0.000	0.000	0.000	0.000
		W	0.515						0.515
58	5	L	0.000	0.250	0.000	0.250	0.250	0.250	3.250
		W		0.418		0.546	0.594	0.707	0.566
59	4	L	0.000	0.200	0.400	0.200	0.200	0.000	2.400
		W		0.641	0.545	0.641	0.641		0.603
60	1	L	0.667	0.333	0.000	0.000	0.000	0.000	0.333
		W	0.355	0.202					0.304
61	0	L	1.000	0.000	0.000	0.000	0.000	0.000	0.000
		W	0.515						0.515
62	3	L	0.200	0.400	0.200	0.200	0.000	0.000	1.400
		W	0.626	0.391	0.411	0.293			0.422
63	4	L	0.600	0.200	0.000	0.000	0.200	0.000	1.000
		W	0.574	0.641			0.641		0.601
64	4	L	0.000	0.222	0.222	0.333	0.222	0.000	2.556
		W		0.502	0.488	0.567	0.627		0.548
65	4	L	0.250	0.125	0.375	0.125	0.125	0.000	1.750
		W	0.396	0.236	0.437	0.217	0.226		0.348
66	3	L	0.000	0.333	0.167	0.500	0.000	0.000	2.167
		W		0.446	0.398	0.518			0.474
67	1	L	0.667	0.333	0.000	0.000	0.000	0.000	0.333
		W	0.393	0.547					0.444
68	2	L	0.000	0.667	0.333	0.000	0.000	0.000	1.333
		W		0.462	0.570				0.498
69	2	L	0.000	0.800	0.200	0.000	0.000	0.000	1.200
		W		0.438	0.531				0.456
70	2	L	0.000	0.500	0.500	0.000	0.000	0.000	1.500
		W		0.570	0.570				0.570
71	0	L	1.000	0.000	0.000	0.000	0.000	0.000	0.000
		W	0.515						0.515
72	3	L	0.143	0.143	0.286	0.429	0.000	0.000	2.000
		W	0.381	0.517	0.530	0.608			0.540
73	4	L	0.000	0.000	0.286	0.286	0.429	0.000	3.143
		W			0.423	0.583	0.602		0.545
74	3	L	0.000	0.400	0.400	0.400	0.000	0.000	2.400
		W		0.313	0.475	0.583			0.548
75	4	L	0.143	0.143	0.000	0.286	0.429	0.000	2.714
		W	0.495	0.379		0.612	0.622		0.566

Table C-9. PLIV-PWV Condensed Catalogs for Ω = 0.5 (continued)

No.	Tornado F/EF	L or W	EF0	EF1	EF2	EF3	EF4	EF5	Mean F/EF and Mean ω for Epistemic Ω = 0.5 (F/EF in L row and ω in W row)
76	1	L	0.000	1.000	0.000	0.000	0.000	0.000	1.000
		W		0.547					0.547
77	3	L	0.167	0.167	0.167	0.500	0.000	0.000	2.000
		W	0.407	0.532	0.626	0.521			0.521
78	2	L	0.000	0.000	1.000	0.000	0.000	0.000	2.000
		W			0.570				0.570
79	3	L	0.000	0.500	0.250	0.250	0.000	0.000	1.750
		W		0.539	0.521	0.626			0.556
80	4	L	0.000	0.286	0.143	0.286	0.286	0.000	2.571
		W		0.475	0.570	0.570	0.546		0.536
81	3	L	0.000	0.000	0.250	0.750	0.000	0.000	2.750
		W			0.209	0.408			0.358
82	1	L	0.000	1.000	0.000	0.000	0.000	0.000	1.000
		W		0.547					0.547
83	3	L	0.000	0.250	0.500	0.250	0.000	0.000	2.000
		W		0.478	0.534	0.478			0.506
84	1	L	0.000	1.000	0.000	0.000	0.000	0.000	1.000
		W		0.547					0.547
85	4	L	0.000	0.000	0.500	0.333	0.167	0.000	2.667
		W			0.349	0.609	0.641		0.484
86	2	L	0.000	0.500	0.500	0.000	0.000	0.000	1.500
		W		0.499	0.570				0.535
87	2	L	0.333	0.333	0.333	0.000	0.000	0.000	1.000
		W	0.570	0.403	0.503				0.492
88	0	L	1.000	0.000	0.000	0.000	0.000	0.000	0.000
		W	0.515						0.515
89	1	L	0.667	0.333	0.000	0.000	0.000	0.000	0.333
		W	0.418	0.547					0.461
90	1	L	0.833	0.167	0.000	0.000	0.000	0.000	0.167
		W	0.474	0.456					0.471
91	3	L	0.000	0.000	0.333	0.667	0.000	0.000	2.667
		W			0.469	0.594			0.553
92	1	L	0.667	0.333	0.000	0.000	0.000	0.000	0.333
		W	0.528	0.547					0.534
93	4	L	0.000	0.200	0.400	0.000	0.400	0.000	2.600
		W		0.310	0.531		0.608		0.517
94	3	L	0.167	0.333	0.167	0.333	0.000	0.000	1.667
		W	0.313	0.404	0.495	0.574			0.461
95	3	L	0.000	0.333	0.333	0.500	0.000	0.000	2.500
		W		0.270	0.427	0.559			0.512
96	3	L	0.000	0.000	0.333	0.667	0.000	0.000	2.667
		W			0.328	0.521			0.457
97	4	L	0.375	0.125	0.125	0.125	0.250	0.000	1.750
		W	0.496	0.410	0.513	0.641	0.551		0.519
98	4	L	0.200	0.000	0.200	0.200	0.400	0.000	2.600
		W	0.446		0.502	0.641	0.558		0.541
99	3	L	0.167	0.167	0.333	0.333	0.000	0.000	1.833
		W	0.626	0.521	0.386	0.355			0.438
100	2	L	0.000	0.500	0.500	0.000	0.000	0.000	1.500
		W		0.570	0.456				0.513

Table C-9. PLIV-PWV Condensed Catalogs for Ω = 0.5 (continued)

No.	Tornado F/EF	L or W	EF0	EF1	EF2	EF3	EF4	EF5	Mean F/EF and Mean ω for Epistemic Ω = 0.5 (F/EF in L row and ω in W row)
101	1	L	0.000	1.000	0.000	0.000	0.000	0.000	1.000
		W		0.547					0.547
102	1	L	0.600	0.400	0.000	0.000	0.000	0.000	0.400
		W	0.511	0.511					0.511
103	1	L	0.667	0.333	0.000	0.000	0.000	0.000	0.333
		W	0.446	0.547					0.480
104	3	L	0.000	0.200	0.400	0.400	0.000	0.000	2.200
		W		0.626	0.417	0.536			0.506
105	3	L	0.000	0.667	0.000	0.333	0.000	0.000	1.667
		W		0.626		0.626			0.626
106	2	L	0.333	0.333	0.333	0.000	0.000	0.000	1.000
		W	0.570	0.273	0.570				0.471
107	5	L	0.000	0.111	0.000	0.333	0.333	0.222	3.556
		W		0.424		0.628	0.542	0.589	0.568
108	4	L	0.143	0.143	0.143	0.286	0.286	0.000	2.429
		W	0.379	0.379	0.466	0.510	0.597		0.491
109	4	L	0.091	0.000	0.091	0.273	0.545	0.000	3.182
		W	0.261		0.404	0.372	0.515		0.443
110	3	L	0.000	0.500	0.250	0.250	0.000	0.000	1.750
		W		0.385	0.578	0.626			0.493
111	3	L	0.250	0.000	0.500	0.250	0.000	0.000	1.750
		W	0.344		0.501	0.626			0.493
112	5	L	0.190	0.095	0.286	0.333	0.000	0.095	2.143
		W	0.353	0.372	0.423	0.464		0.458	0.422
113	3	L	0.333	0.167	0.250	0.250	0.000	0.000	1.417
		W	0.484	0.566	0.596	0.596			0.554
114	4	L	0.105	0.421	0.368	0.053	0.053	0.000	1.526
		W	0.449	0.449	0.539	0.641	0.641		0.502
115	2	L	0.000	0.000	1.000	0.000	0.000	0.000	2.000
		W			0.570				0.570
116	3	L	0.000	0.200	0.600	0.200	0.000	0.000	2.000
		W		0.566	0.497	0.626			0.536
117	0	L	1.000	0.000	0.000	0.000	0.000	0.000	0.000
		W	0.407						0.407
118	2	L	0.500	0.000	0.500	0.000	0.000	0.000	1.000
		W	0.570		0.570				0.570
119	0	L	1.000	0.000	0.000	0.000	0.000	0.000	0.000
		W	0.515						0.515
120	1	L	0.000	1.000	0.000	0.000	0.000	0.000	1.000
		W		0.547					0.547
121	2	L	0.000	0.000	1.000	0.000	0.000	0.000	2.000
		W			0.570				0.570
122	1	L	0.000	1.000	0.000	0.000	0.000	0.000	1.000
		W		0.547					0.547
123	1	L	0.000	1.000	0.000	0.000	0.000	0.000	1.000
		W		0.547					0.547
124	3	L	0.000	0.333	0.000	0.667	0.000	0.000	2.333
		W		0.408		0.598			0.535
125	3	L	0.000	0.000	0.800	0.200	0.000	0.000	2.200
		W			0.428	0.626			0.468

Table C-9. PLIV-PWV Condensed Catalogs for Ω = 0.5 (continued)

No.	Tornado F/EF	L or W	EF0	EF1	EF2	EF3	EF4	EF5	Mean F/EF and Mean ω for Epistemic Ω = 0.5 (F/EF in L row and ω in W row)
126	1	L	0.500	0.500	0.000	0.000	0.000	0.000	0.500
		W	0.547	0.489					0.518
127	0	L	1.000	0.000	0.000	0.000	0.000	0.000	0.000
		W	0.515						0.515
128	2	L	0.000	0.333	0.667	0.000	0.000	0.000	1.667
		W		0.456	0.485				0.475
129	3	L	0.200	0.400	0.200	0.200	0.000	0.000	1.400
		W	0.324	0.301	0.487	0.626			0.408
130	4	L	0.167	0.167	0.333	0.167	0.167	0.000	2.000
		W	0.379	0.641	0.583	0.612	0.612		0.568
131	3	L	0.000	0.250	0.500	0.250	0.000	0.000	2.000
		W		0.358	0.566	0.626			0.529
132	4	L	0.000	0.000	0.000	0.800	0.200	0.000	3.200
		W				0.593	0.641		0.603
133	0	L	1.000	0.000	0.000	0.000	0.000	0.000	0.000
		W	0.515						0.515
134	2	L	0.500	0.250	0.250	0.000	0.000	0.000	0.750
		W	0.480	0.415	0.467				0.460
135	0	L	1.000	0.000	0.000	0.000	0.000	0.000	0.000
		W	0.515						0.515
136	0	L	1.000	0.000	0.000	0.000	0.000	0.000	0.000
		W	0.515						0.515
137	1	L	0.000	1.000	0.000	0.000	0.000	0.000	1.000
		W		0.547					0.547
138	2	L	0.333	0.333	0.333	0.000	0.000	0.000	1.000
		W	0.455	0.469	0.462				0.462
139	4	L	0.000	0.000	0.500	0.250	0.250	0.000	2.750
		W			0.523	0.641	0.641		0.582
140	0	L	1.000	0.000	0.000	0.000	0.000	0.000	0.000
		W	0.515						0.515
141	0	L	1.000	0.000	0.000	0.000	0.000	0.000	0.000
		W	0.515						0.515
142	0	L	1.000	0.000	0.000	0.000	0.000	0.000	0.000
		W	0.515						0.515
143	0	L	1.000	0.000	0.000	0.000	0.000	0.000	0.000
		W	0.515						0.515
144	0	L	1.000	0.000	0.000	0.000	0.000	0.000	0.000
		W	0.515						0.515
145	0	L	1.000	0.000	0.000	0.000	0.000	0.000	0.000
		W	0.515						0.515
146	0	L	1.000	0.000	0.000	0.000	0.000	0.000	0.000
		W	0.307						0.307
147	1	L	0.000	1.000	0.000	0.000	0.000	0.000	1.000
		W		0.547					0.547
148	3	L	0.000	0.375	0.375	0.250	0.000	0.000	1.875
		W		0.399	0.489	0.554			0.471
149	1	L	0.500	0.500	0.000	0.000	0.000	0.000	0.500
		W	0.547	0.547					0.547
150	1	L	0.000	1.000	0.000	0.000	0.000	0.000	1.000
		W		0.547					0.547

Table C-9. PLIV-PWV Condensed Catalogs for Ω = 0.5 (continued)

No.	Tornado F/EF	L or W	EF0	EF1	EF2	EF3	EF4	EF5	Mean F/EF and Mean ω for Epistemic Ω = 0.5 (F/EF in L row and ω in W row)
151	3	L	0.500	0.000	0.000	0.500	0.000	0.000	1.500
		W	0.417			0.626			0.521
152	1	L	0.000	1.000	0.000	0.000	0.000	0.000	1.000
		W		0.547					0.547
153	1	L	0.000	1.000	0.000	0.000	0.000	0.000	1.000
		W		0.547					0.547
154	0	L	1.000	0.000	0.000	0.000	0.000	0.000	0.000
		W	0.515						0.515
155	3	L	0.000	0.000	0.667	0.333	0.000	0.000	2.333
		W			0.435	0.626			0.499
156	1	L	0.750	0.250	0.000	0.000	0.000	0.000	0.250
		W	0.547	0.547					0.547
157	2	L	0.333	0.333	0.333	0.000	0.000	0.000	1.000
		W	0.248	0.570	0.322				0.380
158	1	L	0.000	1.000	0.000	0.000	0.000	0.000	1.000
		W		0.547					0.547
159	2	L	0.500	0.000	0.500	0.000	0.000	0.000	1.000
		W	0.380		0.570				0.475
160	5	L	0.000	0.111	0.407	0.370	0.074	0.037	2.519
		W		0.283	0.424	0.466	0.353	0.353	0.416
161	5	L	0.000	0.000	0.250	0.000	0.250	0.500	4.000
		W			0.661		0.663	0.707	0.684
162	4	L	0.167	0.167	0.167	0.167	0.333	0.000	2.333
		W	0.418	0.455	0.535	0.571	0.641		0.544
163	3	L	0.000	0.333	0.333	0.333	0.000	0.000	2.000
		W		0.537	0.558	0.626			0.574
164	3	L	0.000	0.000	0.500	0.500	0.000	0.000	2.500
		W			0.558	0.626			0.592
165	2	L	0.000	0.333	0.667	0.000	0.000	0.000	1.667
		W		0.502	0.570				0.547
166	3	L	0.000	0.500	0.357	0.143	0.000	0.000	1.643
		W		0.537	0.558	0.626			0.557
167	2	L	0.400	0.400	0.200	0.000	0.000	0.000	0.800
		W	0.509	0.502	0.570				0.518
168	2	L	0.000	0.750	0.250	0.000	0.000	0.000	1.250
		W		0.502	0.570				0.519
169	3	L	0.000	0.600	0.200	0.200	0.000	0.000	1.600
		W		0.537	0.558	0.626			0.559
170	4	L	0.167	0.500	0.167	0.083	0.083	0.000	1.417
		W	0.173	0.321	0.537	0.225	0.641		0.351
171	1	L	0.667	0.333	0.000	0.000	0.000	0.000	0.333
		W	0.368	0.462					0.399
172	4	L	0.235	0.324	0.235	0.059	0.147	0.000	1.559
		W	0.223	0.259	0.365	0.232	0.492		0.308
173	3	L	0.412	0.412	0.118	0.059	0.000	0.000	0.824
		W	0.435	0.381	0.417	0.236			0.399
174	5	L	0.000	0.000	0.600	0.000	0.000	0.400	3.200
		W			0.661			0.707	0.679
175	5	L	0.074	0.185	0.296	0.259	0.111	0.074	2.370
		W	0.206	0.188	0.361	0.395	0.353	0.324	0.323

Table C-9. PLIV-PWV Condensed Catalogs for Ω = 0.5 (continued)

No.	Tornado F/EF	L or W	EF0	EF1	EF2	EF3	EF4	EF5	Mean F/EF and Mean ω for Epistemic Ω = 0.5 (F/EF in L row and ω in W row)
176	3	L	0.222	0.222	0.444	0.111	0.000	0.000	1.444
		W	0.375	0.375	0.313	0.250			0.334
177	2	L	0.429	0.429	0.143	0.000	0.000	0.000	0.714
		W	0.263	0.420	0.541				0.370
178	5	L	0.000	0.125	0.083	0.292	0.417	0.083	3.250
		W		0.169	0.153	0.454	0.343	0.394	0.342
179	5	L	0.000	0.083	0.111	0.278	0.389	0.139	3.389
		W		0.325	0.462	0.344	0.434	0.532	0.417
180	5	L	0.000	0.375	0.250	0.083	0.125	0.167	2.458
		W		0.424	0.509	0.583	0.623	0.652	0.521
181	3	L	0.071	0.214	0.500	0.214	0.000	0.000	1.857
		W	0.191	0.267	0.487	0.490			0.419
Means		L	0.495	0.398	0.378	0.292	0.236	0.190	1.442
		W	0.445	0.456	0.499	0.528	0.557	0.531	0.500

Appendix D. Tornado Wind Field and Swath Modeling

D.1. Translation Speed

Table D-1 provides the figure index for the regional models for tornado translation speed.

Table D-1. Regional Tornado Path Variables

Variable	Region	Page
Translation Speed	1	D-2
Translation Speed	2	D-3
Translation Speed	3	D-4
Translation Speed	4	D-5
Translation Speed	5	D-6
Translation Speed	6	D-7

Note: In the following figures, “Utran” is the translation speed in mph (1 mph = 0.44704 m/s). Path length is given in miles (1 mi = 1.609344 km).

Region 1

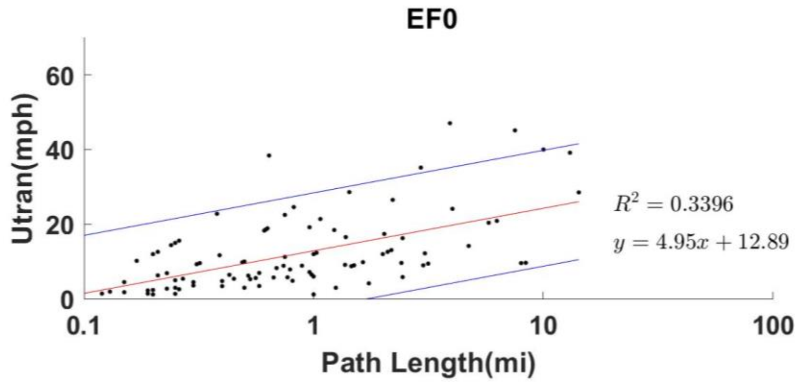
EF0
60
40
20
0
Utran(mph)
0.1
1
10
100
Path Length(mi)
$R^2 = 0.3396$
$y = 4.95x + 12.89$

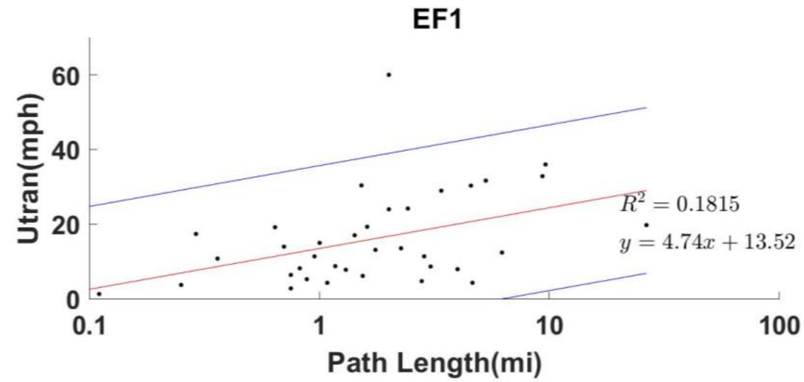
EF1
60
40
20
0
Utran(mph)
0.1
1
10
100
Path Length(mi)
$R^2 = 0.1815$
$y = 4.74x + 13.52$

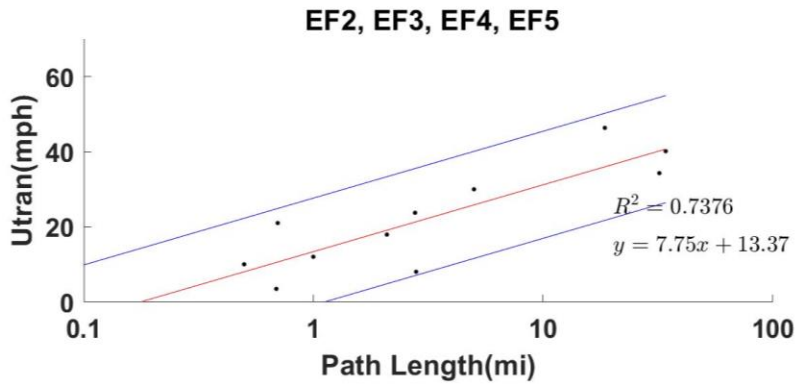
EF2, EF3, EF4, EF5
60
40
20
0
Utran(mph)
0.1
1
10
100
Path Length(mi)
$R^2 = 0.7376$
$y = 7.75x + 13.37$

Region 2

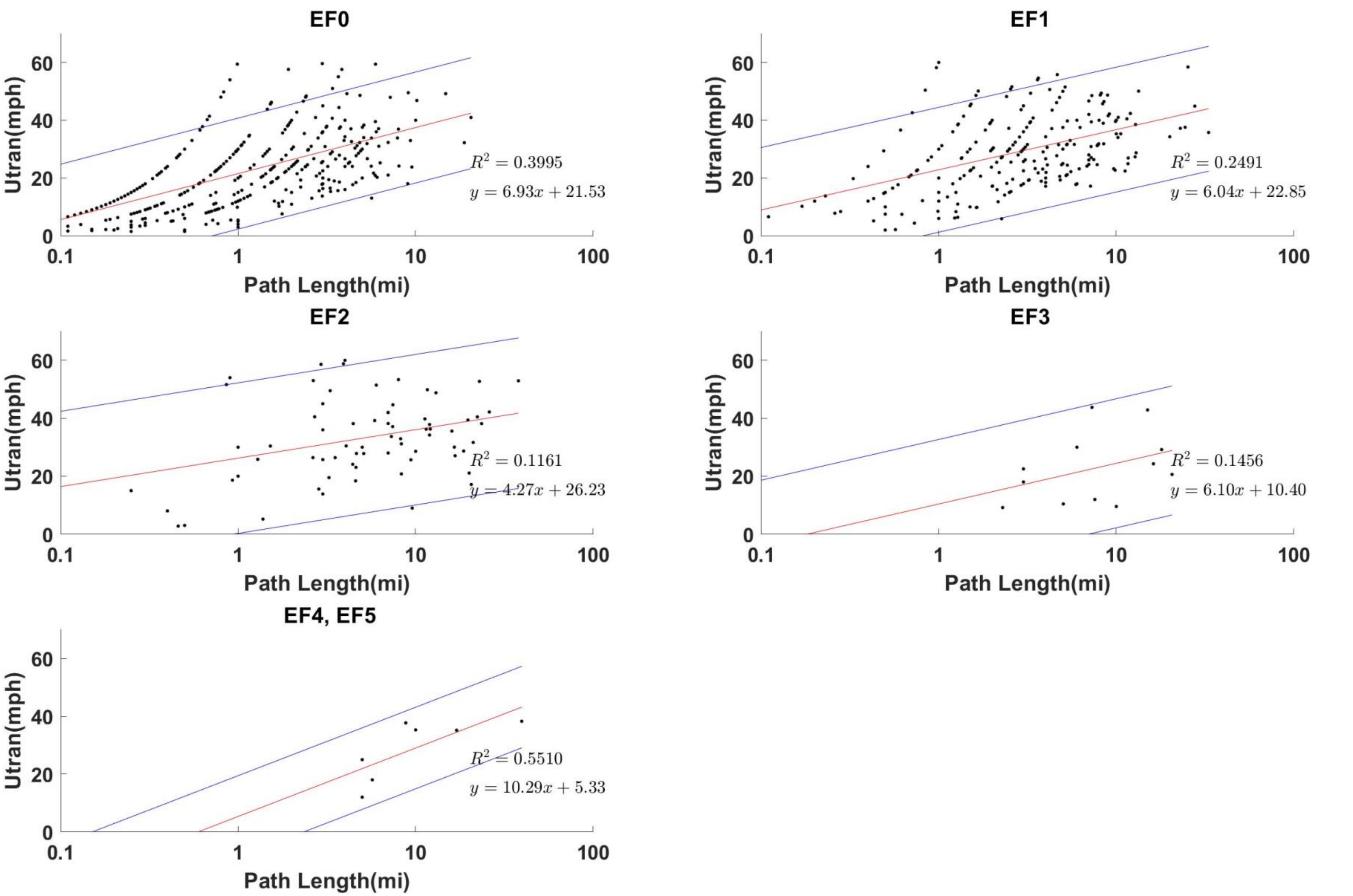
EF0
Utran(mph)
Path Length(mi)
$R^2 = 0.3995$
$y = 6.93x + 21.53$
EF1
Utran(mph)
Path Length(mi)
$R^2 = 0.2491$
$y = 6.04x + 22.85$
EF2
Utran(mph)
Path Length(mi)
$R^2 = 0.1161$
$y = 4.27x + 26.23$
EF3
Utran(mph)
Path Length(mi)
$R^2 = 0.1456$
$y = 6.10x + 10.40$
EF4, EF5
Utran(mph)
Path Length(mi)
$R^2 = 0.5510$
$y = 10.29x + 5.33$

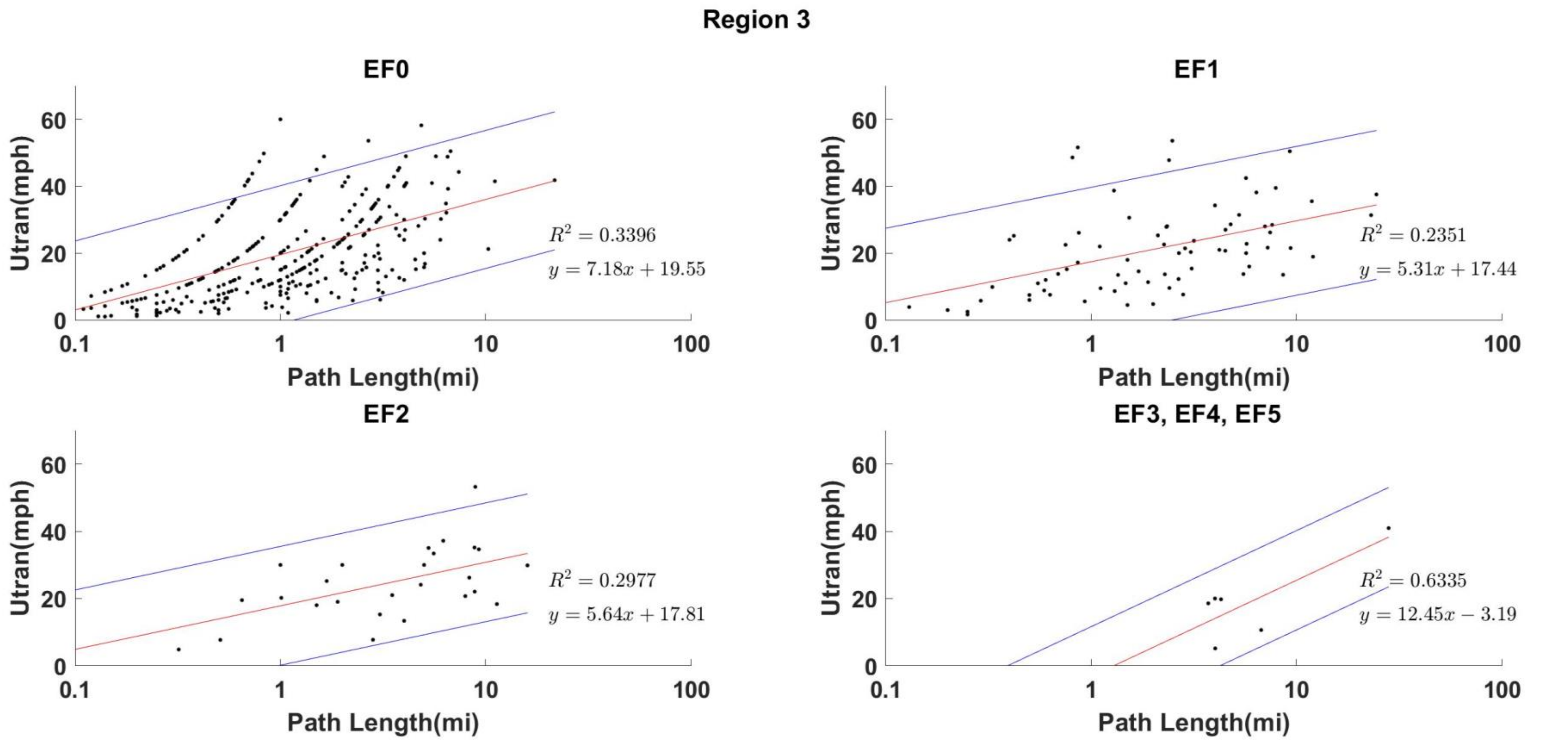
Region 3
EF0
$R^2 = 0.3396$
$y = 7.18x + 19.55$
EF1
$R^2 = 0.2351$
$y = 5.31x + 17.44$
EF2
$R^2 = 0.2977$
$y = 5.64x + 17.81$
EF3, EF4, EF5
$R^2 = 0.6335$
$y = 12.45x - 3.19$
Utran(mph)
Path Length(mi)
0
20
40
60
0.1
1
10
100

Region 4

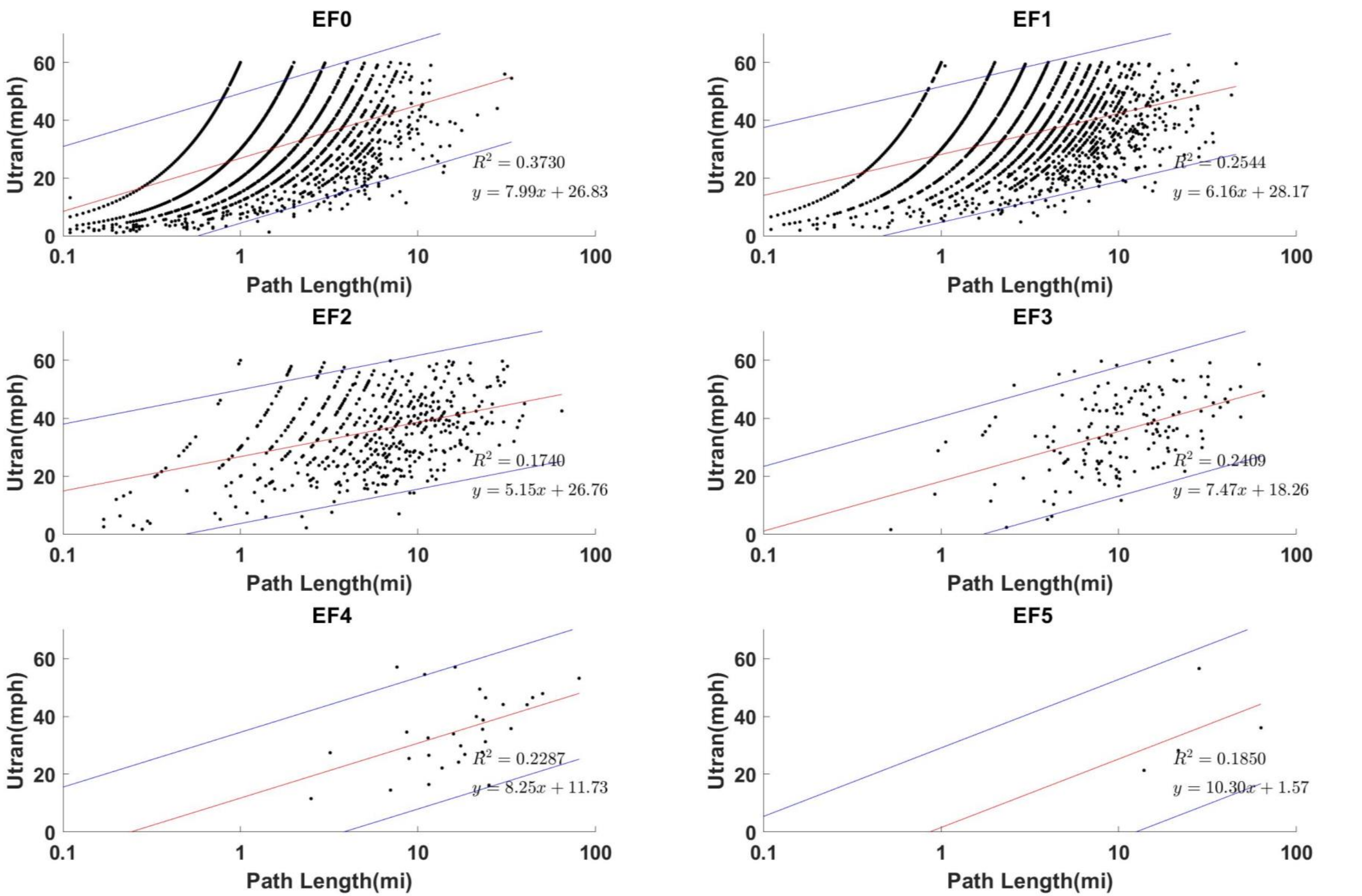
EF0
Utran(mph)
Path Length(mi)
$R^2 = 0.3730$
$y = 7.99x + 26.83$
EF1
Utran(mph)
Path Length(mi)
$R^2 = 0.2544$
$y = 6.16x + 28.17$
EF2
Utran(mph)
Path Length(mi)
$R^2 = 0.1740$
$y = 5.15x + 26.76$
EF3
Utran(mph)
Path Length(mi)
$R^2 = 0.2409$
$y = 7.47x + 18.26$
EF4
Utran(mph)
Path Length(mi)
$R^2 = 0.2287$
$y = 8.25x + 11.73$
EF5
Utran(mph)
Path Length(mi)
$R^2 = 0.1850$
$y = 10.30x + 1.57$

Region 5

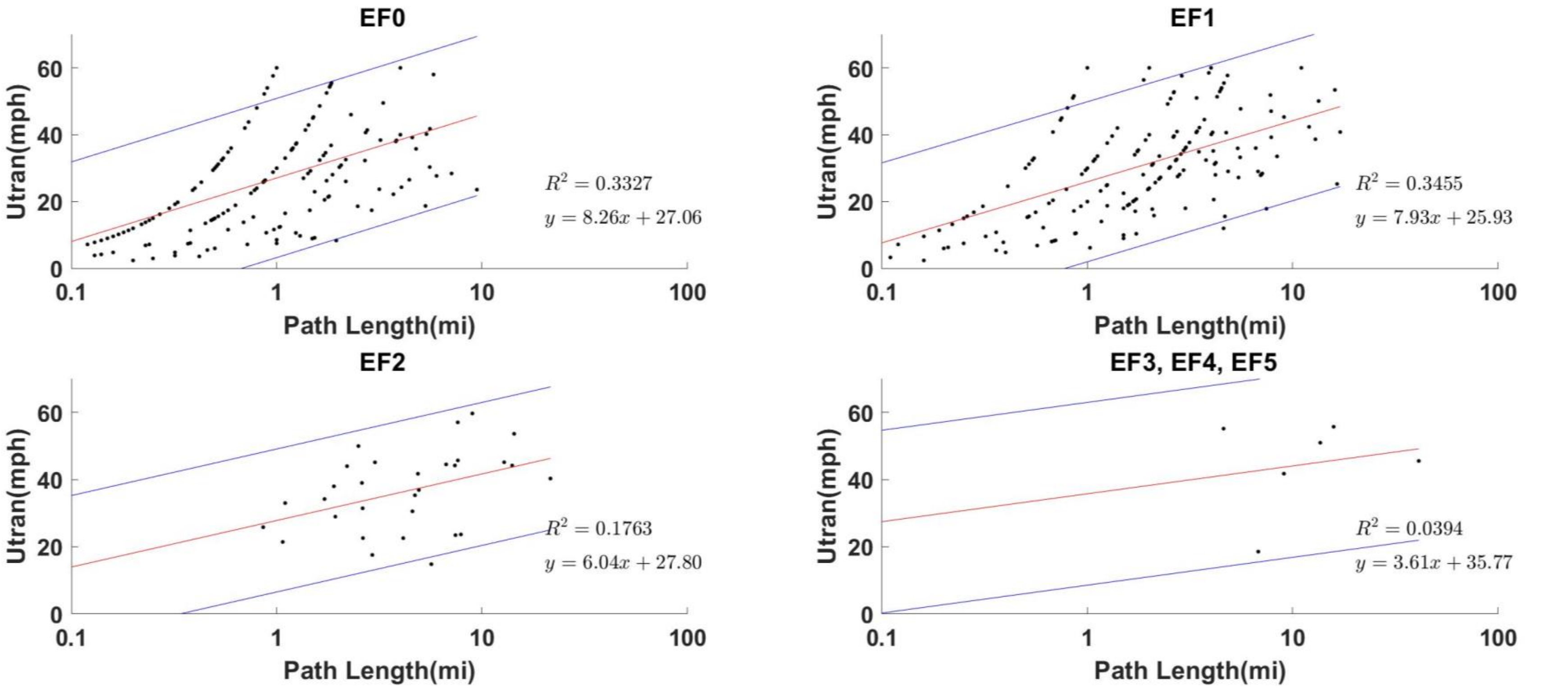

EF0
Utran(mph)
Path Length(mi)
$R^2 = 0.3327$
$y = 8.26x + 27.06$
EF1
Utran(mph)
Path Length(mi)
$R^2 = 0.3455$
$y = 7.93x + 25.93$
EF2
Utran(mph)
Path Length(mi)
$R^2 = 0.1763$
$y = 6.04x + 27.80$
EF3, EF4, EF5
Utran(mph)
Path Length(mi)
$R^2 = 0.0394$
$y = 3.61x + 35.77$

Region 6

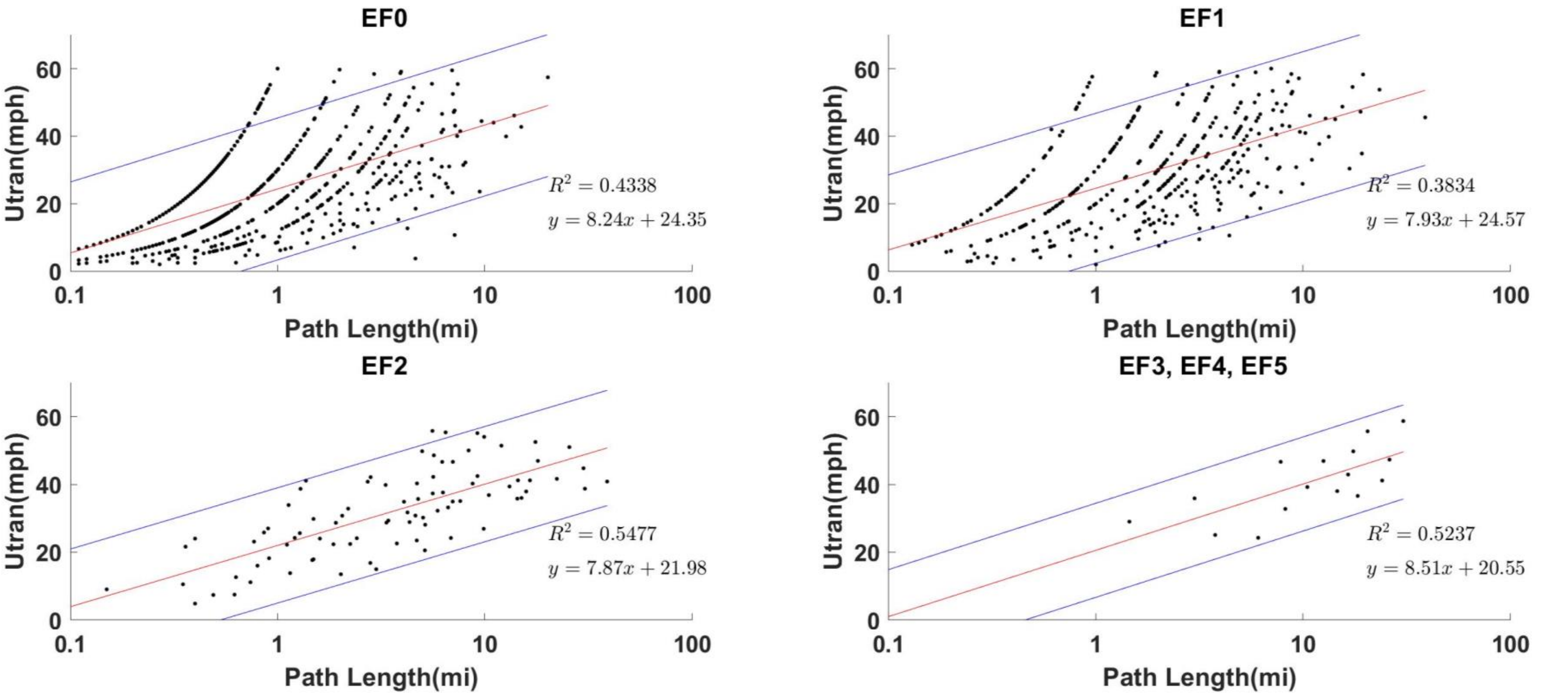
EF0
Utran(mph)
Path Length(mi)
$R^2 = 0.4338$
$y = 8.24x + 24.35$
EF1
Utran(mph)
Path Length(mi)
$R^2 = 0.3834$
$y = 7.93x + 24.57$
EF2
Utran(mph)
Path Length(mi)
$R^2 = 0.5477$
$y = 7.87x + 21.98$
EF3, EF4, EF5
Utran(mph)
Path Length(mi)
$R^2 = 0.5237$
$y = 8.51x + 20.55$

D.2. Path Width Wind Speed Fitting Algorithm

Background. In the synthesized wind field model, the decay of the horizontal wind speed components outside the radius to maximum winds (RMW) is dependent on two parameters namely a and B. These parameters are referred to as path width fitting parameters (Dunn and Twisdale, 1979). The decay function outside the RMW has the following form

$$m(r) = ar + B; \;\; r > RMW \tag{D-1}$$

where $m(r)$ is the decay function at a radius r from the center of a tornado. For values of a that are less than or equal to zero, the decay will approach to zero at a finite distance from the vortex center. For values of a that are greater than zero the decay will be asymptotic. Generally, smaller values of a result steeper decay outside the core. Dunn and Twisdale (1979) established a relationship between a and B by utilizing a function (that controls the magnitude of wind speed components inside RMW) from Kuo's (1970) work. Details of this function and determination of relationship between a and B are given in Dunn and Twisdale (1979). The relationship is shown in the following equation.

$$B = (0.7153 - a) * RMW \tag{D-2}$$

In any given simulation, TORRISK samples path width (PW), maximum wind speed (U_{max}), RMW, translation speed (U_T) and path edge wind speed (V_b) for each EF-Scale. The radial inflow parameter (γ) is based on an RMW-dependent swirl model. After the sampled values are obtained, the following checks are performed before using the path width fitting routine:

1. U_{max}-V_b should be greater than or equal to 20 mph (8.9 m/s). This check is placed to ensure that sampled maximum wind speed is higher than path edge wind speed. If U_{max}-V_b is less than 20 mph (8.9 m/s), then V_b is adjusted such that the difference is 20 mph (8.9 m/s).
2. V_b-U_T should be greater than or equal to 20 mph (8.9 m/s) to ensure a minimum rotational wind speed (at RMW) needed to observe a tornadic damage at the path boundaries.[4] Any rotational wind speed less than the minimum may results wind damage that is indistinguishable from the straight-line wind damage. If V_b-U_T is less than 20 mph (8.9 m/s), then U_T is adjusted such that the difference is equal to 20 mph (8.9 m/s).

Implementation. A non-fibonacci search plan (Hill and Goldstein, 1981) is followed to find the path width fitting parameters. The main goal of this search technique is to reduce the interval of the chosen parameter at subsequent iterations to maximize or minimize the outcome. Figure D-1 describes the steps for the path width fitting of the tornado wind field using this search technique.

[4] The value of 20 mph (8.9 m/s) was assumed as a reasonable minimal observable rotation wind speed for weak tornadoes. Considering the vector sum of U_T, the observable minimal rotational difference across the path width would then typically be 20 mph ± $2U_T$ (8.9 m/s ± $2U_T$ [in m/s]).

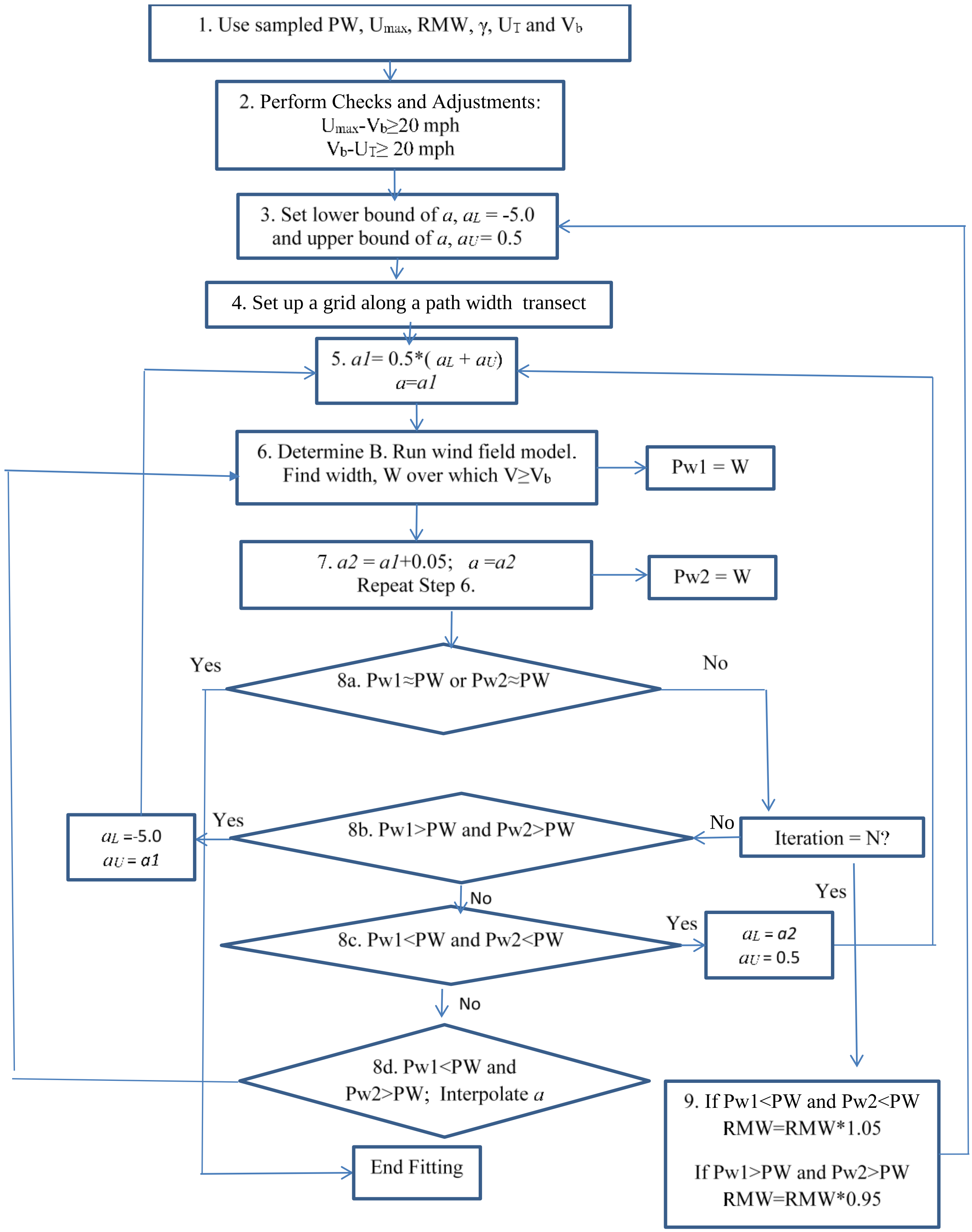

Figure Error! No text of specified style in document.**-8. Flowchart of the Search Procedure**

The steps shown in Figure D-1 are described below:

1. The fitting routine uses the sampled values of PW, U_{max}, RMW, γ, U_T and V_b.
2. We perform the checks on V_b and U_T according to Checks 1 and 2, described previously.
3. The lower and upper bounds of the fitting parameter *a* are set to -5.0 and 0.5 respectively.
4. Across a tornado path width transect, a series of points are placed. The spacing of these points is equal to RMW/20. From the vortex center, the points will cover a distance equals to 6 times of RMW on either side.
5. The initial value of *a* (i.e. *a1*) is the average of lower and upper bounds of *a*.
6. The value of the fitting parameter *B* is determined from the relationship of *a* and *B*. The maximum wind speed that each point experienced during the passage of the storm is determined using the latest values of *a* and *B* and the wind field that uses the sampled values of RMW, *γ*, U_{max} , U_T and V_b. The value of U_T and V_b may be adjusted by Check 1 or Check 2. Then the width over which the maximum wind speeds exceeds V_b is determined. This width is referred to as Pw1.
7. Step 6 is repeated for a value of *a* which is obtained by adding 0.05 to *a1*. This *a* is referred to as *a2*. The obtained width is referred to as Pw2.
8. The widths Pw1 and Pw2 obtained in steps 6 and 7 respectively are compared. Based on the comparison, one of the following steps is implemented.
    a. If the value of either Pw1 or Pw2 is very close to PW, then the search procedure is terminated and the values of *a* and *B* corresponding to that width are used to fit the wind field.
    b. If both Pw1 and Pw2 are greater than PW, then *a1* becomes the upper bound of *a* and the lower bound of *a* (i.e., -5.0) remains the same. The steps are then repeated from Step 5.
    c. If both Pw1 and Pw2 are less than PW, then *a2* becomes the lower bound of *a* and the upper bound of *a* (i.e., 0.5) remains the same. The steps are then repeated from Step 5.
    d. If Pw1 is less than PW and Pw2 greater than PW, then the value of *a* is linearly interpolated using the values of *a1*, *a2*, Pw1, Pw2 and PW. The steps are then repeated from Step 4.
9. If the fitting is not achieved even after sufficient number of iterations of *a*, the value of RMW is modified slightly. If both Pw1 and Pw2 are less than PW, then RMW is increased by 5% otherwise it will be decreased by 5%. The process from Step 3 is repeated for the new RMW value. If this RMW value is not enough to produce a fit, then RMW is re-sampled.

Example. Figure D-2 and Figure D-3 show the wind speed variation across the tornado path for a fixed transect. The wind speed variation is shown for different positions of the tornado center (as a function of RMW) with respect to the transect, where negative is before the storm center reaches the transect. The tornado is translating into the paper such that positive distances (x-axis) are on the right-hand-side of the storm. The dashed green line denotes the maximum wind speed in the storm and the dashed blue line denotes the path boundary wind speed. The two solid red lines show the tornado path.

In Figure D-2, wind speeds plots show that the wind speeds are either lower or equal to V_b at the path boundaries at different position of the tornado center with respect to the transect. Due to the vectorial combination of the horizontal wind speed components (i.e., tangential, radial, and translation speeds), the maximum wind speed is achieved at the transect when the tornado center is about 0.6 RMW past the transect. At this position, the translational speed and rotational velocity vectors add. The maximum wind speed in any of the plots never go beyond the dashed green line, which is U_{max}.

In Figure D-3, the tornado is relatively small (RMW=70 ft (21 m)) compared to that (RMW=250 ft (76 m)) used to create Figure D-2. The path boundary wind speeds in each plot are approximately equal to or lower than V_b. The maximum wind speed is achieved when the tornado center is about 0.1 RMW past the path width transect.

RMW = 250 ft (76 m); PW=1000 ft (300 m); U_{max}=200 mph (89 m/s); U_T=62 mph (27.7 m/s); V_b=82 mph (36.7 m/s);
Tornado Translation = Into the Paper

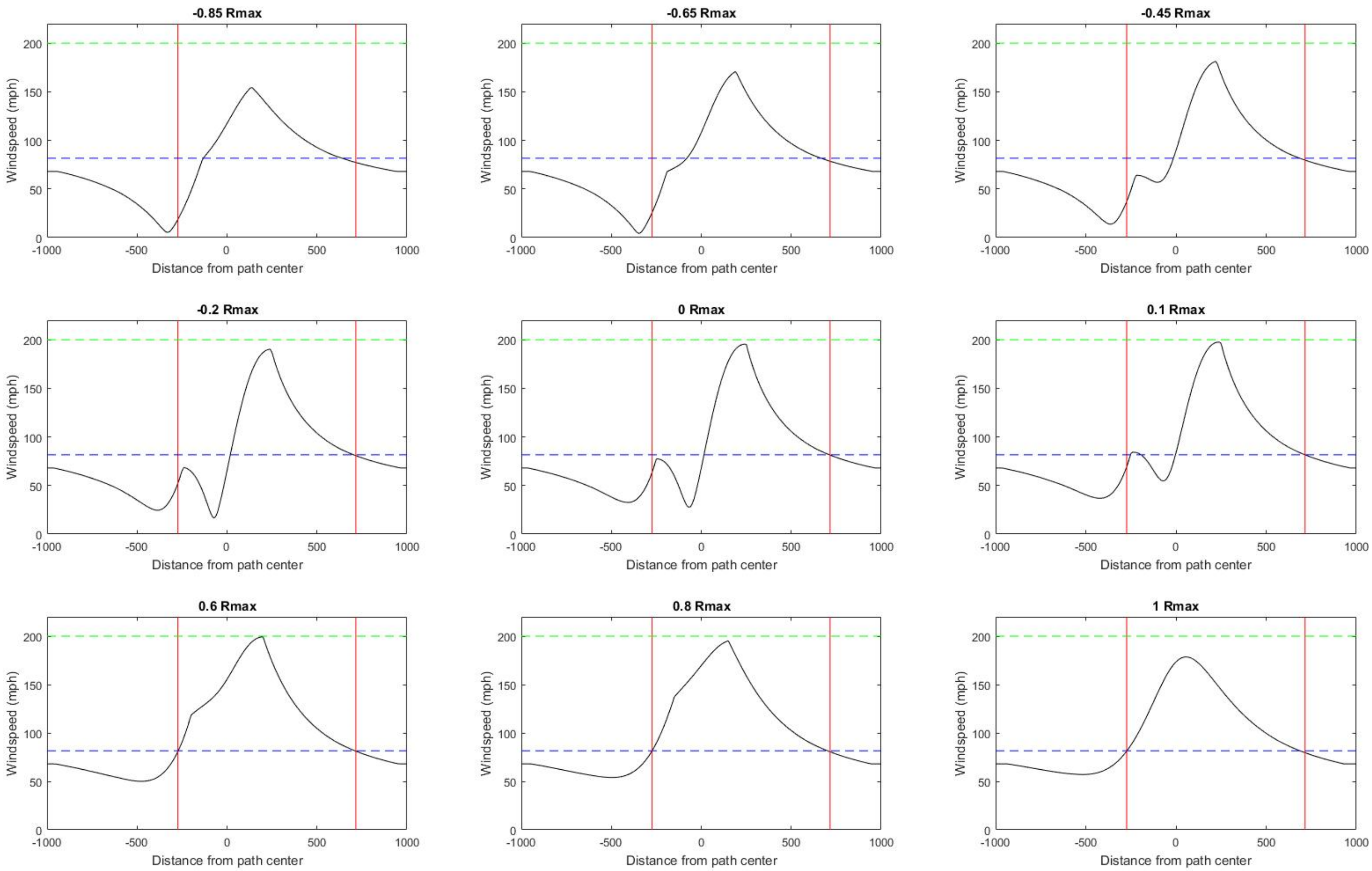

Figure Error! No text of specified style in document.**-9. Example 1 of Wind Field Fitting Results**

RMW =70 ft (21 m); PW=280 ft (85 m); U_{max}=170 mph (76 m/s); U_T=48 mph (21.5 m/s); V_b=68 mph (30.4 m/s);
Tornado Translation = Into the Paper

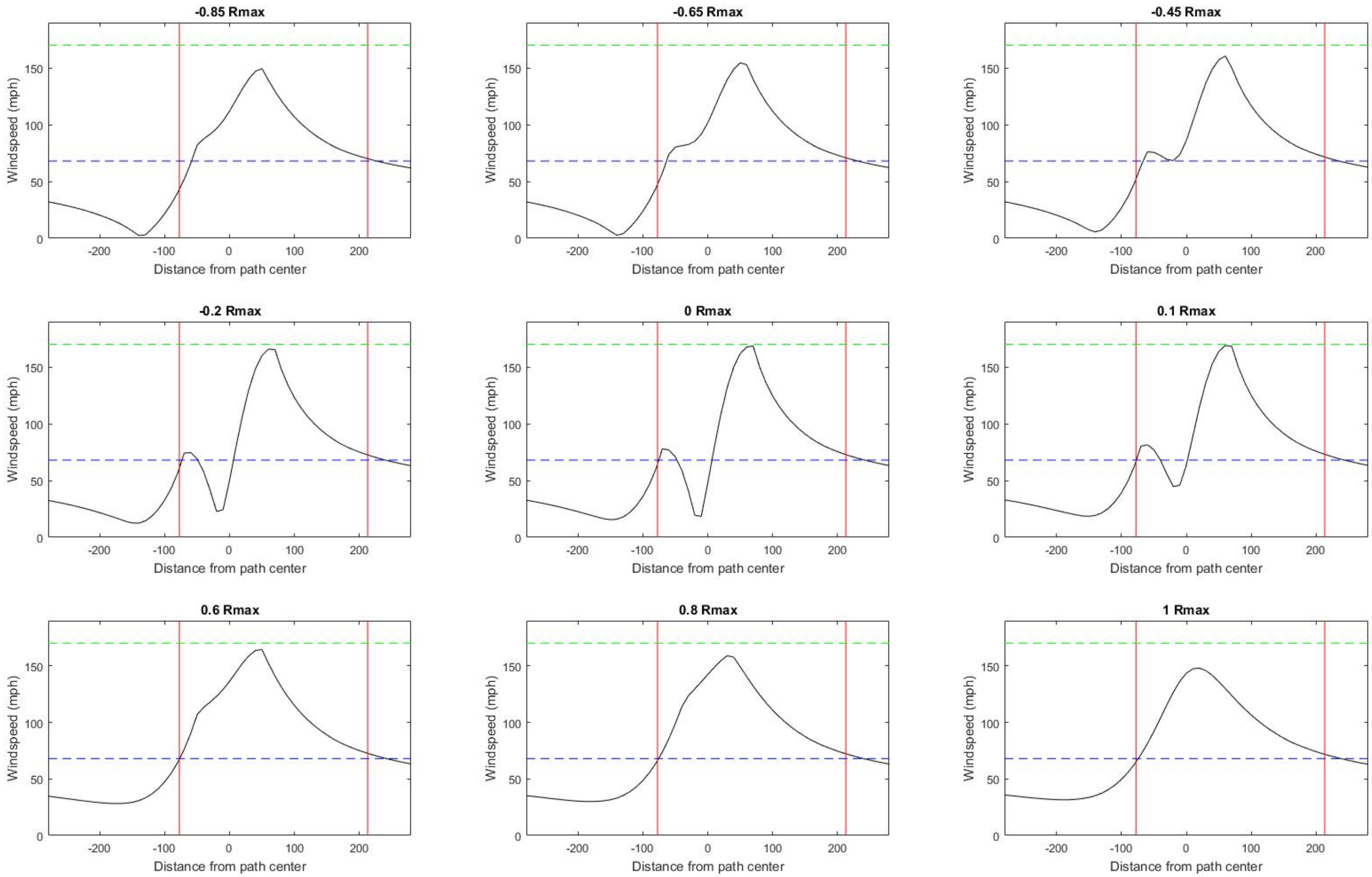

Figure Error! No text of specified style in document.**-10. Example 2 of Wind Field Fitting Results**

Appendix E. Summaries of Tornado Damage Surveys

ARA conducted tornado damage surveys as part of this project and with support from ARA IR&D funding. We had significant help from the NWS in coordinating locations and damage access through NWS field teams.[5] We gained useful information on the NWS survey process and collected detailed data on multiple structures to support our modeling and building stock estimation. The list of events includes:

1. Luther, OK tornado in 2016
2. Illinois tornadoes in 2016
3. Perryville, MO tornado in 2017
4. Galatia and St. James, IL tornadoes in 2018
5. Greensboro, NC tornado in 2018

The following brief descriptions include some of key points in the observed damage. ARA has retained all the survey forms and detailed building-by-building data.

E.1. Luther, OK Tornado

ARA deployed to Oklahoma in coordination with the NWS in anticipation of potentially significant tornado activity on April 26, 2016. We located an EF1 tornado in Luther, OK and surveyed the damage in the northern-most portion of the tornado track. However, the survey was limited to: one community church, 1 mobile home, and 3 one-story houses. Figure **Error! No text of specified style in document.**-1 gives an overview of the NWS damage path and shows where the ARA survey took place.

[5]Our work would not been possible without the help and support of Jim Ladue of the NWS Warning Decision Training Division, Norman, OK.

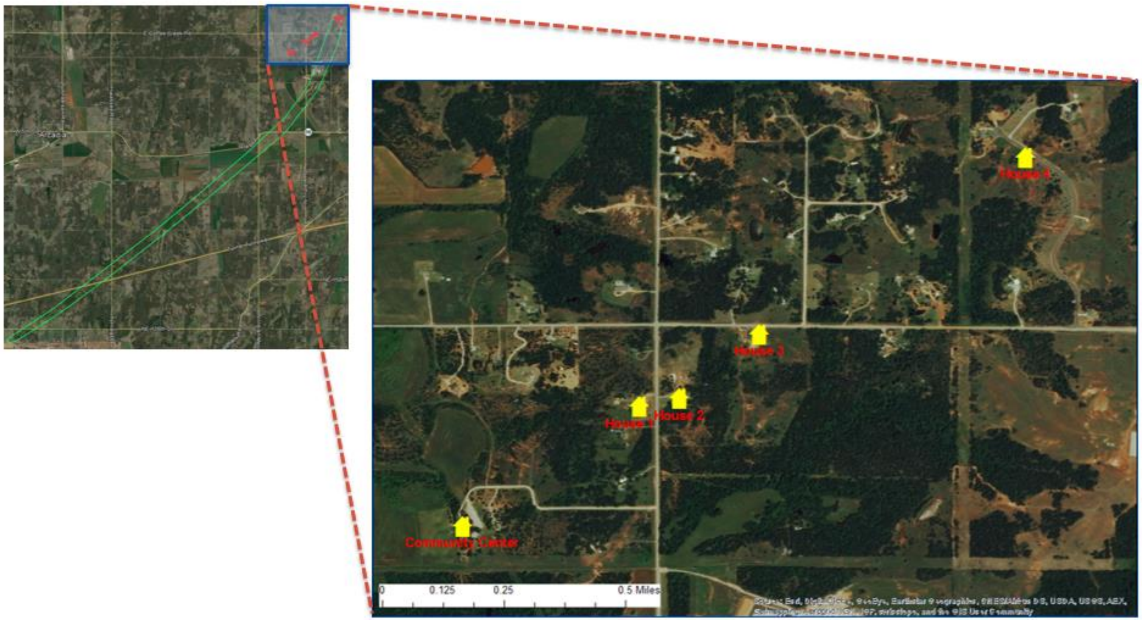

Figure Error! No text of specified style in document.**-1. NWS Damage Path for Luther, OK tornado (1 mi = 1.609344 km)**

The damaged community center was a one and a half stories wood frame building with a metal roof deck. The wall had metal sidings. Portion of the roof structure was failed due to failure of a large overhang structure (18 ft x 36 ft) (5.5 m x 11.0 m) that were attached to the roof and supported by two columns. Connections at column bases were failed due to uplift load. Figure **Error! No text of specified style in document.**-2 shows the damaged portion of the structure.

Figure Error! No text of specified style in document.**-2. Damaged Community Center**

The most damaged house was located on Panther Run Road. Figure **Error! No text of specified style in document.**-3 shows the summary of the survey of this house and pictures of the damaged structure and wind-borne debris.

Figure Error! No text of specified style in document.**-3. Damaged House on Panther Run Road**

The other structures surveyed by ARA had only minor damage such as loss of roof cover or broken windows by wind-borne debris. This tornado was rated an EF1. We used the Panther Run house characteristics and debris translation data in the general calibration of our WBD model for tornadoes.

E.2. Illinois Tornadoes

On June 22, 2016, a tornado event occurred southwest of Chicago, near Seneca, IL. The purpose of this ARA survey was to accompany a NWS team to gain experience in their process for locating areas of maximum damage and path length and width estimation.

An ARA employee followed the Chicago Office NWS team on their damage survey of the area. Three tornado tracks were surveyed, and the tornado tracks that were entered into the DAT by NWS are shown in Figure **Error! No text of specified style in document.**-4.

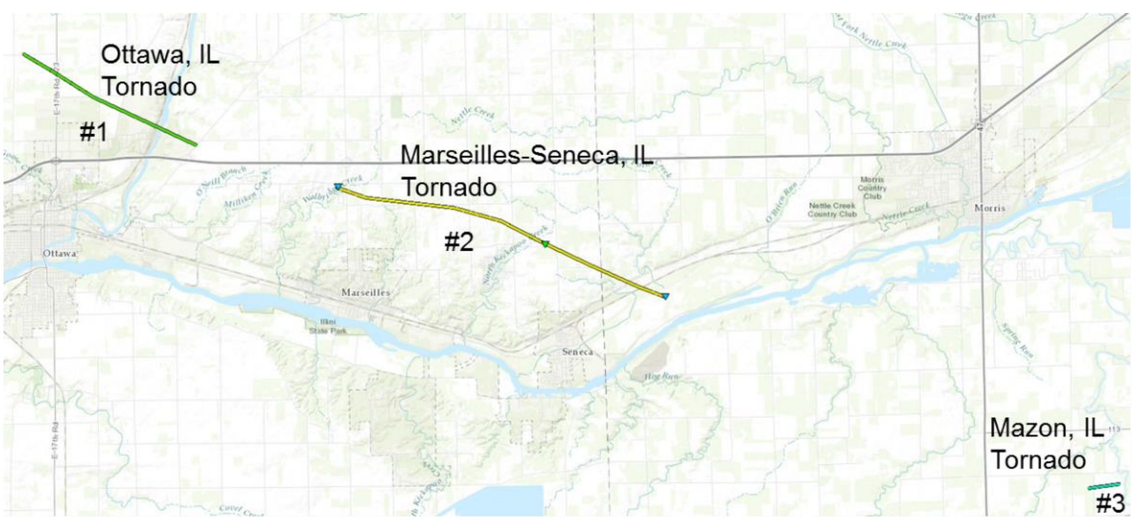

Figure Error! No text of specified style in document.**-4. Three Illinois Tornado Tracks on June 22, 2016 from the NWS DAT**

NWS rating details for the 3 tornado paths are summarized in Table E-1.

Table E-1. **NWS Rating Details for 3 Surveyed Tornadoes**

Variable	Ottawa, IL	Marseilles-Seneca, IL	Mazon, IL
Date	42543	42543	42543
Time	8:48-8:53 PM (CDT)	8:53-9:15 PM (CDT)	9:29-9:36 PM (CDT)
EF-Rating	EF1	EF2	EF0
Est. Peak Winds (mph)	90	116	85
Path Length (mi)	4.5	8.1	1
Path Width (yds)	100	300	100

Note: 1 mph = 1.609344 km/hr; 1 mi = 1.609344 km; 1 yd = 0.9144 m

The most damage occurred in Marseilles-Seneca, IL. Some of the damage consisted of collapsed barn walls, loss of single-family house siding, loss of roof deck, tree damage, and damage to farm silos. Damage photos for the 2 locations (shown in Figure **Error! No text of specified style in document.**-5) with the worst damage are shown in Figure **Error! No text of specified style in document.**-6 and Figure **Error! No text of specified style in document.**-7.

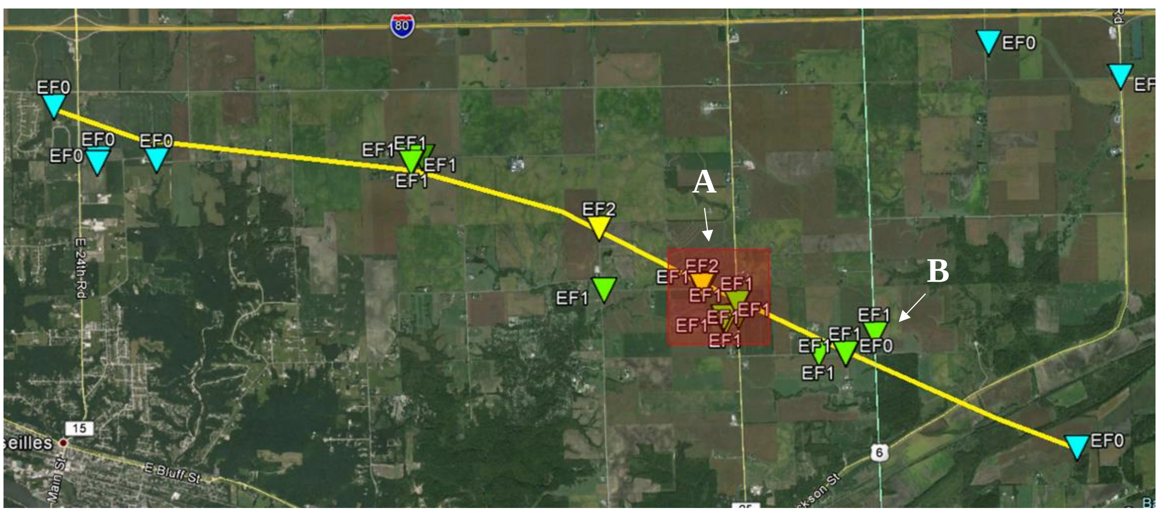

Figure Error! No text of specified style in document.**-5. Damage Track for the Marseilles-Seneca Tornado**

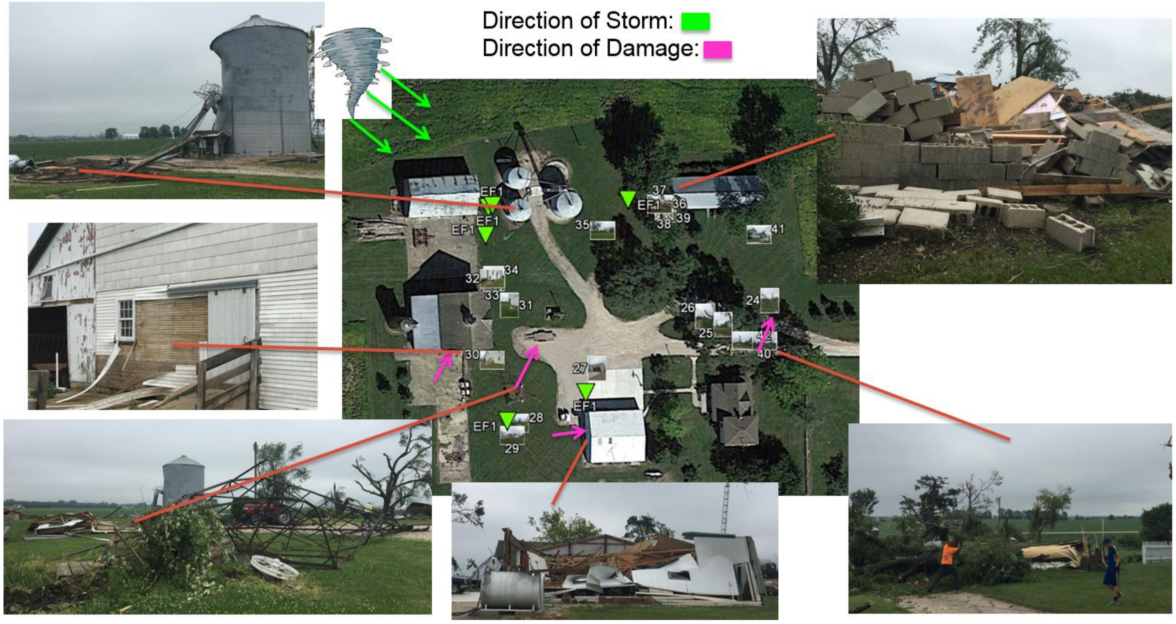

Figure Error! No text of specified style in document.**-6. Damage Area A Photos**

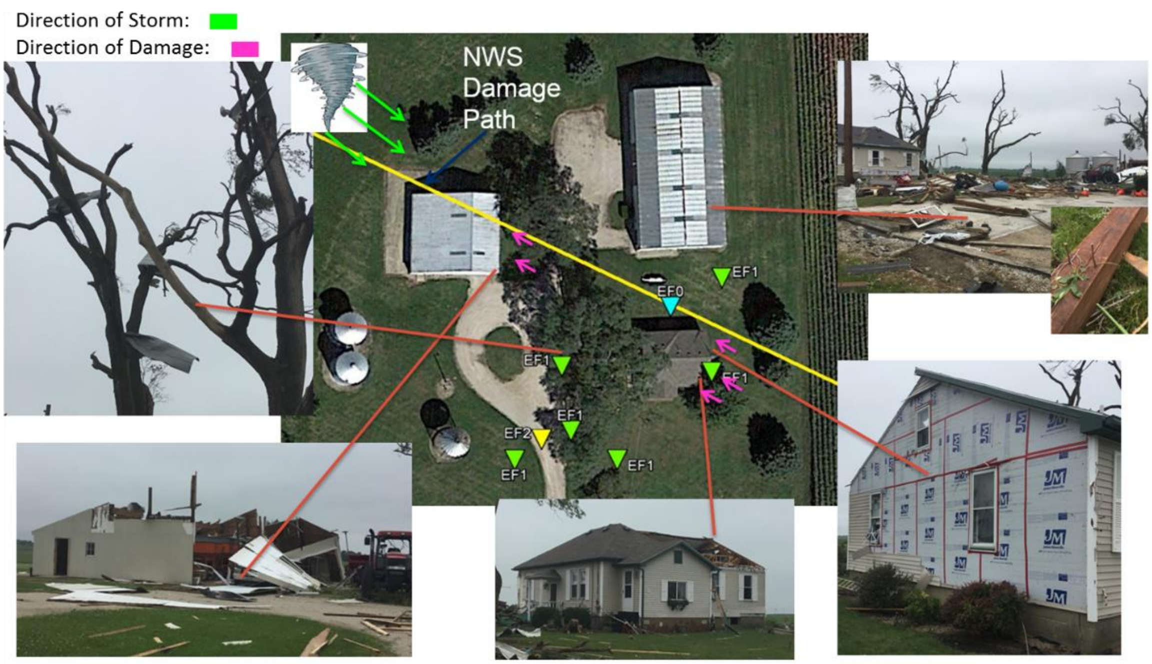

Figure Error! No text of specified style in document.**-7. Damage Area B Photos**

This survey was focused on gathering insights on the NWS tornado damage survey process. NWS used two methods to locate tornado damage and determine the tornado's path. The first method was working with the local emergency management officials, who shared reports of damage and provided access to areas with closed roads due to the damage. The second method to locate areas of damage was to drive to the area where they had a tornado radar signature. If damage was observed in the area, then the team would travel further in all directions around the damage to determine the extent of damage.

The determination of path width was very difficult in this survey because the tornadoes touched down in a rural area with few damage indicators and sparse roads. Although we observed significant corn damage in the area, it was not included in the path width determination. Without an aerial survey, it was too difficult to determine if the corn damage was from a tornado or straight-line winds. This survey highlighted the time required and difficulty in getting accurate tornado path maximum path widths in rural areas.

E.3. Perryville, MO Tornado

On February 28th, 2017, an EF4 tornado touched down about 3.5 miles (5.6 km) northwest of Perryville, MO. A team of 5 ARA employees conducted a survey of the tornado. One of the members followed NWS on their survey, while the other 4 ARA employees conducted detailed surveys of damaged structures. Details from the NWS rating of the tornado are given in Table E-2.

Table E-2. NWS Rating Details for the Perryville, MO Tornado

Variable	Perryville, MO Tornado
Date	42794
Time	7:55-8:57 PM (CST)
EF-Rating	EF4
Est. Peak Winds (mph)	180
Path Length (mi)	50.4
Path Width (yds)	1056

Note: 1 mph = 1.609344 km/hr; 1 mi = 1.609344 km; 1 yd = 0.9144 m

ARA followed NWS for their survey for approximately 25 miles (40.2 km) of the path. Due to time constraints, NWS conducted varying detail level surveys of structures. As much as they could, particularly in the highest damage areas, NWS conducted very detailed surveys of structures. In other cases, some structures were surveyed using a drive-by method. The quick surveys were felt by NWS to be unavoidable due to time constraints with long tornado paths and rapid damage clean-up. NWS went through great lengths to get the most accurate path width and path length measurements as possible, driving from sunrise to sunset and even going into highly forested areas that were difficult to access. A summary of the structures rated by NWS is provided in Table E-2.

Table E-3. Summary of NWS Damage Ratings

NWS DAT Data Summary						
DI	EF0	EF1	EF2	EF3	EF4	All
Barns	0	7	10	0	0	17
Houses	4	8	7	4	8	31
MHDW	0	0	2	0	0	2
ETL	0	1	2	0	0	3
FSP	0	1	0	0	0	1
TH	9	20	12	1	0	42
Other	0	1	2	0	0	3
All	13	38	35	5	8	99

Figure **Error! No text of specified style in document.**-8 gives an overview of the sections of the tornado path that were surveyed. Outlined in blue, is the portion of the NWS survey that ARA surveyed. Outlined in pink are the transects of the damage path that ARA conducted detailed surveys on. Figure **Error! No text of specified style in document.**-9 through Figure **Error! No text of specified style in document.**-12 show aerial views of the transects.

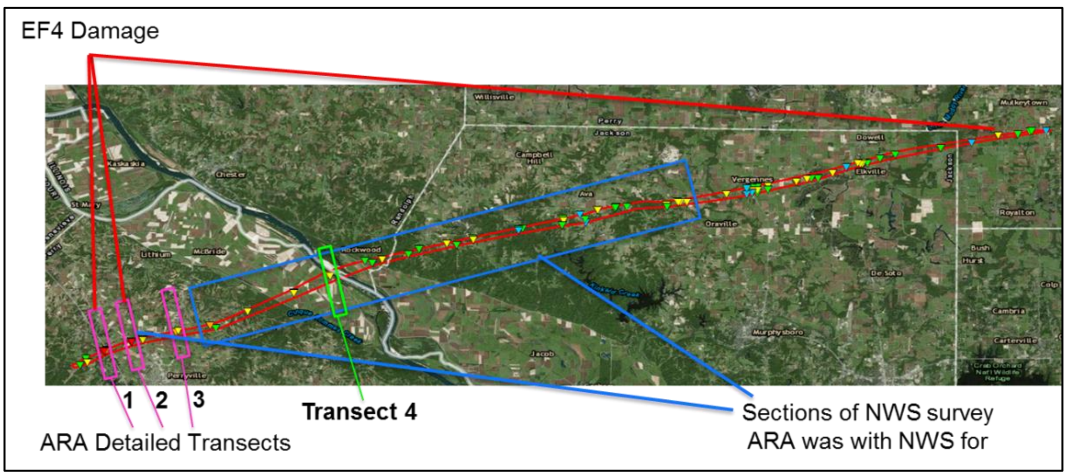

Figure Error! No text of specified style in document.**-8. Overview of Tornado Survey**

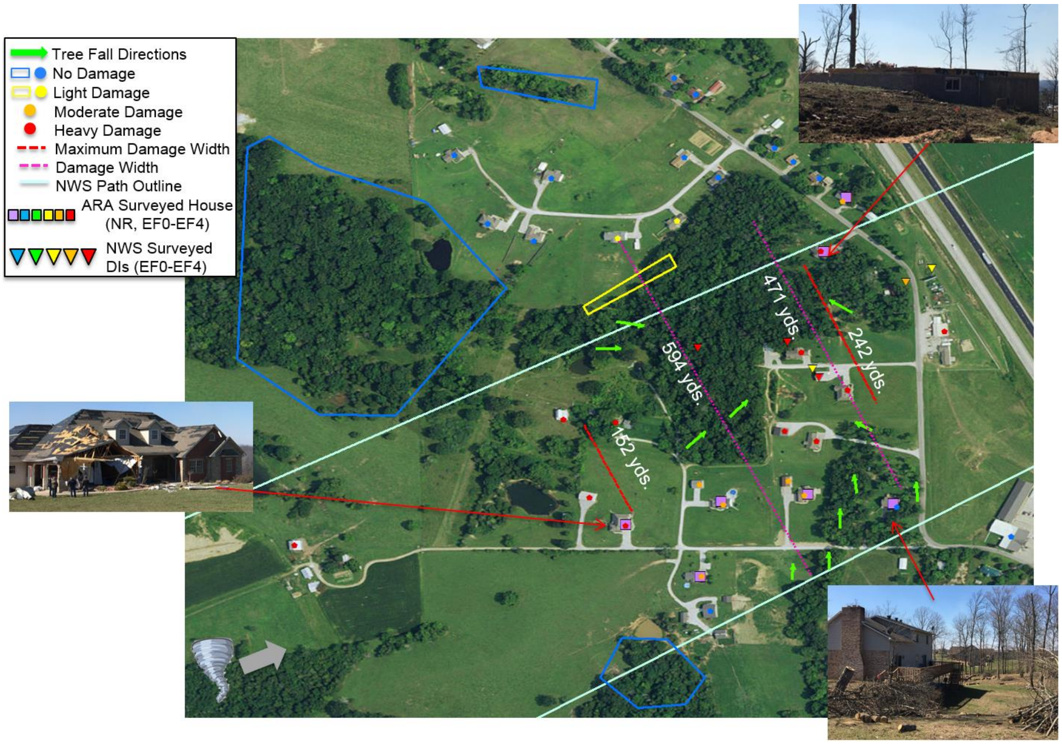

Figure Error! No text of specified style in document.**-9. Transect 1 Overview**

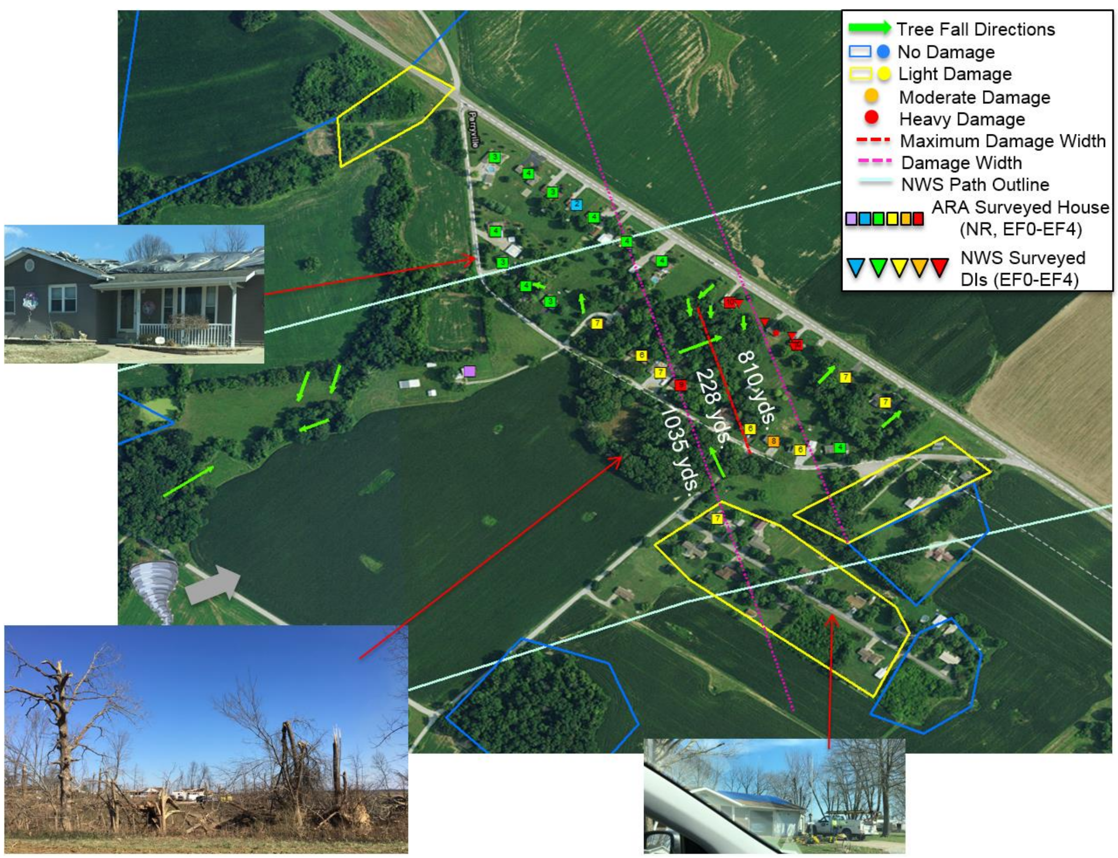

Figure Error! No text of specified style in document.**-10. Transect 2 Overview**

Figure Error! No text of specified style in document.**-11. Transect 3 Overview**

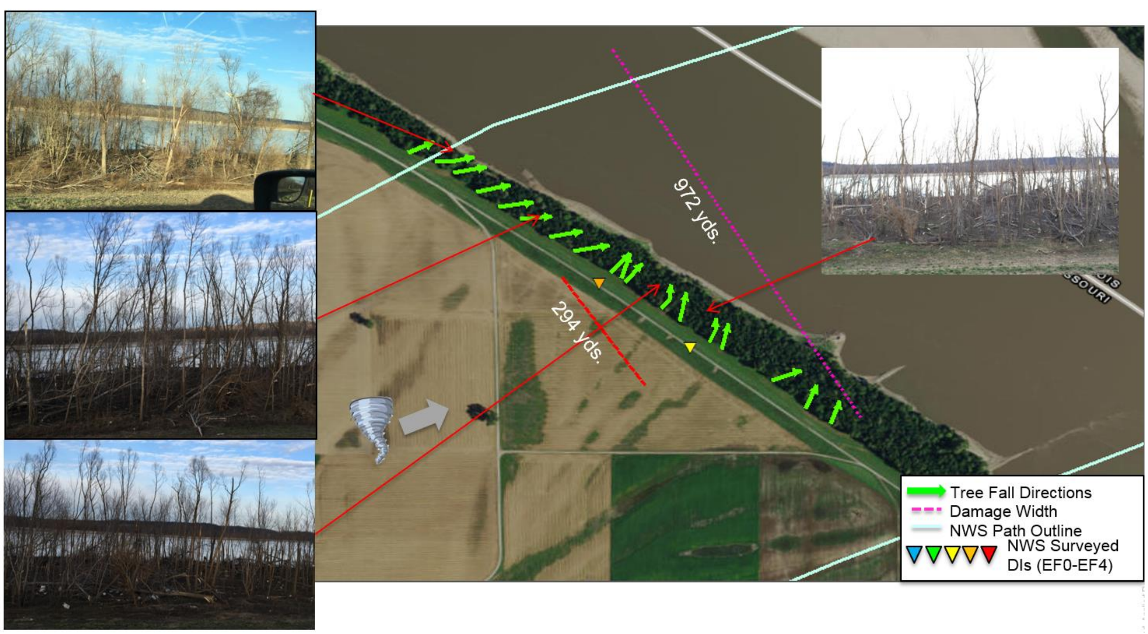

Figure Error! No text of specified style in document.**-12. Transect 4 Overview**

ARA surveyed 45 one and two story houses and documented house characteristics. Figure **Error! No text of specified style in document.**-13 shows a summary of the survey. The common house characteristics that are observed during the survey are given in Table E-4.

- 32 one story and 13 two story wood frame houses were surveyed (45 total).
- Surveyed 7 houses in Transect 1, 25 houses in Transect 2 and 6 houses in Transect 3.
- 90% of the surveyed houses have gable roof.
- Most of the houses had plywood deck with asphalt shingles.
- Most common roof to wall connection observed is Toe-nail connection. Only one house has a clip for roof to wall connection.
- Most of the houses have basement or semi-basement.
- We observed wall to foundation for houses that had major damage or clean foundation. All of such houses had bolted connection.
- Complex houses had less damage compared to simple houses.

Summary of the Perryville Tornado House Survey	
Number of One story House Surveyed	32
Number of Two story House Surveyed	13
No. of Houses with Gable roof	39
No. of Houses with Hip roof	1
No. Houses with flat roof	2
Typical sq. footage one storey house	1500-1800
Typical sq. footage one storey bigger house	3200-3600
No. House with Basement	25

Note: 1 square foot = 0.09290304 m^2

Figure Error! No text of specified style in document.**-13. Summary of the Perryville, MO Tornado Damage Survey**

Table E-4. Perryville Surveyed House Characteristics

Summary of the House Characteristics	
Roof Cover Material	Mostly Ashphalt Shingles
Roof Deck Material	Mostly Plywood
Roof Deck to Frame Connection	8d nails with 6 in to 8 in edge spacing
Roof to Wall Connection	Predominantly 3-16d Toenail
Top plate to stud connection	Mostly 2 Straight Nails
Bottom plate to stud conncetion	Mostly 2 Straight Nails
Sill plate to foundation conncetion	1/2 in anchor bolts with variable spacing
Washer in the Anchor bolt	Most of the Anchor bolt observed have washers
Foundation type	Mostly basement or semi-basement

Note: 1 in = 2.54 cm

A summary of the collected detailed house characteristic data for the surveyed houses are given in Table E-5. This information was useful in our selection of house classes and in the building stock modeling.

Table E-5. Perryville House Characteristics

House No.	No. Stories	Roof Cover Type	Roof Shape	Roof System	Roof Deck Material	Wall Cover Material	Exterior Wall Type	Sheathing	Drywall	Garage Type	Foundation Type	Roof Deck	Roof Deck Connection Length, Dia, Spacing	Roof-Wall	Upper Story Wall-Floor	First Story Wall-Floor	Stud-to-Bottom Plate	Floor Foundation	Floor Foundation Size, Spacing
1	1	S	G	T	P	A, Br	WFr	N	U	D	S	C		TN	SN	SN	SN	B	1/2 in dia, 4'
2	1				U			U	U			U					TN	B	1/2 in dia, 4'
3	2	S	F	R		V, A		Y	Y	N	SW	U		TN					
4	2	S	G	T	P	V	WFr	Y	Y	D	S, SW		2 in long, 7 in edge spacing		TN			U	
5	1	S	G, F	R		Br	WFr			N		C	2.5 in long, 8 in edge spacing						
6	1	S	G			V, Br	WFr	U	Y	S		U		U					
7	1	S	G	T	P	Br	WFr	U	U		SW	C	2.5≈5mm dia, 8"						
8	1			T	P	Br				SD									
9	1	S	G			V	WFr	Y	Y										
10	1	S	G	R		V, Br	WFr	Y		D									
11	1	S	G	R	P	V, Br	WFr	Y	Y	S									
12	1	S	G			V	WFr	Y	Y		SW								
13	1		G	R	P	V		Y		D									
14	1	S		T		V	WFr	Y	Y	S	SW			TN					
15	1			R		Br	WFr	Y	Y		SW			TN		SN		B	1/2 in dia
16	1		G	T	P	Br	WFr	U	Y	D	S, SW	C	2-5", 6", 12"	TN		SN			
17	2	S	G	U	P	V	WFr	Concrete Stucco				U		U					
18	1	S	G	U				U	U	D		U		U					
19	1					O	WFr				SW								
20	1	S	G	T	P	V		Y	Y	N	SW	U	U						
21	1						WFr				SW							B	1/2 dia, 5ft 4in
23	1	S	H	R	P	O	WFr	Y	U	D	O, basement	U		U					
24	1	S	G	T	P	Br	WFr	Y	U	D	S	U	U	TN	U	U	U	U	U
25	1	S	M	U		V, Br		Y		D	S								
26	2	S	G		P	W	WFr	Y	U	N	S								
27	1	S	G	U	U	V	WFr	U	U	M	S								
28	2	S	M	U	P	V	WFr	U	U	M	CB								
29	1	S	G	R	P	V	WFr	Y	Y	N	O, S		2.25", .16"	TN		SN	SN	B	
30	2	S	G	U	U	V, Br	WFr	Y	U	D	O	U	U	U	U	SN	SN	B	3/8", 16"
31	2	U				V, W	WFr	Y	U	M	O			TN	U	U	U	U	U
32	1	S	G	R	P	V	WFr	Y	U	D	O			TN					
33	1	S	G	T	P	Br	WFr	Y	U	D	O								
34	1	S	G	T	P	Br	WFr	Y	Y	D	O			TN					
36	1	S	G		P	W	WFr	U	U	D	S								
37	1	S	G	T	P	Br	WFr	U	U	D	S		2 1/4", 12"						
38	2	S	G	T	P	V	WFr	Y	U	N	O								
39	2	U	G	U	DimLum	V, W	WFr	Y	U	D	O			TN					
40	1	S	G	R	P	Br	WFr	U	U	N	S, O			TN					
41	1	S	M		U	Br	WFr			D	S, O								
42	2	S	G	T	P	V	WFr	Y	U	D	S, O								
43	2	S	G	T	P	V	WFr	Y	U	D	O								
44	1	S	G	T	P	Br	WFr	Y	U	D	S, O								
45	2	S	G	T	P	V, Br	WFr	Y	U	D	O								
46	2	S	G	T	P	V, B, O	WFr	Y	U	D				C		SN			
47	1	S	G	R		V	WFr	Y	Plaster	Detached	SW			TN					

U=Unknown; S=Shingle; G=Gable; H=Hip; F=Falt; M=Mansard; P= Plywood; V=Vinyl; Wfr= Wood Frame; TN=Toe Nail; SN=Straight Nail; Y=Yes; N=No; Br=Brick; B=Bolt; W=Wood; R=Rafter; T=Truss

Note: 1 in = 2.54 cm; 1 ft = 0.3048 m

E.4. Galatia and Saint James, IL Tornadoes

On April 3rd, 2018, two EF2 tornadoes touched down in Galatia, IL and Saint James, IL. ARA surveyed both tornadoes on April 5th. The National Weather Service (NWS) estimated Galatia tornado path length of 12.5 miles (20.1 km) and path width of 1050 ft (320.0 m). ARA surveyed two mobile homes and two single-family homes in Galatia. Figure **Error! No text of specified style in document.**-14 shows the location of these structures along the NWS estimated tornado path in Galatia.

Figure Error! No text of specified style in document.**-14. NWS Estimated Galatia Tornado Path**

Of the two mobile homes surveyed, the one located in 405 Marion Road was overturned and it was observed that the mobile home was not tied down. The damaged structure is shown in Figure **Error! No text of specified style in document.**-15.

Figure Error! No text of specified style in document.**-15. Damaged Mobile Home at 405 Marion Road**

The other mobile home on 1715 Johnston City Road was completely destroyed. The mobile home was built in the mid-90s and was tied down with six anchors per side. It was found that the anchors were partially penetrated in wet soil which caused the structure to roll-over. The damaged structure and the condition of the observed anchor are shown in Figure **Error! No text of specified style in document.**-16.

a. Location of the Damaged Mobile Home

b. Failed Anchor

Figure Error! No text of specified style in document.**-16. Damaged Mobile Home at 1715 Johnston City Road**

Of the two single-family homes surveyed, the one located in 930 Banklick Road was a wood frame house. It lost its roof and detached garage. Wind-borne debris damage was also noticed by ARA surveyors. The debris field and the connection details of this structure are documented. The damaged structure and the wind-borne debris from this structure are shown in Figure **Error! No text of specified style in document.**-17. We analyzed this building as a validation case, as noted in Section 6.

a. Damaged Roof

b. Debris Field

Figure Error! No text of specified style in document.**-17. Damaged Single Family Home at 930 Banklick Road**

The single family home located on 430 Johnston City Road was a wood frame house with metal cladding and roofing. It was a new house built in 2016. The roof-to-wall connection was 2 -16d toe nails. The entire roof of this structure was blown approximately 1,500 ft (460 m). The damaged structure is shown in Figure **Error! No text of specified style in document.**-18.

a. Damaged House *b. Bottom Plate Split at Anchor Bolt*

Figure Error! No text of specified style in document.**-18. Damaged Single Family Home at 430 Johnston City Road**

According to NWS, the St. James tornado path was 18.28 miles (29.42 km) long and 300 ft (91 m) wide. ARA surveyed only one damaged mobile home and three single-family home due to the clean up of most damaged structures. The surveyed mobile home was built in 2009 and was tied down using 10 auger anchors per long sides of the structure. The anchors were penetrated into poured concrete. The failure of the structure was caused by the failure of the ties, which appeared to be rusty. The remains of the structure are visible in Figure **Error! No text of specified style in document.**-19. ARA developed a physics-based mobile home roll-over model and used these observations as part of the overall validation.

a. Location of the Damaged Mobile Home *b. Failed Ties*

Figure Error! No text of specified style in document.**-19**. **Damaged Mobile Home in St. James Tornado**

The three damaged houses that were surveyed were all built in early 1900. All the houses lost their roof due to poor roof to wall connections. The classical failure mode sequence of roof failure followed by wall failure (due to loss of top support) was noted on two of the houses.

E.5. Greensboro, NC Tornado

On April 15, 2018, one EF2 tornado touched down in Greensboro, NC. ARA conducted damage surveys on April 16th and 17th. NWS estimated a tornado path length of 33.6 miles (54.1 km) and a path width of 1,500 ft (460 m). ARA surveyed 18 houses, 3 manufactured units and an elementary school as shown in Table E-6. Figure **Error! No text of specified style in document.**-20 and Figure **Error! No text of specified style in document.**-21 show the NWS surveyed path and ARA surveyed area respectively.

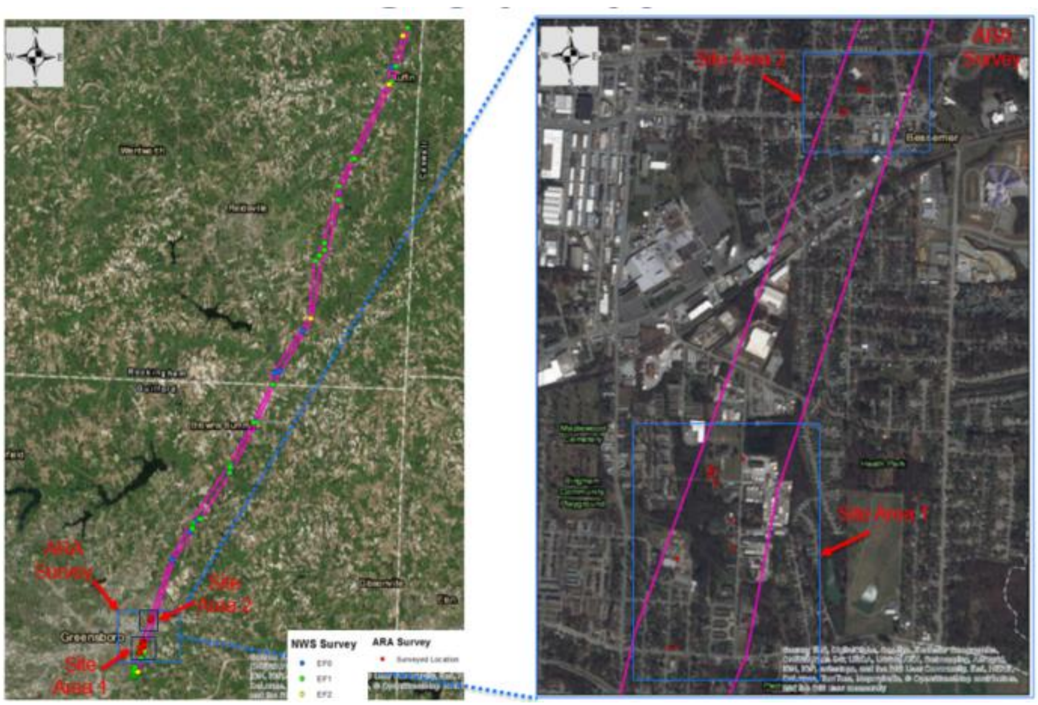

Figure Error! No text of specified style in document.**-20. NWS Surveyed Tornado Path**

Figure Error! No text of specified style in document.**-21. ARA Surveyed Area**

Most of the damaged houses had poor foundation connections such as straight nails or no foundation connections at all. Figure **Error! No text of specified style in document.**-22 shows some of the foundation connections observed during the damage survey. A summary of the house characteristics and observed connections for surveyed houses is given in Table E-7. This data supported our building stock modeling.

a. Failure of Nailed Foundation *b. Failure of Nailed Foundation*

Figure Error! No text of specified style in document.**-22. Observed Foundation Connections**

Three single-wide manufactured units used as classrooms for the elementary school were completely destroyed. In all cases, the failure was due to either failure of the anchors or straps that led to structure rollover. Straps were corroded and the anchors were partially penetrated. Figure **Error! No text of specified style in document.**-23 shows the damaged structures.

a. Damaged Mobile Home

b. Failed Anchors

Figure Error! No text of specified style in document.**-23. Damaged Manufactured Units at Hampton Elementary School**

The damaged elementary school had partial roof damage. Loss of gravel roof cover led to roof decking panel failure/displacement. The school experienced water damage of the inside contents when rainwater entered through the failed roof. None of the exterior walls were failed and there was minor wind-borne debris damage to some of the windows. The damaged structure is shown in Figure **Error! No text of specified style in document.**-24.

Figure Error! No text of specified style in document.**-24. Aerial View of the Damaged Hampton Elementary School**

Table E-6. Summary of the Observed Structures

Type	Structure
On-Story SFH	16
Two-Story SFH	2
Manufactored ome	3
School	1

Table E-7. Greensboro Tornado Surveyed House Characteristics

Address	2402 Apcahe St.	2321 Apache St.	2401 Apcahe St.	510 Banner Ave.	2401 McConnell Rd	3715 Sunnycrest Ave.	3005 E Bessemer Ave	2319 Apache St.	2323 Apache St.	516 Banner Ave.	520 Banner Ave.	2403 McConnell Road	3713 SunnyCrest Ave	3711 SunnyCrest Ave.	3007 E Bessemer Ave	3003 Bessemer	2403 Apache St.	2406 Apache St.
Year Built	1970	1990	2001	1983	1985	1979	2005	1993	1990	U	1945	1953	1958	U	2005	1931	1948	1976
No. Stories	1	1	1	1	1	2	1	1	1	1	1	1	1	1	1	2	1	1
Roof Cover Type	Shingle	Shingle	Shingle	Shingle	Shingle	Shingle	Shingle	Shingle	Shingle	Shingle	U	Shingle	Shingle	Shingle	Shingle	Shingle	Shingle	Shingle
Roof Shape	Gable	Gable	Gable	Gable	Gable	Gable	Gable	Gable	Gable	Gable	U	Gable	Gable	Gable	Gable	Gable	Gable	Hip
Roof System	U	Truss	U	Rafter	U	Rafter	Truss	Truss	Truss	U	U	Truss	U	U	Truss	Truss	Rafter	Rafter
Roof Deck Material	Plywood	Plywood	OSB	Dim. Lumber	Dim. Lumber	Dim. Lumber	OSB	Plywood	Plywood	OSB	U	Plywood	U	U	OSB	OSB	OSB	Dim. Lumber
Wall Cover Material	Masonite	Masonite	Vinyl	Vinyl	Masonite	U	Vinyl	Brick/Vinyl	Vinyl	Asbestus	Asbestus	Vinyl	Vinyl	Vinyl	Vinyl	Vinyl	Vinyl	Vinyl
Exterior Wall Type	Wood frame	Wood frame	Wood frame	Wood frame	Wood frame	URM	Wood frame	Wood frame	Wood frame	Board	Wood frame	Wood frame	Wood frame	U	Wood frame	Wood frame	Wood frame	Wood frame
Sheathing	Full	None	Full	Full	U	URM	Full	Full	Full	Full	Full	Full	Full	U	Full	Full	Full	Full
Foundation Type	Masonry Wall	Masonry Wall	Masonry Wall	Masonry Wall	Masonry Wall	Slab	Masonry Wall	Masonry Wall	Masonry Wall	Concrete wall	Masonry Wall	Masonry Wall	Masonry Wall	Masonry Wall	Masonry Wall	Concrete wall	Concrete wall	Masonry Wall
Roof Deck connection type	nail	nail	U	nail	nail	nail	nail	nail	nail	U	U	nail	U	U	nail	nail	nail	nail
Roof Deck connection length, dia. spacing	U	2.25 in; Edge spacing: 8 inch; Field spacing: 11 inch	U	2.5 in; Edge spacing: 7 inch	U	2.25 in; Edge spacing: 3 inch; Field spacing: 5 inch	Edge spacing: 6 inch; Field spacing: 12 inch	3 in; Edge spacing:6 inch; Field spacing: 6 inch	2.5 in;Edge spacing:6 inch; Field spacing: 6 inch	U	U	2.25 in; Edge spacing:8 inch; Field spacing: 8 inch	U	U	Edge spacing: 6 inch; Field spacing: 6 inch	2.25 inch	U	2.75 in; Edge spacing: 6 inch
Roof-Wall	U	3 TN	U	2-16d TN	U	3 TN; 2-2.5 and 1-3.5	single clip	3 TN ; 36 in oc	2 TN; 16 d and 12 d	U	2-TN	3-TN 3.25 inch	U	U	2-TN	2-TN	2-TN	2-TN
Top plate	Single	Double	U	Single	U	Single	Double	Double	Double	U	Double	Double	U	U	Double	Double	Single	U
Top plate to stud	2-16d SN	2-SN		2-SN	U	2-SN 2.5inch	2-16d SN	1-SN	U	U	2-SN	1-SN	U	U	U	2-TN		U
Stud to Bottom Plate	2-SN	U	U	U	U	U	2-16d SN	1-SN	2-TN	U	2-SN	2-SN	U	U	2-SN	U	U	U
Floor Foundation	U	Nail	U	U	None	U	U	Nail	Nail	U	None	U	U	U	Nail	U	U	U
Fl Fdn size,Spacing	U	2-3.25 inch@ 8 to 10 inch spacing	U	U	No Connection	U	U	3 inch @12 inch oc	12 inch oc	U	No Connection	U	U	U	3.25 inch@10 inch oc	U	U	U
DOD	9	5	3	6	5	7	7	7	6	3	7	7	4	4	4	3	4	6

U=Unknown; S=Shingle; G=Gable; H=Hip; F=Falt; M=Mansard; P= Plywood; V=Vinyl; Wfr= Wood Frame; TN=Toe Nail; SN=Straight Nail; Y=Yes; N=No; Br=Brick; B=Bolt; W=Wood; R=Rafter; T=Truss

Note: 1 in = 2.54 cm

E.6. Summary

We present a few lessons learned and suggestions for damage surveys:

1. Coordination with NWS is essential to productive damage surveys to facilitate access and damage location. In addition, early communications with local emergency management professionals also helps with damage location and access.
2. Rapid deployment of the survey team is essential. Pre-deployment is risky, expensive, and unlikely to position the team in the right part of the state or region. Early arrival on the day-after is essential since structural damage may be covered and debris clean-up underway.
3. Damage surveys should be conducted along several damage path transects to characterize the width of the maximum damage and local path width corresponding to the assigned EF rating in that segment of the storm. The information is useful to characterize the RMW of the storm.
4. Obtaining structural load-path connection details is critical. The connection details should be documented through photograph, measurement and collection of samples from a failed component. A portable ladder may be needed to access roof-to-wall connections and roof-deck connections for one-story buildings.
5. Access is difficult for structures that are not significantly damaged. Owners may not allow access or are not available. Hence, the ability to get the "denominator" in terms of the characteristics of less-damaged buildings remains a major limitation of the damage survey process. Additional efforts through local organizations may be needed to gain access to these structures in following days.
6. More structural details are needed in the EF process. For FR12, these include roof shape, house shape complexity, house plan dimensions, number of stories, roof deck type and attachment, roof cover type, roof slope (low, mid, steep), wall sheathing details, foundation type, connection spacing, and quality information.
7. We believe a better system would be to survey more buildings in detail than performing numerous quick surveys that may miss key elements. Otherwise, wind speed estimation will continue to be more art than science. A tool is needed to collect more of the important data.
8. Locating the storm centerline and maximum damage width (MDW) is essential. The survey should note if the structure is inside the MDW and on the left, center, or right side of the center-line.
9. Unknowns must be allowed on all data collected. Guessing on features and characteristics should not be permitted. This will aid the confidence level in the wind speed estimation.
10. Observation of wind-borne debris field from an isolated structure is very helpful to characterize the debris translation and direction of travel during the tornado. The maximum translation of individual debris type such as roof shingle, roof deck, and roof truss elements should be recorded. If possible, samples of these debris can be

collected and weighed. Center-of-mass location of debris, by component type, is useful.

11. For FR12, DOD 9 and DOD 10 levels of damage need additional data collected regarding walls and debris translation distances and intact-wall section translation.
12. Terrain information is needed and proximity of nearby structures.
13. The wind speed estimation process should be achieved through an engineering-based tool within the DAT. This approach will allow the user to focus on getting key information and letting the tool do the work. Unknowns would be considered and the wind speed uncertainties would reflect the available information, with less guesswork.

Appendix F. Tornado Speed Wind Exceedance Frequencies

F.1. DOD Damage Probability Matrix Plots

This appendix provides the EF* DOD PMF bar plots for four FR12 groups:

1. Simple Plan Area Gables: Classes 1, 13, 17, and 21 (page F-2)
2. Simple Plan Area Hips: Classes 2, 14, 18, and 22 (page F-3)
3. Complex Plan Area Gables: Classes 23, 35, 39, and 43 (page F-4)
4. Complex Plan Area Hips: Classes 24, 36, 40, and 44 (page F-5)

Wind speeds are given in miles per hour (1 mph = 0.44704 m/s).

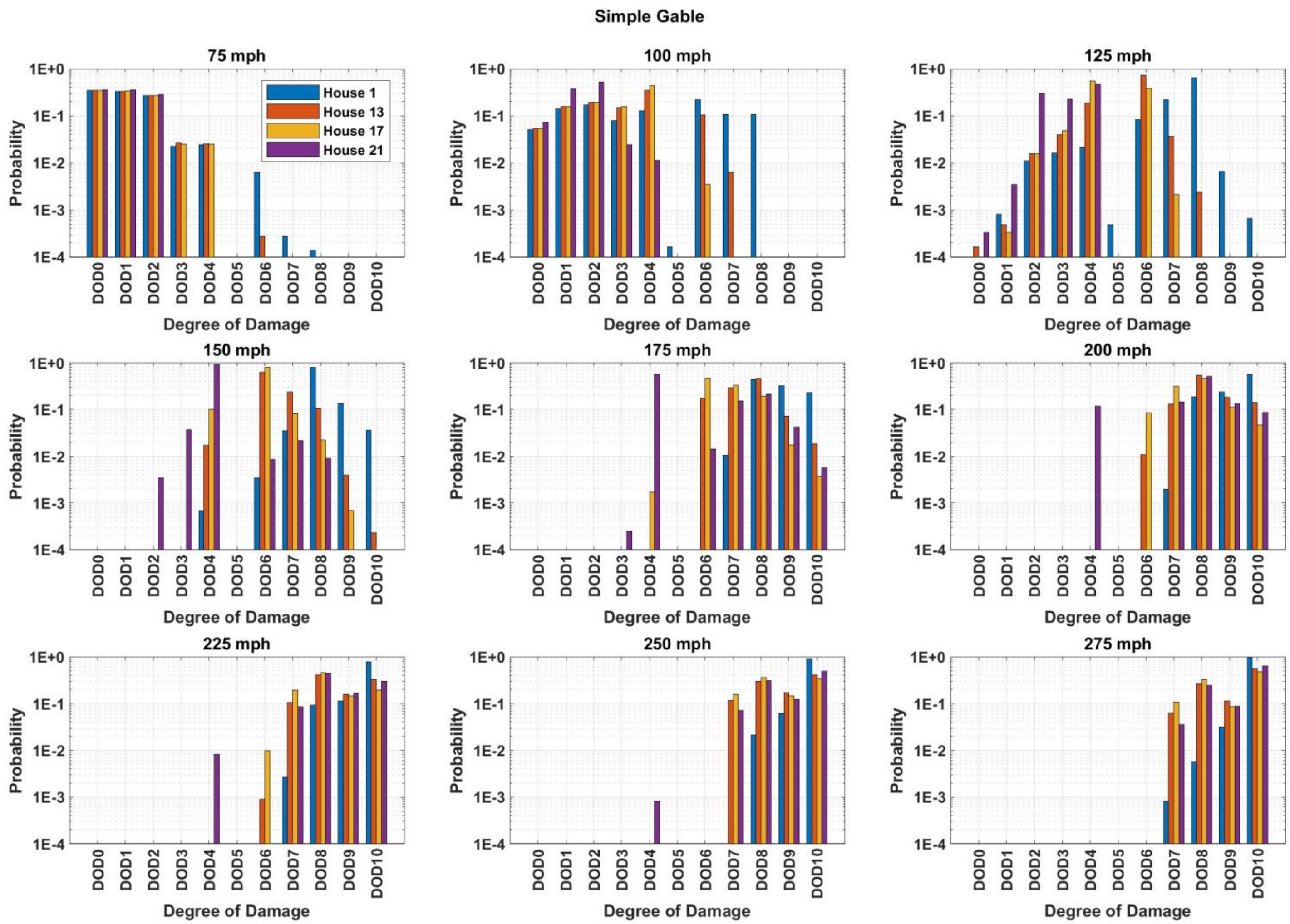
Simple Gable
75 mph
100 mph
125 mph
150 mph
175 mph
200 mph
225 mph
250 mph
275 mph
House 1
House 13
House 17
House 21
Probability
Degree of Damage
1E+0
1E-1
1E-2
1E-3
1E-4
DOD0
DOD1
DOD2
DOD3
DOD4
DOD5
DOD6
DOD7
DOD8
DOD9
DOD10

Simple Hip

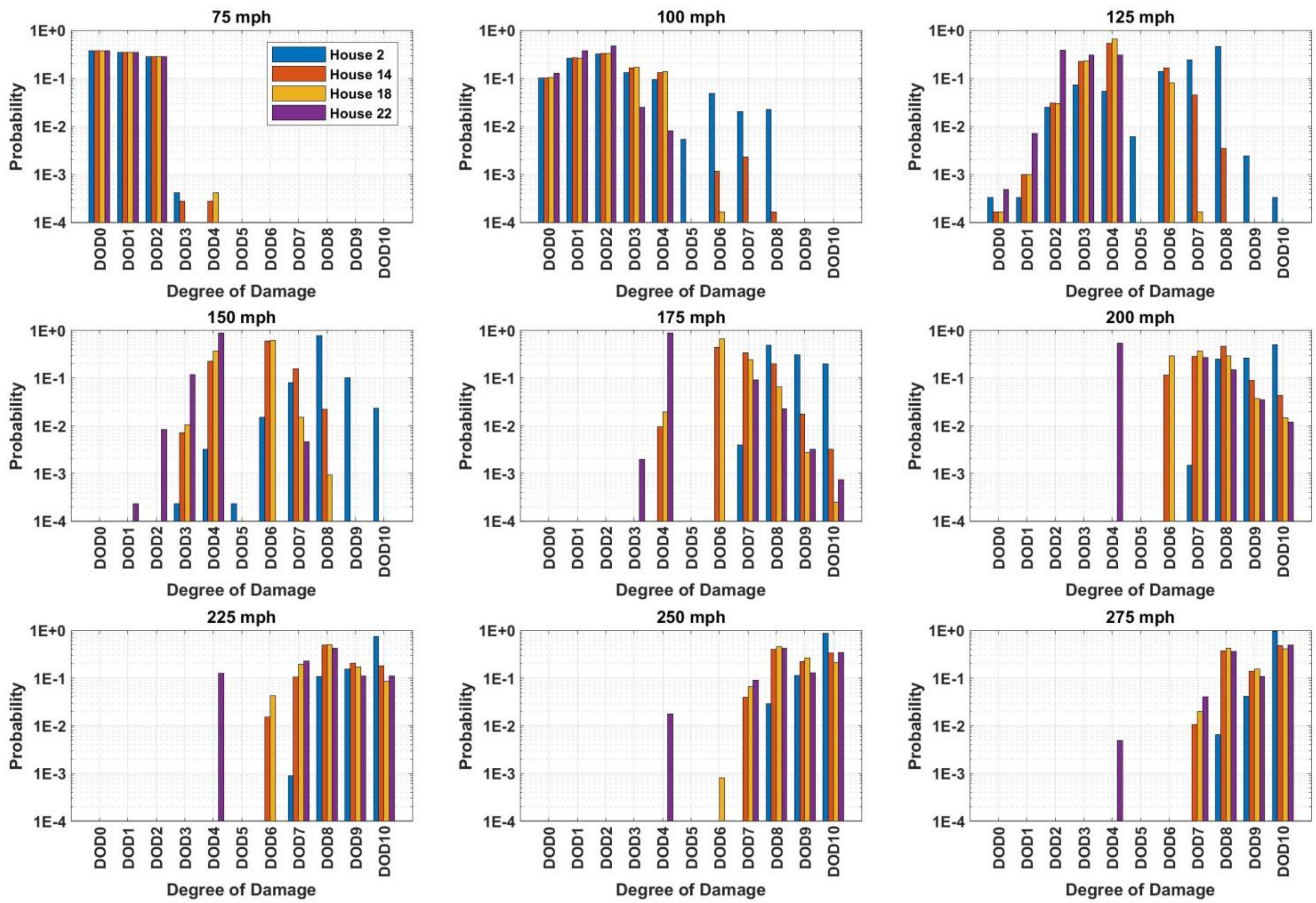
75 mph
100 mph
125 mph
150 mph
175 mph
200 mph
225 mph
250 mph
275 mph
House 2
House 14
House 18
House 22
Probability
1E+0
1E-1
1E-2
1E-3
1E-4
DOD0
DOD1
DOD2
DOD3
DOD4
DOD5
DOD6
DOD7
DOD8
DOD9
DOD10
Degree of Damage

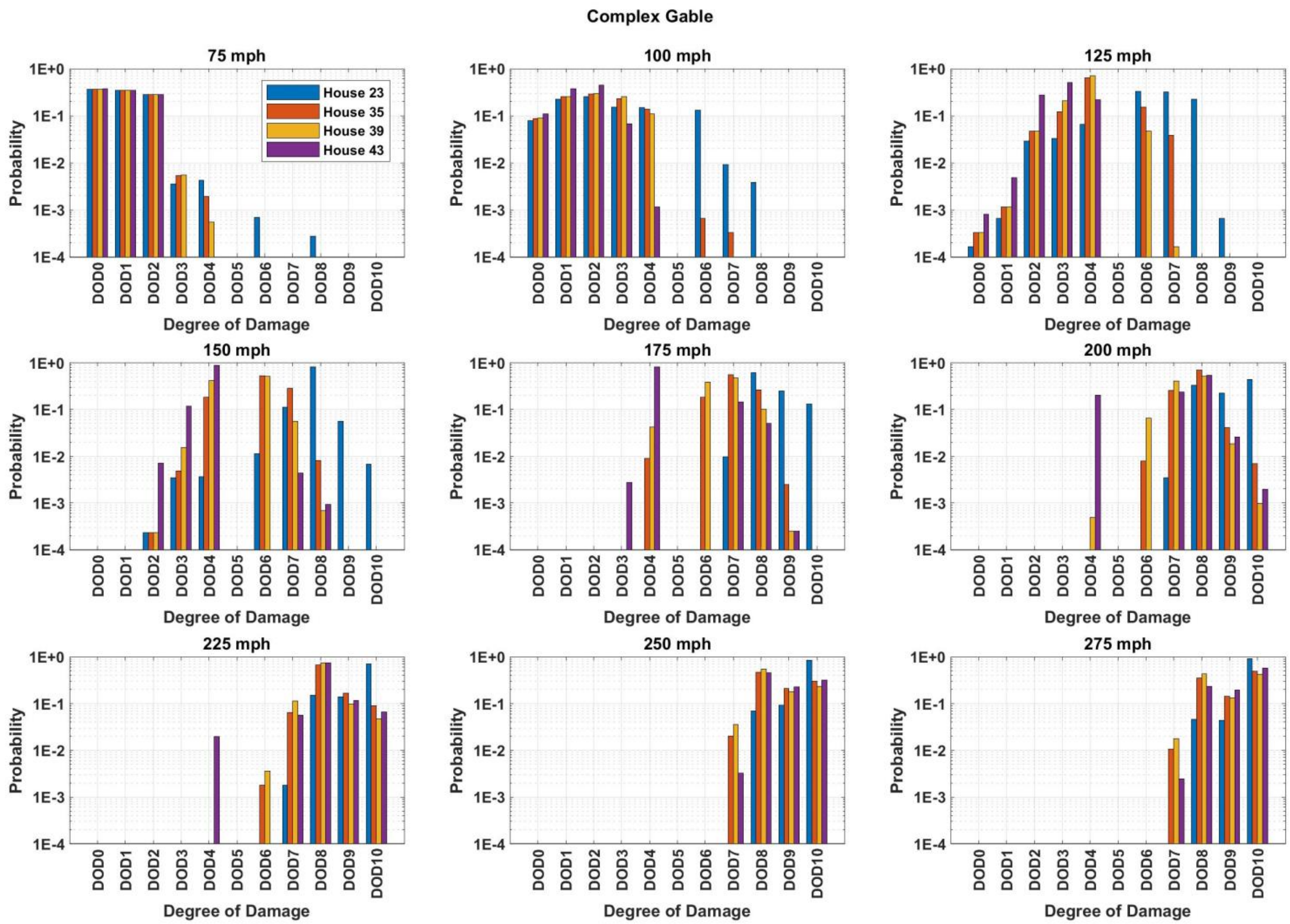

Complex Gable
75 mph
100 mph
125 mph
150 mph
175 mph
200 mph
225 mph
250 mph
275 mph
House 23
House 35
House 39
House 43
Probability
Degree of Damage
1E+0
1E-1
1E-2
1E-3
1E-4
DOD0
DOD1
DOD2
DOD3
DOD4
DOD5
DOD6
DOD7
DOD8
DOD9
DOD10

Complex Hip

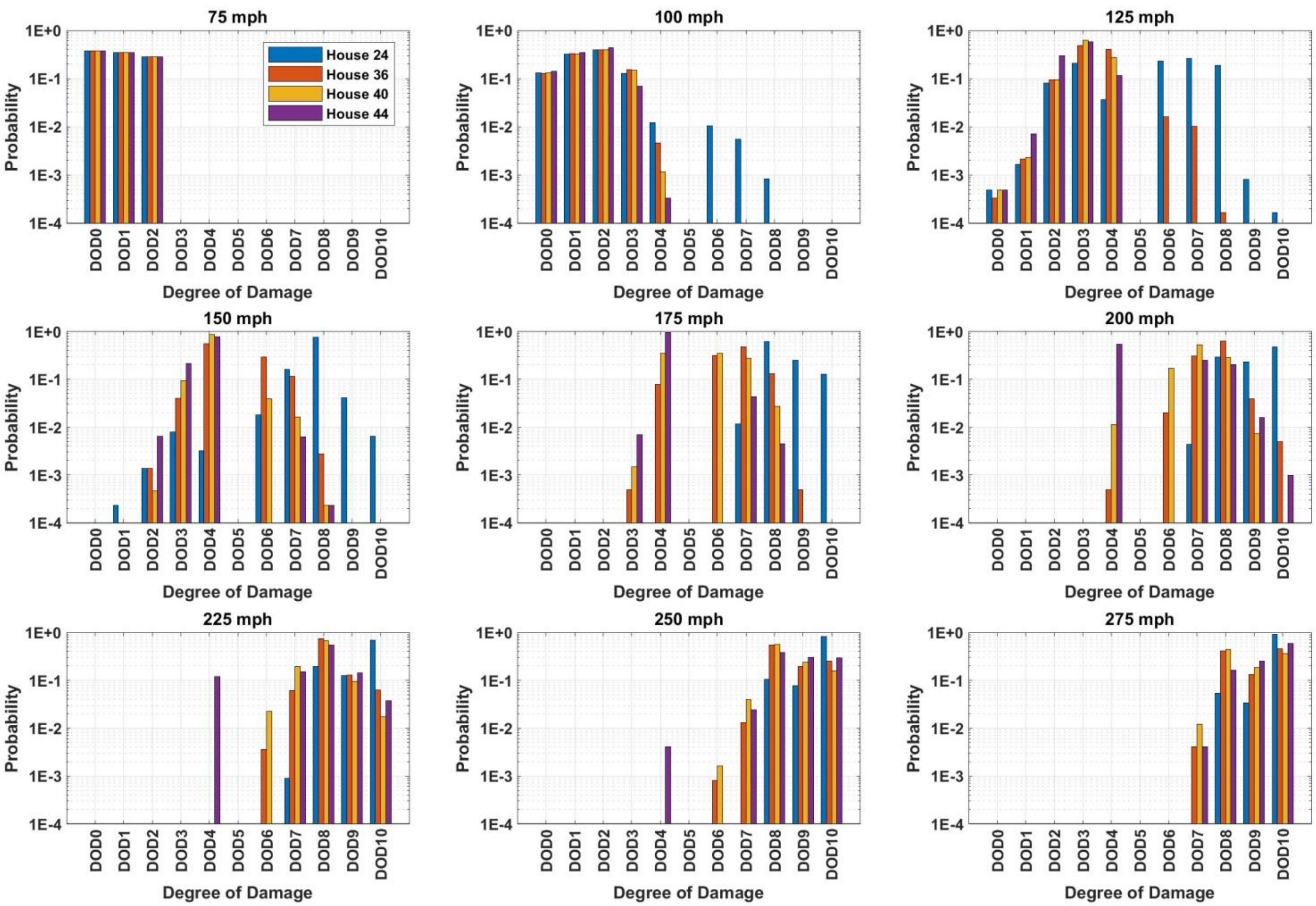
75 mph
100 mph
125 mph
150 mph
175 mph
200 mph
225 mph
250 mph
275 mph
House 24
House 36
House 40
House 44
Probability
Degree of Damage
1E+0
1E-1
1E-2
1E-3
1E-4
DOD0
DOD1
DOD2
DOD3
DOD4
DOD5
DOD6
DOD7
DOD8
DOD9
DOD10

F.2. DOD Wind Speed PMF Plots

FR12 DOD wind speed probability mass distributions (PMF) are provided for the 44 house types defined in Section 6. These distributions are based on the epistemic prior.

Table F-1 provides the order of the PMF plots. These plots are provided on pages F-7 to F-50. The figures include the house class number and label. The label uses notation such as: (1) Strength: W = weak, M = mid, S = strong, and SS = super strong; (2) Roof Deck Nails: 6d, 8d, where 8dpl = 2-8d nails for a plank/board deck; (3) Roof Shape: G = gable and H = hip; and (4) Foundation: B = bolted, N = nailed, all strong houses are bolted. Wind speed is shown in miles per hour (1 mph = 0.44704 m/s).

The first 22 houses in Table F-1 are simple plan shapes and Houses 23 – 44 are complex plan shapes.

Table F-1. DOD Wind Speed PMF Plots

House	File name	PMF Plot Page	House	File name	PMF Plot Page
1	W6dG_tornado_1304G	F-7	23	W6dG_tornado_0014G	F-29
2	W6dH_tornado_1304H	F-8	24	W6dH_tornado_0014H	F-30
3	W8dG_tornado_1304G	F-9	25	W8dG_tornado_0014G	F-31
4	W8dH_tornado_1304H	F-10	26	W8dH_tornado_0014H	F-32
5	W8dpDGN_tornado_1304G	F-11	27	W8dpDGN_tornado_0014G	F-33
6	W8dpDHN_tornado_1304H	F-12	28	W8dpDHN_tornado_0014H	F-34
7	W8dpDGB_tornado_1304G	F-13	29	W8dpDGB_tornado_0014G	F-35
8	W8dpDHB_tornado_1304H	F-14	30	W8dpDHB_tornado_0014H	F-36
9	M6dG_tornado_1304G	F-15	31	M6dG_tornado_0014G	F-37
10	M6dH_tornado_1304H	F-16	32	M6dH_tornado_0014H	F-38
11	M8dG_tornado_1304G	F-17	33	M8dG_tornado_0014G	F-39
12	M8dH_tornado_1304H	F-18	34	M8dH_tornado_0014H	F-40
13	M6dBG_tornado_1304G	F-19	35	M6dBG_tornado_0014G	F-41
14	M6dBH_tornado_1304H	F-20	36	M6dBH_tornado_0014H	F-42
15	M8dBG_tornado_1304G	F-21	37	M8dBG_tornado_0014G	F-43
16	M8dBH_tornado_1304H	F-22	38	M8dBH_tornado_0014H	F-44
17	SG6D_tornado_1304G	F-23	39	SG6D_tornado_0014G	F-45
18	SH6D_tornado_1304H	F-24	40	SH6D_tornado_0014H	F-46
19	SG_tornado_1304G	F-25	41	SG_tornado_0014G	F-47
20	SH_tornado_1304H	F-26	42	SH_tornado_0014H	F-48
21	SSG_tornado_1304G	F-27	43	SSG_tornado_0014G	F-49
22	SSH_tornado_1304H	F-28	44	SSH_tornado_0014H	F-50

House 1: W6dG 1304G Epistemic Prior

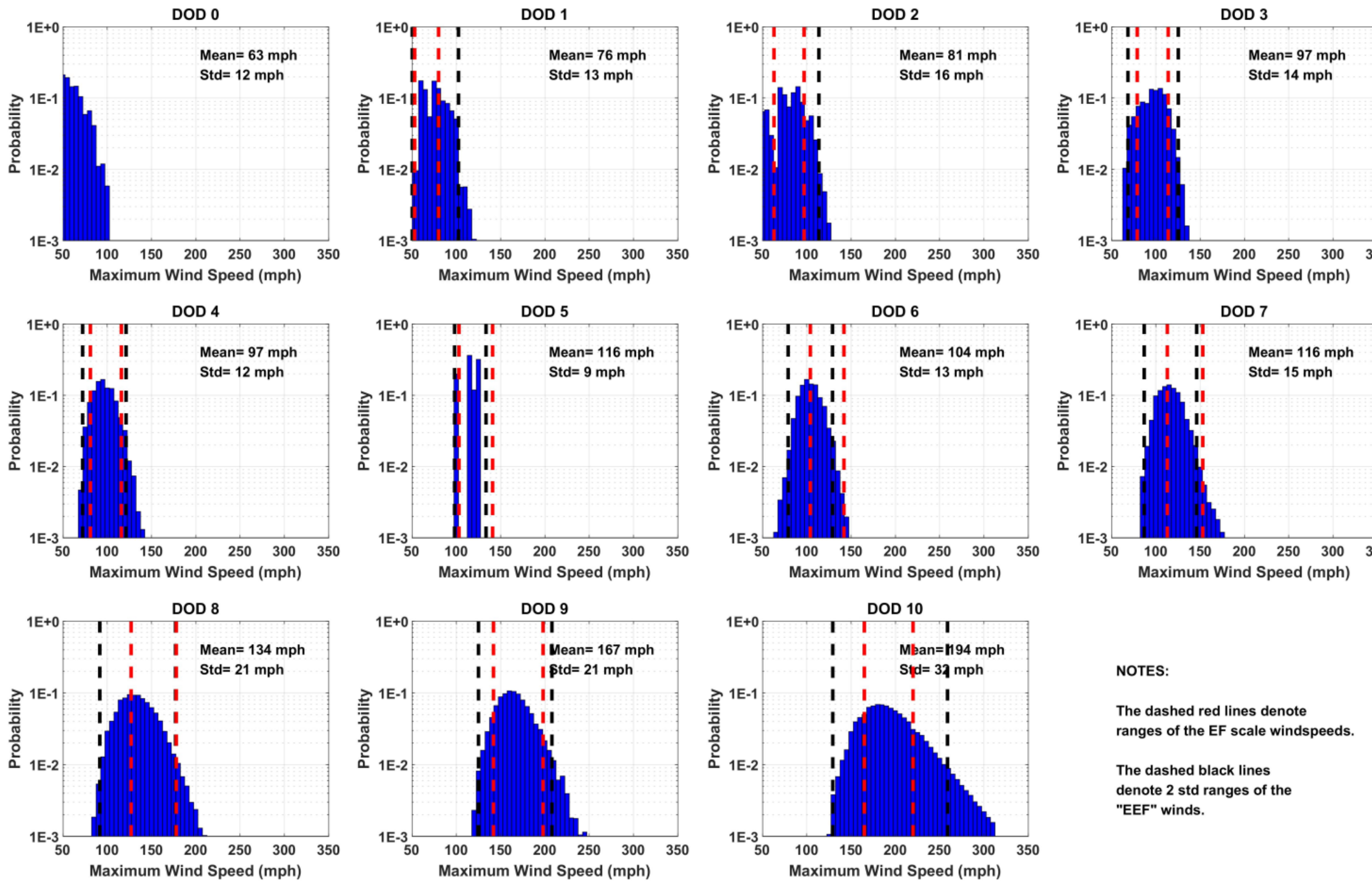

NOTES:

The dashed red lines denote ranges of the EF scale windspeeds.

The dashed black lines denote 2 std ranges of the "EEF" winds.

House 2: W6dH 1304H Epistemic Prior

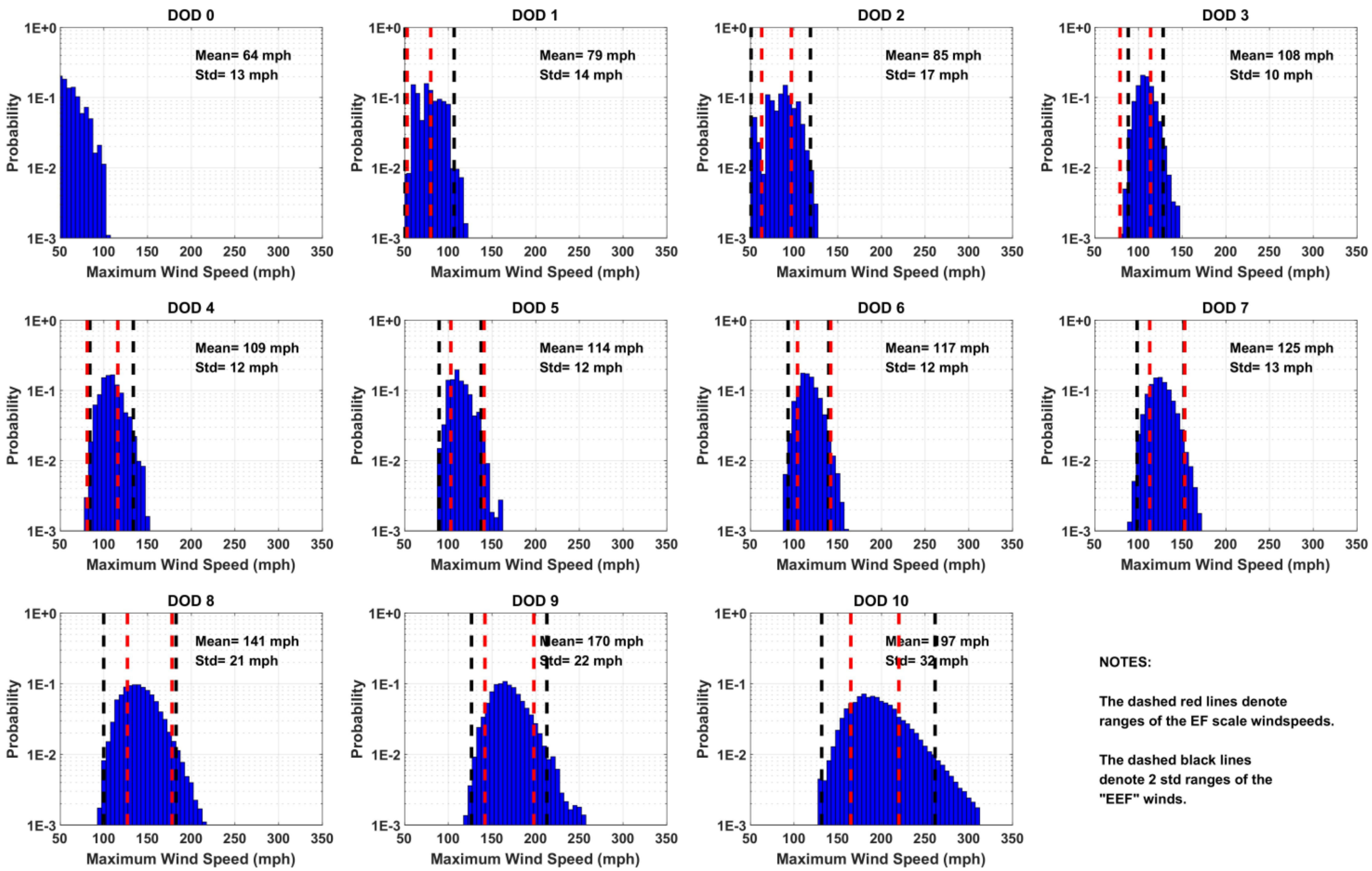

NOTES:

The dashed red lines denote ranges of the EF scale windspeeds.

The dashed black lines denote 2 std ranges of the "EEF" winds.

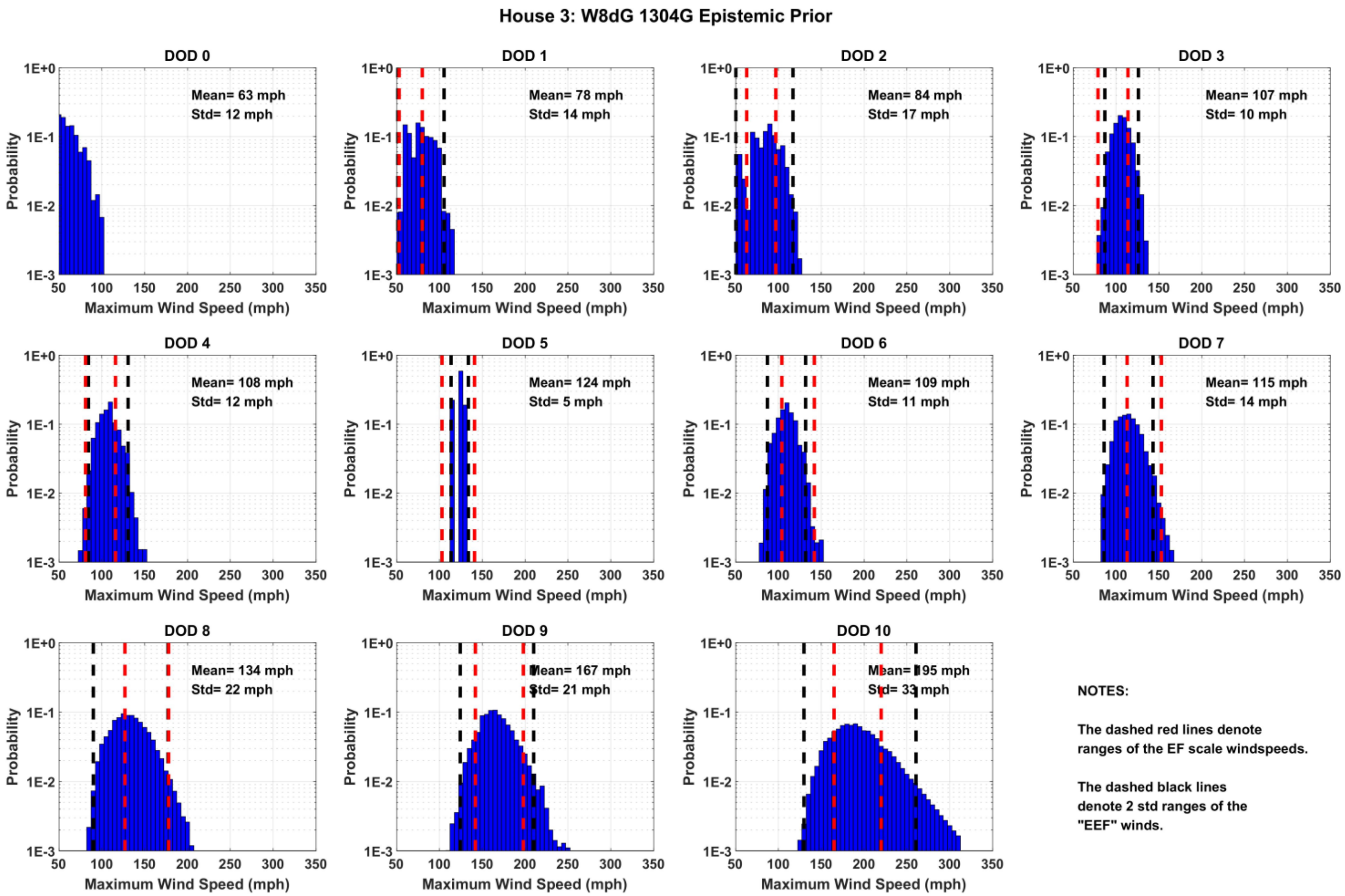
House 3: W8dG 1304G Epistemic Prior
DOD 0
Mean= 63 mph
Std= 12 mph
DOD 1
Mean= 78 mph
Std= 14 mph
DOD 2
Mean= 84 mph
Std= 17 mph
DOD 3
Mean= 107 mph
Std= 10 mph
DOD 4
Mean= 108 mph
Std= 12 mph
DOD 5
Mean= 124 mph
Std= 5 mph
DOD 6
Mean= 109 mph
Std= 11 mph
DOD 7
Mean= 115 mph
Std= 14 mph
DOD 8
Mean= 134 mph
Std= 22 mph
DOD 9
Mean= 167 mph
Std= 21 mph
DOD 10
Mean= 195 mph
Std= 33 mph
Probability
Maximum Wind Speed (mph)
NOTES:
The dashed red lines denote ranges of the EF scale windspeeds.
The dashed black lines denote 2 std ranges of the "EEF" winds.

House 4: W8dH 1304H Epistemic Prior

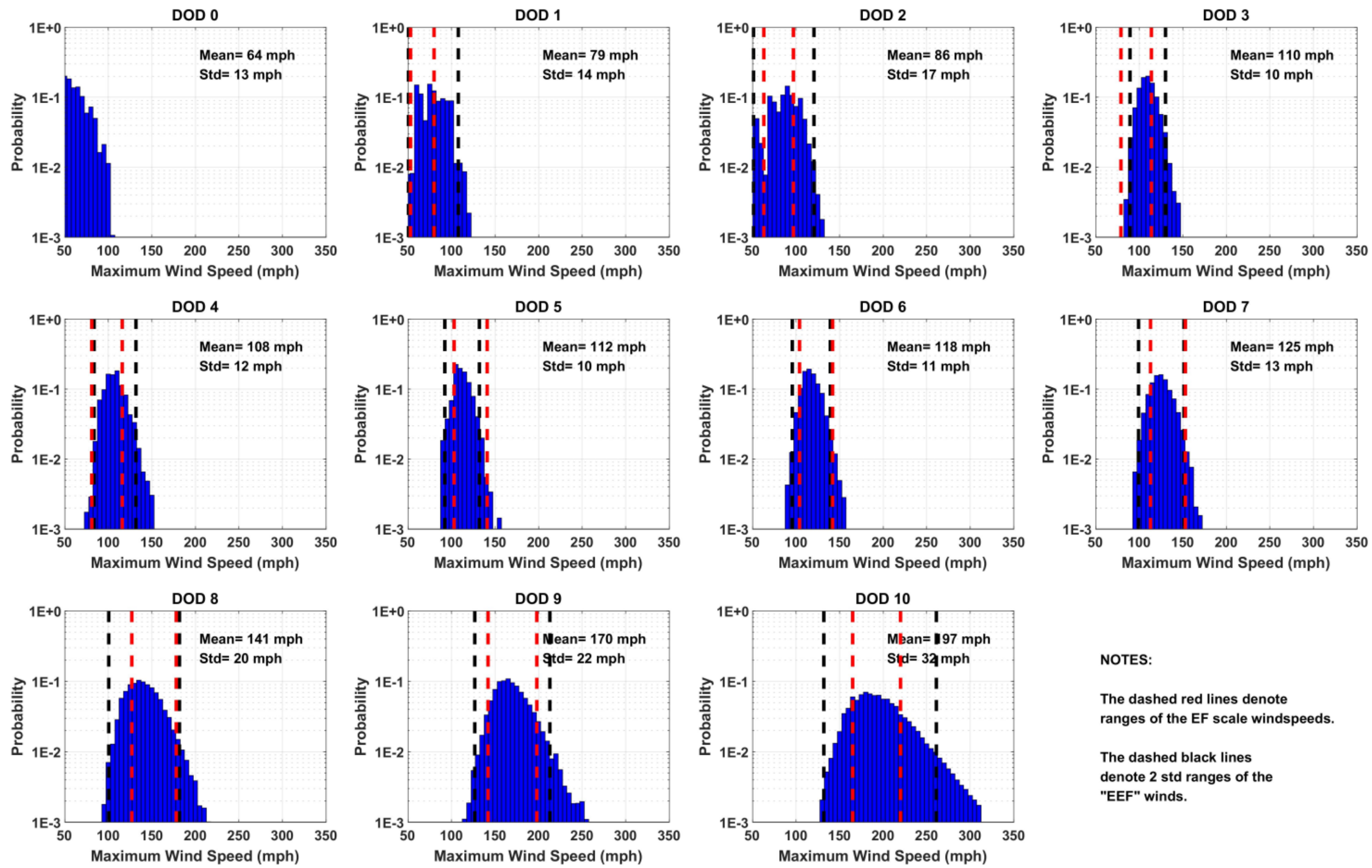

House 5: W8dpDGN 1304G Epistemic Prior

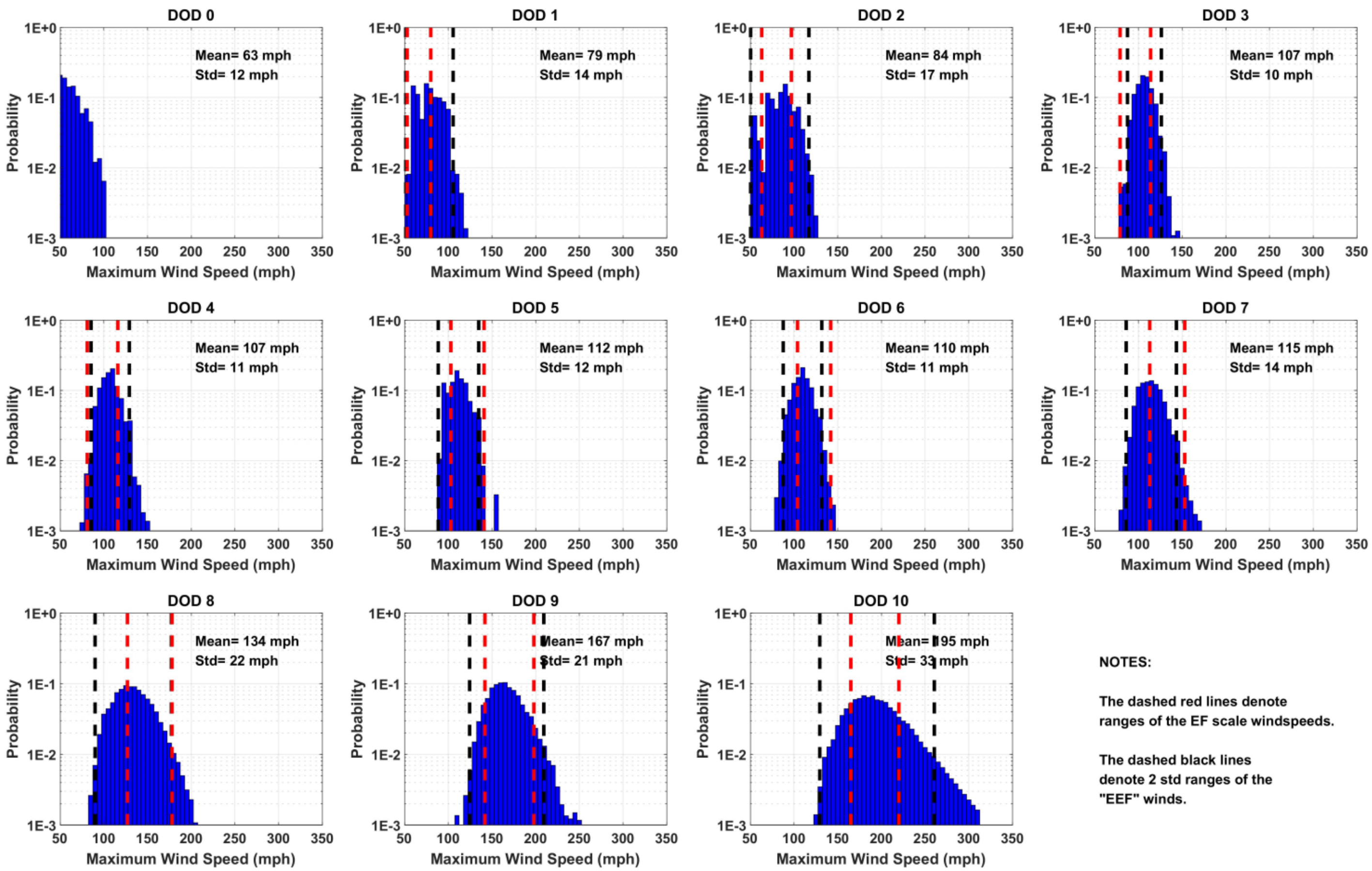

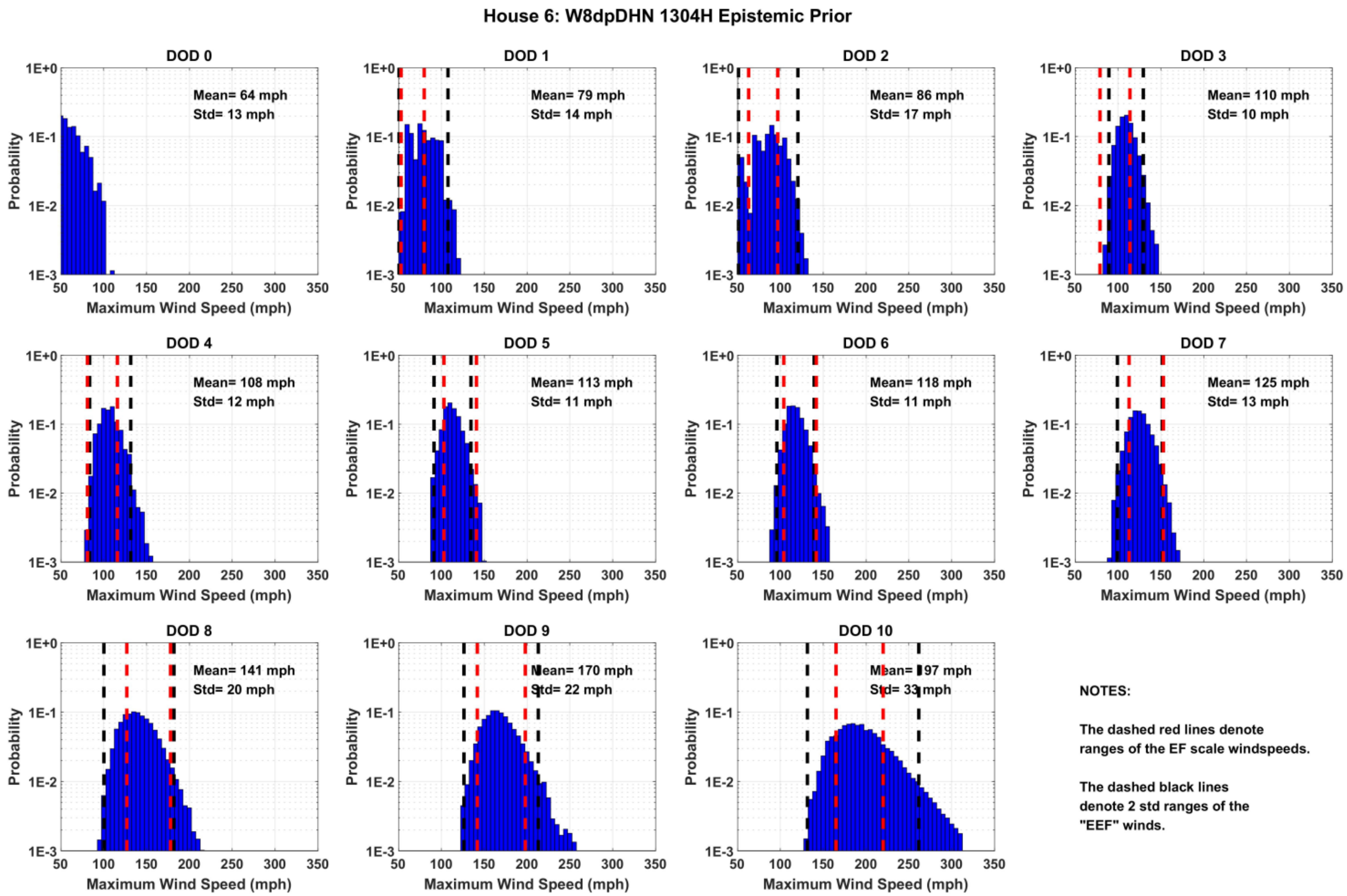
House 6: W8dpDHN 1304H Epistemic Prior
DOD 0
Mean= 64 mph
Std= 13 mph
DOD 1
Mean= 79 mph
Std= 14 mph
DOD 2
Mean= 86 mph
Std= 17 mph
DOD 3
Mean= 110 mph
Std= 10 mph
DOD 4
Mean= 108 mph
Std= 12 mph
DOD 5
Mean= 113 mph
Std= 11 mph
DOD 6
Mean= 118 mph
Std= 11 mph
DOD 7
Mean= 125 mph
Std= 13 mph
DOD 8
Mean= 141 mph
Std= 20 mph
DOD 9
Mean= 170 mph
Std= 22 mph
DOD 10
Mean= 197 mph
Std= 33 mph
Probability
Maximum Wind Speed (mph)
1E+0
1E-1
1E-2
1E-3
50
100
150
200
250
300
350
NOTES:
The dashed red lines denote ranges of the EF scale windspeeds.
The dashed black lines denote 2 std ranges of the "EEF" winds.

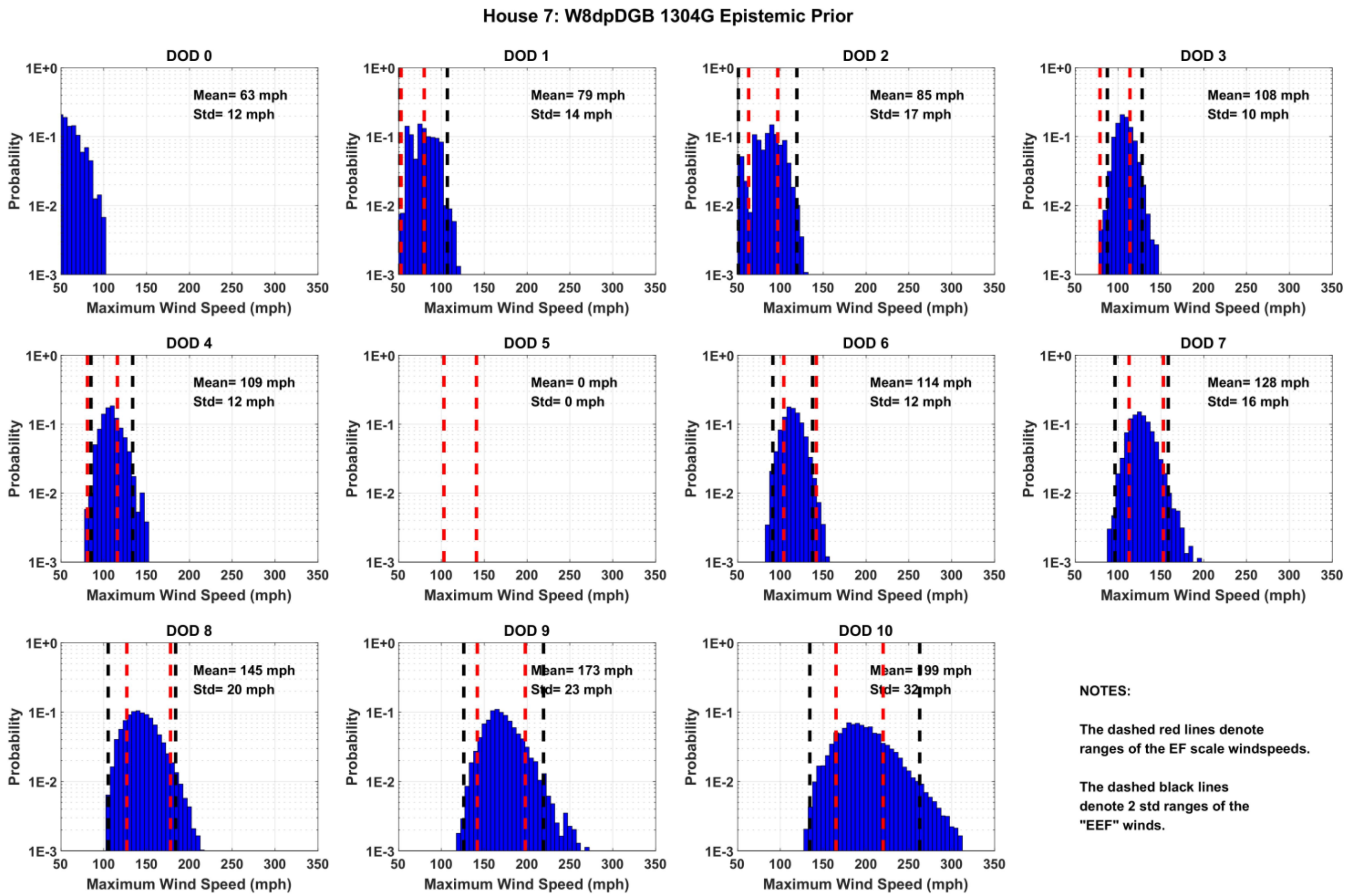
House 7: W8dpDGB 1304G Epistemic Prior
DOD 0
Mean= 63 mph
Std= 12 mph
DOD 1
Mean= 79 mph
Std= 14 mph
DOD 2
Mean= 85 mph
Std= 17 mph
DOD 3
Mean= 108 mph
Std= 10 mph
DOD 4
Mean= 109 mph
Std= 12 mph
DOD 5
Mean= 0 mph
Std= 0 mph
DOD 6
Mean= 114 mph
Std= 12 mph
DOD 7
Mean= 128 mph
Std= 16 mph
DOD 8
Mean= 145 mph
Std= 20 mph
DOD 9
Mean= 173 mph
Std= 23 mph
DOD 10
Mean= 199 mph
Std= 32 mph
Probability
Maximum Wind Speed (mph)
NOTES:
The dashed red lines denote ranges of the EF scale windspeeds.
The dashed black lines denote 2 std ranges of the "EEF" winds.

House 8: W8dpDHB 1304H Epistemic Prior

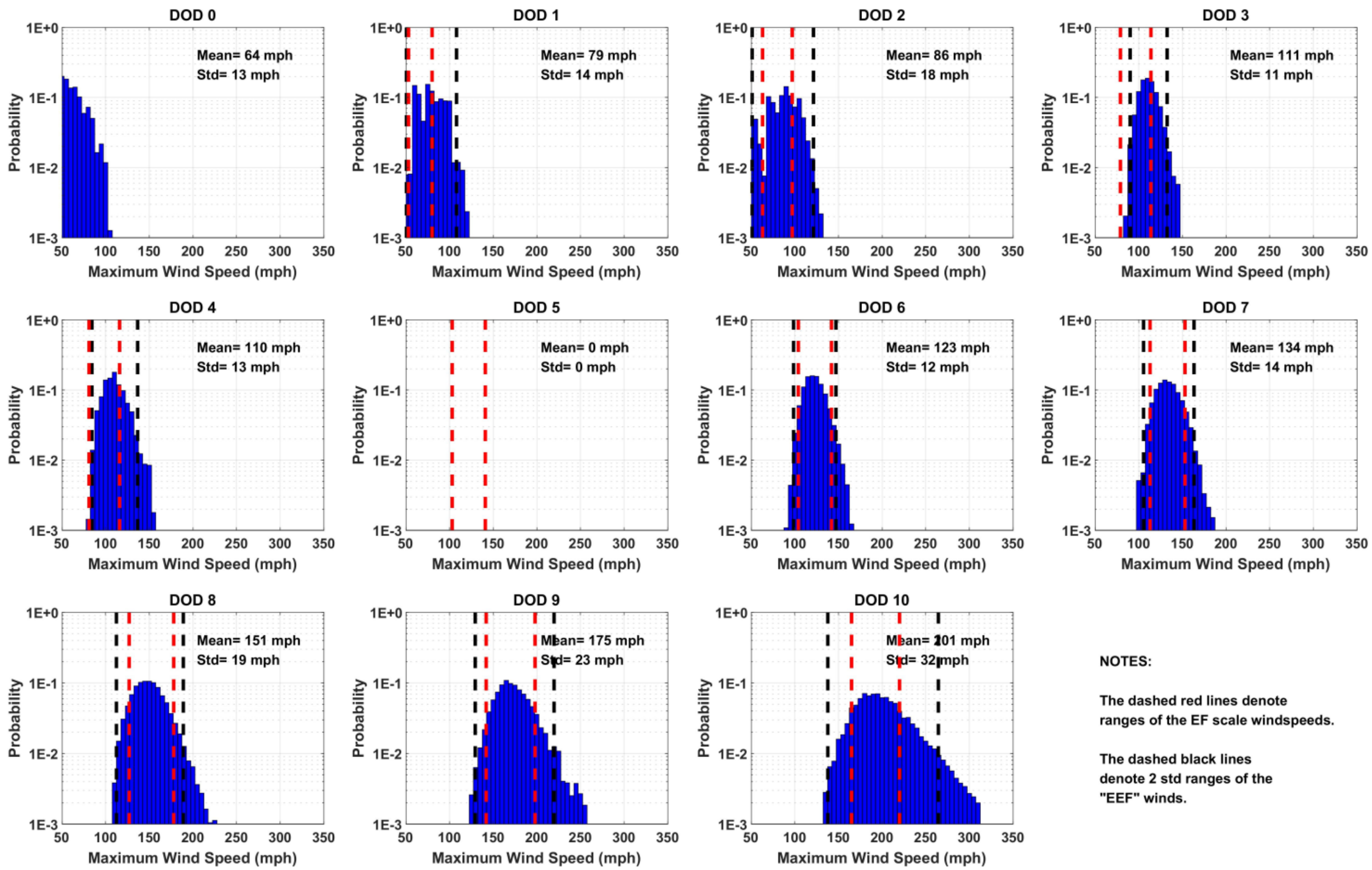

House 9: M6dG 1304G Epistemic Prior

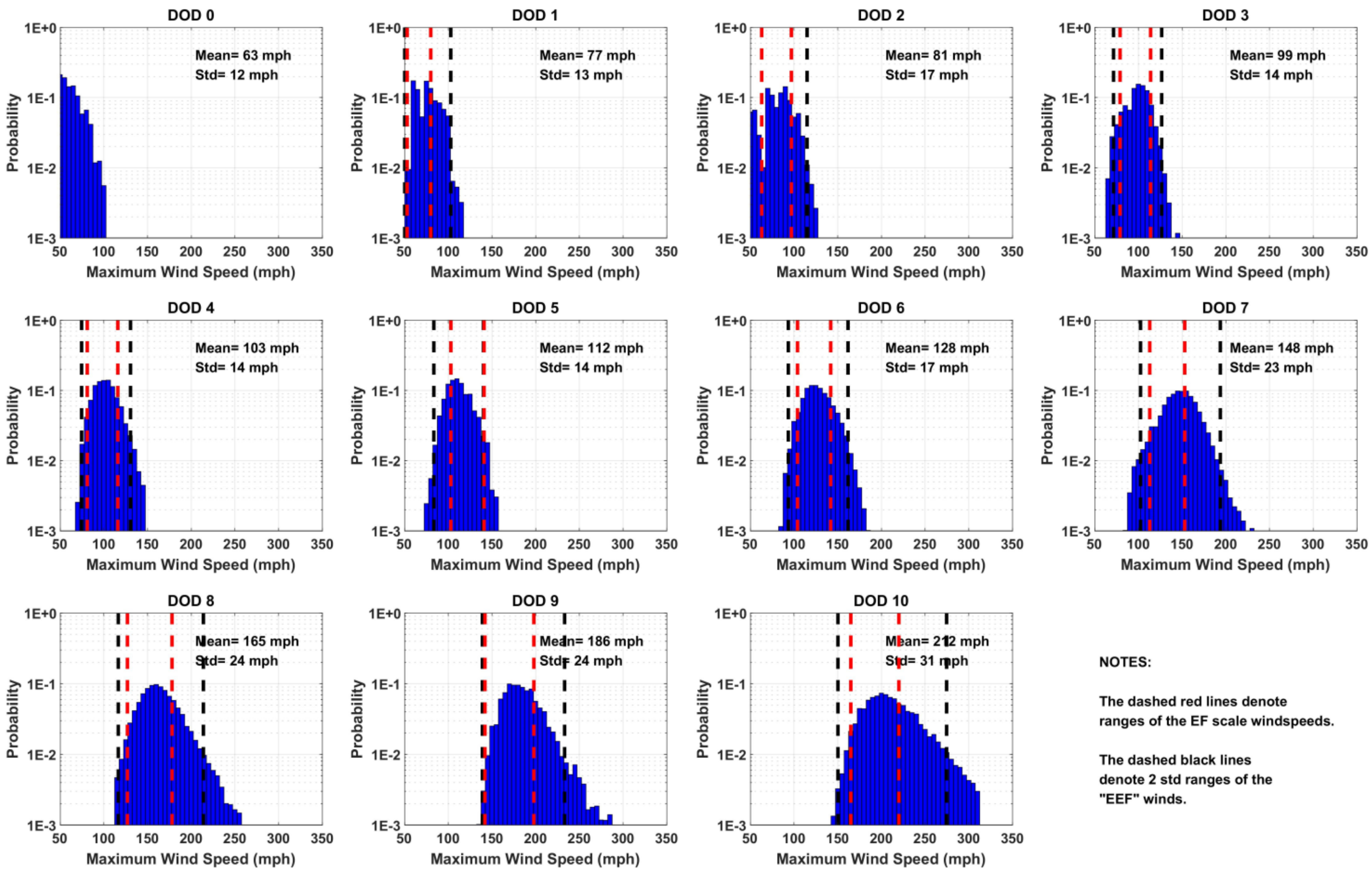

NOTES:

The dashed red lines denote ranges of the EF scale windspeeds.

The dashed black lines denote 2 std ranges of the "EEF" winds.

House 10: M6dH 1304H Epistemic Prior

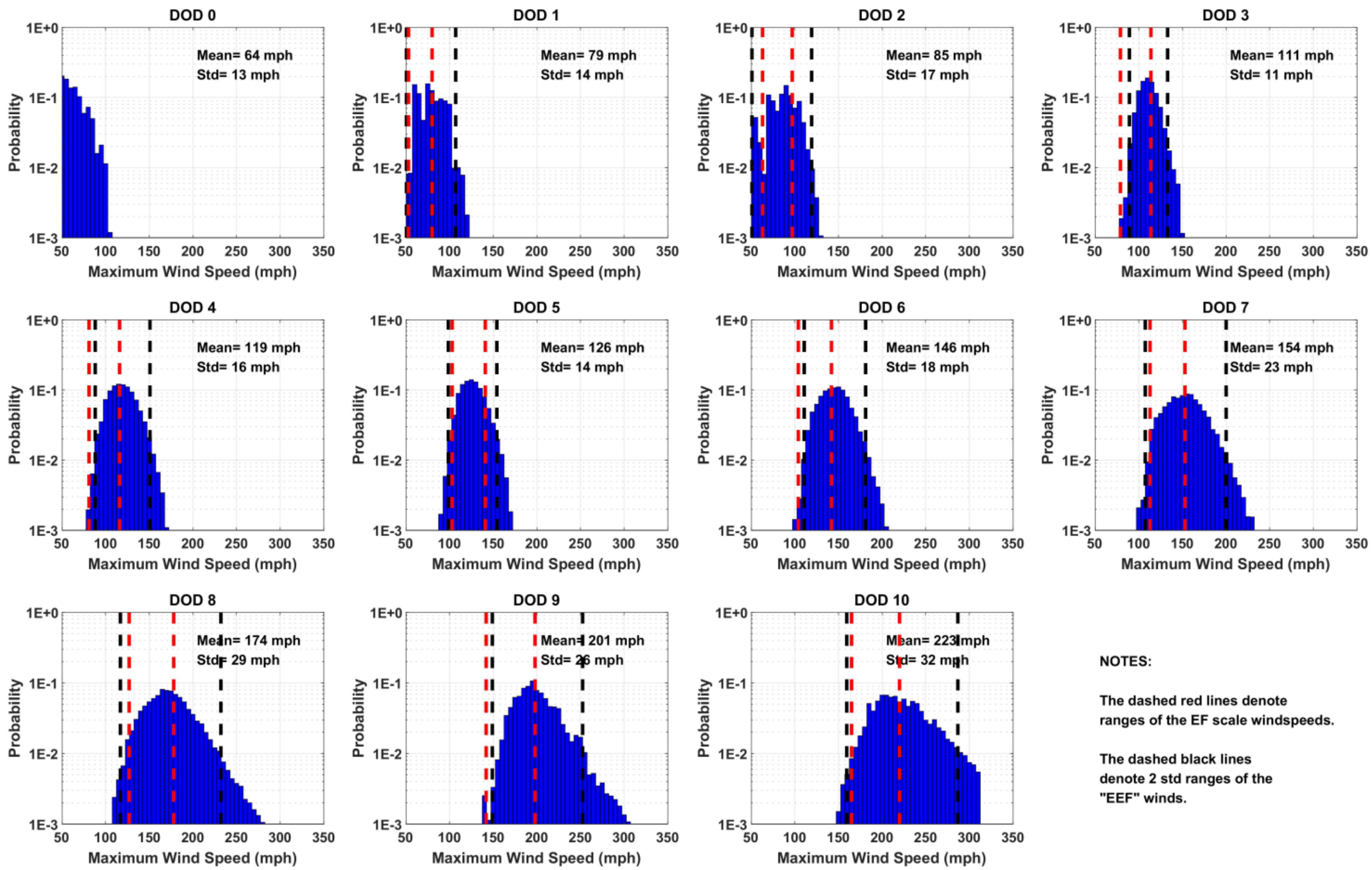

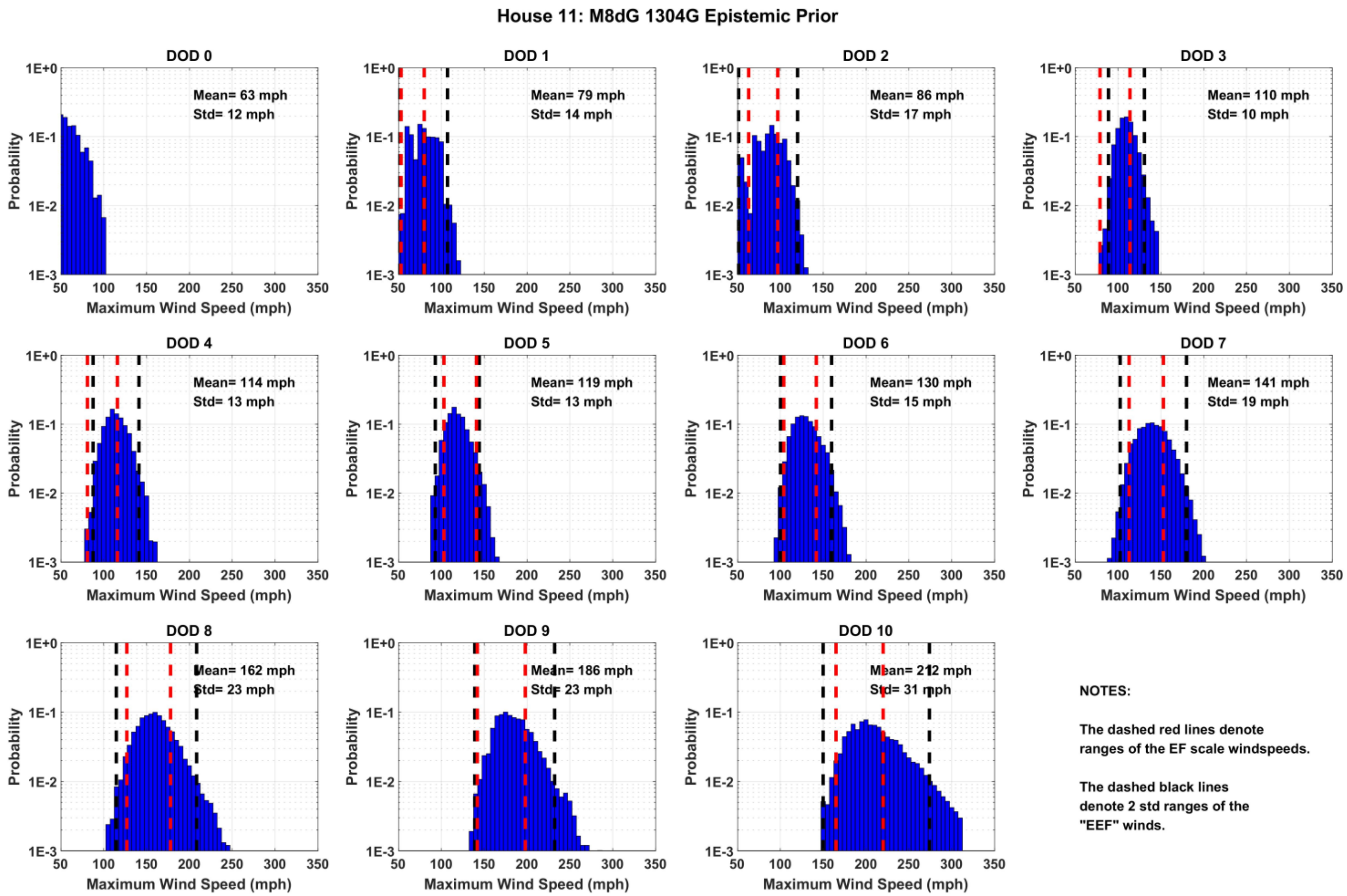
House 11: M8dG 1304G Epistemic Prior
DOD 0
Mean= 63 mph
Std= 12 mph
DOD 1
Mean= 79 mph
Std= 14 mph
DOD 2
Mean= 86 mph
Std= 17 mph
DOD 3
Mean= 110 mph
Std= 10 mph
DOD 4
Mean= 114 mph
Std= 13 mph
DOD 5
Mean= 119 mph
Std= 13 mph
DOD 6
Mean= 130 mph
Std= 15 mph
DOD 7
Mean= 141 mph
Std= 19 mph
DOD 8
Mean= 162 mph
Std= 23 mph
DOD 9
Mean= 186 mph
Std= 23 mph
DOD 10
Mean= 212 mph
Std= 31 mph
Probability
Maximum Wind Speed (mph)
1E+0
1E-1
1E-2
1E-3
50
100
150
200
250
300
350
NOTES:
The dashed red lines denote ranges of the EF scale windspeeds.
The dashed black lines denote 2 std ranges of the "EEF" winds.

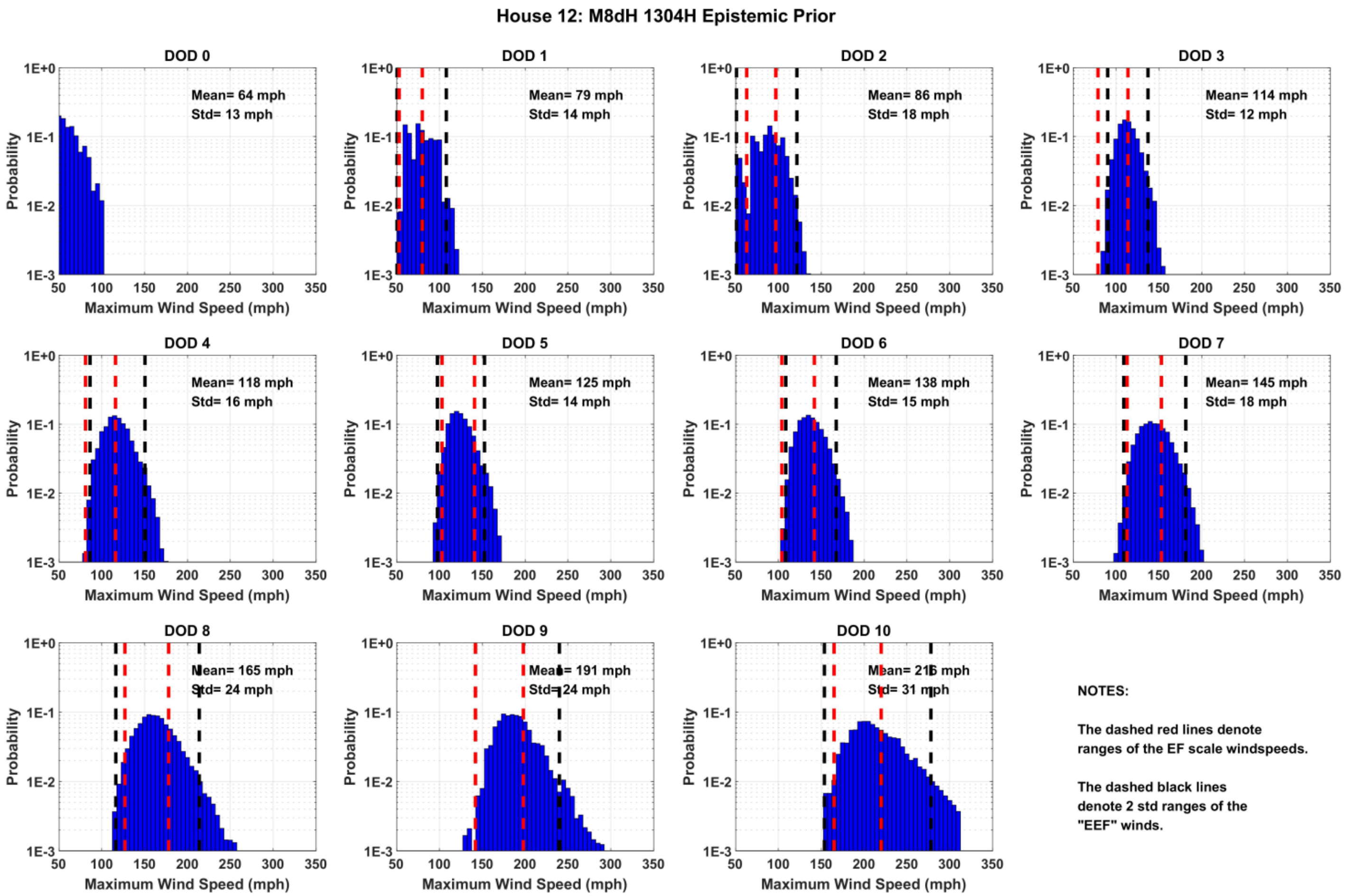

NOTES:

The dashed red lines denote ranges of the EF scale windspeeds.

The dashed black lines denote 2 std ranges of the "EEF" winds.

House 13: M6dBG 1304G Epistemic Prior

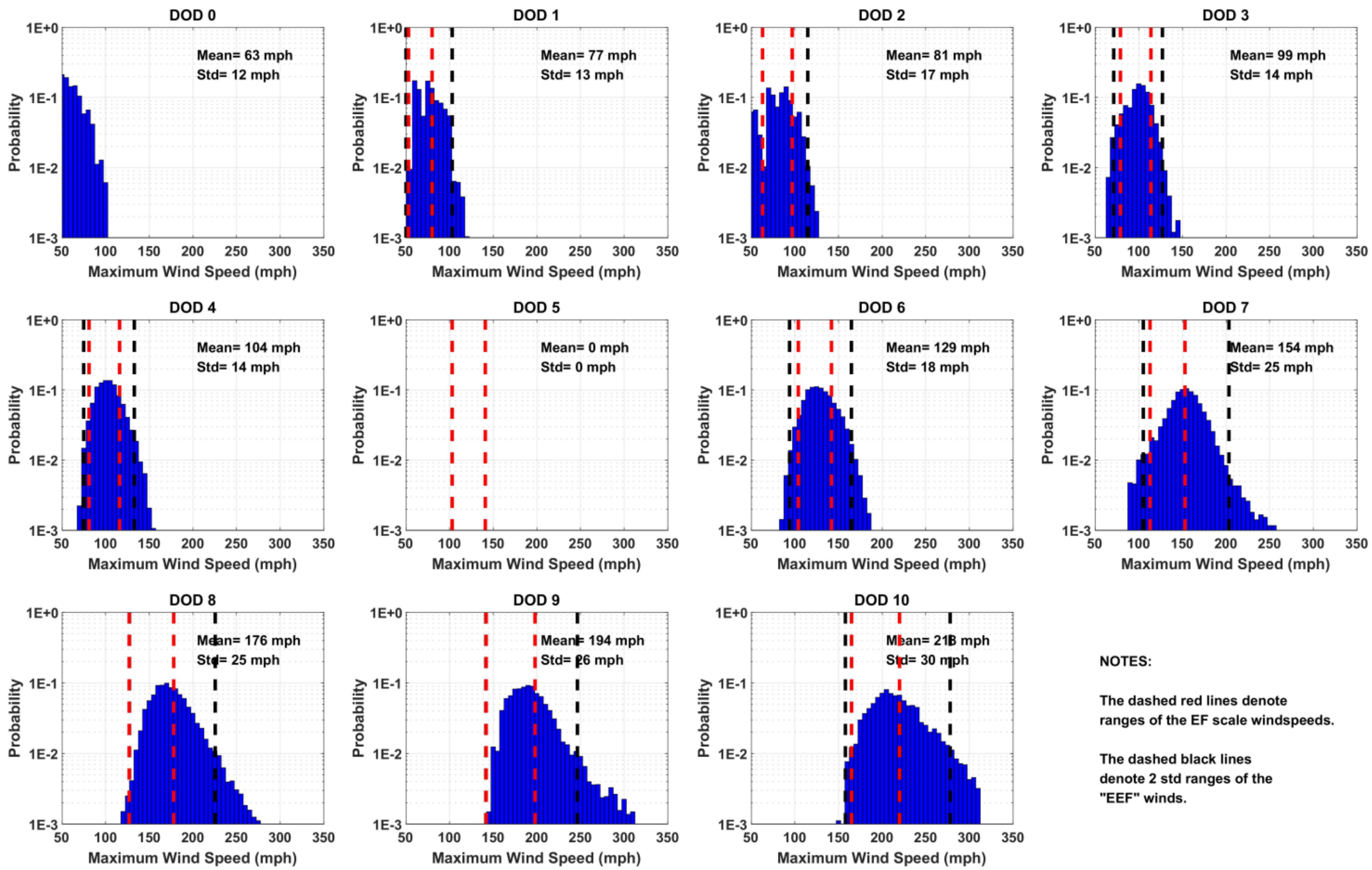

NOTES:

The dashed red lines denote ranges of the EF scale windspeeds.

The dashed black lines denote 2 std ranges of the "EEF" winds.

House 14: M6dBH 1304H Epistemic Prior

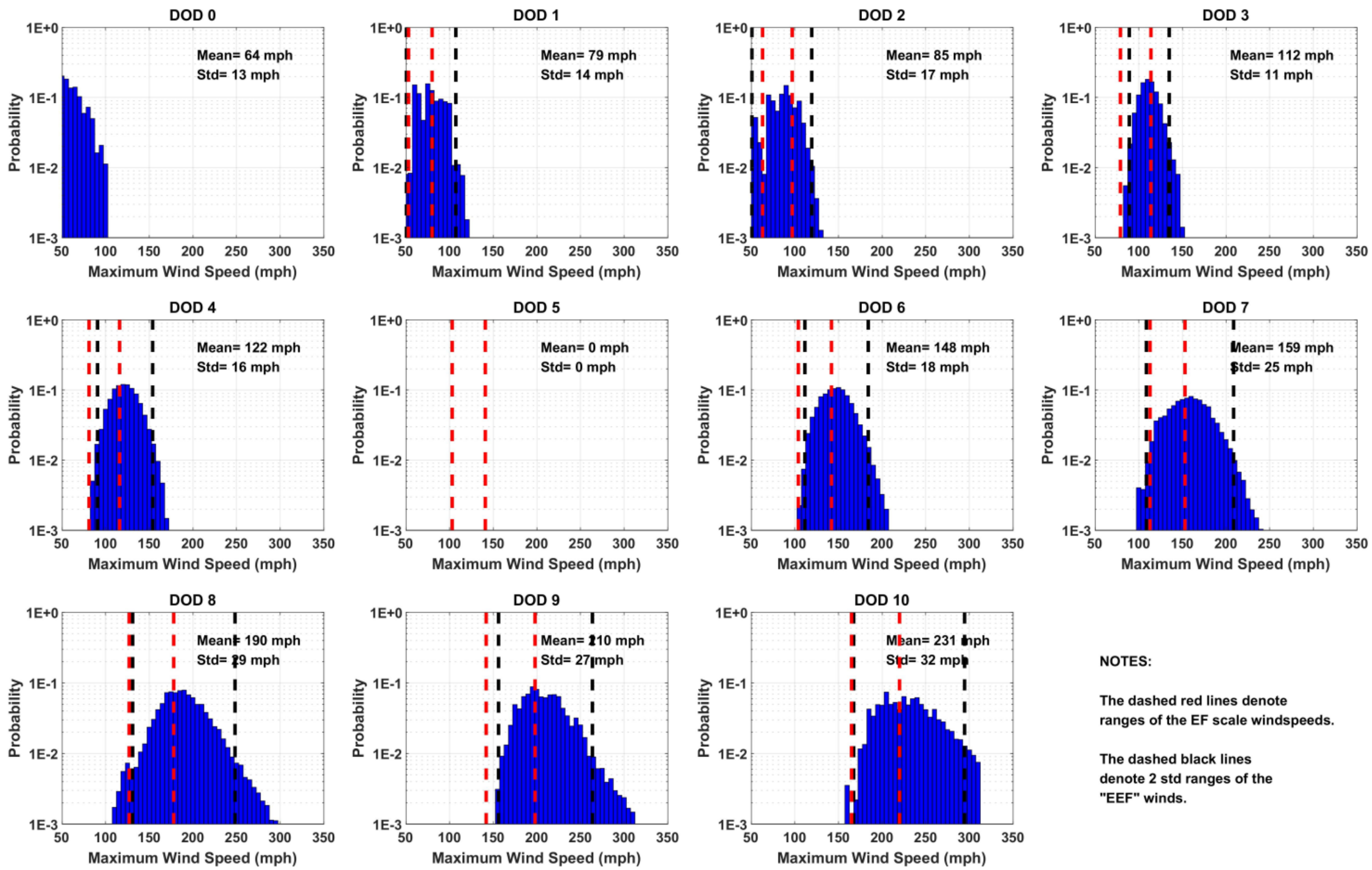

NOTES:

The dashed red lines denote ranges of the EF scale windspeeds.

The dashed black lines denote 2 std ranges of the "EEF" winds.

House 15: M8dBG 1304G Epistemic Prior

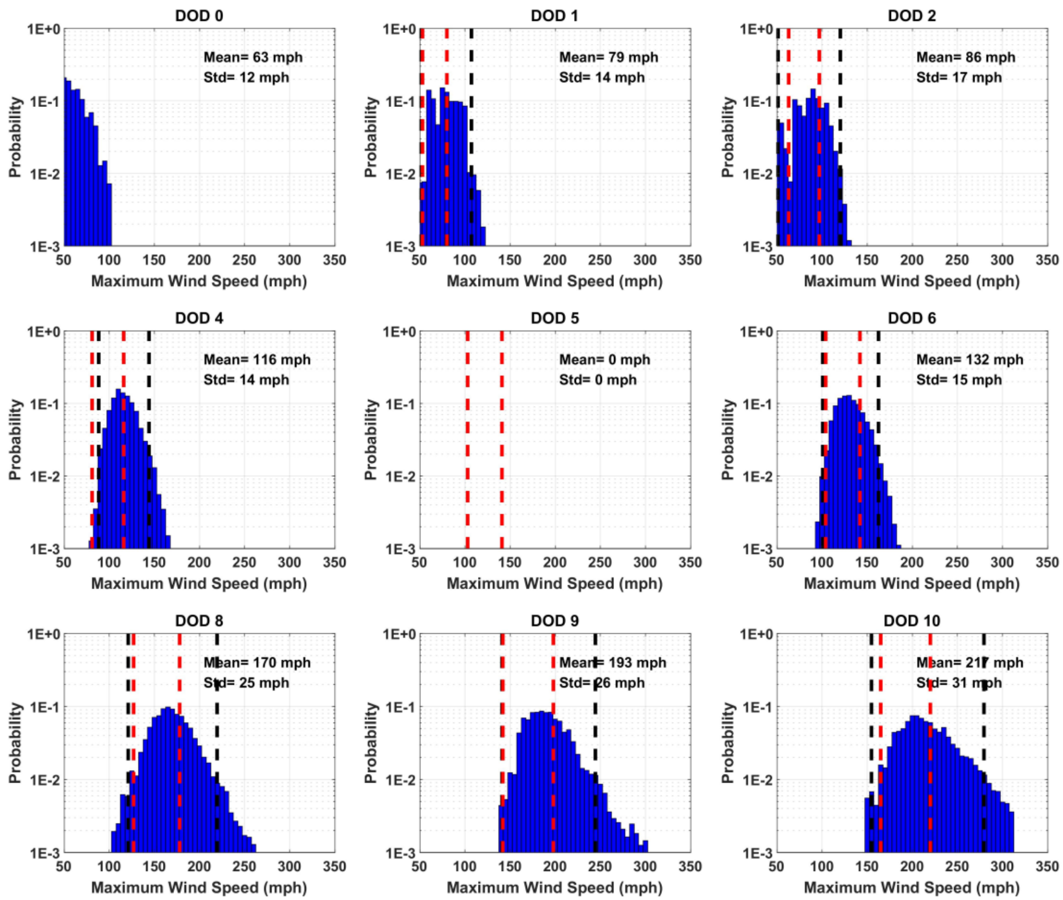

NOTES:

The dashed red lines denote ranges of the EF scale windspeeds.

The dashed black lines denote 2 std ranges of the "EEF" winds.

House 16: M8dBH 1304H Epistemic Prior

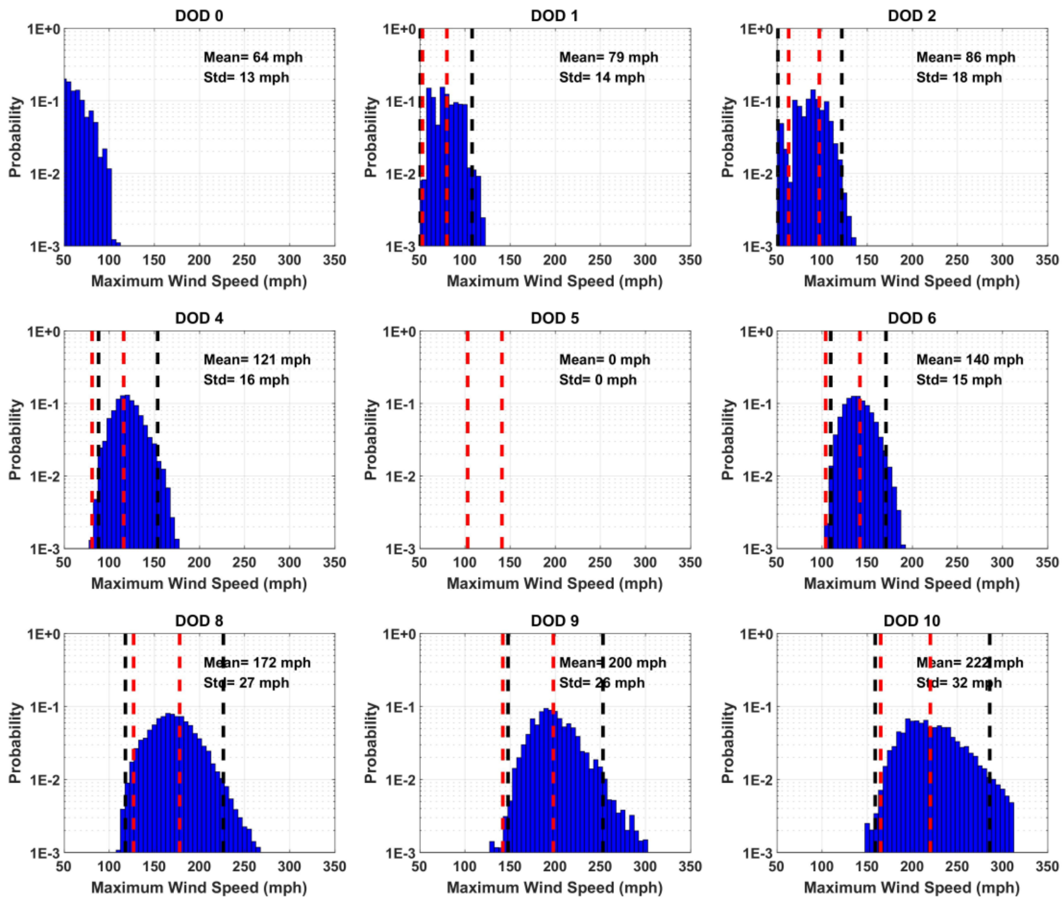

NOTES:

The dashed red lines denote ranges of the EF scale windspeeds.

The dashed black lines denote 2 std ranges of the "EEF" winds.

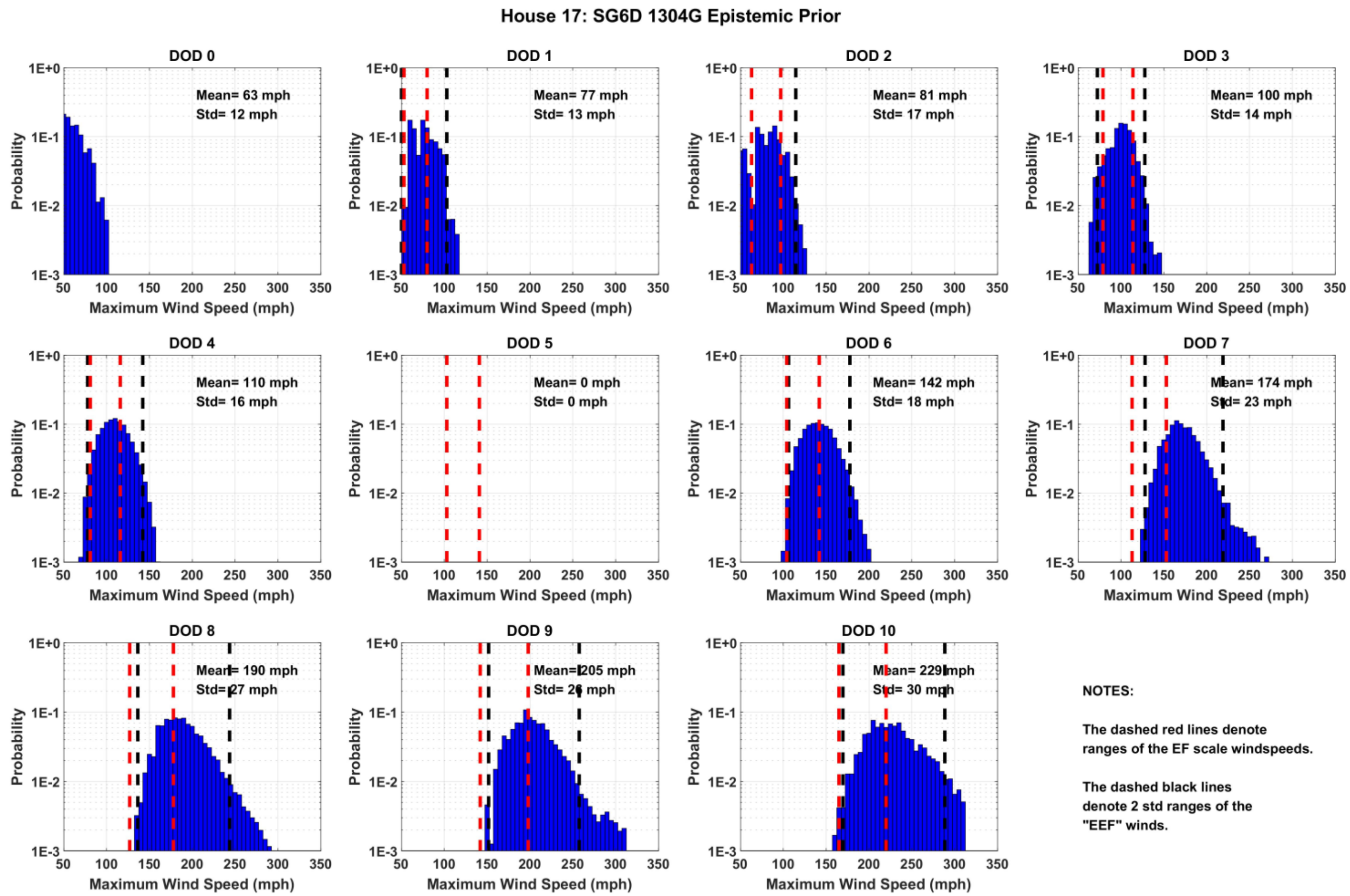
House 17: SG6D 1304G Epistemic Prior
DOD 0
Mean= 63 mph
Std= 12 mph
DOD 1
Mean= 77 mph
Std= 13 mph
DOD 2
Mean= 81 mph
Std= 17 mph
DOD 3
Mean= 100 mph
Std= 14 mph
DOD 4
Mean= 110 mph
Std= 16 mph
DOD 5
Mean= 0 mph
Std= 0 mph
DOD 6
Mean= 142 mph
Std= 18 mph
DOD 7
Mean= 174 mph
Std= 23 mph
DOD 8
Mean= 190 mph
Std= 27 mph
DOD 9
Mean= 205 mph
DOD 10
Mean= 229 mph
Std= 30 mph
Probability
Maximum Wind Speed (mph)
NOTES:
The dashed red lines denote ranges of the EF scale windspeeds.
The dashed black lines denote 2 std ranges of the "EEF" winds.

House 18: SH6D 1304H Epistemic Prior

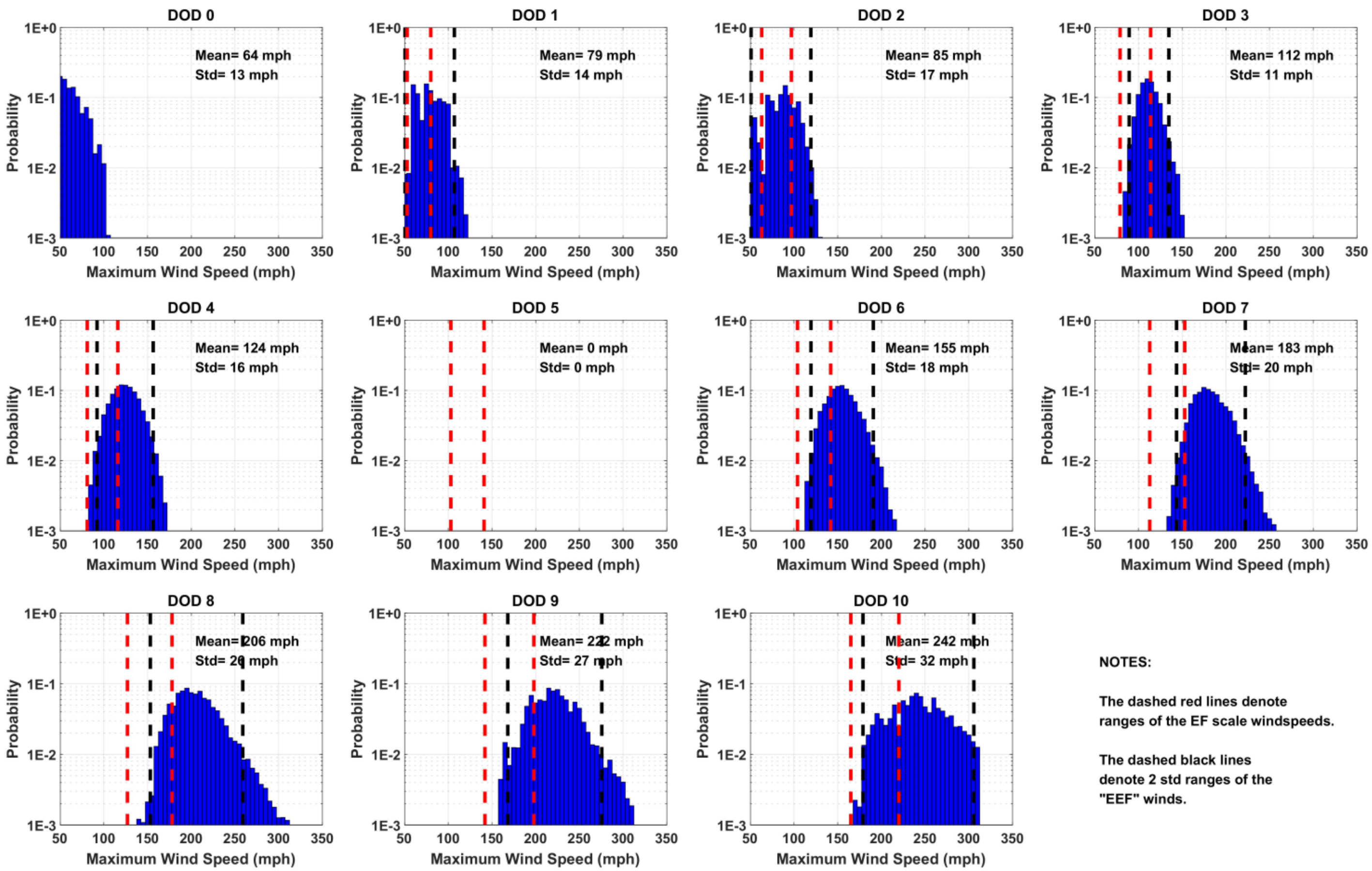

House 19: SG 1304G Epistemic Prior

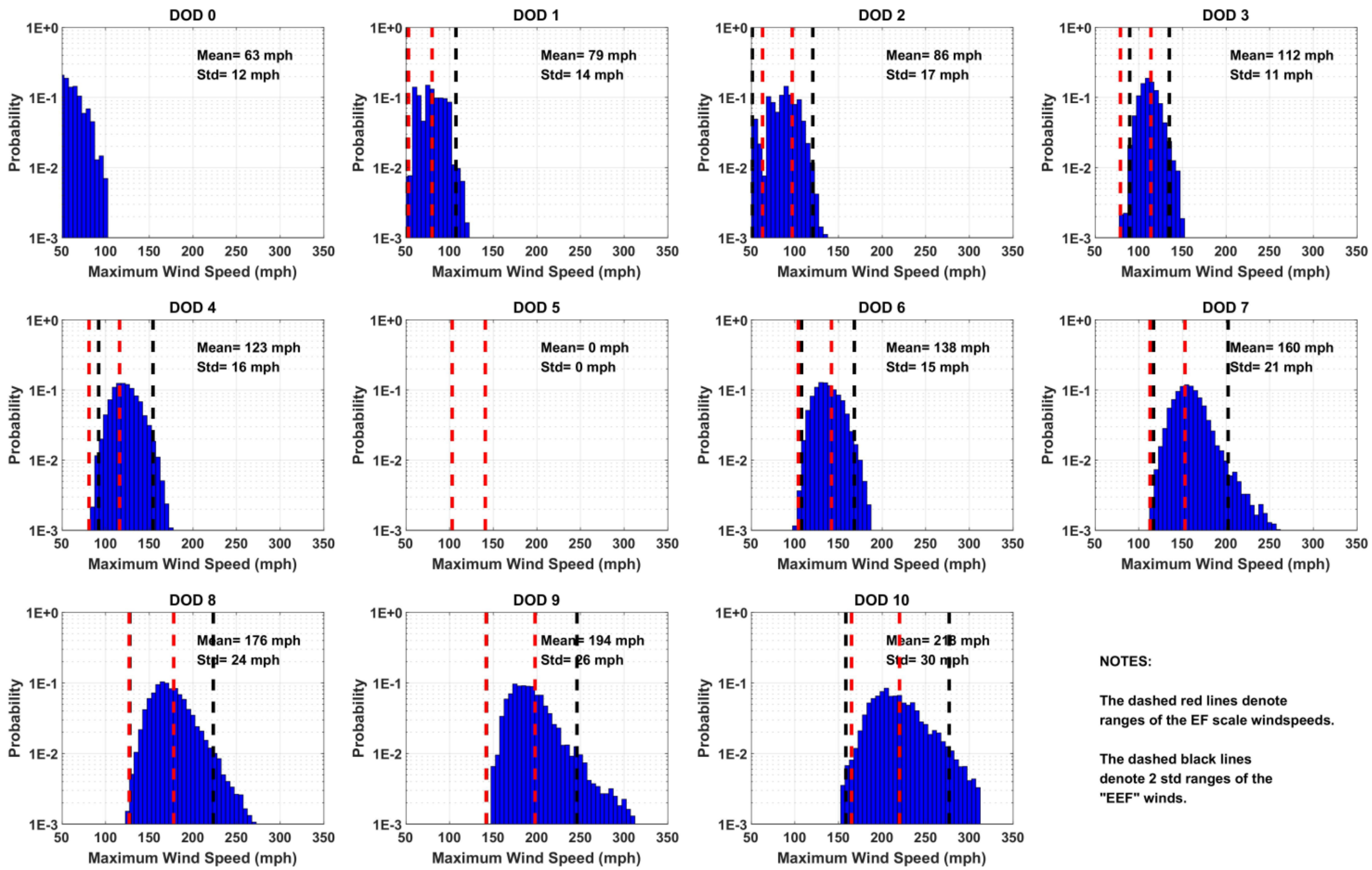

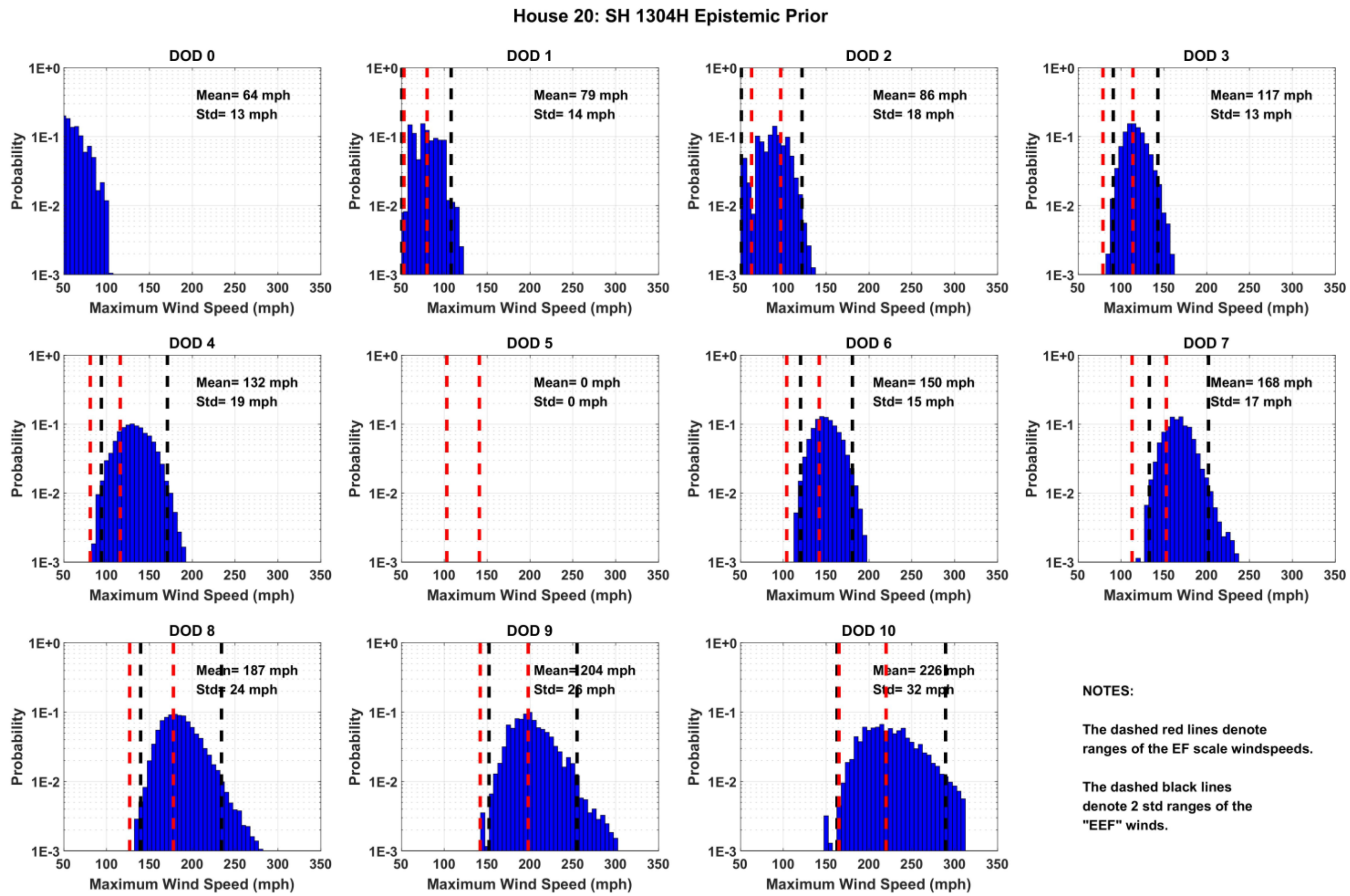
House 20: SH 1304H Epistemic Prior
DOD 0
Mean= 64 mph
Std= 13 mph
DOD 1
Mean= 79 mph
Std= 14 mph
DOD 2
Mean= 86 mph
Std= 18 mph
DOD 3
Mean= 117 mph
Std= 13 mph
DOD 4
Mean= 132 mph
Std= 19 mph
DOD 5
Mean= 0 mph
Std= 0 mph
DOD 6
Mean= 150 mph
Std= 15 mph
DOD 7
Mean= 168 mph
Std= 17 mph
DOD 8
Mean= 187 mph
Std= 24 mph
DOD 9
Mean= 204 mph
Std= 26 mph
DOD 10
Mean= 226 mph
Std= 32 mph
Probability
Maximum Wind Speed (mph)
NOTES:
The dashed red lines denote ranges of the EF scale windspeeds.
The dashed black lines denote 2 std ranges of the "EEF" winds.

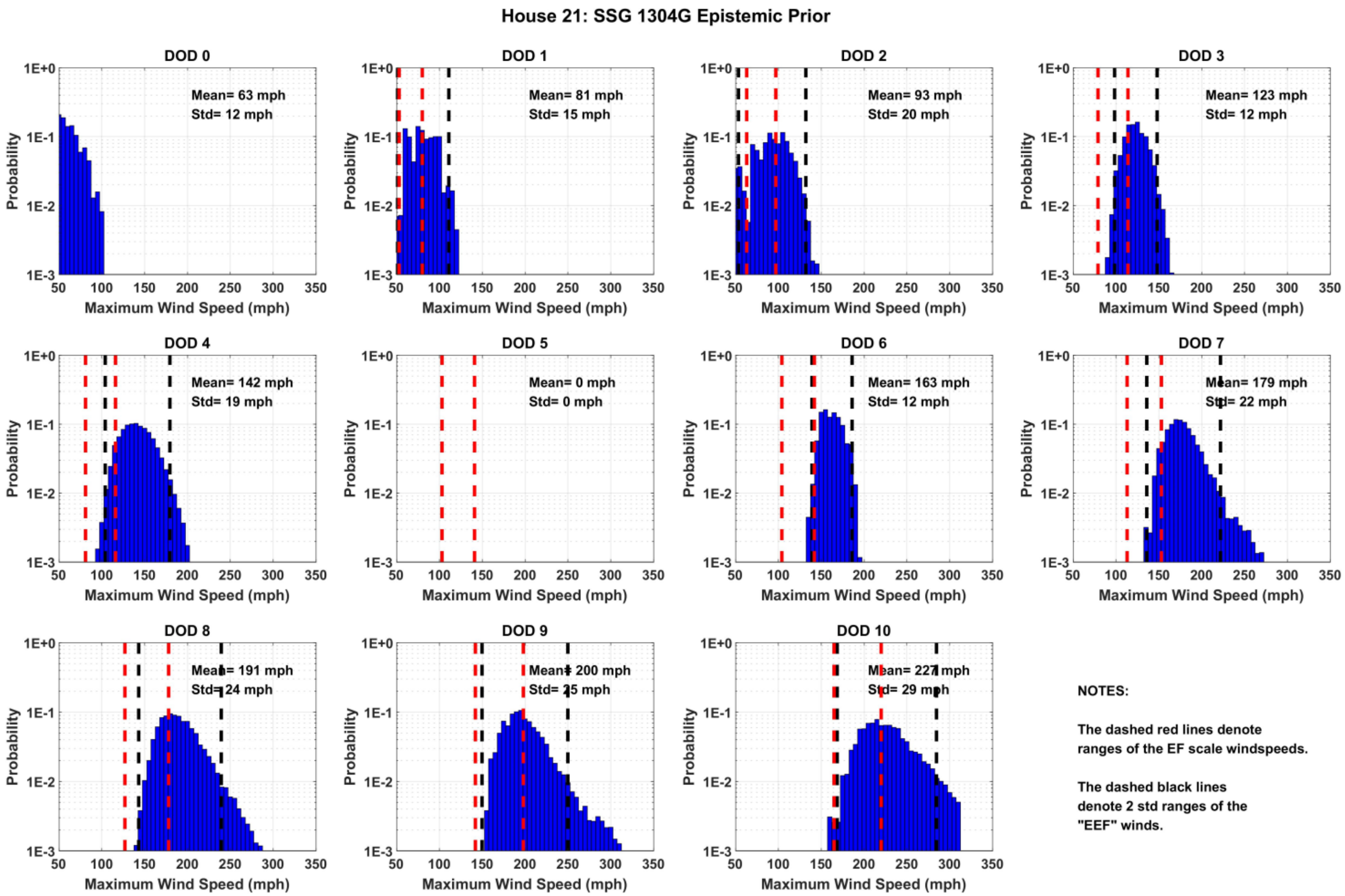
House 21: SSG 1304G Epistemic Prior
DOD 0
Mean= 63 mph
Std= 12 mph
DOD 1
Mean= 81 mph
Std= 15 mph
DOD 2
Mean= 93 mph
Std= 20 mph
DOD 3
Mean= 123 mph
Std= 12 mph
DOD 4
Mean= 142 mph
Std= 19 mph
DOD 5
Mean= 0 mph
Std= 0 mph
DOD 6
Mean= 163 mph
Std= 12 mph
DOD 7
Mean= 179 mph
Std= 22 mph
DOD 8
Mean= 191 mph
Std= 24 mph
DOD 9
Mean= 200 mph
Std= 25 mph
DOD 10
Mean= 227 mph
Std= 29 mph
Probability
Maximum Wind Speed (mph)
NOTES:
The dashed red lines denote ranges of the EF scale windspeeds.
The dashed black lines denote 2 std ranges of the "EEF" winds.

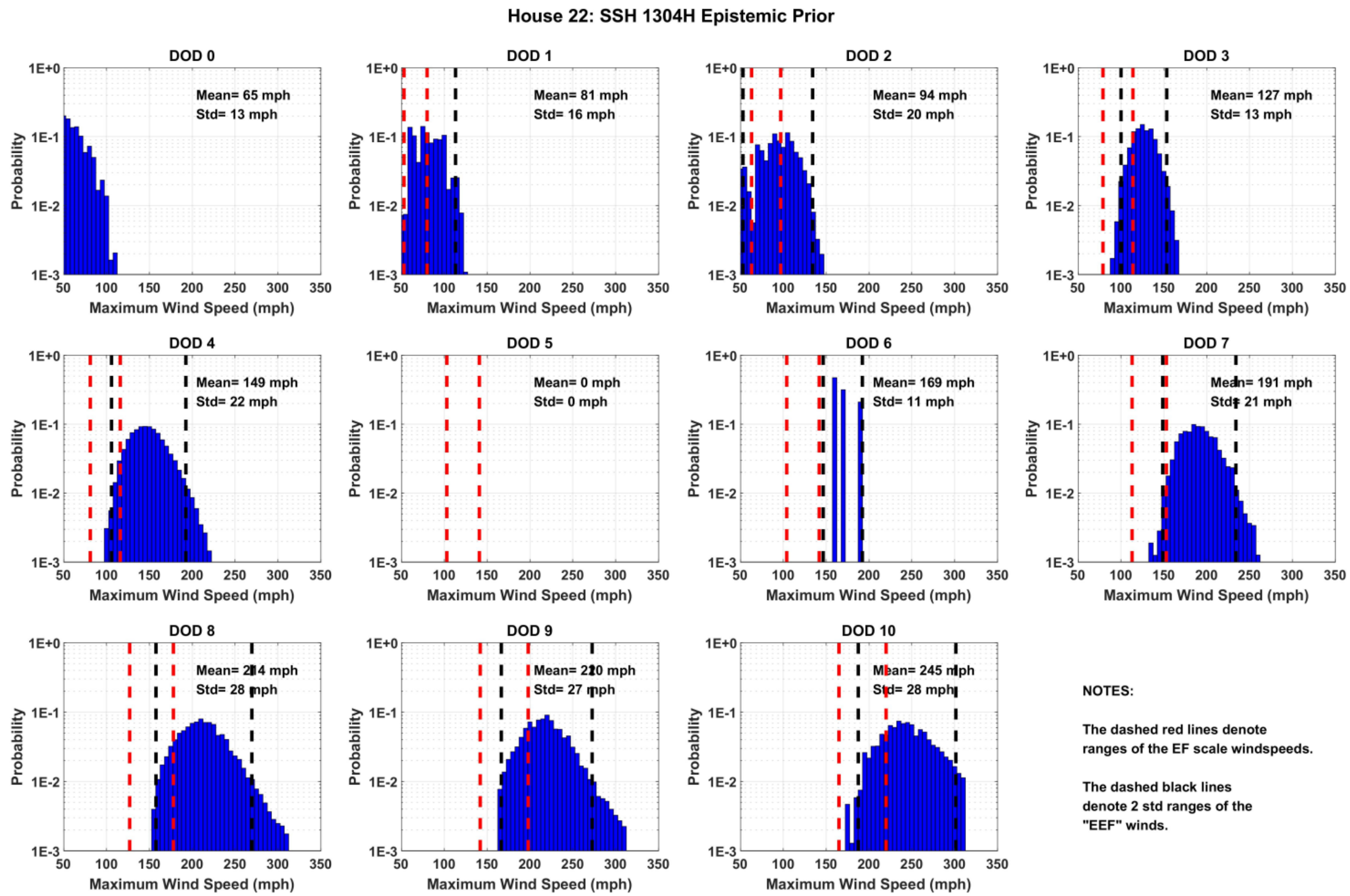
House 22: SSH 1304H Epistemic Prior
DOD 0
Mean= 65 mph
Std= 13 mph
DOD 1
Mean= 81 mph
Std= 16 mph
DOD 2
Mean= 94 mph
Std= 20 mph
DOD 3
Mean= 127 mph
Std= 13 mph
DOD 4
Mean= 149 mph
Std= 22 mph
DOD 5
Mean= 0 mph
Std= 0 mph
DOD 6
Mean= 169 mph
Std= 11 mph
DOD 7
Mean= 191 mph
Std= 21 mph
DOD 8
Std= 28 mph
DOD 9
Std= 27 mph
DOD 10
Mean= 245 mph
Std= 28 mph
Probability
Maximum Wind Speed (mph)
NOTES:
The dashed red lines denote ranges of the EF scale windspeeds.
The dashed black lines denote 2 std ranges of the "EEF" winds.

House 23: W6dG 0014G Epistemic Prior

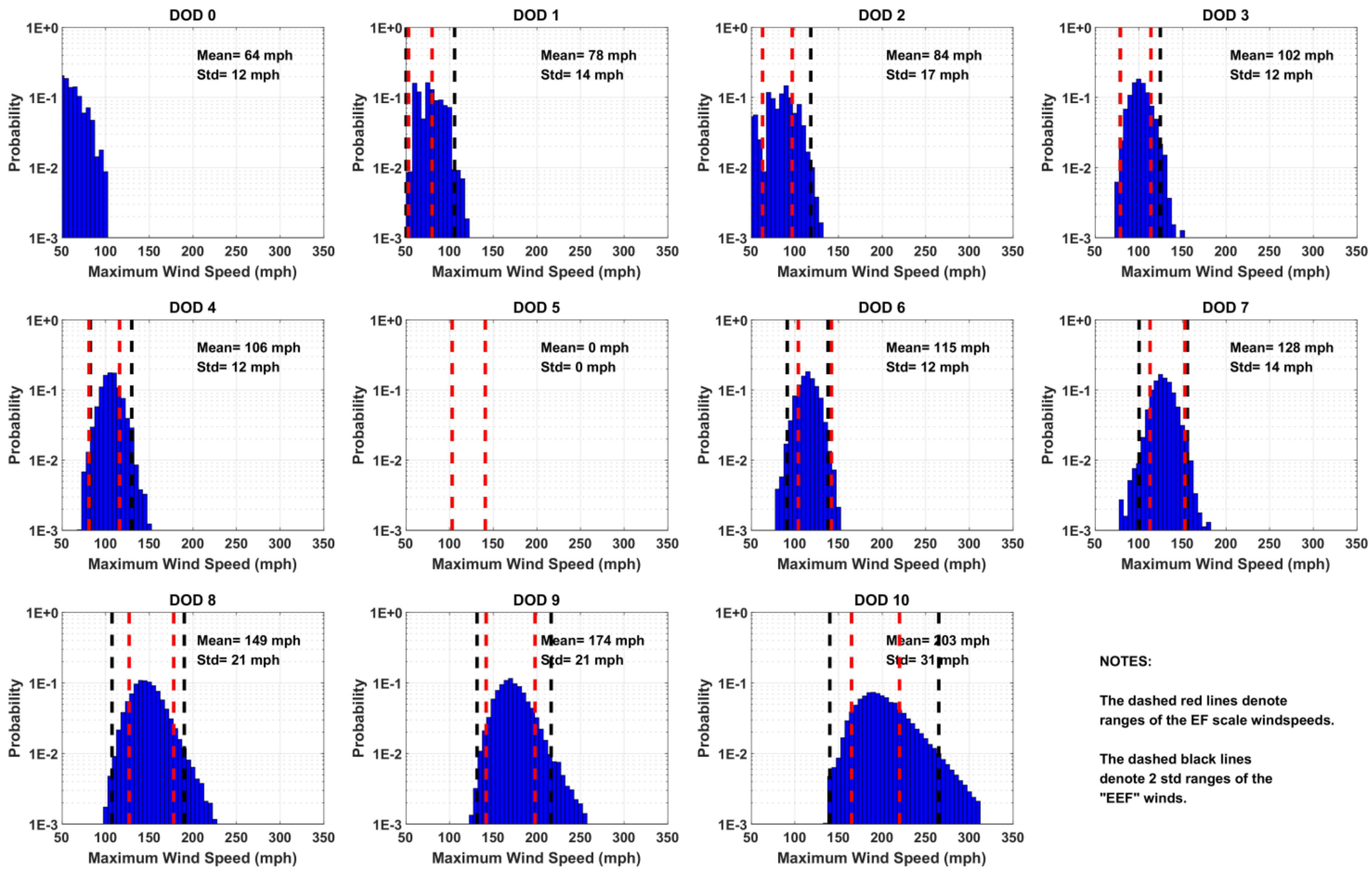

NOTES:

The dashed red lines denote ranges of the EF scale windspeeds.

The dashed black lines denote 2 std ranges of the "EEF" winds.

House 24: W6dH 0014H Epistemic Prior

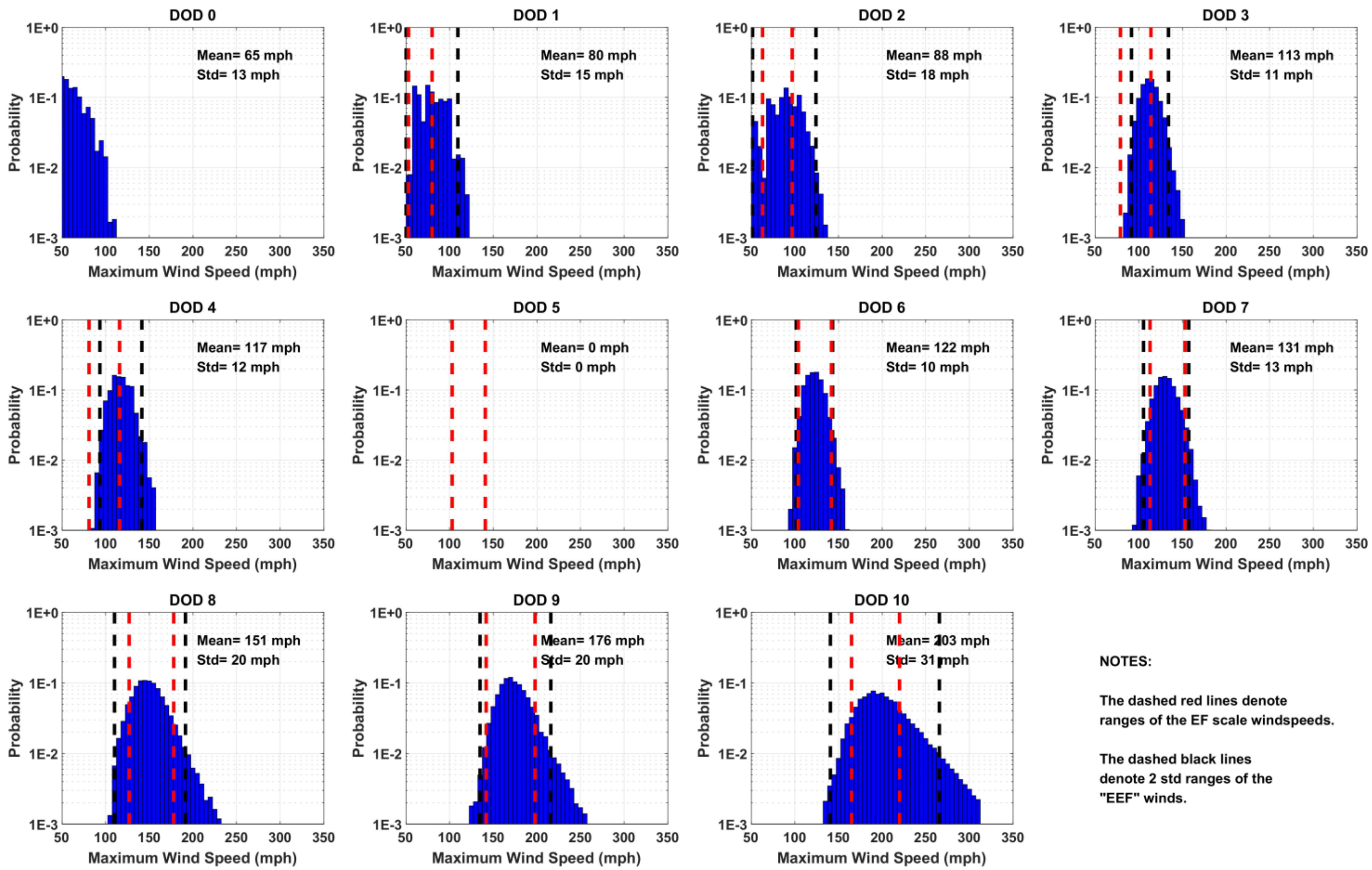

House 25: W8dG 0014G Epistemic Prior

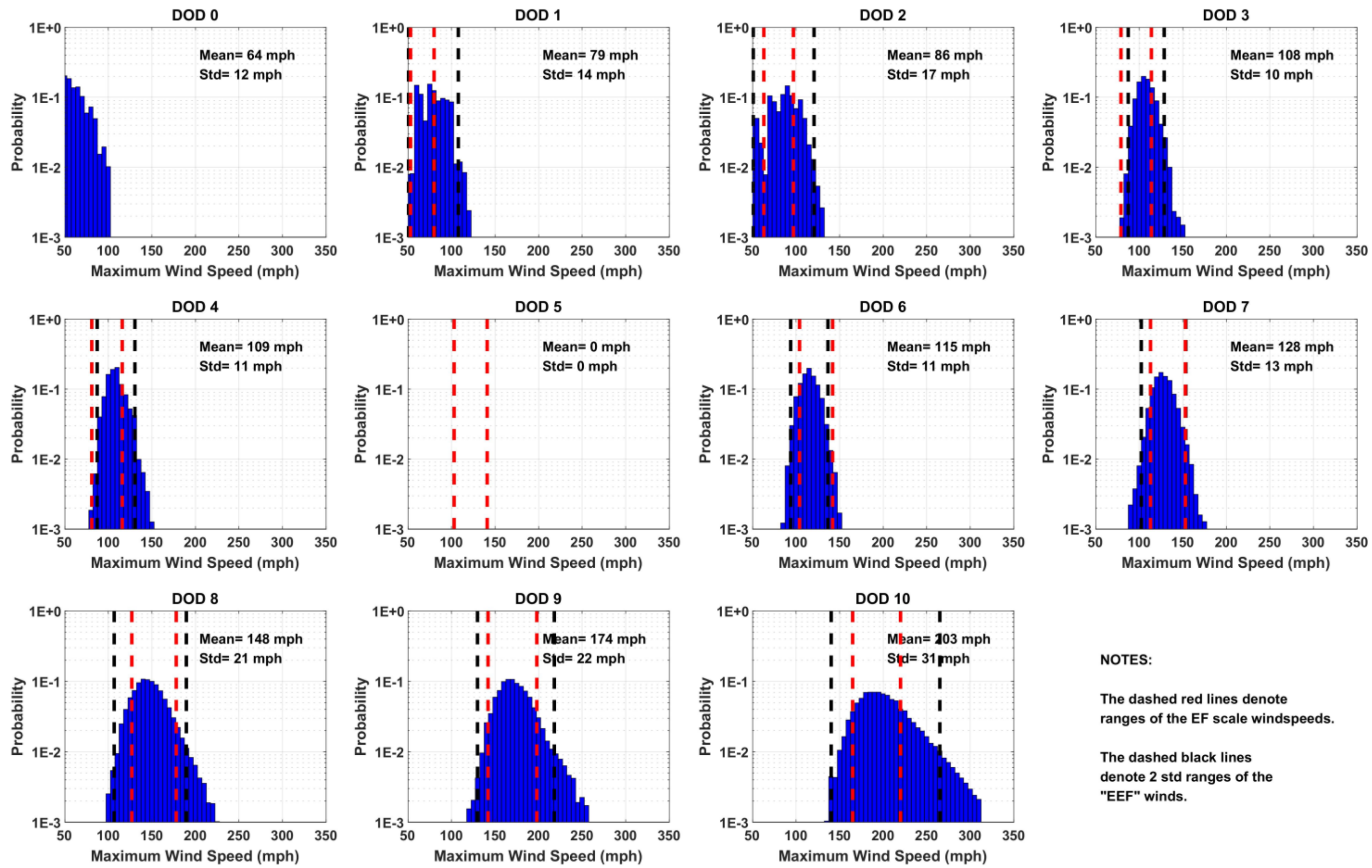

NOTES:

The dashed red lines denote ranges of the EF scale windspeeds.

The dashed black lines denote 2 std ranges of the "EEF" winds.

House 26: W8dH 0014H Epistemic Prior

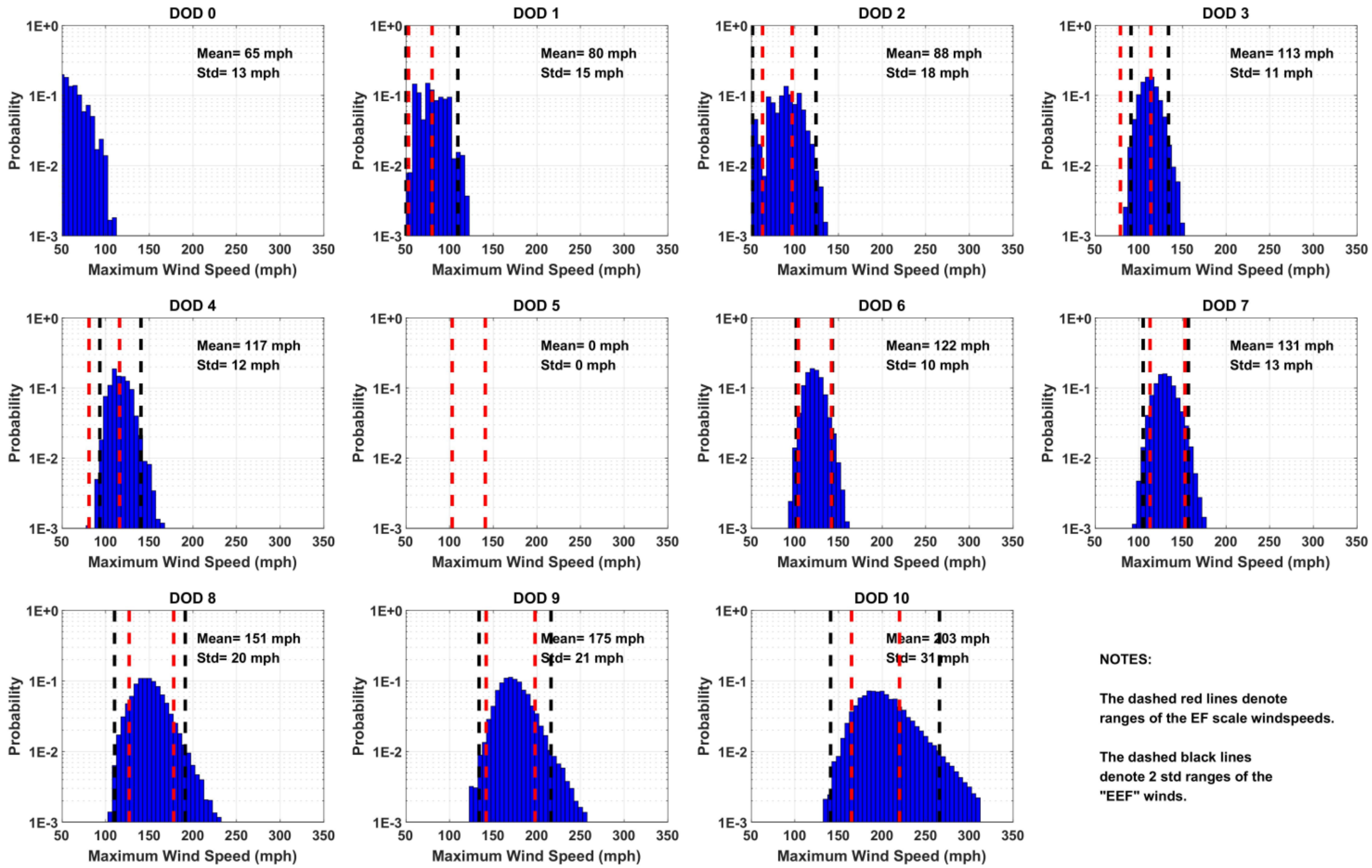

NOTES:

The dashed red lines denote ranges of the EF scale windspeeds.

The dashed black lines denote 2 std ranges of the "EEF" winds.

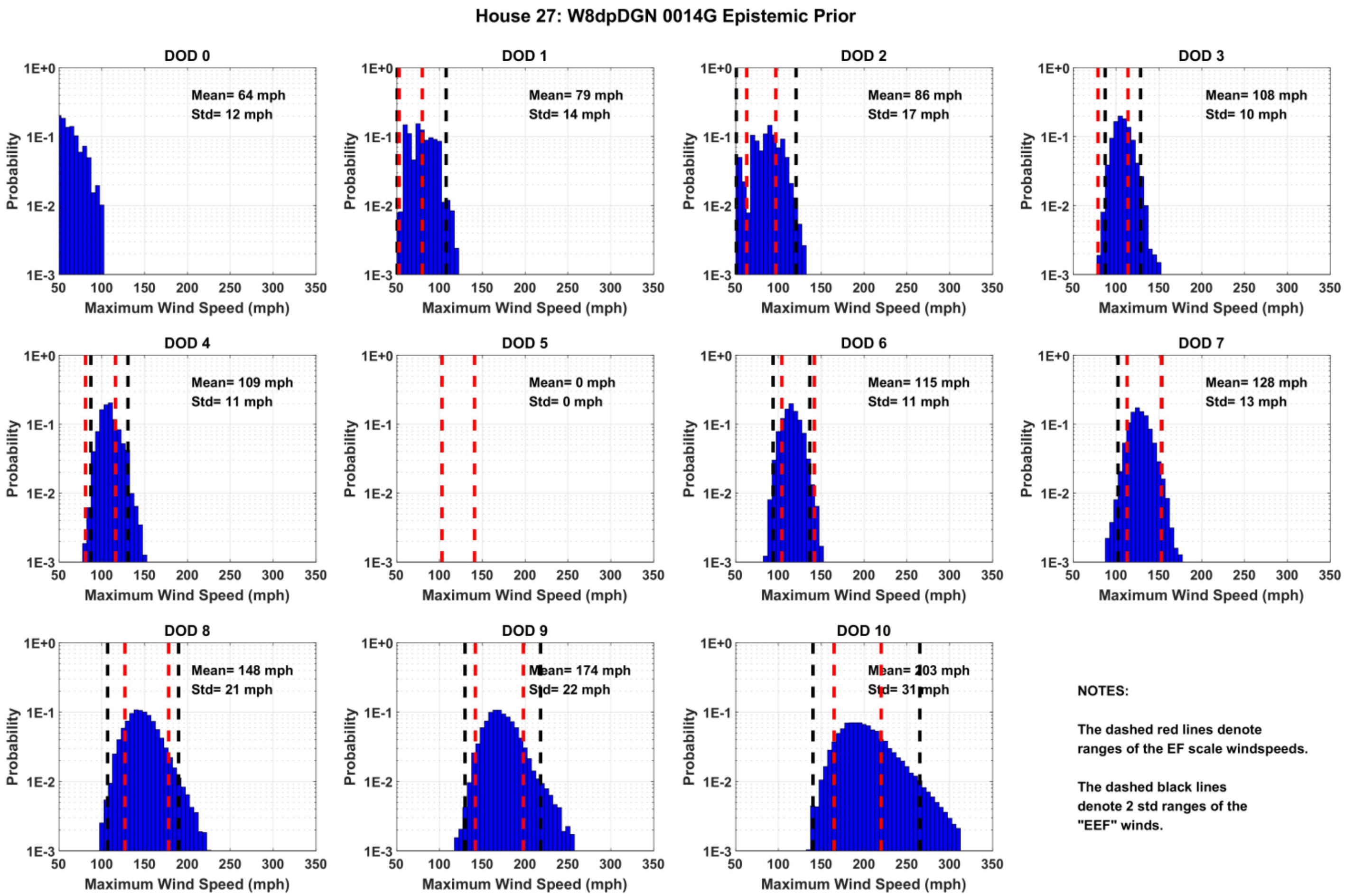
House 27: W8dpDGN 0014G Epistemic Prior
DOD 0
Mean= 64 mph
Std= 12 mph
DOD 1
Mean= 79 mph
Std= 14 mph
DOD 2
Mean= 86 mph
Std= 17 mph
DOD 3
Mean= 108 mph
Std= 10 mph
DOD 4
Mean= 109 mph
Std= 11 mph
DOD 5
Mean= 0 mph
Std= 0 mph
DOD 6
Mean= 115 mph
Std= 11 mph
DOD 7
Mean= 128 mph
Std= 13 mph
DOD 8
Mean= 148 mph
Std= 21 mph
DOD 9
Mean= 174 mph
Std= 22 mph
DOD 10
Mean= 203 mph
Std= 31 mph
Probability
1E+0
1E-1
1E-2
1E-3
Maximum Wind Speed (mph)
50
100
150
200
250
300
350
NOTES:
The dashed red lines denote ranges of the EF scale windspeeds.
The dashed black lines denote 2 std ranges of the "EEF" winds.

House 28: W8dpDHN 0014H Epistemic Prior

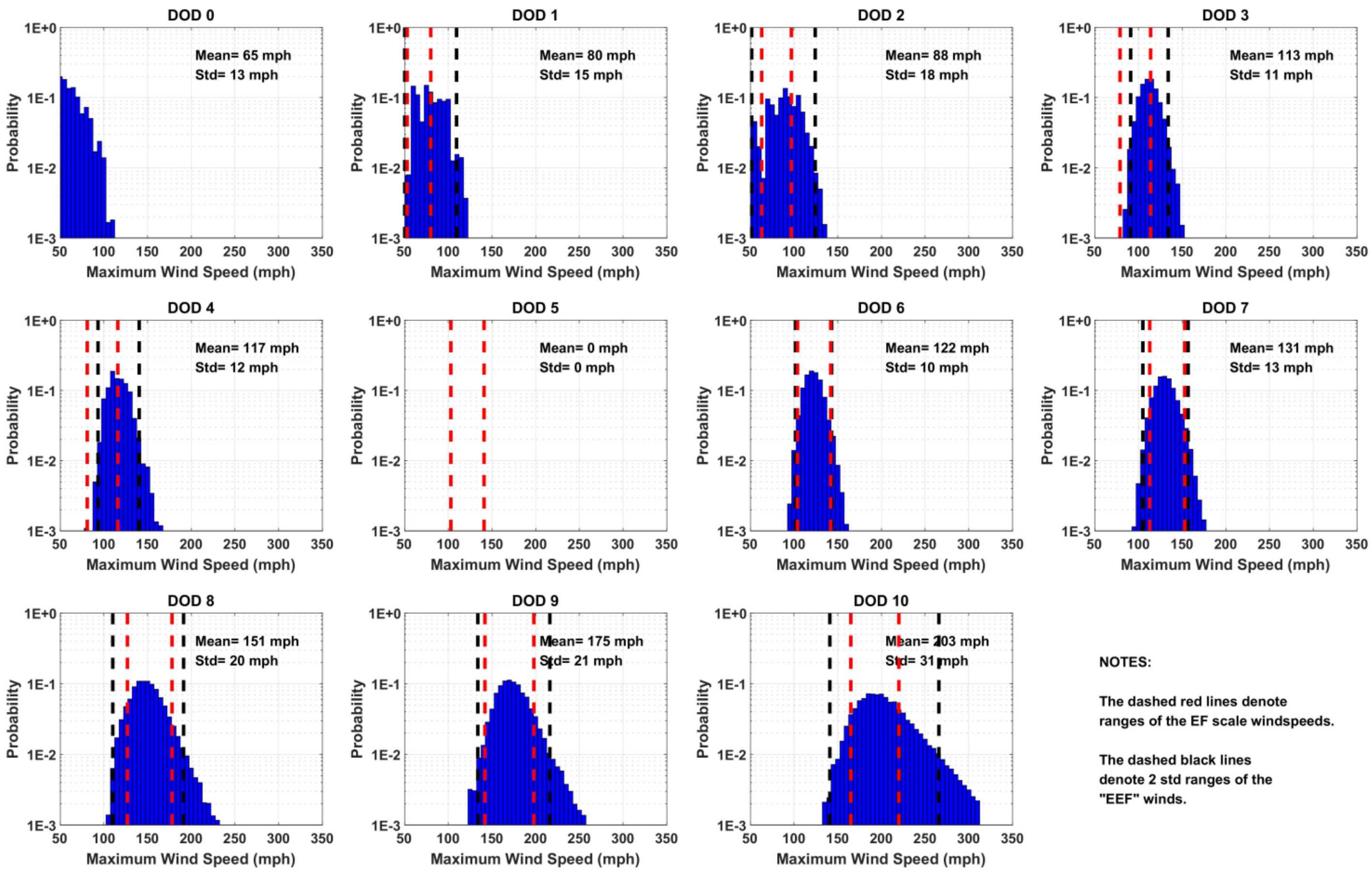

NOTES:

The dashed red lines denote ranges of the EF scale windspeeds.

The dashed black lines denote 2 std ranges of the "EEF" winds.

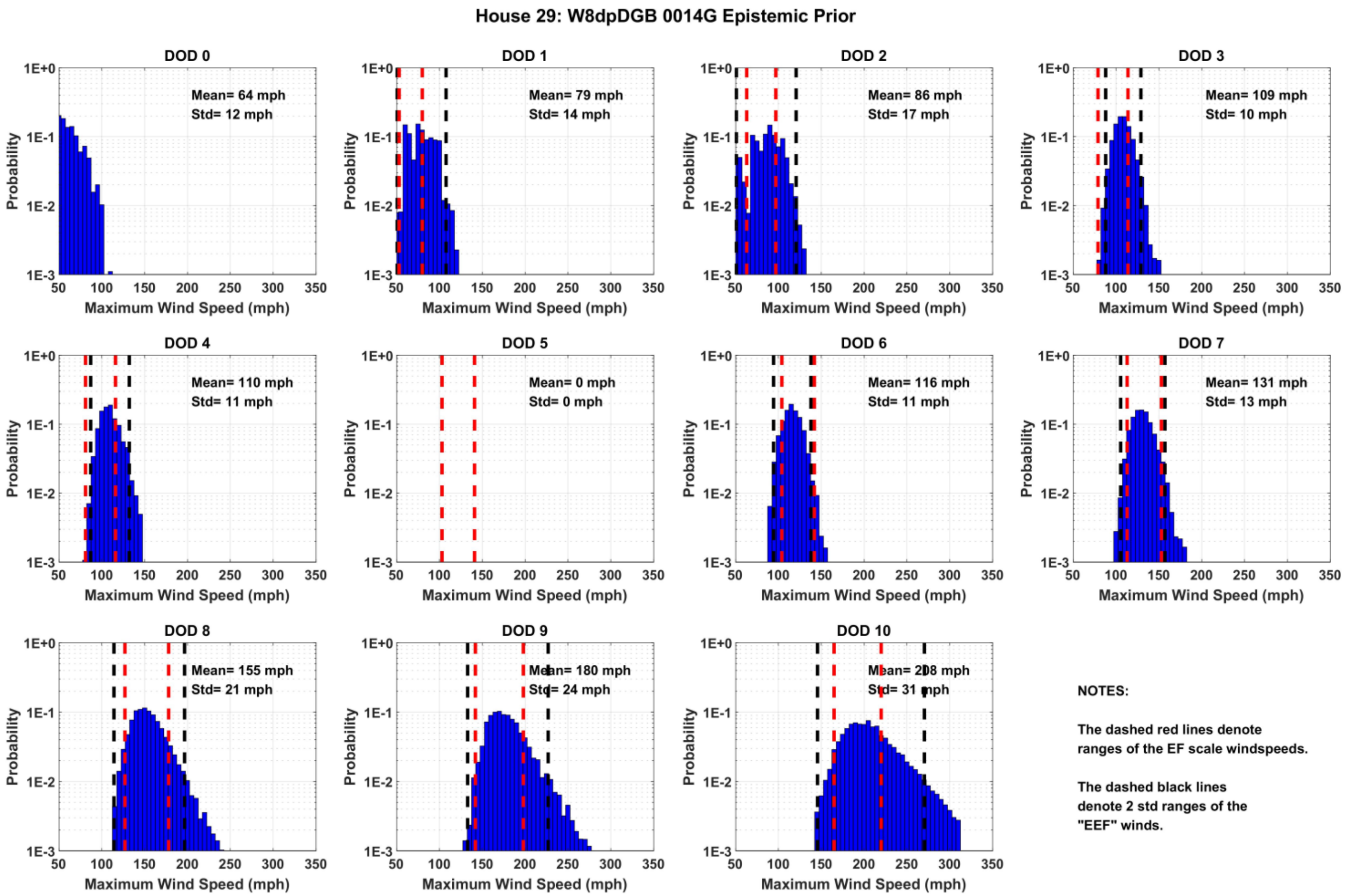
House 29: W8dpDGB 0014G Epistemic Prior
DOD 0
Mean= 64 mph
Std= 12 mph
DOD 1
Mean= 79 mph
Std= 14 mph
DOD 2
Mean= 86 mph
Std= 17 mph
DOD 3
Mean= 109 mph
Std= 10 mph
DOD 4
Mean= 110 mph
Std= 11 mph
DOD 5
Mean= 0 mph
Std= 0 mph
DOD 6
Mean= 116 mph
Std= 11 mph
DOD 7
Mean= 131 mph
Std= 13 mph
DOD 8
Mean= 155 mph
Std= 21 mph
DOD 9
Mean= 180 mph
Std= 24 mph
DOD 10
Mean= 208 mph
Std= 31 mph
Probability
Maximum Wind Speed (mph)
NOTES:
The dashed red lines denote ranges of the EF scale windspeeds.
The dashed black lines denote 2 std ranges of the "EEF" winds.

House 30: W8dpDHB 0014H Epistemic Prior

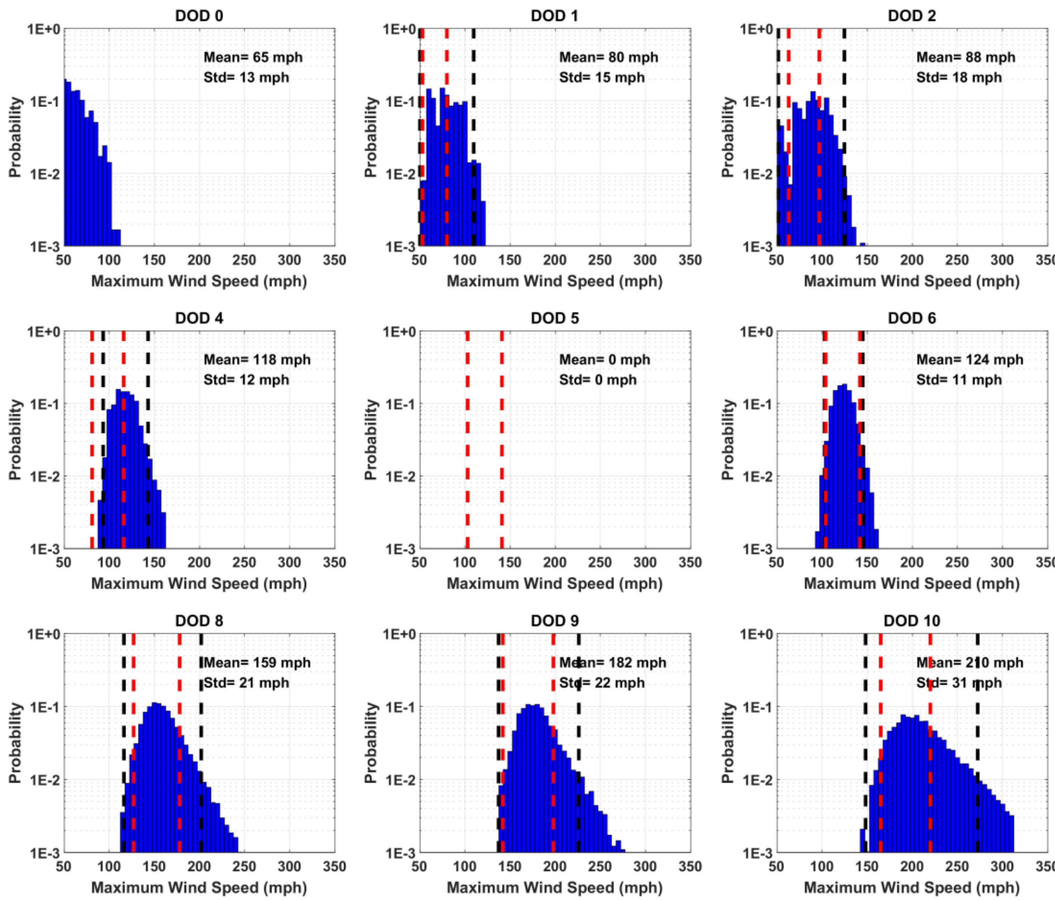

NOTES:

The dashed red lines denote ranges of the EF scale windspeeds.

The dashed black lines denote 2 std ranges of the "EEF" winds.

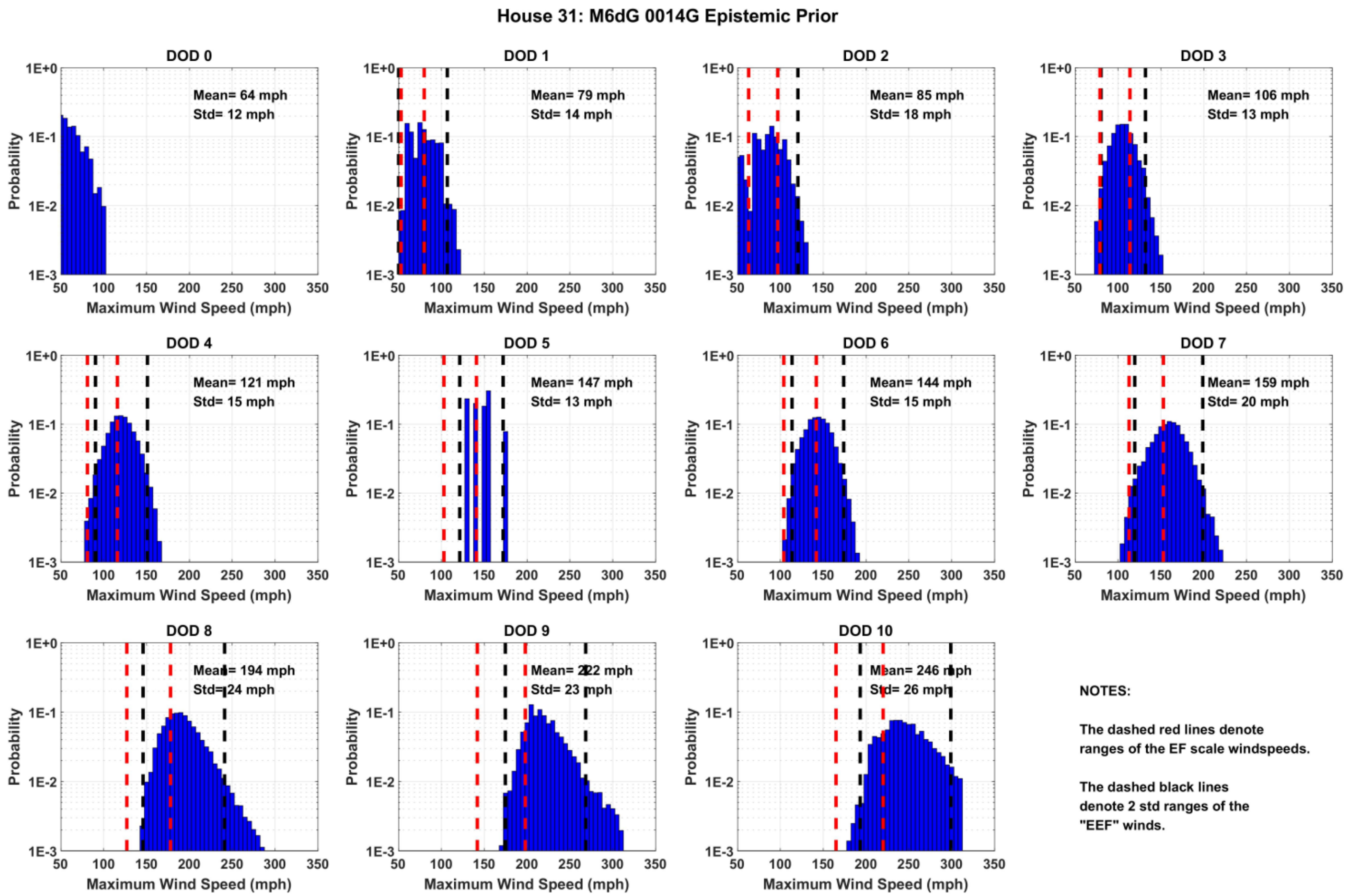
House 31: M6dG 0014G Epistemic Prior
DOD 0
Mean= 64 mph
Std= 12 mph
DOD 1
Mean= 79 mph
Std= 14 mph
DOD 2
Mean= 85 mph
Std= 18 mph
DOD 3
Mean= 106 mph
Std= 13 mph
DOD 4
Mean= 121 mph
Std= 15 mph
DOD 5
Mean= 147 mph
Std= 13 mph
DOD 6
Mean= 144 mph
Std= 15 mph
DOD 7
Mean= 159 mph
Std= 20 mph
DOD 8
194 mph
24 mph
DOD 9
Std= 23 mph
DOD 10
246 mph
26 mph
Probability
Maximum Wind Speed (mph)
NOTES:
The dashed red lines denote ranges of the EF scale windspeeds.
The dashed black lines denote 2 std ranges of the "EEF" winds.

House 32: M6dH 0014H Epistemic Prior

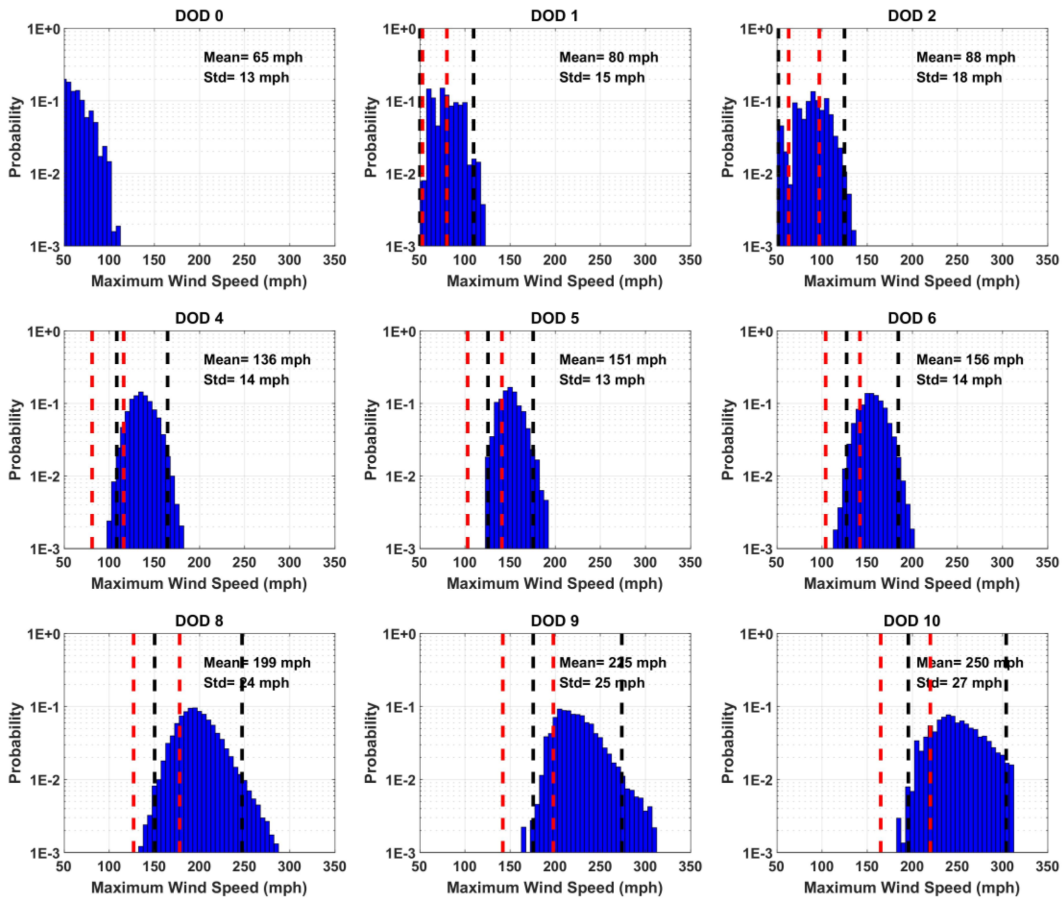

NOTES:

The dashed red lines denote ranges of the EF scale windspeeds.

The dashed black lines denote 2 std ranges of the "EEF" winds.

House 33: M8dG 0014G Epistemic Prior

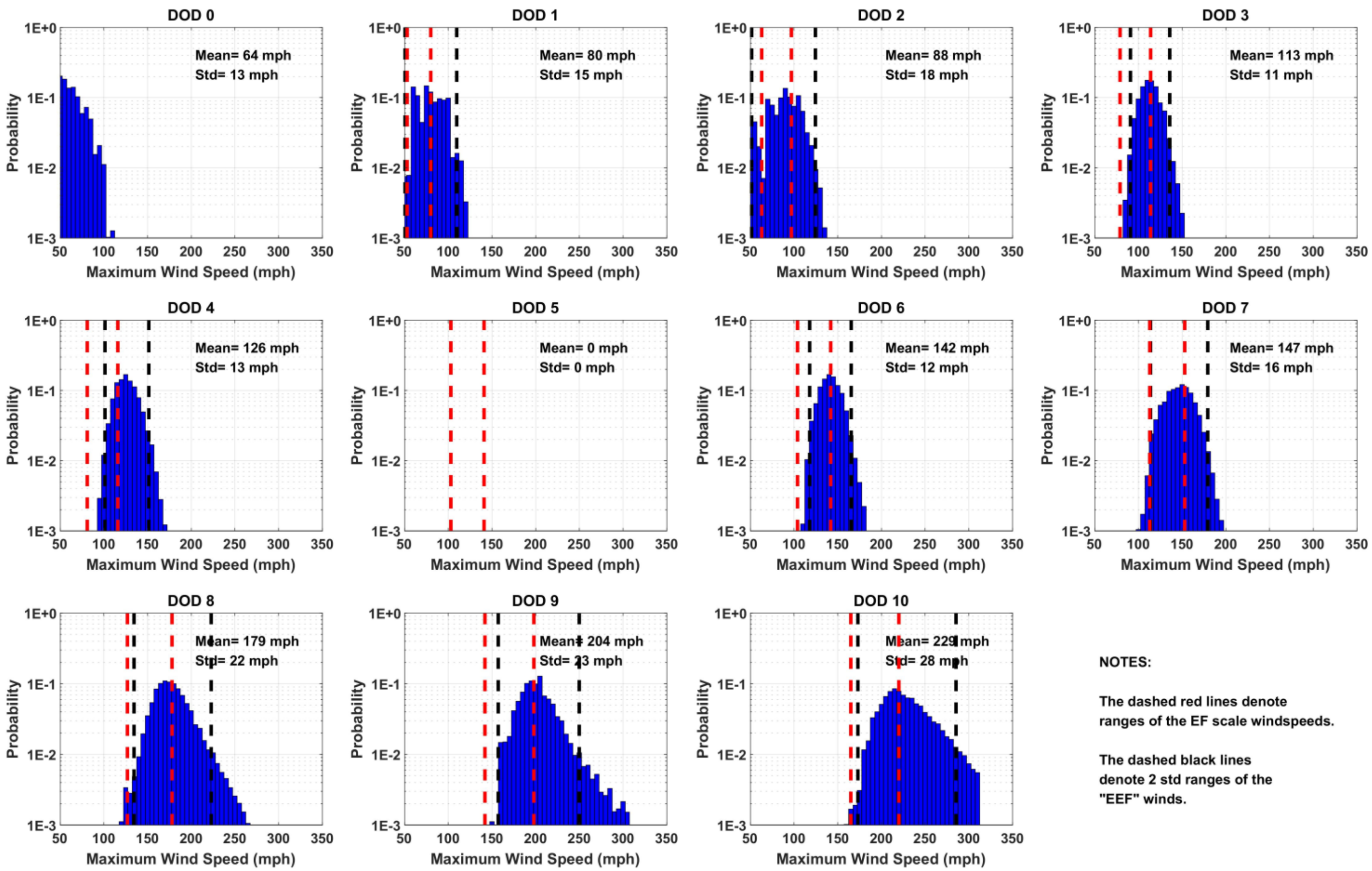

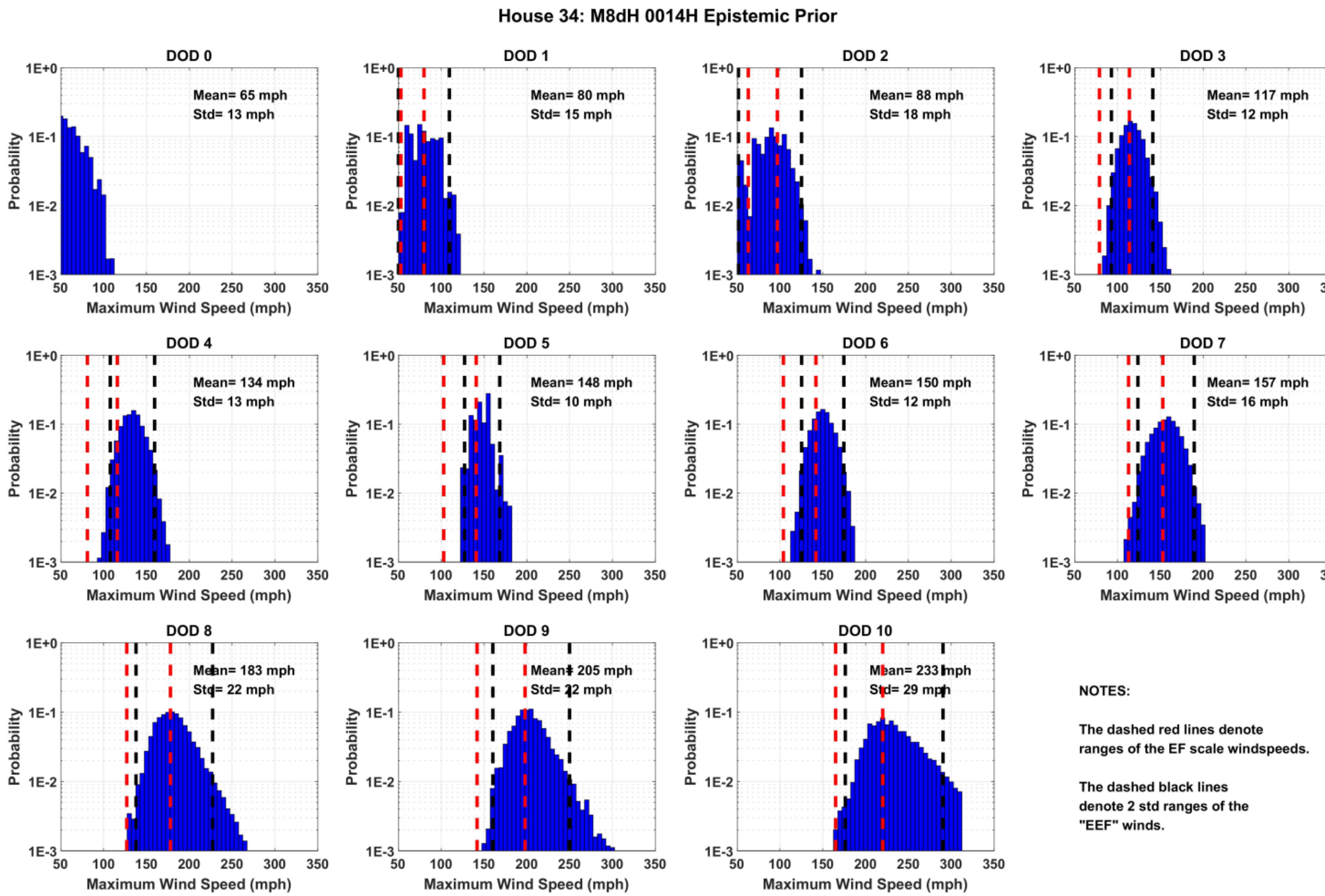
House 34: M8dH 0014H Epistemic Prior
DOD 0
Mean= 65 mph
Std= 13 mph
DOD 1
Mean= 80 mph
Std= 15 mph
DOD 2
Mean= 88 mph
Std= 18 mph
DOD 3
Mean= 117 mph
Std= 12 mph
DOD 4
Mean= 134 mph
Std= 13 mph
DOD 5
Mean= 148 mph
Std= 10 mph
DOD 6
Mean= 150 mph
Std= 12 mph
DOD 7
Mean= 157 mph
Std= 16 mph
DOD 8
Mean= 183 mph
Std= 22 mph
DOD 9
Mean= 205 mph
Std= 22 mph
DOD 10
Mean= 233 mph
Std= 29 mph
Probability
Maximum Wind Speed (mph)
1E+0
1E-1
1E-2
1E-3
50
100
150
200
250
300
350
NOTES:
The dashed red lines denote ranges of the EF scale windspeeds.
The dashed black lines denote 2 std ranges of the "EEF" winds.

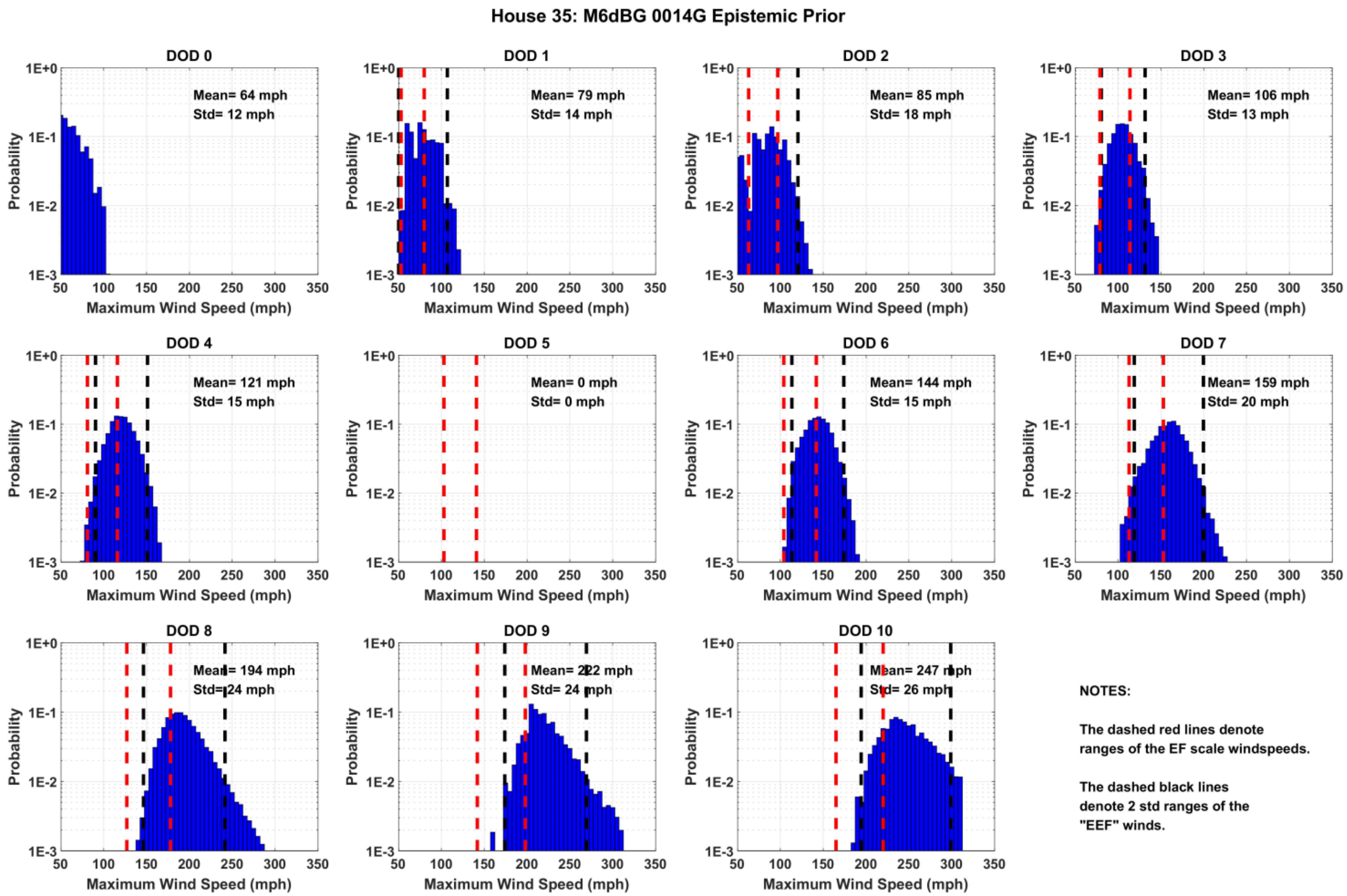
House 35: M6dBG 0014G Epistemic Prior
DOD 0
Mean= 64 mph
Std= 12 mph
DOD 1
Mean= 79 mph
Std= 14 mph
DOD 2
Mean= 85 mph
Std= 18 mph
DOD 3
Mean= 106 mph
Std= 13 mph
DOD 4
Mean= 121 mph
Std= 15 mph
DOD 5
Mean= 0 mph
Std= 0 mph
DOD 6
Mean= 144 mph
Std= 15 mph
DOD 7
Mean= 159 mph
Std= 20 mph
DOD 8
Mean= 194 mph
Std= 24 mph
DOD 9
Std= 24 mph
DOD 10
Mean= 247 mph
Std= 26 mph
Probability
Maximum Wind Speed (mph)
NOTES:
The dashed red lines denote ranges of the EF scale windspeeds.
The dashed black lines denote 2 std ranges of the "EEF" winds.

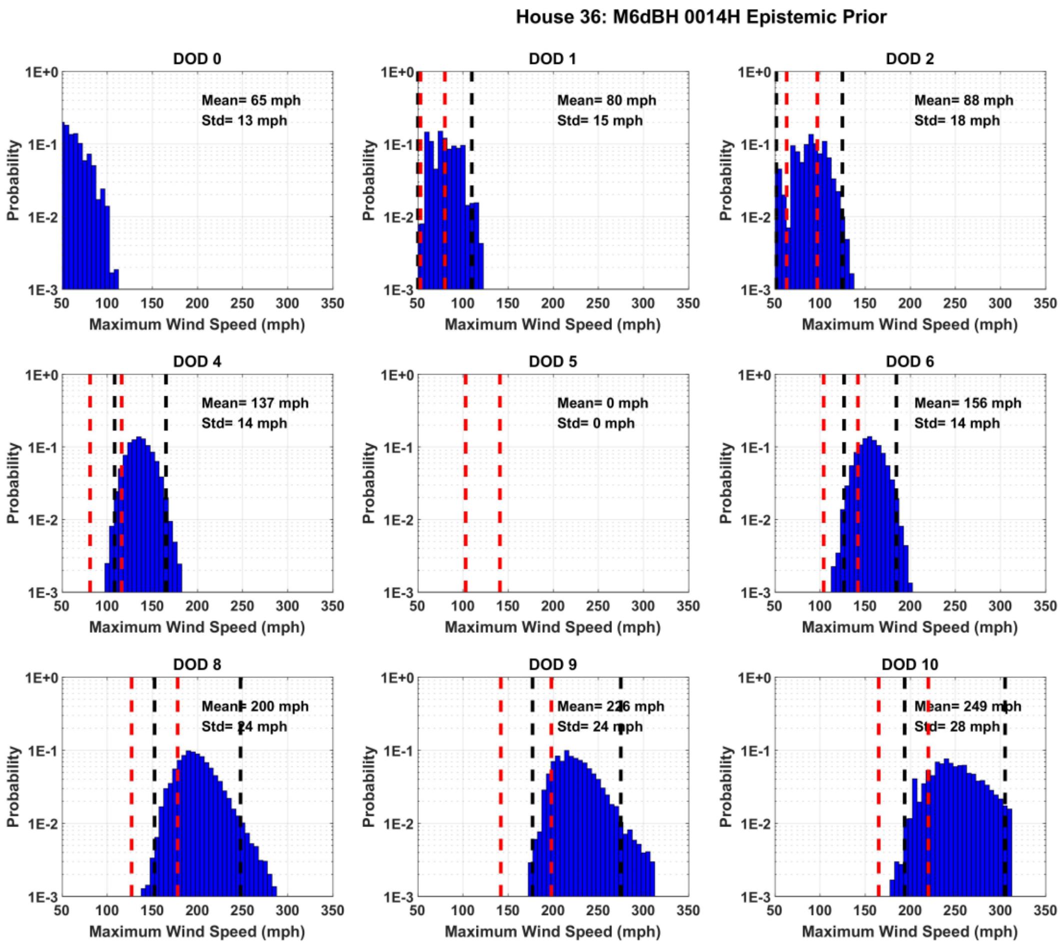

NOTES:

The dashed red lines denote ranges of the EF scale windspeeds.

The dashed black lines denote 2 std ranges of the "EEF" winds.

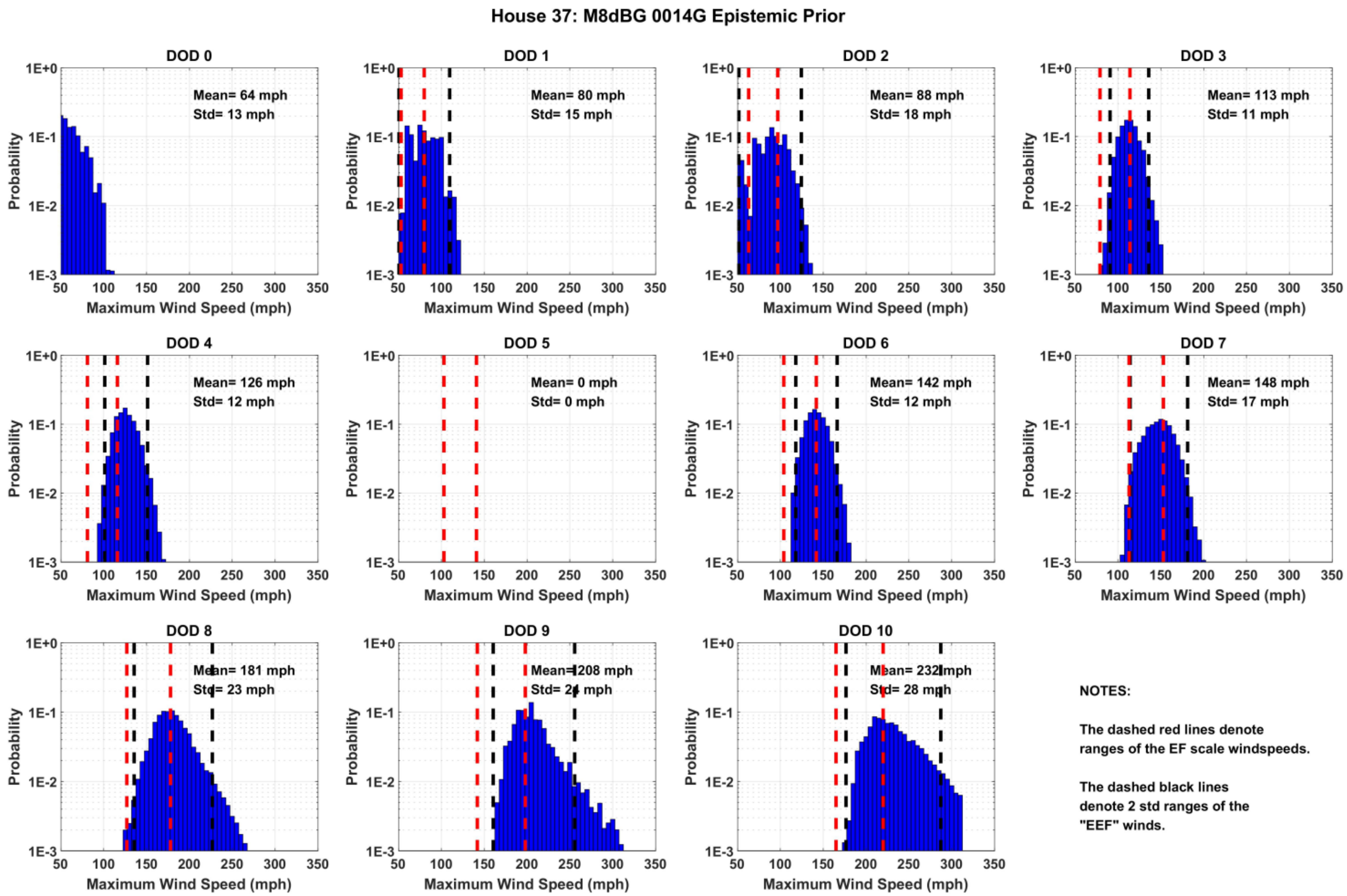
House 37: M8dBG 0014G Epistemic Prior
DOD 0
Mean= 64 mph
Std= 13 mph
DOD 1
Mean= 80 mph
Std= 15 mph
DOD 2
Mean= 88 mph
Std= 18 mph
DOD 3
Mean= 113 mph
Std= 11 mph
DOD 4
Mean= 126 mph
Std= 12 mph
DOD 5
Mean= 0 mph
Std= 0 mph
DOD 6
Mean= 142 mph
Std= 12 mph
DOD 7
Mean= 148 mph
Std= 17 mph
DOD 8
Mean= 181 mph
Std= 23 mph
DOD 9
Mean= 208 mph
DOD 10
Mean= 232 mph
Std= 28 mph
Probability
Maximum Wind Speed (mph)
NOTES:
The dashed red lines denote ranges of the EF scale windspeeds.
The dashed black lines denote 2 std ranges of the "EEF" winds.

House 38: M8dBH 0014H Epistemic Prior

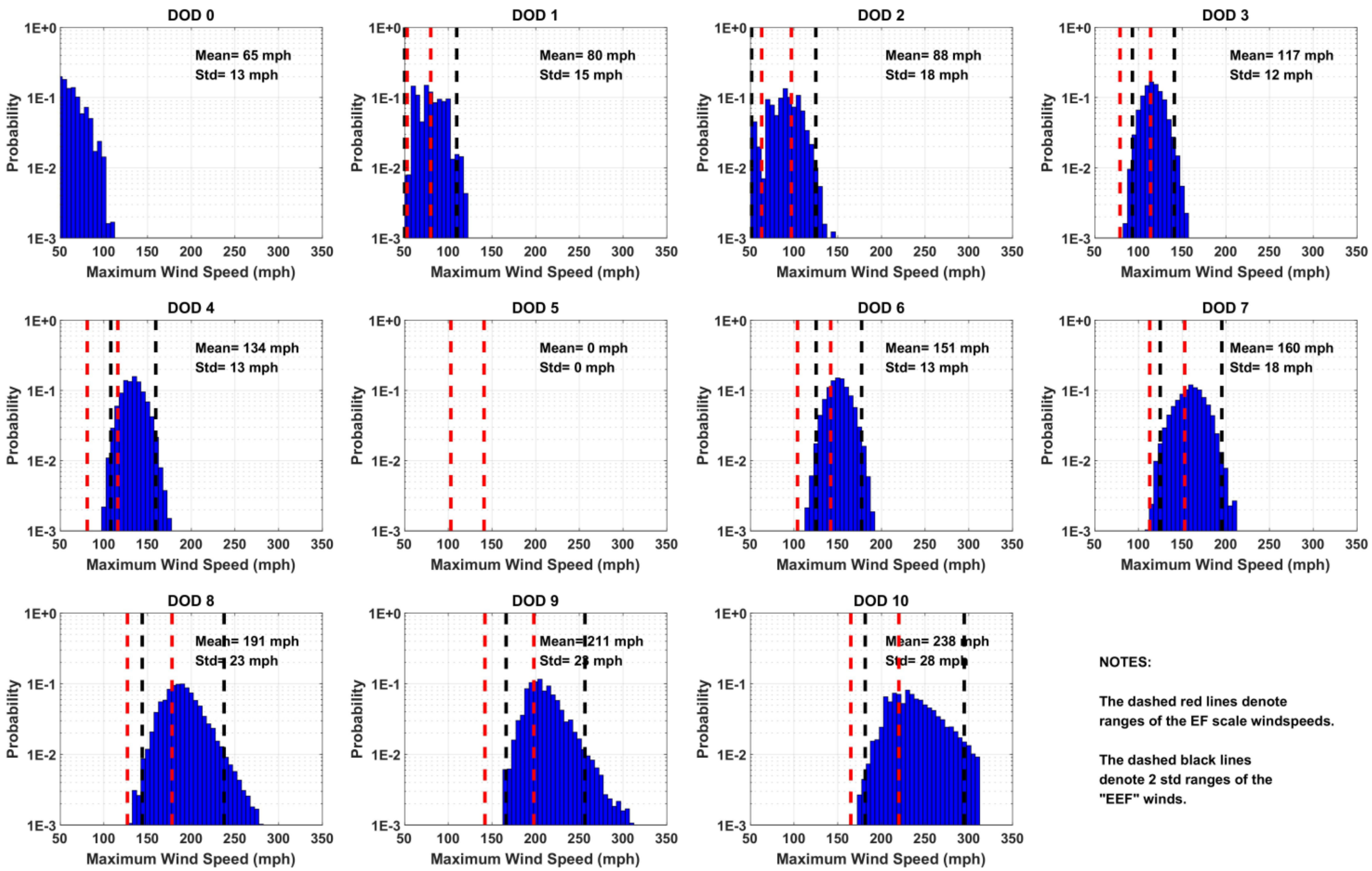

NOTES:

The dashed red lines denote ranges of the EF scale windspeeds.

The dashed black lines denote 2 std ranges of the "EEF" winds.

House 39: SG6D 0014G Epistemic Prior

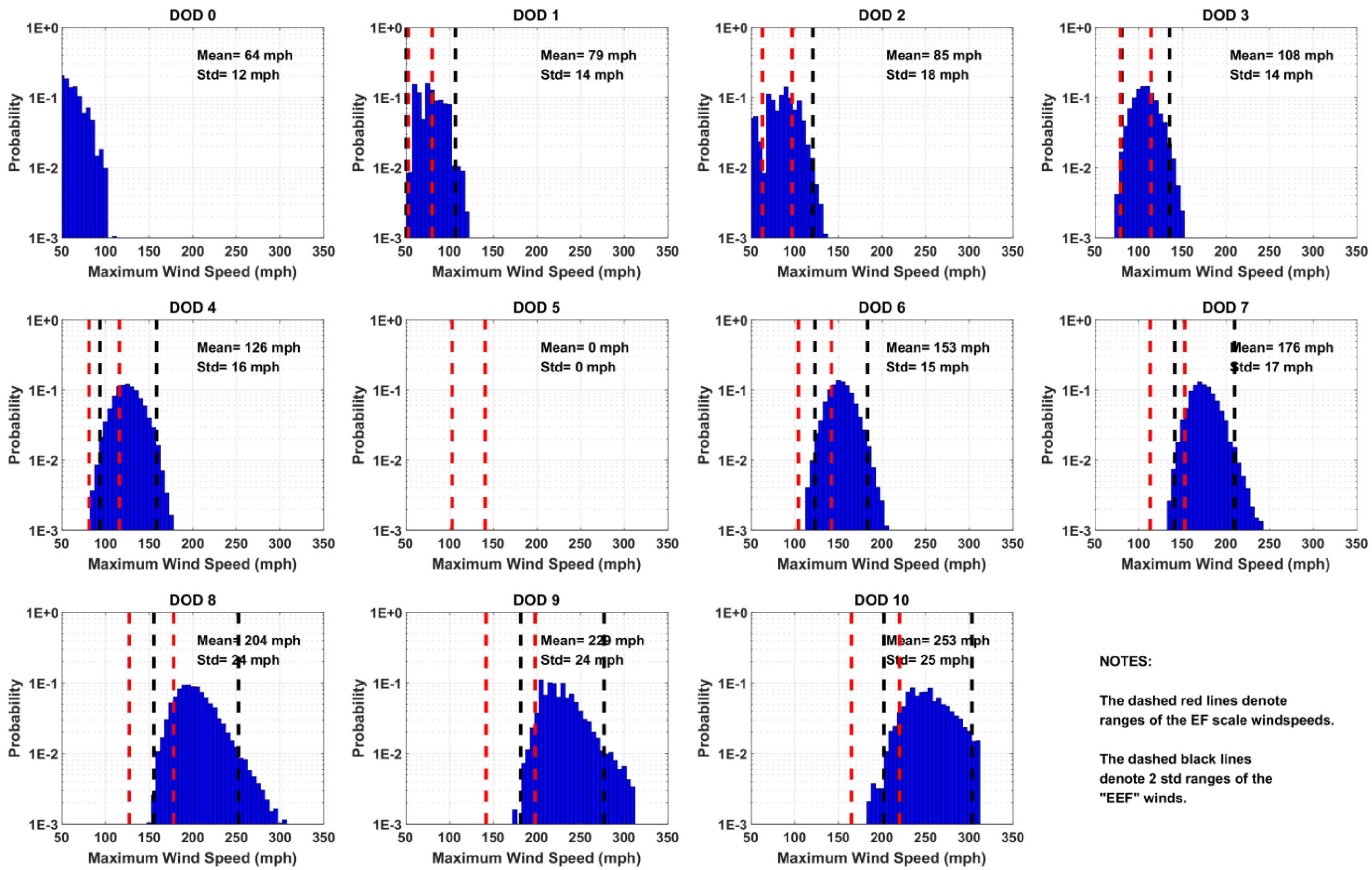

House 40: SH6D 0014H Epistemic Prior

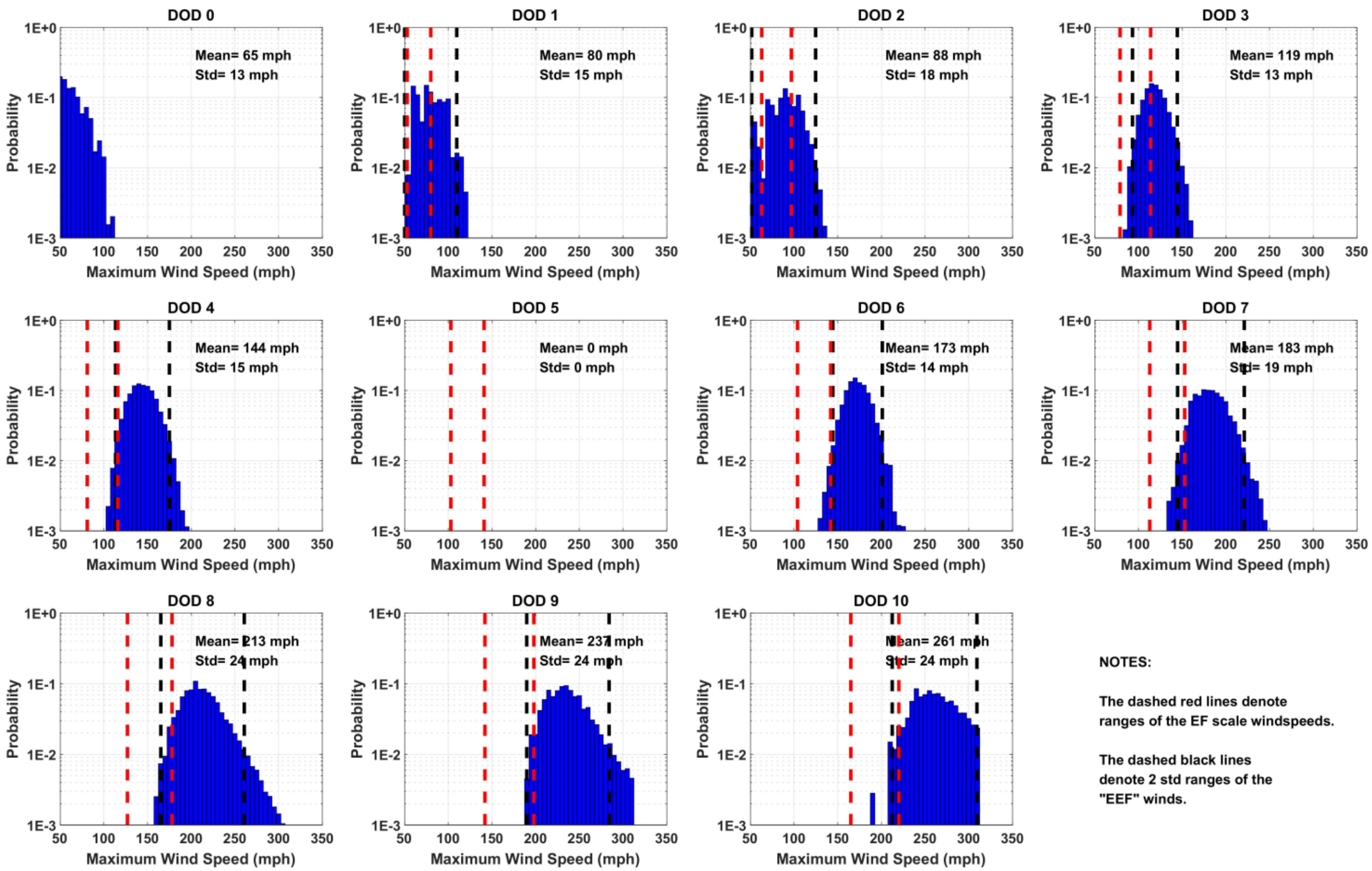

NOTES:

The dashed red lines denote ranges of the EF scale windspeeds.

The dashed black lines denote 2 std ranges of the "EEF" winds.

House 41: SG 0014G Epistemic Prior

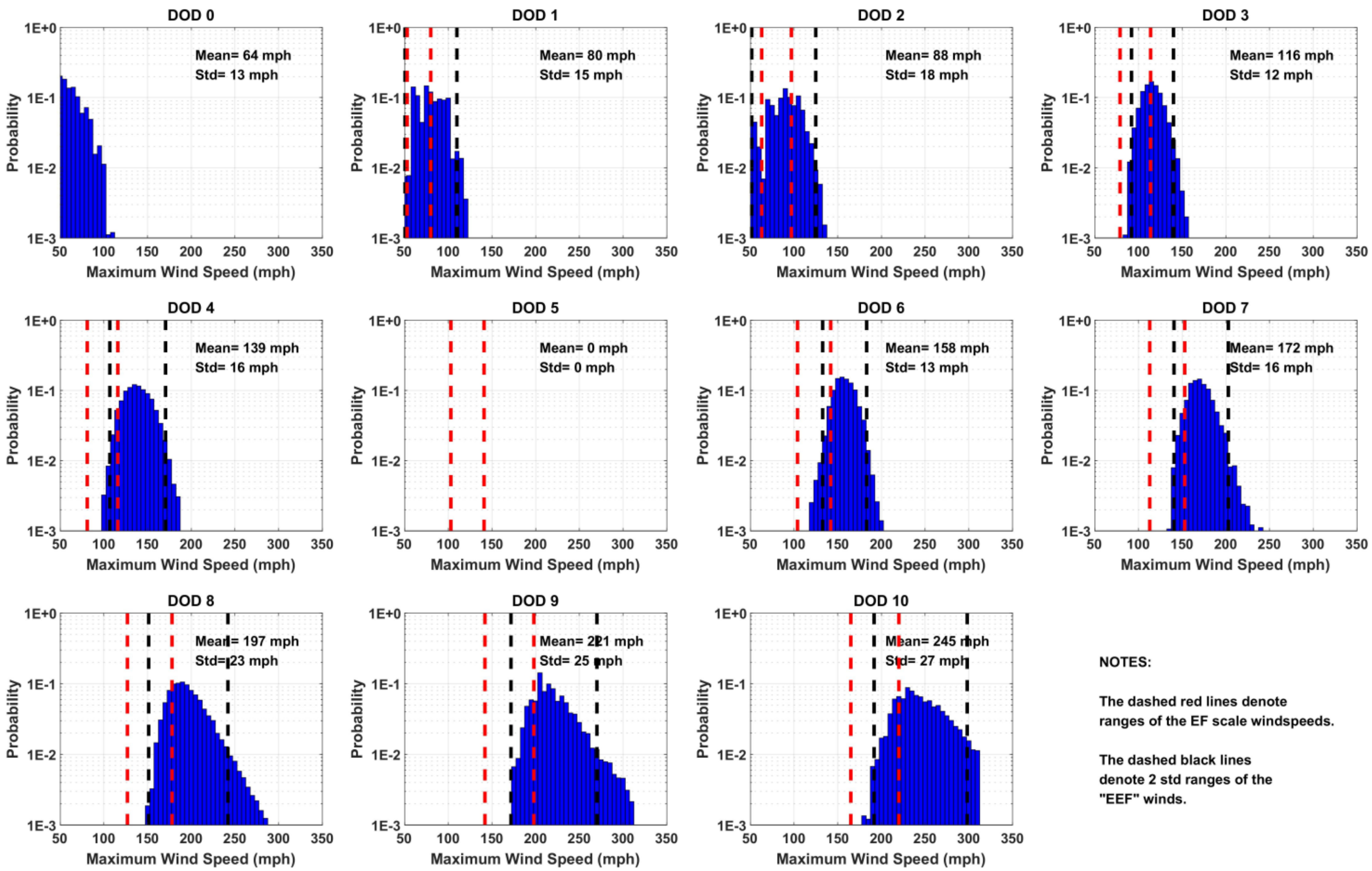

NOTES:

The dashed red lines denote ranges of the EF scale windspeeds.

The dashed black lines denote 2 std ranges of the "EEF" winds.

House 42: SH 0014H Epistemic Prior

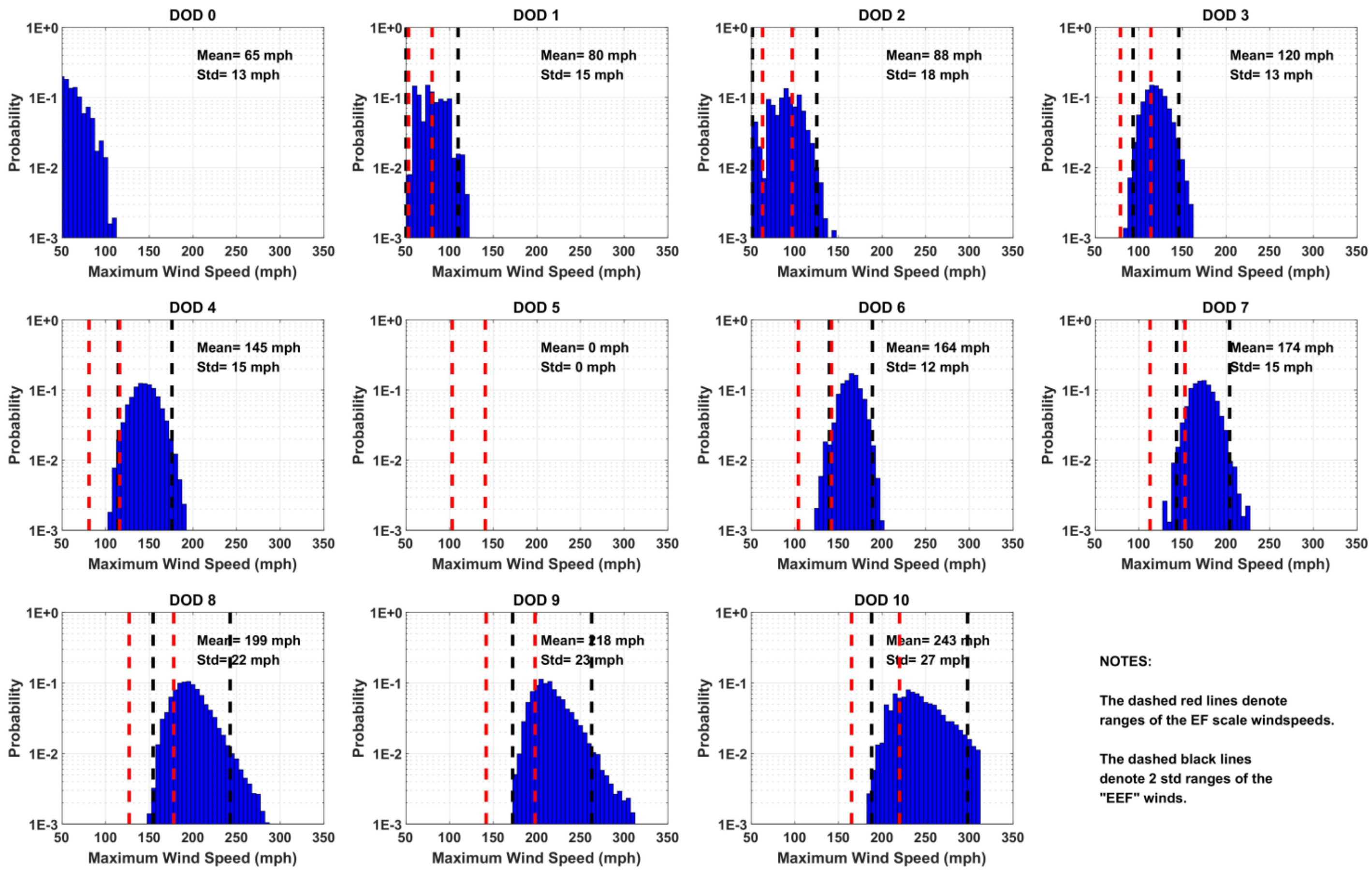

House 43: SSG 0014G Epistemic Prior

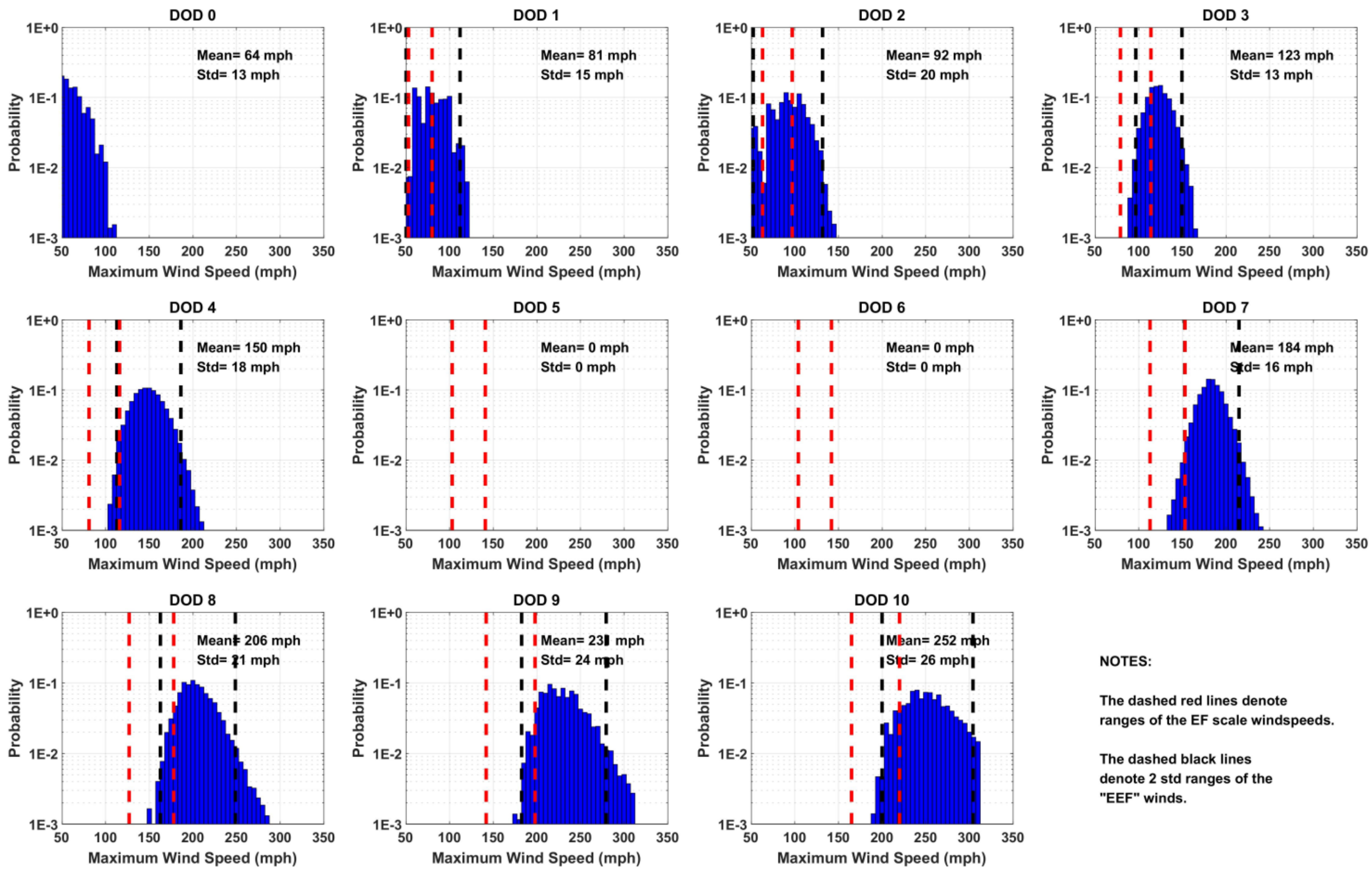

NOTES:

The dashed red lines denote ranges of the EF scale windspeeds.

The dashed black lines denote 2 std ranges of the "EEF" winds.

House 44: SSH 0014H Epistemic Prior

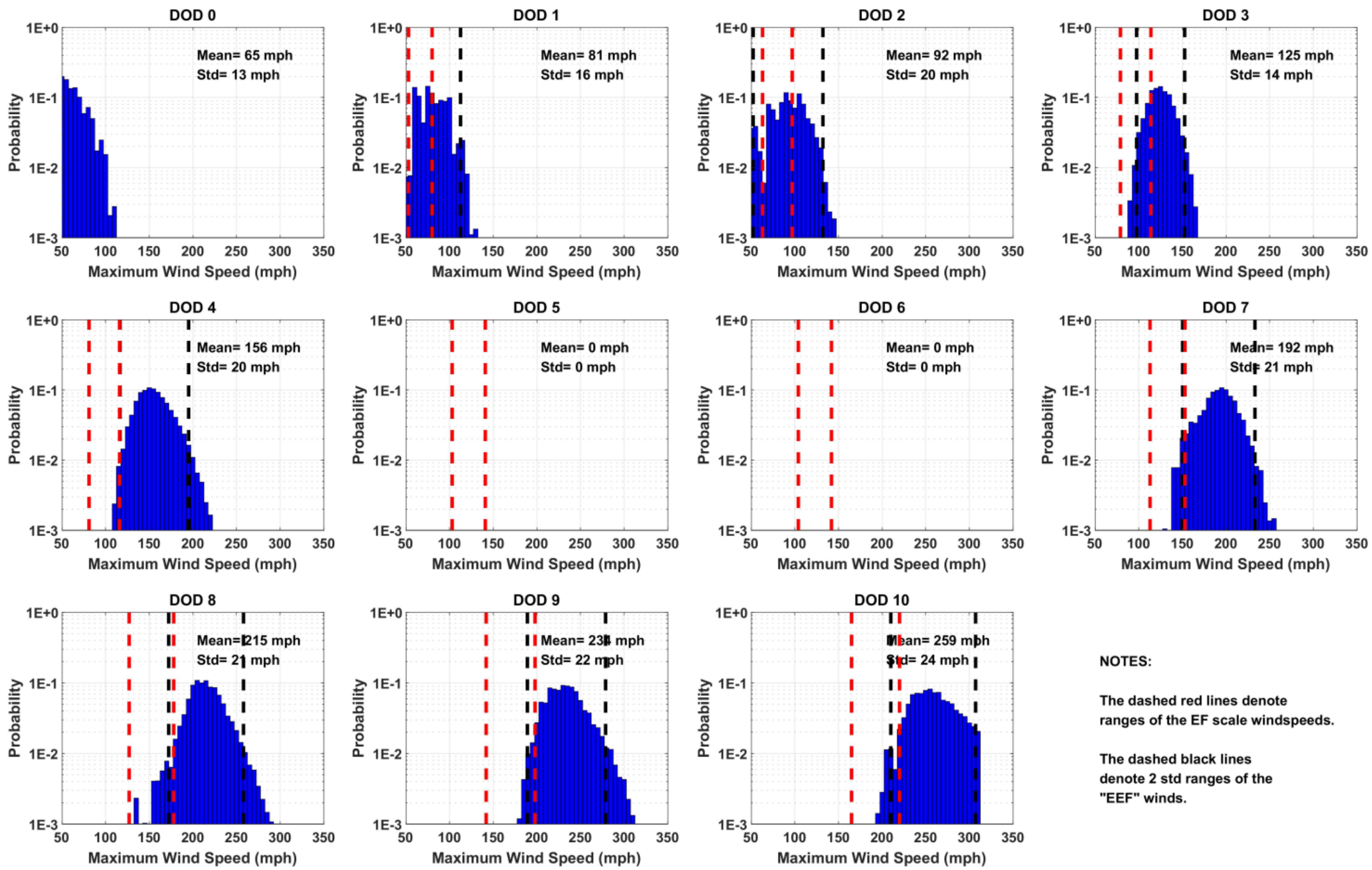

NOTES:

The dashed red lines denote ranges of the EF scale windspeeds.

The dashed black lines denote 2 std ranges of the "EEF" winds.

F.3. DOD Wind Speed CMF Plots

FR12 DOD wind speed and cumulative mass distributions (CMF) are illustrated for the 44 house types defined in Section 6. These distributions are based on the epistemic priors, as described in Section 6. Wind speed is shown in miles per hour (1 mph = 0.44704 m/s). Table F-2 provides the order of the plots.

Table F-2. DOD Wind Speed CMF Plots

House	File name	CMF Plot Page	House	File name	CMF Plot Page
1	W6dG_tornado_1304G	F-52	23	W6dG_tornado_0014G	F-74
2	W6dH_tornado_1304H	F-53	24	W6dH_tornado_0014H	F-75
3	W8dG_tornado_1304G	F-54	25	W8dG_tornado_0014G	F-76
4	W8dH_tornado_1304H	F-55	26	W8dH_tornado_0014H	F-77
5	W8dpDGN_tornado_1304G	F-56	27	W8dpDGN_tornado_0014G	F-78
6	W8dpDHN_tornado_1304H	F-57	28	W8dpDHN_tornado_0014H	F-79
7	W8dpDGB_tornado_1304G	F-58	29	W8dpDGB_tornado_0014G	F-80
8	W8dpDHB_tornado_1304H	F-59	30	W8dpDHB_tornado_0014H	F-81
9	M6dG_tornado_1304G	F-60	31	M6dG_tornado_0014G	F-82
10	M6dH_tornado_1304H	F-61	32	M6dH_tornado_0014H	F-83
11	M8dG_tornado_1304G	F-62	33	M8dG_tornado_0014G	F-84
12	M8dH_tornado_1304H	F-63	34	M8dH_tornado_0014H	F-85
13	M6dBG_tornado_1304G	F-64	35	M6dBG_tornado_0014G	F-86
14	M6dBH_tornado_1304H	F-65	36	M6dBH_tornado_0014H	F-87
15	M8dBG_tornado_1304G	F-66	37	M8dBG_tornado_0014G	F-88
16	M8dBH_tornado_1304H	F-67	38	M8dBH_tornado_0014H	F-89
17	SG6D_tornado_1304G	F-68	39	SG6D_tornado_0014G	F-90
18	SH6D_tornado_1304H	F-69	40	SH6D_tornado_0014H	F-91
19	SG_tornado_1304G	F-70	41	SG_tornado_0014G	F-92
20	SH_tornado_1304H	F-71	42	SH_tornado_0014H	F-93
21	SSG_tornado_1304G	F-72	43	SSG_tornado_0014G	F-94
22	SSH_tornado_1304H	F-73	44	SSH_tornado_0014H	F-95

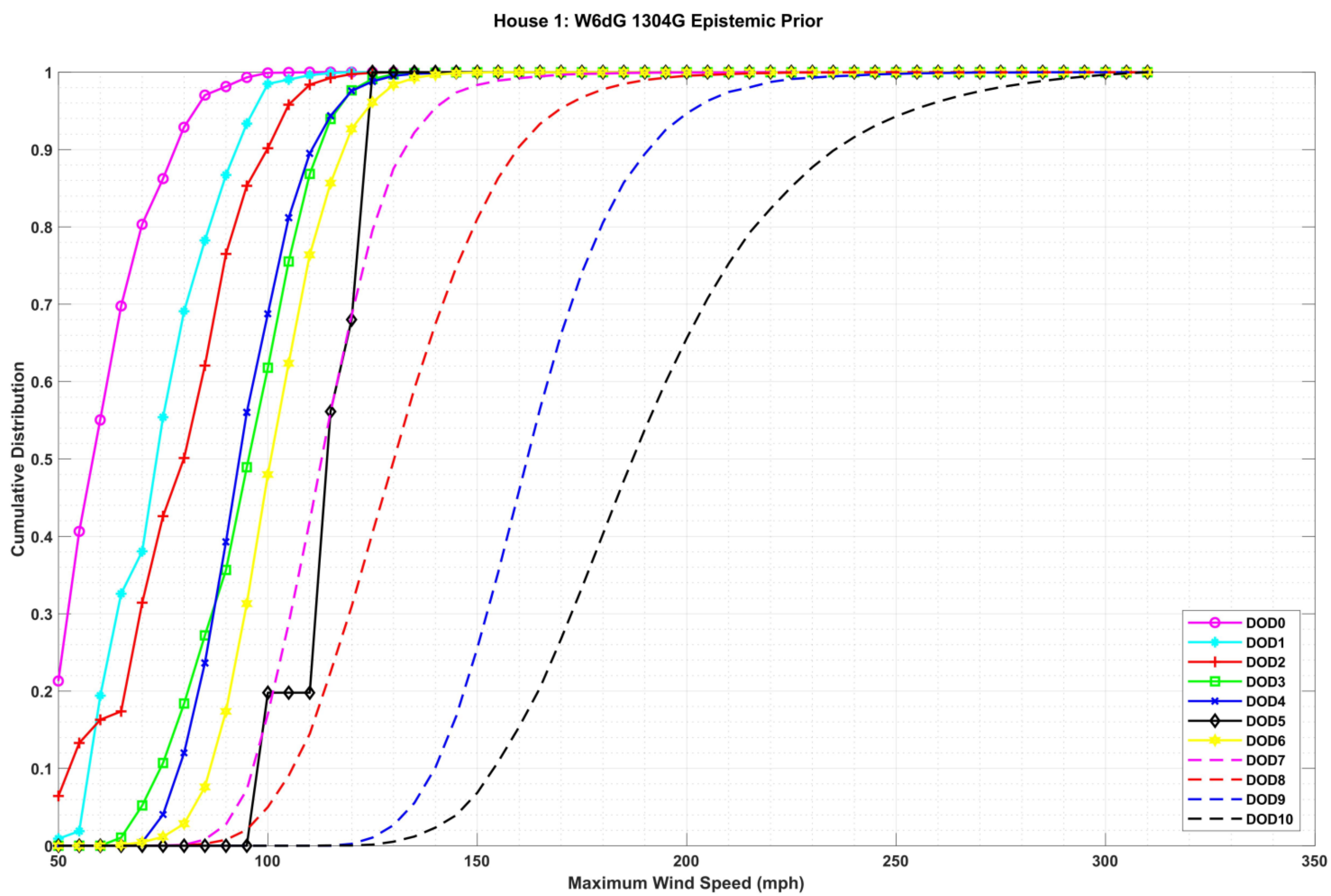
House 1: W6dG 1304G Epistemic Prior
Cumulative Distribution
Maximum Wind Speed (mph)
0
0.1
0.2
0.3
0.4
0.5
0.6
0.7
0.8
0.9
1
50
100
150
200
250
300
350
DOD0
DOD1
DOD2
DOD3
DOD4
DOD5
DOD6
DOD7
DOD8
DOD9
DOD10

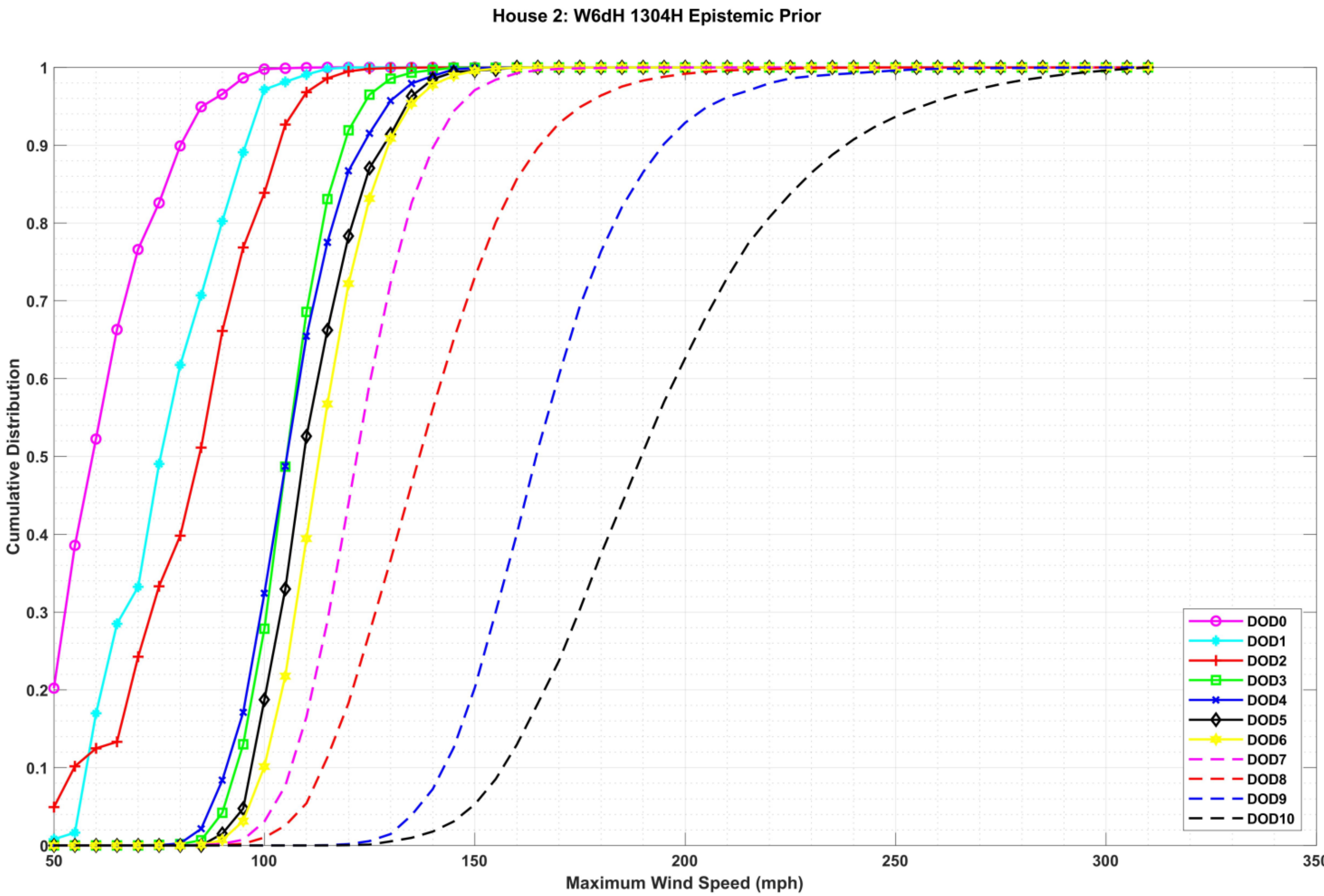
House 2: W6dH 1304H Epistemic Prior
Cumulative Distribution
Maximum Wind Speed (mph)
0
0.1
0.2
0.3
0.4
0.5
0.6
0.7
0.8
0.9
1
50
100
150
200
250
300
350
DOD0
DOD1
DOD2
DOD3
DOD4
DOD5
DOD6
DOD7
DOD8
DOD9
DOD10

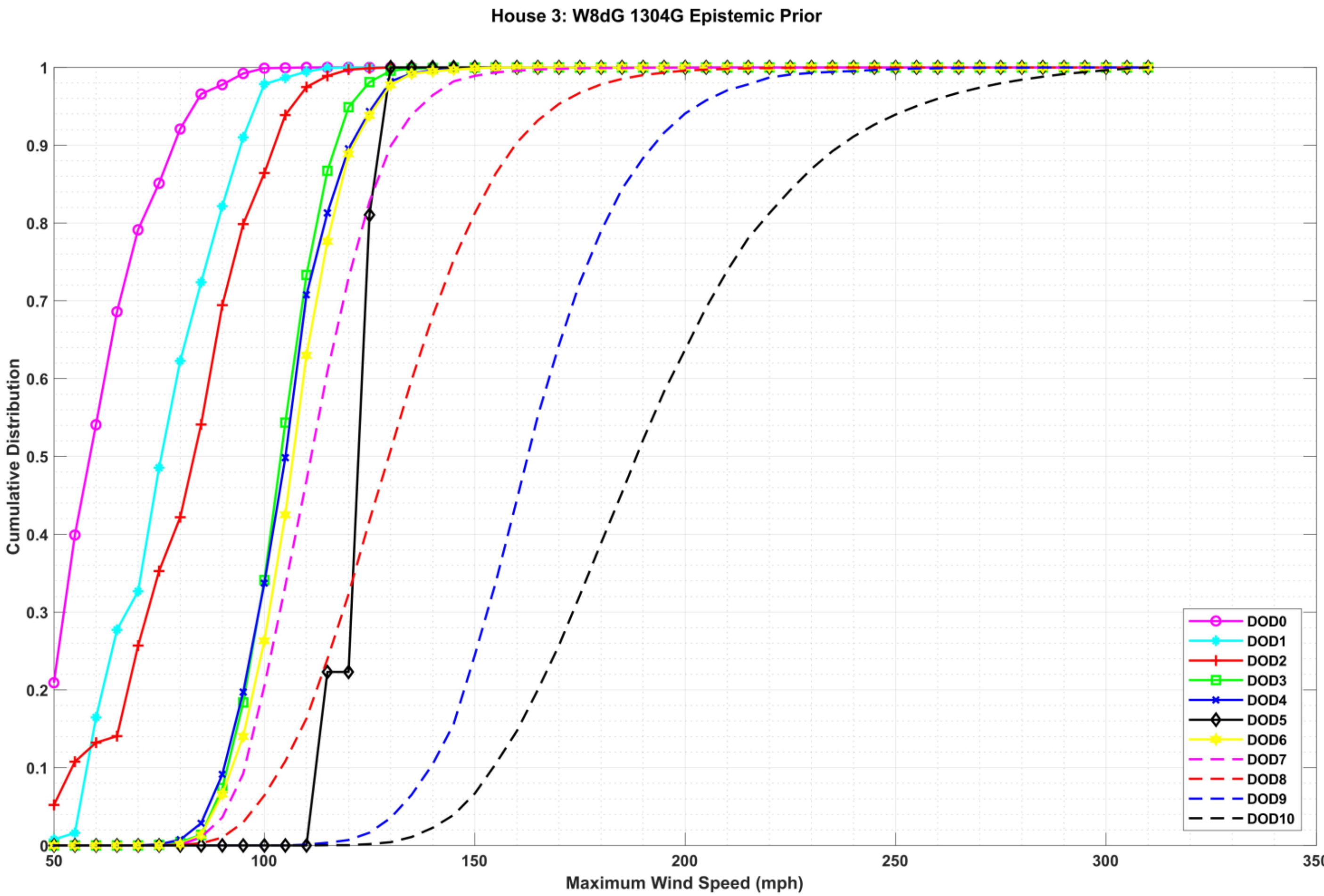

House 3: W8dG 1304G Epistemic Prior
Cumulative Distribution
Maximum Wind Speed (mph)
0
0.1
0.2
0.3
0.4
0.5
0.6
0.7
0.8
0.9
1
50
100
150
200
250
300
350
DOD0
DOD1
DOD2
DOD3
DOD4
DOD5
DOD6
DOD7
DOD8
DOD9
DOD10

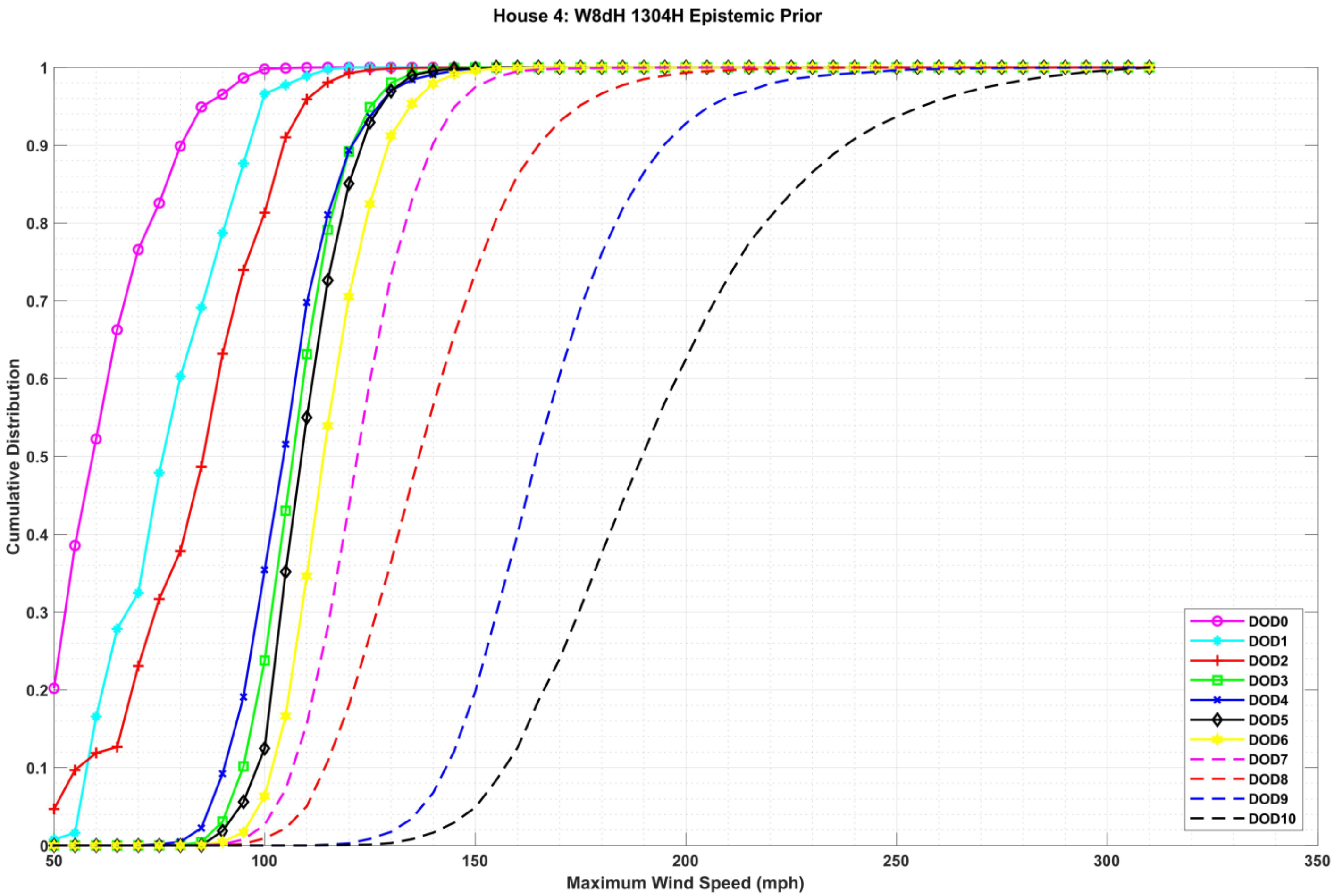
House 4: W8dH 1304H Epistemic Prior
Cumulative Distribution
Maximum Wind Speed (mph)
0
0.1
0.2
0.3
0.4
0.5
0.6
0.7
0.8
0.9
1
50
100
150
200
250
300
350
DOD0
DOD1
DOD2
DOD3
DOD4
DOD5
DOD6
DOD7
DOD8
DOD9
DOD10

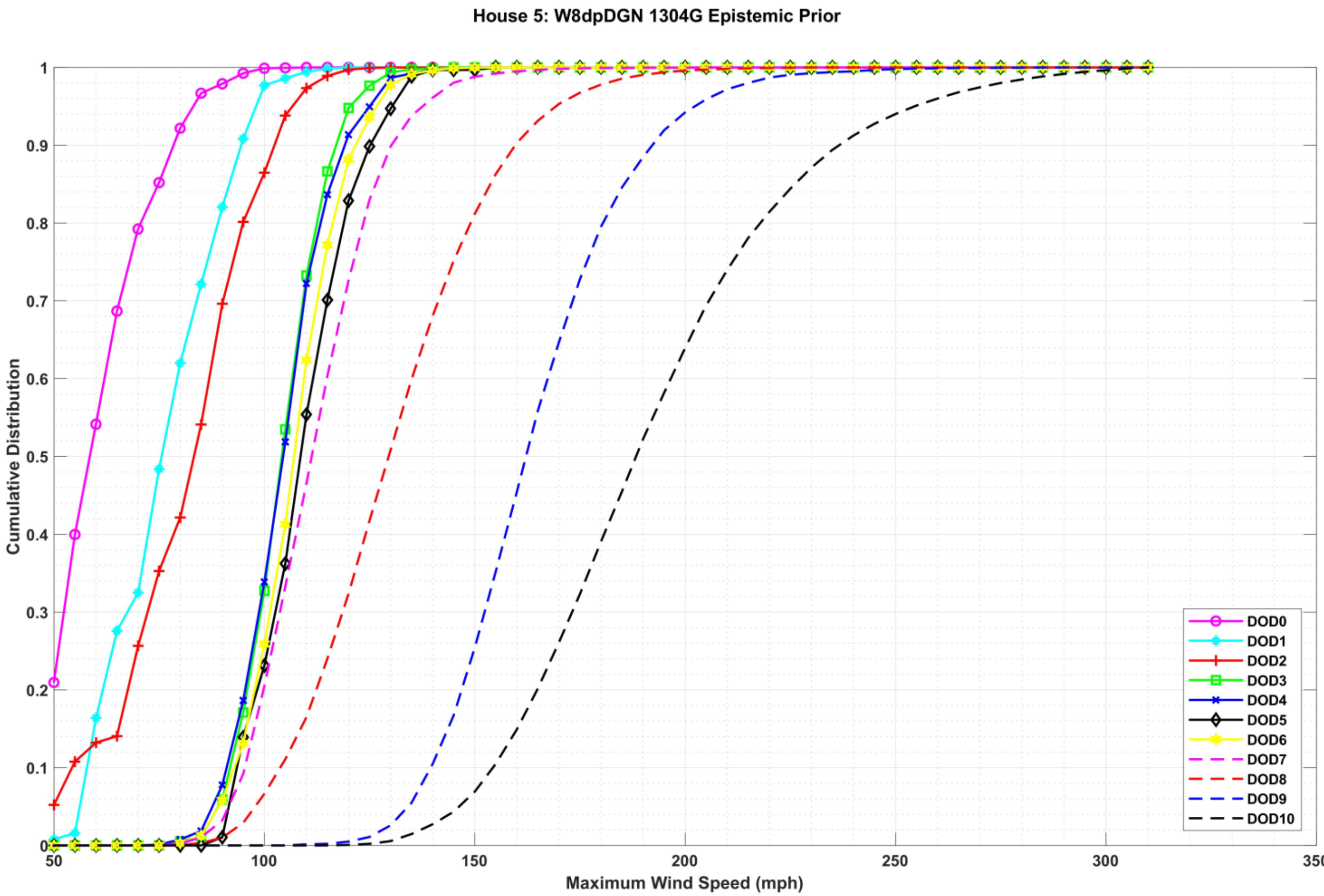
House 5: W8dpDGN 1304G Epistemic Prior
Cumulative Distribution
Maximum Wind Speed (mph)
0
0.1
0.2
0.3
0.4
0.5
0.6
0.7
0.8
0.9
1
50
100
150
200
250
300
350
DOD0
DOD1
DOD2
DOD3
DOD4
DOD5
DOD6
DOD7
DOD8
DOD9
DOD10

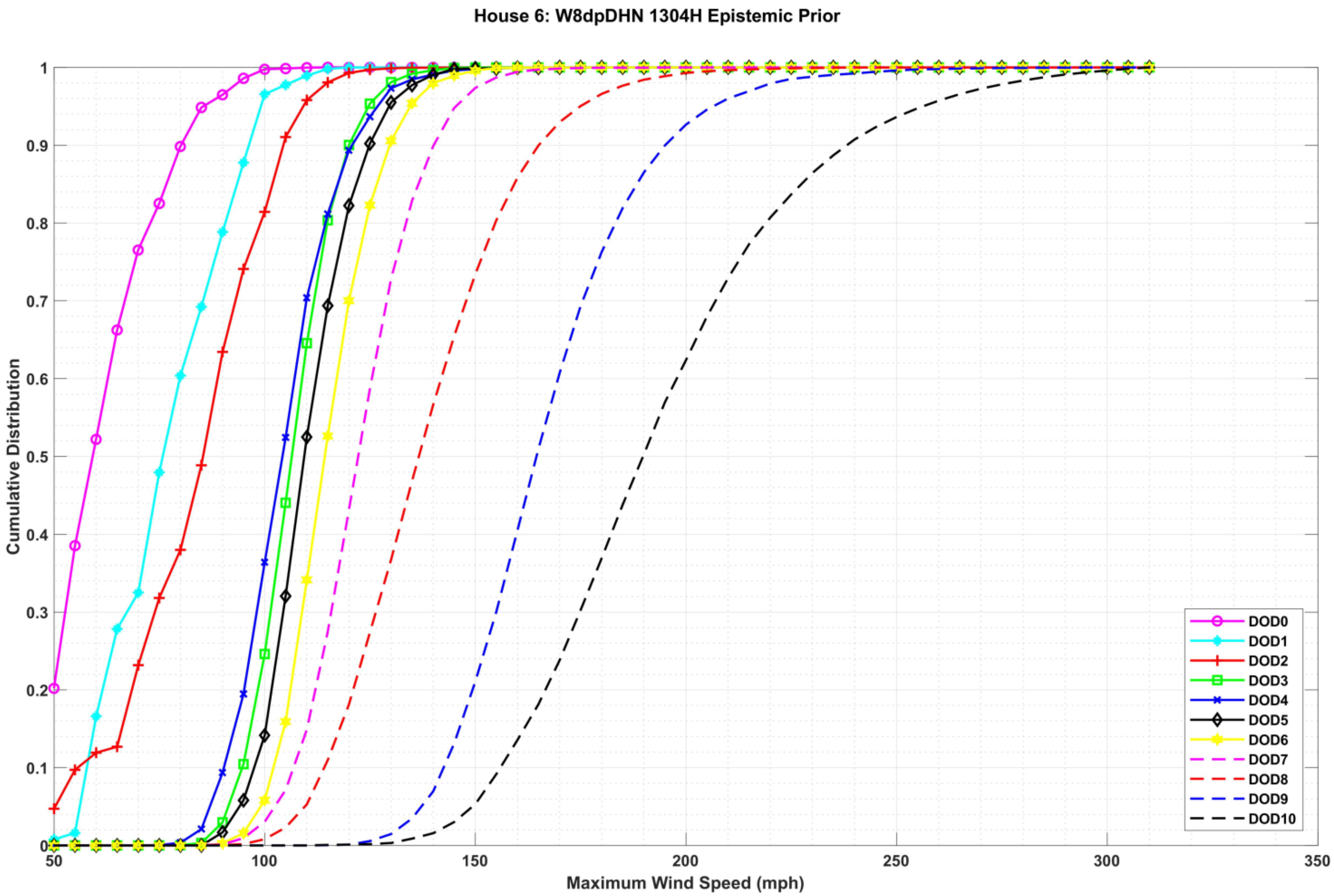

House 6: W8dpDHN 1304H Epistemic Prior
Cumulative Distribution
Maximum Wind Speed (mph)
0
0.1
0.2
0.3
0.4
0.5
0.6
0.7
0.8
0.9
1
50
100
150
200
250
300
350
DOD0
DOD1
DOD2
DOD3
DOD4
DOD5
DOD6
DOD7
DOD8
DOD9
DOD10

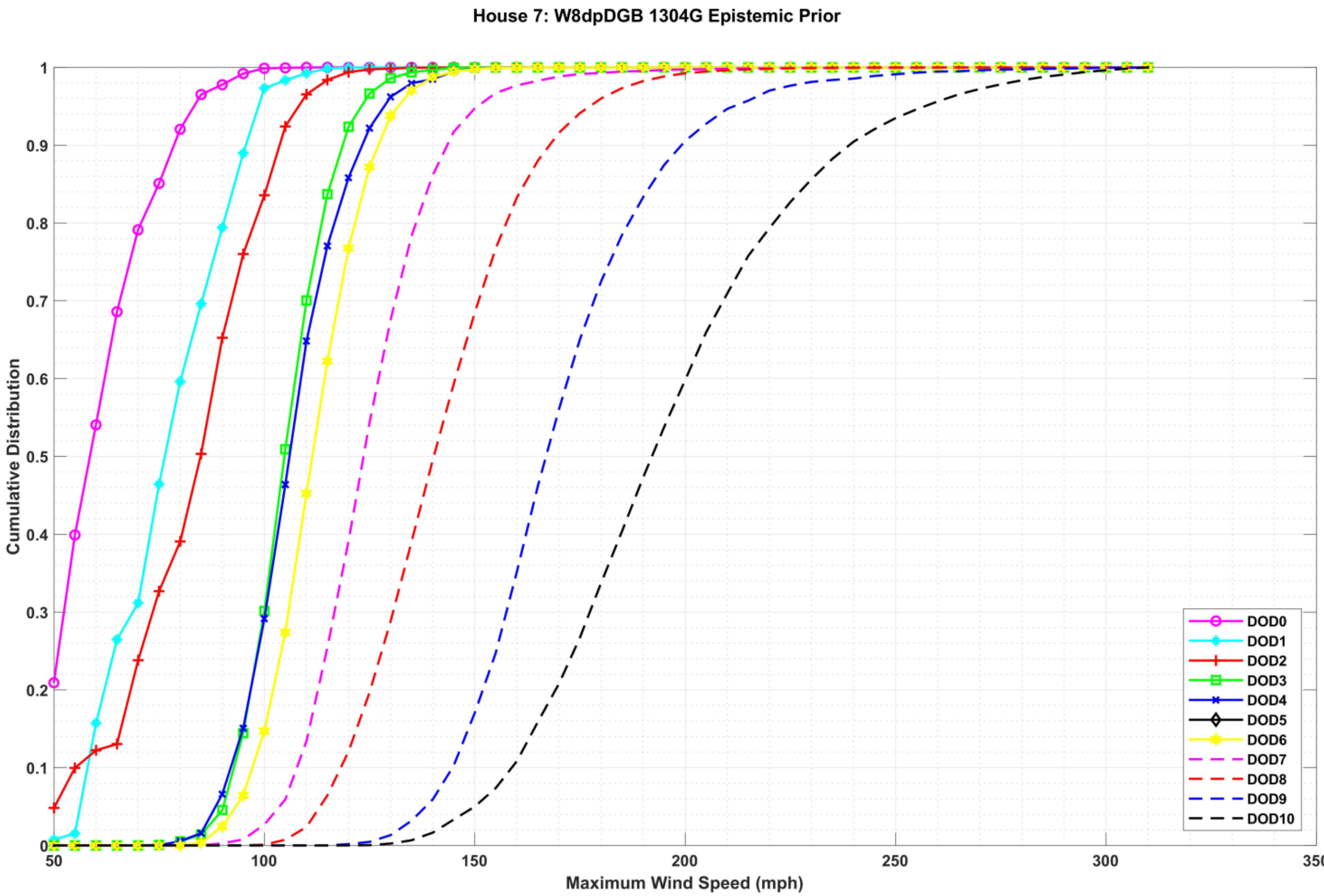
House 7: W8dpDGB 1304G Epistemic Prior
Cumulative Distribution
Maximum Wind Speed (mph)
0
0.1
0.2
0.3
0.4
0.5
0.6
0.7
0.8
0.9
1
50
100
150
200
250
300
350
DOD0
DOD1
DOD2
DOD3
DOD4
DOD5
DOD6
DOD7
DOD8
DOD9
DOD10

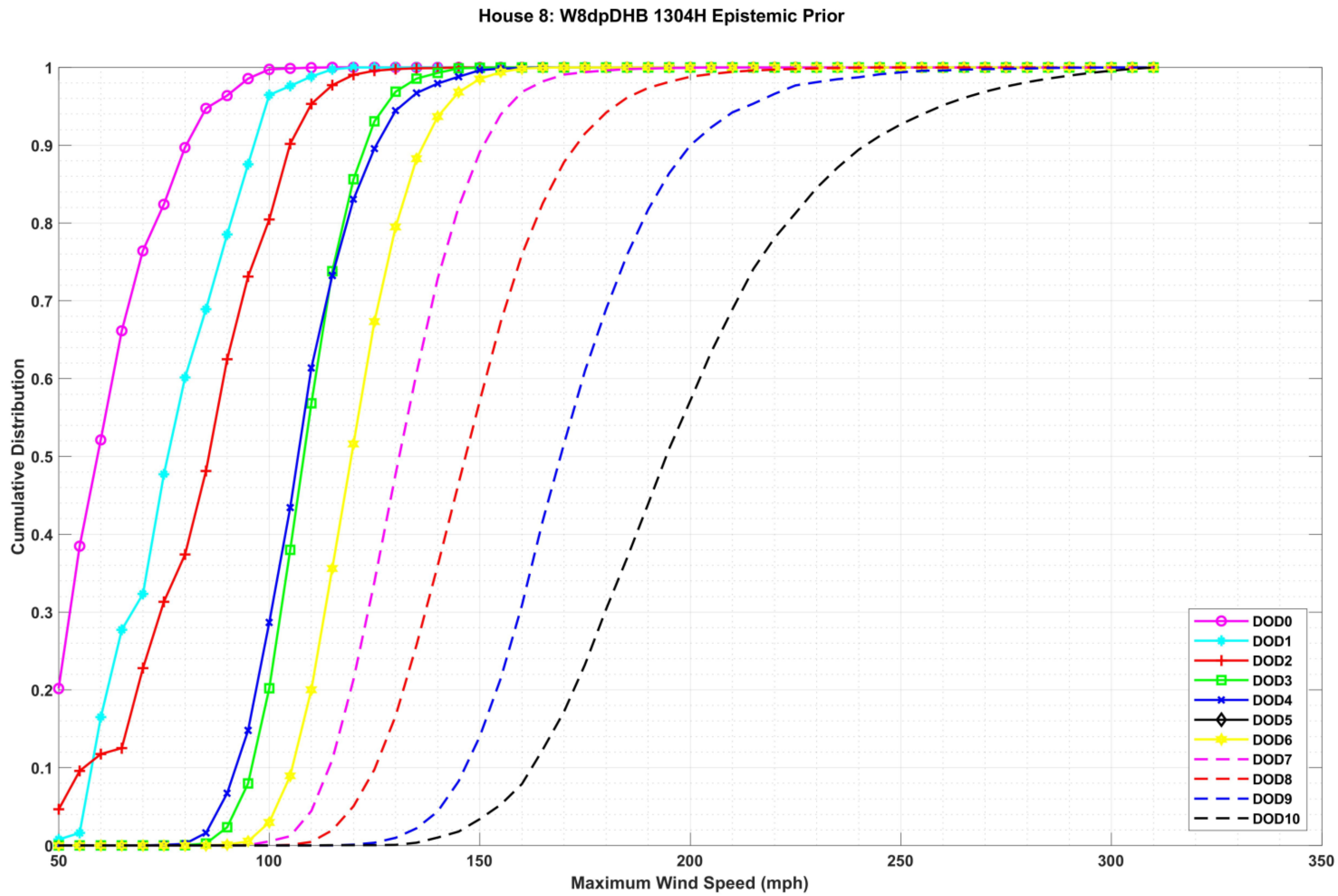

House 8: W8dpDHB 1304H Epistemic Prior
Cumulative Distribution
Maximum Wind Speed (mph)
0
0.1
0.2
0.3
0.4
0.5
0.6
0.7
0.8
0.9
1
50
100
150
200
250
300
350
DOD0
DOD1
DOD2
DOD3
DOD4
DOD5
DOD6
DOD7
DOD8
DOD9
DOD10

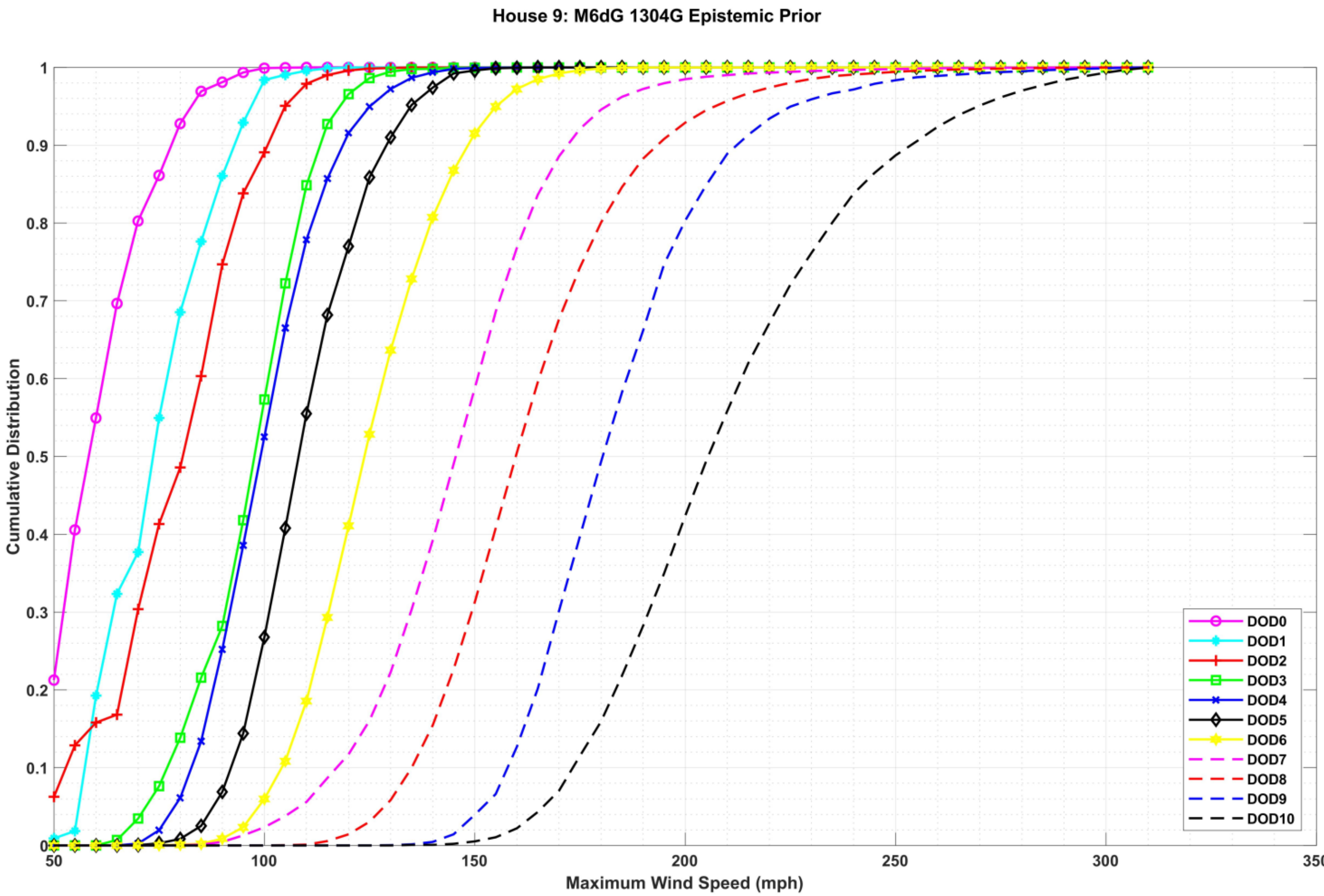
House 9: M6dG 1304G Epistemic Prior
Cumulative Distribution
Maximum Wind Speed (mph)
0
0.1
0.2
0.3
0.4
0.5
0.6
0.7
0.8
0.9
1
50
100
150
200
250
300
350
DOD0
DOD1
DOD2
DOD3
DOD4
DOD5
DOD6
DOD7
DOD8
DOD9
DOD10

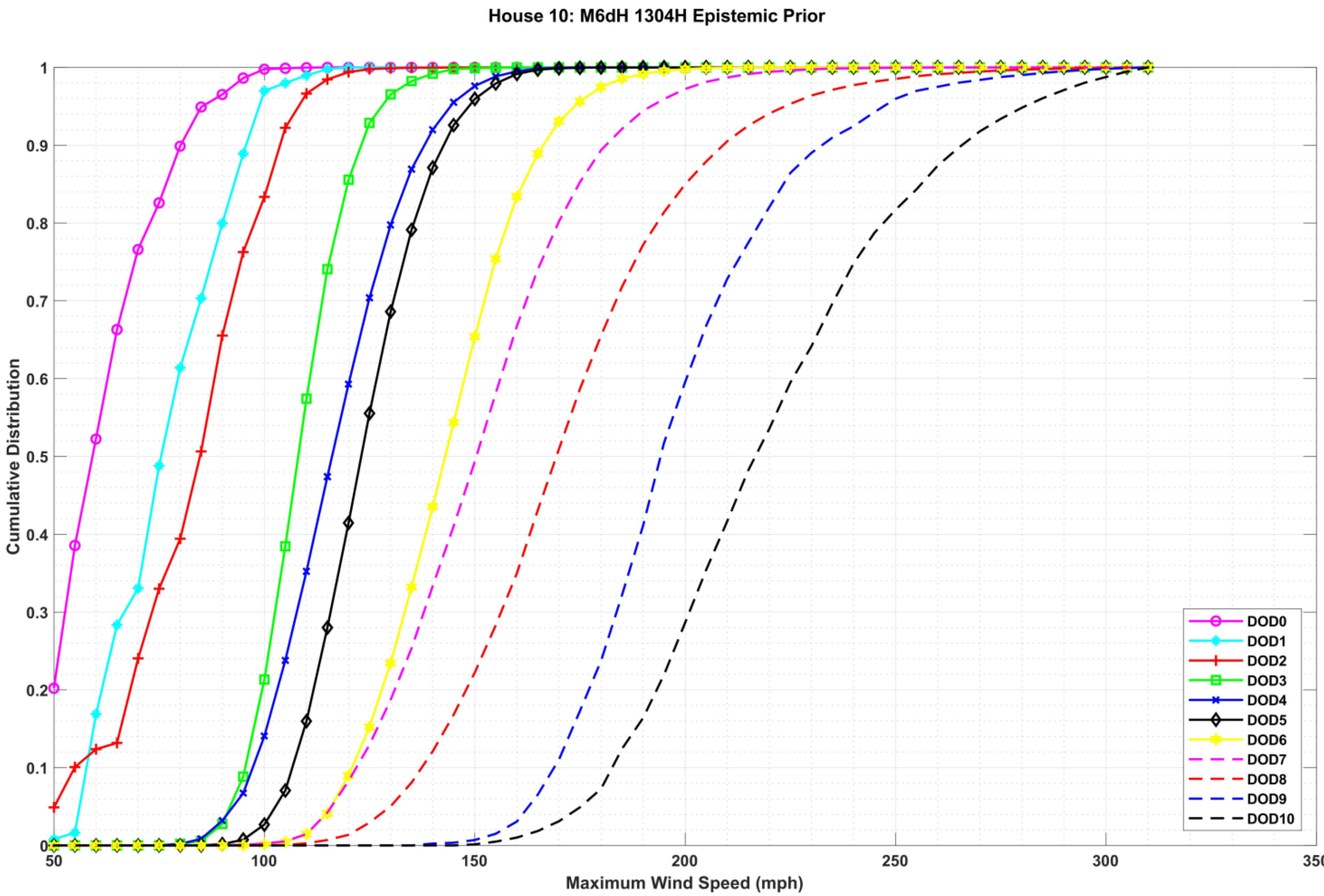

House 10: M6dH 1304H Epistemic Prior
Cumulative Distribution
Maximum Wind Speed (mph)
0
0.1
0.2
0.3
0.4
0.5
0.6
0.7
0.8
0.9
1
50
100
150
200
250
300
350
DOD0
DOD1
DOD2
DOD3
DOD4
DOD5
DOD6
DOD7
DOD8
DOD9
DOD10

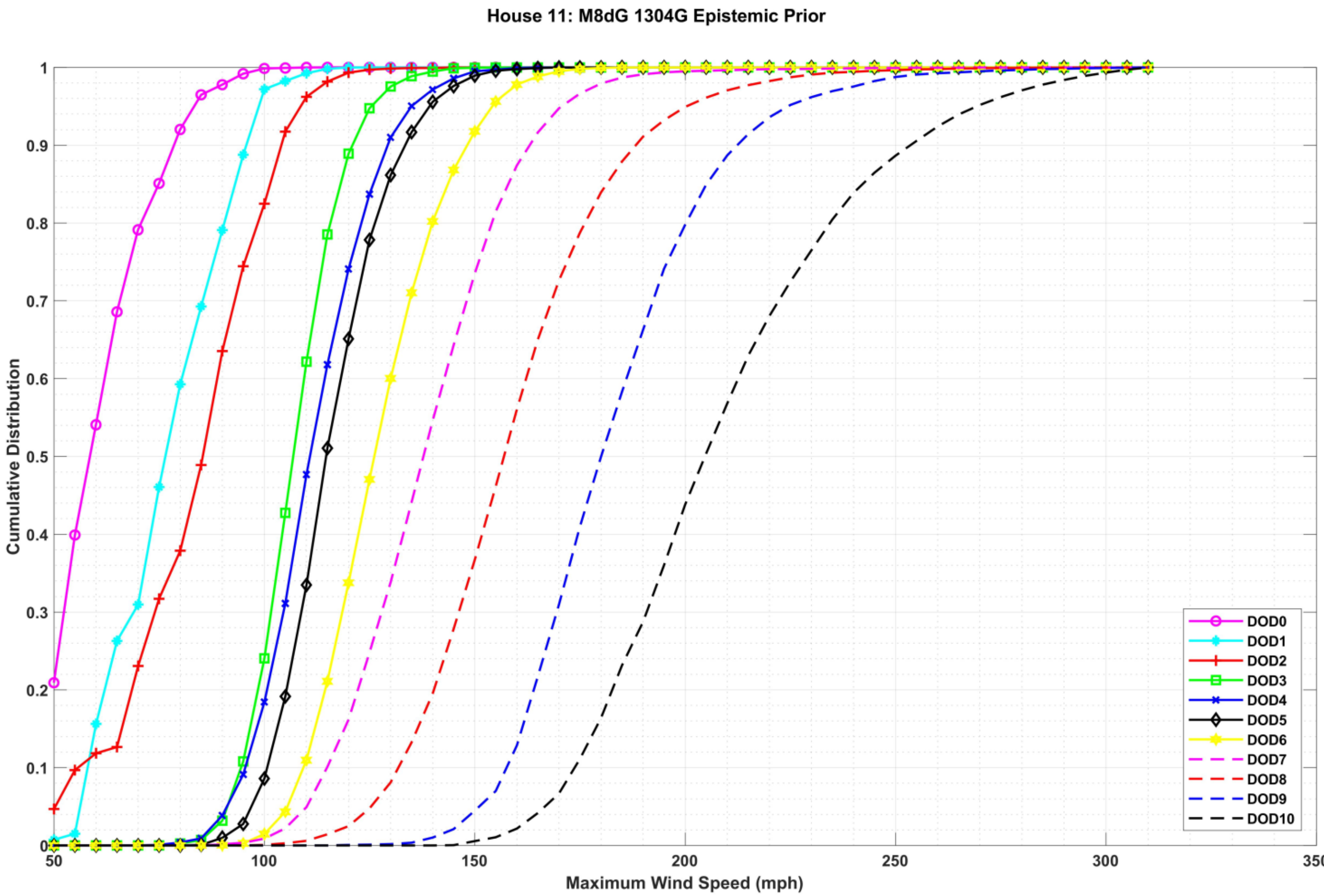
House 11: M8dG 1304G Epistemic Prior
Cumulative Distribution
Maximum Wind Speed (mph)
DOD0
DOD1
DOD2
DOD3
DOD4
DOD5
DOD6
DOD7
DOD8
DOD9
DOD10

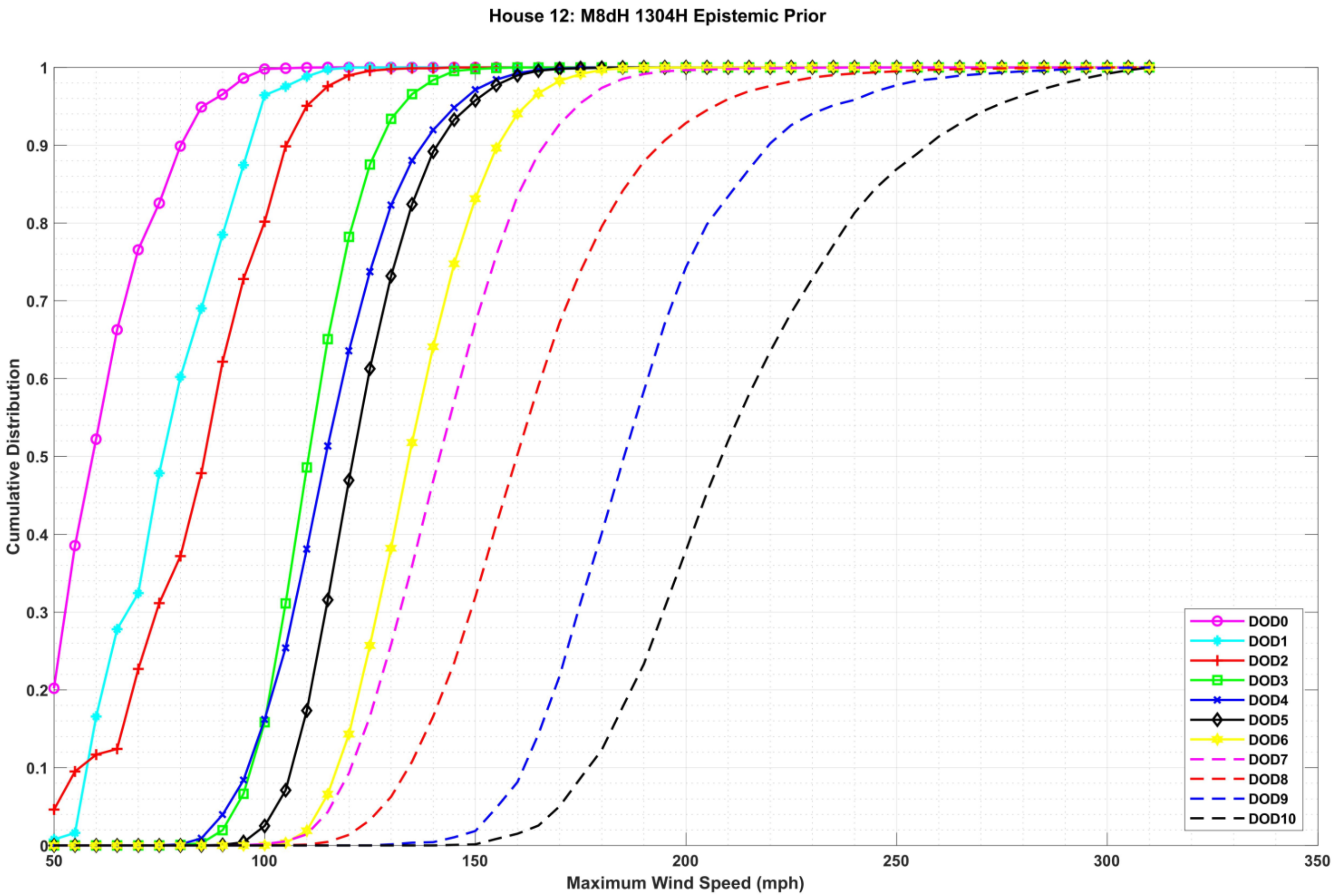

House 12: M8dH 1304H Epistemic Prior
Cumulative Distribution
Maximum Wind Speed (mph)
0
0.1
0.2
0.3
0.4
0.5
0.6
0.7
0.8
0.9
1
50
100
150
200
250
300
350
DOD0
DOD1
DOD2
DOD3
DOD4
DOD5
DOD6
DOD7
DOD8
DOD9
DOD10

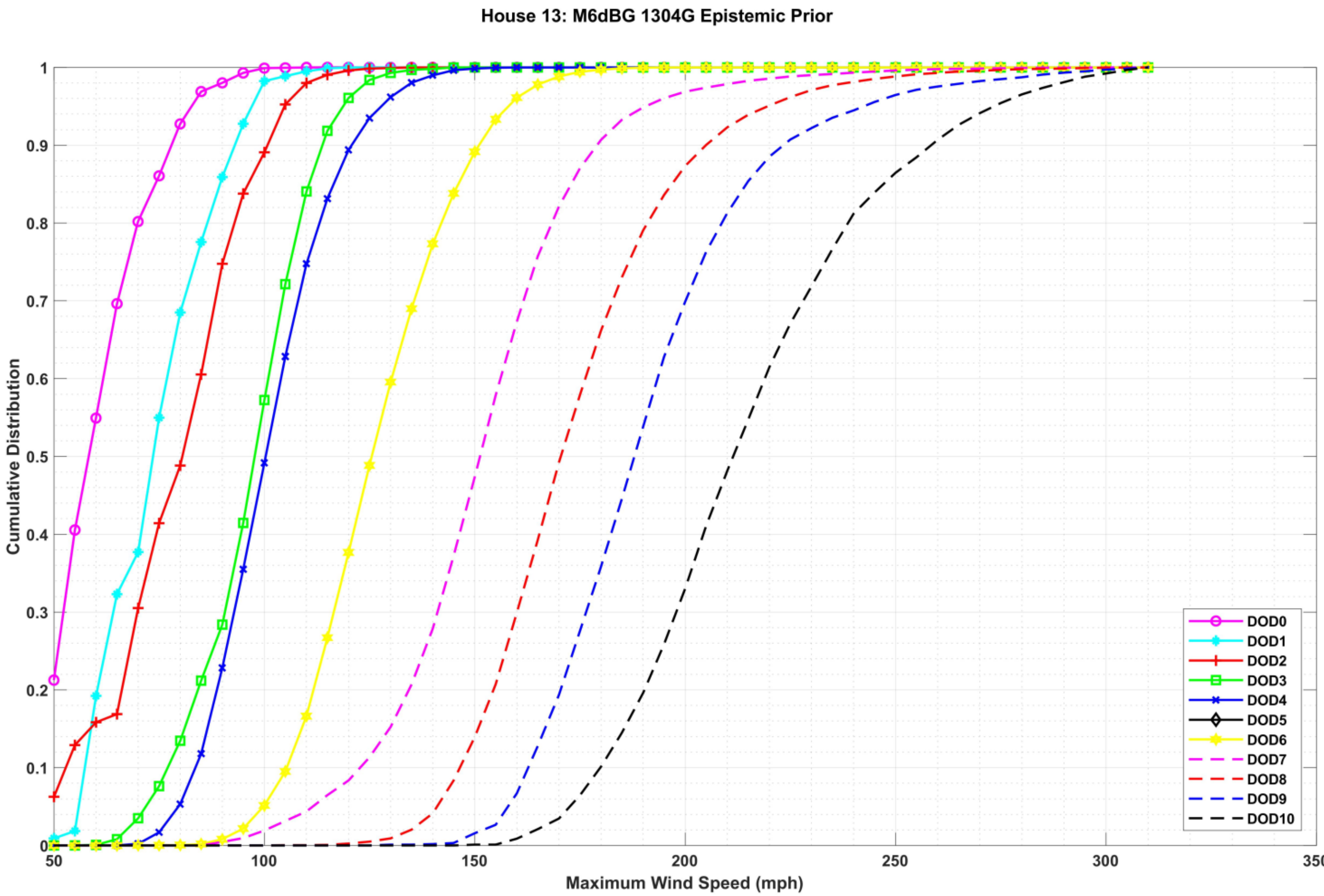
House 13: M6dBG 1304G Epistemic Prior
Cumulative Distribution
Maximum Wind Speed (mph)
0
0.1
0.2
0.3
0.4
0.5
0.6
0.7
0.8
0.9
1
50
100
150
200
250
300
350
DOD0
DOD1
DOD2
DOD3
DOD4
DOD5
DOD6
DOD7
DOD8
DOD9
DOD10

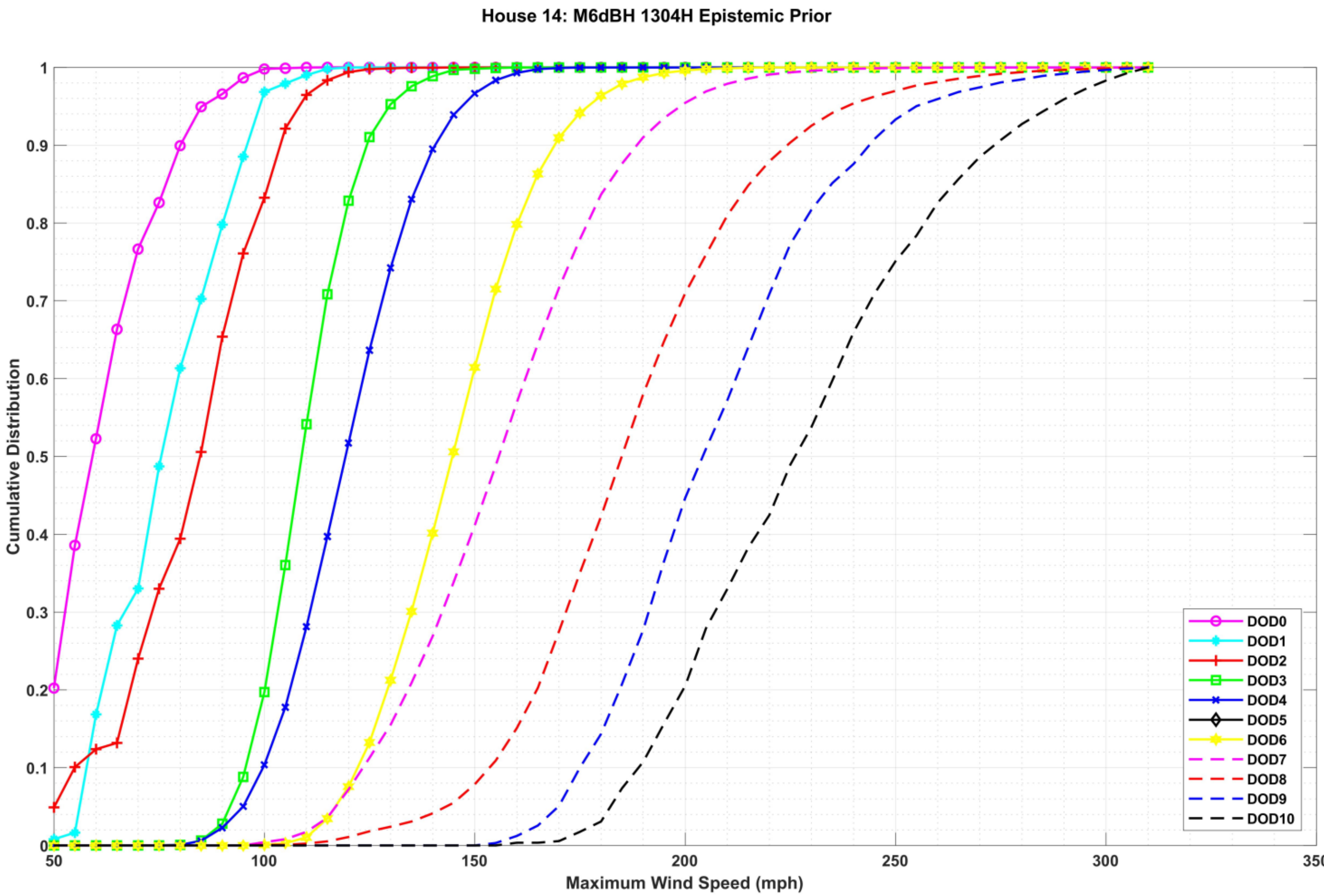
House 14: M6dBH 1304H Epistemic Prior
Cumulative Distribution
Maximum Wind Speed (mph)
0
0.1
0.2
0.3
0.4
0.5
0.6
0.7
0.8
0.9
1
50
100
150
200
250
300
350
DOD0
DOD1
DOD2
DOD3
DOD4
DOD5
DOD6
DOD7
DOD8
DOD9
DOD10

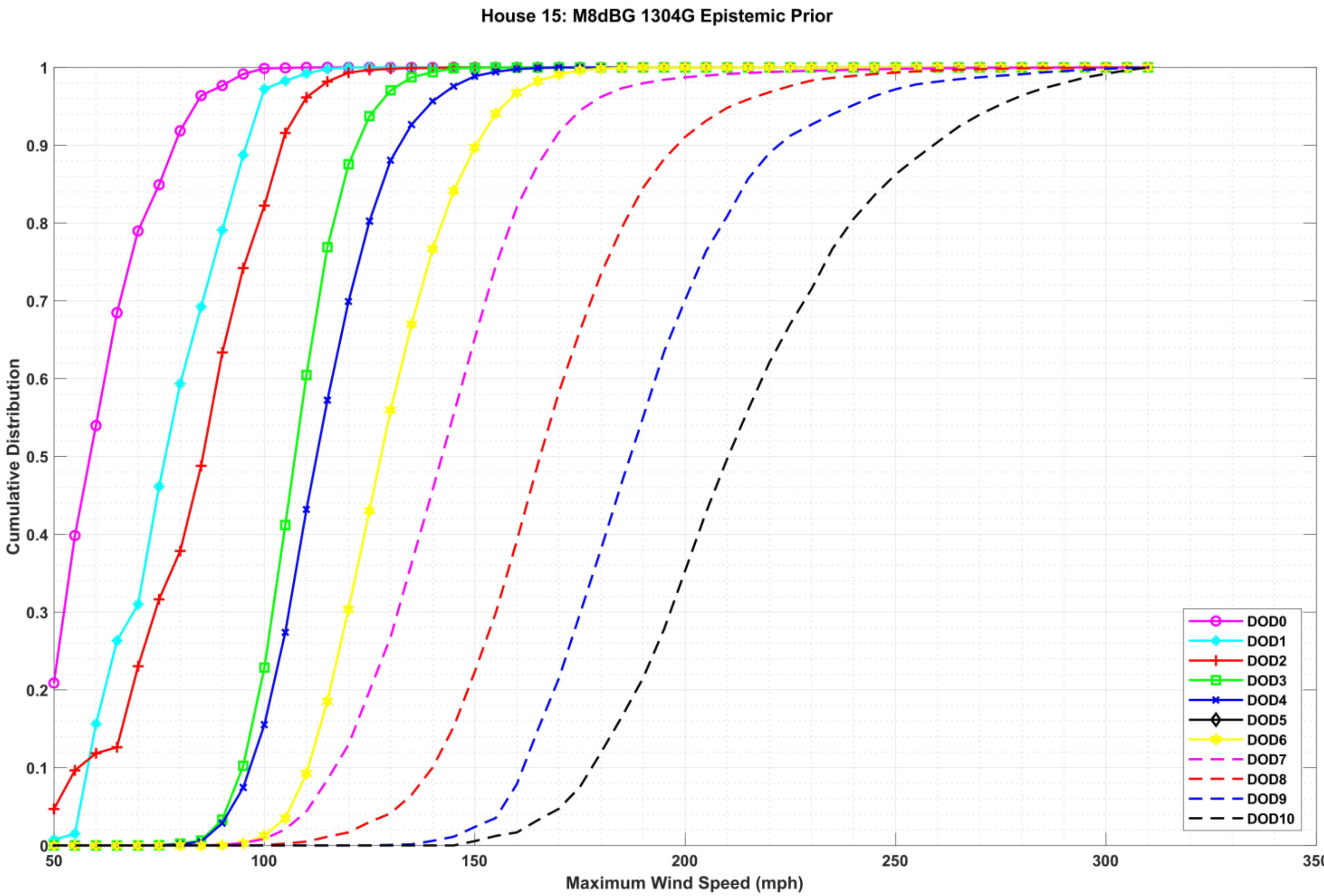
House 15: M8dBG 1304G Epistemic Prior
Cumulative Distribution
Maximum Wind Speed (mph)
0
0.1
0.2
0.3
0.4
0.5
0.6
0.7
0.8
0.9
1
50
100
150
200
250
300
350
DOD0
DOD1
DOD2
DOD3
DOD4
DOD5
DOD6
DOD7
DOD8
DOD9
DOD10

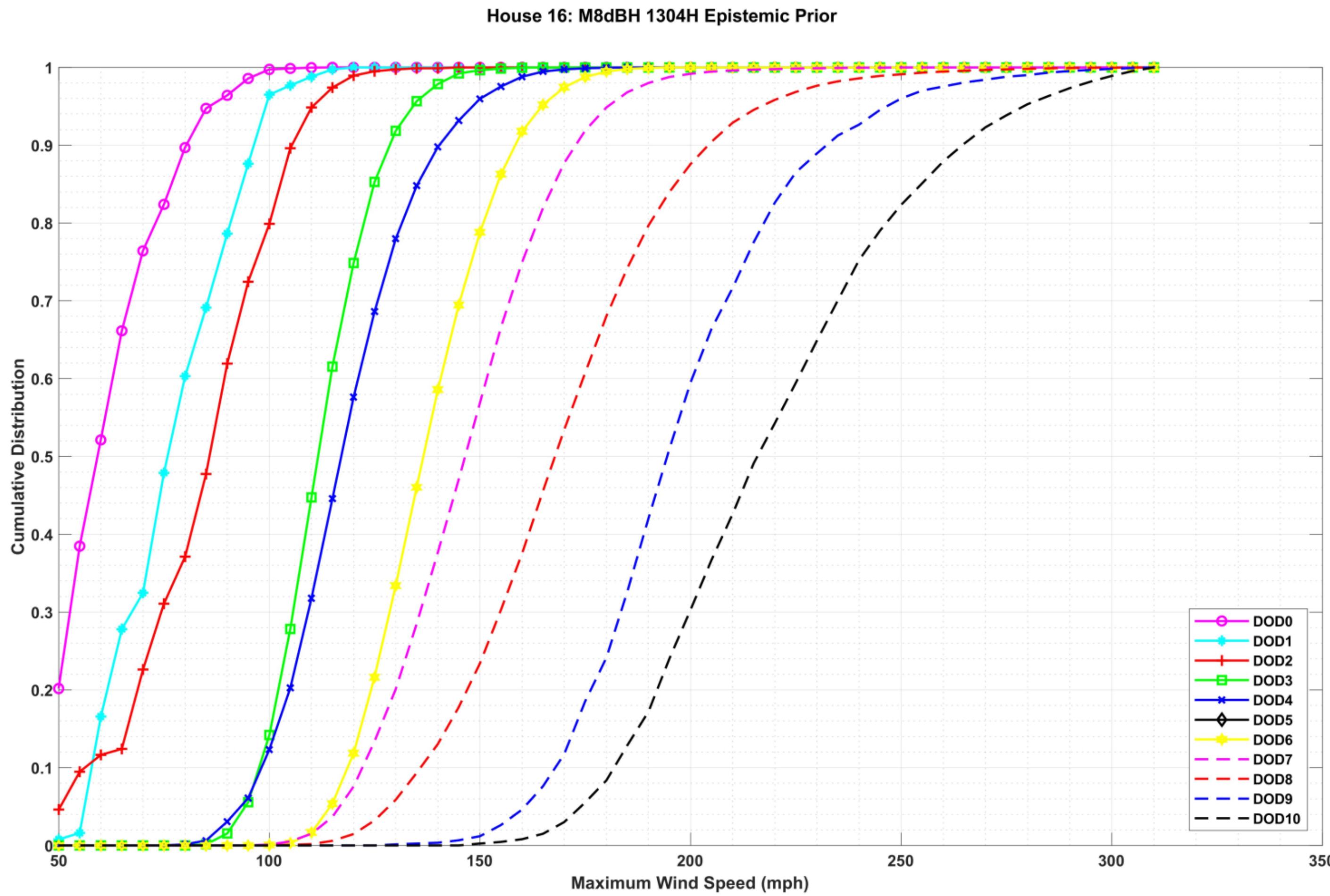

House 16: M8dBH 1304H Epistemic Prior
Cumulative Distribution
Maximum Wind Speed (mph)
0
0.1
0.2
0.3
0.4
0.5
0.6
0.7
0.8
0.9
1
50
100
150
200
250
300
350
DOD0
DOD1
DOD2
DOD3
DOD4
DOD5
DOD6
DOD7
DOD8
DOD9
DOD10

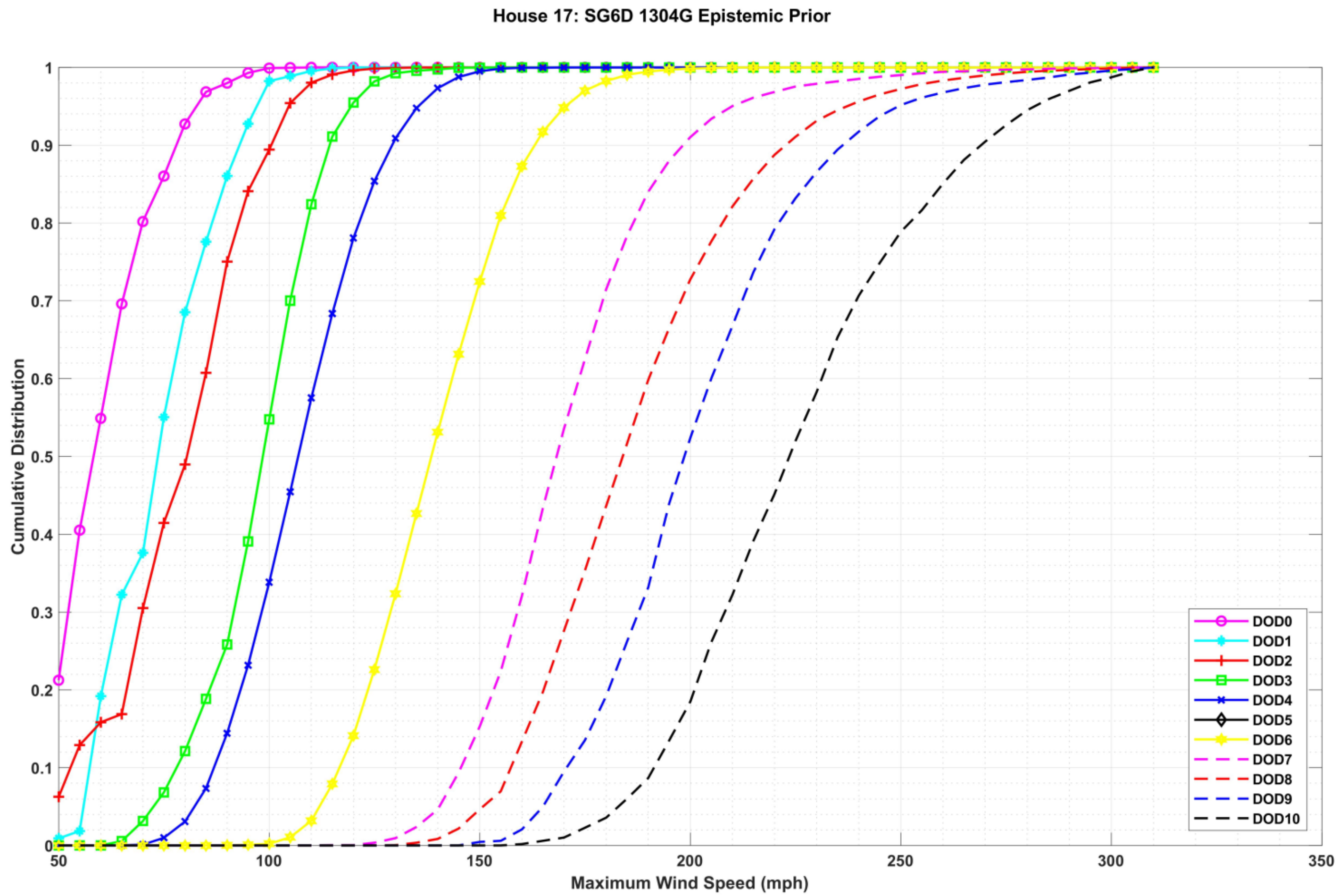
House 17: SG6D 1304G Epistemic Prior
Cumulative Distribution
Maximum Wind Speed (mph)
0
0.1
0.2
0.3
0.4
0.5
0.6
0.7
0.8
0.9
1
50
100
150
200
250
300
350
DOD0
DOD1
DOD2
DOD3
DOD4
DOD5
DOD6
DOD7
DOD8
DOD9
DOD10

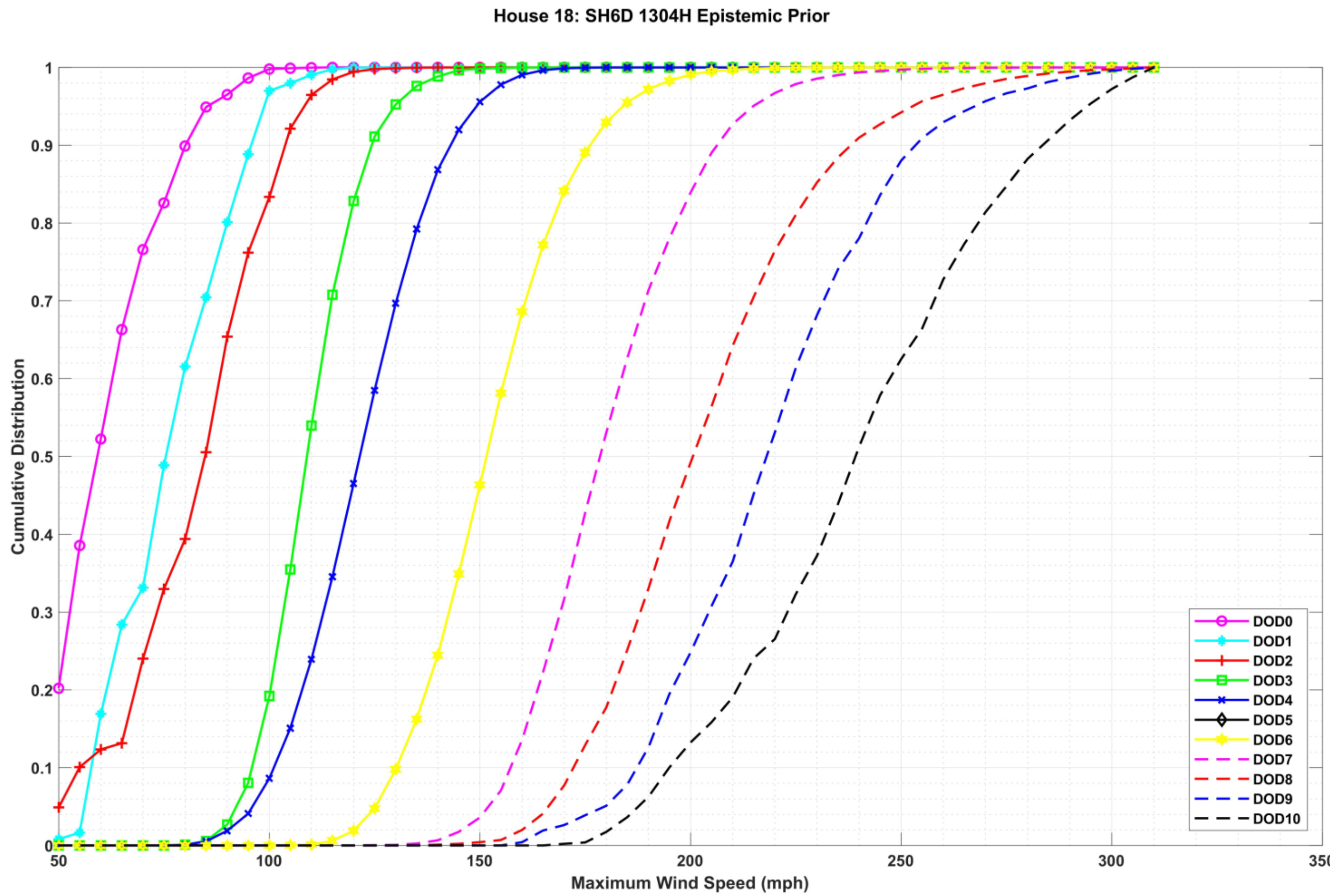
House 18: SH6D 1304H Epistemic Prior
Cumulative Distribution
Maximum Wind Speed (mph)
0
0.1
0.2
0.3
0.4
0.5
0.6
0.7
0.8
0.9
1
50
100
150
200
250
300
350
DOD0
DOD1
DOD2
DOD3
DOD4
DOD5
DOD6
DOD7
DOD8
DOD9
DOD10

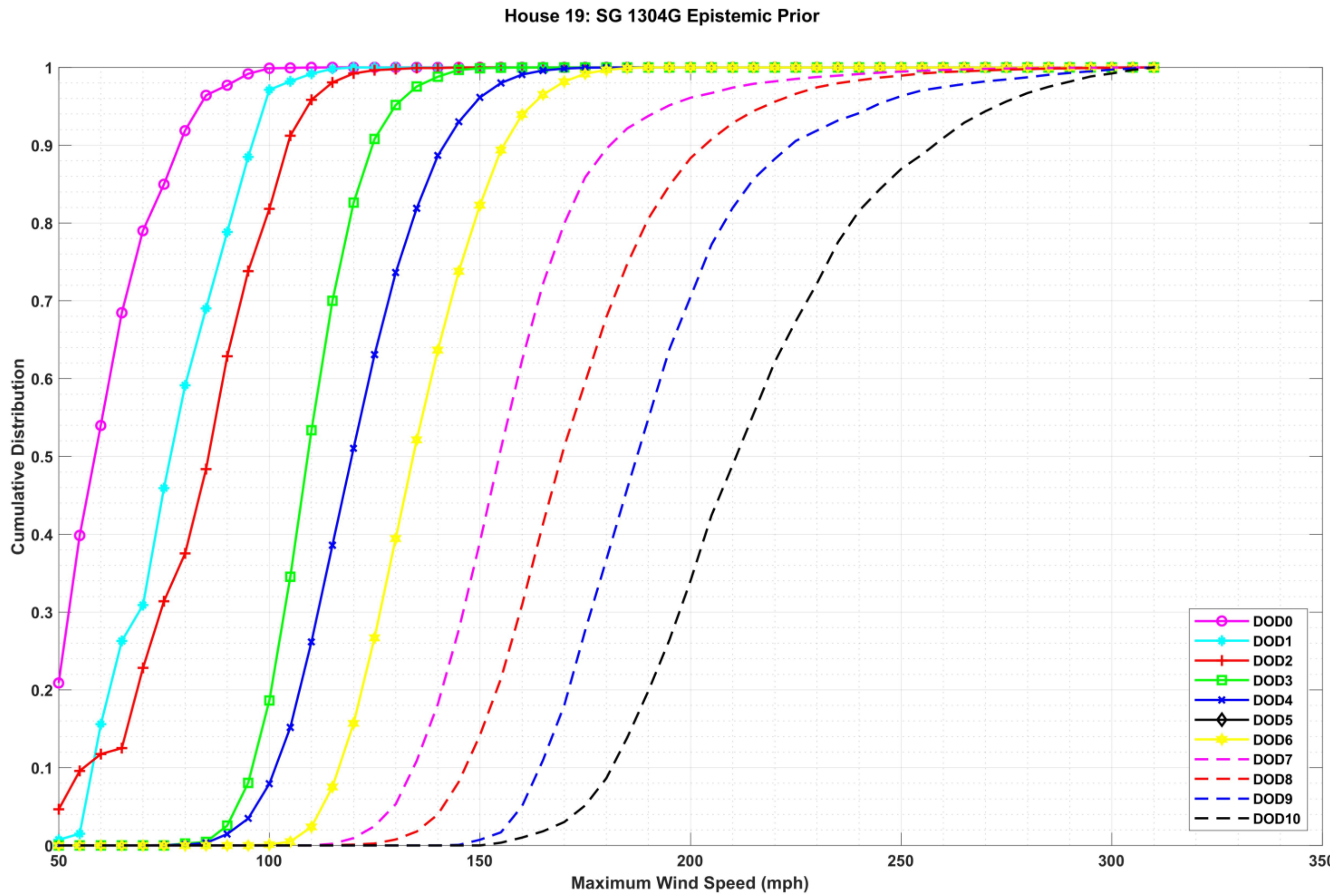
House 19: SG 1304G Epistemic Prior
Cumulative Distribution
Maximum Wind Speed (mph)
0
0.1
0.2
0.3
0.4
0.5
0.6
0.7
0.8
0.9
1
50
100
150
200
250
300
350
DOD0
DOD1
DOD2
DOD3
DOD4
DOD5
DOD6
DOD7
DOD8
DOD9
DOD10

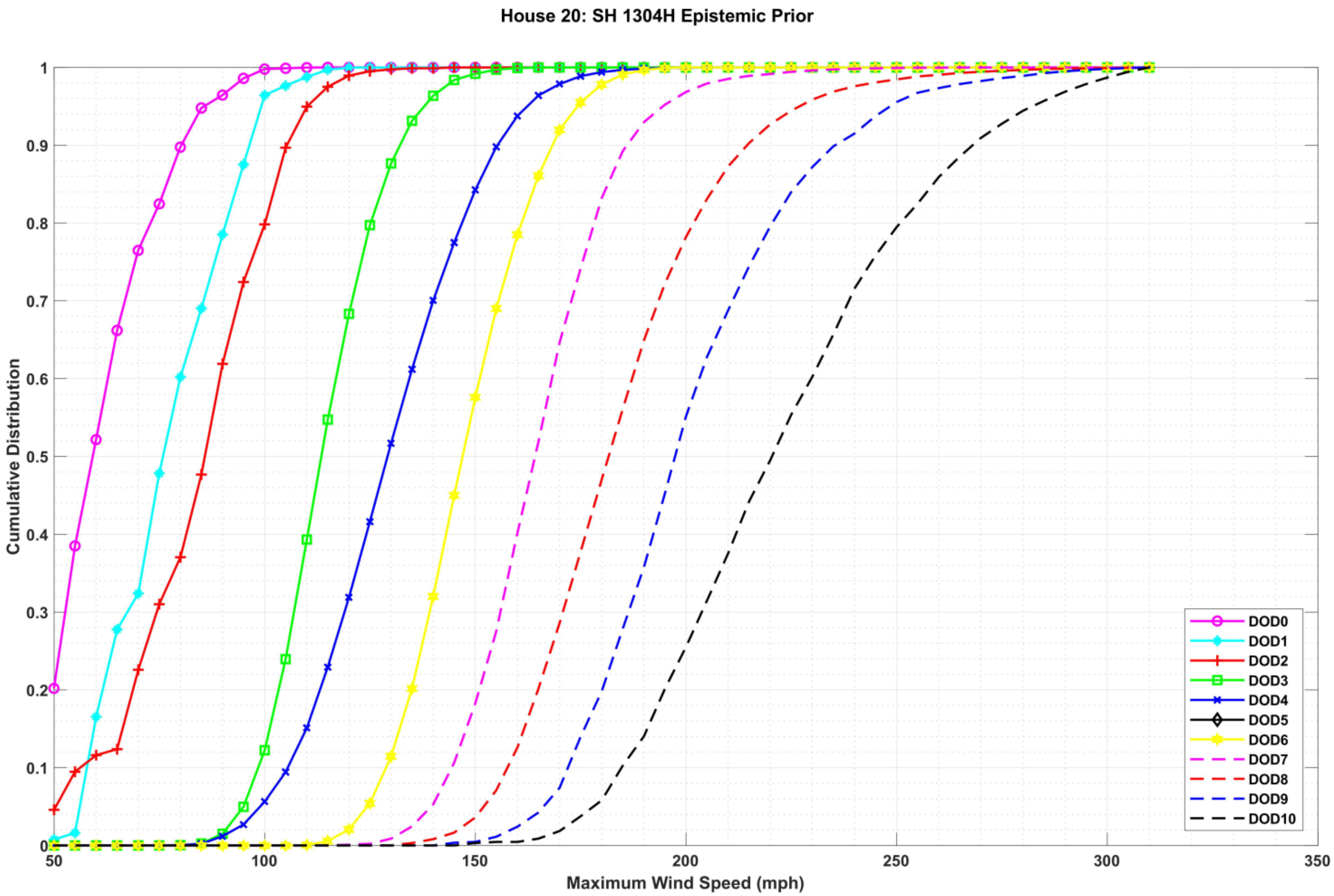
House 20: SH 1304H Epistemic Prior
Cumulative Distribution
Maximum Wind Speed (mph)
0
0.1
0.2
0.3
0.4
0.5
0.6
0.7
0.8
0.9
1
50
100
150
200
250
300
350
DOD0
DOD1
DOD2
DOD3
DOD4
DOD5
DOD6
DOD7
DOD8
DOD9
DOD10

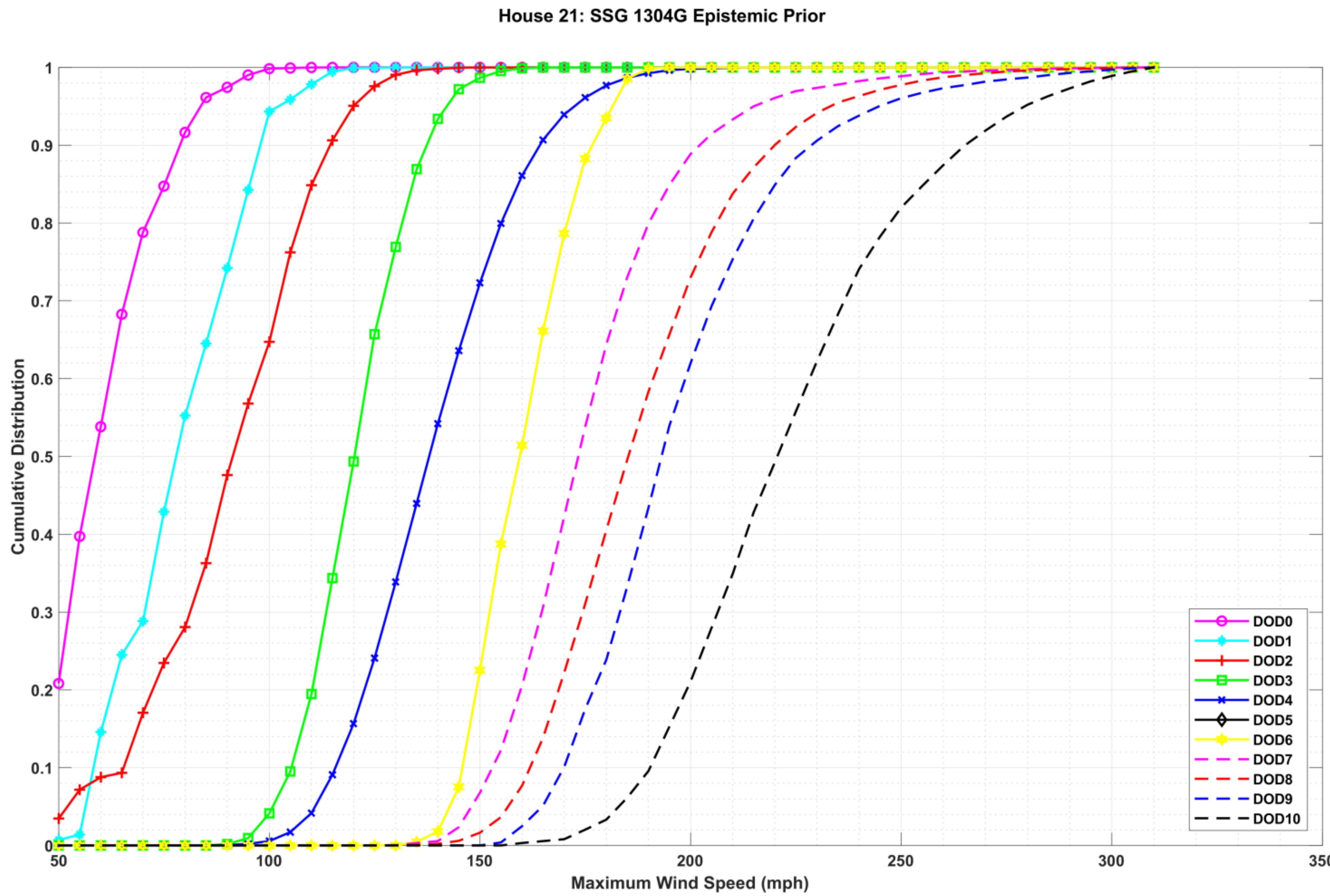
House 21: SSG 1304G Epistemic Prior
Cumulative Distribution
Maximum Wind Speed (mph)
0
0.1
0.2
0.3
0.4
0.5
0.6
0.7
0.8
0.9
1
50
100
150
200
250
300
350
DOD0
DOD1
DOD2
DOD3
DOD4
DOD5
DOD6
DOD7
DOD8
DOD9
DOD10

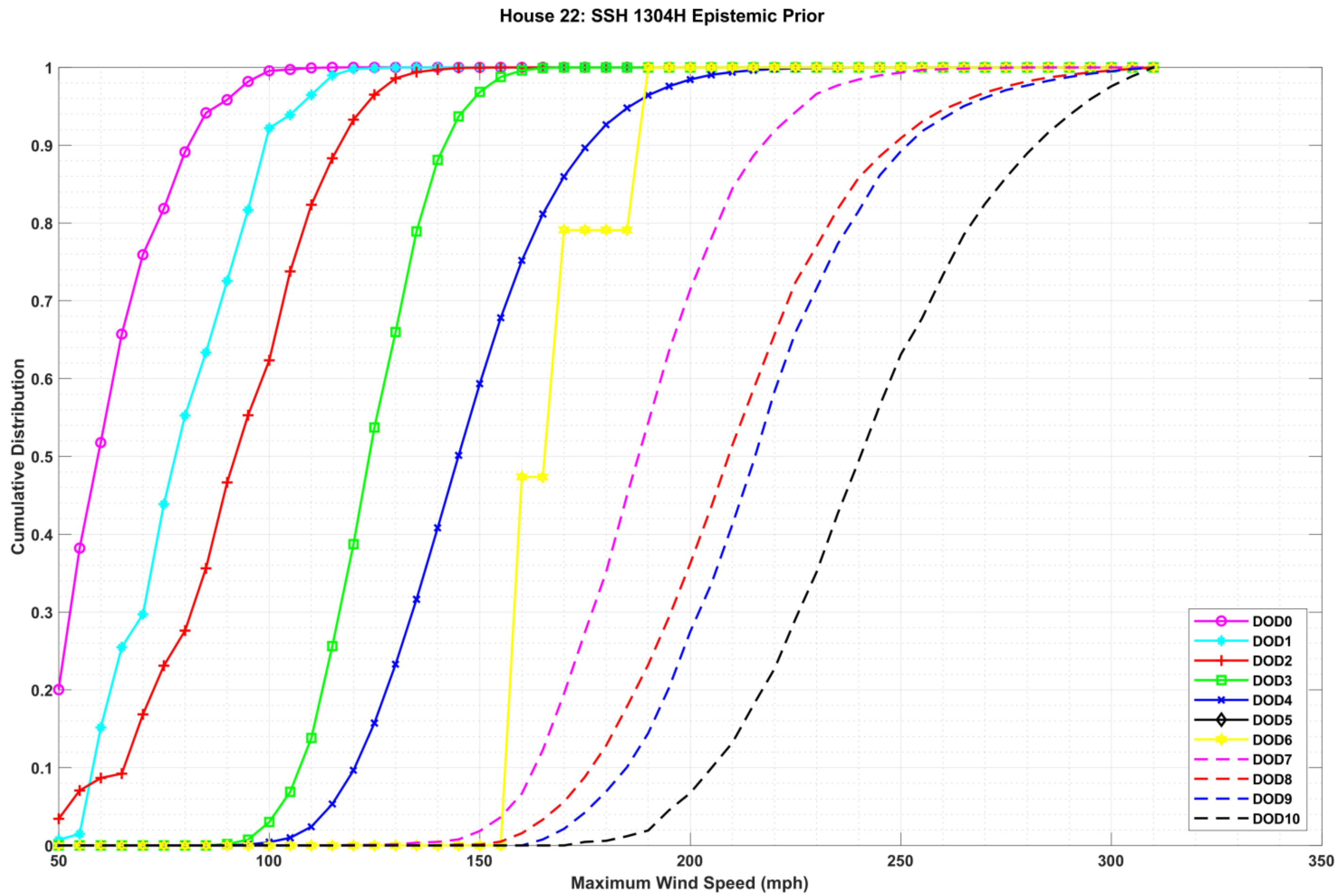
House 22: SSH 1304H Epistemic Prior
Cumulative Distribution
Maximum Wind Speed (mph)
0
0.1
0.2
0.3
0.4
0.5
0.6
0.7
0.8
0.9
1
50
100
150
200
250
300
350
DOD0
DOD1
DOD2
DOD3
DOD4
DOD5
DOD6
DOD7
DOD8
DOD9
DOD10

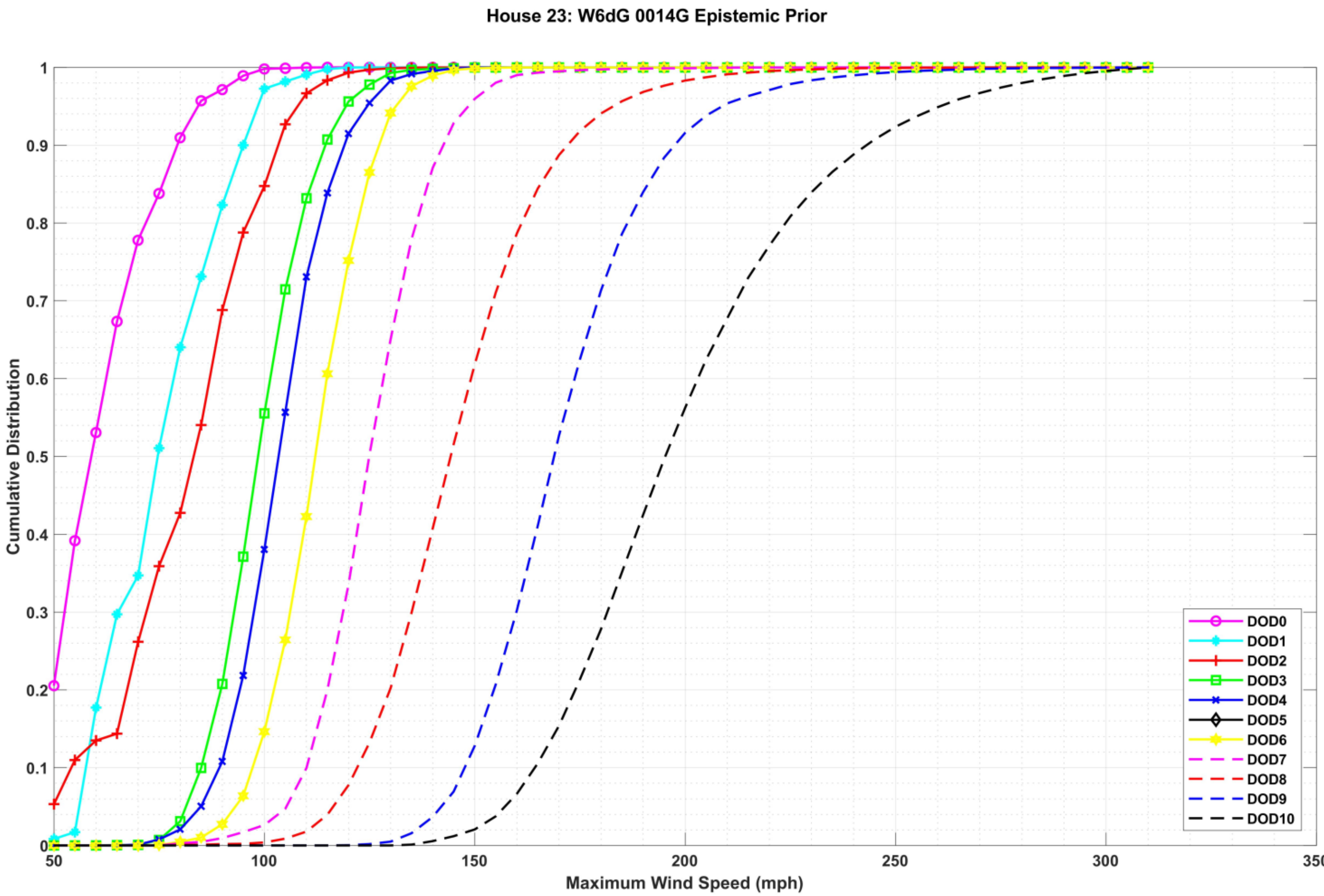
House 23: W6dG 0014G Epistemic Prior
Cumulative Distribution
Maximum Wind Speed (mph)
0
0.1
0.2
0.3
0.4
0.5
0.6
0.7
0.8
0.9
1
50
100
150
200
250
300
350
DOD0
DOD1
DOD2
DOD3
DOD4
DOD5
DOD6
DOD7
DOD8
DOD9
DOD10

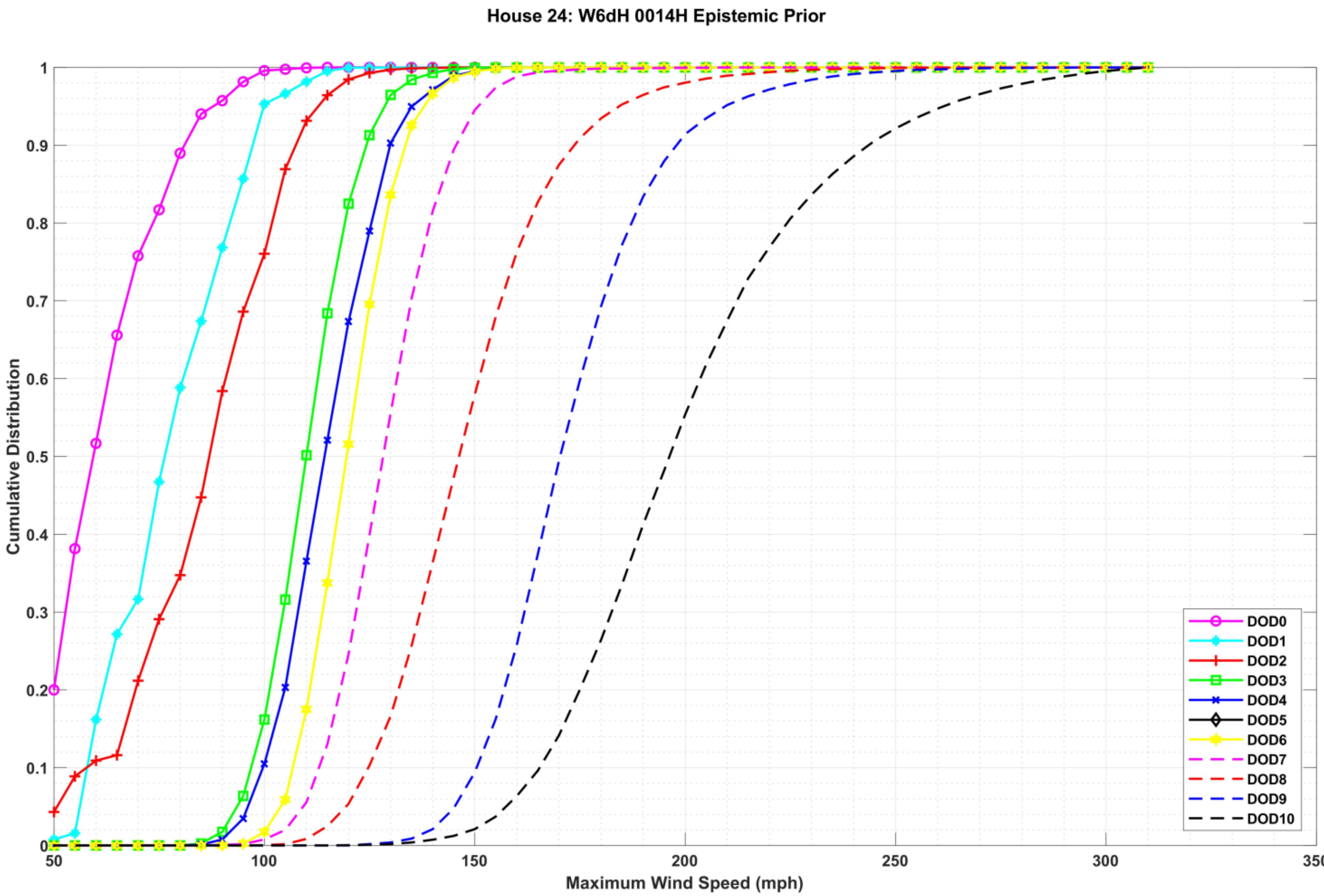

House 24: W6dH 0014H Epistemic Prior
Cumulative Distribution
Maximum Wind Speed (mph)
0
0.1
0.2
0.3
0.4
0.5
0.6
0.7
0.8
0.9
1
50
100
150
200
250
300
350
DOD0
DOD1
DOD2
DOD3
DOD4
DOD5
DOD6
DOD7
DOD8
DOD9
DOD10

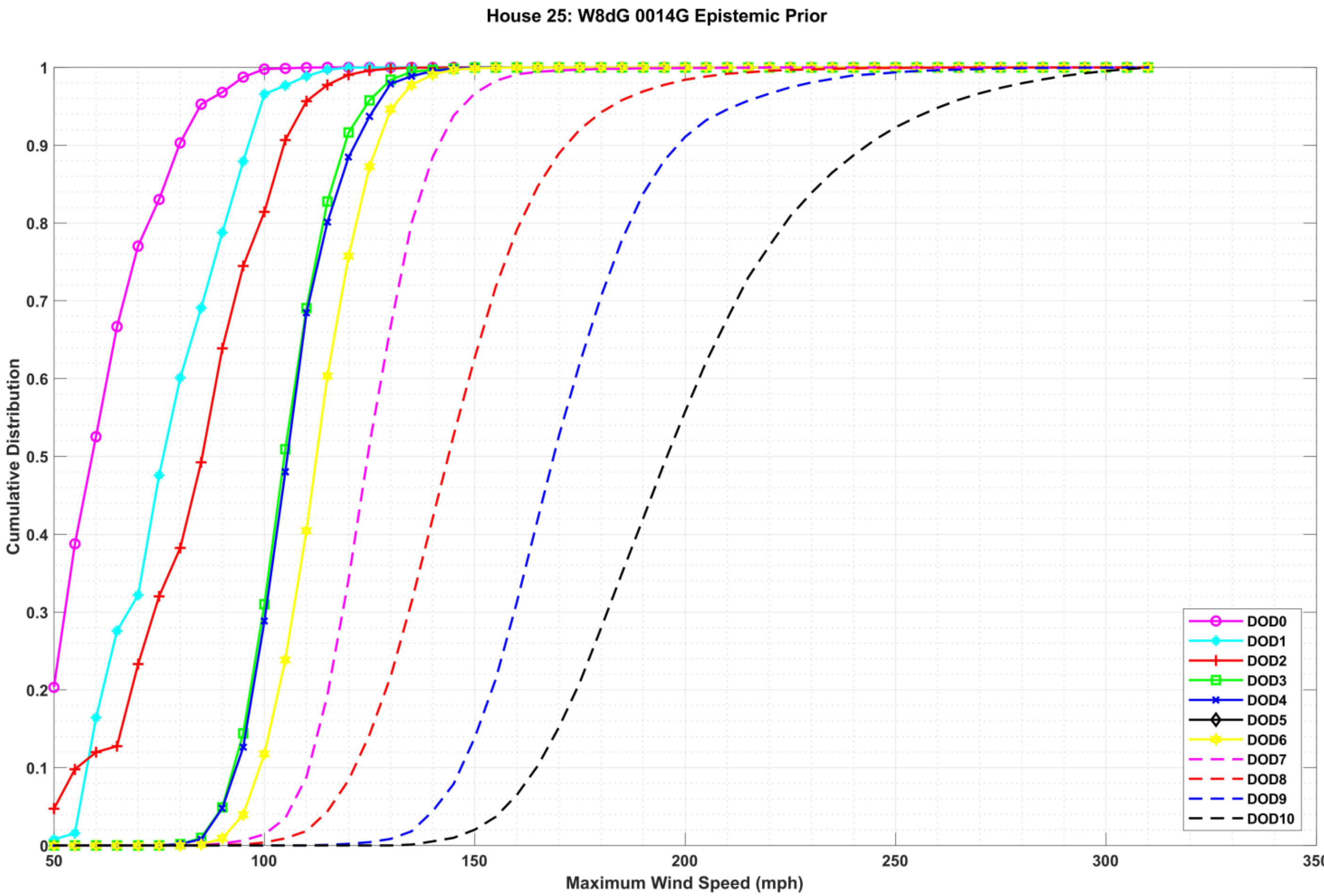
House 25: W8dG 0014G Epistemic Prior
Cumulative Distribution
Maximum Wind Speed (mph)
0
0.1
0.2
0.3
0.4
0.5
0.6
0.7
0.8
0.9
1
50
100
150
200
250
300
350
DOD0
DOD1
DOD2
DOD3
DOD4
DOD5
DOD6
DOD7
DOD8
DOD9
DOD10

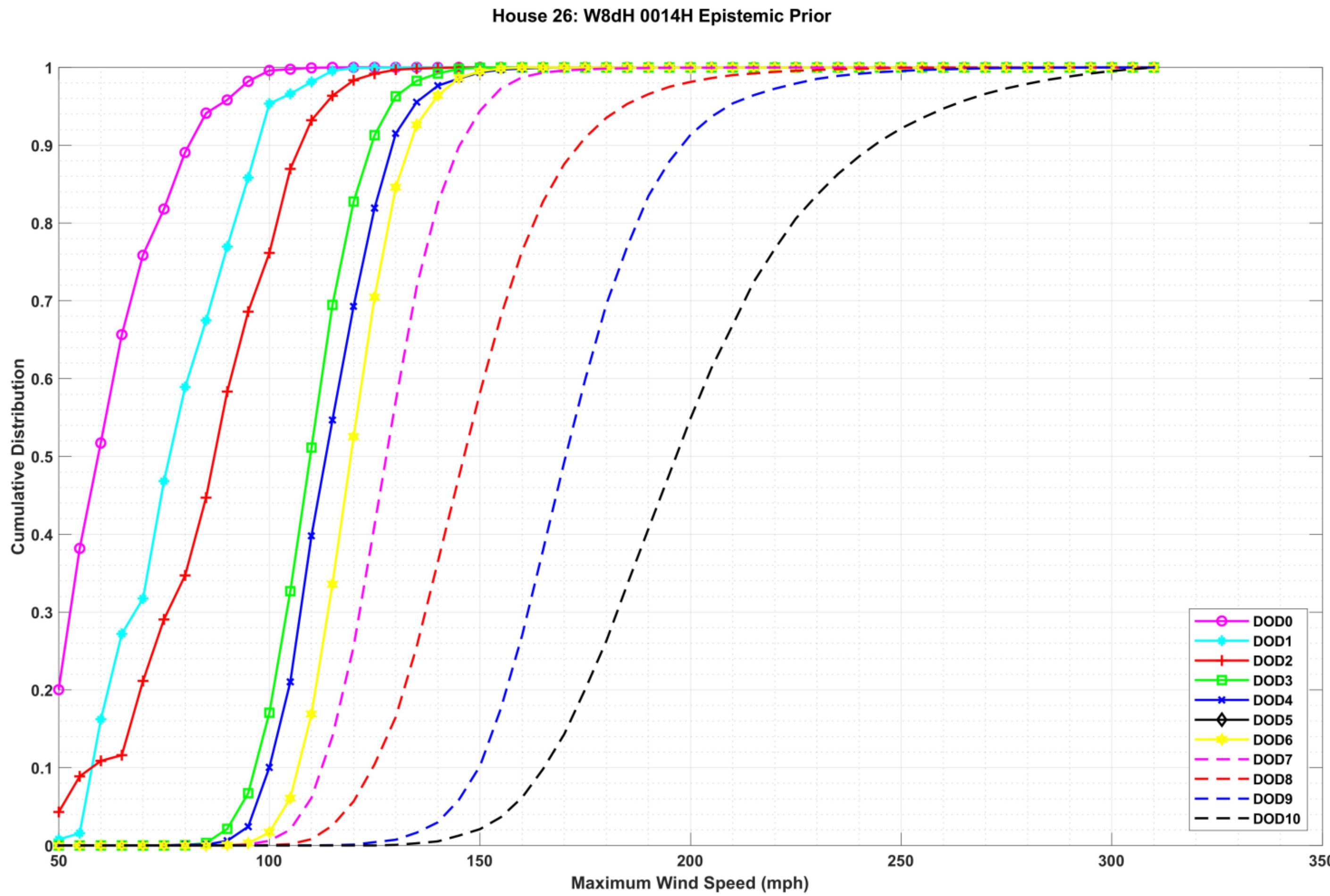
House 26: W8dH 0014H Epistemic Prior
Cumulative Distribution
Maximum Wind Speed (mph)
DOD0
DOD1
DOD2
DOD3
DOD4
DOD5
DOD6
DOD7
DOD8
DOD9
DOD10

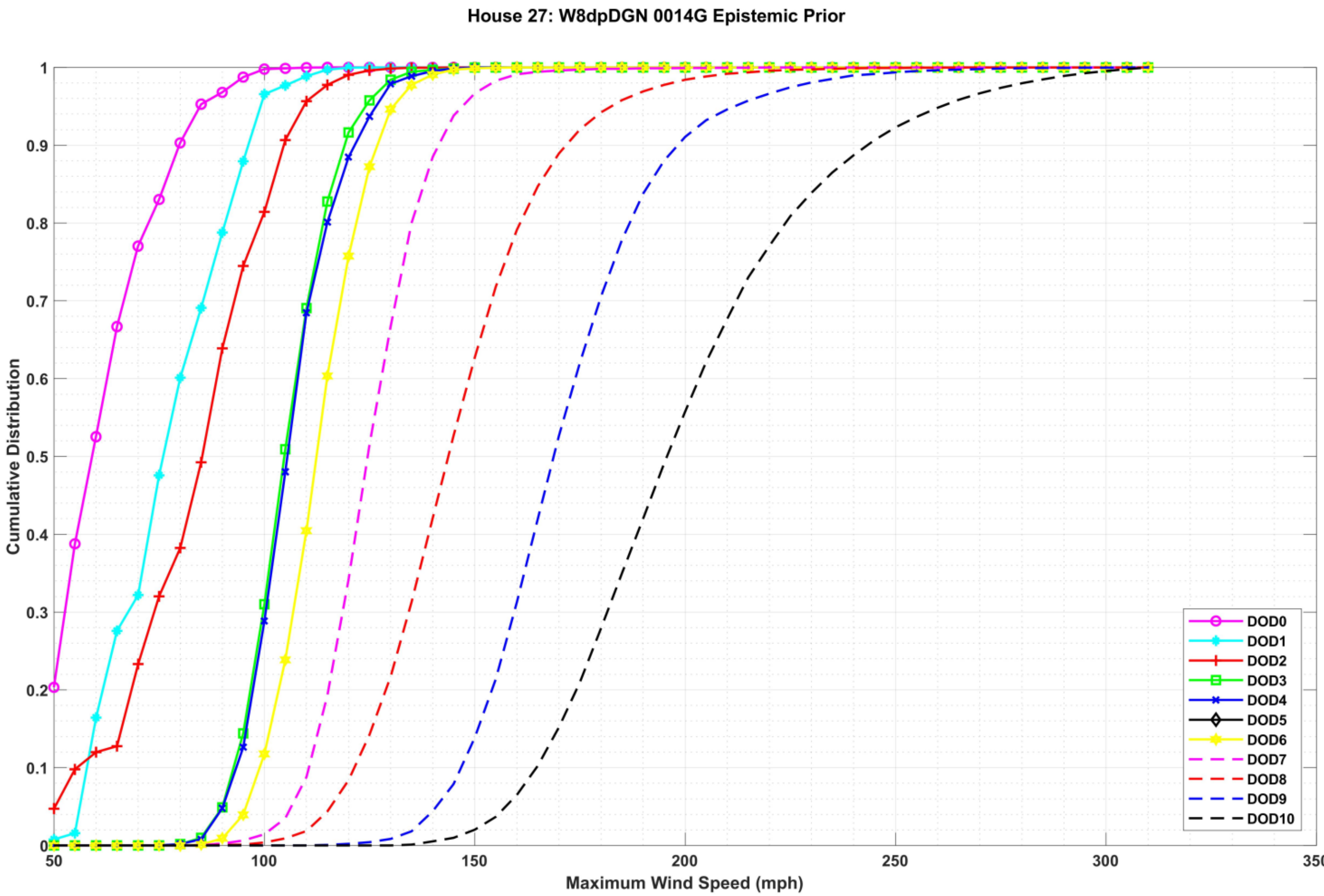
House 27: W8dpDGN 0014G Epistemic Prior
Cumulative Distribution
Maximum Wind Speed (mph)
0
0.1
0.2
0.3
0.4
0.5
0.6
0.7
0.8
0.9
1
50
100
150
200
250
300
350
DOD0
DOD1
DOD2
DOD3
DOD4
DOD5
DOD6
DOD7
DOD8
DOD9
DOD10

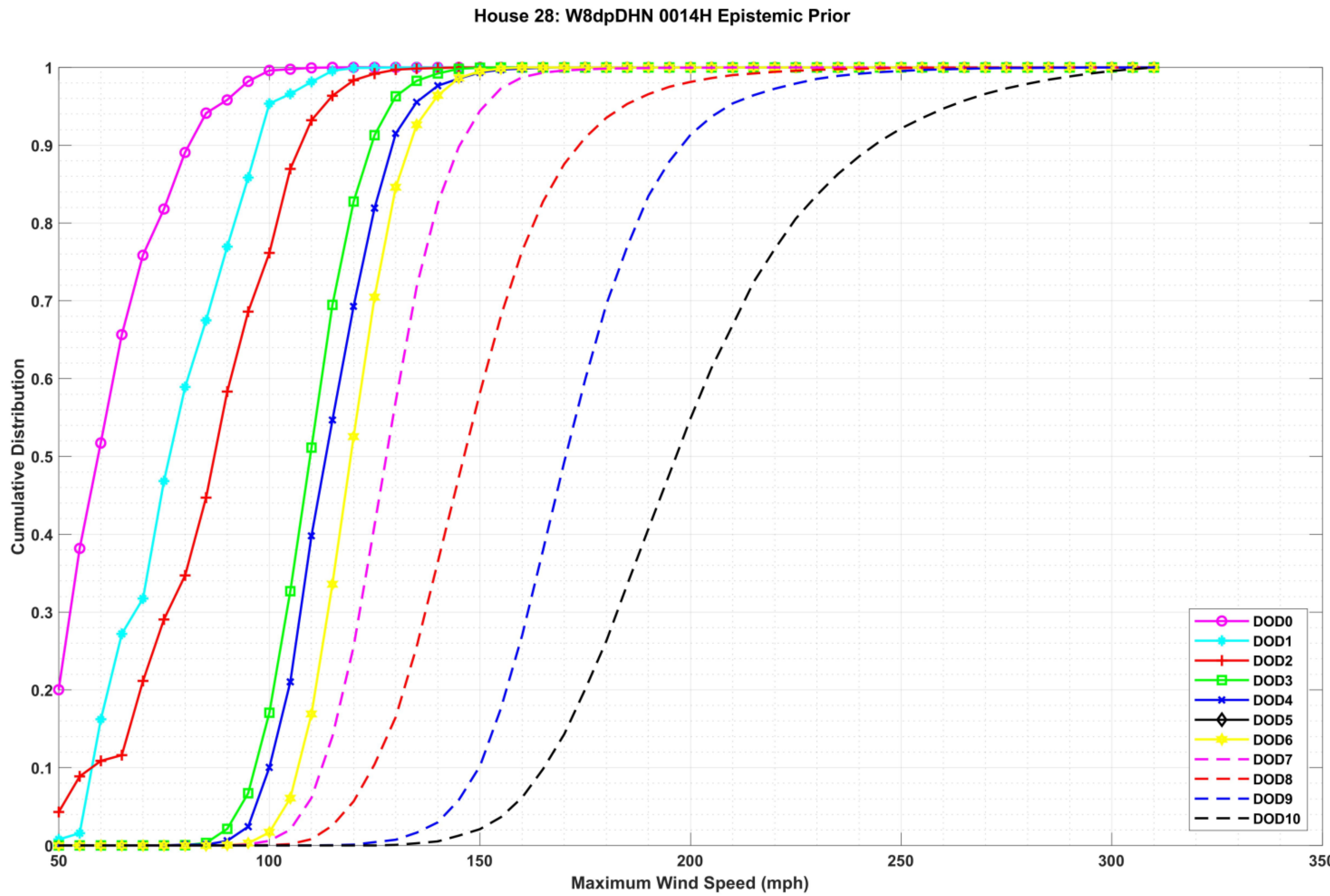
House 28: W8dpDHN 0014H Epistemic Prior
Cumulative Distribution
Maximum Wind Speed (mph)
0
0.1
0.2
0.3
0.4
0.5
0.6
0.7
0.8
0.9
1
50
100
150
200
250
300
350
DOD0
DOD1
DOD2
DOD3
DOD4
DOD5
DOD6
DOD7
DOD8
DOD9
DOD10

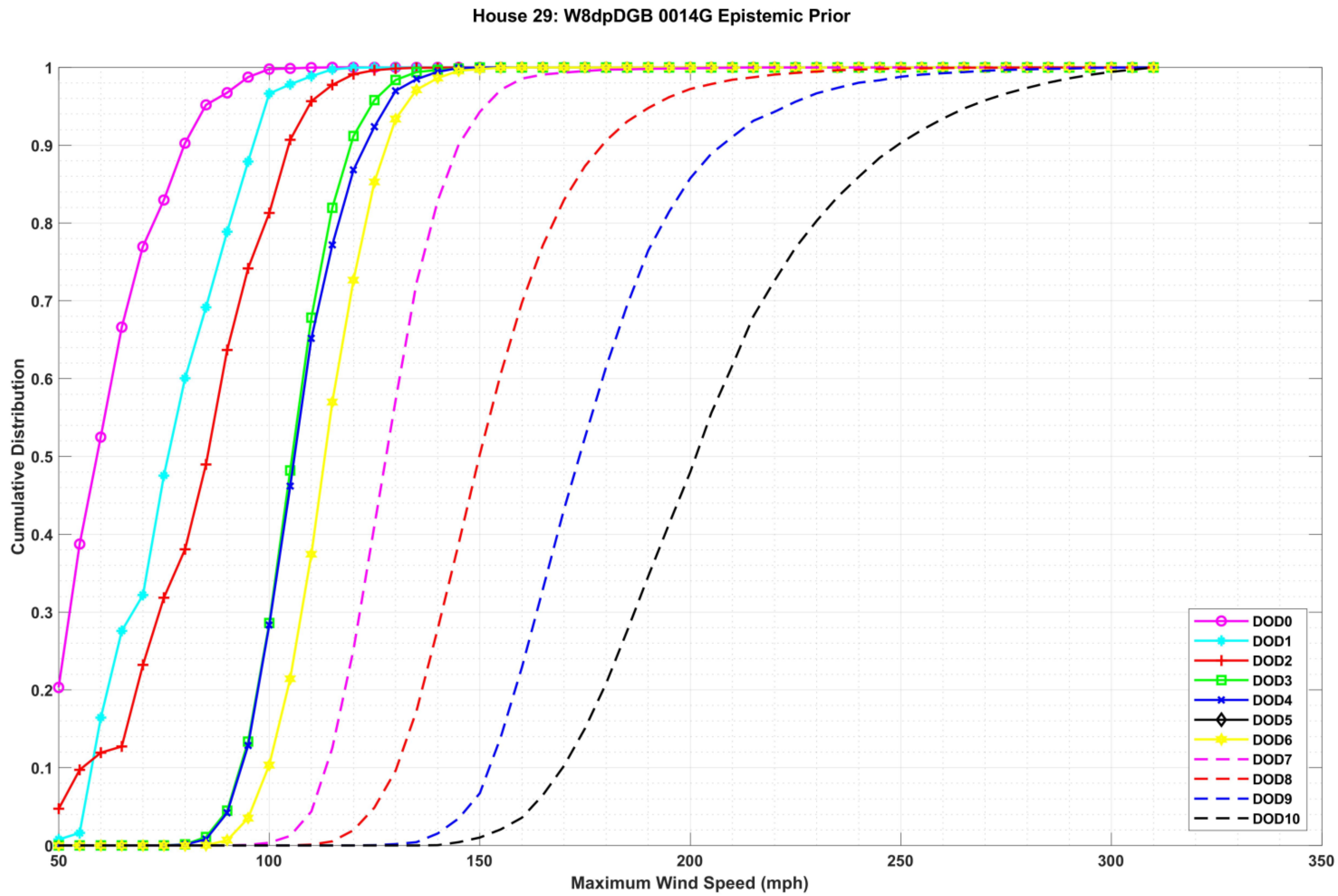
House 29: W8dpDGB 0014G Epistemic Prior
Cumulative Distribution
Maximum Wind Speed (mph)
0
0.1
0.2
0.3
0.4
0.5
0.6
0.7
0.8
0.9
1
50
100
150
200
250
300
350
DOD0
DOD1
DOD2
DOD3
DOD4
DOD5
DOD6
DOD7
DOD8
DOD9
DOD10

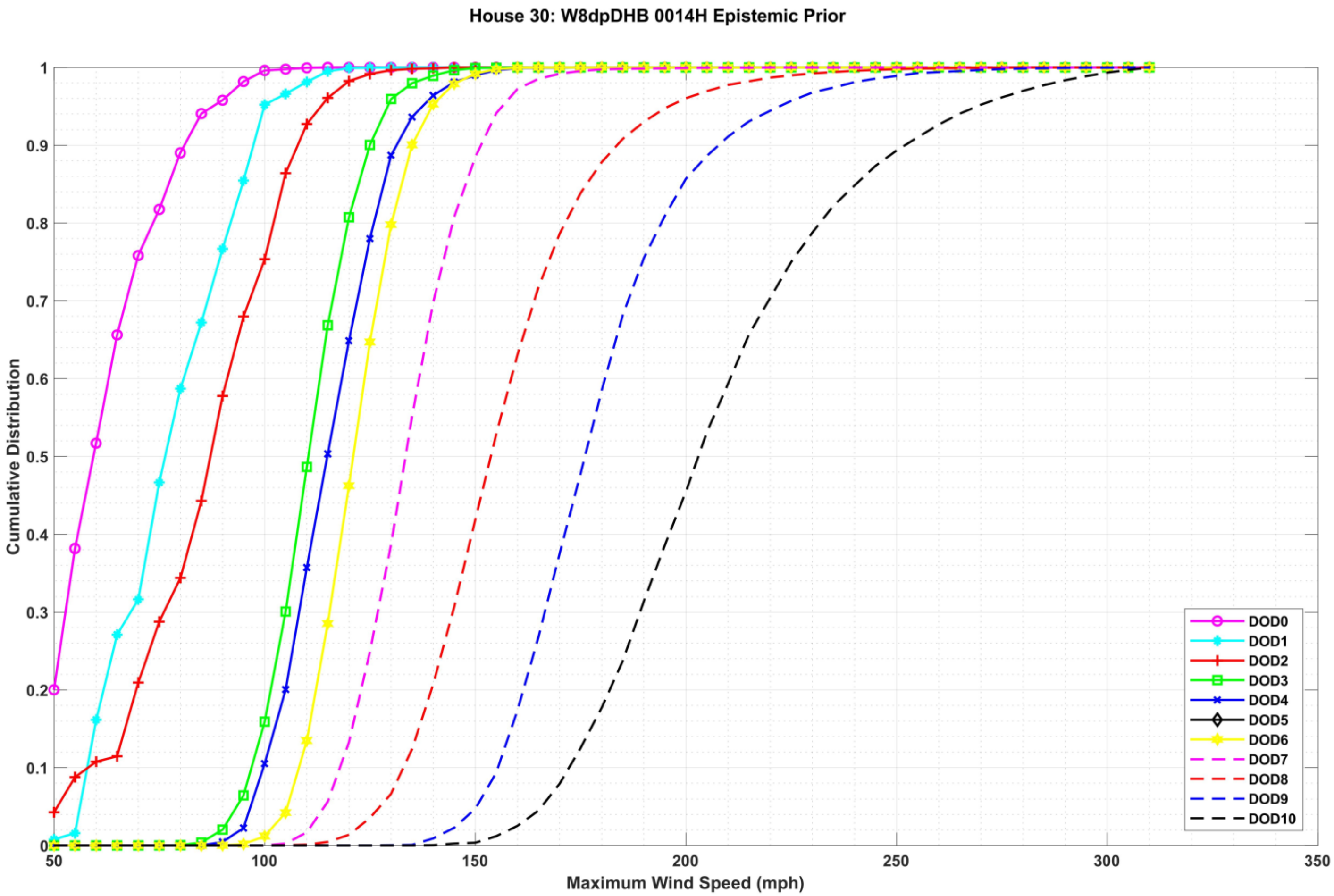
House 30: W8dpDHB 0014H Epistemic Prior
Cumulative Distribution
Maximum Wind Speed (mph)
0
0.1
0.2
0.3
0.4
0.5
0.6
0.7
0.8
0.9
1
50
100
150
200
250
300
350
DOD0
DOD1
DOD2
DOD3
DOD4
DOD5
DOD6
DOD7
DOD8
DOD9
DOD10

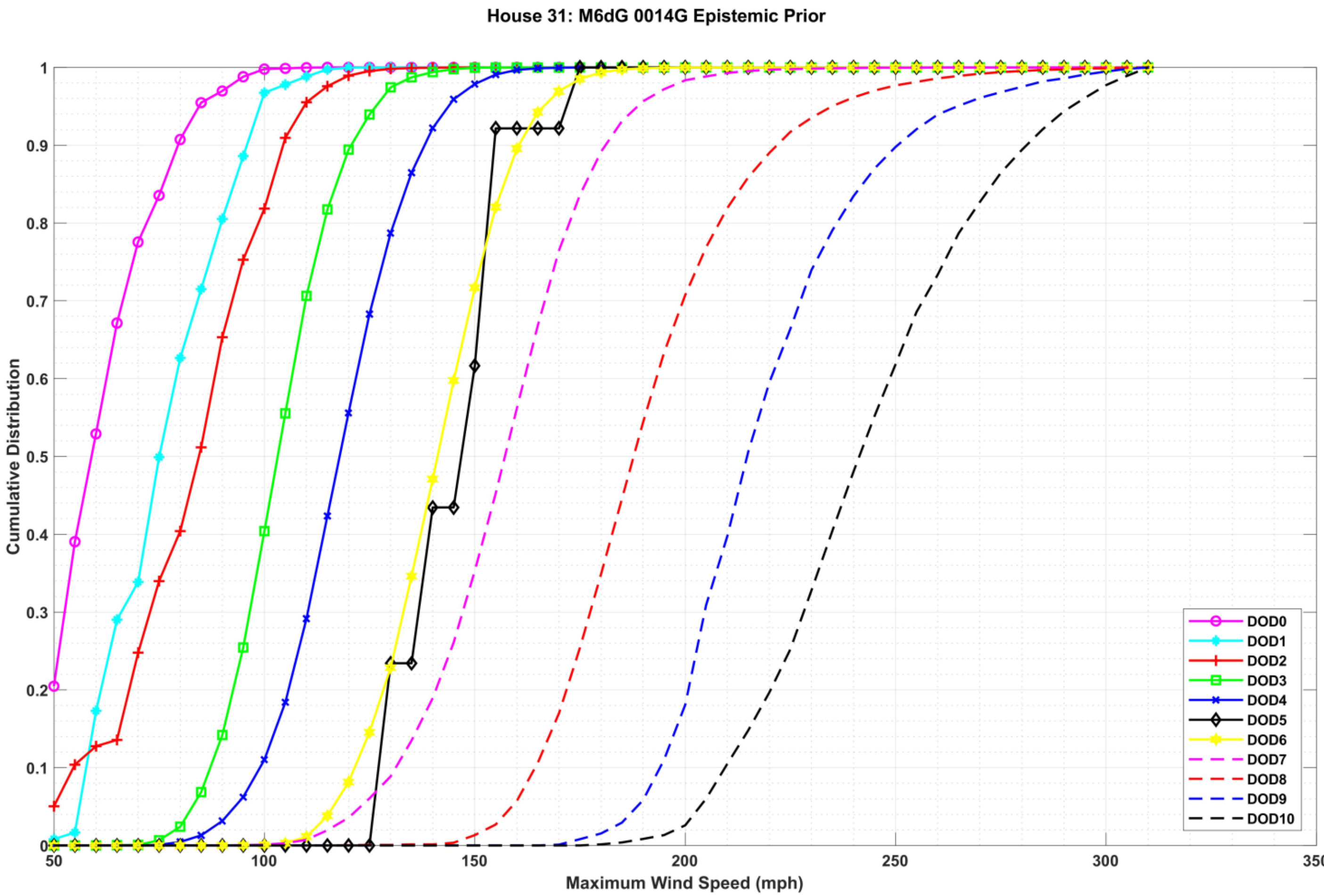
House 31: M6dG 0014G Epistemic Prior
Cumulative Distribution
Maximum Wind Speed (mph)
0
0.1
0.2
0.3
0.4
0.5
0.6
0.7
0.8
0.9
1
50
100
150
200
250
300
350
DOD0
DOD1
DOD2
DOD3
DOD4
DOD5
DOD6
DOD7
DOD8
DOD9
DOD10

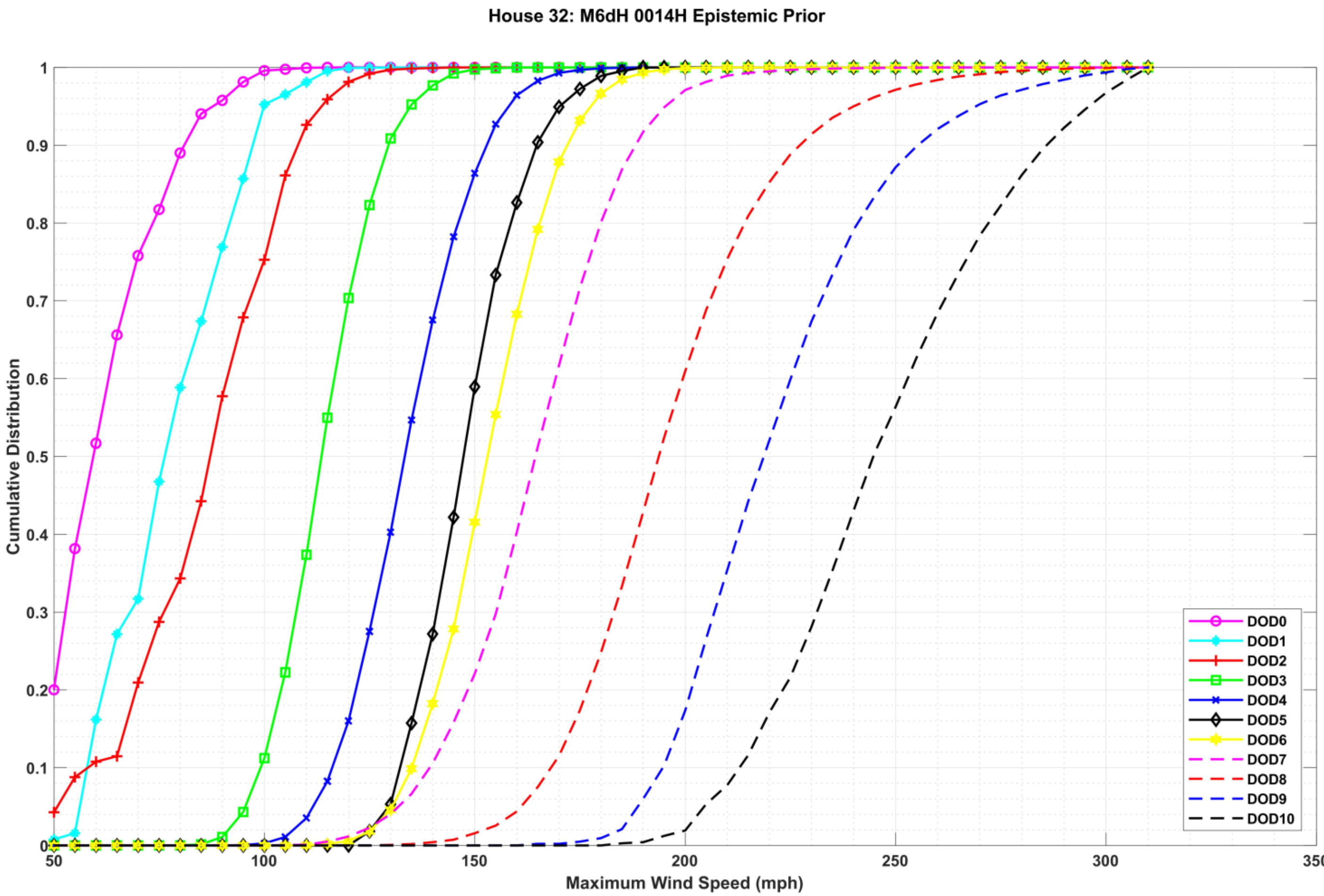
House 32: M6dH 0014H Epistemic Prior
Cumulative Distribution
Maximum Wind Speed (mph)
0
0.1
0.2
0.3
0.4
0.5
0.6
0.7
0.8
0.9
1
50
100
150
200
250
300
350
DOD0
DOD1
DOD2
DOD3
DOD4
DOD5
DOD6
DOD7
DOD8
DOD9
DOD10

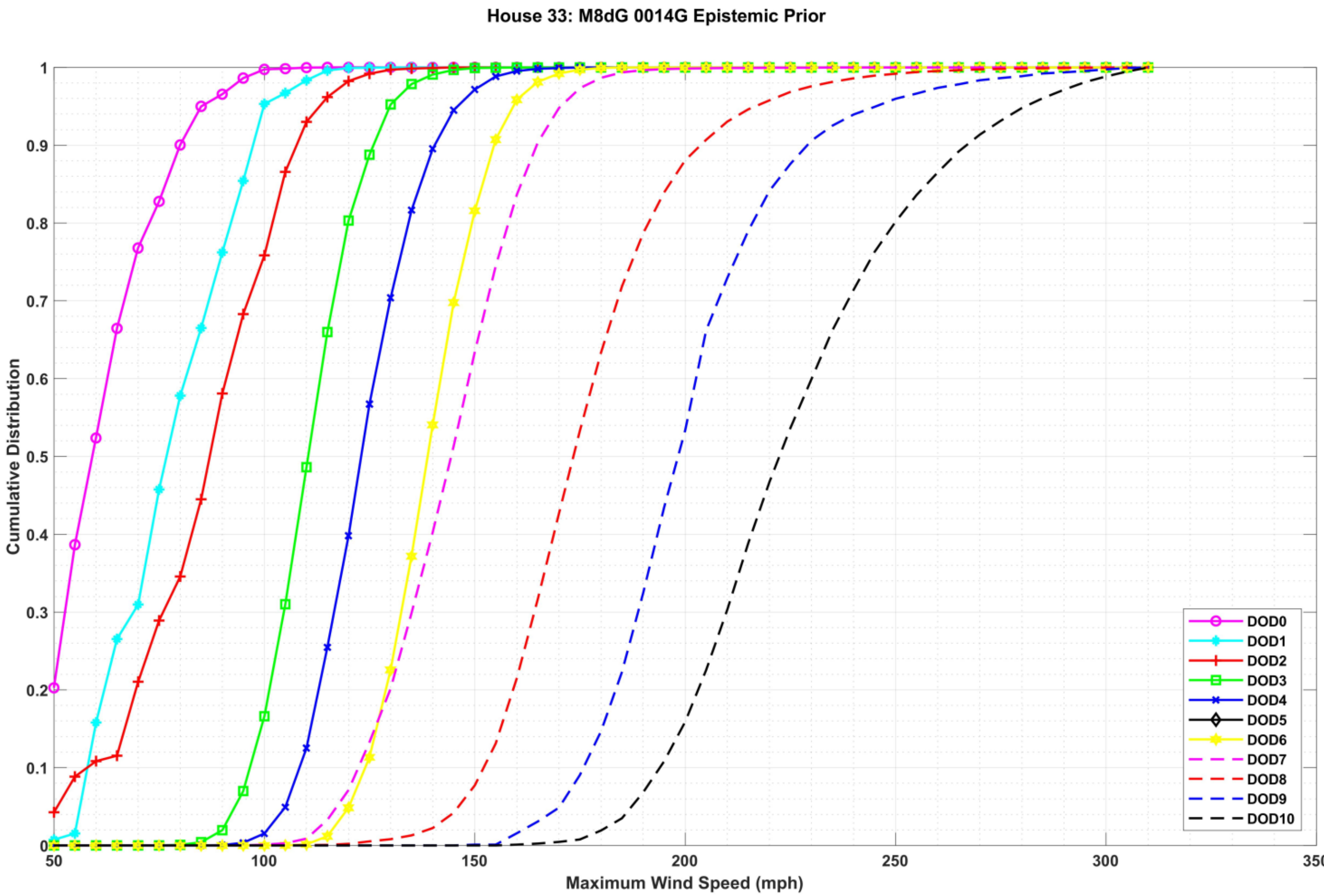
House 33: M8dG 0014G Epistemic Prior
Cumulative Distribution
Maximum Wind Speed (mph)
0
0.1
0.2
0.3
0.4
0.5
0.6
0.7
0.8
0.9
1
50
100
150
200
250
300
350
DOD0
DOD1
DOD2
DOD3
DOD4
DOD5
DOD6
DOD7
DOD8
DOD9
DOD10

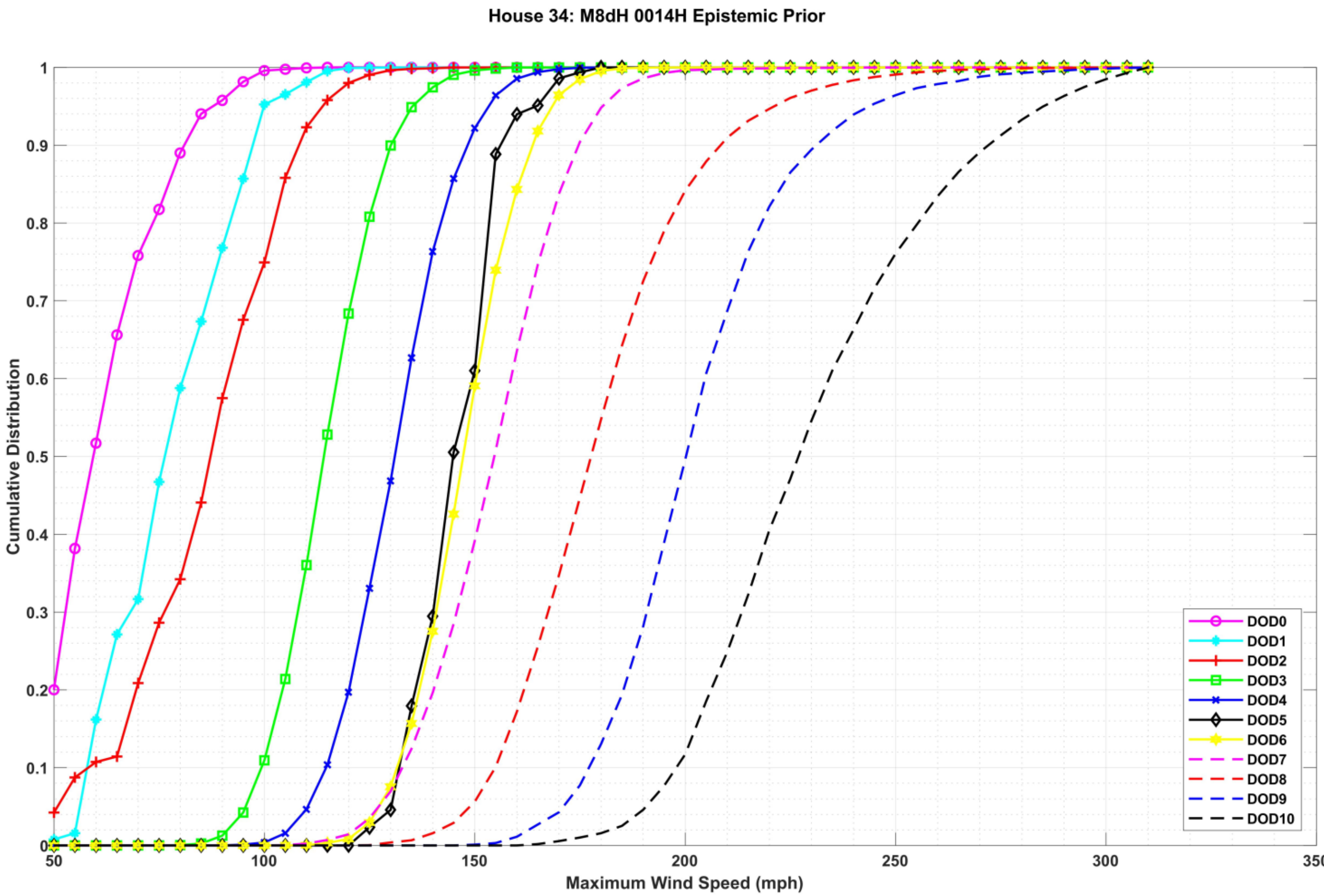
House 34: M8dH 0014H Epistemic Prior
Cumulative Distribution
Maximum Wind Speed (mph)
0
0.1
0.2
0.3
0.4
0.5
0.6
0.7
0.8
0.9
1
50
100
150
200
250
300
350
DOD0
DOD1
DOD2
DOD3
DOD4
DOD5
DOD6
DOD7
DOD8
DOD9
DOD10

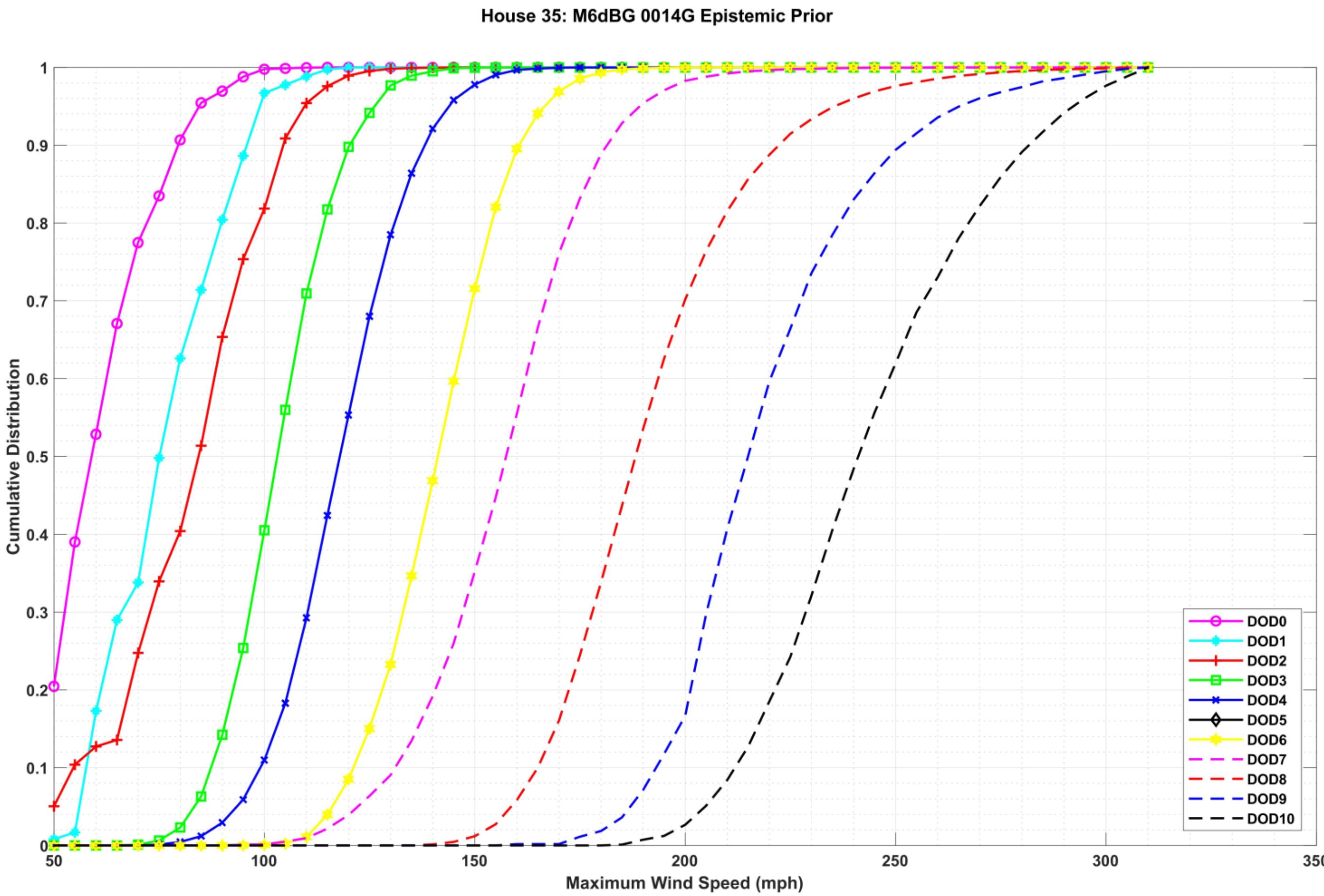
House 35: M6dBG 0014G Epistemic Prior
Cumulative Distribution
Maximum Wind Speed (mph)
0
0.1
0.2
0.3
0.4
0.5
0.6
0.7
0.8
0.9
1
50
100
150
200
250
300
350
DOD0
DOD1
DOD2
DOD3
DOD4
DOD5
DOD6
DOD7
DOD8
DOD9
DOD10

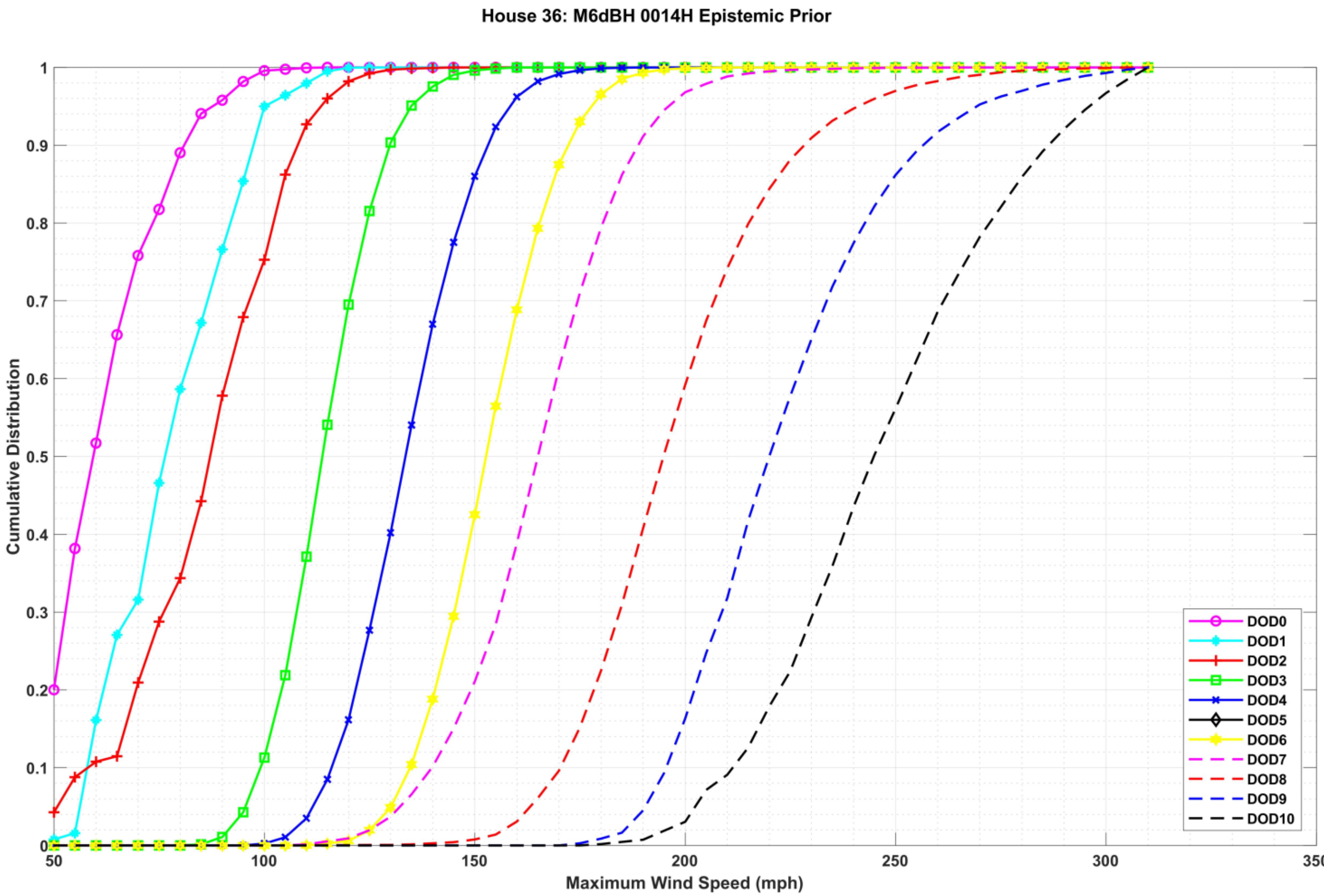

House 36: M6dBH 0014H Epistemic Prior
Cumulative Distribution
Maximum Wind Speed (mph)
0
0.1
0.2
0.3
0.4
0.5
0.6
0.7
0.8
0.9
1
50
100
150
200
250
300
350
DOD0
DOD1
DOD2
DOD3
DOD4
DOD5
DOD6
DOD7
DOD8
DOD9
DOD10

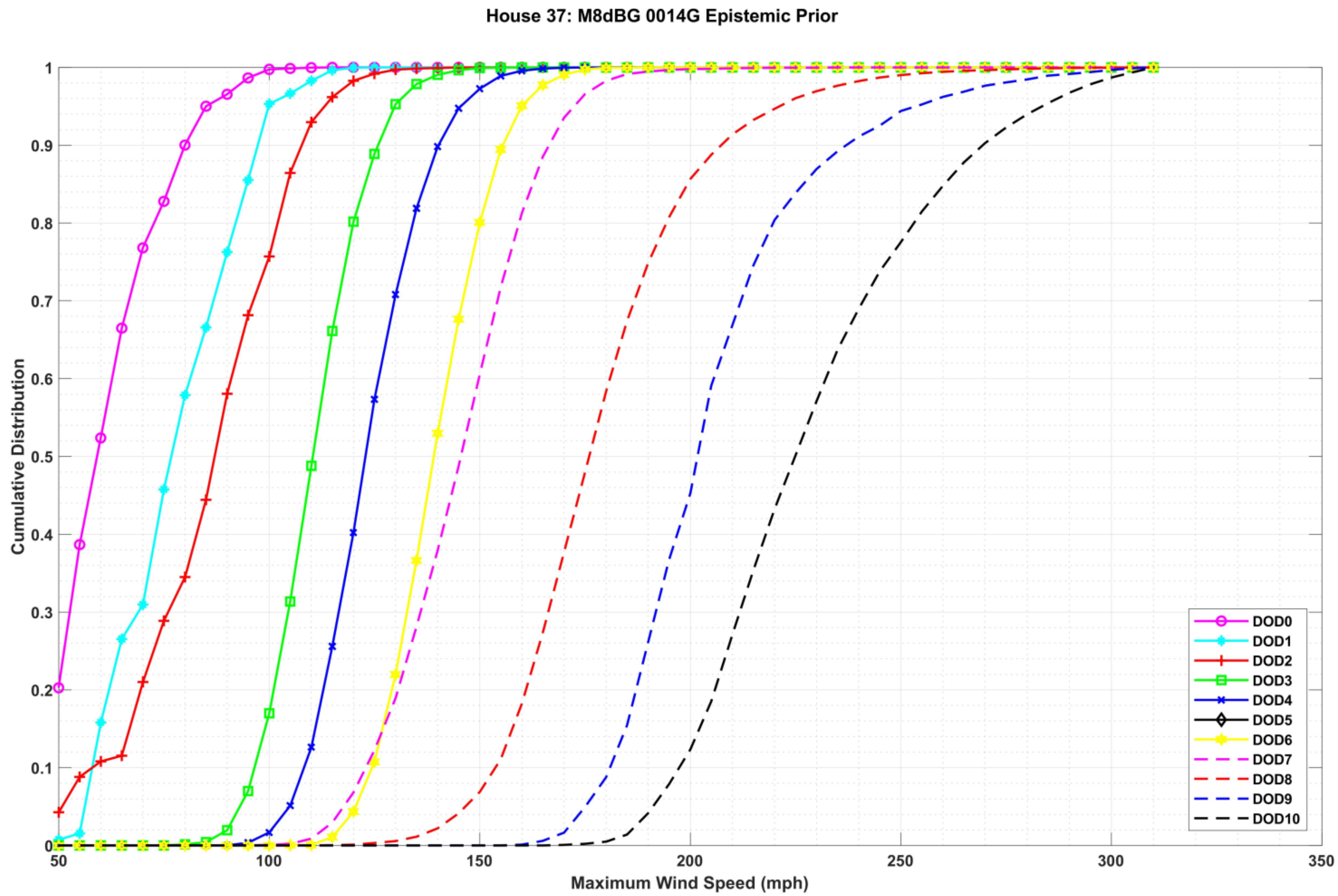
House 37: M8dBG 0014G Epistemic Prior
Cumulative Distribution
Maximum Wind Speed (mph)
0
0.1
0.2
0.3
0.4
0.5
0.6
0.7
0.8
0.9
1
50
100
150
200
250
300
350
DOD0
DOD1
DOD2
DOD3
DOD4
DOD5
DOD6
DOD7
DOD8
DOD9
DOD10

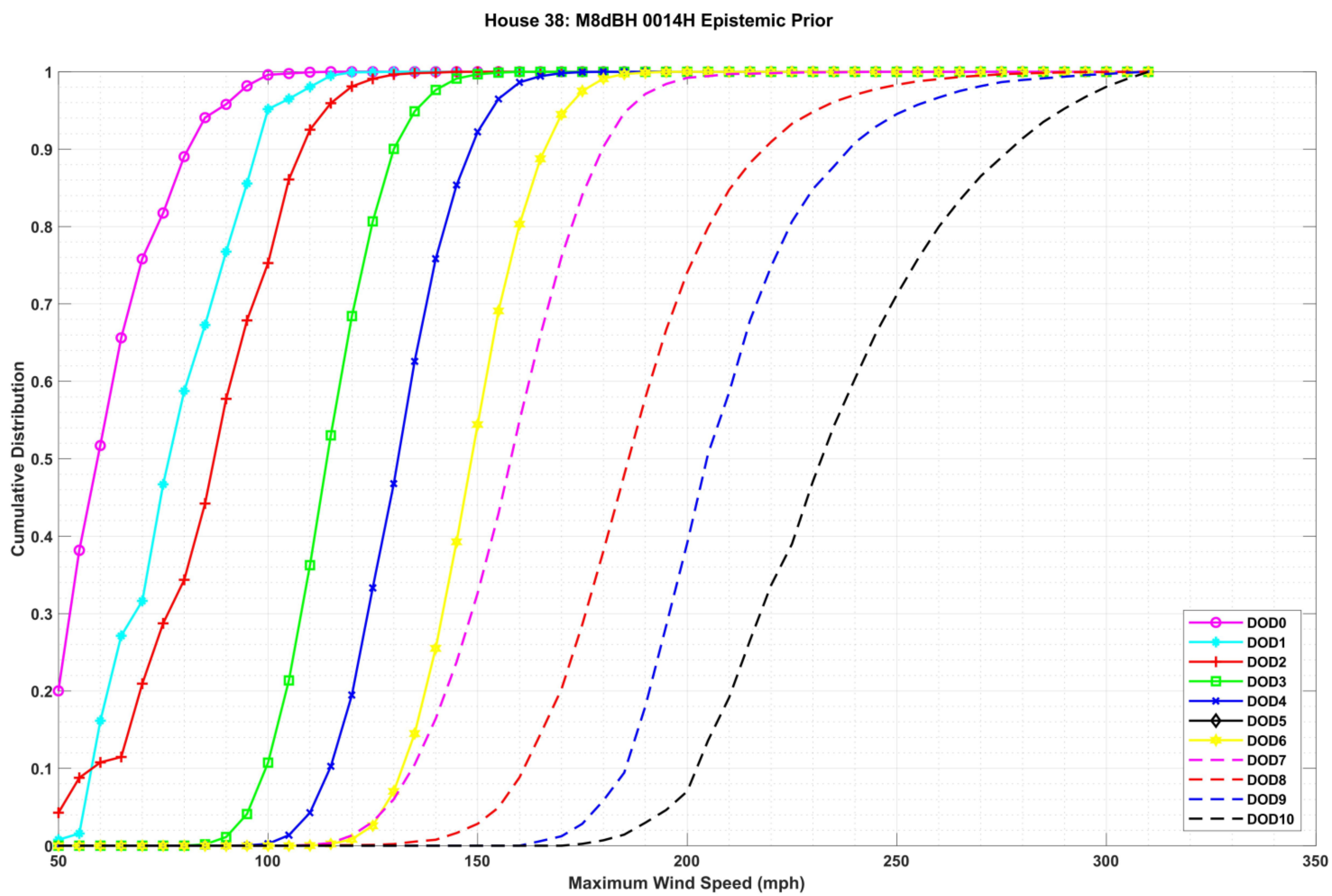
House 38: M8dBH 0014H Epistemic Prior
Cumulative Distribution
Maximum Wind Speed (mph)
0
0.1
0.2
0.3
0.4
0.5
0.6
0.7
0.8
0.9
1
50
100
150
200
250
300
350
DOD0
DOD1
DOD2
DOD3
DOD4
DOD5
DOD6
DOD7
DOD8
DOD9
DOD10

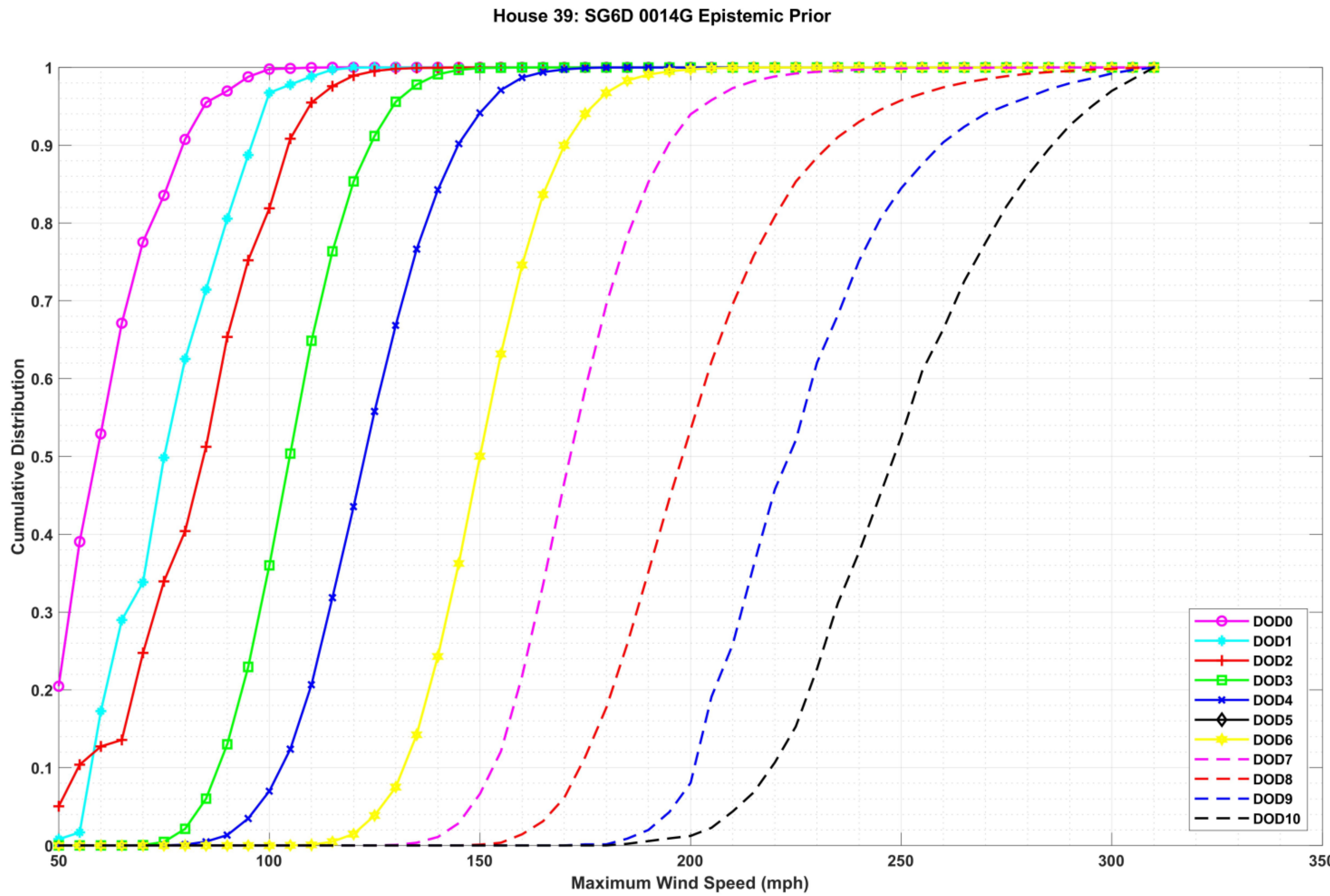

House 39: SG6D 0014G Epistemic Prior
Cumulative Distribution
Maximum Wind Speed (mph)
0
0.1
0.2
0.3
0.4
0.5
0.6
0.7
0.8
0.9
1
50
100
150
200
250
300
350
DOD0
DOD1
DOD2
DOD3
DOD4
DOD5
DOD6
DOD7
DOD8
DOD9
DOD10

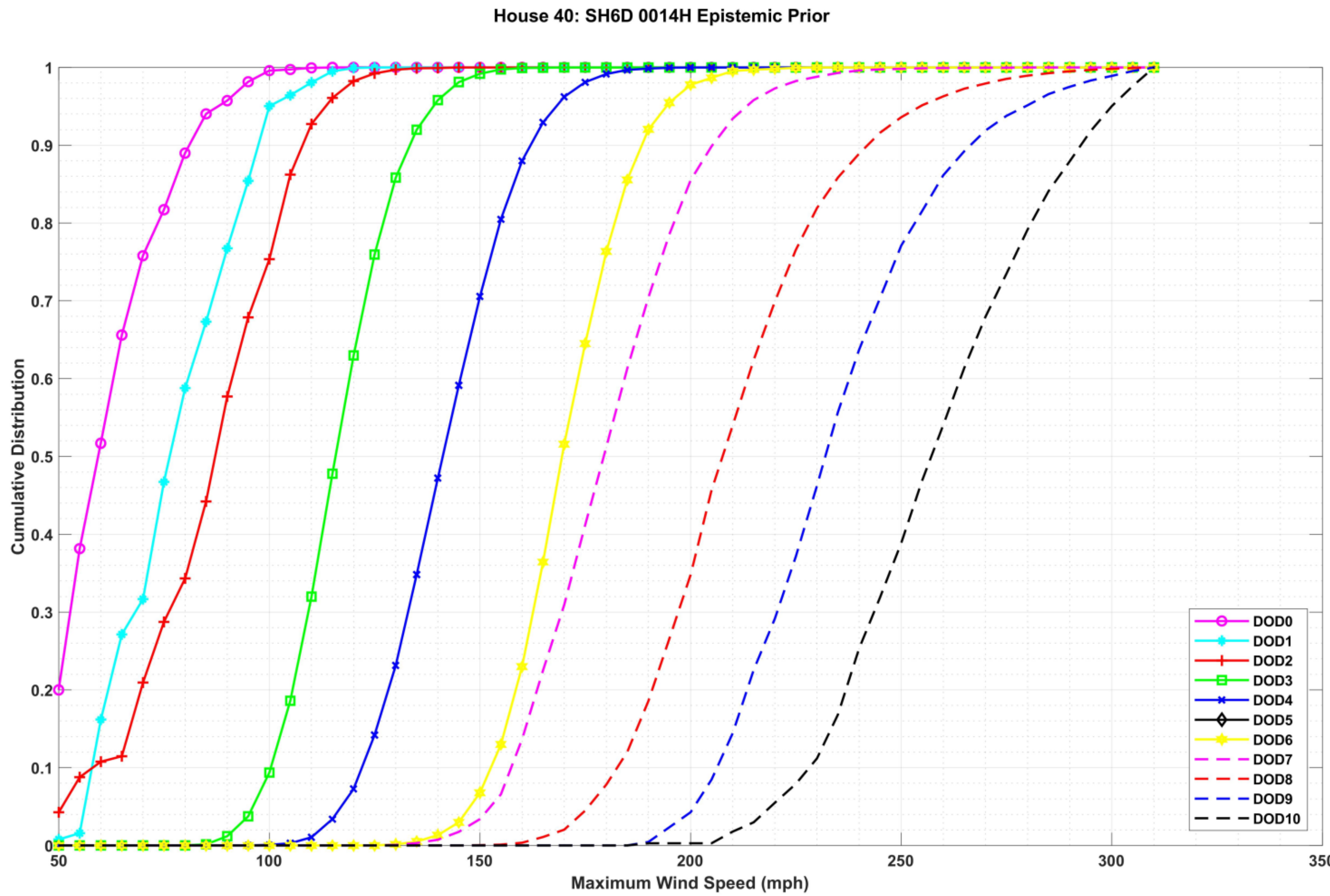

House 40: SH6D 0014H Epistemic Prior
Cumulative Distribution
Maximum Wind Speed (mph)
0
0.1
0.2
0.3
0.4
0.5
0.6
0.7
0.8
0.9
1
50
100
150
200
250
300
350
DOD0
DOD1
DOD2
DOD3
DOD4
DOD5
DOD6
DOD7
DOD8
DOD9
DOD10

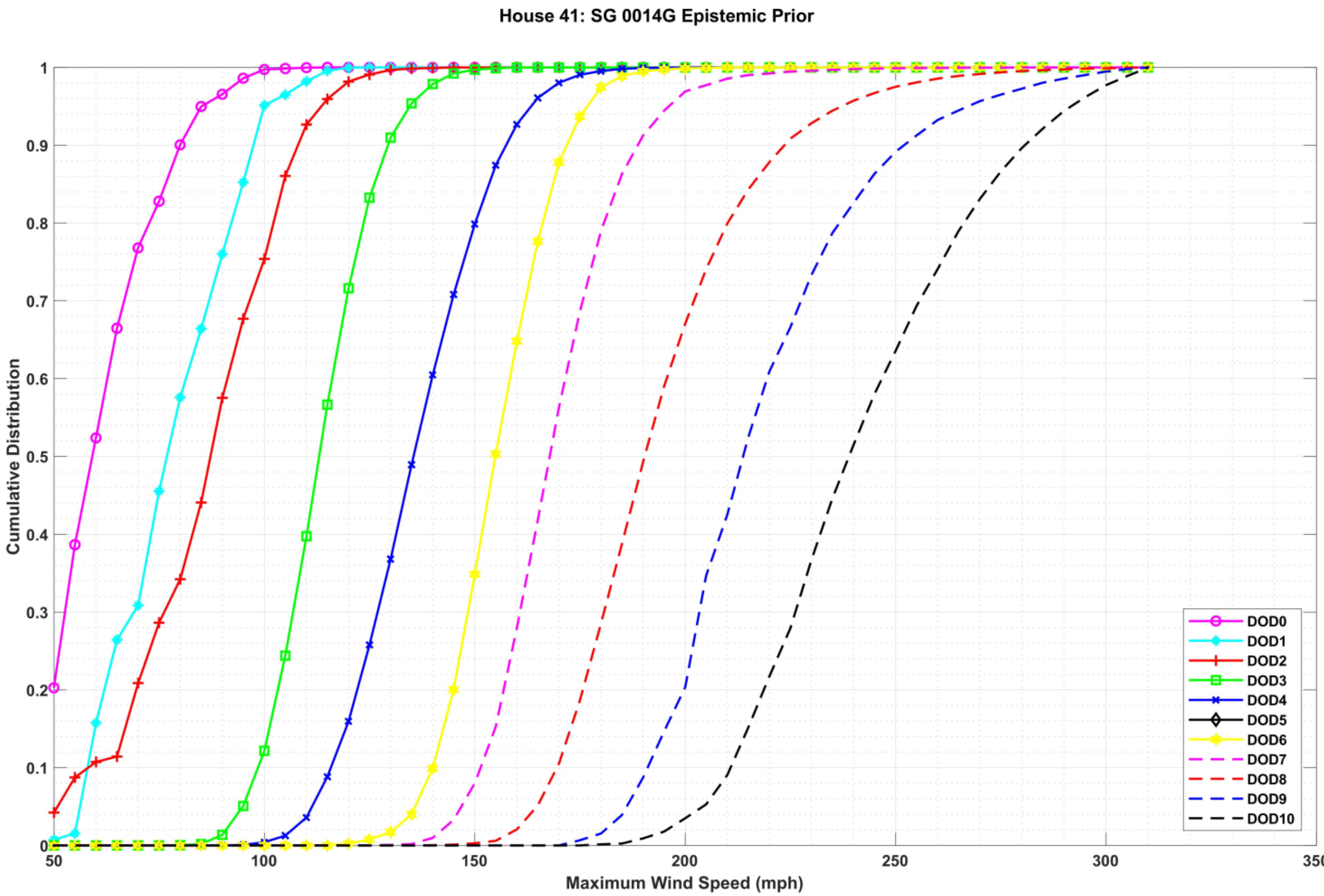
House 41: SG 0014G Epistemic Prior
Cumulative Distribution
Maximum Wind Speed (mph)
0
0.1
0.2
0.3
0.4
0.5
0.6
0.7
0.8
0.9
1
50
100
150
200
250
300
350
DOD0
DOD1
DOD2
DOD3
DOD4
DOD5
DOD6
DOD7
DOD8
DOD9
DOD10

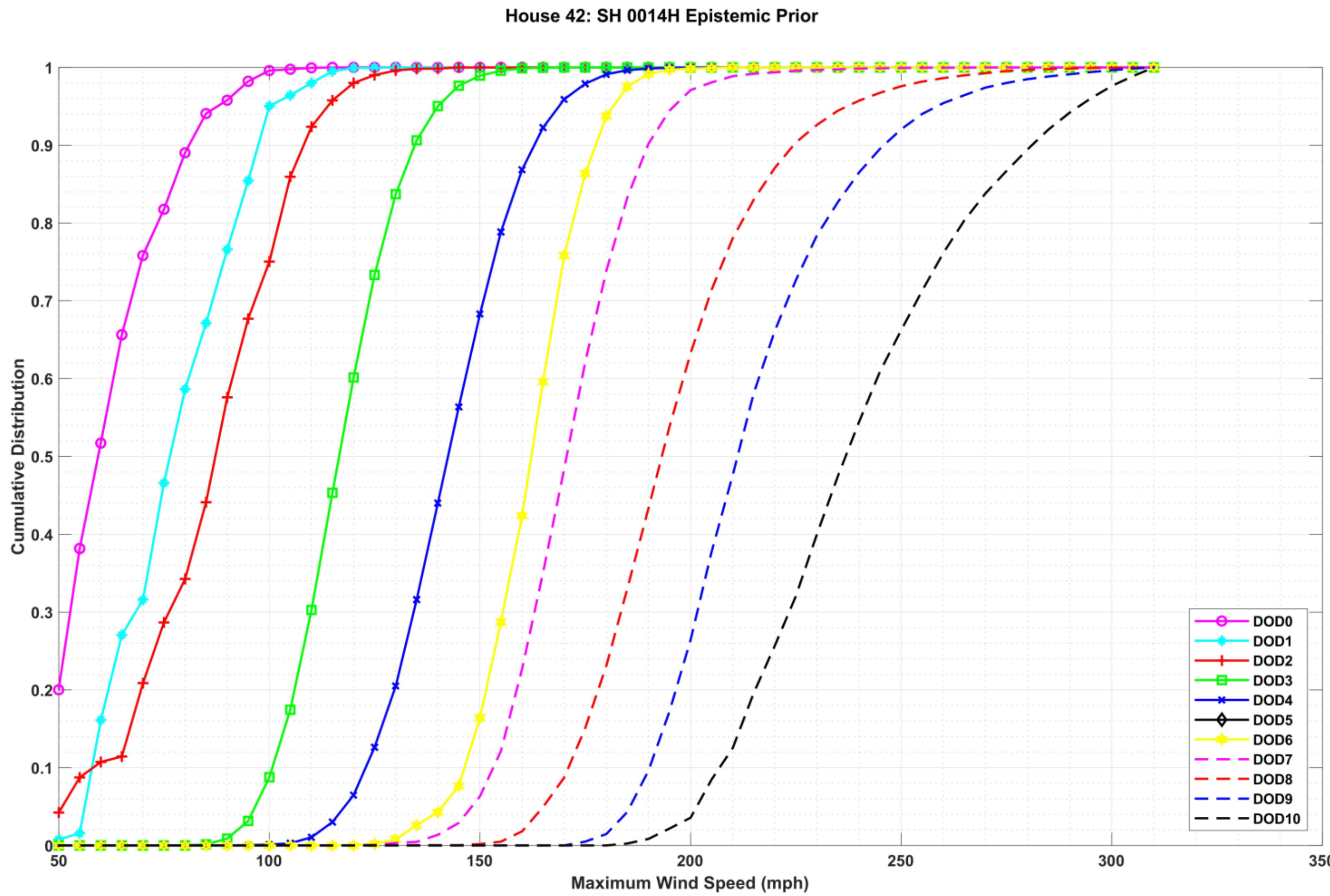
House 42: SH 0014H Epistemic Prior
Cumulative Distribution
Maximum Wind Speed (mph)
0
0.1
0.2
0.3
0.4
0.5
0.6
0.7
0.8
0.9
1
50
100
150
200
250
300
350
DOD0
DOD1
DOD2
DOD3
DOD4
DOD5
DOD6
DOD7
DOD8
DOD9
DOD10

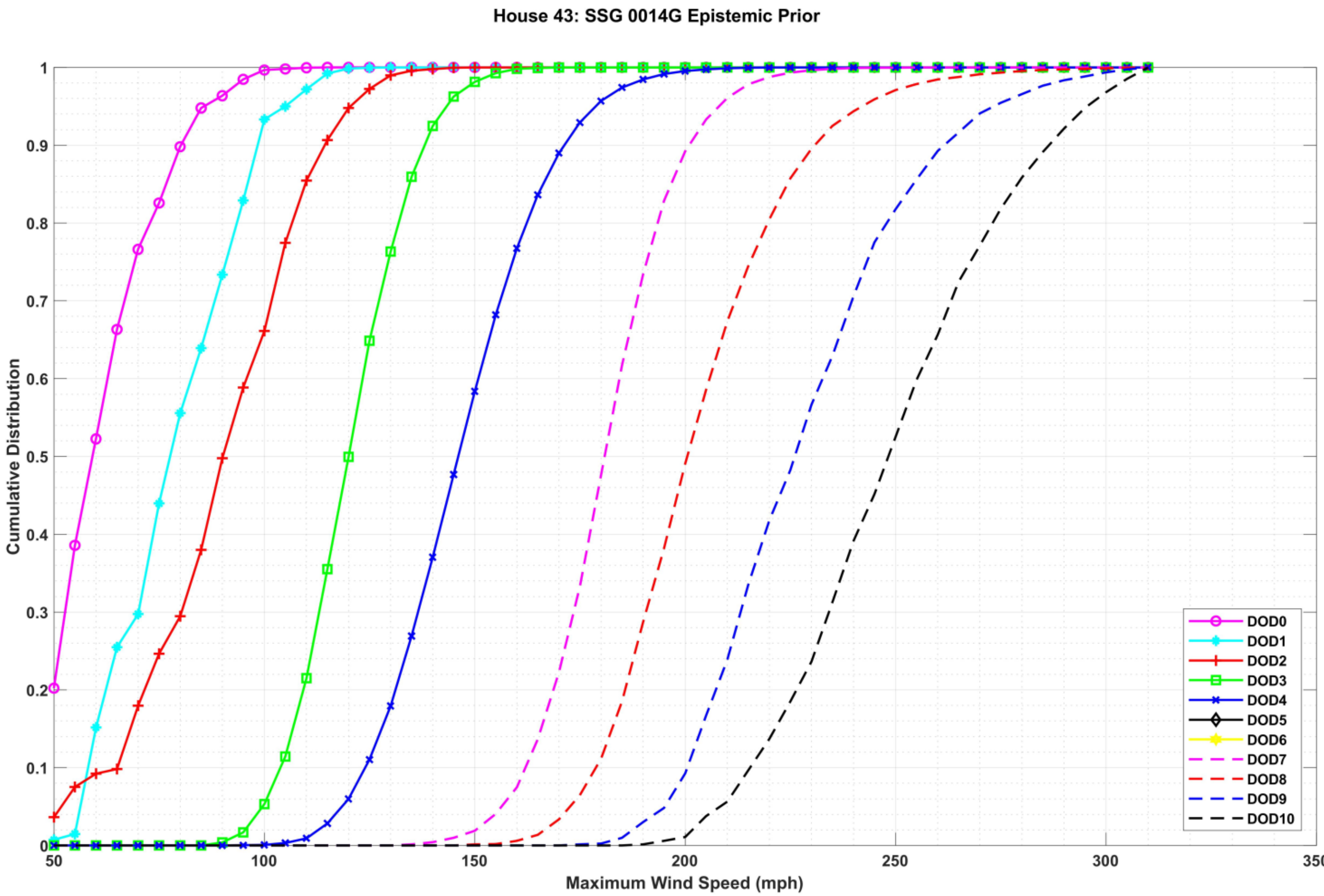
House 43: SSG 0014G Epistemic Prior
Cumulative Distribution
Maximum Wind Speed (mph)
0
0.1
0.2
0.3
0.4
0.5
0.6
0.7
0.8
0.9
1
50
100
150
200
250
300
350
DOD0
DOD1
DOD2
DOD3
DOD4
DOD5
DOD6
DOD7
DOD8
DOD9
DOD10

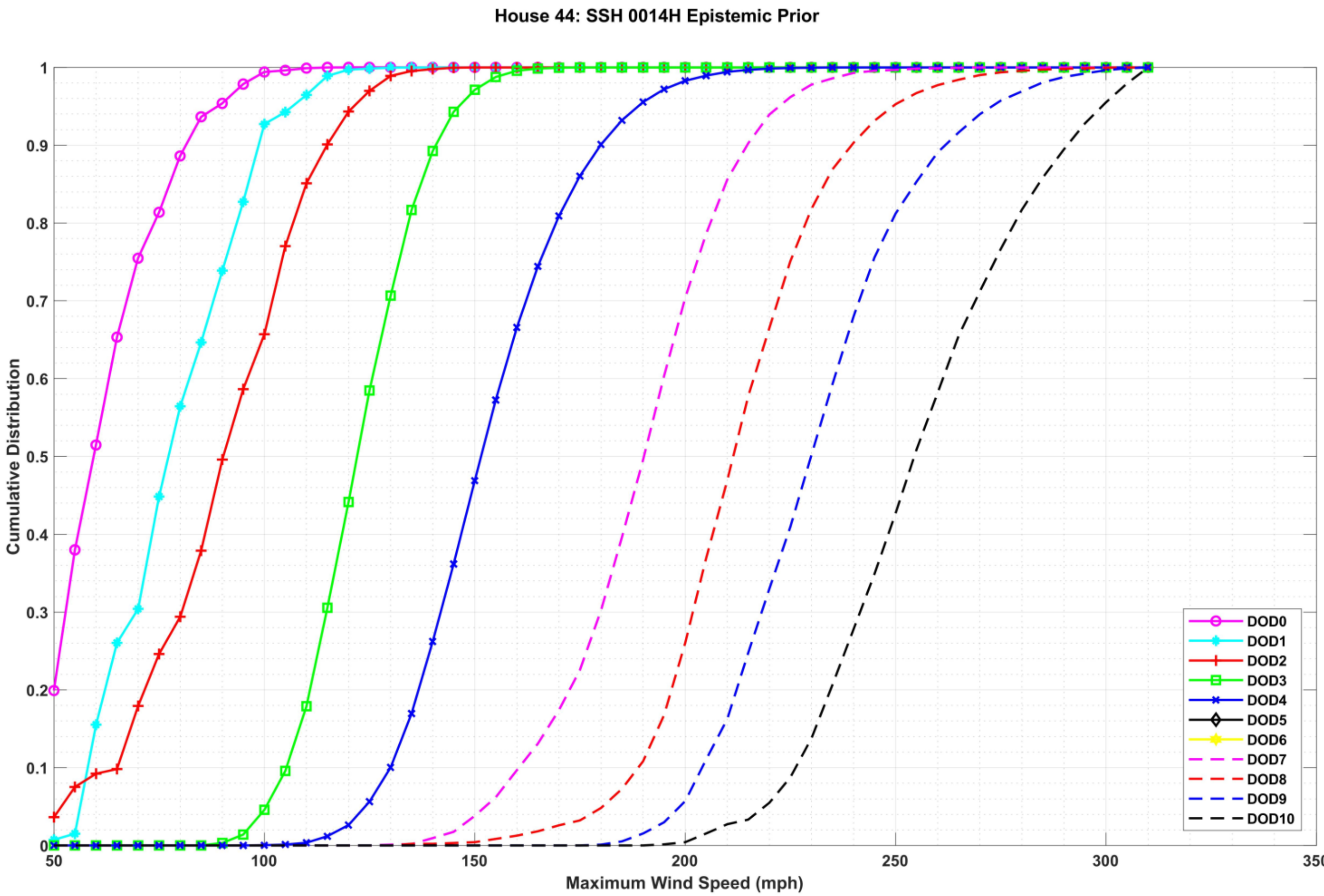
House 44: SSH 0014H Epistemic Prior
Cumulative Distribution
Maximum Wind Speed (mph)
0
0.1
0.2
0.3
0.4
0.5
0.6
0.7
0.8
0.9
1
50
100
150
200
250
300
350
DOD0
DOD1
DOD2
DOD3
DOD4
DOD5
DOD6
DOD7
DOD8
DOD9
DOD10

Appendix G. Tornado Wind Speed Maps

This appendix provides tornado wind speed maps for the 51 return period – target size combinations given in Table 8-1. Mapped tornado wind speeds are nominal 3-second gusts at 33 ft (10 m) height above ground, in mph (1 mph = 0.44704 m/s). Maps are not provided for cases where the tornado wind speeds were nil (less than 50 mph (22 m/s)) for that combination of return period and target size. The map numbers in Table G-1 correspond to the numbers in Table 8-1.

Table G-1. Wind Speed Map Listing

No.	*Map Title*	*Page*
1	Point Target, 1,700 Year Return Period	G-2
2	Point Target, 3,000 Year Return Period	G-3
3	Point Target, 10,000 Year Return Period	G-4
4	Point Target, 100,000 Year Return Period	G-5
5	Point Target, 1,000,000 Year Return Period	G-6
6	Point Target, 10,000,000 Year Return Period	G-7
7	2,000 SF Target, 1,700 Year Return Period	G-8
8	2,000 SF Target, 3,000 Year Return Period	G-9
9	2,000 SF Target, 10,000 Year Return Period	G-10
10	2,000 SF Target, 100,000 Year Return Period	G-11
11	2,000 SF Target, 1,000,000 Year Return Period	G-12
12	2,000 SF Target, 10,000,000 Year Return Period	G-13
13	10,000 SF Target, 1,700 Year Return Period	G-14
14	10,000 SF Target, 3,000 Year Return Period	G-15
15	10,000 SF Target, 10,000 Year Return Period	G-16
16	10,000 SF Target, 100,000 Year Return Period	G-17
17	10,000 SF Target, 1,000,000 Year Return Period	G-18
18	10,000 SF Target, 10,000,000 Year Return Period	G-19
19	40,000 SF Target, 1,700 Year Return Period	G-20
20	40,000 SF Target, 3,000 Year Return Period	G-21
21	40,000 SF Target, 10,000 Year Return Period	G-22
22	40,000 SF Target, 100,000 Year Return Period	G-23
23	40,000 SF Target, 1,000,000 Year Return Period	G-24
24	40,000 SF Target, 10,000,000 Year Return Period	G-25
25	100,000 SF Target, 1,700 Year Return Period	G-26
26	100,000 SF Target, 3,000 Year Return Period	G-27
27	100,000 SF Target, 10,000 Year Return Period	G-28
28	100,000 SF Target, 100,000 Year Return Period	G-29
29	100,000 SF Target, 1,000,000 Year Return Period	G-30
30	100,000 SF Target, 10,000,000 Year Return Period	G-31
31	250,000 SF Target, 1,700 Year Return Period	G-32
32	250,000 SF Target, 3,000 Year Return Period	G-33
33	250,000 SF Target, 10,000 Year Return Period	G-34
34	250,000 SF Target, 100,000 Year Return Period	G-35
35	250,000 SF Target, 1,000,000 Year Return Period	G-36
36	250,000 SF Target, 10,000,000 Year Return Period	G-37
37	1,000,000 SF Target, 700 Year Return Period	G-38
38	1,000,000 SF Target, 1,700 Year Return Period	G-39
39	1,000,000 SF Target, 3,000 Year Return Period	G-40
40	1,000,000 SF Target, 10,000 Year Return Period	G-41
41	1,000,000 SF Target, 100,000 Year Return Period	G-42
42	1,000,000 SF Target, 1,000,000 Year Return Period	G-43
43	1,000,000 SF Target, 10,000,000 Year Return Period	G-44
44	4,000,000 SF Target, 300 Year Return Period	G-45
45	4,000,000 SF Target, 700 Year Return Period	G-46
46	4,000,000 SF Target, 1,700 Year Return Period	G-47
47	4,000,000 SF Target, 3,000 Year Return Period	G-48
48	4,000,000 SF Target, 10,000 Year Return Period	G-49
49	4,000,000 SF Target, 100,000 Year Return Period	G-50
50	4,000,000 SF Target, 1,000,000 Year Return Period	G-51
51	4,000,000 SF Target, 10,000,000 Year Return Period	G-52

Note:
2,000 SF = 185.8 m^2
10,000 SF = 929.0 m^2
40,000 SF = 3716.1 m^2
100,000 SF = 9290.3 m^2
250,000 SF = 23225.8 m^2
1,000,000 SF = 92903.0 m^2
4,000,000 SF = 371612.2 m^2

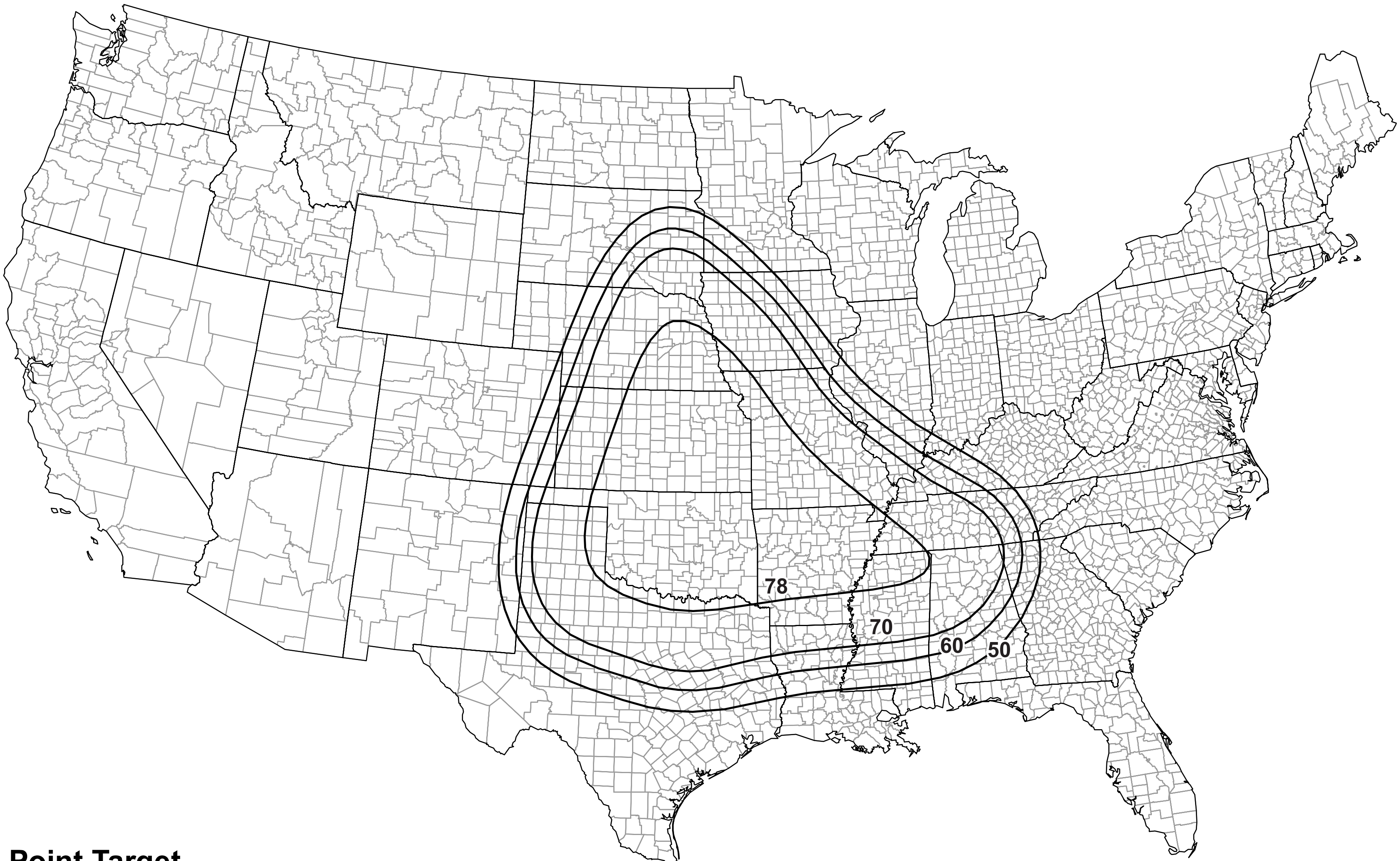

Point Target

Mean Recurrence Interval = 1,700 Yrs
Annual Exceedance Frequency = 5.88×10^{-4}

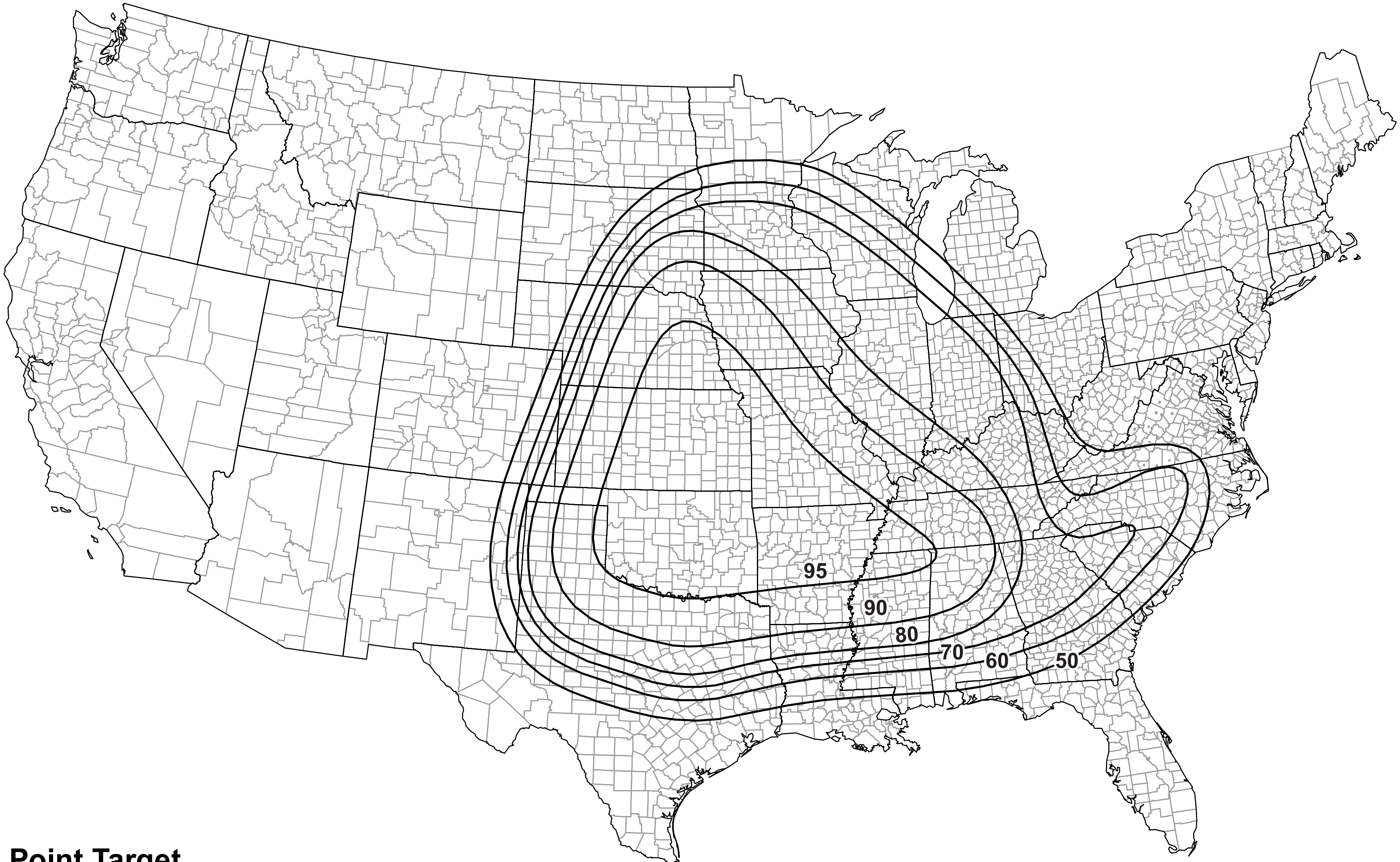

Point Target

Mean Recurrence Interval = 3,000 Yrs
Annual Exceedance Frequency = 3.3×10^{-4}

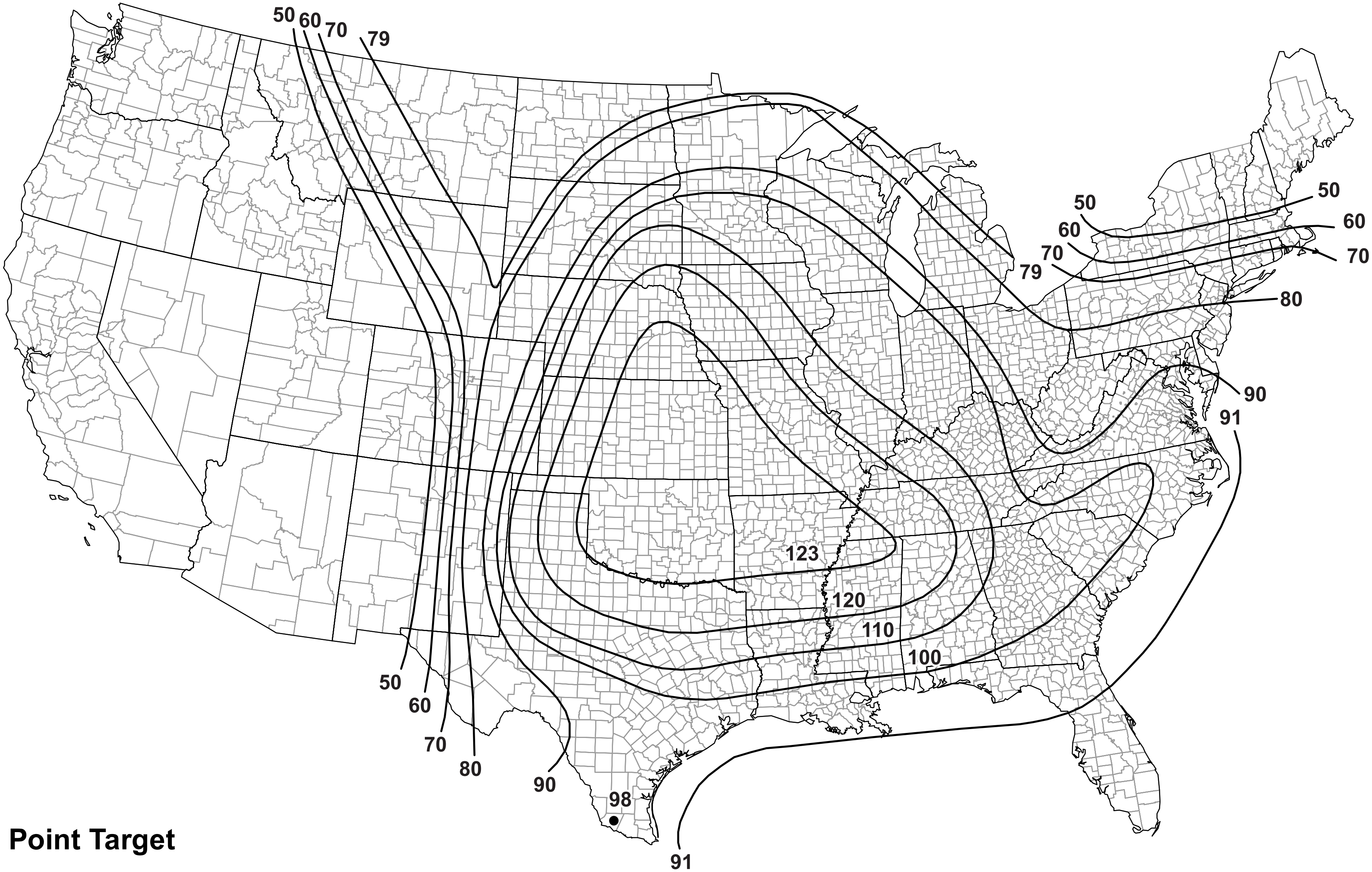

Point Target

Mean Recurrence Interval = 10,000 Yrs
Annual Exceedance Frequency = 1×10^{-4}

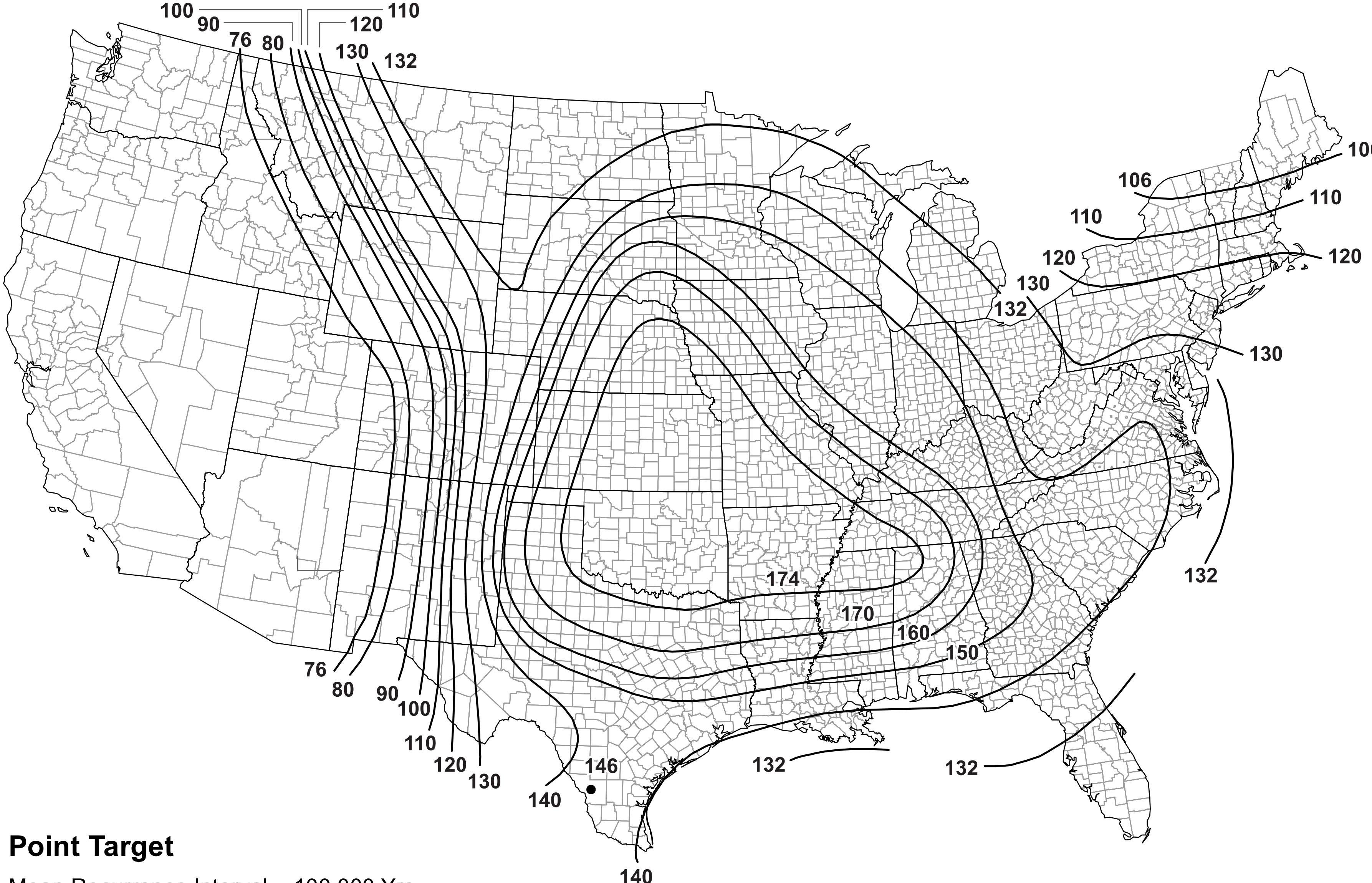

Point Target

Mean Recurrence Interval = 100,000 Yrs
Annual Exceedance Frequency = 1 x 10^{-5}

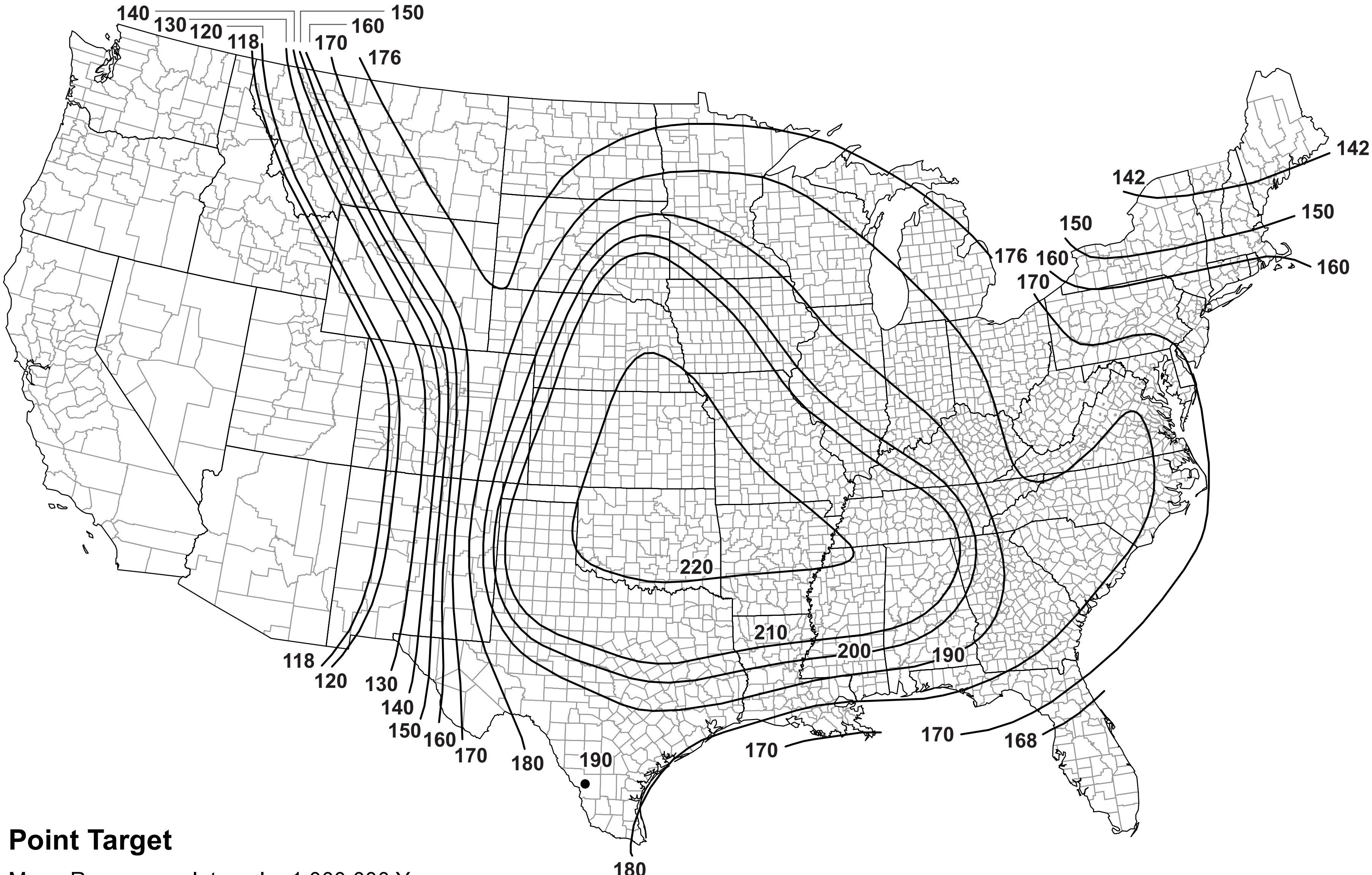

Point Target

Mean Recurrence Interval = 1,000,000 Yrs
Annual Exceedance Frequency = 1 x 10^{-6}

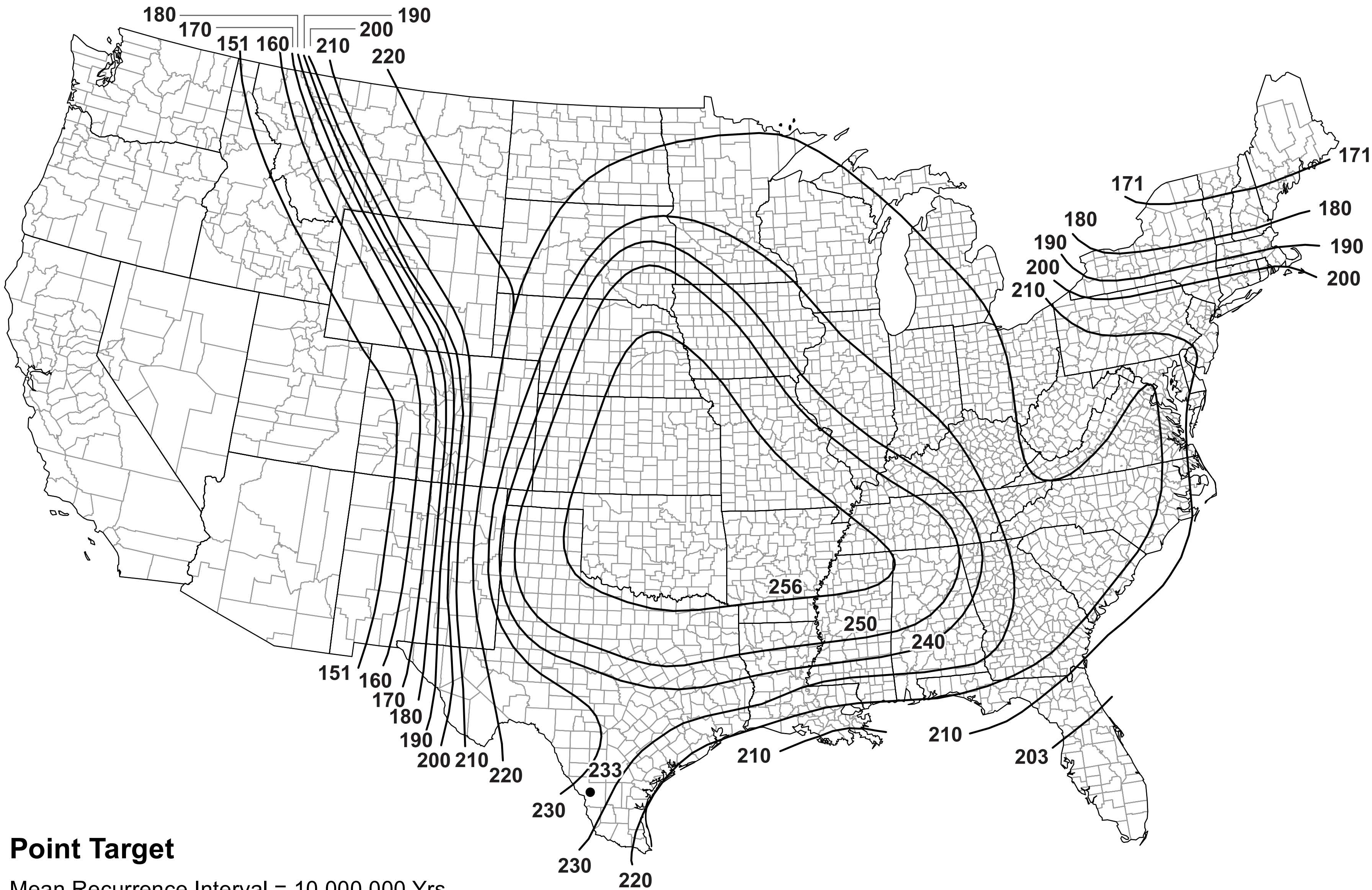

Point Target

Mean Recurrence Interval = 10,000,000 Yrs
Annual Exceedance Frequency = 1 x 10^{-7}

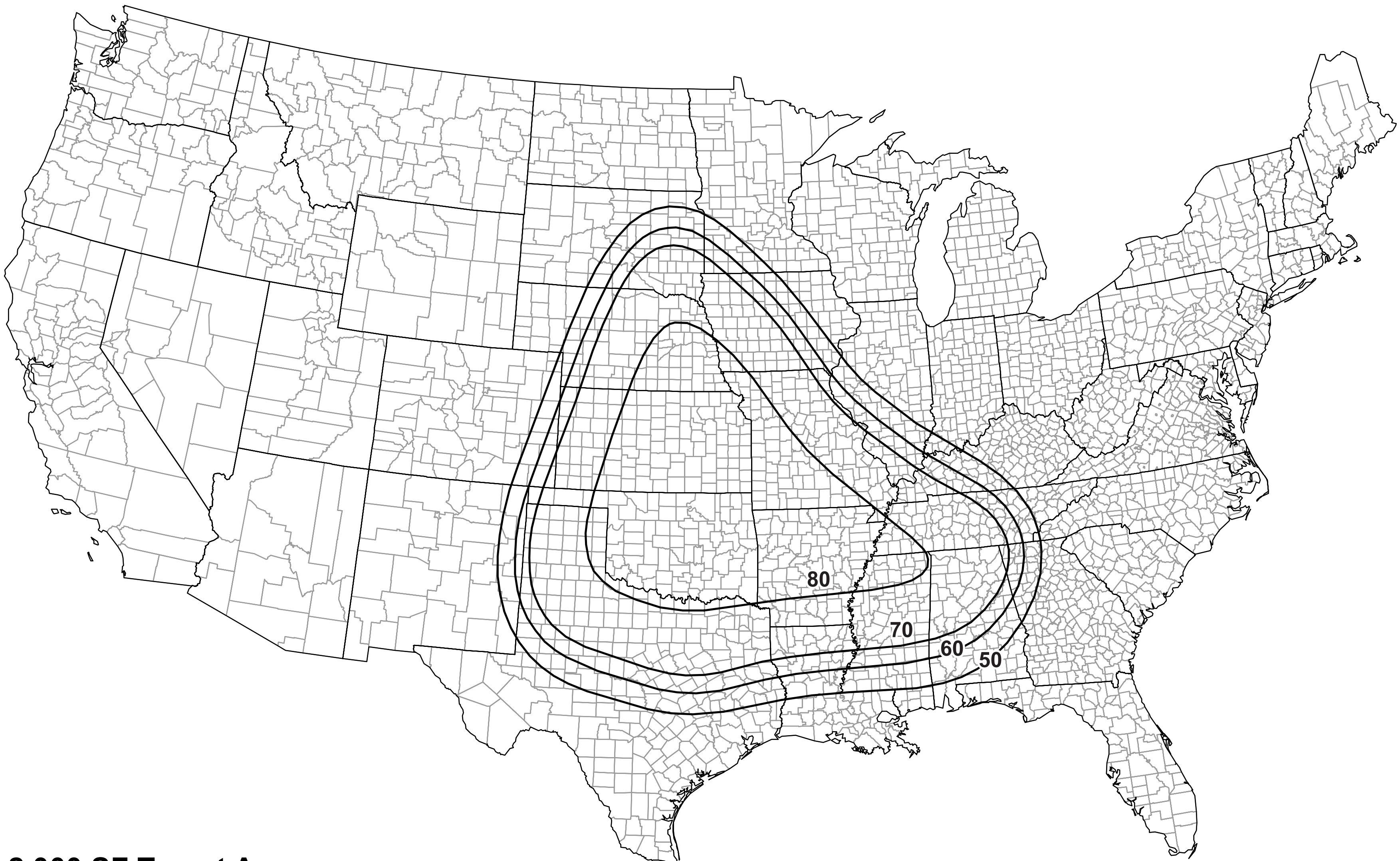

2,000 SF Target Area

Mean Recurrence Interval = 1,700 Yrs
Annual Exceedance Frequency = 5.88×10^{-4}

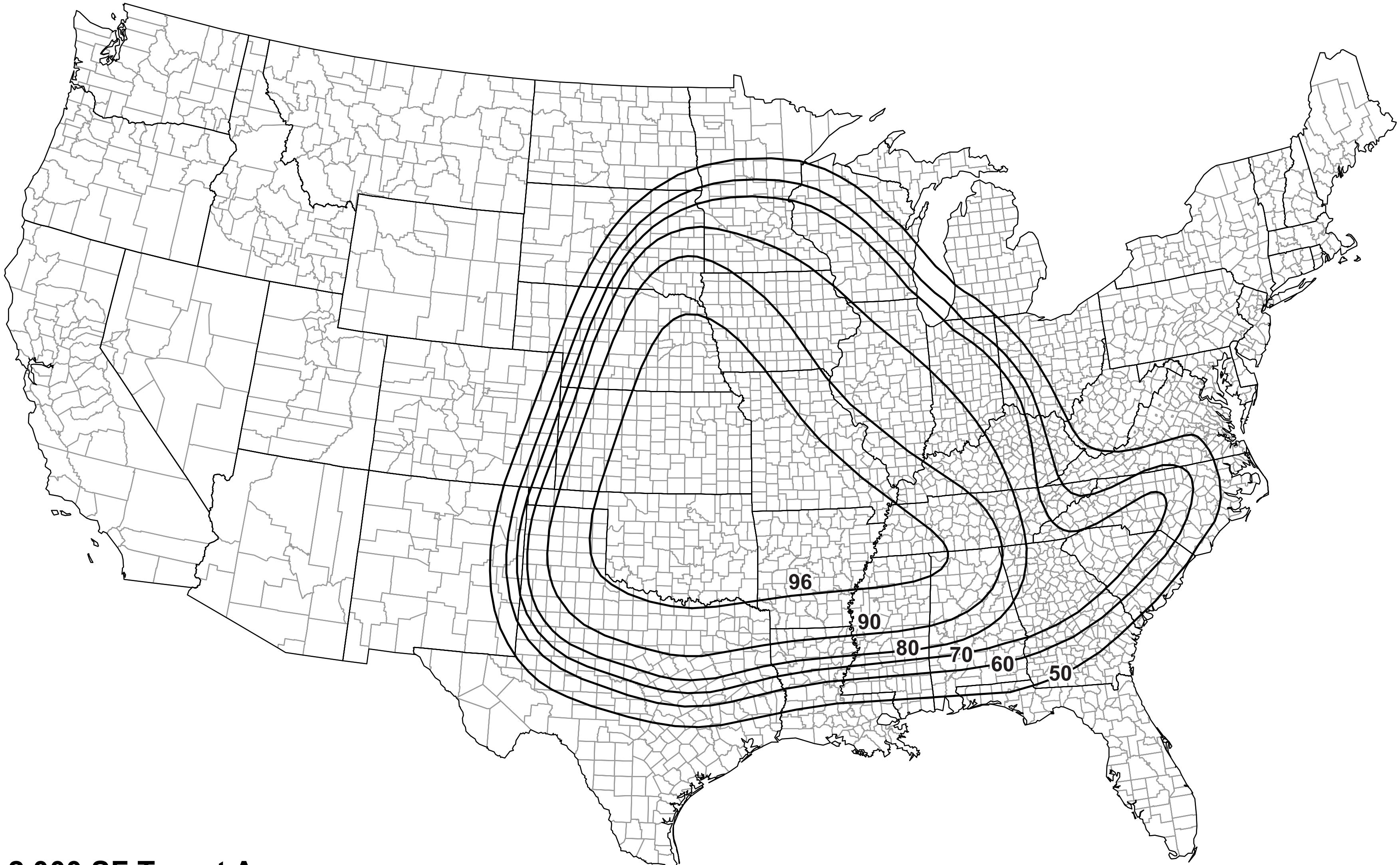

2,000 SF Target Area

Mean Recurrence Interval = 3,000 Yrs
Annual Exceedance Frequency = 3.3 x 10^{-4}

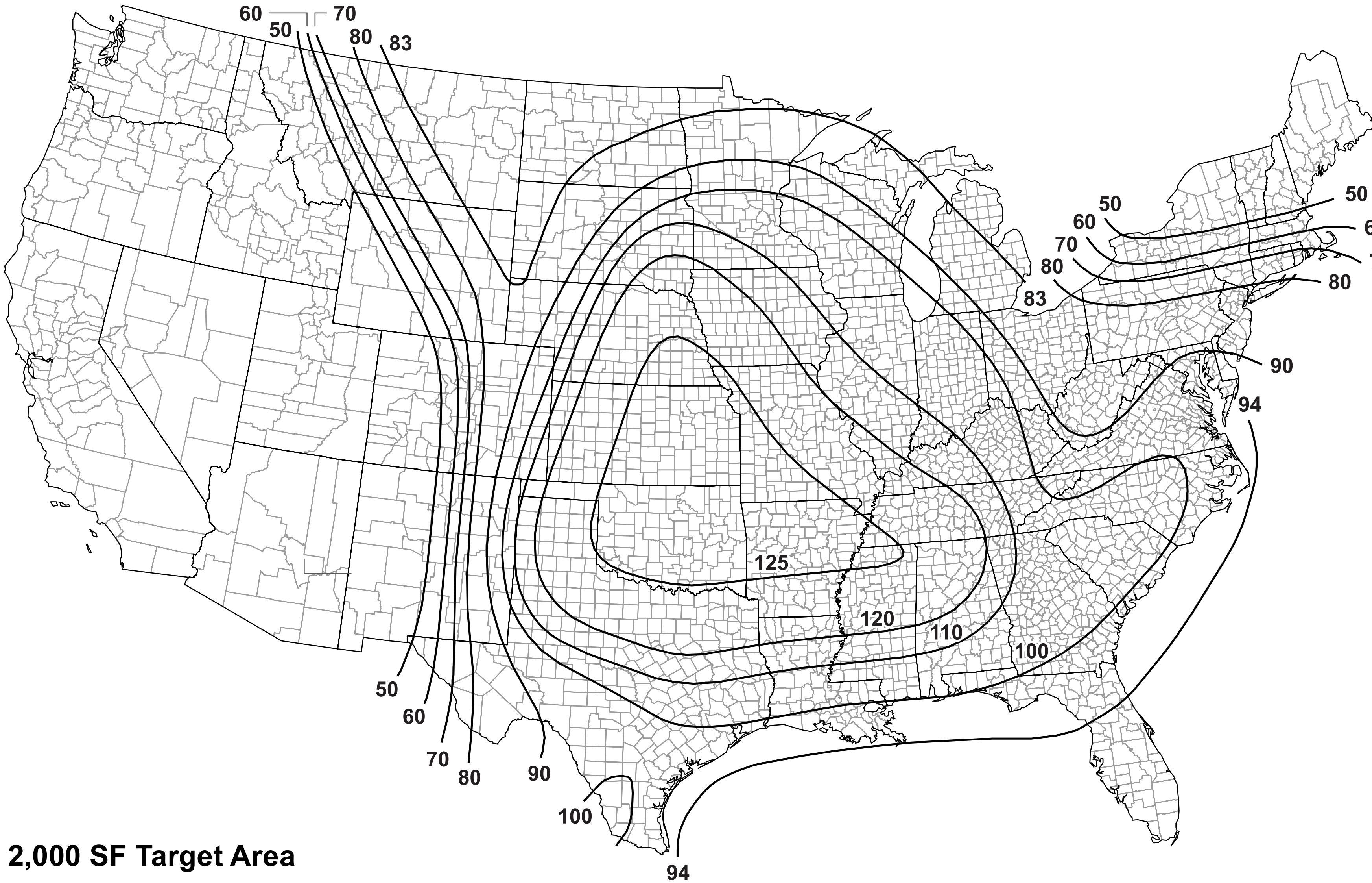

2,000 SF Target Area

Mean Recurrence Interval = 10,000 Yrs
Annual Exceedance Frequency = 1 x 10^{-4}

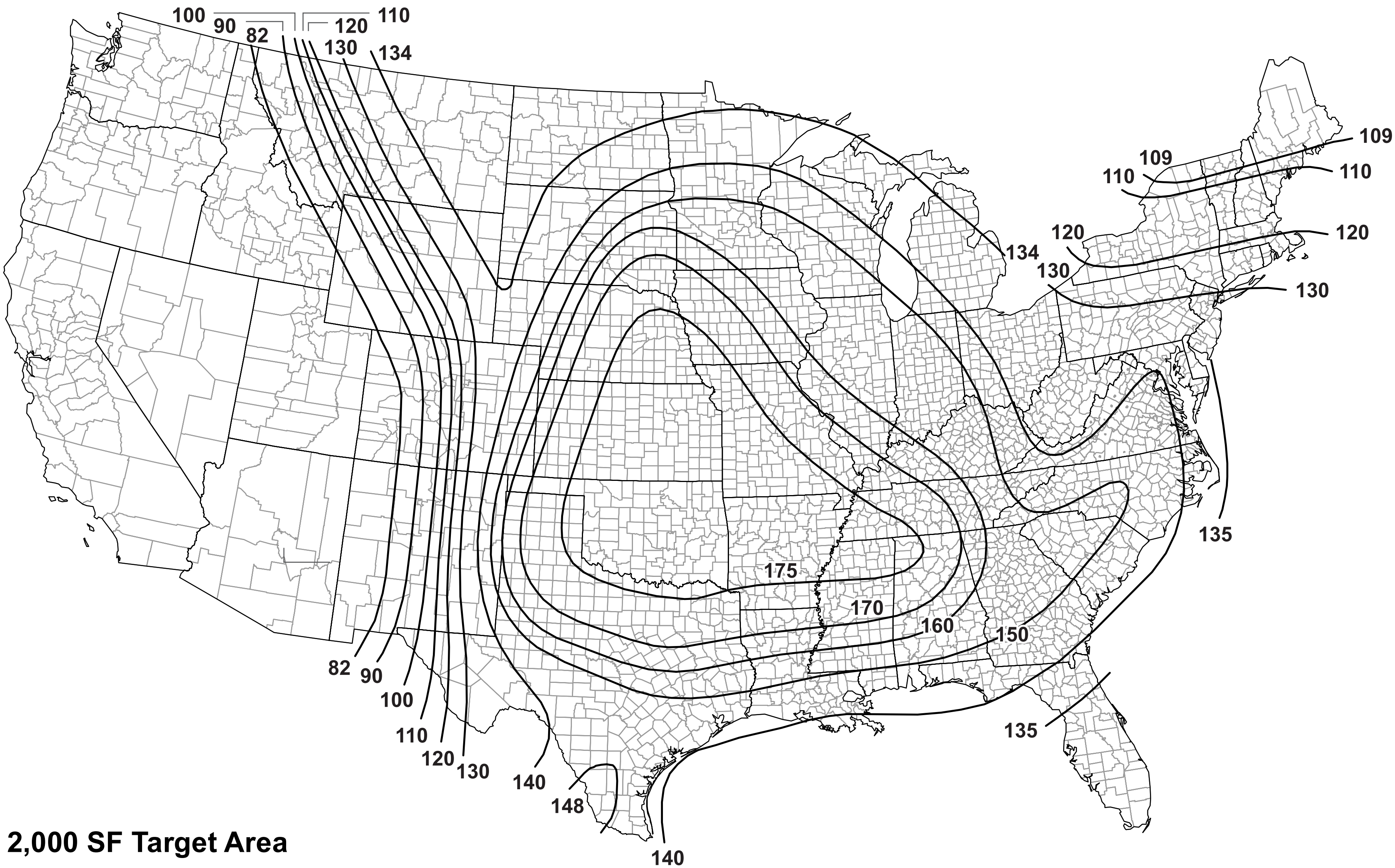

2,000 SF Target Area

Mean Recurrence Interval = 100,000 Yrs
Annual Exceedance Frequency = 1 x 10^{-5}

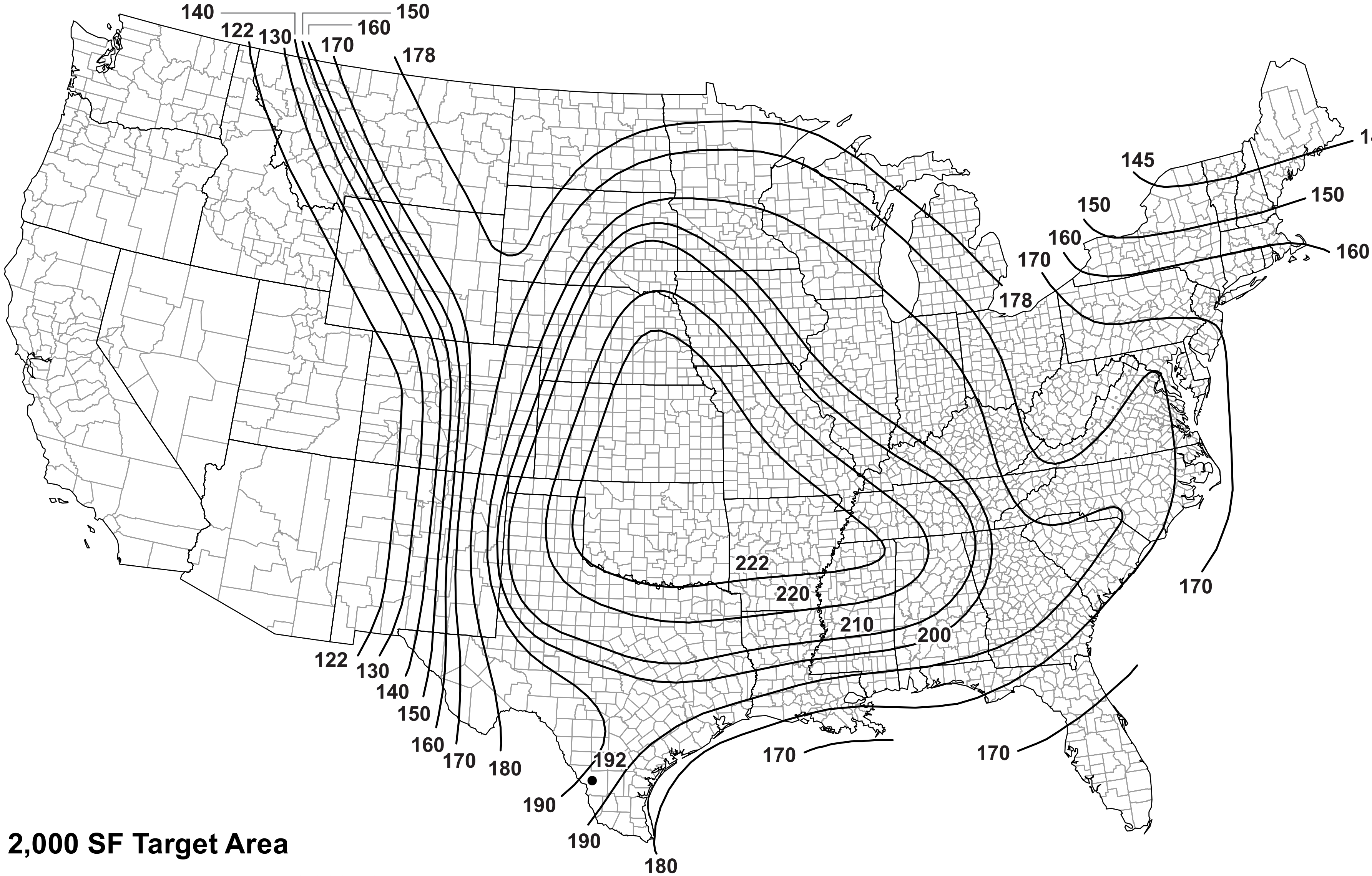

2,000 SF Target Area

Mean Recurrence Interval = 1,000,000 Yrs
Annual Exceedance Frequency = 1 x 10^{-6}

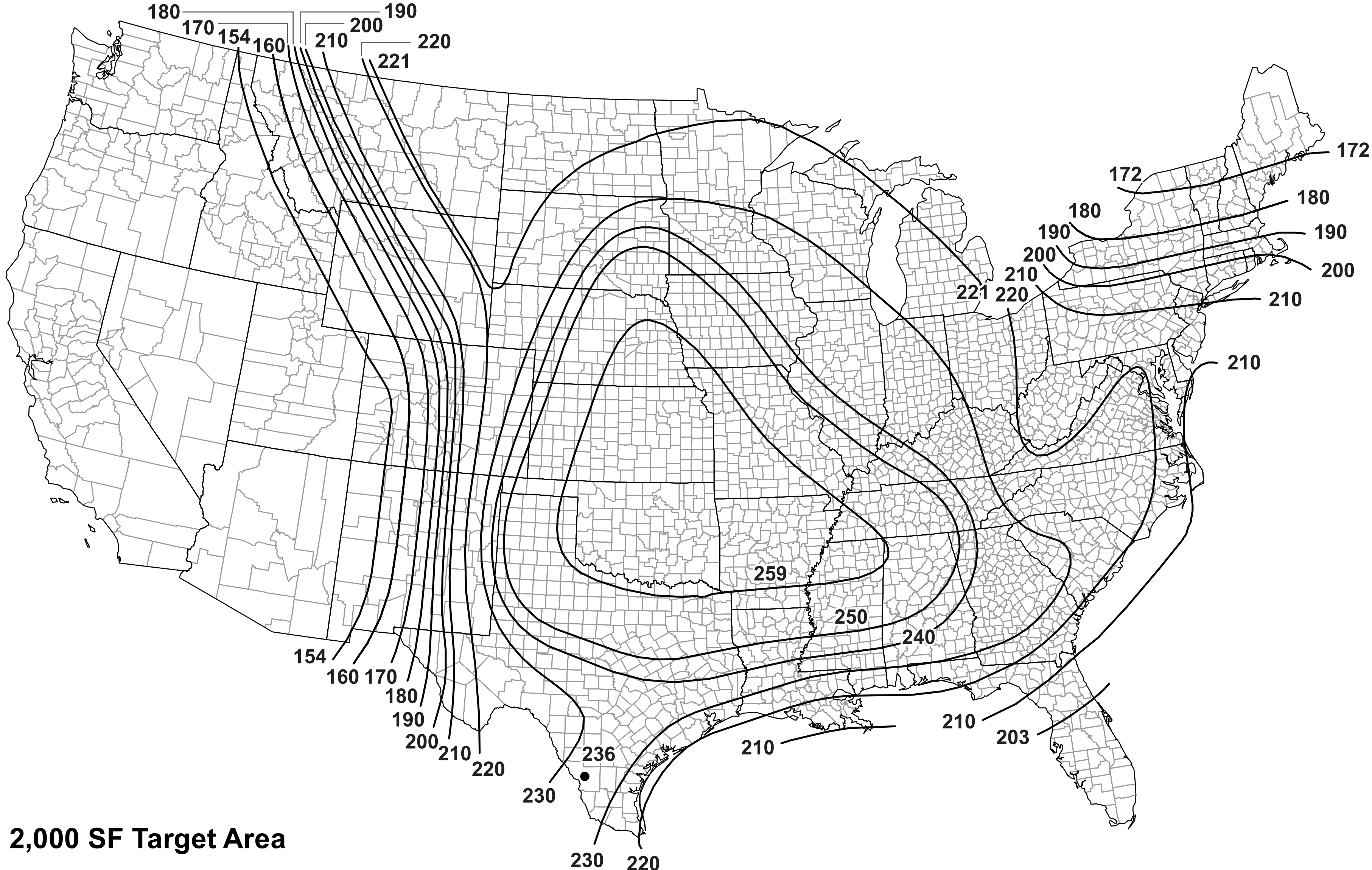

2,000 SF Target Area

Mean Recurrence Interval = 10,000,000 Yrs
Annual Exceedance Frequency = 1 x 10^{-7}

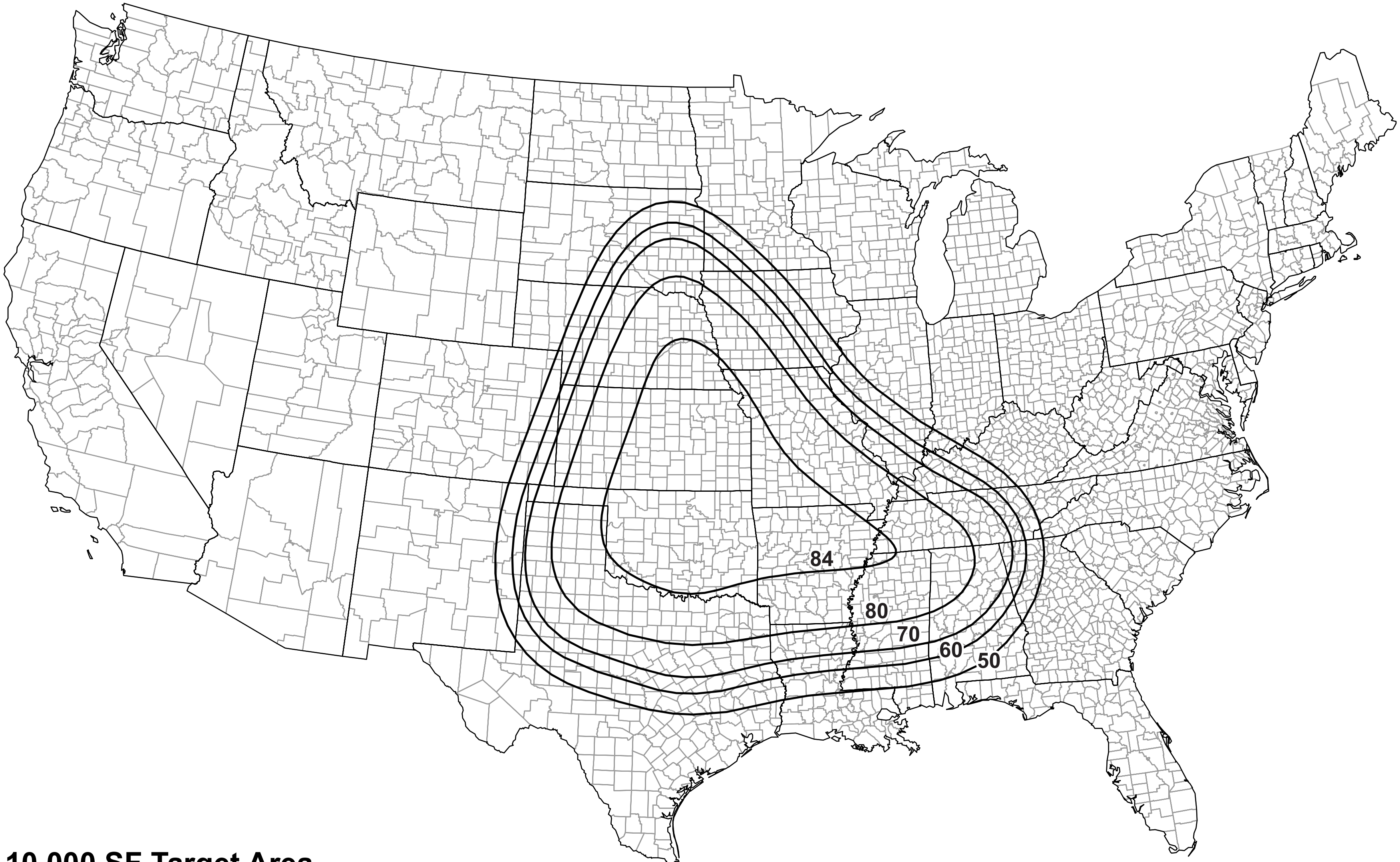

10,000 SF Target Area

Mean Recurrence Interval = 1,700 Yrs
Annual Exceedance Frequency = 5.88×10^{-4}

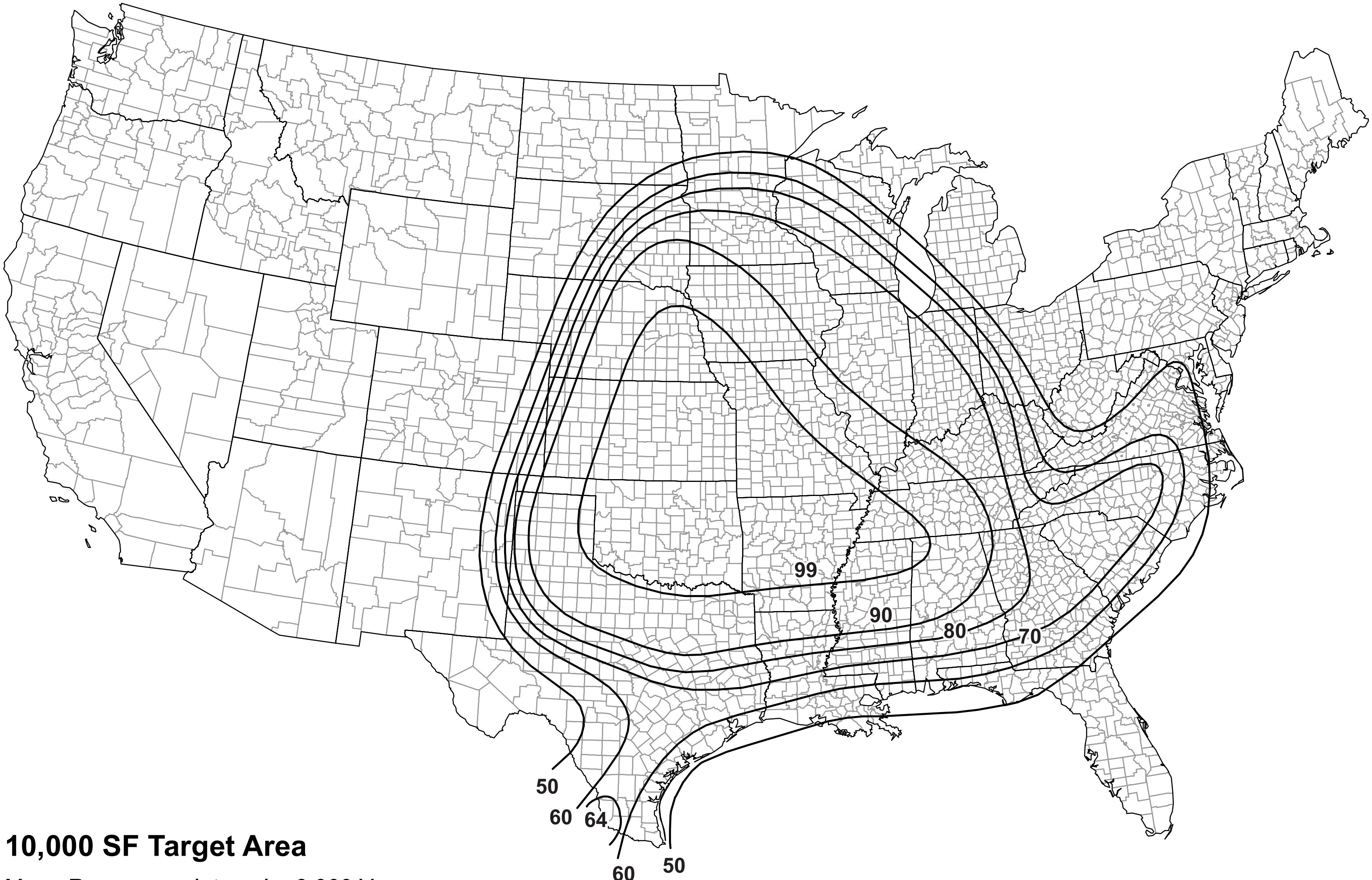

10,000 SF Target Area

Mean Recurrence Interval = 3,000 Yrs
Annual Exceedance Frequency = 3.3×10^{-4}

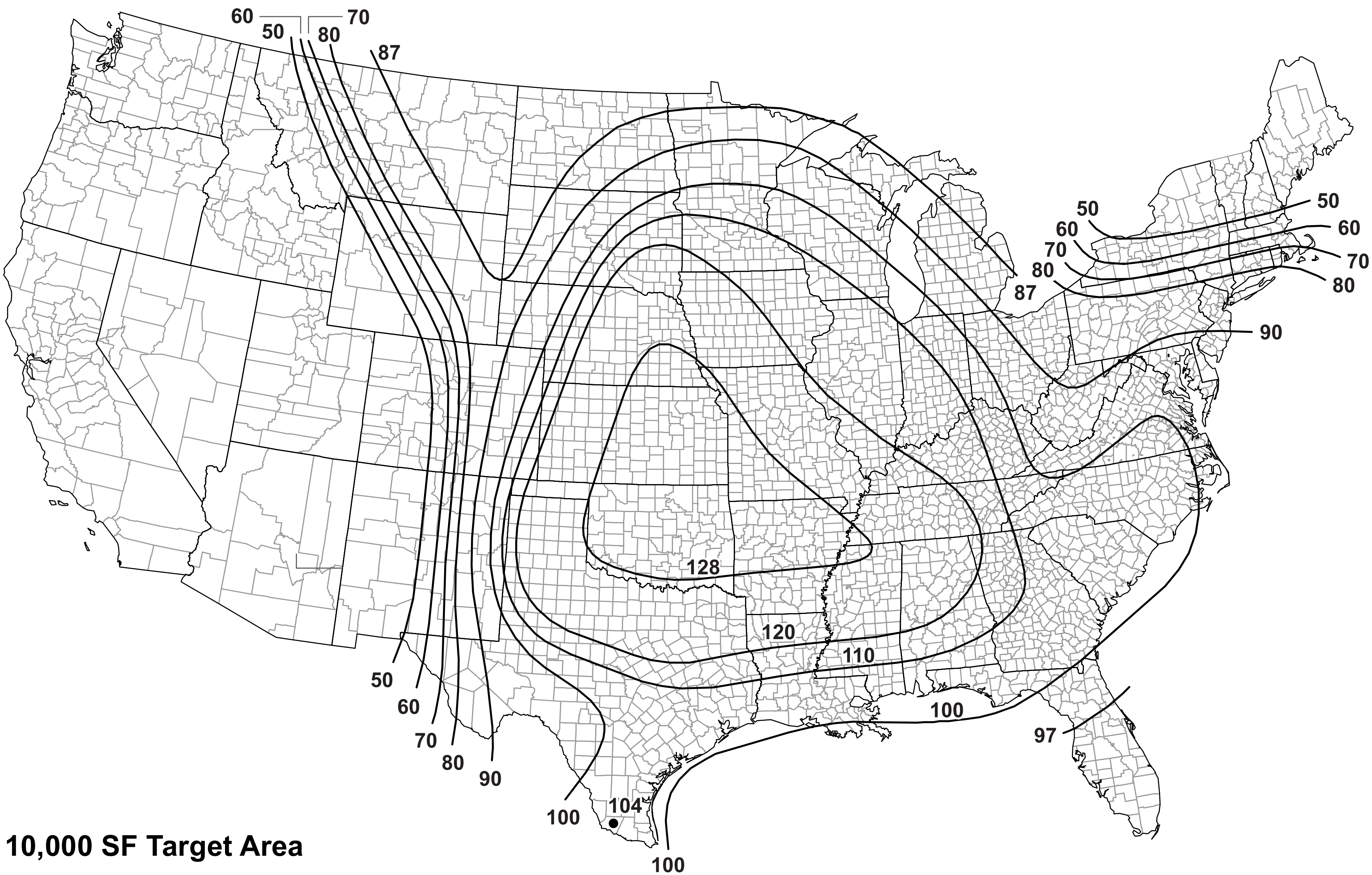

10,000 SF Target Area

Mean Recurrence Interval = 10,000 Yrs
Annual Exceedance Frequency = 1 x 10^{-4}

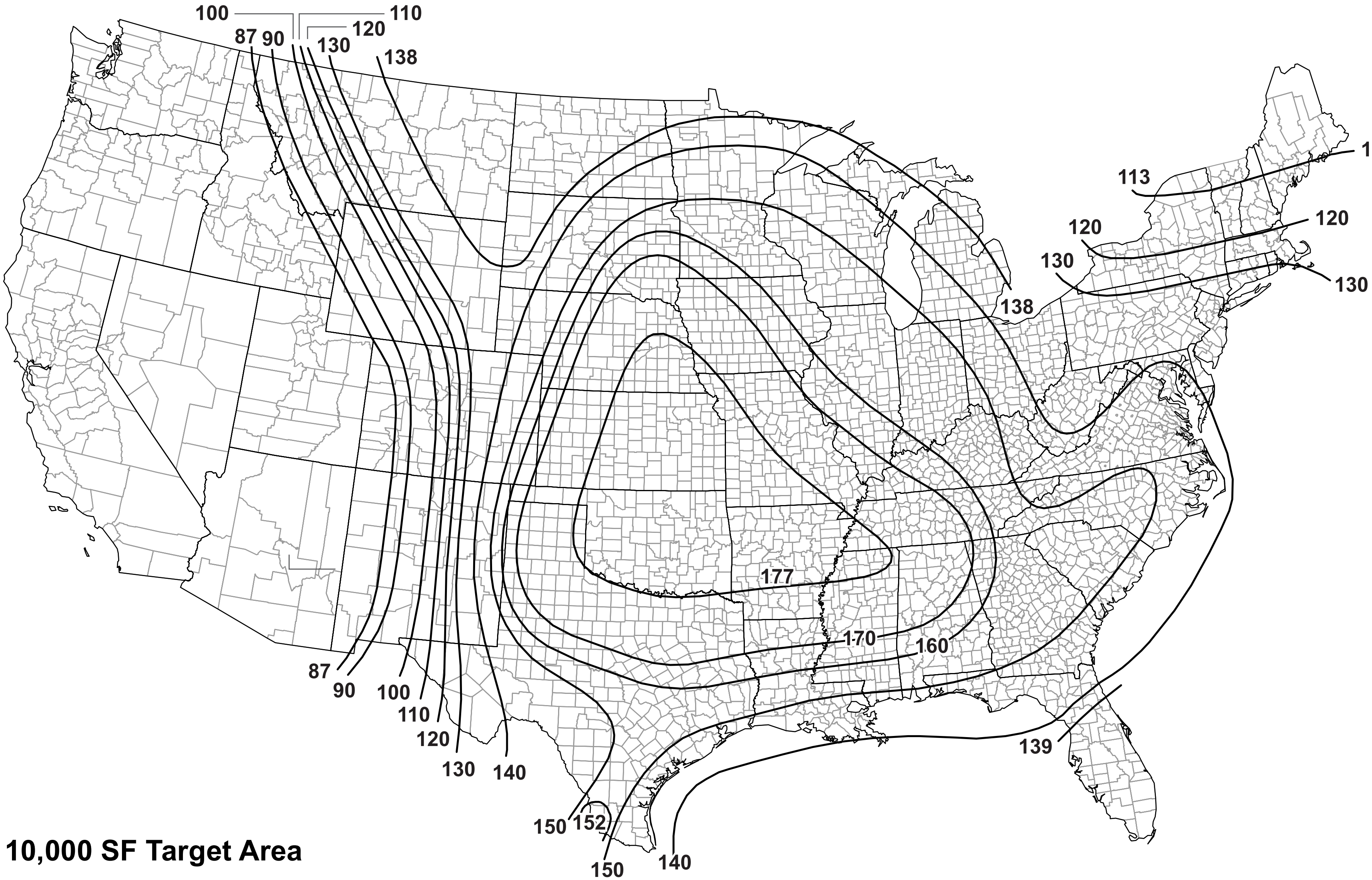

10,000 SF Target Area

Mean Recurrence Interval = 100,000 Yrs
Annual Exceedance Frequency = 1 x 10^{-5}

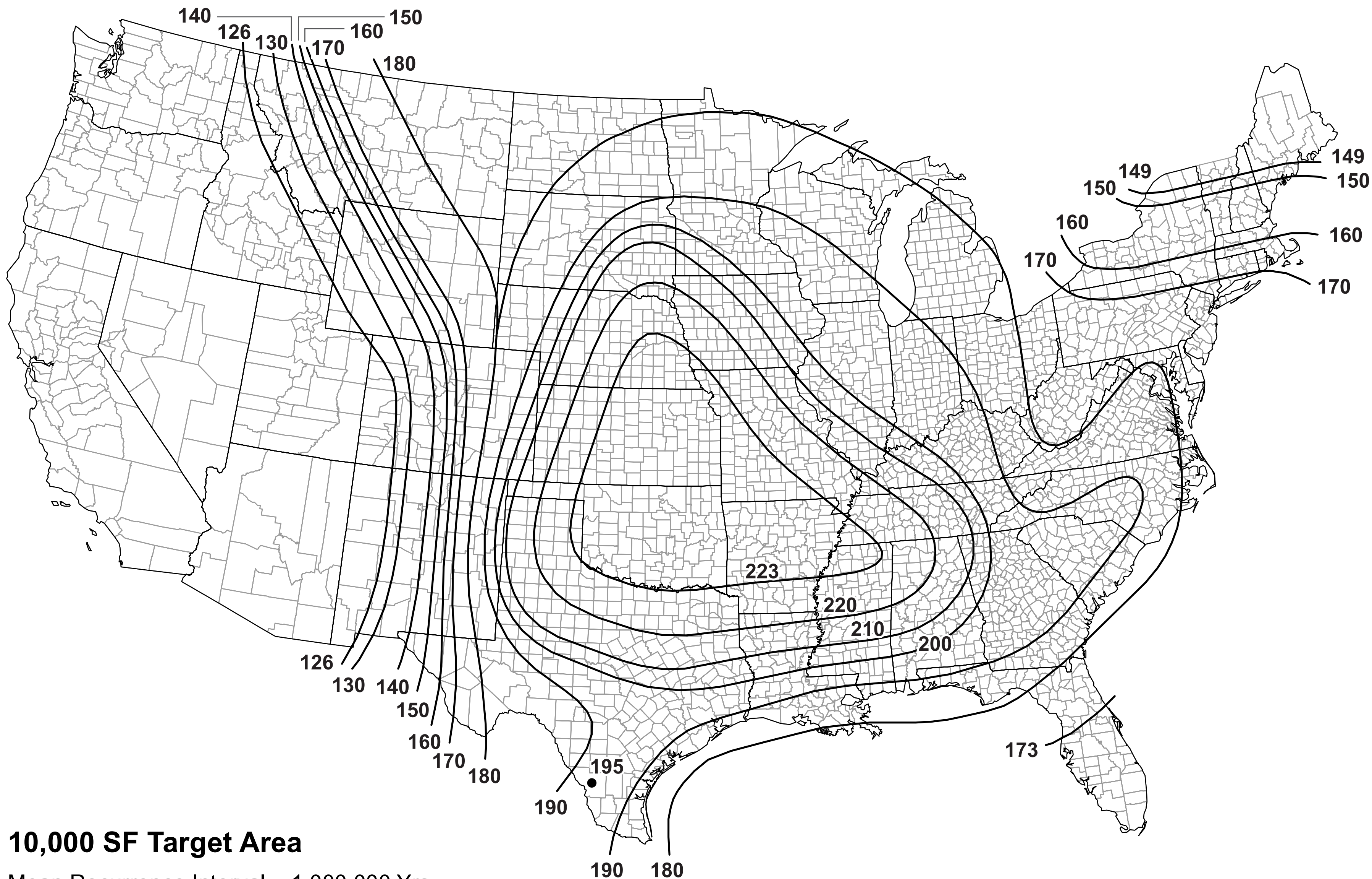

10,000 SF Target Area

Mean Recurrence Interval = 1,000,000 Yrs
Annual Exceedance Frequency = 1 x 10^{-6}

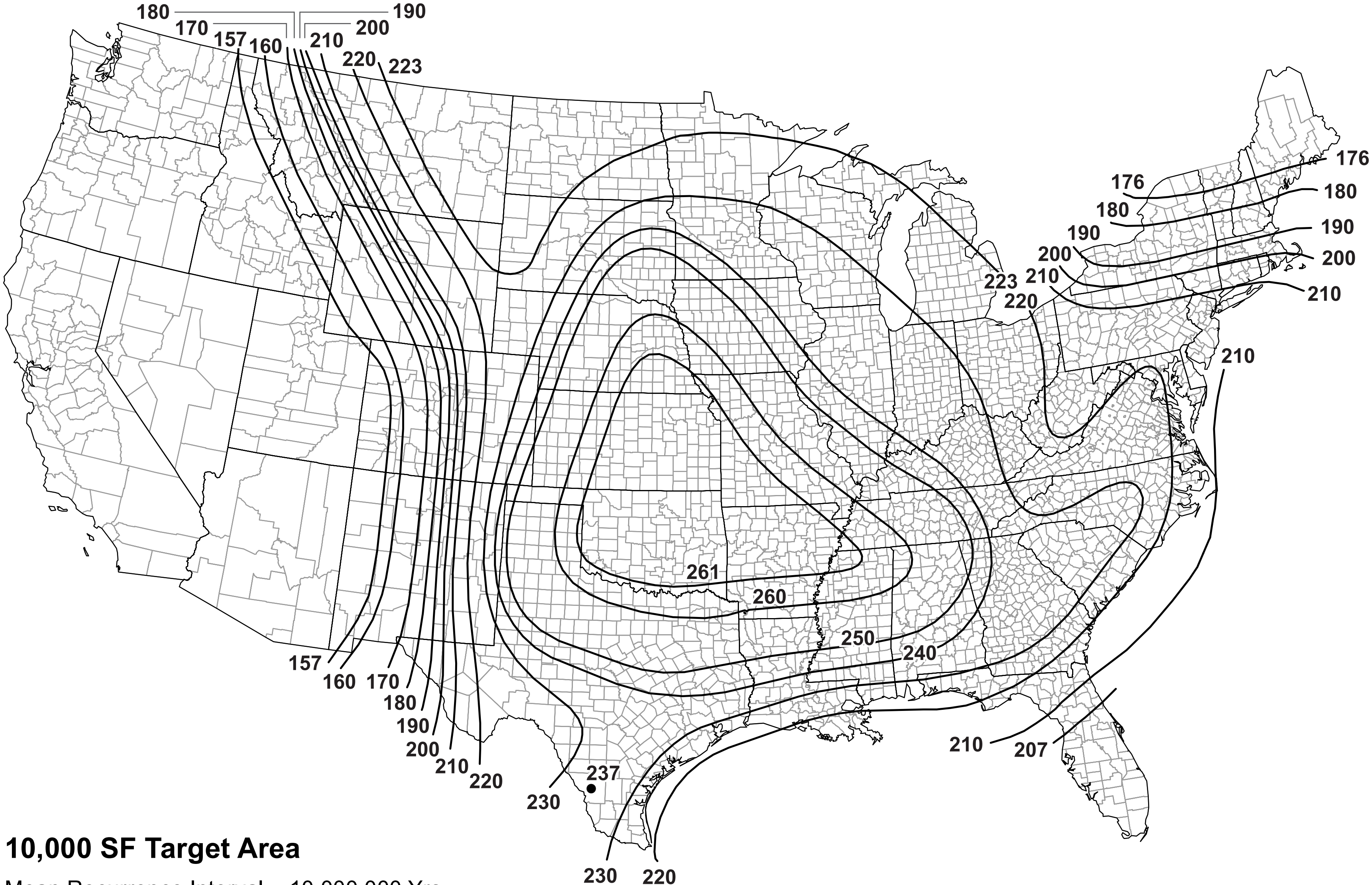

10,000 SF Target Area

Mean Recurrence Interval = 10,000,000 Yrs
Annual Exceedance Frequency = 1 x 10^{-7}

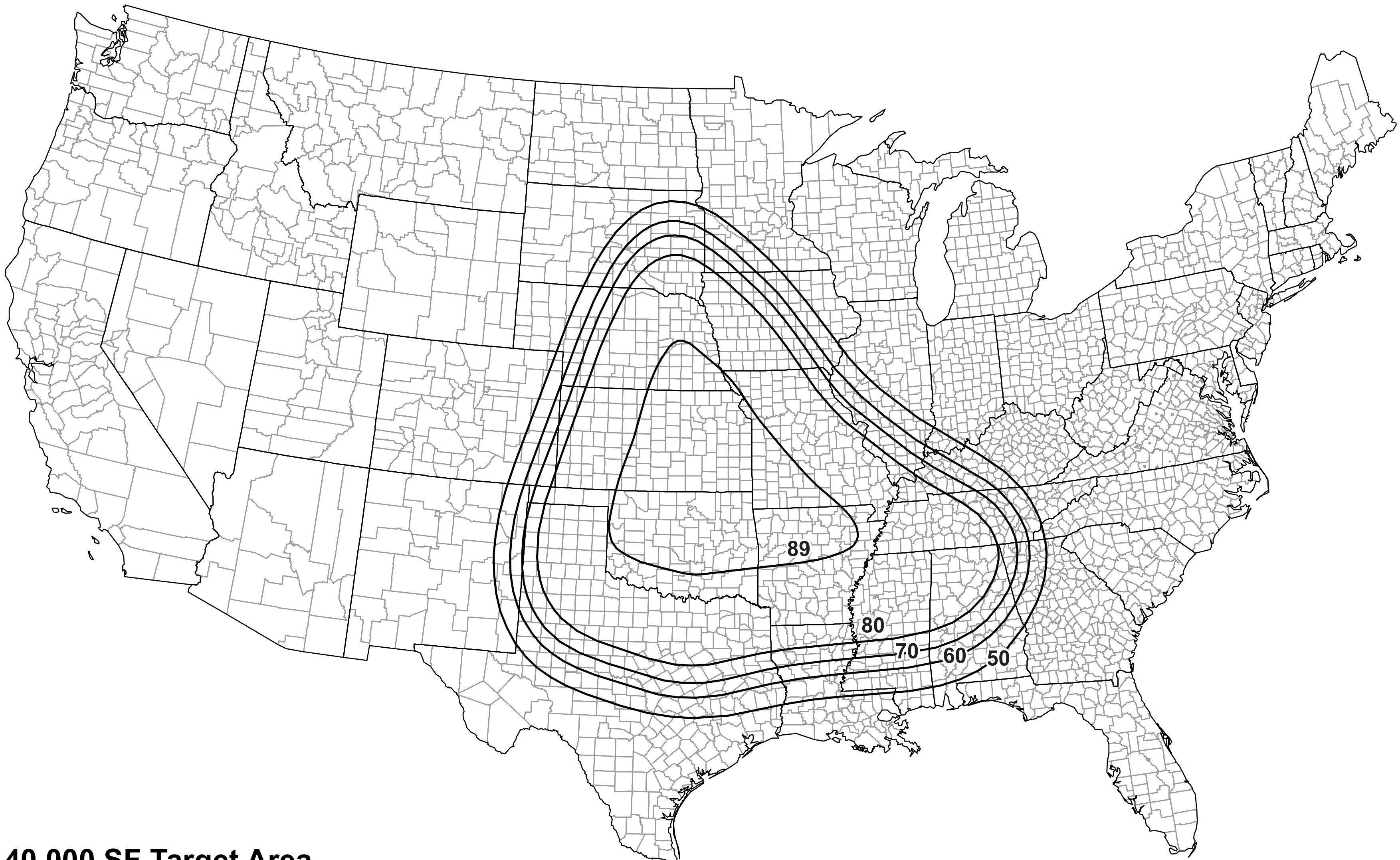

40,000 SF Target Area

Mean Recurrence Interval = 1,700 Yrs
Annual Exceedance Frequency = 5.88 x 10^{-4}

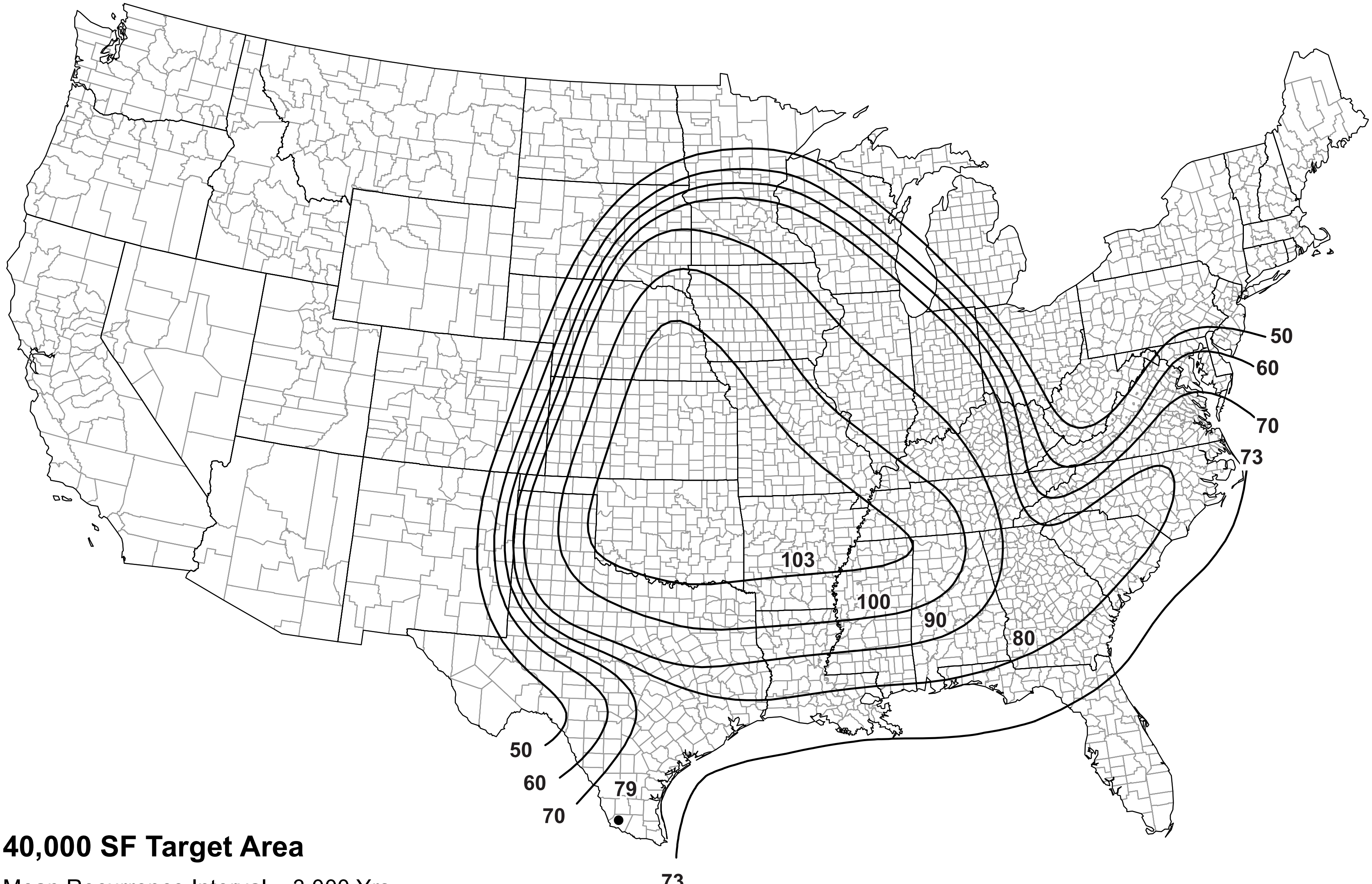

40,000 SF Target Area

Mean Recurrence Interval = 3,000 Yrs
Annual Exceedance Frequency = 3.3 x 10^{-4}

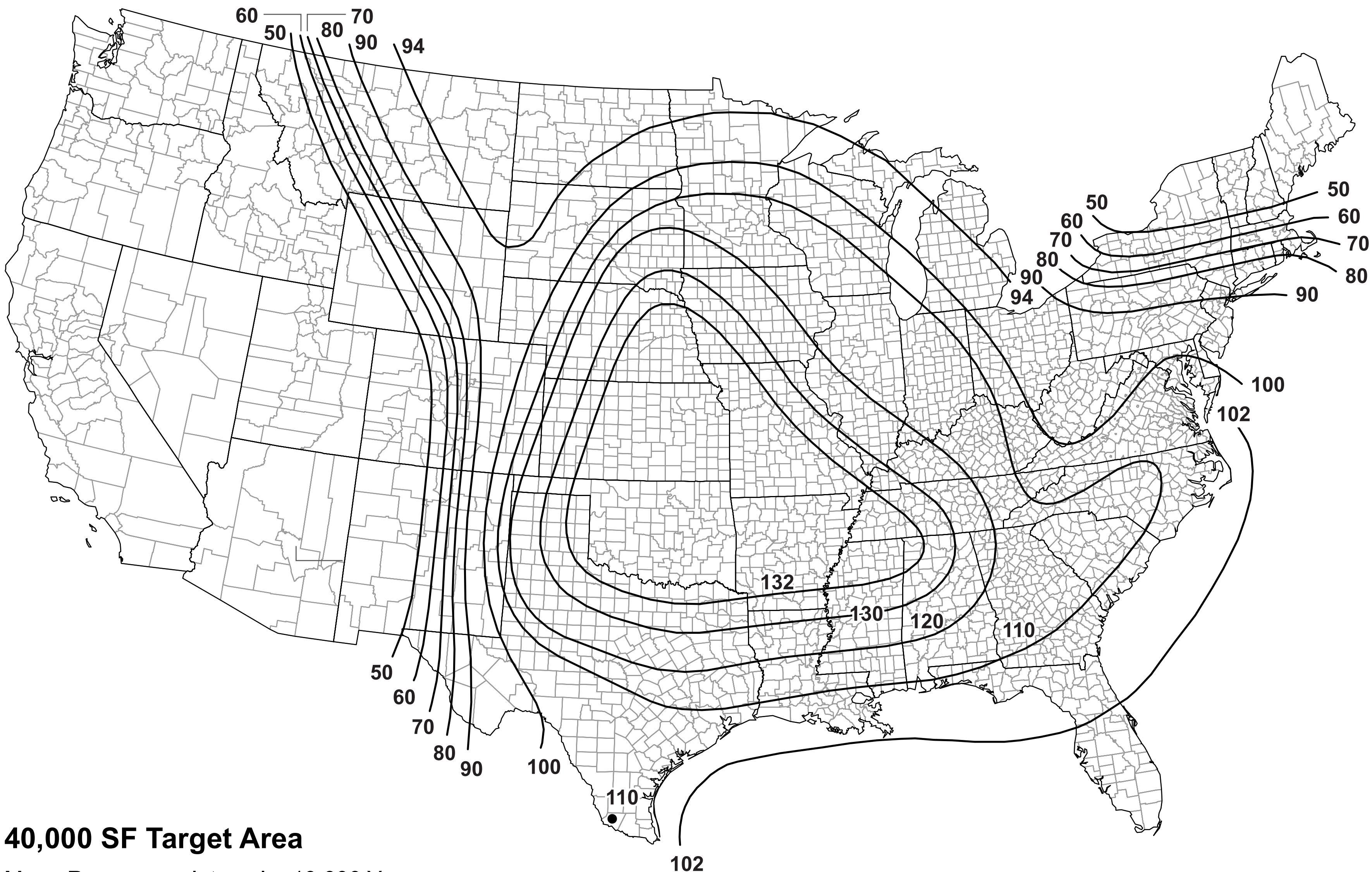

40,000 SF Target Area

Mean Recurrence Interval = 10,000 Yrs
Annual Exceedance Frequency = 1 x 10^{-4}

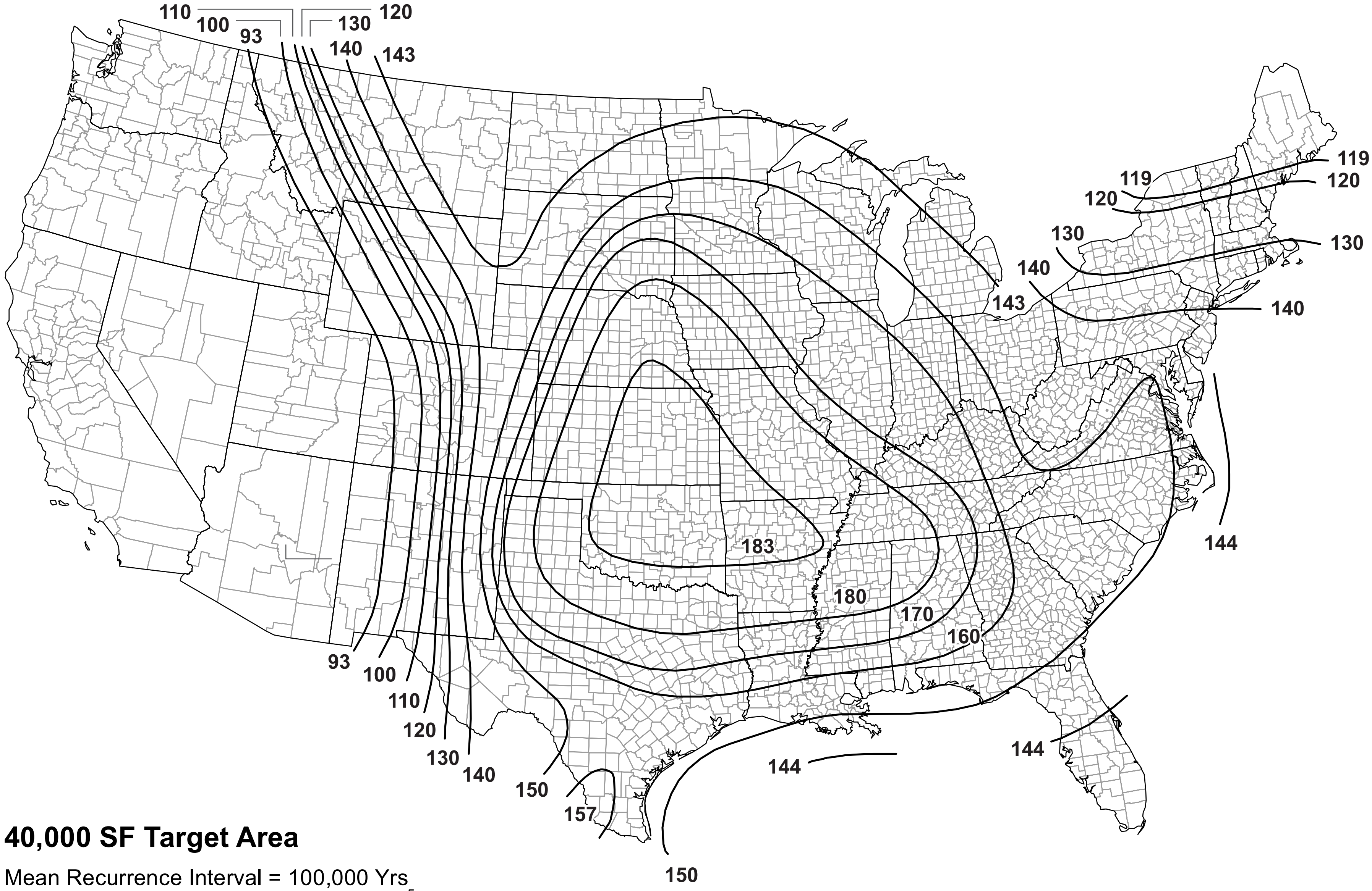

40,000 SF Target Area

Mean Recurrence Interval = 100,000 Yrs
Annual Exceedance Frequency = 1 x 10^{-5}

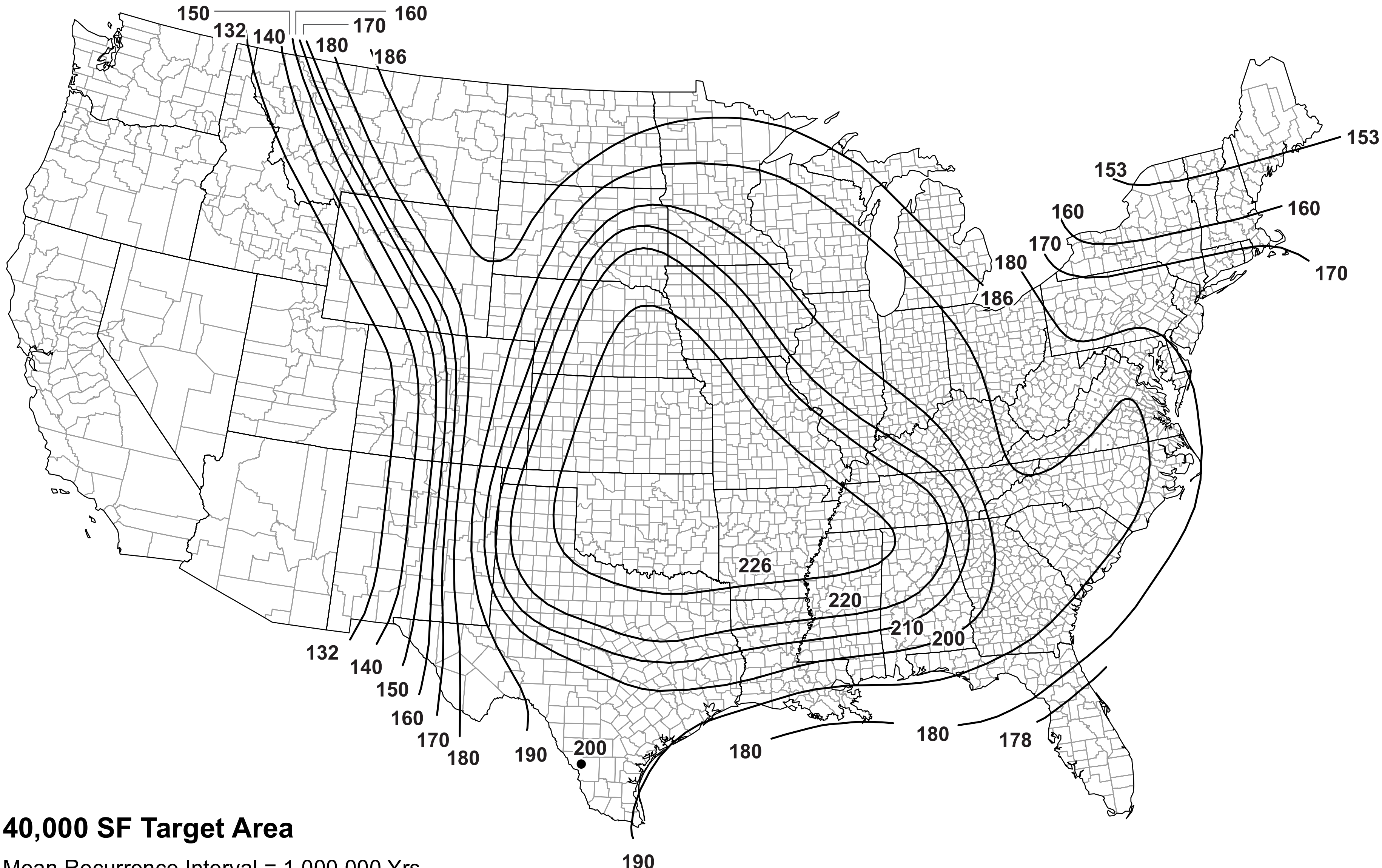

40,000 SF Target Area

Mean Recurrence Interval = 1,000,000 Yrs
Annual Exceedance Frequency = 1 x 10^{-6}

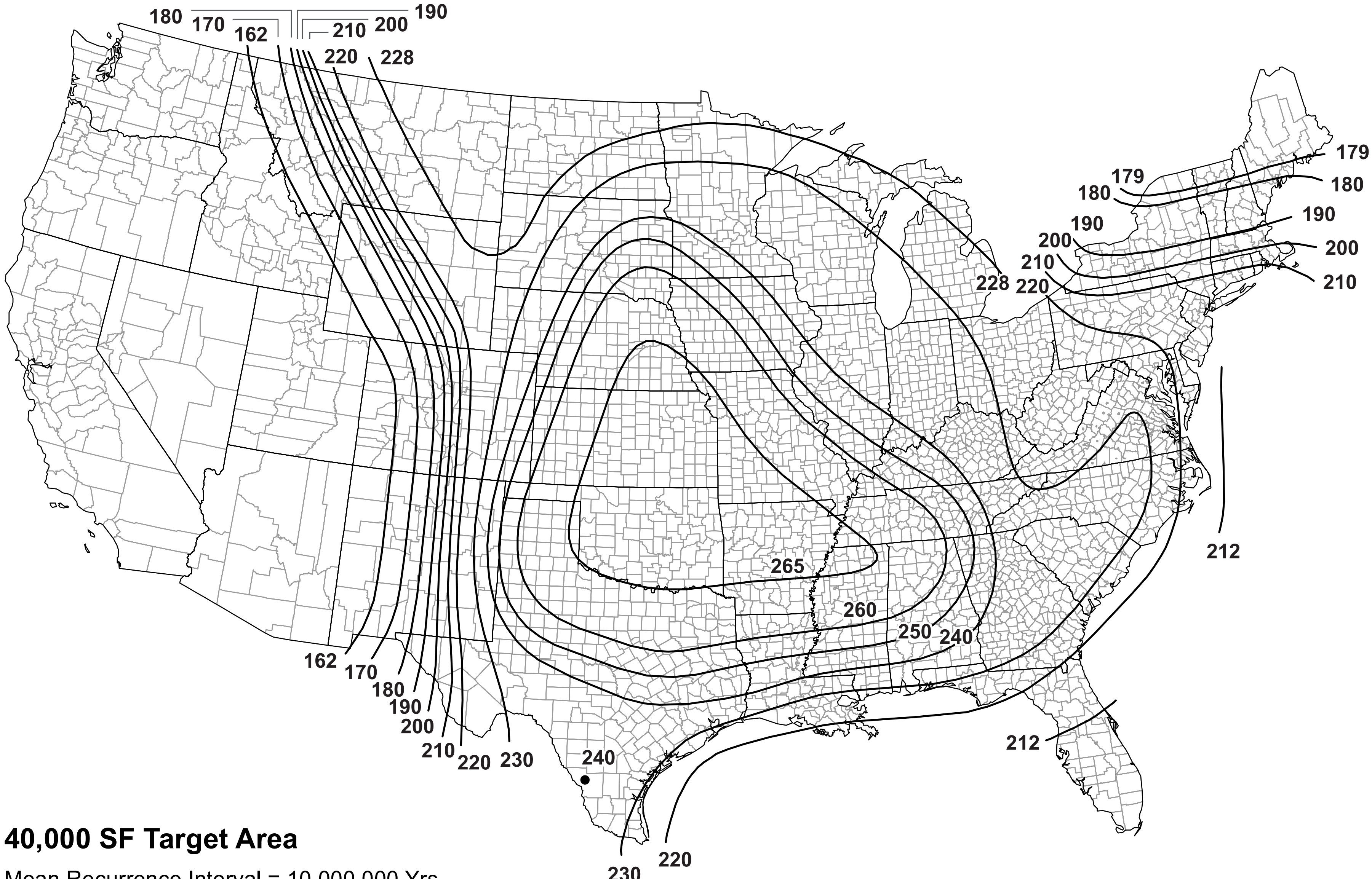

40,000 SF Target Area

Mean Recurrence Interval = 10,000,000 Yrs
Annual Exceedance Frequency = 1 x 10^{-7}

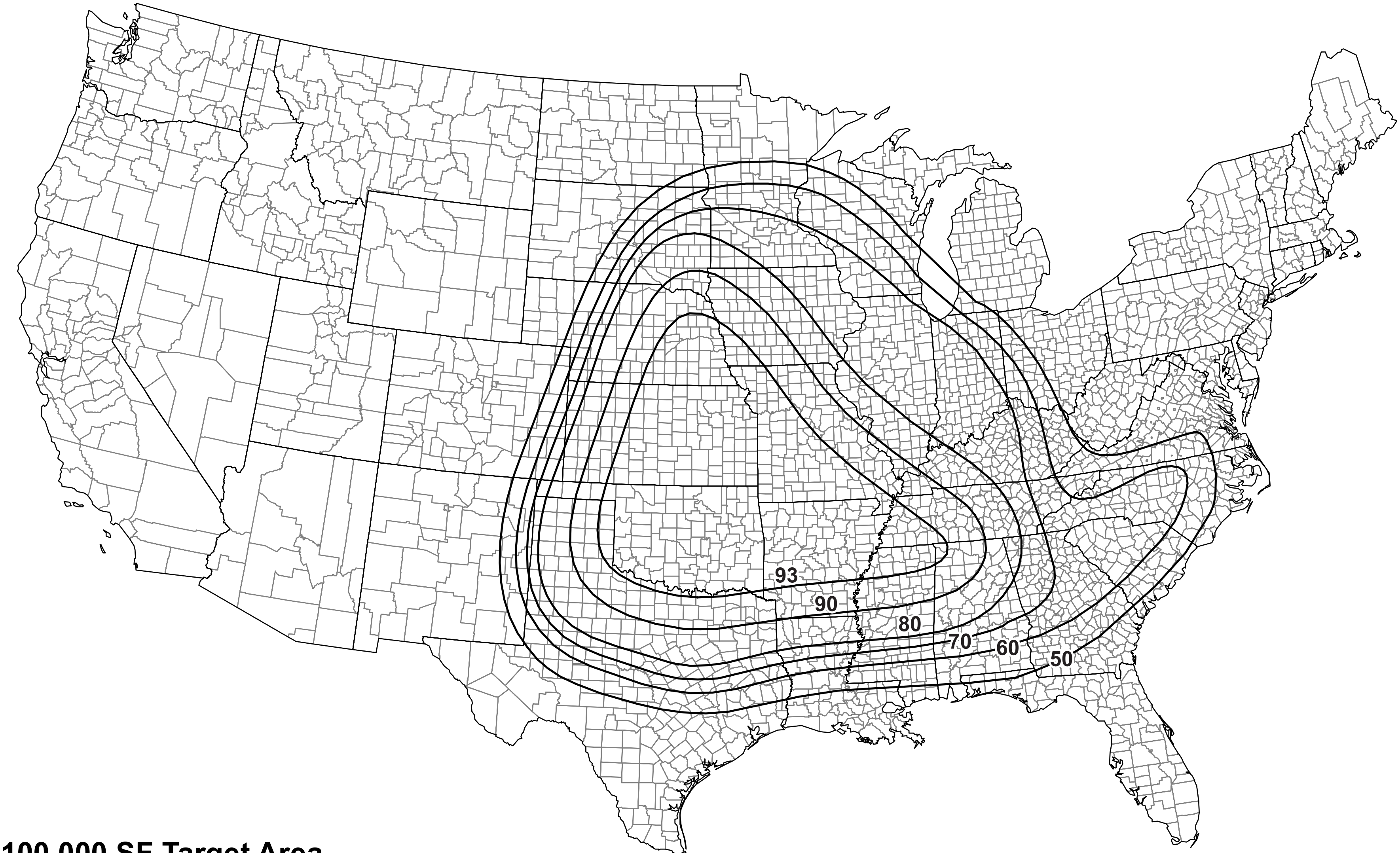

100,000 SF Target Area

Mean Recurrence Interval = 1,700 Yrs
Annual Exceedance Frequency = 5.88×10^{-4}

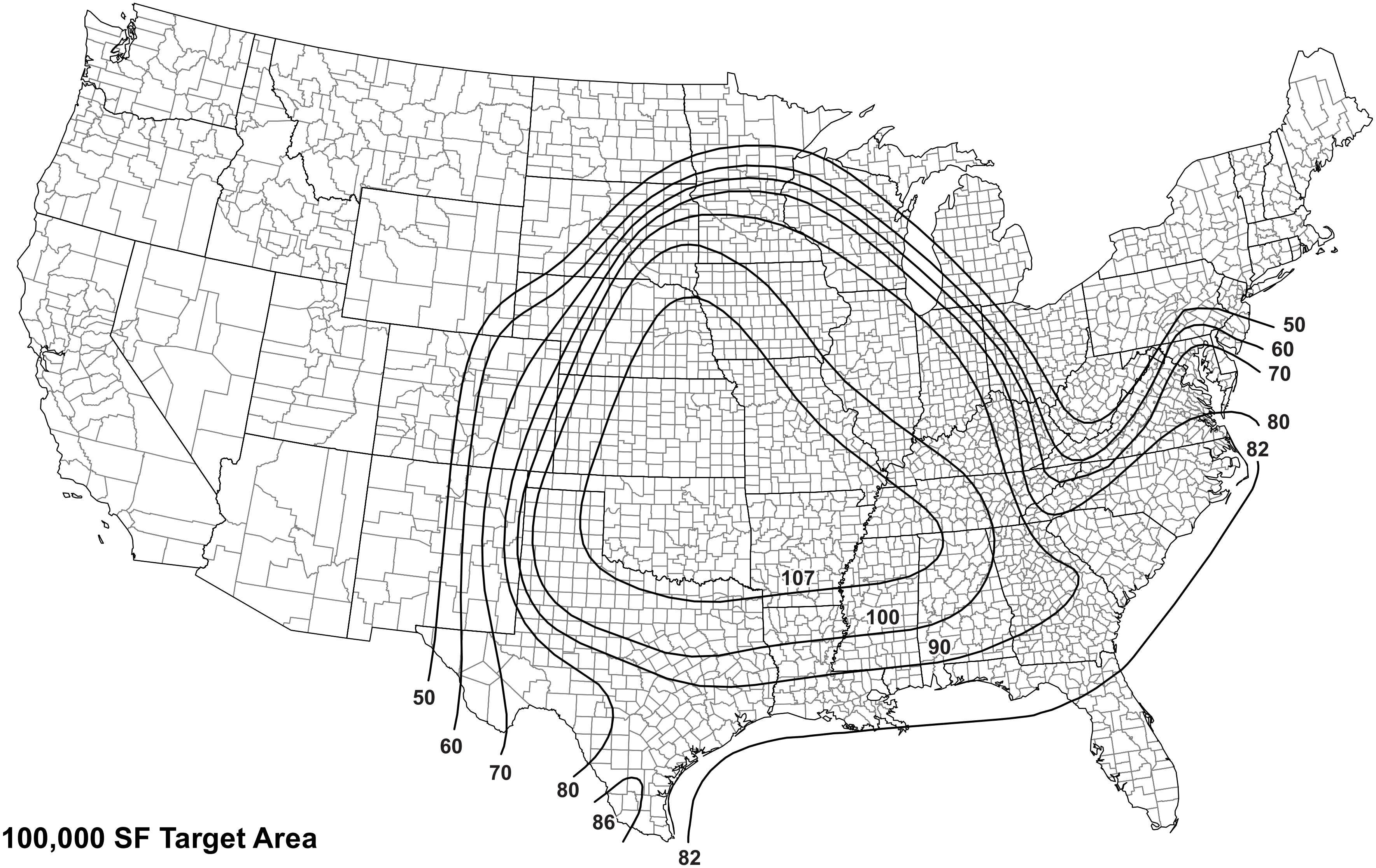

100,000 SF Target Area

Mean Recurrence Interval = 3,000 Yrs
Annual Exceedance Frequency = 3.3 x 10^{-4}

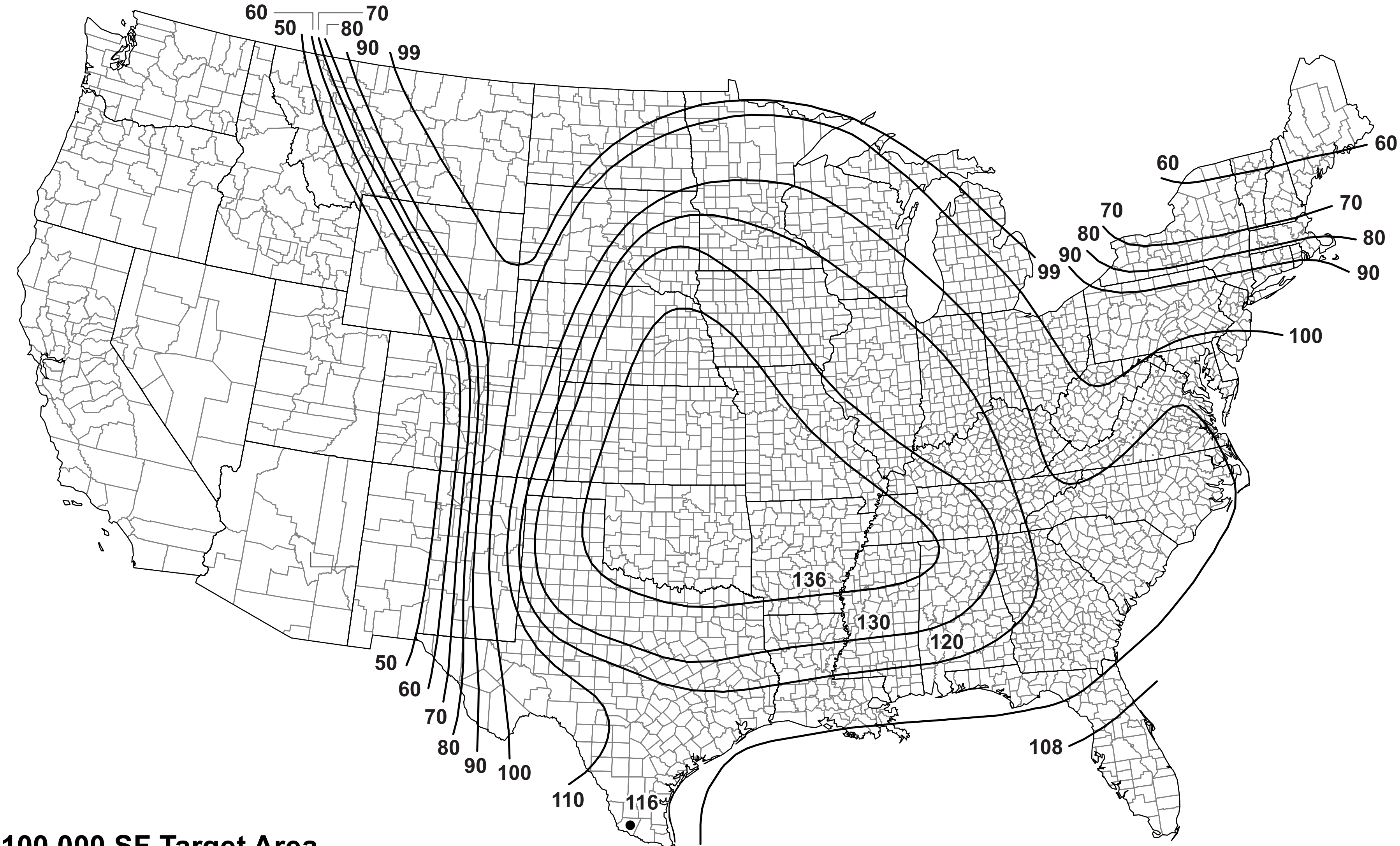

100,000 SF Target Area

Mean Recurrence Interval = 10,000 Yrs
Annual Exceedance Frequency = 1 x 10^{-4}

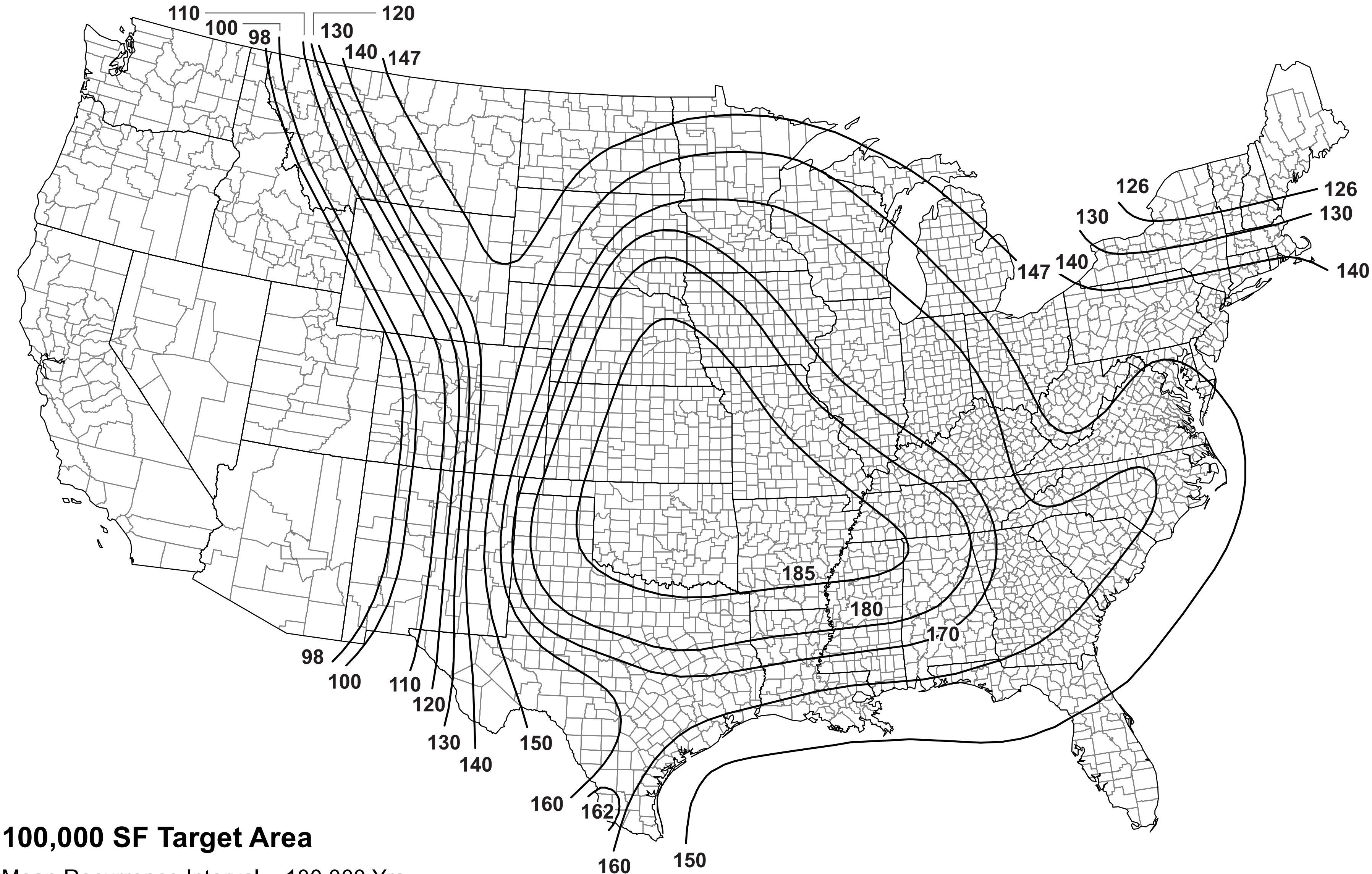

100,000 SF Target Area

Mean Recurrence Interval = 100,000 Yrs
Annual Exceedance Frequency = 1 x 10^{-5}

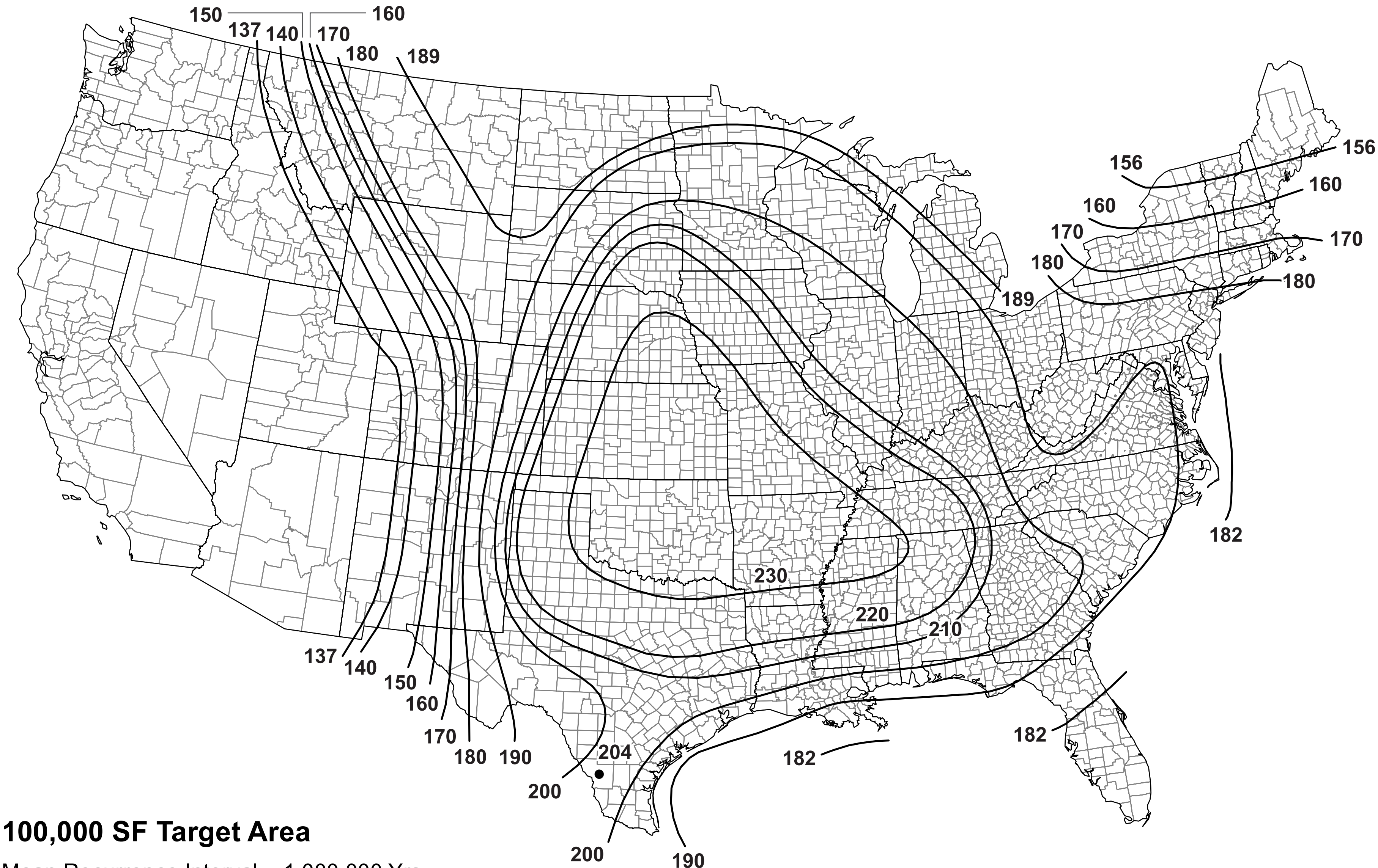

100,000 SF Target Area

Mean Recurrence Interval = 1,000,000 Yrs
Annual Exceedance Frequency = 1 x 10^{-6}

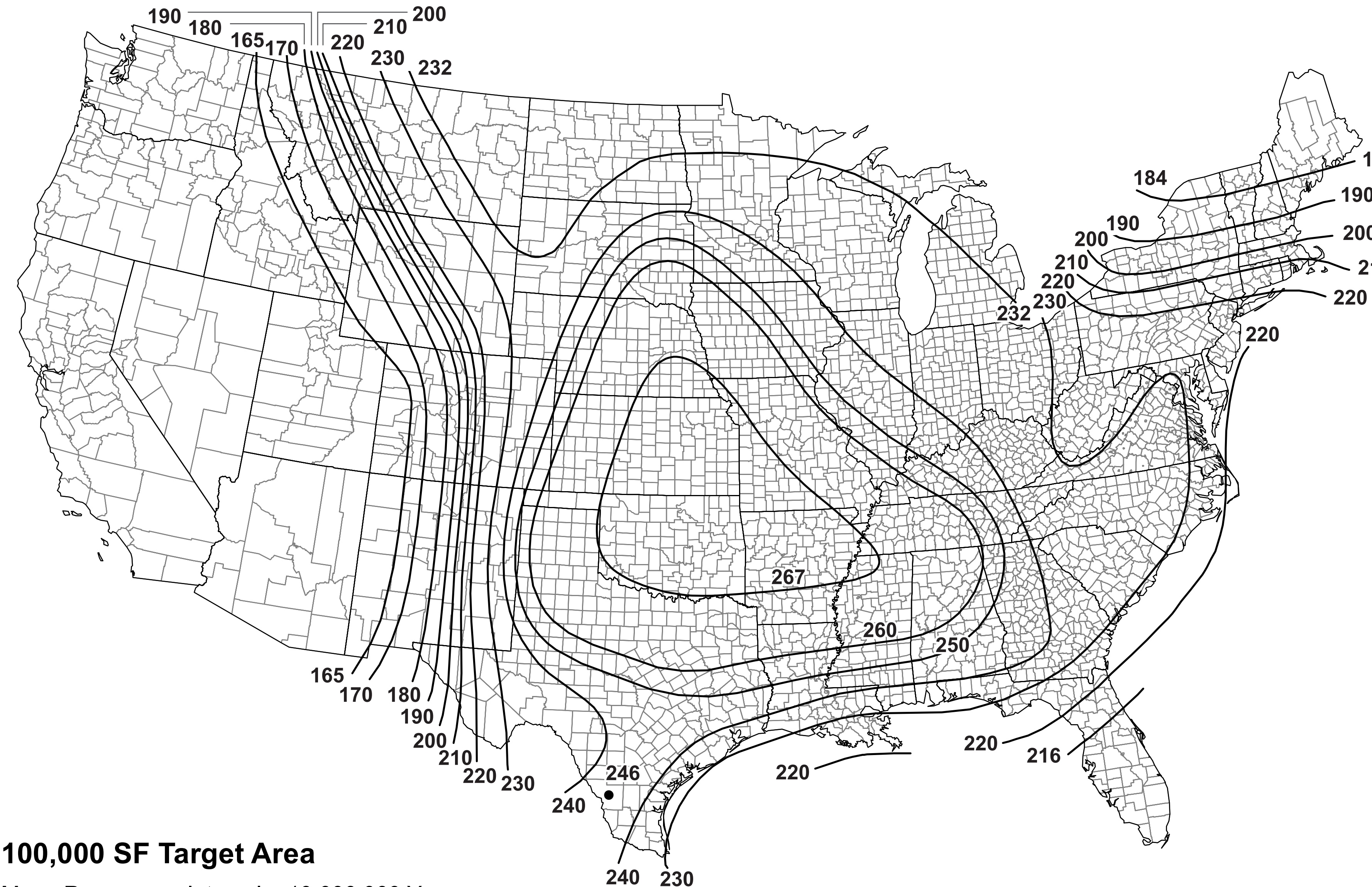

100,000 SF Target Area

Mean Recurrence Interval = 10,000,000 Yrs
Annual Exceedance Frequency = 1 x 10^{-7}

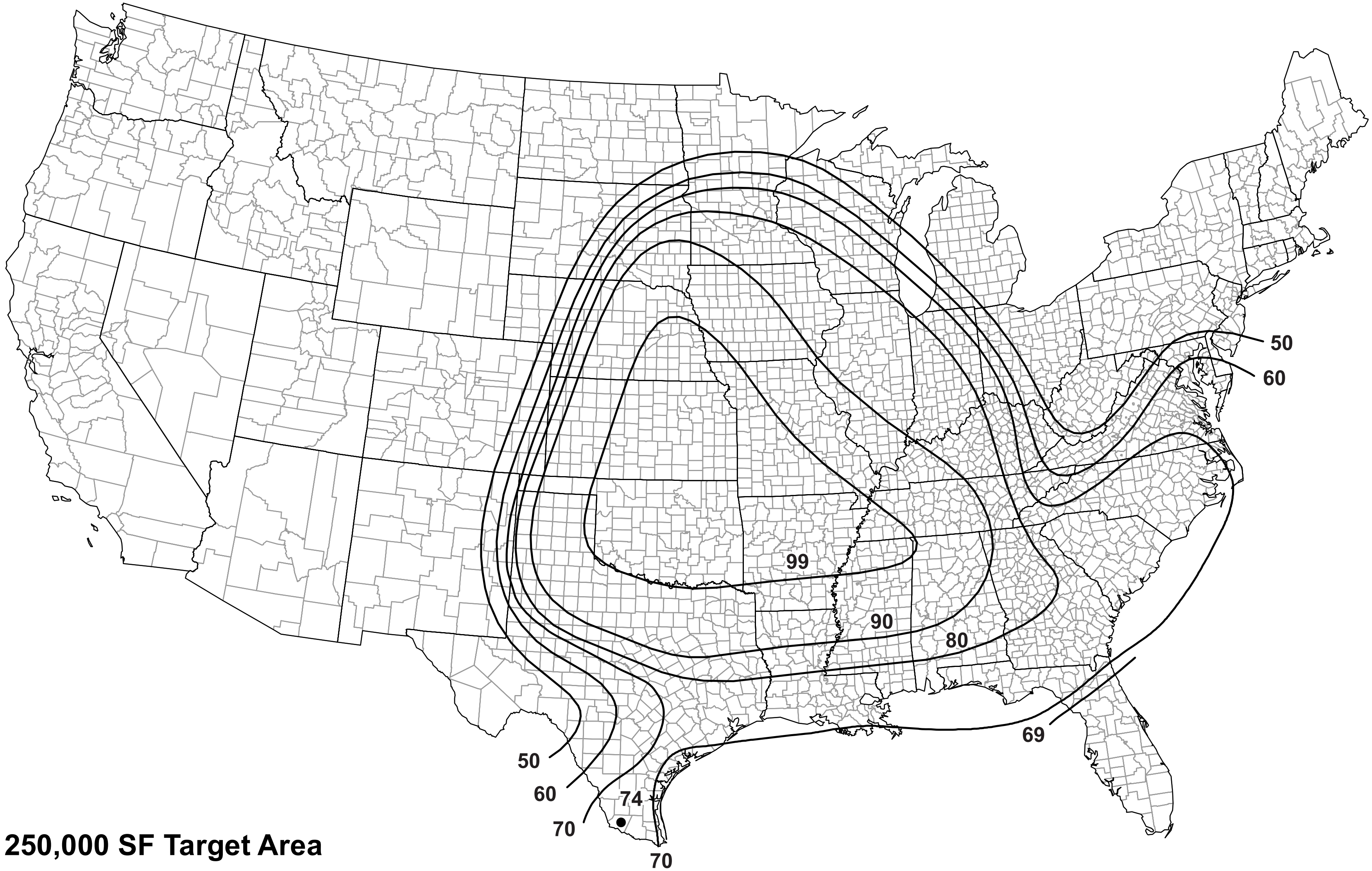

250,000 SF Target Area

Mean Recurrence Interval = 1,700 Yrs
Annual Exceedance Frequency = 5.88×10^{-4}

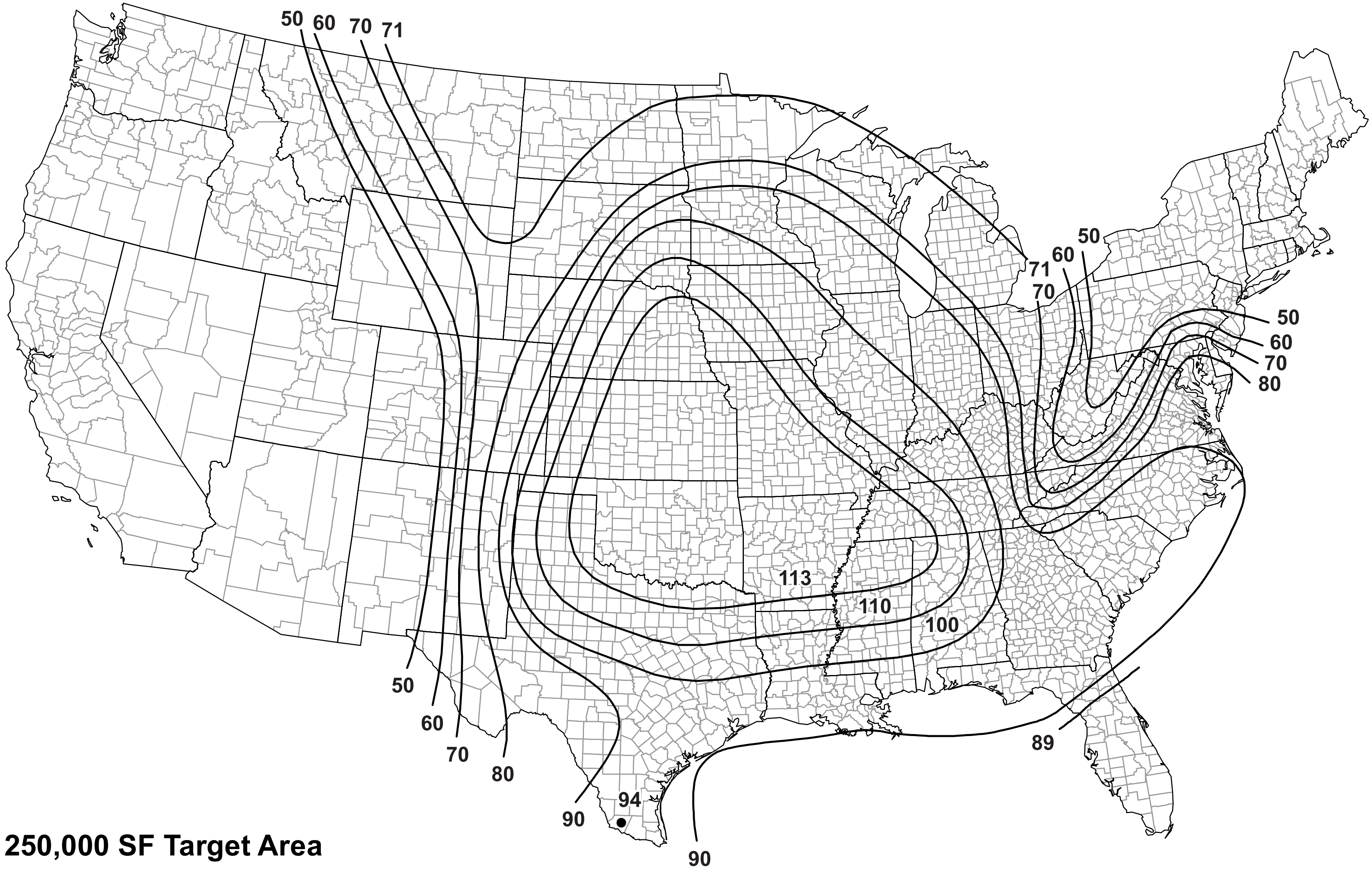

250,000 SF Target Area

Mean Recurrence Interval = 3,000 Yrs
Annual Exceedance Frequency = 3.3 x 10^{-4}

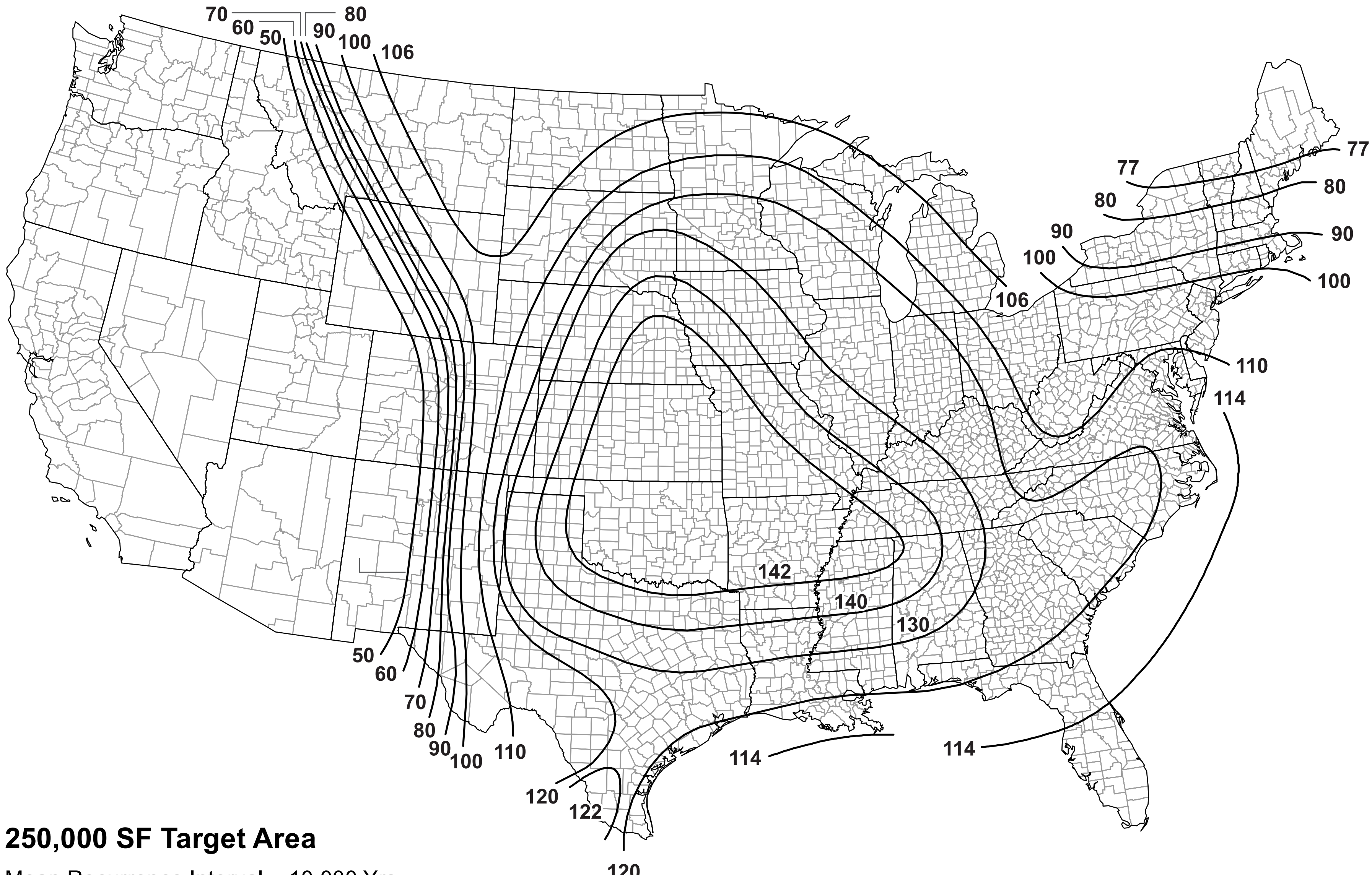

250,000 SF Target Area

Mean Recurrence Interval = 10,000 Yrs
Annual Exceedance Frequency = 1 x 10^{-4}

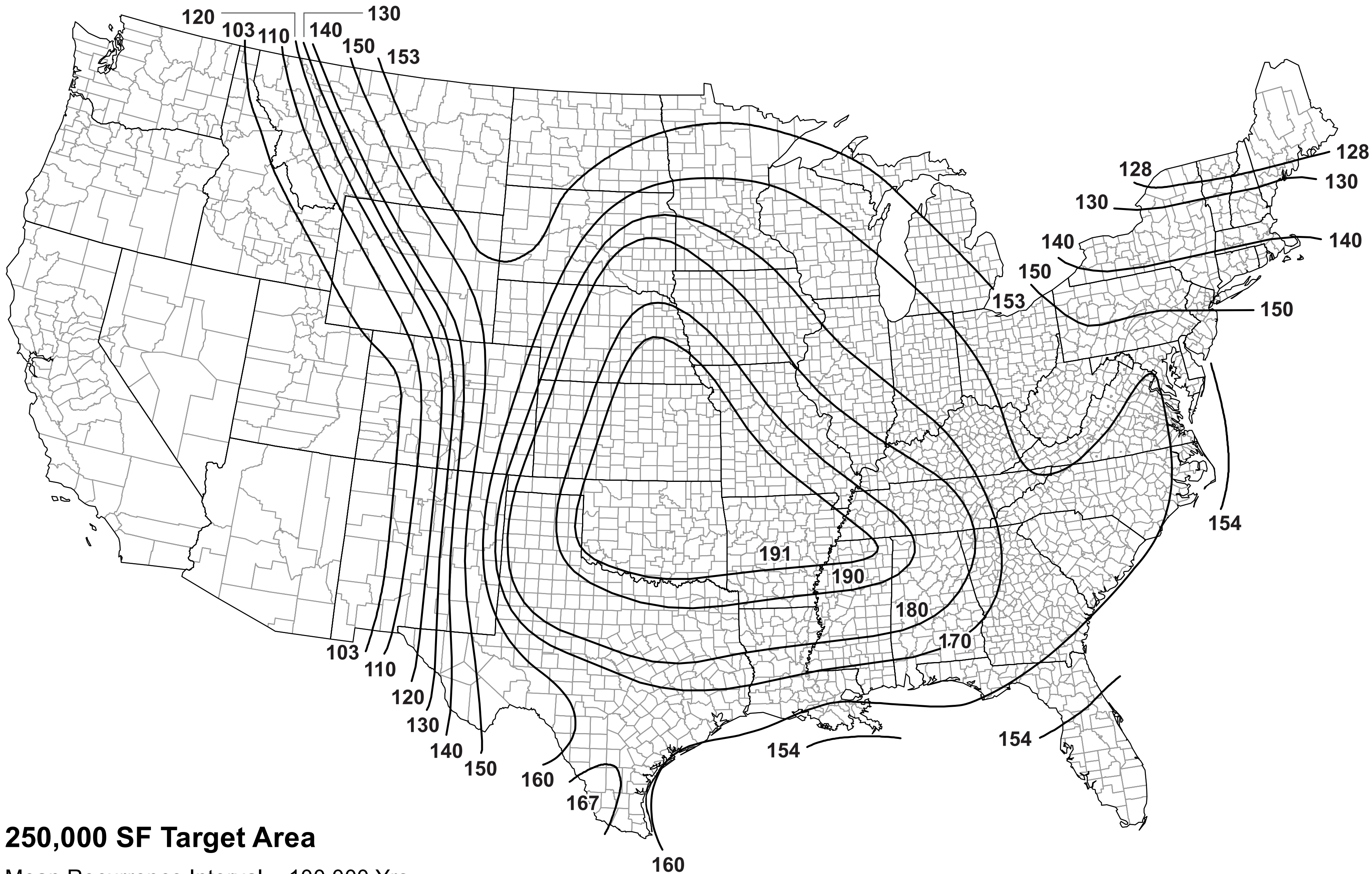

250,000 SF Target Area

Mean Recurrence Interval = 100,000 Yrs
Annual Exceedance Frequency = 1 x 10^{-5}

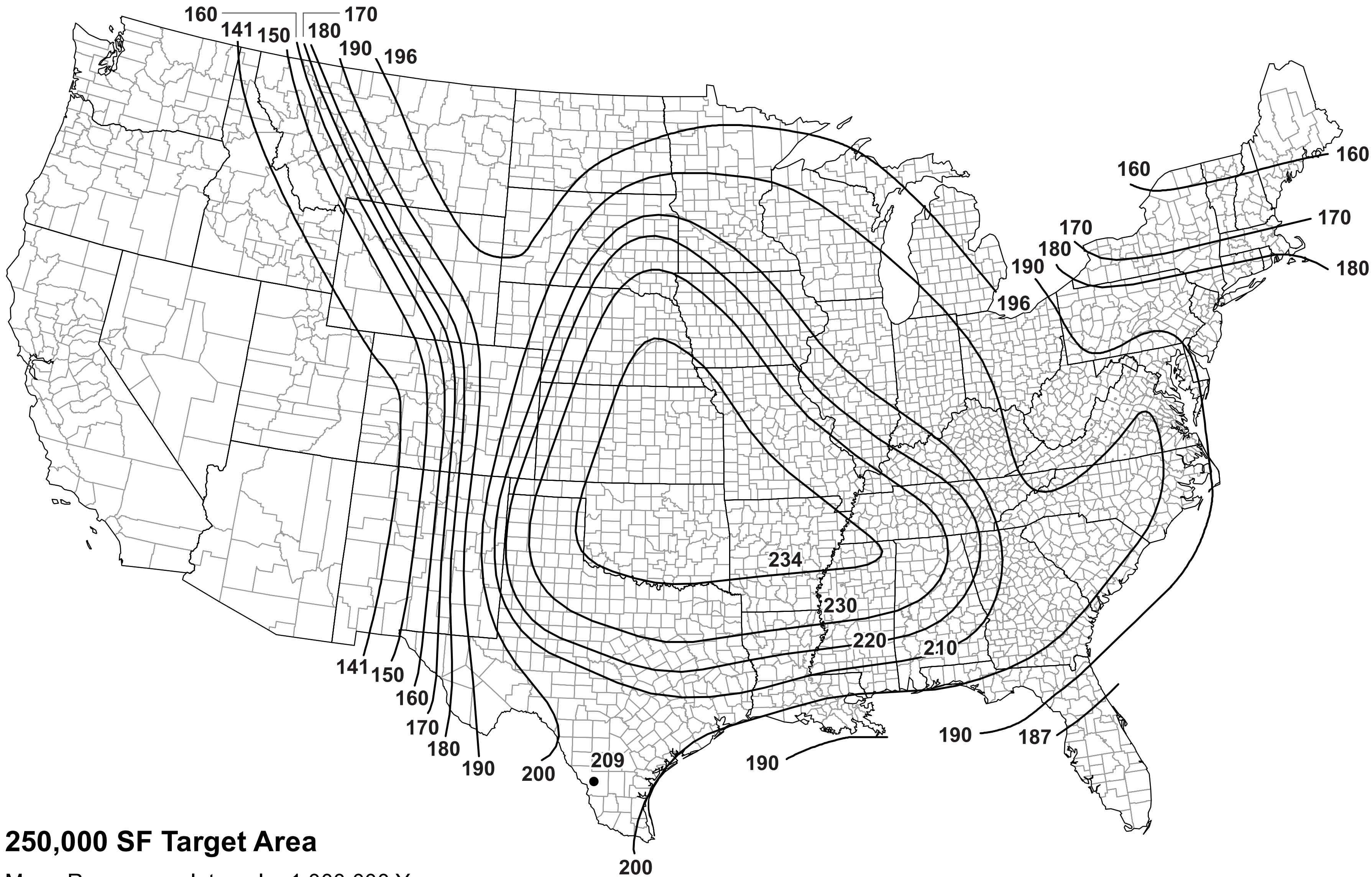

250,000 SF Target Area

Mean Recurrence Interval = 1,000,000 Yrs
Annual Exceedance Frequency = 1 x 10^{-6}

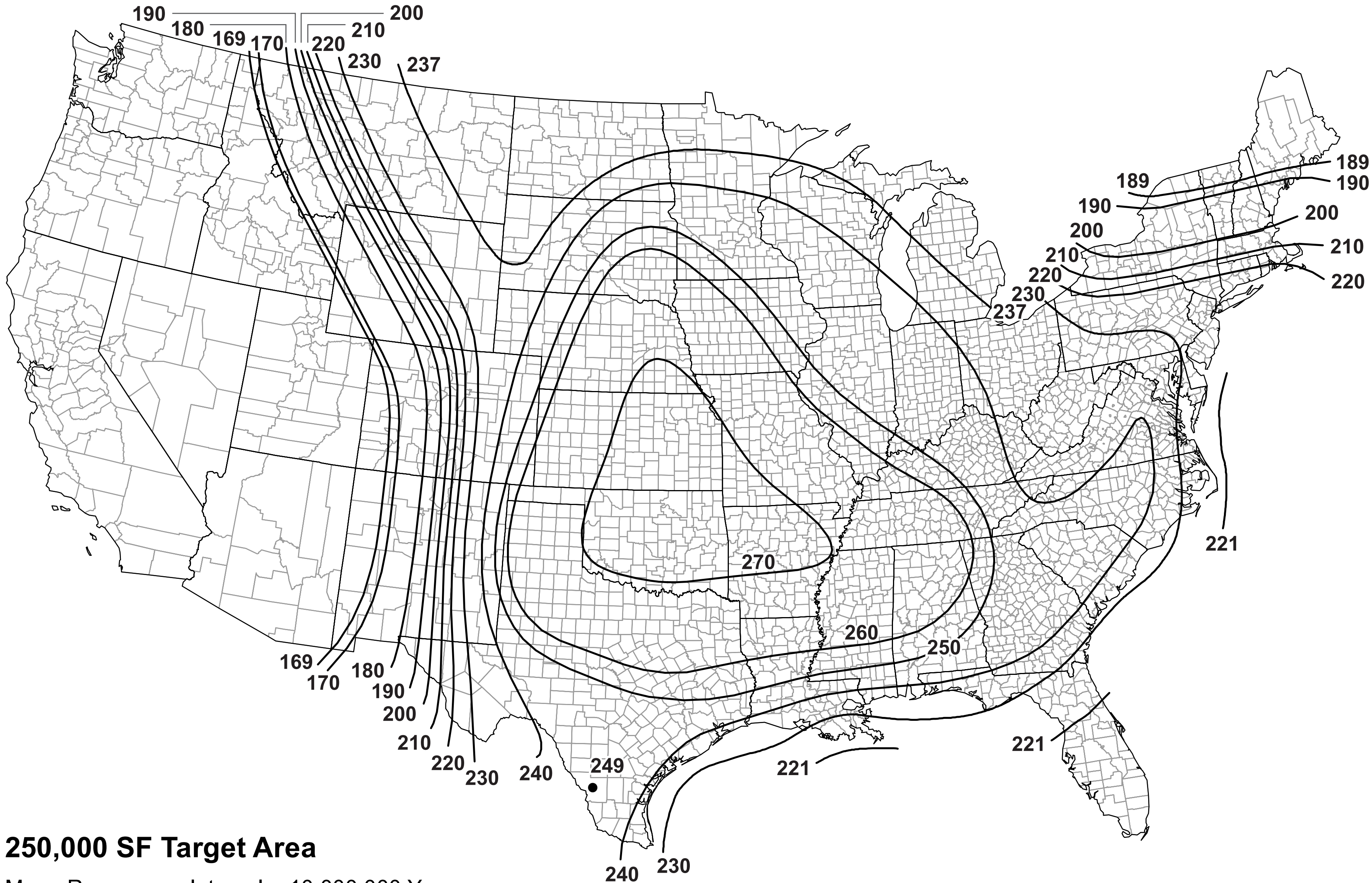

250,000 SF Target Area

Mean Recurrence Interval = 10,000,000 Yrs
Annual Exceedance Frequency = 1 x 10^{-7}

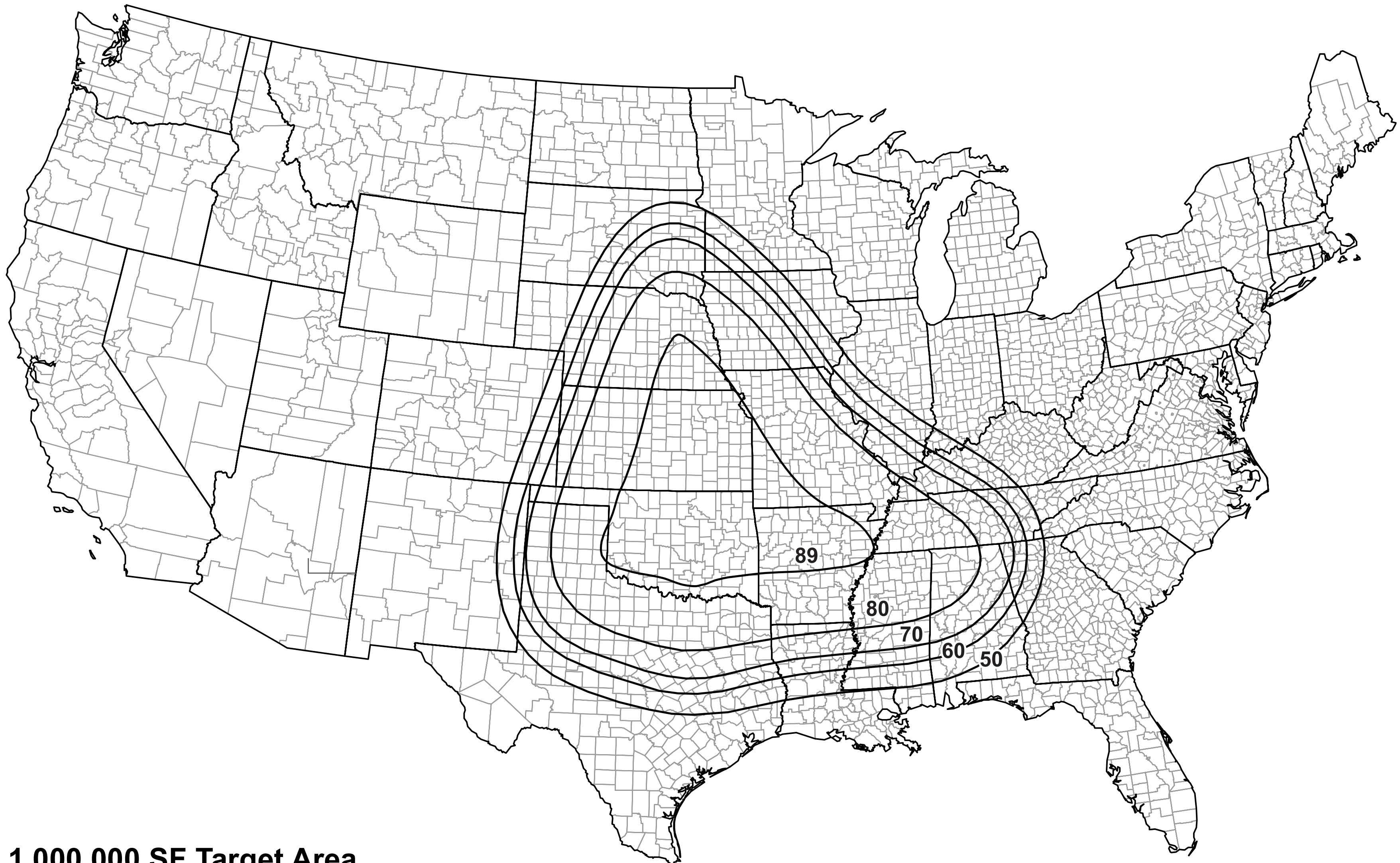

1,000,000 SF Target Area

Mean Recurrence Interval = 700 Yrs
Annual Exceedance Frequency = 1.43 x 10^{-3}

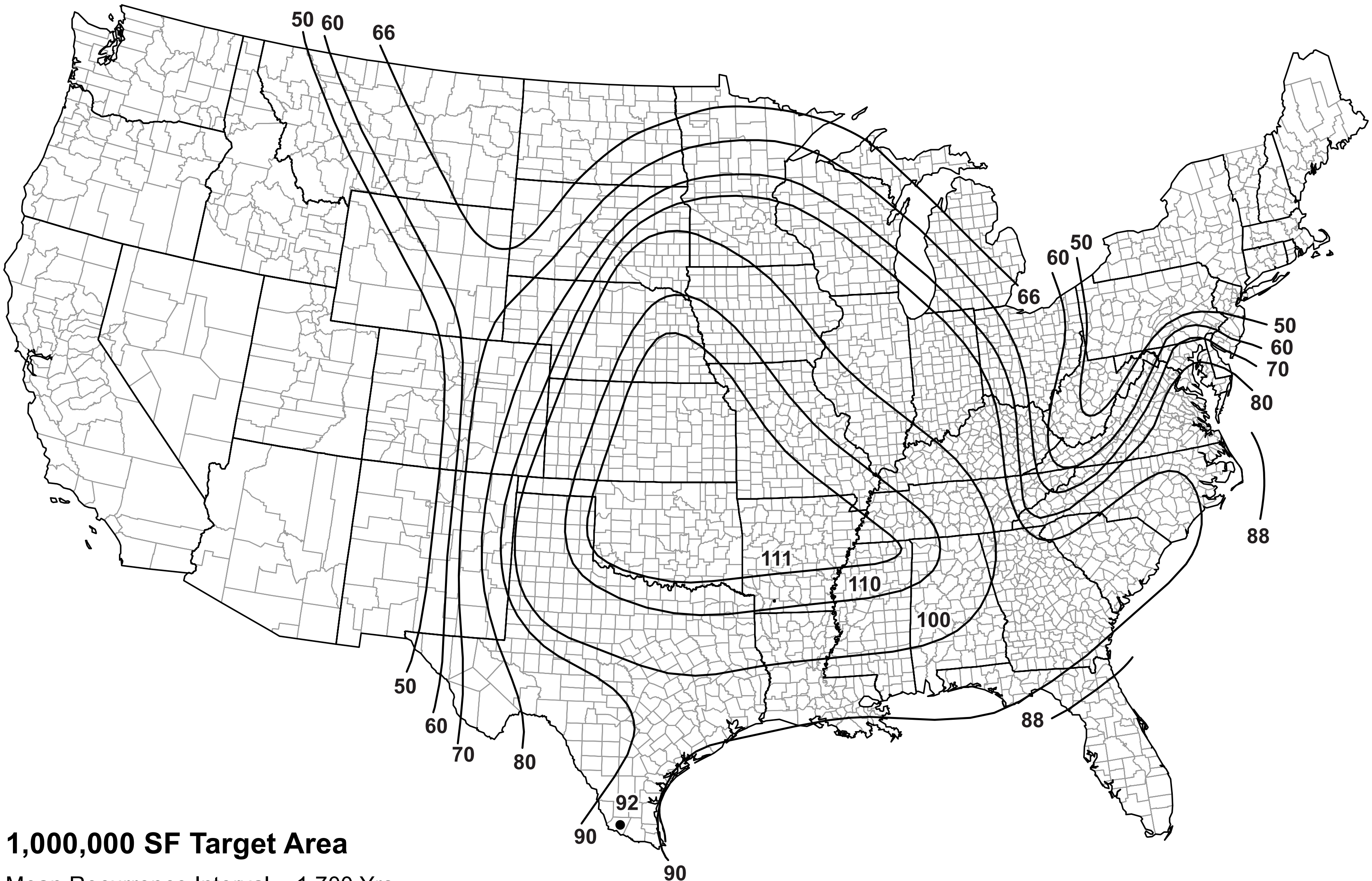

1,000,000 SF Target Area

Mean Recurrence Interval = 1,700 Yrs
Annual Exceedance Frequency = 5.88×10^{-4}

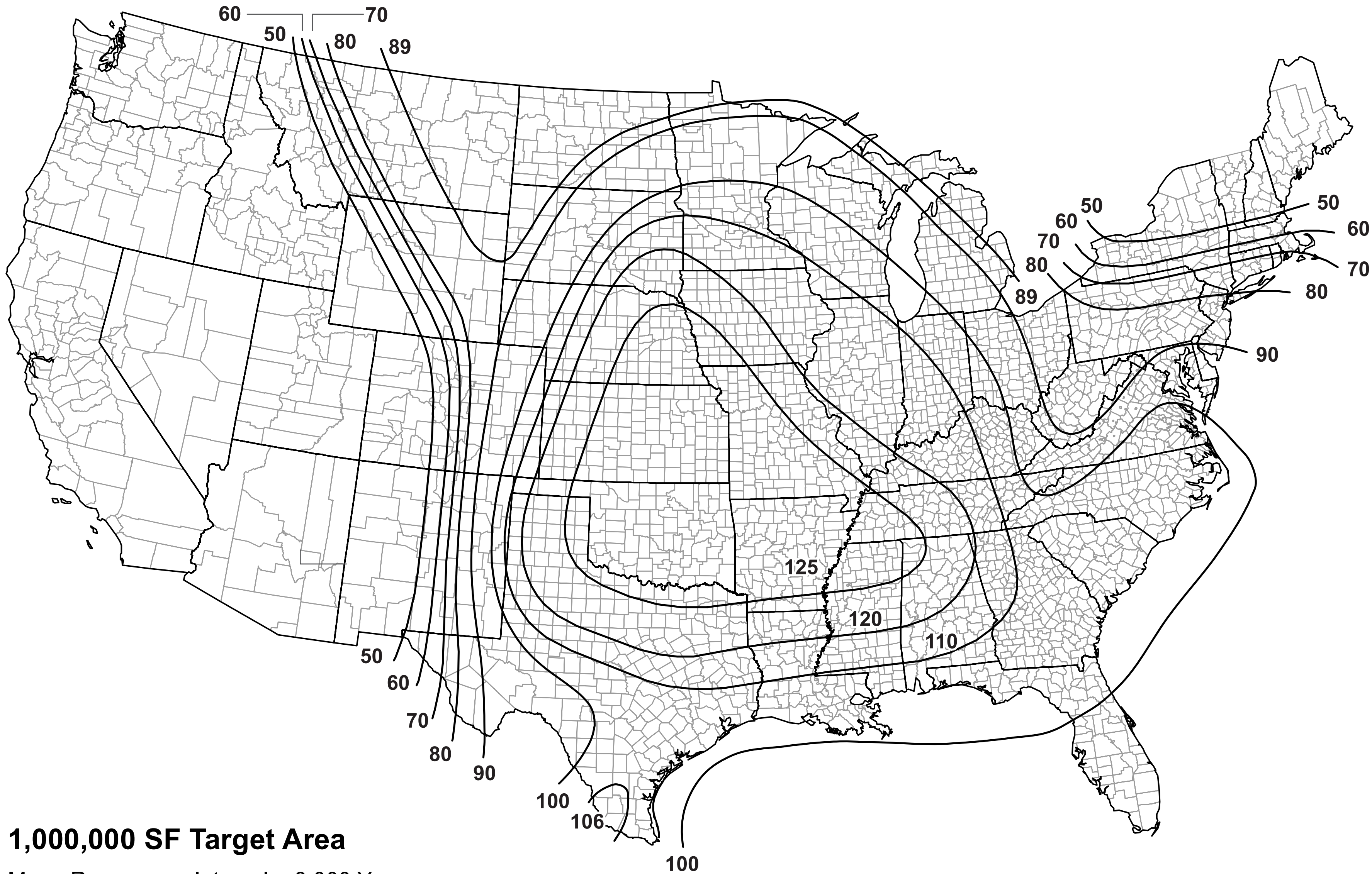

1,000,000 SF Target Area

Mean Recurrence Interval = 3,000 Yrs
Annual Exceedance Frequency = 3.3×10^{-4}

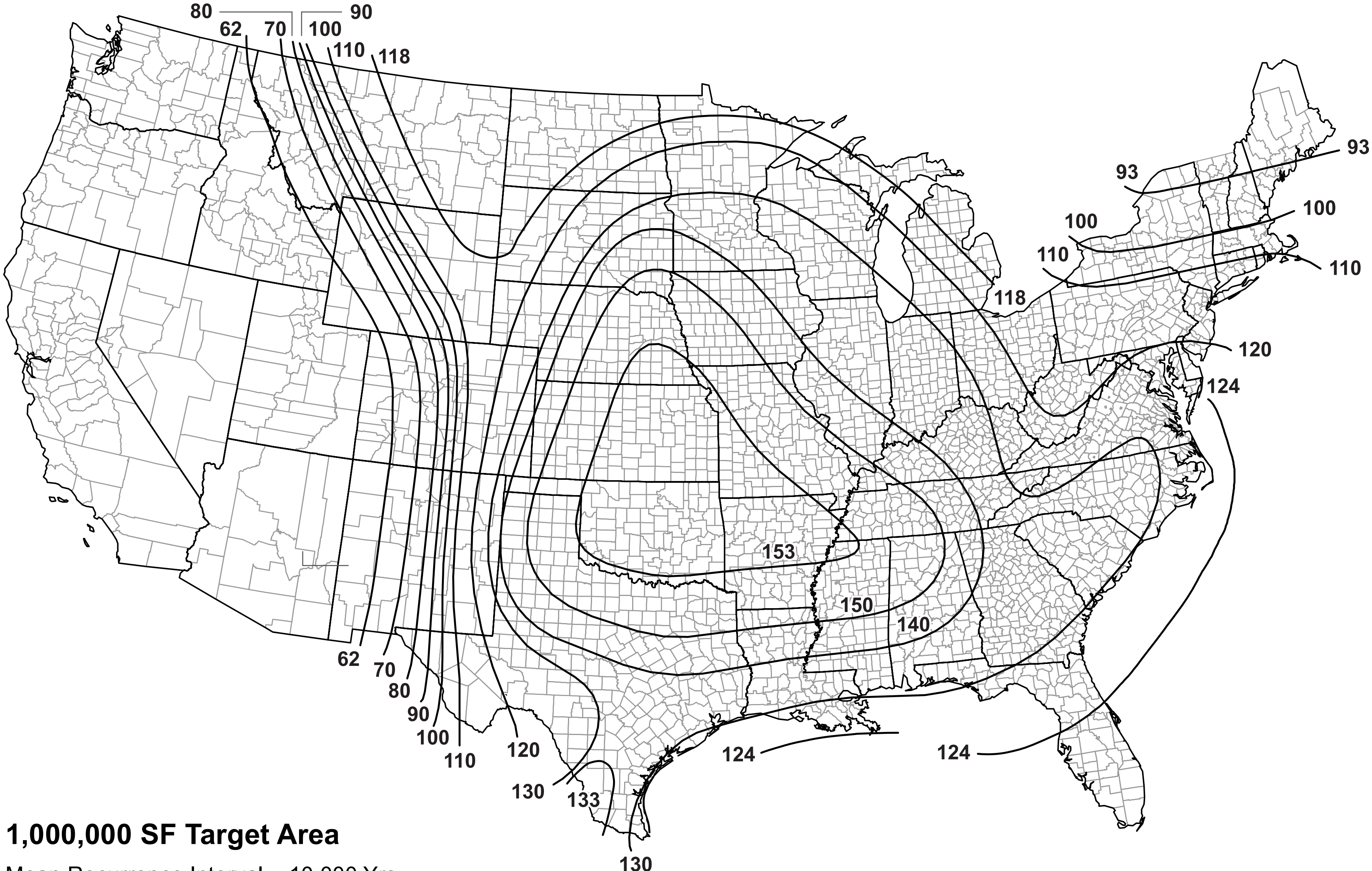

1,000,000 SF Target Area

Mean Recurrence Interval = 10,000 Yrs
Annual Exceedance Frequency = 1 x 10^{-4}

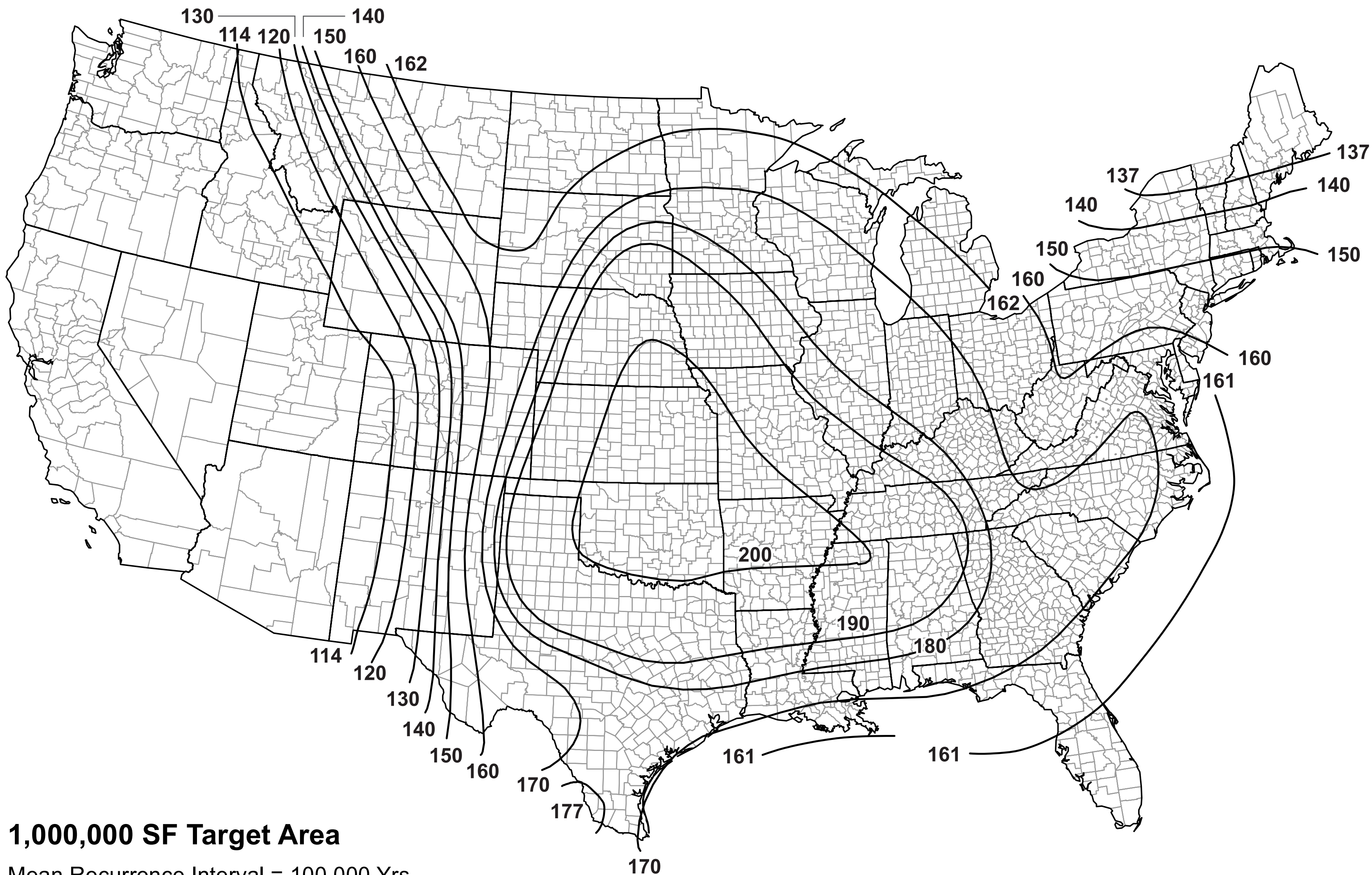

1,000,000 SF Target Area

Mean Recurrence Interval = 100,000 Yrs
Annual Exceedance Frequency = 1 x 10^{-5}

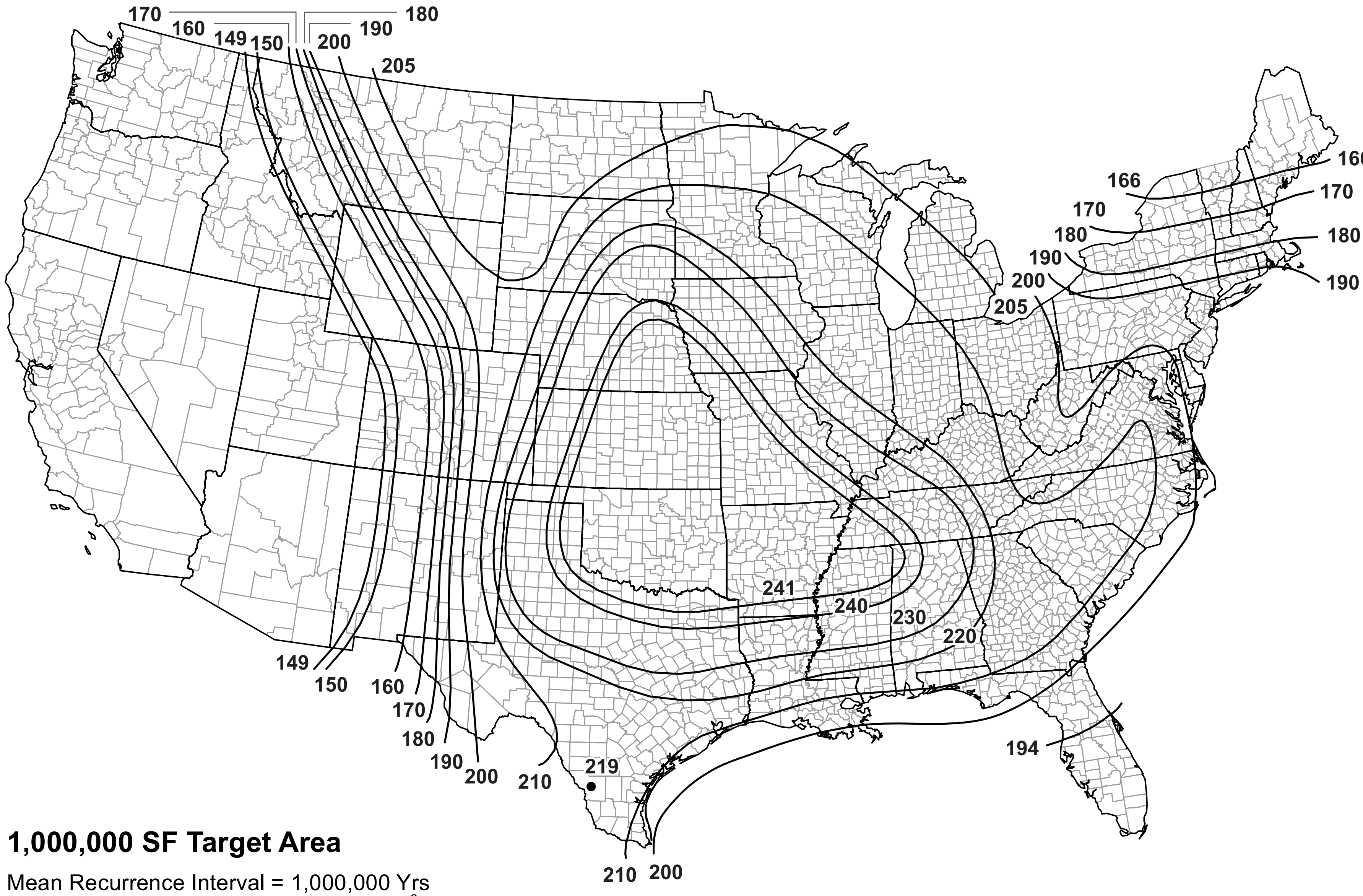

1,000,000 SF Target Area

Mean Recurrence Interval = 1,000,000 Yrs
Annual Exceedance Frequency = 1 x 10^{-6}

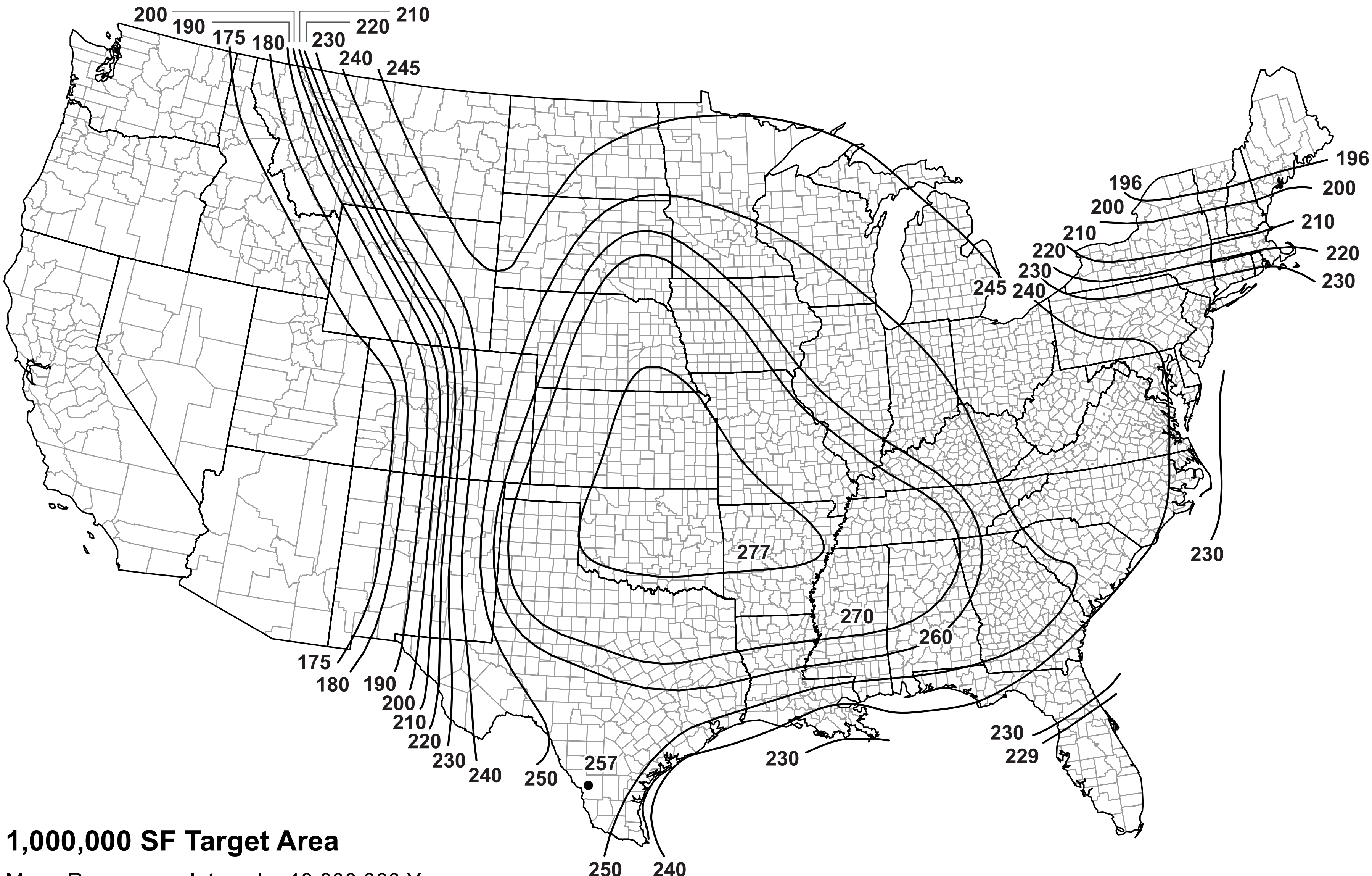

1,000,000 SF Target Area

Mean Recurrence Interval = 10,000,000 Yrs
Annual Exceedance Frequency = 1 x 10^{-7}

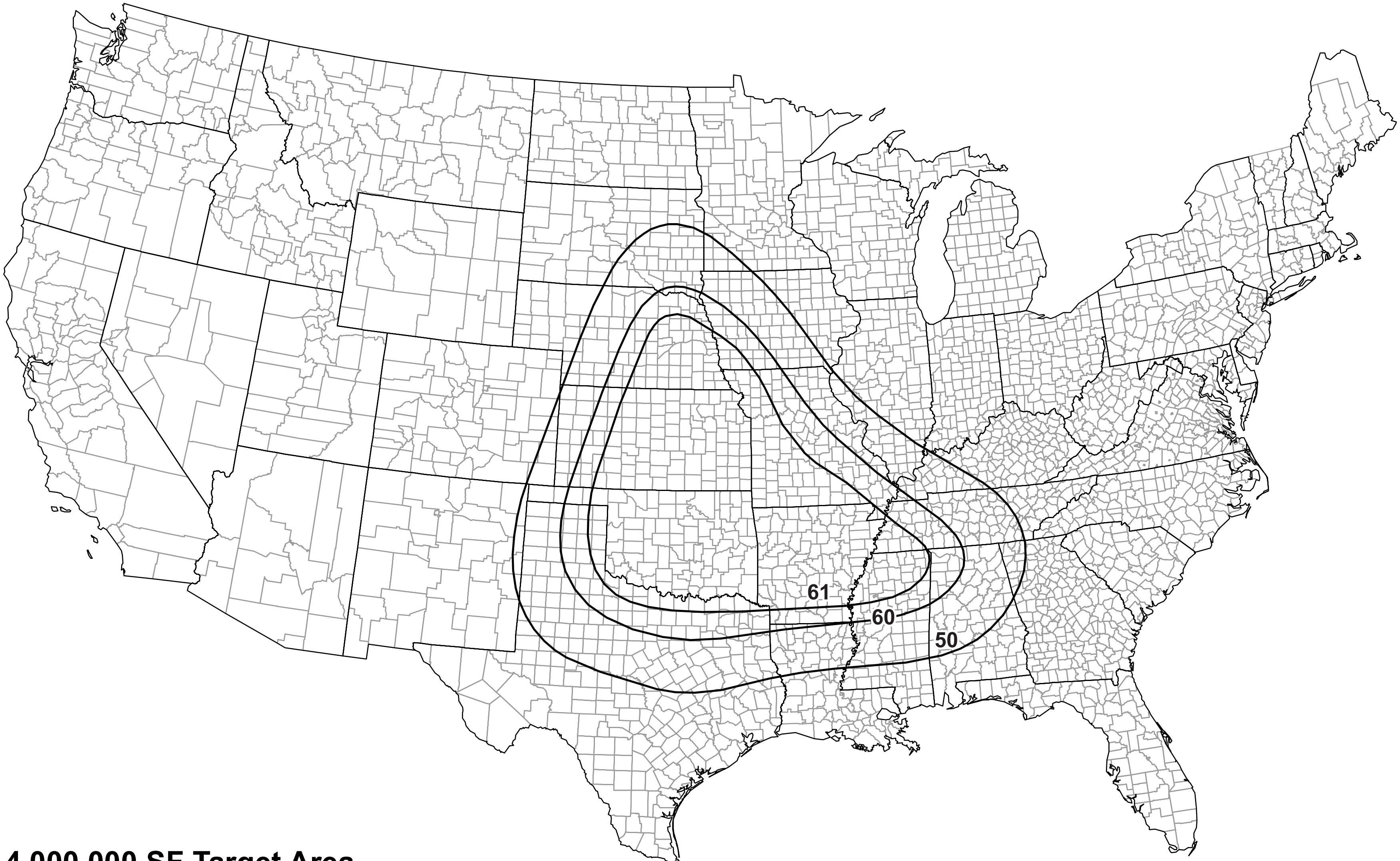

4,000,000 SF Target Area

Mean Recurrence Interval = 300 Yrs
Annual Exceedance Frequency = 3.3 x 10^{-3}

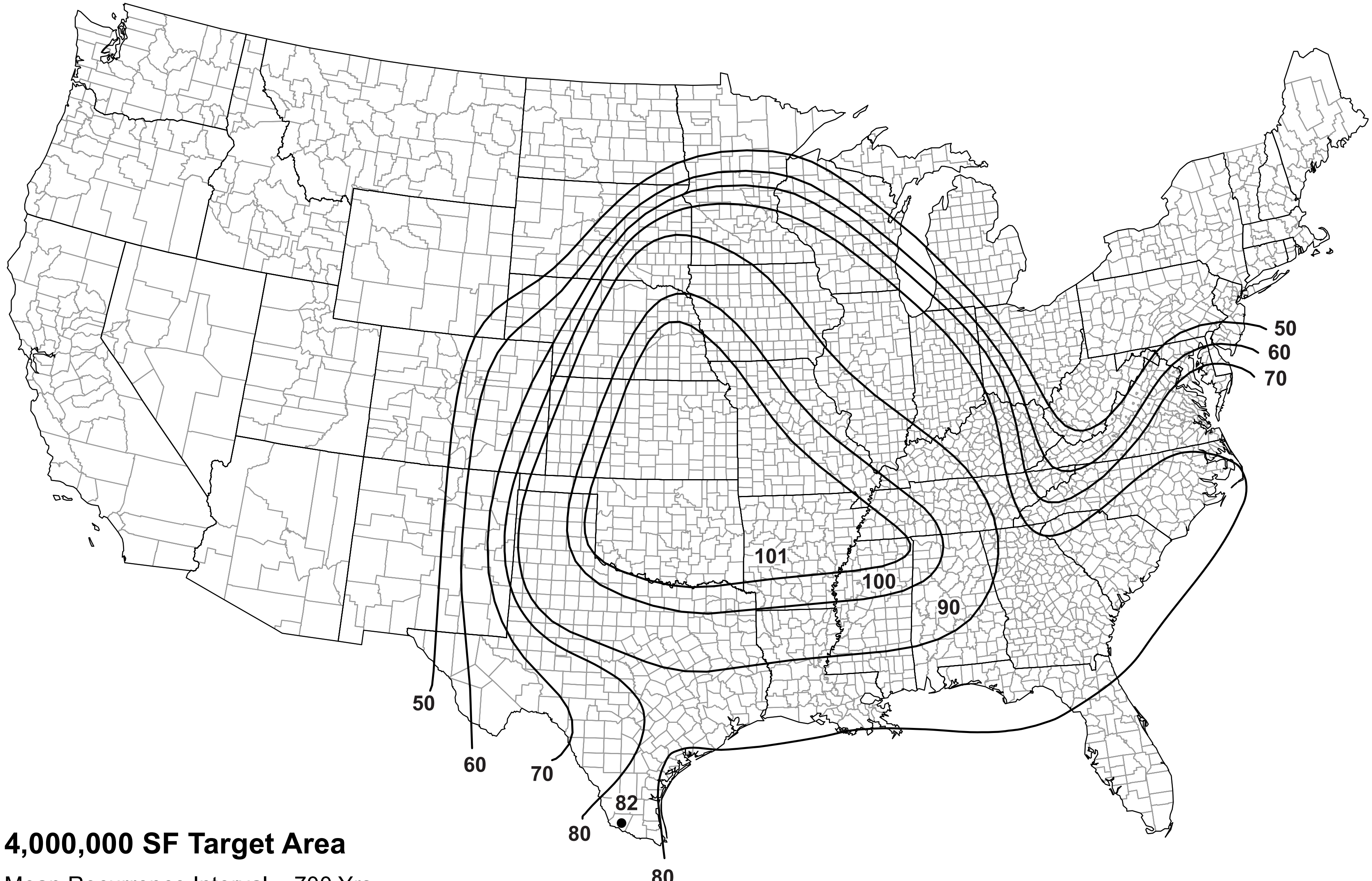

4,000,000 SF Target Area

Mean Recurrence Interval = 700 Yrs
Annual Exceedance Frequency = 1.43×10^{-3}

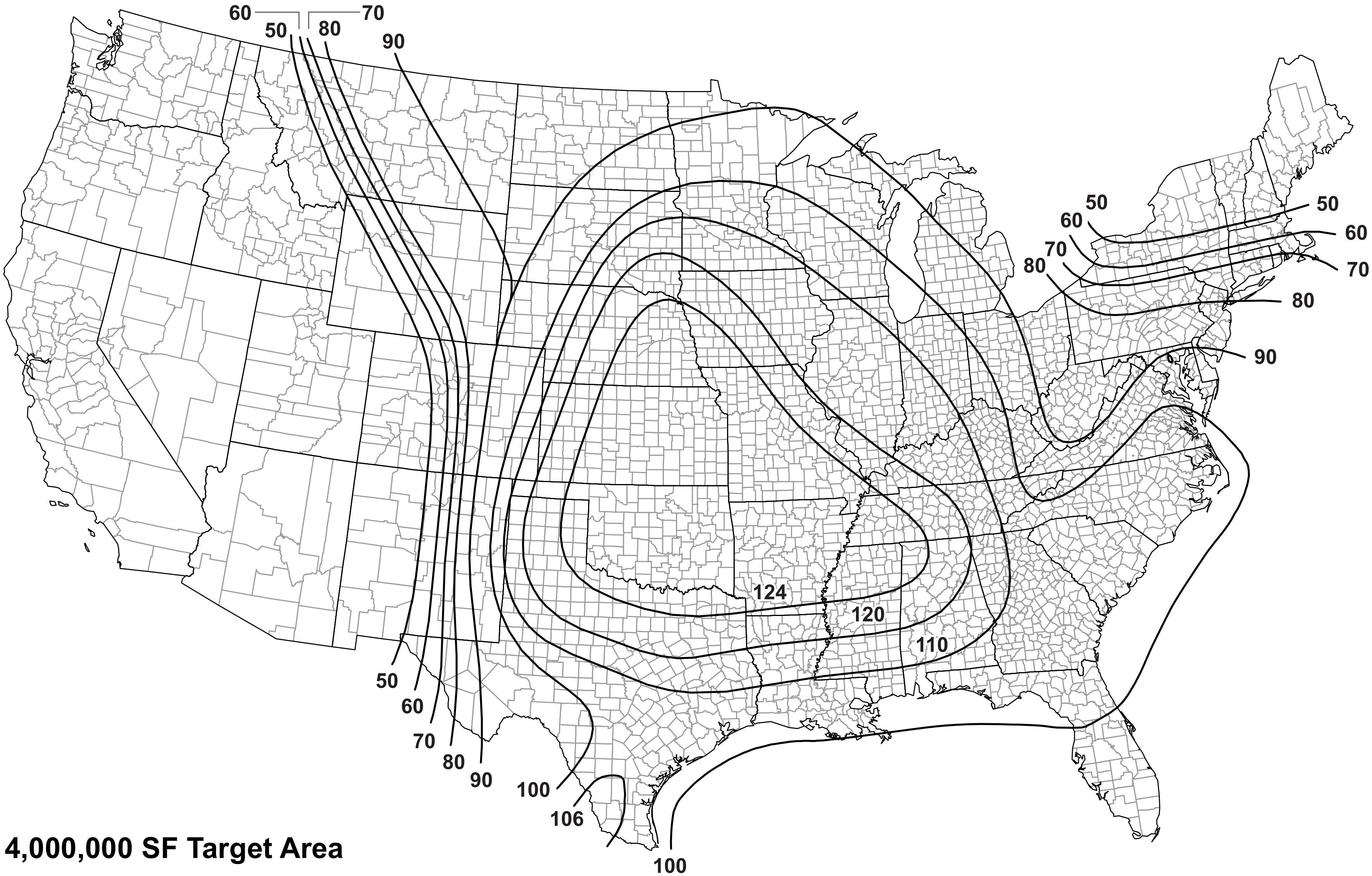

4,000,000 SF Target Area

Mean Recurrence Interval = 1,700 Yrs
Annual Exceedance Frequency = 5.88 x 10^{-4}

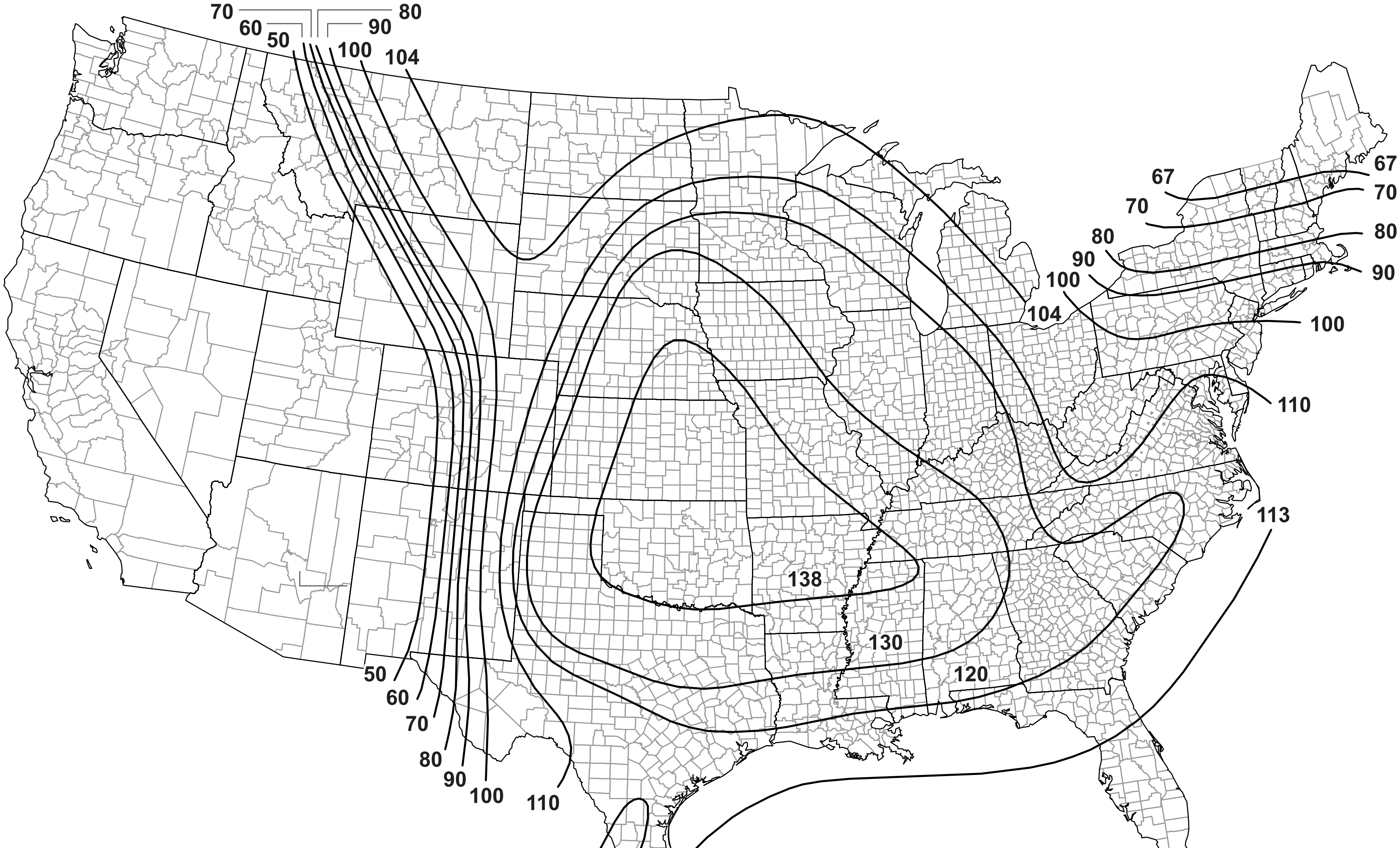

4,000,000 SF Target Area

Mean Recurrence Interval = 3,000 Yrs
Annual Exceedance Frequency = 3.3×10^{-4}

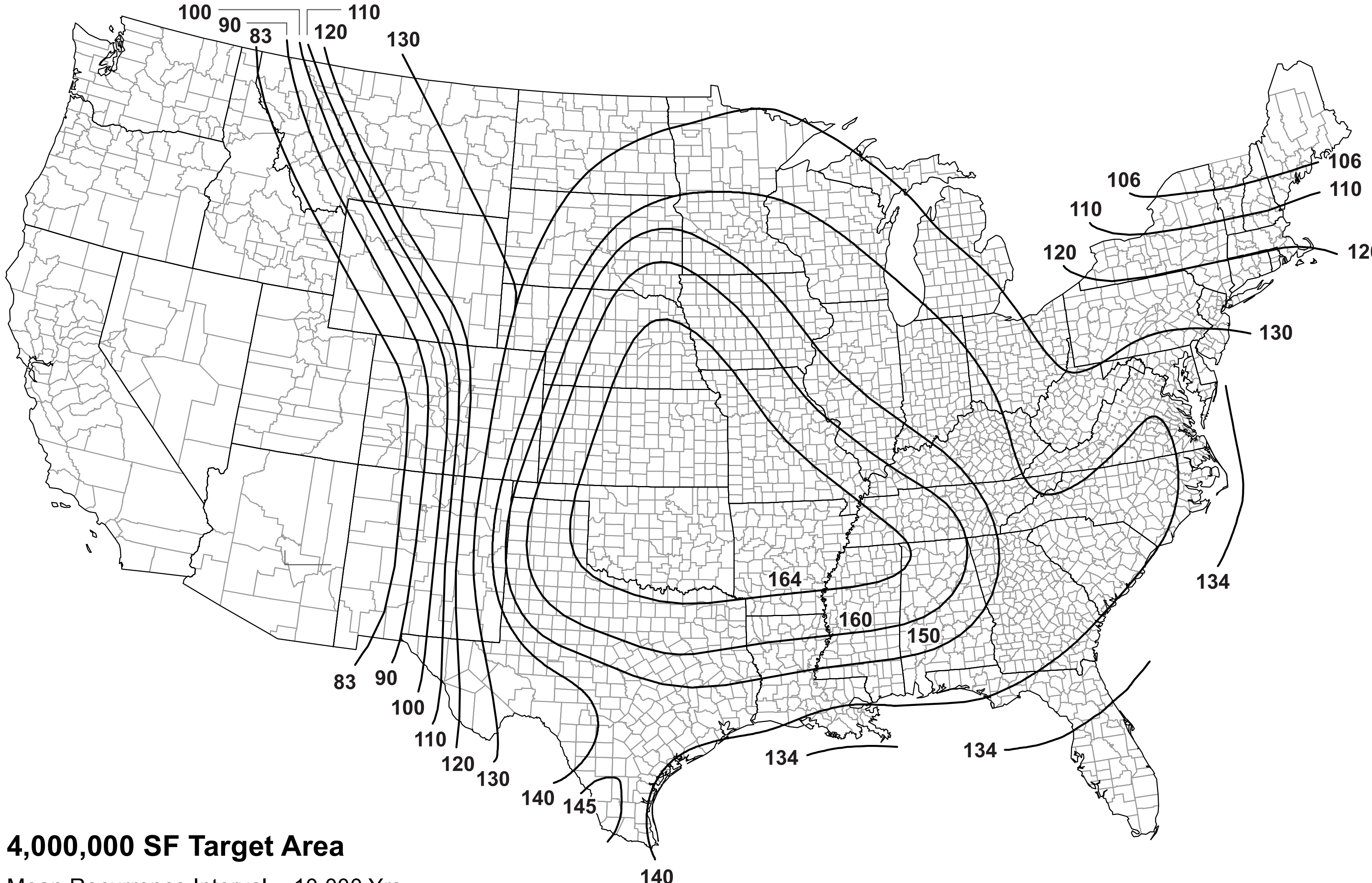

4,000,000 SF Target Area

Mean Recurrence Interval = 10,000 Yrs
Annual Exceedance Frequency = 1 x 10^{-4}

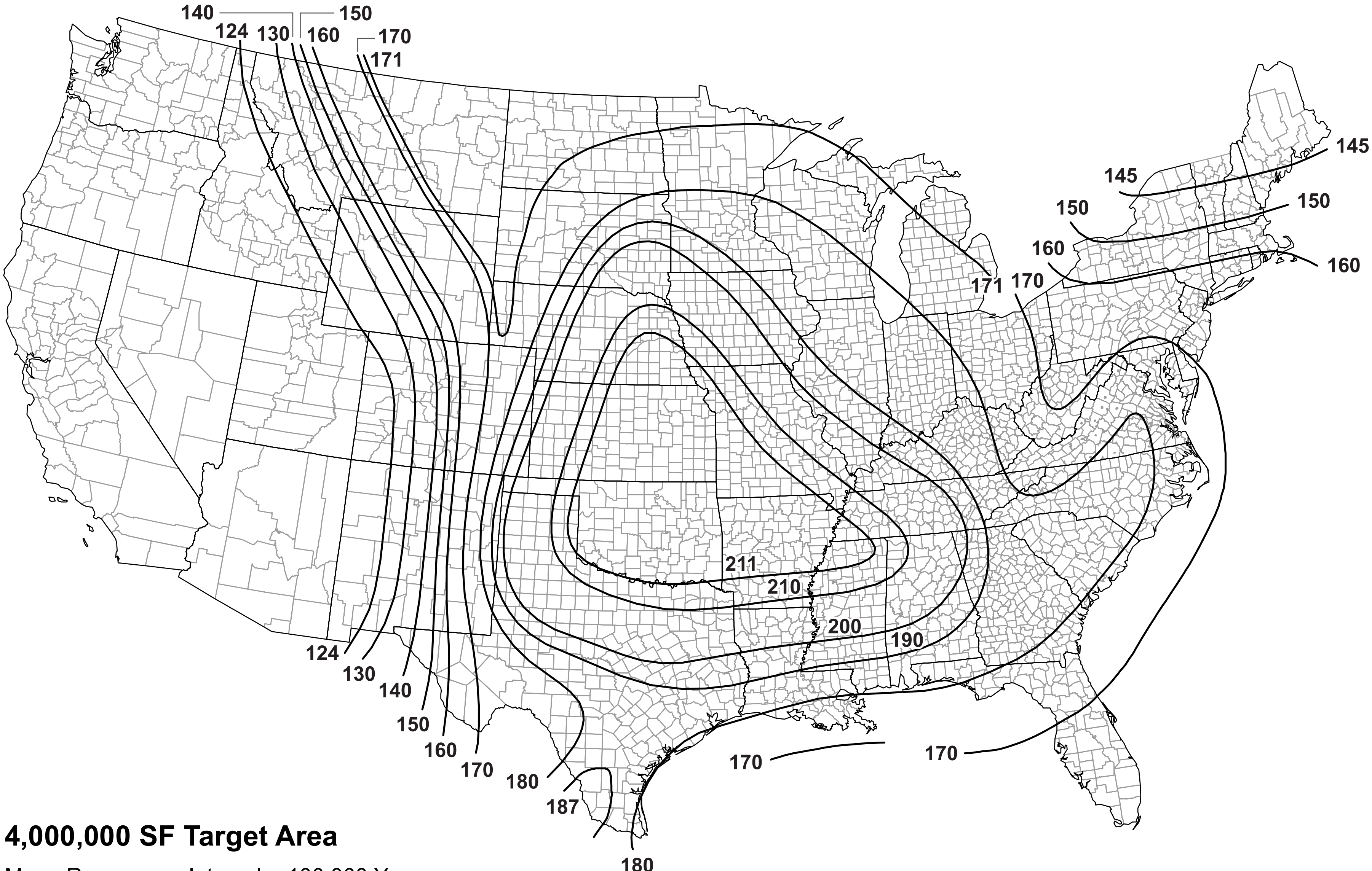

4,000,000 SF Target Area

Mean Recurrence Interval = 100,000 Yrs
Annual Exceedance Frequency = 1 x 10^{-5}

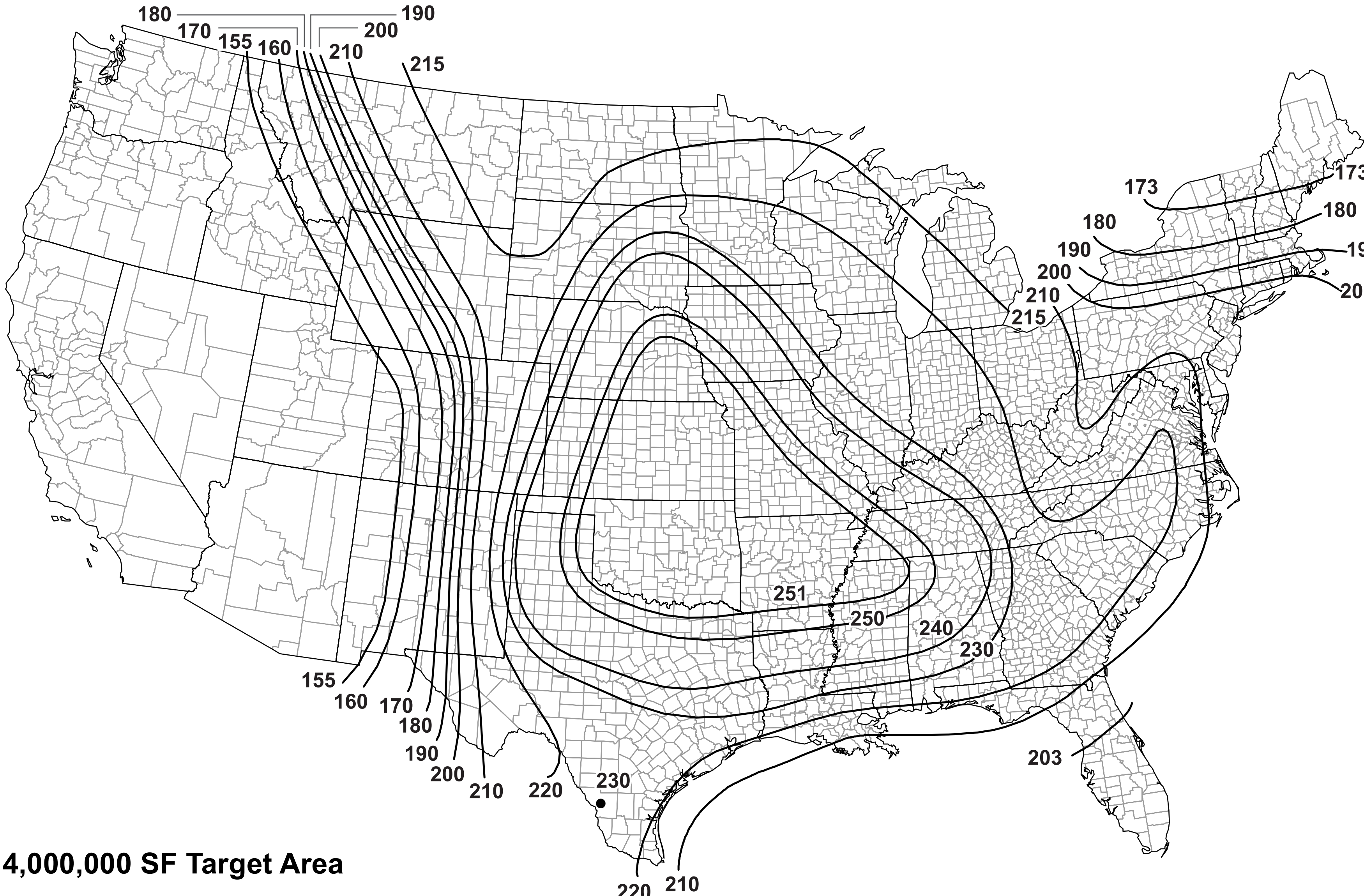

4,000,000 SF Target Area

Mean Recurrence Interval = 1,000,000 Yrs
Annual Exceedance Frequency = 1 x 10^{-6}

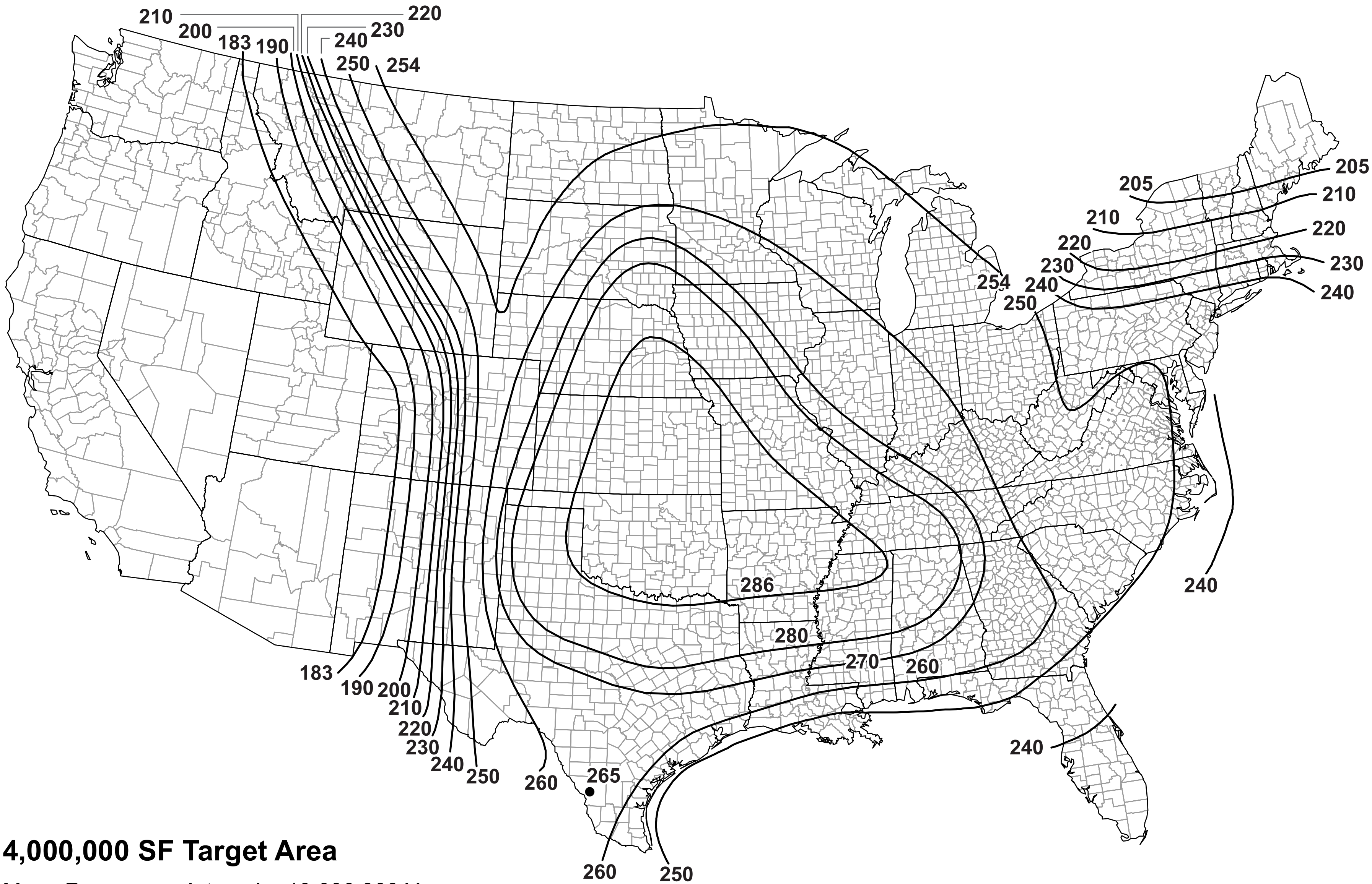

4,000,000 SF Target Area

Mean Recurrence Interval = 10,000,000 Yrs
Annual Exceedance Frequency = 1 x 10^{-7}